

# Laser Surface Engineering

Processes and Applications

Edited by J. Lawrence and D. G. Waugh

# **Laser Surface Engineering**

## **Related titles**

*Lasers for medical applications*  
(ISBN 978-0-85709-237-3)

*Handbook of solid-state lasers*  
(ISBN 978-0-85709-272-4)

*Semiconductor lasers*  
(ISBN 978-0-85709-640-1)

**Woodhead Publishing Series in Electronic and  
Optical Materials: Number 65**

# **Laser Surface Engineering**

## **Processes and Applications**

*Edited by*

***J. Lawrence and D. G. Waugh***



AMSTERDAM • BOSTON • CAMBRIDGE • HEIDELBERG  
LONDON • NEW YORK • OXFORD • PARIS • SAN DIEGO  
SAN FRANCISCO • SINGAPORE • SYDNEY • TOKYO  
Woodhead Publishing is an imprint of Elsevier



Woodhead Publishing is an imprint of Elsevier  
80 High Street, Sawston, Cambridge, CB22 3HJ, UK  
225 Wyman Street, Waltham, MA 02451, USA  
Langford Lane, Kidlington, OX5 1GB, UK

Copyright © 2015 Elsevier Ltd. All rights reserved.

No part of this publication may be reproduced, stored in a retrieval system or transmitted in any form or by any means electronic, mechanical, photocopying, recording or otherwise without the prior written permission of the publisher.

Permissions may be sought directly from Elsevier's Science & Technology Rights Department in Oxford, UK: phone (+44) (0) 1865 843830; fax (+44) (0) 1865 853333; email: [permissions@elsevier.com](mailto:permissions@elsevier.com). Alternatively you can submit your request online by visiting the Elsevier website at <http://elsevier.com/locate/permissions>, and selecting Obtaining permission to use Elsevier material.

#### Notice

No responsibility is assumed by the publisher for any injury and/or damage to persons or property as a matter of products liability, negligence or otherwise, or from any use or operation of any methods, products, instructions or ideas contained in the material herein. Because of rapid advances in the medical sciences, in particular, independent verification of diagnoses and drug dosages should be made.

#### British Library Cataloguing-in-Publication Data

A catalogue record for this book is available from the British Library

#### Library of Congress Control Number: 2014940214

ISBN 978-1-78242-074-3 (print)

ISBN 978-1-78242-079-8 (online)

For information on all Woodhead Publishing publications  
visit our website at <http://store.elsevier.com/>

Typeset by SPi Global

[www.spi-global.com](http://www.spi-global.com)

Printed and bound in the United Kingdom



Working together  
to grow libraries in  
developing countries

[www.elsevier.com](http://www.elsevier.com) • [www.bookaid.org](http://www.bookaid.org)

# Contents

<b>List of contributors</b>	xiii
<b>Woodhead Publishing Series in Electronic and Optical Materials</b>	xvii
<b>Preface</b>	xxiii
<b>Part One Thermal surface treatments using lasers</b>	<b>1</b>
<b>1 Structures, properties and development trends of laser-surface-treated hot-work steels, light metal alloys and polycrystalline silicon</b>	<b>3</b>
<i>L.A. Dobrzański, T. Tański, A.D. Dobrzańska-Danikiewicz, E. Jonda, M. Bonek, A. Drygała</i>	
1.1 Introduction	3
1.2 Laser treatment of hot-work alloy tool steels	4
1.3 Laser treatment of light metal casting alloys	11
1.4 Texturization of polycrystalline silicon for the purpose of photovoltaics	15
1.5 Development trends of selected laser-treated engineering materials determined using new computer-integrated prediction methodology	21
1.6 Conclusion	27
1.7 Comments	30
References	30
<b>2 Laser nitriding and carburization of materials</b>	<b>33</b>
<i>D. Höche, J. Kaspar, P. Schaaf</i>	
2.1 Introduction	33
2.2 Overview on surface alloying of materials by laser irradiation	34
2.3 Laser nitriding of titanium	37
2.4 Laser carburization of materials	44
2.5 Future trends	50
2.6 Sources of further information and advice	51
Acknowledgment	51
References	51
<b>3 Mechanical properties improvement of metallic rolls by laser surface alloying</b>	<b>59</b>
<i>G. Sun, R. Zhou</i>	
3.1 Introduction	59
3.2 Mechanical properties improvement of metallic rolls by laser surface alloying: experimental procedures	60

---

3.3	Laser surface alloying of C-B-W-Cr nano-powders on nodular cast-iron rolls (NCIR)	62
3.4	Laser surface alloying of NiCr-Cr <sub>3</sub> C <sub>2</sub> powders on semisteel rolls	72
3.5	Laser surface alloying of NiCr-Cr <sub>3</sub> C <sub>2</sub> powders on cast steel rolls	80
3.6	Wear behavior of the three kinds of alloyed layers and three roll substrates	89
3.7	Conclusions	91
	References	92
<b>4</b>	<b>Laser surface treatment of AISI 304 steel with the presence of B<sub>4</sub>C particles at the surface</b>	<b>97</b>
	<i>B.S. Yilbas, F. Patel, C. Karatas</i>	
4.1	Introduction	97
4.2	Experimental producers	98
4.3	Results and discussion	99
4.4	Conclusion	104
	Acknowledgment	104
	References	105
<b>5</b>	<b>Characterization and modification of technical ceramics through laser surface engineering</b>	<b>107</b>
	<i>P. Shukla, J. Lawrence</i>	
5.1	Introduction	107
5.2	Background of laser surface treatment of technical ceramics	108
5.3	Materials and experimental procedures	109
5.4	Establishment of laser processing parameters and associated issues	111
5.5	Modifications of Si <sub>3</sub> N <sub>4</sub> and ZrO <sub>2</sub> technical ceramics through laser surface treatment	112
5.6	Compositional changes	119
5.7	Microstructural modifications	122
5.8	Fracture toughness ( $K_{1C}$ ) modifications	128
5.9	Temperature distribution and phase transition	129
5.10	Conclusions	131
	References	132
<b>Part Two</b>	<b>Laser additive manufacturing in surface treatment and engineering</b>	<b>135</b>
<b>6</b>	<b>Compositional modification of Ni-base alloys for laser-deposition technologies</b>	<b>137</b>
	<i>I. Hemmati, V. Ocelík, J.Th.M. De Hosson</i>	
6.1	Introduction	137
6.2	Microstructural design to improve toughness	139
6.3	Selection of the refining element	140
6.4	Experimental procedure	142

---

6.5	Microstructures and phases	145
6.6	Analysis of crack growth paths	153
6.7	Microstructural evolutions	156
6.8	The microstructural refinement–cracking relationship	158
6.9	Conclusions	160
	Acknowledgments	160
	References	160
<b>7</b>	<b>New metallic materials development by laser additive manufacturing</b>	<b>163</b>
	<i>Dongdong Gu</i>	
7.1	Introduction	163
7.2	Selective laser melting of TiC/Ti nanocomposites parts with novel nanoscale reinforcement and enhanced wear performance	164
7.3	Development of porous stainless steel with controllable microcellular features using selective laser melting	172
7.4	Conclusion	177
7.5	Future trends	177
	Acknowledgments	178
	References	179
<b>8</b>	<b>Innovations in laser cladding and direct laser metal deposition</b>	<b>181</b>
	<i>C. Leyens, E. Beyer</i>	
8.1	Introduction	181
8.2	Fundamentals of laser cladding and direct laser metal deposition	182
8.3	High precision 2D- and 3D-processing	185
8.4	High productivity processing	187
8.5	Process control	189
8.6	Conclusions and future trends	191
	Acknowledgments	191
	References	191
<b>9</b>	<b>Laser-enhanced electroplating for generating micro/nanoparticles with continuous wave and pulsed Nd-YAG laser interactions</b>	<b>193</b>
	<i>J. Lin, S.-H. Chen</i>	
9.1	Introduction	193
9.2	Experimental setup	196
9.3	Results and discussion	200
9.4	Conclusions	210
	Acknowledgment	210
	References	210
<b>10</b>	<b>Laser hybrid fabrication of tunable micro- and nano-scale surface structures and their functionalization</b>	<b>213</b>
	<i>M. Zhong, T. Huang</i>	
10.1	Introduction	213
10.2	Fabrication of nanoporous copper structures	215
10.3	Fabrication of 3D manganese-based nanoporous structure (3D-Mn-NPS)	220

10.4	Fabrication of micro-nano hierarchical Cu/Cu <sub>2</sub> O structure	223
10.5	Functionalization of tunable micro-nano surface structures	228
10.6	Conclusion	233
	References	234
<b>11</b>	<b>Laser-controlled intermetallics synthesis during surface cladding</b>	<b>237</b>
	<i>I.V. Shishkovsky</i>	
11.1	Introduction	237
11.2	Laser control of self-propagated high-temperature synthesis (SHS) as synergism of the two high-tech processes	238
11.3	Overlapping of laser cladding and SHS processes for the fabrication of the functional graded (FG) iron, nickel, and titanium aluminides in the surface layers	248
11.4	Temperature distribution during the layerwise surface laser remelting of exothermal powder compositions	263
11.5	Theoretical and numerical modelling of selective laser sintering/melting (SLS/M) and SHS hybrid processes	268
11.6	Conclusion	278
	Acknowledgment	282
	References	282
<b>12</b>	<b>Deposition and surface modification of thin solid structures by high-intensity pulsed laser irradiation</b>	<b>287</b>
	<i>A.C. Popescu, M. Ulmeanu, C. Ristoscu, I.N. Mihailescu</i>	
12.1	Introduction	287
12.2	Thin films with patterned surfaces obtained by laser deposition methods	288
12.3	Direct femtosecond laser surface processing in far- and near-field	303
12.4	Resources	307
12.5	Conclusions	308
	Acknowledgments	309
	References	309
<b>Part Three Laser strutting and surface modification</b>		<b>315</b>
<b>13</b>	<b>Tailoring material properties induced by laser surface processing</b>	<b>317</b>
	<i>H.Y. Zheng, Y.C. Guan, X.C. Wang, Z.K. Wang</i>	
13.1	Introduction	317
13.2	Laser texturing of silicon for improving surface functionalities	318
13.3	Femtosecond laser interactions with polymethyl methacrylate (PMMA)	333
13.4	Nd:YAG laser melting of magnesium alloy for corrosion resistance and surface wettability improvement	342

---

13.5	Conclusions	351
	Acknowledgments	352
	References	353
<b>14</b>	<b>Femtosecond laser micromachining on optical fiber</b>	<b>359</b>
	<i>D.N. Wang, Y. Wang, C.R. Liao</i>	
14.1	Introduction	359
14.2	Femtosecond laser micromachining of optical fibers	361
14.3	Optical fiber microstructures fabricated by femtosecond laser micromachining	363
14.4	Optical sensing devices based on optical fiber microstructures	367
14.5	Current and future trends	375
	References	378
<b>15</b>	<b>Spatiotemporal manipulation of ultrashort pulses for three-dimensional (3-D) laser processing in glass materials</b>	<b>383</b>
	<i>F. He, J. Ni, B. Zeng, Y. Cheng, K. Sugioka</i>	
15.1	Introduction	383
15.2	Tailoring the focal spot by spatiotemporal manipulation of ultrashort laser pulses	385
15.3	Three-dimensional (3-D) istropic resolutions at low numerical apertures (NAs) using the combination of slit beam shaping and spatiotemporal focusing methods	389
15.4	Visualization of the spatiotemporally focused femtosecond laser beam using two-photon fluorescence excitation	393
15.5	Enhanced femosecond laser filamentation using spatiotemporally focused beams	397
15.6	Conclusion and future trends	400
	Acknowledgment	400
	References	400
	Appendix: derivation of the angular chirp coefficient	403
<b>16</b>	<b>Tribology optimization by laser surface texturing: from bulk materials to surface coatings</b>	<b>405</b>
	<i>Q. Ding, L. Wang, L. Hu</i>	
16.1	Introduction	405
16.2	Laser ablation behaviors of different materials	405
16.3	Tribological application of laser surface texturing (LST) to bulk materials	411
16.4	Tribological application of LST to surface coatings	415
16.5	Conclusion and future trends	418
	Acknowledgments	419
	References	419

<b>17 Fabrication of periodic submicrometer and micrometer arrays using laser interference-based methods</b>	<b>423</b>
<i>A.F. Lasagni, E. Beyer</i>	
17.1 Introduction	423
17.2 Multibeam interference patterns	424
17.3 Laser interference lithography	425
17.4 Direct laser interference patterning	430
17.5 Laser interference patterning systems	436
References	436
<b>18 Ultrashort pulsed laser surface texturing</b>	<b>441</b>
<i>E. Toyserkani, N. Rasti</i>	
18.1 Introduction	441
18.2 Physics of thermal versus nonthermal ultrashort pulsed laser surface texturing	441
18.3 Nanosecond pulsed surface texturing	447
18.4 Picosecond pulsed surface texturing	448
18.5 Femtosecond pulsed laser surface texturing	450
18.6 Attosecond pulsed laser surface texturing: would it reasonably be applicable to surface modifications?	450
18.7 Conclusion	451
References	451
<b>19 Laser-guided discharge surface texturing</b>	<b>455</b>
<i>Z.-T. Wang, M.-J. Yang</i>	
19.1 Introduction	455
19.2 Mechanisms of laser-guided discharge texturing (LGDT)	456
19.3 Experiments of LGDT	458
19.4 Comparison with Nd:YAG laser-textured surfacing (YAGLT) and electrical discharge surfacing (EDT)	465
19.5 Conclusions	465
References	466
<b>20 Laser surface treatment to improve the surface corrosion properties of nickel-aluminum bronze</b>	<b>469</b>
<i>R. Cottam, M. Brandt</i>	
20.1 Introduction	469
20.2 Solid-state laser treatment and development of laser-processing parameters	470
20.3 Experimental procedure	474
20.4 Characterization of laser-processed microstructure	475
20.5 Corrosion performance	478
20.6 Conclusion	479
Acknowledgments	480
References	481

---

<b>21</b>	<b>Laser surface engineering of titanium and its alloys for improved wear, corrosion and high-temperature oxidation resistance</b>	<b>483</b>
<i>J. Dutta Majumdar, I. Manna</i>		
21.1	Introduction	483
21.2	Titanium and its alloys	484
21.3	Physical metallurgy of titanium and its alloys	485
21.4	Alloy classification	486
21.5	Surface dependent engineering properties	487
21.6	Surface engineering	489
21.7	Laser surface engineering	489
21.8	Laser surface engineering of titanium and its alloys	493
21.9	Conclusion and future trends	519
	References	520
<b>22</b>	<b>Laser-initiated ablation of materials</b>	<b>523</b>
<i>C. Dowding, A. Borman</i>		
22.1	Introduction	523
22.2	Mechanisms involved in ablation	524
22.3	Demagnified image ablation machining using excimer laser beams	527
22.4	Issues arising from ablation	532
22.5	Possible solutions to such issues	535
22.6	Methods of examining ablation mechanisms	539
22.7	Conclusion	542
	References	543
<b>Part Four Chemical and biological applications of laser surface engineering</b>		<b>547</b>
<b>23</b>	<b>Luminescence spectroscopy as versatile probes for chemical diagnostics on the solid–liquid interface</b>	<b>549</b>
<i>N. Aoyagi, T. Saito</i>		
23.1	Introduction	549
23.2	Chemical analysis of lanthanide and actinide ions by time-resolved laser-induced fluorescence spectroscopy (TRLFS)	551
23.3	Analysis of TRLFS data	553
23.4	Recent progress in chemical analysis of actinides by laser spectroscopy	554
23.5	Recent trends in chemical analysis of actinides by laser spectroscopy	559
23.6	Future trends in laser spectroscopy	562
	References	562
<b>24</b>	<b>Ablation effects of femtosecond laser functionalization on surfaces</b>	<b>565</b>
<i>B. Raillard, F. Mücklich</i>		
24.1	Introduction	565
24.2	Laser techniques and materials	565

24.3	Topographical effects	566
24.4	Chemical and microstructural effects	572
24.5	Potential applications	576
24.6	Conclusions	579
	References	579
<b>25</b>	<b>Laser surface engineering in dentistry</b>	<b>583</b>
	<i>R.S. Oliveira, J.T. Pereira, C.M. Assunção, S.B. Werle, J.A. Rodrigues</i>	
25.1	Introduction	583
25.2	Effect of lasers on soft tissues	584
25.3	Effect of lasers on hard tissues	590
25.4	Future trends	595
	References	596
<b>26</b>	<b>Laser-assisted fabrication of tissue engineering scaffolds from titanium alloys</b>	<b>603</b>
	<i>I.V. Shishkovsky</i>	
26.1	Introduction	603
26.2	Influence of the selective laser sintering (SLS)-technique-obtained 3-D porous matrix for tissue engineering on the culture of multipotent mesenchymal stem cells	607
26.3	Preclinical testing of SLS-obtained titan and nitinol implants' biocompatibility and biointegration	623
26.4	Finite-element optimization of SLS-obtained implants' porous structure	637
26.5	The SLS-assisted functional design of porous drug delivery systems based on nitinol	644
26.6	Future remarks	647
	Acknowledgments	649
	References	649
<b>27</b>	<b>Laser melting of NiTi and its effects on <i>in vitro</i> mesenchymal stem cell responses</b>	<b>653</b>
	<i>D.G. Waugh, J. Lawrence, C.W. Chan, I. Hussain, H.C. Man</i>	
27.1	Introduction	653
27.2	Experimental details	657
27.3	Results and discussion	660
27.4	Conclusions	672
	References	673
<b>Index</b>		<b>677</b>

# List of contributors

**N. Aoyagi** Japan Atomic Energy Agency (JAEA), Ibaraki, Japan

**C.M. Assunção** Federal University of Rio Grande do Sul (UFRGS), Porto Alegre, Brazil

**E. Beyer** Fraunhofer Institute for Material and Beam Technology (IWS), Dresden, Germany; Technische Universität Dresden, Dresden, Germany

**M. Bonek** Silesian University of Technology, Gliwice, Poland

**A. Borman** University of Lincoln, Lincoln, UK

**M. Brandt** Defence Materials Technology Centre, Melbourne, VIC, Australia; RMIT University, Melbourne, VIC, Australia

**C.W. Chan** The Hong Kong Polytechnic University, Hong Kong, China

**S.-H. Chen** National Cheng Kung University, Tainan, Taiwan

**Y. Cheng** Chinese Academy of Sciences, Shanghai, China

**R. Cottam** Swinburne University of Technology, Melbourne, VIC, Australia; Defence Materials Technology Centre, Melbourne, VIC, Australia

**Q. Ding** Chinese Academy of Sciences, Shanghai, China

**A.D. Dobrzańska-Danikiewicz** Silesian University of Technology, Gliwice, Poland

**L.A. Dobrzański** Silesian University of Technology, Gliwice, Poland; The Institute of Advanced Manufacturing Technology, Cracow, Poland

**C. Dowding** University of Lincoln, Lincoln, UK

**A. Drygała** Silesian University of Technology, Gliwice, Poland

**Dongdong Gu** Nanjing University of Aeronautics and Astronautics (NUAA), Nanjing, PR China

**Y.C. Guan** Singapore Institute of Manufacturing Technology, Singapore; Beihang University (formerly Beijing University of Aeronautics and Astronautics), Beijing, PR China

**F. He** Chinese Academy of Sciences, Shanghai, China

**I. Hemmati** University of Groningen, Groningen, The Netherlands

**J.Th.M. De Hosson** University of Groningen, Groningen, The Netherlands

**D. Höche** Helmholtz-Zentrum Geesthacht, Geesthacht, Germany

**L. Hu** Chinese Academy of Sciences, Shanghai, China

**T. Huang** Tsinghua University, Beijing, China

**I. Hussain** University of Lincoln, Lincoln, UK

**E. Jonda** Silesian University of Technology, Gliwice, Poland

**C. Karatas** Hacettepe University, Ankara, Turkey

**J. Kaspar** Fraunhofer Institute for Material and Beam Technology—IWS, Dresden, Germany

**A.F. Lasagni** Fraunhofer Institute for Material and Beam Technology (IWS), Dresden, Germany; Technische Universität Dresden, Dresden, Germany

**J. Lawrence** University of Chester, Chester, UK

**C. Leyens** Fraunhofer Institute for Material and Beam Technology (IWS), Dresden, Germany; Technische Universität Dresden, Dresden, Germany

**C.R. Liao** The Hong Kong Polytechnic University, Hong Kong, China; Shenzhen University, Shenzhen, China

**J. Lin** National Cheng Kung University, Tainan, Taiwan

**J. Dutta Majumdar** Indian Institute of Technology, Kharagpur, India

**H.C. Man** The Hong Kong Polytechnic University, Hong Kong, China

**I. Manna** Indian Institute of Technology, Kharagpur, India

**I.N. Mihailescu** National Institute for Lasers, Plasma and Radiation Physics, Măgurele, Romania

**F. Mücklich** Saarland University, Saarbrücken, Germany

**J. Ni** Chinese Academy of Sciences, Shanghai, China

**V. Ocelík** University of Groningen, Groningen, The Netherlands

**R.S. Oliveira** Federal University of Rio Grande do Sul (UFRGS), Porto Alegre, Brazil

**F. Patel** King Fahd University of Petroleum & Minerals, Dhahran, Saudi Arabia

**J.T. Pereira** Federal University of Rio Grande do Sul (UFRGS), Porto Alegre, Brazil

**A.C. Popescu** National Institute for Lasers, Plasma and Radiation Physics, Măgurele, Romania

**B. Raillard** Saarland University, Saarbrücken, Germany

**N. Rasti** University of Waterloo, Waterloo, ON, Canada

**C. Ristoscu** National Institute for Lasers, Plasma and Radiation Physics, Măgurele, Romania

**J.A. Rodrigues** Federal University of Rio Grande do Sul (UFRGS), Porto Alegre, Brazil

**T. Saito** The University of Tokyo, Tokyo, Japan

**P. Schaaf** Technische Universität Ilmenau, Ilmenau, Germany

**I.V. Shishkovsky** Lebedev Physics Institute (LPI) of Russian Academy of Sciences, Samara, Russia; Moscow State Technological University named “STANKIN”, Moscow, Russia

**P. Shukla** University of Chester, Chester, UK

**K. Sugioka** RIKEN Center for Advanced Photonics, Wako, Japan

**G. Sun** Southeast University, Nanjing, China

**T. Tański** Silesian University of Technology, Gliwice, Poland

**E. Toyserkani** University of Waterloo, Waterloo, ON, Canada

**M. Ulmeanu** National Institute for Lasers, Plasma and Radiation Physics, Măgurele, Romania

**D.N. Wang** China Jiliang University, Hangzhou, China; The Hong Kong Polytechnic University, Hong Kong, China; Hubei Polytechnic University, Huangshi, China

**L. Wang** Chinese Academy of Sciences, Shanghai, China

**X.C. Wang** Singapore Institute of Manufacturing Technology, Singapore

**Y. Wang** The Hong Kong Polytechnic University, Hong Kong, China;  
Wuhan Institute of Technology, Wuhan, China

**Z.-T. Wang** Chinese Academy of Sciences, Shanghai, China

**Z.K. Wang** Singapore Institute of Manufacturing Technology, Singapore

**D.G. Waugh** University of Chester, Chester, UK

**S.B. Werle** Federal University of Rio Grande do Sul (UFRGS), Porto Alegre, Brazil

**M.-J. Yang** Chinese Academy of Sciences, Shanghai, China

**B.S. Yilbas** King Fahd University of Petroleum & Minerals, Dhahran, Saudi Arabia

**B. Zeng** Chinese Academy of Sciences, Shanghai, China

**H.Y. Zheng** Singapore Institute of Manufacturing Technology, Singapore

**M. Zhong** Tsinghua University, Beijing, China

**R. Zhou** Jiangsu University of Science and Technology, Zhenjiang, China

# Woodhead Publishing Series in Electronic and Optical Materials

- 1 **Circuit analysis**  
*J. E. Whitehouse*
- 2 **Signal processing in electronic communications: For engineers and mathematicians**  
*M. J. Chapman, D. P. Goodall and N. C. Steele*
- 3 **Pattern recognition and image processing**  
*D. Luo*
- 4 **Digital filters and signal processing in electronic engineering: Theory, applications, architecture, code**  
*S. M. Bozic and R. J. Chance*
- 5 **Cable engineering for local area networks**  
*B. J. Elliott*
- 6 **Designing a structured cabling system to ISO 11801: Cross-referenced to European CENELEC and American Standards Second edition**  
*B. J. Elliott*
- 7 **Microscopy techniques for materials science**  
*A. Clarke and C. Eberhardt*
- 8 **Materials for energy conversion devices**  
*Edited by C. C. Sorrell, J. Nowotny and S. Sugihara*
- 9 **Digital image processing: Mathematical and computational methods**  
*Second edition*  
*J. M. Blackledge*
- 10 **Nanolithography and patterning techniques in microelectronics**  
*Edited by D. Bucknall*
- 11 **Digital signal processing: Mathematical and computational methods, software development and applications**  
*Second edition*  
*J. M. Blackledge*
- 12 **Handbook of advanced dielectric, piezoelectric and ferroelectric materials: Synthesis, properties and applications**  
*Edited by Z.-G. Ye*
- 13 **Materials for fuel cells**  
*Edited by M. Gasik*
- 14 **Solid-state hydrogen storage: Materials and chemistry**  
*Edited by G. Walker*
- 15 **Laser cooling of solids**  
*S. V. Petrushkin and V. V. Samartsev*
- 16 **Polymer electrolytes: Fundamentals and applications**  
*Edited by C. A. C. Sequeira and D. A. F. Santos*
- 17 **Advanced piezoelectric materials: Science and technology**  
*Edited by K. Uchino*
- 18 **Optical switches: Materials and design**  
*Edited by S. J. Chua and B. Li*

- 19 **Advanced adhesives in electronics: Materials, properties and applications**  
*Edited by M. O. Alam and C. Bailey*
- 20 **Thin film growth: Physics, materials science and applications**  
*Edited by Z. Cao*
- 21 **Electromigration in thin films and electronic devices: Materials and reliability**  
*Edited by C.-U. Kim*
- 22 **In situ characterization of thin film growth**  
*Edited by G. Koster and G. Rijnders*
- 23 **Silicon-germanium (SiGe) nanostructures: Production, properties and applications in electronics**  
*Edited by Y. Shiraki and N. Usami*
- 24 **High-temperature superconductors**  
*Edited by X. G. Qiu*
- 25 **Introduction to the physics of nanoelectronics**  
*S. G. Tan and M. B. A. Jalil*
- 26 **Printed films: Materials science and applications in sensors, electronics and photonics**  
*Edited by M. Prudenziali and J. Hormadaly*
- 27 **Laser growth and processing of photonic devices**  
*Edited by N. A. Vainos*
- 28 **Quantum optics with semiconductor nanostructures**  
*Edited by F. Jahnke*
- 29 **Ultrasonic transducers: Materials and design for sensors, actuators and medical applications**  
*Edited by K. Nakamura*
- 30 **Waste electrical and electronic equipment (WEEE) handbook**  
*Edited by V. Goodship and A. Stevels*
- 31 **Applications of ATILA FEM software to smart materials: Case studies in designing devices**  
*Edited by K. Uchino and J.-C. Debus*
- 32 **MEMS for automotive and aerospace applications**  
*Edited by M. Kraft and N. M. White*
- 33 **Semiconductor lasers: Fundamentals and applications**  
*Edited by A. Baranov and E. Tournie*
- 34 **Handbook of terahertz technology for imaging, sensing and communications**  
*Edited by D. Saeedka*
- 35 **Handbook of solid-state lasers: Materials, systems and applications**  
*Edited by B. Denker and E. Shklovsky*
- 36 **Organic light-emitting diodes (OLEDs): Materials, devices and applications** *Edited by A. Buckley*
- 37 **Lasers for medical applications: Diagnostics, therapy and surgery**  
*Edited by H. Jelínková*
- 38 **Semiconductor gas sensors**  
*Edited by R. Jaaniso and O. K. Tan*
- 39 **Handbook of organic materials for optical and (opto)electronic devices: Properties and applications**  
*Edited by O. Ostroverkhova*
- 40 **Metallic films for electronic, optical and magnetic applications: Structure, processing and properties**  
*Edited by K. Barmak and K. Coffey*
- 41 **Handbook of laser welding technologies**  
*Edited by S. Katayama*
- 42 **Nanolithography: The art of fabricating nanoelectronic and nanophotonic devices and systems**  
*Edited by M. Feldman*
- 43 **Laser spectroscopy for sensing: Fundamentals, techniques and applications**  
*Edited by M. Baudelet*
- 44 **Chalcogenide glasses: Preparation, properties and applications**  
*Edited by J.-L. Adam and X. Zhang*

- 
- 45 **Handbook of MEMS for wireless and mobile applications**  
*Edited by D. Uttamchandani*
- 46 **Subsea optics and imaging**  
*Edited by J. Watson and O. Zielinski*
- 47 **Carbon nanotubes and graphene for photonic applications**  
*Edited by S. Yamashita, Y. Saito and J. H. Choi*
- 48 **Optical biomimetics: Materials and applications**  
*Edited by M. Large*
- 49 **Optical thin films and coatings**  
*Edited by A. Piegari and F. Flory*
- 50 **Computer design of diffractive optics**  
*Edited by V. A. Soifer*
- 51 **Smart sensors and MEMS: Intelligent devices and microsystems for industrial applications**  
*Edited by S. Nihtianov and A. Luque*
- 52 **Fundamentals of femtosecond optics**  
*S. A. Kozlov and V. V. Samartsev*
- 53 **Nanostructured semiconductor oxides for the next generation of electronics and functional devices: Properties and applications**  
*S. Zhuiykov*
- 54 **Nitride semiconductor light-emitting diodes (LEDs): Materials, technologies and applications**  
*Edited by J. J. Huang, H. C. Kuo and S. C. Shen*
- 55 **Sensor technologies for civil infrastructures**  
Volume 1: **Sensing hardware and data collection methods for performance assessment**  
*Edited by M. Wang, J. Lynch and H. Sohn*
- 56 **Sensor technologies for civil infrastructures**  
Volume 2: **Applications in structural health monitoring**  
*Edited by M. Wang, J. Lynch and H. Sohn*
- 57 **Graphene: Properties, preparation, characterisation and devices**  
*Edited by V. Skákalová and A. B. Kaiser*
- 58 **Silicon-on-insulator (SOI) technology**  
*Edited by O. Kononchuk and B.-Y. Nguyen*
- 59 **Biological identification: DNA amplification and sequencing, optical sensing, lab-on-chip and portable systems**  
*Edited by R. P. Schaudies*
- 60 **High performance silicon imaging: Fundamentals and applications of CMOS and CCD sensors**  
*Edited by D. Durini*
- 61 **Nanosensors for chemical and biological applications: Sensing with nanotubes, nanowires and nanoparticles**  
*Edited by K. C. Honeychurch*
- 62 **Composite magnetoelectrics: Materials, structures, and applications**  
*G. Srinivasan, S. Priya and N. Sun*
- 63 **Quantum information processing with diamond: Principles and applications** *Edited by S. Prawer and I. Aharonovich*
- 64 **Advances in non-volatile memory and storage technology**  
*Edited by Y. Nishi*
- 65 **Laser surface engineering: Processes and applications**  
*Edited by J. Lawrence and D. G. Waugh*
- 66 **Power ultrasonics: A handbook of materials, design and applications of high power ultrasound transducers**  
*Edited by J. A. Gallego-Judréz*
- 67 **Advances in delay-tolerant networks (DTNs): Architecture and enhanced performance**  
*Edited by J. J. P. C. Rodrigues*

- 68 **Handbook of flexible organic electronics: Materials, manufacturing and applications**  
*Edited by S. Logothetidis*
- 69 **Machine-to-machine (M2M) communications: Architecture, performance and applications**  
*Edited by C. Anton-Haro and M. Dohler*
- 70 **Ecological design of smart home networks: Technologies, social impact and sustainability**  
*Edited by N. Saito and D. Menga*
- 71 **Industrial tomography: Systems and applications**  
*Edited by M. Wang*
- 72 **Vehicular communications and networks: Architectures, protocols, operation and deployment**  
*Edited by W. Chen*
- 73 **Modeling, characterization, and production of nanomaterials: Electronics, photonics and energy applications**  
*Edited by V. Tewary and Y. Zhang*
- 74 **Reliability characterisation of electrical and electronic systems**  
*Edited by J. Swiniger*
- 75 **Handbook of industrial wireless sensor networks: Monitoring, control and automation**  
*Edited by R. Budampati S. Kolavennu*
- 76 **Epitaxial growth of complex metal oxides: Techniques, properties and applications**  
*Edited by G. Koster, G. Rijnders and M. Huijben*
- 77 **Semiconductor nanowires: Materials, synthesis, characterization and applications**  
*Edited by J. Arbiol and Q. Xiong*

*To my mum who is a source of real inspiration; and to  
Louise, Ethan, and  
Lydia who make it all worthwhile.*

*J. Lawrence*

*To Emma, my world, whose love and support drives me forward;  
and to my Mum, Dad, Brother and Nana. Thank you for the love,  
support, laughter and memories.*

*D.G. Waugh*

This page intentionally left blank

# Preface

Optical energy and its uses are actually nothing new to us. The temperature of the very planet we inhabit is governed by optical radiation, and most forms of life on it need sunlight to generate vitamins and complex chemicals. Nonetheless, mankind was not able to generate large and controllable quantities of optical energy until the advent of the laser in 1960. It is instructive to consider the parallels between the development of optical energy and electricity. Since its first industrial use in the 1870s, we have seen electricity lead to corollary inventions such as lighting, telephones, large-scale metal production, computers, and small motors. It has totally altered the quality of life around the world, and optical energy is unlikely to have any less of an effect because it is considerably more versatile than electricity as a source of energy.

Half a century after its inception and being termed “A solution looking for a problem,” the laser has most certainly provided the solution to many problems. Rather than simply acting as a replacement energy source for an existing technology or process, lasers have, in most cases, provided unique solutions. This has opened up completely new avenues of research and delivered brand new processes and products.

A prime example is the way in which the laser has become a mainstream tool in surface engineering. This has happened because lasers have an inherent ability for continuous development and flexibility of use, and in many cases lasers offer the only effective means of altering the surface properties of materials. More importantly, on account of these characteristics, lasers will be the driving force that propels the science and technology of surface engineering into new and as yet unknown areas, opening up a whole host of novel uses for materials in both new and existing applications and products.

Engineering a surface to perform a radically different function for the bulk, using the reliable, noncontact method offered by lasers, presents tremendous possibilities, especially when one considers the following statement by Dr. Matts Andersson of Nobel Biocare Inc.: “No more can be done to improve a biomaterial’s performance by working from the surface into the bulk; it is now time to concentrate on the surface to body to start to specify materials that signal to cells.” By way of a small insight, just consider the huge steps forward, or even paradigm shifts, that new, engineered surfaces would bring to diverse fields, such as aerospace and biotechnology, given that the shape of functional surfaces could aid aerodynamic performance or stem cell response and growth.

Professor William Steen, the great pioneer of laser materials processing and advocate of better utilizing optical energy, quite rightly points out that “the real break through will come when universities train engineering graduates in the use of optical energy. Only then will engineers be as fluent with electromagnetic radiation as physicists.” This book is therefore timely because it describes the state-of-the-art

technology in laser surface engineering, as well as the advances that should emerge from the current research around the world. The contributions from internationally renowned researchers working in every corner of the globe have resulted in this comprehensive, yet detailed book on the many varied advances in laser surface engineering.

*J. Lawrence and D.G. Waugh*

## **Part One**

# **Thermal surface treatments using lasers**

This page intentionally left blank

# **Structures, properties and development trends of laser-surface-treated hot-work steels, light metal alloys and polycrystalline silicon**

**1**

L.A. Dobrzański<sup>1,2</sup>, T. Tański<sup>1</sup>, A.D. Dobrzańska-Danikiewicz<sup>1</sup>, E. Jonda<sup>1</sup>,  
M. Boniek<sup>1</sup>, A. Drygata<sup>1</sup>

<sup>1</sup>Silesian University of Technology, Gliwice, Poland; <sup>2</sup>The Institute of Advanced  
Manufacturing Technology, Cracow, Poland

## **1.1 Introduction**

Several examples of application have been chosen for presentation from a broad array of laser surface treatment technologies currently researched into and used in industry and the examples are distinguished by their extensive possibilities for future and current applications, especially in the tooling, automotive, and power industry.

Hot-work tool steels still represent a widely used group of tool materials that are especially interesting for their advantageous quality-to-price relation and very good functional properties. Heat treatment, heat and chemical treatment, and heat and mechanical treatment have been used traditionally to improve their properties. The laser treatment of surface layers of hot-work alloy tool steels, including laser remelting and/or alloying to enhance their functional properties, especially hardness and wear resistance, is an attractive alternative. The remelted zone (RZ) and the heat-affected zone (HAZ) are created as a result of the laser remelting of steels in the surface layer with their thickness increasing proportionally to the power of the laser used for remelting. If steel remelting is carried out without using carbide powders, then a noticeable, yet slight improvement in the properties of the surface layers of the steels examined is seen as compared to their respective properties obtained in conventional heat treatment, depending on the laser beam power used for remelting. If alloying additives such as different kinds of carbide powders, for example, niobium (NbC), tantalum (TaC), titanium (TiC), vanadium (VC), and tungsten (WC), are introduced into the liquid metal pool, a marked improvement of mechanical and functional properties of the examined steels is seen as compared to those undergoing conventional heat treatment as well as laser remelting without using the powders.

The surface laser treatment of light metal alloys, that is, casting magnesium and aluminum alloys, consisting of cladding carbide particles (TiC, WC, VC, SiC) or

oxide particles ( $\text{Al}_2\text{O}_3$ ) into their surface has an advantageous effect on their quality and structure and brings a promising enhancement of mechanical and functional properties of the examined material, especially hardness, and is largely dependent on laser power and a concentration of alloy elements. The laser cladding of carbide and oxide powders influences the fragmentation of the structure within the entire range of laser power, and the varied grain size in the specific zones of the investigated alloys' surface layer. Two zones occur in surface layers: a RZ and a HAZ with their characteristic values (e.g., layer thickness) dependant upon the laser power used and the carbide or oxide powders cladded.

The laser surface treatment of polycrystalline, the crystallization process of which, preceding the production of photovoltaic cells is much faster and cheaper than the crystallization of its monocrystalline form, consists of the texturization of its surface to reduce light reflectivity and ensure reabsorption of a photon already reflected from the surface. Laser texturization involves creating parallel or intersecting grooves on the entire surface of material. The advantage of this technology is that it is contact-free and selective; its drawback is the damages done to the layer in the place where a laser beam operates and in the contiguous area. Therefore, the laser-treated material must next undergo chemical etching to reveal the proper texture in the form of parallel grooves in two directions perpendicular to each other.

All the laser surface treatment technologies mentioned here have very extensive developmental and application prospects, therefore, further scientific and research efforts to develop and improve them are justified. A newly developed methodology of the computer-integrated prediction of materials surface engineering development has thus been employed to make an objective evaluation of the particular technologies; to determine the positive and negative factors conditioning their future development; and to identify the applicable, recommended action strategy. Contextual matrices, road maps, and technology information sheets allowing for the quantitative and qualitative comparisons of the individual technologies according to harmonized materials science and technological and economic criteria are the outcome of the investigations conducted [1–3].

## 1.2 Laser treatment of hot-work alloy tool steels

A primary aim of the laser remelting of material surface layers is to formulate their structure and properties, which takes place in the process of creating a chemically homogenous, fine-crystalline surface layer without changing the chemical composition of the material [4–6]. Alternatively, laser alloying aims to improve the mechanical and functional properties of the material as a result of strengthening its surface layer with alloying elements from the partially dissolved particles of hard phases of carbides, oxides, or nitrides [7,8]. The following are the strengths of laser surface treatment versus other surface engineering methods: short process duration, flexibility and precision of manufacturing operations that can be performed with various materials, starting with the ones that are hard to work with through the soft ones,

ending with brittle materials, and ensuring accuracy and performance of other methods applied up till now [9]. By being able to adjust accurately such process parameters as surface scanning speed and laser beam power, alloying material type and thickness, and/or gas shield, an alloyed layer with the expected properties can be achieved depending on the operating conditions.

The laser surface treatment of hot-work alloy tool steels causes changes to the steel surface structure, as evidenced by observations with the scanning electron microscope (SEM) ([Figures 1.1–1.4](#)). Steel, following remelting and laser alloying, features a dendritic structure in the RZ and is characterized by the occurrence of areas with a highly varied morphology connected with the material solidification process. Heat in the central area of the RZ is evacuated in all directions and the structure thus formed is made of fine equiaxial crystals with a lattice of carbides as shown in some examples of photographs of the central RZ of the surface layer ([Figure 1.1](#)) of the steels analyzed. A clear structure change is seen at the limit of the RZ and HAZ of steel alloyed with carbide powders ([Figure 1.2](#)). Carbide agglomerates used in the laser alloying process exist near the surface in some cases ([Figure 1.3](#)). Structure changes caused

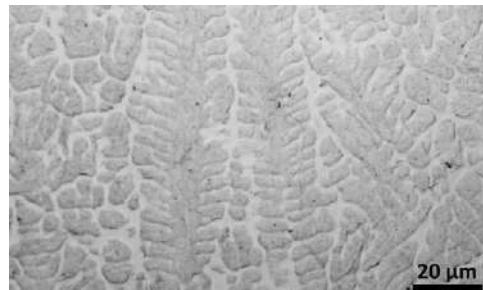


**Figure 1.1** Central zone of remelted surface layer of X40CrMoV5-1 steel after TiC alloying, laser power of 1.2 kW; SEM.

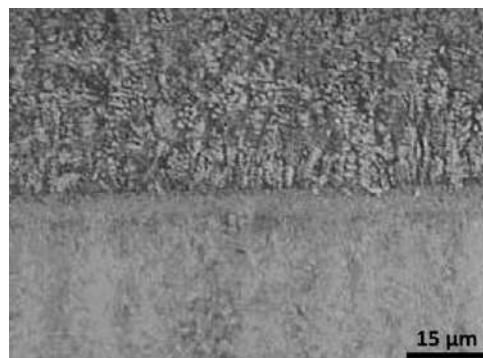


**Figure 1.2** RZ limit of surface layers of X40CrMoV5-1 steel after NbC alloying, laser power of 2.3 kW; SEM.

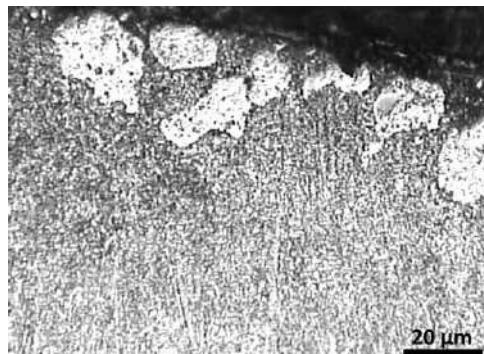


**Figure 1.3** 32CrMoV12-28 steel surface after TaC alloying; laser power of 1.6 kW; SEM.

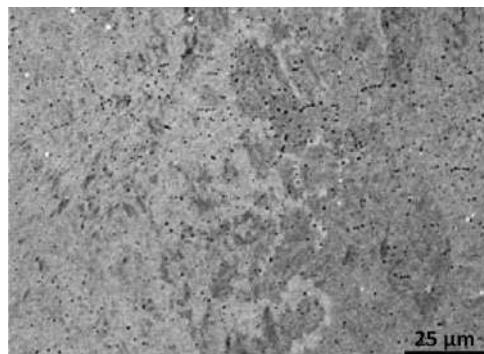


**Figure 1.4** Zone structure of the surface layer of X40CrMoV5-1 steel sample after remelting with laser, the laser beam power of 1.2 kW; SEM.

by laser remelting ([Figure 1.4](#)) are smaller than after alloying the investigated steels using carbide powders.

A number of thorough structure investigations were performed for the various grades of steels comprising, in particular, a linear and point analysis of chemical composition using the scattered X-ray radiation spectroscope; diffraction investigations of thin foil structures in the transmission electron microscope ([Figure 1.5](#)) and microscale investigations; the depth of the RZ and the HAZ, and the width of the bead face [10,11].

The selected mechanical properties, other physical properties, and functional properties of hot-work tool steels subjected to laser remelting and alloying were also examined in the course of the materials science research pursued. Hardness, microhardness, roughness, wear resistance, and thermal fatigue strength were measured. In the majority of cases, laser treatment improves the hardness of the investigated steels, and the hardness of the surface layer alloyed with carbide powders grows significantly with the laser power and depends on the type of carbide powders

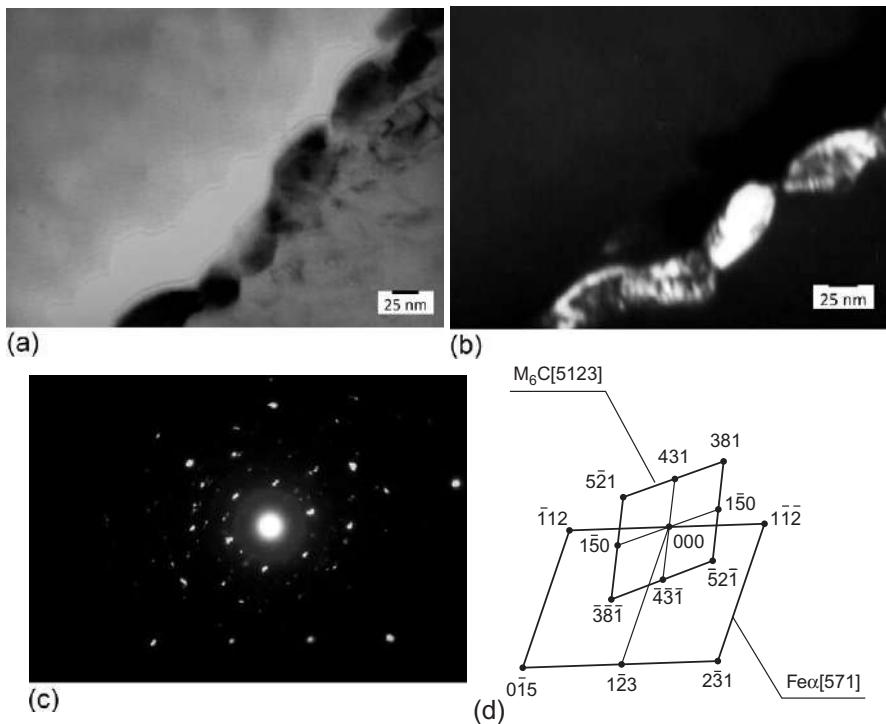


**Figure 1.5** Structure of thin foil made of X40CrMoV5-1 steel after alloying with niobium carbide; laser beam power of 1.3 kW; (a) image in light field, (b) image in dark field from  $(\bar{5}21)$   $M_6C$  reflex, (c) diffraction pattern from the area as in (a), (d) diffraction pattern solution for figure (c); transmission electron microscope.

used in the alloying process. Likewise, the surface roughness of the steels alloyed with carbide powders grows as the power of the laser beam increases within the entire range. Laser remelting and/or alloying using carbide powders usually enhances microhardness at the lateral section of the surface layer according to the distance from the surface of samples (Figure 1.6). As surface layer hardness increases after laser alloying as a consequence of fragmented steel structure, the tribological properties of steel improve (Figure 1.7). Thermal fatigue strength for the steels investigated in the case of the material subjected to laser remelting is only slightly higher than the strength achieved after standard heat treatment, and it grows substantially after alloying with carbide powders.

Variations in the hardness of surface layers achieved by remelting and alloying with carbides using the high power diode laser (HPDL) are accompanied by improved tribological properties as compared to conventional hot-worked steel [12,13]. Differences in the mass loss of specimens after a test of tribological properties after standard hot working in remelted and alloyed steel for various carbides are negligible (Figures 1.8 and 1.9). A loss in specimen mass is dependent upon laser energy for all the tested methods of surface layer modification. A decrease in mass loss in the

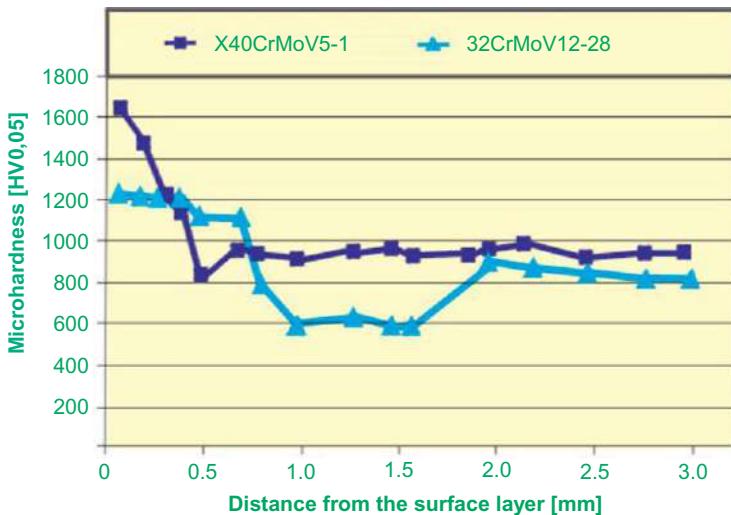


**Figure 1.6** Changes to microhardness of surface layer of 32CrMoV12-28 steel laser alloyed with TaC powder and X40CrMoV5-1 steel NbC-alloyed; the laser power of 1.6 kW.

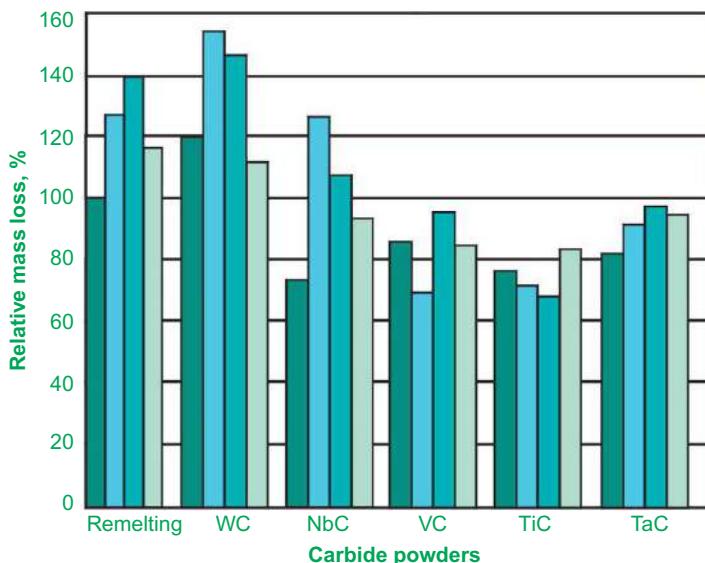


**Figure 1.7** Relative mass loss measured after testing the wear resistance of X40CrMoV5-1 steel remelted and alloyed by laser with carbide powders within the laser power range of, respectively: 1.2, 1.6, 2.0, and 2.3 kW.

material remelted and alloyed with carbides along with growth in laser beam power does not occur. Despite large disparities in outcomes obtained for steel alloyed with tungsten carbide, an increase in mass loss is accompanied by higher laser beam power; the minimum mass loss of 0.41 mg corresponds to the lowest laser beam power of 0.5 kW. For alloyed specimens, mass loss for steel specimens during the test is seen

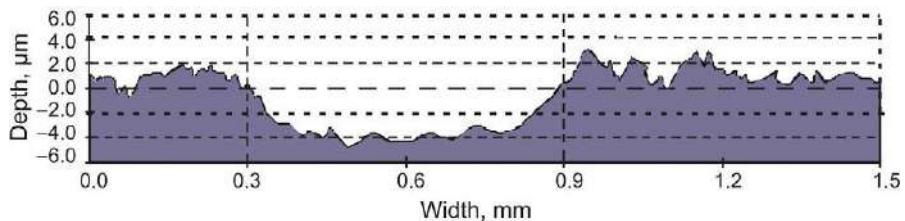


**Figure 1.8** Surface layer wear profile after the pin-on-disc test of X40CrMoV5-1 steel hot worked conventionally.

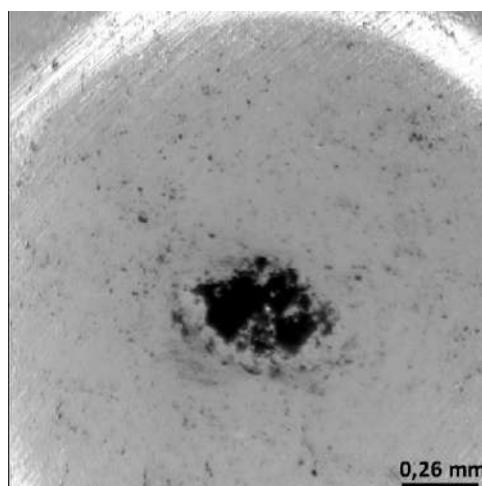


**Figure 1.9** The  $\text{Al}_2\text{O}_3$  counterspecimen wear after 1000 m of friction distance with the surface layer of the steel after the standard heat treatment.

for the entire width, not only due to the wear of the specimens themselves but also due to the intensive wear of the tester ball (Figures 1.10 and 1.11). This broadens the contact surface of the counterspecimen with the steel surface and changes the width and depth of wear on the specimens' surface after a tribological test.

The friction coefficient of surface layers subjected to laser treatment was declining along with heightened steel hardness due to the structure being refined. A friction coefficient for steels alloyed with tungsten carbides is growing as laser power is rising (Figure 1.12). The minimum friction coefficient is  $\mu=0.762$  with the beam power of 0.5 kW. The maximum friction coefficient is  $\mu=0.844$  with the beam power of 1.9 kW.

If laser beam power rises, then the remelted material volume also rises. The volume of the alloying material with specific fraction is mixed and partly dissolved in the growing volume of the remelted steel. As a consequence, wear resistance resulting from tungsten carbide content in the matrix material is falling.

It was revealed in the results of the investigations that if surface layers are fabricated by remelting and alloying with tungsten carbide of X40CrMoV5-1 steel using the HPDL, functional properties are improved as compared to the properties of the conventionally hot-worked steel. In all probability, the layers may determine

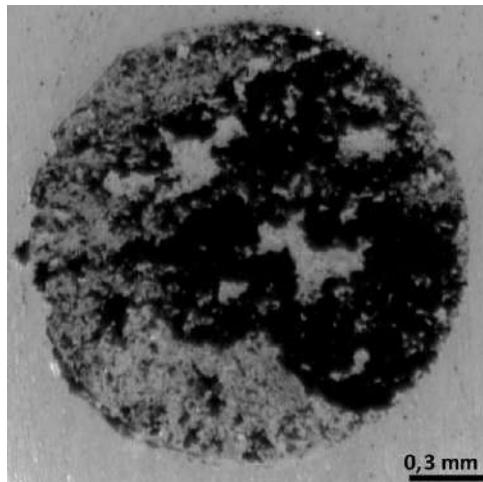


**Figure 1.10** The  $\text{Al}_2\text{O}_3$  counterspecimen wear after 1000 m of friction distance with the surface layer of the steel after alloying with the 0.7 kW laser beam; traverse speed—0.5 m/s, thickness of the coating—0.11 mm.

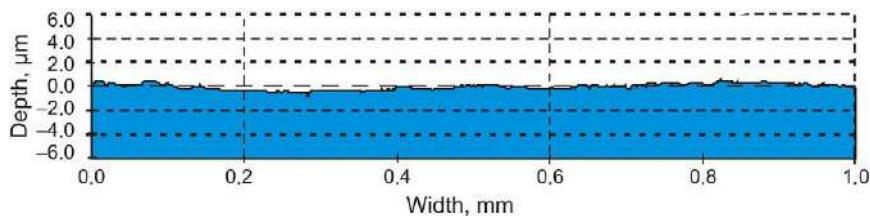


**Figure 1.11** Surface layer wear profile after the pin-on-disc test of X40CrMoV5-1 steel after laser alloying; beam power of 0.7 kW, WC coating thickness of 0.11 mm, and alloying rate of 0.5 m/min.

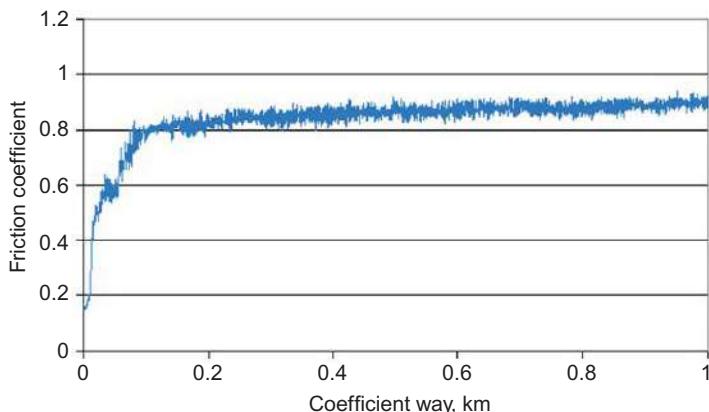


**Figure 1.12** Characteristic of  $\text{Al}_2\text{O}_3$  friction coefficient and of surface layer of X40CrMoV5-1 steel after laser alloying; beam power of 1.7 kW, WC coating thickness of 0.11 mm, and alloying rate of 0.5 m/min.

the enhanced usable properties of tools made of tool steel by additionally improving hardness and abrasive wear resistance. It should be thought that the surface layers so produced may be used for new tools employed mainly for hot plastic working, as well as in other mechanical forming processes, including, in particular, for the cutting of some materials and for regenerating the worn surfaces of working tools made of such steels. This application aspect encourages continued attention to this issue and investigations into the behavior of the examined laser-treated steel in the conditions corresponding to the working conditions of hot-work tools.

Thermal fatigue strength for the steels investigated in the case of the material subjected to laser remelting is only slightly higher than the strength achieved after a standard heat treatment, and it grows substantially after alloying with carbide powders.

Correctly selected conditions of alloying, such as laser power and scanning rate, permit the user to achieve high-quality surface layers that are free of cracks and feature a regular, flat shape of the remelting face. The results achieved for the materials science research reveal that it is reasonable to develop the laser treatment technology of alloy hot-work tool steels and substantiates the technology's development in the future.

### 1.3 Laser treatment of light metal casting alloys

The laser surface treatment of light metal alloys enables the production of a surface layer with a thickness of under a millimeter to several millimeters and with special functional properties: high hardness and wear resistance, while maintaining the properties of the substrate material [14–19]. Laser power and the type of the powder cladded into the surface conditions the structure and properties of the light metal casting alloy's surface layer. The material, following laser treatment made with the HPDL, exhibits different properties from those made with other high-power lasers; especially, it features a more homogenous remelting area and smaller surface roughness [14–19]. The advantages stem from the unique properties of the HPDL, that is, high efficiency of approximately 30–50% (2.0 kW laser consumes 7.5 kW together with a laser cooling system), a very high radiation absorption coefficient, as well as a linear shape of a laser radiation beam. HPDLs are also relatively low-priced, highly durable (over 10,000 h), do not need extra maintenance apart from optic system cleaning, and are easy to use and mobile [14–19].

The structure of the solidified material after laser treatment is characterized by a zonal construction with diversified morphology related to the crystallization of magnesium alloys (Figures 1.13 and 1.14) [14–24]. Multiple changes in crystal growth direction have been observed for these areas. In the area located on the boundary between the solid and liquid phase, minor dendrites occur on the main axes oriented along the heat disposal directions (Figures 1.15 and 1.16) [14,15,19].

The results obtained from the microstructure investigation performed using a SEM (ZEISS Supra 25) with a magnification of up to 500 times reveal the presence of the SiC used (Figure 1.12) and WC ceramic powder (Figure 1.13). For microstructure

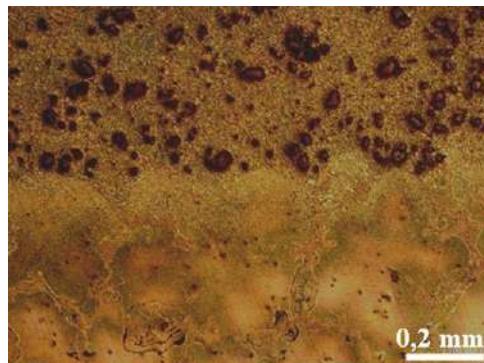


**Figure 1.13** Border between the RZ and the HAZ of the surface layer of MCMgAl12Zn1 alloy after titanium carbide powder cladding, the laser power of 1.6 kW, alloying speed of 0.75 m/min; SEM.

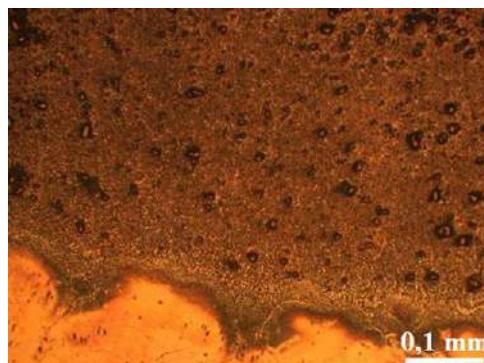


**Figure 1.14** MCMgAl12Zn1 alloy remelting border after cladding TiC powder, laser power of 1.6 kW, alloying speed of 0.75 m/min; SEM.

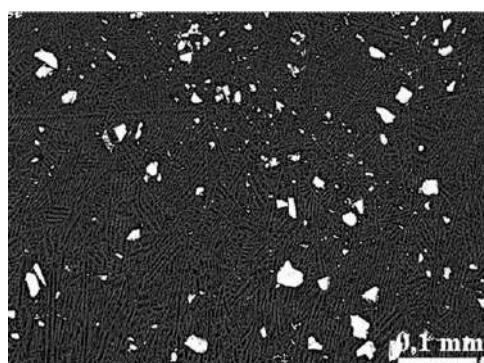


**Figure 1.15** Central zone of the MCMgAl3Zn1 alloy surface layer after cladding with TiC particles; scan rate of 0.75 m/min, laser power of 1.2 kW.

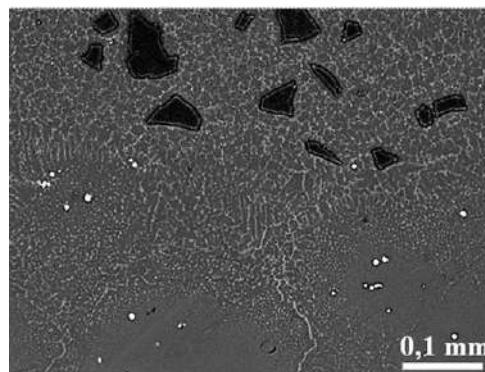


**Figure 1.16** Structure of the interface between the laser-melted zone, HAZ, and the substrate of the MCMgAl9Zn1 alloy after laser treatment with SC particles; scan rate of 0.75 m/min, laser power of 2.0 kW.

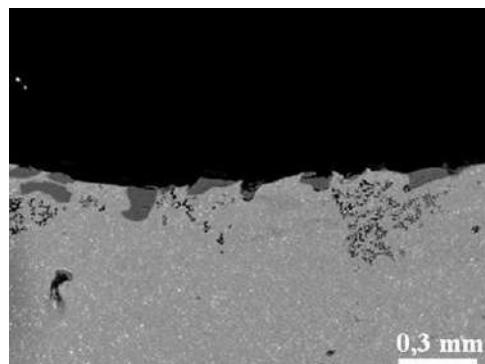


**Figure 1.17** Surface layer of the AlSi9Cu alloy after laser alloying with SiC particles; scan rate of 0.25 m/min, laser power of 2.0 kW, powder feed rate of 8.0 g/min.

evaluation, the backscattered electrons detection method was used, with an accelerating voltage of 20 kV. Based on these investigations, the distribution of the powder particles in the surface layer of the AlSi7Cu and AlSi9Cu aluminum casting alloys was presented. It was also found that in the laser-treated surface layer, there were no pores or cracks in the coating produced, nor did any defects or failures occur in this layer.

Occasionally, discontinuity of the layer can be seen as a product of the heat transfer process and may be neutralized by properly adjusted powder quality and powder feed rate. It is also possible, on the basis of the cross-section micrograph, to evaluate the thickness of the powder feed depth, which is ca. 120 µm in the case of SiC (Figure 1.17) and ca. 1.2 mm in the case of WC powder (Figure 1.18).

In the case of the WC powder, the particles are located mainly on the bottom of the RZ. It was also found that the examined layers consisted of three subzones—the RZ, the heat influence zone, and the substrate material. Further investigations will

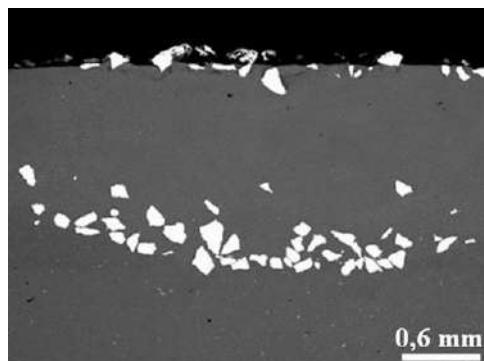


**Figure 1.18** Surface layer of the AlSi7Cu alloy after laser alloying with WC particles; scan rate of 0.25 m/min, laser power of 2.0 kW, powder feed rate of 3.0 g/min.

be needed to reveal the morphology and nature of these zones that occur after alloying with different process parameters and different ceramic powders [14,15].

As a result of the metallographic observations, it was confirmed that the structure of the composite layers produced is free of defects, with distinct grain refinement containing evenly distributed dispersion particles of TiC, WC, SiC carbide, or  $\text{Al}_2\text{O}_3$  oxide applied, which was also confirmed by EDS (Figure 1.19) or electron graphic tests (Figure 1.20).

The alloys with laser-cladded particles of vanadium carbide (their share in the remelting zone being slight) are the exception to the rule. A strong circulation of the liquid metal took place during laser cladding. After the laser bundle remelting, rapid solidification of the initially liquid material took place. The thickness of the laser-formed surface layer is of vital importance in the determination of the material properties, period of use, and final application of the material obtained [14–19].

Three zones occur in the surface layer of cast magnesium alloys: a zone rich with unsolved particles cladded on the surface of magnesium alloys, a RZ, and a HAZ. Both RZ and HAZ (depending on the concentration of aluminum in the magnesium matrix, laser power applied, and ceramic powder) are of different thickness and shape (Figures 1.13–1.18). It was proven that along with the growth of the power applied, the area of occurrence of both RZ and HAZ increased (Figure 1.21), as well as the face of weld changes, which is also confirmed by the reference studies. The MCMgA112Zn1 alloys are characterized with the largest thickness of the surface layer, 3.59 mm, processed with a laser power of 2.0 kW, with silicon carbide cladded into their surface [14,15].

The power of the laser within the range of 1.2–2.0 kW provides the possibility to obtain flat regular remelting welds with a highly smooth surface (Figures 1.22 and 1.23).

An intensive heating of the surface causes the creation of the uneven areas and hollows in the surface layer of the Mg-Al-Zn and Al-Si-Cu cladded using carbide particles. The formation of the melted material in the remelting lake depends on parameters such as the type of substrate, laser power, cladding rate, and the laser powder. Some of the alloy and ceramic parts embedded in the remelting zone are evaporated at

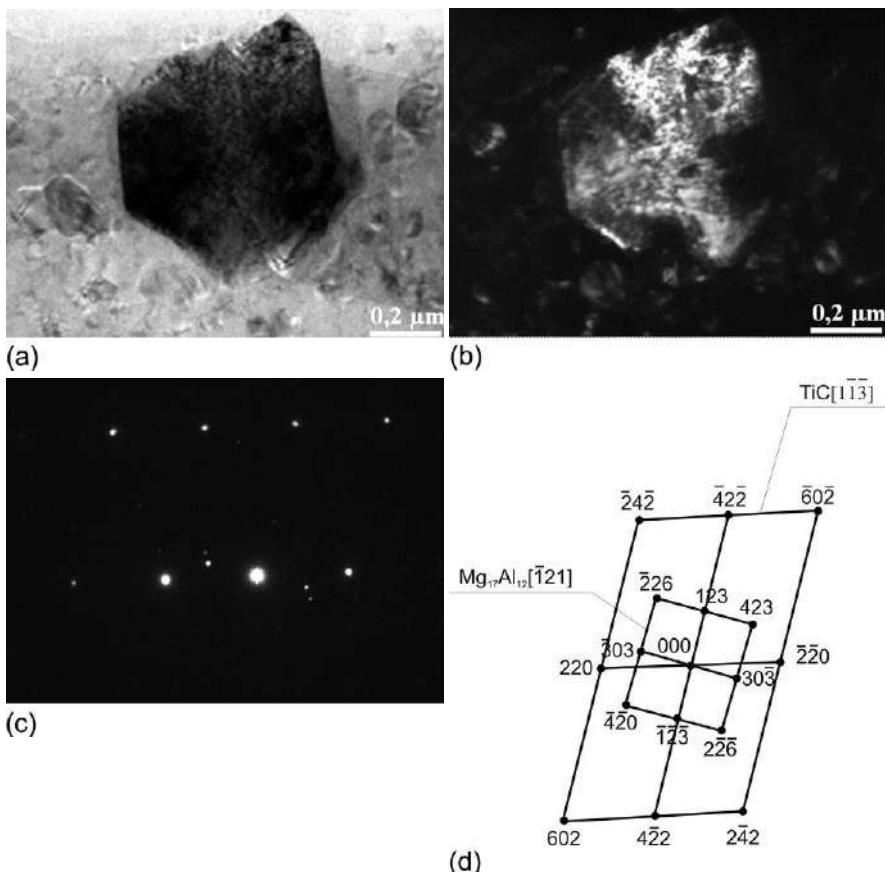


**Figure 1.19** Structure of the thin foil of casting magnesium alloy MCMgAl12Zn1 after laser treatment with TiC (TEM), laser power: 1.6 kW: (a) light field; (b) dark field from the [220] reflex TiC; (c) diffraction pattern from the area as in (a); (d) solution of the diffraction pattern from (c).

high temperature occurring during laser treatment, therefore the characteristic hollows appear on the remelting surface. It was also found that, disregarding the ceramic powder used, in the laser power range from 1.2 to 2.0 kW, the porosity of the composite layers obtained increases, in comparison to that of the raw casting surfaces of magnesium alloys.

## 1.4 Texturization of polycrystalline silicon for the purpose of photovoltaics

Economic reasons underlie an interest in polycrystalline silicon texturization technologies. Silicon occurs in the earth crust in abundance primarily as silica and this is the reason why it is important to search for its widespread industrial applications. In an era

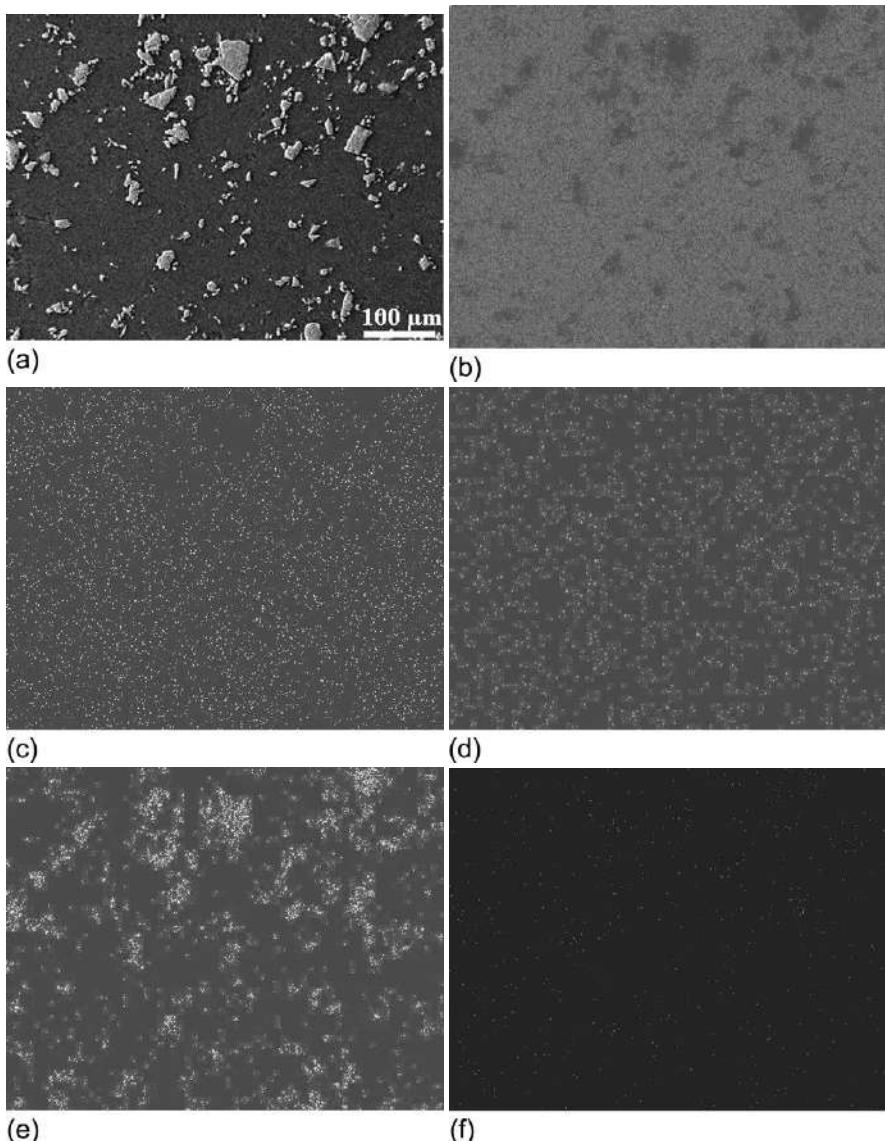


**Figure 1.20** Surface layer structure of the magnesium alloy MCMgAl6Zn1 subjected to laser treatment using titanium carbide: (a) the image obtained using secondary electrons and the surface distribution of elements, (b) Mg, (c) Al, (d) Zn, (e) Ti, (f) C; scanning speed of 0.75 m/min, laser power of 1.6 kW; SEM.

of growing energy demand, depleting conventional energy sources, controversies surrounding the security of nuclear fuel utilization, and the society's growing environmental awareness, a feasible use of silicon in the processes of converting solar radiation energy into electric energy paves the way for its extensive utilization in the future [25]. The production of solar cells from silicon is preceded with a

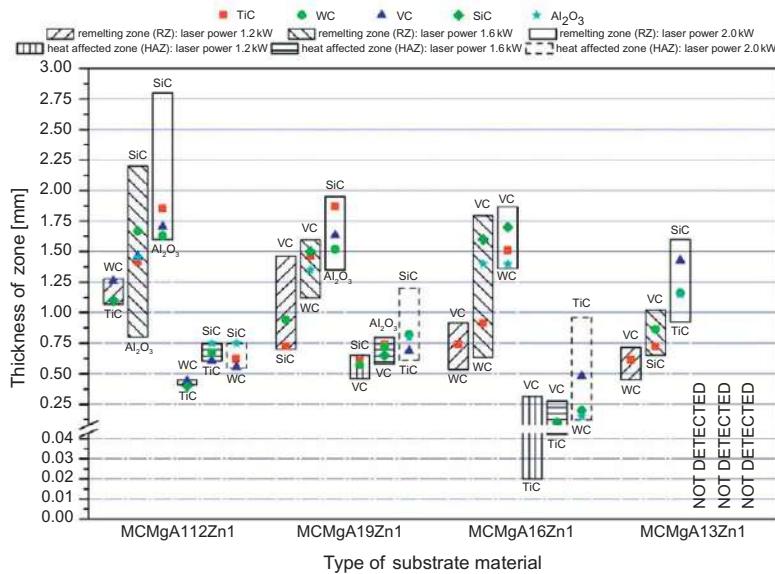


**Figure 1.21** Influence of laser power on thickness of the RZ, HAZ, and the surface layer of casting magnesium alloys after cladding.



**Figure 1.22** View of the MCMgAl9Zn1 casting magnesium alloy face of weld after laser treatment with WC powder, scan rate: 0.5 m/min, laser power: 2.0 kW.



**Figure 1.23** View of the MCMgAl9Zn1 casting magnesium alloy face of weld after laser treatment with SiC powder, scan rate: 0.5 m/min, laser power: 2.2 kW.

crystallization process that produces two forms: mono- and polycrystalline. It is more expensive to produce monocrystalline silicon with grains of a uniform crystallographic orientation; however, the solar cells produced are highly efficient [26]. The crystallization process of polycrystalline silicon with a random crystallographic orientation of grains is faster and cheaper; however, the solar cells produced from them offer lower efficiency than the cells produced of its monocrystalline form due to structural defects present [27]. It is justified, therefore, to seek new cells manufacturing technologies with polycrystalline silicon ensuring higher efficiency at relatively low cost.

The outcome of such quests is the technology of laser texturization of polycrystalline silicon with chemical etching; indispensable due to the fact that the hollows formed due to the activity of a laser beam are secondarily filled with a molten and incompletely evaporated material [28]. A conventional method of monocrystalline silicon surface texturization is anisotropic etching taking place in alkali solutions, for example, KOH or NaOH [29,30]. Using this conventional method, a crystal is etched at various rates according to different crystallographic directions. It creates immense opportunities for its spatial shapening, and randomly arranged pyramids are formed on the surface in the case of monocrystalline silicon with crystallographic orientation (100) (Figure 1.24).

Unfortunately, the use of such etching reagents for the texturing of polycrystalline silicon is restricted due to their high selectivity, which often leads to large faults between grains, mounting an obstacle in the subsequent phases of photovoltaic cells' production (Figure 1.25). By employing a nonstandard texturization method with laser treatment, a homogenous texture can be achieved across the polycrystalline silicon surface. A layer of damaged material is formed on the entire laser-textured area immediately after creating a lattice of grooves. The areas between the flashes of the neighboring grooves are covered with clotted material ejected from the grooves (Figure 1.26) and with products deposited from the gaseous phase released when the material is evaporated outside the groove. Microcracks and microgrooves are present at the surface subjected to texturing, both in the hollows (Figure 1.27) and in the flashes.

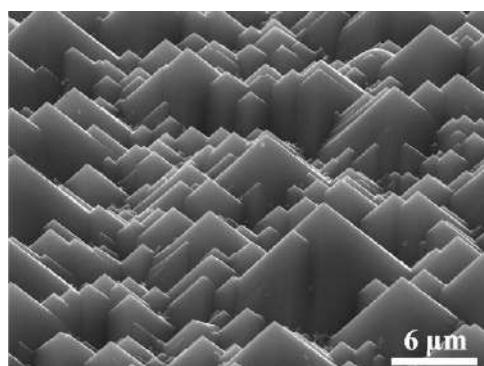


**Figure 1.24** Topography of monocrystalline silicon surface after alkaline texturization; SEM.

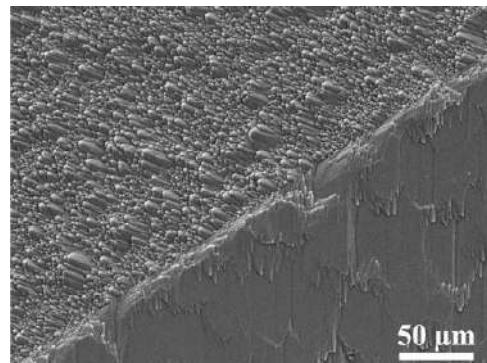


**Figure 1.25** Topography of polycrystalline silicon surface after alkaline texturization; SEM.

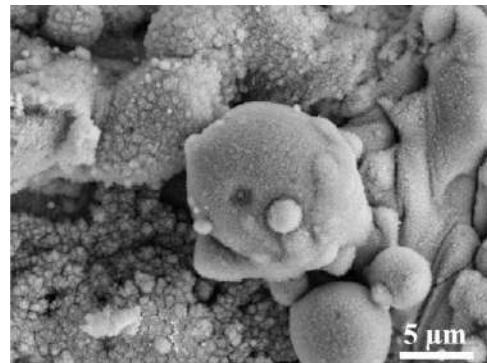


**Figure 1.26** Topography of polycrystalline silicon surface after laser texturization between grooves; SEM.

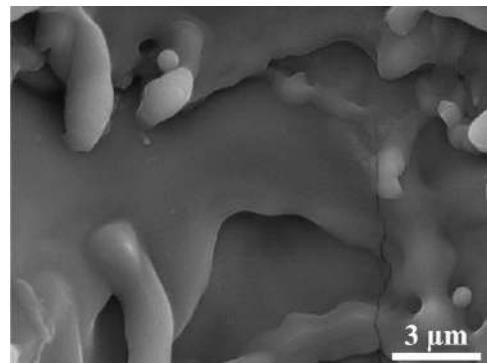


**Figure 1.27** Topography of polycrystalline silicon surface after laser texturization inside groove; SEM.

The laser-treated material undergoing chemical etching allows the proper texture in the form of parallel grooves in two directions perpendicular to each other. A topography of a polycrystalline silicon surface after laser texturization and chemical etching is shown, respectively, in [Figures 1.28](#) and [1.29](#).

The technology of laser texturization of polycrystalline silicon with chemical etching allows the user to improve the optical and electrical properties of photovoltaic cells prepared from them. The light reflection coefficient was examined for untextured wafers after removing the surface layer damage formed while cutting a silicon block. The optical properties of the laser-textured wafers are highly dependable upon the laser processing conditions. If the surface of wafers is textured corresponding to the lattice of grooves, this causes a decrease in the light reflection coefficient as compared to the coefficient for untextured wafers. As the etching of laser-textured wafers is progressing gradually, the  $R_{\text{eff}}$  coefficient is clearly growing only after removing 80  $\mu\text{m}$  ([Figure 1.30a](#)). Laser polycrystalline silicon surface texturing deteriorates the electrical properties of photovoltaic cells made of wafers prepared this way. A layer of the damaged material is formed on the entire laser-textured area

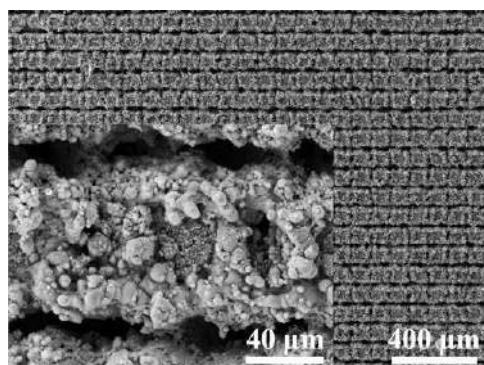


**Figure 1.28** Topography of polycrystalline silicon surface after laser texturization; SEM.

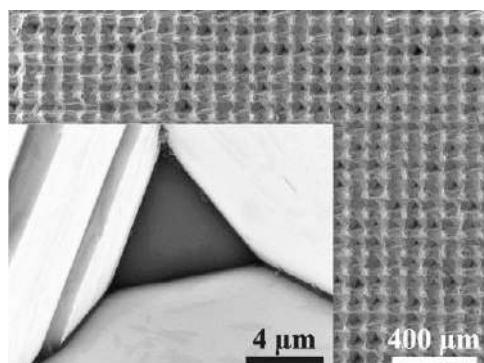


**Figure 1.29** Topography of polycrystalline silicon surface after laser texturization with chemical etching; SEM.

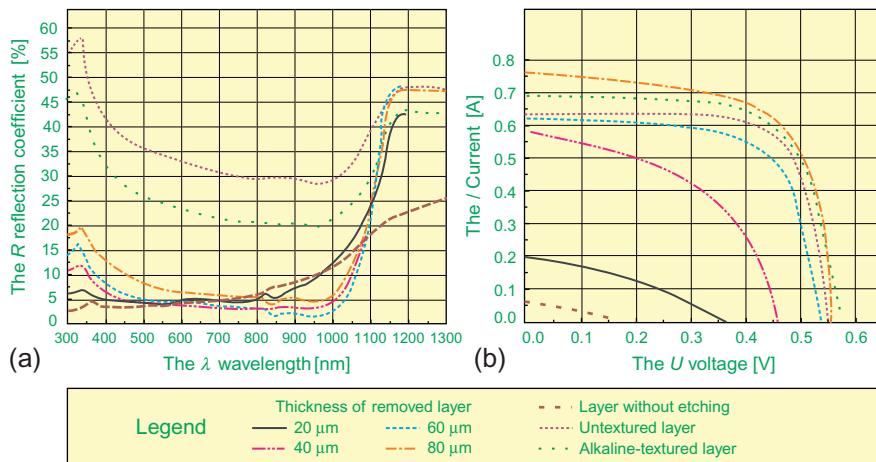


**Figure 1.30** Values of light reflection coefficient (a) and voltage-current characteristics (b) of photovoltaic cells for untextured wafers, alkaline-textured wafers, laser-textured wafers, and textured wafers with laser with chemical etching considering the thickness of layers removed during the process.

immediately after creating a lattice of grooves due to the condensation of the liquid-gaseous phase occurring during laser treatment. When the damaged layer of material is removed through etching, the efficiency of photovoltaic cells is boosted and is largest when a 80  $\mu\text{m}$  thick layer has been etched (Figure 1.30b). Surface layers shaping (using in the order to appropriate technology) can be often used in order to improve engineering material properties [31–35].

The application of laser technology in the manufacturing process of solar cells with high solar radiation conversion efficiency has become an inherent part of the modern photovoltaic technology. Laser texturization is one of the most promising methods of formatting a polycrystalline silicon surface. Laser radiation features a variety of unique properties including directivity, small divergence (collimation), focusing ability, monochromaticity, consistency, and polarization. Additional characteristics of laser treatment, such as the lack of contact, selectivity, and full automation, permit the accurate working of the substrate with fine-tuned depth and width.

## 1.5 Development trends of selected laser-treated engineering materials determined using new computer-integrated prediction methodology

A newly developed methodology of the computer-integrated prediction of materials surface engineering development has been employed to make an objectivized evaluation of the selected technologies described in this chapter, to determine the positive and negative factors affecting their future development, and to identify the

recommended action strategy. The accuracy of the computer-integrated methodology has been verified with 36 different technologies [2] used for metal materials with diversified properties, that is, different steel grades, light metal alloys, soft alloys of nonferrous metals, as well as sintered materials and nonmetal materials (i.e., silicon and polymers). The hidden knowledge of experts has been obtained through the heuristic research performed according to the idea of e-foresight and converted using newly established analytical methods and techniques into knowledge expressed quantitatively with the universal scale of relative states (1-min.; 10-max.). A set of contextual matrices has been created encompassing the dendrological matrix of the technology value, the metrological matrix of environment influence, and a matrix of strategies for technologies [1].

The dendrological matrix of technology value (Figure 1.31) presents graphic results of evaluating specific technology groups, with special attention paid to the

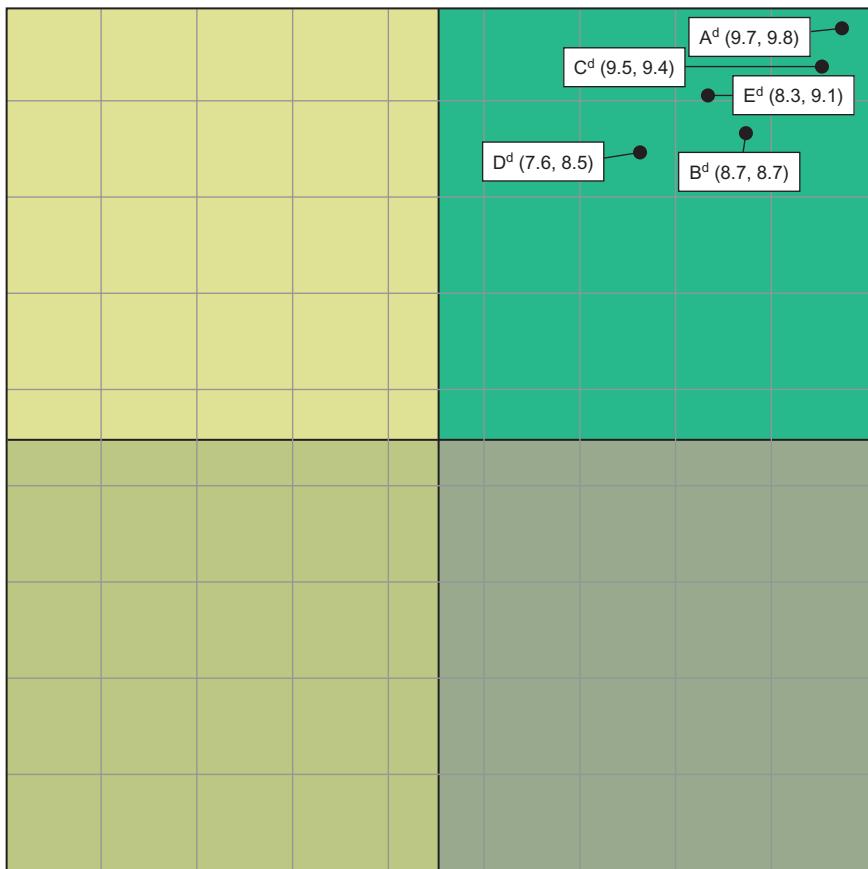


**Figure 1.31** An exemplary dendrological matrix of technology value for the laser cladding and remelting of casting magnesium alloys using TiC (A), WC (B), VC (C), SiC (D), carbide and  $\text{Al}_2\text{O}_3$  oxide (E) powders.

potential constituting the real objective value of a given technology and to the attractiveness reflecting how a given technology is subjectively perceived among its potential users. The potential of a given technology group expressed through a 10-point universal scale of relative states, marked on the horizontal scale of the dendrological matrix, is the result of a multicriteria analysis carried out based on expert opinions taking into account, in suitable proportions, the following types of potential: creative, application, qualitative, developmental, and technical. On the vertical scale of the dendrological matrix, the level of attractiveness was marked by a given technology group, which is the mean weighed expert opinions based on detailed criteria corresponding to the business, economic, liberal, environmental, and system attractiveness. Depending on the type of potential and level of attractiveness determined as part of the expert opinion, a given technology may be placed in one of the quarters of the matrix. The following quarters were distinguished in the dendrological matrix of technology value:

- *Quaking aspen* is a weak technology with limited potential, included within the range  $\langle 1, 5.5 \rangle$  and with limited attractiveness within the range  $\langle 1, 5.5 \rangle$ , whose future success is unlikely.
- *Soaring cypress* corresponds to a technology with limited potential within the range  $\langle 1, 5.5 \rangle$ , but with huge attractiveness included in the range  $(5.5, 10)$ , which causes the success of a given technology to be possible.
- *Rooted dwarf mountain pine* is a technology with limited attractiveness within the range  $\langle 1, 5.5 \rangle$ , but with huge potential included in the range  $(5.5, 10)$ , thanks to which its future success is possible.
- *Wide-stretching oak* corresponds to the best possible situation in which the analyzed technology is characterized by huge potential within the range  $(5.5, 10)$ , as well as huge attractiveness within the range  $(5.5, 10)$ , and this connection guarantees future success.

The meteorological matrix of environment influence (Figure 1.32) presents graphic results of evaluating the impact of external factors on specific groups of technologies that had been divided into difficulties with a negative impact and chances that positively influence the analyzed technologies. The testing of expert opinions on the subject of positive and negative factors that influence specific technologies was carried out based on a survey comprising several dozens of questions pertaining to the micro- and macroenvironment in strictly defined proportions. Sixteen percent of the questions pertain to the competitive environment, while the remaining 84% are questions regarding specific constituents of the macroenvironment, and especially the following types of environment: technological, economic, social, political-legal, international, and natural ones. External difficulties expressed with the use of a 10-point universal scale of relative states, which are the result of a multicriteria analysis conducted based on the expert opinions, have been placed on the horizontal scale of the meteorological matrix. On the other hand, chances (i.e., positive environment factors), being a mean weighed expert opinion based on detailed criteria, were placed on the vertical scale. Depending on the level of influence of positive and negative environment factors on the analyzed technology, determined as part of the expert opinions on a 10-point scale, it is placed in one of the matrix quarters. The following quarters were distinguished in the meteorological matrix of technology value:

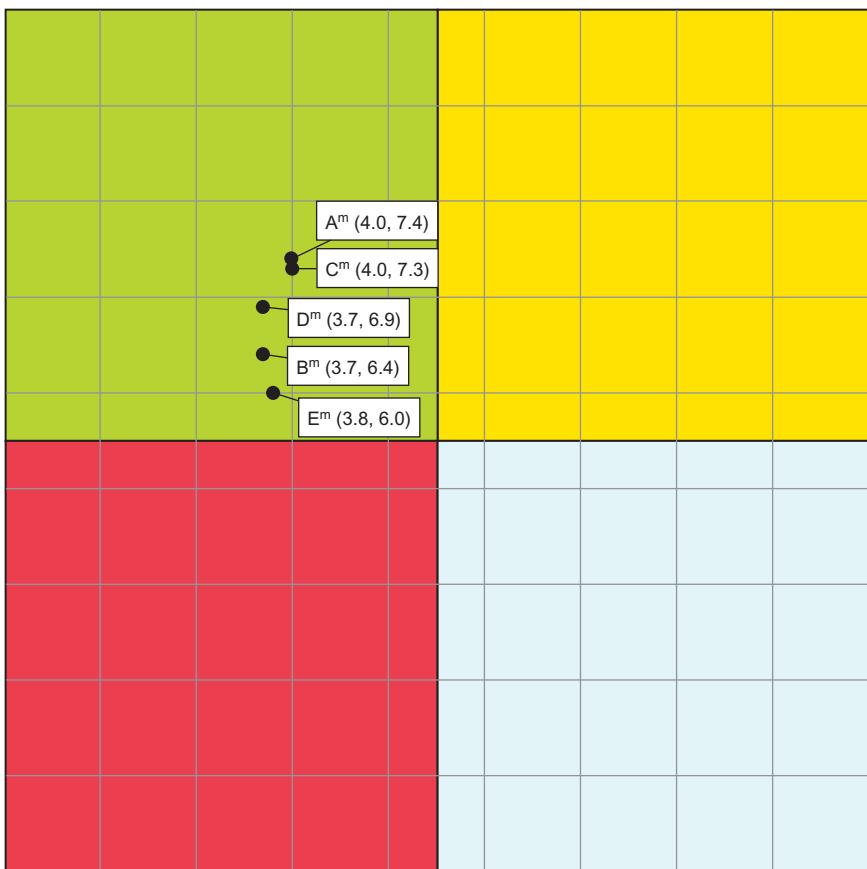


**Figure 1.32** An exemplary meteorological matrix of environment influence for the laser cladding and remelting of casting magnesium alloys using TiC (A), WC (B), VC (C), SiC (D), carbide and Al<sub>2</sub>O<sub>3</sub> oxide (E) powders.

- *Frosty winter* corresponds to the worst possible situation in which the environment carries a large number of difficulties included in the range  $\langle 5.5, 10 \rangle$  and a small number of chances within the range  $\langle 1, 5.5 \rangle$ , which causes the success in a given environment to be difficult or impossible to obtain.
- *Hot summer* corresponds to a situation in which the environment brings many chances included within the range  $\langle 5.5, 10 \rangle$ , but which is also accompanied by many difficulties from the range  $\langle 5.5, 10 \rangle$ ; this causes the success of the technology under these conditions to be possible but charged with risk.
- *Rainy autumn* corresponds to a neutral situation in which there are no dangers awaiting for a given technology, which corresponds to the range  $\langle 1, 5.5 \rangle$ , but also the environment does not carry many chances, which is reflected by the range  $\langle 1, 5.5 \rangle$ .
- *Sunny spring* is the best possible variant because it denotes a friendly environment with a large number of chances from the range  $\langle 5.5, 10 \rangle$  and a small number of difficulties included within the range  $\langle 1, 5.5 \rangle$ , which will guarantee success of a given technology under such good conditions.

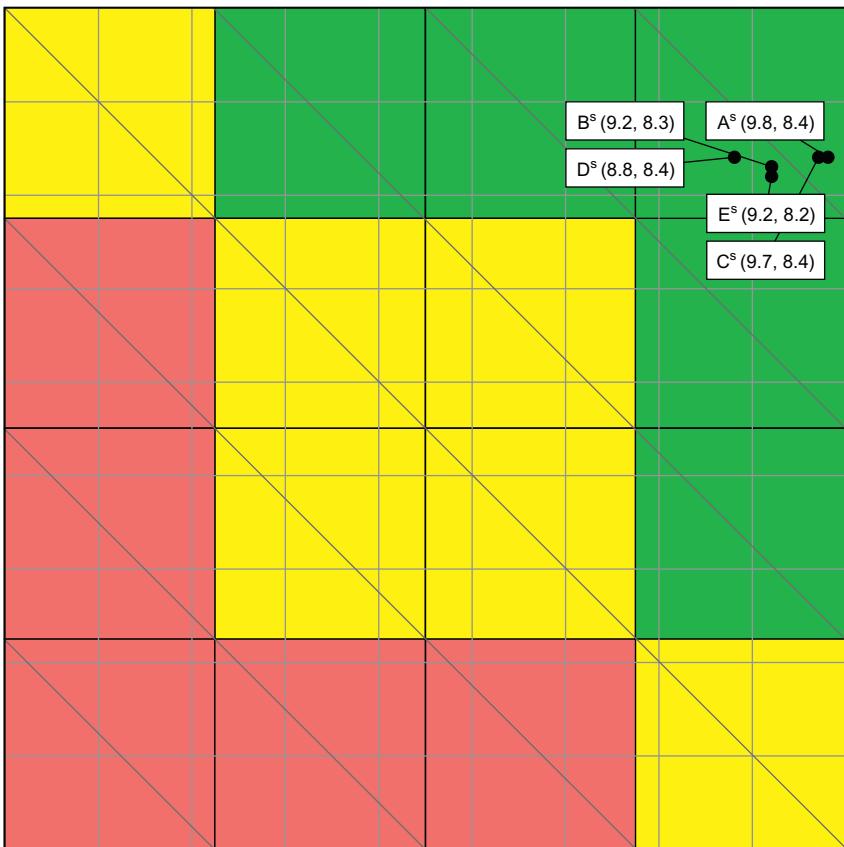


**Figure 1.33** The matrix of strategies for technology called the laser cladding and remelting of casting magnesium alloys using TiC (A), WC (B), VC (C), SiC (D), carbide and Al<sub>2</sub>O<sub>3</sub> oxide (E) powders.

A *matrix of strategies for technologies* (Figure 1.33) includes the research results transformed from a dendrological matrix of technology value, as well as a meteorological matrix of environment influence. A matrix of strategies for technologies consists of 16 fields corresponding to each set of versions resulting from the combination of the types of technology and the types of environments.

To facilitate the transfer of specific numeric values from the dendrological matrix [2 × 2] and the meteorological matrix [2 × 2] to the matrix of strategies for technologies with the dimensions of [4 × 4], mathematical relations and simple software were formulated [1] that enable the rescaling and objectivizing of test results.

In order to enable a comparative analysis of the relevant laser surface treatment technologies according to harmonized materials science, technological, organizational, and economic criteria, technology road maps were created for them and technology information sheets detailing them out [3]. A layout of the custom *technology road map* (Figure 1.34) corresponds to the first quarter of the Cartesian system of

Technology roadmap		Technology name	<i>Laser treatment of hot-work alloy tool steels using niobium carbide powders</i>		Catalogue no.
		Research scope	<i>Laser technologies in surface engineering</i>		M1-03/2010-12
When?	Time intervals	Today 2010-2012		2020	2030
Why?	All society and economic perspectives	Creating scenarios of future events Creating the Book of information cards concerning future technologies Development of information society and intellectual capital	Development of priority innovation technologies Using chances and avoiding difficulties Cooperation to increase innovativeness and competitiveness of economy and intellectual	Statistically high quality of technologies Sustainable development Knowledge-based economy	
	Strategy for technology Environment influence Technology value	Hot summer Wide stretching oak	Strategy of an oak in summer		
What?	Product	Casting moulds, stamping dies, dies, tools working under high temperature gradient conditions			
	Product quality at the background of foreign competitors Surface	Quite high (7)	High (8)	High (8)	
	Kind of surface coatings/layers	NbC niobium carbide			
	Improved material properties	Increase in mechanical and functional properties of elements, especially hardness; increase in resistance to heat fatigue and increase in abrasive resistance			
How?	Diagnostic-research equipment	High-Power Diode Laser (HDPL), light, scanning and transmission electron microscopes, microhardness tester, scratch tester, X-ray diffractometer, X-ray microanalyzer, a device for testing of heat fatigue and abrasive resistance			
	Technology	Alloying and/or cladding of hot-work alloy tool steels using NbC niobium carbide powders			
	Life cycle period	Emбриonic (10)	Experimental (9)	Prototype (8)	
	Production type	Unit scale	Medium-scale serial	Large-scale serial	
	Production organization form	Cellular	Cellular	Cellular rhythmic	
	Machine park modernity	Excellent (10)	Excellent (10)	Excellent (10)	
	Automation & robotization	Quite high (7)	High (8)	Very high (9)	
Where?	Quality and reliability	Quite high (7)	High (8)	Quite high (7)	
	Proeology	High (8)	High (8)	Quite high (7)	
Who?	Organization type	Research and scientific centers		Research and scientific centers, medium-sized enterprises	
	Represented industrial branches	Heavy, automotive, and machine-building industry		Large and medium-sized enterprises	
How much?	Staff education level	High (8)	High (8)	Quite high (7)	
	Engagement of scientific-research staff	Very high (9)	High (8)	Quite high (7)	
	Capital requirements	Excellent (10)	Very high (9)	Moderate (6)	
Production size determining profitability in firm		Medium (5)	Quite high (7)	High (8)	
Production size in the country		Minimal (1)	Low (3)	Medium (5)	
<b>Legend:</b> ---> Cause and effect connections   ----> Capital connections   -----> Time correlations   -> Two-way transfer of data and/or resources					

Figure 1.34 A demonstrated technology road map prepared for the laser treatment of hot-work alloy tool steels using NbC niobium carbide powders.

coordinates. Three time intervals for, respectively, 2010-2012, 2020, and 2030, are given on the axis of abscissa, and the time horizon for the overall results of the research provided on the map is 20 years. Seven main layers are provided on the axis of coordinates of the technology road map responding, respectively, to following more detailed questions: When? Why? What? How? Where? Who? How much? *Technology information sheets* ([Figure 1.35](#)) contain technical details very helpful in implementing a specific technology in the industrial practice, especially in the SMEs not having the capital to conduct research in this field.

The heuristic investigations conducted are of a utilitarian nature, as it is expected to broaden the objectives of e-foresight to include the domain of application and implementation of knowledge on the selected engineering materials surface properties and structure formation technologies and, in general, material processes technologies and engineering materials processing. A new technology transfer center is represented by a group of thematic workshops and teams. The relevant teams are to fulfill the tasks of technology transfer, without, however, providing services and dedicating offers to specific entrepreneurs. By offering for free, via an appropriately prepared Web platform, information and knowledge on engineering materials and surface treatment and material processes technologies resulting from the performed e-foresight research [[36,37](#)], the ongoing monitoring of materials science issues is facilitated. Such tasks are considered to be technology e-transfer (technology electronic transfer) [[38](#)] to be conducted on a continuous basis without any limitations and for free, using an openly available (Open Access) Web platform.

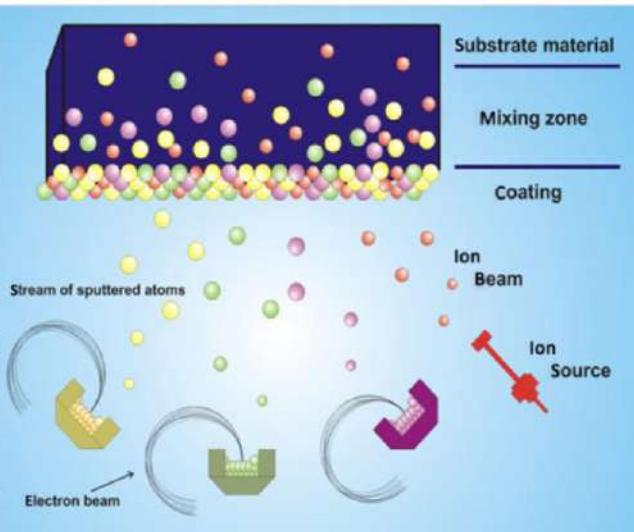
## 1.6 Conclusion

The selected outcomes of the work presented in this book, consisting of laser surface treatment of diverse materials: hot-work tool steels, cast magnesium and aluminum alloys, and polycrystalline silicon, represent promising technologies with broad application opportunities across various industries. Hot-work tool steels continue to represent a widely used group of tool materials in industry due to their excellent functional properties and availability at a reasonable cost. The laser treatment of such steels' surface layers, where their surface layers are remelted and alloyed with powders of hard carbides, allows the enhancement of their functional properties, especially hardness and wear resistance. Demand for light metal alloys is communicated by the automotive and aviation sector, especially cast magnesium alloys and cast aluminum alloys with robust mechanical and functional properties. The properties can be improved through laser treatment of the cladding of hard carbide particles (e.g., TiC, WC, VC, SiC) or oxides (e.g., Al<sub>2</sub>O<sub>3</sub>) into the worked material's surface. Massive interest is seen from the power industry, which is constantly seeking alternative sources of renewable energy. The outcomes of investigations concerning laser surface treatment of polycrystalline silicon indicate that they are much cheaper than the alternative, monocrystalline form. All the laser surface treatment technologies described in this chapter, which has been a subject of specialized research pursued in recent years by the Institute of Engineering Materials and Biomaterials of the Silesian University

Technology information sheet	Technology	<i>Ion implantation</i>				Catalogue no.					
	Thematic area	<i>Non-metallic structural materials surface engineering</i>				P3-05-2010/11					
The essence of the physiochemical phenomenon				Influence of technology application on the predicted and expected material properties		Level					
Ion implantation is a process of introducing ionised atoms of any element into a foreign body, with a high energy (of more than ten keVs to several dozens of MeVs) they gain in a vacuum in an electrical field accelerating and forming ions into a beam. Ion implantation is a treatment process aimed at modifying the properties of non-metallic construction materials, most of all ceramics and plastics. A 0.1±1 µm thick layer is formed as a result of implantation joined integrally with the substrate with its properties being different, better than the substrate. Ions can be implanted into a solid in a continuous and pulse manner.				Biocompatibility	Quite high (7)						
				Resistance to high temperature	Quite high (7)						
				Wear resistance	Moderate (6)						
				Hardness	Moderate (6)						
				Erosion resistance	Moderate (6)						
				Fatigue strength	Moderate (6)						
				Corrosion resistance	Moderate (6)						
				No brittleness	Moderate (6)						
Type of possible coating/surface layer or of the process occurring on the substrate surface				Efficiency of technology's counteracting the results of wear	Level						
Monolayer	Multi-phase	Amorphous		Abrasive wear	High (8)						
Multilayer	Graded	Nanocrystalline		Pitting	High (8)						
Multilayer (>100 layers)	Composite	Hybrid		Scuffing	Quite high (7)						
Phase transformations of Substrate surface	Change of chemical composition on Substrate surface	Physical processes on Substrate surface		Fretting	Quite high (7)						
Special properties of coatings/surface layers/substrate surface due to processes				Erosion	Quite high (7)						
✗ Mechanical	Magnetic	Optic	✗ Tribological	Diffusive wear	Quite high (7)						
✗ Chemical	Diffusion	Thermal	✗ Anticorrosive	Plastic wear	Quite high (7)						
Electrical	Hydromechanical	Acoustic	Others	Industry sector with the highest applicability of technology acc. to the PKD classification	Level						
Advantages		Disadvantages									
Any element can be implanted and the concentrations of the implanted elements are achievable exceeding their solubility in the treated material.		A high apparatus cost; process directivity; items with complicated shapes cannot be treated.									
The most prospective specific technologies and/or areas of applications											
Ion implantation based on ceramic elements of mechanical devices and ceramic elements of electronic circuits (including microelectronic circuits) and based on polymers to improve tribological, electrical and magnetic properties.											
Substitute/alternative technologies											
Electron techniques.											
Recommended references											
1 E. Knystautas (ed.), <i>Engineering Thin Films and Nanostructures with Ion Beams</i> , Taylor & Francis Group, Boca Rato - London - New York - Singapore, 2005.											
2 Lic Books (ed.), <i>Thin Film Deposition: Evaporation, Chemical Vapor Deposition, Sol-Gel, Focused Ion Beam, Thermal Spraying, Diamond-Like Carbon</i> , Books LLC, Tennessee, 2010.											
3 R. Hellborg, H.J. Whitlow, Y. Hang (eds.), <i>Ion beams in nanoscience and technology</i> , Springer Verlag, Berlin-Heidelberg, 2009.											
(a)											

**Figure 1.35** An example of a technology information sheet prepared for ion implantation in the thematic area of nonmetallic construction materials:  
 (a) Page 1 and (b) Page 2.

Technology information sheet	Technology	<i>Ion implantation</i>			Catalogue no.			
	Thematic area	<i>Non-metallic structural materials surface engineering</i>			P3-05-2010/11			
Description of the manufacturing process progress								
<ul style="list-style-type: none"> <li>The charge surface is initially prepared before implantation;</li> <li>A thin layer is deposited onto the surface of the implanted material (optionally);</li> <li>The charge is placed into the implantator working chamber;</li> <li>The implantator working chamber is pumped off;</li> <li>Ion implantation;</li> <li>Charge cooling;</li> <li>The charge is taken out from the implantator working chamber.</li> </ul>								
<p>Ion implantation is a process of doping materials based on the use of a high kinetic energy. The dope atoms are ionised in the ion source and then accelerated in an electrical field. Any material can be doped with almost any element due to the kinematic character of the process. The concentrations of alloying additives exceeding their solubility in the material used can be achieved by means of the ion implantation technology (usually 20%, maximum to over 50%) and independence from the adhesion effect can be attained.</p>								
General physicochemical conditions of technological process performance								
Standard range of process temperature	Unit	from	to					
Temperature	°C	20	600					
Pressure	Pa	$10^{-3}$	$10^{-4}$					
Current and voltage conditions	kV	mA	20	1	200			
Time	min.		30		90			
Environment/atmosphere	Vacuum							
Specific conditions of process performance	High vacuum							
Method(s) of initial substrate material preparation								
Initial cleaning: mechanical, chemical, physical, physicochemical cleaning; ultrasound cleaning.								
Device type/kind								
Ion implantators (ion accelerators)								
Specific accessories								
Ion source; focusing and accelerating system.								



Example scheme of ion implantation process progress with the IBAD (Ion Beam Assisted Deposition) method

(b)

Figure 1.35 Continued.

of Technology, Gliwice, Poland, enjoy very extensive developmental and application prospects in the coming two decades.

Foresight research is also the subject of research conducted by the authors of this chapter. This research focused on an objectivized evaluation of the particular technologies' value in order to formulate (ultimately) such actions as to enable the optimum exploitation of all the external and internal drivers contributing to the stimulated development of a particular technology. To this end, the methodology of the computer-integrated prediction of materials surface engineering development was developed and implemented for the selected technologies. Contextual matrices, road maps, and technology information sheets (being the outcome of the heuristic research conducted) based on the results of multistage and multichannel surveys of experts, allow for the quantitative and qualitative comparisons of the individual technologies according to the harmonized materials science, technological, and economic criteria. This is of practical importance and reassures the industry that the utilitarian aim of the research conducted has been accomplished.

## 1.7 Comments

All the results, photos, and diagrams have been developed in the framework of materials science research and the multiannual foresight project being currently pursued pertaining to surface properties formation, leading technologies of engineering materials, and biomaterials.

## References

- [1] A.D. Dobrzańska-Danikiewicz, Foresight methods for technology validation, roadmapping and development in the surface engineering area, *Arch. Mater. Sci. Eng.* 44 (2) (2010) 69–86.
- [2] A.D. Dobrzańska-Danikiewicz (Ed.), Materials surface engineering development trends, Open Access Library 6 (2011) 1–594.
- [3] A.D. Dobrzańska-Danikiewicz, The book of critical technologies of surface and properties formation of engineering materials, Open Access Lib. 8 (26) (2013) 1–823 (in Polish).
- [4] M. Bonek, Effect of high power diode laser surface alloying of tool steels, *Chiang Mai J. Sci.* 40 (5) (2013) 849–856.
- [5] C. Karatas, B.S. Yilbas, A. Aleem, M. Ahsan, Laser treatment of cemented carbide cutting tool, *J. Mater. Process. Technol.* 183 (2–3) (2007) 234–240.
- [6] M. Bonek, G. Matula, L.A. Dobrzanski, Effect of laser surface melting on structure and properties of a high speed tool steel, *Adv. Mater. Res.* 291–294 (2011) 1365–1368.
- [7] L.A. Dobrzański, M. Bonek, E. Hajduczek, A. Klimpel, A. Lisiecki, Application of high power diode laser (HPDL) for alloying of X40CrMoV5-1 steel surface layer by tungsten carbides, *J. Mater. Process. Technol.* 155–156 (2004) 1956–1963.
- [8] T. Slatter, H. Taylor, R. Lewis, P. King, The influence of laser hardening on wear in the valve and valve seat contact, *Wear* 267 (5) (2009) 797–806.

- [9] G. Matula, M. Bonek, L.A. Dobrzański, Comparison of structure and properties of hard coatings on commercial tool materials manufactured with the pressureless forming method or laser treatment, *Mater. Sci. Forum* 638–642 (2010) 1830–1835.
- [10] B.S. Yilbas, F.M. Arif, C. Karatas, M. Ahsan, Cemented carbide tool: laser processing and thermal stress analysis, *Appl. Surf. Sci.* 253 (12) (2007) 5544–5552.
- [11] R. Sturm, J. Grum, The influence of retained austenite on residual stresses in laser remelted cast iron, *J. Mater. Eng. Perform.* 20 (9) (2012) 1671–1677.
- [12] Q.J. Wang, Y.-W. Chung (Eds.), *Encyclopedia of Tribology*, Springer-Verlag, Berlin, Heidelberg, 2013, p. 4139.
- [13] M. Bonek, L.A. Dobrzański, Characterization performance of laser melted commercial tool steels, *Mater. Sci. Forum* 654–656 (2010) 1848–1851.
- [14] A.D. Dobrzańska-Danikiewicz, T. Tański, J. Domagała-Dubiel, Unique properties, development perspectives and expected applications of laser treated casting magnesium alloys, *Arch. Civil Mech. Eng.* 12 (2012) 318–326.
- [15] C. Taltavull, B. Torres, A.J. Lopez, P. Rodrigo, E. Otero, J. Rams, Selective laser surface melting of a magnesium-aluminium alloy, *Mater. Lett.* 85 (2012) 98–101.
- [16] M. Piec, L.A. Dobrzański, K. Labisz, E. Jonda, A. Klimpel, Laser alloying with WC ceramic powder in hot work tool steel using a high power diode laser (HPDL), *Adv. Mater. Res.* 15–17 (2007) 193–198.
- [17] L.A. Dobrzański, K. Labisz, M. Piec, A.J. Lelątko, A. Klimpel, Structure and properties of the 32CrMoV12-28 steel alloyed with WC powder using HPDL laser, *Mater. Sci. Forum* 530–531 (2006) 334–339.
- [18] S. Katayama (Ed.), *Handbook of Laser Welding Technologies*, In: Woodhead Publishing Series in Electronic and Optical Materials No. 41, June 2013.
- [19] N. Subhasisa, P. Sisa, D.M. Jyotsna, Laser surface alloying of aluminium with WC+Co+NiCr for improved wear resistance, *Surf. Coat. Technol.* 206 (15) (2012) 3333–3341.
- [20] L.A. Dobrzański, T. Tański, Influence of aluminium content on behaviour of magnesium cast alloys in bentonite sand mould, *Solid State Phenom.* 147–149 (2009) 764–769.
- [21] T. Tański, L.A. Dobrzanski, L. Cizek, Influence of heat treatment on structure and properties of the cast magnesium alloys, *Adv. Mater. Res.* 15–17 (2007) 491–496.
- [22] T. Tański, Characteristics of hard coatings on AZ61 magnesium alloys, *J. Mech. Eng.* 59 (3) (2013) 165–174.
- [23] T. Tański, K. Labisz, Electron microscope investigation of PVD coated aluminium alloy surface layer, *Solid State Phenom.* 186 (2012) 192–197.
- [24] T. Tański, K. Lukaszkowicz, Structure and properties of PVD coatings deposited on the aluminium alloys, *Surf. Eng.* 28 (8) (2012) 598–604.
- [25] L.C. Hirst, Principles of solar energy conversion, reference module in earth systems and environmental sciences, *Compr. Renewable Energy* 1 (2012) 293–313.
- [26] T.M. Razykov, C.S. Ferekides, D. Morel, E. Stefanakos, H.S. Ullal, H.M. Upadhyaya, Solar photovoltaic electricity: current status and future prospects, *Solar Energy* 85 (8) (2011) 1580–1608.
- [27] M. Heuer, Metallurgical grade and metallurgically refined silicon for photovoltaics, *Semicond. Semimetals* 89 (2013) 77–134.
- [28] L.A. Dobrzański, A. Drygała, Influence of laser processing on polycrystalline silicon surface, *Mater. Sci. Forum* 706–709 (2012) 829–834.
- [29] W. Sievert, K.U. Zimmermann, B. Hartmann, C. Klimm, K. Jacob, H. Angermann, Surface texturization and interface passivation of mono-crystalline silicon substrates by wet chemical treatments, *Solid State Phenom.* 145–146 (2009) 223–226.

- [30] C. Sethi, V.K. Ananad, K. Walia, S.C. Sood, Optimization of surface reflectance for alkaline textured monocrystalline silicon solar cells, *Int. J. Comput. Sci. Commun. Technol.* 5 (1) (2012) 785–788.
- [31] K. Lukaszkowicz, J. Sondor, A. Kriz, M. Pancielejko, Structure, mechanical properties and corrosion resistance of nanocomposite coatings deposited by PVD technology onto the X6CrNiMoTi17-12-2 and X40CrMoV5-1 steel substrates, *J. Mater. Sci.* 45 (2010) 1629–1637.
- [32] L.A. Dobrzański, M. Musztyfaga, A. Drygała, Final manufacturing process of front side metallisation on silicon solar cells using convectional and unconventional techniques, *Strojnicki vestnik J. Mech. Eng.* 59 (2013) 175–182.
- [33] L.A. Dobrzański, L.W. Żukowska, J. Mikuła, K. Gołombek, D. Pakuła, M. Pancielejko, Structure and mechanical properties of gradient PVD coatings, *J. Mater. Process. Technol.* 201 (2008) 310–314.
- [34] A.D. Dobrzańska-Danikiewicz, D. Łukowiec, Synthesis and characterisation of Pt/MWCNTs nanocomposites. *Phys. Status Solidi B* (2013) <http://dx.doi.org/10.1002/pssb.201300083>.
- [35] L.A. Dobrzanski, M. Kremzer, K. Gołombek, Structure and properties of aluminum matrix composites reinforced by Al<sub>2</sub>O<sub>3</sub> particles, *Mater. Sci. Forum* 591–593 (2008) 188–192.
- [36] A.D. Dobrzańska-Danikiewicz, E-foresight of materials surface engineering, *Arch. Mater. Sci. Eng.* 44 (1) (2010) 43–50.
- [37] A.D. Dobrzańska-Danikiewicz, Foresight of material surface engineering as a tool building a knowledge-based economy, *Mater. Sci. Forum* 706–709 (2012) 2511–2516.
- [38] A.D. Dobrzańska-Danikiewicz, L.A. Dobrzański, J. Mazurkiewicz, B. Tomiczek, E. Reimann, E-transfer of materials surface engineering e-foresight results, *J. Achieve. Mater. Manuf. Eng.* 52 (2) (2011) 87–100.

# Laser nitriding and carburization of materials

2

D. Höche<sup>1</sup>, J. Kaspar<sup>2</sup>, P. Schaaf<sup>3</sup>

<sup>1</sup>Helmholtz-Zentrum Geesthacht, Geesthacht, Germany; <sup>2</sup>Fraunhofer Institute for Material and Beam Technology—IWS, Dresden, Germany; <sup>3</sup>Technische Universität Ilmenau, Ilmenau, Germany

## 2.1 Introduction

In recent years, many industrial applications of laser-based processes have been developed. Beside laser cutting, drilling, welding, alloying, hardening or cladding, laser nitriding and carburizing have been applied successfully on various alloys. The latter surface treatment is used to improve the mechanical properties, wear, or even the corrosion resistance of metals. The laser has been developed into a multiple-choice tool in this context.

Meanwhile, it is well established that the irradiation of titanium, iron, and other metals with continuous wave (cw) or pulsed laser beams in a nitrogen atmosphere, in air or in other process gases such as CH<sub>4</sub>, leads to a take-up of nitrogen or carbon. The laser “gas” nitriding or carburizing effect has been demonstrated for various materials and for different laser systems where even the formation of stoichiometric TiN was reported [1]. Carburization has been extensively studied in [2]. In this context it has to be noted that carburizing can also be performed by remelting a graphite-coated surface with a laser [3], which at least is a different type of process.

Further activities were published on iron treatments that show improved hardness and corrosion resistance of the irradiated samples [4]. Aluminium and AlSi alloys were investigated in [5,6] or [7] who reported the formation of AlN. Carbide formation on silicon or iron has been reported in [8]. Actual investigations show the successful application of laser nitriding on bearings [9] or to modify niobium for accelerator cavities [10]. Further work of Yilbas *et al.* [11] extends the application field on phosphor bronze modification. Carburizing regarding automotive applications was carried out by Abboud *et al.* [12] on iron-based components where they increase the carbon amount up to 6 wt.%.

New efforts are in progress to develop hybrid processing technologies. Liu *et al.* [13] and Zhang *et al.* [14] synthesized TiN/TiAl<sub>3</sub> composites by combining laser nitriding and plasma spraying. Duplex treatments of laser-nitrided and then PVD-coated Ti-6Al-4V were carried out in [15]. In [16] the method was used to improve the adhesion strength of plasma-spraying hydroxyapatite coatings and titanium alloy substrates for biotechnological applications.

Particular interesting opportunities are provided by pulsed laser treatments. It has been established that short laser pulses of high energy can induce a direct synthesis

of thin wear-resistant layers if the surface of, for example, titanium alloys is irradiated in a reactive atmosphere [4,17,18]. Successful tests of the direct laser synthesis have been carried out with Excimer [19,20], Nd:YAG [1,21–24], titanium-Sapphire [2], and free electron lasers [25–28] in nitrogen and methane atmospheres. Pulsed treatments have the benefit that they occur very locally in the material leading to reduced heat entry and only local stresses. This enables the ability of local engineering.

The goal of this chapter is to give a review of the state of the art of laser nitriding and carburizing. This will include fundamental aspects in the next section followed by exemplary descriptions on titanium and iron, including application possibilities. Finally, the reader will be instructed in the following primary aspects of the subject:

- to rate the method in competition to other processing technologies
- to get an idea of the physics and chemistry involved
- to derive correlations between the structure, the mechanical properties, the wear resistance, and the processing parameters
- to get an insight into the structural modification of the alloys and their surfaces
- to draw conclusions on the applicability and the benefit of applying the method, and
- to give an outlook on future trends.

## 2.2 Overview on surface alloying of materials by laser irradiation

Besides well-known surface treatment methods that apply laser irradiation for cladding or powder alloying, the laser-induced nitrogen and carbon uptake has been developed to an established method to enhance the performance of alloys and their surfaces. In order to understand and to control this kind of surface engineering, a detailed view on the phenomena involved seems necessary.

### 2.2.1 Principles of laser nitriding and carburizing

The entire process of laser nitriding and carburizing is a very complex interaction of various fields of science, and thus difficult to describe. For a deeper understanding, it is necessary to define and to quantify the individual physical and chemical sequences that arise in different process chains. A flow chart illustrated in [Figure 2.1](#) has been created that helps to improve the understanding of processes taking place being mainly determined by heat.

The entire process is dominated by the local heating and the resulting surface temperature. This indeed determines the uptake of nitrogen and carbon. Depending on melting or evaporation effects, different process chains are involved. Finally, the coatings and their properties are determined in an interlinking way. Recognize that a process chain sets up itself, whereby each subprocess causes consequences for the resulting synthesis. In order to improve the *in situ* process understanding,

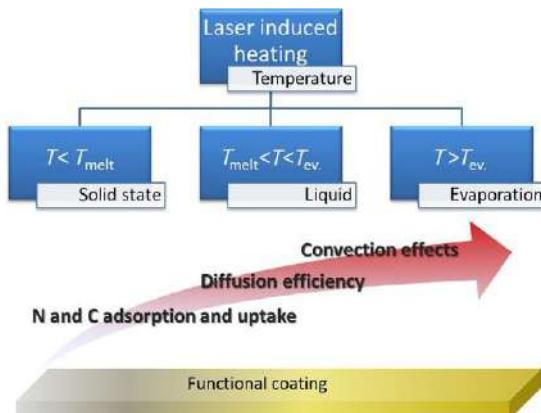


**Figure 2.1** Scheme of temperature dependencies and mechanisms involved.

the aim is to clarify and if necessary to quantify these influences. In relation to a complete description and to enable process control of the synthesis (also for technical application), investigations, measurements, and simulations were compared and coupled.

### 2.2.1.1 Physical and chemical processes

Contrary to the more or less simple experimental setup for the processing, which is usually based on a gas chamber or a gas nozzle, the physical and chemical mechanisms are very complex and closely linked to each other. In order to understand and finally to control the processing for applications in technology, each subprocess has to be examined and weighed. The following list shows and explains the substantial ones:

- *Laser absorption and local heating:* First, the virgin material is irradiated and a strong local heating takes place via optical absorption. This depends on the absorptivity respective to the optical characteristics (dielectric function), on the thermal conductivity, and on the specific heat of the irradiated material.
- *Melt and evaporation processes:* After reaching or exceeding the melting point and bringing in the latent heat of fusion, a liquid phase (melt) develops. The material properties change rapidly. Regarding the process efficiency in particular, the improvement of the diffusion behavior has to be considered. Besides, convection effects can arise, which affect the synthesis process, especially the surface quality, significantly. A further energy entry leads to the excess of the evaporation threshold. The so-called laser ablation and plasma formation occurs. All these processes are coupled to the energy density and the interaction time of the laser beam, which is consistent to the three cases in Figure 2.1.
- *Plasma expansion into the background gas:* Due to the pressure of the ambient gas, the expansion gets strongly absorbed. This interaction provides recoil forces, which can affect the melting bath strongly (possible melt ejection).
- *Dissociation and/or ionization:* As a result of the following shock wave and due to the immense high pressure and temperature rise on top of the surface, molecules are dissociated.

The ablated Ti- and gas-atoms will be ionized as well. Besides, free electrons arise, which can cause the so-called plasma shielding, which leads to the absorption of the laser beam in the plasma and a further heating of the plasma. A fluctuating and oscillating behavior can be observed.

- *Gas adsorption and absorption:* Activated gas above the surface is now available. This can be ad- and absorbed more effectively by the surface. This takes place in first approximation according Sievert's law (ratio of partial pressures).
- *Gas atomic transport (diffusion, convection):* If the nitrogen or carbon is within the metal (liquid/solid), then it is transported by diffusion or convection (depending on the time scale). After a sufficient time, a specific depth profile develops. Finally, the metallic phases and precipitates arise according to the phase diagram.
- *Nucleation and solidification:* After the nucleation processes, certain solidification morphologies evolve depending on gradients of temperature and concentrations at the solid-liquid interface. The grain size and induced stress of these phases now determine considerably the macroscopic characteristics, and at least the process result being the benchmark for its industrial application performance.
- *Solid-state phase transformation:* It has to be taken into account that during cooling to room temperature, phase transformations occur that determine the properties of the surface treated materials as well. The kind of phase transformation taking place depends on the surface chemistry and also on the cooling conditions.

### 2.2.1.2 Process control

To be able to handle the processing, widespread experience is needed. First, you have to be concerned about all parameters of the laser and its beam. Probably, the most important parameter here is the power density, which, for example, can be varied by the spot size  $D_b$ . Users also have to choose between pulsed- and continuous wave mode (cw-mode). All-encompassing, they determine the energy incorporation, the temporal distribution, and the interaction time. For the cw-mode, the scan velocity  $v_s$  is an important parameter, while in pulsed mode the pulse frequency can become the determining one. By the variation of geometrical scan parameter (lateral shift  $\delta$ , spot size  $D_b$ , velocity  $v_s$ , pulse frequency  $f$ , and number of scans  $n$ ) it is arbitrarily possible to steer and thus to handle the total process. It allows achieving custom-made coating characteristics, obtained by a skillful combination of parameters.

A further parameter of the procedure is the gas pressure or gas flow. Pressure dependency has been studied in various publications [29–32] for different systems. Depending on the local gas conditions, N or C uptake varies, which is attributed to the arising process chain at the very surface. Moreover, this indirectly affects the surface quality and morphology. In this context, the N or C content within the gas or the gas mixture amounts to a crucial parameter. The most neglected variable is the material itself. During processing, optical, thermodynamical, and mechanical properties of the material are modified. Due to changes in the aggregate state, the mechanisms mentioned are strongly influenced. At least, all contribute to the solidification behavior and the quality of the functional coatings.

The classification of the process in terms of time scales is very important, because the synthesis mechanisms must be assigned and related to correct "physics." Generally, the range extends from femtoseconds, the duration of the shortest laser

pulses, up to minutes or hours in the case of processing durations. For the laser material processing on different timescales, various investigations, review articles [33], or books [34,35] exist. The treatment by ns-pulses by Nd:YAG- or Excimer lasers can be handled as shown in the upcoming sections. Convective effects can influence the process as well. They determine the surface quality and the material transport at cw-mode nitriding at millisecond timescale. Strong surface deformations and problems with the homogeneity are expected. Treatment and processing durations/periods differ from some seconds up to a few minutes per square centimeter. This is short compared to the classical PVD procedures (hours) and regarding engineering tasks of special interest for localized treatments.

## 2.2.2 Materials and applications

Coating synthesis in reactive atmospheres applying lasers was examined in detail by Schaaf *et al.* [4] for different systems. Iron and silicon carbide were synthesized in methane. It revealed a significant change of the physical and chemical characteristics. Interesting experiments in silicon were accomplished in [36]. A very stable SiC phase was produced. In [37], essential characteristics of steel are changed by this method. Nitriding seems to be the most frequently used method among them. Thus, for example the very interesting iron nitrides in [38] were observed, which entailed an enormous increase of the tribological properties. This is also observed for AlN in [39]. The most examined system for this method is probably TiN. For this reason it was selected for the investigations accomplished here. It allows a detailed insight into the process as well as the physics.

## 2.3 Laser nitriding of titanium

The attempts and progress that have been made in improving the wear properties of titanium-based materials have been reviewed in several papers [4,40–46]. The production of TiN-coatings in reactive atmospheres by means of laser irradiation goes back to the 1980s and 1990s [40,47–59]. All exhibit an enormous improvement of the properties of the surfaces. For example, in [60] characteristics of medical components have been improved. Utilizing CO<sub>2</sub> laser [61–63] coatings of some hundred micrometers thicknesses were realized.

The work of Labudovic and co-authors [64] and Nwobu *et al.* [65] tries to analyse the entire process more exactly. Labudovic indicates that the following reactions arise during the layer synthesis on titanium (assuming a temperature below the evaporation threshold):

1. adsorption:  $[Ti] + N_2 \rightarrow [Ti] + [N_2]$
2. dissociation:  $[N_2] \rightarrow 2N$
3. diffusion:  $[N](surface) \rightarrow [N](surface)$
4. TiN-formation:  $[Ti(N)] \rightarrow TiN + [Ti(N)]'$
5. solidification:  $[Ti(N)]' \rightarrow TiN + \alpha-Ti(N)$

The square brackets [ ] describe liquid phases. It becomes clear, which complex sequences take place and what effort is required. Besides TiN formation nitrogen, dissolution in the pure hexagonal  $\alpha$ -titanium (solid solution) occurs. Nwobu discusses the problem in a similar way. He postulates nitrogen incorporation by convection into the liquid titanium followed by an exothermal reaction in the melt. Various other authors, for example, in [66–72] have already verified the results. Following the subject becomes a more detailed discussion.

### 2.3.1 cw-Mode laser nitriding

#### 2.3.1.1 Processing technologies

The general experimental equipment required for the laser nitriding process includes a high power cw-mode laser, equipment that allows the mixing of nitrogen with argon or helium and delivering the so-called processing gas to the melt pool, as well as a machine that permits the exact positioning and movement of the laser or the sample. Most workers utilized high-power CO<sub>2</sub> lasers and, to a lesser extent, Nd:YAG lasers with average power above 1 kW. In the last few years, high power diode lasers are utilized more for cw-mode laser nitriding of titanium showing a high potential, especially for the generation of thick wear-resistant layers [73,74].

Generally, there are four different experimental setups for the delivering of the processing gas to the working area:

- (a) *A side nozzle gas supply*: This configuration was and is frequently used because of its simplicity [40,49,52,75]. However, drawbacks connected with this setup are the alignment of the nozzle, emerging gas turbulences, and an insufficient shielding from the atmosphere leading to process instability and unsatisfactory reproducibility.
- (b) *A coaxial nozzle gas supply*: This enables the possibility for improved nozzle alignment and hence reproducibility [50,72,76–78]. There are still possible turbulences induced by the gas flow and restricted shielding from the atmosphere can limit process control and stability.
- (c) *A shroud arrangement*: The limitations of side and coaxial nozzle gas supplies can be overcome by the application of purpose-designed shrouds [56,60,79]. Here, a precise control of the composition of the processing gas atmosphere and an accurate shielding from the atmosphere, which prevents uncontrolled oxidation, can be accomplished.
- (d) *A gas chamber arrangement*: The use of a gas chamber is a second way to supply optimized conditions for laser nitriding with respect to process stability and reproducibility [80]. However, if compared to the shroud arrangements, a more complex equipment, which is more restrictive with respect to sample size and flexibility of the processing, is required.

In order to facilitate laser nitriding of larger components on an industrial scale, special equipment that combines the advantages of a shroud and gas chamber equipment was developed [73]. The developed equipment consists of a sealed process chamber with an integrated rotating or swivelling clamping device and a mounted shielding device, such as the one shown in [Figure 2.2](#). The shielding device is constructed in such a way that it can be controlled by a robot or machine axis and it can



**Figure 2.2** Modern equipment for flexible laser nitriding of large parts at Fraunhofer IWS.

contain the optic of a modern fiber-coupled diode laser and the required gas supply. Given this arrangement of equipment, complex shaped parts of different titanium alloys, with dimensions of up to  $400\text{ mm} \times 50\text{ mm} \times 10\text{ mm}$ , were successfully laser-nitrided.

### 2.3.1.2 *Laser nitriding of Ti-6Al-4V*

Most investigations regarding the metallurgy of laser nitriding were carried out on the widely used high-strength ( $\alpha+\beta$ )-Ti alloy Ti-6Al-4V. For this reason, the general aspects of phase formation, structural evolution, mechanical properties, and wear behavior, depending on the processing parameters, will be initially described for this alloy. Depending on the processing parameters applied, complex microstructures are formed in laser-nitrided Ti-6Al-4V. Typical parameters that influence the microstructural evolution are the average laser power, spot diameter, transverse speed, and overlap ratio, as well as the nitrogen content of the processing gas and flow rates. Because it was found that the nitrogen content of the processing gas was the key processing parameter influencing surface structure, hardness and wear resistance get the most attention regarding the effect of this parameter.

It is known that complex microstructures contain face-centered cubic (fcc) titanium nitride ( $\delta$ -TiN), tetragonal (tet) titanium nitride ( $\text{Ti}_2\text{N}$ ), and hexagonal (hex) titanium nitride ( $\text{TiN}_{0.3}$ ), as well as hexagonal  $\alpha$ - and  $\alpha'$ -titanium ( $\alpha$ - and  $\alpha'$ -Ti) and body-centered cubic (bcc)  $\beta$ -titanium ( $\beta$ -Ti) [77,78,81–83]. It was shown in this work that the type, volume fraction, and distribution of the phases formed during laser nitriding were strongly determined by the nitrogen content of the processing gas. The solidification reactions and the solid-state phase transformations taking place in laser-nitrided

**Table 2.1 Metallic phase transformations during cw-mode laser nitriding at different nitrogen process gas conditions**

Nitrogen content	Solidification	Solid state transformations
Low	$\text{melt} \Rightarrow \beta\text{-Ti}$	$\beta\text{-Ti} \Rightarrow \alpha'$ (martensitic) $\beta\text{-Ti} \Rightarrow \alpha\text{-Ti} + \beta\text{-Ti}$
Medium	$\text{melt} \Rightarrow \text{TiN}_{0.3}$ and $\text{melt} + \text{TiN}_{0.3} \Rightarrow \beta\text{-Ti}$	$\beta\text{-Ti} \Rightarrow \alpha\text{-Ti} + \beta\text{-Ti}$
High	$\text{melt} \Rightarrow \delta\text{-TiN}$ and $\text{melt} + \delta\text{-TiN} \Rightarrow \text{TiN}_{0.3}$ and $\text{melt} + \text{TiN}_{0.3} \Rightarrow \beta\text{-Ti}$	$\delta\text{-TiN} + \text{TiN}_{0.3} \Rightarrow \text{Ti}_2\text{N}$ and $\beta\text{-Ti} \Rightarrow \alpha\text{-Ti} + \beta\text{-Ti}$

Ti-6Al-4V in dependence of the nitrogen content of the processing can be summarized in the following manner in [Table 2.1](#).

If the processing gas contains only small amounts of nitrogen, the whole absorbed nitrogen is dissolved interstitially in the  $\alpha'$ - or  $\alpha$ -Ti lattice. In contrast, medium and high nitrogen concentration within the processing gas inevitably leads to formation of titanium nitrides ( $\delta\text{-TiN}$  and  $\text{TiN}_{0.3}$ ) during solidification.

Cracking is a major concern connected with the process of laser nitriding, especially if very thick layers are produced. Because the formation of large and brittle titanium nitrides strongly promotes crack formation, the most effective way to prevent it is to reduce the nitrogen content of the processing gas in order to impede nitride formation [\[84\]](#). However, choosing this approach causes losses in layer hardness and wear resistance that usually have to be accepted. Other approaches such as preheating [\[85\]](#), additional remelting [\[86\]](#), and the use of spinning laser beams [\[87\]](#), even though they mainly avoid the loss in hardness and wear resistance, usually have only small benefit and involve considerably more experimental effort.

Applying high-power cw-mode lasers and processing gas with different nitrogen concentration laser nitriding enables the production of layers of up to 1.5 mm thick exhibiting hardening from 400 to 2000 HV. It was shown that the hardness of laser-nitrided Ti-6Al-4V increased with the nitrogen content of the processing gas [\[82\]](#). At low nitrogen concentrations, the increase in hardness was mainly attributed to solid solution hardening of the titanium by nitrogen. However, at high nitrogen concentrations, the main hardening mechanism is the increased formation of  $\delta\text{-TiN}$ .

Over the last few decades, the beneficial effect of laser nitriding on abrasion [\[60,88\]](#), sliding [\[63,89–91\]](#), cavitation [\[56,69,81,92\]](#), and water-droplet-induced wear [\[93,94\]](#) was reported for Ti-6Al-4V. The abrasive wear resistance of Ti-6Al-4V can only be improved if thick layers exhibiting hardness above 800 HV are generated. Thick nitride layers with such a high hardness normally contain large cracks, so that the application of laser nitriding for abrasive wear protection is hindered. Because layer hardness values above 600 HV could already significantly improve sliding wear resistance, the laser nitriding process can normally be controlled in such a way that crack formation can be avoided. Therefore, sliding wear protection of titanium alloys by cw-mode laser nitriding appears much more promising than abrasive wear protection.

The results being published in the literature demonstrate that the process of cw-mode laser nitriding seems to be most promising for the wear-protection of Ti-6Al-4V against cavitation and water droplet induced wear phenomena. Already, a moderate hardness in the range of 400–600 HV has proven to be appropriate to improve the cavitation and water droplet erosion resistance of Ti-6Al-4V. It was found that an optimum protection against cavitation wear could already be achieved using a low nitrogen content of the processing gas during laser processing, typically in the range from 10% to 15% [81].

From early experiments, the detrimental effects of laser nitriding on the static and cyclic strength of Ti-6Al-4V was documented [40,49,60,93]. By qualifying a 4-point bending test equipped with an acoustic emission analysis system it was possible to assess the load-carrying capacities of laser-nitrided Ti-6Al-4V in an extensive study [95]. According to this work, the crack sensitivity increased significantly with increasing nitrogen content of the processing gas already in the early range from 5% to 25%. Careful surface grinding reduced the crack sensitivity up to a level of 16% of nitrogen in the processing gas. Titanium nitrides forming in the nitrided layer for higher nitrogen concentrations are thought responsible for a high crack sensitivity leading to early crack initiation during 4-point bending.

From comprehensive fatigue testing (Figure 2.3), it was concluded that the formation of titanium nitrides and tensile residual stresses are mainly responsible

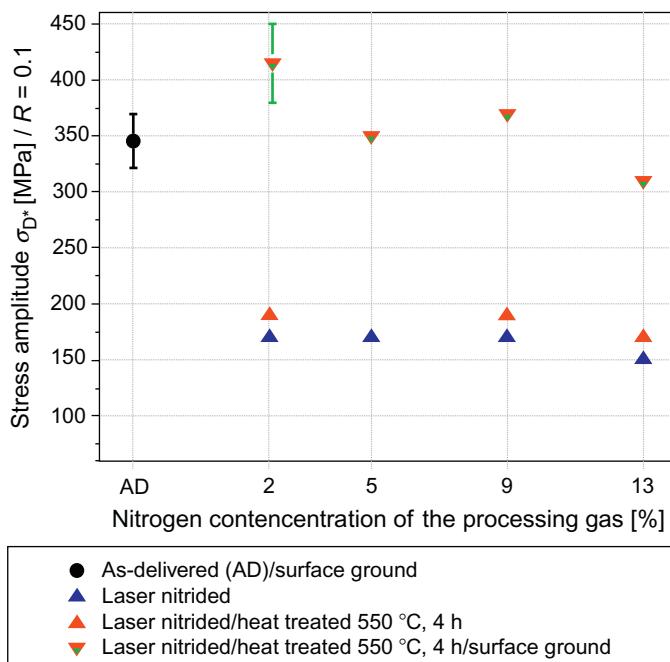


**Figure 2.3** Fatigue strength of laser nitride Ti-6Al-4V in the dependence of surface state and nitriding conditions.

for the loss of fatigue strength in laser-nitrided Ti-6Al-4V. Generally, high fatigue strengths can only be obtained if the laser-nitrided layer contains no massive titanium nitrides. Typically, this means that the layer hardness has to be kept below approximately 550 HV. This can only be achieved by reducing the nitrogen content of the processing gas. Furthermore, the fatigue strength of laser-nitrided Ti-6Al-4V also depends on the surface condition with respect to nitride formation in top layers, roughness, and residual stresses. The fatigue strength of Ti-6Al-4V laser nitrided under processing gases containing little nitrogen can reach very high levels of the as-delivered state, if a combined surface treatment consisting of grinding or shot peening to remove thin top layers and a stress-relief heat treatment is performed. The positive effect of surface grinding can be understood, if you take into consideration that thin continuous top layers form on top of all laser-nitrided samples, which consist of brittle titanium nitrides and contain pores and microcracks [81].

### 2.3.1.3 *Laser nitriding of other titanium alloys*

Among the other alloys, titanium of commercial purity (cp-Ti) was mainly addressed. The predominant structural feature detected in laser-nitrided cp-Ti was a mixture of  $\alpha'$ -Ti and  $\delta$ -TiN [59,62,87]. With increasing nitrogen content of the processing gas, the volume fraction of  $\delta$ -TiN rises at the expense of the  $\alpha'$ -Ti leading to a higher surface hardness.

It will be revealed by previously unpublished work that the composition of the alloy has a significant impact on the structural evolution within the laser-nitrided surface region. In this work, a detailed comparative structural analysis was conducted on laser-nitrided cp-Ti ( $\alpha$ -Ti alloy), Ti-6Al-4V, Ti-4, 5Al-3V-2Mo-2Fe (SP700) (( $\alpha$ + $\beta$ )-Ti alloys), and Ti-10V-2Fe-3Al ( $\beta$ -Ti alloy). Generally, for all types of Ti alloys, the structure in the laser-nitrided zone changes from pure metallic ( $\alpha'$ -Ti,  $\alpha$ -Ti,  $\beta$ -Ti) to a mixture of titanium nitrides ( $TiN_{0.3}$ ,  $\delta$ -TiN) embedded in a metallic matrix, if the nitrogen content of the processing gas increases. However, with increasing  $\beta$ -stabilization of the Ti alloy, the onset of nitride formation during solidification shifts to lower nitrogen concentrations (Figure 2.4). From this behavior, it is concluded that low-alloyed materials such as cp-Ti or Ti-6Al-4V can dissolve more nitrogen interstitially than heavier alloyed materials such as SP700 and Ti-10V-2Fe-3Al. This structural development has a strong impact on the resulting mechanical properties and the wear behavior. Hence, the largest increase in hardness was attained in cp-Ti, followed by Ti-6Al-4V, SP700, and Ti-10V-2Fe-3Al. It is remarkable that using medium nitrogen concentrations for laser processing, similar hardness in the range of 450-550 HV can be attained for the different alloys, even though the hardness in the as-delivered state differed considerably. A similar behavior has been observed for the wear behavior under cavitation erosion [84]. Initially, the cavitation erosion resistance distinctly improved with increasing nitrogen content of the processing gas for all considered titanium alloys in a very similar manner. But, already at a very low nitrogen concentration, the resistance against cavitation wear reaches an optimum and cannot be further improved. The same optimum wear-resistance level could be

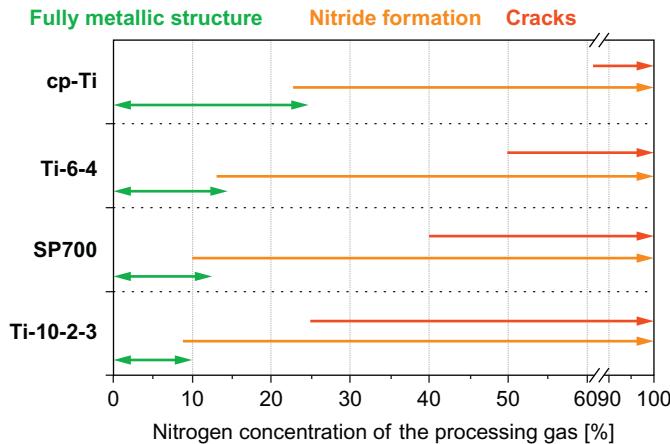


**Figure 2.4** Schematic sketch-up of the structural evolution in different laser nitrided Ti alloys.

achieved for the different types of alloy, even though they exhibit a very different cavitation wear resistance in the as-delivered state.

Generally, in metals and alloys all metallurgical measures leading to strengthening should also improve cavitation erosion resistance except the alloy is too brittle to deform plastically [96,97]. As long as the strengthening is mainly caused by solid solution hardening of the nitrogen, the cavitation erosion resistance increases. But the development of structural inhomogeneities with increasing nitrogen content of the processing gas prevents a further improvement of cavitation wear resistance with strength. Especially, differences in strength between the metallic matrix and titanium nitrides lead to a selective erosion attack along the softer  $\alpha$ - and  $\beta$ -Ti phases. As a result, the wear of harder phases is governed by the erosion of the softer phases and, therefore, the overall wear performance deteriorates. Because  $\beta$ -Ti alloys can dissolve less nitrogen interstitially than  $\alpha$ - and  $(\alpha+\beta)$ -Ti alloys, their potential for improvements of cavitation wear performance is significantly lower. Accordingly, the maximum benefit of cw-mode laser nitriding with respect to cavitation and also water droplet wear protection will be achieved in cp-Ti and other reasonably priced low-alloyed titanium.

### 2.3.2 Pulsed laser nitriding

Compared to conventional nitriding methods such as plasma nitriding, the use of short laser pulses has several advantages. Due to the small heat-affected zone, both in depth and lateral dimension, pieces sensitive to heat and of complex shape can be modified. Laser nitriding is a very efficient technique, allowing accurate spatial control of the surface treatment without any undesired heating of the substrate.

Laser pulses usually will be classified by their timescales and energy densities. This is very important with respect to nitriding control and the required understanding of involved phenomena because the inducing processes of coating formation have to be

related to correct “physics.” An overview on selected publications within this field will be given in this subsection. Considering the extensive demands in surface engineering, pulsed laser nitriding becomes an alternative way, offering some advantages but also disadvantages. The fast treatment leads to further hardening compared to conventional processing due to rapid cooling rates. The well-known fatigue issue during prolonged heat treatments on titanium will be minimized, too. Nevertheless, the process is very sensitive to the huge amount of process parameters and is hard to control. The process window is small and engineering and technical challenges have to be solved.

The laser material processing by laser pulses on different timescales has been discussed in various overview articles [18,33] or books [34,35]. For example, nanosecond pulses refer to very short interaction times and arise in coating thicknesses on a hundred nanometer scale. Pulse durations within the range of microseconds are again different in their performance. Convective effects can influence the process, determine the surface quality, and affect the material transport. The variation in the process efficiency is not only related to the pulse duration. Besides, geometrical aspects (substrate, technical equipment), the scanning parameters (meandering, spot overlap, scan speed, etc.), or the gas respective to nitrogen flow (nozzle) or background pressure (chamber) are influencing the performance. Table 2.2 shows important aspects for different timescales.

During the last few decades, an impressive number of process variations and applications have been developed. Hybrid engineering, or coating processing systems, became and will become important. In this context, surface engineering by pulsed lasers can be assisted by PVD or spraying processes or, for example, by applying mechanical stress fields during processing in order to minimize thermal-induced cracking, especially on the millisecond timescale. Besides nitriding, the use of carbon for alloying according a laser carburization has been investigated as well and will be described now.

## 2.4 Laser carburization of materials

Besides laser nitriding and laser carburization, even the hydriding of metals has been successfully proven [117–119]. Carburization (carbiding) is a common method for improving hardness, mechanical properties, and wear and corrosion resistance of steels [4,120,121]. The well-studied Fe-C system has a great metallurgical importance, because iron is the most employed material for construction and tool fabrication. And carbon is its most important alloying element.

The Fe-C phase diagram can be expressed both with the metastable  $\text{Fe}_3\text{C}$  and with the graphite system, because they build up the only thermodynamically stable phases in iron. The orthorhombic  $\theta\text{-Fe}_3\text{C}$  (cementite) has an enormous technological importance due to its extreme hardness (900–1100 HV). There still exist many carbides (the orthorhombic  $\eta\text{-Fe}_2\text{C}$  and  $\text{Fe}_{20}\text{C}_9$ , the hexagonal  $\varepsilon\text{-Fe}_2\text{C}$ ,  $\text{Fe}_7\text{C}_3$  and  $\varepsilon\text{-Fe}_{(1-x)}\text{C}_x$ , the monoclinic  $\chi\text{-Fe}_5\text{C}_2$ , and the cubic  $\text{Fe}_4\text{C}$  [121], but they are invariably less stable

**Table 2.2 Pulsed treatment and its performance**

Time scale	Pro and contra	References
fs Nitriding	The fundamental approach revealed an inefficiency of the process. Due to the ultra-short interaction time direct ablation takes place arising in insufficient nitrogen uptake. Here, the duration of efficient melting, nitrogen absorption and diffusion is too short. Only the very first top layer is treated and modified. The properties and the quality of the materials surfaces have been strongly decreased.	[17,98–101]
ns Nitriding	<i>Nd:YAG laser nitriding:</i> The surface structure is strongly determined by the overlap of the individual laser pulses and the energy entry per surface area element. The short interaction and diffusion time limits the thickness. For the case of exceeding the evaporation threshold it can be recognized that a weak melt ejection at the interaction zone edges, referring to the so-called Piston effect occurs. Fundamental studies showed the strong dependency on the laser energy density and on the gaseous conditions. High complexity is one of the main reasons for the challenges in process controlling. <i>Excimer laser nitriding:</i> Treatments reveal in bronze-yellow coloured surfaces with a roughness determined by the multi-pulse scans and of compound layer thickness of about 200 nm. Other studies verified the strong dependence of phase formation on the induced nitrogen ionization and the plasma interaction. Diffusion-like profiles indicate the nitrogen transport limits the coating properties. At least, all experiments at UV offer a high efficiency being related to the high energy coupling (high optical absorption coefficient) in the UV range, especially for titanium.	[1,17,22–24, 102–108]
μs Nitriding	One of the very first successful experiments in 1985 on laser nitriding on cp-Ti was performed applying a microsecond pulsed CO <sub>2</sub> laser. It has been proposed that the melting depth determines nitrogen uptake and the coating thickness. Optical breakdown and plasma shielding are further affecting mechanisms being involved. Non equilibrium conditions arise during the irradiation offering unstable and inhomogeneous nitriding results. All-encompassing, there is not much literature available in this regime, because the processing efficiency will be significantly increased by longer pulses or even cw-mode irradiation. Secondly, most commercial available laser systems do work on that time regime and supplemental equipment becomes necessary.	[17,20,30, 109–114]

(Continued)

**Table 2.2 Continued**

Time scale	Pro and contra	References
ms Nitriding	This is most widely spread “version” of pulsed nitriding. Anyway, cw-mode treatments are still more distributed but the reviewing of previous results appears in very interesting information. At adequate conditions hardness values of 13 GPa were achieved. After further optimization of the scan parameters a coating thickness of 30 $\mu\text{m}$ having a surface roughness of about 2 $\mu\text{m}$ has been produced. The microstructure developed according the solidification conditions in needle-like TiN phases and dendrites. Cracks can be avoided by controlling the pulse energy and the related cooling rate. 100 $\mu\text{m}$ coatings containing dendritic TiN embedded in $\alpha$ -titanium with dissolved nitrogen. According the binary phase $\text{Ti}_2\text{N}$ was observed at the underneath diffusion zone. Dendritic structures were strongly affected by convective and thermo-capillary effects.	[21,72,78,116]

than  $\theta\text{-Fe}_3\text{C}$ . The  $\varepsilon\text{-Fe}_{(1-x)}\text{C}_x$  reveals a large range of the carbon concentration with  $0.143 < x < 0.333$ . The formation of these carbides can be arranged as follows: carbon clusters  $\Rightarrow \varepsilon\text{-phase} \Rightarrow \chi\text{-carbide} \Rightarrow \theta\text{-phase}$ . The same sequence also holds for the increase in hardness [122]. A serious disadvantage is that pure  $\text{Fe}_3\text{C}$  cannot be obtained as a single phase due to its embedding in the iron matrix. In some recent investigations, the successful formation of pure  $\text{Fe}_3\text{C}$  layers [2] and several metastable iron carbides was reported. The issue still remains a challenge.

#### **2.4.1 Laser carburization of iron and carbon steel**

Irradiations of iron (Armco, Fe > 99.85%) substrates in controlled methane atmospheres have been performed with nanosecond pulses of an excimer laser, leading to the formation of carbide surface layers, with different stoichiometry and crystallographic structures. The evolution and abundance of each phase is correlated to the experimental parameters, such as the number of laser pulses, the laser energy fluence, and the ambient gas pressure.

The results revealed that under proper experimental conditions, the laser treatment can produce almost homogeneous layers of nitride/carbide, where the composition and the structure are determined only by the parameters of irradiation. As an example for pure iron, the phase formation upon laser irradiation in a methane atmosphere at various pressures is shown in Figure 2.5. It is seen that, for higher pressure, almost a pure cementite surface layer is formed. Amazing potential for upcoming applications occurs.

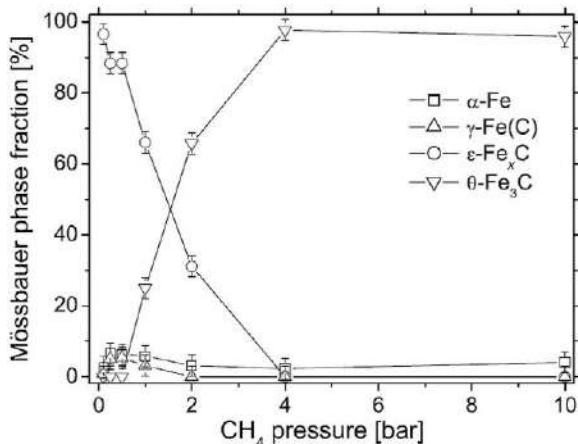


**Figure 2.5** Phase fractions obtained from the Mössbauer analysis versus the methane gas pressure. The sample surface was irradiated with  $11 \times 12$  meandering pulses [8].

#### 2.4.2 Laser carburization of austenitic stainless steel

The carburization of austenitic stainless steel has been successfully implemented, too. This treatment leads to the interstitial incorporation of carbon atoms into the fcc lattice of the austenitic stainless steel [2,123–125]. If the carbon content exceeds the solubility limit, the supersaturated austenite lattice transforms into an amorphous carbon-containing phase [126].

#### 2.4.3 Carburization of various nonferrous materials

Nonferrous materials have been investigated for the laser carburization process as well. There have been experiments carried out for aluminium [8] and silicon in methane atmospheres. Considering the aluminium case, where nitriding leads to nice layers of AlN [29], aluminium carbide ( $\text{Al}_4\text{C}_3$ ) does not meet the technological “fortune” of aluminium nitride. Few publications and little attention have been given to this compound in comparison to its nitride counterpart. Nevertheless, the laser irradiation of aluminium substrates in a methane atmosphere has been performed in order to demonstrate that the carbon incorporation is effective. The sample treated with the  $16 \times 16$  meander scan at the laser fluence of  $4 \text{ J/cm}^2$  in 3 bar CH<sub>4</sub> has been analyzed by means of RBS, XRD, and nanoindentation.

The RBS measurement revealed an average carbon content of about 20 at.%, as shown in Figure 2.6. The nanoindentation measurement results in Figure 2.7 showed a considerable increase of the surface hardness after the treatment (about 4 times larger than the virgin substrate). Nevertheless, very poor crystallinity has been observed by GIXRD (with incidence angle of  $1^\circ$ ): a broad peak centered at the Bragg angle  $2\theta = 31.6^\circ$  ( $7.2^\circ$  FWHM) appears in the diffraction pattern of the irradiated

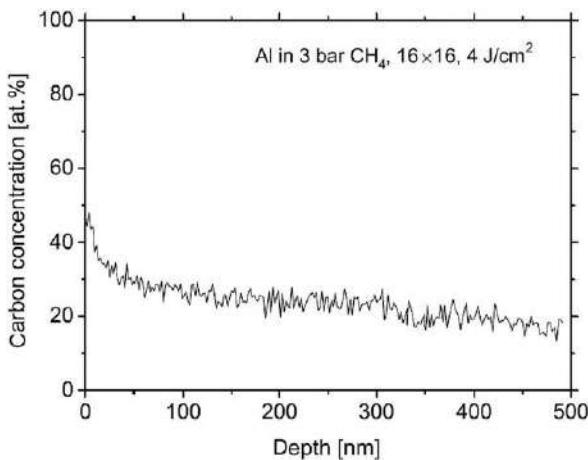


**Figure 2.6** RBS carbon depth profile of the aluminium sample meandered in 3 bar CH<sub>4</sub>. Data from Ref. [2].

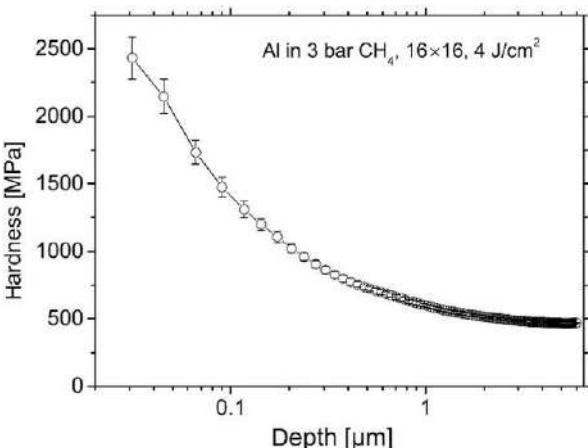


**Figure 2.7** Nanoindentation hardness profile of the laser carburized Al substrate.

specimen, as reported in Figure 2.8. The position of the Bragg reflection is in good agreement with the value of the most intense diffraction peak of crystalline Al<sub>4</sub>C<sub>3</sub> ( $\langle 0\bar{1}2 \rangle$  peak at  $2\theta = 31:74^\circ$ ), suggesting the formation of amorphous aluminium carbide. The poor crystallinity is attributed to the more complex atomic arrangement of the Al<sub>4</sub>C<sub>3</sub> phase compared to AlN. The rapid quenching rate obtained with nanosecond laser pulses might hinder the long-range atomic order. Thus, even if the basic Al<sub>4</sub>C<sub>3</sub> arrangement is locally formed, the crystallites are not large enough to give a clear XRD signal, and only the main interatomic distance is observed (i.e., the most intense XRD peak).

Similar effects have been found in the silicon substrates irradiated in a nitrogen atmosphere, where the stoichiometry of the nitride phase is  $\text{Si}_3\text{N}_4$  (the role of Al atom in the aluminium carbide is played by the N atom in the silicon nitride).

Aiming to the formation of SiC, the influence of the number of laser pulses on the carbon incorporation into the silicon matrix has been investigated by Carpene *et al.* in [8]. As was shown in [36], the synthesis of SiC is successful, but its optimization is required (Figure 2.9).

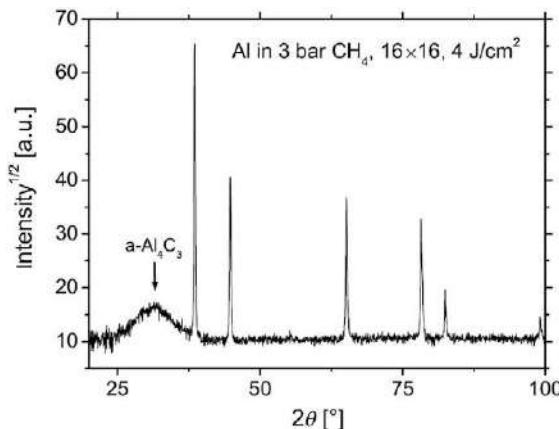


**Figure 2.8**  $1^\circ$  GIXRD pattern of the laser carburized aluminium sample. The broad peak at  $2\theta = 31.6^\circ$  indicates the formation of amorphous  $\text{Al}_4\text{C}_3$ , all other peaks belong to the fcc Al matrix.

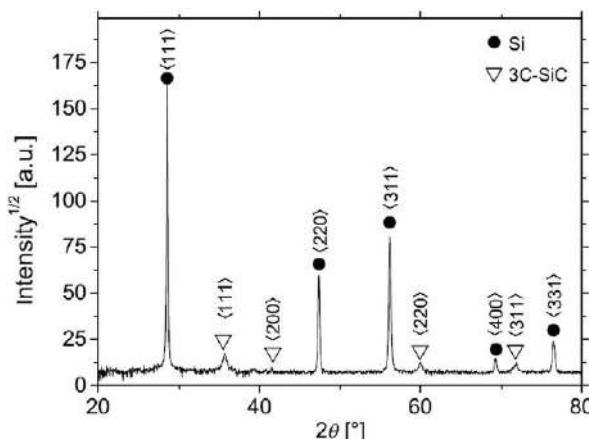


**Figure 2.9**  $2^\circ$  GIXRD diffractogram of the pure Si sample irradiated in  $\text{CH}_4$  with 256 pulses: ( $\nabla$ ) cubic SiC, ( $\bullet$ ) polycrystalline Si.  
From [36].

$\text{Al}_4\text{C}_3$  formation was shown by Fariaut *et al.* [127] during excimer laser irradiation in propylene. They proposed improved carburization efficiency compared to methane. The use of this setup seems to be a candidate for further innovative studies.

#### **2.4.4 Nitrocarburization of materials**

This type of laser surface treatment was carried out by Shapochkin and Smirnov [128] but in a step-by-step way. The alloying effect is based on a classical furnace treatment followed by laser irradiation leading to a high resistance to contact fatigue. All-encompassing, a comprehensive number of studies in terms of pure laser-based processes does not exist, hence future possibilities should be fathomed out. New studies on AISI H12 tool steel [129] applying a nitrogen gas flow might be a base for extending application-oriented research.

### **2.5 Future trends**

Scientists and engineers have been making efforts to improve and optimize laser nitriding and carburization of materials and related methods. It has been shown that a wide range of possible applications for such laser processing technologies have been set up. Especially for niches in surface engineering, beside the common deposition methods such as CVD, PVD, or salt bath nitriding, the method has become a serious competitor. Surface treatments requiring specific demands, very special local engineering issues, or tailor-made product developments will be the field of application. The widespread aspects of materials processing, the involved phenomena, the flexibility of laser irradiation, and the success on treating titanium clearly show the technological potential of laser-assisted nitriding and carburizing methods. Lasers in pulsed or cw-mode can be used to control the interaction time and the heat entry. The ambient gas (flow, nozzle, and chamber) can be applied to offer a wide pressure range. Engineers and coaters get a unique surface property control panel.

The chapter clearly revealed that the method consists of a complicated interaction of many occurring physical and chemical processes and phenomena: laser material interactions itself, heating, phase transformations, diffusion, plasma formation, pressure-induced effects, and many more have to be understood and controlled. Thus, it is obvious that there is a need for optimization of the process for each desired application. Trends show that hybrid treatments can lead to a better performance. “Tailor-made” can be a trade market offering the flexibility to achieve superior properties of the laser beam modified materials for almost every application. By taking care to consider the economic aspects of the development of new flexible and cheaper laser sources and the presented increase in the ability to control the underlying and interacting processes, this is still an issue to be tackled. A far-reaching establishment in different industrial branches, which means being a serious competitor to conventional methods, requires further endeavors of research in terms of performance, processing time, results/quality, and, as always, cost.

## 2.6 Sources of further information and advice

More information on the subject from scientific point of view is available in review articles [4,18]. Reports on application developments and further action inside the topic can be found at the Fraunhofer Institutes IPT and IWS. A very useful common introduction on steel hardening is shown in [130].

## Acknowledgment

This work was partially funded by the Deutsche Forschungsgemeinschaft DFG (grants Scha 632/3, Scha 632/4, Scha 632/10, Scha 632/11, and KA 1812/1).

## References

- [1] D. Höche, H. Schikora, H. Zutz, R. Queitsch, A. Emmel, P. Schaaf, Microstructure of TiN coatings synthesized by direct pulsed Nd:YAG laser nitriding of titanium: development of grain size, microstrain, and grain orientation, *Appl. Phys. A: Mater. Sci. Process.* 91 (2008) 305–314.
- [2] P. Schaaf, M. Kahle, E. Carpene, Reactive laser synthesis of carbides and nitrides, *Appl. Surf. Sci.* 247 (2005) 607–615.
- [3] A.F. Saleh, J.H. Abboud, K.Y. Benyounis, Surface carburizing of Ti–6Al–4V alloy by laser melting, *Opt. Lasers Eng.* 48 (2010) 257–267.
- [4] P. Schaaf, Laser nitriding of metals, *Prog. Mater. Sci.* 47 (2002) 1–161.
- [5] J. Barnikel, K. Schutte, H.W. Bergmann, Nitrieren von Aluminiumlegierungen mit UV-laserstrahlung, *HTM—Härterei-Tech. Mitt.* 52 (1997) 91–93.
- [6] J. Barnikel, T. Seefeld, K. Schutte, H.W. Bergmann, Erhöhung der Korrosionsbeständigkeit von Aluminiumlegierungen durch Excimerlaserstrahlung, *HTM—Härterei-Tech. Mitt.* 52 (1997) 94–96.
- [7] C. Meneau, P. Andreazza, C. Andreazza-Vignolle, P. Goudeau, J.P. Villain, C. Boulmer-Leborgne, Laser surface modification: structural and tribological studies of AlN coatings, *Surf. Coat. Technol.* 100–101 (1998) 12–16.
- [8] E. Carpene, Excimer laser treatments of iron, aluminum and silicon substrates in nitrogen and methane atmospheres (Ph.D. Thesis), Göttingen, 2002.
- [9] E.C. Santos, K. Kida, J. Rozwadowska, T. Honda, H. Koike, Y. Kashima, K. Kanemasu, R. Matsumoto, Wear resistance improvement of titanium bearings by laser gas nitriding, *Appl. Mech. Mater.* 152 (2012) 1227–1232.
- [10] S. Singaravelu, J. Klopf, G. Krafft, M. Kelley, Laser Nitriding of Niobium for Application to Superconducting Radio-Frequency Accelerator Cavities, *J. Vac. Sci. Technol. B* 29 (2011) 061803-1 to 061803-6.
- [11] B.S. Yilbas, S.S. Akhtar, C. Karatas, Laser nitriding of the surface of phosphor bronze, *Int. J. Adv. Manuf. Technol.* 65 (2013) 1553–1565.
- [12] J.H. Abboud, K.Y. Benyounis, A.G. Olabi, M.S.J. Hashmi, Laser surface treatments of iron-based substrates for automotive application, *J. Mater. Process. Technol.* 182 (2007) 427–431.

- [13] Z.D. Liu, X.C. Zhang, F.Z. Xuan, Z.D. Wang, S.T. Tu, In situ synthesis of TiN/Ti<sub>3</sub>Al intermetallic matrix composite coatings on Ti6Al4V alloy, *Mater. Des.* 37 (2012) 268–273.
- [14] X.C. Zhang, Z.D. Liu, J.S. Xu, F.Z. Xuan, Z.D. Wang, S.T. Tu, Synthesis of TiN/Ti<sub>3</sub>Al composite coatings on Ti-6Al-4V alloy by plasma spraying and laser nitriding, *Surf. Coat. Technol.* 228 (Suppl. 1) (2013) S107–S110.
- [15] N. Al-Aqeeli, B.S. Yilbas, N. Tabet, The effect of laser pulse frequency on the microstructure and morphology of duplex treated Ti-6Al-4V alloy, *Surf. Coat. Technol.* 205 (2011) 3073–3079.
- [16] S. Yang, H.C. Man, W. Xing, X. Zheng, Adhesion strength of plasma-sprayed hydroxyapatite coatings on laser gas-nitrided pure titanium, *Surf. Coat. Technol.* 203 (2009) 3116–3122.
- [17] E. Carpene, P. Schaaf, M. Han, K. Lieb, M. Shinn, Reactive surface processing by irradiation with excimer laser, Nd:YAG laser, free electron laser and Ti:sapphire laser in nitrogen atmosphere, *Appl. Surf. Sci.* 186 (2002) 195–199.
- [18] D. Höche, P. Schaaf, Laser nitriding: investigations on the model system TiN. A review, *Heat Mass Transfer* 47 (2011) 519–540.
- [19] E. D'Anna, G. Leggieri, A. Luches, M. Martino, A.V. Drigo, G. Majni, P. Mengucci, I.N. Mihailescu, Nitridation of titanium by multipulse excimer laser irradiation, *Appl. Surf. Sci.* 46 (1990) 365–370.
- [20] A.L. Thomann, E. Sicard, C. Boulmer-Leborgne, C. Vivien, J. Hermann, C. Andreazza-Vignolle, P. Andreazza, C. Meneau, Surface nitriding of titanium and aluminium by laser-induced plasma, *Surf. Coat. Technol.* 97 (1997) 448–452.
- [21] S. Ettaqi, V. Hays, J.J. Hantzpergue, G. Saïndrenan, J.C. Remy, Mechanical, structural and tribological properties of titanium nitrided by a pulsed laser, *Surf. Coat. Technol.* 100–101 (1997) 428–432.
- [22] D. Höche, H. Schikora, H. Zutz, A. Emmel, R. Queitsch, P. Schaaf, TiN-coating formation by pulsed Nd:YAG laser irradiation of titanium in nitrogen, *J. Coat. Technol. Res.* 5 (2008) 505–512.
- [23] E.C. Santos, M. Morita, M. Shiomi, K. Osakada, M. Takahashi, Laser nitriding of pure titanium by pulsed Nd:YAG laser, in: 2005 Conference on Lasers and Electro-Optics Europe, IEEE, Munich, 2005, p. 655.
- [24] E.C. Santos, M. Morita, M. Shiomi, K. Osakada, M. Takahashi, Laser gas nitriding of pure titanium using CW and pulsed Nd:YAG lasers, *Surf. Coat. Technol.* 201 (2006) 1635–1642.
- [25] E. Carpene, M. Shinn, P. Schaaf, Free-electron laser surface processing of titanium in nitrogen atmosphere, *Appl. Surf. Sci.* 247 (2005) 307–312.
- [26] D. Höche, G. Rapin, J. Kaspar, M. Shinn, P. Schaaf, Free electron laser nitriding of metals: from basis physics to industrial applications, *Appl. Surf. Sci.* 253 (2007) 8041–8044.
- [27] D. Höche, M. Shinn, J. Kaspar, G. Rapin, P. Schaaf, Laser pulse structure dependent texture of FEL synthesized TiN<sub>x</sub> coatings, *J. Phys. D Appl. Phys.* 40 (2007) 818–825.
- [28] M. Satta, D.R. Ermer, M.R. Papantonakis, C. Flamini, R.F. Haglund, A. Mele, Time-resolved studies of electron-phonon relaxation in metals using a free-electron laser, *Appl. Surf. Sci.* 154–155 (2000) 172–178.
- [29] E. Carpene, P. Schaaf, Mass transport mechanisms during excimer laser nitriding of aluminum, *Phys. Rev. B* 65 (2002) 224111.
- [30] M. Han, Laser nitriding of metals (Ph.D. Thesis), Georg-August Universität, 2001.
- [31] M. Han, K.P. Lieb, E. Carpene, P. Schaaf, Laser-plume dynamics during excimer laser nitriding of iron, *J. Appl. Phys.* 93 (2003) 5742–5749.

- [32] P. Schaaf, F. Landry, M. Neubauer, K.P. Lieb, Laser nitriding investigated with Mössbauer spectroscopy, *Hyperfine Interact.* 113 (1998) 429–434.
- [33] B.N. Chichkov, C. Momma, S. Nolte, F. Von Alvensleben, A. Tünnermann, Femtosecond, picosecond and nanosecond laser ablation of solids, *Appl. Phys. A: Mater. Sci. Process.* 63 (1996) 109–115.
- [34] D. Bäuerle, *Laser Processing and Chemistry*, Springer Verlag, 2000.
- [35] H. Weber, G. Herziger, R. Poprawe, *Landolt-Börnstein Numerical Data and Functional Relationships in Science and Technology—Laser Physics and Applications*, Springer, 2004.
- [36] E. Carpene, A.M. Flank, A. Traverse, P. Schaaf, EXAFS investigation of laser nitridation and laser carburization of silicon, *J. Phys. D Appl. Phys.* 35 (2002) 1428–1432.
- [37] A.I. Katsamas, G.N. Haidemenopoulos, Laser-beam carburizing of low-alloy steels, *Surf. Coat. Technol.* 139 (2001) 183–191.
- [38] C. Illgner, P. Schaaf, K.P. Lieb, R. Queitsch, J. Barnikel, Material transport during excimer-laser nitriding of iron, *J. Appl. Phys.* 83 (1998) 2907.
- [39] E. Sicard, C. Boulmer-Leborgne, T. Sauvage, Excimer laser induced surface nitriding of aluminium alloy, *Appl. Surf. Sci.* 127 (1998) 726–730.
- [40] T. Bell, H.W. Bergmann, J. Lanagan, P.H. Morton, A.M. Staines, Surface engineering of titanium with nitrogen, *Surf. Eng.* 2 (1986) 133–143.
- [41] A. Bloyce, P.Y. Qi, H. Dong, T. Bell, Surface modification of titanium alloys for combined improvements in corrosion and wear resistance, *Surf. Coat. Technol.* 107 (1998) 125–132.
- [42] H. Dong, T. Bell, Surface engineering of titanium: an overview, in: G. Lütjering, J. Albrecht (Eds.), *Ti-2003 Science and Technology*, Wiley-VCH, Hamburg, 2003, pp. 867–875.
- [43] P.H. Morton, T. Bell, Surface engineering of titanium, *Mem. Etudes Sci. Rev. Metall.* 86 (1989) 639–646.
- [44] B. Sarma, K.S. Ravi Chandran, Recent advances in surface hardening of titanium, *JOM* 63 (2011) 85–92.
- [45] H.J. Spies, Surface engineering of aluminium and titanium alloys: an overview, *Surf. Eng.* 26 (2010) 126–134.
- [46] Y.S. Tian, C.Z. Chen, S.T. Li, Q.H. Huo, Research progress on laser surface modification of titanium alloys, *Appl. Surf. Sci.* 242 (2005) 177–184.
- [47] J.D. Ayers, Wear behavior of carbide-injected titanium and aluminum alloys, *Wear* 97 (1984) 249–266.
- [48] J.D. Ayers, R.J. Schaefer, W.P. Robey, A laser processing technique for improving the wear resistance of metals, *J. Metals* 33 (1981) 19.
- [49] H.W. Bergmann, Thermochemische Behandlung von Titan und Titanlegierungen durch Laserumschmelzen und Gaslegieren, *Materialwiss. Werkstofftech.* 16 (1985) 392–405.
- [50] C. Hu, H. Xin, L.M. Watson, T.N. Baker, Analysis of the phases developed by laser nitriding Ti-6Al-4V alloys, *Acta Mater.* 45 (1997) 4311–4322.
- [51] M. Ignatiev, E. Kovalev, I. Melekhin, I.Y. Smurov, S. Sturlese, Hardening of a titanium alloy by laser nitriding, *Wear* 166 (1993) 233–236.
- [52] S. Katayama, A. Matsunawa, A. Morimoto, S. Ishimoto, Y. Arata, Laser nitriding of titanium and its alloys, in: E.A. Metzbower (Ed.), *Proceedings of the 3rd International Colloquium on Welding and Melting by Electron and Laser Beam*, September 1983, Lyon, France, 1983, p. 127.
- [53] P.H. Morton, T. Bell, Surface engineering of titanium, in: *Proceedings of the 6th World Conference on Titanium*, Cannes, France, 1988, pp. 1705–1712.

- [54] P.H. Morton, T. Bell, A. Weisheit, J. Kroll, B.L. Mordike, K. Sagoo, Laser gas nitriding of titanium and titanium alloys, *Surf. Modificat. Technol.* V (1991) 593–609.
- [55] S. Mridha, T.N. Baker, Characteristic features of laser-nitrided surfaces of two titanium alloys, *Mater. Sci. Eng. A* 115–124 (1991).
- [56] J.M. Robinson, S. Anderson, R.D. Knutsen, R.C. Reed, Cavitation erosion of laser melted and laser nitrided Ti-6Al-4V, *Mater. Sci. Technol.* 11 (1995) 611–618.
- [57] I. Ursu, I.N. Mihailescu, A.M. Prokhorov, V.I. Konov, V.N. Tokarev, S.A. Uglov, On the mechanism of surface compound formation by powerful microsecond pulsed TEA CO<sub>2</sub> laser irradiation in technical nitrogen, *J. Phys. D Appl. Phys.* 18 (1985) 2547–2555.
- [58] A. Walker, J. Folkes, W.M. Steen, D.R.F. West, Laser surface alloying of titanium substrates with carbon and nitrogen, *Surf. Eng.* 1 (1985) 23–29.
- [59] H. Xin, S. Mridha, T.N. Baker, The effect of laser surface nitriding with a spinning laser beam on the wear resistance of commercial purity titanium, *J. Mater. Sci.* 31 (1996) 22–30.
- [60] S. Bonss, B. Brenner, E. Beyer, Laser gas alloying of titanium—new possibilities for severe wear loaded components in medicine, *Materialwiss. Werkstofftech.* 32 (2001) 160–165.
- [61] A.B. Kloosterman, Surface modification of titanium with lasers (Ph.D. Thesis), Groningen University, 1998.
- [62] A.B. Kloosterman, J.T.M. De Hosson, Microstructural characterization of laser nitrided titanium, *Scr. Metall. Mater.* 33 (1995) 567–573.
- [63] M. Raaij, F.M. El-Hossary, N.Z. Negm, S.M. Khalil, A. Kolitsch, D. Höche, J. Kaspar, S. Maendl, P. Schaaf, CO<sub>2</sub> laser nitriding of titanium, *J. Phys. D Appl. Phys.* 41 (2008) 085208.
- [64] M. Labudovic, R. Kovacevic, I. Kmecko, T. Khan, D. Blečić, Z. Blečić, Mechanism of surface modification of the Ti-6Al-4V alloy using a gas tungsten arc heat source, *Metall. Mater. Trans. A* 30 (1999) 1597–1603.
- [65] A.I.P. Nwobu, R.D. Rawlings, D.R.F. West, Nitride formation in titanium based substrates during laser surface melting in nitrogen-argon atmospheres, *Acta Mater.* 47 (1999) 631–643.
- [66] M. Golebiewski, G. Kruzel, R. Major, W. Mroz, T. Wierzchon, R. Ebner, B. Major, Morphology of titanium nitride produced using glow discharge nitriding, laser remelting and pulsed laser deposition, *Mater. Chem. Phys.* 81 (2003) 315–318.
- [67] M. Labudovic, R. Kovacevic, Modelling of the laser surface nitriding of Ti-6Al-4V alloy: analysis of heat transfer and residual stresses, *Proc. Inst. Mech. Eng. Part C: J. Mech. Eng. Sci.* 215 (2001) 315–340.
- [68] H.C. Man, Z.D. Cui, X.J. Yang, Analysis of laser gas nitrided titanium by X-ray photoelectron spectroscopy, *Appl. Surf. Sci.* 199 (2002) 293–302.
- [69] H.C. Man, Z.D. Cui, T.M. Yue, F.T. Cheng, Cavitation erosion behavior of laser gas nitrided Ti and Ti-6Al-4V alloy, *Mater. Sci. Eng. A* 355 (2003) 167–173.
- [70] H.C. Man, N.Q. Zhao, Z.D. Cui, Surface morphology of a laser surface nitrided and etched Ti-6Al-4V alloy, *Surf. Coat. Technol.* 192 (2005) 341–346.
- [71] J.C. Mori, P. Serra, E. Martínez, G. Sardin, J. Esteve, J.L. Morenza, Surface treatment of titanium by Nd:YAG laser irradiation in the presence of nitrogen, *Appl. Phys. A: Mater. Sci. Process.* 69 (1999) 699–702.
- [72] L. Xue, M. Islam, A.K. Koul, M. Bibby, W. Wallace, Laser gas nitriding of Ti-6Al-4V part 1: optimization of the process, *Adv. Perform. Mater.* 4 (1997) 25–47.
- [73] S. Bonss, System engineering for laser processing in process gas atmospheres, Annual report, IWS, Dresden, 2010.

- [74] J.D. Majumdar, *Laser Gas Alloying of Ti-6Al-4V*. *Lasers in Manufacturing*, Elsevier, Munich, 2011, pp. 472–477.
- [75] S. Katayama, A. Matsunawa, A. Morimoto, S. Ishimoto, Y. Arata, Surface hardening of titanium by laser nitriding, *J. Metals* 35 (1983) 85.
- [76] X.K. Chen, G. Wu, R. Wang, W.T. Guo, J.P. Yang, S.Z. Cao, Y.L. Wang, W.H. Han, Laser nitriding of titanium alloy in the atmosphere environment, *Surf. Coat. Technol.* 201 (2007) 4843–4846.
- [77] C. Hu, T. Baker, Overlapping laser tracks to produce a continuous nitrided layer in Ti-6Al-4V alloy, *J. Mater. Sci.* 32 (1997) 2821–2826.
- [78] L. Xue, M. Islam, A.K. Koul, M. Bibby, W. Wallace, Laser gas nitriding of Ti-6Al-4V part 2: characteristics of nitrided layers, *Adv. Perform. Mater.* 4 (1997) 389–408.
- [79] J.H. Abboud, A.F. Fidel, K.Y. Benyounis, Surface nitriding of Ti-6Al-4V alloy with a high power CO<sub>2</sub> laser, *Opt. Laser Technol.* 40 (2008) 405–414.
- [80] R.R.G.M. Pieters, S. Liu, TiN formed by laser gas alloying of Ti-6Al-4V, in: A. Kumar (Ed.), *TMS, The Minerals, Metals & Materials Society*, San Diego, CA, 1999, pp. 415–428.
- [81] J. Kaspar, J. Bretschneider, S. Jacob, S. Bonß, B. Winderlich, B. Brenner, Microstructure, hardness and cavitation erosion behaviour of Ti-6Al-4V laser nitrided under different gas atmospheres, *Surf. Eng.* 23 (2007) 99–106.
- [82] J. Kaspar, A. Luft, S. Bonß, B. Winderlich, B. Brenner, A detailed study of the microstructure formed during laser nitriding of Ti-6Al-4V under different gas atmospheres, in: G. Lütjering, J. Albrecht (Eds.), *Ti-2003. Science and Technology*, Wiley-VCH, Hamburg, 2003, pp. 949–956.
- [83] H. Xin, C. Hu, T.N. Baker, Microstructural assessment of laser nitrided Ti-6Al-4V alloy, *J. Mater. Sci.* 35 (2000) 3373–3382.
- [84] J. Kaspar, J. Bretschneider, S. Bonß, B. Winderlich, B. Brenner, Laser nitriding: a promising way to improve the cavitation erosion resistance of components made of titanium alloys, in: A. Fischer, K. Bobzin (Eds.), *International Symposium on Friction, Wear and Wear Protection*, Wiley-VCH, Aachen, 2008, pp. 74–80.
- [85] C. Hu, T.N. Baker, The importance of preheat before laser nitriding a Ti-6Al-4V alloy, *Mater. Sci. Eng. A—Struct. Mater. Prop. Microstruct. Process.* 265 (1999) 268–275.
- [86] J. Kaspar, A. Luft, S. Bonß, B. Brenner, Untersuchung der Mikrostruktur der Legierung Ti-6Al-4V nach dem Lasergasnitrieren mit unterschiedlichen Stickstoffgehalten, in: J. Grosch, E.J. Mittermeijer (Eds.), *Nitrieren*, AWT, Aachen, Schlangenbad, 2002.
- [87] S. Mridha, T.N. Baker, Crack-free hard surfaces produced by laser nitriding of commercial purity titanium, *Mater. Sci. Eng. A* 188 (1994) 229–239.
- [88] S. Yerramareddy, S. Bahadur, The effect of laser surface treatments on the tribological behavior of Ti-6Al-4V, *Wear* 157 (1992) 245–262.
- [89] Y.S. Tian, C.Z. Chen, L.B. Chen, J.H. Liu, T.Q. Lei, Wear properties of alloyed layers produced by laser surface alloying of pure titanium with B<sub>4</sub>C and Ti mixed powders, *J. Mater. Sci.* 40 (2005) 4387–4390.
- [90] Y.S. Tian, C.Z. Chen, L.X. Chen, Q.H. Huo, Crack-free wear resistance coatings produced on pure titanium and Ti-6Al-4V by laser nitriding, *Surf. Rev. Lett.* 12 (2005) 741–744.
- [91] Y.S. Tian, C.Z. Chen, D.Y. Wang, Q.H. Huo, T.Q. Lei, Microstructures and wear properties of the composite coatings laser-fabricated on titanium alloy Ti-6Al-4V, *Surf. Rev. Lett.* 12 (2005) 443–447.
- [92] A. Richard, R. Kassing, H. Pulker, K.T. Rie, Fifth international conference on plasma surface engineering, *Surf. Coat. Technol.* 98 (1996) 809–1615.

- [93] C. Gerdes, C. Maggi, H. Bartsch, Oberflächenbehandlungen und Schichten gegen Schädigung durch Wassertropfenerosion, in: K.H. Zum Gahr (Ed.), Reibung und Verschleiß, DGM, Bad Nauheim, 1996.
- [94] J.M. Robinson, R.C. Reed, Water droplet erosion of laser-surface treated Ti-6Al-4V, Wear 186 (1995) 360–367.
- [95] J. Kaspar, A. Luft, J. Bretschneider, S. Jacob, S. Bonß, B. Winderlich, B. Brenner, E. Beyer, Laser nitriding: a promising way to improve the cavitation erosion resistance of Ti-6Al-4V, in: E. Beyer (Ed.), Third International Conference on Lasers in Manufacturing, AT-Fachverlag, München, 2005, pp. 393–398.
- [96] R.H. Richman, W.P. Mcnaughton, Correlation of cavitation erosion behavior with mechanical-properties of metals, Wear 140 (1990) 63–82.
- [97] H. Rieger, Kavitation und Erosion, in: VDI-Berichte, VDI-Verlag, Düsseldorf, 1979.
- [98] V. Kara, H. Kizil, Titanium micromachining by femtosecond laser, Opt. Lasers Eng. 50 (2012) 140–147.
- [99] P. Schaaf, Laser nitriding and laser carburizing of surfaces, in: H.P. Weber, V.I. Konov, T. Graf (Eds.), ALT'02 International Conference on Advanced Laser Technologies, SPIE, Adelboden, 2003, pp. 404–415.
- [100] C. Symietz, E. Lehmann, R. Gildenhaar, R. Koter, G. Berger, J. Krüger, Fixation of bioactive calcium alkali phosphate on Ti-6Al-4V implant material with femtosecond laser pulses, Appl. Surf. Sci. 257 (2011) 5208–5212.
- [101] A.Y. Vorobyev, C. Guo, Femtosecond laser structuring of titanium implants, Appl. Surf. Sci. 253 (2007) 7272–7280.
- [102] E. György, A. Perez Del Pino, P. Serra, J.L. Morenza, Surface nitridation of titanium by pulsed Nd:YAG laser irradiation, Appl. Surf. Sci. 186 (2002) 130–134.
- [103] N. Ohtsu, K. Kodama, K. Kitagawa, K. Wagatsuma, Comparison of surface films formed on titanium by pulsed Nd:YAG laser irradiation at different powers and wavelengths in nitrogen atmosphere, Appl. Surf. Sci. 256 (2010) 4522–4526.
- [104] L. Lavisson, J.M. Jouvard, J.P. Gallien, P. Berger, D. Grevey, P. Naudy, The influence of laser power and repetition rate on oxygen and nitrogen insertion into titanium using pulsed Nd:YAG laser irradiation, Appl. Surf. Sci. 254 (2007) 916–920.
- [105] J.D. Wu, C.Z. Wu, X.X. Zhong, Z.M. Song, F.M. Li, Surface nitridation of transition metals by pulsed laser irradiation in gaseous nitrogen, Surf. Coat. Technol. 96 (1997) 330–336.
- [106] E. György, A.P. Del Pino, P. Serra, J.L. Morenza, Depth profiling characterisation of the surface layer obtained by pulsed Nd:YAG laser irradiation of titanium in nitrogen, Surf. Coat. Technol. 173 (2003) 265–270.
- [107] E. György, A.P. Del Pino, P. Serra, J.L. Morenza, Microcolumn development on titanium by multipulse laser irradiation in nitrogen, J. Mater. Res. 18 (2003) 2228–2234.
- [108] E.C. Santos, M. Morita, M. Shiomi, K. Osakada, M. Takahashi, Influence of pulse shaping in laser gas nitriding of pure titanium, in: Japanese Joint Conference for the Technology of Plasticity, 2004, pp. 503–504.
- [109] E. D'Anna, G. Leggieri, A. Luches, M. Martino, A. Perrone, P. Mengucci, I.N. Mihailescu, Multilayer titanium nitride and silicide structures synthesized by multipulse excimer laser irradiation, Appl. Surf. Sci. 54 (1992) 353–357.
- [110] E. D'Anna, G. Leggieri, A. Luches, M. Martino, A.V. Drigo, I.N. Mihailescu, S. Ganatsios, Synthesis of pure titanium nitride layers by multipulse excimer laser irradiation of titanium foils in a nitrogen-containing atmosphere, J. Appl. Phys. 69 (1991) 1687.

- [111] A.L. Thomann, C. Boulmer-Leborgne, C. Andreazza-Vignolle, P. Andreazza, J. Hermann, G. Blondiaux, Metal surface nitriding by laser induced plasma, *J. Appl. Phys.* 80 (1996) 4673–4684.
- [112] I. Mihailescu, N. Chitica, L. Nistor, M. Popescu, V. Teodorescu, I. Ursu, A. Andrei, A. Barborica, A. Luches, M. De Giorgi, Deposition of high quality TiN films by excimer laser ablation in reactive gas, *J. Appl. Phys.* 74 (1993) 5781.
- [113] I. Mihailescu, N. Chitica, V. Teodorescu, M. De Giorgi, G. Leggieri, A. Luches, M. Martino, A. Perrone, B. Dubreuil, Excimer laser reactive ablation: an efficient approach for the deposition of high quality TiN films, *J. Vac. Sci. Technol. A: Vac. Surf. Films* 11 (1993) 2577–2582.
- [114] I. Mihailescu, E. György, N. Chitica, V. Teodorescu, G. Mavin, A. Luches, A. Perrone, M. Martino, J. Neamtu, A parametric study of the deposition of the TiN thin films by laser reactive ablation of titanium targets in nitrogen: the roles of the total gas pressure and the contaminations with oxides, *J. Mater. Sci.* 31 (1996) 2909–2915.
- [115] E. Carpene, M. Shinn, P. Schaaf, Synthesis of highly oriented  $TiN_x$  coatings by free-electron laser processing of titanium in nitrogen gas, *Appl. Phys. A: Mater. Sci. Process.* 80 (2005) 1707–1710.
- [116] L. Covelli, F. Pierdominici, I. Smurov, S. Tosto, Surface microstructure of titanium irradiated by Nd:YAG pulsed laser in presence of carbon and nitrogen, *Surf. Coat. Technol.* 78 (1996) 196–204.
- [117] M. Schwickert, E. Carpene, K. Lieb, M. Uhrmacher, P. Schaaf, Hydrogen incorporation in titanium via laser irradiation, *Appl. Phys. Lett.* 84 (2004) 5231–5233.
- [118] M. Schwickert, E. Carpene, K. Lieb, M. Uhrmacher, P. Schaaf, H. Gibhardt, Laser hydriding—a novel method to store hydrogen in solids, *Phys. Scr.* 2004 (2004) 113.
- [119] M. Schwickert, E. Carpene, M. Uhrmacher, P. Schaaf, K. Lieb, Laser hydriding of crystalline and amorphous silicon, *Appl. Phys. A* 77 (2003) 793–797.
- [120] J. Häglund, G. Grimvall, T. Jarlborg, A.F. Guillermet, Band structure and cohesive properties of 3d-transition-metal carbides and nitrides with the NaCl-type structure, *Phys. Rev. B* 43 (1991) 14400.
- [121] J. Kunze, Nitrogen and Carbon in Iron and Steel Thermodynamics, Akademie-Verlag, Berlin, 1990.
- [122] M. Ron, Iron-carbon and iron-nitrogen system, in: R.L. Cohen (Ed.), Applications of Mössbauer Spectroscopy, Academic Press, New York, 1980.
- [123] H. Binczycka, M. Kahle, S. Cusenza, E. Carpene, P. Schaaf, Interstitial ordering of nitrogen and carbon in laser nitrided and laser carburized austenitic stainless steel, *J. Phys. Condens. Matter* 18 (2006) 10561.
- [124] E. Carpene, P. Schaaf, Formation of  $Fe_3C$  surface layers by laser plasma cementation, *Appl. Phys. Lett.* 80 (2002) 891–893.
- [125] P. Schaaf, M. Kahle, E. Carpene, Reactive laser plasma coating formation, *Surf. Coat. Technol.* 200 (2005) 608–611.
- [126] P. Schaaf, H. Binczycka, M. Kahle, S. Cusenza, D. Höche, E. Carpene, Transformation of expanded austenite to an amorphous ferromagnetic surface layer during laser carburization of austenitic stainless steel: dedicated to Prof. Dr.-Ing. Hans-Joachim Spies on the occasion of his 75th birthday, *HTM J. Heat Treat. Mater.* 64 (2009) 242–248.
- [127] F. Fariaut, C. Boulmer-Leborgne, N. Semmar, E. Le Menn, High-speed mass-transport phenomena during carburization of aluminum alloy by laser plasma treatment, *Appl. Phys. A* 83 (2006) 95–101.

- [128] V.I. Shapochkin, K.O. Smirnov, Formation of structure in nitrocarburized layers of low-alloy steels subjected to laser heating, *Metal Sci. Heat Treat.* 44 (2002) 440.
- [129] B.S. Yilbas, I.-U.-H. Toor, J. Malik, F. Patel, Laser gas assisted treatment of AISI H12 tool steel and corrosion properties, *Opt. Lasers Eng.* 54 (2014) 8–13.
- [130] J.R. Davis, *Surface Hardening of Steels: Understanding the Basics*, ASM International, 2002.

# Mechanical properties improvement of metallic rolls by laser surface alloying

3

G. Sun<sup>1</sup>, R. Zhou<sup>2</sup>

<sup>1</sup>Southeast University, Nanjing, China; <sup>2</sup>Jiangsu University of Science and Technology, Zhenjiang, China

## 3.1 Introduction

Laser surface engineering in this chapter involves the application of laser surface alloying in metallic rolls. In view of this, the laser material processing in this chapter involves intense heating of solid targets/components by laser to enable several types of ultrafast, novel, and economical processing of materials that distinguish themselves from their conventional counterparts in terms of quality, productivity, and efficiency [1]. This laser material processing consists of laser quenching, laser remelting, laser surface alloying, laser cladding, laser rapid prototyping, laser welding, and so on.

Application of the laser to material processing can be grouped into two major classes [1]: applications requiring limited energy/power and causing limited microstructural changes only within a small volume/area without change of state, and applications requiring substantial amount of energy to induce the change in state and phase transformation in large volume/area. The first category includes annealing [2–6], polymer curing [7–11], scribing/marketing [12–15] of integrated circuit substrates, and so forth. The second type of application encompasses cutting [16–18], welding [19–22], surface hardening [23–25], cladding [26–29] and alloying [30–34]. The average power or energy input is relatively low in the first category, while that for the second category is higher as the processes involve single or multiple phase changes within a very short time. Almost all varieties of lasers can perform both types of operations in CW and pulsed mode provided appropriate power/energy density and interaction time for the given wavelength are applied.

Laser surface alloying offers a versatile approach to the production of surface layers of a wide range of structures and compositions on a variety of substrates. The structures can be of a fine-grained nature as a result of the relatively rapid cooling rates that can be achieved from the melt [35]. Consequently, the improvement in corrosion and wear resistance may be achieved by laser surface alloying via homogenization and refinement of the microstructure, and/or formation of new alloys on the surface [36]. It has a variety of industrial applications in the metallurgy industry [37–40], automobile industry [41], petroleum industry, chemical industry, and power industry.

### 3.2 Mechanical properties improvement of metallic rolls by laser surface alloying: experimental procedures

Rolls are the main deformation tools in rolling mills. They withstand cyclic heating and cooling, very high loads, thermal fatigue, and severe environmental attack. As a result, they often fail due to cracks, spalling, and wear [42–46]. The service lives of rolls can be prolonged by improving their wear resistance, because the wear characteristic of rolls is the key factor in determining roll performance. In this part, nodular cast-iron rolls (NCIR), semisteel rolls, and cast steel rolls are strengthened by laser surface alloying.

Metallic rolls such as NCIR, semisteel rolls, and cast steel rolls are used as the substrate material. The chemical composition of the rolls is listed in Table 3.1. A DL-HL-T10000 continuous wave CO<sub>2</sub> laser is used for laser alloying. Prior to laser surface alloying, the roll was polished to remove the oxide layer and then cleaned with acetone and deionized water. Powders used for the alloying materials are C-B-W-Cr composite carbide powders (30–500 nm) and NiCr-Cr<sub>3</sub>C<sub>2</sub> powders. The particle size of the (25 wt.%) Ni-Cr+(75 wt.%) Cr<sub>3</sub>C<sub>2</sub> powder is 13–18 μm. The ratio of Ni and Cr in Ni-Cr is 3:1 in weight. The powders were preplaced on the roll with different thicknesses (0.01–0.05 mm). Several trials were done before the final processing parameters were determined.

After laser treatment, specimens were sectioned, mounted, ground, polished, and etched with an etchant (FeCl<sub>3</sub> 20 g+HCl 50 mL+H<sub>2</sub>O 100 mL). The microstructure was examined using an OLYMPUS-GX71 optical microscope (OM) and a JEOL JSM 7001 F scanning electron microscope (SEM) with energy dispersive X-ray (EDX) analysis. The thicknesses of the layers were measured using the OLYMPUS-OLS3100 laser confocal stereo microscope. The measurement was along central lines in each molten pool. The distances between the layer surface and the bonding line on these lines are defined as the thickness of the alloyed layer. Phases presented in the layers were identified using an X-ray diffractometer (XRD, X'Pert Pro MPD-PW 3040/60) with Cu Kα generated at 40 kV and 40 mA, and scanning speeds of 4°/min (0.5°/min for accurate observation of certain phases). The microhardness of the cross section from the layer surface to the substrate was measured using a Wilson Wdpert 401MVDTM microhardness tester at a load of 50 or 100 g and a dwell time of 10 s. An average value of hardness was taken from three measurements of points along the central line of the molten pool of the cross section of the laser-alloyed specimens.

Taking the real work conditions of hot rolls (high temperature, high load, severe wear, and so on) into consideration, 500 °C is taken as the wear test temperature [47–50]. Sliding wear tests were conducted with a pin-on-disk apparatus (MG-2000 tester, Materials Tester Company, Xuanhua, Hebei Province, China) under dry sliding conditions at ambient and 500 °C. The temperature in the furnace was measured by the thermocouple inserted in it. The dimensions of the pins, whose sliding surface was made of the laser-alloyed layers, are Φ6 mm × 12 mm. The surfaces of the wear test samples were ground and polished with 2000# grit paper.

**Table 3.1 Chemical composition of metallic rolls (wt.%)**

<b>Roll</b>	<b>C</b>	<b>Si</b>	<b>Ni</b>	<b>Cr</b>	<b>Mo</b>	<b>Mn</b>	<b>P</b>	<b>V</b>	<b>Fe</b>
Nodular cast iron (A)	3.2-3.3	2-2.5	1.5-1.8	1.2-1.5	0.5-0.7	-	<0.035	-	Bal.
Semi steel (B)	1.3-2.2	0.3-1.0	0.2-2.5	0.5-3.5	0.2-1.0	0.6-1.4	-	-	Bal.
Cast steel (C)	0.7	0.2-0.6	-	-	0.2-0.45	1.2-1.3	<0.035	0.4-0.5	Bal.

A fixed rotating speed of 250 rpm and an applied load of 100 N were used, and each test was performed for 904.32 m. The sliding disk (60# steel, hardness of 60HRC) with 70 mm in diameter was used as the counterbody. Wear mass loss was measured by a BS 224S electron balance with an accuracy of 0.1 mg after each test. The disk was dressed prior to each test to remove any debris from previous tests and ensure reproducibility in the testing conditions. The average values of the mass losses from the laser-treated layers and the substrates were compared. The microstructure of the samples after the pin-on-disk wear test was observed with SEM and the wear mechanism was discussed.

### **3.3 Laser surface alloying of C-B-W-Cr nano-powders on nodular cast-iron rolls (NCIR)**

NCIR are widely used in steel mills because of their low price, good castability, and good machinability; all desirable features in the production of machine parts [51]. The unique combination of carbide, nodular graphite, and matrix structure offers an advantageous working capacity, such as surface roughening resistance and seizing resistance, to resist severe circumstances [52]. Several trials were done before the final processing parameters were determined, which were as follows: laser power 4 kW, scanning speed 4 m/min, spot diameter of laser 1.5 mm, and an overlap ratio between tracks 33.3%.

#### ***3.3.1 Microstructure of the cross section of the laser alloyed NCIR***

The microstructure of the NCIR substrate is shown in [Figure 3.1a](#), which indicated that the substrate is of hypoeutectic structures, composed of perlite, ledeburite, and nodular graphite. The laser-alloyed layer was composed of dendrites and interdendrites, as indicated in [Figure 3.1b](#). One graphite can be detected in the alloyed layer due to the forces in the molten pool when the powders and substrate are irradiated by the laser. In the nodular iron, graphite nodules gradually dissolved in the molten pool and, at the same time, due to hydrodynamic forces and buoyancy forces, they moved toward the surface. According to the results of Grum *et al.* [53], detailed dimensional analysis of the graphite nodules has shown that only larger nodules reach the surface (they were not completely dissolved) where they may be blown away at the top surface by the protecting gas or carbon combustion of the laser beam energy.

The microstructure varies in the cross section of the alloyed layer as shown in [Figure 3.2](#), among which [Figure 3.2a-c](#) correspond to the top part, middle part, and lower part of the alloyed layer, respectively, and [Figure 3.2d](#) is from the bonding zone between the alloyed layer and the substrate. The microstructure in the alloyed layer is dependent on the cooling rate in the molten pool during heating and cooling. [Figure 3.2a-c](#) shows that the microstructure of the alloyed layer consists of dendrites and eutectics, especially [Figure 3.2b](#). The microstructure in [Figure 3.2a and c](#) is composed of a majority of dendrites and the eutectics can hardly be detected. Furthermore,

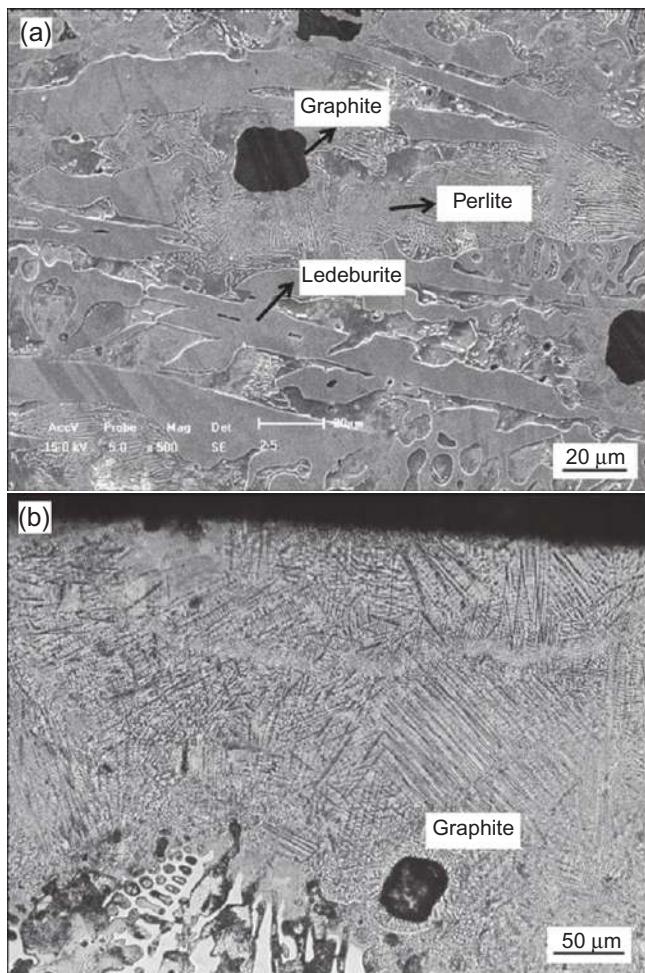


**Figure 3.1** Microstructure of the cross section of (a) NCIR substrate and (b) alloyed layer.

the dendrites size increased from the top to the lower part of the alloyed layer, as can be seen in [Figure 3.2a-c](#). Chemical composition of the spots in [Figure 3.2b](#) is shown in [Table 3.2](#). The combination of [Figure 3.2b](#) and [Table 3.2](#) shows that both the dendrites and eutectics were mainly composed of Fe and C, while the eutectics had a little higher content of Cr, Mo, and W. The carbon content in the molten pool was high enough to qualify the hypereutectic reaction due to the partial dissolution of graphite nodules and the addition of carbides from the alloying powders. A lot of carbides can be formed in the alloyed layer through the reaction of carbon and other elements. The bonding area is at the bottom of the molten pool with a lot of substrate materials melted into it. The solidification and the subsequent microstructure of this area are different from the top part of the alloyed layer. There is a coral structure (indicated by the arrow) in addition to the typical dendrite structure bonded with the substrate.

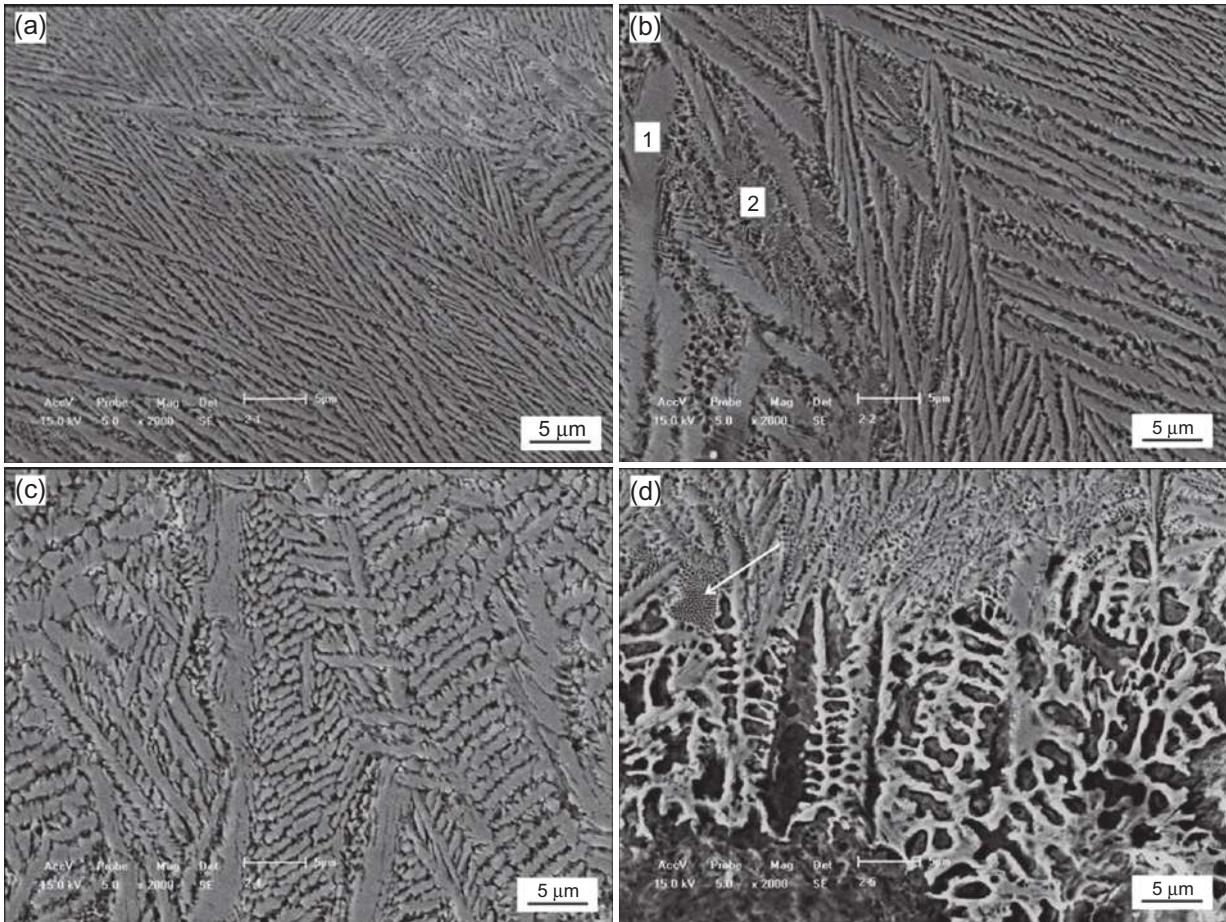


**Figure 3.2** Microstructure of the cross section of the alloyed layer on NCIR, (a) top part, (b) middle part, (c) lower part, and (d) bonding zone.

### 3.3.2 Phases in the alloyed layer on NCIR

[Figure 3.3](#) shows the XRD pattern of the alloyed layer. As can be seen, the alloyed layer was composed of residual austenite, Ni-Cr-Fe solid solution, martensite, a lot of carbides, and W<sub>2</sub>B. It is worthwhile to mention that a solid solution of Ni, Cr, and Fe could be easily obtained, because they have similar atom radii, among which Ni (0.352 nm), Cr (0.288 nm), and Fe (0.287 nm). This Fe-rich solid solution could perform as the tough matrix for hard phases. It is easy to conclude from [Figure 3.2b](#), [Table 3.2](#), and [Figure 3.3](#) that the dendrites were primary carbides and the eutectics were austenite + carbides + W<sub>2</sub>B, with some of the austenite transformed into martensite afterwards. The microstructure here was hypereutectic. Cr<sub>7</sub>C<sub>3</sub> and M<sub>23</sub>C<sub>6</sub> instead of Cr<sub>3</sub>C<sub>2</sub> are detected in the alloyed layer. This observation can be explained by appreciating that the temperature in the molten pool was almost certainly much higher than the melting point of the Cr<sub>3</sub>C<sub>2</sub> (1890 °C); consequently, the Cr<sub>3</sub>C<sub>2</sub> powder would have melted into the molten pool. The formula (3.1)–(3.3) proposed by Anthonysamy [54], provides a basis for the calculation of the formation Gibbs energies of chromium carbides in the temperature range 973–1173 K. Their reported values are also in good agreement with the other study at a higher temperature range.

**Table 3.2 Chemical composition of spots in [Figure 3.2b](#) (at.%)**

Element	C	Fe	Cr	Ni	Mo	W
Spot 1	29.254	68.181	0.277	0.905	0.347	1.036
Spot 2	30.151	65.913	0.622	0.712	0.618	1.984

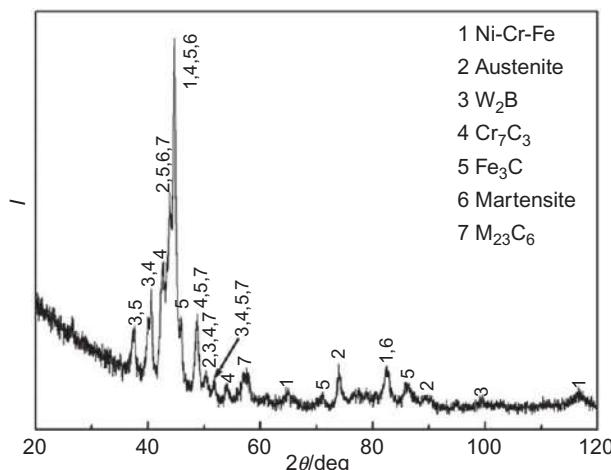


**Figure 3.3** XRD pattern of the alloyed layer on NCIR.

These formulas are used here to calculate the Gibbs formation energies of carbides at about 2000 K.

$$\Delta G\langle \text{Cr}_{23}\text{C}_6 \rangle = -236,331 - 86.2T(\pm 10,000) \text{ J/mol} \quad (3.1)$$

$$\Delta G\langle \text{Cr}_7\text{C}_3 \rangle = -92,067 - 41.5T(\pm 2800) \text{ J/mol} \quad (3.2)$$

$$\Delta G\langle \text{Cr}_3\text{C}_2 \rangle = -54,344 - 19.57T(\pm 9400) \text{ J/mol} \quad (3.3)$$

The calculated values for the Gibbs formation energies for  $\text{Cr}_{23}\text{C}_6$ ,  $\text{Cr}_7\text{C}_3$ , and  $\text{Cr}_3\text{C}_2$  at 2000 K are  $-408,731$ ,  $-175,067$  and  $-93,484$  J/mol, respectively. As the free energy changes of the formation of  $\text{Cr}_{23}\text{C}_6$  and  $\text{Cr}_7\text{C}_3$  are lower than that of  $\text{Cr}_3\text{C}_2$  (at 2000 K), the more stable  $\text{Cr}_{23}\text{C}_6$  and  $\text{Cr}_7\text{C}_3$  would have formed from the reaction of Cr and C. Due to the fast heating and cooling rate in the molten pool, a lot of metastable phases can also be formed.

### **3.3.3 Crack propagation in the alloyed layer and the NCIR substrate**

Crack propagation in the alloyed layer, bonding zone, and the substrate is shown in [Figure 3.4](#). The cracks in the cross section propagated through the layer into the bonding zone and even penetrated into the substrate. They extended for some distance in the ledeburite before a total stop due to the bad toughness of the ledeburite, as shown in [Figure 3.4a](#). Furthermore, a flaking of the alloyed material occurred at the top surface due to the interconnection of cracks. A flaking will be caused when the crack extends to a certain degree with the coating surface or even parallel to it. If a crack originating from a contact surface extends in the direction of the load movement, it is likely to extend farther [43]. When the roll contacts with the steel plate in the real rolling process, cracks on its surface must have similar tendency. [Figure 3.4b](#) shows the crack propagation along pores in the alloyed layer. Areas close to pores in the laser-alloyed layers are prone to generate cracks as the result of the stress concentration. In this case, the crack in the left part of [Figure 3.4b](#) propagated along its original direction (from top to bottom) after meeting the pore, with the width of the crack decreasing. Some flaking material from the alloyed layer can be detected in the crack gap. The crack at the lower right bottom in [Figure 3.4b](#) originated from the bonding zone between the alloyed layer and the substrate and propagated into the alloyed layer. The high temperature gradient and the differences between the thermal expansion coefficients of the alloyed layer and the substrate would cause high thermal stress in the solidifying molten pool, introducing cracks in it. Furthermore, the low strength and fracture strain of the alloyed layer in semisolid-state accelerated the origin and propagation of cracks. The crack propagation in the bonding zone between the alloyed layer and the substrate is shown in [Figure 3.4c](#). The long crack in the alloyed layer ended at the bonding zone, while cracks originated in the bonding zone extended in two directions, that is, both into the alloyed layer and into the substrate. The crack propagation in the alloyed layer stops after a short distance, while the case in the

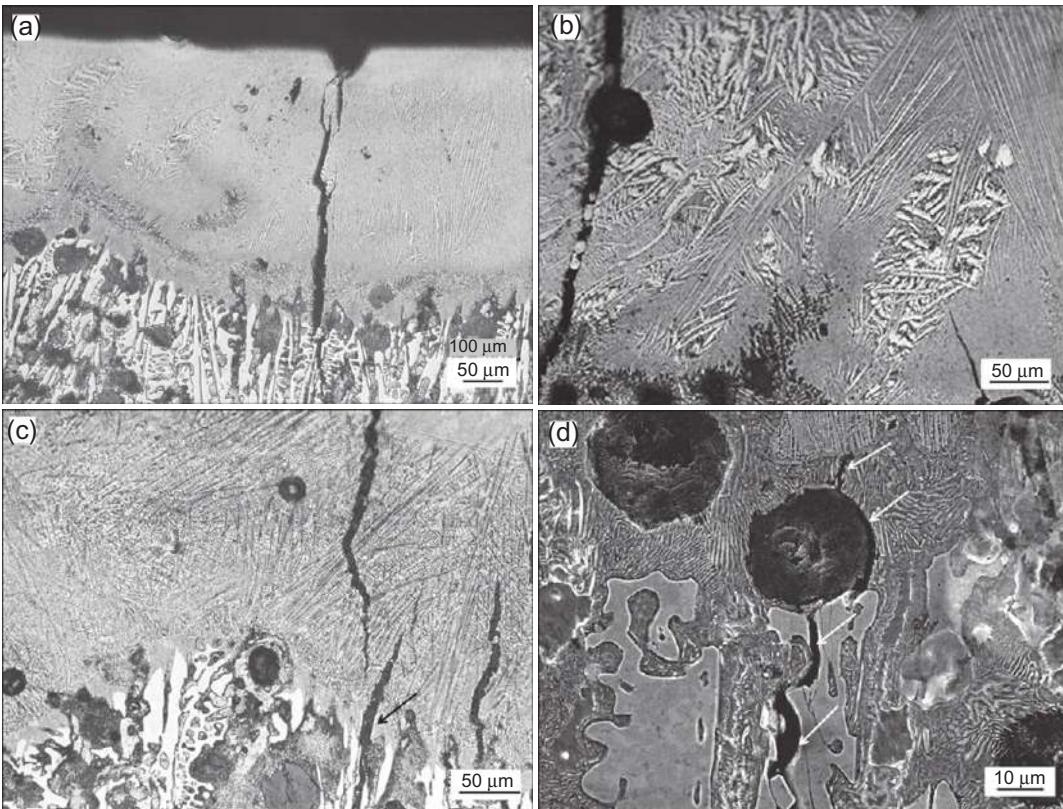


**Figure 3.4** Microstructure of the crack propagation in (a, b) alloyed layer, (c) bonding zone, and (d) NCIR substrate.

substrate can be divided into two cases depending on the microstructure in front of the cracks. The crack will propagate for a distance if the crack extends into the brittle ledeburite (see the one indicated by the arrow in Figure 3.4c), but if it extends into the ductile pearlite, it will come to a stop immediately (see the rightmost one in Figure 3.4c). Furthermore, the propagation direction of cracks in the bonding zone is parallel to the growth direction of dendrites. Crack distribution in the substrate is shown in Figure 3.4d. NCIR substrate is taken as a periodic array of loosely bonded spherical inclusions in the matrix material. Due to the round shape of it, the stress concentration is mild when loaded and the cutting effect to the substrate was reduced to a large extent, enabling the substrate with high strength, toughness, and plasticity. As can be seen in Figure 3.4d, the crack extends along the ledeburite before it meets the nodular graphite. It propagates along the periphery of graphite and turns into the pearlite at the point where the direction is the same as it meets the graphite. At last, the crack ends in the pearlite. Fang's study also indicated the positive effect of the nodular graphite over the flake-like graphite on the wear resistance because the latter one can cause great stress concentration to the iron matrix during wear [55]. The reasons for all the cracks in the alloyed layer, substrate, and the bonding zone between the alloyed layer and the substrate are the thermal stress caused by the differences between the alloyed layer and the substrate and the transformation stress caused by the phase transformation in the molten pool.

When it goes into the real rolling work condition, real contact between the roll and the rolling materials must be taken into consideration. It is worth emphasizing that according to a study by Limodin *et al.* [56], crack closure occurs when the crack surfaces come into contact before the minimum load of the fatigue cycle is reached. The underlying mechanisms are diverse and may operate simultaneously. Further work needs to be done in order to evaluate the influence of the wear conditions on the crack behavior of this type of materials.

The schematic view of the crack propagation along the nodular graphite and in the alloyed layer is shown in Figure 3.5. The substrate near the graphite endures radial compressive stress and tensile hoop stress in the solidifying process after laser treatment due to the differences of the Young's modulus and thermal expansion coefficient between the graphite (12 GPa) and the steel (210 GPa). When encountering the graphite particle, instead of extending into it, the crack deviates from its

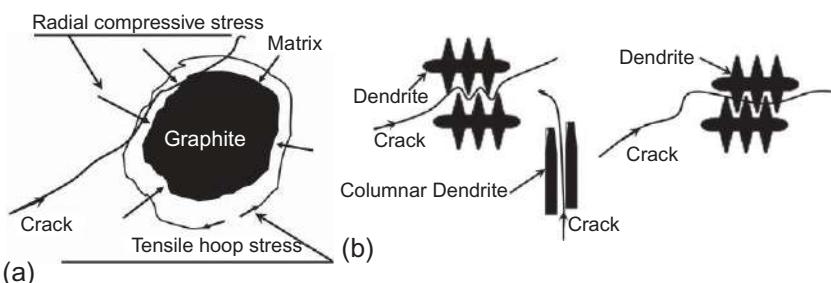


**Figure 3.5** (a, b) Schematic view of the crack propagation in the alloyed layer on NCIR.

original propagating direction to the direction where it is parallel to the hoop stress and perpendicular to the radial stress; namely, along the periphery of the nodular graphite. Furthermore, the radial stress in the substrate increases to its highest value at the interface between the particle and the substrate when the crack approaches the particle, deviating the crack to the interface between the particle and the substrate. The crack turns into its original direction when it leaves the nodular graphite particle. The conclusion that the existence of nodular graphite is positive as a suppression of the propagation of cracks in the NCIR substrate can be derived from the above discussion. The positive effect of the nodular graphite, which can control crack propagation and thermal conductivity, was also found in Ghaderi's research [57].

The crack propagation in the alloyed layer is schematically shown in Figure 3.5b, among which the left and right one show the intergranular crack and transgranular crack in the alloyed layer, respectively, and the middle one shows the intergranular crack along the columnar dendrite in the bonding zone between the alloyed layer and the substrate.

### 3.3.4 Microhardness distribution and wear properties of the alloyed layer on NCIR

The microhardness distribution along the depth in the cross section of the alloyed layer is shown in Figure 3.6. As can be observed, the average microhardness of the alloyed layer is  $1201 \text{ HV}_{0.05}$ , which is 1.4 times higher than that of the substrate ( $500 \text{ HV}_{0.05}$ ). The microhardness decreases to about  $1000 \text{ HV}_{0.05}$  when it goes to the bonding zone between the alloyed layer and the substrate. Measurement in the substrate was avoided due to the nonuniform microstructure in it.

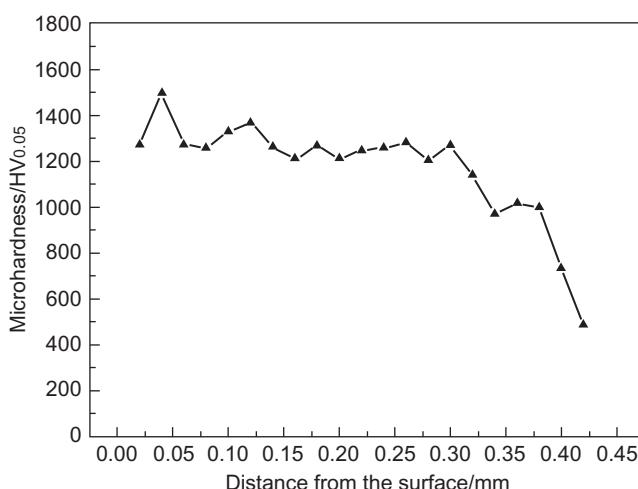
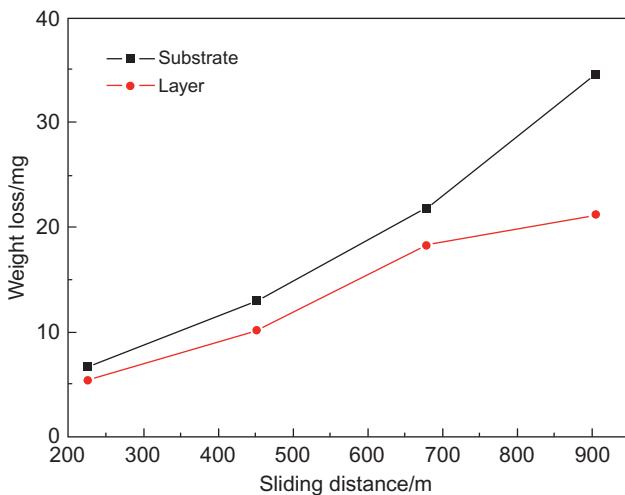


Figure 3.6 Microhardness distribution of laser-alloyed specimen.



**Figure 3.7** Weight loss against sliding time of the NCIR and laser-alloyed layer.

Comparison of the wear weight loss of the roll substrate and the alloyed layer after different wear times is shown in [Figure 3.7](#). The wear rate was high for both of the substrate and the alloyed layer, indicating the running-in stage. Surface roughness was introduced by mechanical machining of the wear counterpart, which reduced the real contact area between them. As time increased, both surfaces of the counterparts were worn smooth, increasing the real contact area and reducing the wear rate. The wear then went into steady stage. The increasing rate of wear mass loss with time for the laser-alloyed layer was less compared with that of the NCIR substrate. The wear mass loss of the substrate was 1.2 times of that of the laser-alloyed layer after wear for 226.08 m. The ratio increased to 1.6 when the wear distance increased to 904.32 m, where the wear mass loss of the substrate and the alloyed layer were 34.6 and 21.2 mg, respectively, indicating the improvement in the wear resistance of the laser-alloyed layer on the NCIR substrate.

The wear morphology of the worn surface of the substrate and alloyed layer after wear for 904.32 m is shown in [Figure 3.8](#), among which [Figure 3.8a](#) and [b](#) is from the laser confocal stereomicroscopy, and [Figure 3.8c](#) and [d](#) is from the SEM, [Figure 3.8a and c](#) is from the substrate, and [Figure 3.8b and d](#) is from the alloyed layer. After sliding for 904.32 m, wear of the substrate is largely abrasive, in which debris served as wear particles. The worn surface was characterized by deep and fairly long continuous grooves ([Figure 3.8a](#)), which may be formed by the fragments of the particles produced in the wear process, indicating an abrasive wear. Microploughing and some patches of iron transfer could be detected ([Figure 3.8c](#)), indicating adhesive wear. Plastic deformation can also be observed. In adhesive wear, if the shear strength of the contacting area is between those of the two contacting materials, material will be easily transferred from the soft one to the hard one. The hardness

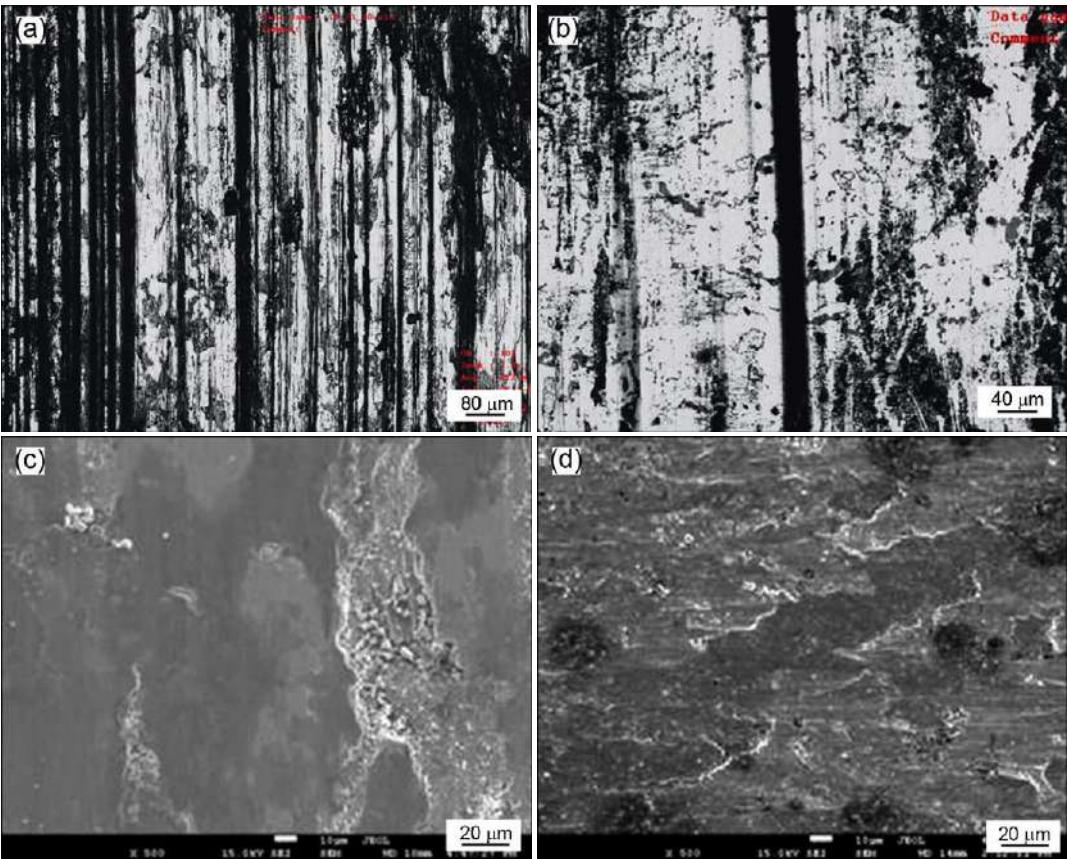


**Figure 3.8** Micrographs of the worn surfaces of (a, c) NCIR substrate and (b, d) alloyed layer after wear test for 904.32 m.

of the counterpart 60# steel (713 HV) is higher than that of the substrate (500 HV), so at high temperature, the material transfer in the adhesive wear must be from the NCIR substrate pin to the disk.

In contrast, the worn surface of the laser-alloyed layer appeared smooth after sliding for 904.32 m, indicating improved adhesive wear, as shown in [Figure 3.8b and d](#). The attached material on the surface of the alloyed layer (1201 HV<sub>0.05</sub>) was the disk material from the 60# steel (713 HV<sub>0.05</sub>). While there were also minor cutting wear grooves on the wear surface, the number of grooves was greatly reduced compared with that of the substrate, indicating an improved abrasive wear resistance.

### **3.3.5 Conclusions of NCIR laser-alloyed with C-B-W-Cr powders**

1. The alloyed layer on NCIR with C-B-W-Cr powders, which was composed of dendrites and eutectics, has pores and cracks in it.
2. XRD results indicated the existence of solid solution, retained austenite, martensite, and a lot of carbides, improving the microhardness from 500 HV<sub>0.05</sub> of the substrate to an average of 1201 HV<sub>0.05</sub> of the alloyed layer on NCIR.
3. Wear test results at 500 °C in ambient air showed that the wear resistance of the alloyed layer on NCIR was 0.6 times higher than that of the NCIR substrate.

## **3.4 Laser surface alloying of NiCr-Cr<sub>3</sub>C<sub>2</sub> powders on semisteel rolls**

Semisteel rolls have high hardness but low toughness, due to the existence of large carbides. NiCr-Cr<sub>3</sub>C<sub>2</sub> powder was used as the alloy powder to form metal matrix systems. The effects of the thickness of the prelayer on the microstructure, phases, hardness, and wear resistance were examined. The powder was preplaced on the rollin different thicknesses. Several trials were done before the final processing parameters (listed in [Table 3.3](#)) were determined. All the experiments were done with the spot diameter of 1.5 mm and the overlapping rate of 33.3%.

**Table 3.3 Processing parameters for the laser surface alloying on semisteel rolls**

Specimen no.	Laser power (kW)	Scanning speed (m min <sup>-1</sup> )	Thickness of the pre-layer (μm)	Average thickness of the alloyed layer (mm)
1	4	1.8	30	0.69
2	4	1.8	18	0.64

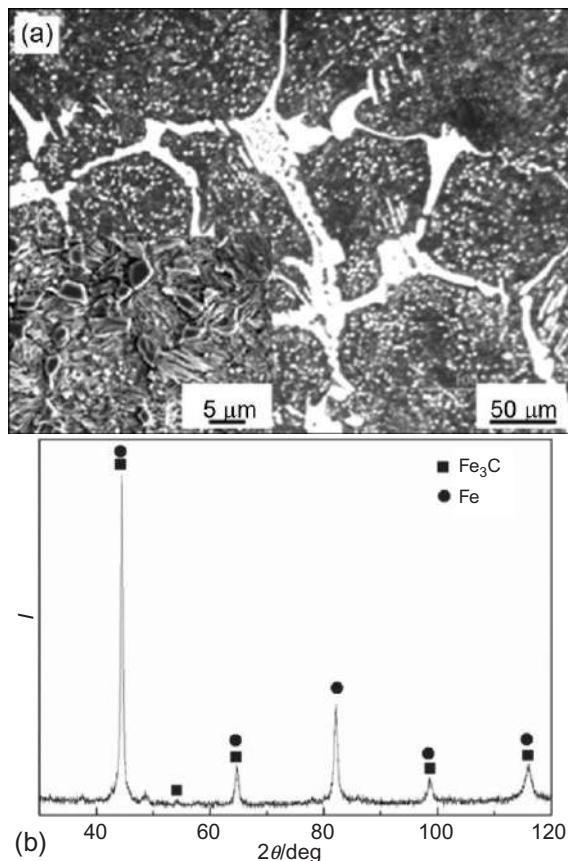


**Figure 3.9** Microstructure (a) and XRD pattern (b) of semisteel rolls.

### 3.4.1 Microstructure and phases of the semisteel rolls

The microstructure and phases of the semisteel roll are shown in Figure 3.9. It can be seen that the substrate was composed of pearlite, ledeburite, net-shaped cementite, and a lot of fine carbides with various shapes.

### 3.4.2 Morphology of the cross sections of the alloyed layers on semisteel rolls

Values of the thicknesses of the two layers are listed in Table 3.3. According to them, the thicknesses of the alloyed layers went up with the thickness of the prelayer. With a laser power and spot diameter of the same value, thicker prelayers were associated with more material melting into the molten pool caused by the interaction between the laser and the prelayer. This phenomenon also indicated that the laser energy was enough to melt the prelayer of specimen 2, which had a thinner prelayer, and that

there must be more substrate material in the alloyed layer of specimen 2 than in the same layer of specimen 1.

The morphology of the cross sections of the alloyed layers of specimens 1 and 2 is shown in [Figure 3.10](#). As can be seen, both of the alloyed layers were pore- and crack-free, and there were heat-affected zones (HAZ) beneath them.

[Figure 3.11](#) shows the microstructure of the two alloyed layers. Both of them were composed of dendrites and interdendrites, which was typical for laser-treated layers. The second arm distance of dendrites in the layer of specimen 1 ( $2.1\text{ }\mu\text{m}$ ) was close to that of specimen 2 ( $2\text{ }\mu\text{m}$ ). Spots 1 and 2 in [Figure 3.4b](#) are taken from the dendrite and interdendrite in the layer of specimen 2, respectively. Their composition is listed in [Table 3.3](#). The composition of C is not accurate, but the comparison of its content between the dendrite and interdendrite can be useful. According to [Figure 3.4](#) and [Table 3.3](#), one can tell that the dendrite was rich in Si, Ni, and Fe, while the interdendrite was rich in C and Cr. The existence of Si indicated the large degree of the mixture of the substrate material in the alloyed layer.

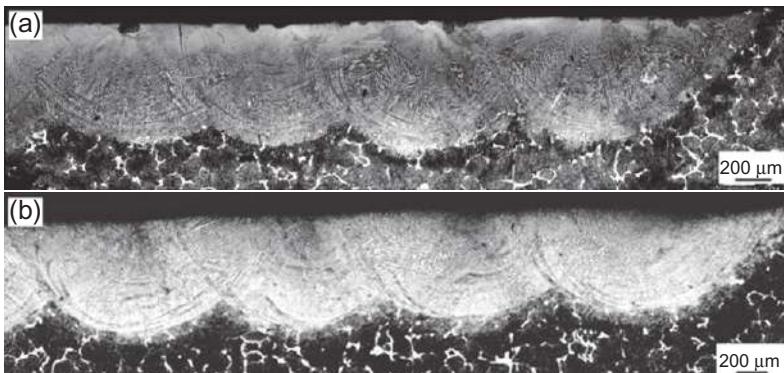


**Figure 3.10** Morphology of the cross sections of (a) specimen 1 and (b) specimen 2.

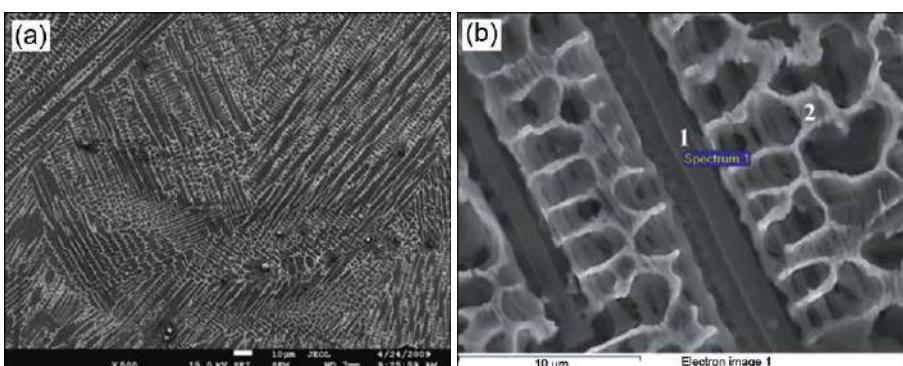


**Figure 3.11** Microstructure of the alloyed layers of (a) specimen 1 and (b) specimen 2.

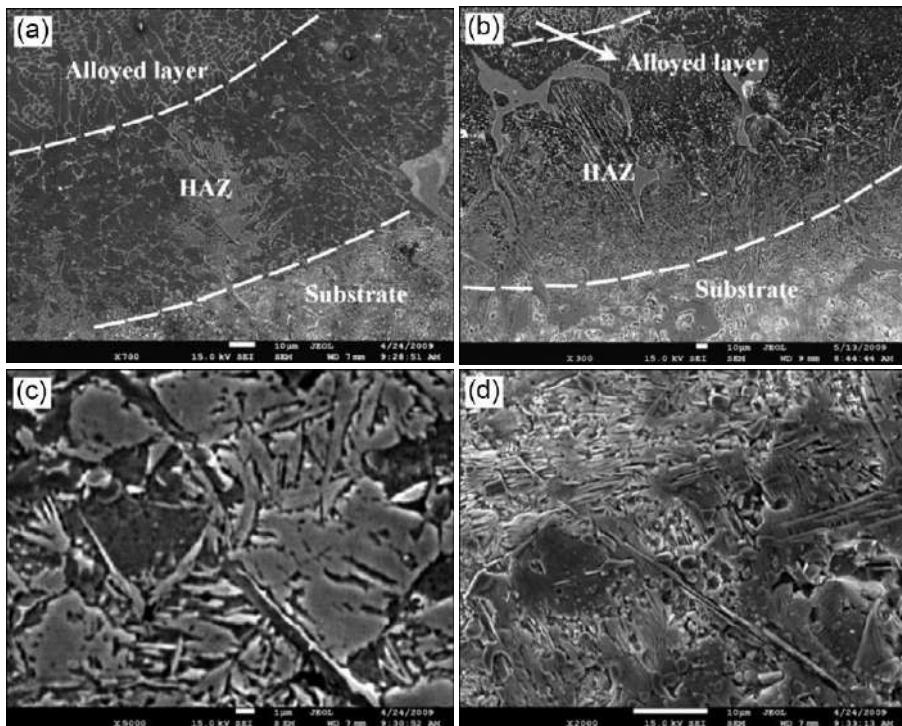


**Figure 3.12** SEM images of (a, c) HAZ of specimen 1, (b) HAZ of specimen 2, and (d) semisteel substrate.

### 3.4.3 Microstructure of the heat-affected zones

As can be seen in [Figure 3.12a and b](#), the bonding area can be divided into three zones: the alloyed layer, HAZ, and the substrate. As the result of the heat effect passed from the molten pool, a lot of carbides dissolved partially in the HAZ of specimen 2, as shown in [Figure 3.12b](#). At the same time, in the HAZ of specimen 1, some large carbide decomposed and got blurred at the fringe ([Figure 3.12a](#)), and some martensite could also be observed ([Figure 3.12c](#)). [Figure 3.12d](#) shows the microstructure of the substrate beneath the HAZ of specimen 2. As can be observed, a lot of carbide dispersed on the perlite matrix. The fringe of these carbides is not as sharp as the fringe of the carbides in [Figure 3.9a](#) as the result of the heat effect.

### 3.4.4 Phases in the alloyed layers

The XRD pattern of the layers of specimens 1 and 2 are presented in [Figure 3.13](#). As can be seen from the images, austenite, martensite,  $\text{Cr}_7\text{C}_3$ , and cementite were detected on the layer of specimen 1 ([Figure 3.13a](#)), while austenite and  $\text{Cr}_7\text{C}_3$  were detected on the layer of specimen 2 ([Figure 3.13b](#)). The difference is that the alloyed

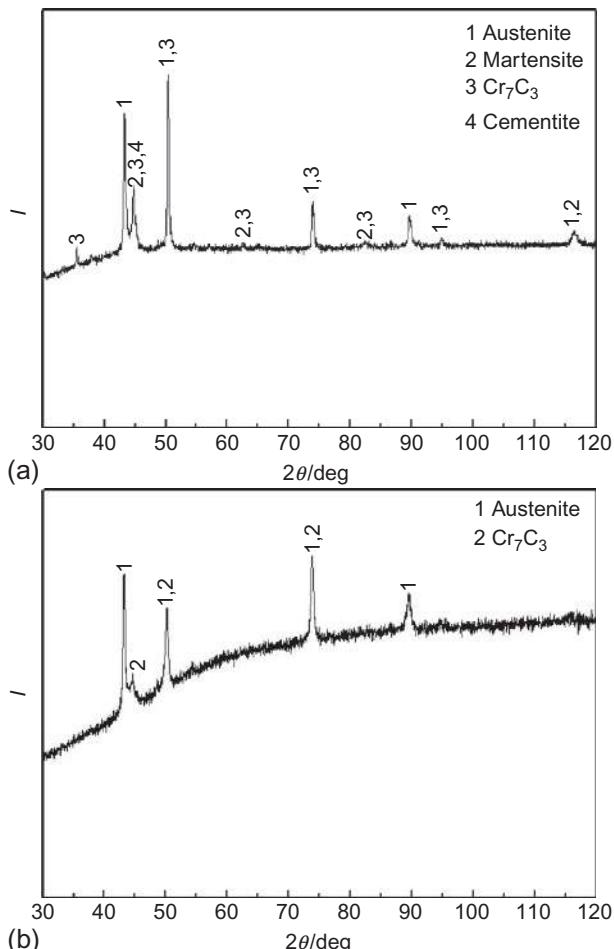
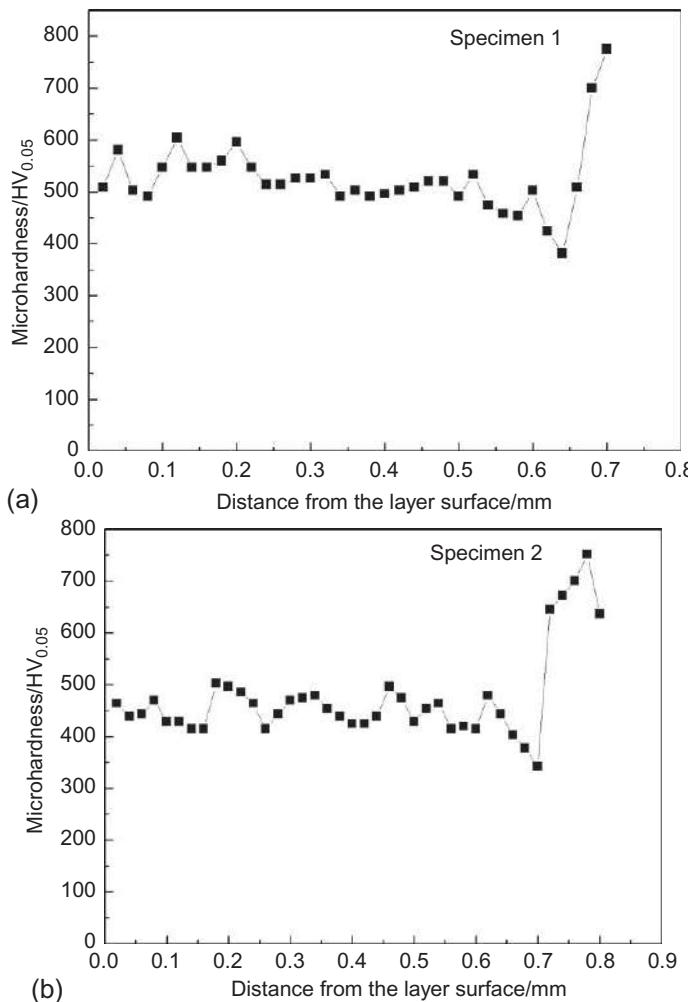


Figure 3.13 XRD pattern of layers of (a) specimen 1 and (b) specimen 2.

layer of specimen 2 did not have the martensite and cementite peaks in the XRD pattern. Furthermore, there was more austenite in the layer of specimen 2 than that of specimen 1.

### 3.4.5 Microhardness and wear properties of the alloyed layer on semisteel rolls

The variations of microhardness along the depth of the alloyed layer of specimen 1 and specimen 2 are given in Figure 3.14. The hardness fluctuation was relatively small throughout both layers of specimen 1 and specimen 2. The partial dissolution of carbides and the release of stress in the HAZ contributed to the microhardness



**Figure 3.14** Microhardness distribution along the depth of the layers of (a) specimens 1 and (b) 2.

descent at the HAZ. Additionally, the average hardness values of 510 and 437 HV<sub>0.05</sub> were achieved for the alloyed layers of specimen 1 and specimen 2, respectively. Both of them were smaller than the value for the substrate (716 HV<sub>0.05</sub>), with the difference possibly explained by the fact that there was a large fraction of retained austenite in both of the alloyed layers. The layer of specimen 2 had a lower microhardness compared with that of specimen 1, owing to less carbide and more retained austenite in it.

Table 3.4 shows the weight loss comparison of the substrate and the specimens before and after the wear test. Specimen 2 has the least weight loss (0.0033 g), and

**Table 3.4 Weight loss comparison in the wear test (g)**

	<b>Weight before wear test</b>	<b>Weight after wear test</b>	<b>Weight loss</b>
Specimen 1	2.5347	2.5274	0.0073
Specimen 2	2.5320	2.5287	0.0033
Substrate	2.5274	2.5112	0.0162

specimen 1 follows it (0.0073 g), while the substrate has the most weight loss (0.0162 g). The wear results of the wear test at 500 °C indicated that the weight loss of the substrate was 2.2 and 4.9 times of that of specimen 1 and specimen 2, respectively. Specimen 2 was the most wear-resistant among them.

Worn surfaces of the substrate and the layer of specimens 1 and 2 are shown in [Figure 3.15](#), and the chemical composition of the worn debris on them is given in [Table 3.5](#). After sliding for 904.32 m, wear of the substrate is largely adhesive wear, indicated by the microploughing and some patches of iron transfer ([Figure 3.15a](#)). The worn surface was also characterized by continuous grooves ([Figure 3.15a](#)), indicating abrasive wear in which debris served as wear particles. They may be formed by the fragments of the particles produced in the wear process. According to the EDX analysis ([Table 3.5](#)) of spot 1 in [Figure 3.15b](#), Fe, C, Mn, Cr, and O existed in the debris on the worn surface of the substrate, which indicated that oxidation wear occurred. The content of O and C obtained from the EDX are not accurate, but their relative content can be compared. The relative content of O was pretty high here. The fact that the oxidized fragments of the substrates served as the abrasive particles in the abrasive wear can be concluded. The formed oxidation film was torn off the substrate with the new substrate face outside and only the lower right part had the oxidation film on it.

In contrast, the worn surface of the layer of specimen 1 appeared smooth after sliding for 904.32 m, indicating improved adhesive wear, as shown in [Figure 3.15c and d](#). While there were also minor cutting wear grooves on the wear surface, the groove volume was much smaller than that of the substrate, indicating an improved abrasive wear resistance. EDX analysis of debris on the layer of specimen 1 (spot 2 in [Figure 3.15d](#)) in [Table 3.5](#) indicated Fe, Cr, C, and O existed on the worn surface of it, suggesting oxidation wear. But the relative O content here was less than that in the substrate. From the morphology of the oxidation film one can tell that the oxidation film was fragile with a pretty low toughness.

The wear surface of the alloyed layer of specimen 2 is shown in [Figure 3.15e and f](#). A dark and tough oxidation film was formed on top of the layer during the wear test, indicated by [Figure 3.15e](#). Some of them flaked off the substrate, with new surface exposing itself to the air. Under the shearing stress and wearing heat that acted on the scraps, which were the material removed from the surface during wear, the scraps curved, oxidized, and served as abrasive particles. At the same time, there was some part of the oxidation film still sticking to the layer ([Figure 3.15e](#)). The composition of the debris was close to that on the layer of specimen 2.

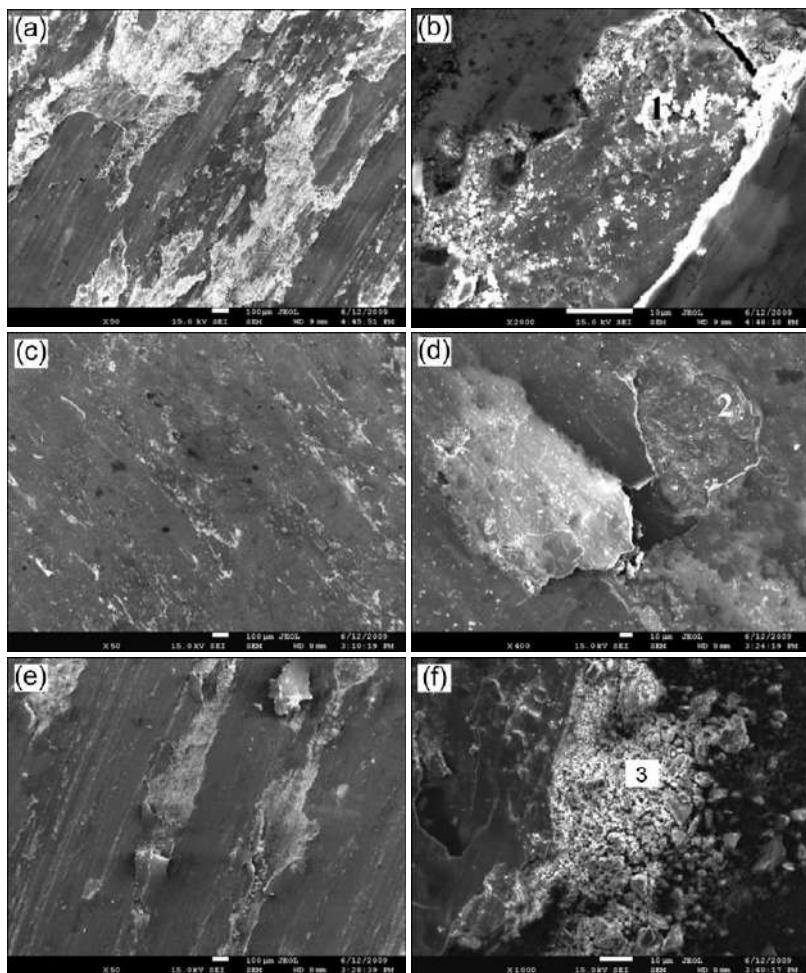


**Figure 3.15** Wear surfaces of (a, b) the substrate, (c, d) layer of specimen 1, and (e, f) layer of specimen 2.

**Table 3.5 Composition of the spots in Figure 3.15 (wt.%)**

Spot	C	Cr	Mn	O	Fe
1	4.29	0.92	0.77	34.52	59.5
2	2.12	1.62	0	26.34	69.91
3	1.9	2.01	0	28	68.09

### **3.4.6 Conclusions of semisteel rolls laser-alloyed with NiCr-Cr<sub>3</sub>C<sub>2</sub> powders**

Laser surface alloying was used to form a wear-resistant layer on semisteel rolls with NiCr-Cr<sub>3</sub>C<sub>2</sub> powders.

1. The alloyed layers were pore and crack free and had a metallurgical bonding with the substrate.
2. The thicknesses of the alloyed layers increased with the thickness of the prelayer.
3. Microhardness of both of the two layers was lower than that of the substrate as the result of the high fraction of retained austenite.
4. Wear test results at 500 °C in ambient air showed that the wear resistance of the alloyed layers on semisteel rolls was 2.2 and 4.9 times that of the semisteel roll substrates.

## **3.5 Laser surface alloying of NiCr-Cr<sub>3</sub>C<sub>2</sub> powders on cast steel rolls**

Cast steel rolls have good toughness but low hardness (220–300 HV). Their poor wear resistance results in a short service life. NiCr-Cr<sub>3</sub>C<sub>2</sub> powders were laser-alloyed on the cast steel rolls to improve their wear resistance. The effects of the processing parameters on the microstructure, phases, hardness, and wear resistance were examined. The effect of retained austenite on the wear resistance was also discussed.

The powder was preplaced on the roll with a thickness of 20 µm. Laser processing parameters are listed in [Table 3.6](#).

### **3.5.1 Microstructure and phases of the cast steel roll substrate**

The microstructure and phases of 70 MnV cast steel are shown in [Figure 3.16](#), which indicated that the substrate was composed of pearlite and ferrite.

### **3.5.2 Morphology of the cross sections of the alloyed layers on cast steel rolls**

Values of the thicknesses of the four layers are listed in [Table 3.6](#). According to them, the thicknesses of the alloyed layers decreased with the increase of the scanning speed. With the laser power and spot diameter of the same value, the larger the scanning

**Table 3.6 Processing parameters for laser surface alloying**

No.	Laser power (kW)	Scanning speed (mm s <sup>-1</sup> )	Spot diameter (mm)	Overlap rate (%)	Average thickness of the layers (mm)
A1	4	26.67	1.5	33.3	0.577
A2	4	30.0	1.5	33.3	0.550
A3	4	33.33	1.5	33.3	0.530
A4	4	36.67	1.5	33.3	0.480

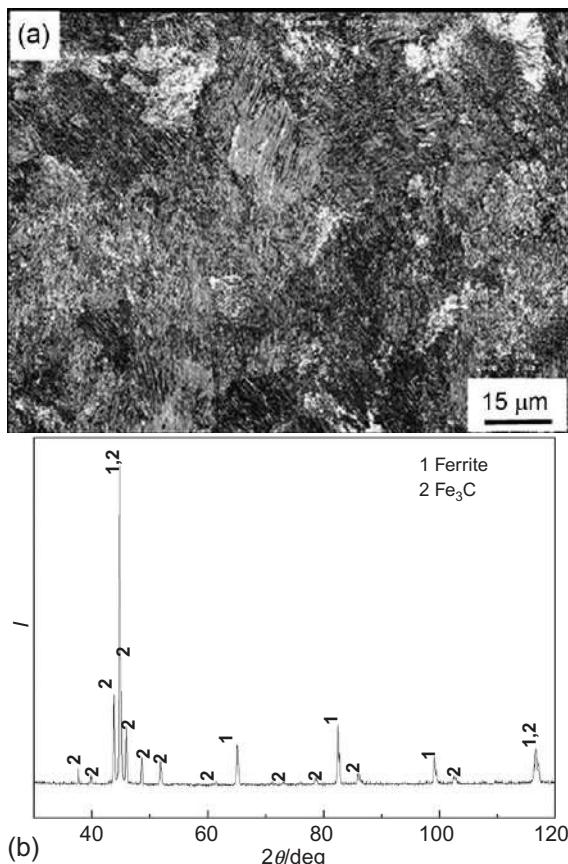


**Figure 3.16** Microstructure (a) and XRD pattern (b) of the 70 MnV cast steel roll.

speed, the shorter the interaction time was between the laser and the substrate. Consequently, less energy was absorbed by the substrate, resulting in a narrower molten pool on the surface of the substrate and leading to a relatively thinner layer than that of the specimen made with a lower scanning speed.

Morphology of the cross sections of the alloyed layers of specimens A1 to A4 is shown in Figure 3.17. Given that the differences among their thicknesses are small, it is hard to differentiate them through the pictures. All four cross sections can be divided into three parts: alloyed layer, heat-affected zone (HAZ, the dark area beneath the layer), and the substrate, as shown in Figure 3.17a-d. Because of the good heat conductivity of the cast steel, heat from the molten pool was conducted to the substrate quickly. The temperature of all the HAZs was over the austenization temperature during the laser processing, resulting in the phase transformation in the subsequent cooling process. The microstructure of the HAZ was different from area to area, as indicated by the morphology of the areas marked as N-1 and N in Figure 3.17d, which is in accordance with the heat course they have undergone.

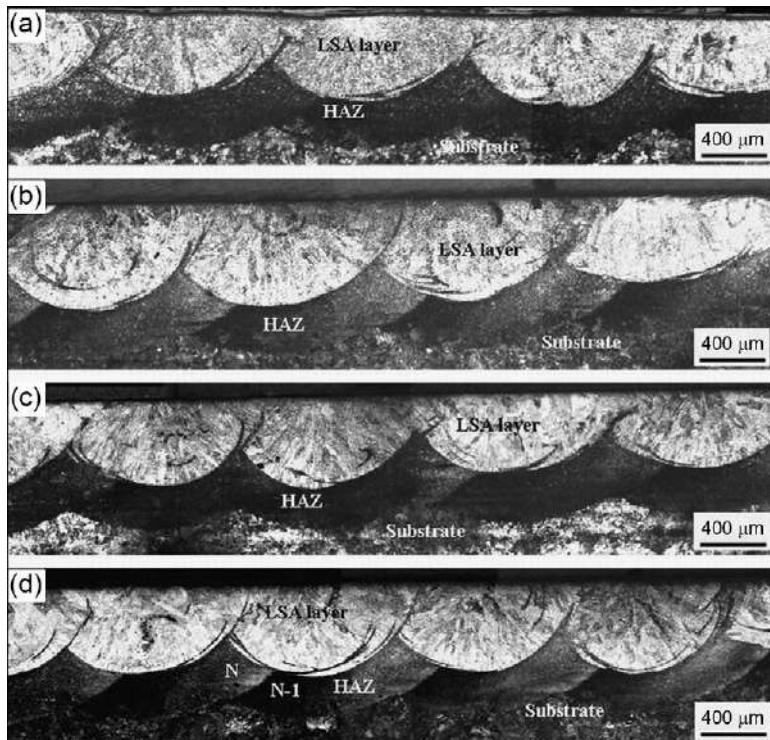


**Figure 3.17** Morphology of the cross sections of the alloyed specimens on cast steel rolls; (a–d) are corresponding to specimens A1 to A4.

### 3.5.3 Microstructure of the alloyed layers on cast steel rolls

The microstructure of the alloyed layers of specimens A1-A4 is shown in Figure 3.18. Martensite, residual austenite, and carbides can be observed in the layers, the morphology of which varied with cooling rates. The morphology of martensite varied with the carbon content. Lath martensite was formed where the carbon content was low, while acicular martensite was formed with a high C content. The alloyed layers were composed of acicular martensite, indicating high carbon content in the molten pool. As far as the carbides are concerned, they precipitated from the austenite during the cooling process. Due to the size effect, some of them could not be observed (see Figure 3.18a), while some of them can be detected as indicated by the arrows in Figure 3.18b-d.

As also can be observed from Figure 3.18, the retained austenite content increased with the scanning speed. In order to differentiate the retained austenite and martensite, different magnifications were used for the pictures. The layers of specimens A1 and A2 consisted of a large amount of martensite, and retained austenite can hardly be distinguished. With the increase of the scanning speed, the cooling rate of the molten pool increased, the time for the convection and diffuse of the alloying elements in the molten pool decreased, resulting in a supersaturated austenite. The high carbon content in austenite might inhibit the martensitic transformation (see also [58,59]), which accounted for the lower martensite with increasing scanning speed. The volume of

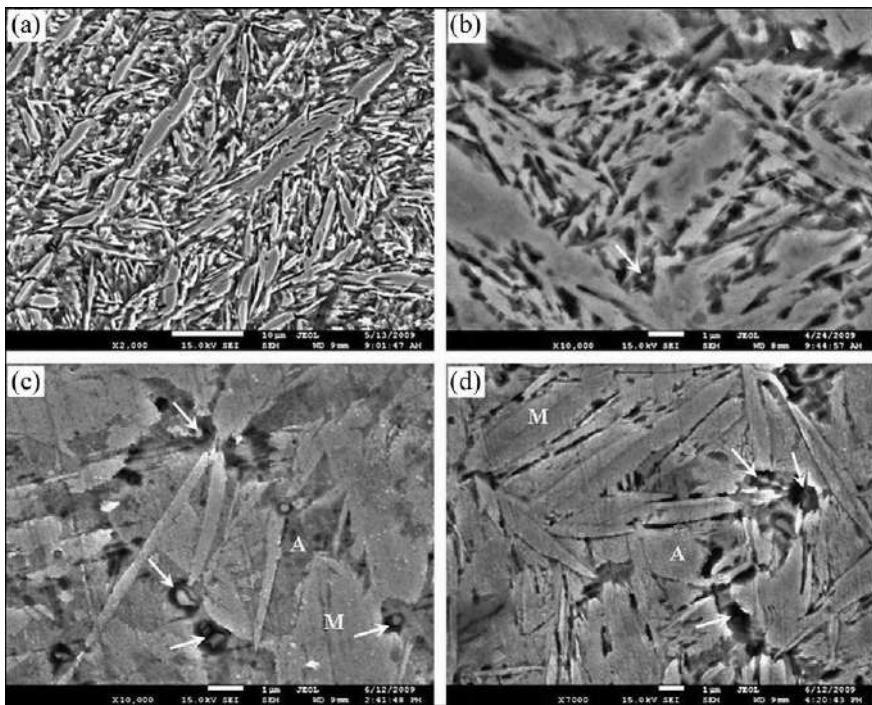


**Figure 3.18** SEM pictures of the alloyed layers of specimen (a-d) A1-A4 on cast steel rolls.

retained austenite was relatively small. The variation of scanning speeds is not as large as the one used in the literature [60], thus the variation of the volume of retained austenite was relatively small.

At the same time, the grain size became smaller with increasing scanning speed, which is also a result of the increase of cooling rate.

### 3.5.4 Phases of the laser-alloyed layers on cast steel rolls

XRD pattern of the layers of specimens A1-A4 is shown in [Figure 3.19](#). In order to be accurate, a slow scanning was conducted when the value of  $2\theta$  is between  $40^\circ$  and  $50^\circ$ , as shown in [Figure 3.19a-d](#). As can be seen from [Figure 3.19](#), martensite, retained austenite,  $\text{Cr}_7\text{C}_3$ , and  $\text{Fe}_3\text{C}$  coexisted in all of the layers. The main phases were retained austenite and martensite. There was a slight difference in the diffraction angle and the intensity of phases. Because the alloyed layers had more than two phases, it is hard to calculate the quantity of martensite and retained austenite. But, the relative content of the retained austenite can be observed from the intensity of them in [Figure 3.19a-d](#). The volume of retained austenite in the alloyed layers increased from specimens A1 to A4. That is to say, the volume of retained austenite increased with increasing scanning speed. This is in good agreement with the observations of the laser surface melted tool steels [60].

The diffraction lines of martensite became broadened as can be obviously seen in [Figure 3.19a-d](#). The broadening of the diffraction peaks indicated the existence of

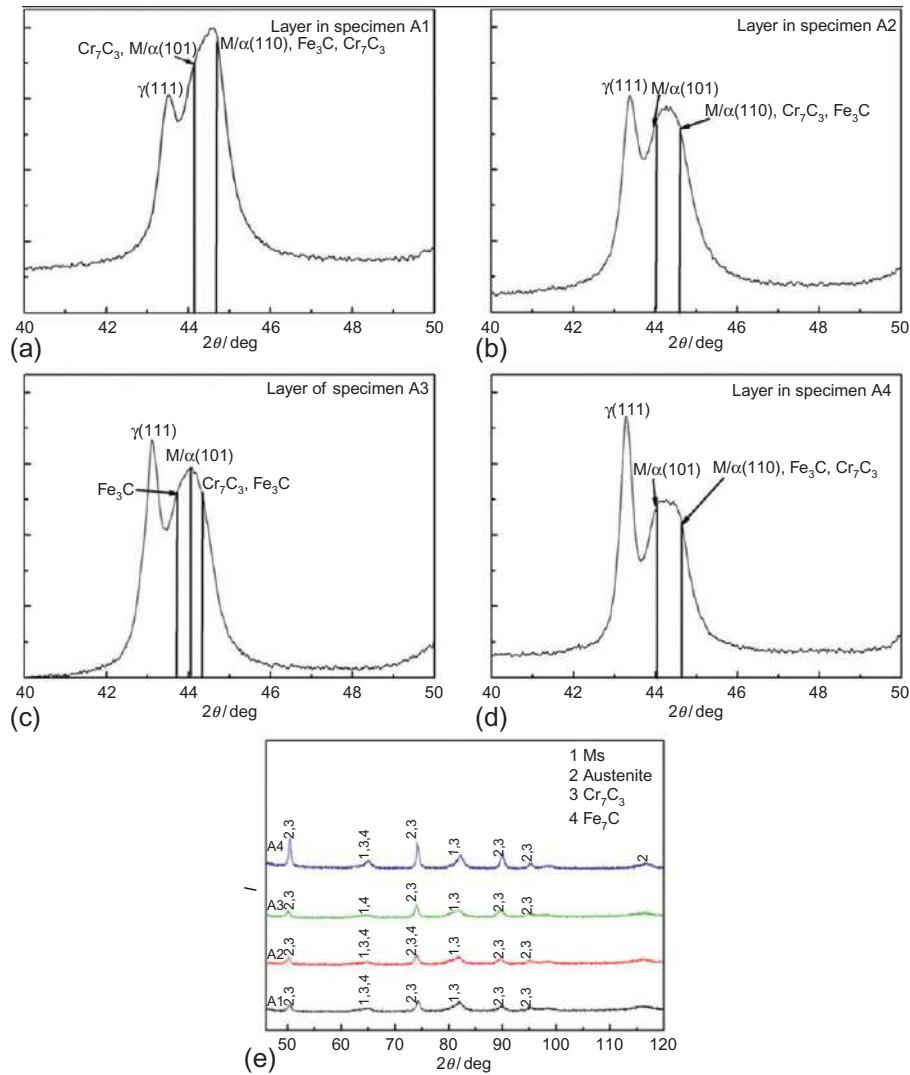


**Figure 3.19** XRD pattern of layers of specimens A1-A4, (a)-(d) slow scan of A1-A4 between 40 and 50 deg ( $2\theta$ ) and (e) fast scan of four of them.

size effect and strain effect (dislocations) [61–63], which also improved the hardness of the alloyed layers.

### 3.5.5 Microhardness and wear behavior of the laser alloyed layers and the cast steel substrate

The variation of microhardness along the depth of the layers of specimen A1-A4 is given in Figure 3.20. The hardness was relatively constant throughout the layer with a decrease at the HAZ and another one at the substrate. All the layers had a much higher

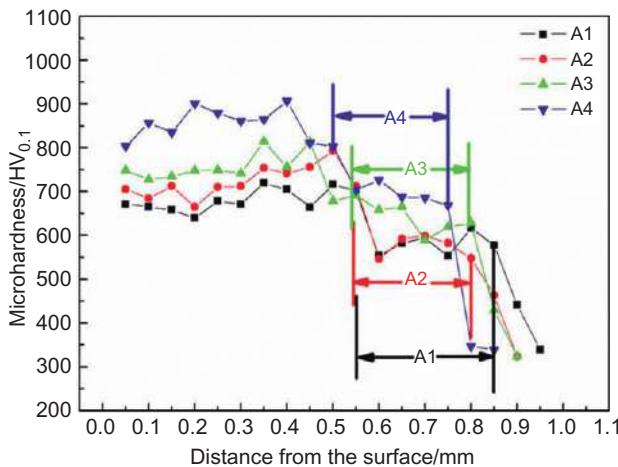


**Figure 3.20** Microhardness distribution along the depth of the layers of specimens A1-A4.

**Table 3.7 Relative wear resistance of the substrate and the layers of specimens A1-A4**

Sliding distance (m)	Substrate	A1	A2	A3	A4
452.16	1	1.4	1.5	3.0	6.3
904.32	1	1.6	1.7	2.7	8.8

microhardness than the substrate did, which may be mainly attributed to the formation of Cr<sub>7</sub>C<sub>3</sub>, Fe<sub>3</sub>C and martensite hard phases in the layers as well as the solid solution strengthening in the supersaturated γ-Fe solid solution. Additionally, in spite the volume of retained austenite increased with increasing scanning speed, the hardness of the layers also increased with the scanning speed, which must be attributed to the fine microstructure, dislocations and the high degree of saturation of the solid solution brought by the high scanning speed (also see [50]). The average value of the microhardness in the layer of specimen A4 was 858 HV<sub>0.1</sub>, which was almost 2.6 times that of the substrate (326 HV<sub>0.1</sub>). The thicknesses of the HAZ decreased with the increasing of the scanning speed, as indicated by the HAZ ranges of each specimen in [Figure 3.20](#).

The relative wear resistance (defined as the ratio of the wear mass loss of the substrate to that of the layer) of the substrate was improved to some extent according to the data in [Table 3.7](#). Furthermore, it increased with the laser scanning speed and the sliding distances, except specimen A3 had a little decrease after sliding for 904.32 m. Among them, specimen A4 had the best relative wear resistance ([Table 3.7](#)), which was 6.3 times that of the substrate after sliding for 452.16 m. This value increased to 8.8 after sliding for 904.32 m at the same temperature. In a word, laser surface alloying can significantly improve the wear resistance of the 70 MnV substrate.

Worn surfaces of the substrate and the layer of specimen A4 are shown in [Figure 3.21](#) and chemical composition of the worn debris on them (spots 1, 2, 3,

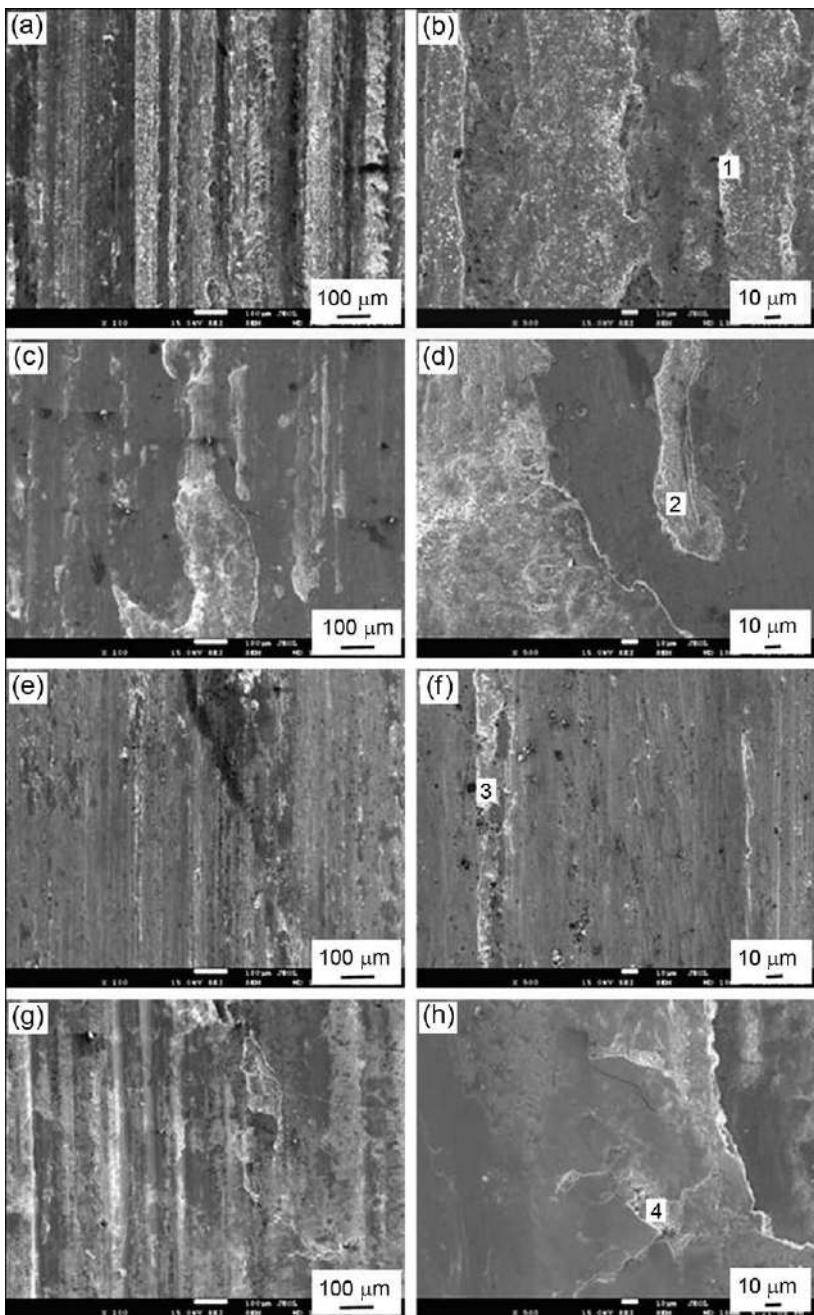


**Figure 3.21** Worn surfaces of the cast steel roll and the layer of specimen A4, (a-d) substrate, (e-h) layer, (a), (b), (e), and (f) sliding for 452.16 m and (c), (d), (g), and (h) sliding for 904.32 m.

**Table 3.8 Composition of debris on the cast steel rolls for different sliding distances**

Wear distance (m)	Composition (at.%)		
	Fe	O	C
452.16	37.64	53.84	7.53
904.32	34.53	61.05	3.61

**Table 3.9 Composition of debris on the layer of specimen A4 for different sliding distances**

Wear distance (m)	Composition (at.%)			
	Fe	O	C	Cr
452.16	72.12	13.9	10.61	1.09
904.32	69.71	24.29	4.74	1.25

and 4) is given in [Tables 3.8](#) and [3.9](#), respectively. After sliding for 452.16 m, wear of the substrate is largely abrasive, in which debris served as wear particles. The worn surface was characterized by deep and fairly long continuous grooves ([Figure 3.21a](#)). The grooves may be formed by the fragments of the particles produced in the wear process. Microploughing and some patches of iron transfer could be detected ([Figure 3.21b](#)), indicating adhesive wear. Plastic deformation can also be observed in [Figure 3.21a and b](#). In adhesive wear, if the shear strength of the contacting area is between those of the two contacting materials, material will be easily transferred from the soft one to the hard one. The hardness of the counterpart 60# steel (713 HV) is higher than that of the substrate (326 HV<sub>0.5</sub>), so the material transfer in the adhesive wear must be from the substrate pin to the disk. According to the EDX analysis (spot 1 in [Table 3.8](#)), Fe, C, and O existed in the debris on the worn surface of the substrate, which indicated that oxidation wear occurred. The content of O and C obtained from the EDX are not accurate, but their relative content can be compared. The relative content of O was pretty high here. The fact that the oxidized fragments of the substrates served as the abrasive particles in the abrasive wear can be concluded.

In contrast, the worn surface of the layer of specimen A4 appeared smooth after sliding for 452.16 m, indicating improved adhesive wear, as shown in [Figure 3.21e and f](#). While there were also minor cutting wear grooves on the wear surface, the groove volume was much smaller than that of the substrate, indicating an improved abrasive wear resistance. EDX analysis of debris on the layer of specimen A4 (spot 3 in [Table 3.9](#)) indicated Fe, Cr, C, and O existed on the worn surface of it, suggesting

oxidation wear. But the relative O content here was much less than that in the substrate.

As the sliding increased to 904.32 m, the surfaces of both the substrate and the layer of specimen A4 turned rougher and severe oxidation could be observed on the substrate (spots 2 and 4 in [Tables 3.8 and 3.9](#), [Figure 3.21c, d, g, and h](#)). For the substrate, some debris flaked off the substrate, with new surface exposing itself to the air. Under the shearing stress and wearing heat that acted on the scraps, which were the materials removed from the surface during wear, the scraps curved, oxidized, and served as abrasive particles. At the same time, there was some debris still sticking to the substrate but severely oxidized ([Figure 3.21c and d](#)). In contrast, obvious oxidation could also be observed on the surfaces of the layer of specimen A4, but no flaking of the layer occurred.

Furthermore, the oxidation of the layer surface was much less than that of the substrate surface, as indicated by the color of the surface. The phases in the alloyed layer of specimen A4 after sliding for 904.32 m was shown in [Figure 3.22](#). As can be seen, they are mainly  $\text{Fe}_2\text{O}_3$  with some  $\text{Fe}_3\text{O}_4$ , which is similar to the wear debris of spray cast high-speed steels when worn at ambient and 300 °C [61].

### **3.5.6 Conclusions of cast steel rolls laser-alloyed with NiCr-Cr<sub>3</sub>C<sub>2</sub> powders**

This work has examined the laser surface alloyed layers of NiCr-Cr<sub>3</sub>C<sub>2</sub> powder on 70 MnV rolls. The major results are as follows:

1. All of the alloyed layers under four processing conditions were pore and crack free, had fully dense and homogeneous structures, as well as a metallurgical bonding with the substrates. When the parameter combination was laser power 4000 W, scanning speed 36.67 mm/s, spot

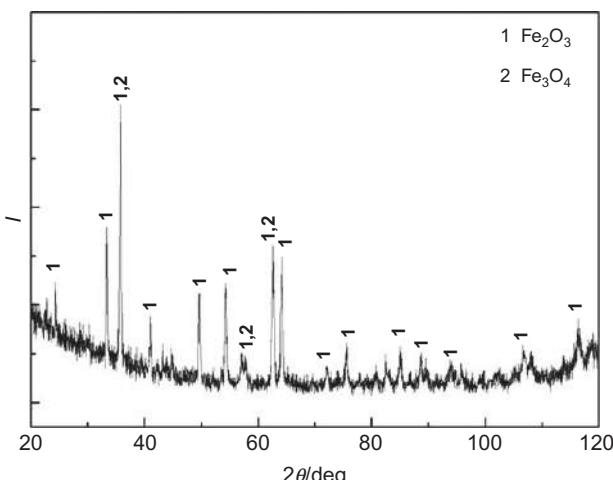


**Figure 3.22** XRD pattern of the worn surface of specimen A4 after wear for 904.32 m at ambient and 500 °C.

diameter 1.5 mm, and overlapping rate 33.3%, the alloyed layer had the highest microhardness and wear resistance. The thickness and average hardness of this layer were 0.48 mm and 858 HV<sub>0.1</sub>, respectively. The wear resistance of the laser-alloyed layer was 8.8 times that of the substrate after sliding for 904.32 m at ambient and 500 °C.

2. As the scanning speed increased, the thickness of the layer and the HAZ decreased, the microstructure of the layer fined, the fraction of austenite was retained, and the hardness and the wear resistance of the layer increased.
3. The phases that occurred in the alloyed layers were martensite, retained austenite, Cr<sub>7</sub>C<sub>3</sub>, and Fe<sub>3</sub>C.

## 3.6 Wear behavior of the three kinds of alloyed layers and three roll substrates

### 3.6.1 The alloyed layers and NCIR

First of all, the increase in the microhardness and wear resistance of the alloyed layer on NCIR mainly contributed to the solid solution strengthening in the austenite and martensite and the grain refinement introduced by the laser treatment. Second, as is well-known, retained austenite was always found in laser-treated layers on steels as the result of the fast cooling rate. It is found that the stress-induced transformation of austenite into martensite plays an important role in the increase of the wear resistance of the material with increasing load at room temperatures in air [64]. Third, Cr<sub>7</sub>C<sub>3</sub> and M<sub>23</sub>C<sub>6</sub>, which are used as one of the hard phases, can improve wear resistances of metallic matrix [65,66]. Obviously, the microstructure and phases of the laser-treated layers will change at elevated temperatures. For example, M<sub>23</sub>C<sub>6</sub> and M<sub>7</sub>C<sub>3</sub> carbides will be formed within the austenite matrix of high Cr white irons when destabilized at 1273 K for 4 h [67]. Consequently, the changes are positive to improve the wear resistance of the materials.

### 3.6.2 The alloyed layers and semisteel rolls

It is found that no matter how high a heat-treatment temperature is used, there is always less carbon in solution after treatment than in the as-cast state [48]. It is easy to conclude that carbides precipitated from the retained austenite and the unstable austenite transformed into martensite partially during the wear test at 500 °C [68], improving the wear resistance. In addition, retained austenite can improve abrasion resistance due to its work-hardening properties [69,70]. It was also observed that the stress-induced Magneli phase formation during the tribological test could decrease the friction coefficient on the oxidized surface [71]. On the one hand, the tough retained austenite improved the adhesion force between the oxide film and the layer. On the other hand, the formed oxide film can protect the inner part of the layer by sacrificing itself. When the adhesion force between the oxide film and the layer was not strong enough to resist the shear force on it, it was torn off the layer. As the sliding went on, new oxide film was formed and a new circle started. The toughness of the oxide film and the high wear resistance of the alloyed layer of specimen 2

as compared to those of specimen 1, owed to the high content of retained austenite in the alloyed layer of specimen 2, indicating the positive effect of retained austenite on improving wear resistance at high temperature.

The positive effect of lots of kinds of oxide films on wear resistance has been reported widely [72–77]. The effects of the temperature, load, and sliding time on the wear behavior of the semisteel substrate and the alloyed layers still need to be studied.

### **3.6.3 The alloyed layers and cast steel rolls**

The wear mechanism of the original cast steel roll substrate shows adhesion, abrasion, ploughing, plastic deformation, and delamination and oxidation, while the mechanisms of the laser-treated layers are mainly minor microcutting, slight adhesive transfer, and oxidation. First, the retained austenite was strengthened by the solution strengthening effect of C, Cr and Ni elements. Second, the retained austenite has a good plasticity, which can reduce the impact. Furthermore, the supersaturated residual austenite is a metastable phase, some of which will change into strain-induced martensite and fine precipitation as carbides at elevated temperatures. This will further improve the wear resistance. Third, the very high hardness of the reinforced carbide phases and the martensite phases prevents the laser-treated layers from wear by severe microcutting and plowing. Fourth, the ductile and tough  $\gamma$ -Fe solid solution matrix could play the very important role of firmly connecting and supporting the hard phases and preventing the reinforced wear-resistant phases and the layer as a whole from wear removal by mechanisms such as microfracturing and fragmentation. As a result, the reinforced carbides can fully exert their wear-resisting abilities.  $\text{Cr}_7\text{C}_3$  is used as one of the hard phases to improve wear resistances of metallic matrix [65,74]. Obviously, the microstructure and phases of the laser-treated layers will change at elevated temperatures. For example,  $\text{M}_{23}\text{C}_6$  and  $\text{M}_7\text{C}_3$  secondary carbides will be formed within the austenite matrix of high Cr white irons when destabilized at 1273 K for 4 h [78]. Finally, the nonequilibrium solidified homogeneous fine microstructure imparts to the layers a good combination of high strength and toughness, which in turn provides the layers with good resistance to spalling and delamination.

### **3.6.4 Comparison between these three-alloyed layers**

From the discussion of the wear mechanism of these three-alloyed layers and substrate, we can see that the improvement in wear resistance is the combined result of the grain refining effect, the solution strengthening effect, the tough  $\gamma$ -Fe matrix, the distribution of the hard phases, and the good bonding between them and the matrix.

As is well-known that retained austenite was always found in laser-treated layers on steels as the result of the fast cooling rate. According to the results of laser surface melting of different steels, the effect of retained austenite on the wear resistance is still a controversial issue [62–64,79,80]. Because a lot of alloying elements were added into the laser surface alloyed layers, the effect of retained austenite on wear resistance

in them might be different from that in the laser surface melted layers. It is found that the stress-induced transformation of austenite into martensite plays an important role in the increase of the wear resistance of the material with increasing load at room temperatures in air [64]. Retained austenite can improve the fracture toughness and the hardness of the materials at certain elevated temperatures as the result of its high toughness and transforming into martensite, respectively [48], which can reduce the impact in rolling and form highly densed dislocations in the working layer. In addition to that, the ductile and tough  $\gamma$ -Fe solid solution matrix could play the very important role of firmly connecting and supporting the hard phases and preventing the reinforced wear-resistant phases and the layer as a whole from wear removal by mechanisms such as microfracturing and fragmentation. As a result, the reinforced carbides can fully exert their wear-resisting abilities.

All the three cases indicated the positive effect of retained austenite on the wear resistance at the same wear conditions.

### 3.7 Conclusions

The authors examined the laser surface alloying with different powders on different rolls, such as C-B-W-Cr powders on high Ni-Cr infinite chilled cast-iron rolls [81], C-B-W-Cr and NiCr-Cr<sub>3</sub>C<sub>2</sub> powders on NCIR [38], NiCr-Cr<sub>3</sub>C<sub>2</sub> powders on semisteel rolls [39], and NiCr-Cr<sub>3</sub>C<sub>2</sub> powders on cast steel rolls [40]. A comparison about the alloyed layer quality (cracks and pores) and the wear resistance improvement of them is summarized in Figure 3.23. First, comparison between the case of the high Ni-Cr infinitesimal chilled cast-iron roll and the NCIR with the C-B-W-Cr as the alloying powder indicated that high content of carbon and alloying elements in the rolls is prone to generating cracks and pores in the laser-alloyed layers. Second, a comparison between the case of the NCIR with the C-B-W-Cr and NiCr-Cr<sub>3</sub>C<sub>2</sub> as alloying powders indicated that the addition of tough bonding powders (NiCr) to the alloying carbides is positive to reduce pores and cracks. Third, laser surface alloying improved the wear resistance of the NCIR, semisteel roll and cast steel roll to different levels

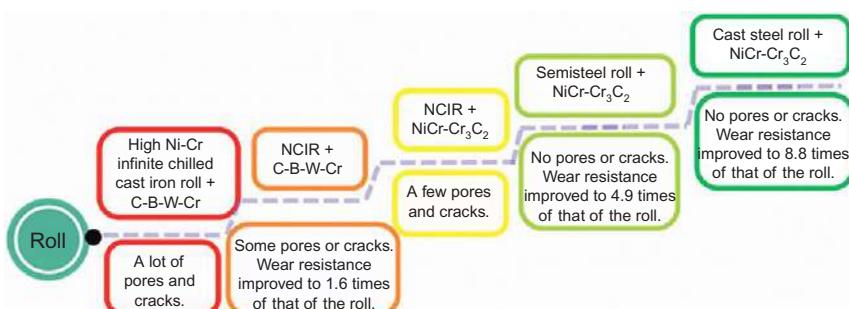


Figure 3.23 Comparison of five different laser surface alloyed layers on different rolls.

compared with the roll substrates with NiCr-Cr<sub>3</sub>C<sub>2</sub> as the alloying powder, indicating that the effect of the laser surface alloying as a strengthening method is especially obvious when the roll material is of low carbon and alloying elements content. A similar result was found in Fang's study that it is suitable to choose a low hardness iron as tribological pairs of ceramics [55]. In a word, rolls with low content of carbon and alloying elements and alloying powders with a tough bonding component are good to obtain a dense and defects free alloyed layer and a large improvement of wear resistance for the substrate. The above-mentioned findings can provide a basic guide for the research of strengthening rolls by laser surface alloying technique.

## References

- [1] J. Dutta Majumdar, I. Manna, *Laser material processing*, Int. Mater. Rev. 5/6 (2011) 341–388.
- [2] H.A. Abdullah, R.A. Siddiqui, Concurrent laser welding and annealing exploiting robotically manipulated optical fibers, Opt. Lasers Eng. 38 (2002) 473–484.
- [3] M.F. Chen, K.M. Lin, Y.S. Ho, Laser annealing process of ITO thin films using beam shaping technology, Opt. Lasers Eng. 50 (2012) 491–495.
- [4] M.R. Viotti, R. Suterio, A. Albertazzi Jr., G.H. Kaufmann, Residual stress measurement using a radial in-plane speckle interferometer and laser annealing: preliminary results, Opt. Lasers Eng. 42 (2004) 71–84.
- [5] H.M. Wang, H.W. Bergmann, Annealing laser-melted ductile iron by pulsed Nd:YAG laser radiation, Mater. Sci. Eng. A 196 (1995) 171–176.
- [6] S.J. Ahn, C.G. Kim, C.G. Park, S.C. Yu, Laser annealing effect of giant magneto-impedance in amorphous Co<sub>66</sub>Fe<sub>4</sub>NiB<sub>14</sub>Si<sub>15</sub> ribbon, Mater. Sci. Eng. A 304–306 (2001) 1026–1029.
- [7] T. Friedel, N. Travitzky, F. Niebling, M. Scheffler, P. Greil, Fabrication of polymer derived ceramic parts by selective laser curing, J. Eur. Ceram. Soc. 25 (2005) 193–197.
- [8] C. Decker, High-speed curing by laser irradiation, Nucl. Instrum. Methods Phys. Res. B 151 (1999) 22–28.
- [9] T.J. Cardwell, R.W. Cattrall, P.J. Iles, I.C. Hamilton, Photo-cured polymers in ion-selective electrode membranes: part 4. An ultraviolet laser cured membrane for potassium, Anal. Chim. Acta 219 (1989) 135–140.
- [10] M.A.F. Scarparo, A. Kiel, Z. Zhiyao, C.A. Ferrari, Q.J. Chen, A.S. Miller, S.D. Allen, Study of resin based materials using CO<sub>2</sub> laser stereolithography, Polymer 38 (1997) 2175–2181.
- [11] J.Y.H. Fuh, L. Lu, C.C. Tan, Z.X. Shen, S. Chew, Processing and characterizing photo-sensitive polymer in the rapid prototyping process, J. Mater. Process. Technol. 89–90 (1999) 211–217.
- [12] J. Daci, D. Bracun, A. Gorkic, J. Mozina, Rapid and flexible laser marking and engraving of tilted and curved surfaces, Opt. Lasers Eng. 49 (2011) 195–199.
- [13] M.F. Chen, Y.P. Chen, W.T. Hsiao, Correction of field distortion of laser marking systems using surface compensation function, Opt. Lasers Eng. 47 (2009) 84–89.
- [14] C. Leone, S. Genna, G. Caprino, I.D. Iorio, AISI 304 stainless steel marking by a Q-switched diode pumped Nd:YAG laser, J. Mater. Process. Technol. 210 (2010) 1297–1303.
- [15] S. Rusu, A. Buzaianu, L. Ionel, D. Ursescu, D.G. Galusca, Titanium alloy nanosecond vs. femtosecond laser marking, Appl. Surf. Sci. 259 (2012) 311–319.

- [16] B.S. Yilbas, C. Karatas, I. Uslan, O. Keles, Y. Usta, Z. Yilbas, M. Ahsan, Wedge cutting of mild steel by CO<sub>2</sub> laser and cut-quality assessment in relation to normal cutting, *Opt. Lasers Eng.* 46 (2008) 777–784.
- [17] F. Quintero, J. Pou, J.L. Fernandez, A.F. Doval, F. Lusquinos, M. Boutinguiza, R. Soto, M. Perez-Amor, Optimization of an off-axis nozzle for assist gas injection in laser fusion cutting, *Opt. Lasers Eng.* 44 (2006) 1158–1171.
- [18] I.A. Choudhury, S. Shirley, Laser cutting of polymeric materials: an experimental investigation, *Opt. Laser Technol.* 42 (2010) 503–508.
- [19] E. Le Guen, R. Fabbro, M. Carin, F. Coste, P. Le Masson, Analysis of hybrid Nd:YAG arc welding processes, *Opt. Laser Technol.* 43 (2011) 1155–1166.
- [20] C.X. Zhao, C. Kwakernaak, Y. Pan, I.M. Richardson, Z. Saldi, S. Kenjeres, C.R. Kleijn, The effect of oxygen on transitional Marangoni flow in laser spot welding, *Acta Mater.* 58 (2010) 6345–6357.
- [21] Z.G. Gao, O.A. Ojo, Modeling analysis of hybrid laser-arc welding of single-crystal nickel-base superalloys, *Acta Mater.* 60 (2012) 3153–3167.
- [22] P. Burdet, J. Vannod, A. Hessler-Wyser, M. Rappaz, M. Cantoni, Three-dimensional chemical analysis of laser-welded NiTi-stainless steel wires using a dual-beam FIB, *Acta Mater.* 61 (2013) 3090–3098.
- [23] T. Miokovic, V. Schulze, O. Vohringer, D. Lohe, Influence of cyclic temperature changes on the microstructure of AISI 4140 after laser surface hardening, *Acta Mater.* 55 (2007) 589–599.
- [24] Y. Van Ingelgem, I. Vandendael, D. Van den Broek, A. Hubin, J. Vereecken, Influence of laser surface hardening on the corrosion resistance of martensitic stainless steel, *Acta Mater.* 52 (2007) 7796–7801.
- [25] A. Bokota, S. Iskierka, Numerical prediction of the hardened zone in laser treatment of carbon steel, *Acta Mater.* 44 (1996) 445–450.
- [26] Y.T. Pei, J.Th.M. De Hosson, Functionally graded materials produced by laser cladding, *Acta Mater.* 48 (2000) 2317–2624.
- [27] X.D. Lu, H.M. Wang, High-temperature phase stability and tribological properties of laser clad Mo<sub>2</sub>Ni<sub>3</sub>Si/NiSi metal silicide coatings, *Acta Mater.* 52 (2004) 5419–5426.
- [28] R. Comesana, F. Quintero, F. Lusquinos, M.J. Pascual, M. Boutinguiza, A. Duran, J. Pou, Laser cladding of bioactive glass coatings, *Acta Biomater.* 6 (2010) 953–961.
- [29] B.J. Kooi, Y.T. Pei, J.Th.M. De Hosson, The evolution of microstructure in a laser clad TiB-Ti composite coating, *Acta Mater.* 51 (2003) 831–845.
- [30] C. Hu, H. Xin, L.M. Watson, T.N. Baker, Analysis of the phases developed by laser nitriding Ti-6Al-4V alloys, *Acta Mater.* 45 (1997) 4311–4322.
- [31] P.A. Carvalho, A.M. Deus, R. Colaco, R. Vilar, Laser alloying of zinc with aluminum: solidification behavior, *Acta Mater.* 46 (1998) 1781–1792.
- [32] P. Mohan Raj, S. Sarkar, S. Chakraborty, G. Phanikumar, P. Dutta, K. Chattopadhyay, Modelling of transport phenomena in laser surface alloying with distributed species mass source, *Int. J. Heat Fluid Flow* 23 (2002) 298–307.
- [33] H.C. Man, K.H. Leong, K.L. Ho, Process monitoring of powder pre-paste laser surface alloying, *Opt. Lasers Eng.* 46 (2008) 739–745.
- [34] X. Tong, M.J. Dai, Z.H. Zhang, Thermal fatigue resistance of H13 steel treated by selective laser surface melting and CiNi alloying, *Appl. Surf. Sci.* 271 (2013) 373–380.
- [35] A. Walker, H.M. Flower, D.R.F. West, The laser surface-alloying of iron with carbon, *J. Mater. Sci.* 20 (1985) 989–995.
- [36] C. Navas, A. Conde, B.J. Fernandez, F. Zubiri, J. de Damborenea, Laser coatings to improve wear resistance of mould steel, *Surf. Coat. Technol.* 194 (2005) 136–142.

- [37] M.Y. Li, Y. Wang, B. Han, W.M. Zhao, T. Han, Microstructure and properties of high chrome steel roller after laser surface melting, *Appl. Surf. Sci.* 255 (2009) 7574–7579.
- [38] G.F. Sun, R. Zhou, P. Li, A.X. Feng, Y.K. Zhang, Laser surface alloying of C-B-W-Cr powders on nodular cast iron rolls, *Surf. Coat. Technol.* 205 (2011) 2747–2754.
- [39] G.F. Sun, Y.K. Zhang, C.S. Liu, P. Li, X.Q. Tao, Microstructure and wear resistance enhancement of semi-steel rolls by laser surface alloying NiCr-Cr<sub>3</sub>C<sub>2</sub>, *Lasers Eng.* 19 (2010) 347–361.
- [40] G.F. Sun, Y.K. Zhang, C.S. Liu, K.Y. Luo, X.Q. Tao, P. Li, Microstructure and wear properties of laser surface alloying coatings of NiCr-Cr<sub>3</sub>C<sub>2</sub> on cast steel roll, *Mater. Des.* 31 (6) (2010) 2737–2744.
- [41] M.L. Zhong, W.J. Liu, H.J. Zhang, Corrosion and wear resistance characteristics of NiCr coating by laser alloying with powder feeding on grey iron liner, *Wear* 260 (2006) 1349–1355.
- [42] R. Colas, J. Ramirez, I. Sandoval, J.C. Morales, L.A. Leduc, Damage in hot rolling work rolls, *Wear* 230 (1999) 56–60.
- [43] Y. Fujii, K. Maeda, Flaking failure in rolling contact fatigue caused by indentations on mating surface (I) reproduction of flaking failure accompanied by cracks extending bi-directionally relative to the load-movement, *Wear* 252 (2002) 787–798.
- [44] K.C. Hwang, S. Lee, H.C. Lee, Effects of alloying elements on microstructure and fracture properties of cast high speed steel rolls: part II. Fracture behavior, *Mater. Sci. Eng. A* 254 (1998) 296–304.
- [45] O.P. Datsyshyn, M.M. Kopylets, Prediction of the service life of rolling bodies according to the development of a subsurface crack, *Mater. Sci.* 39 (2003) 765–779.
- [46] A. Nakajima, T. Mawatari, M. Yoshida, K. Tani, A. Nakahira, Effects of coating thickness and slip ratio on durability of thermally sprayed WC cermet coating in rolling/sliding contact, *Wear* 241 (2000) 166–173.
- [47] L. Zhou, D.L. Sun, C.S. Liu, Q. Wu, Fatigue behavior of high speed steel roll materials for hot rolling by laser impacting, *J. Iron. Steel Res. Int.* 13 (2006) 49–52.
- [48] S.K. Hann, J.D. Gates, A transformation toughening white cast iron, *J. Mater. Sci.* 32 (1997) 1249–1259.
- [49] C.S. Li, H.L. Yu, G.Y. Deng, X.H. Liu, G.D. Wang, Numerical simulation of temperature field and thermal stress field of work roll during hot strip rolling, *J. Iron. Steel Res. Int.* 14 (2007) 18–21.
- [50] R. Vilar, R. Colaco, A. Almeida, Laser surface treatment of tool steels, *Opt. Quantum Electron.* 27 (1995) 1273–1289.
- [51] W.S. Dai, M. Ma, J.H. Chen, The thermal fatigue behavior and cracking characteristics of hot-rolling material, *Mater. Sci. Eng. A* 448 (2007) 25–32.
- [52] T. El-Bitar, E. El-Banna, Contribution of forming parameters on the properties of hot rolled ductile cast iron alloys, *Mater. Lett.* 31 (1997) 145–150.
- [53] J. Grum, R. Sturm, A new experimental technique for measuring strain and residual stresses during a laser remelting process, *J. Mater. Process. Technol.* 147 (2004) 351–358.
- [54] S. Anthonyam, K. Ananthasivan, I. Kalaiappan, V. Chandramouli, P.R. Vasudevarao, C. K. Mathews, K.T. Jacob, Gibbs energies of formation of chromium carbides, *Metall. Mater. Trans. A* 27 (1996) 1919–1924.
- [55] L. Fang, Y.M. Gao, S.H. Si, Q.D. Zhou, Effect of graphitized cast irons hardness on wear of ceramics, *Wear* 221 (1998) 55–60.

- [56] N. Limodin, J. Rethore, J.Y. Buffiere, A. Gravouil, F. Hild, S. Roux, Crack closure and stress intensity factor measurements in nodular graphite cast iron using three-dimensional correlation of laboratory X-ray microtomography images, *Acta Mater.* 57 (2009) 4090–4101.
- [57] A.R. Ghaderi, M.N. Ahmadabadi, H.M. Ghasemi, Effect of graphite morphologies on the tribological behavior of austempered cast iron, *Wear* 255 (2003) 410–416.
- [58] F. Fouquet, E. Szmatala, Laser surface melting of a pearlitic grey cast iron, *Mater. Sci. Eng.* 98 (1988) 305–308.
- [59] N. Zarubova, V. Kraus, J. Cermak, Mechanisms of phase transformations during laser treatment of grey cast iron, *J. Mater. Sci.* 27 (1992) 3487–3496.
- [60] R. Colaco, R. Vilar, Effect of the processing parameters on the proportion of retained austenite in laser surface melted tool steels, *J. Mater. Sci. Lett.* 17 (1998) 563–567.
- [61] D.N. Hanlon, W.M. Rainforth, The rolling sliding wear response of conventionally processed and spray formed high speed steel at ambient and elevated temperature, *Wear* 255 (2003) 956–966.
- [62] K.-H. Zum Gahr, D.V. Doane, Optimizing fracture toughness and abrasion resistance in white cast irons, *Metall. Trans. A* 11 (1980) 613–620.
- [63] C.G. Li, Q.D. Zhou, G.S. Song, Z.S. Fang, Influence of carbon content of martensitic matrix and retained austenite on wear of martensitic ductile iron, *Wear* 162–164 (1993) 75–82.
- [64] R. Colaco, R. Vilar, On the influence of retained austenite in the abrasive wear behavior of a laser surface melted tool steel, *Wear* 258 (2005) 225–231.
- [65] J. Liu, S. Li, Y. Man, Wear resistance of Ni-hard 4 and high-chromium cast iron re-evaluated, *Wear* 166 (1993) 37–40.
- [66] G.L.F. Powell, J.V. Bee, Secondary carbide precipitation in an 18wt%Cr-1wt%Mo white iron, *J. Mater. Sci.* 31 (1996) 707–711.
- [67] J.D. Gates, R. Schmidt, A. Kootsookos, Unpublished microstructural observations, 1991, p. 68.
- [68] S. Turenne, F. Lavallee, J. Masounave, Matrix microstructure effect on the abrasion wear resistance of high-chromium white cast iron, *J. Mater. Sci.* 24 (1989) 3021–3028.
- [69] J. Tong, Y.Z. Zhou, T.Y. Shen, H.J. Deng, The influence of retained austenite in high chromium cast iron on impact-abrasive wear, *Wear* 135 (1990) 217–226.
- [70] T. Akhadejdamrong, T. Aizawa, M. Yoshitake, A. Mitsuo, T. Yamamoto, Y. Ikuhara, Self-lubrication mechanism of chlorine implanted TiN coatings, *Wear* 254 (2003) 668–679.
- [71] D.S.R. Krishna, Y. Sun, Effect of thermal oxidation conditions on tribological behavior of titanium films on 316L stainless steel, *Surf. Coat. Technol.* 198 (2005) 447–453.
- [72] J.L. Sullivan, N.W. Granville, Reciprocating sliding wear of 9-percent Cr steel in carbon dioxide at elevated-temperatures, *Tribol. Int.* 17 (1984) 63–71.
- [73] J.R. Jiang, F.H. Stott, M.M. Stack, The effect of partial pressure of oxygen on the tribological behaviour of a nickel-based alloy, N80A, at elevated temperatures, *Wear* 203 (1997) 615–625.
- [74] P.Q. La, Q.J. Xue, W.M. Liu, S.R. Yang, Tribological properties of  $\text{Ni}_3\text{Al}-\text{Cr}_7\text{C}_3$  composite coatings under liquid paraffin lubrication, *Wear* 240 (2000) 1–8.
- [75] F.H. Stott, High-temperature sliding wear of metals, *Tribol. Int.* 35 (2002) 489–495.
- [76] F.H. Stott, The role of oxidation in the wear of alloys, *Tribol. Int.* 31 (1998) 61–71.
- [77] I. Radu, D.Y. Li, Investigation of the role of oxide scale on Stellite 21 modified with yttrium in resisting wear at elevated temperatures, *Wear* 259 (2005) 453–458.

- [78] G.L.F. Powell, Secondary carbide precipitation in an 18 wt.% Cr–1 wt.% Mo white iron, *J. Mater. Sci.* 31 (1996) 707–711.
- [79] J.L. Arques, J.M. Prado, The dry wear resistance of a carbonitrified steel, *Wear* 103 (1985) 321–331.
- [80] J. Siepak, The influence of contact stress on the wear of a carburized steel case with a high content of retained austenite, *Wear* 80 (1982) 301–305.
- [81] G.F. Sun, C.S. Liu, X.Q. Tao, S.Y. Chen, Research on laser alloying of high Ni–Cr infinite chilled cast iron roller, *J. Northeastern Univ. (Nat. Sci.)* 29 (2008) 845–848.

# Laser surface treatment of AISI 304 steel with the presence of B<sub>4</sub>C particles at the surface

4

B.S. Yilbas<sup>1</sup>, F. Patel<sup>1</sup>, C. Karatas<sup>2</sup>

<sup>1</sup>King Fahd University of Petroleum & Minerals, Dhahran, Saudi Arabia; <sup>2</sup>Hacettepe University, Ankara, Turkey

## 4.1 Introduction

AISI 304 steel is widely used in industry due to its resistance to corrosion. The surface properties of the steel can be further improved without altering the bulk properties. One of the methods to improve the surface properties of the steel is to introduce hard particles in the surface region during the laser-controlled melting. Laser surface processing offers advantages over the conventional surface treatment techniques. Some of these advantages include high-speed processing, precision of operation, local treatment, and low cost. Although high cooling rates during laser processing forms the dense layer in the treated region while improving the surface hardness, the hard particle injection contributes to further enhancement of surface hardness of the laser-treated workpiece. Because the laser heating involves high cooling rates, the temperature gradients in the treated layer remain extremely high during the process. This, in turn, causes the formation of high stress levels in the treated region. In addition, the mismatch between the thermal expansion coefficients of the base alloy and the hard particles contributes to the microstress levels in the surface vicinity, which limits the practical application of the treated surface. Consequently, investigation of the morphological and the metallurgical changes in the laser-treated layer becomes essential.

Considerable research studies were conducted to examine laser treatment of high-speed tool steels. Laser surface melting of high-speed tool steel was studied by Bonek *et al.* [1]. They showed that laser surface melting modified the microstructure in the treated layer and improved the properties at the surface. Laser alloying of high-speed tool steel was investigated by Karaaslan [2]. He indicated that laser alloying at the alloy surface improved high temperature strength and the ductility of the alloy. Microstructural investigation of laser remelted high-speed tool steel was carried out by Kac and Kusinski [3]. They demonstrated that, in general, a laser-treated layer had structures consisting of fine dendrites of austenite crossed by a very fine carbide network and the eutectic without the primary large carbides. Laser-produced, functionally graded tungsten carbide coatings on high-speed tool steel were examined by Riabkina-Fishman *et al.* [4]. Their findings revealed that microhardness of the surface increased significantly after the laser-produced coating. The characteristics of laser-melted high-speed tool steel and its wear resistance were investigated by Darmawan

*et al.* [5]. They showed that the laser-melted surface had improved wear resistance as compared to an as-received alloy surface. Microstructure and mechanical behavior of laser-melted high-speed tool steel surface was studied by Arias *et al.* [6]. They indicated that laser-treated surface had better wear resistance than the untreated steel surface. Laser surface modification of tool steel was investigated by Brabazon *et al.* [7]. Their findings revealed that surface hardness increased because of a complete microstructural transformation to an amorphous state in the glazed samples. Laser surface modification of various tool steels was examined by Kwok *et al.* [8]. They demonstrated that laser treatment improved corrosion resistance of the treated surface due to dissolution of the alloying elements in the solid solution. Laser surface melting of tool steel was studied by Majumdar *et al.* [9]. The results showed that laser surface treatment significantly refined the grain size with the presence of lath martensite. Laser hardening of tool steel surface was examined by Penstar [10]. He showed that the surface hardness was greatly influenced by the dissolution of carbides during desensitization, and the highest hardness values were achieved with slow laser transverse speeds and high surface temperatures. Laser-induced deposition of hard particles into tool steel surface was investigated by Jian and Kovacevic [11]. They showed that the erosion resistance of laser-treated surface decreased with increasing concentration of TiC particles.

Although laser treatment of steel surfaces was investigated previously [12,13], the main emphasis was to introduce laser gas-assisted nitriding at the alloy surface and the influence of microstress levels due to the presence of hard particles left obscure. Moreover, laser gas-assisted processing improves the microhardness considerably at the treated surface. This improvement can further progress through the insertion of hard particles, such as carbides, during the laser gas-assisted processing of the surface. Therefore, in the present study, laser gas-assisted treatment of pre-prepared AISI 304 steel surface is carried out. A thin carbon film accommodating 5% of B<sub>4</sub>C particles is formed at the alloy surface prior to the laser-treatment process. Morphological and metallurgical changes in the treated layer are examined using an optical microscope, scanning electron microscope (SEM), energy dispersive spectroscopy, and X-ray diffraction (XRD). The residual stress developed at the surface is determined, incorporating the XRD technique.

## 4.2 Experimental producers

The CO<sub>2</sub> laser (LC-ALPHAI) delivering nominal output power of 2 kW was used to irradiate the workpiece surface. The laser parameters were selected after conducting several surface treatment tests; the laser parameters resulting in low asperities and a crack-free surface were selected to carry out the experiments. Nitrogen assisting gas emerging from the conical nozzle and coaxially with the laser beam was used. Table 4.1 gives the laser treatment parameters.

AISI 304 samples in 15 × 10 × 3 mm<sup>3</sup> sizes were used as workpieces. The carbon film containing uniformly distributed 5% B<sub>4</sub>C was formed at the workpiece surface prior to the laser treatment process. The method applied for the formation of carbon

**Table 4.1 Laser heating conditions used in the experiment**

Scanning speed (cm/s) (mm/min)	Power (W)	Frequency (Hz)	Nozzle gap (mm)	Nozzle diameter (mm)	Focus setting (mm)	N <sub>2</sub> pressure (kPa)
10	85	1500	1.5	1.5	127	600

film was similar to that presented in the previous study [14]. The laser beam was surface scanned according to the parameters given in [Table 4.1](#).

Jeol 6460 electron microscopy was used for SEM examinations and Bruker D8 Advanced having Cu-K $\alpha$  radiation was used for XRD analysis of the laser-treated surfaces. A Microphotonics digital microhardness tester (MP-100TC) was used to obtain the microhardness at the surface of the laser-treated layer, and the standard test method for Vickers indentation hardness of advanced ceramics (ASTM C1327-99) was adopted. Microhardness measurements were repeated three times at each location for the consistency of the results. The XRD technique was used to measure the residual stresses in the laser-treated surface vicinity. The residual stress measurements rely on the stresses in fine-grained polycrystalline structure. The position of the diffraction peak exhibits a shift as the specimen is rotated by an angle  $\psi$ . The magnitude of the shift is related to the magnitude of the residual stress. The relationship between the peak shift and the residual stress ( $\sigma$ ) is given [15] by:

$$\sigma = \frac{E}{(1+\nu)\sin^2\psi} \frac{(d_n - d_o)}{d_o} \quad (4.1)$$

where  $E$  is Young's modulus,  $\nu$  is Poisson's ratio,  $\psi$  is the tilt angle, and  $d_n$  are the  $d$  spacing measured at each tilt angle. The bcc ferrite steel peak at (211) planes takes place at  $2\theta=88.3^\circ$  with the interplanar spacing of 0.11709 nm. The linear dependence of  $d$ (211) results in the slope of  $3.545 \times 10^{-13}$  m and the intercept of  $1.17 \times 10^{-10}$  m as shown in [Figure 4.1](#). The slope of the curve indicates that the residual stress is compressive and the residual stress determined is of the order of  $520 \pm 20$  MPa.

### 4.3 Results and discussion

Laser treatment of pre-prepared AISI 304 steel surface is carried out. A uniform thickness of carbon film containing 5% B<sub>4</sub>C particles is formed at the workpiece surface prior to the laser treatment process. The presence of the carbon film improved the absorption of the incident film at the workpiece surface and accommodates the uniformly distributed B<sub>4</sub>C particles at the workpiece surface. The analytical tools are used to characterize the resulting surfaces.

[Figure 4.2](#) shows an optical photograph of the laser-treated surface, while SEM micrographs show the top view of the laser-treated surface. The treated surface is free

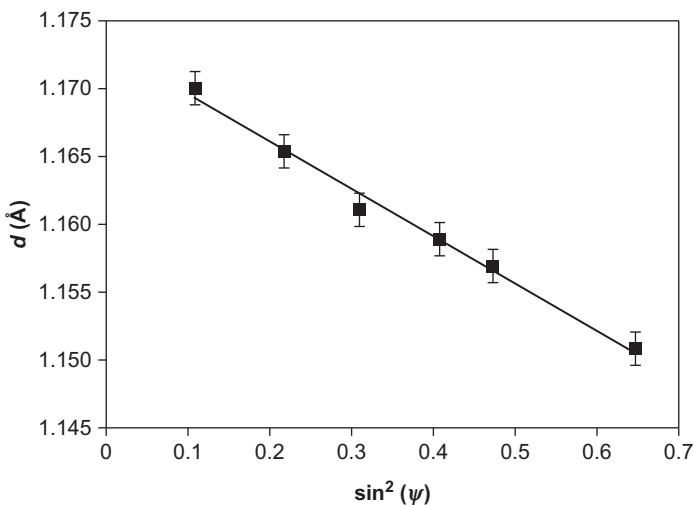


Figure 4.1 Linear variation of  $d(211)$  with  $\sin^2(\psi)$  for the laser-treated surface.

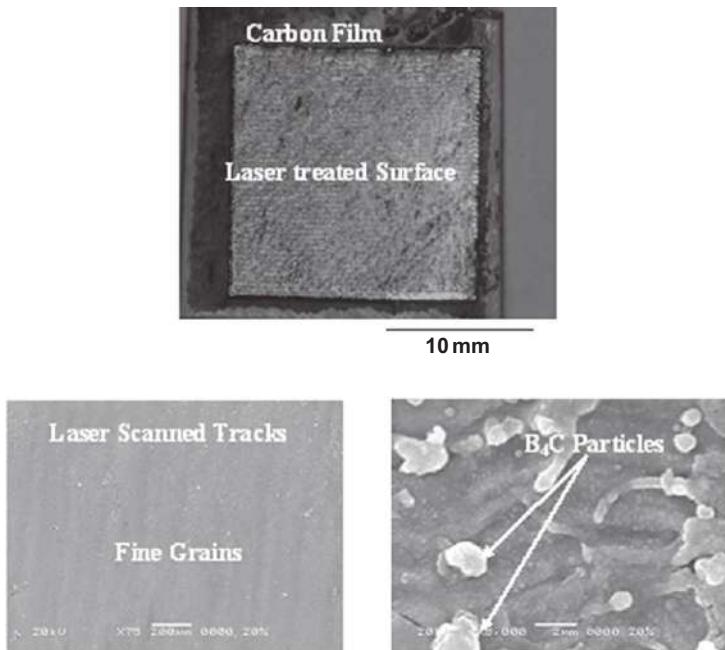
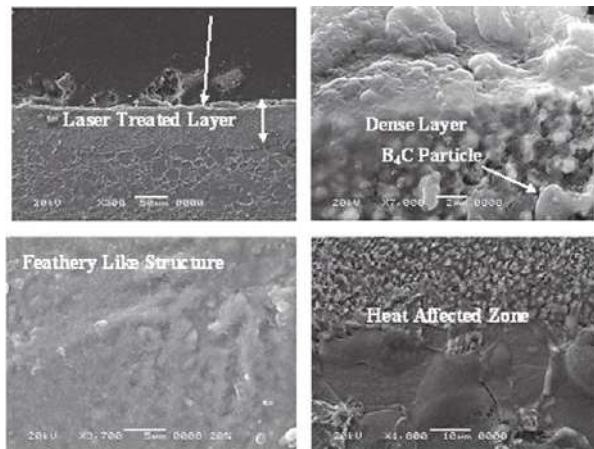


Figure 4.2 Optical photograph (top) and SEM micrographs (bottom) of the laser-treated surface.

from the major defect sites such as large cavities and large-scale cracks. Although the high cooling rates and the mismatch between the thermal expansion coefficients of the base material and B<sub>4</sub>C particles contribute to the stress levels at the treated surface, the major crack-free surface indicates that the stress levels do not reach the critical level to form large-scale cracks at the surface. In addition, the laser power intensity is selected below the critical level such that the power intensity selected does not result in evaporation at the surface. The surface roughness measurements of the treated workpiece reveal that the surface roughness of the treated surface is in the order of 2.5 μm, which is slightly higher than that of the untreated surface (1.5 μm). Consequently, avoiding the evaporation at the surface lowers the surface roughness increase after the treatment process. The slight increase in the surface roughness may occur because of the Marangoni-induced molten flow at the treated surface. In this case, the surface tension of the molten material at the treated surface causes the formation of hill-like structures along the laser scanning tracks. In addition, overlapping of the laser spots contributes to the roughness of the treated surface. It should be noted that the laser beam irradiates the surface via high-frequency pulses (1500 Hz) and this results in overlapping of laser spots along the scanning tracks during the laser beam scanning. A close examination of the optical photograph and the SEM micrographs indicates that the overlapping ratio of the laser spots is in the order of 70%, which results in continuous melting of the surface along the scanning tracks. Because the melting is controlled by proper adjustment of the laser parameters, no melt overflow across the laser scanning tracks is observed from the optical photograph and SEM micrographs. Because the melting temperature of B<sub>4</sub>C is considerably higher than the melting temperature of AISI 304 steel, some of the hard particles appear to be partially embedded at the surface. However, these particles are few at the surface and they are locally scattered without forming a regular pattern. The formation of dense structures is also evident from a SEM micrograph. Although the thermal expansion coefficients of B<sub>4</sub>C particles and the base material are different, only few microcracks are observed at the surface. It should be noted that the crack formation results in stress relaxation at the surface; therefore, few microcracks eliminate the formation of large cracks at the surface through stress relaxation.

Figure 4.3 shows SEM micrographs of the cross section of the laser-treated layer. The treated layer extends uniformly at a depth of 40 μm below the surface. The treated layer is free from asperities and the large-scale defect sites such as internal cavities, cracks, and pores. The formation of a dense layer in the surface region is visible, which is attributed to the high cooling rates and the formation of nitride compounds at the surface due to the use of high-pressure nitrogen assisting gas during the treatment. In this case, volume shrinkage due to the presence of the nitride compounds and fine structure formation results the development of the dense layer at the surface. Although density increases in this layer, no cavitation is observed in the vicinity of the dense layer. In addition, the presence of partially dissolved B<sub>4</sub>C particles is evident from SEM micrographs. Although the geometry of these particles has sharp corners and odd shapes, the total wetting of the particle surface by the base material takes place; in which case, no small voids around the particles are formed. Moreover, the mismatch between the thermal expansion coefficients of B<sub>4</sub>C particles and the base material



**Figure 4.3** SEM micrographs of cross section of the laser-treated layer.

causes the microstress formation in the vicinity of the particles. However, the microstress levels are not high enough to cause microcracks or microcrack networks in the dense layer. Moreover, the self-annealing effect of the initially formed tracks contributes to the stress relaxation in this region, that is, microcrack formation around  $B_4C$  particles is avoided. In the region next to the dense layer, the microstructure, which consists of a phase mixture of ferrite and carbides, transforms into martensite and very fine carbides. The formation of this microstructure is associated with the high cooling rates in this region. In this case, rapid quenching in the surface region contributes to the refinement of carbides in this region. As the depth below the dense layer increases slightly, the feathery structure is observed, which is associated with the presence of the nitride precipitations in this region. Therefore, nitrogen diffusion from the surface along the grain boundaries is responsible for the formation of the feathery structures in this region. Because the nitride phase formation is related to the exothermic reactions, the heat generated in this region contributes to the self-annealing effect occurring in the surface region. The fine dendrites are also observed in this region and the dendrites are martensite with a certain amount of retained austenite due to high cooling rates. As the depth below the surface increases, the dendrite size increases and primary austenite partially transforms into martensite because of the low cooling rates as compared to that corresponding to the surface region. As the depth below the surface increases further, the cellular and homogenized austenitized microstructures are developed because of the relatively slower cooling rates than those of the neighboring region. The sizes of the cells become large and they deform due to slow cooling rates. In the vicinity of the heat-affected zone, the demarcation line between the laser-treated layer and the base alloy becomes visible.

Figure 4.4 shows an X-ray diffractogram for the workpiece surface treated by the laser. The nitride compound peaks are present in the diffractogram. This shows that the use of high-pressure nitrogen as an assisting gas results in the formation of the nitride compounds at the laser-treated surface. In addition, the presence of  $Fe_4N$

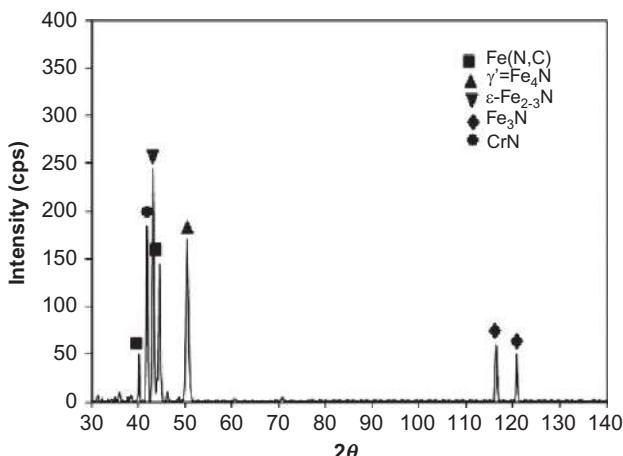


Figure 4.4 XRD diffractogram of the laser-treated surface.

reveals the nitrogen diffusion through grain boundaries while resulting in feathery structures in the vicinity of the surface.  $Fe_3(N, C)$  peak is also seen in the X-ray diffractogram. The carbon film formed at the workpiece surface prior to the laser treatment process is associated with  $Fe_3(N, C)$  phase formation. In addition,  $B_4C$  and CrN peaks are related to the presence of partially dissolved  $B_4C$  particles and chromium nitride phase formation at the surface. Table 4.2 gives the EDS data corresponding to the treated surface. The alloy composition remains almost the same at the treated surface. However, nitrogen is evident from the EDS data, provided that the quantification of light elements, such as nitrogen, involves with error. Table 4.3 gives the microhardness of the treated surface with and without the presence of  $B_4C$  particles and the residual stress formed at the surface vicinity for the laser-treated surface with and without the presence of  $B_4C$  particles. The microhardness increases significantly

Table 4.2 EDS data for laser-treated surface (wt. %)

Spectrum	N	B	Si	Cr	Mn	Ni	Fe
Spectrum 1	4.1	5.1	0.8	18.1	2.0	8.7	Balance
Spectrum 2	5.2	4.9	0.9	17.4	1.9	8.9	Balance
Spectrum 3	5.1	4.9	0.8	17.8	1.8	8.4	Balance

Table 4.3 Microhardness and residual stress obtained from XRD technique for the laser-treated and -untreated surfaces

	Hardness (HV)	Residual stress (MPa)
As received	$150 \pm 25$	—
Laser nitrided	$420 \pm 25$	$380 \pm 15$
Laser treated and $B_4C$	$550 \pm 30$	$520 \pm 20$

at the surface for the treated surface with the presence of  $B_4C$  particles. However,  $B_4C$  particles also increase the residual stress in the treated layer. The enhancement of microhardness at the treated surface is attributed to the following: (i) formation of a dense layer with fine grains at the surface, (ii) nitride phases formed at the surface due to the use of high-pressure nitrogen as an assisting gas, and (iii) microstresses formed in the neighborhood of  $B_4C$  particles.

## 4.4 Conclusion

Laser treatment of AISI 304 steel surface with the presence of  $B_4C$  particles is carried out. A carbon film containing 5%  $B_4C$  particles is formed at the workpiece surface prior to the laser treatment. Nitrogen gas at high pressure is used as an assisting gas during the process. Initial laser scanning tests are carried out to identify the laser processing parameters resulting in minimum defect sites and asperities in the treated region. The parameters resulting in optimum surface treatment conditions are presented in this study. The metallurgical and morphological changes in the laser-treated region are characterized by using optical microscope and SEMs, energy dispersive spectroscopy, and XRD. The residual stress developed at the treated surface is measured by incorporating the XRD technique. It is found that the laser-treated surface consists of regular scanning tracks, which are free from large cavities and large-scale cracks. The treated layer extends uniformly below the thickness of about 40  $\mu m$ . The cross section of the treated layer reveals that no pores and microcracks are present in the treated layer. The self-annealing effect of the lately formed laser scanning tracks minimizes the crack formation in the treated layer. The dense layer is formed at the surface because of the high cooling rates from the surface. The presence of  $B_4C$  particles is observed in the dense layer without defect sites around the particles despite the mismatch of thermal expansion coefficients between the particles and the base material. The microstructure changes in the region next to the dense layer; in which case, phase mixture of ferrite and carbides transforms into martensite and very fine carbides take place in this region. Nitrogen diffusion through the grain boundaries results in the formation of feathery structures in the surface region. The X-ray diffractogram shows the presence of  $Fe_3(N, C)$  peak, which is associated with the carbon film formed at the workpiece surface prior to the laser treatment process. In addition,  $B_4C$  and CrN peaks are related to the presence of partially dissolved  $B_4C$  particles and chromium nitride phase formation at the surface. The presence of  $B_4C$  particles increases the microhardness and the residual stress. The increased microhardness at the treated surface is attributed to the following: (i) formation of a dense layer with fine grains at the surface, (ii) nitride phases formed at the surface due to the use of high-pressure nitrogen as an assisting gas, and (iii) microstresses formed in the neighborhood of  $B_4C$  particles.

## Acknowledgment

The authors acknowledge the support of King Fahd University of Petroleum and Minerals Dhahran, Saudi Arabia for this work.

## References

- [1] M. Bonek, L.A. Dobrzanski, E. Hajduczek, A. Klimpel, Structure and properties of laser alloyed surface layers on the hot-work tool steel, *J. Mater. Process. Technol.* 175 (1–3) (2006) 45–54.
- [2] A. Karaaslan, Laser alloying of high-speed [tool] steel: by heat treatment qualified property changes of laser alloyed high-speed [tool] steel, *Materialprüfung/Mater. Test.* 46 (3) (2004) 102–105.
- [3] S. Kac, J. Kusinski, SEM and TEM microstructural investigation of high-speed tool steel after laser melting, *Mater. Chem. Phys.* 81 (2–3) (2003) 510–512.
- [4] M. Riabkina-Fishman, E. Rabkin, P. Levin, N. Frage, M.P. Dariel, A. Weisheit, R. Galun, B.L. Mordike, Laser produced functionally graded tungsten carbide coatings on M2 high-speed tool steel, *Mater. Sci. Eng. A* 302 (1) (2001) 106–114.
- [5] W. Darmawan, J. Quesada, R. Marchal, Characteristics of laser melted AISI-T1 high speed steel and its wear resistance, *Surf. Eng.* 23 (2) (2007) 112–119.
- [6] J. Arias, M. Cabeza, G. Castro, I. Feijoo, P. Merino, G. Pena, Microstructure and mechanical behavior of laser surface melted AISI M2 high-speed steel, *Surf. Interface Anal.* 42 (6–7) (2010) 752–756.
- [7] D. Brabazon, S. Naher, P. Biggs, Laser surface modification of tool steel for semi-solid steel forming, *Diffus. Defect Data Part B: Solid State Phenom.* 141–143 (2008) 255–260.
- [8] C.T. Kwok, F.T. Cheng, H.C. Man, K.I. Leong, Laser surface modification of various tool steels for improving hardness and corrosion resistance, *Key Eng. Mater.* 384 (2008) 125–155.
- [9] D.J. Majumdar, A.K. Nath, I. Manna, Studies on laser surface melting of tool steel—Part II: mechanical properties of the surface, *Surf. Coat. Technol.* 204 (9–10) (2010) 1326–1329.
- [10] H. Pantsar, Relationship between processing parameters, alloy atom diffusion distance and surface hardness in laser hardening of tool steel, *J. Mater. Process. Technol.* 189 (1–3) (2007) 435–440.
- [11] W.H. Jiang, R. Kovacevic, Laser deposited TiC/H13 tool steel composite coatings and their erosion resistance, *J. Mater. Process. Technol.* 186 (1–3) (2007) 331–338.
- [12] B.S. Yilbas, A.F.M. Arif, C. Karatas, S. Akhtar, B.J. Abdul Aleem, Laser nitriding of tool steel: thermal stress analysis, *Int. J. Adv. Manuf. Technol.* 49 (9–12) (2010) 1009–1018.
- [13] B.S. Yilbas, S.Z. Shuja, S.M.A. Khan, B.J. Abdul Aleem, Laser melting of carbide tool surface: model and experimental studies, *Appl. Surf. Sci.* 255 (23) (2009) 9396–9403.
- [14] B.S. Yilbas, N. Al-Aqeeli, C. Karatas, Laser control melting of alumina surfaces with presence of B<sub>4</sub>C particles, *J. Alloys Compd.* 539 (2012) 12–16.
- [15] Z.A. Khana, M. Hadfield, S. Tobe, Y. Wang, Ceramic rolling elements with ring crack defects—a residual stress approach, *Mater. Sci. Eng. A* 404 (2005) 221–226.

This page intentionally left blank

# Characterization and modification of technical ceramics through laser surface engineering

5

P. Shukla, J. Lawrence  
University of Chester, Chester, UK

## 5.1 Introduction

Laser surface treatment of materials is an important technique because it offers a possibility to enhance various properties such as the surface strength, hardness, roughness, coefficient of friction, chemical resistance, and corrosion of various materials. Such improvements to a material surface are not only ideal for applications when wear rate and shear stresses are high but could also be used for maintaining or elongating the component's functional life by means of covering over the microcracks in surfaces, such as those of technical ceramic-based components. In addition, aesthetics can also be improved using laser surface treatment (for ceramics in particular) by creating a modified surface layer.

Research has advanced in the field of laser machining of ceramics [1–5], surface treatment [6–16], laser cutting [4,15,17–25], and drilling of ceramics [26–29]. But the effects of laser processing of various advanced ceramics are still unknown and are not fully reported in most of the published literature. The unknown aspects, in particular, are the effects during the laser's interaction with oxide and nitride technical grade ceramics. The interaction of the high brightness, and fairly novel, near-infrared (NIR) wavelength fiber laser with such technical ceramics is still not understood from the viewpoint of a compositional, microstructural, internal phases, and mechanical aspects. In this chapter, laser surface treatment process parameters are described for the ceramic material systems used herein, followed by an analysis of the surface finish, material removal, chemical composition,  $K_{1c}$  and the distribution of surface temperature. This should lead to a better understanding of the laser beam-ceramic interactions for future applications, such as laser-assisted joining, because joining technical ceramics-to-ceramics would be useful as an alternative process that could give an opportunity for new applications. On account of this, the interaction of the laser beam with selected ceramics is presented to understand how the laser surface treatment of ceramics can be improved as a process. Furthermore, it is generally difficult to characterize technical ceramics and, particularly if they are laser processed, because the laser-engineered surface becomes amorphous and glassy. This, in turn, does not allow them to be characterized by methods such as X-ray diffraction, which is a conventional tool for the determination of the composition, residual stress, and phase transformation. Having said that, this chapter also indicates the

alternative characterization methods that can be used to analyze the laser engineered technical grade ceramics.

The  $\text{ZrO}_2$  and the  $\text{Si}_3\text{N}_4$  technical ceramics were selected as they both have different mechanical and thermal properties. This, in turn, will create different effects after applying laser surface treatment. Furthermore, both the  $\text{ZrO}_2$  and  $\text{Si}_3\text{N}_4$  technical ceramics are frequently used for many applications within the engineering, medical, and power generation sectors, so undertaking this research contributes to achieving further diversity of current and future applications for the two ceramics employed.

## 5.2 Background of laser surface treatment of technical ceramics

Laser-material interaction in general was reported by Wang *et al.* [30] to be comprised of thermal, physics, dynamic, and many other scientific aspects. Wang *et al.* stated that the factors influencing laser-material interaction are laser output energy, the composition of the material, the specimen thickness, and temperature distributions. Interaction of the laser beam with metals in particular have been thoroughly investigated by many other authors, namely, Prat *et al.* [31,32], Lim [33], and Illyefalvi [34], who discussed the diffusion in material transport caused by laser processing of thin materials. The issues of laser coupling with materials, the effects of plasma with increasing intensity [32,35], the formation of a shock wave and impulse were also addressed [32]. Materials such as C5790 graphite and aluminium alloy AU4G were used for the experimentation [31,32]. Laser-material interaction purely depends on the particular material being processed. Laser beam interaction with metals would produce a different effect to that of the ceramics due to the differences in the material structure. Metals absorb the thermal energy better than ceramics, and the thermal shock results in placing the ceramic under compressive stress when the heat escapes. This does not occur with ceramics, as the thermal shock induced would expand the porous surface and provoke the microcracks and porosity to expand, which in the end causes failures. Failure of ceramics in general through thermal shock is a major issue during laser surface processing. Having said this, it is yet feasible to produce a crack-free laser surface treatment.

Wong *et al.* [36] examined the excimer laser interaction with a partially stabilized  $\text{ZrO}_2$  and suggested that lasers with shorter wavelength than 307 nm are ideal to produce the desired chemical reaction and material removal. The results showed severe surface melting and the formation of columnar structures. This was dependent on the amount of laser fluence and was influenced by the direction of the plasma plume expansion. In this case, the plasma plume expanded away from the normal and led to formation of short columnar structure. Vlasova *et al.* [37] presented the effects of Nd:YAG laser interaction with a sheet of silicon (upper layer) and  $\text{Al}_2\text{O}_3$  (lower layer) to first demonstrate the composition of the ablated element exhibited from the laser-ceramic interaction. The ablated mixture was comprised of silicon, oxygen, and nitrogen. The  $\text{Al}_2\text{O}_3$  layer also fractured after the laser-material interaction, with evidence of oxidation occurring with the top layer of silicon. The interaction of  $\text{Al}_2\text{O}_3$

with  $\text{SiO}_2$  produced the simultaneous nitriding of the melt and decomposition of SIALONs with the formation of mullite, and the ejection of mullite drops also occurred at the thickness of 270–1040 nm.

To date, limited investigations have been performed with respect to achieving an ideal surface treatment of various ceramics with due to the ceramic not being crack free and defect free [38–43]. Ester *et al.* [38] conducted an investigation on  $\text{Al}_2\text{O}_3$  and  $\text{ZrO}_2$ -based oxide ceramics by employing a HPDL. A laser irradiated area of 50 mm × 7 mm was said to have a crack-free surface. This was performed by controlling the laser power, traverse speed, and the sample temperature by preheating the surface of the ceramic. Triantafyllidis *et al.* [39–43] performed several investigations on laser surface treatment of mainly  $\text{Al}_2\text{O}_3$ -based refractory ceramics by employing the HPDL. Earlier work of Triantafyllidis *et al.* identified solidification cracking due to the generation of very large temperature gradients. Furthermore, it was also shown that refractory  $\text{Al}_2\text{O}_3$  can be treated with a combination of laser source (HPDL beam trailed by a  $\text{CO}_2$  laser or vice-versa), to eliminate cracking by controlling the temperature. Having said that, such methods were not always repeatable with ease and efficiency, because it required timely setup and arrangement to take place. Further investigation showed that crack-free surfaces improved the properties of the ceramic surface. Those properties were corrosion resistance, contact characteristics and surface morphology, contact angle, and wetting and water permeability [41,42]. Other studies involved the use of a HPDL to process refractory  $\text{Al}_2\text{O}_3$  without using a post- or preheating method, which are conventional ideas in processing ceramics by using a laser beam [43]. It was reported that a crack free surface treatment was possible with the parameter window speed being 0.4 mm/s and a power density of  $6 \times 10^2 \text{ W/cm}^2$ , which led to a crack free surface treatment for the  $\text{Al}_2\text{O}_3$ . However, these parameters are unique for the refractory  $\text{Al}_2\text{O}_3$  only with the particular composition. Ceramics such as the  $\text{ZrO}_2$  and  $\text{Si}_3\text{N}_4$  are somewhat different due to their chemical composition, which also changes the mechanical and thermal properties and has a different effect during laser processing.

## 5.3 Materials and experimental procedures

### 5.3.1 Details of the technical grade ceramics

The first ceramic material used for the experiment was a cold isostatic pressed  $\text{ZrO}_2$  with 95 wt.%  $\text{ZrO}_2$  and 5 wt.% yttria from Tensky International Company, Ltd. The second ceramic material used for the experiment was a cold isostatic pressed  $\text{Si}_3\text{N}_4$  with 90 wt.%  $\text{Si}_3\text{N}_4$ , 6 wt.% yttria, and 4 wt.% other, unspecified content obtained from the same manufacturer. This initially contained a high content of  $\alpha$ -phase as specified by the manufacturer. Furthermore, the microscopic image of the as-received  $\text{Si}_3\text{N}_4$  with a similar composition was compared to the work of previous researchers to confirm that the  $\text{Si}_3\text{N}_4$  ceramic was in the  $\alpha$ -phase state [44–47]. Each of the samples were obtained in a bulk of 10 × 10 × 50 mm<sup>3</sup> made from a specific rubber mold, to a specified dimension, from which all ceramics were cold isostatically pressed. The as-received surface

roughness was  $1.57 \mu\text{m}$  for the  $\text{ZrO}_2$  and  $1.56 \mu\text{m}$  for the  $\text{Si}_3\text{N}_4$  ceramics. A smoother surface than specified for both ceramics would have much lower surface flaws and microcracks. This in turn, would lead to higher surface strength and wear resistance, but initial experiments showed that polished, shinier surfaces below  $1.57 \mu\text{m}$  for the  $\text{ZrO}_2$  and  $1.56 \mu\text{m}$  for the  $\text{Si}_3\text{N}_4$  would reflect the beam. This, in turn, would reduce beam absorption into the surface and the subsurface of the ceramics, so the surfaces were not ground and polished for a better surface finish. The experiments were conducted in ambient condition at a known atmospheric temperature ( $20^\circ\text{C}$ ).

### **5.3.2 Laser surface treatment methodology**

Experiments were conducted using a 200 W fiber laser (SPI-200c-002; SPI, Ltd.) which emitted a CW mode beam at a wavelength of  $1.075 \mu\text{m}$ . The fiber laser was comprised of a Gaussian beam configuration of  $\text{TEM}_{00}$  with a beam quality factor of  $M^2 = 1.2$ . Experiments were conducted by varying one parameter at a time and by keeping the other parameters constant. Therefore, the laser power was varied from 25 to 200 W (maximum laser power). Concurrently, the traverse speed was varied from 25 to 500 mm/min by keeping the focal position constant for both the technical ceramics. From initial experiments, it was found that laser power of 143.25 W, traverse speed of 100 mm/min for the  $\text{Si}_3\text{N}_4$  treatment ceramic, and the power of 137.5 W at the traverse speed of 100 mm/min for the  $\text{ZrO}_2$  engineering ceramic with a spot size of 3 mm used for both the technical ceramics was found to be an ideal constant to use in order to conduct the surface treatment. From this, identification of the range of laser power and power density required to reach the material threshold was achieved. The processing gas used for this set of experiment was compressed air, which was supplied at a flow rate of 25 l/min. Initial experiments showed that a flow rate in excess of 25 l/min was blowing off excessive material during the laser-ceramic interaction. This was significant during surface cracking of the ceramic, as the cracked surfaces were eventually blown away and produced a large crater. Lower gas pressure would result to lower interaction between the laser beam and the ceramic. Hence, 25 l/min was found to be appropriate for this study. This prevented the ceramic debris from travelling upward into the lens and protected the optics. Programming of the laser was conducted by using an SPI software that integrated with the laser system. A potential beam path was programmed by using numerical control programming, which was transferred by a .dxf file. A larger laser beam was applied as it is more suitable for performing the laser surface treatment as opposed to laser cutting or drilling where high power density is required in the smaller surface area to penetrate through the material. In this case, a defocused beam allows the energy to distribute over a larger surface area, which prevents thermal shocks and severe cracking of the ceramics. In any case, the defocused beam still remained Gaussian.

### **5.3.3 Characterization techniques**

Laser-material interaction was evaluated by studying the surface integrity, morphology, microstructure, and the elemental analysis by using scanning electron microscopy/energy dispersive X-ray (SEM/EDX) by employing a Stereoscan 360, Carl

Zeiss Leo, Ltd., device. In addition, the surface topography was investigated by a focus variation technique (Infinite Focus IFM 2.15; Alicona, Ltd.). The focus variation technique performed a three-dimensional (3-D) surface analysis that generated a 3-D profile of the laser-engineered surfaces of the  $\text{Si}_3\text{N}_4$  and  $\text{ZrO}_2$  technical ceramics. This employed a 2 mm diameter white-light beam. The beam travelled the length of 7 mm across the width of the as-received (laser unaffected) HAZ and the laser-engineered surfaces areas. Mechanical effects such as change in hardness were investigated by using the Vickers indentation (Vickers (HVTM); Armstrong Engineering, Ltd.), which was followed by a calculation of the fracture toughness parameter ( $K_{Ic}$ ) using empirical equations from the literature [48–51]. The temperature measurement was conducted using an infrared thermometer device (Cyclops 100 B; Land instruments international Ltd.) on the surface and also by using a precision fine wire (0.20 diameter  $\times$  152 mm in length), R-type thermocouple (P13R, Omega Instruments Ltd.). All thermocouples were attached to a temperature reader, which was used to record the bulk temperatures during various passes of the laser. Thereafter, the process was modelled by using a finite element model (FEM) using Unigraphics, NX 5.0, Nas-tran designing software, which showed the distribution of temperatures during the laser-material interaction.

## 5.4 Establishment of laser processing parameters and associated issues

In order to find the threshold of both the  $\text{ZrO}_2$  and the  $\text{Si}_3\text{N}_4$  technical ceramics, a systematic approach was used. This is when the laser power was changed while other parameters, such as the spot size of 3 mm, traverse speed of 100 mm/min, and gas flow rate of 25 l/min, were kept constant first during the fiber laser surface treatment of  $\text{Si}_3\text{N}_4$  technical ceramic. The range of powers used were from 25 to 200 W and from 694 to 4761 W/mm<sup>2</sup> along with other associated parameters. During each stage, the effects of the laser-ceramic interaction were recorded. This is when it was found that 143.25 W or 3979 W/mm<sup>2</sup> was ideal for the  $\text{Si}_3\text{N}_4$  producing a surface treatment that comprised of very few cracks on the surface of the  $\text{Si}_3\text{N}_4$  technical grade ceramic. As more laser power was introduced at a constant speed, the surface of the  $\text{Si}_3\text{N}_4$  began to show some effects. Those were a change in color and the appearance of few medium size surface cracks, and then produced high cracking.

Second, for the  $\text{ZrO}_2$  technical ceramic, the approach to determine the threshold was also similar to the  $\text{Si}_3\text{N}_4$ , except that the  $\text{ZrO}_2$  had a different threshold. This was because the  $\text{ZrO}_2$  ceramic comprised of higher thermal conductivity than the  $\text{Si}_3\text{N}_4$ . This meant that the heat was more easily transferred to the  $\text{ZrO}_2$  than the  $\text{Si}_3\text{N}_4$  and the  $\text{ZrO}_2$  generally heated up quickly. This intrinsically would produce higher thermal shock and surface cracking. The power was varied from 25 to 200 W and the traverse speed was initially kept constant to 100 mm/min by using a constant spot size of 3 mm. The fiber laser had began to affect the surface of the  $\text{ZrO}_2$  from changing its color at 75 W to producing a very few to high cracks at various

power intervals. Eventually, it cracked at 200 W of laser power. It was established that the ideal laser power was 137.5 W in order to generate the lowest surface cracks, so the traverse speed was investigated. This is when the laser power, focal spot size, power density, and the gas flow rate were kept constant and the traverse speed was varied from 25 to 500 W. This is how it was confirmed that 100 to 150 mm/min produced the lowest cracks, and beyond the speed of 150 mm/min produced color changes up to 350 mm/min and had no further visual effects on the surface of the  $\text{ZrO}_2$ . Lower speeds of 50–70 mm/min generated high cracking and further shattered the ceramic when the traverse speed was reduced to 25 mm/min. This was obvious as the laser beam was spending more time on the  $\text{ZrO}_2$  surface, which increased the thermal energy input and generated the surface cracks. The  $\text{ZrO}_2$  shattered below 2 mm of spot diameter. Moreover, above 2 mm of spot diameter, the laser beam produced high levels of cracking and then generated the lowest cracks at a beam diameter of 3–3.5 mm. Fiber laser beam diameter larger than 3.5 mm showed some influence on the ceramic, but no visual effects were found beyond 4.5 mm spot diameter. Initial investigations showed that surface cracking occurred due to the difference in the thermal gradient during the laser-ceramic interactions. Minimal cracking was observed using the parameters presented in [Table 5.1](#) for both the technical ceramics and, therefore, such parameters were used for the investigations in this chapter.

## 5.5 Modifications of $\text{Si}_3\text{N}_4$ and $\text{ZrO}_2$ technical ceramics through laser surface treatment

### 5.5.1 Changes in the surface hardness from employing various assist gases

Measuring the surface hardness of the laser engineered-surfaces not only enabled one to detect the location of the HAZ, laser-affected region and the as-received surface of the ceramics. But it was also a good indicator of presenting the surface interaction produced by the various processing conditions and gases compositions. The hardness values obtained from employing a Vickers diamond indentation on different laser-

**Table 5.1 Selected parameters from initial experiments, with a constant spot size of 3 mm, gas flow rate of 25 l/min, by using compressed air assist gas**

Lasers types	Parameters					
	Traverse speed (mm/min)		Laser power (W)		Power density (W/mm <sup>2</sup> )	
	$\text{Si}_3\text{N}_4$	$\text{ZrO}_2$	$\text{Si}_3\text{N}_4$	$\text{ZrO}_2$	$\text{Si}_3\text{N}_4$	$\text{ZrO}_2$
Fiber laser	100	100	143.5	137.5	3979	3719

engineered surfaces can be found in **Figure 5.1a and b** for both the  $\text{Si}_3\text{N}_4$  and  $\text{ZrO}_2$  technical ceramics. The hardness changed from within the untreated zone to the HAZ and the fiber laser irradiated zone. For the  $\text{Si}_3\text{N}_4$  technical ceramic, the softest surface was found from the fiber laser-engineered surface by oxygen assist gas (see **Figure 5.1a**). Then compressed air and ambient air showed similar hardness values compared to nitrogen and argon assist gases. This produced slightly higher hardness values within the laser irradiated region. The HAZs using all the different types of conditions did not seem to make much difference, but it is possible that the spread of heat varied when using different gas compositions.

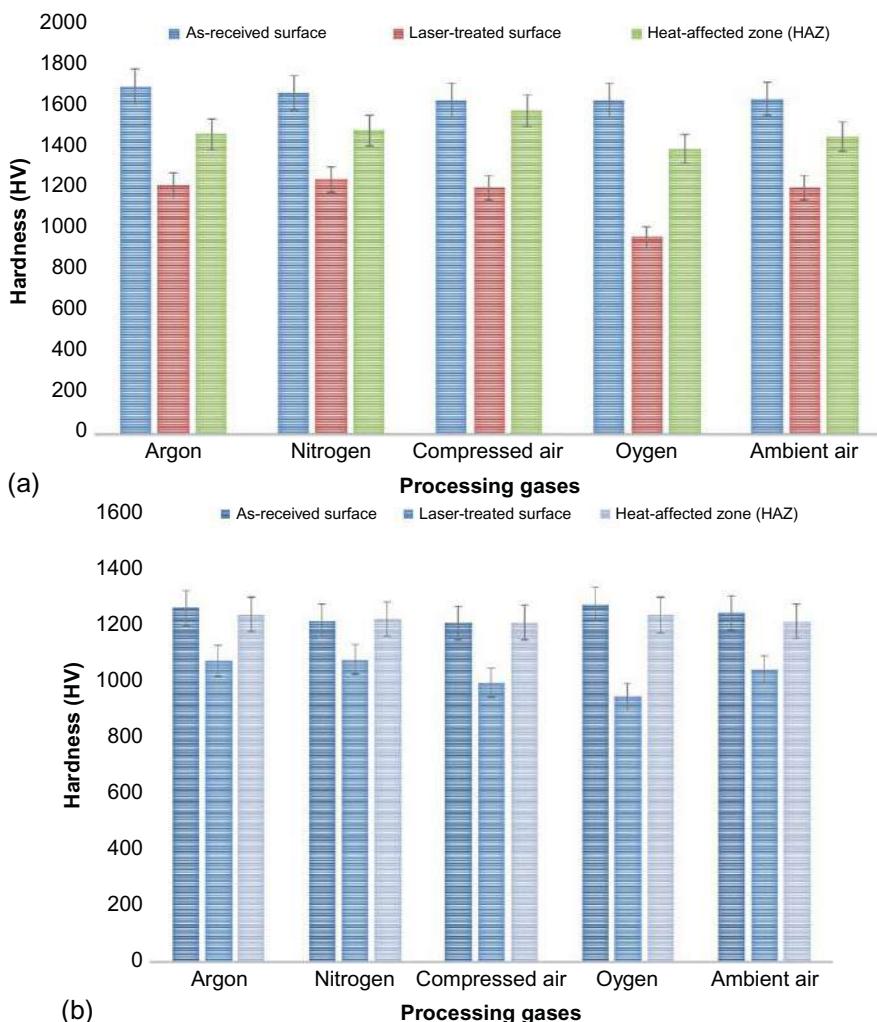


**Figure 5.1** The change in the average hardness (using a 30 kg load) found for the fiber laser treated zone (track) by using various assist gases on the as-received surface and the HAZ of  $\text{Si}_3\text{N}_4$  in (a) the  $\text{ZrO}_2$  technical ceramics in (b).

For the  $\text{ZrO}_2$  technical ceramic, using processing gases such as oxygen, nitrogen, and compressed air also showed much reduction in the surface hardness within the laser engineered track. However, the results were similar to those of the  $\text{Si}_3\text{N}_4$  technical ceramic. From this, it is obvious that the reactive gases such as oxygen, compressed air, and ambient air all produced a considerable amount of interaction zone and would have resulted in higher processing temperature, whereas the nonreactive gases such as nitrogen and argon showed less change in the surface hardness. On account of this, it is indicative that the interaction zone with nonreactive gases was much smaller. This, in turn, produced lower surface temperatures and resulted in low-level activity at the laser-ceramic interface. Further analysis of the topography will show the influence of each gas on both the  $\text{ZrO}_2$  and  $\text{Si}_3\text{N}_4$  technical ceramics.

### **5.5.2 Topographical changes**

*$\text{Si}_3\text{N}_4$  technical ceramic:* The surface topography of a  $\text{Si}_3\text{N}_4$  technical ceramic engineered by the fiber laser using an oxygen assist gas comprised of a new melted and solidified surface layer with some degree of materials removal (see [Figure 5.2a](#)). The gray and white areas present in the laser-treated zone indicate surface oxidation. This was further identified from the microscopic and compositional analysis. In [Figure 5.2b](#), the upper surface profile of the  $\text{Si}_3\text{N}_4$  sample engineered by the fiber laser beam using a compressed air assist gas showed significantly less influenced topography than that of the sample treated with an oxygen assist gas. This indicated that the laser-material interaction during the surface treatment was less reactive in comparison to the surface treated by the fiber laser using the oxygen assist gas. However, the whitening effect on the top surface of the track showed that oxidation took place. From comparison of the compressed air/fiber laser irradiated surface to the oxygen/fiber laser-engineered surface of the  $\text{Si}_3\text{N}_4$  showed similar effects in the near (top) surface layer. Surface oxidation is apparent as well as formation of craters where the surface has become much smoother. This confirmed the melting and the redistribution of the melt zone. More porosity and trapped air holes were also seen in this sample. In [Figure 5.2c](#) the sample fiber laser irradiated with nitrogen assist gas displayed a smaller laser-treated track in comparison to the sample fiber laser treated with oxygen. This is due to nitrogen being a nonreactive gas and, therefore, minimizing the effect of surface oxidation. The surface profile also presents evidence of some morphological changes on the surface of the ceramic resulting from the fiber laser surface treatment. The laser-material interaction between the fiber laser and nitrogen applied on the  $\text{Si}_3\text{N}_4$  technical ceramic may have been less in comparison to other gas types used in this investigation. The surface of the sample fiber laser treated with an argon assist gas, as shown in [Figure 5.2d](#). This revealed similar effects compared to the surface of the sample treated with nitrogen assist gas, which was predictable as argon is an inert gas and would also minimize oxidation and provide a much more protected treatment. The laser-engineered (alone) surface using no assist gas produced a similar result to that of the fiber laser-engineered surface using the compressed air, as shown in [Figure 5.2e](#). This could be due to the compressed air having identical properties to the atmospheric gas properties [52]. Having said that, it can be observed that there

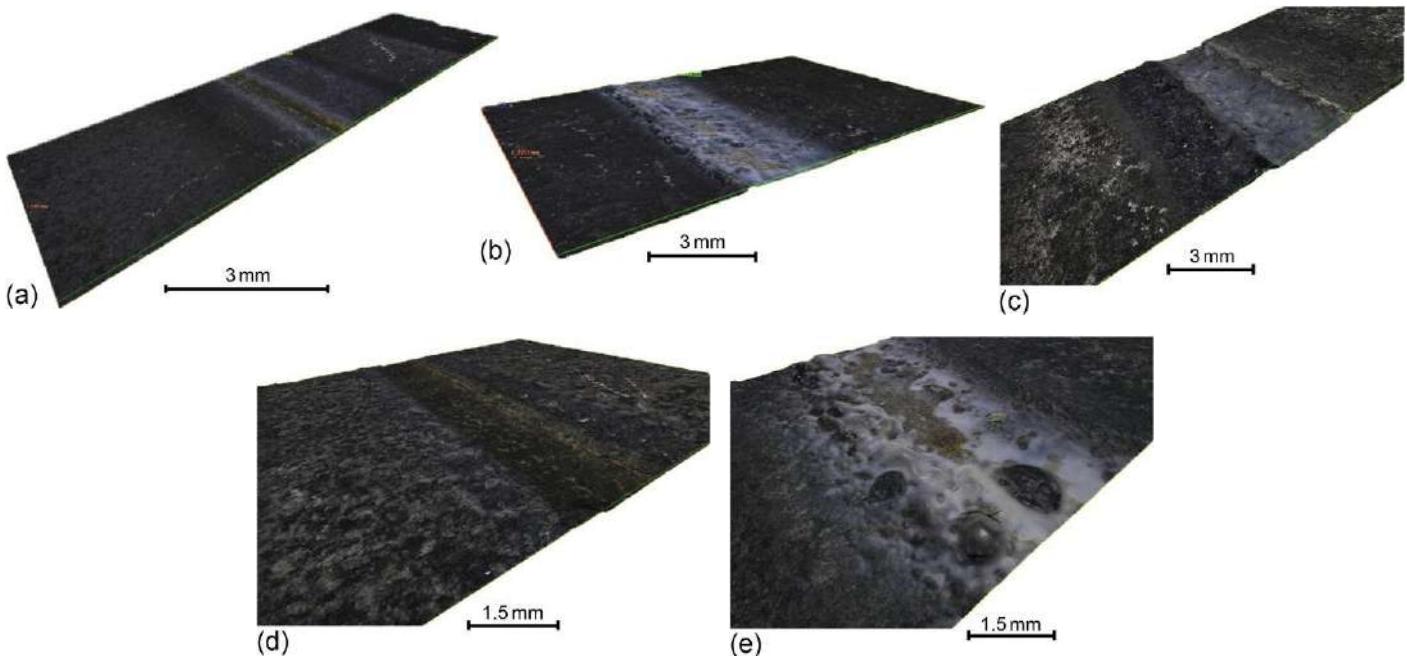


**Figure 5.2** Illustration of the surface topography by a infinite focus variation image of (a) the laser surface engineered by argon, (b) the laser surface engineered by compressed air, (c) the laser surface engineered by oxygen, (d) the laser surface engineered by nitrogen, and (e) the laser surface engineered by ambient air (laser alone) of the  $\text{Si}_3\text{N}_4$  technical ceramics.

are also formations of trapped air holes on the laser-treated zone that were not seen by using other gases compositions, except compressed air and oxygen. In addition, it can also be gathered that the entrapment of holes were formed as the surface melted and formed, leaving the trapped gas to produce a particular surface profile.

*ZrO<sub>2</sub> technical ceramic:* Figure 5.3a presents a topographical image of the fiber laser-engineered surface of the ZrO<sub>2</sub> using oxygen assist gas. The thermal energy induced by the fiber laser has led to some discoloration, as shown in Figure 5.3a-e. The discoloration of the laser surface engineered ZrO<sub>2</sub> was expected due to induction of heat. Thermal exposure of the ZrO<sub>2</sub> at elevated temperatures of over 2500 °C would decompose and transform the ceramic from white to light gray and then to black, which is the case shown in Figure 5.3a-e. Surface melting was not seen in the topographical images, but

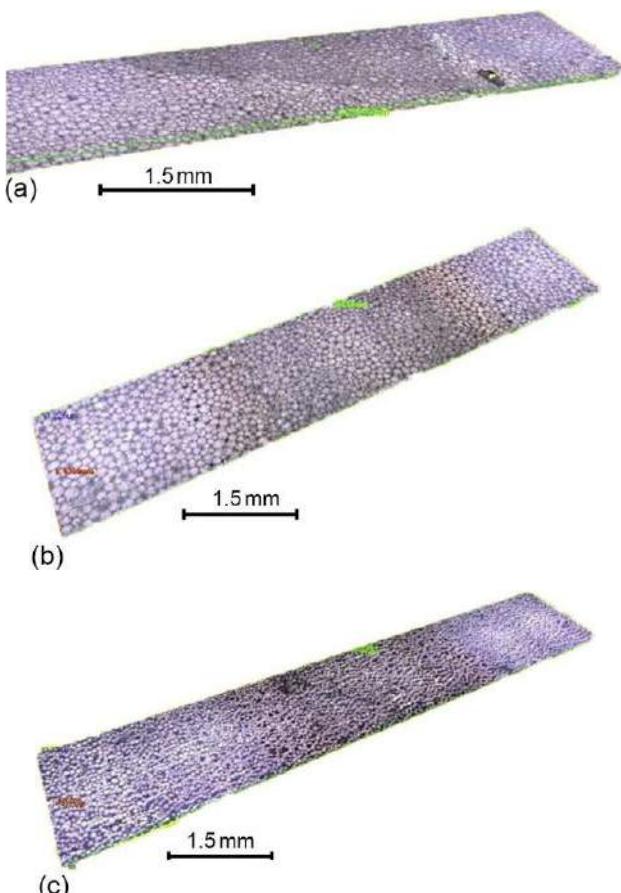


**Figure 5.3** Illustration of the surface topography by infinite focus variation images of (a) the laser surface engineered by argon, (b) the laser surface engineered by compressed air, (c) the laser surface engineered by oxygen, (d) the laser surface engineered by nitrogen, and (e) the laser surface engineered by ambient air (laser alone) of the ZrO<sub>2</sub> technical ceramic.

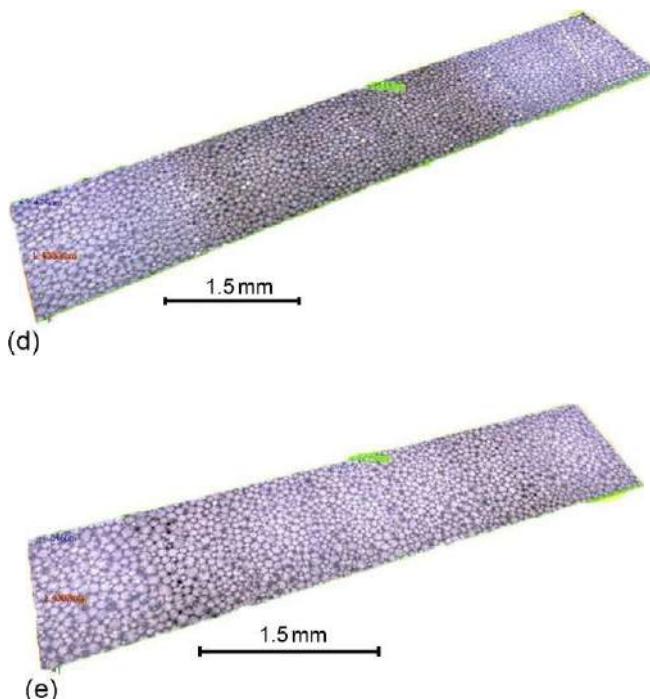


**Figure 5.3** Continued.

further analysis of the microstructure showed some degree of surface melting. From this it could be gathered that the surface temperatures at the fiber laser-ZrO<sub>2</sub> interaction would have ranged from 2300 to 2500 °C and was confirmed from a previous investigation [53]. This is because the oxygen assist gas is generally much more reactive than other gas compositions. This would enhance the fiber laser-ceramic interaction and would produce higher processing temperature to create partial melting of the ceramic, which creates a smoother surface layer than the as-received surface layer. This was also found in a previous investigation [13,14] that described oxygen to be a highly active assist gas for laser processing of ceramic tile material.

The surface of the sample fiber laser engineered using an nitrogen assist gas (see [Figure 5.3c](#)) showed little difference in comparison with the samples fiber laser engineered by using the other gases. The surface finish was improved after the fiber laser treatment in comparison with the surface of the as-received sample. This was due to the nitrogen assist gas being less reactive in comparison to oxygen. Thus, it would produce less interaction between the fiber laser and the ZrO<sub>2</sub> engineering ceramic. Moreover, the processing temperature using nitrogen is also lower compared to oxygen, as an example. This would generate less heat and lower ablation.

The fiber laser-engineered surface using the argon assist gas also presented similar effects to those observed when using nitrogen assist gas (see [Figure 5.3d](#)). This was also to be expected as argon is also an inert gas and would characteristically generate

less of a reactive interaction zone between the fiber laser and the surface of the  $\text{ZrO}_2$  technical ceramic. This proved to be similar when compared to the other samples that were fiber laser engineered using reactive gases. This was due to the laser beam alone coupling with the atmospheric gas molecules to form a similar effect on the  $\text{ZrO}_2$  ceramic, as no assist gas was applied to compliment the laser surface treatment.

### 5.5.3 Material removal

Figure 5.4a and b presents the material removal of both the  $\text{Si}_3\text{N}_4$  and the  $\text{ZrO}_2$  technical ceramics, which were laser engineered using the various assist gases, as mentioned in the previous section. In Figure 5.4a the material removal for the  $\text{Si}_3\text{N}_4$  shows that using oxygen as a processing gas led to the highest material removal, followed by the use of compressed air, ambient air, argon, and nitrogen. The same applied for the results of the laser-engineered  $\text{ZrO}_2$  technical ceramic as shown in Figure 5.4b where the more active gases have a higher material removal than the inert gases. This effect with both ceramics occurred because the oxygen, compressed air, and ambient air all produced an exothermic reaction during the laser-ceramic interaction, whereas the argon and nitrogen are inert and less reactive. This is especially apparent from Figure 5.2a-e for the  $\text{Si}_3\text{N}_4$ ,

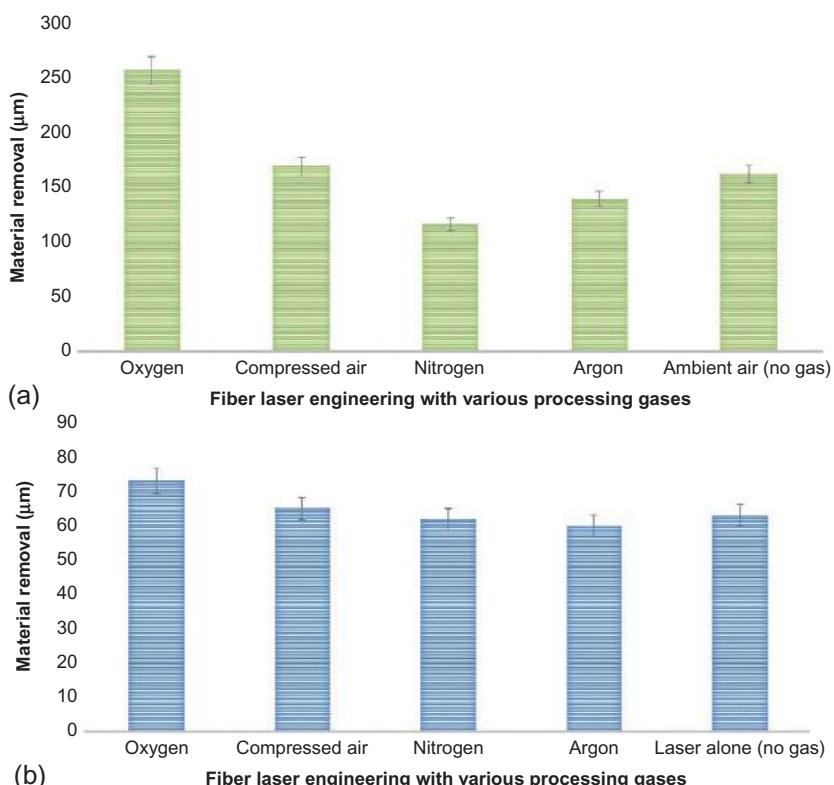


**Figure 5.4** Material removal during laser surface treatment using various processing gases for  $\text{Si}_3\text{N}_4$  in (a) and for the  $\text{ZrO}_2$  technical ceramics in (b).

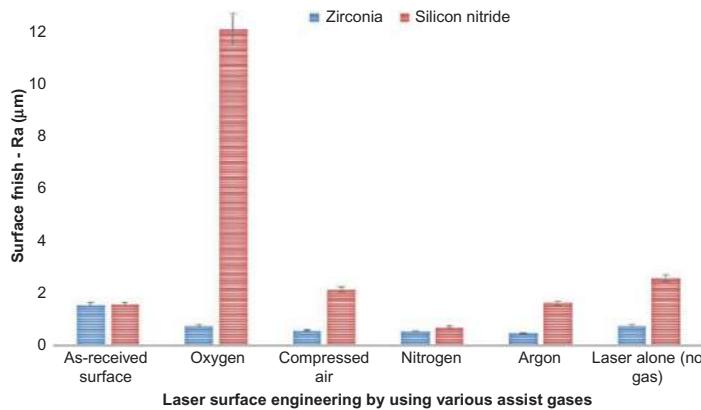


**Figure 5.5** Surface finish of both  $\text{ZrO}_2$  and  $\text{Si}_3\text{N}_4$  technical ceramics after the laser surface treatment.

in which the topographical analysis showed a larger track of the laser-treated zone for the more active gases in comparison to the inert gases.

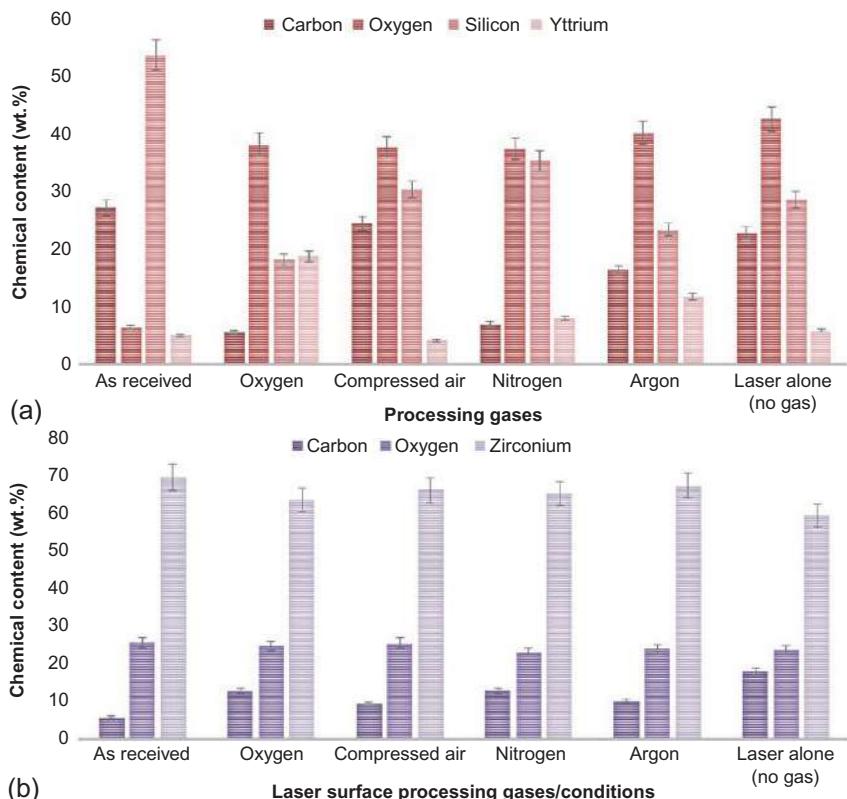
#### 5.5.4 Change in surface finish

Figure 5.5 illustrates the surface finish of the  $\text{ZrO}_2$  and the  $\text{Si}_3\text{N}_4$  technical ceramics after undergoing the laser surface treatment using various assist gases. It is evident that the surface finish for the  $\text{Si}_3\text{N}_4$  was much higher for all conditions applied, in comparison to the conditions applied to  $\text{ZrO}_2$ , despite the surface roughness of the two ceramics being similar for the as-received samples. This occurred first because the  $\text{Si}_3\text{N}_4$  absorbed the NIR wavelength of the fiber laser, while the absorption was low for the  $\text{ZrO}_2$ . The  $\text{ZrO}_2$  also showed very little surface modification, as was evident from the topographical and the microstructural results. The  $\text{Si}_3\text{N}_4$ , on the other hand, heated more than the  $\text{ZrO}_2$  and produced a bigger fusion zone, as well as larger interactions during laser surface treatment. Particularly with the  $\text{Si}_3\text{N}_4$  technical ceramic, the inert gases produced a smoother surface finish, whereas the reactive gases (especially oxygen) produced the roughest finish as a result of high surface interaction ablating significant material by vaporization. For the  $\text{ZrO}_2$  technical ceramic, the surface finish was not apparent. There was a similar regime to that of the  $\text{Si}_3\text{N}_4$ , but reactive gases such as oxygen did not have larger effect on the  $\text{ZrO}_2$  due to the high content of oxygen already present with  $\text{ZrO}_2$  ceramic from its original state.

## 5.6 Compositional changes

### 5.6.1 $\text{Si}_3\text{N}_4$ technical ceramic

Figure 5.6a shows a graphical illustration of the  $\text{Si}_3\text{N}_4$  technical ceramic for the as-received and the laser-surface-engineered samples by using various processing gases. The content of oxygen found on the surface of the sample fiber laser engineered with



**Figure 5.6** Chemical composition of the  $\text{Si}_3\text{N}_4$  in (a) and for the  $\text{ZrO}_2$  technical ceramics in (b) after the fiber laser surface treatment using various processing gases.

oxygen was reasonably high. Up to 37 wt.% of oxygen was observed and was the highest amount relative to the oxygen contents of surfaces treated using other gases. In comparison to the as-received surface, the carbon content of the engineered surface was reduced to 5.56 wt.%, and the silicon content was 17.21 wt.%, as further presented in Figure 5.6. There was also 17.70 wt.% yttrium found in this sample. Based on the content level, it can be observed that a chemical change has occurred in the sample after it underwent the fiber laser surface treatment with oxygen assist gas.

The chemical composition found using compressed air was 24.39 wt.% of carbon, 37.72 wt.% of oxygen, 30.43 wt.% of silicon, and 4.21 wt.% of yttrium. The silicon was decreased in comparison to the as-received surface; however, the decrease was not as great as the decrease in the fiber laser surface engineered with oxygen. This indicated that a compositional change had also occurred as a result of the fiber laser surface treatment using compressed air as an assist gas.

The surface engineered with the fiber laser alone (no assist gas) had the highest oxygen content. Up to 42.60 wt.% of oxygen was found. This probably occurred due to the lack of processing gas being supplied at the surface during the fiber laser- $\text{Si}_3\text{N}_4$  interaction and also because of the extra heat generated at the interaction

zone. This characteristically formed the high oxygen content within the surface layer engineered using the fiber laser. Some areas of the treated zone also comprised of porosity produced from the formation of the new oxide layer. The oxide layer would have prevented the air from escaping during the solidification stage. The carbon content in the laser (alone) treated sample was 27.67 wt.%, and the silicon content was 27.73 wt.%. The elemental analysis given for the nitrogen laser engineered sample in [Figure 5.6a](#) showed 35.47 wt.% of oxygen, 35.45 wt.% of silicon, 6.99 wt.% of carbon, and 10 wt.% of yttrium.

The chemical composition found on this surface was 16.36 wt.% of carbon, 35.72 wt.% of oxygen, 27.43 wt.% of silicon, and 11.70 wt.% of yttrium. The chemical composition herein is similar to that of the nitrogen, except with a fiber laser-engineered surface with argon. This was because there is more oxygen content present due to the argon not coupling well with the  $\text{Si}_3\text{N}_4$  in comparison to nitrogen so that the surface of the  $\text{Si}_3\text{N}_4$  was protected from an atmospheric influence.

A chemical change has been observed on all surfaces fiber laser engineered using the variety of assist gases. Evidence of surface oxidation is also found with all treated samples. However, the effects are remarkable when using reactive gases such as oxygen. The sample treated in ambient condition using no assist gas also showed similar results to that of the oxygen and compressed air assist gases. Overall, the increase in carbon and oxygen content has been seen for all laser processing gasses used (see [Figure 5.6](#)). This formed a new surface layer. From the five different conditions used, carbon, oxygen, and silicon as elements all appear within the treated surfaces to some extent. Owing to this, it can be said that a change in composition has taken place as the fiber laser-engineered surfaces of the  $\text{Si}_3\text{N}_4$  technical grade ceramic were altered to form  $\text{SiO}_2$ . This change was also reported in a previous investigation [52], when the  $\text{SiO}_2$  is produced as a result of heating silicon at a temperature around 1600 °C. The temperature during fiber laser processing in this study using any of the gas compositions was much higher than 1600 °C, as later shown from the thermal analysis. This is evident from the topographical and the microscopic images where melt zones were found. This indicated that the formation of the  $\text{SiO}_2$  layer was unavoidable even by using less-reactive assist gases such as argon and oxygen.

### **5.6.2 $\text{ZrO}_2$ technical ceramic**

The compositional analysis for the fiber laser-engineered surface using oxygen assist gas for the  $\text{ZrO}_2$  technical ceramic showed that the carbon content within the ceramic was increased to 12.77 wt.% compared to the as-received sample by over 50%. This indicated that the laser processing resulted in the ceramic comprising the carbon content due to the carbon content generally present in the atmosphere. The oxygen content maintained in the same region to the as-received surface and was 24.49 wt.% and zirconium was 62.74 wt.% as further presented in [Figure 5.6b](#). With using the compressed air as a processing gas, the carbon content increased to 9.52 wt.% when compared to the laser unaffected surface. The oxygen content remains similar to that of the as-received surface and the zirconium content was 65.22 wt.%. The fiber laser-engineered surface with nitrogen assist gas showed 12.76 wt.% of carbon, 22.73 wt.% of oxygen, and

64.41 wt.% of zirconium. The increase in the carbon content may have occurred during the melting, vaporization, and material removal of the  $\text{ZrO}_2$ . The compositional study of the fiber laser-engineered surface using argon revealed 23.70 wt.% of oxygen, 9.94 wt.% of carbon, and 66.36 wt.% of zirconium. The composition found on the fiber laser-engineered sample with no gas showed 17.91 wt.% carbon, 23.42 wt.% of oxygen, and 57.66 wt.% of zirconium as presented in [Figure 5.6b](#). The carbon content was the highest and zirconium content was the lowest for this sample in comparison to all other samples. Zirconium was found to have reduced in comparison to the as-received surface after the fiber laser surface treatment using ambient air and all other assist gases. The discoloration of all the surfaces was a good indication that this occurred. This was because of the induction of the thermal energy as well as generation of the carbon absorbing within the top layer of the  $\text{ZrO}_2$  and would have led the fiber laser-engineered surfaces to change color and blacken.

The zirconium and oxygen content is generally found within a  $\text{ZrO}_2$  ceramic. However, from [Figure 5.6b](#), it can be seen that a considerable amount of carbon was detected with the laser-engineered  $\text{ZrO}_2$  despite using any gas compositions. In addition, the increase in the carbon content may have occurred during the melting, vaporization, and material removal of the  $\text{ZrO}_2$  engineering ceramic. The content of zirconium was found to have reduced in comparison to the as-received surface after the fiber laser surface treatment was performed by using ambient air and all other assist gases.

## 5.7 Microstructural modifications

### 5.7.1 As-received surface of the $\text{Si}_3\text{N}_4$ technical ceramic

[Figure 5.7a](#) shows the as-received surface of  $\text{Si}_3\text{N}_4$  technical ceramic with the surface appearing to be somewhat coarse, comprised of surface microcracks and closely packed grains, as one can see in [Figure 5.7a](#). The grains were measured to be ranging between 1.5 and 2.5  $\mu\text{m}$  in size. There was no evidence of the porosity pre-existing on the surface of the as-received  $\text{Si}_3\text{N}_4$  from observing the SEM images.

### 5.7.2 Microstructure of the laser-engineered $\text{Si}_3\text{N}_4$ technical ceramic

The SEM images in [Figure 5.7a](#) show the as-received surface of the  $\text{Si}_3\text{N}_4$  technical ceramic, whereas [Figure 5.7b-f](#) presents the different condition of the laser-engineered  $\text{Si}_3\text{N}_4$  technical ceramic by employing various processing gases. The laser-engineered surface using argon and nitrogen shows evidence of partially melted areas (see [Figure 5.7b and c](#)) compared to the surfaces laser engineered by the active gases such as oxygen, compressed air, and ambient air, that all showed considerable melting and oxidation of the surfaces in [Figure 5.7d-f](#). The difference between the microstructure of the surfaces occurred due to the change in fusion zone created by the particular gas compositions. For the reactive gases such as oxygen, compressed air, and ambient air,

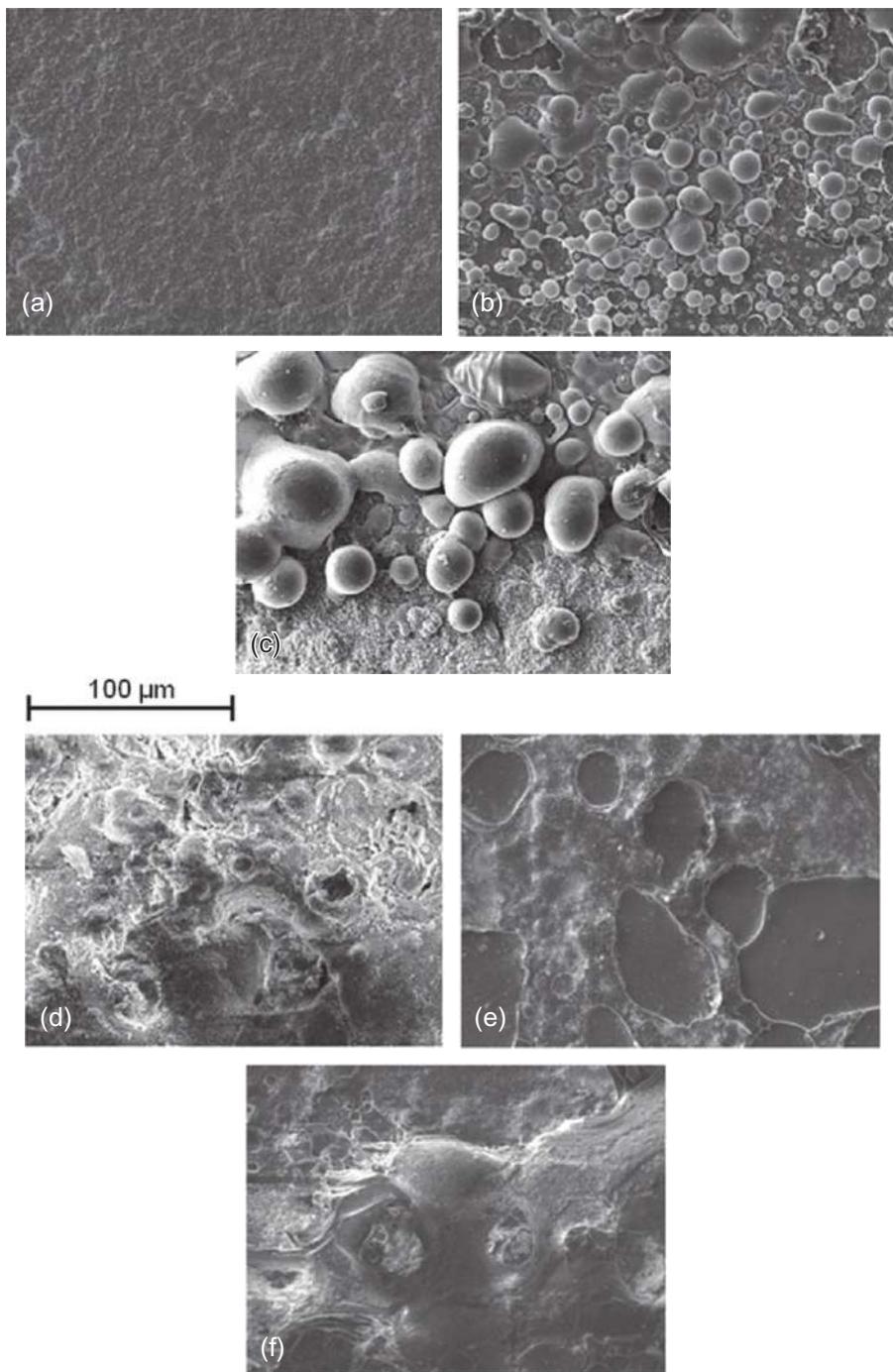


**Figure 5.7** SEM images of the as-received surface in (a), the laser surface engineered with argon in (b); with nitrogen in (c); with oxygen in (d); with compressed air in (e); and the surface engineered with laser alone (no assist gas) in (f) for the  $\text{Si}_3\text{N}_4$  technical ceramic.

it is generally the case that due to an exothermic reaction there tends to be a case where the processing temperature is much higher and may create sufficient level of melting at the laser-ceramic interface.

Observation of the SEM images fiber laser engineered using an oxygen assist gas showed a significantly modified surface profile which comprised of a newly formed surface layer. This can also be seen with images from the other assist gases used but the effects are rather distinct when using oxygen. The surface profile in this case was slightly different to that of the as-received surface as the fiber laser surface treatment had melted the top layer. The melted layer then redistributed unevenly and altered the surface finish and the chemical composition as further seen in this study. The HAZ of the surface treated with the fiber laser beam was also considerably broad in comparison with the samples treated using other assist gases. This was because of oxygen being a reactive gas, where more chemical changes had occurred in comparison to using an inert gas. The reason for the sample treated with oxygen assist gas producing a large area of laser-affected zones was due to the faster burning rate of oxygen than the traverse speed of the laser beam, as stated by Bass [54]. Bass also stated that non-metallic materials such as ceramics are more sensitive to chemical changes from using oxygen. On account of this, a coarser surface finish was found by using the oxygen in this investigation. If the burning rate of oxygen was slower than that of the travelling speed of the laser, then the opposite reaction would occur where the laser-treated zones would be narrow and produce a smoother surface finish. The processing temperature in this case would also be high. In general, the use of oxygen is appropriate for the fiber laser surface treatment for ceramics if deep penetration or faster processing speeds are required. But if the surface roughness and the material removal are more important then argon or nitrogen assist gases are certainly ideal. The fiber laser irradiated sample with compressed air assist gas also showed a significant level of morphological changes along with some decomposition (see [Figure 5.7e](#)). The grains are exposed in comparison to that of the as-received sample. The level of oxidation is not evident as much as the case with samples' fiber laser-treatment using oxygen. This was because of the oxygen content being lower in the elements of compressed air than that of the pure oxygen.

The morphology of a sample fiber laser engineered with compressed air assist gas is shown in [Figure 5.7](#). It can be said that the surface has also undergone some decomposition due to the high temperatures produced during the laser-material interaction, which is later confirmed to be in the region of over 2000 °C. This, in turn, produced material removal that intrinsically changed the surface morphology, as the  $\text{Si}_3\text{N}_4$  was exposed to the atmosphere at such high temperatures. The irregularity of the material removal during the decomposition of the ceramic should also be considered. This is because it has also contributed to the change in the surface morphology and the surface finish. Furthermore, the change in the morphology also depends on how much the grains are covered and the level of bonding between the new surface layer produced by the fiber laser treatment and the secondary phase of the  $\text{Si}_3\text{N}_4$  ceramic. The sample treated in ambient air using the fiber laser has some relation to the sample fiber laser engineered with an oxygen assist gas.

SEM surface images of samples fiber laser irradiated with nitrogen and argon assist gasses are shown in [Figure 5.7b](#) and [c](#) respectively. The HAZ and the fiber laser

surface engineered areas were much smaller and sharper when using nitrogen. The shape of the grains also changed with nitrogen, as presented in [Figure 5.7b](#). For this particular surface, rod-like grains were also formed in some areas that are not seen on other samples. In addition, evidence of porosity formation in the interface between the HAZ and the laser engineered area were also found. This is not apparent in the surfaces engineered using the other assist gases, except argon. This was due to the increase in the cooling rate. The cooling rate allowed a new surface layer to be formed as gases were trapped from escaping. This was also confirmed by previous workers [55]. It can be said that similar effects were achieved when using nitrogen and argon, because they are both inert and less reactive to a chemical change in comparison to the other gases, including ambient air (no gas). This agreed with previous investigations [54,56]. It is also likely that laser interaction temperatures during processing with nitrogen and argon assist gasses were much lower than those using oxygen, compressed air, or ambient assist gasses. Moreover, there was evidence of porosity on the interface between the HAZ and the surface engineered by the fiber laser for both samples that were treated with nitrogen and argon assist gasses, as can be seen in [Figure 5.7b and c](#). The oxygen content within the sample laser engineered with nitrogen assist gas is the lowest in comparison to the other samples, but there is only a small difference between the oxygen content found within each of the samples. However, the use of nitrogen as the assist gas certainly modified the surface profile, as rod-like grains were formed (see [Figure 5.7b](#)). The  $\text{Si}_3\text{N}_4$  surface fiber laser engineered with nitrogen assist gas also showed enlargement of the grains in comparison to the as-received surface.

The microscopic images in [Figure 5.7b](#) show evidence of the surface melting using Ar assist gas. This was somewhat different in comparison to nitrogen as the grain boundaries of the  $\text{Si}_3\text{N}_4$  surface fiber laser irradiated with an Ar assist gas had begun to bind into each other. The interface between the HAZ and the laser treated zone shows that porosity within the ceramic has been covered with the newly formed surface layer. This can relate to the concept of crack healing, where the fiber laser irradiated surface areas were close to their melting temperatures and were solidified and covered the surface cracks and formed a new surface layer. A similar result was also reported by Sun *et al.* [15] when surface treating a  $\text{Si}_3\text{N}_4$  ceramic with a  $\text{CO}_2$  laser. The solidified surface in the interface between the fiber laser-engineered area and the HAZ showed evidence of splatter occurring from the melt zone as the material was pushed to the side of the laser-created track. This appears in all the fiber laser engineered samples but was more evident in the samples treated with nitrogen and argon assist gases. This indicated that there was less heat produced during the interaction of the fiber laser- $\text{Si}_3\text{N}_4$ . Hence, the porosity was formed from the entrapped gases between the HAZ and the fiber laser-engineered surface.

### **5.7.3 Microstructure of the as-received $\text{ZrO}_2$ technical ceramic**

The as-received sample of the  $\text{ZrO}_2$ , with the surface appearing to be somewhat coarse and comprised of the surface microcracks and closely packed grains, is shown in [Figure 5.8a](#). The micrographs in [Figure 5.8a](#) for the  $\text{ZrO}_2$  technical ceramic showed that the as-received surface consisted of agglomerates. The dimensions of the

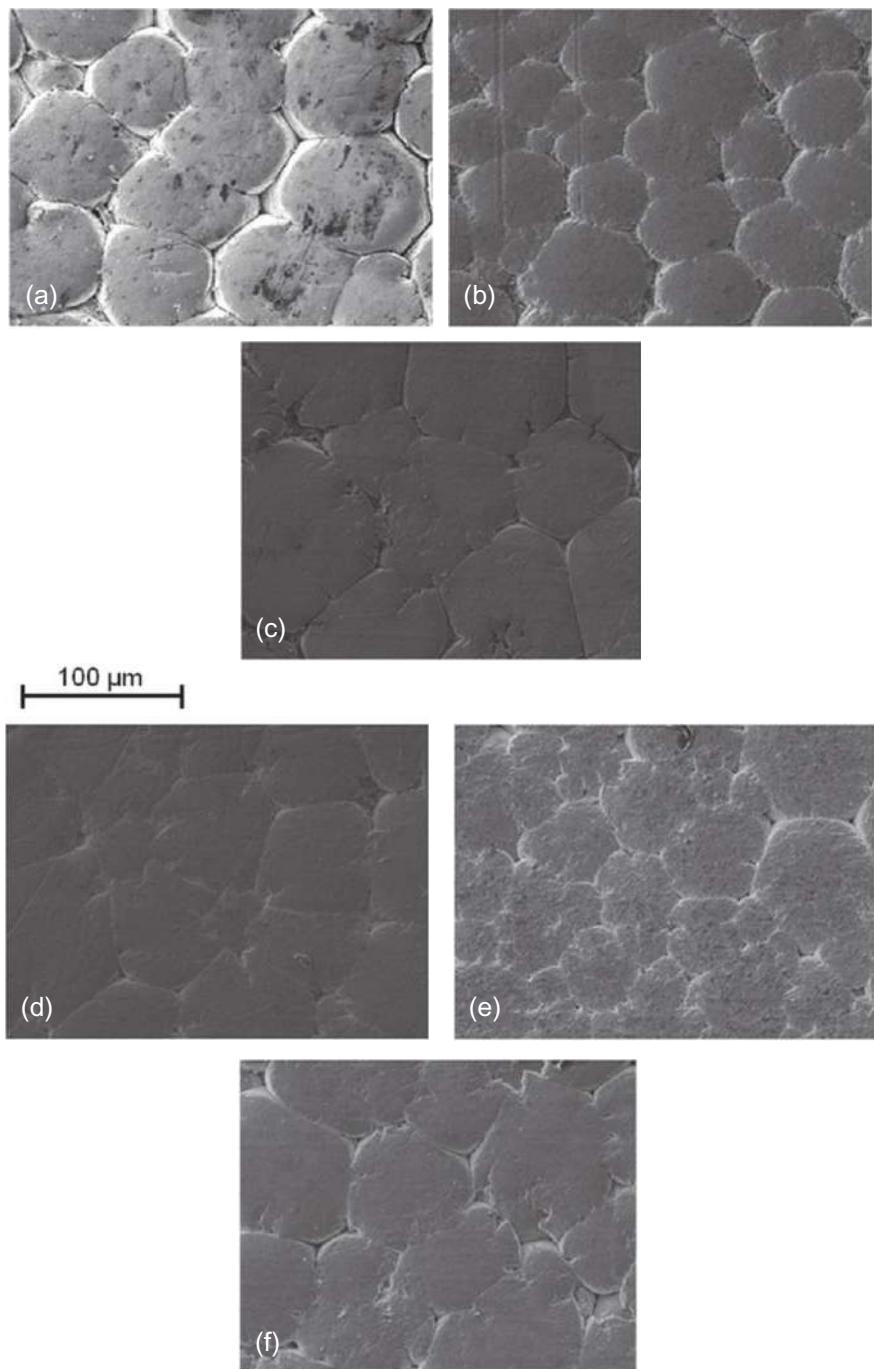


**Figure 5.8** SEM images of (a) the as-received surface, (b) the laser surface engineered with oxygen, (c) with compressed air, (d) with nitrogen, (e) with argon, and (f) with laser alone (no gas) of the  $\text{ZrO}_2$  technical ceramic.

agglomerates ranged between 70 and 100  $\mu\text{m}$  and averaged 95  $\mu\text{m}$ . As one can see, the boundaries of the agglomerates are not so closely packed, which would have increased the level of pores around the edge of the agglomerate boundaries. However, there was minimal porosity seen on the surface of the as-received  $\text{ZrO}_2$ . What is more, during the spray drying stage (when manufacturing the ceramic) and the preparation of the ceramic powder, the powder is generally dispersed in a liquid medium. This is sprayed into hot air so that the droplets will dry and create the spherical agglomerates. The agglomerates enhance the flow of the ceramic powder and, in turn, increase the processing speed during the preparation of the green body (ceramic products) by pressing. It is then sintered to get the final product (the rectangular bar in [Figure 5.8a-f](#)). Moreover, the agglomerates would generally crush during the preparation of the green body by pressing. But, this is not always the case as some agglomerates will only get flattened, especially those near the surface of the sample as presented in the SEM images of the  $\text{ZrO}_2$  technical ceramic. The grains would appear with higher magnification if a magnified analysis through the agglomerates is conducted.

#### **5.7.4 Microstructure of the laser engineered $\text{ZrO}_2$ technical ceramic**

The fiber laser-engineered surface using oxygen assist gas produced some melting of the top surface layer (see [Figure 5.8b](#)). The grain boundaries herein had begun to close-off and bind together. This inherently would produce an interlocking microstructure and enhance the surface strength as well as the resistance to fracture. Upon using compressed air as a processing gas, it was found that there was also some degree of surface melting during laser- $\text{ZrO}_2$  interaction. This is shown in [Figure 5.8b](#), where the agglomerate boundaries have also begun to bond and interlock as the surface had partially melted. Upon observation, the fiber laser-engineered surface with nitrogen assist gas showed the least amount of laser-material interaction. This was due to the surface melting (in this case) being minimal in comparison with other treated surfaces. Yet, the gap between the agglomerate boundaries has decreased in comparison to the as-received surface. However, it generated a minimal amount of material removal. The surface morphology of the sample fiber laser engineered with argon assist gas showed a considerable amount of modification to the near surface layer, as illustrated in [Figure 5.8d](#). The agglomerate boundaries showed some melting and redistribution, which closed off the gaps that existed prior to the fiber laser surface treatment. This is markedly evident in the sample treated by the fiber laser with an argon assist gas in comparison to those treated under other assist gases. Moreover, strengthening of the surface could occur due to a possibility of a phase transformation during heating from ambience and near to the melting temperature of the ceramic. This would have led phase transformation from the monoclinic phase to the tetragonal phase at around 1200  $^{\circ}\text{C}$  followed by a possible change to the cubic phase as later discussed. Thus, during the transformation from monoclinic phase to tetragonal phase would have led to the binding of the agglomerate boundaries and enhanced surface strength. Previous investigation also reported this finding and showed that the fracture strength can be achieved during an active dual phase transformation of tetragonal and

monoclinic within a  $\text{ZrO}_2$  ceramic during a sintering process [57]. This, in comparison with the other samples, was the most influenced by the fiber laser surface treatment when considering the microstructure modifications. Further, it also showed that the interaction of argon with the other samples was better in surface modification  $\text{ZrO}_2$  ceramic. The fiber laser irradiated sample in ambient air (see Figure 5.8f) proved to be less reactive as the gaps between the agglomerate boundaries were not greatly affected, particularly when compared to samples treated by argon, oxygen, and compressed air. The samples fiber laser engineered with nitrogen illustrated similar results but in that case, the material removal and the surface roughness were both slightly higher. This indicated that more interaction between the fiber laser and the  $\text{ZrO}_2$  had also occurred. Hence, it can be summarized that the processing gas of a particular composition is required in order to achieve a considerable amount of effect during the fiber laser irradiation when microstructural modifications are considered.

## 5.8 Fracture toughness ( $K_{1c}$ ) modifications

The investigation of fracture toughness parameter  $K_{1c}$  showed that a modification in the surface hardness led to a change in the  $K_{1c}$  for the laser-engineered surfaces of both the technical ceramics under the applied condition. Modification in hardness and the crack length demonstrated that the hardness acted as an influential parameter in changing the surface  $K_{1c}$ . The hardness and the resulting crack lengths were both an important function of the  $K_{1c}$  calculation. This meant that with changes in the surface hardness and the resulting crack length would generally influence the  $K_{1c}$  of the ceramics. The fiber laser-engineered surfaces in comparison to the as-received surface showed improvement in the  $K_{1c}$  of the top surface layer of both laser engineered  $\text{ZrO}_2$  and  $\text{Si}_3\text{N}_4$  technical ceramics under the applied conditions. The fiber laser had increased the hardness but produced a reduction in the crack length (see Table 5.2). This led to increased  $K_{1c}$  values under the applied conditions.

Several aspects would have resulted to bring about this change. First, it is likely that the heat generated by the laser surface treatment would have caused transformation hardening to take place. For the  $\text{Si}_3\text{N}_4$  technical ceramic, it can be postulated that transformation of the  $\text{Si}_3\text{N}_4$  from *alpha* to *beta* state at 1600 °C could have occurred.

**Table 5.2 The average hardness, crack length, and the  $K_{1c}$  of the laser-engineered surfaces of both the  $\text{Si}_3\text{N}_4$  and  $\text{ZrO}_2$  technical ceramics**

	Average surface hardness (HV)		Average surface crack length (μm)		Average surface $K_{1c}$ (MPa m <sup>1/2</sup> )	
	$\text{Si}_3\text{N}_4$	$\text{ZrO}_2$	$\text{Si}_3\text{N}_4$	$\text{ZrO}_2$	$\text{Si}_3\text{N}_4$	$\text{ZrO}_2$
As-received surface	1106	973	376	277	1.71	2.45
Fiber laser treatment	1154	940	242	170	3.25	5.05

This can be confirmed in [Section 5.4.5](#) by the results of the processing temperatures. A previous investigation by Jiang *et al.* [58] also reported that alpha to beta transformation generally occurs at 1600 °C within a Si<sub>3</sub>N<sub>4</sub>. Because the processing temperature during the fiber laser surface treatment was found to be much higher than 1600 °C (as indicated from the surface melting and decomposition), it would imply that the ceramic was heated to around a temperature of about 1900 °C or above where phase transformation of alpha to beta phase will inherently occur. Strengthening of the ZrO<sub>2</sub> ceramic could have occurred due to a potential change in phases from monoclinic to tetragonal around 1200 °C.

Second, the effect of strain hardening is also a possible cause, as the effect of strain hardening through movement of dislocations at elevated temperatures could induce compression into the surface and the subsurface of the ceramics. Last, the laser-engineered surfaces could have led to an effect of crack healing. This is because the existing surface microcracks on the ceramic were filled and covered by the fiber laser surface treatment, which all led to the modification of the fracture toughness parameter  $K_{Ic}$  of the laser engineered ceramics.

## 5.9 Temperature distribution and phase transition

The measured temperatures of fiber laser surface treatment of both the Si<sub>3</sub>N<sub>4</sub> and the ZrO<sub>2</sub> ceramics are both also presented in [Table 5.3](#) for both the FEM and the experimental model. In addition, the FEM is also presented for both the ceramics in [Figures 5.9](#) and [5.10](#). From both the surface and the bulk temperature measurements, the distribution of the temperature over the length and the depth of the two technical ceramics treated by the fiber laser was also presented, and the FEM was verified with an error of +10%. This was consistent over the estimate of temperature by the FEM, which could have resulted due to the heat losses through the holes drilled into the sample to place the thermocouples, lack of contact of the thermocouples to the material surface, and the response time of the thermocouples. Such aspects were not taken in consideration by the FEM, which produced higher values. The thermal analysis of the fiber laser surface treatment of the ZrO<sub>2</sub> showed that there was also a significant level

**Table 5.3 Comparison of the surface and the bulk temperature obtained by the experimental study and the FEM of the fiber laser surface treatment of the Si<sub>3</sub>N<sub>4</sub> and ZrO<sub>2</sub> technical ceramics**

Experimental model				FEM			
Surface temperature (°C)		Bulk temperature (°C) at 5 mm below surface		Surface temperature (°C)		Bulk temperature (°C) at 5 mm below surface	
Si <sub>3</sub> N <sub>4</sub>	ZrO <sub>2</sub>	Si <sub>3</sub> N <sub>4</sub>	ZrO <sub>2</sub>	Si <sub>3</sub> N <sub>4</sub>	ZrO <sub>2</sub>	Si <sub>3</sub> N <sub>4</sub>	ZrO <sub>2</sub>
2269	2473	1350	1600	2277	2577	1366	1951

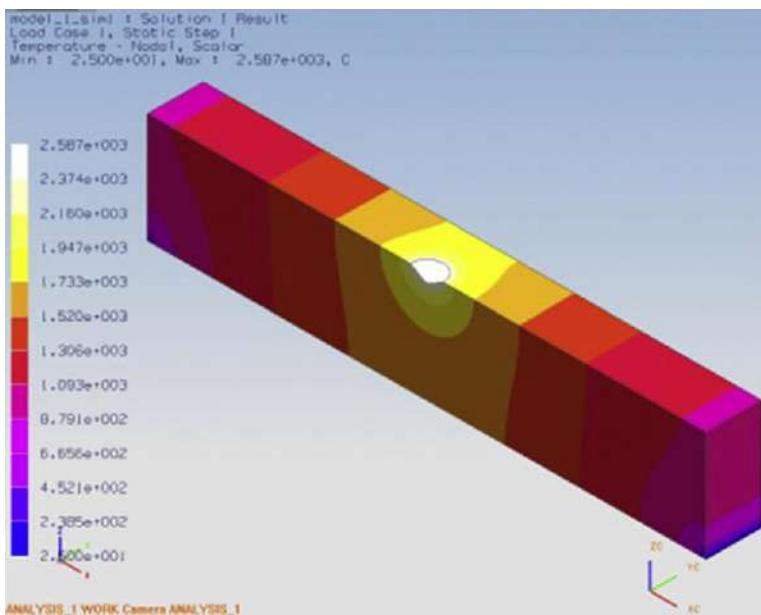


**Figure 5.9** Distribution of temperature for the fiber laser surface treatment of  $\text{ZrO}_2$  technical ceramic obtained from the FEM.

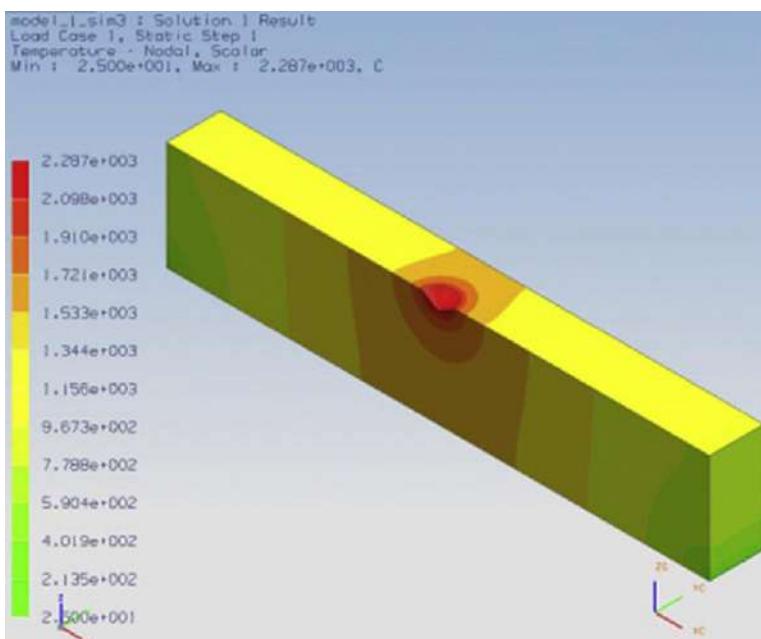


**Figure 5.10** Distribution of temperature during fiber laser surface treatment of  $\text{Si}_3\text{N}_4$  technical ceramic obtained from the FEM.

of temperature difference between the FEM and the experimental temperature readings within both technical ceramics. The measured and verified temperatures by both the experimental and computational methods allows one to postulate that strengthening of the two ceramics through phase transformation as a reason for enhancing the  $K_{1c}$  could be confirmed. This is because the processing temperatures recorded according to the thermals study indicate that the ceramics would have undergone various phase transitions.

For the  $\text{Si}_3\text{N}_4$  technical ceramic it can be postulated that the phase transformation of the  $\text{Si}_3\text{N}_4$  engineering ceramic has started to take place where a large percent of the *alpha*-phase is present and the *beta*-phase has began to form at 1400 °C [59]. Around this temperature, the transition between *alpha*-phase to *beta*-phase would have occurred where *alpha* and *beta* would be found; beyond 1400 °C the phase transformation of *beta*-phase is generally fully formed [59]. Further, at 1450 °C, the  $\text{Si}_3\text{N}_4$  fully transforms to *beta*-phase and shows the end of the phase transformation [59]. Moreover, beyond 1900 °C, the  $\text{Si}_3\text{N}_4$  technical ceramic would generally begin to decompose and vaporize [59].

For the  $\text{ZrO}_2$  technical ceramic, at 700-800 °C a possible phase change could be postulated where a mixture of monoclinic plus tetragonal phase generally occurs [60]. At 1290 °C a further phase transformation of monoclinic to tetragonal would result. From observing the temperature distribution obtained experimentally and from the FEM, one can see that the rapid surface and bulk heating occur. This is followed by the rapid cooling effect, which takes place where the  $\text{ZrO}_2$  is transformed from monoclinic to monoclinic plus tetragonal to a fully tetragonal phase, and finally to tetragonal plus cubic during heating.

## 5.10 Conclusions

This chapter focused on the effects resulting from laser surface treatment of technical grade ceramics, namely,  $\text{Si}_3\text{N}_4$  and  $\text{ZrO}_2$ . Various characterization techniques were used to present the laser-ceramic interaction to demonstrate the topographical, microstructural, compositional, mechanical, and thermal aspects after the laser surface treatment has taken place. The results showed considerable modification in the surface topography, material removal subject to the laser processing conditions. In addition, chemical, microstructural, and compositional changes were also found for both the  $\text{ZrO}_2$  and  $\text{Si}_3\text{N}_4$  technical ceramics. What is more, the fracture toughness parameter  $K_{1c}$  was also modified for the fiber laser-engineered surfaces of the two ceramics by a change in hardness and the resulting crack length from the diamond indentation. This in turn showed a considerable change in the  $K_{1c}$  of the ceramics under the applied conditions. Temperatures during the laser surface treatment were also measured and verified with a computational method, whereby, the distribution of heat over the surface of the  $\text{ZrO}_2$  and the  $\text{Si}_3\text{N}_4$  was found. Through this, phase transformation and internal changes within the material could also be gauged. This research has showed the various methods adaptable to characterize laser surface engineered technical grade ceramics, namely, physical/mechanical, microstructural, topographical,

and compositional. More importantly, the laser-ceramic interaction covers various physical issues that are presented from a wider perspective to enable further process development of laser surface engineering of technical ceramics.

## References

- [1] M. Witt, Industrial applications of excimer lasers, *Hyperfine Interact.* 37 (1977) 415–422.
- [2] J.C. Yamamoto, Laser machining of Silicon Nitride, LAMP'77, 1977.
- [3] A.G. Solomah, L. Mannik, S.K. Brown, Laser machining of silicon nitride ceramics, in: Proceedings of the International Conference on Machining of Advanced Materials, 1993.
- [4] Y.C. Lee, S.H. Kuo, Miniature conical transducer realized by excimer laser micro-machining technique, *Sens. Actuators* 93 (2001) 57–62.
- [5] Y. Tian, Y.C. Shin, Laser assisted machining of damage free-silicon nitride parts with complex geometric features via in process control of laser power, *J. Am. Ceram. Soc.* 79 (2006) 3397–3405.
- [6] J. Lawrence, L. Hao, *Laser Surface Treatment of Bio-Implant Materials*, John Wiley & Sons Ltd. Publications, United Kingdom, 2005.
- [7] P.P. Shukla, Surface treatment of ceramics using contact-less energy beams (M.Sc. by research thesis), Advanced Joining Centre, Coventry University, 2007.
- [8] L. Sun, A.P. Malshe, W. Jiang, P.H. Mccluskey, Effect of CO<sub>2</sub> laser surface processing on fracture behaviour of silicon nitride ceramic, *J. Eng. Mater. Technol.* 127 (July 2006) 460–467.
- [9] L. Sun, A.P. Malshe, J. Wen Ping, P.H. Mccluskey, Experimental investigation of laser surface processing of flexure silicon nitride ceramics, *Trans. Nonferrous Met. Soc. China* 16 (2006) 557–565.
- [10] J. Lawrence, L. Li, On the difference between the beam interactions characteristics of CO<sub>2</sub>, Nd:YAG Excimer and high powered diode lasers with a SiO<sub>2</sub>/Al<sub>2</sub>O<sub>3</sub> ceramic, *Lasers Eng.* 12 (2) (2002) 71–93.
- [11] A. Petitbon, D. Guignot, Laser surface treatment of ceramic coatings, *Mater. Sci. Eng. A* 121 (1979) 545–547.
- [12] J. Lawrence, D.W. Evans, An analysis of crack and porosity formation in laser surface treated magnesia partially stabilized zirconia (MgO-PSZ) and methods for alleviation, *Lasers Eng.* 17 (2007) 255–271.
- [13] J.L. Lawrence, J. Li, T. Spencer, Diode modification of ceramic material surface properties for improved wettability and adhesion, *Appl. Surf. Sci.* 137–139 (1999) 377–393.
- [14] N. Morita, T. Watanabe, Y. Yoshida, Crack free processing of hot-pressed silicon nitride ceramics using pulsed YAG laser, *JSME Int. J. Ser. III* 34 (1) (1991) 149–153.
- [15] M. Mendes, V. Ohveira, R. Vilar, F. Bemhorn, J. Ihleman, O. Conde, Femtosecond ultra-violet laser micromachining of Al<sub>2</sub>O<sub>3</sub>-TiC ceramics, *J. Laser Appl.* 11 (1999) 211–215.
- [16] J. Lawrence, An analysis of the bonding mechanism active in a high powered diode laser generated two stage ceramic tile grout, *Lasers Eng.* 12 (4) (2002) 279–309.
- [17] H.K. Tonshoff, C. Emmelmann, Laser cutting of advanced ceramics, *Laser Zentrum Hannover, Ann. CIRP* 37 (1979) 219–222.
- [18] H. Lei, L. Lijun, A study of laser cutting engineering ceramics, *Opt. Laser Technol.* 31 (1999) 531–537.
- [19] J. Lingfi, Y. Yan, Crack free cutting of thick and dense ceramics with CO<sub>2</sub> laser by single-pass process, *Opt. Lasers Eng.* 46 (2007) 775–790.

- [20] M. Naeem, M.E. Preston, J.R. Tyrer, Processing of engineering ceramics with high powered CO<sub>2</sub> lasers, *Mater. Des.* 10 (1979) 271–375.
- [21] A.S. Kaur, B. Doloi, B. Bhattacharyya, Experimental investigations on Nd:YAG laser cutting of silicon nitride, *Int. J. Manuf. Technol. Manage.* 7 (2/3/4) (2005) 171–191.
- [22] K. Voisey, Laser processing of ceramics, *Ind. Laser User* 33 (2003) 23–25.
- [23] E. Cappelli, S. Orlando, G. Mattel, M. Montozzi, F. Pinzari, D. Seith, Surface modification of carbide ceramics induced by pulsed laser treatment, *Appl. Phys. A* 69S (1999) S515–S519.
- [24] A.G. Solomah, L. Mannik, S.K. Brown, Laser machining of silicon nitride ceramics, in: Proceedings of the International Conference on Machining of Advanced Materials, Gaithersburg, USA 747, 1993, pp. 543–547.
- [25] M. Geiger, W. Becker, T. Rebhan, J. Huttles, N. Luts, Increase of efficiency for the XeCl excimer laser ablation of ceramics, *Appl. Surf. Sci.* 96–97 (1996) 309–315.
- [26] A.J. Murray, J.R. Tyrer, Nd:YAG laser cutting and drilling of PSTZ—Influence of substrate heating temperature on recast layer microcracking, *J. Laser Appl.* 11 (3) (1997) 127–135.
- [27] A.J. Murray, J.R. Tyrer, Pulsed CO<sub>2</sub> and Nd:YAG laser drilling of PSTZ – a study into the wavelength, effects on recast layer micro-cracking, *Lasers Eng.* 9 (1997) 23–37.
- [28] A.J. Murray, J.R. Tyrer, Nd:YAG laser drilling of 7.3 mm thick partially stabilized tetragonal zirconia-control of recast layer micro-cracking using localized heating techniques, *J. Laser Appl.* 11 (4) (1997) 179–184.
- [29] A.J. Murray, The reduction of micro-structural damage during the drilling of ceramics by high power laser (Ph.D. thesis), Loughborough University, 2001.
- [30] X. Wang, J. Takacs, G. Krallics, A. Szilagyi, T. Markovits, Experimental research on laser-material interaction, *Period. Polytech. Ser. Transp. Eng.* 27 (1–2) (2000) 143–152.
- [31] C. Prat, M. Autric, G. Inglesakis, Pulsed CO<sub>2</sub> laser materials interaction: thermomechanical effects, gas flow and chemical lasers, *SPIE* 1710 (1992) 590–593.
- [32] C. Prat, M. Autric, G. Inglesakis, D. Astic, Pulsed CO<sub>2</sub> laser material interaction: mechanical coupling – reflection and scatter radiation, in: Eight International Symposium on Gas Flow and Chemical Lasers, *SPIE* 1397, 1991, pp. 701–704.
- [33] S.Y. Lim, C.R. Chatwin, Special chaos aspects of laser-material interaction, *Opt. Lasers Eng.* 20 (1994) 341–356.
- [34] Z. Illyefalvi-Vitez, Thermal processing of laser-material interaction, *Acta Polytech. Prace. CVUT v Praze* 7 (III, 2) (1979) 13–17.
- [35] X. Zhao, W. Ang, J. Li-jun, Y. Xie, Y.I. Ai-ping, W. Ang, Lh. Liu, J.Y. Uan, X. Liu Jr., Experimental study on 307 nm laser interaction with materials, *Plasma Sci. Technol.* 3 (3) (2001) 727–734.
- [36] K.H. Wong, S.K. Hau, P.W. Chan, L.K. Leung, C.L. Choy, H.K. Wong, XeCl excimer laser interaction with partially stabilized zirconia target, *J. Mater. Sci. Lett.* 10 (1991) 701–703.
- [37] M. Vlasova, P.A. MárquezAguilar, M.C. Reséndiz-González, M. Kakazey, I. González, V. Stetsenko, T. Tomila, A. Ragulya, Laser treatment of Si-Al<sub>2</sub>O<sub>3</sub> two-layer target, *Opt. Laser Technol.* 42 (2010) 7–17.
- [38] F.J. Ester, R.I. Merino, J.Y. Pastor, A. Martin, J. Llorca, Surface modification of Al<sub>2</sub>O<sub>3</sub>–ZrO<sub>2</sub>(Y<sub>2</sub>O<sub>3</sub>) eutectic oxides by laser melting: processing and wear resistance, *J. Am. Ceram. Soc.* 91 (11) (2007) 2552–2559.
- [39] D. Triantafyllidis, L. Li, F.H. Stott, Surface treatment of alumina-based ceramics using combined laser sources, *Appl. Surf. Sci.* 176 (2002) 140–144.
- [40] D. Triantafyllidis, J.R. Bernstein, F.H. Stott, Dual laser beam modification of high alumina ceramics, *J. Laser Appl.* 15 (1) (2003) 49–54.

- [41] D. Triantafyllidis, L. Li, F.H. Stott, Surface properties of laser-treated ceramic materials. EMRS Spring Conference, Strasbourg: France, Thin solid Films 453 (2004) 76–79.
- [42] D. Triantafyllidis, L. Li, F.H. Stott, The effect of laser-induced modification of surface roughness of Al<sub>2</sub>O<sub>3</sub>-based ceramics on fluid contact angle, Mater. Sci. Eng. A Struct. Mater. Prop. Microstruct. Process. 390 (1–2) (2005) 271–277.
- [43] D. Triantafyllidis, L. Li, F.H. Stott, Crack-free densification of ceramics by laser surface treatment, Surf. Coat. Technol. 210 (2006) 3163–3173.
- [44] V.K. Sarin, On the  $\alpha$ -to- $\beta$  phase transformation in silicon nitride, Mater. Sci. Eng. A 105–106 (1971) 151–159.
- [45] D.R. Messier, F.L. Riley, R.J. Brook, The  $\alpha/\beta$  silicon nitride phase transformation, J. Mater. Sci. 13 (1977) 1199–1205.
- [46] G. Ziegler, D.P.H. Hasselman, Effect of phase composition and microstructure on the thermal diffusivity of silicon nitride, J. Mater. Sci. 16 (1971) 495–503.
- [47] P. Sajgalik, D. Galisek,  $\alpha/\beta$  Phase transformation of silicon nitride: homogeneous and heterogeneous nucleation, J. Mater. Sci. Lett. 12 (1993) 1937–1939.
- [48] C.B. Ponton, R.D. Rawlings, Vickers indentation fracture toughness test, part 1 – review of literature and formulation of standardised indentation toughness equations, Mater. Sci. Technol. 5 (1979) 765–772.
- [49] C.B. Ponton, R.D. Rawlings, Vickers indentation fracture toughness test, part 2 – review of literature and formulation of standardised indentation toughness equations, Mater. Sci. Technol. 5 (1979) 961–976.
- [50] P.P. Shukla, J. Lawrence, Evaluation of fracture toughness of ZrO<sub>2</sub> and Si<sub>3</sub>N<sub>4</sub> engineering ceramics following CO<sub>2</sub> and fiber laser surface treatment, Opt. Lasers Eng. 49 (2) (2011) 229–239.
- [51] Y.A. Cengel, R.H. Turner, Fundamentals of Thermal-Fluid Sciences, McGraw Hill International Edition, Singapore, 2001.
- [52] V.S. Lysenko, A.N. Nazarov, M.M. Lokshin, S.B. Kaschieva, Effects of laser irradiation on the structure of silicon dioxide film with implanted phosphorus ions, Fiz. Tekh. Poluprovodn 1 (11) (1977) 2254–2257.
- [53] P.P. Shukla, J. Lawrence, Characterization and compositional study of a zirconia engineering ceramic irradiated with a fiber laser beam, Opt. Laser Technol. 43 (2011) 1292–1300.
- [54] M. Bass, Laser Material Processing, North-Holland Publishing Company, New York, 1997.
- [55] J. Lawrence, L. Li, The influence of shield gases on the surface condition of laser treated concrete, Appl. Surf. Sci. 167 (1–4) (2000) 25–27.
- [56] K. Minami, J. Lawrence, L. Li, R.E. Edwards, A.W. Gale, Effects of gases on high powered laser ablation of tile grout, Appl. Surf. Sci. 176 (1–4) (2002) 264–270.
- [57] T. Sakuma, Y. Zhou, Q.L. Ge, T.C. Lei, Microstructure and mechanical properties of ZrO<sub>2</sub>-2 mol% Y<sub>2</sub>O<sub>3</sub> ceramics, Ceram. Int. 16 (1990) 349–354.
- [58] J.Z. Jiang, F. Kragh, D.J. Frost, K. Stahl, H. Lindelov, Hardness and thermal stability of cubic silicon nitride, J. Phys. Condens. Matter 13 (22) (2001) L515–L520.
- [59] P.P. Shukla, J. Lawrence, Examination of temperature distribution on silicon nitride engineering ceramics during fiber laser surface treatment, Opt. Lasers Eng. 49 (7) (2011) 998–1011.
- [60] P.P. Shukla, J. Lawrence, Mathematical modelling of the fiber laser surface processing of a zirconia engineering ceramic by means of three-dimensional finite element analysis, Proc. Inst. Mech. Eng. Part C J. Mech. Eng. Sci. 225 (4) (2011) 949–964.

## Part Two

# **Laser additive manufacturing in surface treatment and engineering**

This page intentionally left blank

# Compositional modification of Ni-base alloys for laser-deposition technologies

6

*I. Hemmati, V. Ocelík, J.Th.M. De Hosson*  
University of Groningen, Groningen, The Netherlands

## 6.1 Introduction

Laser cladding is being increasingly used for repair and surface protection applications. Despite significant developments, a number of issues, such as comparatively high capital cost, low deposition rates, large residual stresses, and high cracking susceptibility, still need to be resolved for a wider application of this technology [1]. The issues of high capital cost and low deposition rates are being solved by technological advances, such as the introduction of high power diode lasers with a beam as wide as 1 in. and the integration of inductive heating modules into laser cladding heads. For example, with the laser as the only energy source, deposition rates of 9 kg/h of Inconel 625 corrosion protective coatings on large cylindrical components are reported. Furthermore, a deposition rate of 14–16 kg/h of Inconel 625 can be achieved with the simultaneous application of 8 kW laser and 12 kW induction power [2]. Although the induction-assisted laser cladding systems are reported to greatly reduce the cracking problem of laser clad coatings, cracking is still the biggest materials engineering challenge for a more widespread application of laser cladding, especially for hard alloys such as Ni-Cr-B-Si-C [3].

Ni-Cr-B-Si-C alloys are among the most widely used alloys for applications requiring corrosion and wear resistance [4]. These alloys, with their low melting point and self-fluxing properties, were originally developed for spray and fuse applications. In recent years, laser deposition technologies are being increasingly used to produce dense Ni-Cr-B-Si-C coatings with metallurgical bonding to the substrate and superior functional properties [5–7]. Despite desirable corrosion and wear properties of Ni-Cr-B-Si-C alloys and their potential for many surface coating, repair, and additive manufacturing applications [3,8,9], high cracking propensity poses a serious drawback to their usage in laser deposition technologies [10].

In laser deposited coating, cracks could form during solidification and/or during the solid-state cooling. In the case of laser deposited Ni-base coatings, cracking usually occurs during the solid-state cooling [11] when the residual tensile stress exceeds the ultimate tensile strength of the clad material. These stresses originate from a misfit between different regions of the sample, for example, as a result of sharp thermal gradients [12]. In laser deposited coatings, the major source of residual stresses is the

differential thermal contractions of the coating and the substrate caused by steep temperature gradients and different thermal expansion coefficients of the coating and substrate materials [1,12,13]. Thermal stress in a clad layer can be generally expressed as follows:

$$\sigma_{\text{th}} = \frac{E\Delta\alpha\Delta T}{1 - \nu} \quad (6.1)$$

where  $E$  and  $\nu$  are elastic modulus and Poisson's ratio of the clad material, respectively, and  $\Delta\alpha$  and  $\Delta T$  are differences in linear thermal expansion coefficient and temperature between clad and substrate material, respectively [1]. For coatings,  $\sigma_{\text{th}}$  is tensile when the thermal expansion coefficient of the coating is larger than that of the substrate, for example, in the deposition of Ni-base alloys on carbon steel ( $\alpha$  for Ni-base alloys and carbon steel are in the ranges of 13.3-16.8 and 11.3-12.2 ( $10^{-6}$  K $^{-1}$ ), respectively [1]). In addition, increasing the cladding speed or deposition on substrates at lower temperatures increases  $\sigma_{\text{th}}$  because sharper temperature gradients will be established between the clad and its substrate and hence, larger  $\Delta T$  (and probably  $\Delta\alpha$ ) will be produced [13-16].

Nucleation and propagation of cracks in laser deposited coatings depend on the magnitude of the residual tensile stresses, mechanical properties of the clad layer (mainly toughness), and to a lesser extent, the amount of defects (e.g., large pores) in the clad layer. Cracking phenomenon is mainly caused by a combination of high residual tensile stresses and low fracture toughness. Consequently, two major approaches are followed to solve the cracking problem in laser deposited coatings: decreasing the residual tensile stresses in the deposits or increasing the fracture toughness of the deposited alloy. The former approach has been extensively employed using preheating and/or postheating, for example, by induction heating [1,17]. Although preheating is an effective and widely used method to prevent cracking, it makes the process cumbersome and more expensive. It would be preferable if the hardfacing alloy itself is so tough that the deposited coating could resist the thermal stresses without cracking. For hardfacing alloys, this should be realized without a significant loss of hardness.

In engineering materials, normally there is an inverse relationship between hardness and fracture toughness, that is, hard materials usually have low resistance against crack propagation [18]. As a result, developing high-hardness and high-toughness alloys poses some sort of paradox. In normal circumstances, obtaining crack-free coatings with a relatively high hardness would be difficult unless the magnitude of the residual stresses is reduced substantially by proper preheating and/or postheating. However, if the hardness-toughness paradox is resolved (at least partially), hard and tough coatings could be deposited by laser cladding with little or no preheating of the substrate.

The main objective of this chapter is to explore whether a Ni-Cr-B-Si-C alloy could be developed that combines high hardness and high toughness to produce crack-free wear-resistant laser deposited coatings. To realize this goal, microstructural refinement and its effects on the fracture behavior of a Ni-Cr-B-Si-C alloy is investigated as a possible toughening.

## 6.2 Microstructural design to improve toughness

To get an idea of how to improve the toughness of Ni-Cr-B-Si-C alloys, microstructural aspects of the cracking process in these coatings was investigated by analyzing the crack growth path in Colmonoy 69 laser deposited coatings (nominal composition: Ni-13.5Cr-3B-4Si-0.7C-2.1Mo-1.7Cu-4Fe (wt. %)) using scanning electron microscopy (SEM). It can be seen in [Figure 6.1](#) that Cr boride and carbide precipitates such as CrB, Cr<sub>5</sub>B<sub>3</sub>, and Cr<sub>7</sub>C<sub>3</sub>, which are visible as dark phases in the backscatter electron (BSE) SEM image [[19](#)], actively contributed to crack propagation. The role of large Cr boride and carbide precipitates as crack nucleation sites and easy routes for crack growth has been reported previously [[10,20,21](#)]. [Figure 6.1c](#) shows that cracking of Ni-Cr-B-Si-C alloys occurs as a series of cracking phenomena in which cracks grow to their neighboring precipitates. The stress concentration at the tip of an individual fractured Cr-rich precipitate will determine the probability of crack propagation to the neighboring precipitates. The maximum stress  $\sigma_m$  at the crack tip in a brittle phase is directly proportional to the crack length, and can be described as [[20](#)]

$$\sigma_m = 2\sigma_a \left( \frac{a}{2\rho_c} \right)^{0.5} \quad (6.2)$$

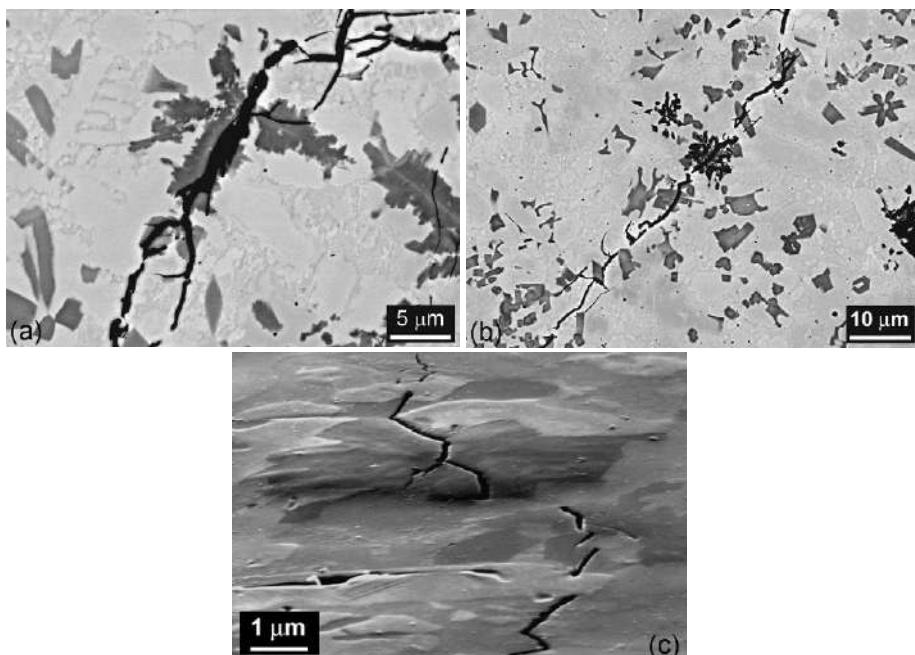


**Figure 6.1** The role of Cr-rich precipitates in crack propagation in Colmonoy 69 laser deposited coatings: (a, b) BSE images, (c) SE image ( $70^\circ$  tilted).

where  $\sigma_a$  is the applied stress,  $\rho_c$  is the crack tip radius of curvature, and  $a$  is the length of the crack (i.e., size of the precipitate).

Given the active contribution of Cr-rich precipitates to the cracking phenomena, it is expected to observe improvements in cracking susceptibility of the deposits with refined precipitates, that is, smaller  $a$ . So, one idea to reduce the cracking susceptibility of the intended coatings would be to refine their microstructure, that is, to reduce the structural scale of the Cr-rich boride and carbide precipitates. Other boride and carbide phases forming at higher temperatures than their Cr-rich counterparts could be potential nucleating agents. For this purpose, early transition metals (ETMs) are good candidates as most of them are strong carbide/boride formers [21–23]. It has been previously suggested that the criterion to select the refining element for Ni-Cr-B-Si-C alloys is that the element should have a high affinity for B or C [24,25], that is, the Gibbs free energy of formation ( $\Delta G_f$ ) for borides or carbides of that element should be more negative than those of Cr-rich precipitates [10]. Although spontaneous formation (negative  $\Delta G_f$ ) is a prerequisite for generation of nucleating sites, lack of microstructural refinement in the Ni-Cr-B-Si-C deposits modified by V [10,26], Ti [24], or Ta [25] raises the question of whether factors other than affinity for B or C play a role in the refinement process.

### 6.3 Selection of the refining element

In our previous work [26], Colmonoy 69 alloy powder modified by different contents of vanadium was deposited by laser cladding. The reason to select vanadium was that its borides have some of the largest negative values of  $\Delta G_f$  and, hence, they are likely to precipitate out preferentially in comparison to Cr borides [21]. In fact, vanadium addition is the limit for the idea of selecting a refining element according to the  $\Delta G_f$  criterion alone. However, the addition of vanadium did not induce microstructural refinement in laser deposited Ni-Cr-B-Si-C coatings. Instead, the morphology and nature of the boride phases were changed and VC precipitates were added to the microstructure. The outcomes of V addition showed that solid solubility of boride or carbides of the additional element in their Cr-rich counterparts as well as their temperature of formation should be considered [26].

Based on the previous results on compositional modification of Ni-Cr-B-Si-C alloys [10,24–26], it can be concluded that a refining element for the intended alloy system should fulfill at least the following three criteria, which will be subsequently elaborated and applied to find potential candidate ETM refining elements:

- (i) Affinity of the refining element for B or C should be higher than affinity of Cr for these elements, that is, it should have the possibility of preferential formation of borides or carbides during solidification.
- (ii) The boride or carbide precipitates of the refining element should have a limited solid solubility in their Cr-rich counterparts.
- (iii) The boride or carbide precipitates of the refining element should form at a higher temperature in comparison to Cr-rich precipitates.

The affinity of ETMs for C is the highest for valence number of 4 and decreases for higher valences, as explained by Cottrell [22]. According to Table 6.1, Ti, Zr, and Hf should have the highest affinity for C. In addition, Ta and Nb should be stronger carbide formers than Cr. The data on heats of formation ( $\Delta H$ ) and  $\Delta G_f$  of carbides such as ZrC, TiC, HfC, and NbC confirm such predictions [21,22]. Similarly, the affinity of Ti, Zr, Nb, and Hf for boron is stronger than that of Cr [21,27].

If a solid solution forms between Cr borides/carbides and the boride/carbides of other ETMs, the ETM atoms will substitute Cr, as was observed for the case of vanadium addition [26]. Hume-Rothery (H-R) rules for substitutional solid solutions (including size, electronegativity, and valence or the electron concentration factors [28]) and their derivatives, such as the methods developed by Darken and Gurry [29] and Chelikowsky [30], could be used as guidelines for judging the extent of solid solubility [31].

The difference of electronegativity between Cr and the rest of the ETMs is less than 0.4, as presented in Table 6.1. Hence, according to the Darken-Gurry criteria [31], electronegativity will play a negligible role in determining the level of solid solubility when Cr and other ETMs are substituted in each other's compounds. The valences of transition metals are variable and complex and due to the valence complication caused by partially filled d orbitals, the transition metal alloys generally do not follow the valence rule when alloyed with other transition metals [31]. As a result, atomic size seems to be the dominant factor in determining the extent of solid solubility in this case. However, the phase constitution of the V-modified system showed that crystal structure of the phases should also be considered [26]. In other words, while the size factor for vanadium calculated as  $\Delta r_V = (r_{Cr} - r_V)/r_{Cr}$  is equal to 5.5%, which is well within the favorable range, VC and Cr<sub>7</sub>C<sub>3</sub> had little solubility as a result of their different crystal structures. Hence, similarity of the crystal structures should also be considered.

**Table 6.1 Properties of early transition metals (ETMs) from groups IV to VI.  $r$ ,  $\Delta r_{ETM}$ ,  $E$  and  $V$  are atomic size, size factor ( $\Delta r_{ETM} = (r_{Cr} - r_{ETM})/r_{Cr}$ ), electronegativity and valence, respectively [23]**

ETM	$r$ (nm)	$\Delta r_{ETM}$ (%)	Electron configuration	$E$	$V$
Cr	0.126	–	[Ar] 3d <sup>5</sup> 4s <sup>1</sup>	1.6	6
V	0.133	5.5	[Ar] 3d <sup>3</sup> 4s <sup>2</sup>	1.6	5
Ti	0.146	15.8	[Ar] 3d <sup>2</sup> 4s <sup>2</sup>	1.5	4
Mo	0.138	9.5	[Kr] 4d <sup>5</sup> 5s <sup>1</sup>	1.8	6
Nb	0.145	15	[Kr] 4d <sup>4</sup> 5s <sup>1</sup>	1.6	5
Zr	0.159	26.1	[Kr] 4d <sup>2</sup> 5s <sup>2</sup>	1.4	4
W	0.139	10.3	[Xe] 4f <sup>14</sup> 5d <sup>4</sup> 6s <sup>2</sup>	1.7	6
Ta	0.145	15	[Xe] 4f <sup>14</sup> 5d <sup>3</sup> 6s <sup>2</sup>	1.5	5
Hf	0.158	25.3	[Xe] 4f <sup>14</sup> 5d <sup>2</sup> 6s <sup>2</sup>	1.3	4

In addition to V, several other ETMs were skipped from the current work for various reasons. Modification of Ni-Cr-B-Si-C alloys by Ti [24] or Ta [25] have been previously done without success. Mo and W were also skipped because none is a strong carbide or boride former [22]. On the other hand, Zr and Hf are very strong carbide and boride formers (Table 6.1 and Ref. [27]) and have the most unfavorable size factors (i.e., favorable for limited solubility in Cr-rich phases). The industrial-grade Zr contains Hf as a natural impurity. So, pure Hf was also skipped. Furthermore, Zr borides and carbide such as  $ZrB_2$  and  $ZrC$  have crystal structures different from their Cr-rich counterparts [23,27]. Consequently, a strong segregation of Cr- and Zr-rich precipitates is expected (as already confirmed experimentally [32]). Finally, Nb has a high affinity for boron and carbon (Table 6.1 and Ref. [27]) and an unfavorable size factor. Nb may form multiple borides/carbides that all have very limited solubility in their Cr-rich counterparts [33,34]. Hence, Zr- and Nb-rich precipitates are expected to remain as independent phases and provide potential nucleation sites. However, these independent phases should also precipitate at high enough temperatures.

According to the binary phase diagrams, both Zr and Nb form borides/carbides at very high temperatures (e.g., above 3000 °C). But, the temperature of boride/carbide precipitation, especially for Zr, drops very quickly by slight compositional variations [32–34]. As a result, the phase formation reactions should be evaluated for the actual alloy composition. For this purpose, the sequence of phase formation reactions in the alloys modified by 5 wt.% of Zr or Nb were simulated using *Thermo-Calc* software (version S, database TTNI version 6.3). In addition to calculations based on the lever rule, the Scheil module was employed to investigate the phase formation reactions in nonequilibrium solidification conditions based on the well-known Scheil-Gulliver model [35] with B and C as fast-diffusing elements. The results of thermodynamic calculations over the entire solidification range are shown in Figure 6.2. For both Zr and Nb additions, the calculated precipitation reactions based on equilibrium and Scheil solidification models were very similar. However, predictions for low-temperature reactions, including eutectic ones (e.g., formation of  $Ni_3B$  [19]), were different. In the case of Zr-modified system,  $ZrB_2$  is expected to solidify first and for the Nb-modified deposits;  $NbC$  should form simultaneously with  $CrB$ . So, both Zr and Nb could form phases at the earliest stages of solidification, which may provide heterogeneous nucleation sites for Cr-rich precipitates. Based on the above-mentioned discussions and calculations, Nb and Zr were selected as additional alloying elements for the experimental part of the work.

## 6.4 Experimental procedure

Colmonoy 69 was selected as the starting alloy powder for subsequent compositional modifications. Single track and five-track coatings (33% track overlapping) of Zr-modified and Nb-modified Colmonoy 69 with a thickness of 0.9–1.1 mm were deposited at a speed of 5 mm/s on 50-mm-diameter S355 low carbon steel rods using a fiber laser beam. A Metco Twin 10C powder feeder was used to simultaneously inject Colmonoy 69 and industrial grade Zr ( $Zr+Hf > 99$  wt.%) or Colmonoy 69

and commercially pure Nb powders through a side cladding powder injection nozzle using argon as powder carrier and melt pool shielding gas. In each case, the two powders were mixed in a cyclone before exiting the deposition nozzle. Zr or Nb powder feeding rates were adjusted to have up to 5 wt.% Zr or up to 10 wt.% Nb in the coatings. Deposits were made using a laser power of 800 W on substrates preheated to 500 °C. Preheating of the substrates was done immediately before cladding using an electric tube furnace. Dilution from the substrate [36] evaluated

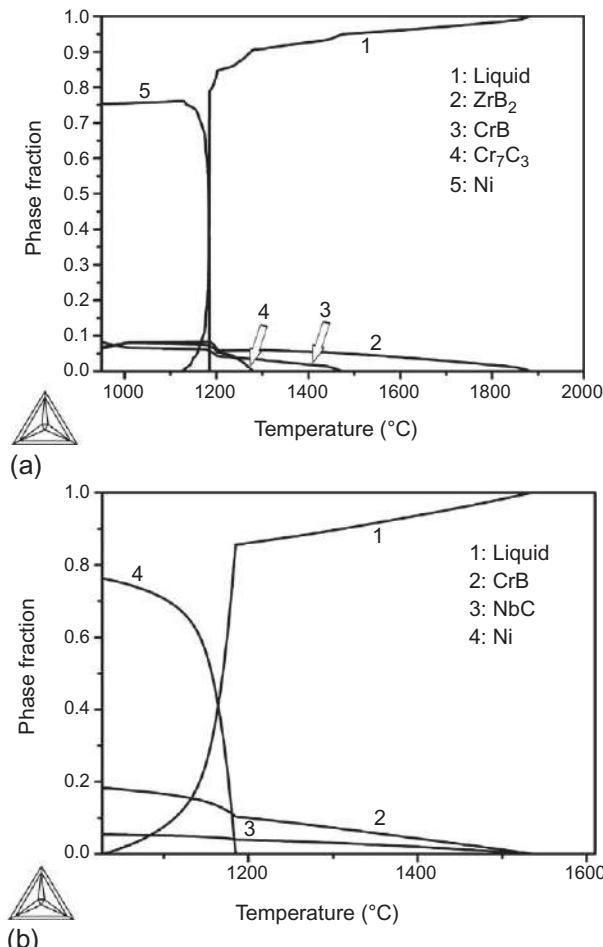


**Figure 6.2** Calculated equilibrium phase fraction versus temperature for the alloys modified by (a) 5 wt.% Zr or (b) 5 wt.% Nb. (c, d) show the solidification sequence of the same alloys as in (a, b) according to the Scheil-Gulliver solidification model. The dashed lines show the equilibrium solidification sequence.

(continued)

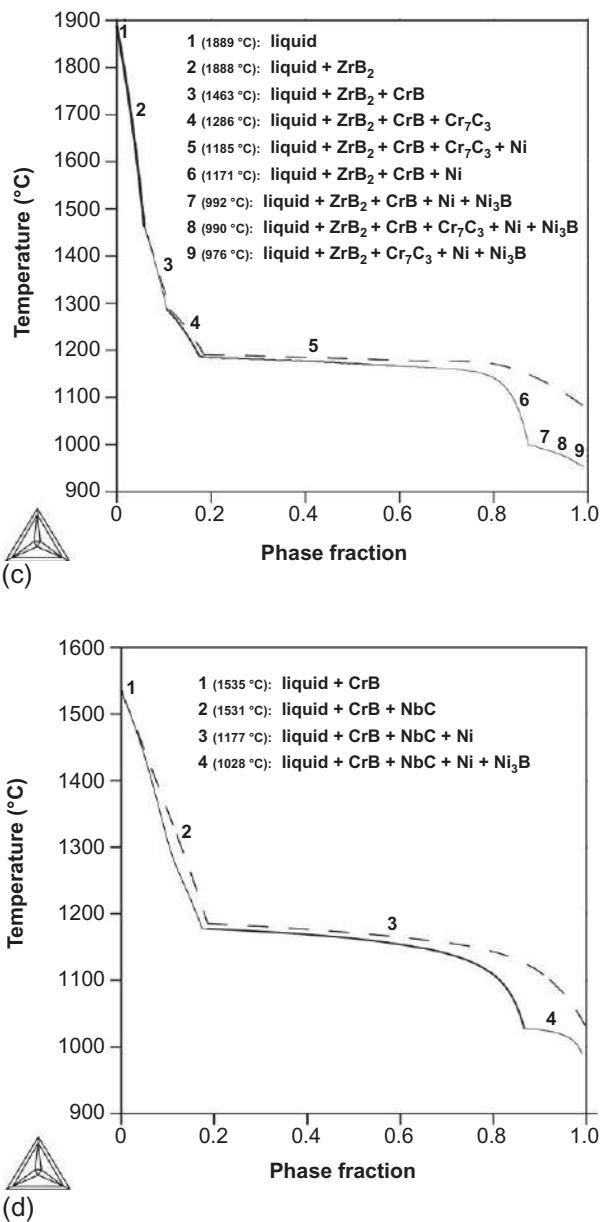


Figure 6.2 Continued.

from optical microscopy (OM) images of transversal cross-sections was kept lower than 10%.

Samples for further characterizations were cut and prepared by standard mechanical grinding with suspensions containing 9 and 3  $\mu\text{m}$  diamond particles and polishing with colloidal  $\text{Al}_2\text{O}_3$ . A Philips XL30 Field Emission Gun Scanning Electron

Microscope (SEM) was used for microstructural observations, mostly in BSE imaging mode. Mutual solubility of the phases was evaluated by quantitative energy dispersive spectroscopy (EDS). To ensure the accuracy and reliability of the EDS measurements, the following steps were taken:

- (i) Large precipitates were analyzed to reduce effects of the surrounding matrix.
- (ii) An accelerating voltage of 5 kV was used to increase the amount of boron and carbon X-ray signals and to maximize the sensitivity of the detector for low-energy X-ray of these elements [37].
- (iii) A standardless element coefficient (SEC) of 4 for boron and 2 for carbon were applied in the EDAX Genesis® software to compensate for the limited detector accuracy for X-ray lines below 1 keV [19].
- (iv) The halographic peak deconvolution (HPD) function in the EDAX Genesis® software was used to compare the model EDS spectra with the experimental ones to distinguish the overlap between B-K and Zr-M or B-K and Nb-M peaks.

Furthermore, a combination of EDS and electron backscatter diffraction (EBSD) was used for phase identification of the Cr-, Zr-, and Nb-rich precipitates. Full details on the application of EDS/EBSD for phase identification of boride and carbide phases in this alloy system could be found elsewhere [19]. As stated before, *Thermo-Calc* simulations were used to determine the sequence and temperature of phase formation reactions. The calculated phase formations were verified against the EDS/EBSD phase identification results. Simulations were repeated using a modified list of expected phases wherever necessary.

An unsuccessful attempt was made to measure the fracture toughness of Colmonoy 69 coatings, using the Palmqvist indentation technique. The procedure and the results are presented in [38]. Alternatively, the cracks in each clad layer were counted using a low-magnification ( $20\times$ ) OM and their number per unit area of the clad layer was used as a measure of toughness. Hardness of the coatings was measured using Vickers indenter at a load of 4.9 N.

## 6.5 Microstructures and phases

**Figure 6.3a and b** shows the microstructure of samples containing 2 and 5 wt.% Zr, respectively. Lower contents of Zr (**Figure 6.3a**) mostly influenced the eutectic structure of the alloy. With the addition of Zr, some Zr-rich precipitates were formed, which are visible with a bright contrast in the SEM-BSE image of **Figure 6.3b**. It can be seen that Zr-rich particles are located at the edges of Cr boride precipitates, indicating that they were present as insoluble components and inactive particles for nucleation during solidification. In comparison to the microstructure of the original alloy [19], no appreciable microstructural refinement happened upon Zr addition.

Unlike the case of Zr addition, the microstructure of Nb-modified deposits was significantly refined, as can be seen by comparing **Figure 6.4a and b**. Submicron Nb-rich precipitates (visible as bright particles in SEM-BSE images) acted as nucleation sites for rod-shaped phases shown in the inset of **Figure 6.4b**. Microstructural observation of samples with different amounts of added Nb confirmed that the refining effect of

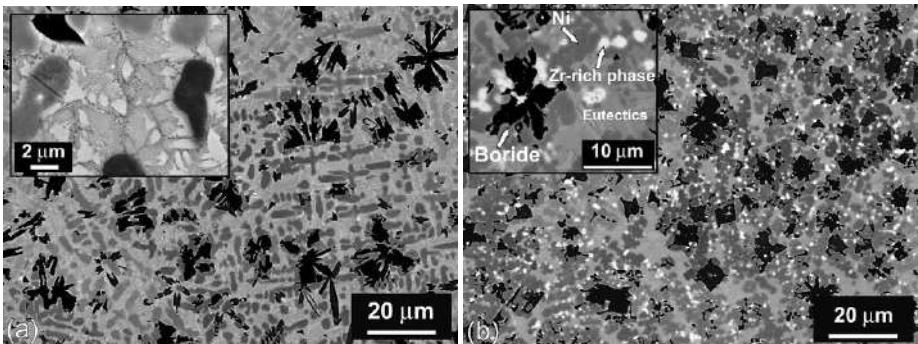


**Figure 6.3** SEM-BSE images showing the microstructure of Zr-modified coatings containing (a) 2 wt.% and (b) 5 wt.% Zr. The insets show the microstructural details.

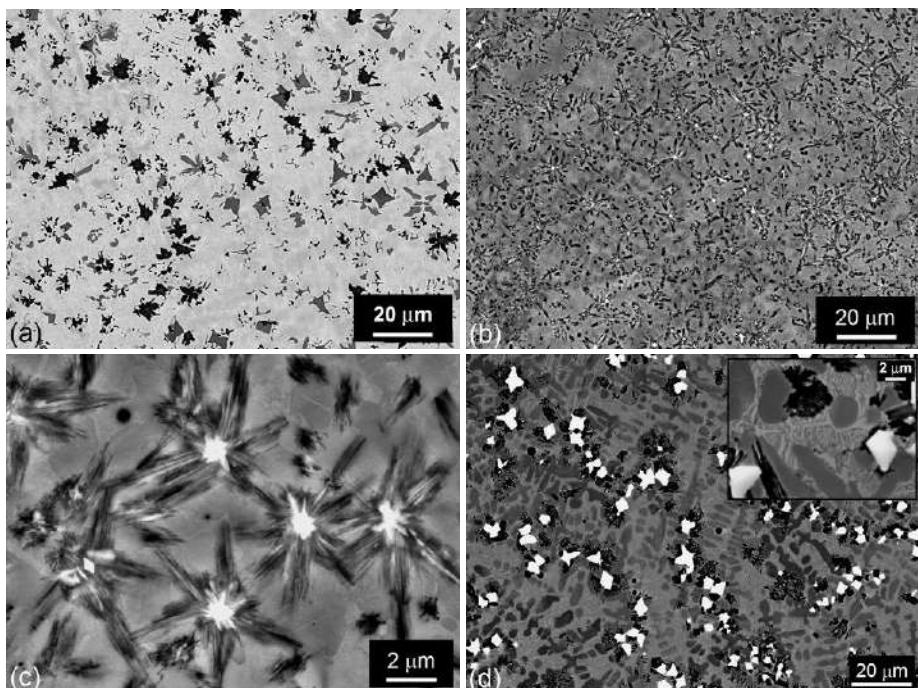


**Figure 6.4** Microstructures of (a) Colmonoy 69 and (b) Colmonoy 69 plus 4 wt.% Nb. In (c), details of the refined microstructure in (b) are shown. In (d), coarse microstructure of the deposits with 9 wt.% of Nb is presented.

Nb was at its peak for Nb contents around 4 wt.%. At higher Nb contents, large Nb-rich precipitates started to appear.

Characterization of the constituent phases was done to determine the composition of all precipitates (Cr-, Zr-, and Nb-rich) and also to conclusively designate their type. Phase characterization could assess the mutual solubility of the phases and

was performed by quantitative EDS measurements. The latter process could reveal which type of phases precipitated as a result of the additional element (carbide, boride, or both). For this purpose, EDS results were combined with crystallographic information from EBSD.

For EDS characterization of Zr-rich precipitates, a careful HPD had to be done because of the proximity of B-K (at 0.188 keV) and Zr-M (at 0.153 keV) characteristic X-ray lines [39]. The HPD profiles, including B-K, Zr-M, and B-K and Zr-M, were generated and superimposed on the experimental EDS spectra obtained from Zr-rich precipitates. As shown in Figure 6.5a, the HPD profiles confirmed that the lowest-energy peak of the spectra does not belong to B and fits much better to the Zr-M. As a result, the EDS peak at around 0.15 keV was assigned to Zr-M, although the Zr-L line was chosen for the quantification procedures. EDS spectra were then obtained from Zr- and Cr-rich precipitates shown in Figure 6.5b and quantified. The ratios of Cr:B and Zr:C atomic percentages in precipitates #1 and #2 were both close to unity. Hence, they were most probably of CrB and ZrC type, respectively (as will be confirmed by the EBSD results later).

EBSD patterns were obtained and indexed using a list of candidate phases developed from the database of the *International Center for Diffraction Data (ICDD)*. Both Zr carbides and borides were included in the list of candidate phases. Figure 6.6a shows the BSE image (70° tilted) form the microstructure of Zr-modified deposits. The EBSD pattern of the Zr carbide precipitates (bright particles) was precisely (with a solution error of less than 0.5°) and reproducibly indexed as ZrC, as shown in

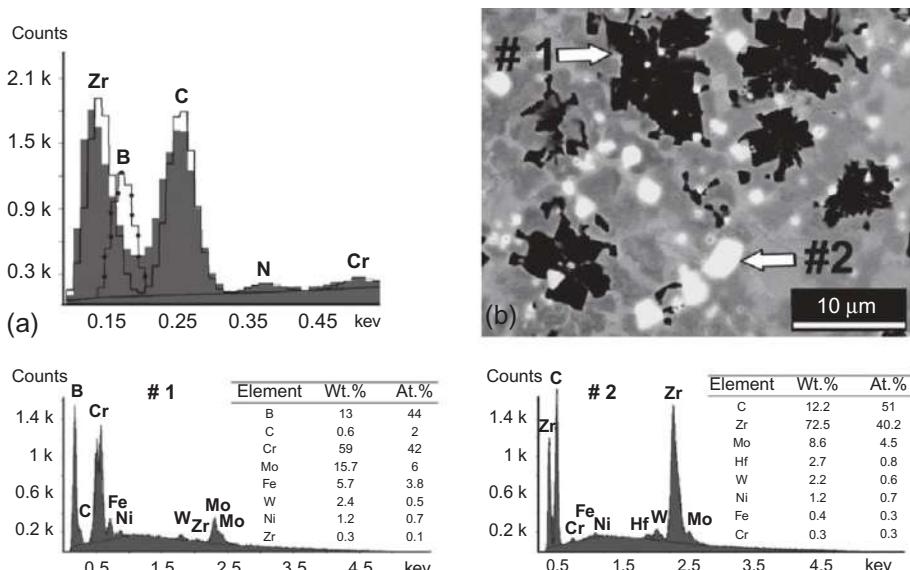


**Figure 6.5** (a) HPD profile including Zr M-line and B K-line superimposed on the experimental EDS spectrum. (b) EDS quantitative analysis of precipitates labeled as #1 and #2 in the SEM image.

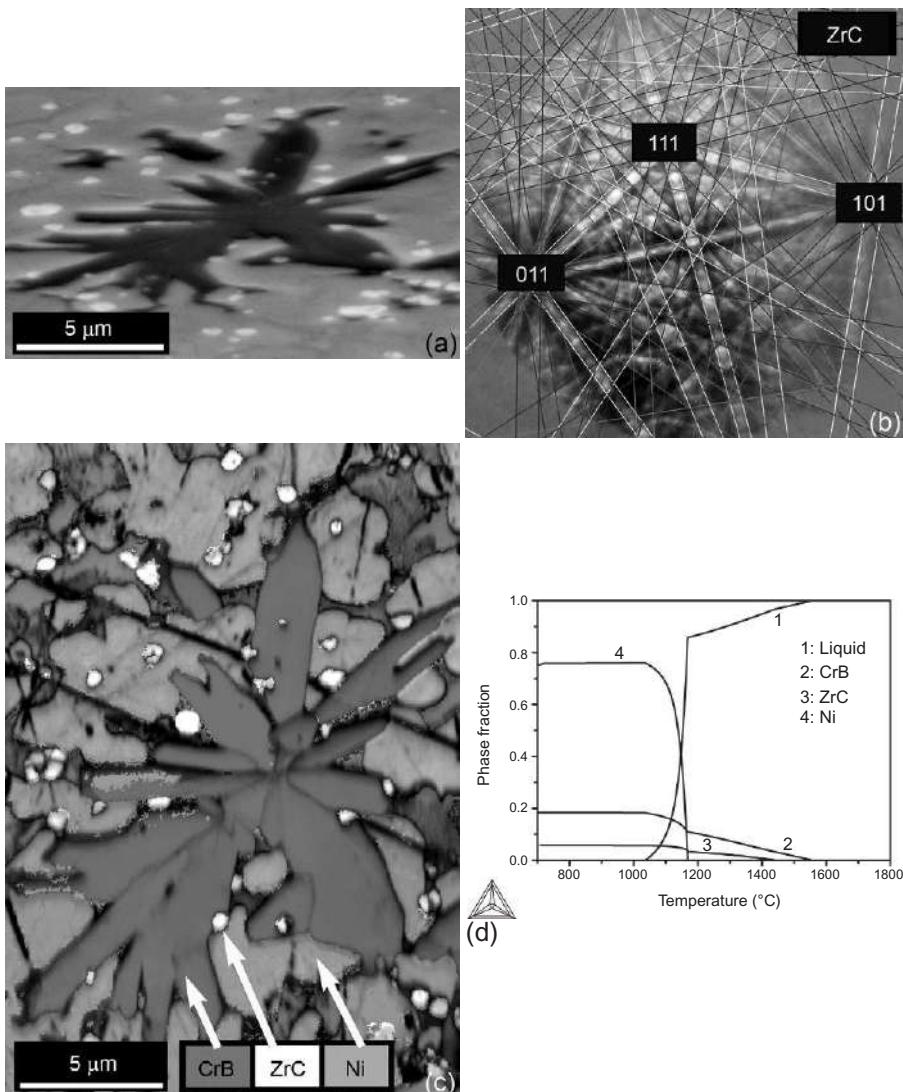


**Figure 6.6** (a) SEM-BSE image ( $70^\circ$  tilted) of the microstructure of coatings containing 5 wt.% Zr. (b) EBSD pattern obtained from bright precipitates visible in (a), which could be indexed as ZrC. (c) The combined phase and image quality maps from the area in (a). (d) Recalculated equilibrium phase fractions based on the phase identification results.

**Figure 6.6b.** The Cr-rich precipitates (the dark phase) could be indexed as CrB. **Figure 6.6c** shows the combination of phase and image quality maps taken from the microstructure of the area shown in [Figure 6.6a](#). Formation of ZrC precipitates on CrB and the Ni dendrite arms surrounding them are clearly visible. Based on the EDS/EBSD phase identifications, the only Zr-rich precipitate in the Zr-modified

alloys was ZrC and not Zr borides such as ZrB<sub>2</sub> as predicted by initial *Thermo-Calc* simulations (Figure 6.2a). As a result, it was necessary to recalculate the solidification of Zr-modified alloy by excluding ZrB<sub>2</sub> from the list of possible phases. The recalculated phase fractions graph presented in Figure 6.6d precisely matches the experimental observations in terms of type and sequence of phase formation, that is, absence of Cr<sub>7</sub>C<sub>3</sub> and formation of ZrC at lower temperatures in comparison to CrB.

The same procedures were followed to assess the mutual solubility of boride/carbide phases in the Nb-modified deposits and to determine their type. The issues that had to be solved before proceeding with the EDS or EBSD analyses were also similar. For example, the X-ray M line of Nb (at 0.171 keV) was very close to the K line for B (at 0.185 keV) [39], which needed a careful comparison of the model spectrum generated by HPD with the experimental one. The SEM image of Figure 6.7 shows a colony of Cr-rich rods formed on an Nb-rich precipitate. Quantification of the EDS spectra proved that the ratios of Nb:C in location #1 and that of Cr:B in location #2 were both close to unity. Hence, the Nb-rich and Cr-rich precipitates were expected to be of NbC and CrB type as confirmed later by EBSD data.

With the same considerations as in the case of Zr carbide, EBSD patterns from Nb carbide precipitate were precisely indexed as NbC (Figure 6.8b). Phase constitution in the intended area was determined by EBSD scanning as shown in the phase map of Figure 6.8c.

In the case of Zr-modified coatings, hardness of the deposits progressively decreased by Zr addition as presented in Figure 6.9a. However, addition of Nb (Figure 6.9b) did not deteriorate the hardness of the original alloy, which was in the range of 700–900 depending on the microstructure [40]. Ni–Cr–B–Si–C alloys are intended for wear applications. Consequently, refinement of the microstructure should be ideally done without deteriorating the high hardness. It can be seen in Figure 6.9b that this goal was largely reached by addition of Nb, as the microstructural refinement shown in Figure 6.4b was obtained at almost the same level of hardness as

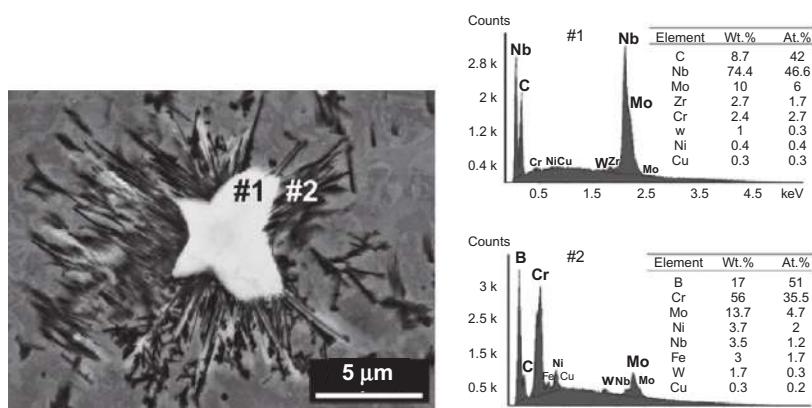


**Figure 6.7** EDS quantitative analysis of precipitates labeled as #1 and #2 in the SEM-BSE image.

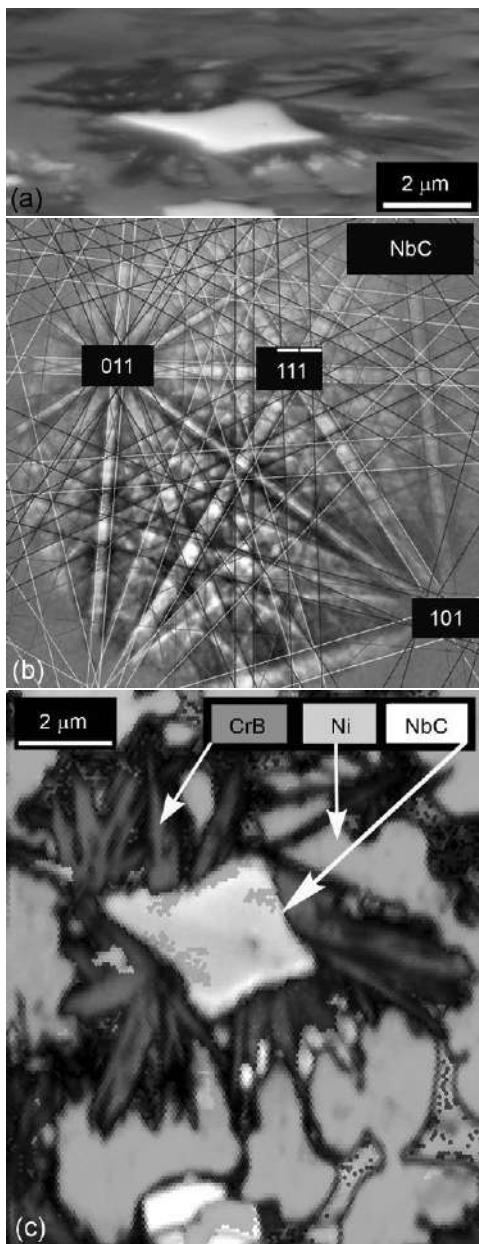


**Figure 6.8** (a) SEM-BSE image ( $70^\circ$  tilted) of the microstructure of Nb-modified coatings. (b) EBSD pattern obtained from bright carbide precipitate in (a), which could be indexed as NbC. (c) The phase map (combined with image quality map) showing the type of constituent phases for the area in (a).

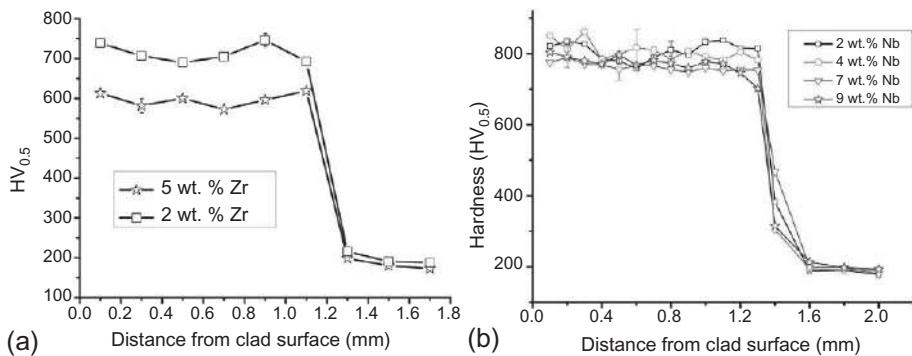


**Figure 6.9** (a, b) Hardness graphs for deposits modified by various percentages of Zr or Nb.

that of the original composition. An interesting feature of the hardness graph in Figure 6.9a is deposits with different Nb additions have almost the same hardness. This may seem strange because Nb added NbC to the microstructure, which has a hardness of around 2000 HV [41]. So, hardness of the coatings should normally increase for higher Nb additions. Nevertheless, the important contribution of the eutectic structure to overall hardness of Ni-Cr-B-Si-C alloys should not be ignored. The eutectic structure of Ni-Cr-B-Si-C alloys with the ratio of Si/B less than 3 mostly consists of hard Ni-Ni<sub>3</sub>B eutectics [19]. Addition of Nb not only produced hard NbC precipitates, but also modified the eutectics. EDS maps showed that the interdendritic eutectics of Nb-modified coatings were rich in Ni and Si and contained some Nb. Hardness of the eutectic areas in Nb-modified coatings measured by Vickers indentations using a force of 0.1 N ( $HV_{0.1}$ ) was in the range of 800-900 HV. It means that a possible increase in hardness because of additional NbC could be compensated by a reduction in hardness of the eutectics phases. Hence, the overall hardness remained mostly unchanged. In the previous compositional modifications of Ni-Cr-B-Si-C alloys, both increase (with Ta [25] addition) and decrease (with Ti [24] or V [10,26] additions) in the hardness of original alloys were reported. Reduction in hardness of V- and Zr-modified Colmonoy 69 deposits was also observed in the current work. These different reports could be explained by the way Ta, Ti, V, Zr, or Nb influence the eutectic structure. Otherwise, all of these elements produce very hard carbide and boride precipitates that should normally increase the hardness.

As the hardness remained unchanged by Nb addition and was comparable for deposits with and without Nb, changes in cracking susceptibility of the samples could be attributed to their microstructures. Figure 6.10 shows the effect of Nb addition on cracking tendency of the samples deposited on 500 °C preheated bars. It can be seen that the cracking susceptibility of the microstructurally refined deposits, that is, those with around 4 wt.% of Nb, was basically the same as that of samples deposited from the original composition. Addition of more Nb even increased the cracking rate.

In this study, the cracking susceptibility of the deposits was evaluated by measuring the cracking rate of multitrack coatings, that is, the number of transversal cracks per

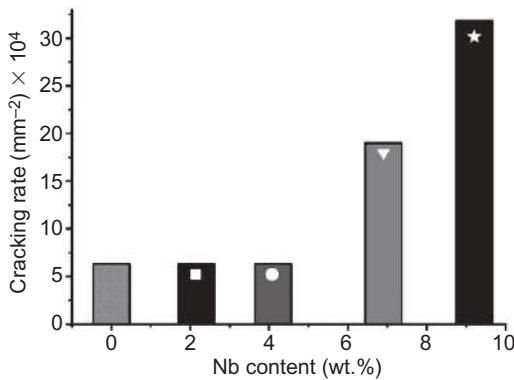


**Figure 6.10** Effect of Nb addition on cracking rate of modified deposits. The markers refer to the respective hardness curves in the graph of [Figure 6.9b](#).

unit area of the deposits. It is well known for laser-clad coatings that the cracking tendency of the coatings depends not only on the intrinsic properties of the coating material such as toughness of the alloy, but also on extrinsic properties of the deposit, including thickness, area, defects (e.g., pores), deposition rate, and temperature of the substrate, among others [11]. Consequently, assessing the cracking tendency of the coating materials based on counting the number of cracks will be meaningful only under very similar extrinsic conditions and, hence, will have a very limited scope.

To overcome such a limitation, indentation by Vickers diamond pyramid indenter under known loads (higher than some threshold necessary to generate cracks) was used to measure fracture toughness [38]. If the material is relatively hard and brittle, cracks will be generated at four corners of the indents. The fracture toughness could then be measured using the following equation [38]:

$$K_{\text{IC}} = \left( \frac{1}{3(1-v^2)\sqrt{\pi}\sqrt[3]{\sqrt{2}\pi\tan\psi}} \right) \sqrt{H} \sqrt{\frac{P}{4a}} \quad (6.3)$$

where  $v$  is Poisson's ratio,  $\psi$  is the half-angle of Vickers indenter ( $68^\circ$ ),  $H$  is the hardness,  $P$  is the applied load, and  $4a$  is the total linear crack length. This technique has been previously used to measure the fracture toughness of several metallic and composite materials such as WC-Co [42], borided steel [43], and plasma transferred arc (PTA) welded Fe-based hardfacing alloys [38].

The idea behind the indentation test for our samples was to measure the toughness on a local scale, that is, on an intended track. Such a local measurement was needed because of variations in microstructure of Colmonoy 69 deposits, as explained earlier. To perform the test, first the upper limit of the indentation load was found as described previously [38] to be around 1500 N and several indentations were made on tracks (at transversal cross-sections) with different microstructures using lower forces. Indentations made at a force of 125 N did not generate any corner cracks and those made at

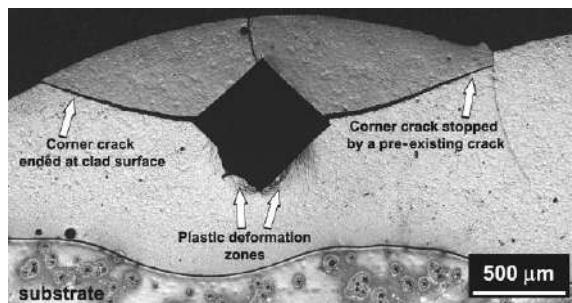


**Figure 6.11** An example of indentations made on the transversal cross section of a Colmonoy 69 coating. This indentation has to be rejected because of the influence from ductile substrate, clad surface, and the preexisting crack.

loads of 250 and 500 N contained very small corner cracks. However, massive and sudden cracks were generated at a load of 1000 N or higher for all microstructures. In the end, it was not possible to obtain a sufficient number of acceptable indents for a reliable measurement of fracture toughness as most of the indents had to be rejected because of proximity to clad-substrate interface and clad surface or closeness to defects such as pores and cracks. Figure 6.11 shows an example of a rejected indent in which effects of the substrate and the diluted layer depicted as a plastic deformation crack-free zone around the lower part of the indent as well as the corner cracks reaching clad surface or being stopped by cracks produced during deposition are visible.

The conclusion is that much thicker deposits are needed for such measurements. In addition, indentations should be made on the top surface of the polished clad layers and not on their cross section. Ultimately, the cracking rate was used to evaluate the cracking susceptibility of clad layers with similar extrinsic characteristics, that is, constant size, geometry and type of the substrate, similar heating and cooling conditions, similar clad thickness and length, and the same deposition rate.

## 6.6 Analysis of crack growth paths

The fact that cracking susceptibility of the microstructurally-refined deposits was basically the same as that of samples with much coarser microstructures shows that the initial analysis about the role of hard precipitates in cracking susceptibility of Ni-Cr-B-Si-C deposits may be inaccurate (or at least incomplete). As a result, the cracking phenomenon should be analyzed in more detail.

The crack growth paths in Colmonoy 69 and Nb-modified Colmonoy 69 were reexamined by SEM and OM to further analyze the microstructural aspects of cracking phenomena. SEM-BSE images of the crack propagation path, such as the one presented in Figure 6.12a, suggested that the main contributors to crack growth in Ni-Cr-B-Si-C deposits are the Cr-rich precipitates (the dark phases) as also reported by previous researchers [10]. This was in line with the previous observation of crack

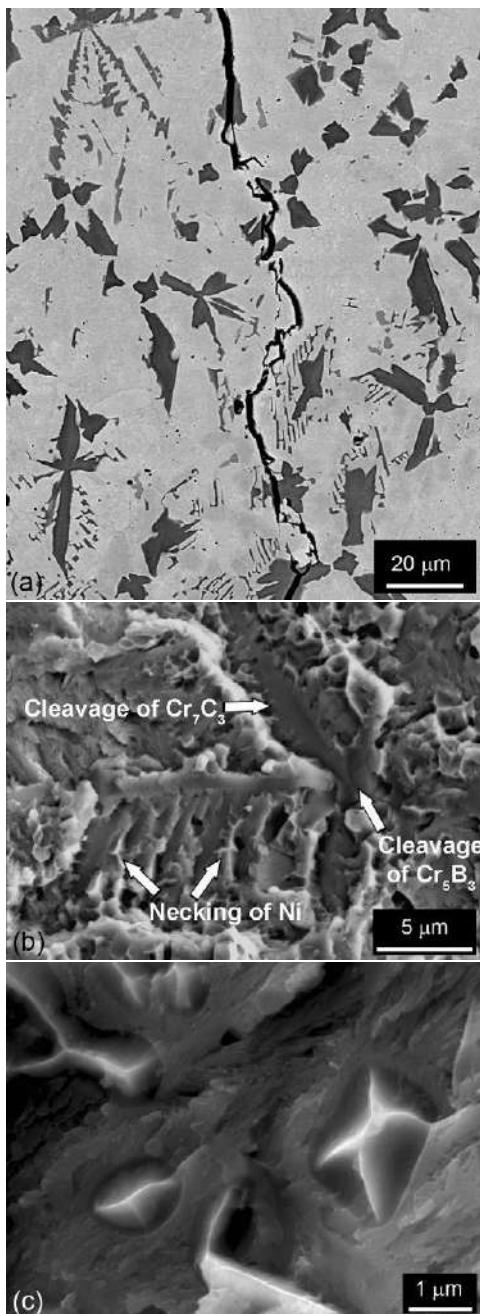


**Figure 6.12** (a) SEM-BSE image showing an example of crack growth path in Colmonoy 69 coatings. The cracks apparently follow the precipitates (dark phases). (b) Fracture surface of Colmonoy 69 coatings showing different fracture modes for Ni and Cr-rich precipitates. (c) Fracture surface showing ductile failure of Ni in comparison to the quasi-cleavage fracture of the interdendritic eutectics.

growth path from which the idea of refining the boride/carbide precipitates emerged. However, the role of the other constituent phases, that is, eutectics and Ni dendrites could not be deduced from BSE imaged because they could not be properly distinguished by BSE imaging [19].

The fracture modes of Cr-rich precipitates, eutectics, and Ni dendrites were assessed by observing the fracture surfaces of Colmonoy 69 deposits. To obtain the fracture surfaces, single tracks of Colmonoy 69 were deposited with zero dilution. Some of the tracks were detached and fractured during deposition. In Figure 6.12b, the cleavage fracture of  $\text{Cr}_5\text{B}_3$  and  $\text{Cr}_7\text{C}_3$  precipitates and the ductile fracture of Ni with clear neck formation are noticeable. Type of the constituent phases was recognized based on their morphologies as characterized previously [19]. Figure 6.12c shows an area of the fracture surface consisting of Ni grains and interdendritic eutectic network. While the ductile behavior of Ni grains and their considerable plasticity are depicted by multiple necks, the eutectic network did not show much plasticity and fractured in a quasi-cleavage mode. These observations suggest that the eutectic structure in Colmonoy 69 deposits should have contributed to crack growth and, clearly, Ni was the only ductile component of the system.

Observation of the crack propagation path using OM revealed other details. Figure 6.13a shows the OM image of crack growth in the same area as in Figure 6.12a. While the BSE image could not explain the tortuous crack path, the OM image in Figure 6.13a clearly shows how cracks propagate not only in the Cr-rich precipitates, but also through the eutectic network. In addition, the OM image of

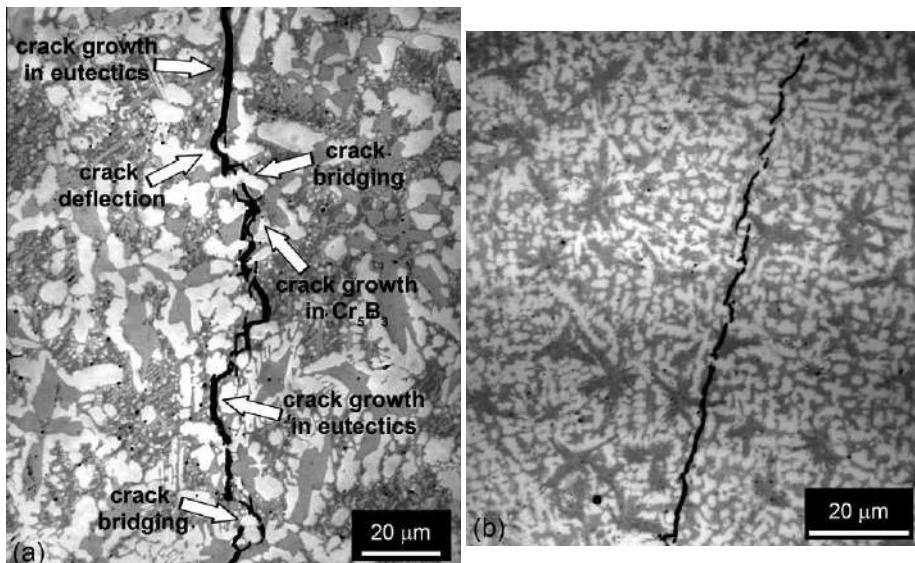


**Figure 6.13** (a) OM image of the area shown in Figure 6.12a in which much more detail about the crack growth path is visible as highlighted; (b) crack growth in the refined microstructure of Nb-modified deposits.

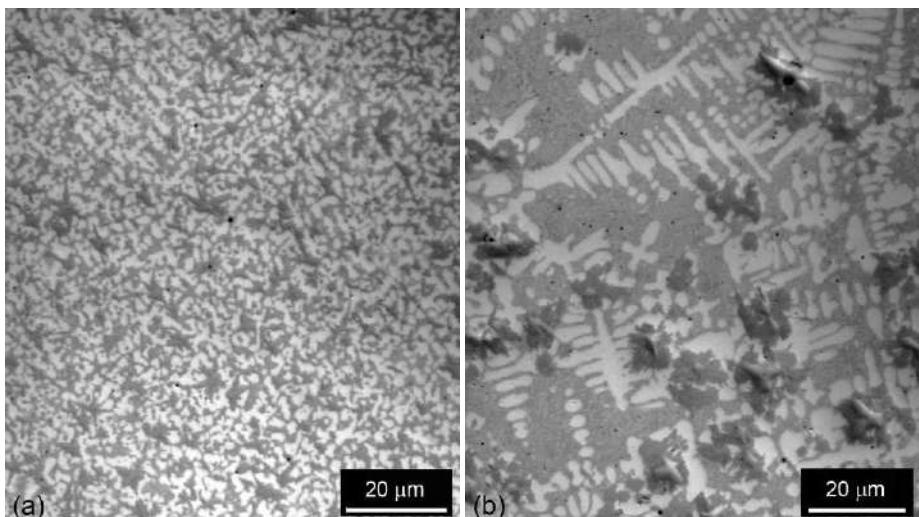


**Figure 6.14** OM microstructural images from coatings modified by (a) 4 wt.% and (b) 9 wt.% of Nb.

[Figure 6.13a](#) reveals the role of Ni dendrites in deflecting the cracks and forcing them to bridge. As OM proved to be more capable of revealing the true nature of crack propagation, crack growth path in the refined microstructure of Nb-modified deposits was observed using OM as shown in [Figure 6.13b](#). The Cr borides in the microstructure shown in [Figure 6.13b](#) are much smaller and are not anymore a major contributor to crack propagation. However, similar to Colmonoy 69 deposits, the continuous network of eutectic phases still provided the easy route for cracks to propagate. These observations confirm the pivotal role of the network of hard eutectics in cracking of Ni-Cr-B-Si-C deposits.

Microstructure of the coatings with different amounts of Nb was reexamined by OM as optical microscopy proved to be a useful tool for microstructural analysis of these alloys, especially to study the crack growth paths as shown above. [Figure 6.14](#) presents the OM microstructural images of deposits with 4 and 9 wt.% of Nb. The differences between the scale of constituent phases and quantity of the interdendritic eutectic are obvious. In comparison to SEM micrographs, OM images give a better overview of the microstructure in these alloys and are especially helpful to observe their eutectic structure.

## 6.7 Microstructural evolutions

It was shown that the proposed procedure to select refining elements based on their ability to form precipitates at high temperatures, which could remain as independent phases and act as heterogeneous nucleation sites, was able to refine the microstructure of Ni-Cr-B-Si-C alloys. Based on the phase formation reactions and

the microstructural evolutions in Nb-, Zr-, and V-modified [26] deposits, the set of proposed rules in the theoretical backgrounds section could be further analyzed.

According to the  $\Delta G_f$  data [21,27], it was expected to form new borides upon addition of Zr or Nb to the original alloy but none were formed. It should be noted that the reported  $\Delta G_f$  data are usually measured or calculated for reactions in which pure elements react or a single chemical reaction occurs to form that compound [21]. Formation of the same compounds may not necessarily happen in a multicomponent system as they may not contribute to bringing the free energy of the whole system to its minimum. From this point of view, application of thermodynamic calculation software to consider competing reactions in the multicomponent system could be very helpful. An example of this was shown for the Nb-modified alloy in which the type and sequence of phase formations (Figure 6.2) were predicted by *Thermo-Calc* simulations with a reasonable precision. Nevertheless, such simulations could not account for the nonthermodynamic effects that could become dominant, especially in processes including rapid solidification, such as laser deposition. In other words, while  $ZrB_2$  plus  $Cr_7C_3$  was the most thermodynamically favorable set in the alloy modified by 5 wt.% of Zr (Figure 6.2a and c), in reality Zr and C content of the alloy precipitated as  $ZrC$ . Such a phase selection phenomena was most probably nucleation-controlled as no borides were detected in the microstructure or predicted by the recalculated phase formation sequence (Figure 6.5d). In an alloy system with numerous phases, competition in the nucleation-controlled regime will be largely determined by the relative magnitudes of  $\Delta G^*$ , that is, the energy barrier to heterogeneous nucleation that can be represented as [35]

$$\Delta G^* = \frac{16\pi\gamma_{SL}^3 T_m^2 f(\theta)}{3L_f^2 \Delta T^2} \quad (6.4)$$

where  $\Delta T$  is undercooling of the liquid phase,  $\gamma_{SL}$  solid-liquid interface energy,  $T_m$  equilibrium melting point,  $L_f$  latent heat of phase formation, and  $f(\theta)$  nucleation potency factor of the heterogeneous site that depends on the wetting angle  $\theta$ . It can be seen that ease of nucleation depends not only on the latent heat of phase formation ( $L_f$  or  $\Delta G_f$ ), but also on other parameters such as the solid-liquid interface energy and the suitable level of undercooling below the equilibrium melting temperature. Selection of the refining element based only on the  $\Delta G_f$  values as suggested before [10] neglects the fact that  $\Delta G_f$  of a compound mostly shows the stability of that phase and not its ease of formation.

In an alloy system with multiple phase formation reactions, the sequence of phase formation should also be assessed. This is particularly important for the refinement process because an obvious prerequisite for an *in situ* formed nucleating agent is its high temperature of formation. The recalculated solidification sequence of the Zr-modified alloy as presented in Figure 6.6d shows that  $ZrC$  started to form more than 100 °C after  $CrB$ . By that stage, the nucleation of  $CrB$  would have been largely completed. As a result,  $ZrC$  particles could not act as nucleation sites and, hence, addition of Zr did not induce any microstructural refinement. A similar phenomenon was observed for V-modified alloys [26] in which  $VC$  precipitates formed at lower temperatures on  $(Cr, V)B$  rods and, consequently, could not function as nucleating agents [26].

Apart from the thermodynamic possibility of spontaneous precipitation as well as ease and temperature of formation, solid-state interaction of the nucleant and Cr borides nucleating on them may influence the final phase constitution of the system. This effect was characterized in detail for the interaction between VB and CrB in V-modified system [26]. As expected from the size factors and differences in crystal structures for Zr- and Nb-rich phases, a strong segregation happened between CrB and ZrC or NbC.

Although the methodology and the rules proposed thus far could explain a good deal about the selection of effective alloying elements for microstructural refinement of Ni-Cr-B-Si-C alloys, they need further elaborations on certain areas. The first one is explaining the role of kinetic effects in the phase selection processes, as briefly mentioned above. This will become pivotal when the additional element could go through multiple precipitation reactions, especially in rapid solidification processes such as laser deposition. The second point is to understand the nucleation mechanism in the refined microstructure of Nb-modified alloys. In the current work, the nucleating capability of NbC was attributed to its high temperature of formation and its lack of solubility in CrB, which gave it the chance to remain as an independent phase. However, such an argument neglects the fact that a good nucleating agent should fulfill more conditions than just being physically available at the right temperature. For example, the surface energy between heterogeneous nucleation site and solid crystal should be lower than the surface energy between heterogeneous nucleation site and the melt [35]. Such a condition is, in turn, controlled by factors including the lattice mismatch and orientation relationship between the nucleant and growing crystal and the chemical nature of the surface layer on the nucleant [44].

## 6.8 The microstructural refinement-cracking relationship

Nb addition and the subsequent refinement of hard Cr-rich precipitates did not fulfill the expectations for enhancement of the coatings' fracture toughness. The outcome was not in line with the findings of a previous research on the correlation between the structural scale of the strengthening components and the fracture toughness of wear-resistant Fe-base alloys, in which the authors hypothesized that "the reduction of the structural scale of the microstructure would enhance the fracture toughness" [45]. In [45], it was shown that microstructural refinement of Fe-base wear-resistant alloy deposits could enhance their fracture toughness while preserving hardness of the deposits. In this way, the so-called hardness-toughness paradox could be solved by preserving the quantity of hard components but reducing their scale. Although a similar phenomenon, that is, microstructural refinement while preserving the level of hardness, happened in Nb-modified Colmonoy 69 coatings, the outcome was not consistent with the above-mentioned hypothesis.

This discrepancy could be explained based on the different phase constitution and microstructure of the laser deposited Ni-Cr-B-Si-C alloys. If the microstructure of the alloy consists of strengthening components in a continuous matrix of ductile phase as in [45], then refinement of the strengthening components may enhance the fracture

toughness. This is so because the ductile phase may effectively isolate cracks in the hard components by providing plastic zones ahead of the cracks. In laser deposited Ni-Cr-B-Si-C alloys such as Colmonoy 69 or Nb-modified Colmonoy 69, although carbide and boride precipitates were engulfed by Ni dendrites, a continuous network of eutectic structure filled the spaces between Ni dendrite arms.

Analysis of the crack growth paths and fracture surfaces showed that besides Cr-rich precipitates, the eutectic network also played an important role in the cracking process. In fact, as it can be seen in [Figure 6.13](#), cracks often propagated through the continuous network of eutectics. This happened because the eutectic structure in Ni-Cr-B-Si-C alloys with the ratio of Si/B less than 3 (Si/B for Colmonoy 69: 1.33) mostly consists of Ni-Ni<sub>3</sub>B, which is very hard and brittle. [Figure 6.12c](#) clearly shows the large difference in plasticity between the eutectic structure and the ductile Ni grains. Although the eutectic network also contains lamella of ductile Ni, these lamellae are too thin to have any significant effect on the toughness. The eutectic phases in the Nb-modified alloy were not as hard as those of Colmonoy 69. However, they still formed an interconnected network that actively contributed to crack propagation, as shown in [Figure 6.13b](#).

In a comprehensive work on the fracture mechanism and toughening of PTA deposited Ni-Cr-B-Si-C alloys, Cockeram [46] concluded that crack bridging mechanism, that is, necking and plastic deformation of Ni dendrites, can explain the fracture behavior of Ni-Cr-B-Si-C alloys. [Figure 6.13a](#) confirms that Ni dendrites effectively deflect the propagating cracks and force them to bridge frequently, which is in line with the findings of Cockeram. Toughening of a brittle matrix by crack bridging ( $\Delta K_{CB}$ ) can be described as [46,47]

$$\Delta K_{CB} = C \cdot E_d [V_f (\sigma_o / E_d) a_o]^{0.5} \quad (6.5)$$

where  $C$  is a material-related constant and  $E_d$ ,  $V_f$ ,  $\sigma_o$ , and  $a_o$  are the elastic modulus, work of rupture, volume fraction, and yield stress and radius of the ductile phase (Ni dendrites), respectively. Measurement of the fracture toughness values for PTA welded Ni-Cr-B-Si-C samples showed that in Equation (6.5),  $V_f$  and  $a_o$  are the main parameters affecting the amount of crack bridging in these alloys [46]. This means that increasing the toughness of Ni-Cr-B-Si-C alloys requires higher percentages and/or coarser Ni dendrites. The phase formation behavior of Ni-Cr-B-Si-C alloys happens in such a way that increasing the percentage of Ni dendrites will inevitably decrease the fraction of the Ni-B-Si eutectics and, hence, reduce the overall hardness of the deposits [40]. In addition, laser deposited samples usually have very fine Ni dendrites as a result of their rapid solidification. Consequently, enhancing the crack bridging phenomena to toughen the Ni-Cr-B-Si-C laser deposited coatings while preserving their high hardness will be inherently difficult. In the Ni-Cr-B-Si-C alloy system, a sole microstructural refinement of the precipitates cannot be a viable toughening mechanism because although the ductile phase may deflect the cracks propagating to and from the precipitates, it cannot prevent them from using the continuous eutectic network as an easy growth path. Consequently, an effective toughening of these alloys will not happen unless the eutectic network is changed in type or its continuity is disrupted.

## 6.9 Conclusions

In this chapter, the idea of reducing the structural scale of Cr-rich precipitates in Ni-Cr-B-Si-C hardfacing alloys by producing *in situ* formed nucleation agents via controlled addition of refining elements was explored. It is proposed that the refining element should be able to spontaneously produce precipitates at high temperatures with little solid solubility in their Cr-rich counterparts. Based on the proposed rules, Zr and Nb were selected to deposit modified Ni-base alloys using laser-cladding process. The results showed that while no microstructural refinement occurred in Zr-modified deposits, Nb addition could significantly refine the scale of Cr borides while preserving the original level of hardness. The mechanism of microstructural refinement in Nb-modified alloys was nucleation of CrB rods on NbC precipitates. Contrary to the expectations, microstructural refinement did not decrease the cracking tendency of Nb-modified coatings. The reason for this failure was that not only the hard precipitates, but also the continuous network of hard eutectics contributed to the cracking process. This means that toughening of Ni-Cr-B-Si-C alloys could not be reached solely by refining hard precipitates. It was suggested that modifying the type of constituent phases in the eutectic structure or disruption of their continuous network is also needed to obtain high hardness-high toughness Ni-base hardfacing alloys.

## Acknowledgments

This research was carried out under project number MC7.06259 in the framework of the Research Program of the Materials Innovation Institute M2i ([www.m2i.nl](http://www.m2i.nl)). R.M. Huizenga from Delft University of Technology is acknowledged for performing *Thermo-Calc*<sup>®</sup> simulations. The Wall Colmonoy Ltd. (UK) is acknowledged for providing Colmonoy 69 powders.

## References

- [1] Y. Huang, X. Zeng, Investigation on cracking behavior of Ni-based coating by laser-induction hybrid cladding, *Appl. Surf. Sci.* 256 (2010) 5985–5992.
- [2] E. Beyer, New Industrial Systems & Concepts for Highest Laser Cladding Efficiency. Continuous Wave, <http://www.lia.org/blog/2011/05/high-performance-laser-cladding/>.
- [3] J. Song, Y. Li, J. Fu, Q. Deng, D. Hu, Cracking behavior of laser cladding forming nickel based alloys, in: Proceedings of International Technology and Innovation Conference (ITIC), IET, 2009, pp. 68–72, <http://dx.doi.org/10.1049/cp.2009.1446>.
- [4] J.A. Ajao, Scanning electron microscopy of some slowly cooled nickel-based hardfacing alloys containing iron additions, *J. Miner. Mater. Charact. Eng.* 9 (2010) 133.
- [5] A. Conde, F. Zubiri, Y.J. de Damborenea, Cladding of Ni-Cr-B-Si coatings with a high power diode laser, *Mater. Sci. Eng. A* 334 (2002) 233–238.
- [6] J.M. Miguel, J.M. Guilemany, S. Vizcaino, Tribological study of NiCrBSi coating obtained by different processes, *Tribol. Int.* 36 (2003) 181–187.

- [7] E. Fernández, et al., Wear behaviour of laser clad NiCrBSi coating, *Wear* 259 (2005) 870–875.
- [8] C.P. Paul, A. Jain, P. Ganesh, J. Negi, A.K. Nath, Laser rapid manufacturing of Colmonoy-6 components, *Opt. Lasers Eng.* 44 (2006) 1096–1109.
- [9] A. Angelastro, S.L. Campanelli, A.D. Ludovico, Characterization of Colmonoy 227-F samples obtained by direct laser metal deposition, *Adv. Mater. Res.* 83–86 (2009) 842–849.
- [10] D. Wang, E. Liang, M. Chao, B. Yuan, Investigation on the microstructure and cracking susceptibility of laser-clad V2O5/NiCrBSiC alloy coatings, *Surf. Coat. Technol.* 202 (2008) 1371–1378.
- [11] F. Wang, H. Mao, D. Zhang, X. Zhao, Y. Shen, Online study of cracks during laser cladding process based on acoustic emission technique and finite element analysis, *Appl. Surf. Sci.* 255 (2008) 3267–3275.
- [12] E. Kannatey-Asibu Jr., *Principles of Laser Materials Processing*, Wiley, 2009.
- [13] F. Brückner, D. Lepski, E. Beyer, Modeling the influence of process parameters and additional heat sources on residual stresses in laser cladding, *J. Therm. Spray Technol.* 16 (2007) 355–373.
- [14] R. Jendrzejewski, G. Śliwiński, M. Krawczuk, W. Ostachowicz, Temperature and stress fields induced during laser cladding, *Comput. Struct.* 82 (2004) 653–658.
- [15] R. Jendrzejewski, I. Kreja, G. Śliwiński, Temperature distribution in laser-clad multi-layers, *Mater. Sci. Eng. A* 379 (2004) 313–320.
- [16] R. Jendrzejewski, G. Śliwiński, M. Krawczuk, W. Ostachowicz, Temperature and stress during laser cladding of double-layer coatings, *Surf. Coat. Technol.* 201 (2006) 3328–3334.
- [17] S. Zhou, X. Dai, H. Zheng, Analytical modeling and experimental investigation of laser induction hybrid rapid cladding for Ni-based WC composite coatings, *Opt. Laser Technol.* 43 (2011) 613–621.
- [18] W.D. Callister, *Materials Science and Engineering: An Introduction*, John Wiley & Sons, 2010.
- [19] I. Hemmati, J.C. Rao, V. Ocelík, J.T.M. De Hosson, Electron microscopy characterization of Ni-Cr-B-Si-C laser deposited coatings, *Microsc. Microanal.* 19 (2013) 120–131.
- [20] J.F. Knott, *Fundamentals of Fracture Mechanics*, Butterworth, 1973.
- [21] I. Barin, *Thermochemical Data of Pure Substances*, VCH, 1995.
- [22] A. Cottrell, *Chemical Bonding in Transition Metal Carbides*, Maney Materials Science, 1995.
- [23] H.O. Pierson, *Handbook of Refractory Carbides and Nitrides: Properties, Characteristics, Processing, and Applications*, Noyes Publications, 1996.
- [24] M.-J. Chao, E.-J. Liang, Effect of TiO<sub>2</sub>-doping on the microstructure and the wear properties of laser-clad nickel-based coatings, *Surf. Coat. Technol.* 179 (2004) 265–271.
- [25] T. Yu, Q. Deng, G. Dong, J. Yang, Effects of Ta on microstructure and microhardness of Ni based laser clad coating, *Appl. Surf. Sci.* 257 (2011) 5098–5103.
- [26] I. Hemmati, J.C. Rao, V. Ocelík, J.T.M. Hosson, Phase formation and properties of vanadium-modified Ni-Cr-B-Si-C laser-deposited coatings, *J. Mater. Sci.* 48 (2013) 3315–3326.
- [27] R.A. Cutler, S.J. Schneider (Eds.), *Engineered Materials Handbook: Ceramics and Glasses*, CRC Press, 1991, pp. 777–803.
- [28] U. Mizutani, *Hume-Rothery Rules for Structurally Complex Alloy Phases*, CRC Press, 2011.
- [29] L.S. Darken, *Physical Chemistry of Metals*, McGraw-Hill Inc., 1953.
- [30] J.R. Chelikowsky, Solid solubilities in divalent alloys, *Phys. Rev. B* 19 (1979) 686–701.

- [31] Y.M. Zhang, S. Yang, J.R.G. Evans, Revisiting Hume-Rothery's Rules with artificial neural networks, *Acta Mater.* 56 (2008) 1094–1105.
- [32] T.F. Fedorov, Y.B. Kuz'ma, Phase equilibria in the system zirconium-chromium-carbon, *Powder Metall. Met. Ceram.* 4 (1965) 234–237.
- [33] T.F. Fedorov, N.M. Popova, L.V. Gorshkova, R.V. Skolozdra, Y.B. Kuz'ma, Phase equilibria in the systems vanadium-chromium-carbon, niobium-chromium-carbon, and tantalum-chromium-carbon, *Powder Metall. Met. Ceram.* 7 (1968) 193–197.
- [34] Y.B. Kuz'ma, V.S. Telegus, D.A. Kovalyk, X-ray diffraction investigation of the ternary systems V-Cr-B, Nb-Cr-B, and Mo-Cr-B, *Powder Metall. Met. Ceram.* 8 (1969) 403–410.
- [35] J. Dantzig, M. Rappaz, *Solidification*, EPFL Press, 2009.
- [36] E. Toyserkani, S. Corbin, A. Khajepour, *Laser Cladding*, CRC Press, 2004.
- [37] I. Hemmati, V. Ocelík, J.T.M. De Hosson, Dilution effects in laser cladding of Ni-Cr-B-Si-C hardfacing alloys, *Mater. Lett.* 84 (2012) 69–72.
- [38] B.E. Meacham, M.C. Marshall, D.J. Branagan, Palmqvist fracture toughness of a new wear-resistant weld alloy, *Metall. Mater. Trans. A* 37 (2006) 3617–3627.
- [39] G.H. Zschornack, *Handbook of X-Ray Data*, Springer, 2007.
- [40] I. Hemmati, V. Ocelík, J.T.M. De Hosson, Evolution of microstructure and properties in laser cladding of a Ni-Cr-B-Si hardfacing alloy, in: WIT Transactions on Engineering Sciences, vol. 71, WIT Press, 2011, pp. 287–296, <http://dx.doi.org/10.2495/SECM110251>.
- [41] J.J. Gilman, *Chemistry and Physics of Mechanical Hardness*, Wiley-Interscience, 2009.
- [42] R. Spiegler, S. Schmudder, L. Sigl, Fracture toughness of evaluation of WC-Co alloys by indentation testing, *J. Hard Mater.* 1 (1990) 147–158.
- [43] I. Campos, et al., Fracture toughness evaluation using Palmqvist crack models on AISI 1045 borided steels, *Mater. Sci. Eng. A* 488 (2008) 562–568.
- [44] B.S. Murty, S.A. Kori, M. Chakraborty, Grain refinement of aluminium and its alloys by heterogeneous nucleation and alloying, *Int. Mater. Rev.* 47 (2002) 3–29.
- [45] D.J. Branagan, M.C. Marshall, B.E. Meacham, High toughness high hardness iron based PTAW weld materials, *Mater. Sci. Eng. A* 428 (2006) 116–123.
- [46] B.V. Cockeram, The fracture toughness and toughening mechanisms of nickel-base wear materials, *Metall. Mater. Trans. A* 33 (2002) 33–56.
- [47] M.F. Ashby, F.J. Blunt, M. Bannister, Flow characteristics of highly constrained metal wires, *Acta Metall.* 37 (1989) 1847–1857.

# New metallic materials development by laser additive manufacturing

7

Dongdong Gu

Nanjing University of Aeronautics and Astronautics (NUAA), Nanjing, PR China

## 7.1 Introduction

Additive manufacturing (AM), also called 3D printing, rapid manufacturing, and solid freeform fabrication, is presently a rapidly developing advanced manufacturing technology [1–3]. Unlike the material removal method in conventional machining processes, AM is based on a completely opposite material incremental manufacturing (MIM) philosophy. AM is processed via the layer-by-layer shaping and consolidation of feedstock (typically powder materials) to a wide range of configurations, normally using a computer-controlled laser as the energy source. Selective laser melting, which is a powder bed-based AM process [4–6], is presently regarded as one of the most versatile AM technologies. First, a computer-aided design (CAD) model of the object to be built is mathematically sliced into thin layers. The object is then created by selective melting and consolidation of the deposited powder layer on the powder bed with a scanning high-energy laser beam. Each shaped layer represents a cross section of the sliced CAD model. SLM technology, accordingly, offers a wide range of advantages such as net-shape fabrication without the need of expensive molds, direct production based on CAD models, high levels of process flexibility, and high material utilization rates [7].

SLM, as implied in its name, is processed based on a metallurgical mechanism of the full melting and subsequent rapid solidification. Typically, SLM involves a unique nonequilibrium physical metallurgical nature. A high-energy laser beam can be focused to a power density up to  $10^{10\text{--}12}$  W/cm<sup>2</sup> during SLM, and can rapidly heat a material surface to a temperature up to 10<sup>5</sup> K, followed by a rapid cooling at a rate of up to 10<sup>6–7</sup> K/s [8]. It thus provides a high potential for obtaining very fine microstructures with superior metallurgical properties. Accordingly, the application of SLM technology to prepare novel structured high-performance functional components is of unique interest. The special MIM processing procedure and highly nonequilibrium nature of the SLM process favor the formation of bulk-form materials with unique microstructures and properties. SLM thus provides a beneficial method to develop new material components with designed 3D configurations, such as nanophase, amorphous, functionally gradient, and porous materials.

In this chapter, two categories of novel metallic materials in bulk form, that is, Ti-based nanocomposites and microcellular stainless steel porous material, were prepared using the SLM process. The microstructural development under different SLM processing was investigated and the mechanical properties in terms of densification level/porosity, microhardness, and wear property were studied. The underlying metallurgical mechanisms responsible for the development of microstructural and mechanical properties were disclosed for SLM-processed novel materials components.

## 7.2 Selective laser melting of TiC/Ti nanocomposites parts with novel nanoscale reinforcement and enhanced wear performance

### 7.2.1 Experimental procedures

The starting powder components included 99.0% purity TiC nanopowder with a near-spherical structure and a mean particle size of 50 nm ([Figure 7.1a](#)) and 99.7% purity Ti powder with a spherical shape and an average particle size of 22.5  $\mu\text{m}$  ([Figure 7.1b](#)). The TiC/Ti nanocomposite powder system with 12.5 wt.% TiC was homogeneously mixed in a Fritsch Pulverisette 4 vario-planetary mill, using a ball-to-powder weight ratio of 5:1, a rotation speed of the main disk of 200 rpm, and a milling duration of 4 h.

The SLM system consisted mainly of a continuous-wave Nd:YAG laser ( $\lambda = 1.064 \mu\text{m}$ ) with a  $\sim 200 \mu\text{m}$  top-hat spot and  $\sim 150 \text{ W}$  power, an automatic powder layering apparatus, an inert argon gas protection system, and a computer system for process control. When specimens were to be prepared, a titanium substrate was fixed on the building platform and levelled. The argon gas was fed into the sealed building chamber and the resultant oxygen content decreased to below 10 ppm. A thin layer of powder with a thickness of 50  $\mu\text{m}$  was then deposited on the substrate by the layering system ([Figure 7.2a](#)). Afterwards, the laser beam scanned the powder bed surface to form a layer-wise profile according to the CAD data of the specimens ([Figure 7.2b](#)). A linear raster scan pattern with a scan vector length of 4 mm and a hatching spacing of 140  $\mu\text{m}$  was used. The laser powers of 90-120 W and scan speeds of 0.1-0.4 m/s were changed by the SLM control program. A parameter “linear laser energy density” ( $\lambda$ ) with a unit of J/m, which was defined by the ratio of laser power to scan speed, was used to assess the laser energy input to the powder layer being melted. Cubic specimens with dimensions of 8 mm  $\times$  8 mm  $\times$  8 mm were prepared ([Figure 7.2c](#)).

Metallographic specimens were prepared according to standard procedures and etched using a solution consisting of 2 ml HF, 4 ml  $\text{HNO}_3$ , and 94 ml distilled water for 25 s. Low-magnification microstructures were analyzed by optical microscopy (OM) and a Quanta 200 scanning electron microscope (SEM). High-resolution characterization of ultrafine nanostructures was performed by a LEO 1550 field emission SEM (FE-SEM). The densities ( $\rho$ ) of SLM-processed parts were determined by the Archimedes principle. The Vickers hardness was measured using a MicroMet 5101

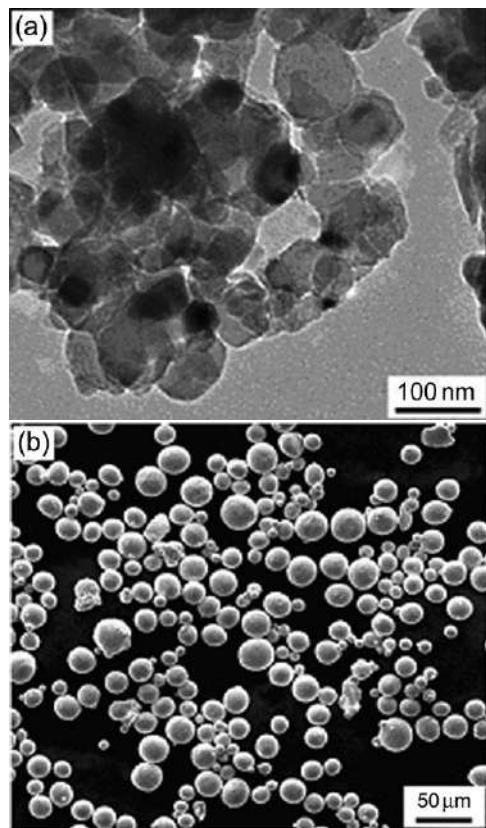


**Figure 7.1** Characteristic microstructures of the starting TiC nanopowder (a) and Ti powder (b).

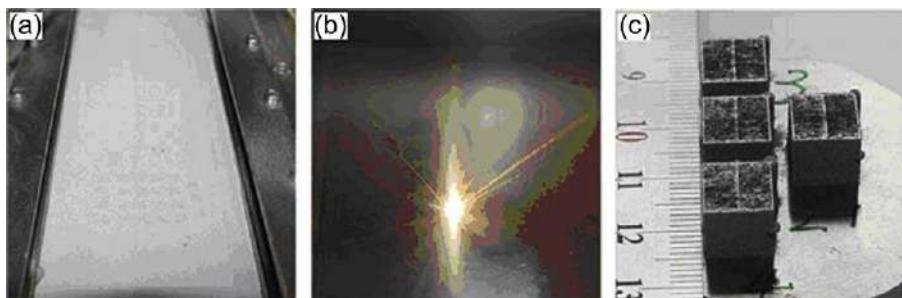


**Figure 7.2** Photographs of SLM process: (a) spreading of powder-on-powder bed; (b) interaction of laser beam with the powder; (c) SLM-processed bulk-form parts.

microhardness tester at a load of 0.2 kg and an indentation time of 20 s. Dry sliding wear tests on SLM-processed parts were conducted in a HT-500 ball-on-disk tribometer at room temperature. A 3 mm diameter bearing steel GCr15 ball was taken as the counter-face material, using a test load of 3 N. The friction unit was rotated at 560 rpm for 30 min and the rotation radius was 2 mm. The COF was recorded during sliding. The wear volume ( $V$ ) was determined gravimetrically using  $V = M_{\text{loss}}/\rho$ , where  $M_{\text{loss}}$  was the weight loss of the specimens after wear tests. The wear rate ( $\omega$ ) was calculated by  $\omega = V/(WL)$ , where  $W$  was the contact load and  $L$  was the sliding distance.

### 7.2.2 *Surface morphology and densification activity of TiC/Ti nanocomposites during SLM*

Figure 7.3 shows characteristic surface morphologies of TiC/Ti parts processed at various SLM parameters. At a relatively high linear laser energy density ( $\lambda$ ), the surface was considerably smoother, denser, and free of any pores (Figure 7.3a). On decreasing the applied  $\lambda$ , although a large area of the surface remained entirely dense, a small amount of irregular shaped pores were occasionally observed on the surface (Figure 7.3b). At an even lower  $\lambda$  of 300 J/m, both the large-scaled balls with a mean size of  $\sim 200 \mu\text{m}$  and the small-sized balls with an average diameter of  $\sim 20 \mu\text{m}$  were observed on the surface (Figure 7.3d), producing a considerable porosity between neighboring balls and scan tracks (Figure 7.3c).

Figures 7.4 and 7.5 illustrate the changes of relative densities and cross-sectional microstructures of TiC/Ti parts with the applied linear laser energy density ( $\lambda$ ). At a relatively high  $\lambda \geq 600 \text{ J/m}$ , the densification levels of SLM-processed parts remained steady and were generally larger than 97%. The cross section of an SLM-processed part at 600 J/m only consisted of a small amount of porosity (Figure 7.5b) and the part processed at 1200 J/m had the dense cross-sectional microstructures free of apparent interlayer pores (Figure 7.5c). However, as the applied  $\lambda$  decreased to 300 J/m, the densification rate decreased markedly to 90.2% (Figure 7.4) and the large-sized, irregular-shaped residual pores were formed on the cross section (Figure 7.5a). Such a kind of interlayer pores was believed to be caused by the balling effect, a typical metallurgical defect associated with the SLM process [9,10].

During SLM of the present TiC/Ti composite system, the dissolution of TiC ceramic in Ti liquid tends to enhance the melt viscosity significantly. A high melt viscosity decreases the overall rheological performance of the composite melt and, accordingly, reduces the wettability, hence causing the melt to undergo a geometric change into individual spheres, rather than flow across the underlying surface [11]. The balling effect thus occurs on the laser-processed surface. The balling effect results in the formation of discontinuous scan tracks and large intertrack pores as a current layer is processed (Figure 7.3c and d). Furthermore, during layer-by-layer SLM process, balling effect is a severe impediment to a uniform deposition of the fresh powder on the previously processed layer and tends to produce porosity induced by poor interlayer bonding (Figures 7.4 and 7.5a). It is reasonable to conclude that laser-induced balling effect is an important factor in influencing the densification activity of SLM-processed parts.

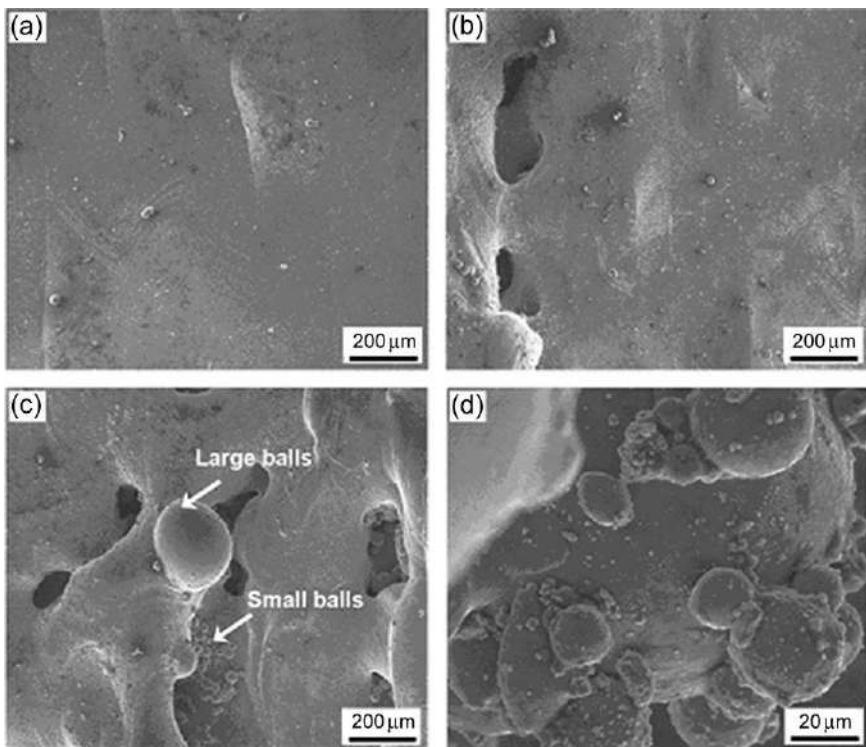


**Figure 7.3** SEM images showing characteristic surface morphologies of SLM-processed TiC/Ti parts at different linear laser energy densities ( $\lambda$ ): (a) 1200 J/m; (b) 600 J/m; (c) 300 J/m. Magnification of (c) showing the occurrence of balling phenomenon (d).

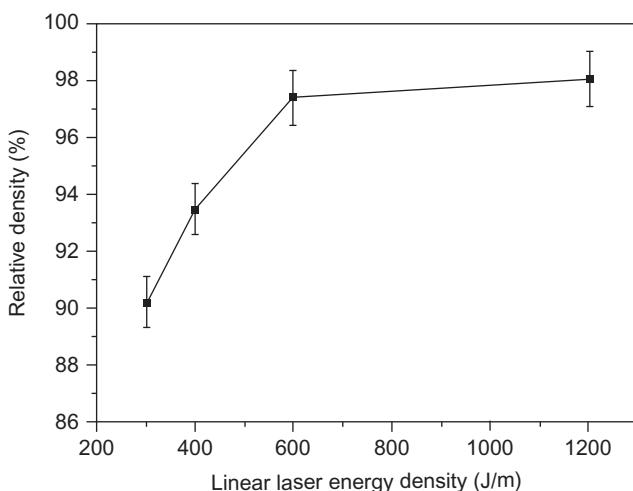


**Figure 7.4** Influence of linear laser energy density ( $\lambda$ ) on densification level of SLM-processed TiC/Ti parts.

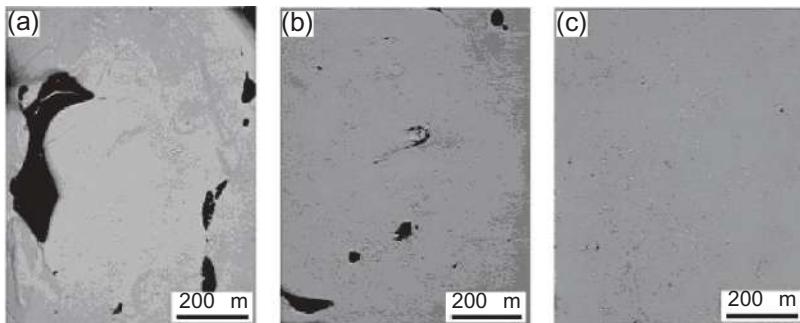
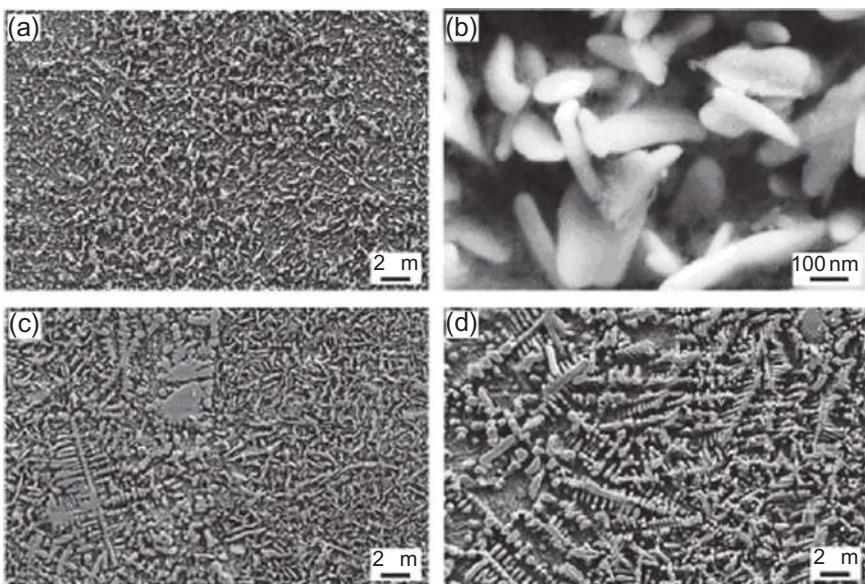


**Figure 7.5** OM micrographs showing low-magnification microstructures on cross sections of TiC/Ti parts at different linear laser energy densities ( $\lambda$ ): (a) 300 J/m; (b) 600 J/m; (c) 1200 J/m.

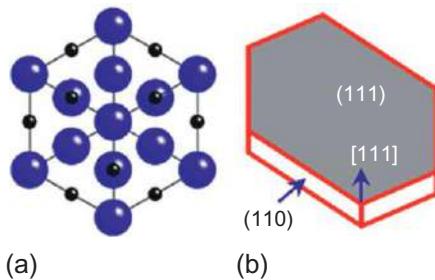
### 7.2.3 Microstructural characteristics of SLM-processed TiC/Ti nanocomposites

Figure 7.6 reveals the typical microstructures of SLM-processed TiC/Ti parts at different linear laser energy density ( $\lambda$ ). It was clear that the TiC reinforcement in SLM-processed composites generally had unique microstructures distinctly different from the initial particulate morphology before SLM (Figure 7.1a). On the other hand, the growth morphology and dispersion state of the TiC reinforcing phase were significantly influenced by the applied  $\lambda$ . At a relatively low  $\lambda$  of 400 J/m, a very homogeneous dispersion of the significantly refined TiC reinforcement was achieved (Figure 7.6a). High-magnification FE-SEM micrographs revealed that the TiC reinforcing phase typically had a nanoscale lamellar structure with an average thickness of  $\sim$ 60 nm (Figure 7.6b). It is known that nanomaterials can be defined as materials that have structured components with at least one dimension less than 100 nm [12]. Following this definition, it was reasonable to consider that the standard nanostructured TiC reinforcement was formed in the SLM-processed structure at 400 J/m. On increasing the applied  $\lambda$  to 600 J/m, the microstructure of TiC reinforcement remained as the ultrafine lamellar nanostructure; however, its dispersion uniformity decreased slightly (Figure 7.6c). At an even higher  $\lambda$  of 1200 J/m, the TiC reinforcement exhibited a uniform network distribution and a typical dendritic morphology (Figure 7.6d). A quantitative measurement during FE-SEM analysis revealed that the average length of the dendrite trunks and the primary dendrite arms reached 9.2 and 1.6  $\mu\text{m}$ , respectively. In this case, the TiC reinforcing phase had not retained the desirable nanostructure after SLM.

Basically, SLM is performed using a complete melting/solidification mechanism, and the TiC is formed through a dissolution/precipitation mechanism by means of the heterogeneous nucleation of TiC nuclei and subsequent grain growth. TiC is a typical faceted crystal and its C atoms occupy the octahedral positions. If viewed along the direction perpendicular to the (111) plane, the Ti and C atoms form a hexagonal shape (Figure 7.7a). The TiC nuclei precipitate from the liquid, and the attendant crystal



**Figure 7.6** FE-SEM images showing characteristic microstructures of TiC reinforcement in SLM-processed TiC/Ti nanocomposites parts at various linear laser energy densities ( $\lambda$ ): (a) 400 J/m; (c) 600 J/m; (d) 1200 J/m. (b) Magnification of (a) showing the lamellar nanostructure of TiC reinforcement.



**Figure 7.7** Atomic projection (a) and crystal structure (b) of TiC along [111] direction.

shape is determined by growth rates of different planes. The formation of lamellar TiC with a nanoscale thickness at a relatively low  $\lambda \leq 600$  J/m (Figure 7.6a-c) implies that the growth rate of {110} side planes along [111] orientation is considerably limited (Figure 7.7b), which is attributed to the unique metallurgical behavior of the molten pool under nonequilibrium laser irradiation. Both theoretical and experimental studies have revealed that there is an effective pressure in a laser-generated molten pool, produced by the combined effect of evaporative recoil under laser irradiation and the surface tension of the melt in the pool [13]. The action of such pressure on the (111) plane increases the contraction of TiC crystals along the [111] orientation, preventing the

thickening of {110} side planes and, thus, maintaining the desirable nanostructures after solidification (Figure 7.6b). Alternatively, the local temperature gradient and chemical concentration gradient within the pool give rise to the surface tension gradient and associated Marangoni convection [14]. The formation of a convective stream within the pool induces liquid capillary force, which, in turn, exerts on the precipitated TiC and accelerates its rearrangement in the liquid, favoring a homogeneous dispersion of the nanoscale TiC reinforcement in the solidified matrix (Figure 7.6a). However, the formation of the relatively coarsened TiC dendrites at an elevated  $\lambda$  of 1200 J/m results in the disappearance of nanostructure (Figure 7.6d). In this instance, the significantly enhanced laser energy input and SLM temperature results in a considerable decrease in melt viscosity, which, in turn, intensifies the Marangoni flow and resultant turbulence within the pool [15,16]. Due to the instability of the solid-liquid interface caused by the perturbation, the TiC precipitates tend to undergo a dendritic growth. Meanwhile, a large amount of heat is accumulated around the growing dendrite tips, which provides a significant internal energy and thermodynamic potential for the coarsening of the developed TiC dendrites.

#### 7.2.4 Microhardness and wear property of SLM-processed TiC/Ti nanocomposites

Figure 7.8a depicts the average microhardness measured on the polished cross sections of TiC/Ti parts. On increasing the applied linear laser energy density ( $\lambda$ ) from 300 to 400 J/m, the microhardness increased considerably from 427 to 518 HV<sub>0.2</sub>. A further increase in  $\lambda$  above 600 J/m led to a steady distribution of even higher microhardness of 551–566 HV<sub>0.2</sub>. For comparison, the microhardness of SLM-processed pure Ti without any reinforcement under the same conditions was 241–287 HV<sub>0.2</sub>. Therefore, regardless of the various  $\lambda$ , the incorporation of nanoscale TiC reinforcement within the laser-processed Ti matrix favored at least a twofold increase in microhardness.

Figure 7.8b and c depicts the average COF and wear rate of SLM-processed TiC/Ti nanocomposite parts at different linear laser energy density ( $\lambda$ ). In general, the TiC/Ti nanocomposite parts had much lower COF relative to the pure Ti part under the same SLM conditions (the average value of  $\sim 1.3$ ) [7]. At a relatively low  $\lambda$  of 300 J/m, a considerably high COF of 0.46 was obtained, resulting in an elevated wear rate of  $7.8 \times 10^{-16}$  m<sup>3</sup>/(Nm). It was accordingly reasonable to consider that the SLM densification level played a basic role in determining the tribological property of SLM-processed parts. An insufficient densification at a low linear laser energy density (Figures 7.4 and 7.5a) resulted in a relatively poor wear performance. When  $\lambda$  was 400 and 600 J/m, the average COF and resultant wear rate decreased markedly to  $\sim 0.25$  and  $\sim 4 \times 10^{-16}$  m<sup>3</sup>/(Nm), respectively. In these two cases, the uniformly dispersed lamellar nanoscale TiC reinforcement in SLM-processed parts (Figure 7.6a–c) had a high tendency to adhere to each other, showing less fragmentation during sliding. Combined with the effect of microhardness enhancement (Figure 7.8a), the strain-hardened tribolayer was easily formed on the worn surface, acting as a protective layer

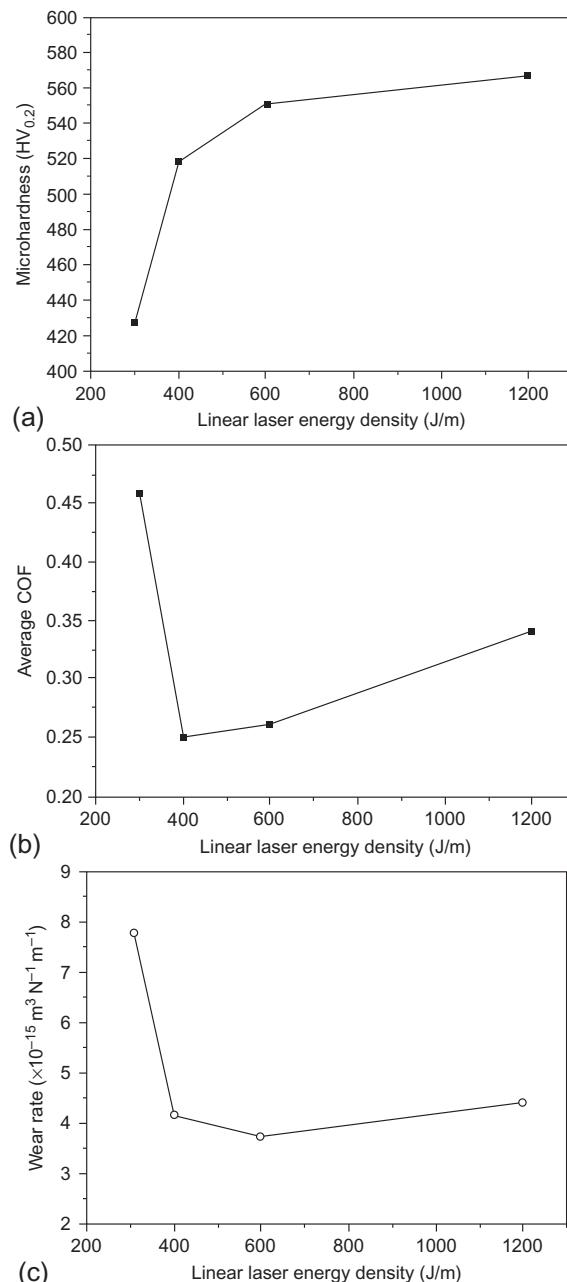


**Figure 7.8** Effect of linear laser energy densities ( $\lambda$ ) on microhardness (a), average COF (b), and wear rate (c) of SLM-processed TiC/Ti nanocomposite parts.

to improve wear resistance. However, the mean COF of the part, processed at an even greater  $\lambda$  of 1200 J/m, increased sharply to 0.34 and the resultant wear rate also increased slightly to  $4.5 \times 10^{-16} \text{ m}^3/(\text{Nm})$ . The decrease in wear performance in this instance was ascribed to the grain coarsening of TiC reinforcement and the resultant disappearance of its favorable nanostructure ([Figure 7.6d](#)). The relatively coarsened TiC dendrites can easily split during sliding, resulting in the spallation of the worn surface and attendant limited wear resistance.

## 7.3 Development of porous stainless steel with controllable microcellular features using selective laser melting

### 7.3.1 Experimental procedures

The starting powder system consisted of 316L stainless steel (SS) powder with a spherical morphology and a mean particle size of 75  $\mu\text{m}$ , and the additive materials, which were composed of 70 wt.%  $\text{H}_3\text{BO}_3$  and 30 wt.%  $\text{KBF}_4$ . The elemental compositions of the SS powder were 16.9Cr, 13.2Ni, 2.7Mo, 1.6Mn, 0.019C, 0.23Si, Fe balance. The SS powder and the additive materials, according to two different weight ratios of 99.95:0.05 and 99.90:0.10, were homogeneously mixed in a planetary mill with a vacuum pumping system at a rotation speed of 100 rpm for 30 min.

The basic procedures of SLM processing and microstructural characterization were addressed in [Section 7.3.1](#). The applied SLM processing conditions were: a continuous wave Gaussian  $\text{CO}_2$  laser ( $\lambda = 10.6 \mu\text{m}$ ), spot size 0.30 mm, laser power 900 W, scan speed 0.03-0.10 m/s, scan line spacing 0.15 mm, and powder layer thickness 0.20 mm.

### 7.3.2 Characteristic microstructural features of SLM-processed porous material

[Figure 7.9](#) shows the characteristic microstructures of SLM-processed porous samples with various contents of additive materials. The microstructures on transverse sections of polished samples showed that cellular structures in micrometer scales were generally formed after laser processing, although the configurations of pores exhibited some differences. When 0.05 wt.% additive materials were used, the pores exhibited an elliptic microcellular shape and the size of pores was typically in a range of 0.8-2.8  $\mu\text{m}$  ([Figure 7.9a](#)). Interestingly, at a higher content of 0.10 wt.%, a regularly round-shaped microcellular structure was formed and a more homogeneous size distribution of pores, with an average value of 2  $\mu\text{m}$ , was obtained ([Figure 7.9b](#)). The metallographic observations on the longitudinal cross-section of the sample were carefully performed to characterize the typical microstructures at different depths within a solidified melt pool. It was observed that near the bottom of the melt pool, cylindrical pores aligned obliquely in one direction ([Figure 7.9c](#)). The SEM

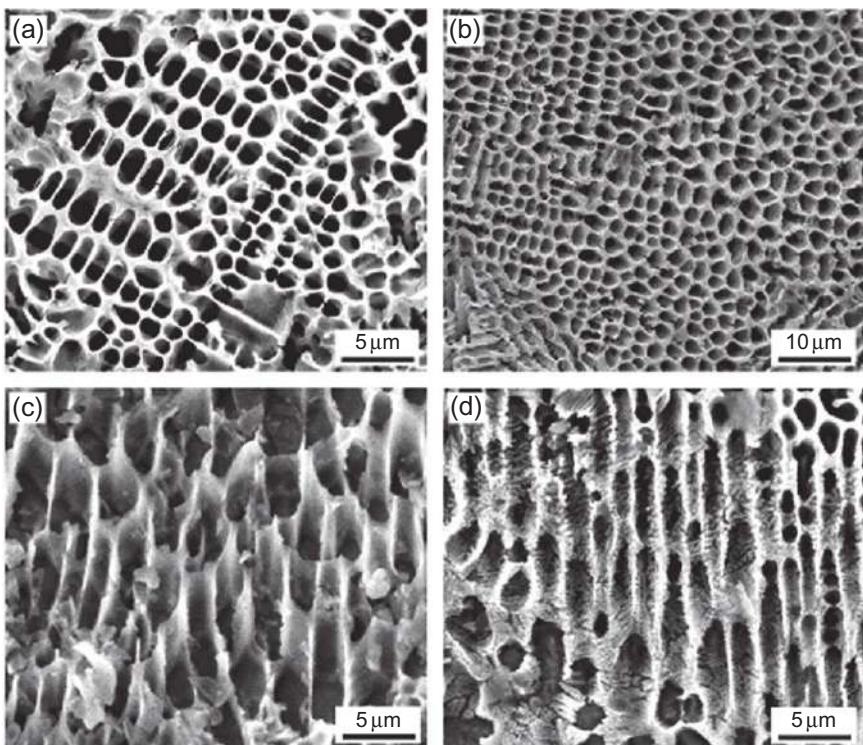


**Figure 7.9** SEM images showing characteristic microcellular features of SLM-processed porous samples with different contents of additive materials: (a) 0.05 wt.%, transverse microstructure; (b) 0.10 wt.%, transverse microstructure; (c) 0.10 wt.%, longitudinal microstructure near the bottom of a melt pool; (d) 0.10 wt. %, longitudinal microstructure in the middle of a melt pool. Laser scan speed was fixed at 0.03 m/s.

micrograph taken from the middle of the melt pool revealed that these unidirectional aligned continuous pore channels had no tendency to merge together (Figure 7.9d).

The typical microstructures of SLM-processed porous samples at different scan speeds are provided in Figures 7.9b and 7.10, respectively. It was clear that by increasing the scan speed from 0.03 to 0.05 m/s, the shape of the pores became longer and narrower and the growth direction of pores had a tendency to incline toward the scan direction of the laser beam (Figures 7.9b and 7.10a). However, at an even higher scan speed of 0.08 m/s, the irregularly shaped pores were randomly distributed and the round-shaped microcellular structures were destroyed (Figure 7.10b).

Figure 7.11 shows the relationship between the measured porosity of samples and the scan speeds used. It was found that when other processing parameters were constant, the porosity decreased with increasing scan speed. As the scan speed reached a critical value ( $\sim 0.08$  m/s), the porosity showed a sharp decrease.

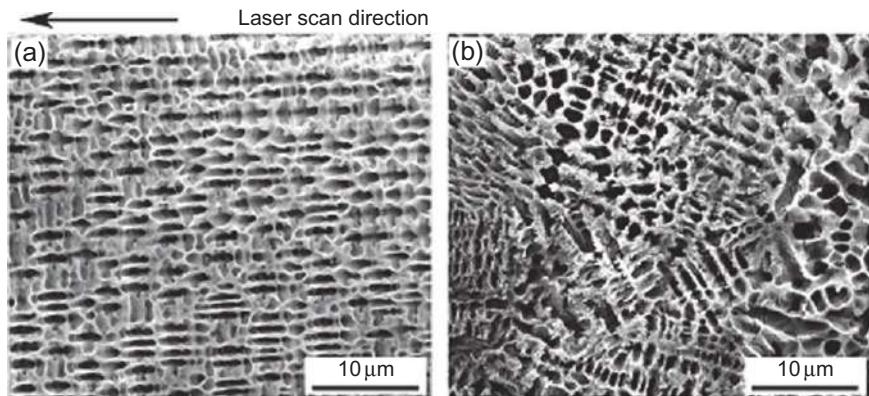


**Figure 7.10** SEM images showing characteristic microstructures of SLM-processed porous samples at different scan speeds: (a) 0.05 m/s; (b) 0.08 m/s. The content of additive materials is fixed at 0.10 wt.%.

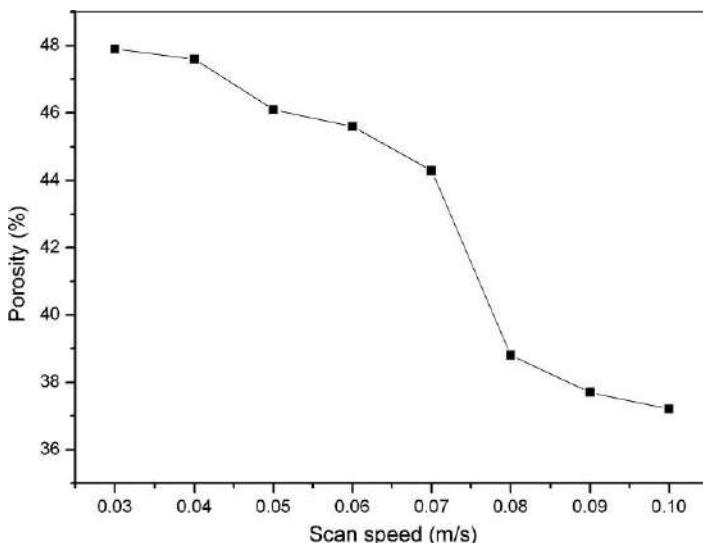
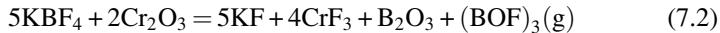
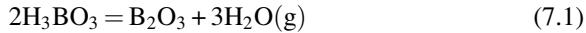


**Figure 7.11** Effect of scan speed on porosity of SLM-processed porous samples.

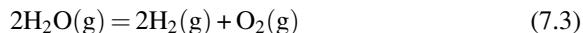
### 7.3.3 Formation mechanisms of microcellular porous structure during the SLM process

Prior to SLM processing, the particles in the powder layer are loosely packed and, thus, there exists a large amount of gas phase in the pores between powder particles. When a laser beam scans over the powder bed, the laser energy is directly absorbed by particles through both bulk coupling and powder coupling mechanisms [17]. The absorbed energy heats up the powder readily, leading to a rapid increase in the operating temperature above

the liquidus temperature of 316L SS powder ( $\sim 1398$  °C) [18]. Consequently, a molten pool is expected to be formed in a laser-irradiated region. In the present pool, the additive materials possessing low decomposition temperatures ( $H_3BO_3$ @ $\sim 185$  °C and  $KBF_4$ @ $\sim 530$  °C) undergo the following chemical reactions [19]:



At an elevated temperature above the liquidus temperature of 316L SS ( $\sim 1398$  °C), the  $H_2O$  vapor is expected to experience the decomposition reaction to generate gas phases in the form of  $O_2$  and  $H_2$ :



Reaction (7.2) reveals that the additive  $KBF_4$  will react with  $Cr_2O_3$ , which is known as the main component of surface oxidation film presented in commercially available SS powder. Shen *et al.*'s work [20] indicates that such oxidation film tends to cause a balling effect, which is detrimental to the SLM of SS powder. Therefore, the functions of additive materials in this study are in two aspects:

- (i) Producing a sufficient amount of gas phase to favor pore formation;
- (ii) Purifying the laser processing system.

Due to a comparatively high solubility of two atomic gases in liquid phase at an elevated temperature, both the originally existing gas (ambient atmosphere) in powder layer (so-called basic gas, main constituents:  $N_2$  and  $O_2$ ) and the additive-generated gas (so-called accessory gas, constituents:  $O_2$  and  $H_2$ , see reaction 7.3) dissolve much more easily in metallic melts. It is known that a high-energy laser beam can produce a significant backpressure on the surface of the melt pool, due to the well-known piston effect occurring during laser irradiation [17]. Furthermore, the weight of the molten liquid also produces pressure on gas bubbles [21]. Consequently, the dissolved gas phase almost fails to escape from the melt pool. From a kinetic viewpoint, the formation of microcellular pore structure is a metallurgical process that occurs by the nucleation and growth of gas phase, as schematically shown in Figure 7.12. During solidification, the dissolved gas phase nucleates heterogeneously to form bubble nuclei at liquid-solid interfaces, due to the significantly reduced solubility of the gas phase in a solid. Because a large amount of microscopic pits and cracks at the solidification front may act as favorable sites for heterogeneous nucleation of gas pores, the required activation energy is small, thereby significantly favoring bubble nucleation. Because the laser beam scans over the powder bed at a fixed speed, the solidification front is expected to advance at a constant velocity. Furthermore, due to a fixed laser scan direction, the maximum heat dissipation direction in the molten pool is constant, thereby fixing the preferential orientation of pore growth. Under these conditions, the bubble nuclei can grow continuously and unidirectionally along with the advancing solidification front in the melt pool, facilitating the formation of regularly shaped parallel pores after SLM (Figure 7.9).

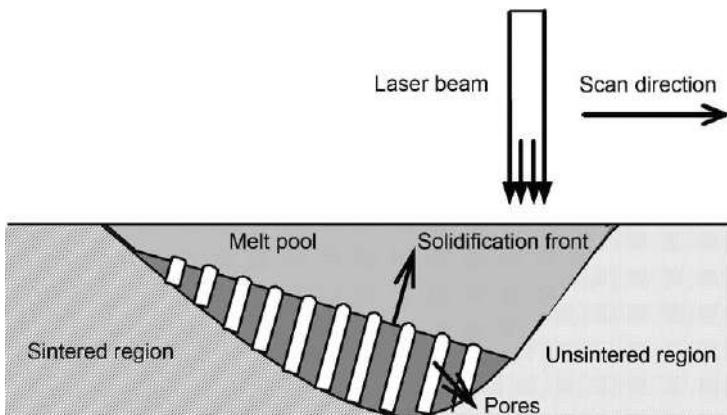


**Figure 7.12** Schematic showing formation mechanisms of pores during SLM.

### 7.3.4 Controlling mechanisms of pore characteristics during the SLM process

The obtained results, as shown in Figures 7.9–7.11, reveal that the morphologies of pores can be adjusted by changing material combinations and processing conditions. On one hand, an increase in the content of additive materials favors the formation of round-shaped microcellular structures with a larger pore size (Figure 7.9a versus b). Under this condition, the concentration of gas phase dissolved in liquid metal increases, due to the presence of a larger amount of “accessorial gas” (see reactions 7.1 and 7.3). Thus the pressure inside the pores increases with respect to the amount of dissolved gas phase [22]. It is known that the essence of pore formation during solidification is the competitive growth of two phases (a solid phase versus a gas phase) [23]. In other words the gas pressure in the bubble is larger than the total pressure around it for pore generation. Therefore, a higher pressure in bubbles, which is realized by adding a larger amount of additive materials, favors the sufficient and continuous growth of bubbles and the formation of microcellular pore structures with a larger pore size (Figure 7.9b). Alternatively, the pore shape, pore direction, and porosity are significantly influenced by the laser scan speed (Figures 7.9b, 7.10, and 7.11). It is known that the growth direction of pores at the liquid-solid interface has a tendency to incline toward the laser scan direction, due to the elliptical configuration of solidification front in the laser-induced molten pool (Figure 7.12). With increasing laser scan speed the advancing velocity of the heat-affected zone increases, leading to the formation of a mobile molten pool with a longer and narrower shape. Thus, the growing pores tend to incline to the scan direction of the laser beam more significantly (Figure 7.10a). This gives an interesting method in controlling pores characteristics; however, using an even higher scan speed (typically larger than 0.08 m/s) greatly decreases the duration of the laser beam at any irradiating zone, thereby shortening the lifetime of the present molten pool considerably. Consequently, the bubble nuclei have insufficient time to grow with the advancing solidification front, resulting in the breakage of the regularly

shaped microcellular pore structures (Figure 7.10b) and, thus, a decrease in the obtainable porosity of SLM-processed samples (Figure 7.11).

## 7.4 Conclusion

In the present study, SLM was applied to build the nanocrystalline TiC/Ti nanocomposite parts and the microcellular 316L stainless steel porous material parts, and the main conclusions were drawn as follows:

- (1) The densification rate of SLM-processed TiC/Ti nanocomposite parts remained above 97% using linear laser energy density  $\lambda \geq 600 \text{ J/m}$ . A decrease in  $\lambda$  lowered the densification level, due to the occurrence of a balling effect. The TiC reinforcing phase in SLM-processed parts had unique microstructures distinctly different from the initial nanoparticle morphology. A proper decrease in  $\lambda$  led to the formation of the uniformly dispersed nano-scale lamellar TiC reinforcement with a mean thickness of  $\sim 60 \text{ nm}$ . The maximum micro-hardness of the optimally processed TiC/Ti nanocomposites reached  $566 \text{ HV}_{0.2}$ . Due to the homogeneous incorporation of nanostructured TiC reinforcement, the SLM-processed parts had a low average COF of  $\sim 0.25$  and a reduced wear rate of  $\sim 4 \times 10^{-16} \text{ m}^3/(\text{Nm})$  during dry sliding tests. The insufficient SLM densification activity at a low  $\lambda$  and the disappearance of nanoscale TiC reinforcement at a high  $\lambda$  generally lowered the wear performance of SLM-processed TiC/Ti nanocomposite parts.
- (2) The regularly shaped microcellular stainless steel porous material with a homogeneous size distribution of micrometer scaled pores ( $2 \mu\text{m}$  in average) was successfully prepared using a SLM process, by adding 0.10 wt.% gas generating materials in the form of  $\text{H}_3\text{BO}_3$  and  $\text{KBF}_4$ . The adjustment of pore morphology, pore direction, and porosity was realized by changing material combinations (such as the content of additive materials) and processing conditions (such as the scan speed of the laser beam).

## 7.5 Future trends

Research on laser-based AM of metallic components is interdisciplinary: integrating materials science, metallurgical engineering, mechanical engineering, and laser technology. Significant research and understanding are still required in the aspects of materials preparation and characterization, process control and optimization, and theories of physical and chemical metallurgy for each AM process. Combined with the opinions proposed by other experts in AM research fields [1,8,24], the author has summarized the following issues that are of particular significance for future development of AM technology.

### 7.5.1 Development of novel materials and “Designed Materials”

The application of AM technology to prepare novel-structured high-performance functional components is of unique interest. The special processing procedure and highly nonequilibrium nature of AM favor the formation of bulk-form materials with unique microstructural and mechanical properties. Besides the nanocomposite material and porous material as investigated in the present work, laser-based AM technology provides a beneficial method to develop other new materials such as amorphous materials,

functionally gradient materials, and in situ composites materials. Laser AM offers a revolutionary approach for manufacturing “Designed Materials” with properties and functions that cannot be easily obtained by other conventional processes.

### **7.5.2 Establishment of an AM processes database**

Comprehensive knowledge is involved in AM processes, including laser technology, material science, powder metallurgy and rapid solidification. The suitable AM processing data for various metallic materials should be accumulated. Combined with the optimization in powder material design and preparation, the corresponding optimal AM processing parameters should be experimentally determined. After sufficient accumulation the material-process database can be established, realizing a simplified, precise, and stable control of AM treatment of versatile powder materials for industrial applications.

### **7.5.3 Microstructure development and metallurgical mechanisms**

AM processes offer a promising potential for the development of novel bulk-form materials of designed compositions, microstructures, and properties. However, due to the significant nonequilibrium nature of laser processing and the complicated mutual influence of material and process parameters, the unpredictability and/or uncontrollability of the formation of phases and microstructures in an AM route still remain as a major challenge. The underlying physical and chemical metallurgical mechanisms responsible for the variation of microstructural and mechanical properties should be determined in order to give a strong theoretical basis for AM processes. The theoretical study of the metallurgical thermodynamics and kinetic behaviors of the melt within nonequilibrium molten pools is of particular importance, including the mass transfer and fluid flow, crystal nucleation and growth, and the melting and mixing behavior of key alloying/additive elements enabling the microstructure to be tailored according to the local performance requirements of the components.

## **Acknowledgments**

The financial support from the National Natural Science Foundation of China (No. 51322509 and No. 51104090), the Outstanding Youth Foundation of Jiangsu Province of China (No. BK20130035), the Program for New Century Excellent Talents in University (No. NCET-13-0854), the Program for Distinguished Talents of Six Domains in Jiangsu Province of China (No. 2013-XCL-028), the Science and Technology Support Program (The Industrial Part), Jiangsu Provincial Department of Science and Technology of China, the Fundamental Research Funds for the Central Universities (No. NE2013103), and the Qing Lan Project of Jiangsu Provincial Department of Education of China is gratefully appreciated.

Reprinted from D.D. Gu, G.Q. Zhang, Virtual and Physical Prototyping 8 (2013) 11-18, Copyright (2013), with permission from Taylor & Francis; and Y.F. Shen, D.D. Gu, P. Wu, Materials Science and Technology 24 (2008) 1501-1505, Copyright (2008), with permission from Maney.

## References

- [1] J. Mazumder, D. Dutta, N. Kikuchi, A. Ghosh, Closed loop direct metal deposition: art to part, *Opt. Lasers Eng.* 34 (2000) 397–414.
- [2] J.P. Kruth, G. Levy, F. Klocke, T.H.C. Childs, Consolidation phenomena in laser and powder-bed based layered manufacturing, *CIRP Ann. Manuf. Technol.* 56 (2007) 730–759.
- [3] X. Wu, A review of laser fabrication of metallic engineering components and of materials, *Mater. Sci. Technol.* 23 (2007) 631–640.
- [4] B.C. Zhang, H.L. Liao, C. Coddet, Microstructure evolution and density behavior of CP Ti parts elaborated by self-developed vacuum selective laser melting system, *Appl. Surf. Sci.* 279 (2013) 310–316.
- [5] E.O. Olakanmi, Selective laser sintering/melting (SLS/SLM) of pure Al, Al-Mg, and Al-Si powders: effect of processing conditions and powder properties, *J. Mater. Process. Technol.* 213 (2013) 1387–1405.
- [6] L. Thijs, M.L.M. Sistiaga, R. Wauthle, Q. Xie, J.P. Kruth, J. Van Humbeeck, Strong morphological and crystallographic texture and resulting yield strength anisotropy in selective laser melted tantalum, *Acta Mater.* 61 (2013) 4657–4668.
- [7] D.D. Gu, Y.C. Hagedorn, W. Meiners, G.B. Meng, R.J.S. Batista, K. Wissenbach, R. Poprawe, Densification behavior, microstructure evolution, and wear performance of selective laser melting processed commercially pure titanium, *Acta Mater.* 60 (2012) 3849–3860.
- [8] M. Zhong, W. Liu, Laser surface cladding: the state of the art and challenges, *Proc. Inst. Mech. Eng. Part C J. Mech. Eng. Sci.* 224 (2010) 1041–1060.
- [9] J.P. Kruth, L. Froyen, J. Van Vaerenbergh, P. Mercelis, M. Rombouts, B. Lauwers, Selective laser melting of iron-based powder, *J. Mater. Process. Technol.* 149 (2004) 616–622.
- [10] D.D. Gu, Y.F. Shen, Balling phenomena in direct laser sintering of stainless steel powder: metallurgical mechanisms and control methods, *Mater. Des.* 30 (2009) 2903–2910.
- [11] M. Agarwala, D. Bourell, J. Beaman, H. Marcus, J. Barlow, Direct selective laser sintering of metals, *Rapid Prototyp. J.* 1 (1995) 26–36.
- [12] P.M. Ajayan, L.S. Schadler, P.V. Braun, *Nanocomposite Science and Technology*, Weinheim, Wiley-VCH, 2003.
- [13] V.V. Semak, G.A. Knorovsky, D.O. MacCallum, R. Allen Roach, Effect of surface tension on melt pool dynamics during laser pulse interaction, *J. Phys. D Appl. Phys.* 39 (2006) 590–595.
- [14] A. Simchi, H. Pohl, Direct laser sintering of iron-graphite powder mixture, *Mater. Sci. Eng. A* 383 (2004) 191–200.
- [15] K. Arafune, A. Hirata, Thermal and solutal Marangoni convection in In-Ga-Sb system, *J. Cryst. Growth* 197 (1999) 811–817.
- [16] D.D. Gu, Y.F. Shen, Influence of Cu-liquid content on densification and microstructure of direct laser sintered submicron W-Cu/micron Cu powder mixture, *Mater. Sci. Eng. A* 489 (2008) 169–177.
- [17] P. Fischer, V. Romano, H.P. Weber, N.P. Karapatis, E. Boillat, R. Glardon, Sintering of commercially pure titanium powder with a Nd:YAG laser source, *Acta Mater.* 51 (2003) 1651–1662.
- [18] Y.K. Guo, D.B. Li, Y. Zhou, X.M. Duan, Microstructure of ZrO<sub>2</sub>(2Y)/316L stainless steel composites, *Chin. J. Nonferrous Met.* 13 (2003) 963–967.
- [19] J. Deng, *Brazing*, China Machine Press, Beijing, 1979.
- [20] Y.F. Shen, D.D. Gu, Y.F. Pan, Balling process in selective laser sintering 316 stainless steel powder, *Key Eng. Mater.* 315–316 (2006) 357–360.

- [21] Y. Liu, Y.X. Li, H.W. Zhang, Fabrication of lotus-structured porous magnesium with GASAR process, *Acta Metall. Sin.* 40 (2004) 1121–1126.
- [22] Y. Liu, Y.X. Li, J. Wan, H.W. Zhang, Evaluation of porosity in lotus-type porous magnesium fabricated by metal/gas eutectic unidirectional solidification, *Mater. Sci. Eng. A* 402 (2005) 47–54.
- [23] Y. Liu, Y.X. Li, J. Wan, H.W. Zhang, Metal-gas eutectic growth during unidirectional solidification, *Metall. Mater. Trans. A* 37 (2006) 2871–2878.
- [24] I. Kelbassa, T. Wohlers, T. Caffrey, Quo vadis, laser additive manufacturing? *J. Laser Appl.* 24 (2012) 050101.

# Innovations in laser cladding and direct laser metal deposition

8

C. Leyens<sup>1,2</sup>, E. Beyer<sup>1,2</sup>

<sup>1</sup>Fraunhofer Institute for Material and Beam Technology (IWS) Dresden, Germany;

<sup>2</sup>Technische Universität Dresden, Dresden, Germany

## 8.1 Introduction

Laser-based material deposition has matured into a well-established industrial technique for precise coating deposition (cladding) as well as additive layer manufacturing (direct laser metal deposition). By means of dedicated nozzle systems, suitable process equipment as well as well-customized manufacturing strategies, the fabrication of both miniaturized and very large area/volume coatings (2D) and components (3D) is feasible. The technology has attracted more and more attention in various fields of application, such as aerospace, energy conversion, the oil and gas industry, medicine, and mechanical engineering in general. It can be used for prototyping, repair, and new parts production purposes. Currently, particular interest is focused on the 3D fabrication of components (additive layer manufacturing).

However, low energy efficiency of the process and comparably low deposition rates conflict profitability and thus limit possible applications, particularly in the area of 2D cladding. This underlines industry's enhanced striving for viable, cost-efficient laser-based processes that combine the indisputable quality advantages with acceptable economic and energy efficiency parameters.

Clearly, manufacturing of near-net-shape components in a layer-by-layer fashion offers a great potential for time and cost savings in comparison to conventional manufacturing technologies, such as casting, forging, and machining [1]. Moreover, innovative materials systems can be produced by gradually changing the chemistry of single layers, thus adjusting the materials composition to the desired component properties. Among others, additive layer manufacturing offers great opportunities regarding the following aspects, most of them are currently under extensive investigation:

- rapid manufacturing/tooling
- exclusive component design for function
- materials/components for function
- individualization for free (lot-size independency)
- complexity for free
- availability for free (on-demand production).

In additive layer manufacturing, quite a number of different process variants are used, which can be summarized in three generic types: powder-bed, powder-feed, and wire-feed processes (Table 8.1). Each process has its own attributes, such as deposition rate,

**Table 8.1 Classification of additive layer manufacturing processes**

ALM process route	Powder-bed		Powder-feed Laser beam	Wire-feed		
	Laser beam	E-beam		Laser beam	E-beam	Arc
Heat source	Major advantages	Part complexity Accuracy		Deposition rate Material quality		
	Major disadvantages	Part size Material quality		Deposition efficiency Deposition rate	Part complexity Accuracy	

Source: Ref. [1].

heat input, processing atmosphere, precision, accuracy, and efficiency of raw material usage, which will determine the most favorable method for specific applications [1]. Wire-feed processes have received less attention than powder-bed and powder-feed processes [2–4] so far; however, wire as feed stock material offers several advantages such as easy handling and reduced contamination [5,6]. Therefore, wire-based processes are currently experiencing increasing interest [2,7], particularly for aerospace components that are machined from costly and oxygen-attracting titanium alloys at a low fly-to-buy ratio.

## 8.2 Fundamentals of laser cladding and direct laser metal deposition

Laser-based surface coatings as well as the generation of complete parts are based on the reabsorption of added material in the laser-induced melt pool. The powder or wire material can be added either laterally or coaxially, the latter giving a higher degree of flexibility regarding workpiece movement; however, it requires a more complex and expensive cladding head. In the coaxial powder cladding head, the powder is pre-heated by the laser beam before being reabsorbed by the melt pool (Figure 8.1a). For wire-based processes, a coaxial laser head design requires a beam split unit that guides the laser beam around the wire center (Figure 8.1b). The wire is continuously fed into the melt pool. Preheating of the wire can be achieved by resistance heating.

After solidification of the melt pool, a strong metallurgical bond between the welding bead and the subjacent material and a dense structure is formed (Figure 8.2). Due to the high precision of the laser beam and its excellent localized energy distribution, only a very thin layer of the substrate is melted, thus leading to low dilution of work-piece material within the bead. Therefore, cladding properties are typically excellent starting from the very first layer on.

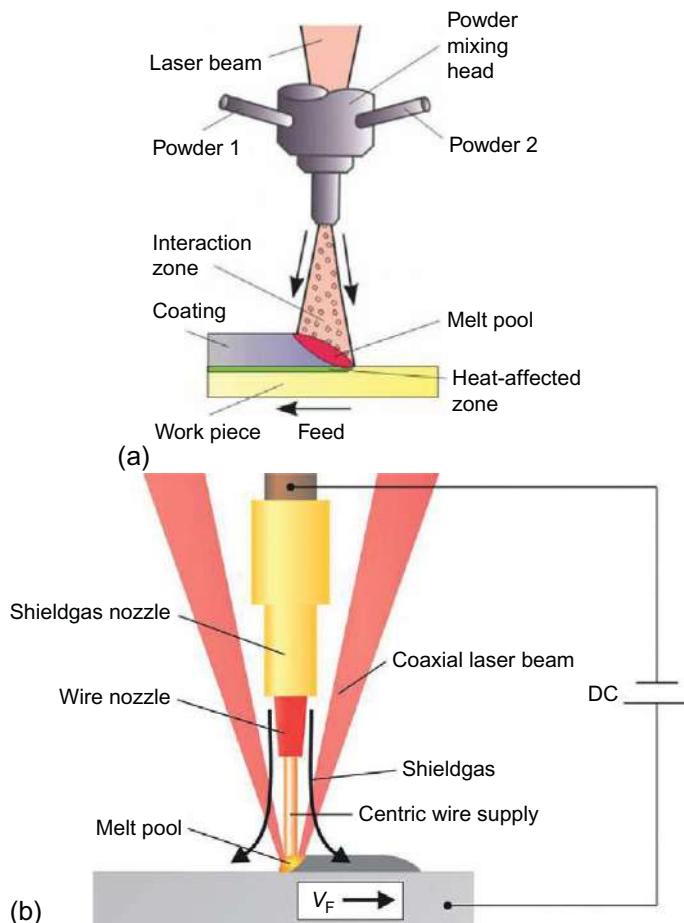


**Figure 8.1** Schematic of a powder-based (a) and wire-based (b) cladding process that can also be used for 3D additive layer manufacturing.

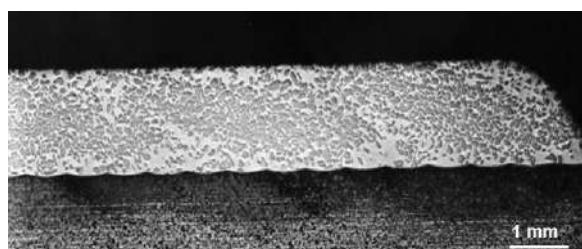


**Figure 8.2** Cross section through a WC/W<sub>2</sub>C+50% NiCrBSi clad showing excellent metallurgical bonding to the steel workpiece.

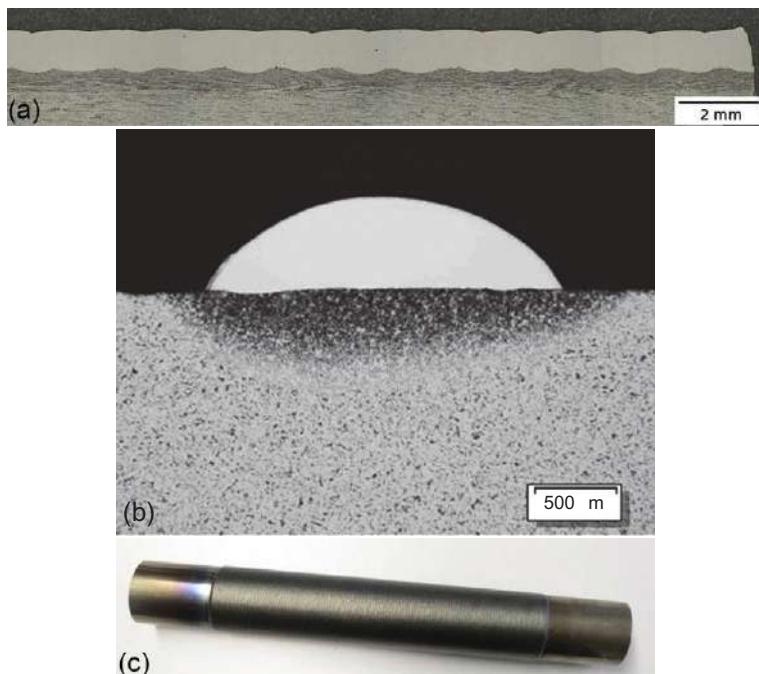


**Figure 8.3** Cross section of a hot-wire INCONEL 625 coating (a), corresponding single bead (b), and corresponding component (diameter 7 cm) (c). Waviness of the coating is  $R_z=63\text{ }\mu\text{m}$  (perpendicular to the beads) only.

In order to cover larger areas with the desired cladding material, an adequate number of welding beads are placed side by side with a certain overlap between single beads to reduce waviness and to ensure full coverage of the surface (Figure 8.3). When thick coatings or 3D build ups are required, material can be deposited layer by layer to achieve the desired thickness of the deposit.

Brandl *et al.* [1] published an extensive basic microstructural study on Ti-6Al-4V blocks fabricated by wire-based processing. The blocks show a morphology of columnar prior  $\beta$ -grains growing epitaxially across several deposition layers. Growth direction is opposed to the direction of heat flow. The microstructure contains layer bands that cannot be attributed to the single layers formed during block fabrication but represent the  $\alpha+\beta/\beta$  transus line. This finding is a clear indication of the importance of solidification and heat treatment conditions present during block formation. Postdeposition heat treatment in the temperature range between 600 and 1200 °C led to significant changes in microstructure and hardness, respectively. While low annealing temperatures led to significant reduction in hardness without any apparent microstructure changes, high temperature annealing was found to completely annihilate the as-built morphology and reduce hardness at the same time. The columnar  $\beta$ -grain morphology transformed into equiaxed grains, presumably as a result of a recrystallization process.

Quite obviously, materials properties of clads and 3D structures fabricated by laser-based processes depend on the specific deposition and postdeposition treatment conditions. Therefore, future progress in this area will strongly depend on the in-depth understanding of the interdependence between processing conditions and materials properties.

### 8.3 High precision 2D- and 3D-processing

For high precision 2D cladding and 3D processing, special nozzle designs are required that provide a precise powder focus (Figure 8.4). Today, minimum bead width is down to 30 µm; however, at the expense of low powder efficiency (typically below 10% as compared to 95% for “conventional” cladding and direct laser metal deposition). For high-precision deposition, a stable powder flow at low flow rate is required. In order to achieve the required geometric precision, a stable and accurate handling system (<10 µm accuracy) is necessary that is capable of highly dynamic workpiece movement. In this case, robot handling systems must be replaced by CNC machines. Due to the low powder flow rate, laser power of the order of 200 W is typically sufficient. However, high beam quality is mandatory, provided by modern disk and fiber lasers ( $M^2 \approx 1.1$ ). Low powder flow rates result in deposition rates as low as 16 g/h.

Despite these limitations in processing speed, delicate structures can be fabricated that currently find their way into applications. New market needs, for example, in the turbine industry and medical engineering, require efficient processing in the submillimeter range. Despite working in a narrow window of process parameters with lower powder efficiency compared to bigger melt-pool sizes, small geometries and structures can be generated quickly and reproducibly as shown in Figure 8.5.

Such filigree functional parts can be used for microimplants in medical technology (e.g., hearing aids that are individually fitted to human patients) or microtooling, rapid prototyping of microcomponents, metallic coding, or the improved stability of thermal barrier coatings (TBCs) for gas turbine applications. The latter is realized by a laser-cladded structure placed on a jet engine part to increase the clamping capability of the subsequently sprayed ceramic TBC [8].

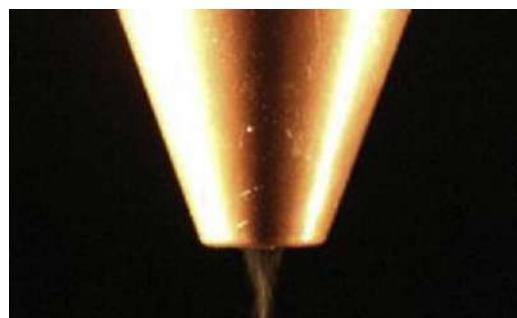
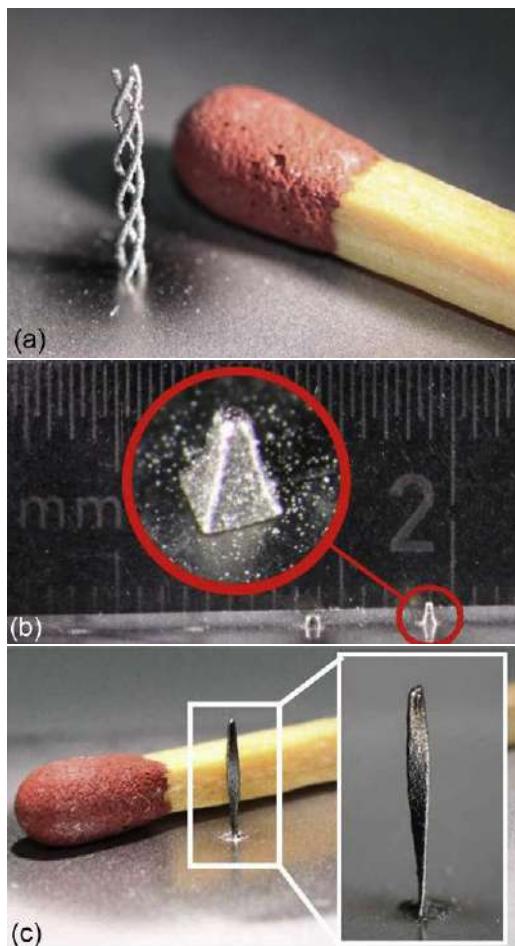
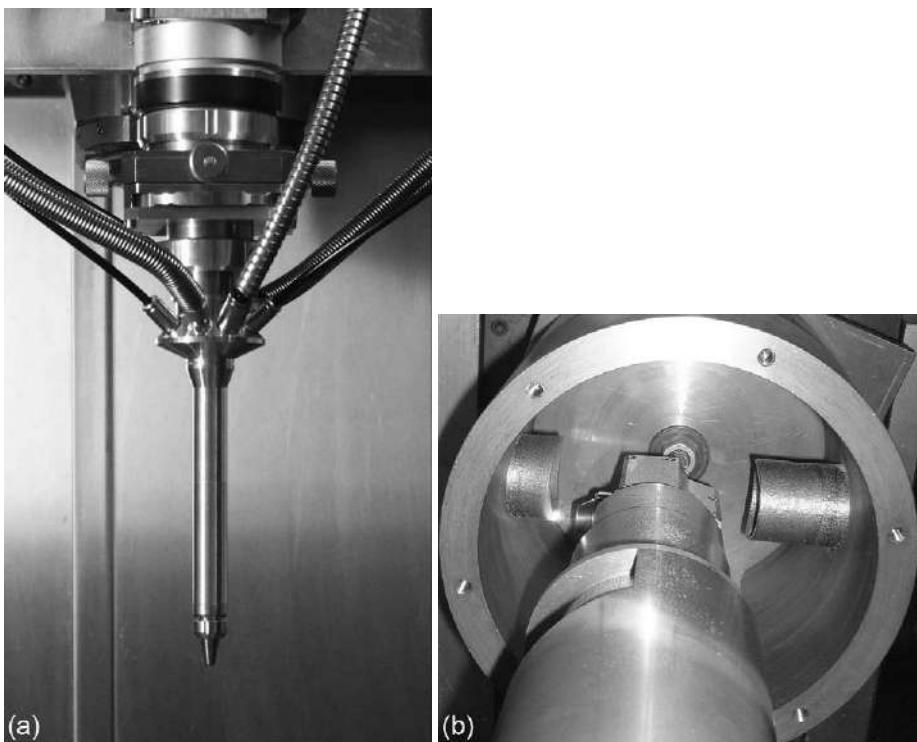


Figure 8.4 High-precision powder nozzle.



**Figure 8.5** (a) Triple-helix structure, (b) pyramid ( $0.5 \times 0.5 \times 1 \text{ mm}^3$ ), and (c) microblade fabricated by high-precision direct laser metal powder deposition.

Another emerging field in laser cladding and 3D direct laser metal deposition is parts fabrication and repair with restricted accessibility. For example, the generation or maintenance of airfoils is a great challenge, especially when processes are required for complete bisk geometries. To handle limited access, very slim nozzle designs are needed that are adapted to the specific application. [Figure 8.6a](#) shows one example of a long and slim nozzle design having an outer diameter of approximately 15 mm only. Further challenges are given regarding the cladding of inner diameters, such as those needed for the repair of (oil drilling) tools or the fabrication of inner structures of jet engine parts. Compared to conventional units for inner diameter (ID) claddings, an advanced multijet nozzle in the ID cladding unit enables the powder supply in any welding position. This allows omnidirectional movements needed, for example, for the generation of a tube in a tube ([Figure 8.6b](#)). Based on a modular concept, varying immersion depths of up to approximately 1 m with a diameter of approximately 10 cm are possible.



**Figure 8.6** (a) Slim nozzle design for improved accessibility; (b) buildup of inner tubes in a tube with the advanced ID cladding unit.

## 8.4 High productivity processing

Compared to a machine setup for cladding in the submillimeter range with a fiber laser source, the use of high-power laser systems with large melt-pool dimensions leads to strongly increased deposition rates. In this area, the earlier dominance of Nd:YAG and CO<sub>2</sub> laser sources is progressively reduced due to the availability of more efficient and cheaper diode laser sources that are currently available up to 15 kW. Especially large surface coatings, as well as the fabrication of modern metal matrix composites used in mining, oil and gas production, and tool and die making, require high-power setups.

However, the technology has so far proven insufficient in terms of deposition rates to coat large areas with protective and functional coatings such as clads for hydraulic cylinders. Industrial users desire the superior quality of the laser-produced coatings but also need high productivity and cost efficiency.

Currently, there are two practical solutions to address this challenge with modern laser and laser-hybrid technologies. The commercial availability of high-power diode lasers up to 10 kW has paved the way for significantly improved deposition rates.



**Figure 8.7** Flat-jet powder nozzle for high deposition rates.

#### **8.4.1 High-power laser cladding with flat-jet powder nozzles**

With the laser as the only energy source in combination with powder jet forming nozzles (Figure 8.7), it is possible to achieve deposition rates of 8-9 kg/h of INCONEL 625 corrosion protective coatings on large cylindrical components. A remarkable track width of more than 20 mm can be achieved using a specially designed flat-jet powder nozzle at 10 kW laser power [9]. This nozzle is currently limited to the use of metallic alloys such as Inconel, Stellite, steel, and bronze.

#### **8.4.2 Induction-assisted laser cladding**

The second approach for high deposition rates in laser cladding is based on hybrid processing. Therefore, a head was developed to integrate a module for additional inductive heating during the laser process (Figure 8.8). This hybrid technology concept further improves the deposition rate and the energy efficiency of the entire process; it is compatible with diode, fiber, and disc lasers. The localized inductive heating directly supports the laser beam and compensates heat losses, which leaves more laser energy to melt a larger amount of powder. As a result, deposition rates increase by a factor of 2-2.5. The coaxial nozzle designed for this application can handle a powder throughput of up to 18 kg/h. Typical practical deposition rates for INCONEL 625 are about 14-16 kg/h with the simultaneous application of 8 kW laser and 12 kW induction power.

Another potential application of this hybrid process is to use the induction coupling to modify coating strategies with tailored heat management. The additional heat leads to a significantly increased cooling time  $t_{8/5}$ , as well as to decreased spatial

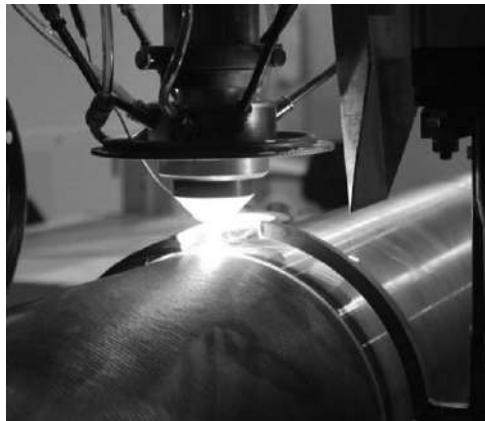


**Figure 8.8** Powder cladding head with full turn induction unit for cylindrical components.

temperature gradients ([Figure 8.9](#)). This configuration facilitates processing of crack free, ultrahard and wear-resistant metal alloys [10]. A good example is a protective coating made from Stellite 20 with a hardness exceeding 60 HRC.

The hybrid process also leads to substantial cost reduction of the technology. The specific investment costs for the required energy sources are reduced by 50% while the overall energetic efficiency of the process is doubled.

## 8.5 Process control

Both, laser cladding with a high precision as well as high deposition rates require a well chosen laser power to obtain a low dilution of substrate material in the coating and excellent resulting properties. Unfortunately, melting of substrate material might be significantly influenced by unstable heat flow into the workpiece during processing. This might occur due to substrate heating (especially in the case of small work-pieces), specific geometrical features of the components, as well as inconstant feed rates. Coating conditions can be kept steady by means of a camera-based process control. An integrated CCD camera, which is sensitive in the near infrared spectrum, records the melt pool coaxially using a coupling cube in the optics. Its band-pass filtered signal is transmitted to a PC where specially developed control software monitors information about temperature and size of the melt pool and calculates adjustments of the power, which are subsequently transferred to the laser source ([Figure 8.10](#)). For robust operation, the camera has to be calibrated before operation using a blackbody radiator.

The process control system can be used to maintain melt pool dimensions. Moreover, it can also be adapted to varying melt pool sizes while processing, as needed, for example, for the generation of turbine blades where outer regions require smaller dimensions compared to the middle section. Combined with an additional second z-axis, which is already integrated in the processing head, and

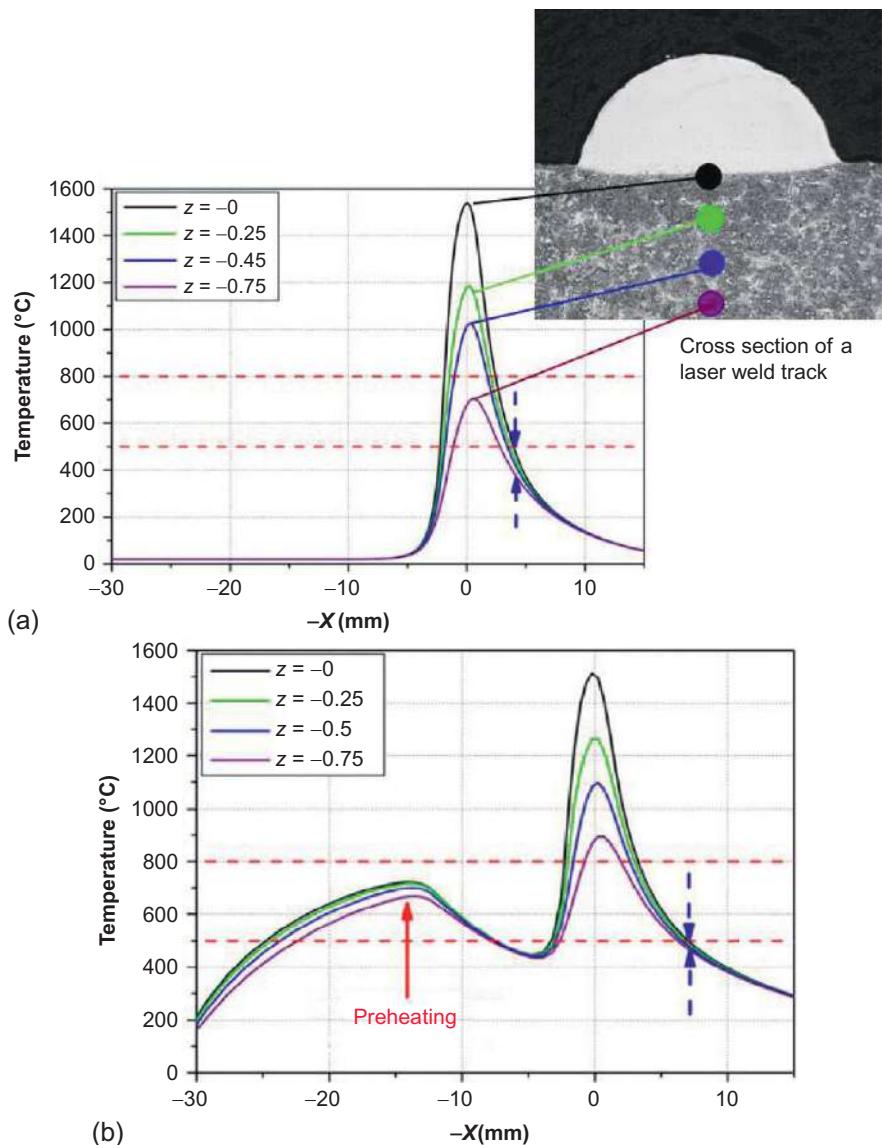
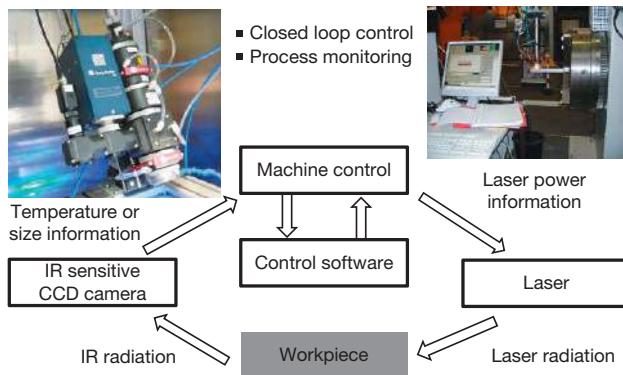


Figure 8.9 Temperature profile at laser cladding without (a) and with (b) inductive preheating.

a data set of the designated melt pool widths, which are backed up in the PC of the control software, the right laser power for varying melt pool sizes can be calculated and transmitted online to the laser source while processing. This online processing diagnostics tool provides invaluable information for complex processing conditions.



**Figure 8.10** General scheme of the camera-based closed loop control.

## 8.6 Conclusions and future trends

2D and 3D laser-assisted direct laser metal deposition has matured from laboratory to industrial scale. Major progress has been made in the areas of hardware components, process control, and understanding of process parameter-materials property relationships. Another important contributor to more widespread application of laser-based processing is the increased cost-effectiveness of the process by increasing deposition rates and thus processing times. Optimized solutions require in-depth knowledge of the process and the materials parameters. Laser cladding as the generic process for two-dimensional coating as well as three-dimensional buildup fabrication will be further improved in terms of precision and productivity as well as the materials selection available. Additive layer manufacturing will become a major driver in this area.

## Acknowledgments

The authors are grateful for valuable contributions from Dr. S. Bonß, Dr. F. Brückner, H. Hillig, T. Finaske, F. Kubisch, Prof. S. Nowotny, M. Riede, S. Scharek, and S. Thieme.

## References

- [1] E. Brandl, A. Schoberth, C. Leyens, Morphology, microstructure, and hardness of titanium (Ti-6Al-4V) blocks deposited by wire-feed additive layer manufacturing (ALM), Mater. Sci. Eng. A 532 (2012) 295–307.
- [2] E. Brandl, V. Michailov, B. Viehweger, C. Leyens, Deposition of Ti-6Al-4V using laser and wire, part I: microstructural properties of single beads, Surf. Coat. Technol. 206 (2011) 1120–1129.
- [3] W.U.H. Syed, A.J. Pinkerton, L. Li, A comparative study of wire feeding and powder feeding in direct diode laser deposition for rapid prototyping, Appl. Surf. Sci. 247 (2005) 268–276.
- [4] T.T. Wohlers, Wohler Report 2010, Wohler Associates, Fort Collins, Colorado, 2010.

- [5] C. Ader, M. Brosemer, C. Freyer, H. Fricke, D. Hennings, F. Klocke, V. Kühne, W. Meiners, C. Over, H. Pleteit, S. Stührmann, I. Wirth, T. Wirtz, K. Wissenbach, Free-form Fabrication Symposium, 26, 2004.
- [6] I.R. Pashby, S.H. Mok, J. Folkes, 23rd International Congress on Applications of Lasers and Electro-Optics, San Francisco (USA), 2004.
- [7] E. Brandl, V. Michailov, B. Viehweger, C. Leyens, Deposition of Ti-6Al-4V using laser and wire, part II: hardness and dimensions of single beads, *Surf. Coat. Technol.* 206 (2011) 1130–1141.
- [8] F. Brückner, S. Nowotny, M. Riede, E. Beyer, Herstellung hochpräziser metallischer 3D-Strukturen durch Auftragschweißen mit brillanten Strahlquellen, in: Proceedings of the International Symposium on Fiber and Disk Lasers, Dresden, 2010.
- [9] J. Tuominen, J. Latokartano, J. Vihinen, P. Vuoristo, T. Mäntylä, T. Naumann, S. Scharek, L. Berger, S. Nowotny, Deposition oft hick wear and corrosion resistant coatings by high power diode laser, in: B.R. Marple, M.M. Hyland, Y.-C. Lau, R.S. Lima, J. Voyer (Eds.), Proceedings of the 2006 International Thermal Spray Conference, ASM International, 2006.
- [10] F. Brückner, Modellrechnungen zum Einfluss der Prozessführung beim induktiv unterstützten Laer-Pulver-Auftragschweißen auf die Entstehung von thermischen Spannungen, Rissen und Verzug (Dissertation TU Dresden, 2011), Fraunhofer Verlag, Stuttgart, 2012.

# Laser-enhanced electroplating for generating micro/nanoparticles with continuous wave and pulsed Nd-YAG laser interactions

9

J. Lin, S.-H. Chen

National Cheng Kung University, Tainan, Taiwan

## 9.1 Introduction

In recent years, controlling the size, shape, and distribution of particles has become an important issue in particle formation with laser ablation [1–3]. Many attempts have been made to use laser ablation on solids, in liquids, or in gases for nanoparticle formations [4–7]. Because metallic nanoparticles can be easily formed by the electroplating method with stabilizers (stabilizing reagent) [8,9], in comparison with the electrochemical method, laser technology lacks the advantages of high production and low cost. The task of controlling the particle size by varying the electrode voltage and current density in electroplating has been investigated broadly [10–13]. Alternatively, many researchers have investigated ultrasonic effects on the formation of nanoparticles in the electroplating process [14–22]. Due to the stress wave induced by the ultrasound elements in the electroplating process, the nanoparticles can be formed without stabilizers, so the deposition efficiency can be raised due to the interference from the ultrasonic wave.

In the early days, Von Gutfeld *et al.* used CW Ar and Kr lasers focused on a confined region to enhance the electroplating deposition [23]. In their results, the particle diameter ranged from 4 to 600 µm with various laser powers and electrode voltages. The deposition rate increased with the laser interaction power, and since then the many possibilities of the laser-enhanced electroplating method have been shown in different applications [24–30]. However, the electrochemical effect on the nanocluster formation with laser interaction is not clear yet.

In this chapter, the formation of copper particles in laser-enhanced electroplating with continuous and pulsed laser output modes, respectively, are discussed. Due to the heating and pulsing effects on the laser interaction region on the cathode in the electroplating process [31], the copper nanoparticles could be produced. In order to characterize the process, the laser power absorbed by the electrolyte and the temperature of the electrode was evaluated. Furthermore the temperature fields of the impinging jet from the laser nozzle were simulated numerically.

### 9.1.1 Laser-enhanced electroplating method

The main device of the laser-enhanced electroplating system is illustrated in [Figure 9.1a and b](#). It includes a CW/Q-switched Nd-YAG laser (wavelength of 1064 nm) and a nozzle with an orifice diameter of 2.5 mm, as shown in [Figure 9.1a](#). In order to increase the transmittance of the laser beam in the electrolyte, the standoff distance from the head of the inner nozzle to the stainless steel cathode is

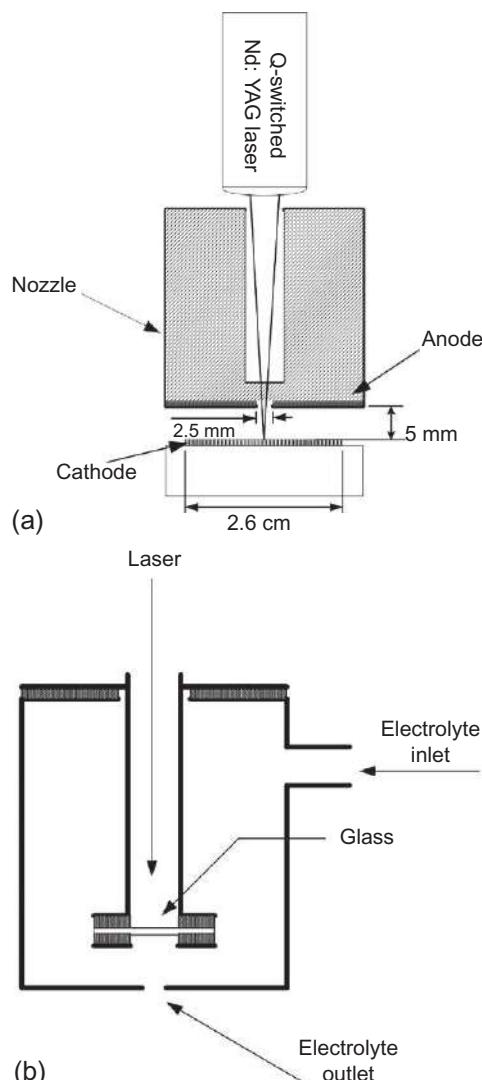


**Figure 9.1** (a) Laser-enhanced electroplating system; (b) the assembly of the nozzle.

reduced to 8 mm, and the standoff distance from the copper anode to the stainless steel cathode is about 5 mm in the present study, as illustrated in Figure 9.1. The laser is focused on the cathode to heat up a confined surface so as to raise the kinetic current and enhance the electrochemical reaction in the heating area. Using 0.05 M copper (II) sulfate liquid solution as electrolyte in the present study, the electroplating process has been made.

### 9.1.2 Mechanisms

From the electrochemical dynamics theory, we know that the increase in temperature will significantly affect the equilibrium potential, exchange current, and dynamic current [32]. The equilibrium potential is the electrode potential when the reaction is under an equilibrium state. The relation of the equilibrium potential among the temperature and concentrations of oxidizer and deoxidizer is expressed by the Nernst equation as Equation (9.1).

$$E = E^0 + \frac{RT}{nF} \ln \frac{[C_{\text{Ox}}^{\text{b}}]}{[C_{\text{Rd}}^{\text{b}}]} \quad (9.1)$$

where  $E$ : equilibrium potential (V);  $E^0$ : standard equilibrium potential (V);  $R$ : gas constant (J/mol K);  $T$ : absolute temperature (K);  $F$ : Faraday constant (96,500 C/mol);  $n$ : number of electron participated in reaction;  $C_{\text{Ox}}^{\text{b}}$ : bulk concentration of oxidant (M);  $C_{\text{Rd}}^{\text{b}}$ : bulk concentration of reductant (M).

In the  $\text{Cu}-\text{Cu}^{2+}$  electrochemical system, Equation (9.1) can be simplified as Equation (9.2) [32]:

$$E = E^0 + \frac{RT}{nF} \ln [\text{Cu}^{2+}]_{\text{bulk}} \quad (9.2)$$

where  $[\text{Cu}^{2+}]_{\text{bulk}}$  is the bulk concentration of copper ion (M).

In an equilibrium state, the exchange current can be expressed by Equation (9.3) [23,32]:

$$j_0 = \frac{nFk_bTC}{h} \exp \left[ -\frac{dG}{RT} \right] \exp \left[ \frac{-\beta nFE}{RT} \right] \quad (9.3)$$

where  $j_0$ : exchange current density ( $\text{A}/\text{m}^2$ );  $n$ : number of electron participated in the reaction;  $F$ : Faraday constant (96,500 C/mol);  $C$ : concentration of electrolyte (M);  $k_b$ : Boltzmann constant ( $1.381 \times 10^{-23}$  J/K);  $T$ : absolute temperature (K);  $h$ : Planck constant ( $6.626 \times 10^{-34}$  J s);  $\beta$ : electron transmission coefficient;  $E$ : equilibrium potential (V);  $dG$ : change of free energy in reaction (J).

According to Equations (9.2) and (9.3) with the process conditions selected in the present study, the equilibrium potential decreases with the increase in the process temperature and the exchange current increases with the process temperature.

In an irreversible reaction near the electrodes, the kinetic current of the electrode and the process overpotential can be expressed by the Butler-Volmer equation as follows:

$$j_k = j_0 \left\{ \left( \frac{C_{\text{Ox}}}{C_{\text{Ox}}^b} \right) \exp \left( \frac{-\beta nF}{RT} \eta \right) - \left( \frac{C_{\text{Rd}}}{C_{\text{Rd}}^b} \right) \exp \left[ \frac{(1-\beta)nF}{RT} \eta \right] \right\} \quad (9.4)$$

$$\eta = V - E - \eta_{\text{loss}} \quad (9.5)$$

where  $j_k$ : kinetic current density;  $j_0$ : exchange current density;  $C_{\text{Ox}}$ : local oxidizer concentration;  $C_{\text{Ox}}^b$ : total oxidizer concentration;  $C_{\text{Rd}}$ : local deoxidizer concentration;  $C_{\text{Rd}}^b$ : total deoxidizer concentration;  $\beta$ : electron transmission coefficient;  $n$ : number of the electron participating in reaction;  $F$ : Faraday constant;  $R$ : gas constant;  $T$ : electrolyte temperature;  $\eta$ : surface overpotential;  $\eta_{\text{loss}}$ : the loss of the overpotential caused by the polarization of concentration.

It can be found that the overpotential and the kinetic current increase at high temperatures, and therefore, the reaction moves toward an irreversible deposition process with the laser heating in the present study and a limit current of the process achieved under certain conditions [33].

## 9.2 Experimental setup

The electroplating setup consists of a pump, flow meter, nozzle, and electroplating cell, as illustrated in Figure 9.2. In the experiments, an Nd-YAG laser with a pulse width of 90 ns in the repetition rate of 2 kHz and 304 stainless steel substrates have been used. The original surface contour of the stainless steel substrate is shown in Figure 9.3. It can be found that the micrograins are uniformly distributed with clear boundaries. The initial flow temperature was controlled at the room temperature of 25 °C. The cathode temperatures with various laser input powers at the interaction zone have been measured by a thermocouple attached on the stainless steel substrate (thickness of 0.08 mm), and the results are listed in Table 9.1. It can be found that the maximum cathode substrate temperature increases with the laser power. Alternatively, a laser power meter measured the absorptivity of the laser beam through the electrolyte without the stainless steel substrate, as shown in Figure 9.2b. The remaining power from the power meter at various flow rates is shown in Figure 9.4. Accordingly, the average absorptivity of the electrolyte flow at 0.5 L/min is about 21% with the laser beam through a flow depth of 8 mm. Alternatively, with an increase of the flow rate to 1.0 L/min, the average absorptivity is about 25%. Based on the absorptivity measurement, the rise of the laser absorptivity at a high flow rate might be caused by the increase in the cooling rate in the electrolyte flow with a considerable drop of the flow temperature. Furthermore, in comparison with the experimental results of the substrate temperature in the laser interaction zone, a similar trend can be found between the experiments and the simulation results of the electrolyte flow temperature at various laser input powers, as shown in Figure 9.5.

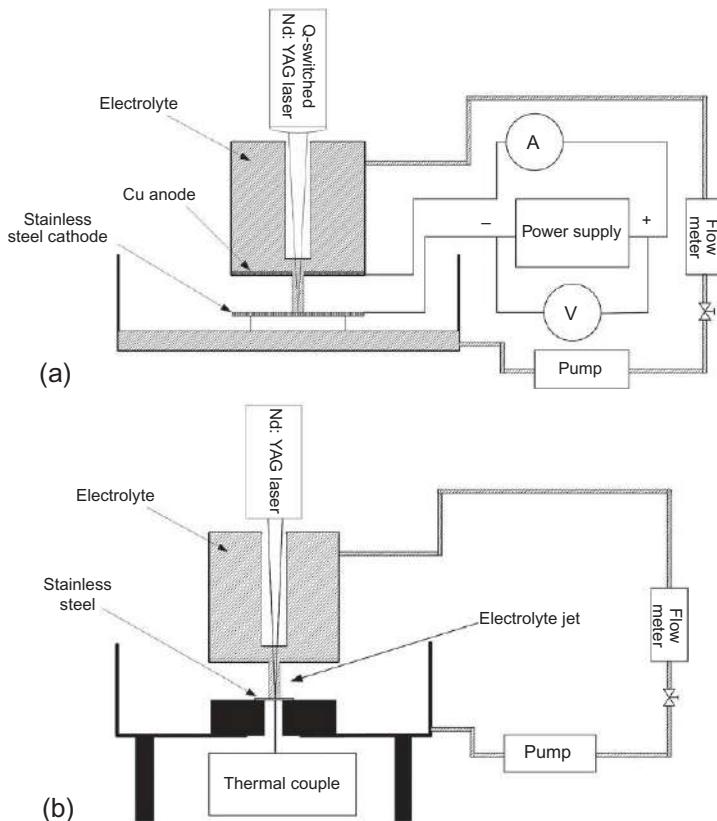


**Figure 9.2** Experimental setups for (a) laser-enhanced electroplating process; (b) laser power measurement.

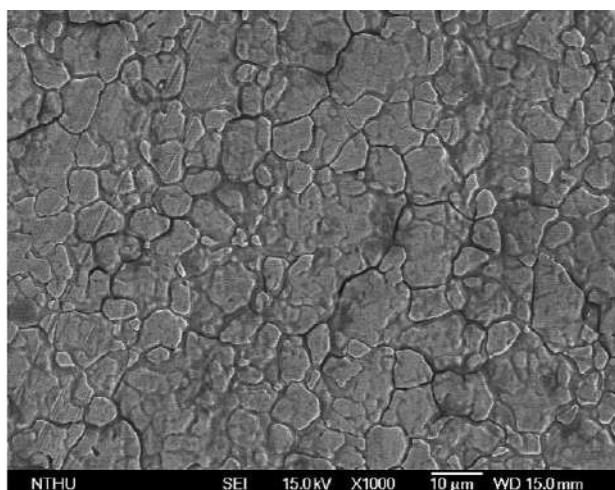


**Figure 9.3** Surface profile of the stainless steel substrate before processing.

**Table 9.1 Temperature rise of the stainless steel substrate with various laser input powers near the interaction zone**

Laser incident power (CW) (W)	Maximum cathode temperature rise (°C)
2.5	6
5	20
7.5	26

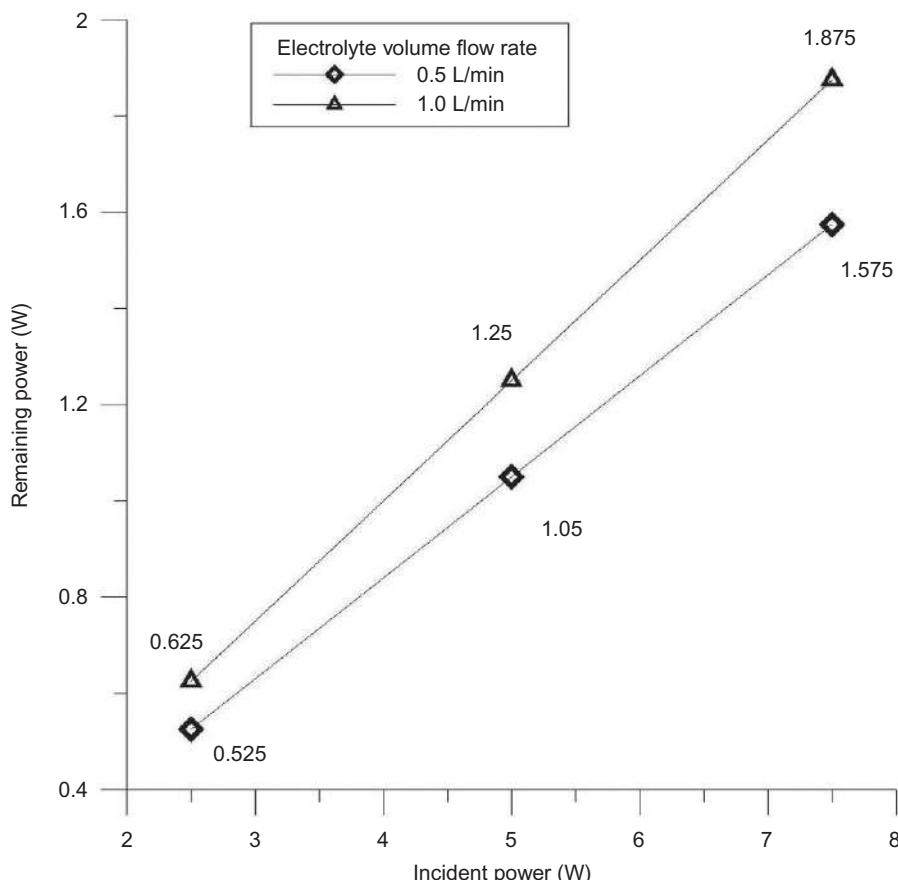


**Figure 9.4** Laser power absorptions at various flow rates with a CW laser interaction.

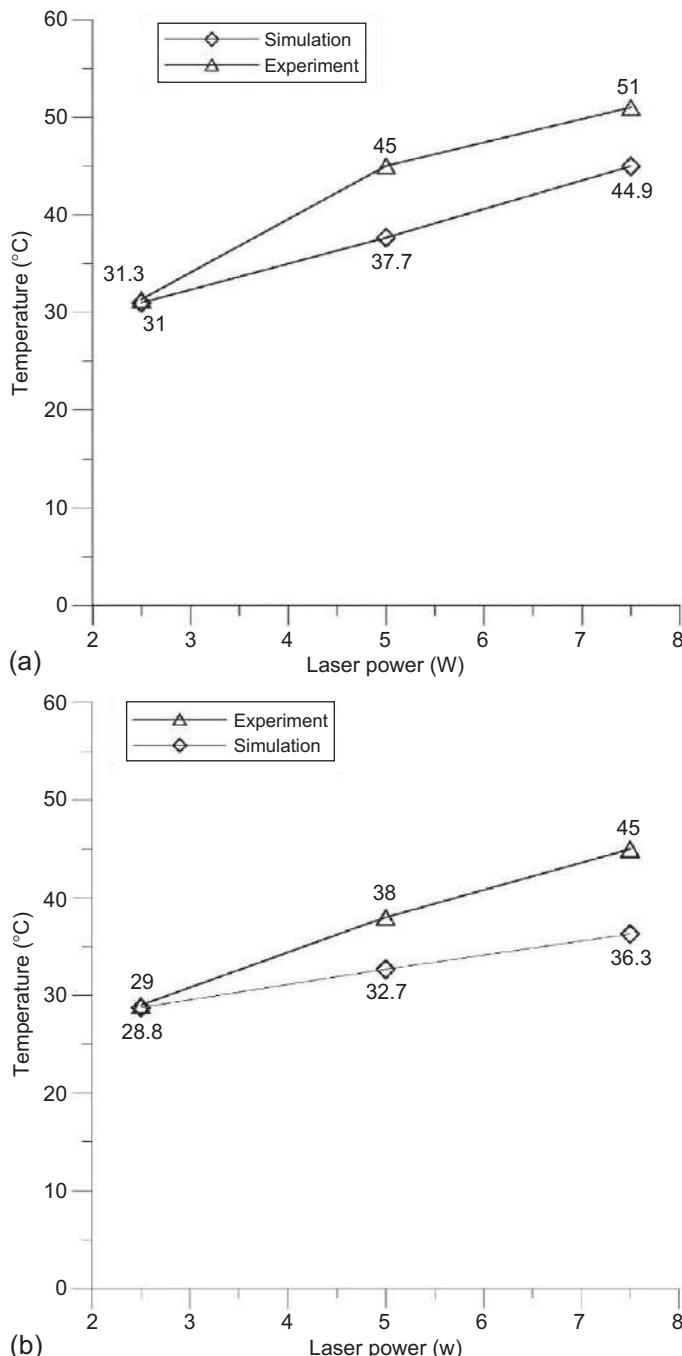


**Figure 9.5** Numerical and experimental results of the peak temperatures at the laser interaction zone at various flow rates of (a) 0.5 L/min and (b) 1.0 L/min.

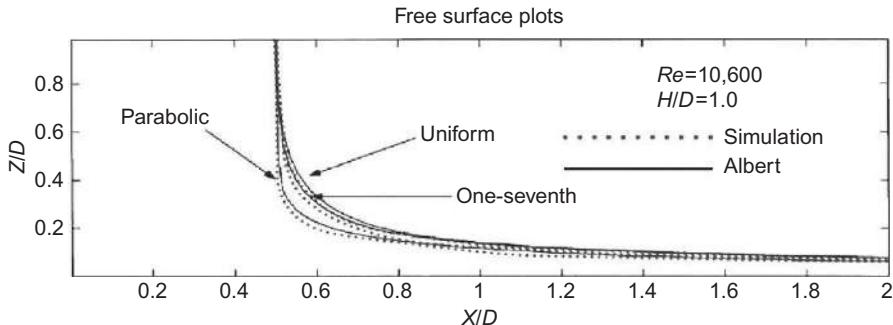


**Figure 9.6** Numerical results of the free surfaces of the impinging water jet in comparison with Albert's results [35].

### 9.2.1 Numerical simulation

The simulation of the electrolyte jet temperatures has been made by the FLUENT software [34] and a testing case has been adopted to evaluate the accuracy of the computation. Based on the results of the Albert's simulation [35] for an impinging water jet, a similar computation domain with various meshed grids was selected and the same assumptions were made. As shown in Figure 9.6, the free surfaces of the impinging jet were plotted with various inlet velocity profiles such as uniform, parabolic, and one-seventh order forms [35]. Because there is a good agreement between the FLUENT simulation and the referred results, the selected domain mesh is acceptable for the similar flow analysis in the present study. Furthermore, the computation domain for the electroplating system is illustrated in Figure 9.7 with a CW laser beam heating. Various laser input powers have been adopted to simulate the temperature fields of the water jet in a confined laser-substrate interaction zone.

## 9.3 Results and discussion

According to the boundary conditions as listed in Table 9.2, the basic assumptions adopted in the numerical simulation include a 2D axi-symmetric steady-state flow with a diameter of 0.3 mm beam spot of Gaussian intensity mode at the wall center, and the inlet velocity profile of the one-seventh order form. The initial flow temperature is 25 °C. Neglecting the laser absorption and electrochemical current effects in the jet flow, but considering the laser absorption on the substrate from the experimental measurement, the computational results of the water flow temperatures along the heating wall with various total laser input powers of 2.5, 5, and 7.5 W at flow rates of 0.5 and 1.0 L/min, respectively, are shown in Figure 9.8. It can be found that with a total laser power input of 7.5 W, the peak temperature at the center of the beam spot rises to 44.9 °C at the absorbed laser power of 1.575 W (absorptivity of 21%) and flow rate of 0.5 L/min. Furthermore, with the absorbed laser power of 1.825 W (absorptivity of 25%) and flow rate of 1.0 L/min, the peak temperature drops to 36.3 °C.

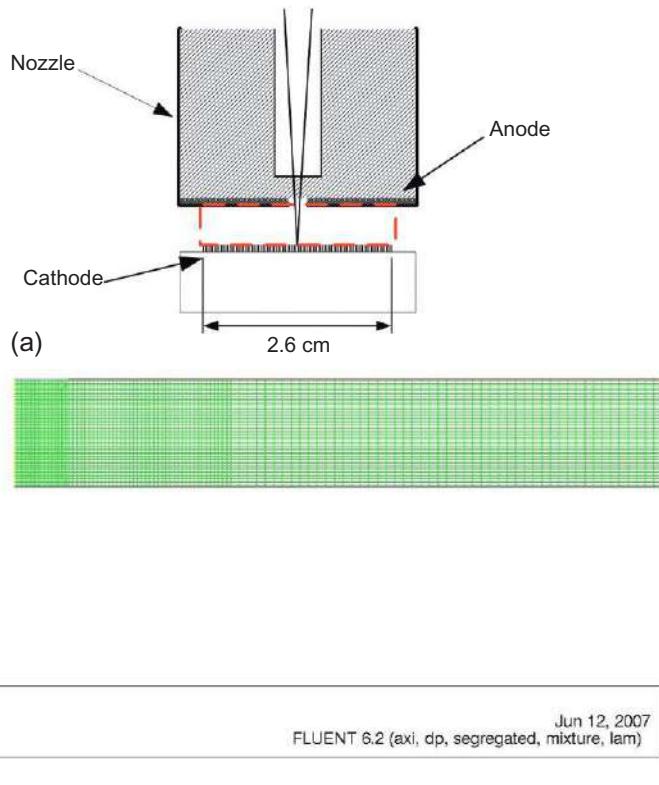


**Figure 9.7** (a) Computation domain; (b) axi-symmetric meshed grids in the present study.

**Table 9.2 Boundary conditions of the simulation of the impinging water jet with laser heating**

Boundaries	Conditions
Inlet velocity profile	$u(r) = 1.22459 u_0 \left(1 - \frac{r}{R_n}\right)^{1/7}$ where $u_0 = 1.6977, 3.3954$ m/s for the flow rate of 0.5 and 1.0 L/min respectively; $r$ is the distance to the laser beam center; $R_n$ is the radius of the nozzle exit
Input laser intensity in the interaction zone	heat flux = $\frac{I_0 \cdot La}{\pi R_l^2} \exp\left(-\frac{r^2}{R_l^2}\right)$ where $I_0$ is the laser input power [W]; La is laser absorptivity at the substrate-flow interface, and determined by experiments; $R_l$ is the radius of the laser beam spot

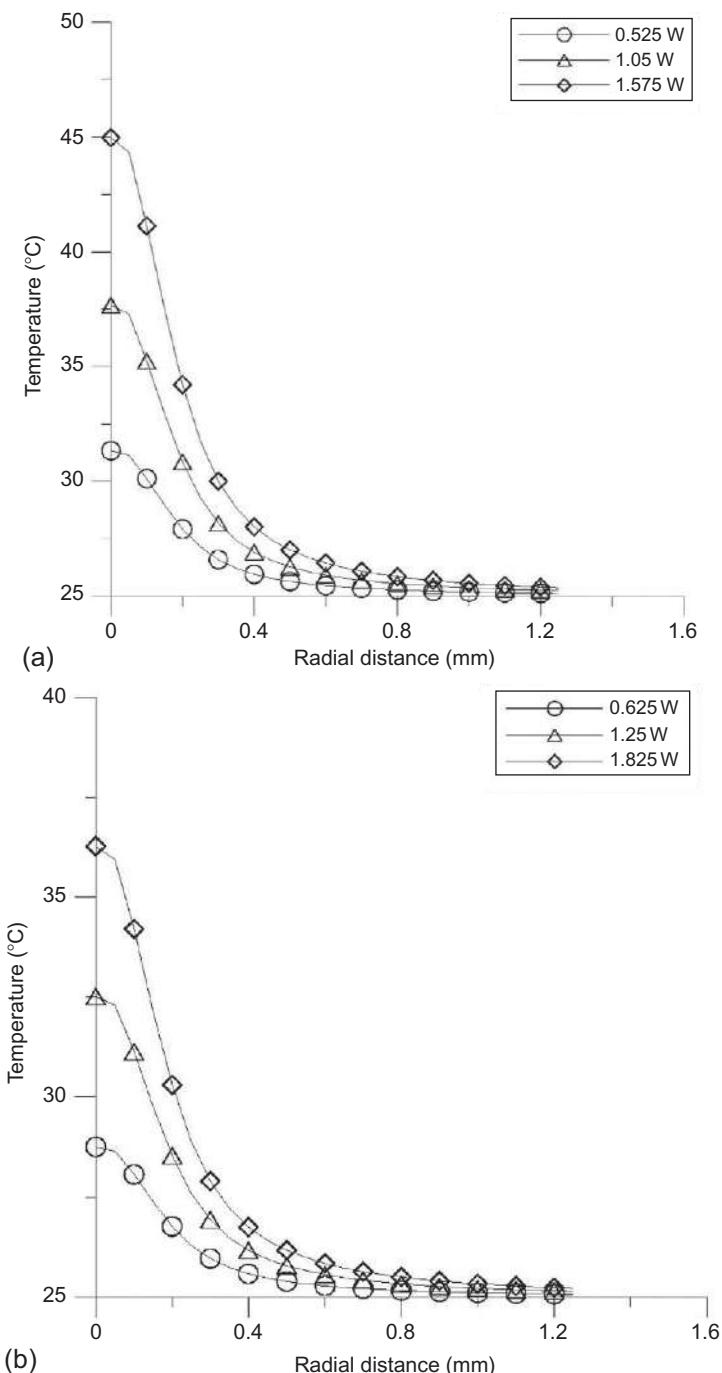


**Figure 9.8** Temperature profiles along the interaction zone at various absorbed laser intensities (a) 0.5 L/min and (b) 1.0 L/min.

The process parameters based on various output modes, laser powers, and irradiation times in the copper particle formation with continuous and pulsed laser modes are tested and listed in [Table 9.3](#). [Figure 9.9a](#) shows the copper particles generated with a CW laser irradiation at 2.5 W (case A) and a group of the microscale copper particles approximately ranged from 4 to 20  $\mu\text{m}$  has been produced at this condition. However, with the increase of the irradiation laser power from 2.5 to 5.0 W, the amount of the particles is increased significantly, as shown in [Figure 9.9b](#). [Figure 9.10](#) is the enlarged image of [Figure 9.9b](#); it can be found that the microscale particles were formed with a leaf shape and mainly accumulated in the grain boundaries of the stainless steel substrate. Alternatively, as shown in [Figure 9.11](#), with a

**Table 9.3 Process parameters of the copper particle formation with continuous and pulsed laser modes**

	Case A	Case B	Case C
Laser output mode	Continuous	2 kHz Q-switched	2 kHz Q-switched
Laser power	2.5, 5.0 W	2.5, 5.0 W	2.5, 5.0 W
Flow rate	0.5 L/min	0.5 L/min	0.5 L/min
Electrode voltage	0.825 V	0.825 V	0.825 V
Processing time	180 s	180 s	30 s

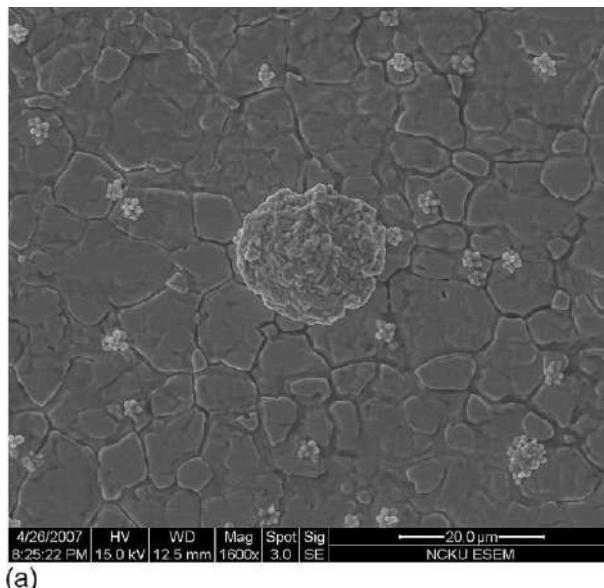
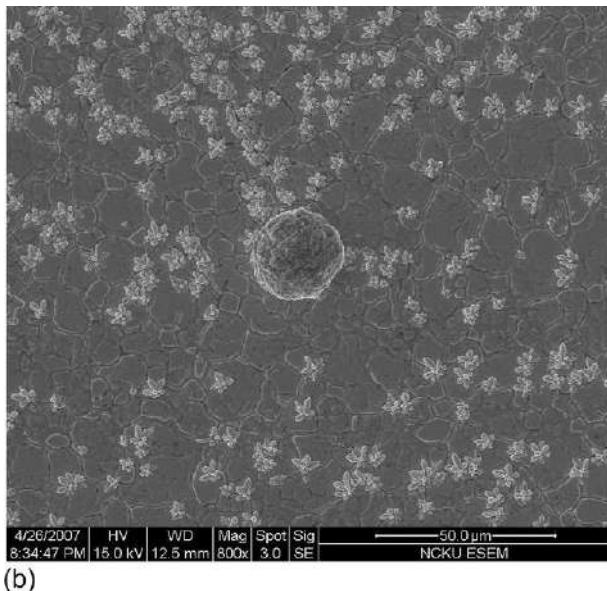


**Figure 9.9** (a) Copper particles generated with a CW 2.5 W laser interaction (case A).

*(Continued)*



(b)

**Figure 9.9** Continued. (b) Copper particles generated with a 5.0 W CW laser interaction (case A).

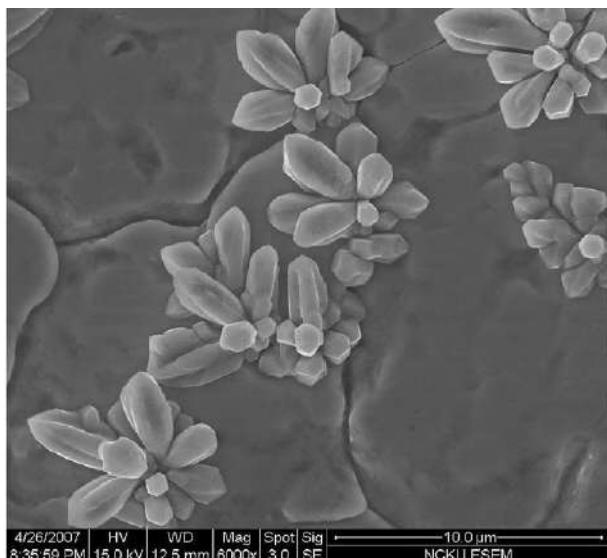


**Figure 9.10** Enlarged image of the copper particles generated with a 5.0 W CW laser interaction (case A).

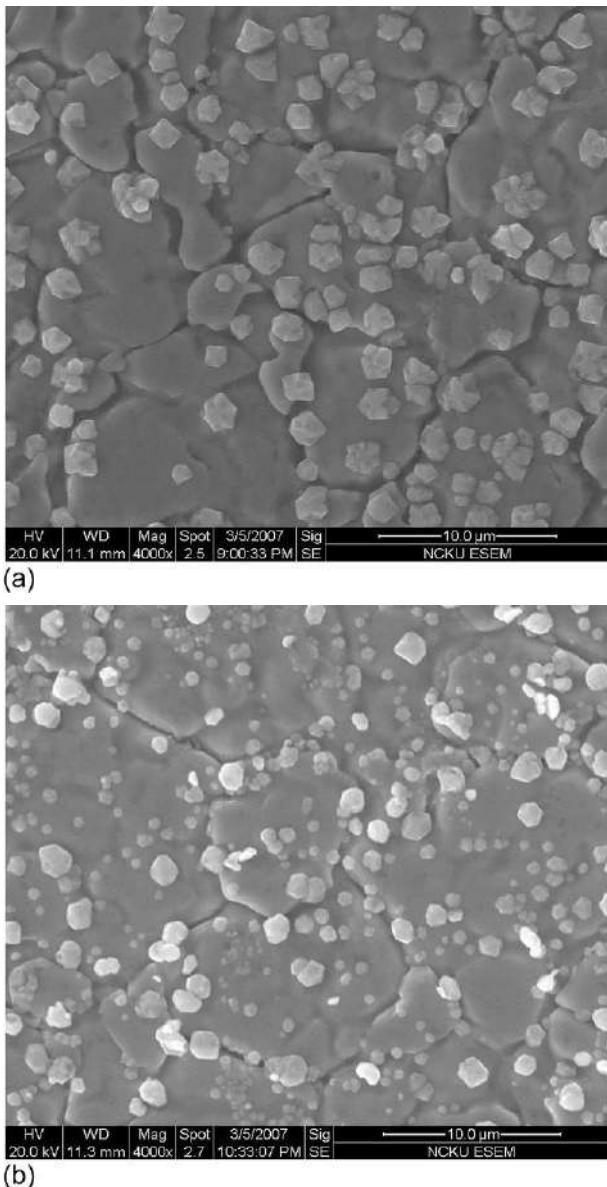


**Figure 9.11** (a) Copper particles generated with a 2.5 W Q-switched laser interaction in 180 s (case B). (b) Copper particles generated with a 5.0 W Q-switched laser interaction in 180 s (case B).

Q-switched laser interaction at average powers of 2.5 and 5.0 W within 180 s respectively (case B), the copper nanoparticles grow with an increase of the laser power interaction. Based on the above observations, it can be concluded that the pulsing stress due to the phase change of the electrolyte jet on the irradiation zone from the Q-switched laser may significantly interrupt the growth of microscale particles in the electroplating process.

As observed in the testing cases above, with a pulsed laser interaction the particles rapidly grow to the nanoscale. The results shown in Figures 9.12 and 9.13 are typical distributions of the number density and the particle diameter with a Q-switched laser interaction in 30 s. As shown in the selected region of Figure 9.12, the particle size distributes from 150 to 350 nm at an average laser power of 2.5 W, and 50 to 400 nm for the selected region of Figure 9.13 at an average laser power of 5.0 W. It can be found that the nanoparticles are mainly formed in a short period of time with pulsed laser interaction. In comparison with Figure 9.11 for Q-switched laser interactions at a long time period, a large amount of the copper particles grow to the microscale range with the increase of the interaction time, but only a very few newly formed particles are in the nanoscale range. Therefore, the formation of the nanoclusters is significantly interrupted with the Q-switched laser mode due to the laser pulsing stress at a high peak power in the present study.

Furthermore, the particles have been inspected by the energy dispersive spectrometer (EDS) method to verify the composition. Figures 9.14 and 9.15 are the typical EDS results about the elements of the copper particles formed on the 304 stainless steel substrate. It can be found that the main portion of compositions of the micro/nanoparticles is copper, but with a small amount of iron and chromium elements coming from the background of the stainless steel substrate.

According to the studies of the laser ablation on solid targets, in liquids and gases with CW, and pulsed laser interactions, it can be found that the liquid solution mainly affects the cooling and stabilizing conditions on the nanoparticle formation via plasmon resonance phenomena [4,5]. In comparison to the pulsed laser ablation process with gas [6], the particle size is sufficiently large in liquids [4]. However, with a high-power CW laser interaction on a metal target in liquid solution or water, various metals, alloys, or metaloxide nanoparticles could be directly generated from the metal target or the surrounding liquids, due to a large amount of heat accumulation from the laser-induced plasma on the target [5,7]. In contrast to the mechanism of the laser ablation processes, the laser-enhanced electroplating method is based on the electrochemical dynamics to reduce the metal ion of the electrolyte into fine particles with the electrical current input. The laser power mainly heats up the electrolyte to trigger the electroplating process with CW and pulsed laser interactions in the present study. Furthermore, the size control of particle formation could be significantly improved with the stress wave generated in a short-pulsed laser radiation. The aggregations of the particle could be limited in the nanoscale range.

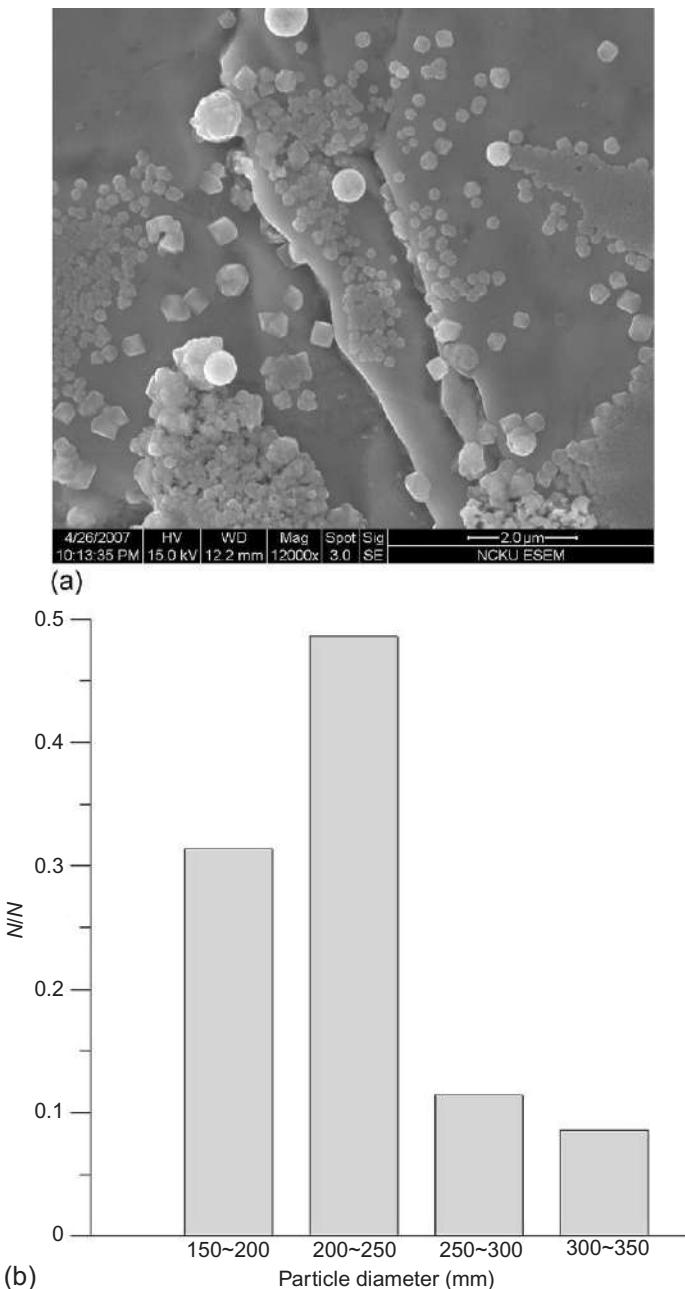


**Figure 9.12** (a, b) Particle distribution with a 2.5 W Q-switched laser interaction in 30 s (case C).

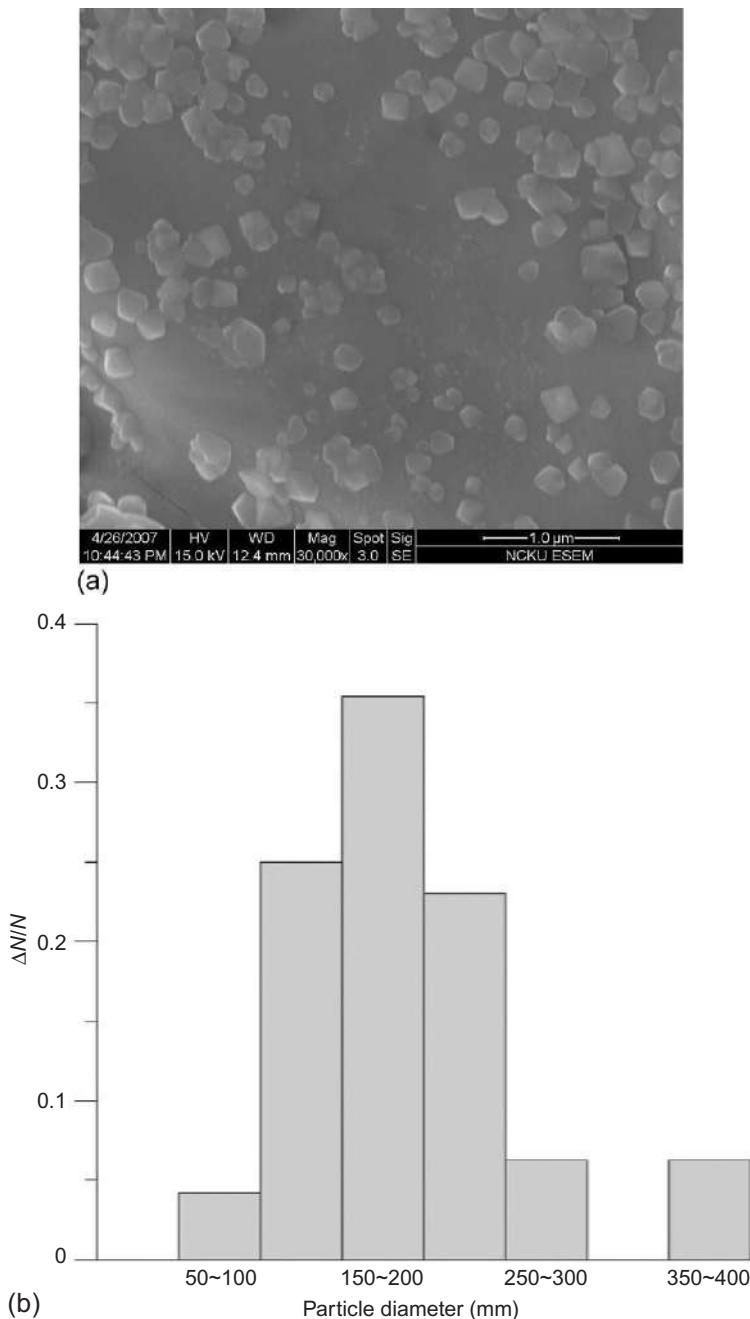


**Figure 9.13** (a, b) Particle distribution with a 5.0 W Q-switched laser interaction in 30 s (case C).

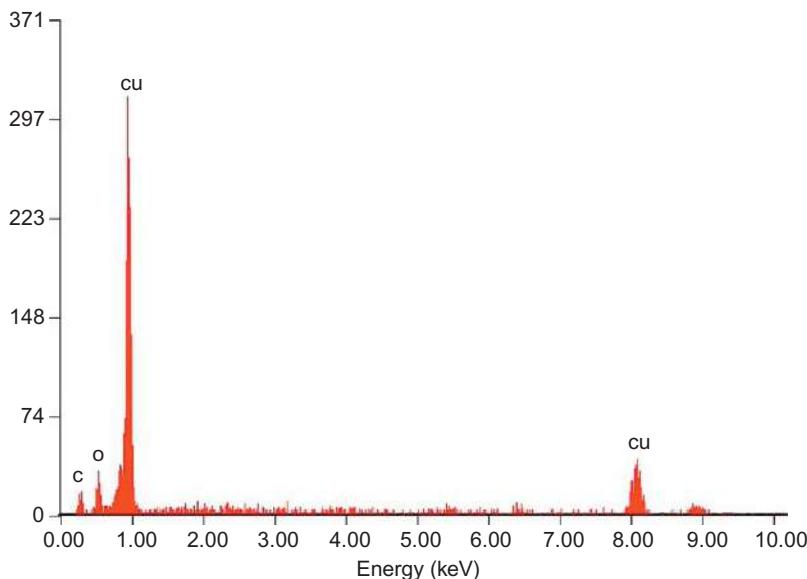


Figure 9.14 Typical EDS results of the copper particles (case A).

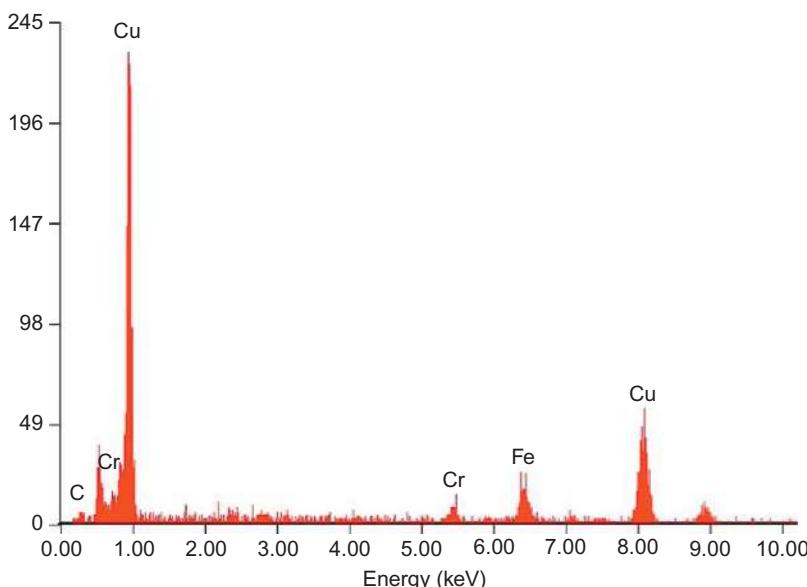


Figure 9.15 Typical EDS results of the copper particles on the 304 stainless steel substrate (case C).

## 9.4 Conclusions

The micro/nanoscale copper particles have been successfully generated by the proposed laser-enhanced electroplating method at various process conditions. With both CW and Q-switched Nd-YAG laser output modes, the copper particle size can be produced from micro- to nanoscales. According to numerical simulation of the flow temperature and the micrographs of the copper particles in the experiments, it shows that the proposed technique generates nanoparticles mainly due to the heating and pulsing effects with a short-pulse laser interaction time of 30 s. The laser energy absorbed by the electrolyte jet and the temperature rise of the electrode during the laser radiation has been examined and the temperature rise of the impinging jet at the laser interaction zone significantly affects the distributions of the particle size. From the experimental observations, copper nanoparticles ranged from 50 to 400 nm generated by Q-switched Nd-YAG laser-enhanced electrochemical method at various laser power inputs from 2.5 to 5.0 W, and this method is successfully applied for producing nano-scale copper particles with the pulsed laser interactions.

## Acknowledgment

This work is sponsored by the NSC (Taiwan) under the grant number NSC97-2212-E-006-227, and part of the contents has been published in the Optics and Lasers Technology.

## References

- [1] W.M. Steen, *Laser Material Processing*, Springer, Berlin, 2001, pp. 255–256.
- [2] H.G. Rubahn, *Laser Applications in Surface Science and Technology*, Wiley, 1999.
- [3] E. Ozawa, Y. Kawakami, T. Seto, Formation and size control of tungsten nanoparticles produced by Nd:YAG laser irradiation, *Scr. Mater.* 44 (2001) 2279–2283.
- [4] F. Mafuné, J.Y. Kohno, Y. Takeda, T. Kondow, H. Sawabe, Formation and size control of silver nanoparticles by laser ablation in aqueous solution, *J. Phys. Chem. B* 104 (2000) 9111–9117.
- [5] D. Poondi, T. Dobbins, J. Singh, A novel laser-liquid-solid interaction technique for synthesis of silver, nickel and immiscible silver-nickel alloys from liquid precursors, *J. Mater. Sci.* 35 (2000) 6237–6243.
- [6] J.H. Jang, J.M. Lin, An investigation of the synthesis of metallic nanoparticles by laser ablation, *Surf. Coat. Technol.* 202 (2008) 6136–6141.
- [7] Z. Liu, Y. Yuan, S. Khan, A. Abdolvand, D. Whitehead, M. Schmidt, L. Li, Generation of metal-oxide nanoparticles using continuous-wave fibre laser ablation in liquid, *J. Micro-mech. Microeng.* 19 (2009) 1–7.
- [8] T.R. Manfred, H. Wolfgang, Size-selective synthesis of nanosturctured transition metal clusters, *J. Am. Chem. Soc.* 116 (1994) 7401–7402.

- [9] M.T. Reetz, M. Winter, R. Breinbauer, T.A. Thomas, W. Vogel, Size-selective electrochemical preparation of surfactant-stabilized Pd-, Ni- and Pt/Pd colloids, *Chem. Eur. J.* 7 (2001) 1084–1094.
- [10] K. Motoi, S. Makoto, Electrochemical reaction of Zn in water and growth of ZnO particles, *J. Electrochim. Soc.* 144 (1997) 809–815.
- [11] B. Allen, C. Chang, Effects of electroplating variables on composition and morphology of nickel-cobalt deposits plated through means of cyclic voltammetry, *Electrochim. Acta* 47 (1997) 3447–3456.
- [12] S.O. Tim, A. Plamen, A.B. Dmitri, Electrodeposition of gold particles on aluminum substrates containing copper, *J. Phys. Chem. B* 109 (2005) 1243–1250.
- [13] B.J. Murray, Q. Li, J.T. Newberg, E.J. Menke, J.C. Hemminger, R.M. Penner, Shape and size-selective electrochemical synthesis of dispersed silver(I) oxide colloids, *Nano Lett.* 5 (2005) 2319–2324.
- [14] Z. Junjie, S.T. Aruna, K. Yuri, A. Gedanken, A novel method for the preparation of lead selenide-pulse sonoelectrochemical synthesis of lead selenide, *Chem. Mater.* 12 (2000) 143.
- [15] Y.C. Liu, L.H. Lin, W.H. Chiu, Size-controlled synthesis of gold nanoparticles from bulk gold substrates by sonoelectrochemical methods, *J. Phys. Chem. B* 108 (2004) 19237–19240.
- [16] S. Liu, W. Huang, S. Chen, S. Avivi, A. Gedanken, Synthesis of X-ray amorphous silver nanoparticles by the pulse sonoelectrochemical method, *J. Non Cryst. Solids* 283 (2001) 231–236.
- [17] Y. Socol, O. Abramson, A. Gedanken, Y. Meshorer, L. Berenstein, A. Zaban, Suspensive electrode formation in pulsed sonoelectrochemical synthesis of silver nanoparticles, *Langmuir* 18 (2001) 4736–4740.
- [18] Y.C. Liu, L.H. Lin, New pathway for the synthesis of ultrafine silver nanoparticles from bulk silver substrates in aqueous solutions by sonoelectrochemical methods, *Electrochim. Commun.* 6 (2004) 1163–1168.
- [19] J. Chen, S. Yao, Synthesis and characterization of silver nanoparticles by sonoelectrodeposition, *Rare Met.* 24 (2005).
- [20] I. Haas, S. Shanmugam, A. Gedanken, Pulsed sonoelectrochemical synthesis of size-controlled copper nanoparticles stabilized by poly(*N*-vinylpyrrolidone), *J. Phys. Chem. B* 110 (2006) 16947–16952.
- [21] H. Lei, Y.J. Tang, J.J. Wei, J. Li, X.B. Li, H.L. Shi, Synthesis of tungsten nanoparticles by sonoelectrochemistry, *Ultrason. Sonochem.* 14 (2007) 81–83.
- [22] X.F. Qiu, J.Z. Xu, J.M. Zhu, J.J. Zhu, S. Xu, H.Y. Chen, Controllable synthesis of palladium nanoparticles via a simple sonoelectrochemical method, *J. Mater. Res.* 18 (2003) 1399–1404.
- [23] R.J. Von Gutfeld, R.E. Acosta, L.T. Romankiw, Laser-enhanced plating and etching: mechanisms and applications, *IBM J. Res. Dev.* 26 (1982) 136.
- [24] R.J. Von Gutfeld, E.E. Tynan, R.L. Melcher, S.E. Blum, Laser-enhanced electroplating and maskless pattern generation, *Appl. Phys. Lett.* 35 (1979) 651.
- [25] J.C. Puippe, R.E. Acosta, R.J. Von Gutfeld, Investigation of laser-enhanced electroplating mechanisms, *J. Electrochim. Soc.* 128 (1981) 2539.
- [26] R.J. Von Gutfeld, L.T. Romankiw, M.H. Gelchinski, D.R. Vigliotti, Laser-enhanced jet plating: a method of high-speed maskless patterning, *Appl. Phys. Lett.* 43 (1983).
- [27] R.J. Von Gutfeld, Laser-enhanced patterning using photothermal effects: maskless plating and etching, *J. Opt. Soc. Am. B* 4 (1987) 272.
- [28] M. Datta, L.T. Romankiw, D.R. Vigliotti, R.J. Von Gutfeld, Jet and laser-jet electrochemical micromachining of nickel and steel, *J. Electrochim. Soc.* 136 (1989) 2251.

- [29] P. Bindra, G.V. Arbach, U. Stimming, On the mechanism of laser-enhanced plating of copper, *J. Electrochem. Soc.* 134 (1987) 2893.
- [30] L.M. Wee, L. Li, Multiple-layer laser direct writing metal deposition in electrolyte solution, *Appl. Surf. Sci.* 247 (2005) 285.
- [31] D.T. Queheillalt, Y. Lu, N.G. Wadley, Laser ultrasonic studies of solid-liquid interfaces, *J. Acoust. Soc. Am.* 101 (1997) 843–853.
- [32] D. Paul, *Double Layer and Electrode Kinetics*, Interscience Publisher, 1966.
- [33] P. Geoffery, *Electrochemical Engineering Principles*, Prentice Hall, 1991.
- [34] FLUENT 6.2 User Guide, Fluent Inc, 2003.
- [35] Y.T. Albert, A numerical study on the hydrodynamics and heat transfer of a circular liquid jet impinging onto a substrate, *Numer. Heat Transfer Part A Appl.* 44 (2003) 1–19.

# Laser hybrid fabrication of tunable micro- and nano-scale surface structures and their functionalization

10

*M. Zhong, T. Huang*  
Tsinghua University, Beijing, China

## 10.1 Introduction

Surface micro-nano structures (SMNS) refer to the regularly or randomly distributed dimple or plump structures with micro, nano, or micro-nano scales. The research on SMNS initiated with the discovery of specific properties of the SMNS associated with some plants and animals after thousands of years of evolution. In the 1980s, Professor Wilhelm Barthlott discovered that lotus leaves have a set of unique micro- and nano-structures, thousands of microscale plumps (20–100  $\mu\text{m}$ ) and distributed thousands of nanoscale wax filament (100–500 nm) on each plump. This unique SMNS results in the superhydrophobic and self-cleaning effect of lotus leaves called the lotus effect [1]. Many other plants also have developed a combination of micro- and nano-structures on their surfaces to minimize the contact area with anything that comes into contact. This is also true for animals. Sharks grow microscale V-shaped ripples on their skin; such microstructure dramatically decreases the friction of the incoming water stream, drives the stream moving fast around the shark's body, and thus makes high-speed swimming possible. The toes of a gecko have millions of microscale fluffs, each with its nanoscale embranchment. When millions of these microfluffs contact the surface of an object, such as a ceiling or a wall, a strong VanderWaals force occurs and enables the gecko to easily hang itself on the ceiling, move on the wall, or to optionally depart from the surface.

All of these super capabilities of the above-mentioned animals or plants have come from the SMNS of their body surfaces. Therefore, SMNS are the wonder behind many natural arcanums and principles such as superhydrophobicity, superhydrophilicity, tribological characteristics, optical absorption, wettability, cell interaction, and aerodynamic and hydrodynamic properties.

SMNS can be fabricated by chemical or physical means, such as lithographic patterning [2–4], chemical vapor deposition [5,6], sol-gel method [7,8], template method [9–11], electrodeposition, plasma fluorination, and so on. Among them, ultrashort pulsed laser ablation is one of the major approaches and a research hotspot [12–14]. Laser ablation by ns, ps, or fs lasers with a near infrared wavelength can typically fabricate controllable and regular microstructures on material surfaces.

However, due to the diffraction limit, it is difficult, if not impossible, to fabricate a designable nanoscale structure at the same time. The smallest feature size for laser ablation on surfaces are diffraction limited to the laser beam wavelength for direct beams and to half of the laser wavelength if interference technique is used. These are generally in the submicrometers ( $>100$  nm) range. In recent years, some near-field patterning techniques have been developed; these include laser integrated scanning near-field optical microscopy, laser-assisted AFM/STM-tip patterning, microlens arrays and contacting particle lens array. These techniques have demonstrated the capability of creating features on a surface smaller than the diffraction limits of the lasers used. Nevertheless, femtosecond (fs) lasers are needed for these near-field approaches.

Consequently, the available laser approaches for SMNS fabrication have the following limitations: (1) Almost all current approaches use fs laser, which is not yet a practical approach; (2) scale tunability is possible but difficult; (3) fabrication is limited to small areas, which are not enough for practical applications; (4) substrate material is normally limited to nonmetal materials, which do not have the required engineering strength; and (5) functionalization is limited. Therefore, currently laser nanofabrication for practical applications remains a challenge.

In recent years, we introduced and developed a novel laser processing-dealloying hybrid approach for SMNS. This approach utilizes conventional high-power industrial continuous wave lasers instead of ultrashort pulsed lasers, and chemical dealloying instead of laser ablation. By combining the physical approach of laser deposition and the chemical approach of dealloying, this engineering nanomanufacturing method enables large-area fabrication of micro, nano, and micro-nano surface structures with tunable size in a thick fusion layer metallurgically bonded to any engineering material substrate for easy functionalization.

Figure 10.1 shows the technical road map for this hybrid method.

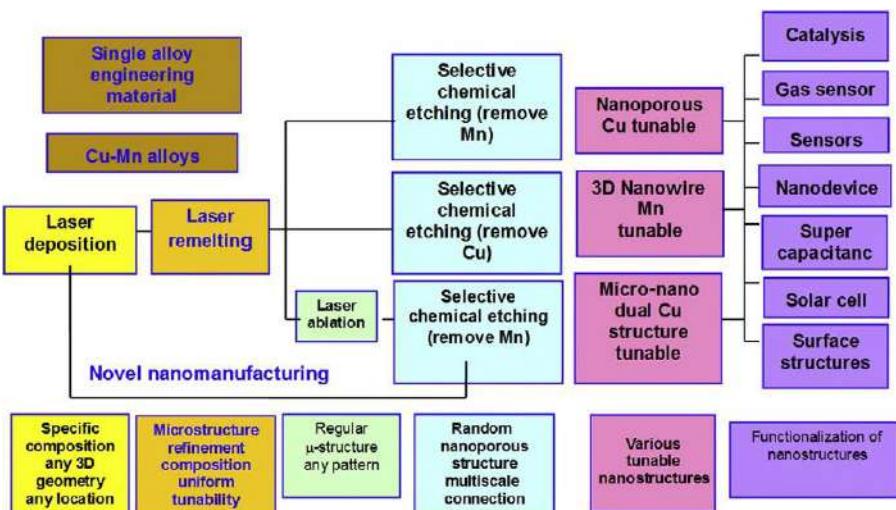


**Figure 10.1** Road map for laser hybrid methods for micro, nano, and micro-nano structure formations.

1. CuMn alloy is chosen for the target material due to the fact that it is a widely used and cost-effective engineering material. In addition, Cu-Mn is a good candidate for chemical dealloying: A dual-element single-phase alloy with a large standard electrode potential difference between the two elements.
2. Laser deposition is applied to deposit the required CuMn alloy onto any location of any kind of substrate or component with designable geometry (coating or 3D structure). Due to the rapid solidification characteristics, the deposited layer has a relatively fine microstructure and a uniform composition.
3. Laser remelting with high scanning speed is applied to process the as-deposited layer to make the microstructure finer and the composition more homogeneous for nanoporous structure formation during the following dealloying process.
4. Chemical dealloying is then used to achieve nanoporous structure. Dealloying is a chemical process by which one element in the single-phase alloy matrix is usually chemically or electrochemically etched owing to its relative higher reactivity. As a result, a dual-connective nanoporous structure can be formed via diffusion, nucleation, and growth. When the relatively active Mn was etched in the single-phase CuMn alloy layer deposited by laser, nanoporous Cu structures were achieved with minimum pore size of 35.2 nm, pore rate of 84.5%, and specific surface area of  $65.3 \text{ m}^2/\text{g}$ .
5. Specific solution was tested for selective dissolution of the more noble element Cu in the single-phase CuMn alloy owing to the passivation of the more active Mn according to the potential-pH diagram in terms of thermodynamics. As a result, three-dimensional manganese-based nanoporous structure was formed consisting of a 3D network of MnO nanowire skeletons and nanoporous channels. The nanopore sizes could be tailored to be less than 25 nm, their surface roughness factor could reach up to 990.
6. Nanosecond laser ablation was introduced to process the as-deposited and remelted CuMn layer for any designable pattern in microscale, then dealloying was further applied to achieve a hierarchical structure, consisting of regular microbumps and bi-continuous nanopores on the surface of the bumps. The hierarchical structure can be tunable by the ratio of Cu and Mn, laser ablation parameters, and dealloying parameters. The height of microbump can be adjusted in the range of 2-120  $\mu\text{m}$ , and the average diameter of nanopores can be changed from 20 nm to 1  $\mu\text{m}$ .
7. The above three kinds of micro, nano, and micro-nano structures were fabricated by laser deposition and chemical dealloying. They are naturally bonded to the engineering material substrate, allowing easy functionalization for potential applications. The fabricated micro-nano structures show good potential for functionalization in catalysis, superhydrophobicity, degradation of methyl orange, surface-enhanced Raman spectrum, and catalysis transform.

## 10.2 Fabrication of nanoporous copper structures

### 10.2.1 *Fabrication of nanoporous copper structures by hybrid laser deposition and chemical dealloying*

A mixture of Cu and Mn powder was deposited on 1045 steel substrate by laser cladding with a continuous wave CO<sub>2</sub> laser to form a 1 mm thick layer of Mn-Cu alloy, which was then immersed into HCl for electrochemical selective etching as part of the dealloying process. The dealloying process was performed at 25 °C. The potential between the electrodes was controlled by a potentiostat made of a platinum plate auxiliary electrode and a saturated calomel reference electrode.

### 10.2.2 Composition and phase characterization

The microstructure and composition of the Mn-Cu in the laser-deposited film before dealloying are shown in [Figure 10.2](#). The dendritic microstructure was formed during laser processing ([Figure 10.1a](#)). Mn showed substantial solid solubility in Cu and was an effective solid solution strengthening agent [15], which was verified by the XRD results shown in [Figure 10.1b](#). The sharp peaks were identified as face-centered cubic (fcc) single-phase solid solution ( $\text{Cu}$ ,  $\gamma\text{Mn}$ ) with the main diffraction peaks of (111), (200), and (220) in all samples ( $\text{Cu25Mn75}$ ,  $\text{Cu40Mn60}$ , and  $\text{Cu60Mn40}$ , at.%).

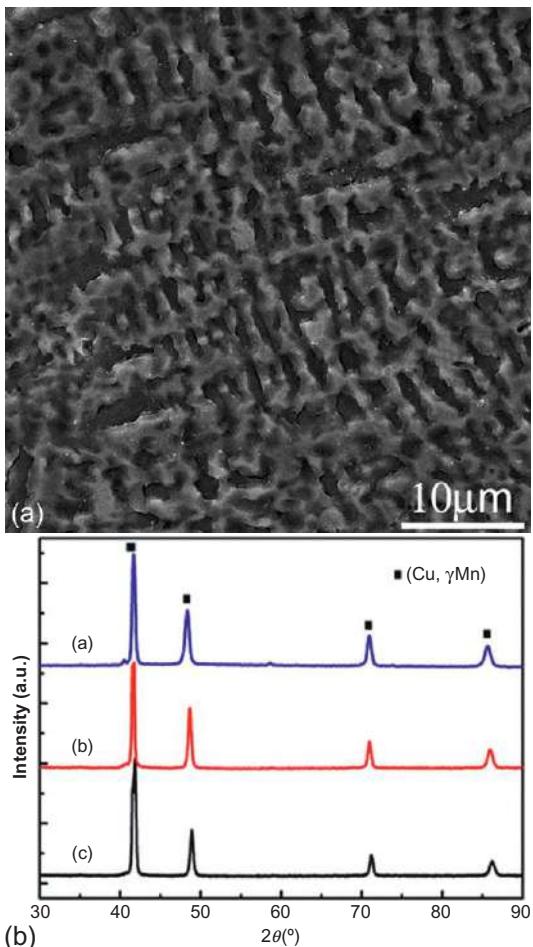


**Figure 10.2** Microstructure and composition of the laser-deposited Mn-Cu precursor:  
 (a) typical morphology of Mn-Cu precursor showing the dendritic microstructure and (b) XRD pattern showing the single-phase solid solution ( $\text{Cu}$ ,  $\gamma\text{Mn}$ ) ((a) blue:  $\text{Cu25Mn75}$ ; (b) red:  $\text{Cu40Mn60}$ ; (c) black:  $\text{Cu60Mn40}$ ).

The nanostructure and composition of the laser-deposited film after dealloying are shown in [Figure 10.3](#). The nanoporous structure was formed ([Figure 10.2a](#)). The XRD results demonstrated that the component gradually changed from  $(\text{Cu}, \gamma\text{Mn})$  to Cu with increase in dealloying time ([Figure 10.2b](#)), suggesting that Mn was dissolved and solubility decreased. Pores form because the less-noble atoms (Mn) are excavated and the more-noble atoms (Cu) are chemically driven to aggregate into two-dimensional clusters by a phase separation process at the solid-electrolyte interface.

After being exposed to air, the nanoporous Cu was oxidized. The final product was examined by XPS, shown in [Figure 10.2c](#). There were two main  $\text{Cu}2\text{p}$  XPS peaks at 931.6 and 951.6 eV, which could be attributed to the  $\text{Cu}^+$  double peak for  $\text{Cu}2\text{p}3/2$  and  $\text{Cu}2\text{p}1/2$ , respectively. There were also two low  $\text{Cu}2\text{p}$  XPS peaks at 942 and 962 eV, which could be attributed to the  $\text{Cu}^{2+}$  double peak. This demonstrated that the main composition of the structure was  $\text{Cu}_2\text{O}$ , and there was also some  $\text{CuO}$  on the surface of the sample. The oxidation happened at the exterior of the structure where the nanoporous morphology still remained. The nanoporous Cu structure was functionalized by oxidation. This unique nanostructure with  $\text{Cu}_2\text{O}$  on the surface exhibits excellent catalysis function for converting CO to  $\text{CO}_2$  gas, this function will be discussed in [Section 10.5.1](#).

### **10.2.3 Tunability of the micro-nano structures**

The dealloying conditions are crucial to the formation of nanoporous structures. Nanopore size can be tunable from 40 to 160 nm by controlling the dealloying conditions [[16](#)]:

$$d \propto (D_s/V)^\mu \quad (10.1)$$

where  $d$  is the diameter of the nanopore;  $D_s$  is the diffusivity;  $V$  is the corrosion velocity of the alloy; and  $\mu$  is a constant suggested to be from 1/6 to 1/4 according to the Cahn-Hilliard equation.  $D_s$  is related to materials, components, and temperature, while  $V$  is influenced by the electrolyte, concentration, and corrosion temperature. Here we take the concentration of HCl and dealloying time as an example.

The fundamental physics of dealloying is marked by nonequilibrium behavior at the alloy/electrolyte interface [[17](#)]. Two primary mechanisms, namely surface dissolution and surface diffusion, operate during the dealloying process and can significantly affect the final nanoporous structure [[18](#)].

The Cu-Mn alloy was more easily etched in 0.1 mol/L HCl. The concentrated acid promoted the dissolution of Mn atoms and prohibited the diffusion of the Cu atoms at the solid-electrolyte interfaces, resulting in a bigger nanoporous structure ([Figure 10.4c](#)). In contrast, the dissolution was prohibited and the diffusion process promoted if the concentration was diluted to 0.025 mol/L, leading to nanoscale pits on the surface ([Figure 10.4a](#)). It is obvious that the desired nanoporous structure can be fabricated only in the appropriate concentration, in which the dissolution and diffusion are balanced with each other ([Figure 10.4b](#)).

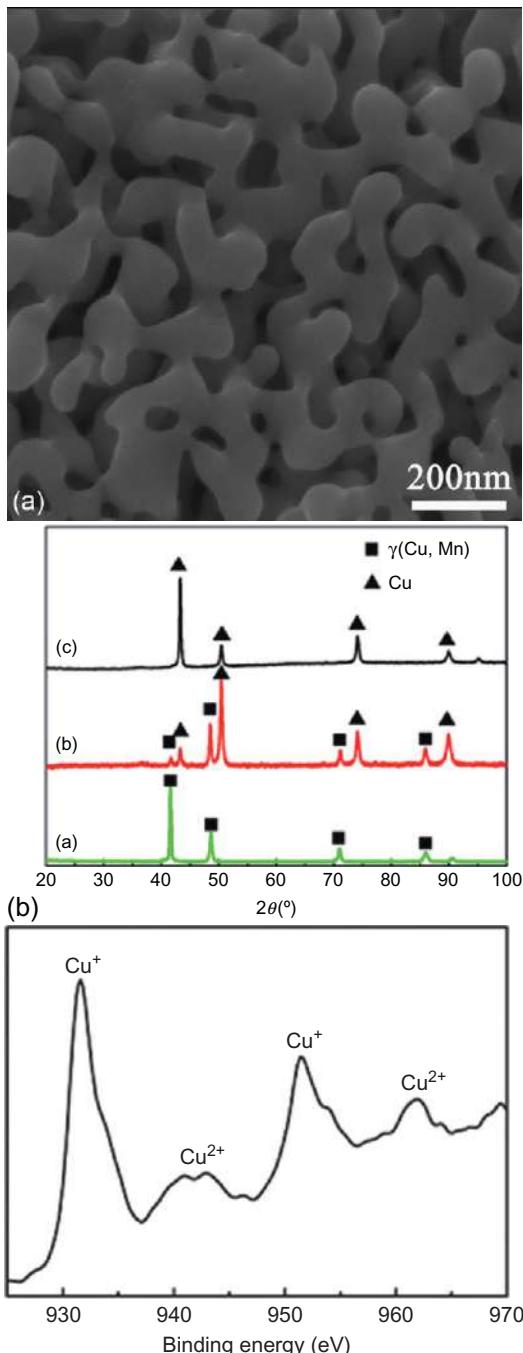


**Figure 10.3** Nanostructure and composition of the dealloyed alloy: (a) typical nanostructure showing nanoporous morphology, (b) XRD pattern showing different component with increase of dealloying time ((a) green: 0 h; (b) red: 25 h; (c) black: 48 h), and (c) XPS result showing  $\text{Cu}^+$  and  $\text{Cu}^{2+}$ .

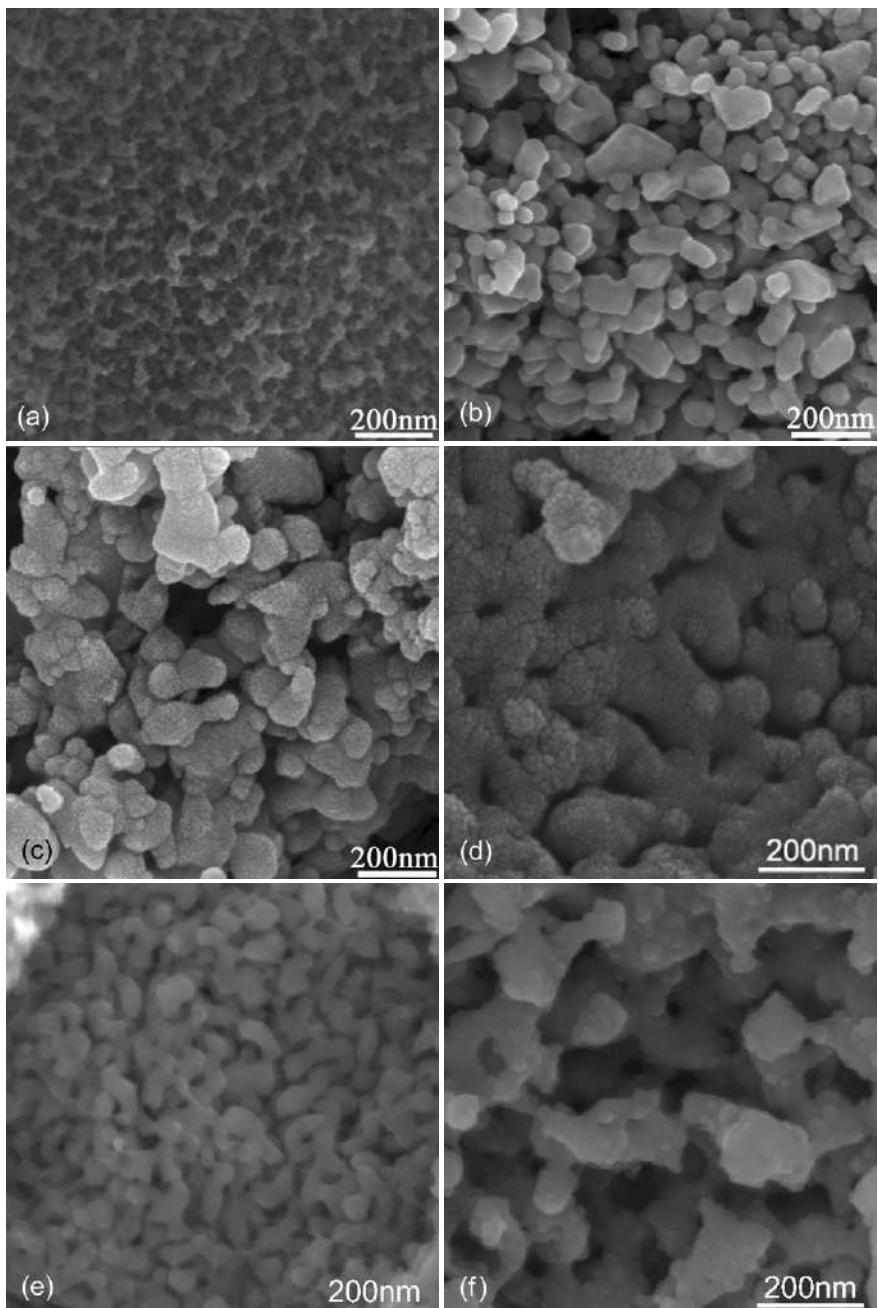


**Figure 10.4** Tunability of nanopore size by controlling dealloying conditions. (a-c) Concentration of HCl: 0.025, 0.05, and 0.1 mol/L. (d-f) Dealloying time: 5, 20, and 50 h.

The influences of dealloying time are shown in Figure 10.4d–f (0.05 mol/L HCl). The etching happened first in places where there was aggregation of defects, resulting in nanoscale pits (Figure 10.3d). When the dealloying time was as long as 20 h, coarsened nanoscale pores contacted each other, forming ligaments about 80 nm in width (Figure 10.4e). With the increase of time, the diffusion between solid and electrolyte became more important. The nanoporous structure formed (Figure 10.4e). Following further etching, the Cu ligaments were dissolved into the acid and the nanoporous structure was destroyed (Figure 10.4f).

## 10.3 Fabrication of 3D manganese-based nanoporous structure (3D-Mn-NPS)

### 10.3.1 Fabrication of 3D-Mn-NPS by hybrid laser deposition and selective electrochemical dealloying

The Cu-Mn alloy precursor was used to fabricate 3D-Mn-NPS through laser deposition and dealloying, the same processes detailed in Section 10.2.1. Here the electrolyte was replaced by  $\text{KNO}_3$  to dealloy Cu. Although as a more-noble element, Cu was removed during dealloying despite that Cu had the higher standard reversible potential (0.342 V versus standard hydrogen electrode (SHE)) compared to Mn (−1.135 V versus SHE) [19], leading to different nanostructure in contrast to nanoporous Cu.

### 10.3.2 Composition and phase characterization

The typical composition and microstructure of the Mn-Cu (Cu<sub>60</sub>Mn<sub>40</sub>, at.%) in the laser-deposited film before dealloying are shown in Figure 10.5. The film is composed of single-phase solid solution (Cu,  $\gamma$ Mn) (Figure 10.4a) with dendritic microstructure (Figure 10.5b), the same as shown in Section 10.2.2. The corresponding auxiliary X-ray energy dispersive spectroscopy (EDS) in Figure 10.5c shows that the bulk Mn-Cu precursor was divided into two different regions: the dendritic cores (embedded dark blots) and the interdendritic region (lighter background). The average compositions of the dendritic core and the interdendritic region were Cu<sub>88</sub>Mn<sub>12</sub> and Cu<sub>58</sub>Mn<sub>42</sub>, respectively, indicating inhomogeneity in the distribution of Cu and Mn between the two regions.

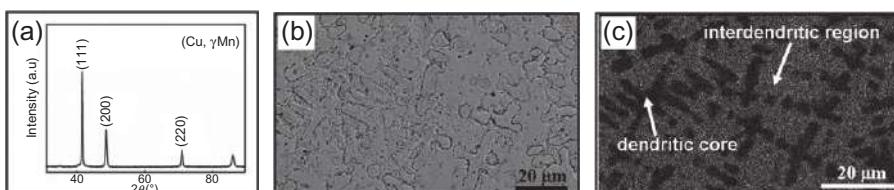


**Figure 10.5** Composition and microstructure of the laser-deposited Mn-Cu precursor (Cu<sub>60</sub>Mn<sub>40</sub>): (a) XRD pattern showing the single-phase solid solution (Cu,  $\gamma$ Mn), (b) top-view of QBSD image of the laser-deposited Mn-Cu precursor, and (c) EDS result showing the phase separation of dendritic cores and interdendritic regions.

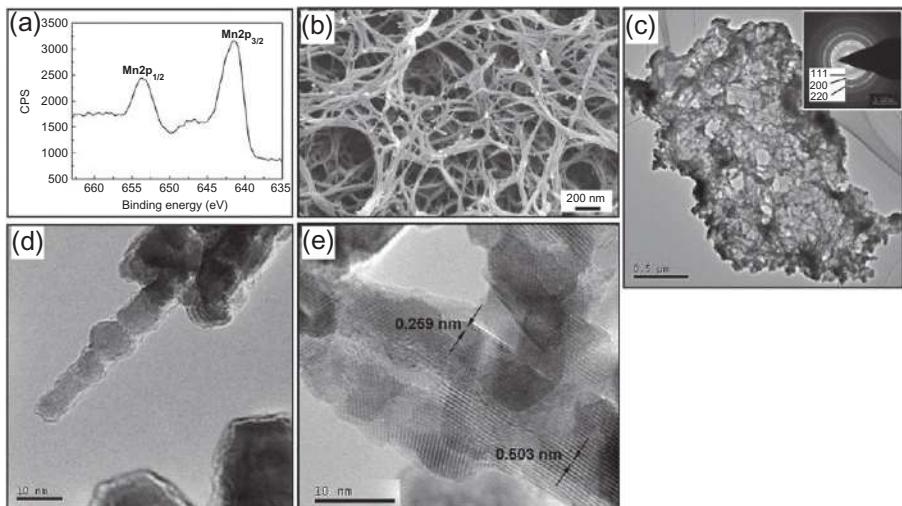


**Figure 10.6** Composition and nanostructure of the 3D-Mn-NPS after dealloying: (a) XPS spectrum of Mn 2p of the as-fabricated 3D-Mn-NPS, (b) top view FESEM image of dealloyed nanoporous film, (c) top view TEM image of dealloyed nanoporous film with inset diffraction pattern indexed as MnO, and (d, e) high-magnification TEM images.

The composition and nanostructure of the 3D-Mn-NPS film after dealloying are shown in Figure 10.6. While the XPS analysis found the presence of a small amount of Cu in the 3D-Mn-NPS surface layer, Mn was determined to be the major component. Specifically, in the Mn 2p spectrum (Figure 10.6a), the binding energy peaked at 641.1 and 652.8 eV, and a satellite peak at 646.2 eV was also identified, matching characteristics of MnO and agreeing with previous literature [20].

Figure 10.6b is the top view of the FESEM image of the dealloyed 3D-Mn-NPS film. The nanostructure consisted of uniform ligaments with a diameter of less than 50 nm and interconnected channels, forming a nanoporous structure. The TEM image of the nanoporous film (Figure 10.6c) and its diffraction pattern (Figure 10.6c inset) indicated that the nanoporous structure maintained the fcc structure. The interplanar spacing corresponded to crystal planes {111}, {200}, and {220}, which was also characteristic of MnO [21], suggesting that, during dealloying, Cu was removed and Mn was passivated and oxidized to form MnO. At higher magnifications (Figure 10.6d and e), it can be clearly seen that the ligaments were composed of randomly oriented nanoparticles. In addition, the wide interplanar spacing (Figure 10.6e) also corroborates the existence of oxide.

### 10.3.3 Tunability of 3D-Mn-NPS

As mentioned in Section 10.2.3, nanopore size is tunable by controlling laser deposition and dealloying parameters. Figure 10.7 shows the evolution in surface structures with respect to dealloying time.

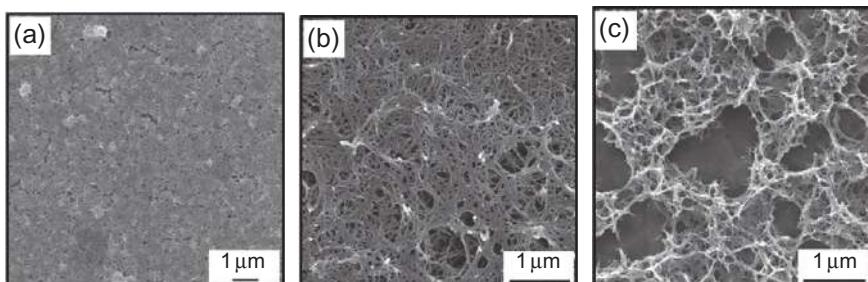


**Figure 10.7** SEM micrographs showing surface structural evolution with different dealloying time: (a) 30 min, (b) 80 min, and (c) 220 min.

Note that in the laser-deposited precursor ([Figure 10.5c](#)), the dendritic cores with higher Cu content were surrounded by the interdendritic regions with a lower Cu content. Therefore, Cu atoms were dissolved at a higher rate in the dendritic cores than in the interdendritic regions. As the Cu atoms started to dissolve on the surface in the dendritic cores, the remaining Cu atoms therein, which were laterally coordinated to the dissolved Cu atoms and thus had fewer bonds, were more susceptible to dissolution, compared to Cu atoms in the interdendritic regions. Therefore, the electrochemical etch front initially spread laterally and developed primarily within the dendritic cores, leading to the formation of small pits ([Figure 10.7a](#)), while the Mn atoms in the dendritic cores in the topmost terrace were detached, diffused to, and agglomerated with the adjacent Mn atoms to form clusters of nanoparticles.

As the pits were developing in the dendritic cores, Cu atoms in the interdendritic regions also started to be attacked and removed to form new pits. Meanwhile, the free Mn atoms, which had resulted from the detachment of adjacent Cu atoms, continued to diffuse, agglomerate into nanoparticles, and join with previously generated Mn clusters to form nanoligaments, and hence the nanostructure formed as shown in [Figure 10.6d](#). Based on this mechanism, it can be inferred that a smaller interdendritic distance facilitates the diffusion and agglomeration of Mn atoms. Concurrent with the formation of nanoligaments was the oxidation of Mn into MnO, demonstrated by the XPS result shown in [Figure 10.6a](#). The coupled formation and development of both pits and ligaments, as well as the oxidation of Mn, eventually resulted in a nanoporous structure ([Figure 10.7b](#)). However, when dealloyed for an excessive amount of time, Cu atoms in deeper layers in the nanoporous film would also be removed, resulting in the detachment of large pieces of MnO clusters/ligaments that had already formed in the top layers, leaving large voids ([Figure 10.7c](#)).

#### 10.3.4 High-temperature performance

The melting point of the 3D-Mn-NPS was found to be between 240 and 320 °C. The initial nanowire structure remains stable below 240 °C. At 320 °C, however, the 3D-Mn-NPS started to melt and displayed a very different structural evolution history from that of the alloy in bulk form ([Figure 10.8](#)). First, melted droplets gradually emerged and

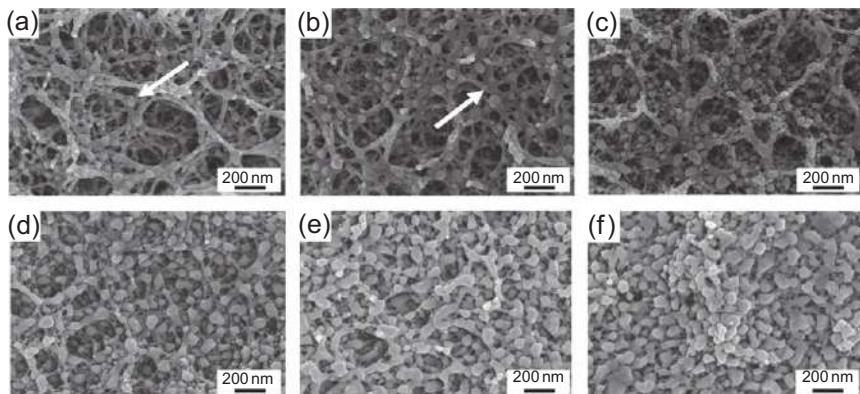


**Figure 10.8** SEM micrographs showing surface structural evolution at 320 °C: (a) 5 min, (b) 10 min, (c) 15 min, (d) 20 min, (e) 30 min, and (f) 40 min.

developed amidst the nanowires. As the droplets developed, they grow first in quantity and then in size. In the end, the nanowire structure in the initial 3D-Mn-NPS was entirely destroyed, replaced by agglomerates of nanoparticles. Also, a small portion of the ( $\text{Cu}$ ,  $\gamma\text{Mn}$ ) phase was oxidized to form  $\text{MnO}$  and  $\text{CuO}$ . It is also noteworthy that the nanowire-nanoparticle complex morphology created during the incomplete transformation from nanowire to nanoparticle in the 3D-Mn-NPS has never been reported before, and may exhibit desirable material properties as it possesses the dual nature of nanowire and nanoparticle, hence suggesting worthiness for further investigation.

## 10.4 Fabrication of micro-nano hierarchical $\text{Cu}/\text{Cu}_2\text{O}$ structure

### 10.4.1 Fabrication of micro-nano hierarchical $\text{Cu}/\text{Cu}_2\text{O}$ structures by hybrid laser ablation and chemical dealloying

The micro-nano hierarchical structure was prepared by a hybrid approach including laser deposition, laser ablation, and chemical dealloying. Figure 10.9 schematically shows the preparing steps: (1) Cu-Mn alloy coatings deposited by laser; (2) microscale structure ablated by laser; and (3) hierarchical structure adjusted by chemical dealloying. The processes of steps 1 and 3 have been detailed in Section 10.2.1. In step 2, a diode laser pumped nanosecond pulse Nd:YAG laser was used to ablate checkerboard trenches and effectively form regular microscale bumps on the deposited Cu-Mn alloy coating.

### 10.4.2 Composition and phase characterization

Figure 10.10a shows the surface morphology of the microscale bumps after laser ablation. The laser-textured surfaces were characterized as high-density microscale dimples/bumps. The spacing between the bumps was about 50  $\mu\text{m}$  and the height was about 100  $\mu\text{m}$ , detected by an interferometer (shown in Figure 10.10b). This

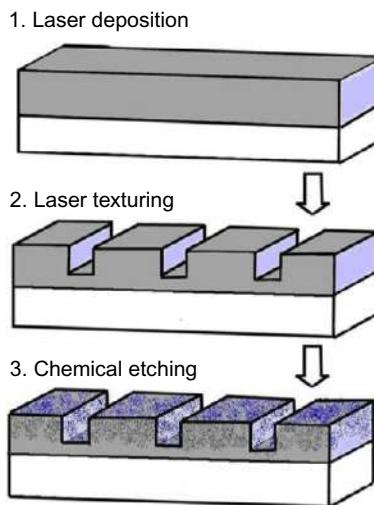


**Figure 10.9** Fabrication process for the micro-nano hierarchical structure: (1) laser deposition, (2) laser ablation, and (3) chemical dealloying.

indicated a uniform and regular microscale structure free of defects on the surface of the substrate.

During dealloying process, Mn reacted with HCl and thus was removed ([Figure 10.11a](#)). The nanoporous Cu was formed on the laser-textured surface, as shown in [Figure 10.2a](#).

[Figure 10.11b](#) shows XRD patterns of the samples fabricated by the hybrid method. The laser deposited Cu-Mn coating can be indexed as an fcc (Cu,  $\gamma$ Mn) phase. The laser ablation process did not change the composition and phase. After the chemical dealloying process, Mn was dissolved and nanoporous Cu formed. After the nanoporous Cu was exposed to air, the color of the nanoporous structures changed immediately to dark green due to oxidation. Peaks of  $\text{Cu}_2\text{O}$  in its XRD pattern indicated that the oxidation occurred at the exterior of the structure. The generated  $\text{Cu}_2\text{O}$  was stable at room temperature, which could be confirmed by XRD pattern of samples aged for 7 days.

#### 10.4.3 Tunability of the micro-nano hierarchical Cu/ $\text{Cu}_2\text{O}$ structures

The mechanisms of laser deposition and dealloying process have been discussed above. Here we focus on the effects of laser ablation. The spacing and the depth of the laser-ablated bumps can be tuned by laser power, scanning speed, and frequency and pulse duration.

The morphologies after laser ablation are presented in [Figure 10.11](#) using a white-light interferometer, and the cross-sectional profiles of the textures are also given. The laser ablation parameters are shown in [Table 10.1](#).

It can be proven that the microstructure was quite uniform without any evident defects shown in [Figure 10.12](#). Laser ablation produced high-density microscale

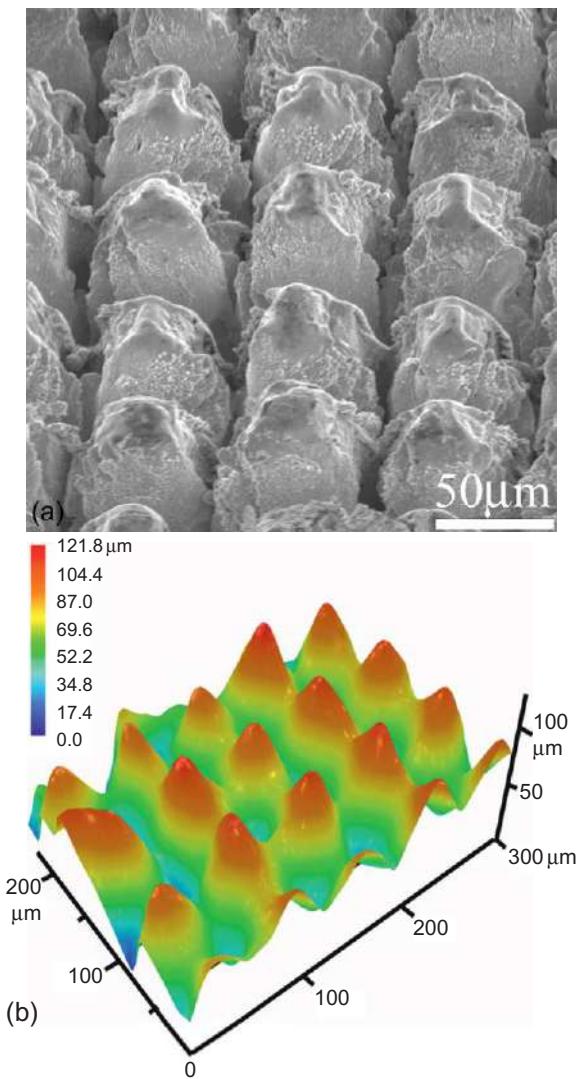


**Figure 10.10** The microstructure of laser ablated surface: (a) SEM micrograph showing morphology of the bumps and (b) light interferometer image of the bumps.

dimples/cones on the substrate. The spacing between the dimples was observed to vary from 25 to 150 μm and the depth is 3–20 μm, as shown in Figure 10.12.

R<sub>a</sub> (arithmetical mean deviation) and R<sub>z</sub> (profile irregularity) measurements, shown in Figure 10.13, were used to distinguish the surface roughness quantitatively, with R<sub>z</sub> in μm scale and R<sub>a</sub> in nm scale. R<sub>a</sub> and R<sub>z</sub> increased as the laser power density increased. The same trend was also observed in the depth and width dimensions. The dimples in the unidirectional (UD) texture direction were disordered and shallow while in the bidirectional (BD) texture direction, the textures were regular and deep.

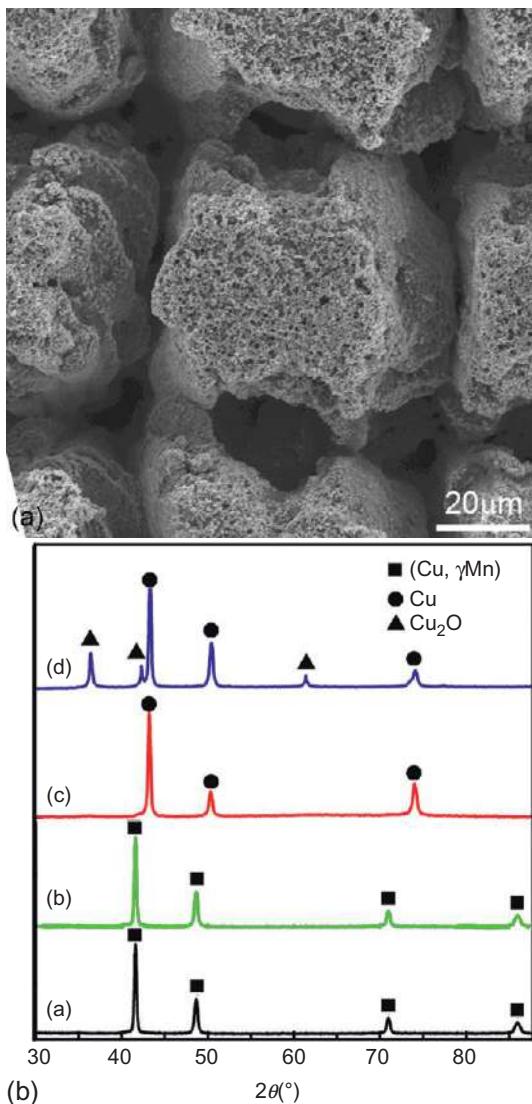


**Figure 10.11** Microstructure and composition of the hierarchical structure by the hybrid approach: (a) SEM micrograph showing morphology of the hierarchical structure and (b) XRD pattern showing different component ((a) black: Cu-Mn alloy coating deposited by laser; (b) green: Cu-Mn alloy coating ablated by laser; (c) red: hierarchical structure by the hybrid method; (d) blue: hierarchical structure under oxidation).

The sample textured surface scanned in both directions showed deeper microstructures than that with a single direction under the same power density. When the same power density was used, the Ra and Rz of the BD textured surfaces were nearly twice those for the UD textured surfaces.

**Table 10.1 Laser ablation parameters for surface texturing**

Sample	Pulse energy (mJ)	Power density (W/cm <sup>2</sup> )	Fluence (J/cm <sup>2</sup> )	Scanning speed (mm/s)	Texture direction
1	5.3	$4.6 \times 10^7$	1.38	100	UD <sup>a</sup>
2	2	$1.7 \times 10^7$	0.52	100	UD
3	1	$8.5 \times 10^6$	0.26	100	UD
4	2	$1.7 \times 10^7$	0.52	200	BD

<sup>a</sup>UD—unidirectional; BD—bidirectional (cross-scan). Sample 5 is untextured for comparison.

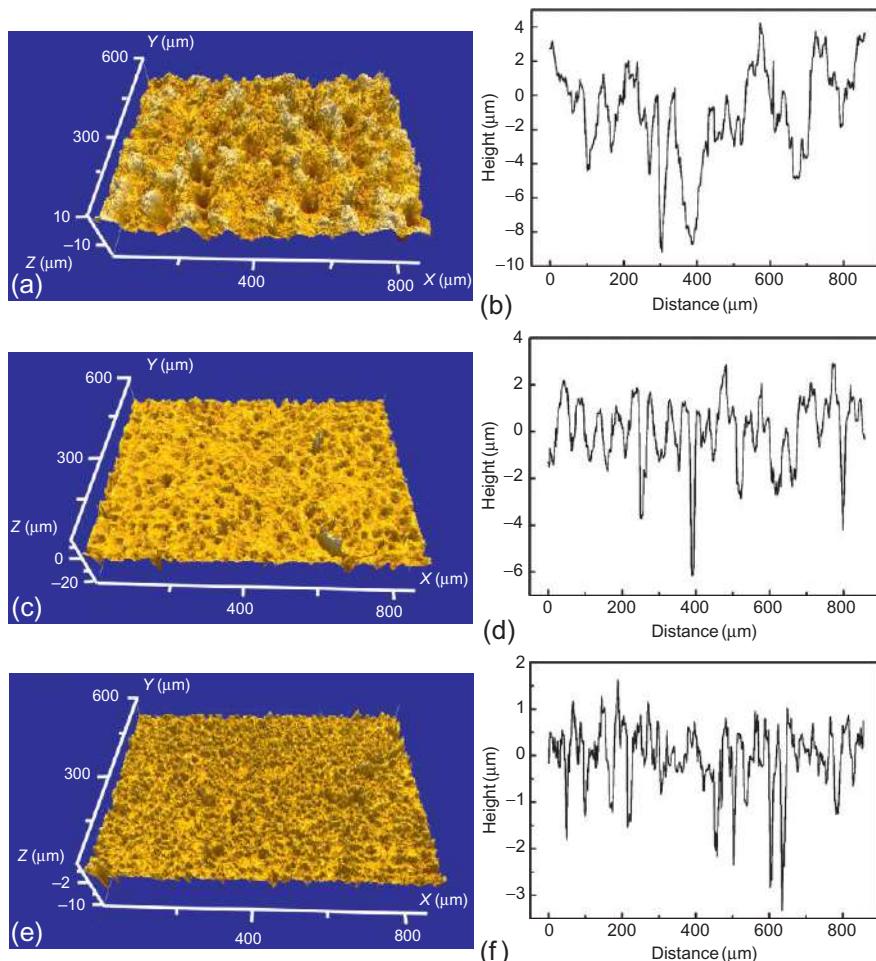


**Figure 10.12** The morphologies with various laser ablation parameters: (a, c, e, g, i) represent the 3D morphologies of the samples 1#, 2#, 3#, 4#, 5#, respectively, and (b, d, f, h, j) represent the surface undulation of the samples 1#, 2#, 3#, 4#, 5#, respectively.

(Continued)

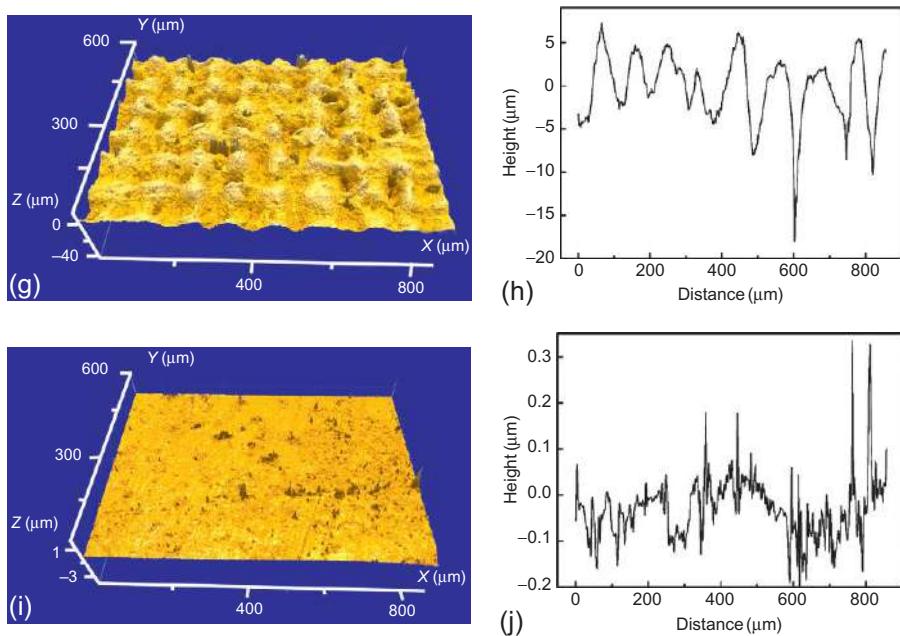


**Figure 10.12** Continued.

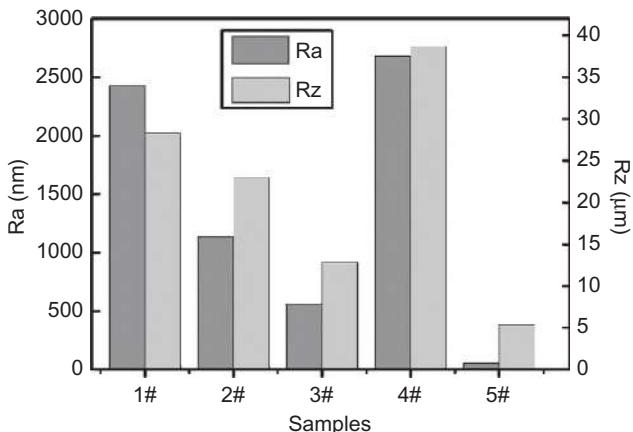


**Figure 10.13** Comparison of Rz and Ra with various laser ablation parameters.

## 10.5 Functionalization of tunable micro-nano surface structures

### 10.5.1 Catalysis performance

Nanoporous metals have been found to exhibit exceptional catalytic activity toward many important reactions, including low-temperature CO oxidation [22–25]. Noble metals, such as Au, Pt, and Zr have been used for CO oxidation. Here, the nanoporous

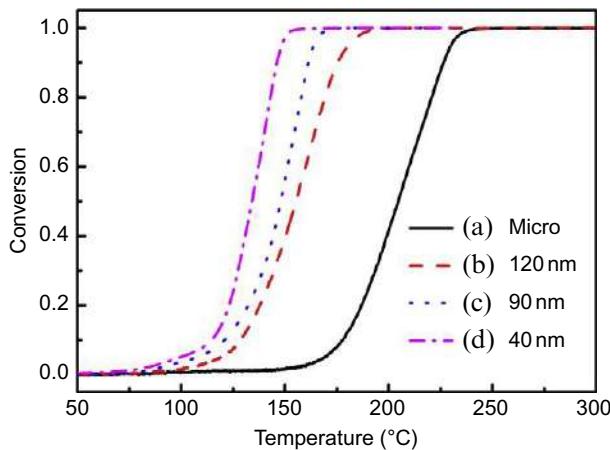


**Figure 10.14** Catalysis of CO under various nanopore sizes: (a) micro, (b) 120 nm, (c) 90 nm, and (d) 40 nm.

Cu fabricated by laser deposition and dealloying exhibits excellent catalysis for converting CO to CO<sub>2</sub> gas.

As shown in Figure 10.3a, the sponge morphology of the nanoporous Cu consisted of interconnecting ligaments with diameters on the order of tens of nanometers. The nanopore size could be tunable by changing the chemical dealloying parameters, as discussed before. Figure 10.14 shows the equilibrium conversion of CO oxidation versus temperature with different pore size. At a fixed temperature, conversion of CO oxidation by the nanostructure were always higher than that by the microstructure. The equilibrium conversion temperatures of CO oxidation were 257, 205, 168, and 153 °C for the pore size of microscale, 120, 90, and 40 nm, respectively. The equilibrium conversion temperatures of CO oxidation decreased sharply with nanopore size of 40 nm. The catalysis was more prominent with smaller nanopores due to the larger surface area, which provided sites for CO adsorption and subsequent reactions at the boundary resulting in rapid turnover of reacting species or high reaction activity.

In addition, the unique composition of Cu<sub>2</sub>O/Cu (as shown in Figure 10.3c) was also important to the excellent catalytic function of the as-produced SMNS. It is generally assumed that oxygen atoms are supplied to the CO molecules adsorbed on the surface by the cuprous oxide lattice, and oxygen lost from the lattice is reloaded through the adsorption and dissociation of gas phase oxygen. The CO then combines with surface oxygen to form CO<sub>2</sub>. White *et al.* [26] pointed out that the CO molecule is found to react with the surface oxygen forming CO<sub>2</sub>, which departs spontaneously from the surface creating an oxygen vacancy. On the other hand, if CO lands on a Cu atom, it approaches the surface without any barrier, diffuses spontaneously to the neighboring surface oxygen, and produces CO<sub>2</sub> as in the earlier step. This explains the high catalytic activity of Cu<sub>2</sub>O observed even at low temperatures. The exposed Cu can easily absorb surface oxygen and be oxidized into Cu<sub>2</sub>O again. Oxygen is then supplied from the surface of the Cu oxide and reacts with CO to form CO<sub>2</sub>. The Cu clusters are stabilized by cuprous oxide through an interfacial interaction

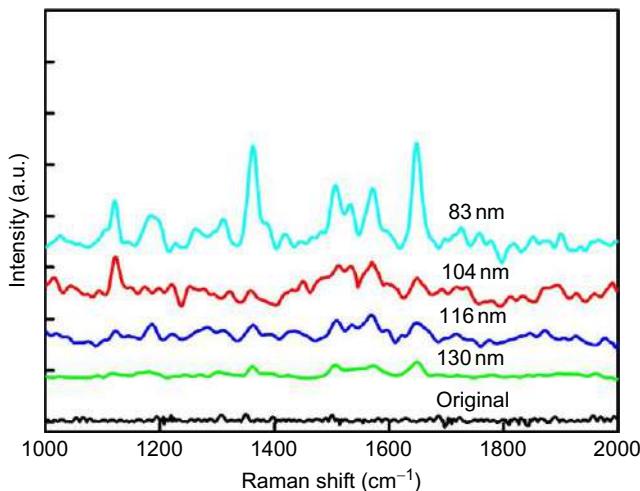


**Figure 10.15** SERS spectra of 3D-Mn-NPS with different pore sizes for 10-6 M R6G aqueous solution.

and, in turn, promote the surface oxygen activation of cuprous oxide. Cu<sub>2</sub>O modifies the physical and chemical properties and provides strong sites for CO adsorption.

### 10.5.2 *Surface Enhanced Raman Spectrum (SERS)*

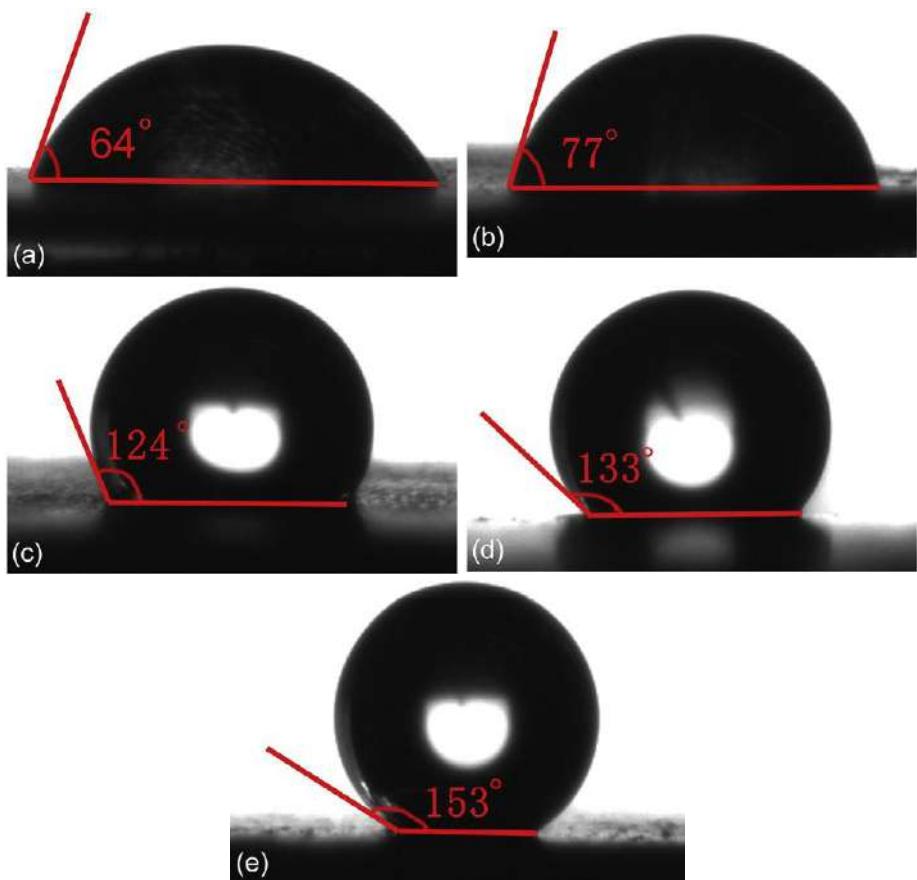
One of the most important applications of nanostructured metals is as active substrates of SERS for detecting molecules and for investigating the interactions between molecules and metal surfaces. The noble and inertia metals, including Au, Ag, and Cu, usually exhibit stronger SERS.

Figure 10.15 shows the SERS spectra of rhodamine 6G (R6G) molecules on the 3D-Mn-NPS with various nanopore sizes. It is obvious that smaller nanopore sizes result in significant improvements in SERS. In general, small nanopore sizes lead to the formation of nanoarchitecture with small metal ligaments and close interligament distances, both of which can significantly improve the SERS enhancement by enforcing localized electromagnetic fields from nanometer-sized metallic ligaments and the electromagnetic coupling among neighboring ligaments.

### 10.5.3 *Superhydrophobic performance*

In general, any surface with a water contact angle (CA) greater than 150° is called a superhydrophobic surface [27]. It is well-known that the wettability of a liquid on a solid surface depends not only on the chemical nature but also on the morphological structure of the surface [28]. Consequently, superhydrophobicity was obtained for the micro-nano hierarchical Cu/Cu<sub>2</sub>O structure.

The CA measurements were performed on various surfaces of the samples shown in Figure 10.16. A polished and smooth Cu sample was chosen as a reference with a CA of 64° (Figure 10.16a), indicating the surface was hydrophilic.



**Figure 10.16** Contact angles in various samples: (a) untreated, (b) laser texturing, (c) dealloying, (d) laser texturing + dealloying, and (e) laser texturing + dealloying + immersed in dodecane-1-thiol.

Surface roughness and surface free energy are the two main factors governing the surface wettability. In respect to the surface roughness, Figure 10.16 demonstrated that the CA of the surface increased when the surface became rough. Compared with the wettability of the smooth surface, both laser texturing (Figure 10.16b) and dealloying (Figure 10.16c) resulted in an increase of CA due to the increased roughness. After laser texturing, CA increased slightly to 77°. It demonstrated that the micro-structures produced by laser texturing did not alter the wettability properties of the surface significantly. After dealloying, the hydrophobic surface was obtained as shown in Figure 10.16c, which indicated that nanoscale structures exhibited good hydrophobicity. The dual-level hierarchies increased the surface roughness to a greater extend (Figure 10.16d). The CA (133°) of the samples with hybrid micro-nano

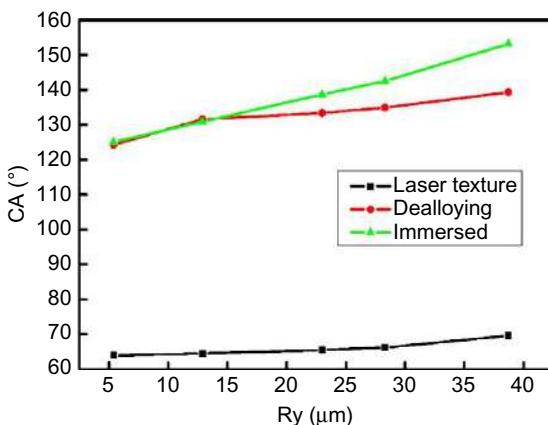


**Figure 10.17** Relationship between the contact angle and roughness.

structures was the highest among other samples treated with laser microtexturing or dealloying alone. This demonstrated that the micro-nano dual hierarchical structures are more capable of achieving the hydrophobicity observed in nature.

In the aspect of the surface energy (Figure 10.17), the samples with dual hierarchical structure were immersed in the ethanol solution to decrease the surface energy and significantly increase the CA. CA increased to  $153^\circ$  to achieve superhydrophobicity (Figure 10.16e).

#### 10.5.4 Photodegradation performance

The photodegradation measurements were performed in 5 mL of 10 mg/L methyl orange with various as fabricated SMNS using an incandescent lamp for 4 h at  $25^\circ\text{C}$ .

Figure 10.18a shows the transmission and visible light driven photocatalytic degradation of methyl orange by four specimens: Laser deposition (milliscale), laser ablation (microscale), dealloying (nanoscale), and hybrid method (micro-nanoscale). The degradation by using these SMNS occurred from 300 to 550 nm, and the transmission peak was 460 nm, very near the peak of sunlight radiation. This indicated that the degradation was due to light irradiation. In addition, the transmission of the specimens with nanoscale structure and the hierarchical structure were obviously better than those of the other two specimens due to the presence of nanoscale structures. Figure 10.18b shows that the concentration of methyl orange in various scale structures decreased with time under visible light irradiation. After 4 h, the concentrations of methyl orange decreased to 32.77%, 46.53%, 82.11%, and 94.54% for micro-nano hierarchical structure, nanoscale structure, microscale structure, and milliscale plate, respectively. Among those, the hierarchical structure displayed the best result in photo degradation. The difference could be attributed to the different scales and compositions of the various structures. The intense absorption in the visible range can be attributed to the high photocatalytic activity of  $\text{Cu}_2\text{O}$  and the properties of the dual-scale structures under visible light irradiation.

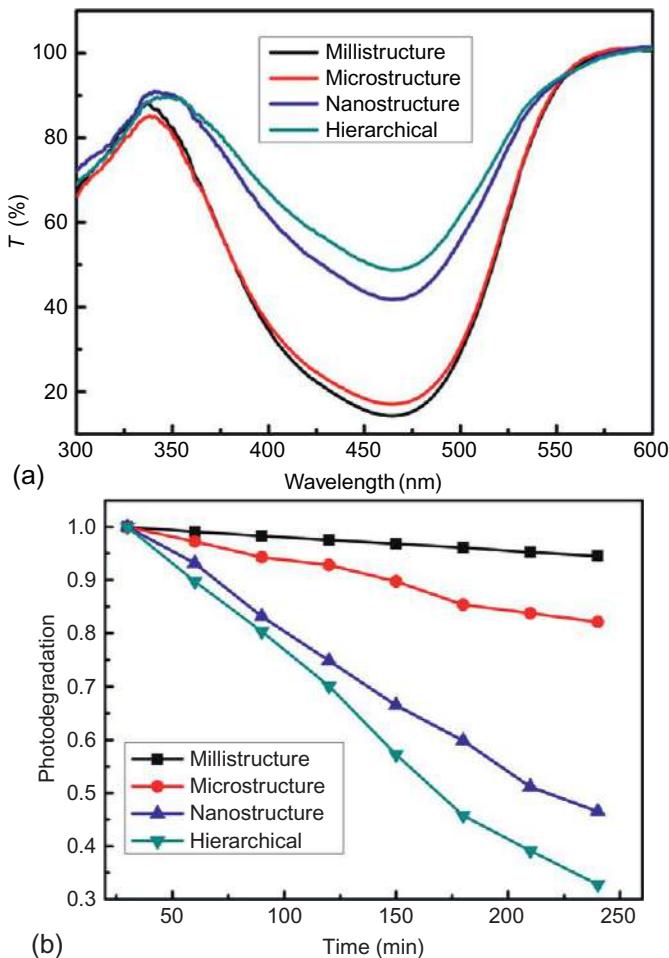


**Figure 10.18** Photo degradation results: (a) transition of methyl orange and (b) photo degradation rate with respect to time.

## 10.6 Conclusion

In this chapter, we introduce a novel laser processing-dealloying hybrid approach for micro-nano structures. This approach enables the fabrication of micro, nano, and micro-nano surface structures with tunable size in a thick fusion layer metallurgically bonded to any engineering material substrate for easy functionalization.

We first deposited a CuMn alloy layer with specific composition onto the surface of an engineering material, then modulated the surface microstructure and composition homogeneity of the as-deposited layer by laser remelting, and finally applied a chemical dealloying process. By the above approach, we were able to fabricate three kinds of micro-nano structures: (1) Nanoporous Cu structures with minimum pore size of

35.2 nm, pore rate of 84.5%, and specific surface area of  $65.3\text{ m}^2/\text{g}$ ; (2) three-dimensional Mn-based nanoporous structure, consisting of a 3D network of  $\text{MnO}$  nanowire skeletons and nanoporous channels—the nanopores could be tailored to be less than 25 nm in diameters, with surface roughness factor reaching up to 990; and (3) micro-nano hierarchical  $\text{Cu}/\text{Cu}_2\text{O}$  structure consisting of regular microbumps and bicontinuous nanopores, with the height of micro bumps tunable in the range of 2–120  $\mu\text{m}$  and the average diameter of nanopores modulated from 20 nm to 1  $\mu\text{m}$ .

The fabricated micro-nano structures showed good potential for functionalization in catalysis, superhydrophobicity, degradation of methyl orange, SERS, and catalysis transform.

## References

- [1] C. Neinhuis, W. Barthlott, Characterization and distribution of water-repellent, self-cleaning plant surfaces, *Ann. Bot.* 79 (6) (1997) 667–677.
- [2] D. Oner, T.J. McCarthy, Ultrahydrophobic surfaces effects of topography length scales on wettability, *Langmuir* 16 (20) (2000) 7777–7782.
- [3] B. He, N.A. Patankar, J. Lee, Multiple equilibrium droplet shapes and design criterion for rough hydrophobic surfaces, *Langmuir* 19 (12) (2003) 4999–5003.
- [4] N.J. Shirtcliffe, G. McHale, M.I. Newton, et al., Dual-scale roughness produces unusually water-repellent surfaces, *Adv. Mater.* 16 (21) (2004) 1929–1932.
- [5] H. Li, X. Wang, Y. Song, et al., Super-amphiphobic aligned carbon nanotube films, *Angew. Chem. Int. Ed.* 113 (9) (2001) 1793–1796.
- [6] Y. Wu, H. Sugimura, Y. Inoue, et al., Thin films with nanotextures for transparent and ultra water-repellent coatings produced from trimethylmethoxysilane by microwave plasma CVD, *Chem. Vap. Deposition* 8 (2) (2002) 47–50.
- [7] Y. Lu, Y. Yin, B.T. Mayers, et al., Modifying the surface properties of superparamagnetic iron oxide nanoparticles through a sol-gel approach, *Nano Lett.* 2 (3) (2002) 183–186.
- [8] U.N. Maiti, P.K. Ghosh, S. Nandy, et al., Effect of Mn doping on the optical and structural properties of  $\text{ZnO}$  nano/micro-fibrous thin film synthesized by sol-gel technique, *Physica B* 387 (1-2) (2007) 103–108.
- [9] H. Masuda, Ordered metal nanohole arrays made by a two-step, *Science* 268 (1995) 1466.
- [10] G. Acharya, C.S. Shin, M. Mcdermott, et al., The hydrogel template method for fabrication of homogeneous nano/microparticles, *J. Control. Release* 141 (3) (2010) 314–319.
- [11] Y. Zhao, L. Jiang, Hollow micro/nanomaterials with multilevel interior structures, *Adv. Mater.* 21 (36) (2009) 3621–3638.
- [12] Z. Ma, C. Guo, Observation of a step change in the optical absorption of gold in a vacuum, *Phys. Rev. B* 74 (23) (2006) 233404.
- [13] A.Y. Vorobyev, C. Guo, Femtosecond laser nanostructuring of metals, *Opt. Express* 14 (6) (2006) 2164–2169.
- [14] A.Y. Vorobyev, C. Guo, Enhanced absorptance of gold following multipulse femtosecond laser ablation, *Phys. Rev. B* 72 (19) (2005) 195422.
- [15] F. Yin, Y. Ohsawa, A. Sato, K. Kawahara, X-ray diffraction characterization of the decomposition behavior of  $\gamma\text{Mn}$  phase in a Mn-30 at.%Cu alloy, *Scr. Mater.* 40 (9) (1999) 993.
- [16] F. Jia, C. Yu, Z. Ai, et al., Fabrication of nanoporous gold film electrodes with ultrahigh surface area and electrochemical activity, *Chem. Mater.* 19 (15) (2007) 3648–3653.

- [17] J. Erlebacher, M.J. Aziz, A. Karma, et al., Evolution of nanoporosity in dealloying, *Nature* 410 (6827) (2001) 450–453.
- [18] W.C. Li, T.J. Balk, Effects of substrate curvature on dealloying of nanoporous thin films, *Scr. Mater.* 61 (12) (2009) 1125–1128.
- [19] L.Y. Chen, J.S. Yu, T. Fujita, et al., Nanoporous copper with tunable nanoporosity for SERS applications, *Adv. Funct. Mater.* 19 (8) (2009) 1221–1226.
- [20] S.P. Jeng, R.J. Lad, V.E. Henrich, Satellite structure in the photoemission spectra of MnO (100), *Phys. Rev. B* 43 (14) (1991) 11971–11977.
- [21] B. Djurfors, J.N. Broughton, M.J. Brett, D.G. Ivey, Electrochemical oxidation of Mn/MnO films: formation of an electrochemical capacitor, *Acta Mater.* 53 (4) (2005) 957–965.
- [22] A. Eichler, CO oxidation on transition metal surfaces: reaction rates from first principles, *Surf. Sci.* 498 (3) (2002) 314–320.
- [23] C. Xu, X. Xu, J. Su, Y. Ding, Research on unsupported nanoporous gold catalyst for CO oxidation, *J. Catal.* 252 (2) (2007) 243–248.
- [24] V. Zielasek, B. Jurgens, C. Schulz, J. Biener, M.M. Biener, A.V. Hamza, M. Baumer, Gold catalysts: nonporous gold foams, *Angew. Chem. Int. Ed.* 45 (48) (2006) 8241–8244.
- [25] F. Maillard, S. Schreier, M. Hanzlik, E.R. Savinova, S. Weinkauf, U. Stimming, Influence of particle agglomeration on the catalytic activity of carbon-supported Pt nanoparticles in CO monolayer oxidation, *Phys. Chem. Chem. Phys.* 7 (2005) 385–393.
- [26] B. White, M. Yin, A. Hall, D. Le, S. Stolbov, T. Rahman, N. Turro, S. O'Brien, Complete CO oxidation over Cu<sub>2</sub>O nanoparticles supported on silica gel, *Nano Lett.* 6 (9) (2006) 2095–2098.
- [27] X. Zhou, X. Guo, W. Ding, Y. Chen, Superhydrophobic or superhydrophilic surfaces regulated by micro-nano structured ZnO powders, *Appl. Surf. Sci.* 255 (2008) 3371–3374.
- [28] Z. Chen, Y. Guo, S. Fang, A facile approach to fabricate superhydrophobic aluminum surface, *Surf. Interface* 42 (2010) 1–6.

This page intentionally left blank

# Laser-controlled intermetallics synthesis during surface cladding

11

I.V. Shishkovsky<sup>1,2</sup>

<sup>1</sup>Lebedev Physics Institute (LPI) of Russian Academy of Sciences, Samara, Russia;

<sup>2</sup>Moscow State Technological University named "STANKIN", Moscow, Russia

## 11.1 Introduction

The selection of promissory powder compositions for laser cladding (LC) is traditionally based on the conditions of a metallurgical miscibility (the possibility to form a eutectic) first in the liquid and then in crystallizing phases after the laser treatment (LT). If the melting point of the cladding powder is lower than the substrate temperature, then a good wettability of the melt provides the required contact conditions. Otherwise, the intermixing of unfused cladding particles occurs in the melting pool of the substrate, and this is called the metal-matrix (MM), ceramic-matrix (CM) hardening after the crystallization. During the melting process, the fusible phase spreads by the grain boundaries of the refractory phase and, being crystallized, serves as a binder that reinforces the surface strength after the laser influence (LI). These hardened inclusions substantially improve the physical and mechanical properties by MM composites.

Hence, in parallel with the search for new challenging possibilities of powdered systems for LC and with the expansion of the synthesized parts of the functional resource, it seems reasonable to concurrently use functionally graded (FG) composite materials, as well as to use combinations of LC with other processes [1]. Thus, the combination of LC with soldering makes it possible to produce three-dimensional (3D) models out of bimetals having a high adhesion of the solder melt to the metallic phase, ensuring the improved mechanical properties of the sample.

Another well-studied hybrid process is plasma spraying with subsequent LT. In comparison with the laser source, the plasma source is less concentrated but more powerful and economical. Therefore, during laser plasma assisted spraying (LPASS) it is possible to achieve the fabrication of high-strength coatings with a sufficient cohesion to the substrate. Lately, there has been a great deal of interest in the combination of a cold spray with LT [2,3]. In the first stage of the laser-assisted cold spray (LACS) process, the FG coatings on the substrate are produced due to the mechanical embedding of the accelerated powdered particles. In the second stage, these FG layers undergo a precision laser remelting, resulting in improved adhesion between dissimilar layers, owing to the creation of chemical bonds and new compositions, in the increase of the coating strength and in the emergence of new and interesting mechanical properties.

In papers by Shishkovsky *et al.* [4], the possibility of a selective laser sintering/melting (SLS/M) process and LC of exothermal powdered mixtures, traditionally applied in self-propagated high-temperature synthesis (SHS), was shown for the first time and theoretically confirmed [5]. Thermal-physical modelling of the SLS/M + SHS and LC+SHS processes will be considered further in [Section 11.5](#) of this chapter, and in [Section 11.4](#) we will describe experiments on the thermal field measurement in the combustion front under such a hybrid combination.

## 11.2 Laser control of self-propagated high-temperature synthesis (SHS) as synergism of the two high-tech processes

### 11.2.1 Self-organization under SLS on exothermal powder composition

When realizing the combination of the LI and the SHS processes, it is necessary to make sure that the controllable exothermal combustion reaction takes place exactly within the spot of the LI, scanning by the powdered composition surface, because only the spaced-selective cladding with high-resolution allows a synthesized object to take a tightly defined shape. This answers the long-term objective of 3D synthesis. The SHS process realized by the SLS/M or LC methods created not only stronger material copies of the complex form [6], but also increased the functional features of these 3D objects, owing to the new phases synthesis (intermetallics, piezoelectric, and ferroelectric, etc.).

We were the first to offer and realize the laser-controlled combination of the SLS/M+SHS processes in the overall technological process using the following powdered compositions [1]:

- metal mixtures for the intermetalide synthesis in systems Ni + Ti, Ni + Al, Ti + Al, Fe + Ti, Fe + Al, Cu + Al + Ni;
- mixtures of metals in the gas phase/analogue of a laser chemical vapor deposition process: Ti + N<sub>2</sub>, Al + N<sub>2</sub>, Ti + O<sub>2</sub>;
- oxide's metal mixtures for the ceramics synthesis TiO<sub>2</sub> + ZrO<sub>2</sub> + PbO, Al(Al<sub>2</sub>O<sub>3</sub>) + Zr(ZrO<sub>2</sub>);
- laser-controlled synthesis of barium hexaferrites and lithium ferrites-spinels from BaO<sub>2</sub> + Fe<sub>2</sub>O<sub>3</sub> + Cr<sub>2</sub>O<sub>3</sub> + Fe, Li<sub>2</sub>CO<sub>3</sub> + Fe<sub>2</sub>O<sub>3</sub> + Cr<sub>2</sub>O<sub>3</sub> + Fe.

Optimal LI regimes for the maintenance of the controllable exothermal reaction exactly within the laser spot were determined. For some systems, the 3D samples made of the above-mentioned compositions were obtained. In this chapter we will discuss the synthesis of intermetallic phases, in particular aluminide of titanium, nickel, and iron in the matrix of the main metal under the layerwise LC.

Among other things, the originality of our approach consists in the fact that the LI is not just reduced to an additional and precise thermal energy input, as in cases for the LPASS and LACS [7,8]. A special frequency and amplitude selection of the external field with respect to the natural oscillation frequencies of the “powder

mixture + synthesized sample” system, can initiate a number of phenomena of the resonance nature. The LI as one of the methods for achieving this resonance state is easily controllable, power consuming, and has a point nature, that is, it is extremely challenging as the source of the external electromagnetic fields. On the whole, the problem of self-similar phenomena, which can arise in such experiments, is interesting by itself and deserves a special separate examination. Note that self-similarity is not the same as self-organization. If we have a coherent structure, and the laser has a coherent property, and the LI acts beyond the multiphase systems, this is one of the conditions of the appearance of the self-organizing media.

The combination of laser alloying with the ultrasonic treatment considerably improves the physical-mechanical properties of the end product, due to the cavitation processes in the liquid phase. The selection of the amplitude and frequency of the ultrasonic vibrations is determined as far as the conditions for the standing acoustic wave’s formation in the laser melting zone.

The LI is an electromagnetic wave with its own amplitude and frequency. In contrast to usual light sources, the LI possesses unique, fundamental physical properties. These are monochromaticity, space and temporal coherence, narrow LI directivity, and strict polarization. If the last two of the LI’s properties are used in the laser technology, then the wave properties are not mentioned. However, considering the ultradispersed (nanodimensional) powders, aerosols (i.e., when particle size is comparative to or less than the light wavelength), and the wave nature of the LI (its amplitude, frequency, and phase) begins to play a not insignificant role. So it is possible to govern such structures by means of the LI parameter variation.

The variation of depth ( $h$ ) of the SHS reaction against specific laser energy input ( $A$ ) is shown in [Figure 11.1](#). It can be noted that with increasing  $A$  the values of  $h$  tends to also increase. If  $A$  is increased beyond the limit shown in [Figure 11.1](#), this results in an uncontrolled thermal explosion across the entire volume of the sample. In the case of lower values of  $A$  (below that listed in the figure), the layers are incompletely sintered and lead to a mechanically weak, friable composite. It is important to note that the slopes of the plots characterize the rate of power supply that is suitable for sustaining the SLS/M process.

For Ni powder of PGSR-4 grade, the  $h$  value is greater than that for pure Ni. It is also clear that the impurities present within the PGSR-4 grade of Ni powder tend to strengthen the sintered layer. Fine Ti powder (PTOM grade 98-99 wt.% Ti) exhibits a higher level of reactivity than the Ti powder of higher purity 99.2 wt.%Ti ([Figure 11.1](#), curves 3 and 4). Therefore, combinations of these powders can also be used to influence the SLS process. As can be seen from [Figure 11.1](#), the process is markedly affected by the composition of the starting mixture. For the Al+Ti mixtures 1:1, and 1:3 stoichiometric ratios in air, and 3:1 in N<sub>2</sub> (absent in [Figure 11.1](#)), no controlled SHS-SLS was achieved. The slopes are indicative of different energy consumption levels in the respective reactions (compare curves 3 and 6 in [Figure 11.1](#)). Curve 7 ([Figure 11.1](#)) refers to the synthesis of the hexaferrite BaFe<sub>12x</sub>Cr<sub>x</sub>O<sub>19</sub> from a mixture of metal and oxides.

Calculated in [4], induction periods for  $P$ ,  $V$ , and  $D$  imply that the Ni<sub>3</sub>Al synthesis takes place only within the laser beam spot. The spot diameter (about 60 μm) is

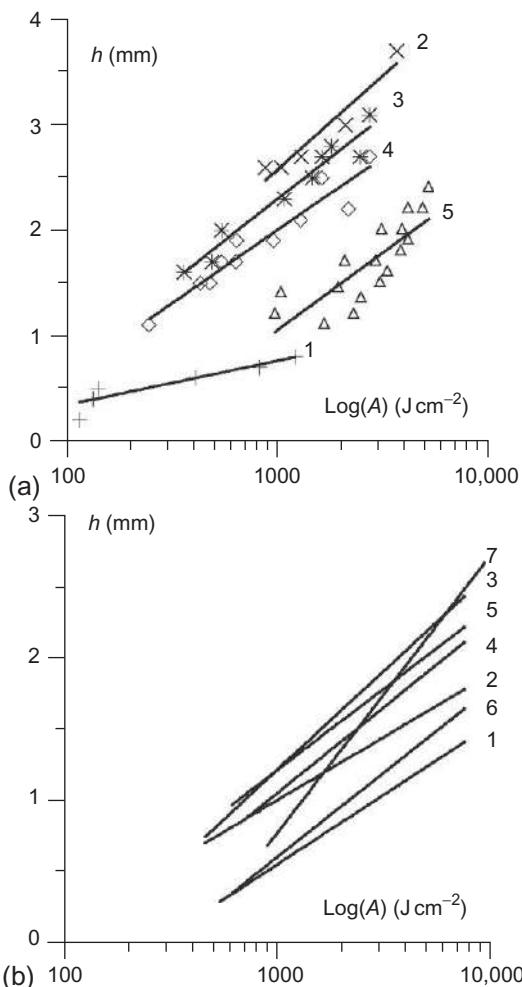


**Figure 11.1** The depth of laser-controlled sintering  $h$  versus  $\log A$  for [7]: (a) (1)  $\text{Ni} + \text{Al}$  (1:1), (2-4)  $\text{Ni} + \text{Ti}$  (1:1), (2) PGSR4+PTH, (3) PGSR4+PTOM, (4) PNK+PTH, (5) PZT. (1, 2, 5) SLS on air, (3, 4) under Ar and (b) (1, 4, 6)  $\text{Al} + \text{Ti}$  (3:1), (2, 5)  $\text{Al} + \text{Ti}$  (1:1), (3)  $\text{Al} + \text{Ti}$  (1:3), (7)  $\text{BaFe}_{12x}\text{Cr}_x\text{O}_{19}$ . (1-3) SLS on air, (4, 7) under Ar, (5, 6) under  $\text{N}_2$ .

comparable with  $D$  and the particle size of the starting powder. X-ray diffraction (XRD) data for the Ni-Al and Al-Ti systems confirm the formation of the respective aluminides. The energy activation of the SHS reaction in the system Ni-Al is significantly higher than in systems Ni-Ti, Ti-Al, so the synthesis process in these systems are badly controlled (see data presented in Tables 11.1 and 11.2). Titanium aluminide under 3D SLS/M+SHS also poses some challenges (Figure 11.1). In particular, the system Al-Ti “burns” practically on all regimes in the  $\text{N}_2$  and/or Ar as on the air, and from this it has been noted that the  $\text{Al}_x\text{Ti}_y$  synthesis requires a careful preparation of mixture (which requires oxygen and nitrogen to be removed from pores).

**Table 11.1 Thermophysical parameters of the Ni-Al system**

Phase	$T_i$ (°C)	$E$ (kJ/mol)	$Q$ (J/kg)
Ni <sub>2</sub> Al <sub>3</sub>	–	–	$1.9 \times 10^6$
NiAl	$910 \pm 25$	$135 \pm 27$	$9.7 \times 10^6$
Ni <sub>3</sub> Al	$925 \pm 16$	$115 \pm 25$	$2.4 \times 10^6$
(Ni+Al) Melt	–	48.24	$1.3 \times 10^6$

Sources: [9,10].

**Table 11.2 Thermophysical properties of the ignition reaction in the Ti-Al system**

Initial powder mixture	$T_i$ (°C) thermocouple/simulation		$E$ (kJ/mol)	$Q$ (J/kg)	X-ray comments
	Beginning	End			
Al: Ti = 1:3	$645 \pm 10/-$	$1150 \pm 50/1244$ (adiabatic)	$18.0 \pm 1$	–	Ti main, Al small, Ti <sub>3</sub> Al, TiAl, TiAl <sub>3</sub> minor
Al: Ti = 1:1	$645 \pm 10/-$	$1400 \pm 50/1245$ (adiabatic)	$19.5 \pm 1$	–	Ti <sub>3</sub> Al main, TiAl, TiAl <sub>3</sub> small
Al: Ti = 3:1	$645 \pm 10/-$	$1200 \pm 50/1271$ (adiabatic)	$22.5 \pm 1$	–	Al main, Ti, TiAl <sub>3</sub> small

Sources: [11,12].

What are the main reasons for conducting the SHS reaction under the LI? The specific characteristics of laser energy dosing for the SHS process is such that (1) it is impossible to consider the laser influence as a heat source only, particularly when using it in the case of soot; (2) the laser influence is a high-energy source (temperature gradients and heating-cooling velocities are comparable and can exceed SHS energy); (3) it is impossible to allow for a united macro front of the SHS reaction under the selective LI, as this process will become uncontrolled and it is impossible to fabricate the 3D object; and (4) temporary and spatial LI shape are not comparable with traditional types of heat sources (such as plasma, arc, and induction heating). Under experimental conditions, a heat explosion has been observed when the laser control under SHS process was lost.

Experimental heat situation studies in the LI area for exothermal powdered mixtures (Section 11.3) [13,14] and a detection of electromotive force occurrence on the combustion front [8] indicate that we have a deal with “laser-controlled” high-temperature syntheses (LHS) of new chemical compounds (more information on this

is given in the chapter on aluminides of the Ti, Fe, and Ni) from the initial mixtures of reactionary powders with stoichiometry ratios.

### **11.2.2 Thermophysical estimations and fractal behavior for laser-controlled high-temperature syntheses**

Analysis of the intermetallic phase substructure synthesized after the SLS/M+SHS overlapping gives very interesting results under great magnification (Figure 11.2). The intermetallic surface has a brightly denominated fractal order. Such order is observed at the LI regimes with a high-energy input. Moreover, such ordering on the elementary level has also been observed under the SLS/M+SHS overlapping. The SLS/M process of prealloying intermetallide (for instance, nitinol graded PN55T45) gives the traditional liquid phase sintered morphology.

The formed nanostructures present an interesting object itself for the study of the system behavior with lowered dimensionality. However, geometric shapes of synthesized nanostructures in reactionary-capable Ni-Ti, Ni-Al, or Ti-Al powdered systems are, in principle, different.

The fine structure in the intermetallic compounds on the micro- and the nanoscale after the SLS/M+SHS overlapping will determine the successful applications of the 3D articles. This area requires further investigation. As it was noted in [4,13,14], there is a clear correlation between the LI parameters and the morphological structure of the sintered surface under the layerwise laser synthesis of intermetallic compounds. It was shown in [11] that the high degree of nitinol implant osteointegration has a great deal of influence on the developed sub- (nano-) structure of porous implants.

The evolution of the micro- and macrostructure (surface morphology), depending on the laser processing parameters, can be tracked through analysis of the fractal dimension of the structure,  $D$  [15,90]. It is obvious that the transition from the nano- to the micro- and macrostructural levels (by process of the atom-by-atom droplet formation under rapid crystallization of the melt) can be interpreted as percolation threshold, that is, the transition of the material to a state when the connection between individual particles (atoms) can be described as fractal cluster formation and segregation. Evolution of the percolation cluster is governed by structurally sensitive characteristics such as pore size, roughness, and specific surface area, dissipative structures appearing in the course of the structure formation, and coagulation and recrystallization processes. At the same time, the formation of new intermetallic phases under SLS/M+SHS can also lead to additional changes in  $D$ . Because the nucleation periods under structural phase transition and in the course of the molten pool crystallization are different, variations of  $D$  should occur [16]. With the increase of the nucleation rate (i.e., laser cooling rate) the percolation cluster's structure becomes more compact while the fractal dimension tends to the Euclid's universal one [17]. In other words, the fractal dimension characterizes the degree of surface roughness.

Highly magnified images of the typical microstructures obtained in Ni-Al, Ti-Al, Fe-Ti, and Ni-Ti systems under SLS/M+SHS are presented in Figure 11.2. It can be

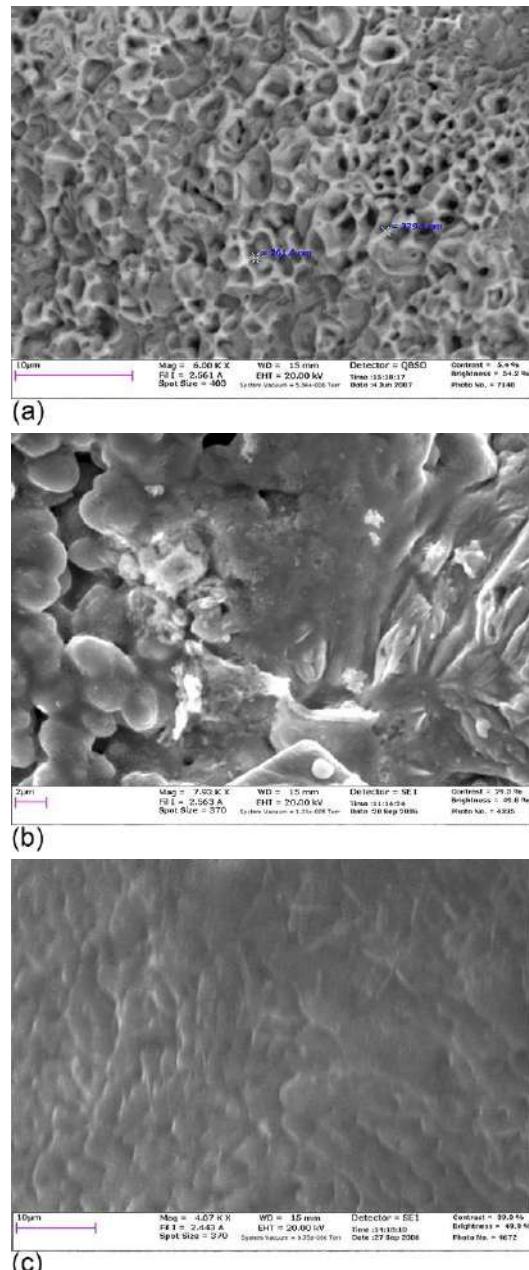


**Figure 11.2** Microstructure of the intermetallic synthesis during SLS/magnification and accelerating voltage are shown on pictures, laser beam diameter  $L_b \sim 100 \mu\text{m}$ : (a)  $\text{Fe-Ti} = 1:1$ ,  $P = 17.8 \text{ W}$ ,  $v = 2.8 \text{ cm/s}$ ; (b)  $\text{Ni-Al} = 1:1$ ,  $P = 30.3 \text{ W}$ ,  $v = 2.8 \text{ cm/s}$ ; (c)  $\text{Ti-Al} = 3:1$ ,  $P = 15.2 \text{ W}$ ,  $v = 1.5 \text{ cm/s}$ ;

*Continued*

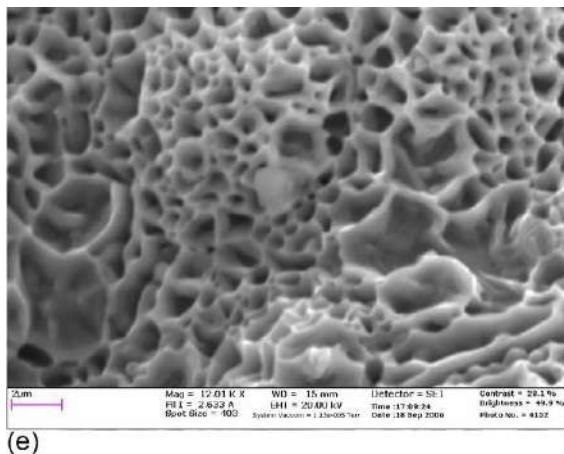
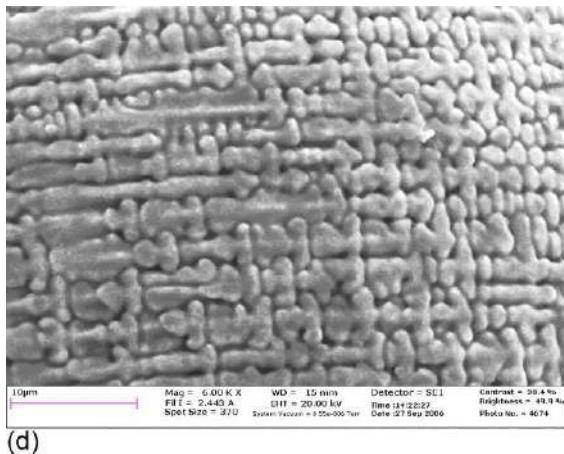


**Figure 11.2** Continued. (d) Ni-Al = 3:1,  $P = 30.3$  W,  $v = 11.4$  cm/s; and (e) Ni-Ti = 1:1,  $P = 13.9$  W,  $v = 5.7$  cm/s [11].

seen that there is a certain correlation between the shapes and the sizes of the obtained substructures (cf. Figure 11.2a, e and c, d). Further on, the intermetallic phase formation process will be analyzed on the basis of the phase diagrams of these systems.

According to the equilibrium phase diagram (EPD) of the NiAl system [4,9], the following phases are observed at the different heating and cooling stages. Under heating to temperatures up to  $T_e = 640$  °C, the metastable  $\text{Ni}_2\text{Al}_3$   $\gamma$ -phase emerges and grows. With further heating,  $\gamma$ - and  $\delta$ -phases coexist, then in the interval of  $1132$  °C <  $T$  <  $1638$  °C the  $\gamma$ -phase melts and the NiAl intermetallic ( $T_3 = 1638$  °C), the NiAl phase, followed by the  $\text{Ni}_3\text{Al}$   $\varepsilon$ -phase emerges in the subsequently cooled melt.

Therefore, depending on the selected LI parameters ( $P$ ,  $v$ ,  $Lb$ ) and the mixture composition, laser irradiation energy may be sufficient or not to achieve the appropriate temperatures and to obtain intermetallic phases predicted by the EPD in the SLS/M + SHS synthesized part. At the same time, a principle difference in the fine substructure in the Ni-Al (1:1) system in Figure 11.2b and in the Ni-Al (3:1) system in Figure 11.2d is evident. Dendritic structure of the NiAl system and mosaic structure of the  $\text{Ni}_3\text{Al}$  system indicate the varying character of the transformations under synthesis of these intermetallic compounds. It can be assumed that these differences in the ordered low-dimensional clusters are induced, among others, by the above-described phase formation conditions.

The EDX microanalysis cannot provide the type of the intermetallic phase, but the presence of phases such as  $\text{Ni}_3\text{Al}$  and NiAl may be established based on the quantitative content of these elements. X-ray phase analysis (XRD) results reported in Ref. [12] (see Section 11.3.3 also) and theoretical assessments in Ref. [1] showed that under laser-controlled synthesis, it will be more advantageous to obtain the  $\text{Ni}_3\text{Al}$  intermetallic phase compared to the NiAl one, as the former is steady. It may be related to the fact that the NiAl phase synthesis reaction is accompanied by a considerable heat release while the formation of this phase starts later than the  $\text{Ni}_3\text{Al}$  one's [4,9].

The XRD, SEM, and backscattered electron microscopy (BSEM) methods were applied in Ref. [18] to establish the sequence of the phase formation in the TiAl system under the temperature increase, including that induced by LI (cf. thermocouple measurement in Ref. [13,14]). It was shown that upon reaching  $T = 645 \pm 10$  °C, the reaction of combustion and synthesis of  $\text{Ti}_x\text{Al}_y$  phases (where  $x, y = 1, \dots, 3$ ) takes place at the boundary melt (Al)/solid (Ti) in the contact area of melted aluminium. As a result, an intermetallic frame consisting of  $\text{Al}_3\text{Ti}$  is formed with the subsequent TiAl phase synthesis from noncombusted Al and Ti. This type of microstructure is presented in Figure 11.2c. There is a certain similarity in the appearance of the substructures in Figure 11.2c and d.

The melting and exothermal reaction in the Fe-Al system starts at the boundary between Al and Fe and probably with participation of its oxides ( $\text{Fe}_2\text{O}_3$ ,  $\text{Fe}_3\text{O}_4$ ). This reaction is called a termite one. The yield of this reaction consists of  $\text{Fe}_x\text{Al}_y$  intermetallic compounds, and probably the alumina formed during the synthesis reaction, while the Al-Fe percentage diminishes [19]. The exothermic heat emission facilitates accelerated melting. The reaction mechanism involves not only the decrease of Fe, the conversion of  $\text{Fe}_2\text{O}_3$  to  $\text{Fe}_3\text{O}_4$  and  $\text{FeO}$ , and the oxygen release, but also aluminium oxidation, interaction of Al with the iron oxides, the formation of the complex Al-Fe-O,  $\text{Al}_2\text{O}_3$  oxide phases and Al-Fe intermetallic compounds proper, depending on the reaction temperature and Fe/Al ratio in the mixture.

During the high-speed laser cooling, the alloys with the aluminium content up to 34 at.% from the high to room temperatures they acquire the structure of  $\alpha$ -solid solution. In the alloys with the Al content ranging from 34 to 52 at.%, the  $\text{FeAl}_2$  structure is exclusively observed. Under the higher aluminium percentage, the different intermetallic compounds ( $\text{FeAl}_2$ ,  $\text{Fe}_2\text{Al}_5$ ,  $\text{FeAl}_3$ ) are formed. The ordered structure of the  $\text{Fe}_3\text{Al}$  type is formed in the alloys containing from 25% to 34% of Al, after a slow cooling. After the quenching of these alloys at the temperature of 600 °C and above, the

$\text{FeAl}_2$  structure appears. The ordering process is characterized by a change in the number of physical properties, in particular, by a lower value of the Curie point, by a change in the crystal lattice spacing at room temperature depending of the content of Al. With its content up to 10 wt.% the crystal lattice spacing increases linearly with the increasing in the content of the alloying element. In the ordered state, the alloys with the Al content ranging from 10 to 20 wt.% are characterized by almost constant lattice spacing.

Finally, the  $\text{Fe}_x\text{Ti}_y$  and  $\text{Ni}_x\text{Ti}_y$  intermetallic phases are synthesized in the equiatomic systems  $\text{FeTi}$  and  $\text{NiTi}$  [1]. The  $\text{Ti}_2\text{Fe}$ ,  $\text{TiFe}_2$ , and  $\text{Ti}_2\text{Ni}$  metastable phases may occur as well, respectively. As can be seen in [Figure 11.2a and e](#), the similarity in the trend of the processes leads to the formation of resembling substructures.

The wall thickness  $h$  of the ordered honeycomb-like nanostructures typical for the Ni-Ti and Fe-Ti systems versus laser energy input is plotted in [Figure 11.3](#). The wall thickens and diminishes with the laser energy input increase, and the substructures become more openwork. As for substructures in the Ni-Al and Ti-Al systems, such boundaries (honeycombs) are hard to distinguish.

The fractal dimension  $D$  is plotted in [Figure 11.4](#). The varying character of the  $D$  change under the increase of the laser energy input  $A$  should be noted.  $D$  grows in the system  $\text{Ni}_3\text{Al}$  that indicates a more complicated character of such nanostructures (cf. also [Figure 11.2d](#)). A similar behavior of  $D=D(A)$  was observed in Ref. [8] concerning the fractal dimension of pores under SLS/M of pure titan. Both increase and decrease of  $D$  occurred in the Ni-Ti and Fe-Ti systems. Variations of the  $D$  orientation indicate a change of the phase formation mechanism, that is, the metastable  $\text{Ti}_2\text{Fe}$ ,  $\text{TiFe}_2$ , and  $\text{Ti}_2\text{Ni}$  phases give place to the more steady  $\text{TiFe}$  and  $\text{TiNi}$  intermetallic phases, respectively. It was found that the reactive capability of the  $\text{NiAl}$  system is

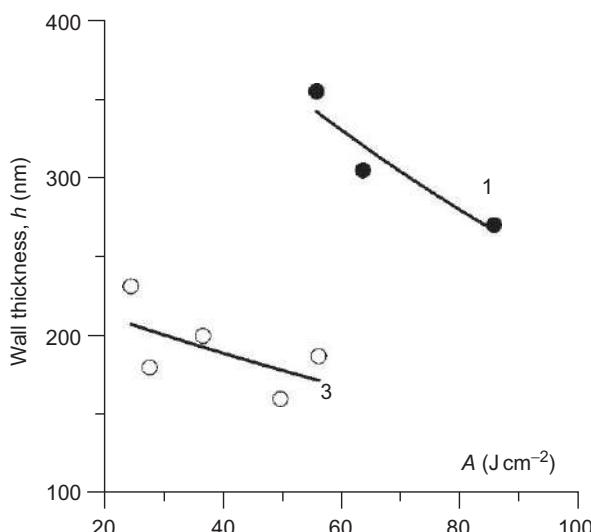


**Figure 11.3** Dependence of the nano wall thickness  $h$  (nm) on laser energy input  $A$  ( $\text{J}/\text{cm}^2$ ): (1) Fe-Ti and (3) Ni-Ti [11].

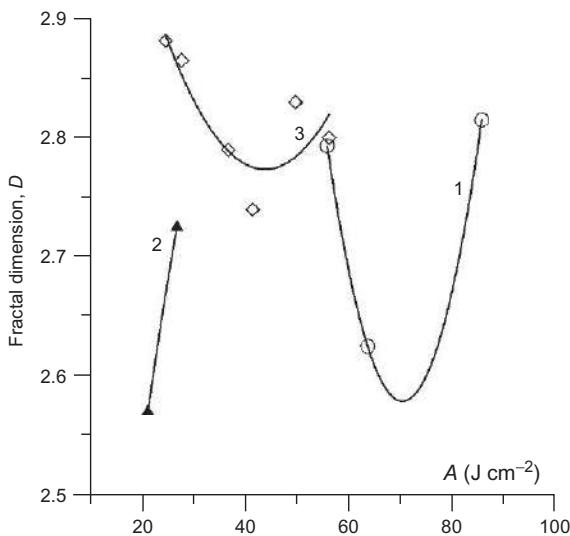


**Figure 11.4** Fractal dimension  $D$  versus laser energy input  $A$  ( $\text{J}/\text{cm}^2$ ): (1) Fe-Ti; (2) 3Ni-Al; and (3) Ni-Ti.

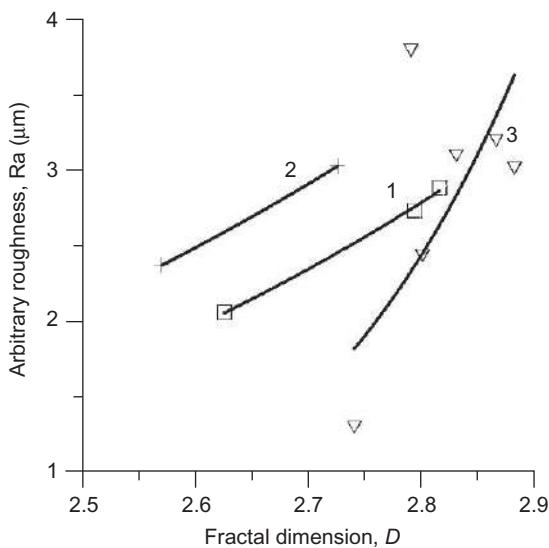


**Figure 11.5** Arbitrary roughness  $R_a$  ( $\mu\text{m}$ ) versus fractal dimension  $D$  [11].

enhanced and  $D$  increases when PGSR4 powder is replaced by pure nickel. The highest  $D=2.91$  was observed in the NiTi system at  $P=13.9$  W and  $v=3.8$  cm/s. Figure 11.5 plots the nanosurface roughness versus the fractal dimension. Thus, it was shown that fractal dimension is a structure-sensitive parameter characterizing the degree of self-similarity of irregularities of different sizes [8].

Thus, the hybrid combination of the SLS/M+SHS and LC+SHS processes is characterized as far as the synergetic effect, which is evinced by obtaining not only functional articles, but also to reaching the synthesis conditions of new intermetallide phases and structures ordering on all levels from the nano- to the microsizes of crystallites.

### 11.3 Overlapping of laser cladding and SHS processes for the fabrication of the functional graded (FG) iron, nickel, and titanium aluminides in the surface layers

As was noted in [Section 11.2](#), we experimentally approved the layerwise laser melting and cladding process in the Me + Al (Me = Ti, Ni or Fe) systems [4,12,20–22] and theoretically substantiated [23] the approach, where the strengthened intermetallide is created directly within the LAM process in the metallic matrix due to the synthesis reaction. Nickel aluminides NiAl and Ni<sub>3</sub>Al are characterized by high heat resistance, including the conditions of high-temperature gas flows. The intermetallic compounds in the Al-Ti system are promising materials for the manufacturing of high-temperature and radiation-resistant coatings. Titanium and nickel aluminides can be used as a carrier matrix for catalytic additives. Titanates of iron are promising in hydrogen power engineering, and nickel titanium is widely known as a biocompatible material.

The LI initiates a chemical reaction between the particles in the powder mixture of stoichiometric composition, thus leading to the intermetallic phase, and the excess substance (a deviation from the stoichiometry) aggregate the material matrix. The synthesis reaction realization is advantageous due to the finer and more uniform distribution of the inclusions in the crystalline structure, its internal stability, and the additional release of the exothermic reaction energy under the structural-phase transformations. The LI does not only activate the synthesis reaction, it also contributes to the acceleration of crystallization and governs the properties of the intermetallide microstructures ([Figures 11.3–11.5](#)). By controlling the poured layer thicknesses (i.e., the volume of the reaction zone) this can influence the motion of exothermic synthesis reactions and the solidification process (due to the change in thermal conditions), and can also have an influence on the size and shape of the microstructures. Furthermore, the laser power and scanning speed also affect the melting-crystallization conditions.

Functionally graded structures (FGS) and FG objects fabricated by applying complex and dissimilar materials ensure the specific properties of the final product. The manufacturing of 3D FG objects by the 3D LC and/or direct metal deposition (DMD) is one of the most promising techniques capable of meeting various industrial challenges [24,91]. This approach permits new freedoms in design and manufacturing, thus allowing, for example, to create an object with the desired shape, internal structure, and engineering composition, including the appropriate physical-mechanical properties, within a single-step fabrication process.

Because LI is reflected well by aluminium, the more refractory Me (Ti, Fe or Ni) must be the matrix material, and, in accordance with the Me-Al phase diagram, it should be expected that it will obtain the next stable intermetallide phases of

aluminides as— $\text{Me}_3\text{Al}$ ,  $\text{MeAl}$ ,  $\text{MeAl}_3$  (plus some metastable phases) in the exothermic reaction of the type:  $x\text{Me} + y\text{Al} \rightarrow \text{Me}_x\text{Al}_y + Q$ , where  $Q$  is the reaction thermal effect. Under the Al selection as the matrix basis, besides problems with the energy transfer from the LI to the material, another factor will appear. Aluminium has a low melting point in comparison with the refractory metal melting point (cf. 660 against 1537 °C for iron), and it will more effectively remove a heat due to the higher thermal conductivity, which ultimately will require a larger laser energy input.

The method of FGS fabrication used in the present study is schematically presented in [Figure 11.6](#). The hatching distance was 2 mm, the layer depth was ~1 mm, and the powder feeding rate was ~10 g/min. The layers were made out of  $\text{Me} = (\text{Ti}, \text{Fe}, \text{or Ni})$  and Al powders on a related substrate by the following strategy: the first two layers were of pure Me, the next two consisted of 70% Me + 30% Al, the third couple of layers were of 50% Me + 50% Al, and lastly the upper 7th and 8th layers had the ratio of 30% Me + 70% Al. Each second layer was formed on the bottom layer after its turning by 90°. Argon was the carrying gas. The laser scanning speed was 500 mm/min, laser power varied within the range of 800–1200 W, and laser beam spot diameter was 3 mm. The first channel of the feeder with the Me powder had a gas flow rate of approximately 20 l/min while the second one with the Al powder was ~10 l/min.

In [Figure 11.7](#) the results of the layer-by-layer 3D synthesis are presented, and the LI passages are clearly visible. In the areas where the LI starts and at the turns from one passage to another, the laser beam speed is slowed down (as showed by the pointers in [Figure 11.7a](#)), and the heat dissipation speed is substantially less than in the central areas, thus leading to the cladded boundary obstruction and degradation

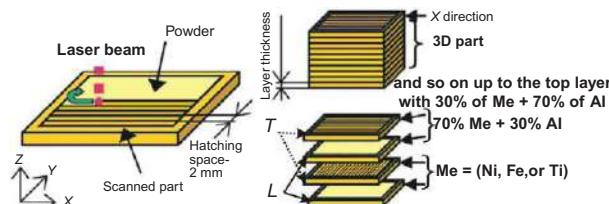


**Figure 11.6** Schematic of the multicomponent graded structure fabrication by 3D laser cladding. Longitudinal L and transversal T [22].

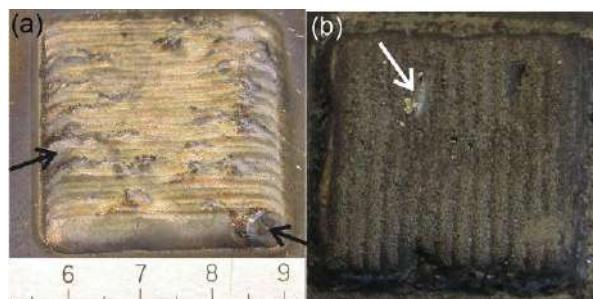


**Figure 11.7** Sample fabricated DMD process: (a) Ti-Al; (b) Fe-Al. Arrows indicate problem areas on the laser cladded surface.

(Figure 11.7b) of the physical and mechanical properties of the structures being synthesized.

### 11.3.1 Laser synthesis in Ti-Al system

Gamma alloys of titanium aluminides in the Ti-Al system have been developed for high-temperature applications in the automotive, aerospace, and power generation industries [25]. The TiAl-based intermetallics have a number of advantages over the conventional titanium alloys; they are a higher elasticity modulus, lower density, and have better mechanical properties at high temperatures [26,27]. In our studies [20,21] the possibility of the laser-induced reaction synthesis of  $Ti_xAl_y$  intermetallics during the 3D laser sintering or cladding was asserted.

In accordance with the phase diagram, we expected to obtain the following stable intermetallic phases of aluminium titanates:  $TiAl_3$ ,  $TiAl$ ,  $Ti_3Al$  in the exothermic reaction of the type  $xTi + yAl \rightarrow Ti_xAl_y + Q$ , where  $Q$  is the thermal reaction effect. This system is widely used in the SHS technology, and its fundamental thermo-physical characteristics ( $T_i$ —an ignition temperature,  $E$ —the energy activation of chemical reaction,  $Q_i$ —the thermal effects of exothermic reactions on one mole) and synthesized phases are known (see Table 11.2).

The following powders were used in the experiments: a titanium powder was TiGd2 grade 99.76 wt.% Ti; and aluminium was grade 99 wt.% Al. Both powders are produced by the TLS Technik GmbH&Co. The powder particles were mainly spherical with a size of  $\sim 80\text{-}100 \mu\text{m}$  for 95% of them. The substrates were round plates with a 65 mm diameter and 5 mm height made of Ti-6Al-4V. The powder size distribution was studied by means of a granulomorphometer ALPAGA 500NANO (OCCHIO s.a.).

The results of the optical metallography are presented in Figure 11.8. A series of photos show the characteristic microstructures based on the lower, middle, and upper

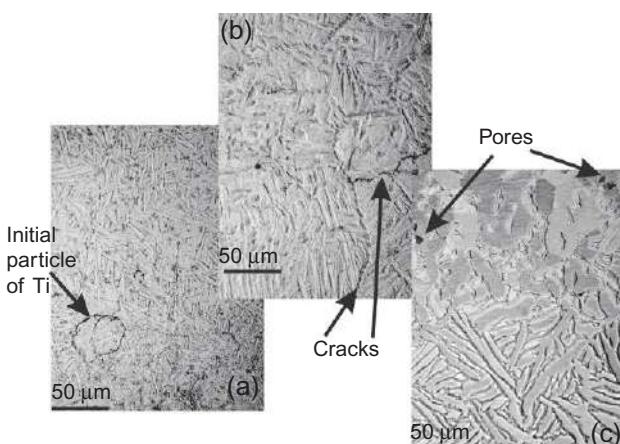


**Figure 11.8** OM micrographs showing the typical microstructures of 3D laser clad coating of Ti-Al multilayer system in Ar: (a) bottom layers  $\sim 250\text{-}300 \mu\text{m}$  from substrate; (b) middle layers  $\sim 900\text{-}1000 \mu\text{m}$  from substrate; and (c) top layers  $\sim 1700\text{-}1800 \mu\text{m}$  from substrate [21].

parts of the 3D laser cladded FG volume, that is, where the proportions of the powdered  $Ti+Al \approx 3:1$ ; 1:1, and 1:3 by weight ratios were comprised.

In the lower layers in the photo (Figure 11.8a), a predominantly lamellar microstructure typical of the single-phase titanium alloys with changing morphology can be observed. In the middle layers, mainly a coarse-grained structure occurs of the “basket netting” type. In the individual sections of near-surface layers, a fine grain is present with the martensite morphology of the  $\beta$ -titanium phase. The pointer in Figure 11.8a shows a nonremelted particle of the initial titanium. The existing structural heterogeneity is obviously connected with the nonuniform alloying, the exothermal reactions of the intermetallic synthesis, and high-speed laser cooling during the crystallization from the melt. In the lower and middle layers, subjected to a longer laser heating after solidification, the recrystallization features of  $\alpha$ -Ti phase are observed. These plates were etched less clearly, so against their background the dispersed precipitations of the second phase ( $\alpha_2$ - $Ti_3Al$  phase) appeared (Figure 11.8b).

These intermetallic phases, being more durable, cause the crack development at the grain boundaries (see Figure 11.8b). Finally, after the LC the upper layers are characterized by the coarse elongated grains of a dendrite type.

The measured microhardness (Figure 11.9) of the cladded layers grows from the substrate to the top irregularly. We believe this to be connected with a local hardness increase in the intermetallic phase locations. As a whole, the microhardness values correspond to similar measurements on the titanium aluminides after the DMD and LENS processes [26].

The X-ray analysis results are presented in Figure 11.10. The lower curve in Figure 11.10 corresponds to the diffractogram of the initial powder  $Ti+Al = 1:1$  mixture without any treatment. As seen from the lower curve, the most intensive lines belong to (111)  $\alpha$ -Al and (101)  $\alpha$ -Ti, still a weak (101) line of  $\beta$ -Ti phase is also visible. These intensive lines of the initial phases completely disappear after the 3D laser cladding. However, there remains a sufficient number of the weaker lines against the large angles of  $\alpha$ -Ti (110), (112) and, probably, of aluminium (220), (222). The

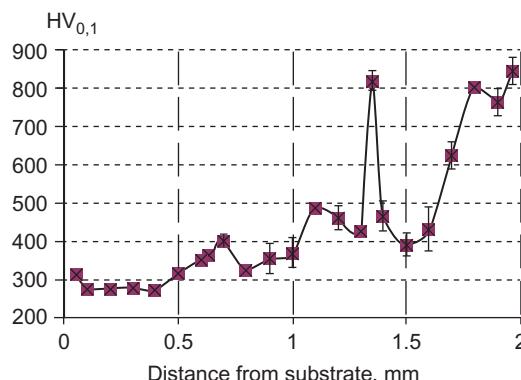
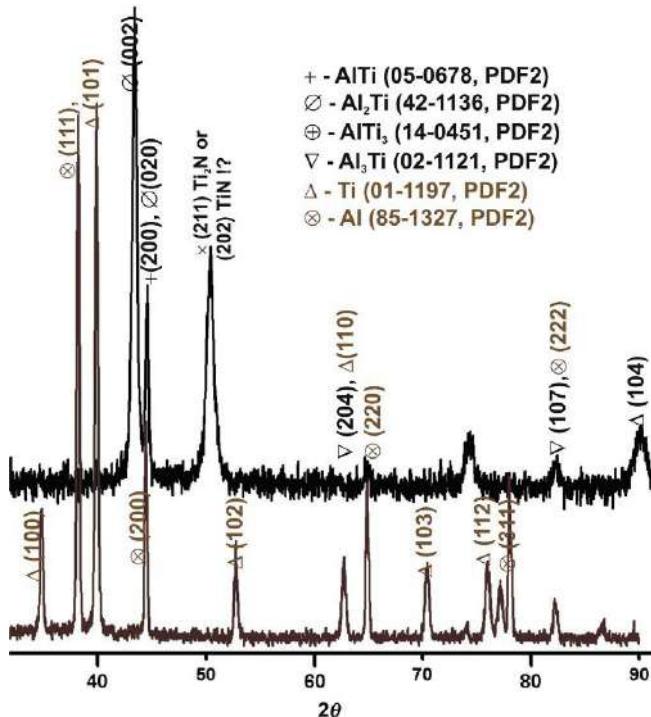


Figure 11.9 Microhardness distributions of Ti-Al FG multilayer system in argon [21].



**Figure 11.10** X-ray diffraction patterns of Ti-Al DMD multilayer system in argon. Lower curve is diffractogram of the initial  $\text{Ti} + \text{Al} = 1:1$  powdered mixture without laser treatment.

presence of these lines attests to the fact that after the DMD process the Ti and Al initial phases have not reacted completely even in the case of the noncontrollable combustion in nitrogen (Figures 11.4b and 11.7b). After the DMD, the strongest lines are located at the angles of  $2\theta \sim 43-45^\circ$ , which in our opinion corresponds to the entire set of intermetallic phases. This is mainly a metastable phase (002), (020) of Al<sub>2</sub>Ti and eutectic tetragonal (200) phase of  $\gamma$ -AlTi. A similar picture was observed in research reported in [26]. Furthermore, at the large angles we identified the lines (204), (107) of a tetragonal Al<sub>3</sub>Ti phase. However, because their intensities are not great, the presence of this phase is doubtful. The element analysis data (Figure 11.11) confirm this suggestion. The presence of the nitrogen associations (200)—Ti<sub>3</sub>AlN, disputably (200)—Ti<sub>3</sub>AIC should also be mentioned. These are probably the intermetallic phases enriched with nitrogen and carbon. We assumed their presence in the Ti-Al system after the DMD process in nitrogen environment [21], while it was amazing to discover the occurrence of a strong peak near the angle of  $2\theta \sim 50^\circ$  in the protective Ar medium. We consider them as nitride phases with lines (200) of the  $\varepsilon$ -phase TiN and (211) Ti<sub>2</sub>N.

On taking into account all the peaks mentioned above, it is reasonable to conclude that this XRD pattern (Figure 11.10) best of all coincides with the set of lines for the TiAl intermetallide. This means that out of all the assumed stoichiometric (3:1, 1:1,

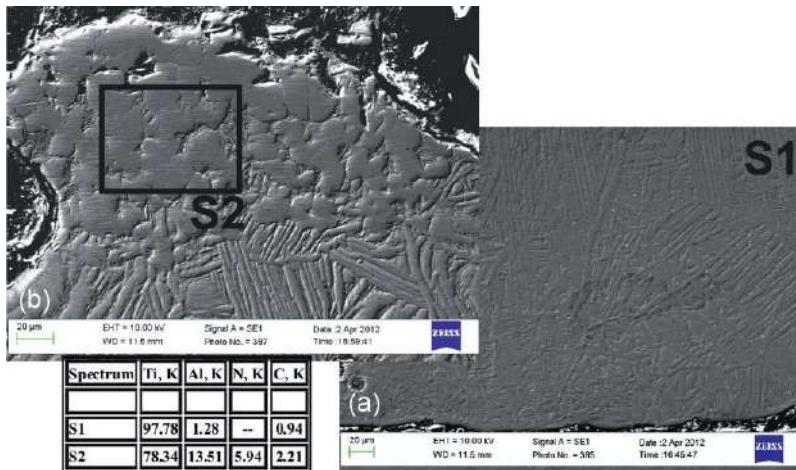


**Figure 11.11** SEM micrographs showing typical solidification microstructures of clad coatings with laser scanning speed of 0.83 cm/s and 400 W with EDS result (S1 and S2 regions) of Ti-Al multilayer system in Ar: (a) bottom layers near substrate and (b) top layers [21].

1:3) mixtures, the combustion reaction of the  $\text{Ti}_x\text{Al}_y$  intermetallic synthesis was going by the following direction:  $\text{Al} + 3\text{Ti} \rightarrow \text{AlTi} + 2\text{Ti}$ . This explains both the presence of a large number of residual nonreacted Ti powder and a very low quantity of pure aluminium.

The SEM images of the micro- and substructures are shown in Figure 11.11, just as in Figure 11.8, from the lower, middle, and upper parts of the cladded layers.

On the whole, their images corresponded to the optical metallography data given above. However, the results of element analysis are the most interesting. They show that, despite the fact that the FGS scheme assumed introduction of up to 50% of Al in the middle layers and more than 80% of Al in the upper layers, this aluminium was practically not fixed. It is possible to suggest that the temperature was enough to evaporate the aluminium, which is why we observe it now on the microphotograph (Figure 11.8) in the form of a whitish coating.

Because the solid but brittle  $\text{AlTi}$ ,  $\text{AlTi}_3$  intermetallic phases identified by us are the second phase inclusions for the titanium matrix of cladded layers, and thus simultaneous with the strengthening of the titanium matrix, they cause its cracking. This phenomenon was visually noted by the authors.

### 11.3.2 Laser synthesis in Fe-Al system

Interest aroused by the intermetallide phases of the Fe-Al system is connected with their high strength per unit weight, corrosive and wear durability, and low price of manufacture [28,29]. High-temperature applications for the iron aluminides include the pipeline of heat exchangers, turbine blades, the valves of complex shapes for

engines, and the substrates for catalytic converters [30–32]. The conventional fabrication method for solid 3D articles through the Fe-Al intermetallic compounds is casting, resulting in partial oxidation and grain growth due to high-temperature aging over a long period of time. The direct manufacturing of 3D articles of these materials is difficult, due to the brittleness at low temperatures inherent in those intermetallics. Furthermore, the subsequent sample-machining from the Fe-Al intermetallic compounds leads to more wear of the cutting tool than does machining with the usual Fe-C alloys.

Therefore, attempts have been made to obtain the Fe-Al intermetallic samples and coating by alternative methods, such as through thermal spraying, magnetron sputtering [33–35], SHS [36,37], and laser additive manufacturing (LAM) (3D laser cladding, DMD, LENS, SLM processes) [19,38–44]. Nevertheless, these methods also have a number of negative factors, which decrease the effectiveness of these approaches, such as porosity and high connection strength due to the difference in the temperature expansion coefficients of the coating and the base layer.

Of particular interest is the fabrication of the metal-the matrix composites (MMC), when the reinforcing  $\text{Fe}_x\text{Al}_y$  intermetallic compounds, are added to the matrix of the base metal (for example, Fe or Al). This process can be realized by several methods. Within the first approach, the preliminary addition of the strengthening prealloying intermetallic particles in the powder mixture occurs before the LAM process [22,40].

In the Fe-Al system this approach was approved in the papers [19,45], where the  $\text{Al}/\text{Fe}_2\text{O}_3$  mixture was combined during the SLM process for the direct creation of articles through the aluminium matrix with the strengthening inclusions. It was shown that the SLM can ensure the homogeneous distribution of the alumina and  $\text{Al}-\text{Fe}(-\text{O})$  particles. In a study [40], the SLM conditions for the prealloying FeAl intermetallic compounds were determined.

Another interesting direction is the laser welding of the dissimilar materials, that is, Fe and Al alloys, which are important for the aerospace and automobile industries for which serious difficulties are caused by the high brittleness of the intermetallide phases generated in the melting pool [46–50,89]. On knowing the succession of the phase-structural transformations in the laser weld joint, it is possible to attain the fabrication of such a barrier layer of the alloying elements (AE) [46–48] that is capable of wetting the joining alloys on the basis of iron and aluminium, protecting them from the contact during the melting and preventing the formation of undesirable phases. There are different methods for the plasticity improvement of such welded joints, including crystallographic structure modification, boundary strengthening, grain-size decrease, columnar structure creation, and micro- and macroalloying, and all of these methods can be completely realized using the LAM methods.

The powders enumerated below were used for the experiments. The iron powder had 99.76 wt.% of Fe (TLS Co.). The alloy 2024 (TLS Co.) was used as the Al powder, which had the following chemical composition: Cu 3.8–4.9, Mg 1.2–1.8, Mn 0.30–0.9, Si 0.50, Fe 0.50, Zn 0.25, Ti 0.15, Cr 0.10 wt.%, bal. Al. The powder particles were mainly spherical with the size of  $\sim 80$ – $100 \mu\text{m}$  for 95% of them. Steel substrates of a square shape with a 50-mm width and 5-mm height were used. The FGS fabrication scheme in the Fe-Al system is shown above (see Figure 11.6).

**Figure 11.12a-c** represents the results of optical metallography. As before, the photo series was selected in order to exhibit the characteristic microstructures from the bottom (a), middle (b), and top (c) parts of the cladded layers, that is, the parts where the weight ratios of Fe-Al in powder were  $\approx 3:1$ ,  $1:1$ ,  $1:3$ , respectively. The bottom cladding layers (**Figure 11.12a**) have a fine-crystalline structure with an almost uniform morphology mainly typical of single-phase iron alloys. In the middle layers (**Figure 11.12b**), the structure becomes more developed (see the supplementary inserts to **Figure 11.12b1-b3**), while in the lower layers (**Figure 11.12b1**) the transition from the fine-crystalline to the grain structure is observed. Further on, this grain structure (with typical grain size of  $20 \mu\text{m}$ ) transforms into the dendrite-type structure (**Figure 11.12b3**). Finally, in the upper layers (**Figure 11.12c1-c3**) an extremely heterogeneous MM structure is clearly visible, with the boundary intermetallic phases being precipitated (**Figure 11.12c2**). The dendrite nature of the Fe matrix structure testifies to the intensive overheating and the subsequent high-speed supercooling of the material in the LC process. In **Figure 11.12b and c** the cracks are arrowed, going in the direction of the layer and the direction of the main heat removal to the substrate base. Obviously, the observed structure heterogeneity is connected with the inhomogeneous intermetallic phases ( $\text{Fe}_3\text{Al}$ ), alloying, and the laser supercooling regime, during the melt crystallization.

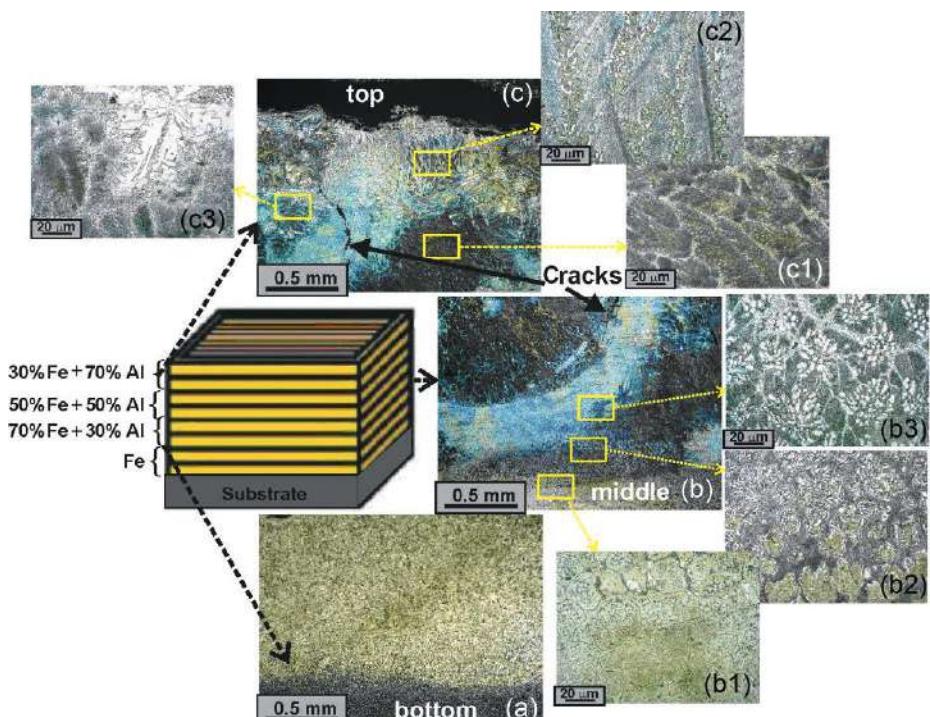


**Figure 11.12** OM micrographs showing the typical microstructures of 3D laser clad coating of Fe-Al multilayer system: (a) bottom layers  $\sim 2\text{-}4$  mm from substrate; (b) middle layers  $\sim 4\text{-}6$  mm from substrate; and (c) top layers  $\sim 6\text{-}8$  mm from substrate [22].

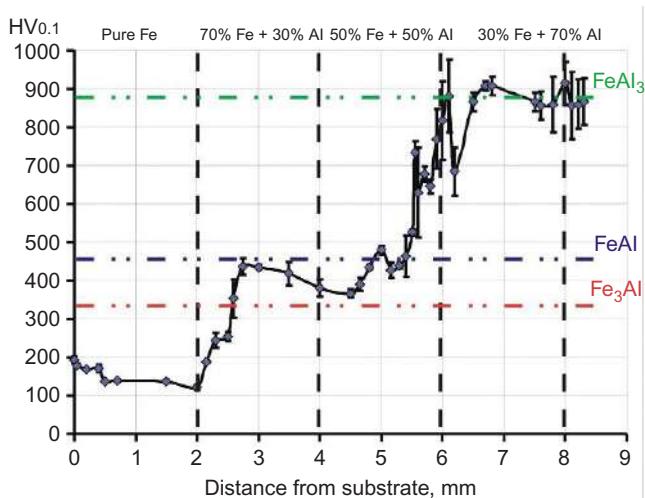


**Figure 11.13** Microhardness distributions of Fe-Al FG multilayer system [22].

The formed intermetallic phases harden the iron matrix, but being low-plastic, they cause crack development along the grain boundaries (see Figure 11.12b and c). The measured layer microhardness (Figure 11.13) grows irregularly from the substrate to the top. We refer to this irregular growth as the local hardness increase in the locations of intermetallide phases. In Figure 11.13, vertical dotted lines indicate the zones from the substrate surface, where the ratio and relationship of Fe and Al changed. Horizontal dot-and-dash lines designate the average microhardness level, characteristic of the Fe-Al intermetallic phases [51]. As follows from Figure 11.13, the microhardness remains equal to 200 HV<sub>0.1</sub> within the layer from the substrate up to the 2-mm level. In the range from 2 to 6 mm it grows up to 300-500 HV<sub>0.1</sub> level and corresponds to the hardness of the Fe<sub>3</sub>Al and FeAl intermetallide phases. Finally, in the last section from 6 to 8 mm the microhardness grows up to 700-900 HV<sub>0.1</sub>, which is characteristic of the FeAl<sub>3</sub> phase.

It is known from the literature [51] that the Al<sub>2</sub>Fe and Al<sub>5</sub>Fe<sub>2</sub> metastable phases can have a microhardness of up to 1058-1070 and 1000-1150 HV<sub>0.1</sub>, respectively. The microhardness dips we connect with the cracks on the grain boundaries. On the whole, the microhardness values correspond to similar measured values for the iron aluminides after the laser welding.

Figure 11.14 shows the results of the X-ray analysis. The lower curve in Figure 11.14 corresponds to the diffractogram of the initial 1:1 ratio Fe + Al powder mixture that has not undergone any treatment. As is evident from this curve, the most intensive lines belong to (111)  $\alpha$ -Al and (110)  $\alpha$ -Fe, although a weak line (200) of  $\beta$ -phase is also visible for the iron. After the LC, the intensive lines of Al disappear completely, while the Fe lines are probably “hidden” behind the intermetallic compound lines at angles of 44.6° and 64.7°. This result testifies to the fact that, after the LC, the entire amount of Al has completely reacted into the exothermic reactions

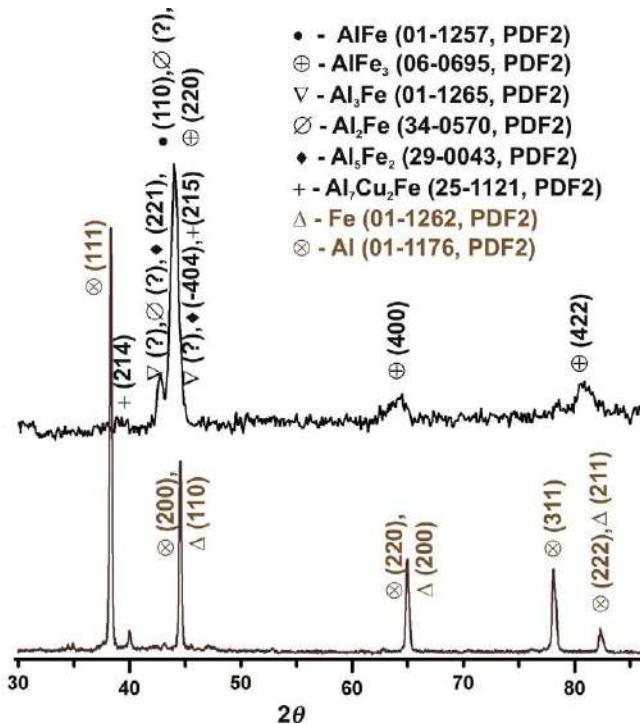


Figure 11.14 X-ray diffraction patterns of Fe-Al DMD multilayer system [22].

of the intermetallic compounds' synthesis. After the layered cladding, the strongest lines are located at the angles of  $2\theta \sim 43-45^\circ$ , which in our opinion, can correspond to the whole set of intermetallide phases. These can, disputably, be both the metastable phases, (222) Al $_5$ Fe $_2$  and Al $_2$ Fe, and stable phases, (110) AlFe and (220) AlFe $_3$ . The existence of the AlFe $_3$  phase is confirmed by the presence of weaker reflexes (400) and (422) at larger angles.

The microelement analysis data (Figures 11.15 and 11.16) confirms our conclusions. A possibility of the presence of complex intermetallide compounds with a copper (215) Al $_{7-8}$ Cu $_2$ Fe should also be noted. This is connected with the copper presence in the initial composition of the Al alloy. So, on taking into account the entire set of peaks, it can be concluded that the lines system (Figure 11.15) best matches the line system of the Fe $_3$ Al and FeAl intermetallic compounds.

Figures 11.15 and 11.16 show the greatly magnified SEM images of the same micro- and substructures, as before in Figure 11.12b and c, from the middle and top parts of the cladded layers. Figure 11.15a, in particular, corresponds to the structure section from Figures 11.12b1, Figure 11.15b from Figure 11.12b3, and Figure 11.16a-c from Figure 11.12c1-c3, respectively.

On the whole, their structures correspond to the above-given data of the optical metallography. However, the interesting results are those of element analysis. Relying on this data, we can assert that the preferred intermetallic yielding of FeAl crystals in

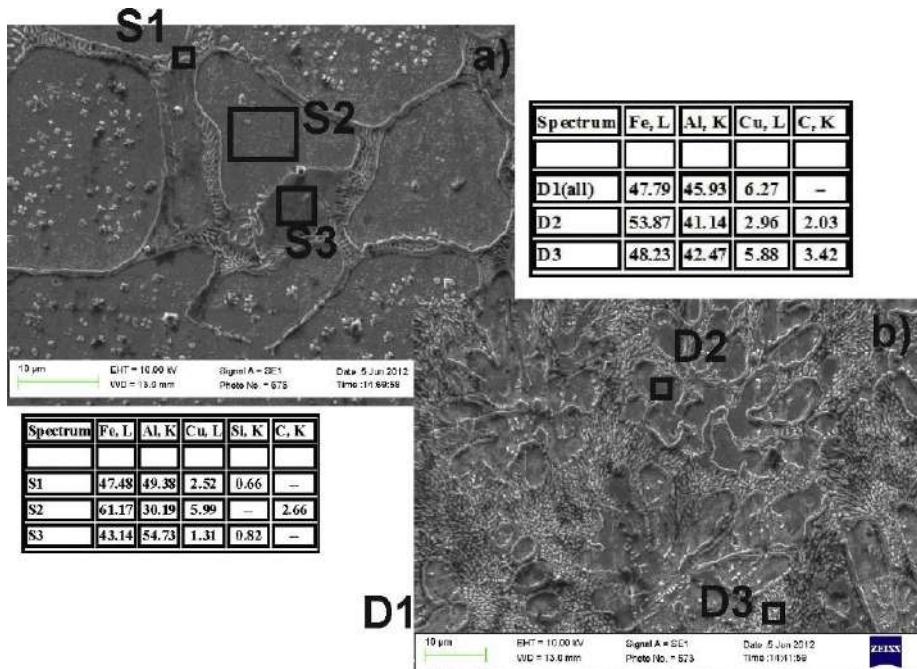


**Figure 11.15** SEM micrographs showing typical solidification microstructures of middle clad coatings with EDS result of Fe-Al multilayer system [22].

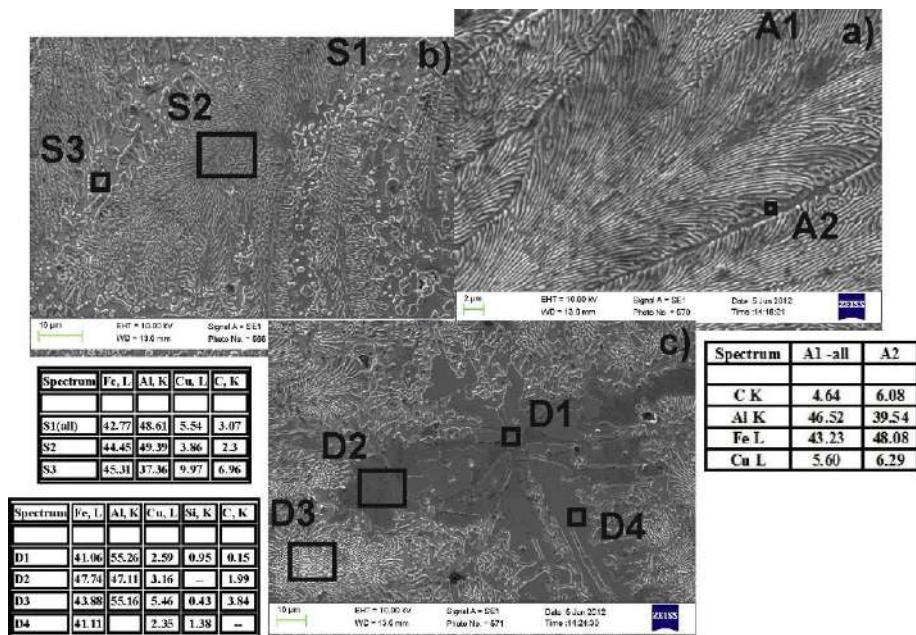


**Figure 11.16** SEM micrographs showing typical solidification microstructures of top clad coatings with EDS results of Fe-Al multilayer system [22].

the middle layers from 4 to 6 mm and of the Fe<sub>3</sub>Al phase in the layers from 2 to 4 mm take place, while in the top cladded layers the phases of FeAl, FeAl<sub>2</sub>, Fe<sub>2</sub>Al<sub>5</sub> are also generated.

Because hard but brittle FeAl<sub>2</sub>, Fe<sub>2</sub>Al<sub>5</sub> intermetallide phases identified by the authors are the second phase inclusions for the iron cladded matrix, they both strengthen this matrix and cause its cracking. An insignificant addition of Cu can smooth over this effect, however.

The element analysis also reveals the presence of carbon (up to 2-5%) and silicon (up to 1.5%), although there must be no trace of them in the initial mixture (see the XRD pattern results in [Figure 11.14](#)). Furthermore, in our opinion, the residual presence of oxygen is completely probable.

### **11.3.3 *Laser synthesis in Ni-Al system***

Superalloys based on nickel are widely used in high-temperature applications, as in turbine blades [[52](#)]. In this case, high-temperature oxidation is a problem.

The next powders were used for the FGS fabrication. The aluminium powder had 99 wt.% of Al (TLS Technik GmbH&Co.). The NiCr superalloy Diamalloy 1005 (Sulzer Metco Co.) was used as the Ni powder, which had the following chemical composition: Cr 21.5, Fe 2.5, Mo 9, Nb 3.7 wt.%, bal. Ni. The powder particles were mainly spherical, with 95% having the size of ~80-100 µm. The steel substrates had a square shape with a width of 65 mm and a height of 5 mm. Diamalloy is equivalent to the Inconel 525 alloy, which was studied earlier in the DMD process [[53](#)]. It combines high strength, creep resistance, and stability to oxidation and corrosion; therefore, it is widely used in space, chemical, and naval applications. Therefore, the intermetallide phase's generation of a nickel aluminide into this superalloy matrix is an interesting task, substantially changing its mechanical properties. The FGS fabrication scheme in the Ni-Al system was shown above ([Figure 11.6](#)).

The optical metallography is presented in [Figure 11.17](#). As described earlier, the photographs are selected in order to show the characteristic microstructures based on the lower (a), middle (b-c), and upper (d) parts of the FGS after 3D laser cladding, that is, where the proportions of the powdered Ni+Al≈3:1; 1:1, and 1:3 by weight ratios were comprised. Under large magnification, these layers are presented on the inserts a1 for (a); b1 for (b); c1 and c2 for (c) and d1 for (d). In the lower layers in the photo ([Figure 11.17a and b](#)), a columnar dendrite pattern was observed that characterized the high-speed quenching of the NiCr superalloy, practically without Al additive participation [[53](#)]. The dendrite growth direction ([Figure 11.17a1 and b1](#)) is stipulated for maximum heat dissipation to the massive substrate. We connect superfluous porosity in [Figure 11.17a and b](#) (shown by arrows) with the nonoptimal selection of the increment height from one layer to the next. At the top layers ([Figure 11.17c and d](#)) the microstructure radically changes. In the middle (bottom of [Figure 11.17c or c1](#)), there is a cellular microstructure, which can testify to the equivalence of the heat dissipation speeds in different directions from this area. The upper layers ([Figure 11.17c2-d2](#)) have a needle-shaped microstructure with the impregnations of intermetallide phases. At the middle layers we also observed the triple eutectic structure, which consists of a γ-solid

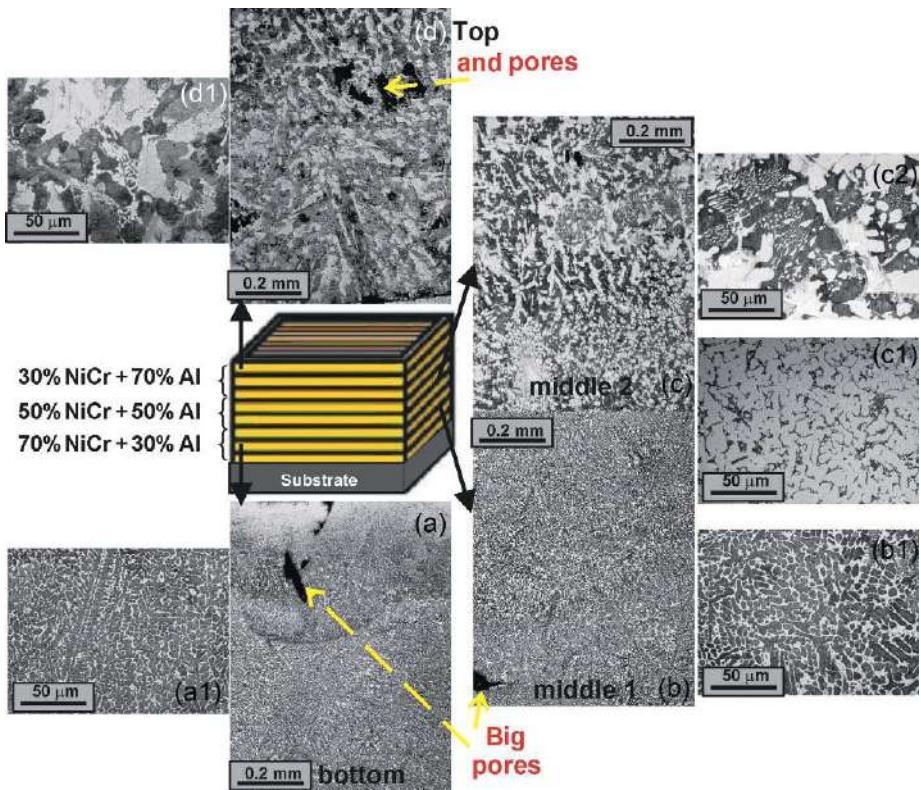


**Figure 11.17** OM micrographs showing the typical microstructures of 3D laser clad coating of NiCr-Al multilayer system: (a) bottom layers ~2-4 mm from substrate; (b) middle layers ~4-6 mm from substrate; and (c) top layers ~6-8 mm from substrate.

solution on the nickel basis,  $\alpha$ -solid solution on the chromium basis, and also  $\beta$ -solid solution on the basis of the  $\text{Ni}_3\text{Al}$  intermetallic compound in the middle and  $\text{NiAl}$  intermetallide phase above. By the boundaries of the  $(\alpha + \gamma + \beta)$  triple eutectic colonies, the two-component eutectic is arranged, which includes the  $\gamma$ -solid solution on the Ni basis and  $\text{AlCr}_2$  intermetallide phase.

The results of a microhardness measurement are shown in Figure 11.18. If at near the base the microhardness is equal to 500-550 HV<sub>0.1</sub>, then it unevenly grows and reaches up to 650-750 HV<sub>0.1</sub>. The separate dips in the microhardness value we connect in the bottom layers (up to 2 mm from the substrate in Figure 11.18) with the superfluous porosity, and in the top layers with the indentor entry into the Diamalloy 1005 matrix. On the whole, the measured microhardness values considerably exceed other researchers' data (500-550 HV<sub>0.1</sub> for the LC of  $\text{NiAl}$  by Yu *et al.* [54]; 200-250 HV<sub>0.1</sub> for the Inconel 625 after the DMD process by Dinda *et al.* [53]).

The XRD pattern of a transverse section after the LC in the NiCr-Al system is shown in Figure 11.19. We can draw the following basic conclusions: After the LC free nickel and aluminium are practically absent, that is, it has completely interacted with the  $\text{Ni}_3\text{Al}$  and  $\text{NiAl}$  intermetallic phase formation. This distinguishes our results

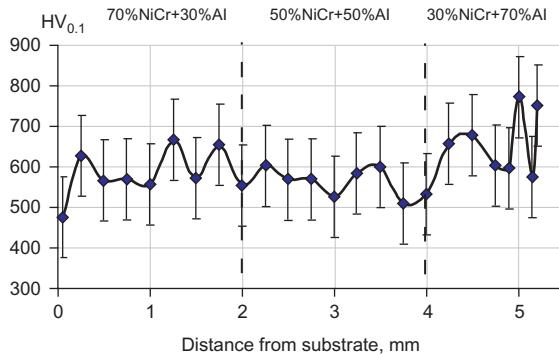


Figure 11.18 Microhardness distributions of NiCr-Al FG multilayer system.

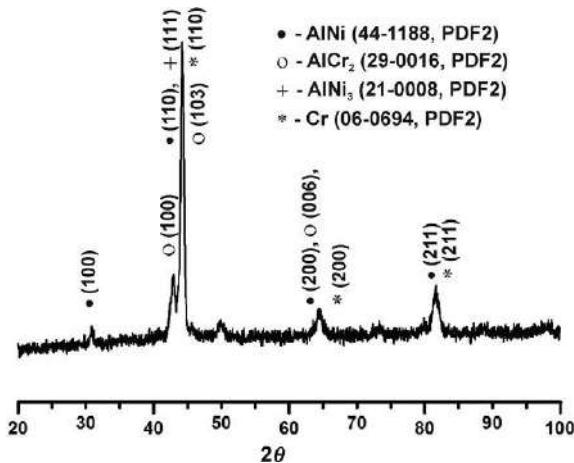
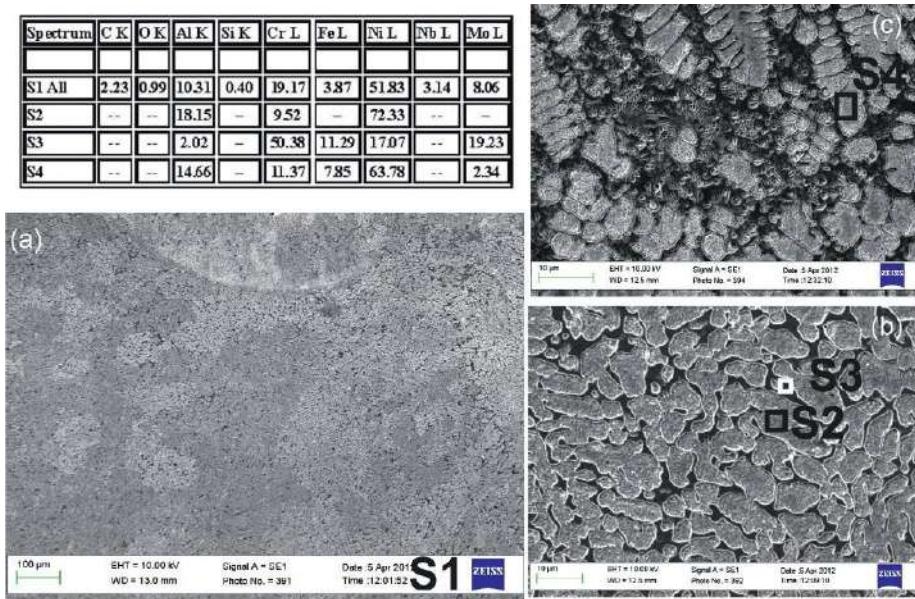


Figure 11.19 X-ray diffraction patterns of NiCr-Al DMD multilayer system.

from the data of the study in Ref. [53], which under similar LC regimes with the subsequent annealing fixed both the free nickel,  $\gamma$ - and  $\delta$ -Ni<sub>3</sub>Nb phases. Because the intensity lines of free chromium practically coincide with the intensity lines for the intermetallic compound AlNi, so it is impossible to assert unambiguously about the free Cr presence. Meanwhile, the presence of intermetallic phase of AlCr<sub>2</sub> is possible.

Figures 11.20 and 11.21 show the SEM data in the bottom, middle, and top layers of the FGS after the layerwise LC in the NiCr-Al system. The “All” index is written with those EDX data, in which information was collected from the whole area of the corresponding figure. Figure 11.20a completely coincides with the middle part of Figure 11.17a. It is evident that its microelement composition (S1-All) practically repeats the initial Diamalloy 1005 composition plus 10 wt.% of Al. Figure 11.20b corresponds to the lower part of Figure 11.17b, and Figure 11.20c to Figure 11.17b1. By the element relationship in the S2 area (Figure 11.20b) we have the Ni<sub>3</sub>Al intermetallic phase, on the boundaries of which have been observed the free Cr extraction (see S3).



**Figure 11.20** SEM micrographs showing typical solidification microstructures of the bottom (a, b) and middle (c) clad coatings with EDS result of NiCr-Al multilayer system.

Finally, a dendritic structure in Figure 11.20c (S4) clearly shows the intermetallide nature of the  $\text{Ni}_3\text{Al}$  phase. Figure 11.21a corresponds to Figure 11.17c1, while Figure 11.21b and c is equivalent to Figure 11.17c2 and d1, respectively. We can assert that in the upper layers the synthesis of the  $\text{NiAl}$  intermetallide phases (D4 and D8) occurs; a precipitation of the  $\text{AlCr}_2$  intermetallide phase on the grain boundaries (D2). We connect sufficiently great carbon (up to 10 wt.%) and oxygen (up to 6 wt.%) content with the possibility of their hit from the environment, although the XRD pattern does not fix these elements.

The applications of the 3D laser cladding for the creation of a functional gradient and building of  $\text{Me}_x\text{Al}_y$  ( $x, y = 1, \dots, 3$ ) intermetallic structures has been experimentally studied. It has been shown that:

- the LAM process implementation has the tendency to form heterogeneous phases of  $\text{Fe}_3\text{Al}$  and  $\text{FeAl}$ . The microhardness growth from 300 to 900 HV was obtained for the same sample due to the change of the elements ratio in the Fe-Al system during the 3D laser cladding. The copper alloying additive is favorable for the smoothing of the crack tendency formation beyond to the intermetallic compound-steel matrix boundaries;
- the DMD process implementation in argon has the tendency to form the heterogeneous  $\gamma$ -phase of  $\text{TiAl}$ . Variations in microhardness from 130 to 800 HV have been obtained within the same sample due to the change of the element relationship in the Al-Ti system with 3D laser cladding;
- under the layerwise LC in the NiCr-Al system the formation of the  $\text{Ni}_3\text{Al}$  and  $\text{NiAl}$  intermetallic compounds was observed. The microhardness values from 500 to 750 HV<sub>0.1</sub> were achieved, which precisely connected with the intermetallide phase's presence in the NiCr matrix.

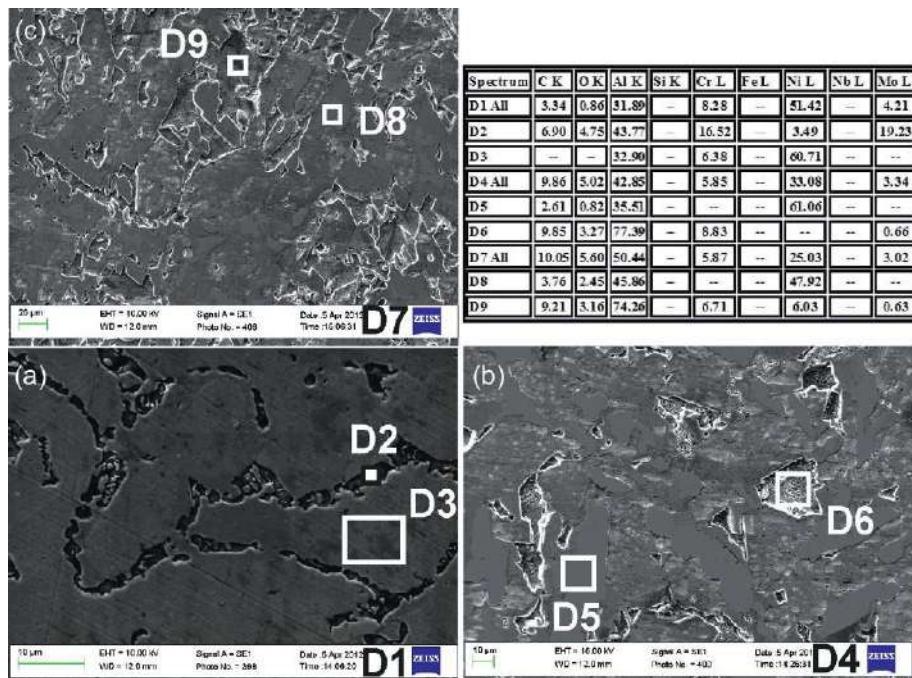


**Figure 11.21** SEM micrographs showing typical solidification microstructures of the middle (a) and top (b, c) clad coatings with EDS results of NiCr-Al multilayer system.

It has been found that the sizes and boundaries of the transition zones between the powder compositions with different components and of corresponding  $\text{Me}_x\text{Al}_y$  intermetallic phases depend on the laser synthesis conditions and, thus, can be controllable.

The possibility of controlling the hardness of the multilayer structure by changing the powder composition and using the appropriate CAD modeling can expand the range of the 3D FGM applicability in the aerospace and nuclear industries. Provoking a further interest is the study of the LAM conditions for the large samples and the control of the residual stress level, which can impede the process application for the fabrication of high-precision samples.

## 11.4 Temperature distribution during the layerwise surface laser remelting of exothermal powder compositions

It is obvious that the determination of LI optimum regimes (power, scanning velocity, the beam diameter, etc.), which make it possible to realize the synthesis reaction of diffusion type for intermetallic compounds (i.e., controlled exactly in the laser beam spot), it is the urgent task both of SLS/M + SHS and LC + SHS processes in the Me + Al reactive powder compositions. The final goal of such a study is the layer-by-layer fabrication of the FG materials (3D parts) via the SLS/M or/and LC + SHS joint method,

using the feedback from the thermocouple measurements to control and guide the process.

A diagram of the setup for thermal measurements during the laser-controlled SHS-process is shown in [Figure 11.22](#) and was developed by Shishkovsky *et al.* [13,14]. Powder compositions were placed on a metal platform. The volume of cuvette was  $\sim 12 \text{ cm}^3$ . The dimensions of the LI zone were  $10 \times 30 \text{ mm}^2$  with a typical sintered/melted monolayer depth of 0.5-3 mm. Thermocouples were inserted into the powder within this zone 5 mm from the zone edge at a depth of 3-5 mm.

[Figures 11.23–11.28](#) describe the character of temperature distribution in the reactive capable powder compositions, where SHS propagation waves can move in front of the laser beam. Regimes of the LI corresponded to the experimentally determined conditions for laser-controlled overlap of the SLS/M and SHS processes. As thermocouples were situated on the periphery of sintering/melting, absolute values of temperatures are not high. In the case of a thermal explosion, all the powder volume ( $\sim 12 \text{ cm}^3$ ) was burned through completely; however, the contact points to the thermoelectric junction were not destroyed. This allowed us to register the temperature change over time for the whole process.

As a whole, the temperature profiles had an understandable sequence for all of the experiments ([Figures 11.23–11.28](#)).

The first response was always from the first thermocouple, which was positioned closest to the starting point for the initiation of the laser scanning. The second (counter) thermocouple, routinely behind the reaction front, does not record a temperature increase until some time later. Measurements from the third and fourth thermocouples are comparable with first one. It is connected as follows: when the reaction front reaches the midpoint of the sintered/melted monolayer ([Figure 11.22](#)), the powder volume is already very hot. If reaction control is lost, the temperature measurements for the third and fourth thermocouples are maximized. Finally, reaction exothermicity is

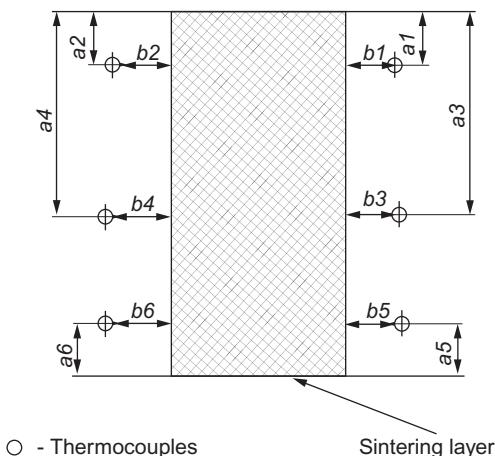


**Figure 11.22** Scheme of thermocouple distribution ( $i=1, \dots, 6$ ,  $a_i, b_i$ —sizes), relative the zone (hatching marked) of laser sintering/melting [13,14].

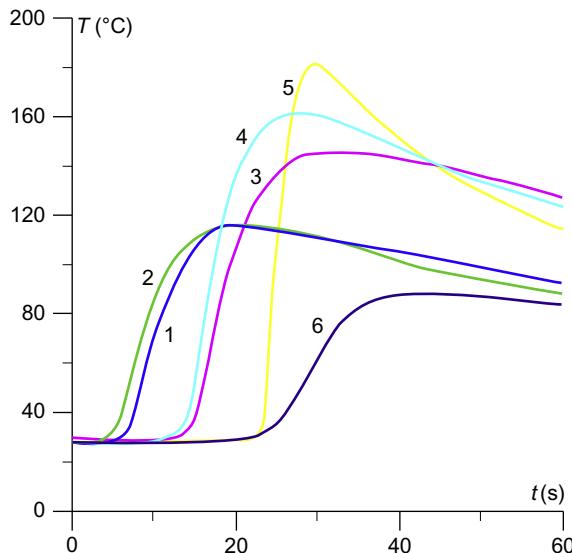


**Figure 11.23** Temperature change on thermocouples ( $i=1,\dots,6$ ) during laser sintering/melting. Power composition  $\text{Ni}+\text{Al}=3:1$ . LI power  $P=24 \text{ W}$ . Laser scan velocity  $v=11.4 \text{ cm/s}$ , beam diameter  $d=100 \mu\text{m}$  [13,14].

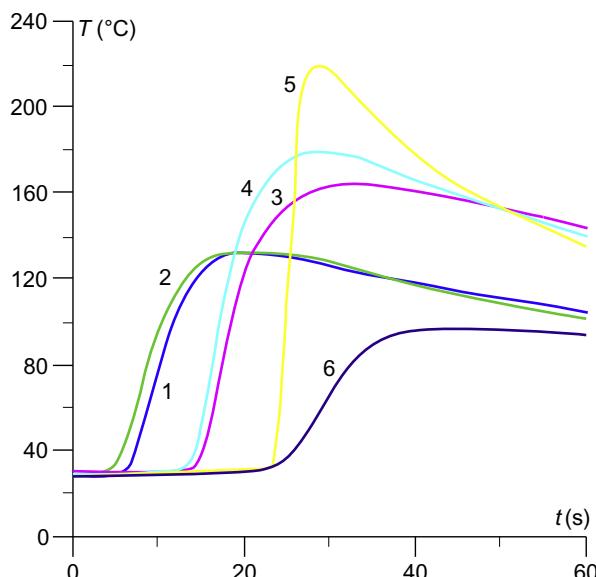


**Figure 11.24** Temperature change on thermocouples ( $i=1,\dots,6$ ) during laser sintering/melting. Power composition  $\text{Ni}+\text{Al}=3:1$ . LI power  $P=30.3 \text{ W}$ . Laser scan velocity  $v=11.4 \text{ cm/s}$ , beam diameter  $d=100 \mu\text{m}$  [13,14].

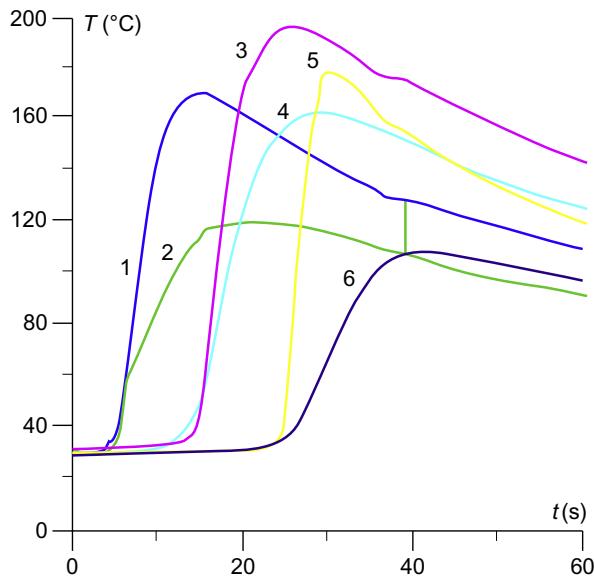


**Figure 11.25** Temperature change on thermocouples ( $i=1,\dots,6$ ) during laser sintering/melting. Power composition Ni + Ti = 1:1. LI power  $P = 24$  W. Laser scan velocity  $v = 11.4$  cm/s, beam diameter  $d = 100$   $\mu\text{m}$  [13,14].

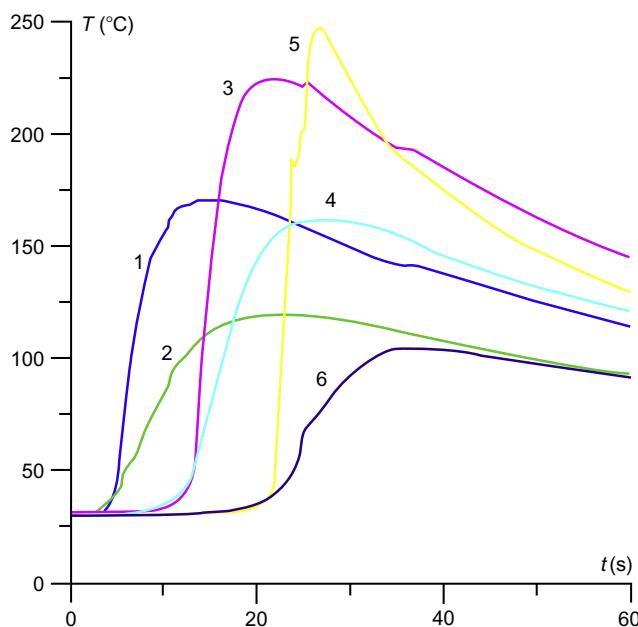


**Figure 11.26** Temperature change on thermocouples ( $i=1,\dots,6$ ) during laser sintering/melting. Power composition Ni + Ti = 1:1. LI power  $P = 30.3$  W. Laser scan velocity  $v = 11.4$  cm/s, beam diameter  $d = 100$   $\mu\text{m}$  [13,14].

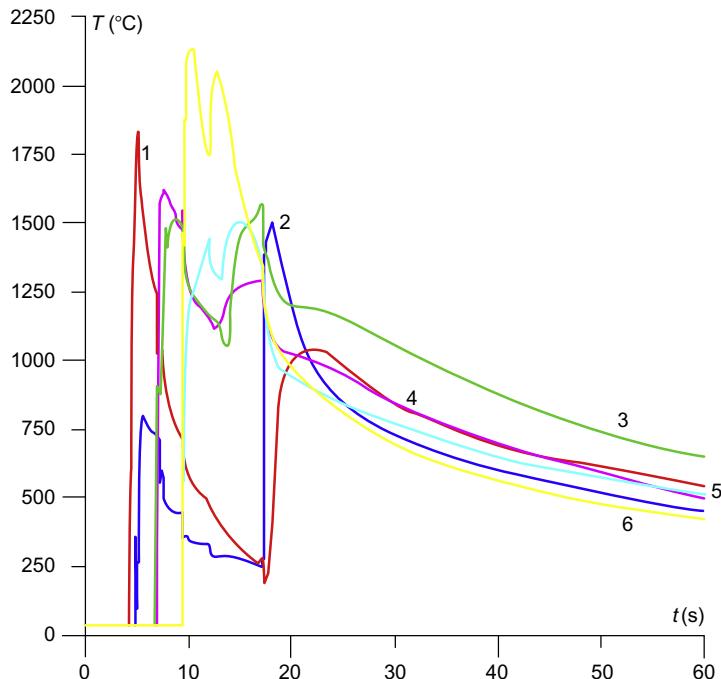


**Figure 11.27** Laser sintering/melting of powder composition  $\text{Ni} + \text{Al} = 1:1$ , beam diameter  $d = 100 \mu\text{m}$ . LI power  $P = 800 \text{ W}$ ,  $v = 11.4 \text{ cm/s}$ —pure nickel. Laser regime:  $P = 8 \text{ W}$ ,  $v = 11.4 \text{ cm/s}$  [13,14].

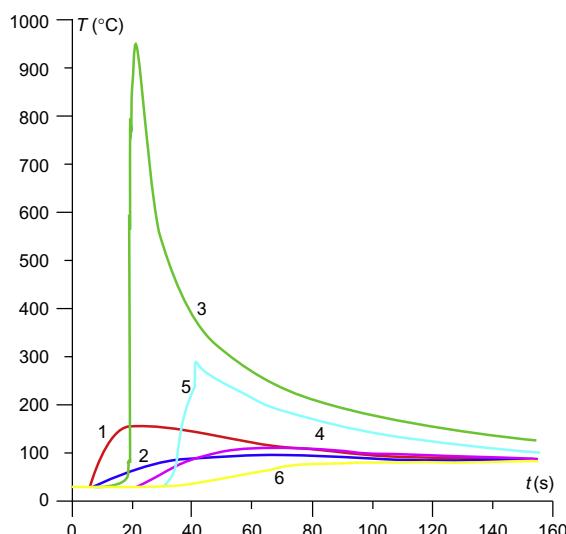


**Figure 11.28** Laser sintering/melting of powder composition  $\text{Ni} + \text{Al} = 1:1$ , beam diameter  $d = 100 \mu\text{m}$ . LI power  $P = 30.3 \text{ W}$ ,  $v = 2.9 \text{ cm/s}$ —PGSR4 nickel power. Laser regime:  $P = 8 \text{ W}$ ,  $v = 11.4 \text{ cm/s}$  [13,14].

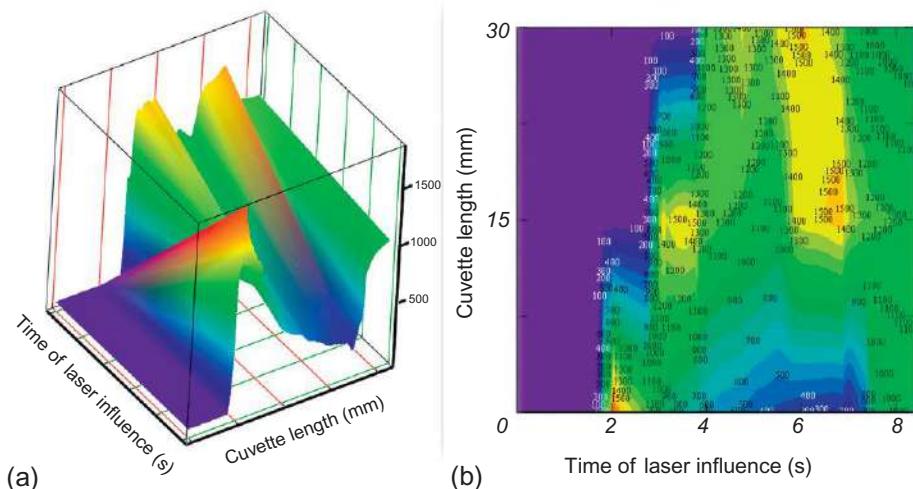


**Figure 11.29** 3D temperature field (a) and a front of exothermal reaction (b) relative to cuvette during LI.

registered from the fifth and sixth thermocouples, which are farther away from the initiation point.

Figure 11.29 shows the digitization results of the previously carried out measurements [13,14] of temperature distribution during the LI on the  $\text{Ni} + \text{Al} = 1:1$  powder composition with parameters that are the same as those in Figure 11.27. As is evident, there is a certain delay ( $\sim 4$  s) between the beginning of laser scanning by means of the powder surface and a real increase in the temperature. These measurements correlate with the calculations on the numerical model in Section 11.4 [23].

A two-dimensional transient theoretical model of the SLS/M and LC for the reactive powder compositions with allowance for chemical reaction kinetics has been developed in Section 11.5 [5]. The experimental data obtained in this study provides a good basis for comparing the numerical and experimental approaches.

## 11.5 Theoretical and numerical modelling of selective laser sintering/melting (SLS/M) and SHS hybrid processes

### 11.5.1 Theoretical modelling of the laser cladding and SHS processes overlapping

In this paragraph we will formulate base equations for the description of the layerwise remelting in reaction-capable powder composition on the substrate according to [55–66]. Because the 3D LC is a thermal process, the known equation of thermal conductivity plays a central role in the process of physical simulation. The equation of thermal conductivity (11.1) describes the energy balance in the selected volume: a

right side of equation includes diffusion and convection heat flows, taking into account all possible heat sources  $Q$ ; and left, a change in the heat quantity per unit of time and of volume. The system must be augmented by the momentum conservation and continuity equations (11.2). In the case of the thermomechanical process analysis, the connected system will consist of the thermal conductivity equations (11.1)–(11.4), plus equation of state (11.6), for the stresses and the strains. Note that Equation (11.6) becomes significant after the beginning of the crystallization process [67–69]. A scan velocity of the laser beam will designate  $V_L$ . It can be seen that an absorbed energy of the LI leads to the surface heating not more than the material boiling point  $T_B$ . Then, the heat losses can be seen to be due to the convection and thermal radiation in the comparison with the value of the absorbed power density  $Q$ .

$$\frac{\partial(\rho c T_L)}{\partial t} + \nabla(\rho c U T_L) = \nabla(\lambda \nabla T_L) + Q \quad (11.1)$$

Conservation equations are

$$\begin{aligned} \frac{\partial(\rho V_L)}{\partial t} + (\rho V_L \nabla) V_L &= \rho g - \nabla p + \mu \nabla(\nabla V_L) \\ \nabla V_L &= 0 \end{aligned} \quad (11.2)$$

where  $\mu$  is the melting viscosity,  $g$  is the gravitational acceleration, and  $c, \lambda$  are the thermophysical parameters of the meting material. Under the reaction-capable powder cladding, the explicit form of  $Q$  includes the heat combustion due to the exothermic reaction. If a powder mixture is multicomponent, we will use an equation of type (11.22) for the thermophysical parameter description. Beyond the surface of the melt pool, the Marangoni force (11.3) acts [70,71], due to the inverse proportion of the surface tension from the temperature, and leading to the formation of the vortex flows in the melt from the center to the bath edges [72].

$$\begin{aligned} \nabla p + \rho g z &= \left( 2\mu \frac{\partial V}{\partial n} \right) + \gamma R \\ V_n &= 0 \end{aligned} \quad (11.3)$$

where  $z$  is directed into the melt bath depth,  $\gamma$  is a surface tension, and  $R$  is a melt surface curvature. Under the surfactant species presence it is necessary to consider not only a temperature dependence of the surface tension coefficient, but the dependence of the chemical segregation concentration also:

$$\begin{aligned} \gamma(T, a_s) &= \gamma_0^m - A(T - T_0) - RT\Gamma_s \ln(1 + K_{\text{seg}} a_s) \\ \frac{\partial \gamma}{\partial T} &= -A - R\Gamma_s \ln(1 + K_{\text{seg}} a_s) - \frac{K_{\text{seg}} a_s \Gamma_s \Delta H_0}{1 + K_{\text{seg}} a_s} \end{aligned} \quad (11.3 \text{ a})$$

where  $K_{\text{seg}} = S_l \exp(-\Delta H_0/RT)$ ;  $\Delta H_0$  [J/mol] is the absorption heat,  $a_s$  [wt.%] is a concentration activity,  $S_l$  a constant of the segregation entropy, and  $\Gamma_s$  [mol/m<sup>2</sup>] the

surplus outcome on the surface unit. This accounting can substantially change the traditional flow direction by Marangoni from the bath boundaries to the center [73].

On the liquid-solid boundary several conditions must also be carried out:

$$\begin{aligned} -\lambda_S \frac{\partial T_S(z=s(t)-0)}{\partial z} &= -\lambda_L \frac{\partial T_L(z=s(t)+0)}{\partial z} \pm \rho L \frac{\partial s}{\partial t} \left( 1 + \left( \frac{\partial s}{\partial t} \right)^2 \right)^{-1} \\ T_S(t, z=s(t, r), r) &= T_L(t, z=s(t, r), r) = T_m \\ V_Z = V_R = V_\phi &= 0 \end{aligned} \quad (11.4)$$

It is through these means that a convection current component on the “of solid-liquid” boundary tends to zero (known “adhesion condition”), the boundary temperature is equal to a crystallization temperature, and the crystallization front moves by law  $s=s(t, R)$ , a heat exchange and a latent heat output of phase transition occurs. The thermal equation for the crystallized phase, obviously, must also be mentioned here for system completeness.

An isotherm shape on the crystallization front ( $T=T_{\text{Melt}}=S(t, z, R)$ ) is found by the method of sequential approximations from the solution of a transcendental equation. For example, in the first approximation on the heating stage this dependence (11.5) can be presented as [71,74,75]

$$s(\zeta, 0) = s(t, 0) \frac{\zeta - t_L}{t - t_L}, \quad t_{LD} \leq t \quad (11.5)$$

where  $t_L$ ,  $t_{LD}$  are the times of the melt appearance and the LI duration, respectively.

A visco-plastic (rheological) melt behavior after the crystallization acquires an elastic-plastic nature. Therefore, in the next elastic task in the cylindrical coordinate system it suffices to write

$$\begin{aligned} \frac{d\sigma_{rr}}{dr} + \frac{d\sigma_{rz}}{dz} + \frac{(\sigma_{rr} - \sigma_{\phi\phi})}{r} &= 0 \\ \frac{d\sigma_{rz}}{dr} + \frac{d\sigma_{zz}}{dz} + \frac{\sigma_{rz}}{r} &= 0 \end{aligned} \quad (11.6)$$

Equation (11.6) is supplemented to the Maxwell equation system, which connects the stresses, deformation, and displacement, taking into account a thermoelastic contribution up to plasticity; that is, on the free boundary (melt surface) an accepted definition is that the stresses are equal to zero. This system is solved, for example, by the thermoelastic potential method (Goodier’s function method) [67,69].

The LI source in the cylindrical coordinate system is described by Equations (11.17) and (11.18), and the boundary conditions take the form of type (11.23). On the remaining boundaries we will use equality conditions of zero temperatures in the semi-infinite thermal task. In the LC of finite quantity layers, the heat exchange according to the Newton law occurs (third order boundary conditions).

Thus, the closed theoretical model was built for the tasks of the laser synthesis of the 3D parts by the SLM/LC methods (analogy of the DMD™, LENST™, and 3D

Welding techniques). The above-formulated thermoelastic task could be solved by numerical methods. For example, in [58] this problem realizes in the ANSYS package, and in the FemLab program (Comsol Ltd.) was used. These solutions had been traditional for the laser surface hardening and alloying era of the 1980s, but contemporary software is now used, and it does not give answers on the some of the most important questions. Which will be the material structure after a high-speed crystallization? How will the AE be distributed, what phases will be obtained, and, as a result, what will the mechanical properties of the cladded layers be? At the moment, these questions are solved by experimental methods. Meanwhile, in the following paragraph some model approaches will be presented, which enables us to answer some of these practical questions.

### ***11.5.2 Kinetic and diffusion processes of high-speed crystallization under laser cladding and intermetallide alloying***

Under the LC+SHS, overlapping the intermetallic compounds are synthesized into the melting bath. As a result of the high-speed quenching of the wide spectrum of the heterogeneous solid solutions with the intermetallic compounds, it is possible to obtain inclusions, which frequently do not correspond to the EPD for the studied system. Specifically, the possibility of retention in the solid lattice of the large intermetallide quantity due to the high cooling rates is the most interesting feature of the LC and MMC synthesis (see Section 11.2 regarding the FG layer's synthesis). The cladded layer thickness can vary from 10 µm to several mm depending on the workable material and LI parameters. The structural phase state and their combination will determine the subsequent mechanical layer properties in many respects. These properties will also depend on the EPD of the corresponding compounds; a quantity of intermetallic phases; the degree of the mutual solubility (connectivity) between the matrix and intermetallic compound as the solid as liquid phases; the diffusion mobility of intermetallide phases on the phase boundaries (liquid-solid); the methods “transit” of these boundaries; the boundary moving speed during crystallization (i.e., from the cooling speed of the processed material); the ways of solid diffusion, and so on.

So the proposed theoretical model of the intermetallic compound redistribution under the LC could give the answers on these process directions and facilitate the optimization of the DMD regimes. It is obvious that because the material final state is most fundamental after the LC (this state is studied by experimental method now), the precisely high-speed crystallization of the melt with solid inclusions has great technological interest. It is assumed that intermetallic compound redistribution occurred already at the melt bath, but all insoluble phases for the LI time (particles of large sizes, compounds with high melting points, etc.) are incorporated at the solid phase directly in such a form as they existed before the fusion. Actually, already the first studies of the 3D LC showed [55,57,64] that the LI time ( $\sim 0.1\text{-}1 \mu\text{s}$ ) is sufficient for the effective mixing of the AE into the melt bath due to the existing of the convection currents there, which characterize the convection speeds up to  $\sim 1\text{-}10 \text{ m/s}$ .

The melt dynamic and the AE were analyzed earlier in sufficient details before the numerous studies (see for example [70, 76–78] and the cited references).

The convective mixing task will not be examined in this study. Instead, a theoretical analysis of diffusion and kinetic redistribution of the AE on the final stage of the LC process will be presented. In particular, the processes on the crystallization front and in the cooling solid phase will be described.

We will assume from this point that the binary powder mixture is (Me + MeAl system), and the AE is an aluminide of the MeAl type (Me = Ni, Fe or Ti). It is reasonable to consider that the initial data is known: the temperature by the laser alloying zone on the moment of the LI finish  $T(x_i, t)$  from the system solution (11.1)–(11.5); a quantity of synthesized intermetallide at the exothermic reaction  $C_L = C_0 + C_{ad} + C_k$  ( $C_0$  in accordance with the EPD); the  $Me_xAl_y$  metastable intermetallide phase quantity (if the same exist); and the EPD itself.

The process of high-speed crystallization of a melt and kinetics of a front moving during a phase transformation (PT) were also analyzed in the literature in detail (refer to monographs [79, 80]). If the PT process of a first-order is interpreted classically, that is, it is realized by a way of thermofluctuational or atomic transitions on the boundary cross section of phases, so the growing velocity of the new phase (crystallized melt) is described as

$$\frac{\partial r}{\partial t} = av \exp\left(-\frac{U}{kT(t)}\right) \left[1 - \exp\left(-\frac{\Delta F}{kT(t)}\right)\right] \quad (11.7)$$

where  $v$  is the characteristic Debye frequency,  $U$  is the activation energy of the atom transition through the interphase boundary cross-section,  $\Delta F$  is the changing of the specific free energy at the appearance the new phase nucleus (usually here it is limited by the volume part  $\Delta F_v = \Delta h[T_m - T(t)]/T(t)$  and the surface part of  $\Delta F_s = \phi\sigma n^{2/3}$  [81], and  $a$  is the lattice parameter. However, if the cooling velocity is very high, on the phase boundary the atoms begin to overcome cooperative [82] and fluctuation-diffusion nature of the transition loses meaning. In the work [81] from the analytical solution for the distribution function by particle number (DFPN) of the new phase  $Z(n, t)$  it was shown that at the high-speed cooling, the melt is crystallized via clusters with the particle value from several tens to several hundred depending on a cooling velocity  $V_{cool}$  and material thermodynamic properties. At last, generally under  $V_{cool} > V_{cr}$  the melting begins amorphously.

Further, we will use conclusions [81], in particular, for the lamellar (dendrite) shape embryos we found the exact form for the distribution function:

$$Z(\alpha, \beta, n) = \sqrt{\frac{n}{\alpha}} \int_0^{\infty} d\xi Z_{in}(\xi^2 e^{\beta}/4) \exp\left(-\frac{4n + \xi^2}{4\alpha}\right) I_1\left(\xi \frac{\sqrt{n}}{\alpha}\right) \quad (11.8)$$

where  $Z_{in}$  is the initial distribution function,  $I_1$  is a modified Bessel function of the first-order,  $T_0$  is a temperature of phase transition, and  $\alpha$  and  $\beta$  are the task parameters, which depend on the temperature changing rate  $T(\tau)$ :

$$\begin{aligned}\alpha(t) &= v \exp(-\beta(t)) \int_0^t \exp\left(\beta(\tau) - \frac{U}{kT(\tau)}\right) d\tau \\ \beta(t) &= -\frac{\Delta h v}{kT_0} \int_0^t \frac{T_0 - T(\tau)}{T(\tau)} \exp\left(-\frac{U}{kT(\tau)}\right) d\tau\end{aligned}\quad (11.9)$$

Then, the relative volume of the new crystallized phase can be defined as

$$\frac{\Delta V}{V} = 1 - \exp(\beta(t)) \quad (11.10)$$

and the average size of the crystalline nucleus or the average number of atoms in the nucleus of the new phase is defined as

$$\langle n \rangle = \frac{3\alpha(t)}{2} \left[ \alpha(t) - 1 - \frac{1}{\alpha(t)} \ln \left( 1 - \frac{\alpha(t)}{3} \right) \right] \quad (11.11)$$

In the paper [81], an asymptotic nature  $\alpha$  and  $\beta$  under  $t \rightarrow \infty$  was explored for the simplest cooling laws (linear, power, and exponential types) only. Here, we will consider that from the solution of the thermal conductivity Equations (11.1)–(11.5), the relative volume of a new phase, and the size of a crystallite we can estimate accurately through these parameters.

The knowledge of the temperature fields  $T(t, z, R)$  in the liquid and solid phases, forms and speeds of the front displacement under the PT ( $L \rightarrow S$ )  $S(t, z, r)$  from Equation (11.5), the volume and the size of the crystallizing phase (11.10) and (11.11) it allows us to mathematically adequately describe the diffusion redistribution process for the MeAl phase under the high-speed cooling from the melt pool during the LC process via an intermetallide alloying. The obtained Equation (11.10) in the physical sense is similar to a well-known Kolmogorov-Avraami equation for the new phase volume [79,80]. It should be considered that on the moving phase boundary the abrupt concentration changing for the AE takes place:  $k_e = C_S/C_L$ , where  $k_e$  is a ratio to a kinetic eutectic coefficient  $C_S$  (i.e., the AE concentration, determined by the solidus line on the EPD), and a  $C_L$  by the liquidus line [83,84]. Due to the closed equilibrium conditions, the equilibrium concentration of the dissolved atoms into the solid state cannot exceed the maximum solubility at the solid phase, therefore the maximum presence of the concentration admixtures after the LI testifies to the predominant role of the kinetic effects on the phase boundary (11.10) and (11.11). Phase reconstruction is accompanied by both the specific free energy decreasing  $\Delta F_{(L \rightarrow S)}$  of the system and the latent heat output, but the atom volume is also decreasing in the concentration space [85]. This process differs from usual diffusion and is described by the specific set of equations [83,85]. For example, the Tiller model works for the very high speeds of the PT front motion, but works badly for low speeds. The Baker and Cahn model uses a thermodynamic approach, the Wood's model is based on the kinetic equations in the assumption of a very "thick" boundary zone, but the Jackson-Aziz model utilizes the kinetic laws. Without entering into the essence of these models, their basic conclusions could be pointed out. For the step-by-step movement of the PT front the

kinetic coefficient dependence of the motion speed for the L→S front could be presented as

$$k(v) = k_e + (1 - k_e) \exp\left(-\frac{v_D}{v}\right) \quad (11.12)$$

where  $v_D = D_L/a$ ,  $D_L$  is the AE diffusion coefficient in the liquid phase. In the continuous front moving model (L→S) this dependence is next:

$$k(v) = \frac{v/v_D + k_e}{v/v_D + 1} \quad (11.13)$$

In the Baker and Cahn model it is

$$k(v) = \frac{v/v_D + \ln(k_e)}{v/v + 1/k_e \ln(k_e) \exp(-v/v_D)} \quad (11.14)$$

The semi-infinite medium thermal problem has been described earlier (11.1)–(11.5). Let's designate the MeAl in a liquid phase  $C_L(t, z, r)$  and in a solid phase  $C_S(t, z, r)$ . Let's assume that convection in the liquid phase is delayed on the distance  $l$  from interphase boundary  $S(t, z, r)$  (i.e.,  $l$  is interface thickness). Then at the boundary front speed  $u = dS/dt$ , the diffusion problem could be described

$$\begin{aligned} \frac{\partial C_{S,L}}{\partial t} &= D_{S,L}(T_{S,L}) \left( \frac{\partial^2 C_{S,L}}{\partial r^2} + \frac{1}{r} \frac{\partial C_{S,L}}{\partial r} + \frac{\partial^2 C_{S,L}}{\partial z^2} \right) + u \nabla C_{S,L} \\ 0 \leq r &\rightarrow \infty, 0 \leq z \rightarrow \infty; C_L(t=0, r, z) = C_L(t, z, r \in L) = C_L \\ C_S(t, r, z \rightarrow \infty) &= C_S \end{aligned} \quad (11.15)$$

$$\begin{aligned} -D_L(T_L) \frac{\partial C_L(z=s(t)-0)}{\partial z} &= -D_S(T_S) \frac{\partial C_S(z=s(t)+0)}{\partial z} \\ &+ \frac{\Delta V_{L-S}}{V} (C_S(t) - C_L(t)) \frac{\partial s}{\partial t} \end{aligned} \quad (11.16)$$

Equation (11.15) is described as the MeAl redistribution at the near-boundary region between the liquid and solid phases ( $i=L, S$ ) and on the boundary itself (11.16). Moreover, the difference  $(C_S - C_L)$  on the PT front can be presented as  $C_L[k(v) - 1]$ , where  $k(v)$  was determined before in (11.12)–(11.14). The concrete form of  $k(v)$  selection makes it possible to realize different situations on the L→S front, when the interface (1) retains the AE in the melt and leads to their superfluous content on the surface, (2) forms the equilibrium redistribution, and (3) leads to the AE extraction at the second phase. The temperature dependence of the diffusion coefficient in the proper phase can be represented as  $D_i = D_{i0} \exp(-E/kT_i(t, z, r))$ .

The system solution can be achieved by numerical methods. Because the front moving speed will be known from the thermal conductivity equation solution (11.1)–(11.5), this facilitates the search for the system solution (11.12)–(11.16). One should consider that with the present definition the average AE concentration could be estimated in the solid phase. The metastable  $\text{Me}_x\text{Al}_y$  intermetallic redistribution requires the complication of system setting (11.12)–(11.16). As was noted earlier, the part of the intermetallic compounds cannot be dissolved completely for the LI time; however, in this case their sizes will decrease and some Al quantity will begin to precipitate in the melt. Undissolved intermetallic compounds will penetrate the phase boundary at the solid phase, to change the surface shape  $S(t, z, R)$  and to create additional channels for the diffusion penetration of the MeAl from the liquid to the solid phase. A similar approach was examined at the [86]. Finally, if as a result of the high-speed cooling in the EPD some types of the intermetallide phases must be observed, and the system set (11.12)–(11.16) must be corrected.

Thus, the model approaches developed above, which include the kinetic and diffusion processes of high-speed crystallization after the LC, are completely closed. Actually, the above-mentioned continuous thermoplasticity task in connection with the AE redistribution under the cladding process can be solved by numerical methods only (ANSYS, Comsol packages). It allows us to give answers on the thermomechanical process's courses, and to facilitate the 3D LC+SHS regime optimization. The kinetic and diffusion laws' addition to this model approach during the high-speed crystallization (Section 11.5.2) completely locks our model. We can estimate the structurally sensitive parameters of the 3D LC technological process, that is, to predict before the experience: the material structure and the phase composition after the high-speed crystallization; the AE redistribution in the case of multicomponent powder compositions uses and the FG layer fabrication; and to forecast the future mechanical properties. At present, these questions are solved only by experimental methods.

### **11.5.3 Numerical simulation of laser-controlled heating of reaction-capable powdered compositions**

In this paragraph we will use the earlier developed [23] two-dimensional model for the theoretical description of SLS/M of powder compositions in which the SHS reaction can be realized. It is necessary to note that, apart from the structural macrokinetics of the SHS processes, we have an interest not only in specifying the quasi-stationary model reaction regimes (their stability, self-propagation velocity, etc.) [87] but also in the conditions of keeping the process controllable due to the relevant modifications of the laser source parameters (power density  $Q_1$ , velocity of laser scanning during SLS/M  $V_L$ ,  $\alpha$  is a volume absorption of the LI and the laser spot diameter— $d_L = 2r_n$ ). Laser power density will be determined as follows:

$$Q_1(t, x, z) = Q_m \exp\left(-\frac{(x - V_L t)^2}{r_n^2}\right) \exp(-\alpha z) \quad (11.17)$$

where  $Q_m$  is maximum density of the LI in the beam spot center:

$$Q_m = \frac{A\alpha P}{\pi r_{\text{II}}^2} \quad (11.18)$$

It is important to understand how the laser scan velocity ( $V_L$ ) will correlate with the moving velocity ( $U$ ) of the combustion reaction front during the SLS/M (or LC)+SHS process's combination. The heat release due to the chemical transformations in the reacting mixture  $Q_2$  will be described in accordance with the well-known macrokinetic approach [88], by the introduction of the dimensionless degree of transformation  $\eta$ , which accepts values from the segment  $[0, 1]$  and satisfies (11.20), as

$$Q_2 = Q_R \rho \frac{\partial \eta}{\partial t} \quad (11.19)$$

$$\frac{\partial \eta}{\partial t} = F_\eta(\eta) k \exp\left(-\frac{E}{RT}\right) \quad (11.20)$$

Mathematically, the model can be formulated inside the two-dimensional half-space  $(x, z) \in (-\infty, \infty) \times (0, \infty) = R \times R^+$ . The positive direction of an  $O_x$  axis coincides with the direction of the laser beam movement, and the positive direction of the  $O_y$  axis is defined as going into the depth of the powder reaction mixture:

$$c\rho \frac{\partial T}{\partial t} = \lambda \left( \frac{\partial^2 T}{\partial x^2} + \frac{\partial^2 T}{\partial z^2} \right) + Q_1 + Q_2 \quad (11.21)$$

In order to simplify the formal part of the model, it is necessary to ensure that the density, heat capacity, and thermal conductivity of the reacting mixture do not change their values during the SLS/M process. For their values, the following approximation was utilized:

$$A = \frac{\rho}{v\rho_1 + (1-v)\rho_2} (vA_1 + (1-v)A_2) + \frac{v\rho_1 + (1-v)\rho_2 - \rho}{v\rho_1 + (1-v)\rho_2} A_a \quad (11.22)$$

where  $A_1, A_2, A_a$  are the heat capacity, thermal conductivity, and heat diffusivity of the initial components in air,  $v$  is the volume fraction of one component, and  $\rho$  is the bulk density of the reacting mixture. Initial and boundary conditions are as follows:

$$\left. \frac{\partial T}{\partial y} \right|_{y=0} = 0, \quad T(t, x=+\infty) = T_0, \quad \left. \frac{\partial T}{\partial x} \right|_{x \rightarrow \pm\infty} = 0 \quad (11.23)$$

$$T(0, x, y) = T_0, \quad \eta(0, x, y) = 0 \quad (11.23a)$$

We will connect the system of coordinates with the laser beam center by introducing a new variable parameter  $z=x-V_L t$ . Then combining (11.21), (11.17)–(11.20) will give

$$\left\{ \begin{array}{l} c\rho \frac{\partial T}{\partial t} - c\rho V_L \frac{\partial T}{\partial x} = \lambda \left( \frac{\partial^2 T}{\partial x^2} + \frac{\partial^2 T}{\partial y^2} \right) + Q_m \exp \left( - \left( 2 \frac{x}{d_L} \right)^2 \right) \exp \left( - \frac{y}{\alpha_L} \right) \\ \quad + Q_R \rho \frac{\partial \eta}{\partial t} - Q_R \rho V_L \frac{\partial \eta}{\partial x} \\ \frac{\partial \eta}{\partial t} - V_L \frac{\partial \eta}{\partial x} = \frac{(1-\eta) \exp \left( \frac{(T-T_R)}{\Delta_R T} \right)}{\Delta_t} \end{array} \right. \quad (11.24)$$

The equation set of (11.24) was solved by using different schemes, known as the alternating direction approach using the sweep method [23].

One of the main parts of the analysis of the proposed model is to examine the problem of interdependence between the laser scan speed and the thickness of the single layer in the completely reacted, chemically active powder mixture immediately behind the LI spot. From a practical point of view, it is of importance to calculate the single-layer thickness when carrying out SLS/M. First of all, it is necessary to note here two extreme scenarios.

*Scenario I.* The velocity of SLS/M is very small. First, when the single layer of powder mixture is thin enough and/or with strong heat release from the system (for example, the powder mixture lays on a cool massive substrate). In this case the thermal wave of chemical transformation will be complicated and unstable. It will permanently overtake the SLS/M, but after a small period of time it will stop and wait for the SLS/M approach, because the wave is not capable of propagating by itself without external heating. Part of the reaction mixture transformation will take place in the front of the thermal wave, and the other part immediately in the SLS/M. The heat from the SLS/M, which will boost an already heated powder mixture, will overheat the reacting system, and, instead of sintering/melting of the reacting layer, combustion will take place. It will break the step-by-step scheme of structure formation by SLS/M. In this case, control is lost from the SLS/M process. Therefore, the extremely unfavorable conditions appearing during the product formation make this regime unacceptable for SLS/M technology.

For the second case of the low laser scan velocity, the other situation is relevant to a relatively thick layer of powder mixture. In this case, there is so much heat released during the SHS reaction that the SHS thermal transformation occurs. This kind of wave is well-known and investigated in the framework of SHS structural macrokinetics. The SLS/M here serves only as a thermal wave initiator and, after a short period of time, lags behind the synthesis wave. It is also a case of complete incompatibility of the combined SHS and SLS/M technologies, when process control by the use of SLS/M is completely lost. Such a regime may be qualitatively described within the framework of the model when a single layer with infinite width was described.

*Scenario II.* The high speed of the  $V_L$ . In this case, the SLS/M process also becomes uncontrollable due to the fact that even a thin layer of the green mixture has no time to react completely in the neighboring area before the laser spot is moved forward. This may lead to one of two possible situations. If the heat quantity in the system appears to be high enough for SHS reaction propagation in the absence of the SLS/M, the reaction again happens to be completely uncontrollable.

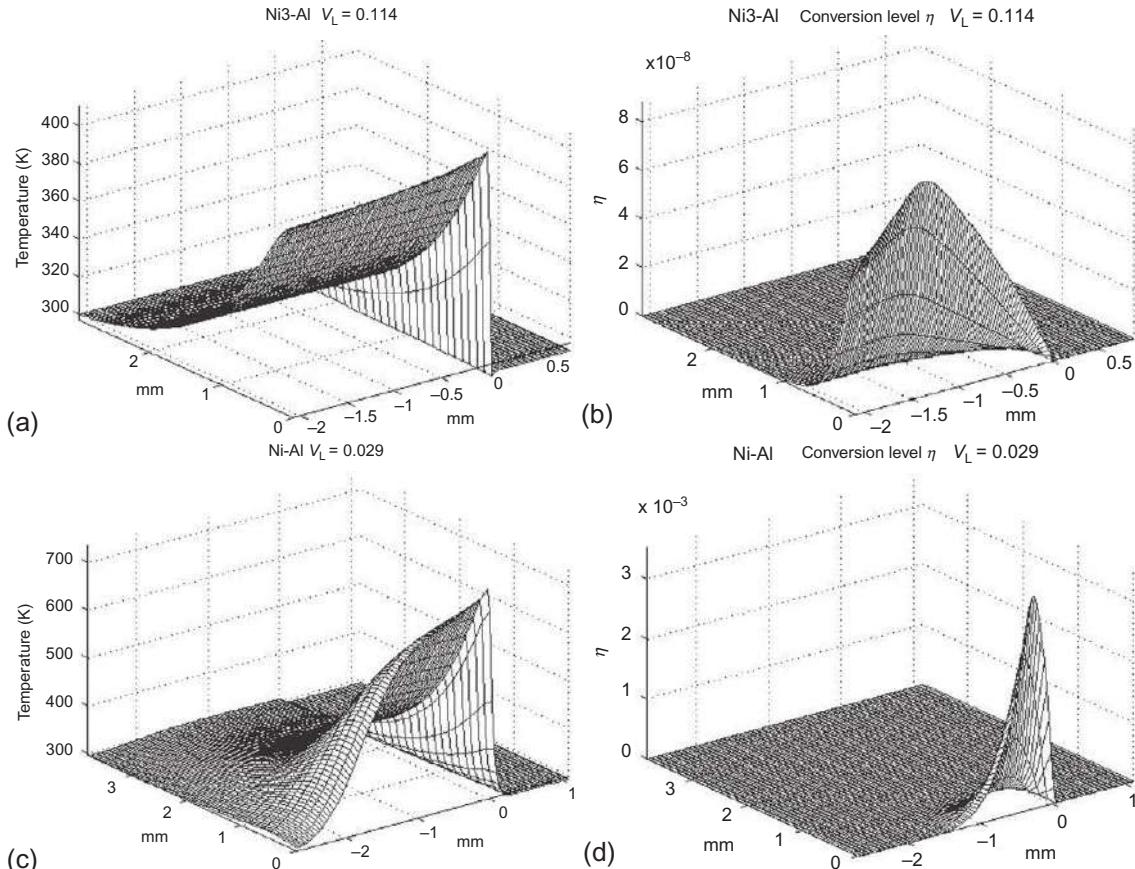
Alternatively, a fast green mixture will appear to be partially reacted. The suggested model allows an estimate of the geometrical characteristics and values of the laser scan velocity, which correspond to the formation of a single layer of completely reacted green mixture. This case takes place after a sufficient period of time from the zero point, in which the SLS/M started to move and has abandoned an observable neighboring area near the laser irradiation spot.

Figure 11.31 shows the numerical results for the LC of a reaction-capable Ni-Al powdered system. As can be seen from the comparisons, the favorable conditions of the intermetallide phase synthesis for the  $\text{Ni}_3\text{Al}$  and  $\text{NiAl}$  (Figure 11.31d and e) take place, and it is not favorable for the  $\text{NiAl}_3$  phase synthesis. Comparison of the measured temperatures (Figures 11.24, 11.27, and 11.28) and calculated temperatures (Figures 11.30a, c and 11.31a-c) ensure that our numerical approach is efficient.

Thus, we presented the model, which makes it possible to estimate the correspondence between the geometric characteristics of the synthesized system and the LI parameter's values, under which the delivered layer completely reacts in the moving laser beam spot. The carried out calculations agree well with the experimental data [4,13,14,20], represented early in Section 11.3.

## 11.6 Conclusion

To summarise the results of this chapter, it is possible to assert that the laser-controlled synthesis of aluminides and regime optimization are solved for the  $\text{Me} + \text{Al}$  ( $\text{Me} = \text{Ni}, \text{Fe}, \text{Ti}$ ) reaction-capable powder composition. The experimental results by the FGS fabrication in the MMC are discussed, where the intermetallic phases strengthened the metal matrix. The control capability by the mechanical properties (microhardness) within such FG cladded layers was shown. The specific fractal features of self-organization in the synthesized substructures have been noted. The self-consistent model of the laser-controlled combination in the SLS/M+SHS and in LC+SHS processes is built. It allows for the indicated class of reaction-capable powder mixtures to calculate the optimum regimes for the LI, in the framework of which it is possible to realize the synthesis of the 3D samples. It was important to understand and to estimate that the laser scanning speed must be located in the dynamic equilibrium with the front speed of the exothermal reaction for the intermetallic phase synthesis. Simultaneously with this, the laser energy input must be sufficient for the effective aluminide synthesis, but it must not exceed the critical values (known as the thermal effects of the exothermic reaction) for each of the synthesized phases in SHS powder mixtures. Our numerical calculations confirm the observed experimental data.



**Figure 11.30** Temperature versus  $O_x$  and  $O_y$  axes (3D graph) (a, c) and conversion degree versus  $O_x$  and  $O_y$  axes (3D graph) (b, d). The case laser controlled SHS in Ni<sub>3</sub>-Al (a, b) system and Ni-Al (c, d) systems. The LI regimes were taken from Figures 11.24 and 11.28, accordingly [23].

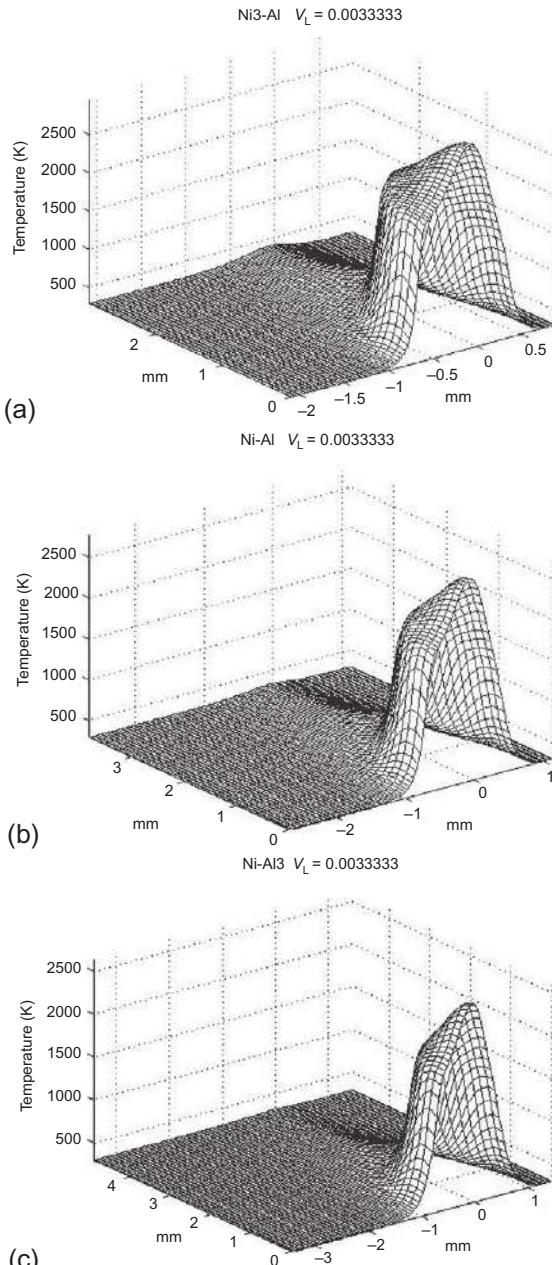


**Figure 11.31** Temperature versus  $O_x$  and  $O_y$  axes (3D graph) (a-c) and conversion degree versus  $O_x$  and  $O_y$  axes (3D graph) (d-f). The case of LC + SHS overlapping in Ni<sub>3</sub>-Al (a, d) system, Ni-Al (b, e), and Ni-Al<sub>3</sub> (c, f) systems. The LI regimes were taken from Figure 11.27 [23].

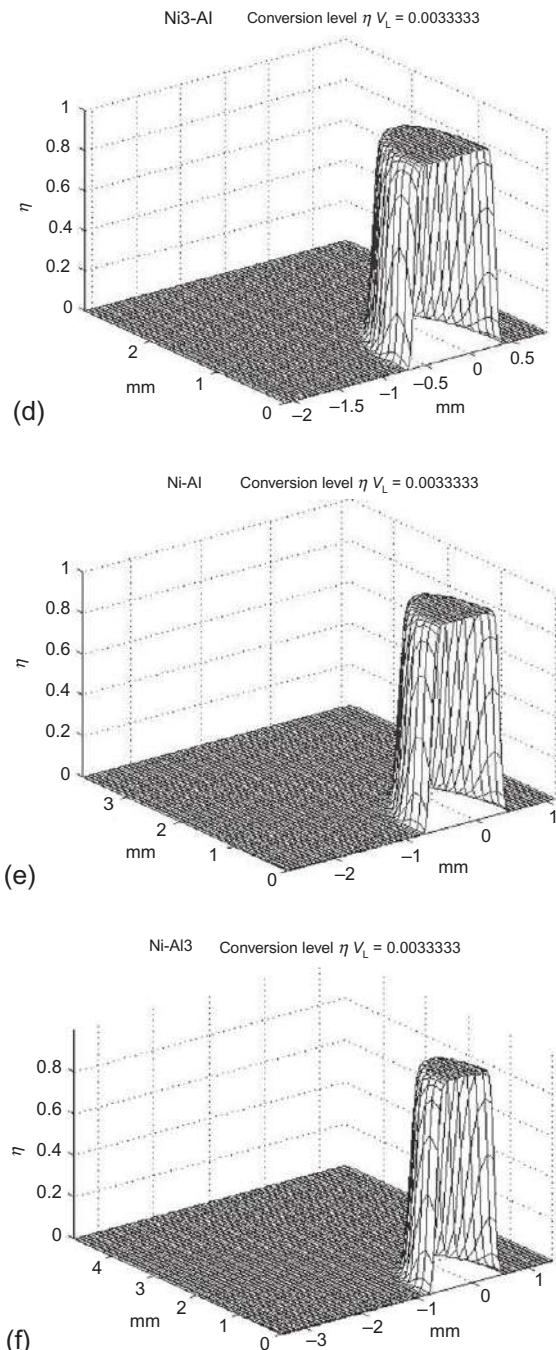


Figure 11.31 Continued.

## Acknowledgment

This chapter was completed while the author was at Moscow State University of Technology “STANKIN” and was supported of the Ministry of Education and Science of Russian Federation in the frame of the Governmental Regulation of the Russian Federation N220 (contract No. 11. G34.31.0077). Separately, author thanks the Russian Science Foundation (grant N 14-19-00992) for continue of those studies (namely, Section 11.3 and numerical simulations mentioned in Sec. 11.5.3 – Figs. 11.31e–f).

## References

- [1] I.V. Shishkovsky, Laser Synthesis of Functional Mesostructures and 3D Parts, Fizmatlit Publishers, Moscow, 2009.
- [2] D.K. Christoulis, M. Jeandin, E. Irissou, J.-G. Legoux, W. Knapp, Laser-assisted cold spray (LACS), in: D.C. Dumitras (Ed.), Nd YAG Laser, InTech, 2012. ISBN 978-953-51-0105-5.
- [3] H.Y. Lee, S.H. Jung, S.Y. Lee, K.H. Ko, Fabrication of cold sprayed Al-intermetallic compounds coatings by post annealing, Mater. Sci. Eng. A 433 (2006) 139–143.
- [4] I.V. Shishkovsky, A.G. Makarenko, A.L. Petrov, Conditions for SHS of intermetallic compounds with selective laser sintering of powdered compositions, Combust. Explos. Shock Waves 35 (2) (1999) 59–64.
- [5] L.P. Kholpanov, S.E. Zakiev, I.V. Shishkovskii, Modeling of thermal processes in laser sintering of reactive powder compositions, J. Eng. Phys. Thermophys. 78 (6) (2005) 1088–1095.
- [6] I.V. Shishkovsky, A.G. Makarenko, A.L. Petrov, Method manufacturing of 3D part from reaction-capable powder compositions, Patent Russian Federation No. 2217265, claim N 2000101975/02, 2000, date of priority 28.01.2000.
- [7] I.V. Shishkovsky, M.V. Kuznetsov, Y.G. Morozov, I.P. Parkin, Laser-induced SHS reactions and sintering of their products: computer-aided prototyping, J. Mater. Chem. 14 (2004) 3444–3448.
- [8] I.V. Shishkovskiy, M.V. Kuznetsov, Y. Morozov, I.P. Parkin, Electromotive force measurements in the combustion wave front during layer-by-layer surface laser sintering of exothermal powder compositions, Phys. Chem. Chem. Phys. 11 (2009) 3503–3508.
- [9] O.V. Lapshin, V.E. Ovcharenko, A mathematical model of high-temperature synthesis of nickel aluminide Ni<sub>3</sub>Al by thermal shock of a powder mixture of pure elements, Combust. Explos. Shock Waves 32 (3) (1996) 299–305.
- [10] M.I. Shilyaev, V.E. Borzykh, A.R. Dorokhov, Laser ignition of nickel-aluminum powder system, Combust. Explos. Shock Waves 30 (2) (1994) 147–150.
- [11] I.V. Shishkovsky, I. Smurov, Y. Morozov, Nanofractal surface structure under laser sintering of titanium and nitinol for bone tissue engineering, Appl. Surf. Sci. 254 (4) (2007) 1145–1149.
- [12] A.V. Kamashev, A.S. Panin, et al., Laser-controlled synthesis of nickel-aluminum intermetallic compounds, Tech. Phys. Lett. 27 (2001) 498–499.
- [13] I.V. Shishkovsky, L.T. Volova, et al., Porous biocompatible implants and tissue scaffolds synthesized by selective laser sintering from Ti and NiTi, J. Mater. Chem. 18 (12) (2008) 1309–1317.
- [14] I.V. Shishkovsky, V.I. Scherbakov, et al., Surface laser sintering of exothermal powder compositions: the thermal and SEM/EDX study, J. Therm. Anal. Calorim. 91 (2) (2008) 427–436.

- [15] H.J. Glass, G. With, Fractal characterization of the compaction and sintering of ferrites, *Mater. Charact.* 47 (2001) 27–37.
- [16] I. Sinha, R.K. Mandal, Simulation studies on the nature of fractal dimensions of glass-ceramics at percolation threshold, *J. Mater. Sci.* 38 (2003) 3469–3472.
- [17] A. Provata, P. Falaras, A. Xagas, Fractal features of titanium oxide surfaces, *Chem. Phys. Lett.* 297 (1998) 484–490.
- [18] N. Bertolino, M. Monagheddu, et al., Ignition mechanism in combustion synthesis of Ti-Al and Ti-Ni systems, *Intermetallics* 11 (2003) 41–49.
- [19] S. Dadbakhsh, L. Hao, In situ formation of particle reinforced Al matrix composite by selective laser melting of Al/Fe<sub>2</sub>O<sub>3</sub> powder mixture, *Adv. Eng. Mater.* 14 (2012) 45–48.
- [20] Y.G. Morozov, S.A. Nefedov, et al., Conditions of selective laser sintering in Al-Ti powdered system, *Izv. Akad. Nauk Ser. Fiz.* 66 (8) (2002) 1156–1159 (in Russian).
- [21] I. Shishkovsky, F. Missemmer, I. Smurov, Direct metal deposition of functional graded structures in Ti-Al system, *Phys. Procedia* 39 (2012) 382–391.
- [22] I. Shishkovsky, F. Missemmer, N. Kakovkina, I. Smurov, Intermetallics synthesis in the Fe-Al system via layer-by layer 3D laser cladding, *Crystals* 3 (2013) 517–529.
- [23] S.E. Zakiev, L.P. Kholpanov, et al., Modeling of the thermal processes that occur in the laser sintering of reacting powder compositions, *Appl. Phys. A Mater. Sci. Proc.* 84 (1–2) (2006) 123–129.
- [24] S. Ocylok, A. Weisheit, I. Kelbassa, Functionally graded multi-layers by laser cladding for increased wear and corrosion protection, *Phys. Procedia* 5 (2010) 359–367.
- [25] D. Srivastava, I.T.H. Chang, M.H. Loretto, The effect of process parameters and heat treatment on the microstructure of direct laser fabricated TiAl alloy samples, *Intermetallics* 9 (2001) 1003–1013.
- [26] W. Liu, J. DuPont, Fabrication of titanium aluminide matrix composites by laser engineered net shaping, in: Proceedings of the Solid Freeform Fabrication Symposium, Austin, TX, 2002, pp. 124–132.
- [27] N.V. Pimenova, T.L. Starr, Electrochemical and corrosion behavior of Ti-xAl-yFe alloys prepared by direct metal deposition method, *Electrochim. Acta* 51 (2006) 2042–2049.
- [28] S.C. Wei, B.S. Xu, et al., Comparison on corrosion-resistance performance of electro-thermal explosion plasma spraying FeAl-based coatings, *Surf. Coat. Technol.* 201 (2007) 5294–5297.
- [29] Y. Yang, I. Baker, The influence of vacancy concentration on the mechanical behavior of Fe-40Al, *Intermetallics* 6 (1998) 167–175.
- [30] T.H. Kim, G.T. Gong, et al., Catalytic decomposition of sulfur trioxide on the binary metal oxide catalysts of Fe/Al and Fe/Ti, *Appl. Catal. Gen.* 305 (2006) 39–45.
- [31] C.T. Liu, E.P. George, et al., Recent advances in B2 iron aluminide alloys: deformation, fracture and alloy design, *Mater. Sci. Eng. A* 258 (1998) 84–98.
- [32] M.M. Pariona, V. Teleginski, et al., AFM study of the effects of laser surface remelting on the morphology of Al-Fe aerospace alloys, *Mater. Charact.* 74 (2012) 64–76.
- [33] T. Chmielewski, D.A. Golanski, New method of in-situ fabrication of protective coatings based on Fe-Al intermetallic compounds, *Proc. Inst. Mech. Eng. Part B J. Eng. Manuf.* 225 (2011) 611–616.
- [34] S. Kumar, V. Selvarajan, et al., Characterization and comparison between ball milled and plasma processed iron-aluminium thermal spray coatings, *Surf. Coat. Technol.* 201 (2006) 1267–1275.
- [35] G.J. Yang, H.T. Wang, et al., Effect of annealing on the microstructure and erosion performance of cold-sprayed FeAl intermetallic coatings, *Surf. Coat. Technol.* 205 (2011) 5502–5509.

- [36] S. Azem, M. Nechiche, K. Taibi, Development of copper matrix composite reinforced with FeAl particles produced by combustion synthesis, *Powder Technol.* 208 (2011) 515–520.
- [37] E. Godlewski, S. Szczepanik, et al., FeAl materials from intermetallic powders, *Intermetallics* 11 (2003) 307–312.
- [38] A. Agarwal, Iron aluminide based coating deposited by high energy density processes, *Surf. Modificat. Technol.* XV (2002) 173–182.
- [39] G. Sharma, R. Awasthi, K. Chandra, A facile route to produce Fe-Al intermetallic coatings by laser surface alloying, *Intermetallics* 18 (2010) 2124–2127.
- [40] B. Song, S. Dong, et al., Fabrication and microstructure characterization of selective laser-melted FeAl intermetallic parts, *Surf. Coat. Technol.* 206 (2012) 4704–4709.
- [41] S. Tomida, K. Nakata, Fe-Al composite layers on aluminum alloy formed by laser surface alloying with iron powder, *Surf. Coat. Technol.* 174 (2003) 559–563.
- [42] K. Uenishi, Y. Ogata, et al., Laser cladding of Fe-Cu based alloys on aluminum, *Solid State Phenom.* 127 (2007) 331–336.
- [43] L. Zhao, M.J. Zhao, et al., Study on Fe-Al-Si in situ composite coating fabricated by laser cladding, *Appl. Surf. Sci.* 258 (2012) 3368–3372.
- [44] L.N. Zhu, B.S. Xu, et al., Microstructure and nanoindentation measurement of residual stress in Fe-based coating by laser cladding, *J. Mater. Sci.* 47 (2012) 2122–2126.
- [45] S. Nayak, L. Riester, et al., Micromechanical properties of a laser-induced iron oxide-aluminum matrix composite coating, *J. Mater. Res.* 18 (2003) 833–839.
- [46] S. Chen, J. Huang, et al., Influence of a Ni-foil interlayer on Fe/Al dissimilar joint by laser penetration welding, *Mater. Lett.* 79 (2012) 296–299.
- [47] H. Laukant, C. Wallmann, et al., Fluxless laser beam joining of aluminium with zinc coated steel, *Sci. Technol. Weld. Joining* 10 (2005) 219–226.
- [48] S. Mukherjee, S. Chakraborty, Transport phenomena in conduction mode laser beam welding of Fe-Al dissimilar couple with Ta diffusion barrier, *Int. J. Heat Mass Transfer* 53 (2010) 5274–5282.
- [49] K. Saida, W. Song, K. Nishimoto, Diode laser brazing of aluminium alloy to steels with aluminium filler metal, *Sci. Technol. Weld. Joining* 10 (2005) 227–235.
- [50] G. Sierra, P. Peyre, Steel to aluminium braze welding by laser process with Al-12Si filler wire, *Sci. Technol. Weld. Joining* 13 (2008) 430–437.
- [51] M. Potesser, T. Schoeber, et al., The characterization of the intermetallic Fe-Al layer of steel-aluminum weldings, in: S.M. Howard, R.L. Stephens, C.J. Newman, J.-Y.J. Hwang, A.M. Gokhale, T.T. Chen (Eds.), EPD Congress 2006, TMS (The Minerals, Metals & Materials Society), 2006, pp. 167–176.
- [52] R. Vilar, E.C. Santos, P.N. Ferreira, et al., Structure of NiCrAlY coatings deposited on single-crystal alloy turbine blade material by laser cladding, *Acta Mater.* 57 (18) (2009) 5292–5302.
- [53] G.P. Dinda, A.K. Dasgupta, J. Mazumder, Laser aided direct metal deposition of Inconel 625 superalloy: microstructural evolution and thermal stability, *Mater. Sci. Eng. A* 509 (2009) 98–104.
- [54] Y. Yu, J. Zhou, J. Jianmin Chen, et al., Preparation, microstructure and tribological behavior of laser cladding NiAl intermetallic compound coatings, *Wear* 274–275 (2012) 298–305.
- [55] J. Choi, L. Han, Y. Hua, Modeling and experiments of laser cladding with droplet injection, *J. Heat Transfer* 127 (9) (2005) 978–986.
- [56] R. Dwivedi, S. Zekovic, R. Kovacevic, A novel approach to fabricate uni-directional and branching slender structures using laser-based direct metal deposition, *Int. J. Mach. Tools Manuf.* 47 (2007) 1246–1256.

- [57] S. Ghosh, J. Choi, Modeling and experimental verification of transient/residual stresses and microstructure formation of multi-layer laser aided DMD process, *J. Heat Transfer* 128 (7) (2006) 662–679.
- [58] M. Labudovic, D. Hu, R. Kovacevic, A three dimensional model for direct laser metal powder deposition and rapid prototyping, *J. Mater. Sci.* 38 (2003) 35–49.
- [59] M.P. Mughal, H. Fawad, et al., Deformation modelling in layered manufacturing of metallic parts using gas metal arc welding: effect of process parameters, *Model. Simul. Mater. Sci. Eng.* 13 (7) (2005) 1187–1204.
- [60] M.P. Mughal, H. Fawad, R. Mufti, Finite element prediction of thermal stresses and deformations in layered manufacturing of metallic parts, *Acta Mech.* 183 (1–2) (2006) 61–79.
- [61] M.P. Mughal, H. Fawad, R. Mufti, Three-dimensional finite-element modelling of deformation in weld-based rapid prototyping, *Proc. Inst. Mech. Eng. Part C J. Mech. Eng. Sci.* 220 (6) (2006) 875–885.
- [62] A.J. Pinkerton, L. Li, An analytical model of energy distribution in laser direct metal deposition, *Proc. Inst. Mech. Eng. Part B J. Eng. Manuf.* 218 (4) (2004) 363–374.
- [63] A.J. Pinkerton, L. Li, The development of temperature fields and powder flow during laser direct metal deposition wall growth, *Proc. Inst. Mech. Eng. Part C J. Mech. Eng. Sci.* 218 (5) (2004) 531–542.
- [64] A.J. Pinkerton, L. Li, An experimental and numerical study of the influence of diode laser beam shape on thin wall direct metal deposition, *J. Laser Appl.* 17 (1) (2005) 47–56.
- [65] H. Qi, J. Mazumder, H. Ki, Numerical simulation of heat transfer and fluid flow in coaxial laser cladding process for direct metal deposition, *J. Appl. Phys.* 100 (2006) 2.
- [66] E. Toyserkani, A. Khajepour, S. Corbin, *Laser Cladding*, CRS Press, 2005.
- [67] I.V. Shishkovskii, Calculation of residual stresses induced during laser quench-hardening of steel, *J. Eng. Phys. Thermophys.* 61 (6) (1991) 1534–1541.
- [68] I.V. Shishkovsky, Thermal field analysis under SLS of metal-polymer powder compositions, *Proc. SPIE* 4644 (2002) 446–449.
- [69] I.N. Zavestovskaja, V.I. Igoshin, et al., Theoretical and numerical analysis of stresses in a laser hardening model, *J. Sov. Laser Res.* 12 (4) (1991) 365–382.
- [70] N.N. Rukalin, *Laser and e-Beam Treatment of Materials*, Handbook, Mashinistrienie Publishers, Moscow, 1986 (in Russian).
- [71] A.A. Vedenov, G.G. Gladush, *Physical Processes of Laser Treatment of Materials*, Energoatomizdat Publishers, Moscow, 1985 (in Russian).
- [72] L.D. Landau, E.M. Lifshitz, *Fluid mechanics*, in: *Course of Theoretical Physics*, vol. 6, second ed., Reed Educational and Professional Publishing Limited, 2000.
- [73] G. Ehlen, A. Ludwig, P.R. Sahm, Simulation of time-dependent pool shape during laser spot welding: transient effects, *Metall. Mater. Trans. A* 34A (2003) 2947–2961.
- [74] A.A. Uglov, O.G. Sagetdinov, Melt simulation and metal crystallization under impulse laser, *Phys. Chem. Mater. Treat.* 5 (1991) 36–40 (in Russian).
- [75] A.A. Uglov, O.G. Sagetdinov, Melt simulation under volume laser influence, *Phys. Chem. Mater. Treat.* 5 (1992) 33–37 (in Russian).
- [76] T.K. Anthony, H.E. Cline, Surface rippling induced by surface-tension gradient during laser surface melting and alloying, *J. Appl. Phys.* 48 (9) (1977) 3888–3894.
- [77] R.V. Arutuynov, V.I. Baranov, et al., *Interaction of Laser Influence with Matter*, Science Publishers, Moscow, 1989 (in Russian).
- [78] T. Change, J. Mazumder, Two-dimensional transient model for mass transport in laser surface alloying, *J. Appl. Phys.* 57 (6) (1985) 2226–2232.
- [79] J. Christian, *Theory of Transformation in Metals and Alloys. Part 1*, World Publishers, Moscow, 1987.

- 
- [80] B.Y. Lubov, Theory of Crystallization in large Volumes, Science Publishers, Moscow, 1975.
  - [81] I. Shishkovsky, Submicron nucleation kinetics during a high-speed laser assisted surface modification, *Phys. Status Solidi A* 207 (5) (2010) 1154–1159.
  - [82] D.M. Gureev, S.I. Mednikov, About of theory of lattice reconstruction under phase transformations in metals, in: FIAN Proceedings, 2017, 1993, pp. 37–41 (in Russian).
  - [83] M.J. Aziz, Model for solute redistribution during rapid solidification, *J. Appl. Phys.* 53 (2) (1982) 1158–1168.
  - [84] M.J. Aziz, Non-equilibrium interface kinetics during rapid solidification: theory and experiment, *Mater. Sci. Eng.* 98 (1988) 369–372.
  - [85] Pout, et al., Modification and Alloying of Surface under Laser, Ion and e-Beam Influence, Mashonostroenie Publishers, Moscow, 1987 (in Russian).
  - [86] R. Sasikumar, T.R. Ramamohan, B.C. Pai, Critical velocities for particle pushing by moving solidification fronts, *Acta Metall.* 37 (7) (1989) 2085–2091.
  - [87] S.E. Zakiev, K.G. Shkadinsky, Thermal influence of high frequency radiation on high-temperature synthesis front, *Chem. Phys. Rep.* 17 (1998) 112–120.
  - [88] A.G. Merzhanov, History and new developments in SHS, *Ceram. Trans.* 56 (1995) 3–25.
  - [89] K.J. Lee, S. Kumai, T. Arai, Interfacial microstructure and strength of steel to aluminum alloy lap joints welded by a defocused laser beam, *Mater. Trans.* 46 (2005) 1847–1856.
  - [90] I.V. Shishkovskij, Fractal dimension of the pores distribution under a laser sintering of Ti powder, *Phys. Chem. Mater. Treat.* 6 (2004) 66–70 (in Russian).
  - [91] I.V. Shishkovsky, I. Smurov, Titanium base functional graded coating via 3D laser cladding, *Mater. Lett.* 73 (2012) 32–35.

# Deposition and surface modification of thin solid structures by high-intensity pulsed laser irradiation

12

A.C. Popescu, M. Ulmeanu, C. Ristoscu, I.N. Mihailescu

National Institute for Lasers, Plasma and Radiation Physics, Măgurele, Romania

## 12.1 Introduction

Section 12.2 is dedicated to laser deposition methods of interest: pulsed laser deposition (PLD) and matrix-assisted pulsed laser evaporation (MAPLE). Advantages and drawbacks are listed. Possible applications that make full use of these laser deposition methods are reviewed. Relevant examples from current activity on the influence of laser and deposition parameters on films structure and morphology are selected. It is noticed that the fluence variation produces porous or melted structures, solvent evaporation or MAPLE target composition induce the generation of periodical structures, and ambient pressure stays at the origin of cauliflower morphology in calcium phosphates. Structure modification with deposition parameters is introduced with two relevant examples: ambient gas that transforms ZnO from transparent to dark, and carbon structures that convert from very soft to quite hard.

Section 12.3 reviews various approaches of direct surface processing using pulsed laser beams. Special emphasis is put on experimental results of surface processing in air or under liquid using fs laser sources. The advantage in using liquids is the possibility to employ all types of light-induced processes for direct single-step surface patterning by ablation, etching, and chemical or structural transformation. In this section it is shown that there is a direct correlation between chemical composition of the liquids and the femtosecond pulse laser interaction with silicon and gallium arsenide substrates. The surface is irradiated at normal incidence, in far- and near-field, under liquid precursors such as acetone ( $C_3H_6O$ ), methanol ( $CH_3OH$ ), carbon tetrachloride ( $CCl_4$ ), or 1,1,2-trichlor-trifluorethan ( $C_2Cl_3F_3$ ). Experimental evidence of periodic arrays on silicon and gallium arsenide surfaces is given. The influence of the irradiation medium on far- and near-field interactions is investigated.

Section 12.4 is devoted to “Resources,” before the chapter ends with conclusions and a reference list including books and review articles on the reviewed topics.

## 12.2 Thin films with patterned surfaces obtained by laser deposition methods

### 12.2.1 Thin film laser deposition methods

#### 12.2.1.1 Pulsed laser deposition

When a high-intensity laser beam interacts with a solid material, the photons absorption can initiate the fusion and the local vaporization of the outer layers. A substance cloud is generated near the surface, consisting of photons, electrons, ions, atoms, molecules, clusters, and liquid or solid particles. The material ejection phenomenon under the action of a laser beam is known in literature as *laser ablation*.

By placing a collector parallel and at a distance of a few centimeters in front of the target, adherent inorganic thin films can be obtained, with possible applications in almost all industrial fields. The thin films synthesis method commonly associated with laser ablation is PLD. This technique emerged out of the necessity to obtain stoichiometric transfer of materials with complex composition in the form of thin films. Historically, the method bared several denominations [1]: pulsed laser evaporation, laser-induced flash evaporation, laser molecular beam epitaxy, laser-assisted deposition and annealing, or laser sputtering. A typical PLD setup is available from many books and Ph.D. theses defended in recent years [1,2].

Whenever the deposition is conducted in a reactive gas and the obtained film has a composition different from that of the target or nonexistent in nature, the synthesis process is called reactive pulsed laser deposition (RPLD).

Even though PLD proved till now difficult to implement industrially, it is a viable laboratory option due to some important advantages:

- the target composition (stoichiometry) can be reproduced with relative ease in the synthesized thin films—due to the congruent vaporization it is possible to deposit materials with complex chemical composition [3];
- the sequential nature of the PLD process allows for a very precise control of the films thickness ( $10^{-1}$  Å per pulse);
- any material can be ablated, so the method is not limited to special classes of compounds;
- using a carousel system with targets of different compositions, a multilayer film can be obtained—the combinations are endless, and new composite materials with improved properties can be obtained [4];
- the target vaporization is induced by photons, so no contamination occurs during the deposition process;
- by varying the deposition parameters, largely different structures can be obtained in terms of macroscopic and microscopic aspect, crystalline status, and physical properties; or
- the number of pulses dictates if the ablated substance is deposited on substrate as thin films or as isolated nanoparticles. Complex structure films-particles can be synthesized, taking advantage of the surface plasmon resonance [5].

The most common PLD/RPLD disadvantages reported in the literature are:

- Deposition areas of a few square centimeters only because the plasma is expanding mainly along the  $z$  direction and at high fluences (necessary for the congruent evaporation) the

- $\theta$  angle is small. Special translation/rotation robotized substrate holders should be used for uniform coating of large substrate areas [6].
- Unpractical for deposition of organic complex molecules. Under the action of intense laser pulses, long organic chains are broken, the deposited material being different from the original target material.
  - The major disadvantage however, comes from the micronic and submicronic aggregates (described in the literature as particulates or droplets) that hinder applications in fields requiring high finesse (micro-, nano-, or optoelectronics). However, special precautions in conjunction with PLD can drastically diminish the droplets in PLD films [7–9].

### 12.2.1.1 Applications

Here follows a list of selected PLD applications from recent literature: complex oxide thin films for superconductors ( $\text{YBa}_2\text{Cu}_3\text{O}_7$  [10],  $\text{Ba}_2\text{Co}_2\text{Fe}_{12}\text{O}_{22}$  [11]), thin film optical components ( $\text{As}_2\text{S}_3$  [12]), active mediums (Er:YAG [13]), wide band-gap electronics (ZnO doped [14] or in conjunction with other semiconductors), oxide sensor devices (zinc oxide for detecting  $\text{NO}_2$  [15]), protective coatings and barriers (e.g., DLC [16], BN [17], TiN [18]), biocompatible coatings (prostheses coatings [19], particles for drug delivery [20]), and organic thin films (i.e., polymethylmethacrylate) [21].

### 12.2.1.2 Matrix-assisted pulsed laser evaporation

For electronic, optical, and biosensor device applications, the materials of choice are (bio)polymers for the fabrication and passivation of electronic coatings; organic dye molecules for nonlinear and optical applications; and biocompatible, protein coatings for microarray biosensor applications, living cells for tissue engineering. The ability to deposit various classes of functional polymeric and organic materials in the form of thin films using a single technique opens the way to the development and implementation of new applications.

When a laser beam acts upon organic targets under the usual conditions for PLD, the material, which is grown in thin film form, will be different from the starting material, the functional groups being altered [22]. The organic chain can be broken and the film consists of small polymeric pieces with different functional groups terminating the ends. It should be mentioned that even small changes in the number of functional groups or the degree of polymerization can preclude the use of these films for desired application. Such modifications might be acceptable for some applications, but in general the use of lasers for depositing thin films of organic or other delicate materials requires more subtle approaches than those offered by PLD.

MAPLE is a laser-based vapor deposition technique derived from PLD that has been invented to deposit thin organic and biologic films without decomposition or other major irreversible damage [23]. Characteristic to MAPLE is the use of a cryogenic composite target made of a dilute mixture of the delicate solute to be deposited and a light absorbent, high vapor pressure solvent matrix (Figure 12.1).



**Figure 12.1** Cryogenic target submitted to multipulse KrF\* laser irradiation for MAPLE deposition.

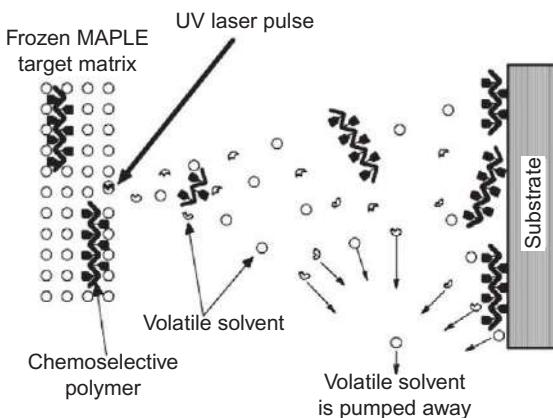


**Figure 12.2** Scheme of the MAPLE desorption process.

When using a frozen composite as a target, the basic laser-material interaction mechanism is changing, so that the major part of the laser energy is absorbed by the solvent molecules and not by the fragile solute. Fast evaporating volatile solvent molecules desorb the solute by soft collisions (Figure 12.2). A uniform thin film is deposited with preserved properties, such as chemical structure and functionality. The receiving substrate is kept at room temperature or in any case low temperature in order to prevent solute molecule degradation or damage. The sticking coefficient of the solvent is close to zero, so the evaporated solvent is efficiently pumped away by the vacuum system.

The major advantages of MAPLE are listed below:

- it enables the thin films deposition from a large choice of delicate materials: polymers, proteins, enzymes, living cells;
- it is a noncontact deposition technique free of pollution risks; and
- it is compatible with masking, allowing to obtain patterned nanostructures.

Due to compatibility issues between laser radiation and solvents, the experimentalist is often forced to choose from a rather narrow offer of solvents. Therefore, restrictions of the method application may arise:

- the solvent when in frozen state should be an efficient laser radiation absorber;
- the solvent should not interact with solute even when exposed to laser irradiation; and
- the freezing point of solvent should not be too low to limit the energy expenses.

#### 12.2.1.2.1 Present-day applications

- Biomaterials for drug delivery, sensing, and tissue engineering: polyethylene glycol [24–26], metalloporphyrins [27,28], polyvinyl alcohol derivatives [29], poly(1,3-bis-(*p*-carboxyphenoxy propane)-co-(sebacic anhydride) [30], collagen [31].
- Polymers for electronic devices (electrically conductive polymers, light-emitting thin films): polythiophene [32], polyfluorene [33], lysosime [34], hybrid composites [35].
- Insulating polymers with controlled roughness [36–38].
- Chemical and gas sensors: polypirrole [39], urease [40].
- Protective coatings: composite carbon/gold nanoparticle films [41].

The following experiments were conducted in a stainless steel enclosure. Excimer laser sources (ArF\*, KrF\*, XeCl\*) generating pulses of tens of ns at 193, 248, or 308 nm, respectively, were used for film depositions. To avoid drilling and obtain a uniform film, the targets were rotated and/or translated during the multipulse irradiation. The laser beam was at oblique incidence, while the deposition torch was always normal to target surface. A low-pressure ambient atmosphere of water vapors, oxygen, or nitrogen was present in the deposition chamber in some experiments.

#### 12.2.2 *Drastic modification of thin films morphology or structure due to one parameter variation during laser deposition*

##### 12.2.2.1 *Target material: cauliflower-like calcium phosphate thin films for implantology applications*

Fifteen millimeter diameter Ti substrates were mechanically polished and submitted to acid etching to get an extended active surface. They were placed parallel to the target at a separation distance of 4 cm and heated during deposition at a temperature of 150 °C. The targets were prepared from octocalcium phosphate (OCP—Ca<sub>8</sub>(HPO<sub>4</sub>)<sub>2</sub>(PO<sub>4</sub>)<sub>4</sub>·5H<sub>2</sub>O) powders. OCP thin film deposition was carried out in 35–80 Pa water vapors. The number of applied laser pulses for the deposition of 1 μm structure was 15,000. To improve the crystalline status, each film was thermally treated postdeposition for 6 h in a flux of hot water vapors at 180 °C [42].

The OCP films exhibited a porous, 3D structure (**Figure 12.3**) similar to cauliflower-like structures, as a result of aggregation of grains, particulates, and droplets of different sizes. In cross section, droplets with diameters of 250–300 nm were visible (**Figure 12.4b**). The measured coating roughness was of Ra = 720 nm, with an accuracy of 10%. X-ray diffraction (XRD) patterns of OCP coatings deposited on Si substrates showed an amorphous-poor crystalline structure.

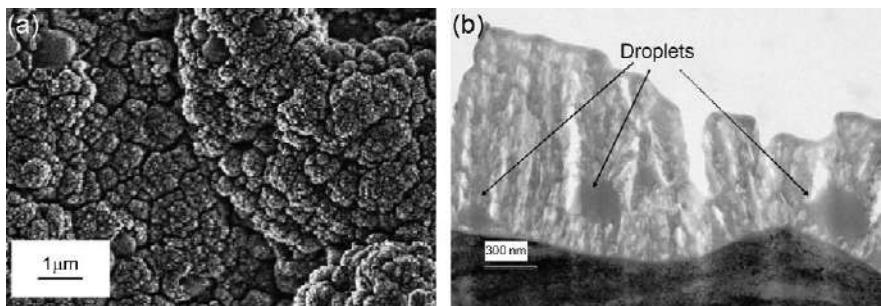


**Figure 12.3** (a) SEM and (b) TEM micrographs showing the porous, 3D morphology of PLD OCP coatings.

Reproduced with permission from [42].

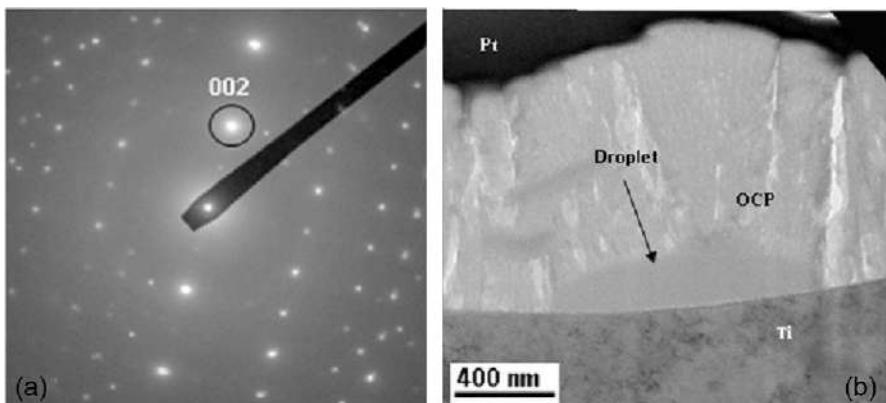


**Figure 12.4** (a) SAED pattern of the OCP samples and (b) global XTEM images. (a, b) show the samples deposited on Ti substrate, heated at 150 °C, and subjected to post-deposition treatment at 150 °C, respectively.

Reproduced with permission from [43].

The layers had a tree-like structure similar to the coral (Figures 12.3a and 12.4b) with a growth direction perpendicular to the substrate [43].

Selected area electron diffraction (SAED) (Figure 12.4a) and HRTEM micrographs [43] evidenced an amorphous phase with dispersed crystalline nanodomains. These particular features are well suited for growing bone tissues and fast osteointegration [44]. The cells contact area is in this case orders of magnitude larger than for equivalent smooth surface. *In vitro* tests proved that both fibroblasts and osteoblasts adhere, reach a normal morphology, proliferate, and remain viable when cultured on OCP coatings, supporting good biocompatibility and absence of any toxicity.

### 12.2.2.2 Deposition ambient: transparent hydrophilic and dark hydrophobic ZnO thin films

ZnO thin films were deposited from high-purity (99.99%) targets. The target-substrate separation distance was of 3-6 cm, but the laser fluence was always set at  $5 \text{ J/cm}^2$ . Pieces of  $(3 \times 3) \text{ cm}^2$  cotton/polyester (56%/44%) were used as deposition substrates. A mask was interposed to deposit a circular spot of 2 cm diameter. The surrounding bare area was used as a reference for color, structural investigations, and wetting tests. Two sets of five samples were prepared in a flux of 13 Pa oxygen or in vacuum. After the application of 100 laser pulses, ZnO completely covered the textiles in the form of a continuous film.

ZnO films were uniform at optical inspection and had an average thickness measured by spectroscopic ellipsometry of 20 nm. The thin films deposited in an oxygen flux were highly transparent ([Figure 12.5a](#)), while the ones obtained in vacuum were opaque, dark-colored ([Figure 12.5b](#)).

The wetting properties of the textiles coated with ZnO were evaluated at room temperature by static contact angle measurements. Thin films deposited in oxygen flux

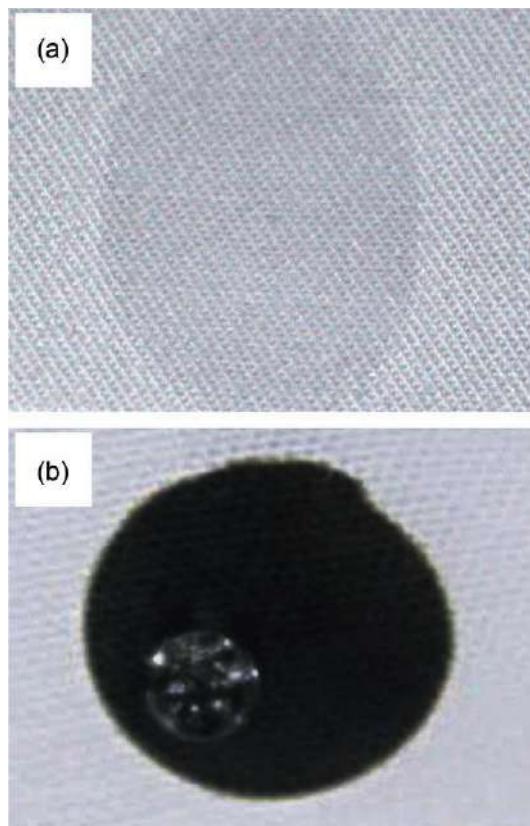


**Figure 12.5** Textile material partially coated with ZnO nanostructures: (a) hydrophilic thin film deposited in 13 Pa oxygen and (b) hydrophobic thin film deposited in vacuum.  
Reproduced with permission from [45].

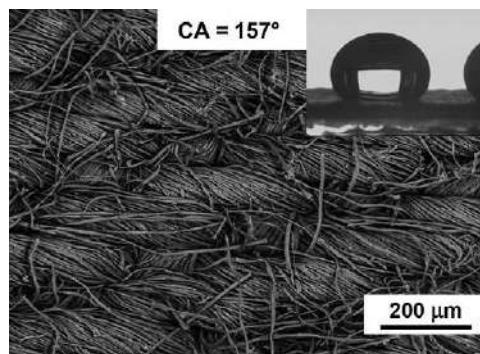


**Figure 12.6** SEM micrograph of the superhydrophobic textile coated with ZnO in vacuum. Inset: Water droplet in static mode with the CA of 157°.  
Reproduced with permission from [45].

were hydrophilic, identical to the surrounding uncoated area (Figure 12.5a). In both cases, the water drop collapsed on textile surface.

Conversely, the thin films deposited in vacuum were hydrophobic (Figure 12.5b). The water droplet in the undeposited area collapsed, while the one poured onto the ZnO thin film preserved its round shape for a matter of minutes. A contact angle of 157° (Figure 12.6) was measured, which qualified these films as superhydrophobic.

Typical XRD patterns of the samples obtained in oxygen flux or in vacuum look rather different (Figure 12.7). All the diffraction lines associated with the films, deposited on either Si or textile, were assigned to the wurtzite phase of hexagonal ZnO. The main difference between the two structures is related to the preferred orientation and mean size of the ZnO crystallites. The preferred orientation was pointed by the modification of relative intensities of the characteristic peaks of ZnO in thin films versus the reference ZnO powder. The oriented growth was much more evident in the case of the films deposited on Si. In the case of the films deposited in oxygen flux, the orientation of crystallites corresponds to the (001) and to (101) planes parallel to the surface. Films deposited in vacuum contain comparable amounts of ZnO crystallites oriented either with (100) or (110) planes parallel to the surface.

The rocking curves of the respective crystal planes were also recorded (Figure 12.7Ab-e). They showed a maximum centered at  $\omega = 2\theta_B/2$ , confirming that these planes were parallel to the surface. The full width at half maximum of the rocking curve was in the range of 8–11° for each plane.

It was concluded that the oxygen flux of 13 Pa favors the (001) texture of ZnO, with a 65° misalignment, the crystallite size along the *c*-axis being relatively large (~85 nm). When the deposition was carried out in vacuum, the crystallites were fairly small, with two different types of grains coexisting in comparable amounts. The first type was oriented with (100) planes parallel to the surface, with an average size of ~9 nm, and a second one was (110)-oriented plane having ~4 nm only.

One notes that the two types of crystal planes parallel to the surface in the films deposited in oxygen flux, (001) and (101), contain a single type of atoms in a plane, Zn or O, in successive layers (Figure 12.8a). To the contrary, the two types of crystal

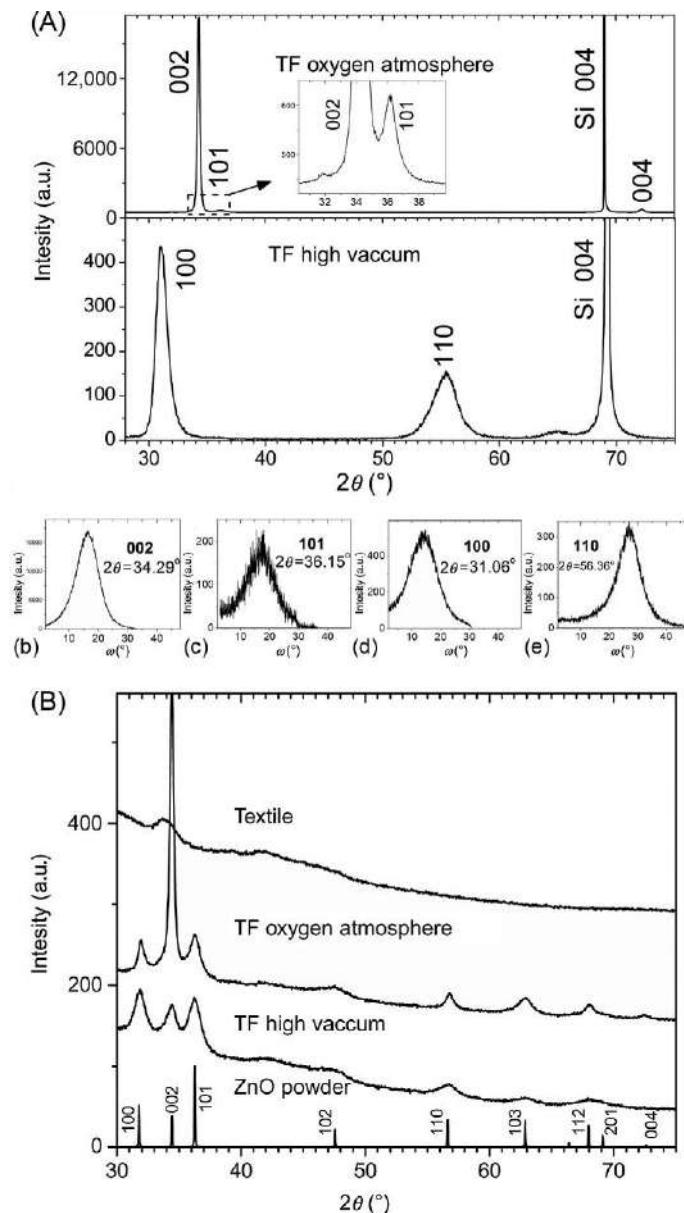


**Figure 12.7** XRD patterns for ZnO TF deposited onto (A) silicon substrate and (B) textile substrate. Rocking curves ( $\chi$  scans) for the involved crystal planes (b) (002), (c) (101), (d) (100), and (e) (110).

Reproduced with permission from [45].

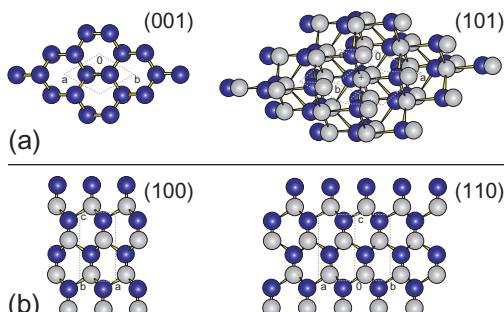


**Figure 12.8** ZnO lattice with the crystal planes parallel to the surface in the ZnO films synthesized in an oxygen flux: (a) (001) and (101) planes containing a single type of atoms, and in the ZnO films synthesized in vacuum, (b) (100) and (110) planes consisting of pairs of Zn (black) plus O (white) atoms.

Reproduced with permission from [45].

planes parallel to the surface in the structures deposited in vacuum, (100) and (110), contain in the same plane pairs of Zn and O atoms (Figure 12.8b).

The electrical charging of the surface can stay at the origin of the affinity or repellency to water of ZnO structures. Indeed, as observed by XRD, the ambience in the deposition chamber also determines the forming combinations between Zn and O atoms in the crystalline lattice. In the case of depositions in a vacuum, there is a mix in each crystalline plane of positive and negative charges that compensate for each other. The water droplet, neutral from the electrical point of view, does not interact electrically with the structure. Conversely, the films deposited in oxygen flux contain only one type of atoms per plane that induce a positive (Zn) or negative (O) charging of the surface. The deposit interacts electrically with the droplet to reach the neutral status, thus attracting the water bubble toward the ZnO surface, causing supplementary stress that contributes to the final collapse of the bubble [45].

### 12.2.2.3 Ambient gas pressure: hard and soft carbon nitride thin films

CNx thin films were predicted to reach a hardness superior to diamond [46,47]. For synthesis by RPLD, graphite targets and a low-pressure ambient nitrogen atmosphere were used. The incident laser fluence was set at 12 or 18 J/cm<sup>2</sup>. A series of 10,000 laser pulses at a repetition rate of 10 Hz were applied for the deposition of one film. The synthesized material was collected on KBr or Si ⟨111⟩ substrates kept at room or 250 °C temperature, placed parallel with the target surface at a separation distance of 4 cm. After evacuation to  $\sim 10^{-4}$  Pa, the chamber was circulated with high-purity nitrogen at a dynamic pressure of 0.2, 1, or 50 Pa.

The mechanical properties of the deposited layers (hardness and Young modulus) were measured with a nanoindenter equipped with a Berkovich triangular pyramidal tip. Six indentation loads of 0.5, 1.5, 2.5, 5, 7.5, and 10 mN were applied. Ten indentations were performed for each load, while the analysis was carried out according to the Oliver and Pharr method [48].

Hardness values corresponding to different depths inside the deposited layers are given in [Figure 12.9](#). The distance  $d$  measured from the surface of the films is the maximum penetration depth for different indentation loads. From [Figure 12.9](#) one can notice that the hardness values rapidly stabilize into the layer's depth. [Table 12.1](#) collects the data on the dependence of the stabilized hardness values upon the nitrogen pressure in the deposition chamber.

Mg K $\alpha$  (1253.6 eV) radiation for excitation and a concentric VSW100 hemispherical analyzer working at a base pressure of  $5 \times 10^{-8}$  Pa have been used for XPS investigations. Integral spectra were recorded in the C1s, N1s, and O1s regions. More accurate recordings were also conducted for the study of the C1s and N1s lines by the deconvolution peak method. XPS analysis was performed immediately after the deposition, as well as about 1 year later [49].

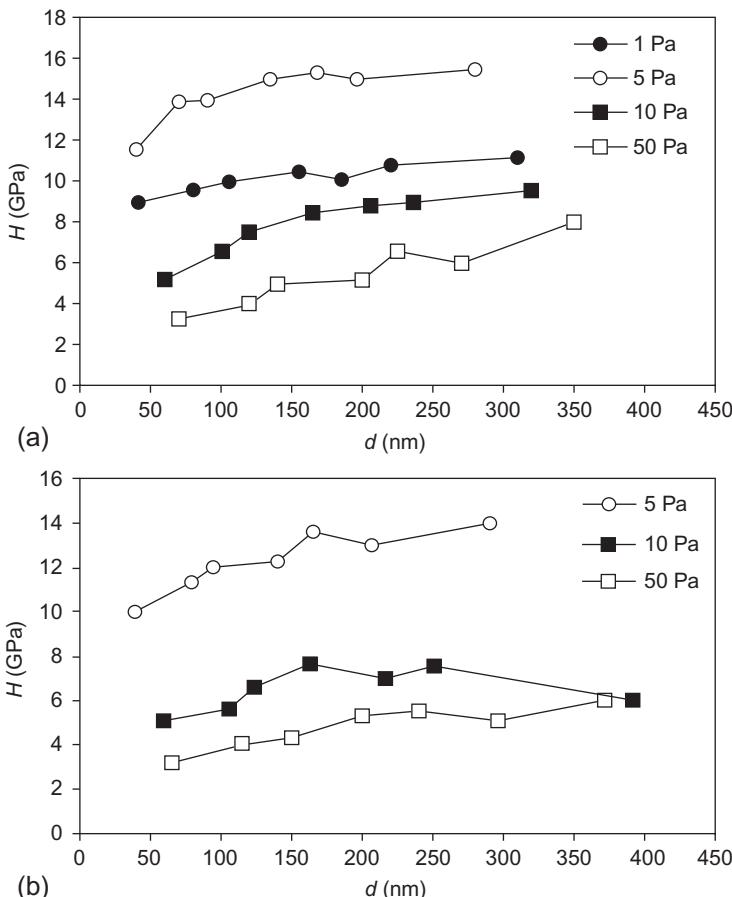


**Figure 12.9** Microhardness values of the films deposited at room temperature (a) and 250 °C collector temperature (b), at different depths,  $d$ , measured from the surface of the obtained structures.

Reproduced with permission from [49].

**Table 12.1 Microhardness values of the films deposited at room temperature and at 250 °C for different pressures of ambient N<sub>2</sub>**

P (Pa)	H (GPa) (RT)	H (GPa) (250 °C)
1	10	—
5	15	14
10	9	7
50	6	4

Source: Reproduced with permission from [49].

Figure 12.10 shows the C1s spectra of the films deposited at 5, 10, and 50 Pa in ambient nitrogen at room temperature. The spectrum of the film deposited at 5 Pa N<sub>2</sub> (Figure 12.10a) was deconvoluted into four lines, corresponding to different bonding states of the carbon atoms. The components of the C1s line were assigned to the C—N single, C=N double, and C≡N triple bonds, and to a pure carbon network (C=C), respectively. The C1s spectra corresponding to the films deposited at 10 Pa N<sub>2</sub> (Figure 12.10b) and 50 Pa N<sub>2</sub> (Figure 12.10c) were deconvoluted, showing maximum intensities at 289.4, 288.0, 286.4, and 285.3 eV. The peak with the highest energy at 289.4 eV was assigned to the C—O bonds, while the line having the maximum intensity at 288.0 eV corresponds to C—N single bonds. The peak at 286.4 eV most probably originates from sp<sup>3</sup> hybridized C singly bonded to C or can be associated with the presence of C—N bonds. Furthermore, the 285.3-eV peak was ascribed to C=N double bonds.

The peak with the highest energy was attributed to oxide contamination by the oxygen impurities in the ambient nitrogen. As expected, this contamination increases with the nitrogen pressure.

Interesting features are the relative intensity change and peak areas of the different components of the deconvoluted C1s and N1s spectra. The C—N/C≡N peaks ratio was calculated for the deconvoluted C1s and N1s spectra (Table 12.2). One notices from Table 12.2 that the C—N/C≡N ratio decreases with the increase in nitrogen pressure.

According to the literature, the hardness of carbon-based films is related to the presence of sp<sup>3</sup> bonding of the carbon atoms. In carbon-nitride materials, this requirement was formulated by Liu and Cohen [46,47]. Thus, in order to get a high-density, low-compressibility, hard carbon-nitride layer, the carbon atoms must be in the sp<sup>3</sup> hybridization state.

Nevertheless, the studies revealed that the increase of the nitrogen concentration in the synthesized structure leads to preferential formation of the sp<sup>2</sup> trigonal C bonded to N. From the data in Table 12.3, one observes that the C—N/C≡N integrated intensity ratio, calculated from the deconvoluted C1s and N1s spectra (Figure 12.10), decreases with the increase of nitrogen pressure in the irradiation chamber and with the nitrogen content of the films.

This change in structure (the reduction of the amount of C—N single bonds in favor of the formation of C≡N double bonds) was considered responsible for the observed

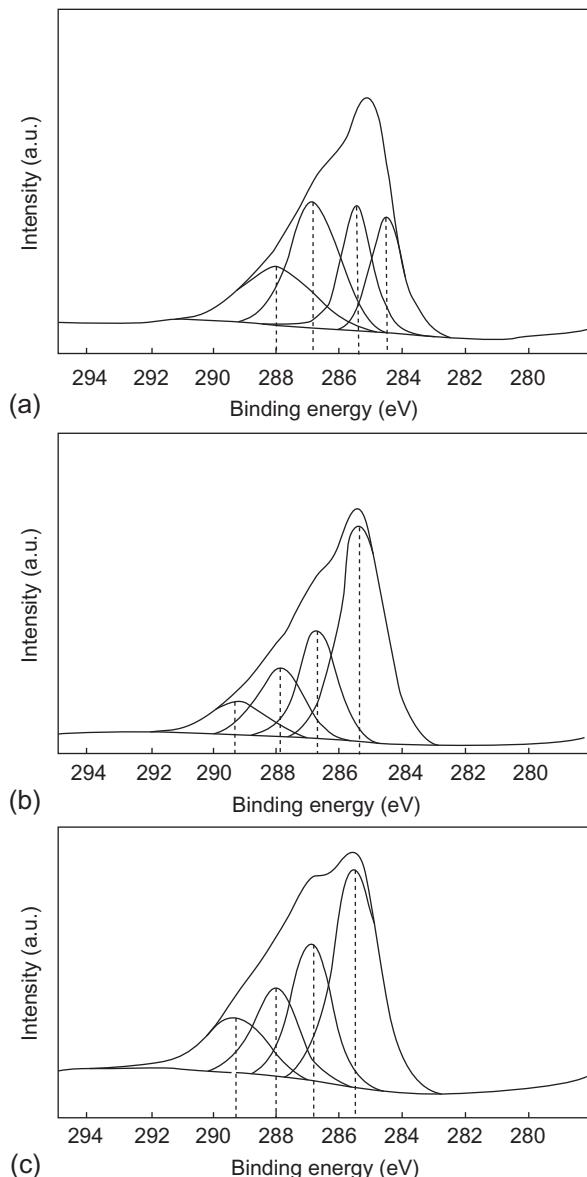


**Figure 12.10** Deconvoluted C1s XPS spectra of the films deposited at 5 Pa (a), 10 Pa (b), and 50 Pa (c)  $\text{N}_2$ .

Reproduced with permission from [49].

decrease of the films hardness along with the increase in nitrogen incorporation. One may conclude that the hardness decrease with the increase in nitrogen content is valid above a certain threshold value of nitrogen incorporation in the obtained structures.

**Table 12.2 Peaks position and  $I_D/I_G$  intensity ratios inferred by the decomposition of the Raman spectra into mixed Lorenzian-Gaussian profiles**

$F$ (J/cm <sup>2</sup> )	$P_{N_2}$ (Pa)	$I_D/I_G$	Thickness (nm)	$N/C$
12	1	1.20	220	0.2
12	5	1.72	150	0.25
12	10	0.88	30	0.3
12	50	0.80	10	0.5
12	100	0.80	<10	0.6
18	100	0.60	<10	0.7

Source: Reproduced with permission from [49].

**Table 12.3 The C—N/C=N ratio between the integrated intensity of the peak corresponding to the C—N single and C=N double bonds calculated from the deconvoluted C1s and N1s spectra, for different  $N_2$  ambient pressures**

$P$ (Pa)	C1s C—N/C=N	N1s C—N/C=N
5	0.98	1.1
10	0.35	0.37
50	0.37	0.37

Source: Reproduced with permission from [49].

#### 12.2.2.4 Laser fluence: sponge-like structure in polymer films for drug delivery systems

PVACOOH (polyvinyl alcohol) thin films were synthesized by MAPLE on both sides polished (100) Si wafers [29]. The target-substrate separation distance was of 4 cm, while the incident laser fluence was varied in these experiments within the range (0.25–0.7) J/cm<sup>2</sup>. Twenty thousand laser pulses have been applied for the deposition of one film.

AFM micrographs were obtained in semicontact mode, error mode, and phase contrast [29]. These experiments were conducted with laser fluences of 300, 500, and 700 mJ/cm<sup>2</sup>. For a fluence of 300 mJ/cm<sup>2</sup>, the surface presented a chained globular morphology that in phase contrast mode examination exhibited a nanoporous structure with a large distribution of pores in the (1–10) nm range. When the fluence was increased to 500 mJ/cm<sup>2</sup>, the porous structures become more compact and independent reticulated enchain globular structures are observed. For a higher laser fluence of 700 mJ/cm<sup>2</sup>, the polymer domains with compact structure are well distinguishable and much more pronounced [29].

FTIR spectra of films were recorded at 50° with an apparatus coupled with an IR microscope and ATR device with ZnSe crystal with 4 cm<sup>-1</sup> resolution. FTIR spectra

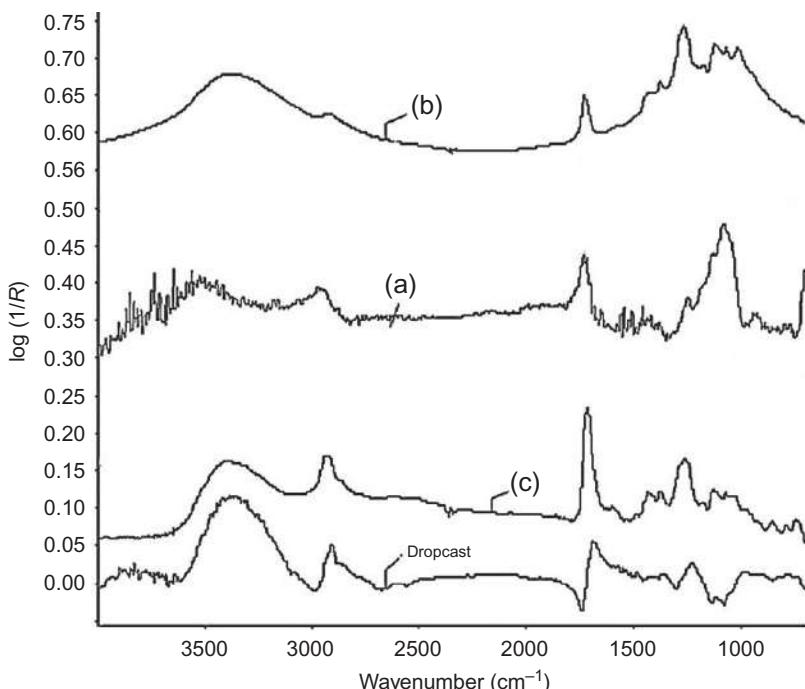


**Figure 12.11** Typical FTIR spectra of PVACOOH dropcast material and thin films prepared at a fluence of  $300 \text{ mJ/cm}^2$  (a),  $500 \text{ mJ/cm}^2$  (b), and  $700 \text{ mJ/cm}^2$  (c). Reproduced with permission from [29].

of PVACOOH dropcast material and of films deposited at a fluence of 300 (a), 500 (b), and  $700 \text{ mJ/cm}^2$  (c) are given in Figure 12.11. In all cases the specific absorption bands of polyvinyllic alcohol were present at hydroxyl groups ( $3384 \text{ cm}^{-1}$ ), C—H vibration modes ( $2855\text{--}2943 \text{ cm}^{-1}$ ), carbonyl function ( $1731 \text{ cm}^{-1}$ ), aromatic nuclei from the anhydride ( $3063$  and  $1600 \text{ cm}^{-1}$ ), C—O groups of esteric function ( $1265 \text{ cm}^{-1}$ ), and C—O—C esteric groups ( $1120 \text{ cm}^{-1}$ ) [50]. The preservation of spectra characteristics demonstrate that the organic material was transferred without chemical degradation.

Following FTIR and AFM results the films deposited at room temperature at fluence of  $300 \text{ mJ/cm}^2$ , which demonstrated the best structure and porosity characteristics have been selected for next *in vitro* microbiological assay.

#### 12.2.2.5 Solvent: 2D parallel gratings in polymeric films for drug delivery and implants

Levan and oxidized levan thin films were synthesized by MAPLE [51]. For the preparation of the targets used in the deposition process, 0.05 g of levan or oxidized levan were dissolved in 10 ml of dimethyl sulfoxide (DMSO) to obtain a homogeneous

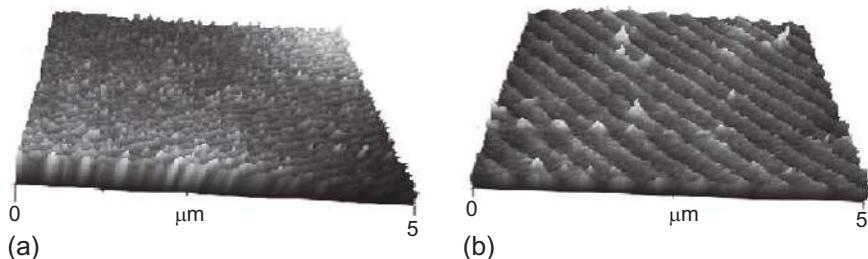


**Figure 12.12** Typical AFM images of sample surface for (a) levan and (b) oxidized levan coatings on Si.

Reproduced with permission from [51].

solution. DMSO is selected as solvent because it does not chemically interact with levan or oxidized levan and it is rather volatile and good absorbent of 248 nm laser wavelength. The appropriate deposition conditions such as fluence, pulse repetition rate, substrate temperature, and separation distance target-substrate have been selected after tests. The optimum fluence value changed from  $280 \text{ mJ/cm}^2$  for levan to  $350 \text{ mJ/cm}^2$  for oxidized levan for a pulse repetition rate of 3 Hz. Both sides polished single-crystalline Si (111) wafers were used as substrates. The substrates were heated to  $100^\circ\text{C}$  and placed parallel at 3.5 cm from target. The dynamic pressure inside the deposition chamber was stabilized at 5 Pa. For the growth of each film, 20,000 laser pulses have been applied.

An AFM apparatus with triangular  $\text{Si}_3\text{N}_4$  cantilevers used in noncontact mode was used for investigating the surface morphology of samples. Typical 3D-AFM images of levan and oxidized levan coatings are shown in Figure 12.12. Surface assembling of levan and oxidized levan can be observed. Films morphology is similar in the two cases with a neat spatial orientation, probably due to the combined effect of evaporation-induced self-assembly and specific linkages between the linear structures of the compounds. It should be mentioned that the nanostructured assembling increases the specific surface area, which could boost surface properties. The measured root mean square values were of 0.972 nm for levan and of 1.203 nm for oxidized levan coatings.

#### 12.2.2.6 Target composition: protein films with periodical surface structuring for biofouling

Mussel adhesive protein analog DOPA-PF68 thin films were obtained by MAPLE on Si (100) wafers at room temperature and placed at 7 cm separation distance from target [52]. The number of applied pulses was 25,000 at a laser fluence of  $410 \text{ mJ/cm}^2$  and repetition rate of 20 Hz. AFM details visible at 10 mm scale revealed a ripple-like structure of the deposited films. The structure height is of about 100 nm. A network of fairly oriented distributed roped chains can be observed for each ripple. The chains have an average width of 200 nm, and are separated by zones of about 100 nm [52].

Contact angle measurements were carried out to characterize the films wettability. The contact angle was of  $65.3^\circ$  and  $31^\circ$  for the dropcast and MAPLE film, respectively. It is considered that the contact angle change is due to modifications of polymer surface tension, roughness, and chemical heterogeneity [53].

## 12.3 Direct femtosecond laser surface processing in far- and near-field

Silicon laser processing, in far-field and by enhanced optical near-field under colloidal sphere particles, is an area that attracted attention due to fundamental and prospective applications. Studies have been reported in the literature on laser ablation of silicon in vacuum [54], air [55], gasses [56,57], or under liquids [58]. Liquid-assisted processes have been introduced as an efficient technique for silicon-based microprocessing. This technique allows one to employ all types of light-induced processes for direct single-step surface patterning by ablation, etching, and chemical or structural transformation. Fluid containment of solid interface is related to a contacting condensed phase, which has a strong physical-chemical influence upon these phenomena [59,60]. When the size of the silicon devices shrinks, the surface nanopatterning with lateral dimensions becomes increasingly important. Besides the conventional processing methods such as e-beam, X-ray, and UV photolithography for nanoscale processing of Si, several near-field laser processing techniques have been demonstrated, among which contacting particle-lens array technique. Very recently, a direct correlation between chemical composition of the liquids and the femtosecond pulse laser interaction with silicon and gallium arsenide was demonstrated [61,62]. The surfaces were irradiated at normal incidence, in far- and near-field, under liquid precursors such as acetone ( $C_3H_6O$ ), methanol ( $CH_3OH$ ), carbon tetrachloride ( $CCl_4$ ), or 1,1,2-trichlor-trifluorethan ( $C_2Cl_3F_3$ ). Experimental evidence of periodic arrays on silicon and gallium arsenide surfaces are reviewed in the following sections. The influence of the irradiation medium on far- and near-field interactions was investigated.

### 12.3.1 Silicon femtosecond laser processing in far-field, in air, or under liquid

The experiments were carried out by direct irradiation with a femtosecond Ti:sapphire laser (200/90 fs pulse duration, 2/1 kHz repetition rate,  $M^2 \sim 1.2$ ) operating at a wavelength of 387/400 nm and focused via a 75 mm focal length lens/microscope objective onto the liquid immersed Si (111) substrate placed at the bottom of an open container. The container, filled with the liquids to be used in the tests,  $C_3H_6O$ ,  $CH_3OH$ , and  $C_2Cl_3F_3$ , was placed on a computer-controlled XYZ-stage positioning (XY stages: 0.1  $\mu m$  resolution and Z stage: 0.5  $\mu m$  resolution and  $\pm 2 \mu m$  repeatability). A circular mask was used to remove the tails of the Gaussian profile. A scheme of the experimental design is given in Figure 12.13. A detailed area of the propagation of a

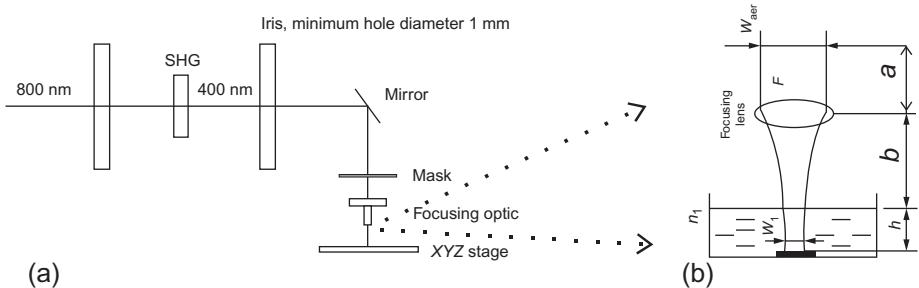


**Figure 12.13** Schematic representation of the experimental setup: (a) standard laser micro-processing setup in air/liquid (SHG—second harmonic generation, XYZ motorized stage) and (b) details of the focusing in liquid medium.

Gaussian beam in a model system of liquid-assisted laser processing is given in Figure 12.13b.

To the difference of air, under liquid the focus spot lies more away from the laser. The  $ABCD$ -matrix for the interval between the beam waists diameter in air,  $w_{\text{air}}$  and in liquids,  $w_l$  (interval  $a-h$ ) can be inferred as the product of the  $ABCD$ -matrices of homogeneous intervals and interfaces [63]:

$$\begin{bmatrix} A & B \\ C & D \end{bmatrix} = \begin{bmatrix} 1 & h \\ 0 & 1 \end{bmatrix} \begin{bmatrix} 1 & b \\ 0 & 1 \end{bmatrix} \begin{bmatrix} 1 & 0 \\ -\frac{1}{f} & 1 \end{bmatrix} \begin{bmatrix} 1 & a \\ 0 & 1 \end{bmatrix}$$

Here  $f$  is the focal length and  $h$  is the liquid thickness.

The beam waist in liquid can be calculated with the equation  $w_l = \sqrt{\frac{w_{\text{air}}}{1 + (\pi^2 w_0^4 / f^2 \lambda_0^2)}}$ .

The beam waist diameter in air is estimated to be 3  $\mu\text{m}$  calculated with the equation  $w_{\text{air}} = \frac{1.27 f \lambda M^2}{CA}$ , where  $\lambda$  is the wavelength and  $CA$  is the clear aperture. The calculated beam waist in liquid,  $w_l$  has a similar value as the one in air. The focusing distance is changing with  $\delta g = h(n_l - 1)$ , where  $n_l$  is the refractive index of the liquid. Single-pass grooves were imprinted on the Si sample, in far-field, by using different laser power and scanning speed values of the XYZ stage, in  $\text{CH}_3\text{OH}$ . The following speed values have been used: 0.1, 0.25, and 0.5 mm/s, in consequence varying the distance between two consecutive shots of the laser from 0.1, 0.25 to 0.5  $\mu\text{m}$ , respectively. The average laser power was varied from 1 to 20 mW, while the groove length was of 1.5 mm. Once parameters have been selected from the data corresponding to one line, surface machining tests have been conducted. The irradiated areas were characterized by SEM and subjected to two-dimensional Fourier transforms (2D-FFT) for quantitative analysis of the spatial period,  $\Lambda$ . It was observed that the surface morphology depends on the scanning speeds and the laser pulse energy. Figure 12.14 shows that by choosing the appropriate parameters it is possible to generate large-scale homogenous Si surface with 2D ordering.

Contact angle measurements have been carried out. Both unprocessed and processed Si have been investigated as visible in Figure 12.15. All samples were measured six times on different places. A decrease of the contact angle can be noticed

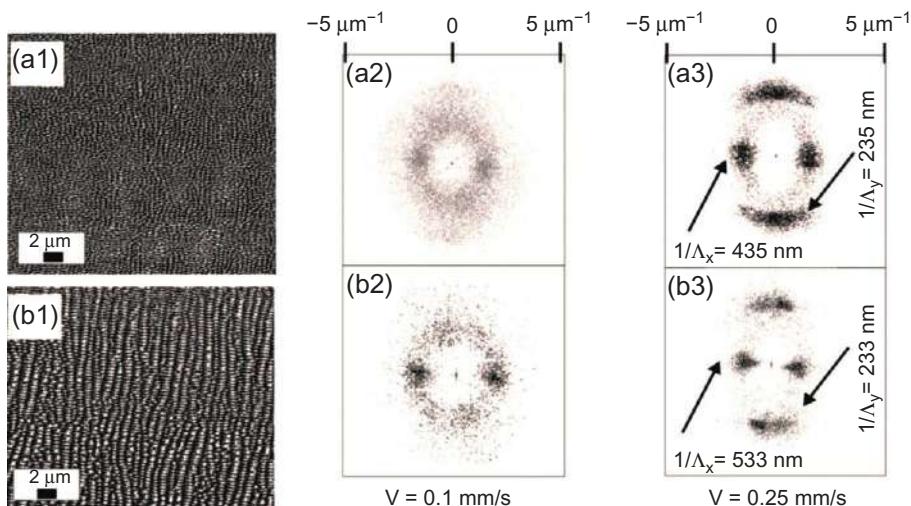


**Figure 12.14** Areas generated by processing of Si substrate in  $\text{CH}_3\text{OH}$  (a1) and  $\text{C}_2\text{Cl}_3\text{F}_3$  (b1). In both cases, the laser power was 5 mW; 2D-FFT analysis for  $v=0.1 \text{ mm/s}$  (a2, b2) and for  $v=0.25 \text{ mm/s}$  (a3, b3).

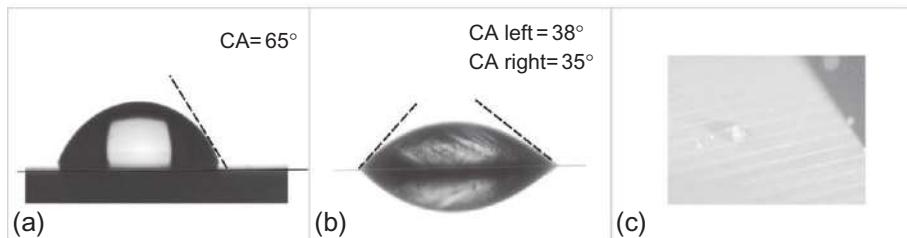


**Figure 12.15** Contact angle measurements for (a) unprocessed Si, (b) processed Si under methanol, and (c) general overview of the drop on the processed Si substrate.

from  $65^\circ$  for the unprocessed Si to  $38^\circ$  for the processed Si. As mentioned, the surface was processed line-by-line, as visible from Figure 12.15c. The lines overlapping was not perfect and the drop size is bigger than the width of a line, but this does not play any significant role in the contact angle measurements.

SEM micrographs in Figure 12.16 represent the scanned area (sizes  $1 \times 1 \text{ mm}^2$ ) on Si surface, in air, at different laser energies and scanning speeds. Figure 12.16a and b presents comparatively the increase of the laser energy,  $E_{\text{las}}$  from 1.8 J (Figure 12.16a) to 2.5 J (Figure 12.16b) at the same scanning speed of 1 mm/s. One can observe that when the incident laser energy increases, the microstructure changes from directional-oriented bacilliform structure (Figure 12.16a) to well-known ripple structure (Figure 12.16b). The ripple structures have a width of about 525 nm and are perpendicular to the laser polarization. The scan velocity was tuned taking into consideration the influence of overlap (OL) between subsequent laser pulses. OL is defined

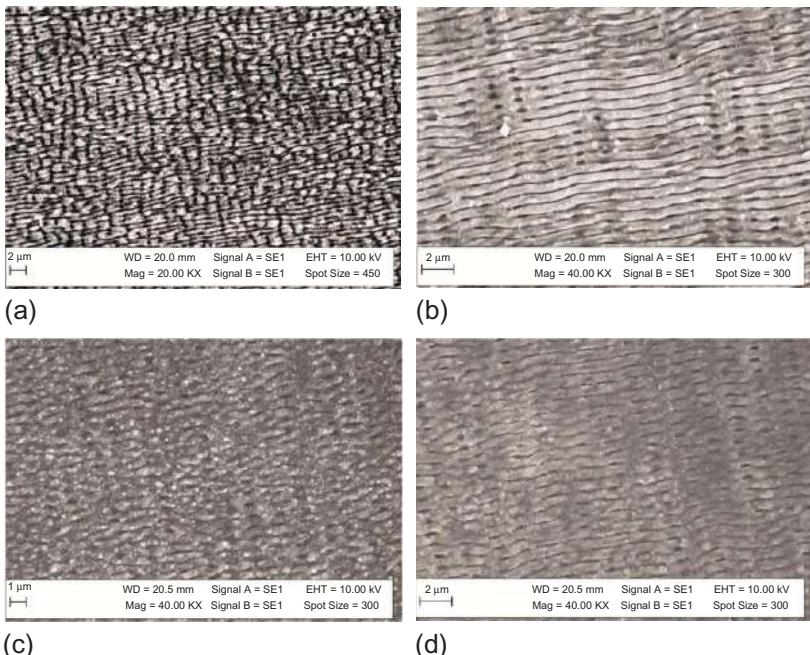


**Figure 12.16** SEM micrographs of the Si surface microstructures induced by the fs laser scanning in air at (a)  $E_{\text{las}} = 1.8 \text{ J}$ ,  $v = 1 \text{ mm/s}$ ; (b)  $E_{\text{las}} = 2.5 \text{ J}$ ,  $v = 1 \text{ mm/s}$ ; (c)  $E_{\text{las}} = 1.8 \text{ J}$ ,  $v = 9 \text{ mm/s}$ ; and (d)  $E_{\text{las}} = 2.5 \text{ J}$ ,  $v = 9 \text{ mm/s}$ .

Reproduced with permission from [60].

as  $\text{OL} = (1 - v/fd) \times 100\%$  where  $d$  [m] denotes the beam diameter,  $f$  [Hz] the frequency repetition rate, and  $v$  [m/s] the velocity of the focal spot relative to the sample. OL factor was 98% in case of 1 mm/s scanning speed. When increasing the scanning speed to 9 mm/s (Figure 12.16c and d), OL factor of 85% decreases the number of shots deposited in a unit area, which diminish the modification of surface morphology at energy levels of 1.8 J (Figure 12.16c) and 2.5 J (Figure 12.16d). The surface morphology in air depends on the scanning speeds and laser pulse energy. Thus, Figure 12.16b indicates that by choosing the appropriate parameters it is possible to generate large-scale homogeneous Si surfaces with subwavelength ripples.

### 12.3.2 Silicon and gallium arsenide femtosecond laser processing in near-field, in air, or under liquid

In the near-field experiments, silica colloidal particles with diameter of 700 and 390 nm were used. The monodisperse silica spheres were applied to an n-doped Si (100)/GaAs substrate after the suspension had been diluted with deionized water. The Si/GaAs substrates, previously kept for some minutes in an oxygen plasma environment in order to convert them from hydrophobic to hydrophilic, were next maintained at room temperature until all of the water had been evaporated. As a result, a

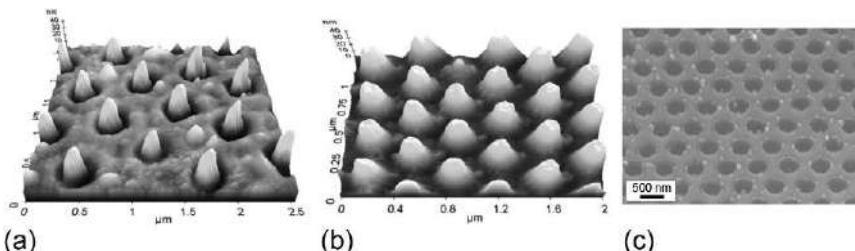


**Figure 12.17** AFM images showing a regular array pattern of Si bumps with a convex shape, with a center-to-center distance for the Si bumps of about 700 nm (a) and 390 nm (b), laser irradiation process in  $\text{C}_2\text{Cl}_3\text{F}_3$ , laser fluence  $30 \text{ J/cm}^2$ , at 387 nm; (c) SEM image of the holes forming on the Si substrate by near-field processing in air.

Reproduced with permission from [61].

silica bead, monolayer array, within a large area (tens of square micrometers) was obtained on the surface. The substrates with the silica colloidal particles on top were placed at the bottom of a glass container filled with a liquid precursor such as  $\text{C}_2\text{Cl}_3\text{F}_3$ ,  $\text{CCl}_4$ . The glass container was mounted on a three-axis translation stage, and the sample with the silica particle array was irradiated at normal incidence. The sample was irradiated with single pulses of 200 fs duration at 387 nm wavelength and with horizontal polarization from a double frequency amplified Ti:sapphire laser. The laser pulses were focused by a 75 mm focal length lens and traveled through 5 mm of liquid before hitting the surface. The laser fluence was set in the range from 1 to  $40 \text{ J/cm}^2$ . The fabricated nanofeatures were analyzed by AFM and SEM.

AFM images in Figure 12.17a and b show that the generated features have a density that is dependent on the silica particle diameter size. The SEM image in the Figure 12.17c evidences the hole structure formation that it is generated by near-field experiments in air.

In Figure 12.18 the holes are presented in the interstitial spacings and at low laser power. The presence of a bump precisely underneath the center of the colloidal particle for both Si and GaAs substrates irradiated in near-field in  $\text{CCl}_4$  can be observed. The image in Figure 12.18b shows that when raising the laser power, the laser etching activity is enhanced and the bump height is increasing.

AFM measurements put into evidence an increase of the bump height from 10 nm (at 10 mW) to 100 nm (at 100 mW), the depth of the hole being about 75 nm (at 100 mW). Because the field enhancement at particle-substrate contacting points is small, one can assume [64] that the convex bumps can be induced by the in-bulk microexplosion processes only, which pushes the materials on top of focal volume.

## 12.4 Resources

For a more in-depth study on pulsed laser methods used for synthesis of composite materials and surface structuring, we recommend to the reader the book edited by Antonio Miotello and Paolo M. Ossi, *Laser-surface interactions for new materials*

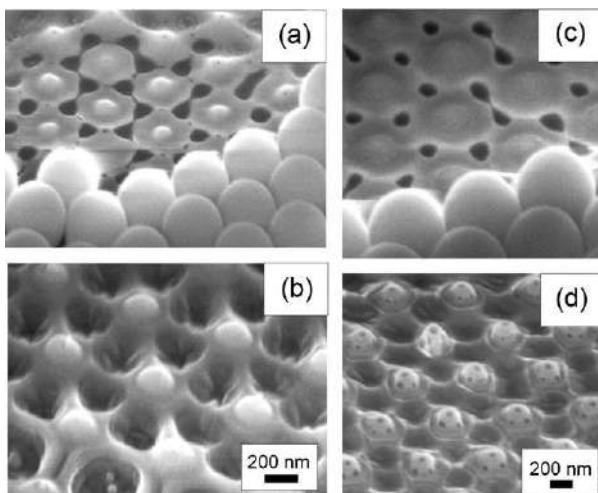


**Figure 12.18** SEM micrographs of Si substrate (a, b) and GaAs (c, d) irradiated under  $\text{CCl}_4$ , laser power 10 mW (a, c) and 100 mW (b, d); center-to-center distance 700 nm.

production, in: Laser-Surface Interactions for New Materials Production, Springer Series in Materials Science, 2010, ISBN: 978-3-642-03306-3. Another reference book on laser-matter interactions and possible applications is Peter Schaaf (editor), Laser Processing of Materials: Fundamentals, Applications and Developments, Springer Series in Materials Science, 2010, ISBN: 978-3-642-13280-3.

For student's introduction in the fields of laser processing, surface structuring, and thin films deposition, we recommend the book by William M. Steen and Jyotirmoy Mazumder, Laser Material Processing, Springer, 2010, ISBN 978-1-84996-062-5, written in a humorous and accessible language, but of high scientific level.

For an emphasis on laser deposition methods and their applications in research and industry, the book of choice is Robert Eason (editor), Pulsed Laser Deposition of Thin Films: Applications-Led Growth of Functional Materials, Wiley, 2007, ISBN: 978-0-471-44709-2.

For a more in-depth study of the liquid-assisted laser processing, we recommend the book by Arvi Kruusing, Handbook of Liquids-Assisted Laser Procession, Elsevier, New York, 2007, ISBN-13: 978-0080444987.

A comprehensive review article is by Ana Menendez-Manjon, Philipp Wagener, and Stephan Barcikowski, Transfer-matrix method for efficient ablation by pulsed laser ablation and nanoparticle generation in liquids, *J. Phys. Chem. C* 115 (2011) 5108-5114.

## 12.5 Conclusions

In the first part of this chapter it is stated that depending on the material nature and by variation of experimental parameters during thin films deposition, different structures

and morphologies can be achieved by PLD or MAPLE with pulsed nanosecond laser sources. These structures can be exploited in specific applications to obtain significant advantages. Examples are reviewed concerning high roughness in the case of calcium phosphates and polymers for cells growth, the use of porous surfaces (polyvinyl alcohol) for drug delivery, and the use of periodical structures (levan or oxidized levan and mussel adhesive protein analog) with high-contact angle for implant coating or biofouling. The variation of the ambient oxygen pressure during deposition results in ZnO films that are either transparent or dark, with hydrophilic or hydrophobic wettability, respectively, or soft or hard carbon nitride thin films by deposition of C in nitrogen.

In the second part, the direct patterning of a surface with pulsed femtosecond laser sources in different media is introduced. Results of the far- and near-field laser processing of Si and GaAs under different liquid precursors are described. Large periodic areas are generated in the far-field on the Si substrate, both in air and under different liquid precursors. The laser irradiation in the near-field, under the liquid precursors, of different size colloidal particle results in regular areas of convex shape bumps on both Si and GaAs substrates.

One may conclude that the pulsed laser processing with either ns or fs pulses has a great potential in controlled modification of samples of surface morphology and structure with prospective applications in nanobiomedicine, chemical catalysis, drug delivery systems, the textile industry, biofouling depositions, and hard coatings, among many others. The selection is mandatory for each particular investigated case of the main experimental parameter, such as laser wavelength and fluence, pulse duration and repetition rate, nature and pressure of the ambient gas, or liquid coverage.

## Acknowledgments

ACP and INM acknowledge with thanks the UEFISCDI under the contract ID304/2011. ACP also acknowledges the support of UEFISCDI under the Contract TE16/2013. MU acknowledges the Euminafab Project no. 1120 and the European Social Fund POSDRU 2007-2013 through the contract POSDRU/89/1.5/S/60746. CR acknowledges UEFISCDI support through the contract TE82/2011.

## References

- [1] R. Eason (Ed.), *Pulsed Laser Deposition of Thin Films: Applications-Lead Growth of Functional Materials*, John Wiley & Sons, 2007.
- [2] D. Bauerle, *Laser Processing and Chemistry*, fourth ed., Springer Verlag, 2011.
- [3] I. Ruiz de Larramendi, S. Vivès, N. Ortiz-Vitoriano, J.I. Ruiz de Larramendi, M.I. Arriortua, T. Rojo,  $\text{La}_{0.6}\text{Sr}_{0.2}\text{Ca}_{0.2}\text{Fe}_{0.8}\text{Ni}_{0.2}\text{O}_3$  thin films obtained by pulsed laser ablation: effect of the substrate on the electrochemical, *Solid State Ionics* 192 (1) (2011) 584–590.
- [4] N. Ortega, P. Bhattacharya, R.S. Katiyar, Enhanced ferroelectric properties of multilayer  $\text{SrBi}_2\text{Ta}_2\text{O}_9/\text{SrBi}_2\text{Nb}_2\text{O}_9$  thin films for NVRAM applications, *Mater. Sci. Eng. B Solid* 130 (1-3) (2006) 36–40.

- [5] G. Socol, E. Axente, C. Ristoscu, F. Sima, A. Popescu, N. Stefan, L. Escoubas, J. Ferreira, S. Bakalova, A. Szekeres, I.N. Mihailescu, Enhanced gas sensing of Au nanocluster-doped or -coated zinc oxide thin films, *J. Appl. Phys.* 102 (2007) 083103.
- [6] J. Greer, Large-area commercial pulsed laser deposition, in: R. Eason (Ed.), *Pulsed Laser Deposition of Thin Films: Applications-Lead Growth of Functional Materials*, John Wiley & Sons, 2006.
- [7] T. Yoshitake, K. Nagayama, The velocity distribution of droplets ejected from Fe and Si targets by pulsed laser ablation in a vacuum and their elimination using a vane-type velocity filter, *Vacuum* 74 (3-4) (2004) 515–520.
- [8] T. Yoshitake, G. Shiraishi, K. Nagayama, Elimination of droplets using a vane velocity filter for pulsed laser ablation of FeSi<sub>2</sub>, *Appl. Surf. Sci.* 197-198 (2002) 379–383.
- [9] E. György, I.N. Mihailescu, M. Komitsas, A. Giannoudakos, Deposition of particulate-free thin films by two synchronized laser sources: effects of ambient gas pressure and laser fluence, *Thin Solid Films* 446 (2) (2004) 178–183.
- [10] D. Xu, Y. Wang, L. Liu, Y. Li, Dependences of microstructure and critical current density on the thickness of YBa<sub>2</sub>Cu<sub>3</sub>O<sub>7-x</sub> film prepared by pulsed laser deposition on buffered Ni-W tape, *Thin Solid Films* 529 (1) (2013) 10–14.
- [11] M. Mohebbi, C. Vittoria, Growth of Y-type hexaferrite thin films by alternating target laser ablation deposition, *J. Magn. Magn. Mater.* 344 (2013) 158–161.
- [12] A. Zakery, Y. Ruan, A.V. Rode, M. Samoc, B. Luther-Davies, Low-loss waveguides in ultra-fast laser-deposited As<sub>2</sub>S<sub>3</sub> chalcogenide films, *J. Opt. Soc. Am. B* 20 (2003) 1844–1852.
- [13] J. Remsa, M. Jelinek, T. Kocourek, J. Oswald, V. Studnička, M. Černanský, F. Uherek, M. Jelínek, Highly oriented crystalline Er:YAG and Er:YAP layers prepared by PLD and annealing, *Appl. Surf. Sci.* 255 (10) (2009) 5292–5294.
- [14] Q.A. Drmosh, S.G. Rao, Z.H. Yamani, M.A. Gonda, Crystalline nanostructured Cu doped ZnO thin films grown at room temperature by pulsed laser deposition technique and their characterization, *Appl. Surf. Sci.* 270 (2013) 104–108.
- [15] D. Padilla-Rueda, J.M. Vadillo, J.J. Laserna, Room temperature pulsed laser deposited ZnO thin films as photoluminescence gas sensors, *Appl. Surf. Sci.* 259 (2012) 806–810.
- [16] H. Cho, S. Kim, H. Ki, Pulsed laser deposition of functionally gradient diamond-like carbon (DLC) films using a 355 nm picosecond laser, *Acta Mater.* 60 (18) (2012) 6237–6246.
- [17] A. Anzai, M. Fuchigami, S. Yamanaka, K. Inumaru, Preparation of calcium-doped boron nitride by pulsed laser deposition, *Mater. Res. Bull.* 47 (8) (2012) 2062–2066.
- [18] D. Craciun, N. Stefan, G. Socol, G. Dorcioman, E. McCumiskey, M. Hanna, C.R. Taylor, G. Bourne, E. Lambers, K. Siebein, V. Craciun, Very hard TiN thin films grown by pulsed laser deposition, *Appl. Surf. Sci.* 260 (2012) 2–6.
- [19] A.A. Ribeiro, R.M. Balestra, M.N. Rocha, S.B. Peripolli, M.C. Andrade, L.C. Pereira, M. V. Oliveira, Dense and porous titanium substrates with a biomimetic calcium phosphate coating, *Appl. Surf. Sci.* 265 (2013) 250–256.
- [20] R.K. Singh, W.S. Kim, M. Ollinger, V. Craciun, I. Coowantwong, G. Hochhaus, N. Koshizaki, Laser based synthesis of nanofunctionalized particulates for pulmonary based controlled drug delivery applications, *Appl. Surf. Sci.* 197/198 (2002) 610–614.
- [21] E. Süske, T. Scharf, P. Schaaaf, E. Panchenko, D. Nelke, M. Buback, H. Kijewski, H.-U. Krebs, Variation of the mechanical properties of pulsed laser deposited PMMA films during annealing, *Appl. Phys. A* 79 (4-6) (2004) 1295–1297.
- [22] T.M. Patz, A. Doraiswamy, R.J. Narayan, N. Menegazzo, C. Kranz, B. Mizaikoff, Y. Zhong, R. Bellamkonda, J.D. Bumgardner, S.H. Elder, X.F. Walboomers, R. Modi, D.B. Chrisey, Matrix assisted pulsed laser evaporation of biomaterial thin films, *Mater. Sci. Eng. C* 27 (3) (2007) 514–522.

- [23] A. Piqué, R.A. McGill, D.B. Chrisey, D. Leonhardt, T.E. Mslna, B.J. Spargo, J.H. Callahan, R.W. Vachet, R. Chung, M.A. Bucaro, Growth of organic thin films by the matrix assisted pulsed laser evaporation (MAPLE) technique, *Thin Solid Films* 355 (1999) 536–541.
- [24] V. Califano, F. Bloisi, L.R.M. Vicari, P. Colombi, E. Bontempi, L.E. Depero, MAPLE deposition of biomaterial multilayers, *Appl. Surf. Sci.* 254 (22) (2008) 7143–7148.
- [25] R. Cristescu, C. Popescu, A. Popescu, S. Grigorescu, I.N. Mihailescu, D. Mihailescu, S.D. Gittard, R.J. Narayan, T. Buruiana, I. Stamatin, D.B. Chrisey, Functional polyethylene glycol derivatives nanostructured thin films synthesized by matrix-assisted pulsed laser evaporation, *Appl. Surf. Sci.* 255 (2009) 9873–9876.
- [26] R. Cristescu, C. Cojanu, A. Popescu, S. Grigorescu, L. Duta, O.-S. Ionescu, D. Mihailescu, T. Buruiana, A. Andronie, I. Stamatin, I.N. Mihailescu, D.B. Chrisey, Laser processing of polyethylene glycol derivative and block copolymer thin films, *Appl. Surf. Sci.* 255 (2009) 5605–5610.
- [27] R. Cristescu, C. Popescu, A.C. Popescu, I.N. Mihailescu, A.A. Ciucu, A. Andronie, S. Iordache, I. Stamatin, E. Fagadar-Cosma, D.B. Chrisey, Functional porphyrin thin films deposited by matrix assisted pulsed laser evaporation, *Mater. Sci. Eng. B* 169 (2010) 106–110.
- [28] R. Cristescu, C. Popescu, A.C. Popescu, S. Grigorescu, I.N. Mihailescu, A.A. Ciucu, S. Iordache, A. Andronie, I. Stamatin, E. Fagadar-Cosma, D.B. Chrisey, MAPLE deposition of Mn(III) metalloporphyrin thin films: structural, topographical and electrochemical investigations, *Appl. Surf. Sci.* 257 (2011) 5293–5297.
- [29] R. Cristescu, C. Cojanu, A. Popescu, S. Grigorescu, L. Duta, G. Caraene, A. Ionescu, D. Mihailescu, R. Albulescu, T. Buruiana, A. Andronie, I. Stamatin, I.N. Mihailescu, D. B. Chrisey, Functionalized polyvinyl alcohol derivatives thin films for controlled drug release and targeting systems: MAPLE deposition and morphological, chemical and in vitro characterization, *Appl. Surf. Sci.* 255 (2009) 5600–5604.
- [30] R. Cristescu, C. Cojanu, A. Popescu, S. Grigorescu, C. Nastase, F. Nastase, A. Doraiswamy, R.J. Narayan, I. Stamatin, I.N. Mihailescu, D.B. Chrisey, Processing of poly(1,3-bis-(*p*-carboxyphenoxy propane)-co-(sebacic anhydride)) 20:80 (P(CPP:SA) 20:80) by matrix-assisted pulsed laser evaporation for drug delivery systems, *Appl. Surf. Sci.* 254 (2007) 1169–1173.
- [31] R. Cristescu, D. Mihailescu, I. Stamatin, G. Socol, I.N. Mihailescu, D.B. Chrisey, Deposition of biopolymer thin films by matrix assisted pulsed laser evaporation, *Appl. Phys. A* 79 (4-6) (2004) 1023–2026.
- [32] F. Bloisi, A. Cassinese, R. Papa, L. Vicari, V. Califano, Matrix-assisted pulsed laser evaporation of polythiophene films, *Thin Solid Films* 516 (7) (2008) 1594–1598.
- [33] T. Tunno, A.P. Caricato, M.E. Caruso, A. Luches, M. Martino, F. Romano, D. Valerini, M. Anni, Matrix-assisted pulsed laser evaporation of polyfluorene thin films, *Appl. Surf. Sci.* 253 (15) (2007) 6461–6464.
- [34] A. Purice, J. Schou, P. Kingshott, M. Dinescu, Production of active lysozyme films by matrix assisted pulsed laser evaporation at 355 nm, *Chem. Phys. Lett.* 435 (4-6) (2007) 350–353.
- [35] R. Pate, K.R. Lantz, A.D. Stiff-Roberts, Resonant infrared matrix-assisted pulsed laser evaporation of CdSe colloidal quantum dot/poly[2-methoxy-5-(2'-ethylhexyloxy)-1,4-(1-cyano vinylene)phenylene] hybrid nanocomposite thin films, *Thin Solid Films* 517 (24) (2009) 6798–6802.
- [36] N. Mirchin, M. Gankin, U. Gorodetsky, S.A. Popescu, I. Lapsker, A. Peled, L. Duta, G. Dorcioman, A. Popescu, I.N. Mihailescu, Estimation of polyethylene nano-thin layer

- morphology by differential evanescent light intensity imaging, *J. Nanophotonics* 4 (2010) 041760.
- [37] I. Lapsker, N. Mirchin, U. Gorodetsky, S.A. Popescu, A. Peled, L. Duta, G. Dorcioman, A.C. Popescu, I.N. Mihailescu, Morphology of polyethylene nanolayers: a study by evanescent light microscopy, *J. Mater. Sci.* 45 (23) (2010) 6332–6338.
  - [38] S.A. Popescu, B. Apter, N. Mirchin, U. Gorodetsky, I. Lapsker, A. Peled, L. Duta, G. Dorcioman, A. Popescu, C. Ristoscu, I.N. Mihailescu, Study of polyethylene nanolayers by evanescent light microscopy, *Appl. Phys. A* 104 (3) (2011) 997–1002.
  - [39] D. Kopecký, M. Vrňata, F. Vysloužil, V. Myslík, P. Fitl, O. Ekrt, P. Matějka, M. Jelínek, T. Kocourek, Polypyrrole thin films for gas sensors prepared by matrix-assisted pulsed laser evaporation technology: effect of deposition parameters on material properties, *Thin Solid Films* 517 (6) (2009) 2083–2087.
  - [40] E. Gyorgy, F. Sima, I.N. Mihailescu, T. Smazú, B. Hopp, D. Predoi, S. Ciucă, L.E. Sima, S.M. Petrescu, Biomolecular urease thin films grown by laser techniques for blood diagnostic applications, *Mater. Sci. Eng. C* 30 (2010) 537–541.
  - [41] C.N. Hunter, M.H. Check, J.E. Bultman, A.A. Voevodin, Development of matrix-assisted pulsed laser evaporation (MAPLE) for deposition of disperse films of carbon nanoparticles and gold/nanoparticle composite films, *Surf. Coat. Technol.* 203 (3-4) (2008) 300–306.
  - [42] I.N. Mihailescu, P. Torricelli, A. Bigi, I. Mayer, M. Iliescu, J. Werckmann, G. Socol, F. Miroiu, F. Cuisinier, R. Elkaim, G. Hildebrand, Calcium phosphate thin films synthesized by pulsed laser deposition: physico-chemical characterization and in vitro cells response, *Appl. Surf. Sci.* 248 (2005) 344–348.
  - [43] G. Socol, P. Torricelli, B. Bracci, M. Iliescu, F. Miroiu, A. Bigi, J. Werckmann, I.N. Mihailescu, Biocompatible nanocrystalline octacalcium phosphate thin films obtained by pulsed laser deposition, *Biomaterials* 25 (2004) 2539–2545.
  - [44] A. Bigi, B. Bracci, F. Cuisinier, R. Elkaim, M. Fini, I. Mayer, I.N. Mihailescu, G. Socol, L. Sturba, P. Torricelli, Human osteoblast response to pulsed laser deposited calcium phosphate coatings, *Biomaterials* 26 (2005) 2381–2389.
  - [45] A.C. Popescu, L. Duta, G. Dorcioman, I.N. Mihailescu, G.E. Stan, I. Pasuk, I. Zgura, T. Beica, I. Enculescu, A. Ianculescu, I. Dumitrescu, Radical modification of the wetting behavior of textiles coated with ZnO thin films and nanoparticles when changing the ambient pressure in the pulsed laser deposition process, *J. Appl. Phys.* 110 (2011) 064321.
  - [46] A.Y. Liu, M.L. Cohen, Prediction of new low-compressibility materials, *Science* 245 (1989) 841.
  - [47] A.Y. Liu, M.L. Cohen, Structural properties and electronic structure of low compressibility materials:  $\beta$ -Si<sub>3</sub>N<sub>4</sub> and hypothetical  $\beta$ -C<sub>3</sub>N<sub>4</sub>, *Phys. Rev. B* 41 (1990) 10727.
  - [48] W.C. Oliver, G.M. Pharr, An improved technique for determining hardness and elastic modulus using load and displacement sensing indentation experiments, *J. Mater. Res.* 7 (1992) 1564.
  - [49] E. Gyorgy, V. Nelea, I.N. Mihailescu, A. Perrone, H. Pelletier, A. Cornet, S. Ganatsios, J. Werckmann, Correlation between hardness and structure of carbon-nitride thin films obtained by reactive pulsed laser deposition, *Thin Solid Films* 388 (2001) 93–100.
  - [50] KnowItAll Database by Bio, <http://www.bio-rad.com>.
  - [51] F. Sima, E. Cansever Mutlu, M.S. Eroglu, L.E. Sima, N. Serban, C. Ristoscu, S.M. Petrescu, E. Toksoy Oner, I.N. Mihailescu, Levan nanostructured thin films by MAPLE assembling, *Biomacromolecules* 12 (2011) 2251–2256.
  - [52] R. Cristescu, T. Patz, R.J. Narayan, N. Menegazzo, B. Mizaikoff, D.E. Mihailescu, P. B. Messersmith, I. Stamatin, I.N. Mihailescu, D.B. Chrisey, Processing of mussel adhesive

- protein analog thin films by matrix assisted pulsed laser evaporation, *Appl. Surf. Sci.* 247 (1-4) (2005) 217–224.
- [53] T. Patz, R. Cristescu, R. Narayan, N. Menegazzo, B. Mizaikoff, P.B. Messersmith, I. Stamatin, I.N. Mihailescu, D.B. Chrisey, Processing of mussel-adhesive protein analog copolymer thin films by matrix-assisted pulsed laser evaporation, *Appl. Surf. Sci.* 248 (1-4) (2005) 416–421.
  - [54] B.N. Chichkov, C. Momma, S. Nolte, F. Von Alvensleben, A. Tunnerman, Femtosecond, picosecond and nanosecond laser ablation of solids, *Appl. Phys. A* 63 (2) (1996) 109–115.
  - [55] F. Sanchez, J.L. Morena, R. Aguiar, J.C. Delgado, M. Varela, Whiskerlike structure growth on silicon exposed to ArF excimer laser irradiation, *Appl. Phys. Lett.* 69 (5) (1996) 620–622.
  - [56] A.J. Pedrazza, J.D. Fowlkes, D.H. Lowndes, Laser ablation and column formation in silicon under oxygen-rich atmospheres, *Appl. Phys. Lett.* 77 (19) (2000) 3018–3020.
  - [57] T.-H. Her, R.J. Finlay, C. Wu, S. Deliwalla, E. Mazur, Microstructuring of silicon with femtosecond laser pulses, *Appl. Phys. Lett.* 73 (12) (1998) 1673–1675.
  - [58] M.Y. Shen, C.H. Crouch, J.E. Carey, E. Mazur, Femtosecond laser-induced formation of submicrometer spikes on silicon in water, *Appl. Phys. Lett.* 85 (23) (2004) 5694–5696.
  - [59] C. Radu, S. Simion, M. Zamfirescu, M. Ulmeanu, M. Enculescu, M. Radoiu, Silicon structuring by etching with liquid chlorine and fluorine precursors using femtosecond laser pulses, *J. Appl. Phys.* 110 (1) (2011) 034901–034906.
  - [60] M. Ulmeanu, F. Jipa, C. Radu, M. Enculescu, M. Zamfirescu, Large scale microstructuring on silicon surface in air and liquid by femtosecond laser pulses, *Appl. Surf. Sci.* 258 (23) (2012) 9314–9317.
  - [61] M. Ulmeanu, I. Anghel, M. Filipescu, C. Luculescu, M. Enculescu, M. Zamfirescu, Periodic arrays of nanostructures in silicon and gallium arsenide by near-field enhanced laser irradiation in liquid precursors, *Colloids Surf. A* 418 (1) (2013) 47–51.
  - [62] M. Ulmeanu, I. Anghel, F. Jipa, M. Filipescu, M. Enculescu, M. Zamfirescu, Silicon bump arrays by near-field enhanced femtosecond laser irradiation in fluorine liquid precursors, *Appl. Surf. Sci.* 278 (1) (2013) 301–304.
  - [63] W. Silfvast, *Laser Fundamentals*, Cambridge University, 1996.
  - [64] Z.B. Wang, W. Guo, A. Pena, D.J. Whitehead, B.S. Luk'yanchuk, L. Li, Z. Liu, Y. Zhou, M.H. Hong, Laser micro/nano fabrication in glass with tunable-focus particle lens array, *Opt. Express* 16 (24) (2008) 19706–19711.

This page intentionally left blank

## Part Three

# **Laser structuring and surface modification**

This page intentionally left blank

# Tailoring material properties induced by laser surface processing

13

H.Y. Zheng<sup>1</sup>, Y.C. Guan<sup>1,2</sup>, X.C. Wang<sup>1</sup>, Z.K. Wang<sup>1</sup>

<sup>1</sup>Singapore Institute of Manufacturing Technology, Singapore; <sup>2</sup>Beihang University (formerly Beijing University of Aeronautics and Astronautics), Beijing, PR China

## 13.1 Introduction

In recent years, laser surface processing has been employed in many applications to modify materials surface properties [1,2]. For instance, laser annealing to recrystallize amorphous-Si is a mature technology in the manufacture of thin film transistor (TFT) displays [1], and laser texturing of silicon to enhance light trapping has been widely reported [2]. In this chapter, we report some recent research and development in laser surface processing of silicon, polymethyl methacrylate (PMMA), and magnesium alloys in respective sections.

With increasing attention toward carbon-free energy production, solar electricity has been considered as a potentially widespread approach for sustainable energy production. However, the present cost of solar electricity is still high for general use, mainly because photovoltaic (PV) modules are fabricated using expensive silicon wafers.

Considering the trade-off between the preparation cost and the material quality, recrystallization of amorphous-Si films is regarded as a promising solution for solar cells to be competitive in the longer term. Among various recrystallization techniques, laser annealing provides an effective approach to recrystallizing amorphous-Si films within a short time period without damaging the underlying substrates [3–5]. In order to increase the efficiency of solar cells, surface texturing has been widely used in the fabrication process, and surface texturing of the front surface of a solar cell can lead to both a reduction in reflection and an increase in light trapping [6–8]. As the most commonly used method to texture monocrystalline wafers, anisotropic alkaline etching techniques are ineffective on randomly oriented grains that make up multicrystalline wafers and amorphous/polycrystalline thin films. Therefore, it is necessary to develop an advanced texturing technique that will isotropically shape the front surface, regardless of the crystallographic orientation, in both an electrical and optical way [9,10]. In the following section, we introduce our work in fs laser surface processing of Si. The ultrashort pulse duration and extremely high peak power enable the crystallization of amorphous-Si and simultaneous surface nanostructuring on a-Si:H surface in a one-step process. The absorbance of the a-Si:H thin film is increased due to the crystallization and surface nanotexturing. We also report our work with an excimer laser, inducing

nanobumps on an n-doped (100) Si wafer with silica microspheres. With a single shot of 248 nm excimer laser irradiation on a monolayer of self-organized hexagonally close-packed silica microspheres formed on Si surface, an array of Si-based nanobumps is formed. The near-field enhancement effect in laser-sphere interaction and the mechanisms for the nanobumps formation are discussed. In addition, laser direct pit ablation induced texturing on Si surface is shown to produce uniform and consistent microsurface structure on Si substrate. The laser-textured Si substrate is demonstrated as a template for generating micro/nanostructures on a smooth sol gel coating so as to enhance its hydrophobicity.

Controlled surface modification to achieve either hydrophilicity or hydrophobicity on selected surfaces is useful in various applications. For example, superhydrophobic surfaces are good for self-cleaning of contaminations [11], but hydrophobic surfaces are difficult to wet and bond. In this case, hydrophilic surfaces are preferred. Wettability also determines flow behavior in microfluidic channels and enhances cell adhesion. Modification of PMMA surface wettability is highly desirable, as PMMA is commonly used in various microfluidic devices [12]. In the following section, we introduce how microfluidic channels with controlled surface wettability can be achieved and fabricated using femtosecond laser direct ablation of PMMA at various fluences.

Magnesium alloys have been increasingly used in the industries and biomaterial fields due to their low density, high specific strength, and biodegradability [13–15]. Unfortunately, actual use at present is limited mainly due to inferior surface properties [16,17]. Previous work shows that laser processing can produce surface layers with fine microstructures that reduce the size of galvanic couples and expand the solid solution range of alloying elements [18–20]. Abbas *et al.* [21] and Liu *et al.* [18] found that the improved corrosion resistance of AZ31, AZ61, and WE43 Mg alloys following laser treatment was associated with the increased concentration of Al and microstructure refinement in the laser-melted zone. The present work investigates fundamental mechanisms of kinetics of phase transformation under nonequilibrium conditions, microstructural evolution, and surface performance of laser-treated surfaces, as well as laser-Mg interaction. This work demonstrates the capability of millisecond pulse laser in achieving the enhanced corrosion resistance and surface wettability of Mg alloy. It also analyzes heat flow and rapid solidification in the molten pool as well as material loss during laser irradiation.

## 13.2 Laser texturing of silicon for improving surface functionalities

### 13.2.1 Femtosecond laser-induced surface nanostructuring and simultaneous crystallization of amorphous thin silicon film

Figure 13.1 shows an optical microscope image of fs laser-treated and -untreated surfaces of a-Si:H film deposited on a Corning 1737 glass substrate where the laser fluence was  $6.9 \text{ mJ/cm}^2$  and the scanning speed was 20 mm/s. It can be clearly seen that

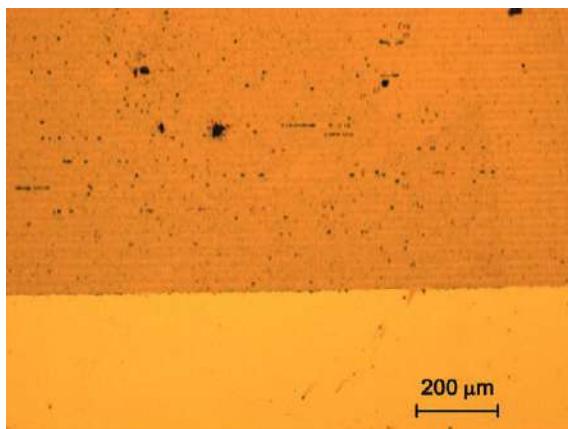


**Figure 13.1** Optical microscope image of fs laser-treated a-Si:H thin film.

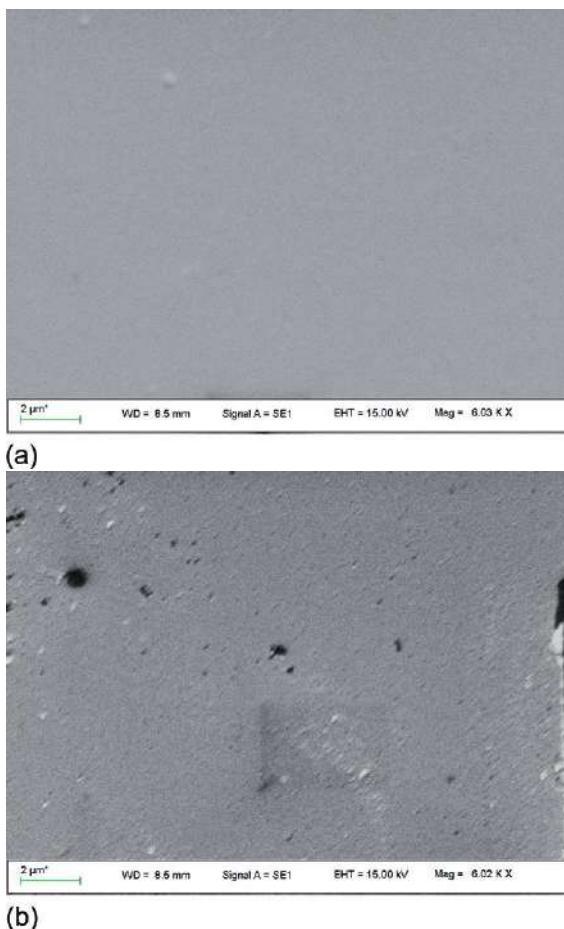
after laser irradiation the a-Si film was turned into a dark brown from the original shiny light yellow color, which indicates the surface properties such as surface finish, and phase state might change after laser treatment.

Figure 13.2 shows scanning electron microscope (SEM) images of original and laser-treated Si surfaces. It is obvious from the images that surface nanostructures have been formed upon laser treatment. Further enlarged by AFM images as shown in Figure 13.3, it was observed that a regular nanospike-patterned texture was formed after fs laser irradiation. The distance between the nanospikes is about 200 nm and the diameter of the formed nanobump is about 90 nm at full width at half maximum (FWHM) and its height is about 20 nm.

The produced nanospike pattern is expected to be beneficial to reducing the light reflectance, so as to increase light trapping. Actually, femtosecond laser-induced nanospike-patterned “black silicon” has been achieved and extensively studied by Mazur’s group on crystalline bulk silicon substrate [22,23], where the crystalline Si substrate was processed in the presence of a sulfur-containing gas such as SF<sub>6</sub>. The nanospike-patterned black silicon surface was demonstrated to be strongly light absorbing and the surface of silicon, normally gray and shiny, turned deep black. Also, the surface textured black silicon has been realized with reactive ion etching (RIE) on monocrystalline and multicrystalline silicon wafers [24,25]. The etched silicon surface showed significantly reduced reflectance in the visible region as well as in the near-IR region.

To study the crystalline property of the laser-treated area, micro-Raman analysis was conducted. Raman spectroscopy is a sensitive probe to local atomic arrangement and vibrations (phonons) in solids [26] and this technique has been used to characterize nanostructures that provide information about the nature of crystalline structure or amorphous disorder structure.

Figure 13.4 showed micro-Raman spectra for as-grown a-Si thin film and fs laser-treated a-Si thin film, where the Gaussian line profiles fitting has been conducted to



**Figure 13.2** SEM images of (a) original a-Si:H thin film surface and (b) fs laser-treated a-Si:H thin film surface.

the Raman spectra of untreated and fs laser-treated a-Si:H film as the dashed lines. As shown in [Figure 13.4](#), it can be seen that for as-grown a-Si:H, the Raman spectrum consists mainly of two broad peaks, one peak centered at  $465.55\text{ cm}^{-1}$ , which is characteristic of amorphous-Si corresponding to the TO zone-edge phonon, and another broad peak centered at  $332.20\text{ cm}^{-1}$ , which is attributed to LO amorphous phonon mode [27].

After fs laser treatment, interestingly, besides two broad bands at  $477.97$  and  $347.78\text{ cm}^{-1}$ , the Raman spectra show a sharp Raman peak centered at  $511.7\text{ cm}^{-1}$ , which is evidence of a crystalline phase. However, the sharp peak is shifted by an amount of  $8.3\text{ cm}^{-1}$  from the peak at  $520\text{ cm}^{-1}$  that corresponds to bulk crystalline silicon. This shift might be attributed to phonon confinement [28], possibly due to the presence of nanocrystals embedded in a-Si:H environment. Stress-induced effects

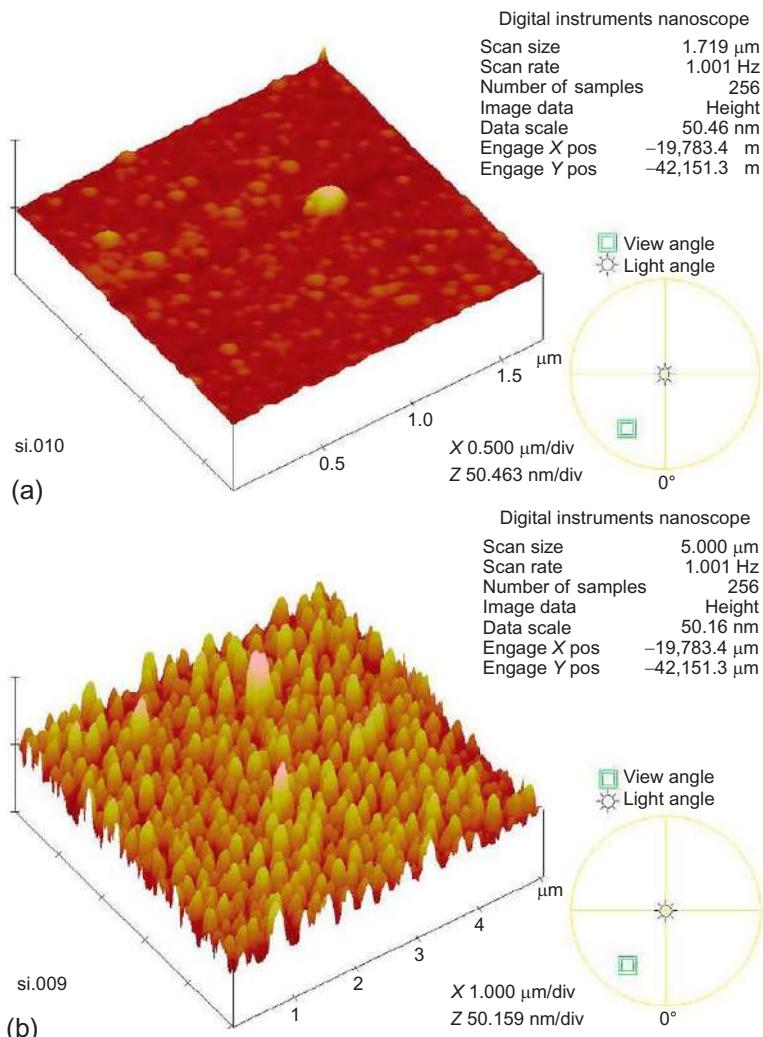


**Figure 13.3** AFM images of (a) original a-Si:H thin film surface and (b) fs laser-treated a-Si:H thin film surface.

are also reported to cause this behavior. As a result, in [Figure 13.4](#), the two distinct peaks at 511.7 and 477.97 cm<sup>-1</sup> for the fs laser treated a-Si:H thin film are believed to be corresponding to an mixed phase silicon consisting of an amorphous phase and crystalline phase. In mixed phase silicon, the momentum selection rule of the Raman process is more relaxed compared to crystalline silicon. With increasing momentum the TO photon energy lowers, leading to broadening of the Raman peak toward the lower energies [27,29]. The crystalline volume fraction of the fs laser-treated sample can be calculated from the integrated intensities of the Raman peaks with Gaussian fits

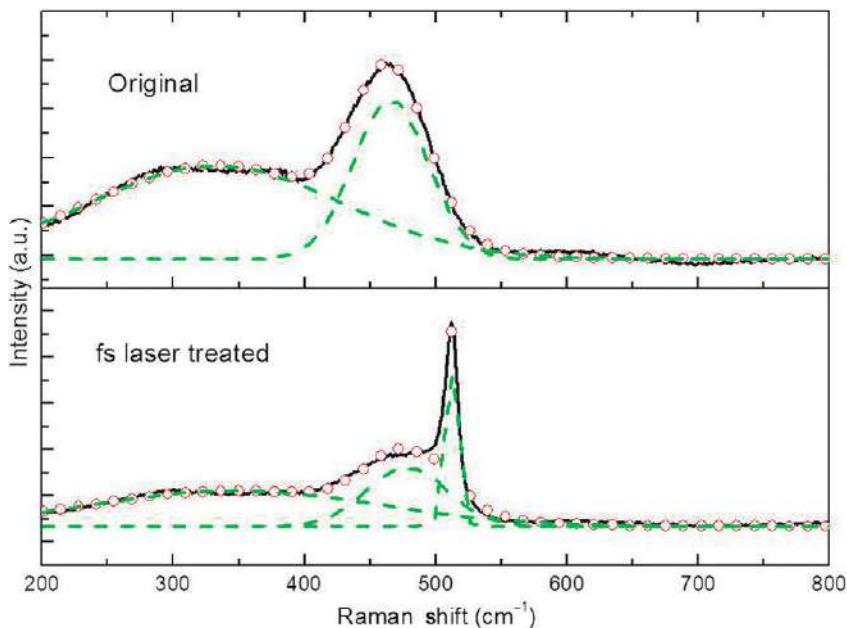


**Figure 13.4** Raman spectra of original and laser-treated a-Si:H thin film, the dashed lines are Gaussian profile fittings.

for the amorphous peak ( $I_a$ ) and the crystalline peak ( $I_c$ ), as shown in Figure 13.4. The calculation was done as proposed by Tsu *et al.* with crystalline volume fraction ( $X_c$ ) given by Equation (13.1), where  $\gamma$  is the ratio of the backscattering cross section of amorphous and crystalline phases [30],

$$X_c = \frac{I_c}{I_c + (\gamma)I_a} \quad (13.1)$$

The selection of a value of  $\gamma$  is complex due to its dependency on absorption coefficient of amorphous and crystalline silicon [31].  $\gamma$  has been calculated to be between 0.8 and 0.9, the most widely used value being 0.8 for mixed phase silicon [29,31]. Here,  $\gamma$  was taken to be 0.8. According to Equation (13.1), based on the integrated intensities of crystalline part and amorphous part in Figure 13.4, the crystalline volume fraction of fs laser-treated a-Si:H thin film was determined to be approximately 34.7%.

In order to study the optical characteristics, we measured the reflectance and transmittance of as-grown and laser-treated a-Si thin film with an area of  $20 \times 20 \text{ mm}^2$  using a spectrophotometer. The reflectance ( $R$  in %) and transmittance ( $T$  in %) were then used to obtain the absorbance ( $\alpha$  in %) of the samples:  $\alpha = 1 - R - T$ . Figure 13.5 shows the absorbance of laser treated and original a-Si films. It is clear from Figure 13.5 that there is a significant enhancement in the optical absorption below the a-Si:H band gap (1.7 eV) in the case of laser-treated films.

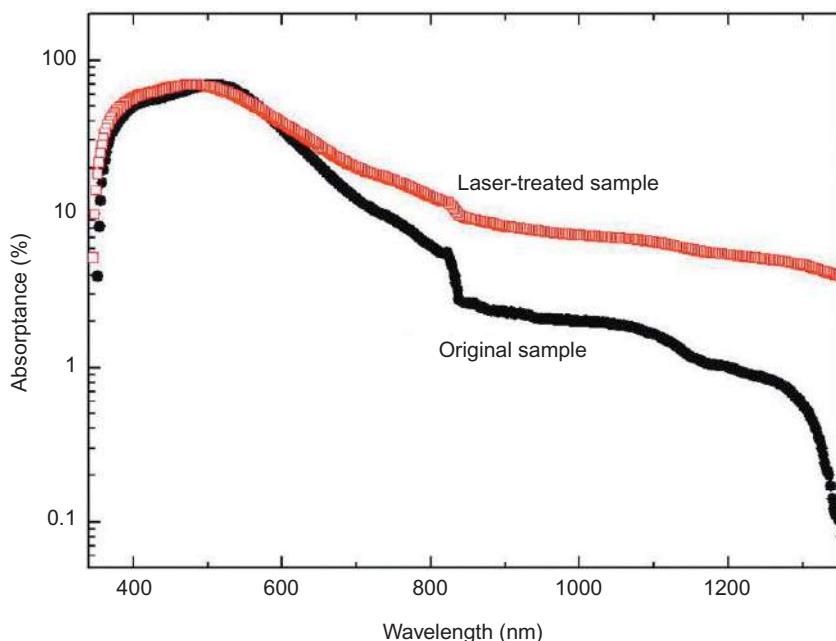


**Figure 13.5** Absorptance of original and laser-treated a-Si:H thin film.

It is suggested that the increase in below band edge absorption might be due to the textured surface resulting from laser treatment, by helping to trap the light due to multiple reflection. Furthermore, the increase in the absorption is most probably caused by the reduction in the reflection, which could be due to the antireflective properties of the fs laser formed nanospikes, which may have gradient index structure [3]. Also, structural defects induced during the laser surface texturing process may likely produce bands of defect and impurity states in the band gap and, thus, enhance the overall absorption further.

Unlike continuous wave laser annealing and excimer laser annealing, the fact that very low laser fluence of  $6.9 \text{ mJ/cm}^2$  is required for fs laser annealing suggests that ultrafast or nonthermal melting of silicon is the dominant mechanism involved in the process. Femtosecond optical pulses can excite a significant number of the valence electrons in the semiconductor through nonlinear absorption. This high level of electronic excitation can severely weaken interatomic bonds so that “cold” atomic motion can lead to disordering of the lattice and then cause structural transformation such as recrystallization. This can occur while the electronic system and lattice are not in a thermal equilibrium. The ultrafast transition caused by the high-density electron hole plasma inherently carries no conventional molten phase. The studies with femtosecond time-resolved optical microscopy and reflectivity measurements [4,32,33] suggested the existence of a liquid layer whose properties and transient behavior differ from normal thermal melting. Also, the distortion of the silicon diamond lattice structure was shown to be related to lattice instability in the timescale of hundreds

of femtoseconds following the ultrashort pulsed laser irradiation. Electronic excitation effects were suggested as the likely cause for the crystallization of amorphous semiconductor thin films by laser pulses shorter than 800 fs [5,34,35].

### 13.2.2 Fabrication of silicon nanobump arrays by near-field enhanced laser irradiation

A hexagonally close-packed silica sphere monolayer array was first obtained on the silicon surface as shown in Figure 13.6. The silica monolayer array was then exposed to a single shot of a KrF excimer laser. The pulsed KrF excimer laser operated at 248 nm wavelength with a pulse duration of 23 ns at FWHM. A homogenizer was used to produce a uniform laser beam over an area of approximately  $3 \times 3 \text{ mm}^2$  with a  $4 \times$  demagnification lens. The laser power was adjusted with a motor-controlled beam attenuator.

The laser irradiation on the silica particle array was conducted at different incident laser energy densities of 270, 300, 350, and 450 mJ/cm<sup>2</sup>. It was found that the formation of nanobumps was quite dependent on the incident laser powers. When the laser energy density was set at about 270 mJ/cm<sup>2</sup>, no structures were formed. When the laser energy density was set at about 350 mJ/cm<sup>2</sup> or above, the nanoscale pit array was formed. When the laser energy density was set at about 300 mJ/cm<sup>2</sup>, the uniformly distributed nanobump array was fabricated. Figure 13.7 shows an AFM image of a small area of the Si substrate that was irradiated by a single laser shot at 300 mJ/cm<sup>2</sup>. It can be clearly seen that a regular 2-D array of nanobumps were formed. Also it is found that the arrangement of bumps generated on the Si surface reveals the hexagonal lattice structure of the microspheres. The distance between the bumps is 1.5  $\mu\text{m}$ , which is equal to the diameter of spheres. From Figure 13.8, it can be seen

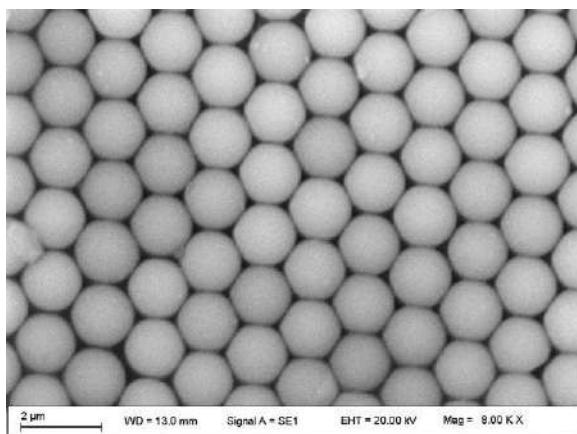


**Figure 13.6** SEM image of a hexagonally close-packed monolayer of silica microspheres with a diameter of 1.5  $\mu\text{m}$  on a n-doped Si (100) substrate.

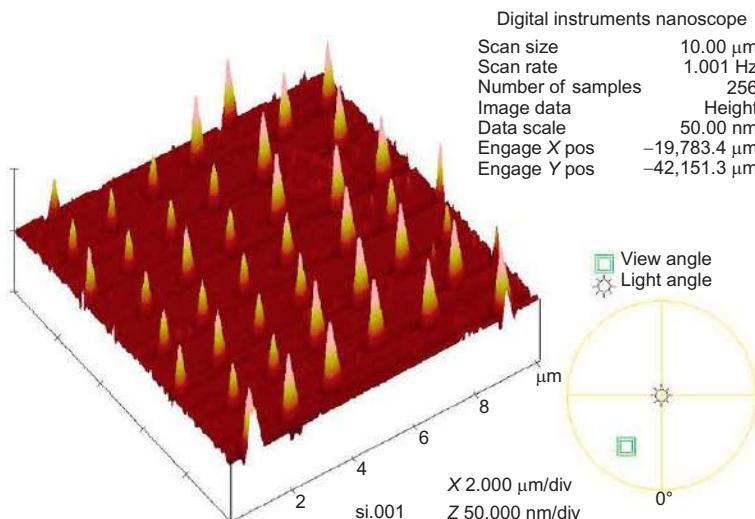


**Figure 13.7** Si nanobump arrays fabricated on a Si (100) surface by single-shot 248 nm KrF excimer laser irradiation at a fluence of  $300 \text{ mJ/cm}^2$  with a monolayer of silica microspheres.

that the diameter of the formed nanobump is about 162 nm at FWHM and its height is about 43 nm. Both quantities are measured with respect to the surface of the Si wafer. It is also observed in Figure 13.8b that the bumps are surrounded by a ring-shaped trench whose volume is, within  $\pm 10\%$ , equal to the volume of the bump. Figure 13.4 showed the SEM images and EDX spectra of laser fabricated nanobump arrays. Together with AFM characterization as shown in Figures 13.7 and 13.8, it is confirmed that a regular array pattern of nanobumps surrounded by ring-shaped trenches is produced. Also from EDX result as shown in Figure 13.9, only Si was detected in the nanobumps and no oxygen was detected. So, the fabricated nanobumps are Si-based nanobumps.

Huang *et al.* [9] demonstrated the formation of “nanobump” arrays on silicon. In their work, Huang *et al.* applied a 23 ns laser pulse, with a wavelength of 248 nm and a fluence of  $150 \text{ mJ/cm}^2$ , to a surface array of polystyrene (PS) spheres with a diameter of  $1.0 \mu\text{m}$ . The heights and widths at FWHM of the nanobumps were 42 and 260 nm, respectively. However, they did not specify the nanobumps’ composition and no ring-shaped trench was observed [9]. Also, Wysocki *et al.* reported submicrometer Si cones produced by silica microspheres. They used  $\text{SiO}_2$  microspheres of  $6 \mu\text{m}$  diameter as sphere lens arrays with the Si substrate placed in the focal plane of microspheres deposited on a quartz support [36]. With this approach, it may be critical and time-consuming to align and adjust the distance between quartz support substrate and Si substrate for the Si substrate to be at the focal position of the microspheres.

The work used a monolayer of silica microspheres directly on the Si surface as the focusing lens and template to form a nanobumps array. The method is simple and straightforward. The distance between nanobumps can be adjusted via changing the diameter of microspheres. Two mechanisms for nanobump formation with

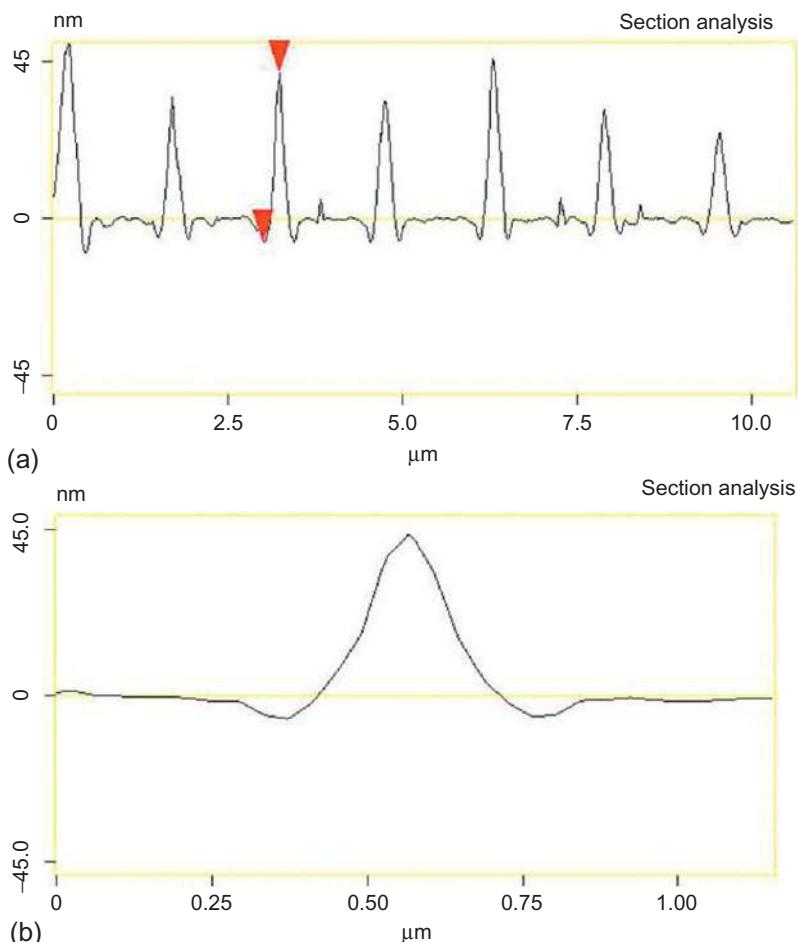


**Figure 13.8** (a) AFM sectional profile of a row of silicon nanobumps and (b) magnified view of the profile of one Si nanobump.

microspheres have been proposed. It is known that there is an optical enhancement by micro/nanospheres in the near-field region, which can be explained by Rayleigh scattering and Mie scattering. Rayleigh scattering takes place when the diameter of the sphere is less than the wavelength of the light. In this case, the sphere is treated as dipole radiator. When the diameter of the sphere is larger than the wavelength, light is scattered elastically according to the Mie scattering law. It has been reported that the intensity distribution changes dramatically with the size of the sphere and also the distance between the sphere and the substrate. For the sphere diameter larger than the laser wavelength as in the present work, according to Mie theory, the electric field is enhanced by several times toward the forward area of the sphere [37].

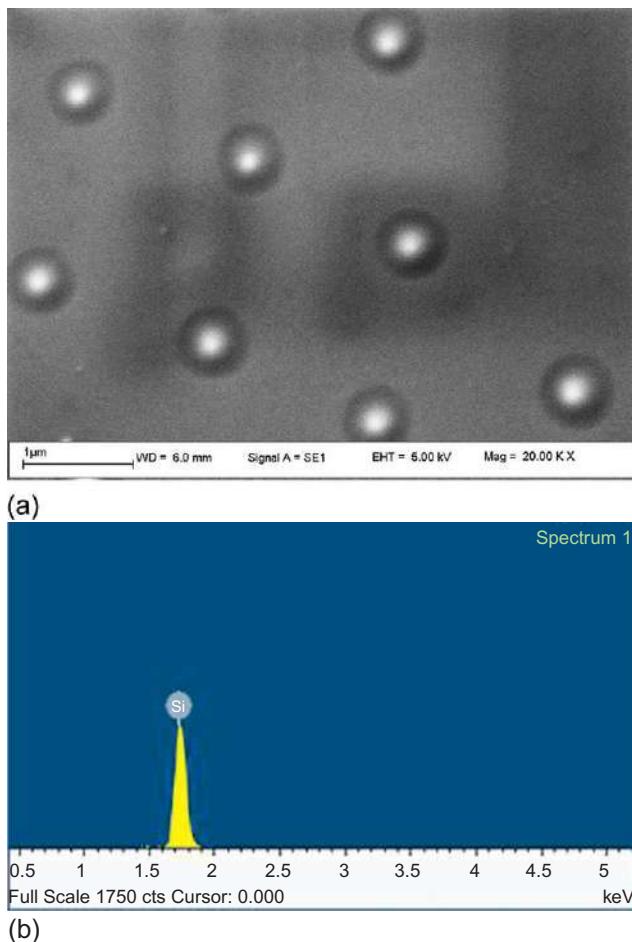


**Figure 13.9** (a) SEM image of the fabricated Si nanobump arrays and (b) EDX spectrum on the nanobump area.

Such optical enhancement will lead to local melting of the Si substrate materials. The anomalous behavior of the density of solid and liquid silicon can explain the nanobump formation. With the experimental conditions employed, the silicon surface becomes molten within the focal area generated by the microsphere. After laser-induced melting, the silicon resolidifies. Resolidification starts at the edge of the molten zone and proceeds and pushes the remaining liquid silicon to the center. Also, in contrast to the usual behavior of materials with melting, the density of liquid Si,  $\rho_l(l\text{-Si})=2.52 \text{ g/cm}^3$ , is bigger than the density of solid Si,  $\rho_s(c\text{-Si})=2.32 \text{ g/cm}^3$  [8]. Thus, the volume of silicon increases during solidification. As a consequence, during cooling, the liquid silicon is squeezed radially to the center and forms a protrusion. As a result, a solid bump surrounded by a ring-shaped trench is formed as shown in

[Figure 13.8b](#). On the other hand, Grigoropoulos *et al.* has demonstrated that Marangoni-driven flow is mainly responsible for the redistribution of surface material upon laser texturing of NiP on a microscale [6,7]. The Marangoni effect involving shear stress refers to the motion of liquid due to surface tension gradients. Thermocapillary and chemicapillary are two distinct components, which result from the thermal potential of a temperature gradient and the chemical potential of a compositional gradient, respectively. In the current experiment, the enhanced optical field is known to have a Gaussian-like intensity distribution [10]. This creates a temperature field in the silicon substrate that decreases from the center to its edge of the molten zone upon pulsed laser irradiation. The temperature-gradient-induced thermocapillary force results in an outward flow. However, the highest surface tension exists in the center of the molten zone [38], which induces a chemicapillary force. The chemicapillary force results in an inward flow of the molten material toward the center. The Si nano-bump formation as shown in [Figure 13.9](#) indicates the chemicapillary force may dominate [39–41].

### 13.2.3 *Laser microstructuring on a Si substrate for improving surface hydrophobicity*

Three hundred and fifty-five nanometer DPSS UV laser direct pit ablation induced texturing process was conducted at a pulse energy of 24  $\mu\text{J}$  and 40 kHz repetition rate for different spot separations and pulse number on each spot. [Figure 13.10](#) shows the surface texture produced under different spot separation of 10, 15, and 35  $\mu\text{m}$ . It can be clearly seen that for too small spot separation of 10  $\mu\text{m}$ , the laser ablated pits overlapped and connected together so the induced texture is not regular and consistent as shown in [Figure 13.10a](#). When the spot separation is too big at 35  $\mu\text{m}$ , the laser ablated pits are separated for some distance and not continuously connected so the induced texturing is not continuously consistent as shown in [Figure 13.10c](#). There existed an optimum spot separation of 15  $\mu\text{m}$  as shown in [Figure 13.10b](#) where the laser-induced texturing was quite uniform and consistent. [Figure 13.11](#) shows the laser textured surface profile for 15  $\mu\text{m}$  spot separation measured by surface profilometer. It can be seen that the surface texturing obtained with a spot pitch of 15  $\mu\text{m}$  has a uniform texturing. The diameter of the textured pit is about 15  $\mu\text{m}$  and its depth is about 8  $\mu\text{m}$ .

[Figure 13.12](#) shows the laser-induced texturing at a fixed spot pitch of 15  $\mu\text{m}$  for different pulse numbers of 2, 4, and 8. It can be seen that the induced texture is uniform. It was also found that with an increase in pulse number, the pit shape is changing from square-conical to circular-conical. And the pit depth is also increasing as shown in [Table 13.1](#). [Table 13.1](#) shows patterned pit depth for different pulse numbers. It can be seen that through controlling the pulse number, the pattern pit depth can be adjusted from 7 to 9  $\mu\text{m}$ .

Surface contact angle measurement is the simplest surface analysis technique in determining the hydrophilicity and hydrophobicity. [Figure 13.13](#) shows the measured

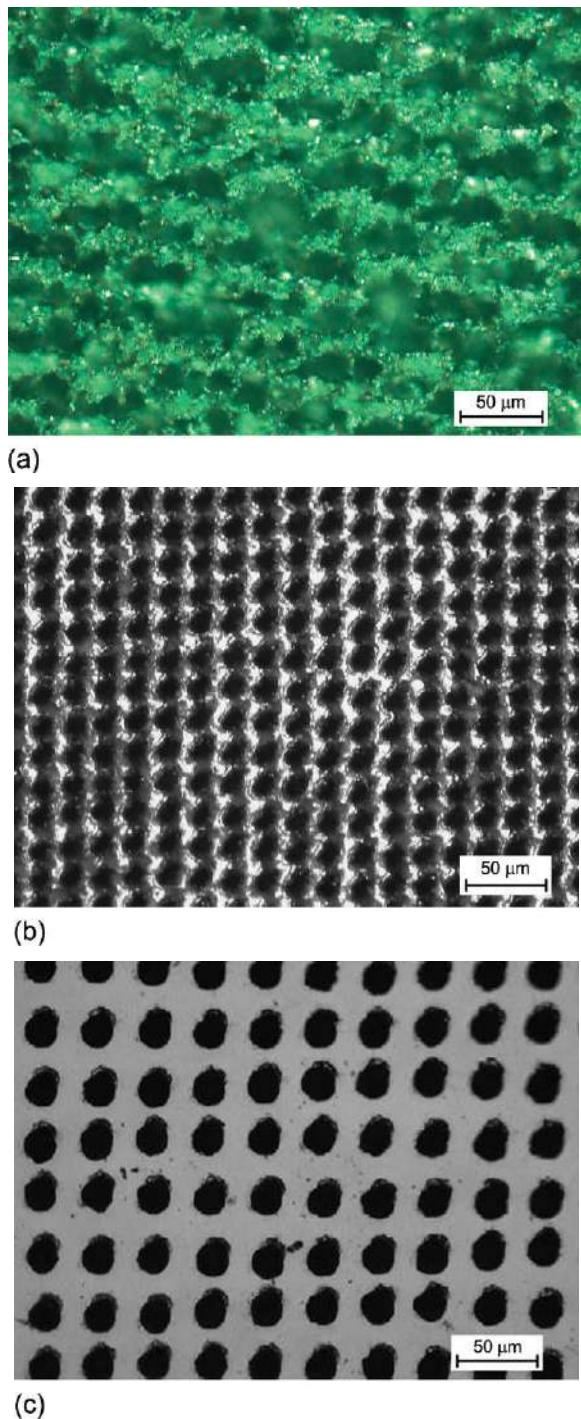


**Figure 13.10** Laser direct pit ablation induced texturing on Si substrate for four pulses at different spot separations: (a) 10  $\mu\text{m}$ , (b) 15  $\mu\text{m}$ , and (c) 35  $\mu\text{m}$ .

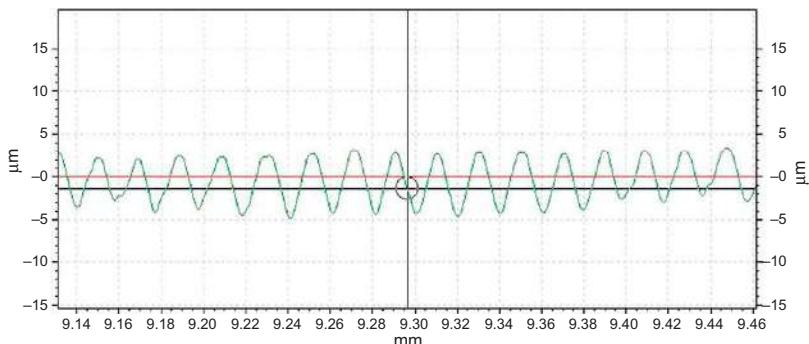


**Figure 13.11** Surface profile of laser-induced texture on Si substrate for 15  $\mu\text{m}$  pit pitch.

surface contact angle of original and laser-textured Si sample. The original silicon surface without texturing is hydrophilic with a surface contact angle of  $64.2^\circ$ . It was found that after laser texturing, the surface contact angle was increased up to  $97.5^\circ$  from  $64.2^\circ$  for original surface indicating the Si surface was changed from hydrophilicity to hydrophobicity.

The surface roughness has a large effect on the surface contact angle. As shown in Figure 13.13, the surface contact angle was greatly changed with laser surface structuring. The change in surface contact angle is due to the fact that the pit-like structuring on the surface of the silicon induced by laser treatment enhances the Si surface roughness as shown in Figure 13.12. Furthermore, it was observed that besides the micro-sized pit structures, there were some nanoscale ripple structures on the edge of the pits as shown in Figure 13.14. The imprinted structures that were the replica of the pit structure are also characterized with the two-scale roughness combination of microscale and nanoscale (as shown in Figure 13.15). The literature suggested that protruding structures with two-scale roughness combination of microscale roughness plus nanoscale roughness are beneficial for obtaining high water contact angles [42,43].

The laser-textured Si substrate was used as a template to produce bump-like surface texturing on sol gel film through imprinting processes. Figure 13.15 showed the surface morphology of patterned sol gel film. It can be clearly seen that the micro-sized bump texturing was produced. The diameter of the bump was approximately 10  $\mu\text{m}$  and separation of the bumps was measured to be about 15  $\mu\text{m}$ , as shown in Figure 13.15. From Figure 13.15c, it was further observed that there existed nano features formed on the micro-sized bumps. The result indicated that the details of laser-induced pattern on the Si surface was transferred and duplicated onto the sol gel film through an imprinting process. After imprinting, the surface contact angle of the patterned sol gel film was increased by about  $30^\circ$  up to  $138^\circ$ , as shown in Figure 13.16.

Compared to other methods such as conventional photolithography cum RIE, the laser direct pit ablation texturing method is fast, efficient, and cost-effective for

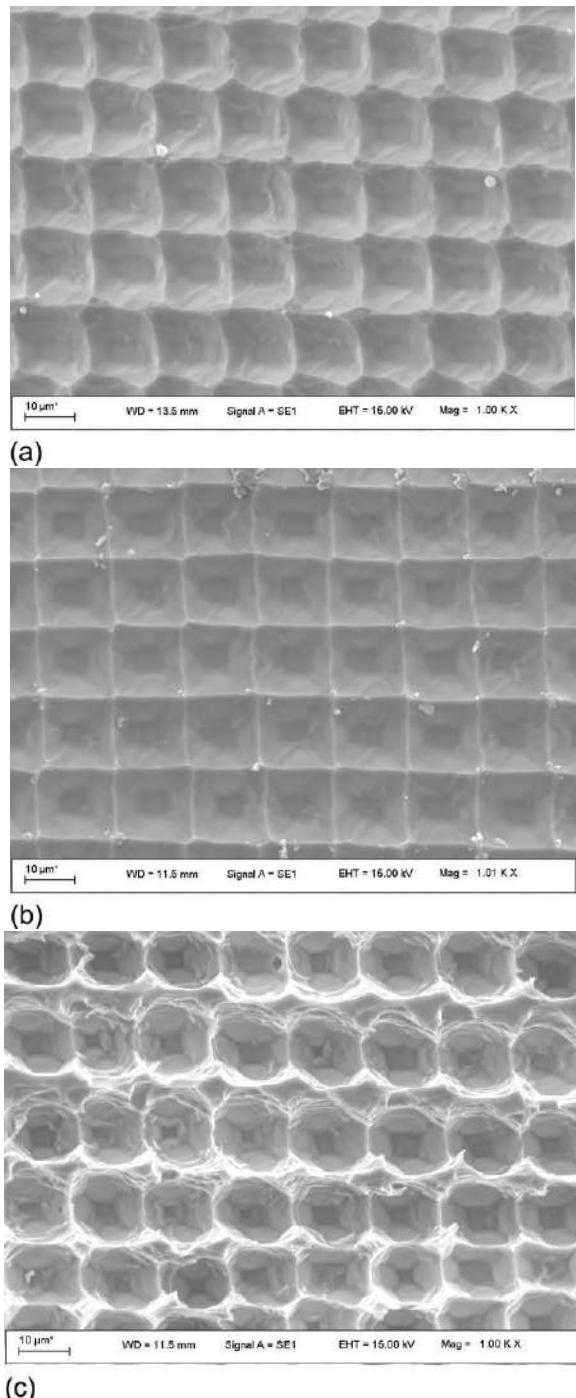
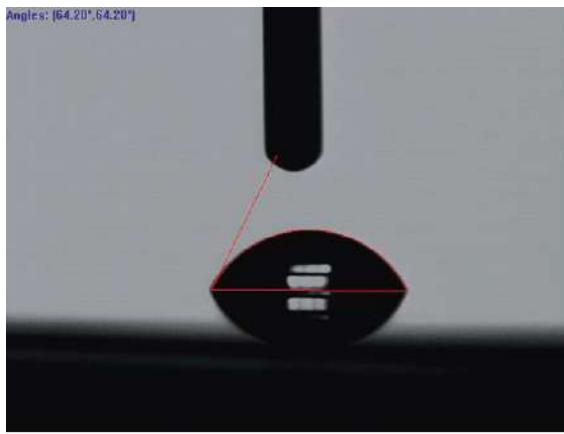


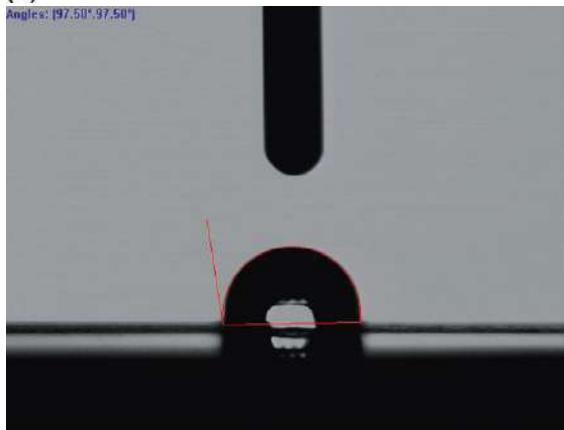
**Figure 13.12** Laser-induced texture on Si substrate for different pulse number under fixed spot separation of 15  $\mu\text{m}$ : (a) 2 pulses, (b) 4 pulses, and (c) 8 pulses.

**Table 13.1 The pit depth for different pulse numbers**

	Pulse number				
	1	2	4	6	8
Pit depth ( $\mu\text{m}$ )	7	7.2	7.5	7.7	9



(a)



(b)

**Figure 13.13** Surface contact angle measurement for (a) original sample and (b) laser-textured sample.

making a texture-imprinting mold. However, as shown in [Figure 13.15a](#) it was found that some arrayed bumps are somewhat nonuniform and misaligned. It is believed that this misalignment was caused by the tracking error of the galvanometer scanner. The issue is expected to be resolved by optimizing the beam positioning speed or using a high-performance (high accuracy, high stability, high repeatability) scanner.

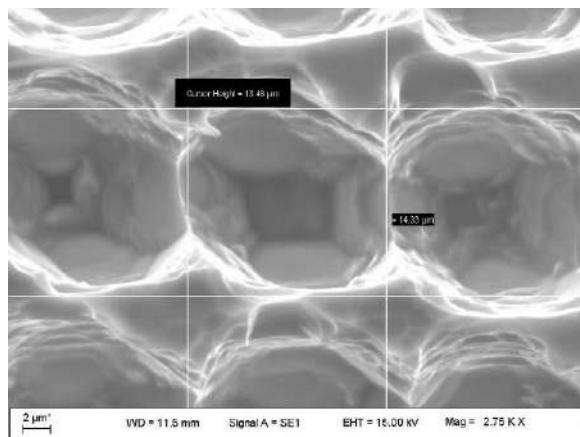


Figure 13.14 Close-up view on laser-textured Si surface morphology.

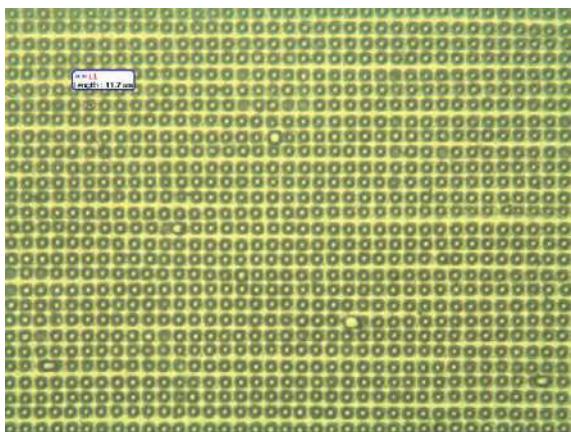
### 13.3 Femtosecond laser interactions with polymethyl methacrylate (PMMA)

#### 13.3.1 Laser-induced surface hydrophilicity and hydrophobicity

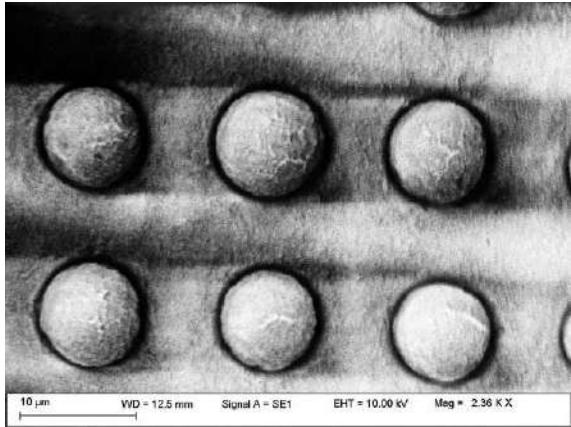
##### 13.3.1.1 Wettability modification by laser irradiation

Commercially available 1-mm-thick PMMA substrate was irradiated by a fs laser (CPA2001 Clark-MXR, wavelength 775 nm). At 1 kHz repetition rate and 300 mW attenuated power, the laser beam was focused by a conventional focusing lens (focal length of 100 mm). Through a galvanometer scanner, a 5 mm by 5 mm surface area was horizontally raster-scanned at a shifting pitch of 25  $\mu\text{m}$ . The scanning speed was 2 mm/s. Surface was modified with various laser fluences by adjusting the defocusing distance  $Z$ , with positive or negative  $Z$  indicating that the focal plane is above or below the sample surface, respectively. To characterize surface wettability, WCA (variation within  $\pm 1^\circ$ ) was measured in room temperature and ambient air conditions (relative humidity 60%) using VCA Optima XE, by releasing a 0.5  $\mu\text{l}$  droplet onto the surface.

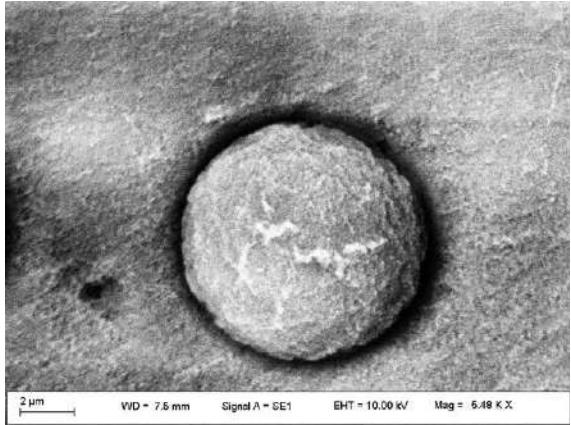
Figure 13.17 is a plot of WCA of the irradiated surface and the laser fluence against the defocusing distance  $Z$ . When the sample surface was on the laser focal plane, water droplets spread rapidly across the surface with a boundary beyond the field of view of the microscope. Thus, WCA was deduced to approach  $0^\circ$ , indicating superhydrophilicity. WCA increased with the increasing magnitude of defocusing distance, indicating a decrease of surface hydrophilicity. With  $Z$  more than 3 mm, WCA exceeded  $90^\circ$ , indicating a hydrophobic surface. Maximum WCA of approximately  $125^\circ$  was achieved for  $Z$  of 7 mm. For  $Z$  greater than 8 mm, WCA decreased to  $76\text{--}78^\circ$ , which was similar to that of a raw PMMA surface. Figure 13.17 shows the symmetry of WCA with respect to  $Z$ , that is, similar WCA value for the same  $Z$ . For a given laser power, the same  $Z$  will have the same laser fluence, indicating that



(a)

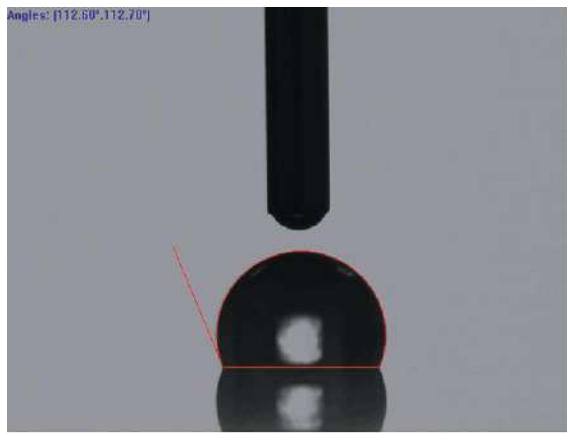


(b)

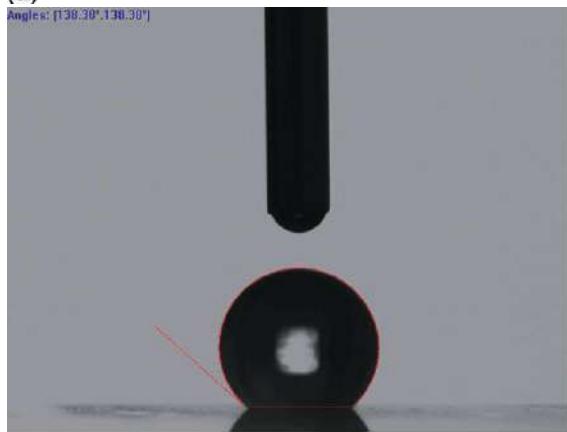


(c)

**Figure 13.15** Imprinted pattern on sol gel film surface with laser-textured Si substrate: (a) overview of the imprinted pattern, (b) SEM images of the imprinted pattern, and (c) close-up view of the imprinted bump.



(a)



(b)

**Figure 13.16** Surface contact angle measurement for (a) original sol gel film and (b) imprinted sol gel film.

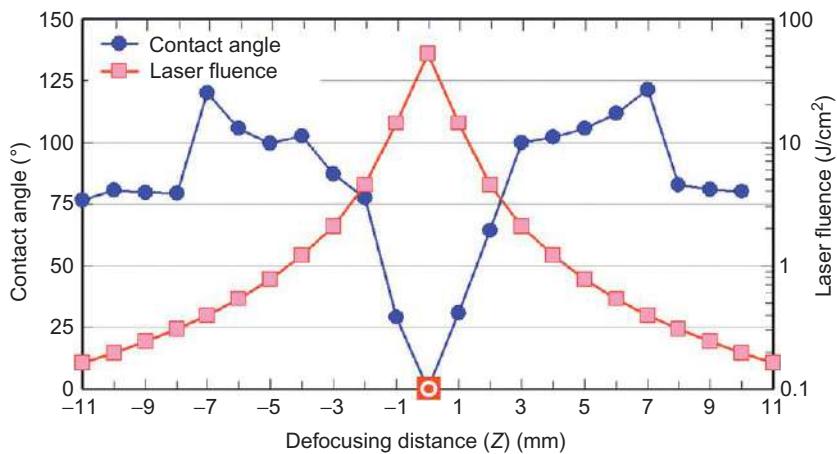


**Figure 13.17** Effect of defocusing distance  $Z$  on water contact angle (WCA).

laser fluence is the key determining factor of WCA. The change in WCA over the range of fluence investigated was significant. Near zero degree in WCA was achieved at a high fluence of  $52.7 \text{ J/cm}^2$  ( $Z$  of 0 mm), and  $125^\circ$  at a fluence of  $0.40 \text{ J/cm}^2$  ( $Z$  of 7 mm). Fluences below  $0.31 \text{ J/cm}^2$  ( $Z$  of 8 mm or more) remained WCA similar to that of the raw PMMA surface, indicating the level of fluence was below the threshold to cause any noticeable changes to the PMMA surface [40,41,44,45].

### 13.3.1.2 Mechanism of laser-induced wettability modification

Oxygen-containing groups on polymer surfaces, such as  $\text{C}-\text{O}$ ,  $\text{C}=\text{O}$ , and  $\text{O}-\text{C}=\text{O}$ , are responsible for the change of surface hydrophilicity [46–48]. As the polarity of the  $\text{C}=\text{O}$  bond is more intense than that of the  $\text{C}-\text{O}$  bond, the  $\text{C}=\text{O}$  double bond is most important for hydrophilicity of polymer surfaces [47]. To gain an insight on the changes in surface wettability induced by laser irradiation, X-ray photoelectron spectroscopy (XPS) analysis using a VG ESCALAB 220i-XL was employed to identify the chemical bonds. Using the O 1s XPS spectra from a raw PMMA sample, samples irradiating at high fluence of  $52.7 \text{ J/cm}^2$  and low fluence of  $0.40 \text{ J/cm}^2$  ( $Z=0$  and  $-7 \text{ mm}$ , respectively) were measured. Figure 13.18 shows that at high fluence of  $52.7 \text{ J/cm}^2$ , the  $\text{O}-\text{C}$  and  $\text{O}=\text{C}$  peak merged into one much higher peak, indicating the generation of methane and carbon oxide as the degradation products of the free methyl formate radical [49]. This increases the surface oxygen concentration and hydrophilicity. This is similar to that of a PMMA surface treated by ns UV laser [50], DC-plasma, or microwave plasma [51]. In contrast, at fluence  $0.40 \text{ J/cm}^2$ , the  $\text{O}-\text{C}$  and  $\text{O}=\text{C}$  peaks decreased, thus decreased hydrophilicity, as compared to that of the raw PMMA. The nonlinear absorption of fs laser causes photodegradation [52–54], which is different from the thermal degradation associated with linear absorption in ns pulses [55,56]. The observed modification of PMMA surface wettability by fs laser over a wide range of WCA (from around  $0^\circ$  to approximately

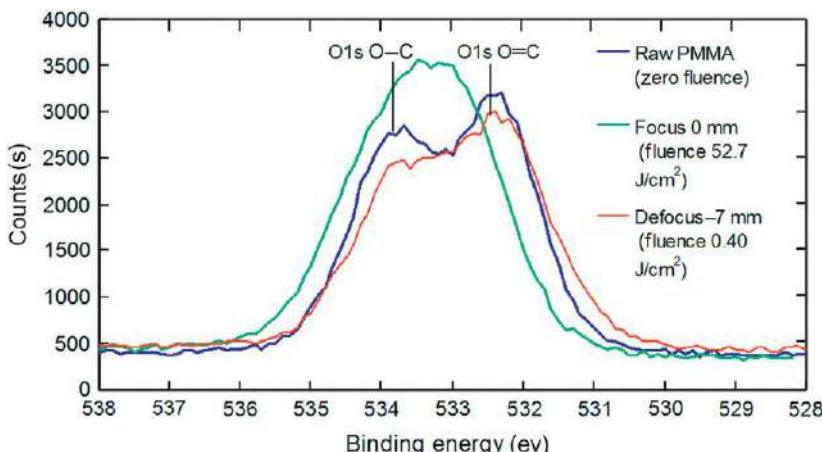


**Figure 13.18** O 1s XPS-spectra of PMMA sample before and after fs laser irradiation.

125°) could be attributed to this photodegradation. The level of laser fluence determines the degree and nature of photodegradation, which dictates the level of wettability [44,45].

To understand the photochemical process caused by this photodegradation, the C 1s XPS spectra of these three samples were measured. The deconvolution of the C 1s and O 1s XPS spectra allows identification of the variations of chemical bonds for polar and nonpolar functional groups. The relative amount of the chemical bonds was summarized in Table 13.1. In agreement with Figure 13.18, Table 13.2 shows that high fluence produced the highest concentration of polar group O 1s O=C and the lowest concentration of nonpolar group C 1s C—C, indicating high hydrophilicity. In contrast, the sample surface subjected to low fluence has the highest concentration of nonpolar group C 1s C—C, and low total concentration of polar groups as compared to raw PMMA surface, indicating increased hydrophobicity. Thus, by controlling the fluence level, controlled modification of WCA was achieved by surface chemical changes to be rich in either polar groups or nonpolar groups as indicated in Figure 13.18 and Table 13.2.

To confirm if surface wettability could also be a function of surface morphology such as roughness [50,57,58], surface roughness was measured using a stylus profilometer (Dektak 3-D surface profiler). Samples of various roughness were prepared with single directional laser scan (samples 1<sup>#</sup> and 4<sup>#</sup>), or parallel and perpendicular scans (samples 2<sup>#</sup>, 3<sup>#</sup>, 5<sup>#</sup> and 6<sup>#</sup>). All scanning speeds were 2 mm/s except for the perpendicular scanning speeds of samples 3<sup>#</sup> and 6<sup>#</sup>, which were 4 mm/s. These samples were subjected to either high fluence (52.7 J/cm<sup>2</sup>) or low fluence (0.40 J/cm<sup>2</sup>). Figure 13.19 indicates that for surfaces irradiated with the same fluence, WCA had similar values despite their significant differences in roughness. In addition, there was no obvious spreading of water droplets along the laser scan track for these samples. Thus, the observed surface wettability modification is predominantly caused by

**Table 13.2 Relative amount of oxygen/carbon functional groups (at.%)**

	Chemical bond	Raw PMMA	High fluence 52.7 J/cm <sup>2</sup>	Low fluence 0.40 J/cm <sup>2</sup>
Nonpolar groups	C 1s C—H C 1s C—C	40.25 13.84	29.78 1.38	39.88 20.35
Sum		54.09	31.16	60.23
Polar groups	C 1s C—O C 1s O—C=O O 1s O=C O 1s O—C	13.44 10.39 — 11.43 10.64	10.97 6.38 — 29.99 21.50	10.85 8.07 — 11.57 9.28
Sum		45.90	68.84	39.78

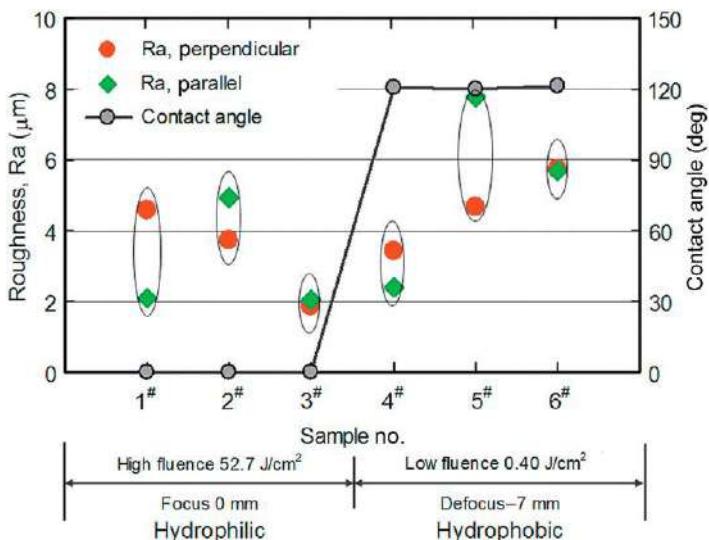


**Figure 13.19** WCA and surface roughness for various samples showing WCA is independent of roughness but dependent on fluence.

laser-induced chemical bond modification and not by a change in surface roughness. These results are in agreement with reported observations that the observed surface wettability modification was dominantly caused by laser-induced chemical bond modification [47]. However, there would be no reason to completely rule out the possibility that other differences in physical morphology of the surface, such as a change in surface porosity, could contribute to a change in the absolute value of WCA [40,41,44,45]. Furthermore, the micron scale roughness could have an influence on the wettability [47].

### 13.3.2 *Laser-induced wettability modification of microfluidic channels for fluid flow control*

#### 13.3.2.1 *Fabrication of microchannels with varied surface wettability*

According to the values in WCA for different laser fluences in Figure 13.17, three types of microchannels, namely, with a highly hydrophilic surface, low hydrophilic surface, and a hydrophobic surface, were prepared for the evaluation of the effect of channel surface wettability on liquid medium flowing behavior in microchannels. A Y-chip was designed and fabricated through laser direct writing on a PMMA substrate, as shown in Figure 13.20. One of the two branch channels was written at low laser fluences, thus a hydrophobic or low hydrophilic surface of the channel, while the other written at high fluences was highly hydrophilic. The WCA for the surface of branch channel (a) of the Y-chips was measured to be  $64.1^\circ$  and

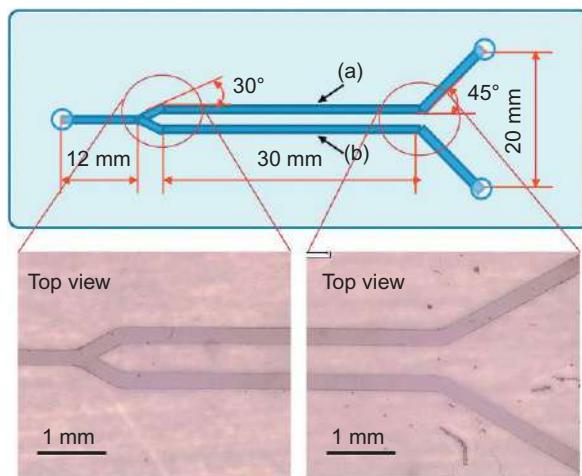


**Figure 13.20** Y-chip with different levels in surface wettability for channels (a, b).

102.5°, respectively, for laser fluences of 5.6 and 1.3 mJ/cm<sup>2</sup> used to fabricate the channel. The WCA for the surface of branch channel (b) of the Y-chips was measured to be below 10° for laser fluence of 45.9 mJ/cm<sup>2</sup> used to fabricate the channel. The remaining channels of the Y-chip were fabricated with a WCA of below 10°. Overlapped scans of the laser beams horizontally and/or vertically were used to ensure the similar channel profiles for different laser fluences. The focal spot size in our laser system was around 29 μm in diameter. Eight scans were carried out with a shifting pitch of 25 μm along the channel for all laser fluences applied. These scans determined the width of the microchannel. A single scan was carried out at laser fluence of 45.9 mJ/cm<sup>2</sup>. Three and five overlapped scans, respectively, were carried out at the laser fluences of 5.6 and 1.3 mJ/cm<sup>2</sup>. These scans determined the depth of the channel. The different scan passes were selected based on the fact that a deeper depth was produced at a higher fluence without significant increase in width. As such, nearly identical channel dimensions were achieved for the channels with three types of surface wetting properties. The geometric dimensions of the microchannels were characterized using a stylus profilometer (Taylor-Hobson Form Talysurf Series 2). The cross section of the channel was measured to be close to a trapezoid shape 230 μm in top width, 150 μm in bottom depth, and 55 μm in height. An observation of the microchannels under an optical microscope was also carried out. [Figure 13.20](#) shows a top view of the microchannel chips. [Figure 13.21](#) shows the images of the cross section and the bottom of a microchannel.

### 13.3.2.2 Effect of laser-induced various wettability on liquid flow

The PMMA substrate of [Figure 13.20](#) was bonded with a PDMS substrate by mechanical pressure without adhesives or elevated temperature. When water was injected into the channel from the front of the two branch channels (a) and (b) using a syringe at a

controlled constant flow rate, the different flowing velocity in the two channels was clearly observed as shown in Figure 13.22. This indicates the varied water separation ratio in the two channels due to the varied surface wetting behaviors. When the water was injected into the Y-chip at a flow rate of 1.0  $\mu\text{l}/\text{min}$ , the velocity ratio of the water flow in the two branches calculated from the flowing distance was to be approximately 3.5 for highly hydrophilic channel to low hydrophilic channel (top two rows, Figure 13.22a) and 3.9 for highly hydrophilic channel to hydrophobic channel (bottom

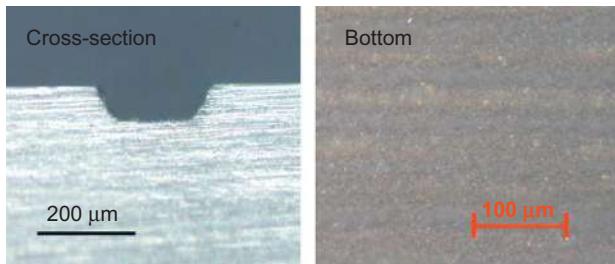


**Figure 13.21** Optical views of the cross section and bottom of a microchannel.

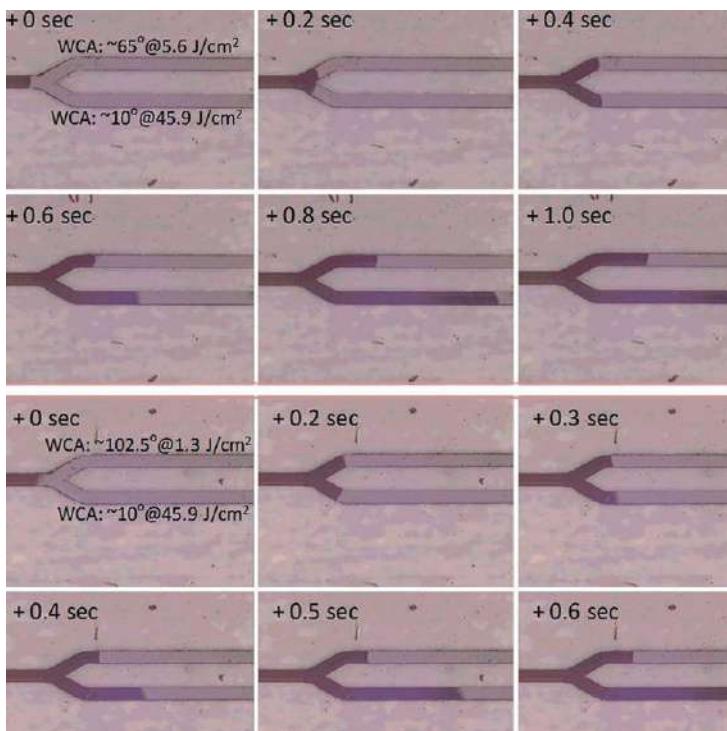


**Figure 13.22** Effect of surface wettability on flow behavior in microfluidic channels.

two rows, [Figure 13.22b](#)). The similarity in bottom surface roughness and dimensions of the cross section for channel branch (a) and (b) enabled us to conclude that the surface wettability of the channels controlled the flowing behavior. The separation ratio of water in different microchannels could be simply controlled by varied channel surface wetting characteristics. As the initial pump rate changed from the injection syringe, the separation velocity and ratio in the two channels were able to be consequently adjusted. Of more interest to note is that it could be difficult to flexibly fabricate such a device with its channel in varied surface wettability using other techniques except fs laser ablation.

To understand the fluid flow behavior, a Y-mixer was fabricated by laser direct writing of PMMA then was thermally bonded with another PMMA plate at 4.3 MPa and 106 °C for 20 min. Using the same protocol as described earlier, different wetting behaviors at the channel bottom surface were obtained by controlling the laser fluences. Furthermore, in order to determine if any flow difference in microchannels fabricated between fs laser and other routine methods, a Y-mixer was thus fabricated using hot embossing technique. A commercial red dye (COCHINEAL RED, from KA Foodlink, Singapore) was diluted with DI water at a ratio of 1–5 (V/V). After dilution, the same procedure of syringe injection was used to fill the dye into the different Y-mixers. The fluid flow front was photographed in static equilibrium after releasing the syringe. It was observed that a concave flow front appeared on the super hydrophilic surface, a convex flow front on the hydrophobic surface, and a straight flow front on the raw surface ([Figure 13.23](#)). The results could also imply that the laser-induced wettability in channel surface was not noticeably influenced by the routine thermal bonding. The modified surface wettability could remain stable during thermal bonding [[44,45](#)].

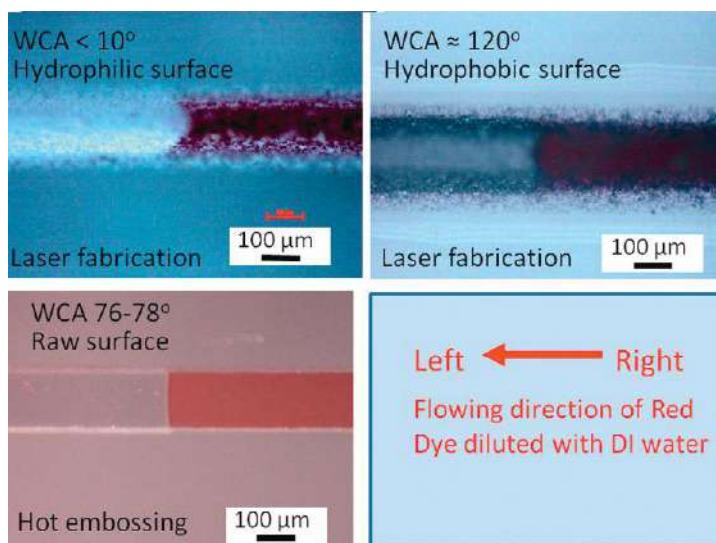


**Figure 13.23** Water flow front in microchannels with controlled surface wettability.

## 13.4 Nd:YAG laser melting of magnesium alloy for corrosion resistance and surface wettability improvement

### 13.4.1 Heat transfer and liquid flow as well as material loss during laser-Mg interaction

In the AZ91D Mg alloy molten pool induced by millisecond pulse Nd:YAG laser, surface tension at the cooler edge is higher than that in the center due to a negative temperature gradient of surface tension [59,60]. It is known that Marangoni flows arise whenever a nonuniform temperature or concentration distribution exists along the interface between two fluids. Therefore, radially outward Marangoni flow creates a depression of liquid surface beneath the laser beam and the ridging of liquid surface elsewhere [61]. As the laser beam passes to other areas of the surface, this distortion of liquid surface is frozen in, creating a roughened ripples surface. It is believed that convection is the predominant heat transport mechanism, and the liquid flow is driven by buoyancy and surface tension forces [62–64]. Buoyancy effects originate from spatial variation of the liquid material density due to temperature variation and composition differences.

The relative importance of buoyancy and surface tension forces for liquid flow in the molten pool can be determined from the ratio of surface tension Reynolds number ( $Ma$ ) to Grashof number ( $Gr$ ) [63–66]:

$$R_{s/b} = \frac{Ma}{Gr} = \left( \frac{\rho L_R \Delta T |\partial\gamma/\partial T|}{\mu^2} \right) / \left( \frac{g\beta L_b^3 \Delta T \rho^2}{\mu^2} \right) = \frac{L_R |\partial\gamma/\partial T|}{g\beta L_b^3 \rho} \quad (13.2)$$

where  $\rho$  is the density of materials,  $g$  is gravitational acceleration,  $\beta$  is thermal expansion coefficient,  $L_R$  is characteristic length taken as the pool radius at the top surface of the molten pool,  $L_b$  is characteristic length for the buoyancy force in the liquid pool, which is approximated by one-eighth of the pool radius,  $\mu$  is typical liquid velocity, and  $\partial\gamma/\partial T$  is the temperature coefficient of surface tension, and  $\Delta T$  is the temperature difference between the peak pool temperature and solidus temperature. According to physical properties of AZ91D Mg alloy in the literature [13,67] and the measured molten pool radius as 432  $\mu\text{m}$  in this work, the ratio of surface tension force to buoyancy force was calculated as  $4.07 \times 10^5$  based on Equation (13.2). Therefore, the liquid flow is driven mainly by Marangoni flows and, to much lesser extent, by the buoyancy force.

During the laser irradiation process, vaporization of alloying elements and liquid metal ejection are two main mechanisms of material loss [68,69]. Moreover, selective vaporization is a key factor responsible for enrichment of alloying element in a laser-treated surface [18–20]. As a result, vaporization of alloying elements was examined in this work using Si wafer to collect generated plume from the laser process. Figure 13.24a shows surface morphology of the deposited plume on Si sheet. The deposited plume reveals an ellipse shape with dimension around 500  $\mu\text{m} \times 1500 \mu\text{m}$ ,

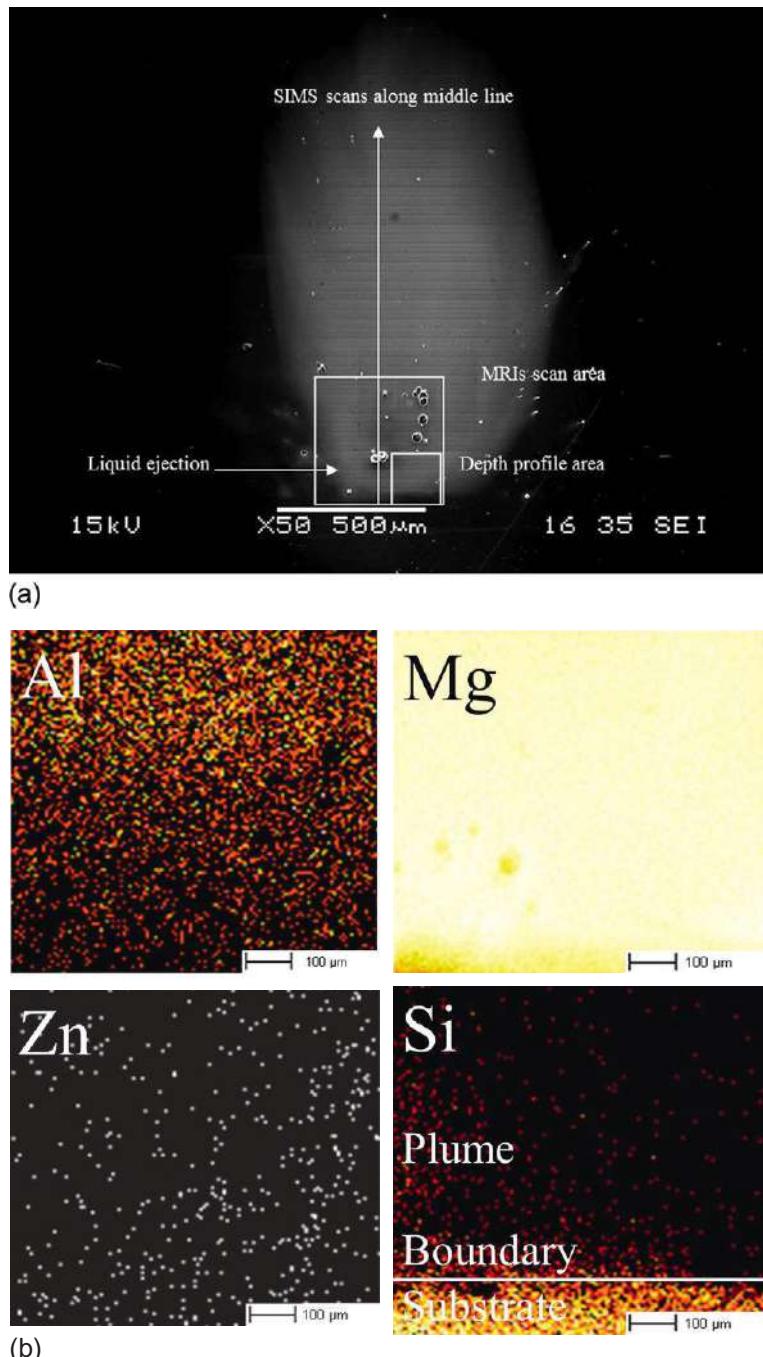


**Figure 13.24** Morphology of deposited plume on Si wafer: (a) SEM image indicating locations of SIMS analysis and (b) MRIs showing chemical mapping of main elements.

and the average thickness was measured as 322 nm. Location of MRIs analysis is also illustrated in Figure 13.24a. A few liquid ejections of molten material were observed, indicating phase explosion phenomenon with a mixture of liquid and vapor during laser process. The MRIs results are shown in Figure 13.24b. According to color contrast of Si, boundary between the deposited plume and the Si substrate was indicated as a white line. The concentration of Mg is found to be quite uniform in the whole area, while the concentration of Al increases with the distance starting from the boundary. There were very few Zn elements in the deposited plume. The signal of Mg, Al, and Zn elements below the boundary line was due to edge effect during the deposition process. In addition, the chemical content ratio of vaporized Mg and Al species in the deposited plume was found to be more than 50:1. This was mainly due to the different vaporization rate of Mg and Al as well as the original base metal composition. Transport rate of vaporized Al was further found to be higher than that of Mg, and this was attributed to relatively high diffusivity of Al vapors in Ar gas during the laser process [70,71].

### 13.4.2 Microstructural evolution and phase transformation in the melted zone

Figure 13.25 shows typical XRD patterns of AZ91D alloy before and after laser treatment. Both  $\alpha$ -Mg phase and  $\beta$ - $Mg_{17}Al_{12}$  intermetallics are shown in the as-received and laser-treated microstructures. Figure 13.26 indicates whole morphology of solidification microstructure within the laser-melted zone. Al-Mn intermetallics were also found in both the laser-melted zone (they did not melt during laser processing due to a

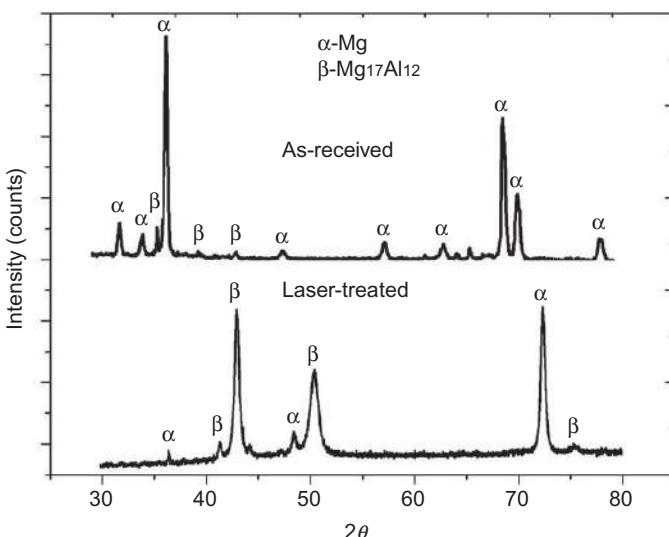


**Figure 13.25** XRD patterns of AZ91D Mg alloy, showing the presence of  $\alpha$ -Mg phase and  $\beta$ - $Mg_{17}Al_{12}$  intermetallics: (a) as-received and (b) laser-treated layer.

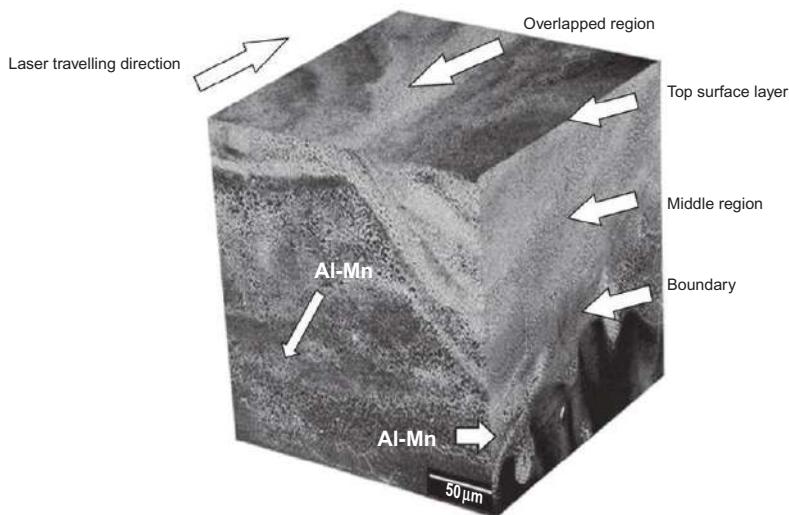


**Figure 13.26** Three-dimensional image of typical solidification microstructure of AZ91D Mg alloy in the laser-melted zone.

high melting point) and the substrate microstructure. Typical cellular/dendrite structure was observed, and the penetration depth of the laser-melted zone was more than 100 μm. Moreover, the refined microstructure was not uniform in the melt zone and coarse network of  $\beta$ -Mg<sub>17</sub>Al<sub>12</sub> along the overlapped regions might be formed due to the inadequate energy distribution near the tail of Gaussian distribution in the laser beam together with the remelt process during laser irradiation [18,72,73]. Heat-affected zone (HAZ) in our experiment was very small due to the rapid laser heating and subsequent rapid cooling, and the depth of HAZ is typically less than 50 μm.

The distribution of main elementary compositions based on EDS analysis is shown in Figure 13.27. Average Al content increased in the melted zone, which is likely due

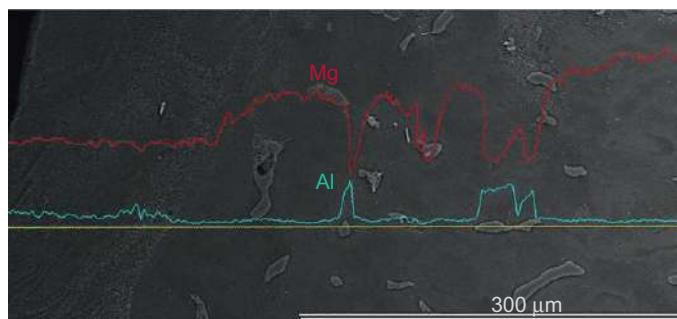


**Figure 13.27** Distribution of main elements Al and Mg in the laser-melted zone and substrate of AZ91D Mg alloy.

to relatively more Mg evaporation during the laser process, as discussed before, and fine  $\beta\text{-Mg}_{17}\text{Al}_{12}$  precipitation during laser-induced solidification [20,72–75]. Quantitative analyses of the micrographs confirmed that the Al content in the  $\alpha\text{-Mg}$  matrix (79.2–82.4 wt.% Mg) was in the range of 10.7–12.1 wt.% and was enriched at the dendrite/cellular boundaries (61.3–65.8 wt.% Mg) in the range of 30.8–33.3 wt.%, which were higher than the value of 9.0 wt.% in the untreated substrate (89.9 wt.% Mg).

Phase transformation of refined  $\alpha\text{-Mg}$  and  $\beta\text{-Mg}_{17}\text{Al}_{12}$  phase was further investigated by TEM, as shown in Figure 13.28. Figure 13.28a and b shows the typical cellular/dendrite structure in the overlapped region. Moreover, Figure 13.28b reveals that many individual particles were observed to be distributed randomly in the matrix, and the sizes of these particles were in the range of 50–200 nm. SAD patterns show that these particles exhibit the BCC crystal structure. Quantitative analyses of elementary compositions in the particles were analyzed by EDS, including 63.11 wt.% Mg, 32.83 wt.% Al, 3.48 wt.% Zn, and 0.68 wt.% Mn. Therefore, these nanoparticles were identified as  $\beta\text{-Mg}_{17}\text{Al}_{12}$  phase. It should be noted that various types of Mg-Al, Mg-Mn, and Mg-Ca precipitates are generated in sizes ranging from nanometers to microns in Mg alloys processed via different methods [76,77]. However, rapid solidification induced by laser treatment results in a more homogeneous distribution as well as a relatively more refined scale. Figure 13.28c and d shows there is a typical orientation relationship (OR) between the individual nanoparticle and the matrix. The OR between the  $\alpha\text{-Mg}$  matrix and plate-shape  $\beta\text{-Mg}_{17}\text{Al}_{12}$  phase was found to be Burgers OR ((0001) $_{\alpha}$ ||(110) $_{\beta}$ ), as shown in Figure 13.28c. It has been known that Burgers OR was the predominant Burgers OR of  $\beta\text{-Mg}_{17}\text{Al}_{12}$  precipitation in AZ91D Mg alloy [77–79]. Moire fringes were observed in the particles due to the overlapping effect between the nanocrystal and the  $\alpha\text{-Mg}$  matrix [80]. Additionally, the OR between the  $\alpha\text{-Mg}$  matrix and the spherical-shaped  $\beta\text{-Mg}_{17}\text{Al}_{12}$  phase was found to be (10 $\overline{1}$ 2) $_{\alpha}$ ||(113) $_{\beta}$ , as shown in Figure 13.28d.

### 13.4.3 Degradation behavior in modified body simulated fluid

In order to understand the effect of microstructural features on the corrosion mechanism, original surfaces and corroded surfaces of 2 h and 2 weeks exposures in modified body simulated fluid (m-SBF) were analyzed under SEM, as shown in Table 13.3. Selected SEM micrographs for corroded surfaces of as-received specimen and laser-irradiated specimens A–C conditions are shown. In the initial 2 h exposure time, corrosion of the as-received microstructure occurred preferentially in  $\alpha\text{-Mg}$  matrix and the eutectic area, and intergranular and pitting corrosion was found along the original  $\beta\text{-Mg}_{17}\text{Al}_{12}$  phase. For laser-irradiated A–C microstructures, deep corrosion was observed along the overlapped regions while some localized corrosion was found within the matrix. Coarse dendrite structure in A specimen and a small crack in C were the reasons for the increased corrosion rate [18,81]. After immersion for 2 weeks, the microgalvanic corrosion at  $\alpha\text{-Mg}$  matrix and eutectic phase accelerated in the as-cast microstructure. In the A microstructure, localized pits were found to spread laterally along the laser passages and cover the whole surface resulting in uniform corrosion. Although localized pitting corrosion in B microstructures was

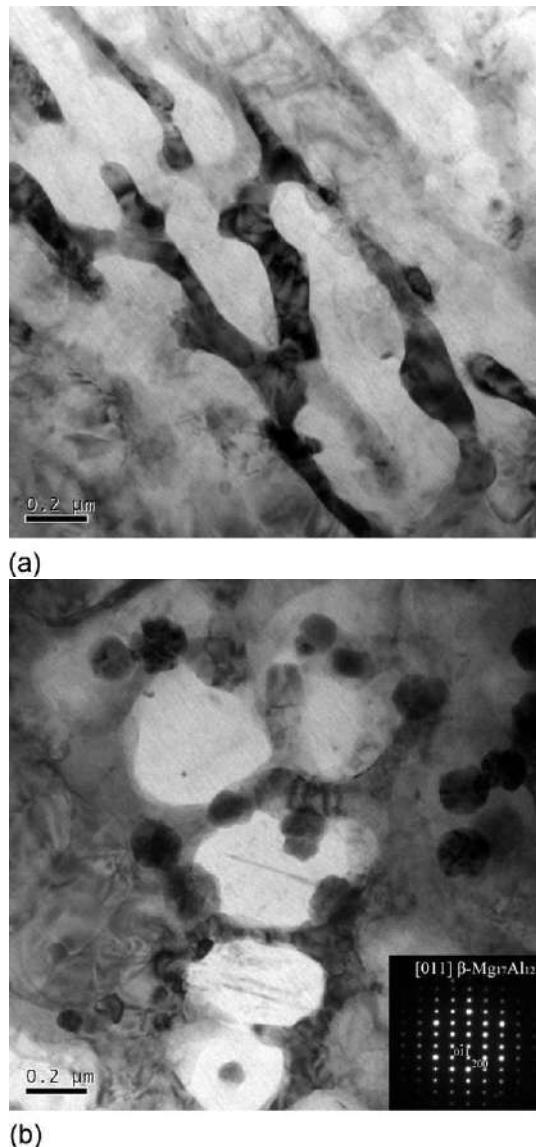
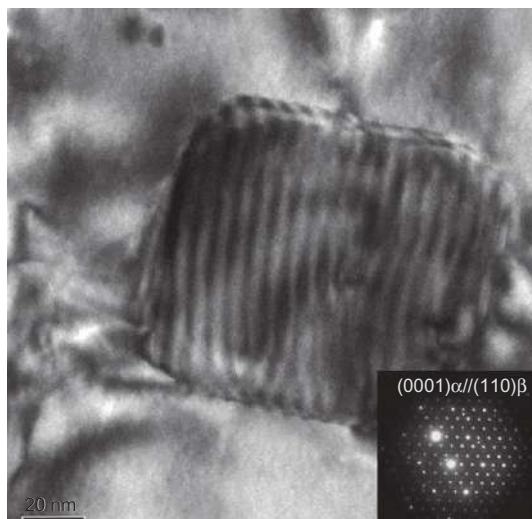
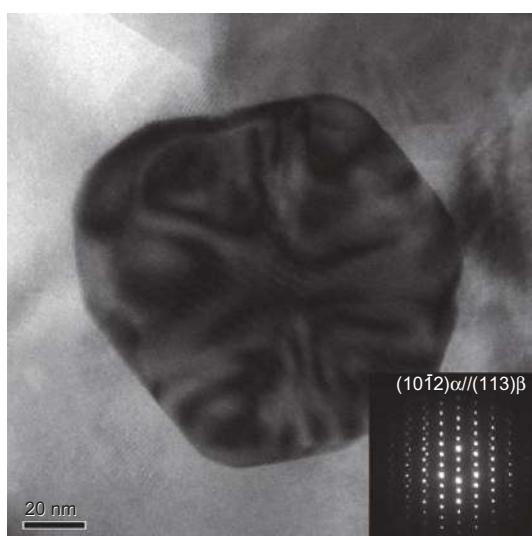


**Figure 13.28** (a) Bright-field TEM image of nonoverlapped region in laser-melted AZ91D Mg alloy, showing lath-shaped  $\beta\text{-Mg}_{17}\text{Al}_{12}$  formed along the cellular/dendrite structure. (b) Bright-field TEM image showing  $\beta\text{-Mg}_{17}\text{Al}_{12}$  formed along cellular/dendrite structure and submicron and nanometer scale particles distributed within the matrix, SAD pattern from one of these particles exhibiting BCC structure.

(continued)



(c)



(d)

**Figure 13.28** Continued. (c) Bright-field TEM image of one individual plate-shape nanoparticle, SAD pattern showing Burgers OR  $(0001)_\alpha \parallel (110)_\beta$  between the particle and  $\alpha$ -Mg matrix. (d) Bright-field TEM image of one individual spherical-shape nanoparticle, SAD pattern showing OR  $(10\bar{1}2)_\alpha \parallel (113)_\beta$  between the particle and  $\alpha$ -Mg matrix.

**Table 13.3 Microstructural evolution of AZ91D Mg alloy before and after immersion test**

	As-received specimen	Specimens A	Specimens B	Specimens C
Before immersion tests				
After 2 h exposure in m-SBF				
After 2 weeks exposure in m-SBF				

propagated, the degree of corrosion was lower than that of A. Moreover, cracks in C accelerated the corrosion rate to a large extent.

The electrochemical corrosion behavior of laser-irradiated microstructures was investigated by comparing them with that of as-received microstructures. The potentiodynamic polarization curves of all the microstructures in m-SBF are shown in [Figure 13.29](#). Corrosion potential  $E_{corr}$  for laser-treated microstructures was shifted to less negative values than that of as-received alloy, indicating less corrosion susceptibility for the laser-treated microstructures. It is further noted that cathodic current  $i_{corr}$  was much lower for all laser-treated microstructures at all potentials, indicating that the laser-treated samples had lower corrosion rates. This observation is found to be in only partial agreement with the results of immersion tests: after the laser treatment, the immersion corrosion rate is indeed lower for microstructures A and B but, in fact, higher for microstructures C and D. However, the discrepancy can be explained because the cracks in microstructures C and D are shown to accelerate corrosion during immersion tests [[72,73](#)].

#### 13.4.4 Surface energy and wettability characteristics

Contact angle measurement was carried out for the as-received alloy and laser-treated specimens to study the effect of the laser irradiation on the surface property. Contact angles were found to be considerably smaller for the laser-treated specimens than for the as-received alloy for all the three types of liquids used ( $47.34^\circ$  versus  $70.21^\circ$  for formamide,  $51.55^\circ$  versus  $72.88^\circ$  for deionized water, and  $32.97^\circ$  versus  $63.75^\circ$  for ethylglycol), as shown in [Figure 13.30](#). This indicates that irradiation by Nd:YAG laser increased the surface wettability of AZ91D Mg alloy significantly.

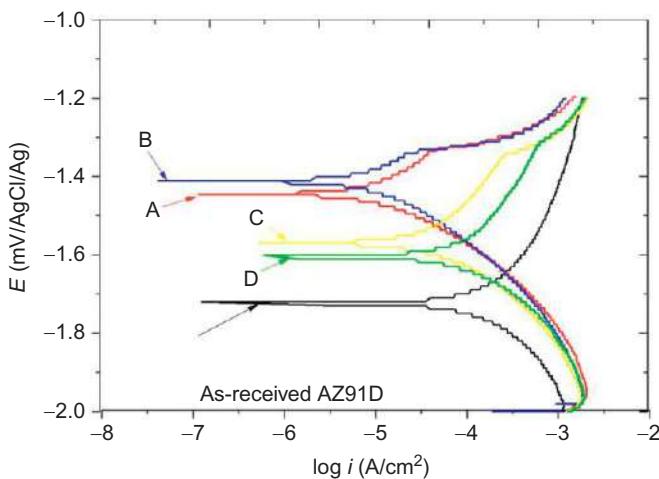


**Figure 13.29** Potentiodynamic polarization curves for as-received and laser-treated AZ91D alloy in m-SBF.

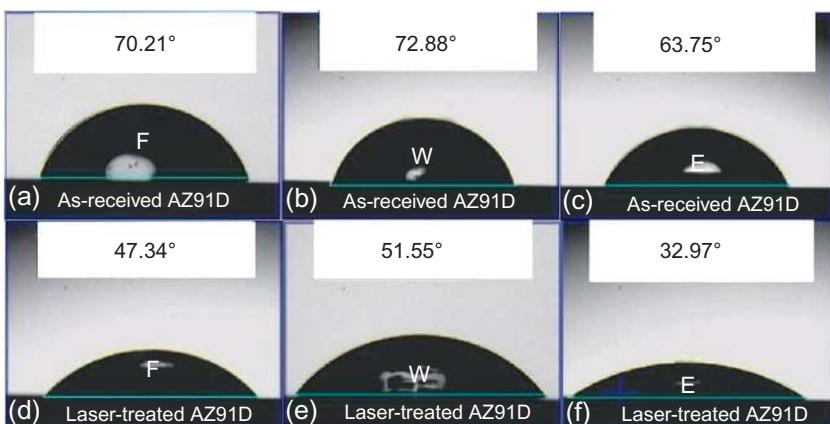


**Figure 13.30** Contact angles for formamide (F), deionized water (W), and ethylglycol (E) on (a-c) as-received AZ91D alloy and (d-f) laser-treated AZ91D Mg alloy.

Acid-base theory or three-liquid method was used in the work, solid/liquid interfacial tension can be described by the following equations [82,83]:

$$2 \left( \sqrt{\gamma_{sv}^{LW} \gamma_{lv}^{LW}} + \sqrt{\gamma_{sv}^+ \gamma_{lv}^-} + \sqrt{\gamma_{sv}^- \gamma_{lv}^+} \right) = \left( \gamma_{lv}^{LW} + 2 \sqrt{\gamma_{lv}^+ \gamma_{lv}^-} \right) (1 + \cos \theta) \quad (13.3)$$

where  $\gamma_{sv}^{LW}$  and  $\gamma_{lv}^{LW}$  are Lifshitz-van der Waals components (the dispersive component  $\gamma_{sv}^d$  and  $\gamma_{lv}^d$ ),  $\gamma_{sv}^{AB}$  and  $\gamma_{lv}^{AB}$  are Lewis acid-base components (the polar component  $\gamma_{sv}^P$  and  $\gamma_{lv}^P$ ),  $\gamma_{sv}^+$  and  $\gamma_{lv}^+$  are the electron-acceptor parameters of the acid-base surface free energy component, and  $\gamma_{sv}^-$  and  $\gamma_{lv}^-$  are the electron-donor parameters of the acid-base surface free energy component. The calculated results are summarized in [Table 13.4](#).

**Table 13.4 Surface energy components and total surface energy ( $\gamma_{sv}$ ) obtained, mJ/m<sup>2</sup>**

Specimen	$\gamma_{sv}^{LW}(=\gamma_{sv}^d)$	$\gamma_{sv}^{AB}(=\gamma_{sv}^p)$	$\gamma_{sv}(=\gamma_{sv}^{AB} + \gamma_{sv}^{LW})$
As-received	20.97	4.83	25.80
Laser-treated	27.23	13.53	40.76

**Table 13.5 Adhesion energies of three test liquids to the laser-treated surface, mJ/m<sup>2</sup>**

Specimen	$W_{ad}$ for F	$W_{ad}$ for W	$W_{ad}$ for E
As-received	77.64	94.23	69.22
Laser-treated	97.30	118.07	88.25

The table shows clearly that the laser surface melting leads to a significant increase (by 58%) in the total surface energy  $\gamma_{sv}$  from 25.80 to 40.76 mJ/m<sup>2</sup>, while also increasing the polar component of the surface energy  $\gamma_{sv}^p$ , from 4.83 to 13.53 mJ/m<sup>2</sup>. Adhesion energies of three test liquids to the laser-treated surface  $W_{ad}$  (work of adhesion) are also calculated by the Young-Dupre equation [84]  $W_{ad} = \gamma_{lv}(1 + \cos \theta)$ , and summarized in Table 13.5. The increased surface energy of laser-treated alloy has a positive effect upon the action of wetting and adhesion.

The increase in surface energy and wettability of the laser-treated AZ91D Mg alloy is thought to be related to the laser-induced change in resolidification microstructure and chemical composition. The dendrite and cellular structure in the molten zone is known to affect an increase in  $\gamma_{sv}$ , and thus an improvement in the wettability characteristics and an increase in the adhesion at the interface in contact with the control liquids. This conclusion is in strong agreement with the findings of Lawrence and Li [84], who studied the increased polar component of surface energy resulting from the melting and resolidification of the mild steel surface, thus creating a different microstructure that quite possibly improved the action of wetting and adhesion. Magnesium alloys have been increasingly used as structural materials for the aerospace, automotive, and electronic industries, but the alloys' poor corrosion resistance limits their wider application [16,85,86]. The current study indicates that laser irradiation may be used to improve wetting and adhesion of the magnesium alloy substrates for better coating quality [72,73].

## 13.5 Conclusions

### 13.5.1 Laser texturing of silicon for improving surface functionalities

One step fs laser processing to produce surface nanostructuring and crystallization of amorphous thin film simultaneously was discussed. The crystalline volume fraction of fs laser-treated a-Si:H thin film was about 34.7%. The process has potential

applications for high-efficiency Si thin film solar cells, TFTs, large area sensors, and other optoelectronic devices. A regular array of Si nanobumps surrounded by ring-shaped trench was fabricated on Si substrate by a single shot excimer laser irradiation of a monolayer of silica microspheres. The developed Si nanobump pattern has potential applications for sensitive detectors, efficient PV cells, field-emitter arrays, and displays. DPSS UV laser direct pit ablation induced surface texturing on Si substrates was demonstrated. Through finely adjusting laser beam fluence, pulse number, and beam spot separation, uniform consistent surface texturing could be formed. The reported process was demonstrated to be a fast, cost-effective approach for making an imprinting mold compared with other conventional methods.

### **13.5.2 Femtosecond laser interactions with PMMA**

Controlled modification of wettability could be achieved over a wide range of WCA by controlling the level of the laser fluence irradiated on the PMMA surface. This modification is mostly caused by laser-induced chemical bond changes. A controlled liquid sample separation ratio in different microfluidic channels can be obtained through the tailored surface wetting characteristics of the channels. These results offer greater possibilities in microfluidic chip design with surfaces of various wetting properties.

### **13.5.3 Nd:YAG laser melting of magnesium alloy for corrosion resistance and surface wettability improvement**

Marangoni convection played a predominant role in determining the solidification microstructure of laser-treated AZ91D Mg alloy, and typical cellular/dendrite structures and  $\beta\text{-Mg}_{17}\text{Al}_{12}$  nanoparticles as well as enhanced Al concentration were observed due to rapid solidification and selective vaporization as well as laser reheating cycles. Refined homogeneous microstructure led to improved corrosion resistance of laser-treated surface in modified body simulated fluid. However, coarse structure in the overlapped regions caused by microstructure inhomogeneities and small cracks attributed to high thermal stress provided preferential site for corrosion, resulted in poorer corrosion resistance. Results obtained from contact angle measurements revealed that laser treatment enhanced wettability significantly and led to a drastic increase in total surface energy and in the polar component of the surface energy, thus improving the action of wetting and adhesion.

## **Acknowledgments**

This work is supported by Singapore Institute of Manufacturing Technology (SIMTech), Project code U09-M-006SU, Project C08-M-042, and Project C09-M-052. The authors would like to express grateful thanks to Prof. Zhou Wei and Prof. Yee Cheong Lam from Nanyang Technology University and Dr. Li Zhongli from SIMTech for valuable discussions.

## References

- [1] W.T. Silfvast, *Laser Fundamentals*, second ed., Cambridge University Press, 2004.
- [2] W.M. Steen, “Laser” industry: an introduction to laser processing and its industrial application, in: J. Lawrence, J. Pou, D.K.Y. Low, E. Toyserkani (Eds.), *Advances in Laser Materials Processing*, Woodhead Publishing Limited, CRC Press, 2010.
- [3] Y.F. Huang, S. Chattopadhyay, Y.J. Jen, C.Y. Peng, T.A. Liu, Y.K. Hsu, C.L. Pan, H.C. Lo, C.H. Hsu, Y.H. Chang, C.S. Lee, K.H. Chen, L.C. Chen, Improved broadband and quasi-unidirectional anti-reflection properties with biomimetic silicon nanostructures, *Nat. Nanotechnol.* 2 (2007) 770–774.
- [4] C.V. Shank, R. Yen, C. Hirlmann, Time-resolved reflectivity measurements of femtosecond-optical-pulse-induced phase transitions in silicon, *Phys. Rev. Lett.* 50 (6) (1983) 454–457.
- [5] J. Solis, C.N. Afonso, S.C.W. Hyde, N.P. Barry, P.M.W. French, Existence of electronic excitation enhanced crystallization in GeSb amorphous thin films upon ultrashort laser pulse irradiation, *Phys. Rev. Lett.* 76 (14) (1996) 2519–2522.
- [6] T.D. Bennett, D.J. Krajnovich, C.P. Grigoropoulos, P. Baumgart, A.C. Tam, Marangoni mechanism in pulsed laser texturing of magnetic disk substrates, *J. Heat Transfer* 119 (1997) 589–596.
- [7] S.C. Chen, D.G. Cahill, C.P. Grigoropoulos, Melting and surface deformation in pulsed laser surface micromodification of Ni-P disks, *J. Heat Transfer* 122 (2000) 107–112.
- [8] S.D. Unamuno, E. Fogarassy, A thermal description of the melting of c- and a-silicon under pulsed excimer lasers, *Appl. Surf. Sci.* 36 (1989) 1–11.
- [9] S.M. Huang, Z. Sun, B.S. Luk'yanchuk, M.H. Ming, L.P. Shi, Nanobump arrays fabricated by laser irradiation of polystyrene particle layers on silicon, *Appl. Phys. Lett.* 86 (2005) 161911.
- [10] B.S. Luk'yanchuk, N. Arnold, S.M. Huang, Z.B. Wang, M.H. Hong, Three-dimensional effects in dry laser cleaning, *Appl. Phys. A* 77 (2003) 209–215.
- [11] E. Chibowski, L. Holysz, K. Terpilowski, M. Jurak, Investigation of super-hydrophobic effect of PMMA layers with different fillers deposited on glass support, *Colloids Surf. A. Physicochem. Eng. Aspects* 291 (2006) 181–190.
- [12] R. Lin, M.A. Burns, Surface-modified polyolefin microfluidic devices for liquid handling, *J. Micromech. Microeng.* 15 (2005) 2156–2162.
- [13] R.S. Busk, Magnesium and its alloys, in: M. Kutz (Ed.), *Handbook of Materials Selection*, John Wiley & Sons, Inc., New York, 2002.
- [14] M.P. Staiger, A.M. Pietaka, J. Huadmaia, G. Diasb, Magnesium and its alloys as orthopedic biomaterials: a review, *Biomaterials* 27 (9) (2006) 1728–1734.
- [15] F. Witte, The history of biodegradable magnesium implants: a review, *Acta Biomater.* 6 (5) (2010) 1680–1692.
- [16] R. Ambat, N.N. Aung, W. Zhou, Evaluation of microstructural effects on corrosion behaviour of AZ91D magnesium alloy, *Corros. Sci.* 42 (8) (2000) 1433–1455.
- [17] E. Ghali, W. Dietzel, K.U. Kainer, General and localized corrosion of magnesium alloys: a critical review, *J. Mater. Eng. Perform.* 13 (1) (2004) 7–23.
- [18] Z. Liu, P.H. Chong, P. Skeldon, P.A. Hilton, J.T. Spencer, B. Quayle, Fundamental understanding of the corrosion performance of laser-melted metallic alloys, *Surf. Coat. Technol.* 200 (18–19) (2006) 5514–5525.

- [19] J.D. Majumdar, R. Galun, B.L. Mordike, I. Manna, Effect of laser surface melting on corrosion and wear resistance of a commercial magnesium alloy, *Mater. Sci. Eng. A Struct. Mater.: Prop. Microstruct. Process.* 361 (1-2) (2003) 119–129.
- [20] A.K. Mondal, S. Kumar, C. Blawert, N.B. Dahotre, Effect of laser surface treatment on corrosion and wear resistance of ACM720 Mg alloy, *Surf. Coat. Technol.* 202 (14) (2008) 3187–3198.
- [21] G. Abbas, Z. Liu, P. Skeldon, Corrosion behaviour of laser-melted magnesium alloys, *Appl. Surf. Sci.* 247 (1-4) (2005) 347–353.
- [22] T.H. Her, R.J. Finlay, C. Wu, S. Deliwal, E. Mazur, Microstructuring of silicon with femtosecond laserpulses, *Appl. Phys. Lett.* 73 (12) (1998) 1673–1675.
- [23] T.H. Her, R.J. Finlay, C. Wu, E. Mazur, Femtosecond laser-induced formation of spikes on silicon, *Appl. Phys. A70* (2000) 383–385.
- [24] H. Jansen, M. de Boer, R. Legtenberg, M. Elwenspoek, The black silicon method: a universal method for determining the parameter setting of a fluorine-based reactive ion etcher in deep silicon trench etching with profile control, *J. Micromech. Microeng.* 5 (1995) 115–120.
- [25] J.S. Yoo, I.O. Parm, U. Gangopadhyay, K. Kim, S.K. Dhungel, D. Mangalaraj, J. Yi, Black silicon layer formation for application in solar cells, *Sol. Energy Mater. Sol. Cells* 90 (2006) 3085–3093.
- [26] K. Arora, M. Rajalakshmi, T.R. Ravindran, Phonon confinement in nanostructured materials, in: *Encyclopedia of Nanoscience and Nanotechnology*, vol. 8, 2004, pp. 499–512.
- [27] C. Smit, R.A.C.M.M. Van Swaaij, H. Donker, A.M.H.N. Petit, W.M.M. Kesels, M.C. M. van de Sanden, Determining the material structure of microcrystalline silicon from Raman spectra, *J. Appl. Phys.* 94 (5) (2003) 3582–3588.
- [28] E. Fogarassy, H. Pattyn, M. Elliq, A. Slaoui, B. Prevot, R. Stuck, S. de Unamuno, E. L. Mathe, Pulsed-laser crystallization and doping for the fabrication of high-quality poly-Si TFTs, *Appl. Surf. Sci.* 69 (1-4) (1993) 231–241.
- [29] T. Voutsas, M.K. Hatalis, J. Boyce, A. Chiang, Raman spectroscopy of amorphous and microcrystalline silicon films deposited by low-pressure chemical vapor deposition, *J. Appl. Phys.* 78 (12) (1995) 6999–7006.
- [30] R. Tsu, J. Gonzalez-Hernandez, S.S. Chao, S.C. Lee, K. Tanaka, Critical volume fraction of crystallinity for conductivity percolation in phosphorus-doped Si-F-H alloys, *Appl. Phys. Lett.* 40 (6) (1982) 534–535.
- [31] E. Bustarret, M.A. Hachicha, M. Brunel, Experimental-determination of the nanocrystalline volume fraction in silicon thin films from Raman-spectroscopy, *Appl. Phys. Lett.* 52 (20) (1988) 1675–1677.
- [32] M.C. Downer, R.L. Fork, C.V. Shank, Femtosecond imaging of melting and evaporation at a photoexcited silicon surface, *J. Opt. Soc. Am. B* 2 (4) (1985) 595–599.
- [33] K. Sokolowski-Tinten, J. Solis, J. Bialkowski, J. Siegel, C.N. Afonso, D. Von der Linde, Dynamics of ultrafast phase changes in amorphous GeSb films, *Phys. Rev. Lett.* 81 (17) (1998) 3679–3682.
- [34] X.C. Wang, H.Y. Zheng, C.W. Tan, F. Wang, H.Y. Yu, K.L. Pey, Femtosecond laser induced surface nanostructuring and simultaneous crystallization of amorphous thin silicon film, *Opt. Express* 18 (18) (2010) 19379.
- [35] X.C. Wang, H.Y. Zheng, C.W. Tan, F. Wang, H.Y. Yu, K.L. Pey, Fabrication of silicon nano-bump arrays by near-field enhanced laser irradiation, *Appl. Phys. Lett.* 96 (2010) 084101.
- [36] G. Wysocki, R. Denk, K. Piglmayer, N. Arnold, D. Bäuerle, Single-step fabrication of silicon-cone arrays, *Appl. Phys. Lett.* 82 (2003) 692–693.

- [37] H.J. Munzer, M. Mosbacher, M. Bertsch, J. Zimmermann, P. Leiderer, J. Boneberg, J. Microsc., Localfield enhancement effects for nanostructuring of surfaces, *J. Microsc.* 202 (2001) 129–135.
- [38] Y. Lu, S. Theppakutai, S.C. Chen, Marangoni effect in nanosphere-enhanced laser nanopatterning of silicon, *Appl. Phys. Lett.* 82 (2003) 4143–4145.
- [39] Y.L. Linda Wu, Q. Shao, X.C. Wang, H.Y. Zheng, C.C. Won, Hierarchical structured sol-gel coating by laser textured template imprinting for surface superhydrophobicity, *Soft Matter* 8 (2012) 6232–6238.
- [40] X.C. Wang, Y.L. Linda Wu, Q. Shao, H.Y. Zheng, Laser micro structuring on a Si substrate for improving surface hydrophobicity, *J. Micromech. Microeng.* 19 (2009) 085025.
- [41] Z.K. Wang, H.Y. Zheng, C.P. Lim, Y.C. Lam, Polymer hydrophilicity and hydrophobicity induced by femtosecond laser direct irradiation, *Appl. Phys. Lett.* 95 (11) (2009) 111110.
- [42] L. Vogelaar, R.G.H. Lammertink, M. Wessling, Superhydrophobic surfaces having two-fold adjustable roughness prepared in a single step, *Langmuir* 22 (2006) 3125–3130.
- [43] L.B. Zhu, Y.H. Xiu, J.W. Xu, P.A. Tamirisa, D.W. Hess, C.P. Wong, Superhydrophobicity on two-tier rough surfaces fabricated by controlled growth of aligned carbon nanotube arrays coated with fluorocarbon, *Langmuir* 21 (2005) 11208–11212.
- [44] Z.K. Wang, H.Y. Zheng, Y.C. Lam, Investigation on femtosecond laser irradiation energy in inducing hydrophobic polymer surfaces, *Appl. Surf. Sci.* 257 (2011) 10427–10433.
- [45] Z.K. Wang, H.Y. Zheng, H.M. Xia, Femtosecond laser-induced modification in surface wettability of PMMA for fluid separation in microchannels, *Microfluid. Nanofluid.* 10 (2011) 225–229.
- [46] S. Han, Y. Lee, H. Kim, G. Kim, J. Lee, J.-H. Yoon, G. Kim, Polymer surface modification by plasmasource ion implantation, *Surf. Coat. Technol.* 93 (1997) 261–264.
- [47] J. Lai, B. Sunderland, J. Xue, S. Yan, W. Zhao, M. Folkard, B.D. Michael, Y. Wang, Study on hydrophilicity of polymer surfaces improved by plasma treatment, *Appl. Surf. Sci.* 252 (2006) 3375–3379.
- [48] R.L. McCarley, B. Vaidya, S.Y. Wei, A.F. Smith, A.B. Patel, J. Feng, M. Murphy, S. A. Soper, Resist-free patterning of surface architectures in polymer-based microanalytical devices, *J. Am. Chem. Soc.* 127 (2005) 842–843.
- [49] C. Wochnowski, S. Metev, G. Sepold, UV-laser-assisted liquid phase fluorination of PMMA, *Appl. Surf. Sci.* 253 (2000) 9435–9442.
- [50] J. Lawrence, L. Li, Modification of the wettability characteristics of polymethyl methacrylate (PMMA) by means of CO<sub>2</sub>, Nd:YAG, excimer and high power diode laser radiation, *Mater. Sci. Eng. A* 303 (2001) 142–149.
- [51] U. Schulz, P. Munzert, N. Kaiser, Surface modification of PMMA by DC glow discharge and microwave plasma treatment for the improvement of coating adhesion, *Surf. Coat. Technol.* 142-144 (2001) 507–511.
- [52] H. Kumagai, K. Midorikawa, K. Toyoda, S. Nakamura, T. Okamoto, M. Obara, Ablation of polymer films by a femtosecond high-peak-power Ti:sapphire laser at 798 nm, *Appl. Phys. Lett.* 65 (1994) 1850.
- [53] S. Küper, M. Stuke, Femtosecond uv excimer laser ablation, *Appl. Phys. B* 44 (1987) 199–204.
- [54] R. Srinivasan, E. Sutcliiffe, B. Braren, Self-developing photo etching of poly(ethylene terephthalate) films by far-ultraviolet excimer laser radiation, *Appl. Phys. Lett.* 51 (1987) 1285.

- [55] T. Lippert, Interaction of photons with polymers: from surface modification to ablation, *Plasma Processes Polym.* 2 (2005) 525–546.
- [56] T. Lippert, J.T. Dickinson, Chemical and spectroscopic aspects of polymer ablation: special features and novel directions, *Chem. Rev.* 103 (2003) 453–485.
- [57] H.J. Busscher, A.W.J. Van Pelt, P. De Boer, H.P. De Jong, J. Arends, The effect of surface roughening of polymers on measured contact angles of liquids, *Colloids Surf.* 9 (1984) 319–331.
- [58] H. Qi, T. Chen, L. Yao, T. Zuo, Hydrophilicity modification of poly(methyl methacrylate) by excimer laser ablation and irradiation, *Microfluid. Nanofluid.* 5 (2008) 139–143.
- [59] S.A. David, T. DebRoy, Current issues and problems in welding science, *Science* 257 (5069) (1992) 497–502.
- [60] B. Xiao, Y.W. Zhang, Laser sintering of metal powders on top of sintered layers under multiple-line laser scanning, *J. Phys. D Appl. Phys.* 40 (21) (2007) 6725–6734.
- [61] J.J. Valencia, P.N. Quested, Thermophysical properties, Casting, in: ASM Handbook, vol. 15, ASM International, 2008, pp. 468–481.
- [62] X. He, J.W. Elmer, T. DebRoy, Heat transfer and fluid flow in laser microwelding, *J. Appl. Phys.* 97 (8) (2005) 084909.
- [63] P.S. Wei, C.N. Ting, J.S. Yeh, T. DebRoy, F.K. Chung, G.H. Yan, Origin of wavy weld boundary, *J. Appl. Phys.* 105 (5) (2009) 053508.
- [64] Z. Yang, T. DebRoy, Modeling macro- and microstructures of gas-metal-arc welded HSLA-100 steel, *Metall. Mater. Trans. B Process Metall. Mater. Process. Sci.* 30 (3) (1999) 483–493.
- [65] X. He, P.W. Fuerschbach, T. DebRoy, Heat transfer and fluid flow during laser spot welding of 304 stainless steel, *J. Phys. D Appl. Phys.* 36 (2) (2003) 1388–1398.
- [66] S. Mishra, T. DebRoy, Measurements and Monte Carlo simulation of grain growth in the heat-affected zone of Ti-6Al-4V welds, *Acta Mater.* 52 (5) (2004) 1183–1192.
- [67] P.A. Molian, Estimation of cooling rates in laser surface alloying processes, *J. Mater. Sci. Lett.* 4 (3) (1985) 265–267.
- [68] P.A.A. Khan, T. DebRoy, Alloying element vaporization and weld pool temperature during laser-welding of AISI 201 stainless-steel, *Metall. Trans. B Prog. Metall.* 15 (4) (1984) 641–644.
- [69] P.R. Willmott, J.R. Huber, Pulsed laser vaporization and deposition, *Rev. Mod. Phys.* 72 (1) (2000) 315–328.
- [70] M.M. Collur, A. Paul, T. Debroy, Mechanism of alloying element vaporization during laser welding, *Metall. Trans. B* 18B (4) (1987) 733–740.
- [71] K. Mundra, Interfacial phenomena in welding: vaporization and gas dissolution (Ph.D. thesis), The Pennsylvania State University, University Park, PA, 1994.
- [72] Y.C. Guan, W. Zhou, H.Y. Zheng, Effect of laser surface melting on corrosion behaviour of AZ91D in simulated-modified body fluid, *J. Appl. Electrochem.* 39 (9) (2009) 1457–1464.
- [73] Y.C. Guan, W. Zhou, H.Y. Zheng, Effect of Nd:YAG laser melting on surface energy of AZ91D Mg alloy, *Surf. Rev. Lett.* 16 (6) (2009) 801–806.
- [74] Y.C. Guan, W. Zhou, H.Y. Zheng, Z.L. Li, Solidification microstructure of AZ91D Mg alloy after laser surface melting, *Appl. Phys. A: Mater. Sci. Process.* 101 (2) (2010) 339–344.
- [75] N. Pierron, P. Sallamand, S. Matteï, Study of magnesium and aluminum alloys absorption coefficient during Nd:YAG laser interaction, *Appl. Surf. Sci.* 253 (6) (2007) 3208–3214.
- [76] R.S. Coelho, A. Kostka, H. Pinto, S. Riekehr, M. Kocak, A.R. Pyzalla, Microstructure and mechanical properties of magnesium alloy AZ31B laser beam welds, *Mater. Sci. Eng. A Struct. Mater.: Prop. Microstruct. Process.* 485 (1-2) (2008) 20–30.

- [77] C.P. Luo, X.L. Xiao, J.W. Liu, J.F. Nie, B.C. Muddle, Multi-orientation relationship and {112} gamma pseudo-twin relationship of gamma-Mg<sub>17</sub>Al<sub>12</sub> precipitates in an AZ91 Mg-Al alloy, *Acta Metall. Sin.* 38 (7) (2002) 709–717.
- [78] Y. Wang, G. Liu, Z. Fan, Microstructural evolution of rheo-diecast AZ91D magnesium alloy during heat treatment, *Acta Mater.* 54 (3) (2006) 689–699.
- [79] J.P. Zhou, D.S. Zhao, R.H. Wang, Z.F. Sun, J.B. Wang, J.N. Gui, O. Zheng, In situ observation of ageing process and new morphologies of continuous precipitates in AZ91 magnesium alloy, *Mater. Lett.* 61 (25) (2007) 4707–4710.
- [80] W.Z. Zhang, G.C. Weatherly, On the crystallography of precipitation, *Prog. Mater. Sci.* 50 (2) (2005) 181–292.
- [81] D. Dubé, M. Fiset, A. Couture, I. Nakatsugawa, Characterization and performance of laser melted AZ91D and AM60B, *Mater. Sci. Eng. A Struct. Mater.: Prop. Microstruct. Process.* 299 (1-2) (2001) 38–42.
- [82] M. Gindl, G. Sinn, W. Gindl, A. Reiterer, S. Tschegg, A comparison of different methods to calculate the surface free energy of wood using contact angle measurements, *Colloids Surf. A. Physicochem. Eng. Aspects* 181 (1-3) (2001) 279–287.
- [83] C.J. van Oss, R.J. Good, M.K. Chaundhury, Additive and nonadditive surface-tension components and the interpretation of contact angles, *Langmuir* 4 (4) (1988) 884–891.
- [84] J. Lawrence, L. Li, Wettability characteristics of an Al<sub>2</sub>O<sub>3</sub>/SiO<sub>2</sub>-based ceramic modified with CO<sub>2</sub>, Nd:YAG, excimer and high-power diode lasers, *J. Phys. D Appl. Phys.* 32 (10) (1999) 1075–1082.
- [85] C.H. Olk, D.B. Haddad, Growth and structure of a combinatorial array of mixed-phase magnesium-aluminum thin-film alloys, *Appl. Phys. A Mater. Sci. Process.* 88 (2) (2007) 249–253.
- [86] X.P. Zhang, S.R. Yu, Z.M. He, Y.X. Miao, Wetting of rough surfaces, *Surf. Rev. Lett.* 11 (1) (2004) 7–13.

This page intentionally left blank

# Femtosecond laser micromachining on optical fiber

14

D.N. Wang<sup>1,2,3</sup>, Y. Wang<sup>2,4</sup>, C.R. Liao<sup>2,5</sup>

<sup>1</sup>China Jiliang University, Hangzhou, China; <sup>2</sup>The Hong Kong Polytechnic University, Hong Kong, China; <sup>3</sup>Hubei Polytechnic University, Huangshi, China; <sup>4</sup>Wuhan Institute of Technology, Wuhan, China; <sup>5</sup>Shenzhen University, Shenzhen, China

## 14.1 Introduction

The advent of femtosecond pulsed lasers in the 1980s brought remarkable advances in the field of laser processing. Femtosecond laser pulses exhibit ultrashort pulse durations ( $\sim 10^{-15}$  s), extremely high peak power ( $\sim 10^{14}$  W/cm<sup>2</sup>), and strong nonlinearity during the laser-material interaction. They can be used to process nearly all kinds of materials including metals, semiconductors, and dielectrics such as crystals, glasses, and ceramics with micrometer and submicrometer scale micromachining accuracies and negligible heat effects [1–3]. Femtosecond laser micromachining is of great interest for the processing of transparent materials, such as glasses, in which “true” three-dimensional micromachining can be readily achieved [4].

The mechanism of the femtosecond laser-matter interaction differs among metals, semiconductors, and transparent materials. Metals can absorb both visible and near infrared light because they possess large numbers of free electrons, while photons with these frequencies cannot be directly absorbed by semiconductors and transparent dielectrics as electrons are in bound states in these materials. However, the nonabsorption behavior changes when the laser beam intensity is sufficiently high in semiconductors and transparent materials, where a nonlinear interaction between laser light and material occurs. When femtosecond pulses are propagating in transparent materials such as fused silica, nonlinear processes including self-focusing, self-phase modulation, group velocity dispersion, and supercontinuum generation can be induced by the ultrahigh beam intensity [5–7].

When a femtosecond laser beam is focused into transparent dielectrics, bound electrons can absorb the energy of femtosecond pulses through multiphoton absorption and avalanche ionization processes; thus, the substances in the focal volume can be ionized to plasma immediately, further absorbing the laser pulse energy and resulting in Coulomb explosion, local heating, or optical breakdown of materials [4,8–11].

### 14.1.1 Multiphoton ionization and tunneling ionization

There are two nonlinear photoionization processes to ionize bound electrons from the valence band (bound state) to the conduction band (free state) of the dielectrics, which are multiphoton ionization and tunneling ionization, respectively [12]. Multiphoton

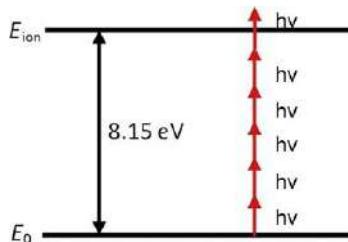


**Figure 14.1** Multiphoton ionization process in silicon due to simultaneous absorption of 6 photons.  $h\nu$  is the photon energy,  $E_0$  is the ground state, and the first ionization energy ( $E_{\text{ion}}$ ) of silicon is  $\sim 8.15$  eV.

ionization occurs with extremely high photon degeneracy of the laser light where the valence electron can be ionized through the absorption of several photons simultaneously and the ionization probability is proportional to the  $k$ th order of the laser intensity  $I$  ( $k$  is the minimum number of photons, the total energy of which is no smaller than the ionization energy of the valence electron). Figure 14.1 shows the schematic of multiphoton ionization process of silicon. The first ionization energy ( $E_{\text{ion}}$ ) of silicon is  $\sim 8.15$  eV, which requires 6 photons of 800-nm-wavelength laser pulses to be absorbed simultaneously to ionize the bound electron from the ground state ( $E_0$ ) to the free state.

Electrons in the bound state can also be excited into the free state through a tunneling ionization process, that is, the bound electron can move across the quantum potential barrier in dielectrics through the tunneling effect to become free electrons. In fact, tunneling ionization and multiphoton ionization can be described with the same theoretical system and distinguished by the well-known Keldysh parameter  $\gamma$

$$\gamma = [I_p / (2U_p)]^{1/2} \quad (14.1)$$

where  $I_p$  and  $U_p$  are the ionization and ponderomotive energy of the atom, respectively.  $\gamma > 1$  corresponds to the multiphoton ionization process, while  $\gamma < 1$  corresponds to the tunneling ionization process.

### 14.1.2 Avalanche ionization

There are always a few free electrons (also called seed electrons) that can absorb the energy of laser pulses through the inverse bremsstrahlung process [13]. Seed electrons mainly originate from the thermal excitation (or Zener tunneling process) of the impurity in materials. Once the kinetic energy of a seed electron is larger than the potential energy of the bound electrons, the seed electron is able to ionize the bound electron through collision and two free electrons with lower kinetic energy are produced. This procedure repeats and leads to avalanche ionization [14]. It is worth noting that multiphoton ionization dominates the ionization process during femtosecond laser-matter interaction, because the ionization rate of multiphoton ionization is larger than that of the avalanche ionization for ultrashort laser pulses.

### 14.1.3 Coulomb explosion

Electrons will be ionized and escape from the femtosecond laser irradiated region due to the ultrahigh peak power, leaving ions behind with relatively low temperature and extremely high charge density and static electric field. Once the electrostatic force is beyond that between the crystal lattice, the chemical bond breaks and leads to the lattice fracture, which is known as “Coulomb explosion” [15]. Theoretical and experimental results obtained indicate that Coulomb explosion can be observed in dielectrics, but not in metals and semiconductors, during the ultrashort pulsed laser-matter interactions [16].

## 14.2 Femtosecond laser micromachining of optical fibers

Optical fibers are commonly made of fused silica, which is a typical transparent dielectric material. Near infrared femtosecond laser pulses can be focused onto the surface or into the bulk of the glass fibers to ablate fiber materials or modify their refractive index distribution within the fiber [10,17]. Thus, techniques for femtosecond laser micromachining of dielectrics, including interference, direct writing, optical lithography, and so on, can be implemented on optical fibers [17–19]. Among them, femtosecond laser beam interference and direct ablation/modification are the most commonly used.

### 14.2.1 Femtosecond laser beam interference

Figure 14.2 shows the experimental two-beam interference arrangement of femtosecond laser pulses, which is the same as in traditional optical interference experiments. The femtosecond laser beam is launched onto a phase mask, by which the incident

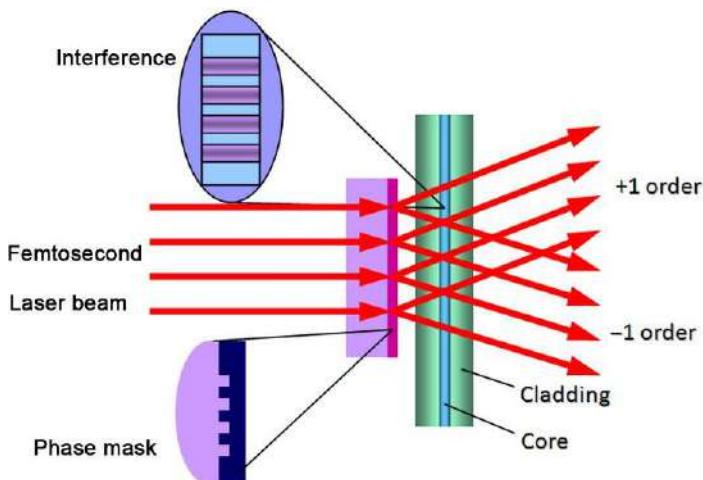


Figure 14.2 Two-beam interference of the femtosecond laser assisted with a phase mask.

beam is diffracted to  $\pm 1$  order beams causing an interference pattern to be produced at the exit of the phase mask. The interference periodicity is determined by the incident wavelength and the Bragg angle of the phase mask. When an optical fiber is positioned at the interference region, the periodic distributed light intensity will result in a periodic modulation of the refractive index in the fiber core and hence the fiber grating forms. The grating resonance can be monitored by use of a broadband light source and an optical spectrum analyzer in real time to avoid oversaturation.

#### 14.2.1.1 Phase mask

The fiber Bragg gratings (FBGs) fabricated by use of the femtosecond laser interference have been broadly investigated, which exhibit advantages such as H<sub>2</sub>-load-free and high temperature durability [20,21].

#### 14.2.2 Femtosecond laser direct writing

Direct writing is a basic method for femtosecond laser micromachining; this is flexible and possesses a high degree of freedom to fabricate microstructures from 0 to 3 dimensions. In-fiber microstructures such as microcavity interferometers, point-by-point or line-by-line inscribed gratings, and other structural devices have been fabricated based on this method [22–25].

Figure 14.3 shows the experimental setup for femtosecond laser direct writing of optical fibers. The laser beam is launched into a microscope objective to be focused

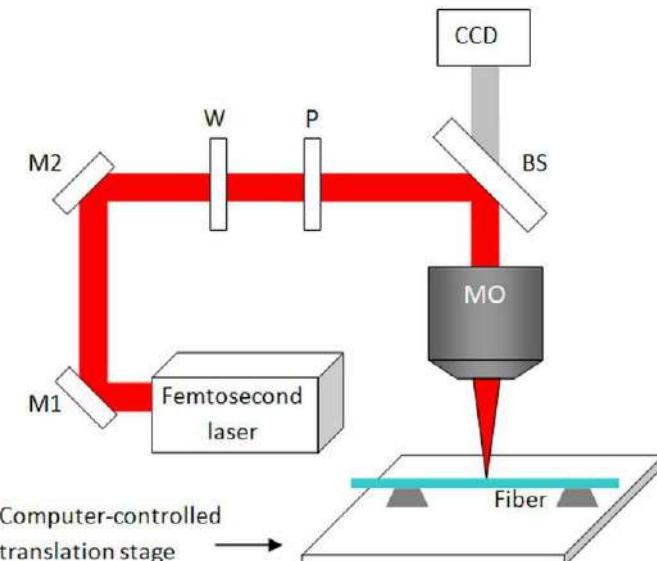


**Figure 14.3** Experimental setup for femtosecond laser direct writing of optical fibers. CCD, charge-coupled device camera; MO, microscope objective; BS, beam splitter; W, half-wave plate; P, polarizer; M1, M2: optical mirrors.

onto the optical fiber, which is mounted on a computer-controlled three-dimensional translation stage. The pulse energy can be adjusted through the combination of a half-wave plate and polarizer, then the micromachining process is monitored by CCD in real time.

The micromachining quality is mainly determined by the writing directions (parallel or perpendicular to the beam direction), repetition rate, pulse energy, and scanning speed. Perpendicular writing is often used to perform line scanning, either with ablation or refractive index modification. For drilling applications, parallel writing is often required. The spot size and spatial intensity distribution of the focused laser beam can be modified by use of microscope objectives with different numerical apertures or optical beam-shaping elements to fulfill the requirements of various applications.

## 14.3 Optical fiber microstructures fabricated by femtosecond laser micromachining

### 14.3.1 Fiber Bragg grating

Recently, FBGs fabricated by use of femtosecond laser pulse irradiation have attracted considerable attention, especially in high-temperature sensing applications. The first FBG was inscribed on standard Ge-doped telecom fiber (Corning SMF-28) by use of 800 nm, 120 fs laser irradiation and a deep-etch silica zero-order nulled phase mask by Mihailov's group in 2003 [20]. In 2004, direct point-by-point inscription of FBGs by femtosecond laser was reported by Bennion's group; this method did not require a phase mask and offered remarkable technological flexibility [26]. Figure 14.4a and b shows the axial and the cross-sectional morphology of the damaged FBG fabricated by femtosecond laser. A clear grating structure was obtained and the groove structure induced by the severe laser ablation goes beyond the core and the material modification in the core is highly disordered, being quite analogous to the birefringence zone of Type II damage [27].

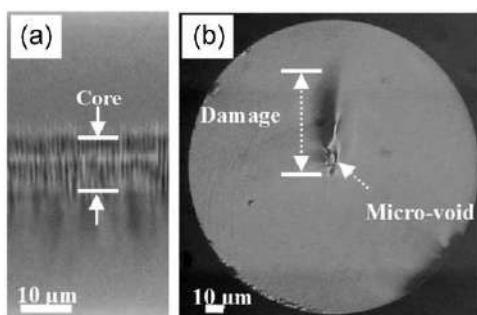


**Figure 14.4** (a) The axial morphology of damaged FBG fabricated by femtosecond laser and (b) the cross-sectional morphology in grating area.

### 14.3.2 Long period fiber grating (LPFG)

A femtosecond laser was also used to write LPFGs of which the grating period is approximately 100–1000  $\mu\text{m}$ . The first experimental realization of LPFGs written in SMF via focused irradiation of infrared femtosecond laser pulses was carried out by Kondo *et al.* in 1999 [28]. Successively, LPFGs have been successfully inscribed in the fiber with pure silica core [29] and the near-single-mode  $\text{GeO}_2$  glass fiber [30] by femtosecond laser inscription. In 2008, Allsop *et al.* reported a series of symmetric and asymmetric LPFGs inscribed in photonic crystal fiber (ESM fiber from Crystal Fiber A/S) [31]. In light of the fast growth of photonic crystal fiber and its special structure property, femtosecond laser writing of LPFGs is currently attracting much more attention.

Figure 14.5 illustrates the schematic diagram of the experimental setup for LPFG fabrication by use of femtosecond laser with a line-scanning method [25]. The beam was focused onto the fiber core by a microscope objective and the fiber was fixed to a computer-controlled XYZ-translation stage. During the inscription process, the stage was moved at a constant speed along the designed pattern, translating the fiber with respect to the focal point of the beam. In this figure, the period of the LPFG was chosen as 640  $\mu\text{m}$ . The transmission spectrum of the LPFG was measured *in situ* by a broadband source and an optical spectral analyzer.

### 14.3.3 Microhole structure

By local irradiation of femtosecond laser, a single microhole can be drilled without moving the laser focus point transversely. The single pulse energy and the femtosecond laser irradiation time will decide the dimensions of the fabricated microhole. Normally, larger pulse energy together with longer laser irradiation time will result in a

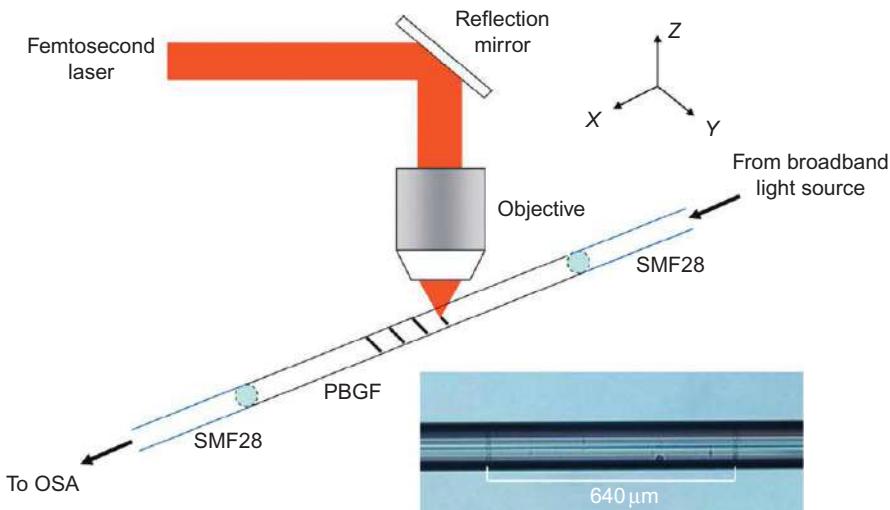


**Figure 14.5** Schematic diagram of the experimental setup for LPFG fabrication by use of femtosecond laser with line-scanning method. Insets: optical microscope image of the side view of LPFG.

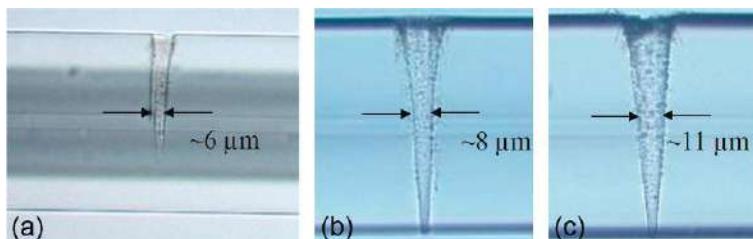


**Figure 14.6** Microholes with different  $D$  values: (a) 6  $\mu\text{m}$ , (b) 8  $\mu\text{m}$ , and (c) 11  $\mu\text{m}$ .

larger diameter and depth of the microhole. The numerical aperture value of the focusing objective will also affect the microhole morphology.

Using this method, microholes can be directly drilled in fibers without any chemical etching procedure. This has the advantages of easy fabrication and high robustness [32]. Three types of microholes are fabricated with individual average diameter ( $D$ ) values chosen for smaller than, close to, and larger than the fiber core diameter. The morphologies of each microhole are shown in Figure 14.6a–c. The directly drilled microholes possess a cone shape.

In 2006, researchers from Aston University reported the fabrication of microchannels within SMFs based upon femtosecond laser exposure combined with chemical etching [33]. In the fabrication process, the desired structure was inscribed into the fiber by use of a tightly focused femtosecond laser beam followed by etching in a solution of 5% hydrofluoric acid for selective removal of the laser-modified region. This method takes advantage of high spatial resolution inherent to femtosecond laser inscription and the preferential chemical etching of the modified material to realize the designed microchannels within fiber.

Strong structural modulated LPFG can be made by periodically drilling multiple microholes along the fiber. The airhole structured LPFG introduces a strong and asymmetric structural modulation in the fiber core and cladding. This couples light from the fiber core mode to the cladding mode in a relatively efficient way by supporting a small grating dimension. The microhole-structured LPFG can be formed in different types of optical fibers such as SMF and PCFs [34–36]. Figure 14.7 shows the morphologies and the transmission spectrum evolution of the microhole-structured LPFG in SMF. The depth of the resonance peak of around 1517 nm becomes saturated when 15 grating periods are created, which is over 20 dB with an insertion loss of ~15 dB. The depth would dramatically decay if the number of grating periods were further increased due to overcoupling. The resonance peak near 1404 nm is created due to the coupling of the fundamental core mode to another lower-order cladding mode.

#### 14.3.4 Fiber in-line interferometer

In recent years, fiber in-line interferometers have attracted considerable research interests because of their compactness, ease of construction, and convenient operation in many sensing applications. Various types of fiber in-line interferometer configurations have been demonstrated, such as the Fabry-Perot interferometer, Mach-Zehnder

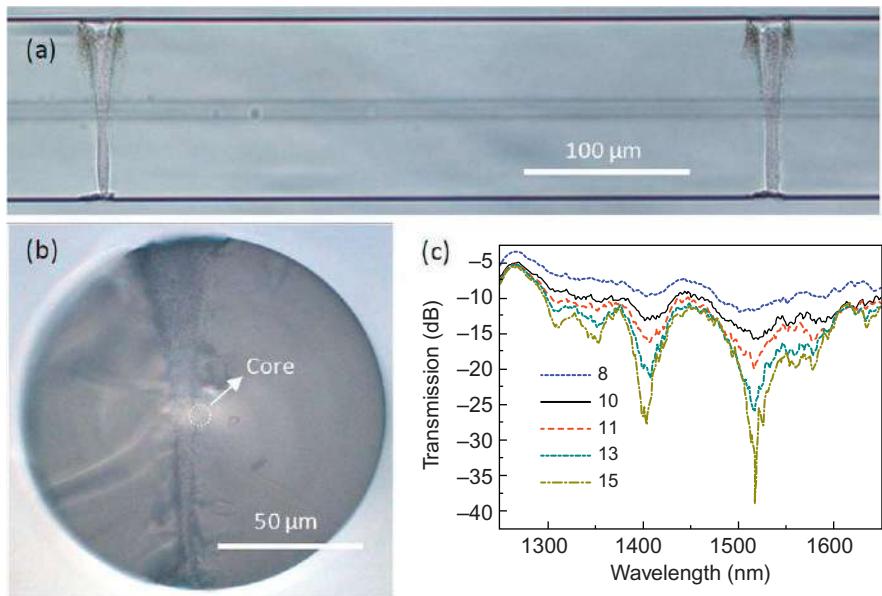


**Figure 14.7** (a) Morphology of an microhole-structured LPFG with the grating period of 450  $\mu\text{m}$ . (b) Cross-section view of the grating pitch, that is, the microholes. (c) Evolution of the transmission spectrum of the LPFG.

interferometer, and Michelson interferometer, based on the open air-cavity fabricated by femtosecond laser drilling in the fiber [22,23,37–39].

Due to the small laser spot of femtosecond laser, the length of the cavity could be accurately controlled in the micrometer order. The first fiber in-line Fabry-Perot interferometer was fabricated by use of femtosecond laser micromachining of a rectangular nonthrough hole into a SMF [22]. The length of the hole was only 80  $\mu\text{m}$ . This Fabry-Perot interferometer had a fringe visibility of 2 dB. Later, Wei *et al.* also demonstrated a fiber in-line Fabry-Perot interferometer with a better fringe visibility of 16 dB by femtosecond laser one-step micromachining of a micronotch on a SMF [37].

In a fiber in-line Mach-Zehnder interferometer, one of the interferometer arms contains a microcavity created by removing part of the fiber core near the core and cladding interface; the other lies in the remaining part of the fiber core. The light was split into two portions and transmitted in the two arms individually. Interference occurs when the two output rays combine at the other core-cavity wall, which forms a Mach-Zehnder interferometer, as shown in Figure 14.8.

In a fiber in-line Michelson interferometer, part of the fiber core near one of the fiber ends is removed. High-reflectivity metal film is deposited on the fiber core and end surfaces to increase the reflectivity. The input light beam is split into two portions denoted by  $E_1$  and  $E_2$ , respectively, with a splitting ratio that depends on the diameter of the remaining fiber core. After being reflected back by the fiber end,  $E_1$  is recombined with  $E_2$  at the cut end of the removed fiber core, resulting in interference.

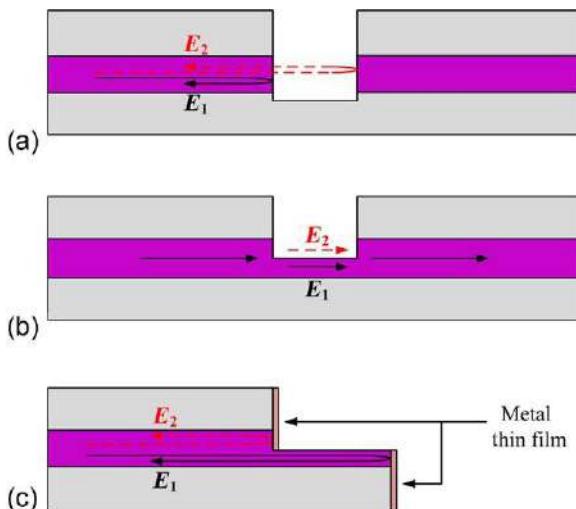


**Figure 14.8** Configuration of various fiber in-line interferometers fabricated by use of femtosecond laser micromachining: (a) Fabry-Perot interferometer; (b) Mach-Zehnder interferometer; and (c) Michelson interferometer.

## 14.4 Optical sensing devices based on optical fiber microstructures

### 14.4.1 Femtosecond laser fabricated FBG sensors

It is known that FBGs inscribed by UV laser usually exhibit poor stability at temperatures greater than 500 °C. Damaged FBGs fabricated by use of femtosecond laser pulses have a local refractive index change range on the order of  $10^{-2}$ , which is thermally stable above 1000 °C [28]. Thus, femtosecond laser-inscribed FBGs have become a promising candidate in high-temperature sensing applications.

Femtosecond laser-induced FBGs in SMF exhibit stable performance below 1050 °C. The glass transition temperature ( $T_g$ ) of pure silica is approximately 1330 °C but material doping in silica fiber reduced the  $T_g$  to a certain degree. Experiments showed that the highest temperature that silica fiber can survive is lower than 1330 °C. Li *et al.* believed the residual stress that existed in the fiber had some negative effects on the fiber reliability and grating quality and, consequently, the thermal stability. In their experiment, the damaged FBGs were inscribed in SMFs with relaxed residual stress by the use of an annealing treatment at high temperature. The FBG with a preannealing treatment at 1100 °C demonstrates excellent thermal stability at temperatures of up to 1200 °C for more than 20 h [21]. Being superior to silica fiber, single crystal sapphire has a higher melting temperature (~2050 °C). Grobnić *et al.* reported the FBGs fabricated in multimode sapphire fiber by use of femtosecond laser irradiation; such FBGs were tested to be thermally stable up to 1500 °C [40].

Pressure sensors operated at high temperature have many important applications in the energy industry, such as operation of gas turbines, coal boilers, nuclear power plants, and others. A novel FBG pressure sensor based on femtosecond laser-fabricated FBG in airhole microstructured fibers was developed for high-temperature operation above 800 °C [41]. In comparison with other fiber optical pressure sensors, such FBG pressure sensors can be easily multiplexed for a sensor network.

#### 14.4.2 Femtosecond laser fabricated LPFG sensors

LPFG fabrication by UV-laser irradiation has a problem with an aging stability because the index change relaxes even below 100 °C. Femtosecond laser-induced LPFGs are more thermally stable and exhibit no degradation of grating performance from 20 to 500 °C. Kondo *et al.* reported the temperature sensitivity of such LPFG within SMF of 0.098 nm/°C [28]. This sensitivity value is almost the same as the values of LPFGs fabricated by UV-light irradiation in SMFs.

LPFG fabricated in all-solid photonic bandgap fibers by use of femtosecond laser with line scanning was reported in 2010 [25]. The coupling from the fundamental core mode to LP<sub>11</sub> mode can be readily obtained. Figure 14.9a shows the transmission spectrum evolution of the LPFG. The resonance wavelength of the LPFG created is located at 1542.3 nm, with a full-width at half-maximum value of ~24 nm; the strongest resonance was measured as ~19 dB. The resonant wavelength of the grating is found to be highly sensitive to tensile strain. Figure 14.9b shows the result of tensile strain test. There is a linear “blue” shifting for the resonant wavelength with the increase of applied tensile strain. The measured sensitivity is  $-1.8 \text{ nm/m}\varepsilon$ , this being four times higher than those of LPFGs in conventional SMFs.

Microhole-structured LPFGs within SMF fabricated by femtosecond laser drilling shows a good performance in liquid refractive index sensing [36]. The average refractive index sensitivity obtained is  $\sim 190 \text{ nm/RIU}$  (refractive index unit) between 1.31 and 1.38. With the increase of the surrounding refractive index value, the resonance wavelength of the LPFG experiences a “red shift,” being different from the “blue shift” characteristics of the traditional LPFGs fabricated by UV light or CO<sub>2</sub> laser

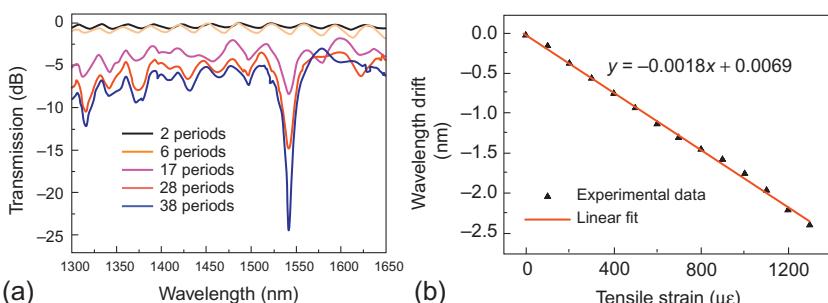


**Figure 14.9** (a) Evolution of the transmission spectrum of LPG with the increase of period number (from 2 to 38), the grating pitch is 640 μm and (b) tensile strain measurement.

in SMF. The “red shift” can be explained by use of the phase-matching curve of the microhole-structured LPFG. The waveguide dispersion is defined as

$$\gamma = (\mathrm{d}\lambda_{\mathrm{res}}/\mathrm{d}A)/\Delta n_{\mathrm{eff}}$$

where  $\lambda_{\mathrm{res}}$  is the resonant wavelength,  $A$  is the grating period, and  $\Delta n_{\mathrm{eff}}$  is the effective index difference between the fundamental core mode and the cladding mode. In general, the  $\mathrm{d}\lambda_{\mathrm{res}}/\mathrm{d}A$  term is negative for UV or CO<sub>2</sub> laser written LPFG in SMF; however, this term becomes positive for the microhole-structured LPFGs.

#### **14.4.3 Femtosecond laser fabricated fiber in-line interferometer sensors**

In 2007, Rao *et al.* first reported to directly machine a micro Fabry-Perot interferometer on SMF and PCF by using a near infrared femtosecond laser [22]. The wavelength-strain sensitivity of the SMF Fabry-Perot interferometer sensor and the PCF Fabry-Perot interferometer sensor were measured to be 0.006 and 0.0045 nm/ $\mu\epsilon$ , respectively. Such a sensitivity is about five times larger than that of an in-line SMF etalon sensor. Besides, the wavelength-temperature sensitivity of the SMF Fabry-Perot interferometer sensor is  $-0.0021 \text{ nm}/^{\circ}\text{C}$ , which is close to that of the PCF Fabry-Perot interferometer sensor, that is,  $-0.002 \text{ nm}/^{\circ}\text{C}$ . Accordingly, these sensors could find wide applications in practice due to their outstanding advantage of having high strain sensitivity and low temperature sensitivity.

In 2008, Wei *et al.* reported a similar fiber in-line Fabry-Perot interferometer configuration, with an open micronotch cavity fabricated by one-step femtosecond laser micromachining, for highly sensitive refractive index measurement [37]. The sensitivity for measurement of refractive index change was 1163 nm/RIU at 1550 nm. The temperature cross-sensitivity of the device was about  $1.1 \times 10^{-6} \text{ RIU}/^{\circ}\text{C}$ . The small size, all-fiber structure, small temperature dependence, linear response, and high sensitivity make the device attractive for chemical and biological sensing.

In 2010, a compact fiber in-line Mach-Zehnder interferometer was obtained by femtosecond laser micromachining [23]; this solution is different to the configuration of the fiber in-line Fabry-Perot interferometer because one arm of the Mach-Zehnder interferometer contains a microcavity created by removing part of the fiber core near the core-cladding interface and the Fabry-Perot lies in the remaining part of the fiber core. The interference occurs when the two output light beams are combined at the other core-cavity wall, which forms a Mach-Zehnder interferometer. The side view optical microscopic image of the Mach-Zehnder interferometer and the SEM cross-section image of the microcavity are shown in Figure 14.10a and b, respectively. Figure 14.10c shows the result of liquid refractive index measurement. The interferometer exhibits a high refractive index sensitivity of  $\sim -9370 \text{ nm}/\text{RIU}$  within the refractive index range between 1.31 and 1.335. Moreover, a precise sensing location can be ensured owing to the small size of the interferometer.

This fiber in-line Mach-Zehnder interferometer can also be employed in high-temperature measurements [42]. Figure 14.11a shows the transmission spectra at

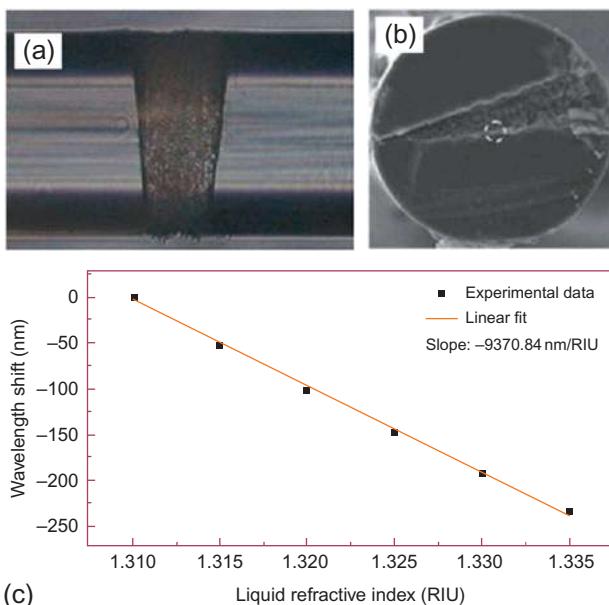


**Figure 14.10** (a) Optical microscope image of the microcavity (side view); (b) SEM image of the microcavity, the dashed white circle indicates the fiber core (cross-section view); and (c) fringe dip wavelength shift versus the liquid refractive index.

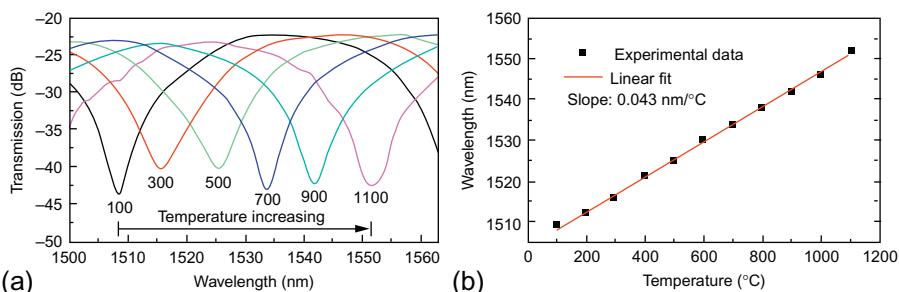


**Figure 14.11** Interference fringes of the Mach-Zehnder interferometer at different temperatures.  
(a) Transmission spectra and (b) wavelength shift versus the temperature increasing.

several temperature points, and it can be clearly seen that the dip shifts toward the longer wavelength with the increase of temperature. Figure 14.11b presents the wavelength shift of the dip versus temperature and exhibits a sensitivity of  $\sim 0.043 \text{ nm/}^{\circ}\text{C}$ . The temperature sensitivity originates from the difference of the temperature coefficients of refractive index between the fiber core and air.

In 2012, a fiber in-line Michelson interferometer was fabricated by the combination of femtosecond laser micromachining and thin-film coating for refractive index measurement [43]. The optical microscope image of the fiber interferometer is shown in Figure 14.12a and the interferometric spectrum with a cavity length of  $\sim 38 \mu\text{m}$  in air

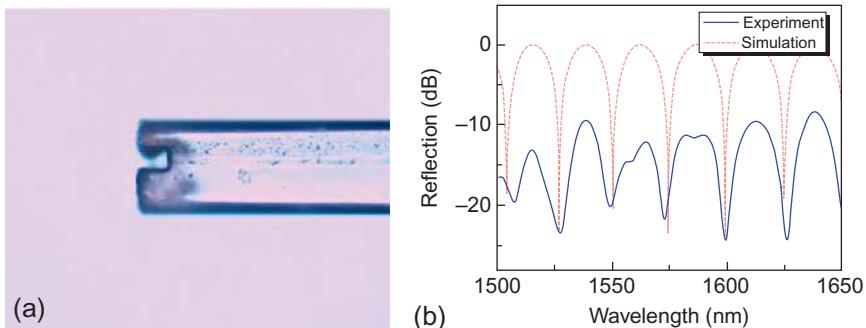


**Figure 14.12** (a) Optical microscope image of the fiber in-line Michelson interferometer and (b) output spectrum of the fiber interferometer with a cavity length of  $\sim 38 \mu\text{m}$ .

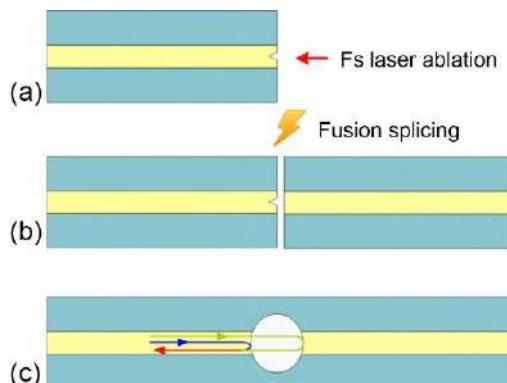


**Figure 14.13** (a) Microhole produced by femtosecond laser ablation; (b) fiber tip with microhole spliced together with another cleaved SMF; and (c) hollow sphere formed in SMF.

is shown in [Figure 14.12b](#), where the red dotted line represents the calculated spectrum based on two-beam interferometry. In refractive index sensing, such an interferometer shows a wide measurement range and a high sensitivity of  $\sim 975 \text{ nm/RIU}$  at the refractive index value of 1.484 and it can be operated at the reflection mode, which is attractive in many sensing applications.

The micro-open-cavity interferometer is easily cracked due to the laser-induced damage within fiber. [Figure 14.13](#) shows a novel fiber in-line Fabry-Perot interferometer fabricated by femtosecond laser micromachining and fusion splicing [44]. A hollow-sphere cavity is formed by drilling a microhole at the end facet of SMF, followed by fusion splicing. The incident light beam along the SMF is reflected by the two surfaces of the sphere, respectively, and recombined in the fiber core, resulting in an interference spectrum at the output. By using different initial microhole sizes and fusion splicing parameters, different sizes of hollow sphere and hence different cavity lengths could be created.

[Figure 14.14a](#) shows three hollow spheres with different cavity lengths of 30, 65, and  $93 \mu\text{m}$ , respectively, corresponding to the initial microhole diameter of 1, 1, and  $10 \mu\text{m}$ ; the fusion current of 15.3, 16.8, and 17.3 mA; and the fusion duration of 1.5,

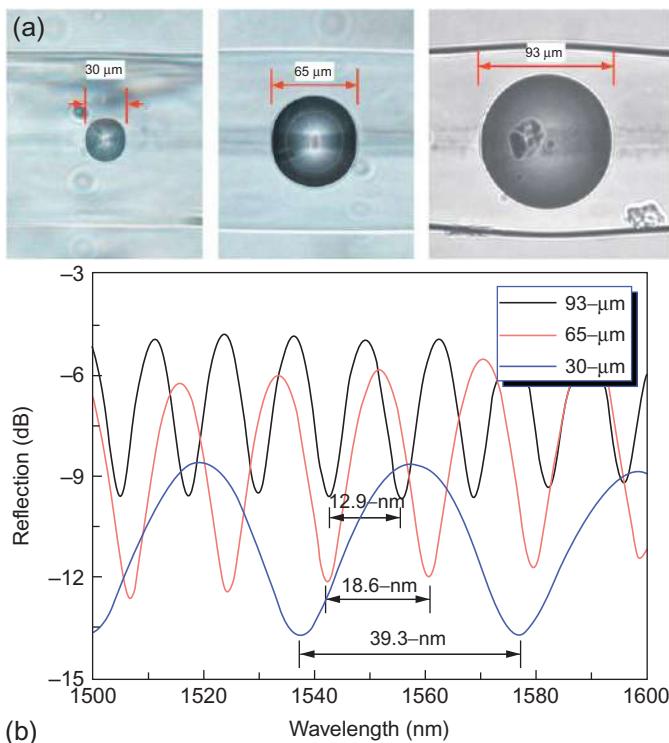


**Figure 14.14** (a) Optical microscope images of the Fabry-Perot interferometer cavity with lengths of 35, 70, and 105  $\mu\text{m}$ , respectively and (b) reflection spectra of fiber in-line Fabry-Perot interferometer with different cavity lengths.

2.0, and 2.0 s, respectively. The reflection spectra corresponding to different cavity lengths are displayed in Figure 14.14b.

To realize liquid refractive index sensing, microchannels were machined vertically cross the FP cavity, which allowed the refractive index liquid to readily flow in or out of the cavity. Figure 14.15 shows the reflection spectra in different refractive index liquids and the wavelength dip experiences a “red shift” with the increase of refractive index. The refractive index sensitivity obtained is  $\sim 994 \text{ nm/RIU}$ ; the temperature cross-sensitivity of the sensor is  $\sim 4.8 \times 10^{-6} \text{ RIU/}^{\circ}\text{C}$ . Such a device is simple in configuration; easy for fabrication and reliable in operation due to extremely low temperature cross sensitivity.

#### 14.4.4 Combined microstructures in optical fiber for multiple parameter sensing

In situ monitoring of liquid RI is of great importance for many chemical/biological applications. One of the major concerns in the determination of refractive index value is the temperature cross-sensitivity, which leads to an unreliable measurement. It is

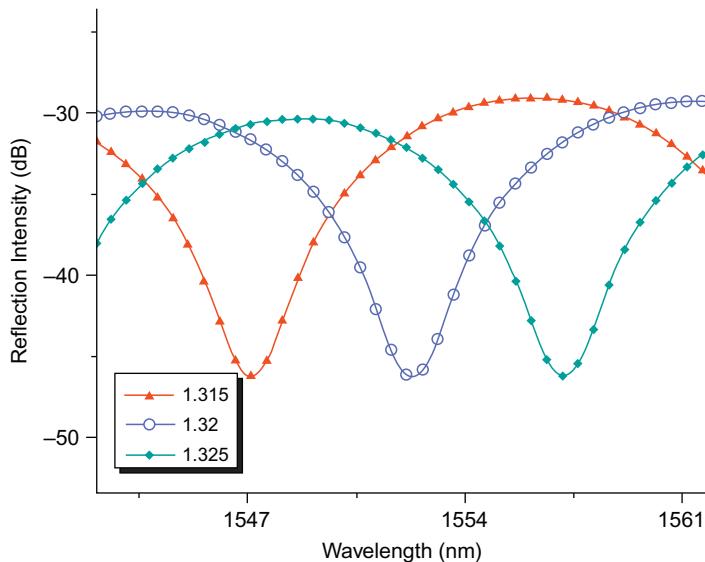


**Figure 14.15** The reflection spectra at the refractive index of 1.315, 1.32, and 1.325, respectively.

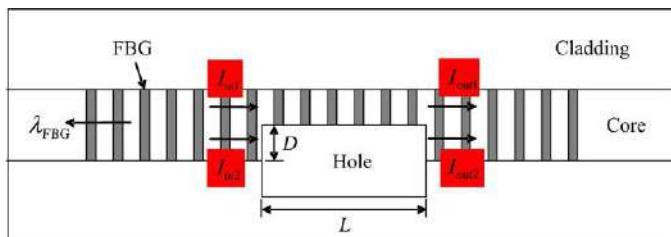


**Figure 14.16** Schematic diagram of the sensor based on a Mach-Zehnder interferometer embedded in FBG.

critical that the temperature and refractive index be simultaneously and unambiguously measured. A compact optical fiber refractive index sensor based on an in-line Mach-Zehnder interferometer embedded in FBG was fabricated by use of femtosecond laser micromachining [39]. **Figure 14.16** shows the schematic diagram of the combined two-parameter sensor.

**Figure 14.17a** shows the transmission spectrum of the sensor for different refractive index values, that is,  $n = 1$  (air), 1.30, 1.31, and 1.32. It can be clearly observed that an increase of the refractive index value leads to a “blue shift” of Mach-Zehnder interferometer spectrum, while the resonance wavelength of the FBG is essentially unchanged. **Figure 14.17b** shows that the Mach-Zehnder interferometer spectrum is extremely sensitive to the refractive index change with an almost linear response, whereas the resonance wavelength of the FBG remains to be a constant. The sensitivity coefficient obtained is  $-9148 \text{ nm/RIU}$  within the range between 1.30 and 1.325.

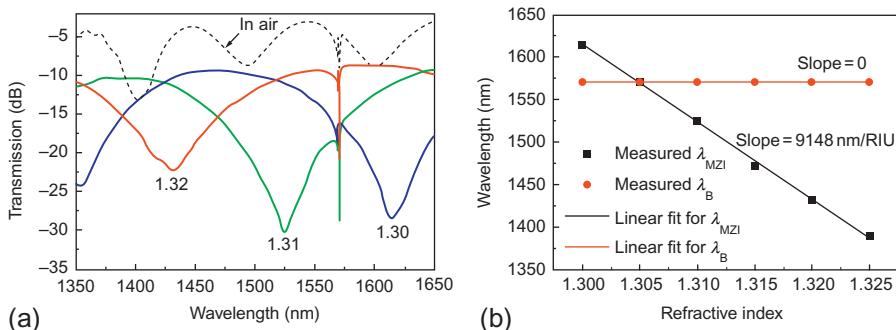


**Figure 14.17** (a) Transmission spectrum of the sensor in different refractive indexes (air, 1.30, 1.31, and 1.32) and (b) relationship between the resonance wavelength of the FBG,  $\lambda_B$ , Mach-Zehnder interferometer fringe dip wavelength,  $\lambda_{MZI}$ , and refractive index.

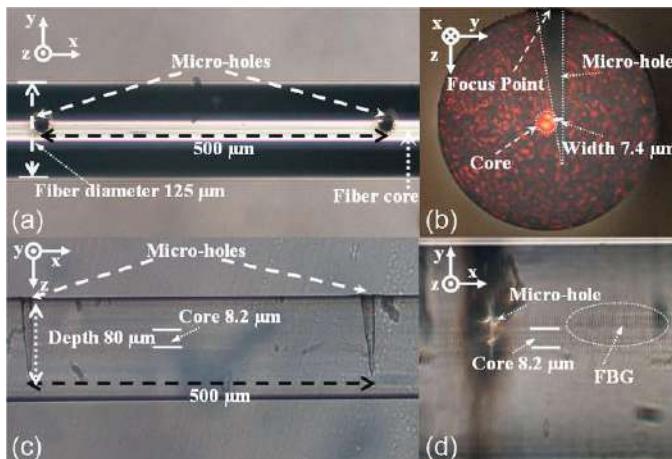


**Figure 14.18** Morphology of the device. (a) Top view (focused at fiber cladding surface); (b) cross-section view; (c) side view; and (d) top view (focused at fiber core).

Based on the matrix method, a simultaneous and unambiguous refractive index and temperature sensing can be achieved. Owing to the ultracompact size of the Mach-Zehnder interferometer cavity, a precise sensing location can be guaranteed.

Another microstructure embedded FBG sensor for simultaneous measurement of refractive index and temperature is achieved by placing asymmetrical located microholes along the fiber length [45]. These microholes can introduce scattering loss in the transmission without significantly destroying the FBG periodical structure in the core center. In order to enhance the refractive index sensing, multiple microholes are drilled. The configuration of the sensing element is shown in Figure 14.18.

Due to the temperature insensitive property of the microhole, this device can achieve simultaneous and independent temperature and refractive index sensing by direct detection of the FBG resonant wavelength shift and its intensity variation.

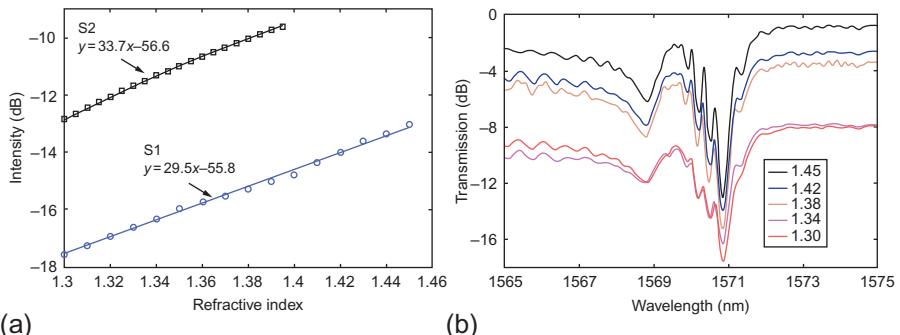


**Figure 14.19** Individual refractive index measurement. (a) FBG dip intensity versus refractive index (circles: S1; squares: S2) and (b) selected transmission spectra of S1 in different refractive index liquids.

The two parameters can be determined by tracing only one characteristic wavelength, which can largely simplify the detection system.

Figure 14.19a shows the FBG response of the two samples to the refractive index change, where the intensity was measured at the FBG resonant dip. The refractive index sensitivity obtained for S1 is  $\sim 29.5$  dB/RIU in the RI region 1.300-1.450. Both the samples exhibit similar refractive index sensitivity and linear regression values, which ensure a good linearity. Meanwhile, both the resonant dips do not shift with the increase of refractive index, owing to the fact that only a small portion of the fiber core is actually exposed to the external medium. This means that light energy is mainly bounded inside the fiber core and, thus, the effective refractive index of the core mode hardly changes with the variation of external refractive index. Figure 14.19b shows the transmission spectra of S1 in different refractive index liquids, and no shift of dip wavelength is observed.

Individual temperature measurement was performed by placing S1 in an oven, exposed to air, detecting the shift when the temperature was increased from 20 to 90 °C. The sensitivity obtained is 10.7 pm/°C, as shown in Figure 14.20.

## 14.5 Current and future trends

The microstructures fabricated by femtosecond laser micromachining such as micro-holes and open air cavities [22,23,32–36] have poor robustness, which essentially limits their application. One of the efficient ways to enhance the robustness of the optical fiber devices is to fabricate inner microstructures in optical fibers.

Figure 14.21 shows the schematic diagram of a fiber in-line Mach-Zehnder interferometer based on an inner air cavity adjacent to the fiber core [46]. The air cavity is fabricated by using femtosecond laser micromachining together with the fusion splicing technique. Light propagating in the fiber core is divided into two portions: one passing through the air cavity and the other traveling along the fiber core, before recombining at the air cavity end. Such an inner air cavity-based Mach-Zehnder

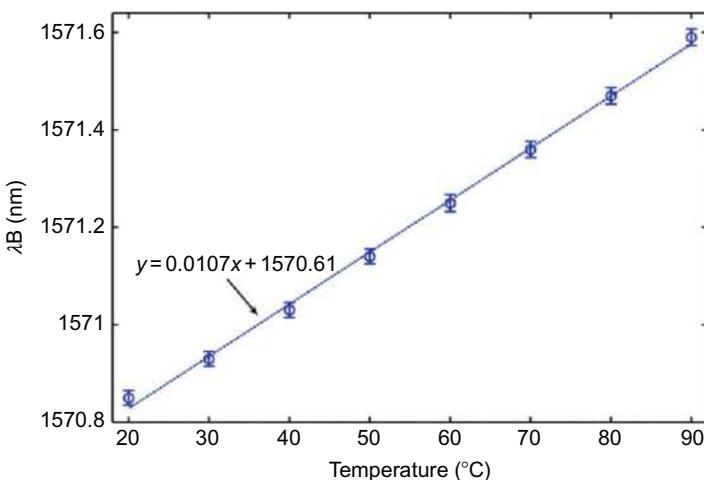


**Figure 14.20** Individual temperature measurement: FBG resonant wavelength of S1 versus temperature (circles: experimental results; dotted line: linear fitted).

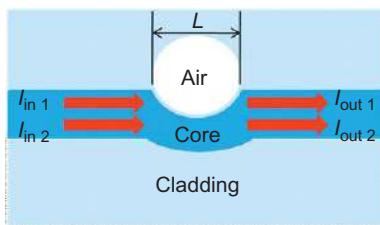


**Figure 14.21** Schematic diagram of the fiber in-line Mach-Zehnder interferometer.

interferometer is miniature and robust, responds linearly to temperature, with high sensitivity of  $\sim 43.2 \text{ pm}^\circ\text{C}$  up to  $1000^\circ\text{C}$ , while being insensitive to the surrounding refractive index variation.

A long-standing goal of optical fiber devices is the development of a miniature and versatile optical fiber component that is capable of performing multiple functions; thus, enabling a simple and efficient system. A promising candidate to achieve miniaturization is to use microfiber [47–51]. Microfiber has a small size but a large evanescent field for the guided light, making it easy to manipulate and highly sensitive to the surrounding medium. Such unique and interesting properties help create novel optical fiber devices. An ultracompact optical fiber device would be realized if microstructures could be created within microfibers.

Recently, by use of femtosecond laser micromachining, fusion splicing, and flame brushing techniques, a novel optical fiber device based upon microfiber with inner air cavity has been fabricated [52]. The fabrication process of a hollow sphere in SMF is the same as that shown in Figure 14.13, redrawn in Figure 14.22, but with the addition of the flame brushing technique in Figure 14.22d.

Figure 14.23a shows the cleaved fiber end facet with a microhole fabricated by femtosecond laser ablation. After fusion splicing with another section of SMF, a

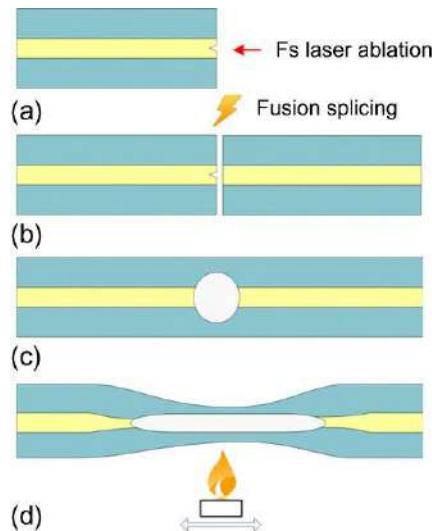


**Figure 14.22** Schematic diagram of fabrication process of the microfiber with inner air cavity. (a) Microhole produced by fs laser; (b) fiber tip with microhole spliced together with another cleaved SMF; (c) hollow sphere formed in SMF; and (d) microfiber with inner air cavity produced by flame brushing technique.

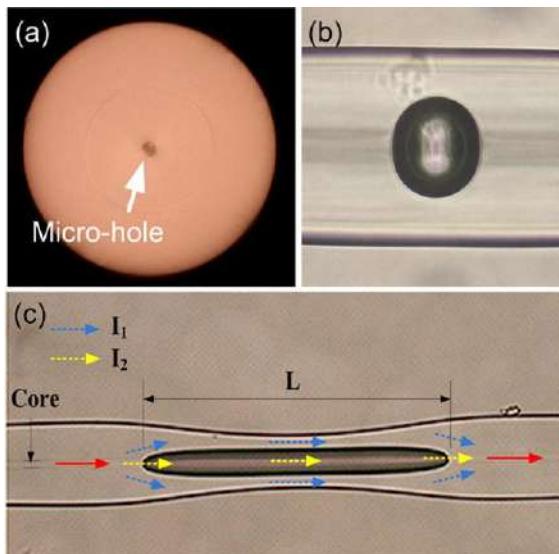


**Figure 14.23** (a) The microhole fabricated by femtosecond laser ablation at the center of cleaved SMF end facet; (b) the hollow sphere formed after fusion splicing; and (c) microfiber Mach-Zehnder interferometer with an inner air cavity.

hollow sphere is formed in the SMF, as shown in Figure 14.23b. The inner wall of the air cavity is rather smooth, due to the high temperature experienced in the hollow sphere formation. Figure 14.23c displays the microscope image of the tapered microfiber with an inner air cavity which essentially forms a microfiber in-line Mach-Zehnder interferometer. In the tapered section, the input light beam is split into two portions denoted by  $I_1$  and  $I_2$ , respectively. While  $I_1$  travels along the silica cavity wall,  $I_2$  propagates through the inner air cavity, and the interference takes place when the two output beams recombine at the cavity end.

Compared with the conventional microfiber of similar size, the thinner cavity wall supports a larger evanescent field and hence an enhanced light interaction with the surrounding medium. Thus, the microfiber in-line Mach-Zehnder interferometer opens a promising way to achieve a miniature, versatile, and highly sensitive optical fiber sensing device.

Femtosecond laser micromachining has become an efficient tool to fabricate various types of microstructures on optical fibers, which can be used in a wide range of photonics applications. The future development trend indicates the continued use of femtosecond laser micromachining together with the techniques such as fusion splicing, flame brushing, and others to fabricate combined microstructures on optical fibers to realize miniature, robust, and multifunctional optical fiber devices.

## References

- [1] M.D. Shirk, P.A. Molian, A review of ultrashort pulsed laser ablation of materials, *J. Laser Appl.* 10 (1) (1998) 18–28.
- [2] A. Ruf, F. Dausinger, Interaction with metals, *Top. Appl. Phys.* 96 (2004) 105–113.
- [3] J. Kruger, W. Kautek, Ultrashort pulse laser interaction with dielectrics and polymers, *Adv. Polym. Sci.* 168 (2004) 247–289.
- [4] E. Glezer, E. Mazur, Ultrafast laser driven micro explosions in transparent materials, *Appl. Phys. Lett.* 71 (7) (1997) 882–884.
- [5] R. Gattass, E. Mazur, Femtosecond laser micromachining in transparent materials, *Nat. Photonics* 2 (2008) 219–225.
- [6] D. von der Linde, H. Schüler, Breakdown threshold and plasma formation in femtosecond laser-solid interaction, *J. Opt. Soc. Am. B* 13 (1) (1996) 216–222.
- [7] N. Nguyen, A. Saliminia, W. Liu, S.L. Chin, R. Vallee, Optical breakdown versus filamentation in fused silica by use of femtosecond infrared laser pulses, *Opt. Lett.* 28 (17) (2003) 1591–1593.
- [8] S. Sundaram, C. Schaffer, E. Mazur, Microexplosions in tellurite glasses, *Appl. Phys. A* 76 (3) (2003) 379–384.
- [9] G. Zhou, M. Gu, Anisotropic properties of ultrafast laser driven microexplosions in lithium niobate crystal, *Appl. Phys. Lett.* 87 (24) (2005) 24110721–24110723.
- [10] M. Lenzner, J. Kruger, S. Sartania, Z. Cheng, C. Spielmann, G. Mourou, W. Kautek, F. Krausz, Femtosecond optical breakdown in dielectrics, *Phys. Rev. Lett.* 80 (18) (1998) 4076–4079.
- [11] B. Stuart, M. Feit, S. Herman, A. Rubenchik, B. Shore, M. Perry, Nanosecond to femtosecond laser induced breakdown in dielectrics, *Phys. Rev. B* 53 (4) (1996) 1749–1761.

- [12] L.V. Keldysh, Ionization in the field of a strong electromagnetic wave, Sov. Phys. JETP 20 (5) (1965) 1307–1314.
- [13] J. Lindl, Development of the indirect drive approach to inertial confinement fusion and the target physics basis for ignition and gain, Phys. Plasmas 2 (11) (1995) 3933–4024.
- [14] J. Posthumus, The dynamics of small molecules in intense laser fields, Rep. Prog. Phys. 67 (5) (2004) 623–665.
- [15] T. Ditmire, J. Tisch, E. Springate, M. Mason, N. Hay, R. Smith, J. Marangos, M. Hutchinson, High energy ions produced in explosions of superheated atomic clusters, Nature 386 (6620) (1997) 54–56.
- [16] R. Stoian, A. Rosenfeld, D. Ashkenasi, I. Hertel, Surface charging and impulsive ion ejection during ultrashort pulsed laser ablation, Phys. Rev. Lett. 88 (9) (2002) 97603–97606.
- [17] K. Davis, K. Miura, N. Sugimoto, K. Hirao, Writing waveguides in glass with a femtosecond laser, Opt. Lett. 21 (21) (1996) 1729–1731.
- [18] T. Kondo, S. Matsuo, S. Juodkazis, H. Misawa, Femtosecond laser interference technique with diffractive beam splitter for fabrication of three dimensional photonic crystals, Appl. Phys. Lett. 79 (6) (2001) 725–727.
- [19] Y. Nakata, T. Okada, M. Maeda, Lithographical laser ablation using femtosecond laser, Appl. Phys. A 79 (426) (2004) 1481–1483.
- [20] S. Mihailov, C. Smelser, P. Lu, R. Walker, D. Grobnic, H. Ding, G. Henderson, J. Unruh, Fiber Bragg gratings made with a phase mask and 800-nm femtosecond radiation, Opt. Lett. 28 (12) (2003) 995–997.
- [21] Y. Li, M. Yang, D.N. Wang, J. Lu, T. Sun, K. Grattan, Fiber Bragg gratings with enhanced thermal stability by residual stress relaxation, Opt. Express 17 (2009) 19785–19790.
- [22] Y. Rao, M. Deng, D. Duan, X. Yang, T. Zhu, G. Cheng, Micro Fabry-Perot interferometers in silica fibers machined by femtosecond laser, Opt. Express 15 (21) (2007) 14123–14128.
- [23] Y. Wang, M. Yang, D.N. Wang, S. Liu, P. Lu, Fiber in-line Mach-Zehnder interferometer fabricated by femtosecond laser micromachining for refractive index measurement with high sensitivity, J. Opt. Soc. Am. B 27 (2010) 370–374.
- [24] E. Wikszak, J. Burghoff, M. Will, S. Nolte, A. Tuennemann, T. Gabler, Recording of fiber Bragg gratings with femtosecond pulses using a “point by point” technique, in: Conference on Lasers and Electro-Optics (CLEO), paper CThM7, 2004.
- [25] C. Liao, Y. Wang, D.N. Wang, L. Jin, Femtosecond-laser inscribed long period gratings in all-solid photonic crystal fibers, IEEE Photon. Technol. Lett. 22 (2010) 425–427.
- [26] A. Martinez, M. Dubov, I. Khrushchev, I. Bennion, Direct writing of fiber Bragg gratings by femtosecond laser, Eletron. Lett. 40 (2004) 1170–1172.
- [27] C.W. Smelser, S.J. Mihailov, D. Grobnic, Formation of Type I-IR and Type II-IR gratings with an ultrafast IR laser and a phase mask, Opt. Express 12 (2005) 5377–5386.
- [28] Y. Kondo, K. Nouchi, T. Mitsuyu, M. Watanabe, P. Kazansky, K. Hirao, Fabrication of long period fiber gratings by focused irradiation of infrared femtosecond laser pulses, Opt. Lett. 24 (1999) 646–648.
- [29] F. Hindle, E. Fertein, C. Przygodzki, F. Durr, L. Paccou, R. Bocquet, N. Pierre, H. Limberger, M. Douay, Inscription of long period gratings in pure silica and Germano-Silicate fiber cores by femtosecond laser irradiation, IEEE Photon. Technol. Lett. 16 (1861–1863) 2004.
- [30] R. Suo, Y. Lai, K. Zhou, L. Zhang, I. Bennion, X. Jiang, J. Lousteau, A. Jha, Long period gratings in near-single-mode  $\text{GeO}_2$  glass fiber by IR femtosecond laser inscription, OSA/BGPP, BWB5, 2007.

- [31] T. Allsop, K. Kalli, K. Zhou, Y. Laia, G. Smith, M. Dubov, D. Webb, I. Bennion, Long period gratings written into a photonic crystal fibre by a femtosecond laser as direction bend sensors, *Opt. Commun.* 281 (2008) 5092–5096.
- [32] Y. Wang, D.N. Wang, M. Yang, W. Hong, P. Lu, Refractive index sensor based on a microhole in single-mode fiber created by the use of femtosecond laser micromachining, *Opt. Lett.* 34 (2009) 3328–3330.
- [33] Y. Lai, K. Zhou, I. Bennion, Microchannels in conventional single-mode fibers, *Opt. Lett.* 31 (2006) 2559–2561.
- [34] M. Yang, D.N. Wang, Y. Wang, C.R. Liao, Long period fiber grating formed by periodically structured microholes in all-solid photonic bandgap fiber, *Opt. Express* 18 (2010) 2183–2189.
- [35] S. Liu, L. Jin, W. Jin, D.N. Wang, C.R. Liao, Y. Wang, Structural long period gratings made by drilling micro-holes in photonic crystal fibers with femtosecond infrared laser, *Opt. Express* 18 (2010) 5496–5503.
- [36] Y. Wang, D.N. Wang, M.W. Yang, C.R. Liao, Asymmetric microhole-structured long-period fiber gratings, *Sens. Actuators B* 160 (2011) 822–825.
- [37] T. Wei, Y. Han, Y. Li, H. Tsai, H. Xiao, Temperature-insensitive miniaturized fiber inline Fabry-Perot interferometer for highly sensitive refractive index measurement, *Opt. Express* 16 (2008) 5764–5769.
- [38] J.L. Kou, J. Feng, L. Ye, F. Xu, Y.Q. Lu, Miniaturized fiber taper reflective interferometer for high temperature measurement, *Opt. Express* 18 (2010) 14245–14249.
- [39] C.R. Liao, Y. Wang, D.N. Wang, M.W. Yang, Fiber in-line Mach-Zehnder interferometer embedded in FBG for simultaneous refractive index and temperature measurement, *IEEE Photon. Technol. Lett.* 22 (2010) 1686–1688.
- [40] D. Grobnic, S.J. Mihailov, C.W. Smelser, D. Huimin, Sapphire fiber Bragg grating sensor made using femtosecond laser radiation for ultrahigh temperature applications, *IEEE Photon. Tech. Lett.* 16 (2004) 2505–2507.
- [41] C.M. Jewart, Q.Q. Wang, J. Canning, D. Grobnic, S.J. Mihailov, K.P. Chen, Ultrafast femtosecond-laser-induced fiber Bragg gratings in air-hole microstructured fibers for high-temperature pressure sensing, *Opt. Lett.* 35 (2010) 1443–1445.
- [42] Y. Wang, Y.H. Li, C.R. Liao, D.N. Wang, M.W. Yang, P.X. Lu, High-temperature sensing using miniaturized fiber in-line Mach-Zehnder interferometer, *IEEE Photon. Tech. Lett.* 22 (2010) 39–41.
- [43] C.R. Liao, D.N. Wang, M. Wang, M.W. Yang, Fiber in-line Michelson interferometer tip sensor fabricated by femtosecond laser, *IEEE Photon. Technol. Lett.* 24 (2012) 2060–2063.
- [44] C.R. Liao, T.Y. Hu, D.N. Wang, Optical fiber Fabry-Perot interferometer cavity fabricated by femtosecond laser micromachining and fusion splicing for refractive index sensing, *Opt. Express* 20 (2012) 22813–22818.
- [45] M. Yang, D.N. Wang, C.R. Liao, Fiber Bragg grating with micro-holes for simultaneous and independent refractive index and temperature sensing, *IEEE Photon. Technol. Lett.* 23 (2011) 1511–1513.
- [46] T.Y. Hu, Y. Wang, C.R. Liao, D.N. Wang, Miniaturized fiber in-line Mach-Zehnder interferometer based on inner air-cavity for high-temperature sensing, *Opt. Lett.* 37 (2012) 5082–5084.
- [47] L. Tong, R.R. Grattass, J.B. Ashcom, S. He, J. Lou, M. Shen, I. Maxwell, E. Mazur, Sub-wavelength-diameter silica wires for low-loss optical wave guiding, *Nature* 426 (2003) 816–819.

- [48] G. Brambilla, V. Finazzi, D.J. Richardson, Ultra-low-loss optical fiber nanotapers, *Opt. Express* 12 (2004) 2258–2263.
- [49] M. Sumetsky, Y. Dulashko, A. Hale, Fabrication and study of bent and coiled free silica nanowires: self-coupling microloop optical interferometer, *Opt. Express* 12 (2004) 3521–3531.
- [50] P. Polynkin, A. Polynkin, N. Peyghambarian, M. Mansuripur, Evanescent field-based optical fiber sensing device for measuring the refractive index of liquids in microfluidic channels, *Opt. Lett.* 30 (2005) 1273–1275.
- [51] X. Fang, C.R. Liao, D.N. Wang, Femtosecond laser fabricated fiber Bragg grating in microfiber for refractive index sensing, *Opt. Lett.* 35 (2010) 1007–1009.
- [52] C.R. Liao, D.N. Wang, Y. Wang, Microfiber in-line Mach-Zehnder interferometer for strain sensing, *Opt. Lett.* 38 (2013) 757–759.

This page intentionally left blank

# Spatiotemporal manipulation of ultrashort pulses for three-dimensional (3-D) laser processing in glass materials

15

F. He<sup>1</sup>, J. Ni<sup>1</sup>, B. Zeng<sup>1</sup>, Y. Cheng<sup>1</sup>, K. Sugioka<sup>2</sup>

<sup>1</sup>Chinese Academy of Sciences, Shanghai, China; <sup>2</sup>RIKEN Center for Advanced Photonics, Wako, Japan

## 15.1 Introduction

Ultrashort pulses are generally defined as laser pulses with durations in the scale of femtoseconds ( $1 \text{ fs} = 10^{-15} \text{ s}$ ) to a few of tens of picoseconds ( $1 \text{ ps} = 10^{-12} \text{ s}$ ). The peak intensity of a focused femtosecond laser beam can be as high as  $10^{15} \text{ W/cm}^2$ , producing a highly localized light field that is sufficient to ionize almost any atom. It's since the 1990s that Ti:sapphire lasers have revolutionized ultrafast science, and that ultrafast laser material processing has been extensively explored [1,2]. In 1996, Hirao's group [3] and Mazur's group [4] demonstrated that the modification in the bulk of various glass materials could be tailored to produce a permanent refractive index increase, which pioneered the internal modification of transparent materials using tightly focused ultrashort pulses.

The interaction of ultrafast pulses and materials is generally considered to be a multiphoton absorption (MPA) initiated process [5]. Compared with conventional laser fabrication techniques that use continuous wave lasers or long pulse lasers, ultrashort laser-material processing has several distinct advantages: (i) Owing to the nonlinear excitation mechanism, the tightly focused ultrashort pulses can produce a strong absorption even in the transparent material. Therefore, the light matter interaction occurs only near the focal volume where the peak intensity is sufficiently high to induce MPA, thus reducing the out-of-focus absorption. This unique property makes it possible for true 3-D microfabrication inside the transparent material using ultrashort pulses. (ii) Ultrashort pulses significantly reduce the thermal effect during the laser-material processing, due to that when the pulse duration is shorter than the electron-phonon coupling time (in the order of 10 ps), most of the energy is absorbed by the electrons and is very rapidly transferred to the lattice so that the energy is not dissipated through thermal diffusion. This suppression of the heat-affected zone (HAZ) enables fabrication of fine structures with micro- and nanoscale features [6]. (iii) The combination of HAZ suppression and MPA of laser-material processing using ultrashort pulses enables the fabrication resolution far beyond the optical diffraction limit. This can be easily achieved by adjusting the laser intensity to

match the intensity threshold of the modification [7,8]. (iv) The ultrashort pulses (particularly femtosecond lasers) can be used to finely modify or even change the physical and chemical properties of the material in a spatially selective manner, which enables multiple functions to be integrated in a single substrate [9,10].

Owing to the above advantages, ultrashort pulses particularly femtosecond laser direct writing has attracted significant attention and promised a wide variety of intriguing applications in not only integrated photonic devices (e.g., waveguide writing, polarization sensitive optics, quantum circuits) but also integrated microfluidic and optofluidic systems (e.g., lab on a chip devices, micro-total analysis systems) [9–14]. In the meantime, this new way of interaction of femtosecond laser with matter, that is, irradiation of intense ultrafast pulses inside transparent materials such as glass and crystals, has led to many intriguing phenomena, such as refractive index modification [3,4], formation of nanovoids and periodic nanogratings [15–17], element redistribution [18], nanocrystallization [19], and nonreciprocal writing [20–22]. Several review papers [9,10,14] as well as books [23–26] are available on femtosecond laser micromachining, providing comprehensive overviews on its fundamental physics, the basic processing systems, and many novel applications.

Most of the laser direct-write (LDW) processes have taken the manner of transverse direct write, namely, the writing direction is perpendicular to the laser propagation direction. Unfortunately, the focal spot produced by an objective lens typically has an asymmetrical shape elongated in the direction of propagation, resulting in unbalanced lateral and axial resolutions, as shown in Figure 15.1. Unlike the traditional planar lithography in which the feature size is only determined by the lateral resolution, spatial resolutions in all three dimensions in space have to be taken into account in femtosecond laser direct writing for fabricating 3-D microstructures.

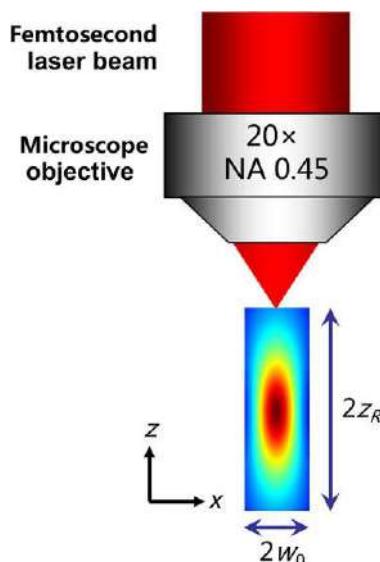


**Figure 15.1** Intensity distribution of a tightly focused femtosecond laser beam.

To date, several beam shaping techniques have been developed to solve this problem. For instance, in the widely used transverse writing scheme (i.e., the writing direction is perpendicular to the direction of laser propagation), by shaping the input femtosecond laser beams with either a pair of cylindrical lenses [27] or a narrow slit [28,29] placed before the objective lens, one can obtain a circular cross section of focal spot in the plane perpendicular to the transverse writing direction, whereas the cross sections in the planes perpendicular to the writing direction are still elliptical. Moreover, isotropic 3-D spatial resolution in femtosecond laser micromachining has been demonstrated by means of the crossed-beam irradiation method, whereas the stringent requirement on the alignment of two objective lenses introduces additional complexity and cost as compared to the beam-shaping techniques requiring only one objective lens [30]. Thus, beam-shaping techniques that could enable 3-D isotropic resolution is still in high demand. Moreover, for high-precision 3-D micro- and nanomachining, control of these novel phenomena at micrometer and even nanometer scales requires precise tailoring of the light field within a focal spot, including the spatial (in all three dimensions) and/or temporal profiles, polarization direction, pulse front tilting, and so forth [31,32]. Thus, manipulation of spatiotemporal characteristics of ultrashort pulses represents a stimulating challenge in the field of 3-D laser material processing.

This chapter focuses on the development of spatiotemporal beam-shaping techniques for 3-D laser-material processing. The remainder of this chapter is organized as follows. In [Section 15.2](#), the concept of spatiotemporal focusing of a femtosecond laser beam is introduced. The application of this technique in controlling of the cross-sectional shape of microstructures using femtosecond laser direct writing is also demonstrated. [Section 15.3](#) describes achieving a 3-D isotropic resolution at low NAs using a combination of slit beam shaping and spatiotemporal focusing methods. [Section 15.4](#) discusses spatiotemporal characteristics of spatiotemporally focused ultrashort pulses near the focus. The underlying mechanism behind this exotic phenomenon is discussed. [Section 15.5](#) extends the application of spatiotemporally focused ultrafast laser pulses to femtosecond laser filamentation, and models the propagation dynamics of spatiotemporally shaped beams. Finally, a summary and a future outlook are given in [Section 15.6](#).

## 15.2 Tailoring the focal spot by spatiotemporal manipulation of ultrashort laser pulses

In 2005, the spatiotemporal focusing technique was first developed by the bioimaging community for suppressing the background signal in two-photon fluorescence microscopy, thus improving the axial resolution, as well as achieving high-speed imaging [33,34]. The principle of spatiotemporal focusing involves directing the laser pulse through an optical dispersive element (e.g., prisms, gratings) to produce an angularly dispersive beam. In this situation, the spectral components that comprise the ultrashort pulse are not spatially overlapped, and, thereby, cannot add together to produce a transform-limited pulse in time. Then the spatially separated frequencies can be

recombined together through an objective lens, producing a shortest pulse only at the focal plane while the out-of-focus pulse is stretched, as shown in [Figure 15.2](#). This focusing mode can localize the peak intensity in both space and time domains, thus achieving an improved axial resolution. In 2010, the spatiotemporal focusing method was implemented into 3-D femtosecond laser micromachining, leading to tremendous advances in improving the fabrication resolution, eliminating nonlinear self-focusing, and increasing the fabrication efficiency [[35–39](#)].

Intuitively, improving the axial resolution can be used to match the lateral resolution, thus realizing a symmetrical cross-sectional shape of microstructure when using femtosecond LDW. A schematic of the experimental setup for spatiotemporally focused LDW is shown in [Figure 15.3](#). The femosecond lasers (Libra-He/Rega-9000/Legend-Elite; Coherent Inc.) employed for the direct writing are the chirped pulse amplification (CPA) systems, with pulse durations of 40–200 fs, center wavelengths of 800 nm, which have been described in detail elsewhere [[35,36,40,41](#)]. In this experiment, the input laser beam size is controlled by an adjustable circular aperture. A pair of parallel gratings (blazing at 800 nm) are used to separate the spectral components of the incident pulse in  $X$  coordinate; that is, to produce a spatial dispersion, which is different from the

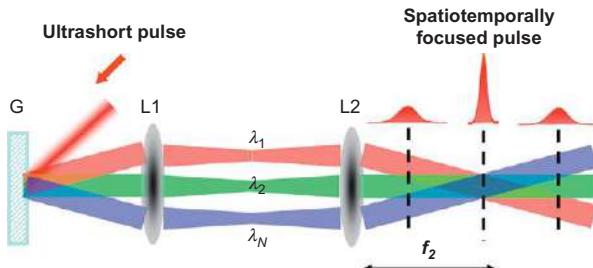


**Figure 15.2** Principle illustration of spatiotemporal focusing of ultrashort pulses. G is the grating, L1 and L2 are lenses.

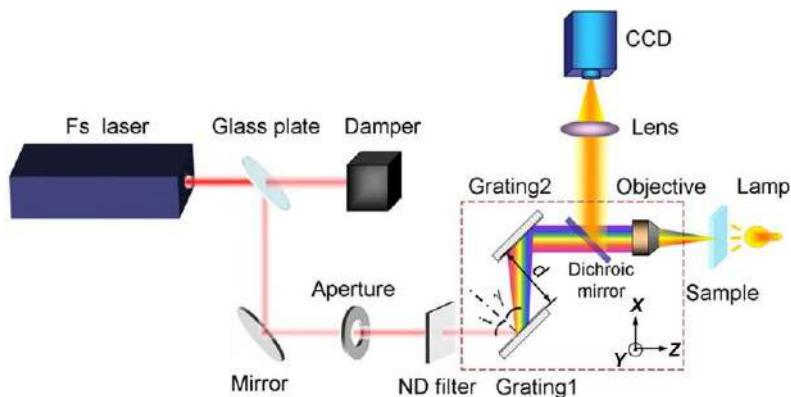


**Figure 15.3** The experimental setup of femtosecond laser micromachining using spatiotemporal focusing technique.

grating-lens setup used in spatiotemporal focusing bioimaging system. To precompensate all the chirps through the optics, the input pulse is positively prechirped by decreasing the distance between the grating pair of the CPA pulse compressor. The best precompensation of dispersion can be achieved when the strongest ionization (i.e., the brightest plasma) of the air was observed at the focus of the objective. The power of the spatial dispersed pulse is adjusted by neutral density (ND) filters, before being focused by an objective lens ( $20\times$ , 0.46 NA,  $f=8$  mm; BX-51, Olympus Inc.) into a glass sample. The glass can be arbitrarily translated by a PC-controlled XYZ stage (P-545; Physik Instrumente Inc.).

Theoretically, calculation of the spatiotemporally focused femtosecond laser beam propagation can be achieved using Fresnel-Kirchhoff's diffraction theory [42]. Assuming that the temporal chirp of the incident pulse is precompensated, and that the input spectral phase is  $\phi(\omega)=0$ , the normalized light field of a spatially dispersed pulse  $E_1$  at the entrance aperture of the lens thus can be expressed as

$$E_1(x, y, z=0, \omega) = A_0 \exp\left[-\frac{(\omega - \omega_0)^2}{2\Omega^2} + i\phi(\omega)\right] \exp\left\{-\frac{[x - \Delta x(\omega)]^2}{2W_x^2}\right\} \exp\left(-\frac{y^2}{2W_y^2}\right) \quad (15.1)$$

where  $A_0$  is the constant field amplitude,  $\omega_0$  the carrier frequency,  $\Omega$  the bandwidth ( $1/e^2$ ) of the pulses, and  $W_x$  and  $W_y$  are the beam waist ( $1/e^2$ ) along the major and minor axes, respectively.  $\Delta x(\omega)$  is the linear shift of each spectral component at the entrance aperture of the lens. For the grating pair dispersion system, neglecting the high-order chirp induced by the grating pair, the linear shift of each spectral component at the entrance aperture can be written as  $\Delta x(\omega) \approx \alpha(\omega - \omega_0)$ . Details of the derivation of the analytical expression of  $\alpha$  are given in [Appendix](#) [36].

After passing through the lens and propagating a distance  $z$  from the lens, the light field can be written as [36]

$$\begin{aligned} E_2(x, y, z, \omega) &= \frac{\exp(ikz)}{i\lambda z} \int \int_{-\infty}^{\infty} E_1(\xi, \eta, \omega) \exp\left(-ik\frac{x^2 + y^2}{2f}\right) \\ &\times \exp\left[ik\frac{(x - \xi)^2 + (y - \eta)^2}{2z}\right] d\xi d\eta \end{aligned} \quad (15.2)$$

where  $k$  is the wave vector and  $f$  is the focal length of the lens. The intensity distribution in the time domain can be obtained by performing an inverse Fourier transform of  $E_2(x, y, z, \omega)$  as

$$I_{TF}(x, y, z, t) = |E_2(x, y, z, t)|^2 = \left| \int_{-\infty}^{\infty} E_2(x, y, z, \omega) \exp(-i\omega t) d\omega \right|^2 \quad (15.3)$$

The intensity distributions of the focused spatially dispersed beam in both XZ and YZ planes can be obtained according to Equation (15.3). In the numerical simulation, the pulse duration and the spectrum bandwidth are 40 fs, 30 nm, respectively. The distance between the gratings (1200 lp/mm, blazing at 45°) is set to be  $\sim 180$  mm. The beam waist of the input laser is  $2 W_0 = 5$  mm. The intensity distribution of the conventional focusing laser beam can be obtained by substituting  $\Delta x = 0$  into Equation (15.1). As shown in Figure 15.4a-c, one can clearly see that a near spherical-shaped intensity distribution has been obtained with the spatiotemporal focusing.

We also demonstrate experimental proofs of the cross-sectional shape control by comparing the conventional focusing with the spatiotemporal focusing direct writing method. To do so, 3-D microfluidic channels are fabricated in fused silica by femtosecond LDW followed by chemical wet etching. The laser power and scanning speed are chosen to be 3.5 mW and 50  $\mu\text{m}/\text{s}$ , respectively. Other parameters are chosen according to the above simulation. After the laser irradiation, the sample is subjected to a 150-min wet chemical etching in a solution of 10% HF diluted with water in an ultrasonic bath. We examine the cross sections of the channels by cutting and polishing the sample. The optical micrographs of the cross sections of microfluidic channels, shown in Figure 15.4d-f, are clear evidence of the validity of this shape control method.

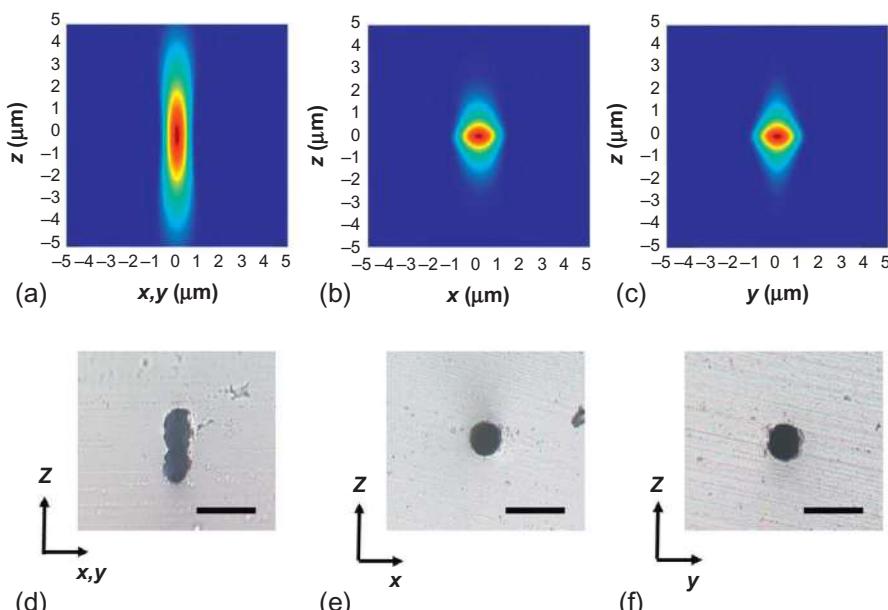


**Figure 15.4** Theoretical calculations of laser intensity distributions at the focus produced by an objective lens with (a) conventional focusing and with (b, c) spatiotemporal focusing technique in XZ and YZ planes, respectively. Optical micrographs of the cross section of microfluidics channels fabricated by femtosecond LDW (d) with a conventional focusing system and with (e, f) spatiotemporal focusing system in XZ and YZ planes, respectively. The scale bars in (d-f) are 50  $\mu\text{m}$ .

It should be specifically noted that the threshold intensity of femtosecond laser fabrication of the transparent materials not only strongly depends on the peak intensity but also can be affected by the ultrashort laser pulse duration [9]. In addition, the axial resolution would also be affected by the order of optical nonlinearity of the interaction between the femtosecond laser pulse and the transparent material (e.g., the  $n$ th-order optical nonlinearity means simultaneous absorption of  $n$  photons during the light-matter interaction in this situation). Therefore, because the order of optical nonlinearity of the interaction between the femtosecond laser and fused silica [43] is not clearly defined in our experiment, quantitative reproduction of the experimental results by theoretical simulation is difficult.

### 15.3 Three-dimensional (3-D) isotropic resolutions at low numerical apertures (NAs) using the combination of slit beam shaping and spatiotemporal focusing methods

It is well known that self-focusing can typically occur before the focal volume due to the high peak power of short pulses, and can result in elongated structures when using laser direct-writing. In the spatiotemporal focusing mode, the peak power only increases near the focal volume and filamentary damage tracks could be avoided, in particular in highly nonlinear materials such as polymers and crystals. Recently, Vitek *et al.* [37] demonstrated that temporal focusing of spatially chirped femtosecond laser pulses overcomes previous limitations for ablating high aspect ratio features with low NA beams. For instance, when 50  $\mu$ J, 60 fs pulses (centered at 800 nm) are focused through a 6 mm thick fused silica sample at 0.05 NA without spatiotemporal focusing, its observed that the beam self-focuses and collapses into a filament. It is conventionally unable to selectively ablate the back surface of the sample, and the entire thickness of the glass is modified along the direction of propagation. Conversely, with spatiotemporal focusing and for the same pulse energy and duration and focal spot size, it allows for selective ablation of only the back surface of the sample, leaving the glass volume nearly unblemished. However, we further point out that when the spatiotemporal focusing technique is employed with an objective lens of low NA values, the lateral cross section (i.e., in the plane perpendicular to the propagation direction) of the focal spot will no longer be circular. We also demonstrate this issue in both theoretical and experimental perspectives.

In order to obtain an analytical expression of the peak-intensity distributions near the focus for the spatiotemporally focused femtosecond laser beams, we simplify the calculations by employing the slow varying envelope approximation to Equation (15.3), namely, assuming that the wave vector  $k$  for each frequency is approximately at the center wavelength of the pulse  $k_0$ , which is valid for pulse widths on the order of 100 fs [33]. The peak intensity can then be expressed as [36]

$$I_{\text{TF}}(x, y, z, t) = \left| CR(z) \exp\left(-\frac{x^2}{Q_x} - \frac{y^2}{Q_y}\right) \exp\left[-\frac{\Omega^2}{2(1+\psi)}(t + f\alpha x/P)^2\right] \right|^2 \quad (15.4)$$

where  $C$  is a constant, and

$$\psi = i \frac{(z-f)\alpha^2 \Omega^2}{P} \quad (15.4a)$$

$$R(z) = \frac{1}{\sqrt{1 - \frac{z}{f} + i \frac{z}{kW_x^2}}} \frac{1}{\sqrt{1 - \frac{z}{f} + i \frac{z}{kW_y^2}}} \frac{1}{\sqrt{1 + \psi}} \quad (15.4b)$$

$$P = \frac{zf}{k} + i(z-f)W_x^2 \quad (15.4c)$$

$$Q_x = \left( \frac{zf}{k^2 W_x^2} + i \frac{z-f}{k} \right) / \left( 1 - \frac{if}{kW_x^2} \right) \quad (15.4d)$$

$$Q_y = \left( \frac{zf}{k^2 W_y^2} + i \frac{z-f}{k} \right) / \left( 1 - \frac{if}{kW_y^2} \right) \quad (15.4e)$$

The lateral dimensions of the focal spot at the geometric focus can be calculated by substituting  $z=f$  and  $t=0$  into Equation (15.4), and it is obtained as

$$W'_x = \frac{\sqrt{2}f}{k \sqrt{W_x^2 + 2\alpha^2 \Omega^2}}, \quad (15.5)$$

$$W'_y = \frac{\sqrt{2}f}{kW_y}$$

It is obvious that the size of the focal spot decreases along the  $X$ -direction due to the term of spatial chirp. The most important information given by Equation (15.5) is that with the spatiotemporal focusing, the cross section of the lateral focal plane (i.e.,  $XY$  plane) is noncircular if the incident Gaussian beam has a circular beam profile (i.e.,  $W_x=W_y$ ). It is also shown that the asymmetry becomes more severe for low NA values. In the meantime, Equation (15.5) suggests that the resolutions in  $X$ - and  $Y$ -directions can be balanced by using a noncircular incident Gaussian beam (i.e.,  $W_x < W_y$ ). Moreover, from Equation (15.4), one can also derive the expression of the pulse width, which depends only on the propagation distance  $z$  and reaches its shortest value at the position  $z=f$ . Detailed discussion about the pulse duration could also be found in Ref. [33].

For femtosecond laser micromachining deep inside the transparent samples, objective lenses of low NA values are required because of their long work distances. In this case, the asymmetric peak intensity distribution illustrated in Equation (15.5) must

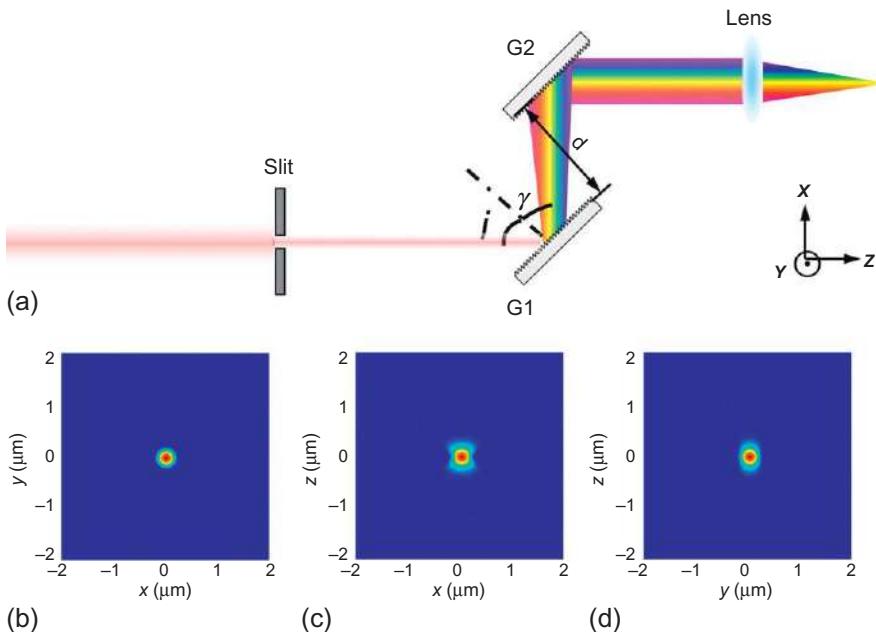


**Figure 15.5** (a) Side view schematic illustration of the focal system combining spatiotemporal focusing and slit beam-shaping methods for femtosecond laser micromachining. G1 and G2 are gratings. Numerically calculated laser focal intensity distributions produced by an elliptical Gaussian beam with  $W_x=1$  mm,  $W_y=6$  mm in (a) XY, (b) XZ, and (c) YZ planes, respectively.

be corrected for achieving 3-D isotropic resolution. To solve for this issue, we simply insert a slit before the grating pair to adjust the aspect ratio of the beam profile in the transverse section. A schematic of the experimental setup is shown in Figure 15.5. After passing through the slit, the circular Gaussian can be approximately considered as an elliptical Gaussian beam. In this calculation, the grating pair G1-G2 is ruled with 1500 lp/mm, the distance between them is set to be  $\sim 250$  mm, and a 10 $\times$  objective with a NA of 0.25 is employed, which is different from those in Section 15.2. Typically, when we choose  $W_x=1$  mm and  $W_y=6$  mm, both the axial and lateral aspect ratios of the cross sections of focal spot can be tuned to be  $\sim 1$ , thus warranting a 3-D isotropic resolution.

We also use a photosensitive glass, Foturan, to record and inspect the 3-D intensity distribution of femtosecond pulses at the focus. (In this case, the Foturan glass can be regarded as a 3-D photographic recording medium.) The experimental conditions are chosen in accordance with the above theoretical analysis. We then compare the conventionally focused Gaussian beam, the spatiotemporal focusing, and the combination of slit beam shaping and spatiotemporal focusing technique by inscribing parallel lines in both X- and Y-directions in Foturan glass samples, respectively. The diameter of the laser beam used for conventionally focusing is 12 mm. In the spatiotemporal focusing scheme, the circular incident Gaussian beam is chosen to be 2 mm, thus corresponding

to a low NA value of  $\sim 0.06$ , while the incident Gaussian beam profile becomes  $2W_x = 2$  mm,  $2W_y = 12$  mm for the combination of slit beam shaping and spatiotemporal focusing. The writing speed is chosen to be  $100 \mu\text{m/s}$  and the average laser power is  $3 \text{ mW}$ , for all the above three direct-writing schemes.

After the femtosecond laser exposure, the sample is subjected to a programmed heat treatment. The temperature is first ramped from room temperature to  $520^\circ\text{C}$  at  $5^\circ\text{C}/\text{min}$  and held at this temperature for 2 h. After the samples are naturally cooled down to room temperature, we polish them and observe the inner areas modified by the femtosecond laser irradiation under the optical microscope. As shown in [Figure 15.8a and b](#), under the conventional focusing direct-writing scheme, the cross-sectional shapes in both XZ and YZ planes are turned to be seriously asymmetrical. However, when it comes to spatiotemporal focusing using a low NA objective, although the cross-sectional profile in the YZ plane becomes symmetrical, the cross-section shape in the XZ plane is still elliptical ([Figure 15.6c and d](#)), which renders it impractical for 3-D isotropic resolution control. This issue can be finally addressed by using the combination of slit beam shaping and temporal focusing methods, as it can be observed clearly that the cross-sectional profiles in both XZ and YZ planes are becoming symmetrical ([Figure 15.6e and f](#)), which is in good agreement with the calculated results presented in [Figure 15.5](#).

Therefore, introducing the slit beam shaping method can effectively compensate for the lateral asymmetry of the focal spot caused by spatiotemporal focusing in the case of using low-NA objective lenses. On the other hand, this new technique also allows for independently tuning the aspect ratios of intensity distributions in both lateral and axial cross sections.

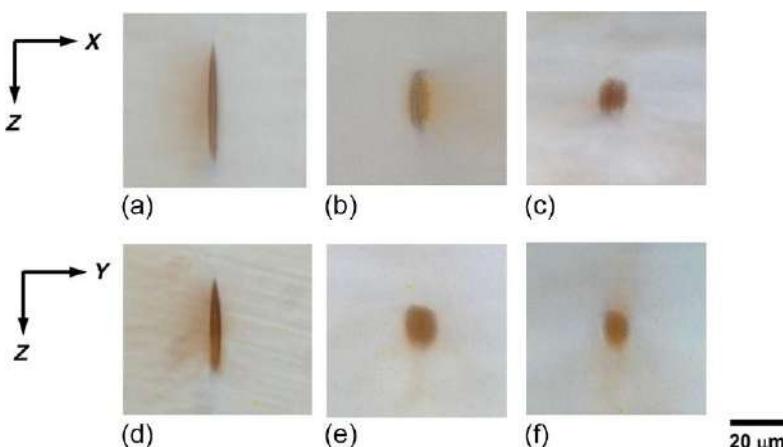


**Figure 15.6** Optical micrographs of transverse profiles of the patterns inscribed inside Foturan glass with (a, d) conventional focusing, (b, e) spatiotemporal focusing, and (c, f) the combination of slit beam shaping and spatiotemporal focusing.

## 15.4 Visualization of the spatiotemporally focused femtosecond laser beam using two-photon fluorescence excitation

The optical nonreciprocal writing, or optical “quill” writing, is referred to as the effect that the characteristics of the modification change when the scan direction of laser direct-writing is reversed, which was initiated by Kazansky *et al.* [20–22] and has become another hot topic in femtosecond laser micromachining. They also theorized that the intensity gradient established across the focal spot by the presence of pulse front tilt (PFT) acts to displace electrons in the plasma by virtue of the ponderomotive force. In practice, PFT may be imposed on the laser beam by tuning the laser’s grating compressor. However, any adjustment to the parallelism of the gratings produces angular dispersion that necessarily results in spatial and temporal distortions at focus. Consequently, the conditions for generating PFT are not easily translated between systems, so that deciphering the effect of PFT on nonreciprocal writing is confounded.

At first sight, this phenomenon is completely understandable, as PFT has long been regarded as the major cause responsible for the nonreciprocal writing process. However, recently several groups have also shown that if the focal spot has only an asymmetric intensity distribution but no PFT, it can also induce the nonreciprocal writing. This discovery raises the question on the origin of the nonreciprocal writing, which is still hotly disputed. It should be stressed that a complete characterization of spatiotemporally focused spot is critical for gaining deeper insight into this question, which so far has not been done.

Although the spatiotemporal focusing method is originally proposed to improve the axial resolution, it could meanwhile yield interesting applications in nonreciprocal writing. Recently, Vitek *et al.* [39] have reported that the spatiotemporally focused laser beam, which naturally creates a focal spot with several orders of magnitude larger PFT, can induce nonreciprocal writing in glass more quickly and efficiently.

In this section, we attempt to characterize the spatiotemporally focused femtosecond laser beam based on the two-photon fluorescence excitation (TPFE) process. In such a manner, instead of examination of the fluence distribution in the focal volume, we focus more on the peak intensity distribution, which is more relevant to the nonlinear absorption processes during irradiation of femtosecond laser in glass. We then perform a theoretical analysis to reveal the origin of such tilted peak intensity distribution. Finally, we experimentally show that the tilted intensity distribution alone is sufficient for inducing the well-known nonreciprocal writing effect by use of a new direct-writing scheme in which the optical axis of the objective lens deviates from the normal incident direction. Our results suggest that the role of PFT in inducing the nonreciprocal writing effect observed in glass should be reexamined because of the intrinsically tilted intensity distribution within the spatiotemporally focused spot.

The experimental setup is in common with that employed in Figures 15.3 and 15.5(a), except that no aperture or slit is used. The incident Gaussian beam is shrunk to be within a 1 mm diameter, so as to increase the spatial chirp rate. To visualize the spatiotemporally focused spot, a lens with a focal length of ~500 mm is employed to

focus the spatially chirp beam into a 0.12 mg/mL sodium fluorescein diluted with water. The total volume of the fluorescein is  $\sim$ 1200 mL, which is contained in a 240 mm  $\times$  160 mm  $\times$  160 mm cuvette. The laser power measured after the ND filter is  $\sim$ 20 mW. The TPFE image can be captured by the digital camera from both top view and side view.

**Figure 15.7a and c** shows digital camera captured images of TPFE using the spatiotemporal focusing scheme, observed from the XZ and YZ planes, respectively. It can be seen that the fluorescence intensity distribution in the XZ plane is tilted while in the YZ plane it appears symmetrical. Such tilted intensity distribution in the XZ plane has never been reported before, whose characteristics are fundamentally different from the well-known PFT.

For comparison, we also focus the femtosecond laser beam with a conventional focusing system, namely, without use of the spatiotemporal focusing to perform the similar TPFE experiment. In this situation, the incident beam has a diameter of 12 mm, while the laser power and the focal lens are the same as that used above. The TPFE image is shown in **Figure 15.7e**, which demonstrates a much longer focal

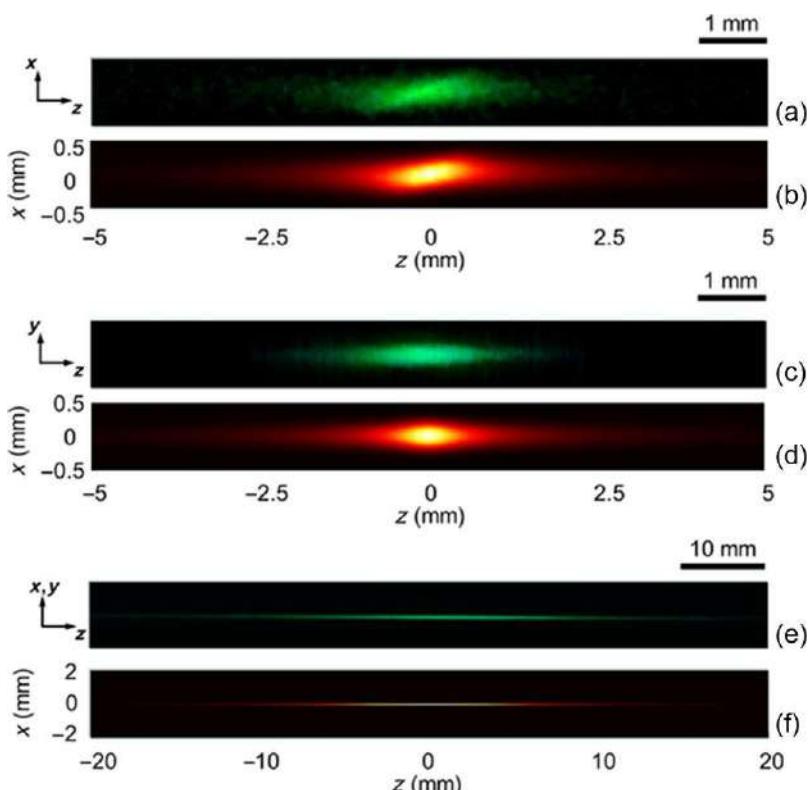


**Figure 15.7** TPFE images (a-d) with spatiotemporal focusing and (e, f) without spatiotemporal focusing. (a) and (c) are TPFE images captured in the XZ and YZ planes, respectively, and (b, d, f) are corresponding numerical simulation TPFE signals.

depth than that obtained with the spatiotemporal focusing. The result is consistent with the observation of highly localized focal spot in a thick glass sample enabled by the use of spatiotemporal focusing with a low NA lens [37].

Theoretically, simulation of the two-photon excitation of dye with a spatiotemporally focused femtosecond laser beam can be achieved using Fresnel-Kirchhoff's diffraction theory. The two-photon fluorescence signal at the focus can be obtained as

$$I_{\text{TPFE}}(x, y, z) \propto \int_{-\infty}^{\infty} I_{\text{TF}}^2(x, y, z, t) dt = \int_{-\infty}^{\infty} |E_2(x, y, z, t)|^4 dt \quad (15.6)$$

where  $E_2(x, y, z, t)$  is the light field of the spatiotemporal focused beam written in the time domain, and  $I_{\text{TF}}(x, y, z, t)$  is the intensity distribution of simultaneous spatiotemporal focused beam.

The TPFE intensity distribution at the focus of the spatiotemporally focused beam, in both the  $XZ$  and  $YZ$  planes, can be obtained with Equation (15.3), as shown in Figure 15.7b and d, respectively. On the other hand, TPFE intensity distribution obtained without using the spatiotemporal focusing can be calculated by substituting  $\Delta\omega(x)=0$  into Equation (15.1). One can clearly see that the theoretical results are in good agreement with the experiment results. It should be noted that the long focal length of the lens used in our experiment makes it reasonable to use the Fresnel-Kirchhoff's diffraction theory for our simulation.

The PFT, the dependence of the arrival time of the pulse on the transverse coordinate, is controlled by the combination of angular or lateral spatial chirp with spectral chirp [44]. In the present case of the spatiotemporal focusing, the temporal chirp is precompensated and  $\phi_2=0$ , the PFT is introduced by the angular dispersion alone. In our experiment the pulse is only spatially chirped before the lens, and the lens converts this spatial chirp to angular chirp. The Gaussian beam written in terms of the amplitude and phase as

$$E(x, y, z, \omega) = A(x, y, z, \omega) \exp[i\phi(x, y, z, \omega)] \quad (15.7)$$

Following the analysis in Ref. [45], we can treat a particular frequency component as an individual beamlet. After focused by the lens, the amplitude function for the beamlet propagating at a frequency-dependent angle  $\theta_x$  can be written

$$A(x, y, z, \omega) = \frac{A(\omega)w_0}{w(z)} \exp\left[-\frac{(x - z \tan \theta_x)^2 + y^2}{w^2(x)}\right] \quad (15.8)$$

and the phase function, under the paraxial approximation can be written as

$$\phi(x, y, z, \omega) = k_0 x \sin \theta_x + k_0 z \cos \theta_x - \eta(z) + k_0 \frac{(x - z \tan \theta_x)^2 + y^2}{2R(z)} \quad (15.9)$$

where  $k_0$  is the central wave vector of the pulses,  $R(z)$  is the radius of the curvature of the beam's wavefront, and  $\eta(z)$  is the Gouy phase shift. We define the frequency

dependence of the beamlet angle as  $\sin\theta_x \approx \tan\theta_x \approx \theta_x = \frac{\alpha(\omega - \omega_0)}{f}$ , and thus  $\cos\theta_x \approx 1 - \frac{1}{2}\theta_x^2$ . When the spectral phase is expanded to second order we can obtain the spatial dependence of the pulse chirp [45]:

$$\phi_2(x, z) = \frac{1}{1 + z^2/z_R^2} \frac{2\alpha}{cf} \left( x - \frac{\alpha\omega_0}{2f} z \right) \quad (15.10)$$

This spectral phase originates from the evolution of the wavefront curvature of each of the beamlets. It is evident in this expression that there is a line in the  $x$ - $z$  plane where this geometric phase is zero. Solving for where  $\phi_2=0$  we can get

$$x(z) = \frac{\alpha\omega_0}{2f} z \quad (15.11)$$

Thus, the value of the IPT angle  $\theta_t$  can be evaluated as:  $\tan\theta_t = \frac{\alpha\omega_0}{2f}$ .

Intuitively, the slope of IPT is proportional to the angular chirp rate and inverse proportional to the focal length  $f$ . In our experiment, the IPT angle is calculated to be  $\sim 33^\circ$  by using Equation (15.11).

To add to the evidence about the mechanisms behind the nonreciprocal writing with femtosecond laser pulses, we performed an experiment to test for nonreciprocal writing where the beam is tilted with respect to the sample, but with conventional focusing. The beam was inspected at the focus to ensure that it did not have spatial chirp. This was easily accomplished by simultaneously rotating the incident beam and the objective ( $20\times$ , NA = 0.46) at an angle of  $\theta = 15^\circ$  in the YZ plane, as illustrated in Figure 15.8. In this experiment, another femtosecond laser (Libra-He,

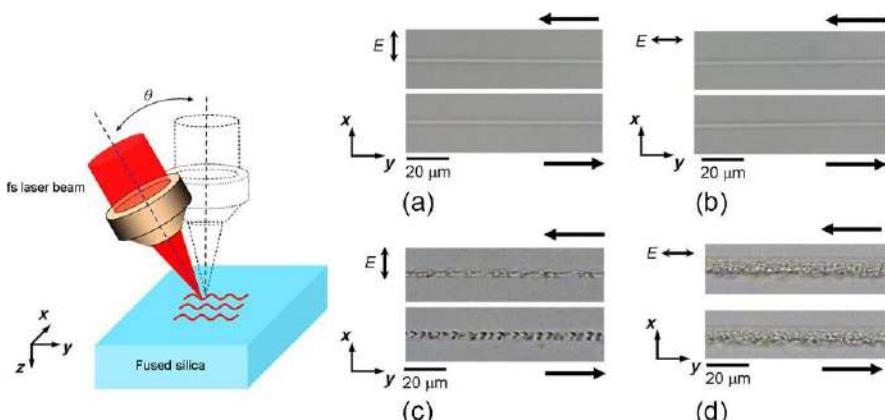


**Figure 15.8** Schematic of femtosecond LDW using a tilted focal plane (left) and optical micrographs of fs direct-writing structures in fused silica glass using (a, b) normal and (c, d) oblique incident beams, respectively. The polarization is along  $x$ - and  $y$ -directions in (a, c) and (b, d), respectively. The black arrows denote the laser writing directions.

Coherent Inc.) was used that emits 800 nm, 50 fs pulses with a maximum pulse energy of 4.5 mJ and a repetition rate of 1 kHz. The laser beam was linearly polarized along the  $Y$ -axis. The material used in the experiment is commercially available fused silica (JGS1), cut to small coupons with dimensions of  $10\text{ mm} \times 5\text{ mm} \times 2\text{ mm}$ , and with six sides polished. The sample was placed on a XYZ stage with a resolution of 1  $\mu\text{m}$ . The laser power and the scanning speed were 1.5 mW and 20  $\mu\text{m}/\text{s}$ , respectively. The location of the focal plane is  $\sim 300\text{ }\mu\text{m}$  beneath the surface of the sample.

When the beam was at normal incidence, no nonreciprocal writing effect was observed, as shown in [Figure 15.8a and b](#). While in the oblique incident scheme as depicted above, nonreciprocal writing structures were observed when the orientation of the electric field  $E$  was arranged perpendicular to the laser scanning direction ( $S$  polarization), as shown in [Figure 15.8c](#). In contrast, when the electric field  $E$  was arranged to be parallel to the laser scanning direction ( $P$  polarization), no reciprocal writing effect was observed, as shown in [Figure 15.8d](#). We note that for  $P$ -polarization there is a component of the electric field that is perpendicular to the surface, allowing for resonance absorption in the plasma gradient. The more effective energy absorption in this case may play a role in the difference between [Figure 15.8c and d](#). If we consider the intensity distribution tilting in a spatiotemporally focused laser beam, our results in [Figure 15.8c and d](#) are consistent with that reported in Ref. [46]. In that experiment, the change in incident angle was accomplished by displacing the beam from the center of the lens, so there was the potential for spatial chirp owing to the prismatic effect of the lens. More importantly, this simple experiment shows that a PFT relative to the surface may be sufficient for inducing the nonreciprocal writing effect. Thus, the role of PFT in inducing the nonreciprocal writing will require reexamination with further experimental and theoretical investigations.

This finding is a big step in our understanding of this exotic phenomenon, and suggests that for achieving a complete understanding on the nonreciprocal writing effect in glass observed with spatiotemporally focused laser pulses, the roles of the pulse front tilting and the peak-intensity distribution tilting should be separately investigated and weighed, which requires development of more sophisticated beam manipulation techniques in both space and time domains.

## 15.5 Enhanced femosecond laser filamentation using spatiotemporally focused beams

We extend the application of spatiotemporally focused ultrafast laser pulses from 3-D micromachining to femtosecond laser filamentation. It is well known that the peak intensity in the filament core is inherently limited by the intensity clamping effect during femtosecond laser filamentation. We experimentally demonstrate the significant enhancement of the peak intensity beyond the clamped intensity using the spatiotemporally focused femtosecond laser pulses. The experimental setup is similar to [Figure 15.3](#). Laser pulses at a center wavelength of 800 nm with a spectral bandwidth of  $\sim 30\text{ nm}$  were derived directly from the amplifier without compression. A cylindrical convex lens and a cylindrical concave lens were employed to reduce the beam size

by five times in the horizontal direction. Then, the beam was dispersed by a parallel pair of gratings in the horizontal direction. The distance between the gratings was optimized to compensate for the temporal dispersion of different spectral components. It was then focused with a 1000 mm focal length lens into the air. The fluorescence from the filament was imaged to the entrance slit of the spectrometer in a 4-f geometry configuration. For comparison, the fluorescence spectrum of the filamentation generated without using the spatiotemporal focusing was also measured.

**Figure 15.9a and b** shows the filament profiles generated with and without the spatiotemporal focusing technique captured by a digital camera from the side of the filaments. When using the 1000 mm focal lens to focus the 40 fs laser pulse without spatiotemporal focusing directly, the length of the filament is  $\sim$ 100 mm. However, when the spatial-temporal focusing technique is employed, the length of the filament decreases to less than 4 mm. The shortened filament implies that the peak intensity of the pulse decays quickly away from the focus. The rapid decrease of the peak intensity beyond the focus is caused by two reasons. First, as different spectral components of the beam are separated spatially, only at the focus will all the spectral components converge to form an ultrashort intense pulse. While before or after the focus, different spectral components of the beam diverge spatially resulting in a spatially chirped narrow spectral bandwidth, thus a longer pulse. Second, as different spectral components are spatially dispersed, only in the geometric focus is the pulse chirp free, while before (after) the focus the pulse is highly positively (negatively) chirped. The large chirp elongates the temporal pulse duration. Both these two effects ensure that the shortest pulse duration can only be achieved in the focus, while away from the focus the pulse duration grows quickly.

To investigate the clamped intensity in the filament, we measured the fluorescence of nitrogen molecules and ions generated by focusing the laser beam into the air with a 100 cm focal lens (both with and without spatiotemporal focusing configuration). Two representative spectra are demonstrated by the insets of **Figure 15.9a and b**,

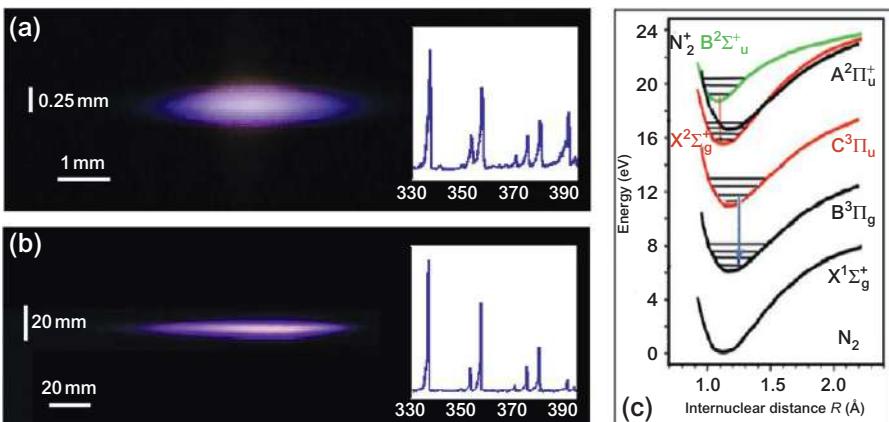


**Figure 15.9** Filamentation profiles captured by a digital camera (a) with and (b) without using spatiotemporal focusing. Please note the scale change from (a) to (b). Insets show the corresponding N<sub>2</sub> fluorescence spectra. (c) Indicates the energy diagram of nitrogen molecule.

respectively. Both spectra in the insets feature “continuum free,” as reported previously. Particularly, the 337 and 391 nm lines in the spectra can be assigned to the second positive band of  $N_2(C^3\Pi_u \rightarrow B^3\Pi_g)$  and the first negative band system of  $N_2^+(B^2\Sigma_u^+ \rightarrow X^2\Sigma_g^+)$ , respectively. The strength ratio between the two nitrogen fluorescence lines is given by the following:

$$R \equiv \frac{S_{391}}{S_{337}} = \frac{aI^{n1}}{k(aI^{n1} + bI^{n2})} \propto \frac{1}{1 + (b/a)I^{n2-n1}} \quad (15.12)$$

From Equation (15.12), we know that higher laser intensity will give rise to a larger ratio, because  $n_2 < n_1$  in view of higher ionization potential of the inner electrons.

The experimentally measured strength ratios of the 391 and 337 nm lines is plotted in Figure 15.10 as a function of the laser energy with and without spatiotemporal focusing. It can be seen that in the case without using spatiotemporal focusing, the ratio shows a first rapid rise with the increase of the input laser energy. While the energy is higher than 1 mJ, the ratio remains almost constant because the peak intensity does not increase due to the intensity clamping. However, when the spatial-temporal focusing technique was employed, the intensity ratio of the 391-337 nm first grows with the increase of the incident energy, and then it reaches a plateau at  $\sim 0.15$  when the laser energy is larger than 4.5 mJ, which indicates that the intensity clamping occurs at a higher energy level with higher intensity.

The peak intensity can then be calculated by the empirical formula [47]:

$$I_0 = 79 \times (2.6/R - 1)^{-0.34} \times 10^{12} \text{ W/cm}^2 \quad (15.13)$$

According to Equation (15.13), the peak clamped intensity in the filament is estimated to be enhanced by  $\sim 50\%$  using spatiotemporal pulses as compared to compressed pulses when using the 100 cm focal length lens. Although this experiment is carried

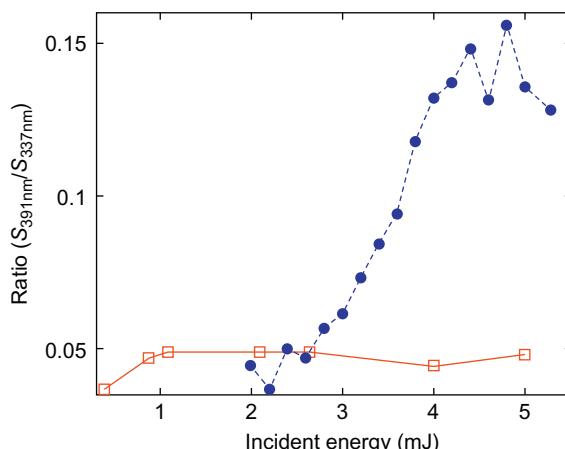


**Figure 15.10** Experimentally measured intensity ratio of the 391 and 337 nm lines as a function of the laser energy with (solid cycles) and without (open squares) using spatiotemporal focusing.

out in air, we expect a similar effect can occur in glass, which can lead to stronger modification inside glass materials. This effect may enable new applications such as synthesis of new materials by femtosecond laser-induced shock wave.

## 15.6 Conclusion and future trends

To summarize, this chapter focuses on 3-D femtosecond laser materials processing with spatiotemporally focused laser pulses. Previously, in the femtosecond laser materials processing, major efforts were made on the development of spatial and/or temporal beam shaping methods. With the introduction of simultaneous spatial and temporal focusing of femtosecond laser pulses, we show that several long-standing difficulties in femtosecond laser micromachining can be resolved, including achieving true 3-D isotropic resolutions, avoiding nonlinear self-focusing in thick samples, and enhancing the peak intensity at the focus spot by overcoming the intensity clamping. Specifically, we further reveal an unexpected tilted peak intensity distribution at the focus of a spatially chirped femtosecond laser beam, which will play important roles in applications such as femtosecond laser micromachining and bioimaging.

The implementation of the spatiotemporal focusing technique into the field of femtosecond laser micromachining provides us with new and exciting opportunities to manipulate the ultrashort pulse for 3-D laser-material processing. It will offer great opportunities for further fundamental research as well as technological applications in 3-D laser-material processing. On the other hand, this technique allows for precisely tailoring the ultrashort pulses simultaneously in the space and time domains, which exhibits great promise for deciphering the physics behind the exotic phenomenon of ultrafast laser-materials processing.

## Acknowledgment

The authors would like to thank Prof. C.G. Durfee from Colorado School of Mines for his helpful discussions. This work is supported by NSFC (Nos. 61327902 and 11104294).

## References

- [1] D. Strickland, G. Mourou, Compression of amplified and chirped optical pulses, *Opt. Commun.* 56 (1985) 219, [http://dx.doi.org/10.1016/0030-4018\(85\)90151-8](http://dx.doi.org/10.1016/0030-4018(85)90151-8).
- [2] D.E. Spence, P.N. Kean, et al., 60-fsec pulse generation from a self-mode locked Ti: sapphire laser, *Opt. Lett.* 16 (1991) 42, <http://dx.doi.org/10.1364/OL.16.000042>.
- [3] K.M. Davis, K. Miura, N. Sugimoto, K. Hirao, Writing waveguides in glass with a femtosecond laser, *Opt. Lett.* 21 (1996) 1729, <http://dx.doi.org/10.1364/OL.21.001729>.

- [4] E.N. Glezer, M. Milosavljevic, L. Huang, R.J. Finlay, T.-H. Her, J.P. Callan, E. Mazur, Three-dimensional optical storage inside transparent materials, *Opt. Lett.* 21 (1996) 2023–2025, <http://dx.doi.org/10.1364/OL.21.002023>.
- [5] M. Lenzner, J. Kruger, S. Sartania, et al., Femtosecond optical breakdown in dielectrics, *Phys. Rev. Lett.* 80 (1998) 4076, <http://dx.doi.org/10.1103/PhysRevLett.80.4076>.
- [6] B.N. Chichkov, C. Momma, S. Nolte, et al., Femtosecond, picosecond and nanosecond laser ablation of solids, *Appl. Phys. A* 63 (1996) 109, <http://dx.doi.org/10.1007/BF01567637>.
- [7] S. Kawata, H.B. Sun, T. Tanaka, et al., Finer features for functional microdevices, *Nature* 412 (2001) 697, <http://dx.doi.org/10.1038/35089130>.
- [8] A.P. Joglekar, H. Liu, E. Meyhofer, et al., Optics at critical intensity: applications to nanomorphing, *Proc. Nat. Acad. Sci. USA* 101 (5856) (2004), <http://dx.doi.org/10.1073/pnas.0307470101>.
- [9] R.R. Gattass, E. Mazur, Femtosecond laser micromachining in transparent materials, *Nat. Photonics* 2 (2008) 219, <http://dx.doi.org/10.1038/nphoton.2008.47>.
- [10] R. Osellame, H.J.W.M. Hoekstra, G. Cerullo, et al., Femtosecond laser microstructuring: an enabling tool for optofluidic lab-on-chips, *Laser Photonics Rev.* 5 (2011) 442, <http://dx.doi.org/10.1002/lpor.201000031>.
- [11] L. Sansoni, F. Sciarrino, G. Vallone, P. Mataloni, A. Crespi, R. Ramponi, R. Osellame, Polarization entangled state measurement on a chip, *Phys. Rev. Lett.* 105 (2010) 200503, <http://dx.doi.org/10.1103/PhysRevLett.105.200503>.
- [12] M. Beresna, P.G. Kazansky, Polarization diffraction grating produced by femtosecond laser nanostructuring in glass, *Opt. Lett.* 35 (2010) 1662, <http://dx.doi.org/10.1364/OL.35.001662>.
- [13] Y. Shimotsuma, M. Sakakura, P.G. Kazansky, M. Beresna, J. Qiu, K. Miura, K. Hirao, Ultrafast manipulation of self-assembled form birefringence in glass, *Adv. Mater.* 22 (2010) 4039–4043, <http://dx.doi.org/10.1002/adma.201000921>.
- [14] K. Sugioka, Y. Cheng, Femtosecond laser processing for optofluidic fabrication, *Lab Chip* 12 (2012) 3576–3589, <http://dx.doi.org/10.1039/C2LC40366H>.
- [15] Y. Shimotsuma, P.G. Kazansky, J. Qiu, K. Hirao, Self-organized nanogratings in glass irradiated by ultrashort light pulses, *Phys. Rev. Lett.* 91 (2003) 247405, <http://dx.doi.org/10.1103/PhysRevLett.91.247405>.
- [16] V.R. Bhardwaj, E. Simova, P.P. Rajeev, C. Hnatovsky, R.S. Taylor, D.M. Rayner, P. B. Corkum, Optically produced arrays of planar nanostructures inside fused silica, *Phys. Rev. Lett.* 96 (2006) 057404, <http://dx.doi.org/10.1103/PhysRevLett.96.057404>.
- [17] S. Kanehira, J. Si, J. Qiu, K. Fujita, K. Hirao, Periodic nanovoid structures via femtosecond laser irradiation, *Nano Lett.* 5 (2005) 1591–1595, <http://dx.doi.org/10.1021/nl0510154>.
- [18] Y. Liu, M. Shimizu, B. Zhu, Y. Dai, B. Qian, J. Qiu, Y. Shimotsuma, K. Miura, K. Hirao, Micromodification of element distribution in glass using femtosecond laser irradiation, *Opt. Lett.* 34 (2009) 136, <http://dx.doi.org/10.1364/OL.34.000136>.
- [19] S.K. Sundaram, E. Mazur, Inducing and probing non-thermal transitions in semiconductors using femtosecond laser pulses, *Nat. Mater.* 1 (2002) 217–224, <http://dx.doi.org/10.1038/nmat767>.
- [20] P.G. Kazansky, W. Yang, E. Bricchi, J. Bovatsek, A. Arai, Y. Shimotsuma, K. Miura, K. Hirao, “Quill” writing with ultrashort light pulses in transparent materials, *Appl. Phys. Lett.* 90 (2007) 151120, <http://dx.doi.org/10.1063/1.2722240>.
- [21] W. Yang, P.G. Kazansky, Y.P. Svirko, Non-reciprocal ultrafast laser writing, *Nat. Photonics* 2 (2008) 99–104, <http://dx.doi.org/10.1038/nphoton.2007.276>.

- [22] W. Yang, P.G. Kazansky, Y. Shimotsuma, M. Sakakura, K. Miura, K. Hirao, Ultrashort-pulse laser calligraphy, *Appl. Phys. Lett.* 93 (2008) 171109, <http://dx.doi.org/10.1063/1.3010375>.
- [23] K. Sugioka, M. Meunier, A. Piqué, *Laser Precision Microfabrication*, Springer Publishing, 2010, <http://dx.doi.org/10.1007/978-3-642-10523-4>.
- [24] K. Sugioka, Y. Cheng, *Ultrafast Laser Processing: From Micro- to Nanoscale*, Pan Stanford Publishing, 2013.
- [25] K. Sugioka, Y. Cheng, *Femtosecond Laser 3-D Micromachining for Microfluidic and Optofluidic Applications*, Springer, London, 2012, <http://dx.doi.org/10.1007/978-1-4471-5541-6>.
- [26] R. Osellame, G. Cerullo, R. Ramponi (Eds.), *Femtosecond Laser Micromachining: Photonic and Microfluidic Devices in Transparent Materials*, Springer, 2012, <http://dx.doi.org/10.1007/978-3-642-23366-1>.
- [27] R. Osellame, S. Taccheo, M. Marangoni, R. Ramponi, P. Laporta, D. Polli, S.D. Silvestri, G. Cerullo, Femtosecond writing of active optical waveguides with astigmatically shaped beams, *J. Opt. Soc. Am. B* 20 (2003) 1559, <http://dx.doi.org/10.1364/JOSAB.20.001559>.
- [28] Y. Cheng, K. Sugioka, K. Midorikawa, M. Masuda, K. Toyoda, M. Kawachi, K. Shihoyama, Control of the cross-sectional shape of a hollow microchannel embedded in photostructurable glass by use of a femtosecond laser, *Opt. Lett.* 28 (2003) 55, <http://dx.doi.org/10.1364/OL.28.000055>.
- [29] M. Ams, G. Marshall, D. Spence, M. Withford, Slit beam shaping method for femtosecond laser direct-write fabrication of symmetric waveguides in bulk glasses, *Opt. Express* 13 (2005) 5676, <http://dx.doi.org/10.1364/OPEX.13.005676>.
- [30] K. Sugioka, Y. Cheng, K. Midorikawa, F. Takase, H. Takai, Femtosecond laser microprocessing with three-dimensionally isotropic spatial resolution using crossed-beam irradiation, *Opt. Lett.* 31 (2006) 208–210, <http://dx.doi.org/10.1364/OL.31.000208>.
- [31] R. Stoian, M. Boyle, A. Thoss, A. Rosenfeld, G. Korn, I.V. Hertel, E.E.B. Campbell, Laser ablation of dielectrics with temporally shaped femtosecond pulses, *Appl. Phys. Lett.* 80 (2002) 353, <http://dx.doi.org/10.1063/1.1432747>.
- [32] C. Maclair, A. Mermilliod-Blondin, N. Huot, E. Audouard, R. Stoian, Ultrafast laser writing of homogeneous longitudinal waveguides in glasses using dynamic wavefront correction, *Opt. Express* 16 (2008) 5481–5492, <http://dx.doi.org/10.1364/OE.16.005481>.
- [33] G. Zhu, J. Howe, M.E. Durst, W. Zipfel, C. Xu, Simultaneous spatial and temporal focusing of femtosecond pulses, *Opt. Express* 13 (2005) 2153–2159, <http://dx.doi.org/10.1364/OPEX.13.002153>.
- [34] D. Oron, E. Tal, Y. Silberberg, Scanningless depth-resolved microscopy, *Opt. Express* 13 (2005) 1468–1476, <http://dx.doi.org/10.1364/OPEX.13.001468>.
- [35] F. He, H. Xu, Y. Cheng, J. Ni, H. Xiong, Z. Xu, K. Sugioka, K. Midorikawa, Fabrication of microfluidic channels with a circular cross section using spatiotemporally focused femtosecond laser pulses, *Opt. Lett.* 35 (2010) 1106, <http://dx.doi.org/10.1364/OL.35.001106>.
- [36] F. He, Y. Cheng, J. Lin, J. Ni, Z. Xu, K. Sugioka, K. Midorikawa, Independent control of aspect ratios in the axial and lateral cross sections of a focal spot for three-dimensional femtosecond laser micromachining, *New J. Phys.* 13 (2011) 083014, <http://dx.doi.org/10.1088/1367-2630/13/8/083014>.
- [37] D.N. Vitek, D.E. Adams, A. Johnson, P.S. Tsai, S. Backus, C.G. Durfee, D. Kleinfeld, J. A. Squier, Temporally focused femtosecond laser pulses for low numerical aperture micromachining through optically transparent materials, *Opt. Express* 18 (2010) 18086–18094, <http://dx.doi.org/10.1364/OE.18.018086>, <http://www.opticsinfobase.org/oe/abstract.cfm?URI=oe-18-17-18086>.

- [38] D. Kim, P.T.C. So, High-throughput three-dimensional lithographic microfabrication, Opt. Lett. 35 (2010) 1602–1604, <http://dx.doi.org/10.1364/OL.35.001602>.
- [39] D.N. Vitek, E. Block, Y. Bellouard, D.E. Adams, S. Backus, D. Kleinfeld, C.G. Durfee, J. A. Squier, Spatio-temporally focused femtosecond laser pulses for nonreciprocal writing in optically transparent materials, Opt. Express 18 (2010) 24673–24678, <http://dx.doi.org/10.1364/OE.18.024673>.
- [40] F. He, Y. Cheng, Z. Xu, Y. Liao, J. Xu, H. Sun, C. Wang, Z. Zhou, K. Sugioka, K. Midorikawa, Y. Xu, X. Chen, Direct fabrication of homogeneous microfluidic channels embedded in fused silica using a femtosecond laser, Opt. Lett. 35 (2010) 282–284, <http://dx.doi.org/10.1364/OL.35.000282>.
- [41] F. He, Y. Cheng, L. Qiao, et al., Two-photon fluorescence excitation with a microlens fabricated on the fused silica chip by femtosecond laser micromachining, Appl. Phys. Lett. 96 (2010) 041108–041108-3, <http://dx.doi.org/10.1063/1.3294627>.
- [42] J.W. Goodman, *Introduction to Fourier optics*, Roberts and Company Publishers, 2005.
- [43] A. Tien, S. Backus, H. Kapteyn, M. Murnane, G. Mourou, Short-pulse laser damage in transparent materials as a function of pulse duration, Phys. Rev. Lett. 82 (1999) 3883, <http://dx.doi.org/10.1103/PhysRevLett.82.3883>.
- [44] S. Akturk, X. Gu, E. Zeek, R. Trebino, Pulse-front tilt caused by spatial and temporal chirp, Opt. Express 12 (2004) 4399–4410, <http://dx.doi.org/10.1364/OPEX.12.004399>.
- [45] C.G. Durfee, M. Greco, E. Block, D. Vitek, J.A. Squier, Intuitive analysis of space-time focusing with double-ABCD calculation, Opt. Express 20 (2012) 14244–14259, <http://dx.doi.org/10.1364/OE.20.014244>.
- [46] B. Zeng, W. Chu, H. Gao, W. Liu, G. Li, H. Zhang, J. Yao, J. Ni, S. Chin, Y. Cheng, Z. Xu, Enhancement of peak intensity in a filament core with spatiotemporally focused femtosecond laser pulses, Phys. Rev. A 84 (2011) 063819, <http://dx.doi.org/10.1103/PhysRevA.84.063819>.
- [47] P.S. Salter, M.J. Booth, Dynamic control of directional asymmetry observed in ultrafast laser direct writing, Appl. Phys. Lett. 101 (2012) 141109, <http://dx.doi.org/10.1063/1.4756904>.

## Appendix: derivation of the angular chirp coefficient

This appendix [36] is used to derive the analytical expression of coefficient  $\alpha$  in Equation (15.1). The configuration of the gratings pair is shown in Figure 15.11, where  $i$  is the incident angle,  $\gamma$  the first order diffractive angle,  $d$  the distance between the gratings, and  $\sigma$  the grating constant, respectively. The first order diffraction must satisfy the following equation

$$\sin \gamma = \sin i - \lambda/\sigma \quad (15.14)$$

The left and right sides of Equation (15.14) can be written using the Taylor expansion to the first order as

$$\sin \gamma = \sin \gamma_0 + \Delta \gamma \cos \gamma_0 + \dots \quad (15.14a)$$

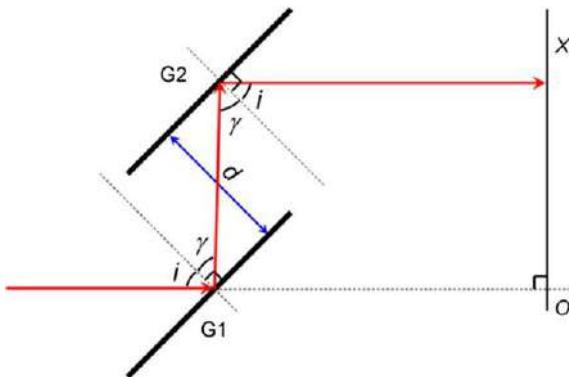


**Figure 15.11** Configuration of the gratings pair used in the spatiotemporal focusing scheme for dispersing and collimating different spectral components of the laser pulses.

$$\begin{aligned}\sin i - \lambda/\sigma &= \sin i - \frac{\lambda_0 + \Delta\lambda}{\sigma} + \dots \\ &= \sin i - \frac{\lambda_0}{\sigma} + \frac{\lambda_0}{\sigma\omega_0}\Delta\omega + \dots\end{aligned}\quad (15.14b)$$

where  $\lambda_0$  and  $\omega_0$  are the center wavelength and center frequency, respectively. It is noted that in Equation (15.14b) the approximation  $\Delta\lambda \approx -\lambda\Delta\omega/\omega$  is used. Combining Equations (15.14a) and (15.14b), it can be derived that

$$\Delta\lambda \approx \frac{\lambda_0}{\sigma\omega_0 \cos \gamma_0} \Delta\omega \quad (15.15)$$

The position of different spectral components along the  $x$ -direction is given as

$$x = d \sin(i + \gamma) / \cos \gamma \quad (15.16)$$

Both sides of Equation (15.16) can be written using the Taylor expansion as

$$x = x_0 + \Delta x + \dots \quad (15.16a)$$

$$\begin{aligned}d \sin(i + \gamma) / \cos \gamma &= d(\sin i + \cos i \tan \gamma) \\ &= d(\sin i + \cos i \tan \gamma_0) - \frac{d \cos i}{\cos^2 \gamma_0} \Delta\lambda + \dots\end{aligned}\quad (15.16b)$$

Substituting Equation (15.15) into Equation (15.16b), we obtain

$$\Delta x = -\frac{d\lambda_0 \cos i}{\sigma\omega_0 \cos^3 \gamma_0} \Delta\omega + o(\Delta\omega) + \dots \quad (15.17)$$

Hence the coefficient  $\alpha = -d\lambda_0 \cos i / (\sigma\omega_0 \cos^3 \gamma)$ .

# Tribology optimization by laser surface texturing: from bulk materials to surface coatings

16

*Q. Ding, L. Wang, L. Hu*

Chinese Academy of Sciences, Shanghai, China

## 16.1 Introduction

Surface texturing, that is, introducing specific patterns on sliding surfaces, is a well-known approach to improve the tribological properties of mechanical components, and relevant research has been conducted for many years in both the theoretical and industrial application aspects. Theoretical work mainly focuses on the simulation and structure optimization, based on the hydrodynamic and elastohydrodynamic lubrication theories [1–4], while application-oriented work explores the application potential of surface texturing on various mechanical components, including automotive components, forming tools, thrust bearings, seal rings, magnetic storage devices, and microelectromechanical system devices [5–8]. Generally speaking, the tribological effects of surface texturing could be summarized as follows: the microstructure on sliding surfaces could induce extra hydrodynamic pressure and increase the film stiffness of lubricant oil; meanwhile, the micropits or grooves could act as reservoirs for lubricants and could trap debris to reduce abrasive wear. To obtain textured surfaces, several technologies can be used, such as reactive ion etching (RIE), photoetching, laser surface texturing (LST), and mechanical machining, among which LST is thought of as the most promising solution because it is extremely fast, clean to the environment, and provides excellent control of patterns size and shape.

Section 16.2 first summarizes the laser ablation behaviors of typical materials such as metals, ceramics, and hard coatings. Through investigating the basics of laser-material interactions, the potential of the laser to be used as a texturing technique for different materials is discussed. Then Sections 16.3 and 16.4 provide a brief review of the recent research works on the application of LST to improve the tribological performances of various materials from bulk materials to surface coatings.

## 16.2 Laser ablation behaviors of different materials

For precise laser processing, high material removal efficiency with a small heat-affected region, good reproducibility, and the controllability of the pattern size are the central goals to be aimed for, and the processing results are strongly dependent

on the laser parameters, such as wave length, pulse duration, frequency, and peak power. However, the pulse duration ( $\tau$ ) is recognized as the most important parameter affecting the processing quality. The nanosecond (ns) laser is mature and has been widely used in the industrial field due to its simple construction and low price. It has been found that the ns-laser is very suitable for processing metals, including steels and light metal alloys. With the appropriate choice of laser parameters and processing strategies, high-quality micromachining with ns-lasers could also be realized on ceramics. However, because of the inherent thermal effects, the ns-laser is not suitable for texturing the nonmetal hard surface coatings. In the case of ultrashort (picosecond and femtosecond) laser pulses, due to the extreme nonequilibrium ablation mechanisms, the ultrashort laser ablation is expected to significantly lower the thermally affected zone and produce fine surface structures on metals, ceramics, and surface coatings.

### 16.2.1 *Laser ablation behavior of metals*

Metals are one of the most widely used engineering materials, and laser treatment has proved to be very efficient in patterning metals. Even with ns-laser pulses, high-quality textures can be rapidly produced on metal surfaces including steels, titanium alloys, and aluminum alloys. Hu studied the ablation behavior of the above-mentioned materials by multipulse irradiation with a Nd:YAG ns-laser ( $\lambda = 1.064 \mu\text{m}$ ,  $\tau = 4 \text{ ns}$ ) at the power of 9.8 W and 20 kHz frequency. It turned out that differences in thermo-physical properties might result in different ablation rates. With up to 40 times irradiation, the depth of the produced micropits on steel could reach 25  $\mu\text{m}$  with a diameter of 50  $\mu\text{m}$ , while the depth of micropits on titanium alloys and aluminum alloy could reach 80  $\mu\text{m}$  with a diameter of 40  $\mu\text{m}$ . Thus, a surface structure with a high  $h/d$  (depth versus diameter) ratio, which is a key factor for tribological optimization, could be more easily obtained on titanium alloys and aluminum alloy. Additionally, due to the severe thermal effects of ns-laser pulses, the ablated surfaces need to be polished to remove the sharp bulges around the irradiated spots.

In order to produce structures with large dimensions, such as wide channels or micropits that are larger than the focused laser spot, several laser tracks have to be put side-by-side with a defined offset. Schreck compared the machining results on steel with a Nd:YAG ns-laser system ( $\lambda = 1.064 \mu\text{m}$ ,  $\tau = 100-200 \text{ ns}$ , 5 W, 5 kHz) that operated in the pulsed mode (Q-switch) and continuous wave (cw) mode [9]. Operated in pulsed mode, the produced channels show a rather ragged surface, while with the cw-mode and a multistage process strategy, large dimension structures with high quality could be achieved, as shown in [Figure 16.1a](#).

The appropriate choice of wavelength  $\lambda$  could also improve the machining quality. Since the reflectivity of most metals is high in the near-infrared but decreases at shorter wavelengths, Knowles suggested that the visible wavelength such as frequency-doubled Nd lasers (532 or 527 nm) and copper vapor laser (CVL) (511 nm) are often the best choice for the micromachining of metals with ns-lasers [10]. For process strategy, the optimum quality is most often achieved by using low-pulse energy to remove only a small volume per pulse, with a high-pulse

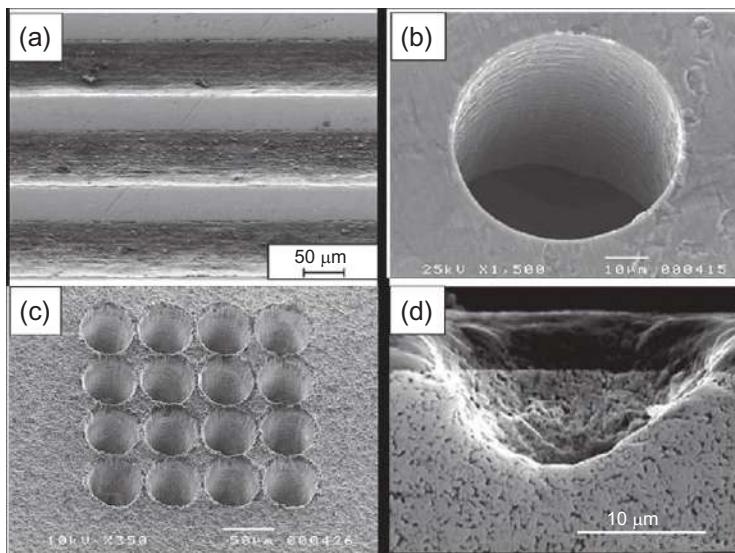


**Figure 16.1** SEM micrographs of different structures: (a) channels in steel generated by the Nd: YAG ns-laser in cw-mode; (b) hole drilled through stainless steel by a CVL ns-laser system; (c) high density holes drilled in alumina ceramic by a CVL ns-laser system; and (d) laser ablated pore in coated WC-Co by a Ti:sapphire fs-laser system [9–11]. Reproduced with permission from Ref. [9]. Copyright (2005) Elsevier B.V.; reproduced with permission from Ref. [10]. Copyright (2007) Springer; reproduced with permission from Ref. [11]. Copyright (2004) Springer.

frequency to ensure adequate material removal rates. Using a CVL system ( $\lambda=511\text{ nm}$ ,  $\tau=20\text{ ns}$ , 45 W, 10 kHz), very high-quality laser micromachining was realized on stainless steel, as shown in Figure 16.1b.

### 16.2.2 Laser ablation behavior of ceramics

Advanced ceramics are regarded as ideal tribomaterials for harsh working conditions due to their excellent physical, chemical, and mechanical properties, such as high wear resistance, stability at high temperatures, and good corrosion resistance. In particular, silicon nitride ( $\text{Si}_3\text{N}_4$ ) and silicon carbide ( $\text{SiC}$ ) have gained much attention due to their extremely low friction in water lubrication, making them promising materials for mechanical seals and sliding bearings of hydraulic machines [12]. Lots of research has proved that the hydrodynamic lubrication performance and antiseizure ability of ceramic components could be further improved by surface texturing.

However, compared with metals, the laser texturing of ceramics is challenging due to the large scattering at common laser wavelengths and high ablation threshold [10]. Sciti investigated the ablation behavior of  $\text{SiC}$  ceramics with a  $\text{CO}_2$  laser system [13]. In the experimental condition ( $\lambda=1.064\text{ }\mu\text{m}$ ,  $\tau=0.5\text{--}2\text{ ms}$ ,  $P_{\text{cw}}=1.5\text{ kW}$ ), hole diameters ranging from 100 to 200  $\mu\text{m}$  and depth up to 400  $\mu\text{m}$  were obtained. Although a

high material removal rate was achieved, a ring-like heat-affected zone was observed in all the treated samples, with thermal stress-induced microcracks extending around the hole. Such a heat-affected zone was also observed by Wang *et al.* [14]. Thus, as proposed by Knowles, for ceramics such as alumina and silicon nitride, a combination of short pulse and short wavelength should be the best choice. Using a CVL system ( $\lambda = 511$  nm,  $\tau = 20$  ns), high-quality hole (50  $\mu\text{m}$  in diameter and 250  $\mu\text{m}$  in depth) arrays were created on alumina ceramics as shown in Figure 16.1c [10]. Since the thermal stress-induced cracking is related to the formation of intense laser-induced plasma, to avoid this, the power was set at 3 W to keep the heat input to the bulk material low. Actually, even for a fs-laser, high energy fluence-induced plasma could also impair the precision and regularity of the processing results [11]. Thus multiablation with low single pulse energy is still the optimum processing strategy for an ultrashort laser system.

Besides generating microscale structures and periodic nanostructured arrays, the so-called ripple structure, can also be simultaneously produced on irradiated surfaces by a fs-laser. Such a ripple structure is thought to be related to the second-harmonic wave and can be fabricated by irradiating the material near the ablation threshold. Friction tests showed that such nanostructures also exhibit certain beneficial effects in the tribological optimization of ceramics [15,16].

### 16.2.3 *Laser ablation behavior of surface coatings*

Depositing protective coatings is a mature technology to prolong the lifetime of tools. For example, electroplated chromium processing has been widely used in industry to enhance the wear resistance and corrosion resistance of steel components. With the emergence of new deposition technologies, such as physical vapor deposition (PVD) and chemical vapor deposition (CVD), new coating materials with superior properties have been developed, such as titanium nitride (TiN) and chromium nitride (CrN), which exhibit high hardness, excellent wear resistance, and low stick properties, and have been applied in various cutting and machining tools. Among the newly developed surface coatings, diamond-like carbon (DLC) coating gained wide attention due to its excellent tribological properties, such as high hardness, very low friction, and chemical inertness [17].

In recent years, to combine the advantages of protective coatings and the beneficial effects of surface texturing, coatings with well-defined surface structures have been prepared. Such textured coatings can be prepared either by depositing the coating material on a textured substrate or directly structuring the coating by etching or laser ablating. Because the etching technology involves a complicated technical procedure, laser direct ablating has the advantage in convenience and efficiency [18]. However, in practice, it is found that the ns-laser pulse is unsuitable for direct ablating of hard surface coatings, due to the inherent heat-affected zone, which has the same order of magnitude as the film thickness [19]. The thermal stress induced in the film lowers its adherence to substrates. Passing from ns-laser to fs-laser could improve the quality of laser processing. In the case of fs-laser ablation, the absorption of the energy needed for material ablation is highly confined to a superficial layer and occurs via different

material-specific phenomena in practically all materials, which enables the processing of both the surface coating and the substrate with the same laser beam [20]. To avoid the adverse effects caused by laser-induced plasma, the combination of low fluences and high repetition rates is a preferred processing strategy.

Dumitru drilled the TiN and TiCN coated surfaces with a Ti:sapphire fs-laser system ( $\lambda = 800$  nm,  $\tau = 100$  fs,  $E = 2$  J/cm<sup>2</sup>). After 100 incident pulses, the micropits with a depth of 18  $\mu\text{m}$  were produced on the TiN coated steel, while the micropits with a depth of 15  $\mu\text{m}$  were produced on the TiCN coated hard metal (WC-Co) [20]. Morphology analyses did not reveal any coating delamination or other coating damage after laser processing as shown in Figure 16.1d [11]. It is proposed that after the first dozen pulses, the film was penetrated and the subsequent pulses induced ablation on the substrate. By using the fs-laser pulses, similar precise processing was also achieved on DLC coated surfaces [21].

Besides changes in morphology, changes in phase structure could also be induced by laser ablation. For inert coatings like TiN, an oxidation phenomenon was observed inside the irradiated spots. However, for DLC, the laser-induced structure change is more complicated. As a metastable form of amorphous carbon, the properties of DLC are strongly dependent on the microstructure, that is, the relative fraction of sp<sup>2</sup> and sp<sup>3</sup> carbon bonds and the energy imposed by laser pulses is enough to trigger the phase transformation (0.5 J/cm<sup>2</sup>) in DLCs.

The basics of laser-DLC interaction have been discussed in many research papers. The transfer of energy from the laser pulse to the carbon film causes structural modification of a surface layer, including transformation of existing sp<sup>3</sup>-bonds to sp<sup>2</sup>-bonds and crystallization of the original amorphous matrix. This structural modification (usually called graphitization) is accompanied by significant changes in the DLC's physical properties, for example, mechanical properties, optical absorption, thermal conductivity, and tribological behavior. Simulation studies, which investigated the influence of the pulse duration on the graphitization process, demonstrated that for fs-pulses a layer-by-layer graphitization occurs, whereas for longer laser pulses (ns or longer) graphitization propagates vertically into bulk [22]. Dumitru experimentally investigated the effects of laser pulse duration on structural changes of DLC [23]. Confirmed by Raman analysis, they found both nonequilibrium (fs) and equilibrium (ns) laser interactions induced the graphitization process of DLC, but the fs-laser irradiation lowered the in-plane order, whereas the ns-laser treatment increased it.

As occurred in ceramics, when irradiated by fs-laser pulses around the ablation threshold, a "ripple" structure could also be formed on the irradiated coatings, such as DLC and TiN. The ripples can be attributed to the periodic enhancement of the local field through the excitation of surface plasmon polaritons (SPPs) in the surface layer. However, for DLC coatings, due to the unique graphitization process during ablation, a swelling morphology could be formed when the bonding structure is changed from DLC to glassy carbon (GC), making the DLC exhibit a special nanoscale ablation behavior. By observing the initial stage of ablation, Miyaji found that the nanostructure formation is initiated on the swelled surface and the presence of surface roughness in nanosize, resulted from the structural change, is crucial for the SPP excitation [24].

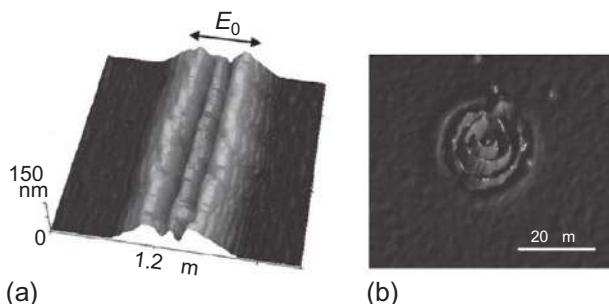


**Figure 16.2** The unique laser ablation behavior of DLC: (a) micro-nano structure induced by fs-laser on DLC and (b) spalling effect induced by ns-laser on DLC:H [24,25]. Reproduced with permission from Ref. [24]. Copyright (2008) OSA; reproduced with permission from Ref. [25]. Copyright (2011) AIP Publishing LLC.

On the swelled surface with a high curvature, the local field is generated to enhance the incident  $E$ -field and initiate nanoscale ablation. It is noteworthy that such unique ablation behavior enables us to rapidly and conveniently construct the nano/micro multiscale structure on DLC surfaces, as shown in Figure 16.2a.

Recently, Ding found that the hydrogen in DLC structure could cause significant impact on the laser processing results [25]. Based on the hydrogen content, the DLC can be generally divided into two major categories: the hydrogenated DLCs (DLC:H), which could be deposited from different source gases such as  $\text{CH}_4$ ,  $\text{C}_2\text{H}_2$ ,  $\text{C}_2\text{H}_4$ , and  $\text{C}_6\text{H}_6$ , and the nonhydrogenated DLCs, which use graphite as a carbon source. When irradiated with a Nd:YAG ns-laser ( $\lambda = 1.064 \mu\text{m}$ ,  $\tau = 4 \text{ ns}$ ) system, the nonhydrogenated DLC and DLC:H exhibit totally different ablation behavior. The processing results of nonhydrogenated DLC could be facilely controlled (from microbulges to micropits) by adjusting the laser power. However, as shown in Figure 16.2b, for DLC:H, a distinct multilayer spallation phenomenon was observed, which brings the uncertainty and limits the precision and reproducibility of the laser texturing process.

Kononenko first reported the laser-induced spalling effect in DLC:H, and showed that such effect existed for a wide range of laser parameters ( $\lambda = 539, 800, 1064$ , and  $1078 \text{ nm}$ ;  $\tau = 100 \text{ fs}, 300 \text{ ps}, 10 \text{ ns}$ , and  $150 \text{ ns}$ ) [26–28]. They suggested that the spallation effect belongs to the fundamental aspects of the pulsed laser interaction with DLC films, and proposed a dynamic tensile stresses mechanism, in which the dynamic tensile stress is caused by the interference between the compressive and rarefaction waves. The tensile stress has a maximum at a variable distance from the surface, and if the maximum reaches the fracture threshold, a crack would appear in the corresponding region. However, the model could not successfully explain the experimental results that such spallation effects could only be observed on DLC:H, but not on nonhydrogenated DLC.

Then based upon the simulation results, Ding found that the temperature distributions are nearly identical in both coatings for the same laser parameter. Therefore, the different ablation behavior between nonhydrogenated DLC and DLC:H might

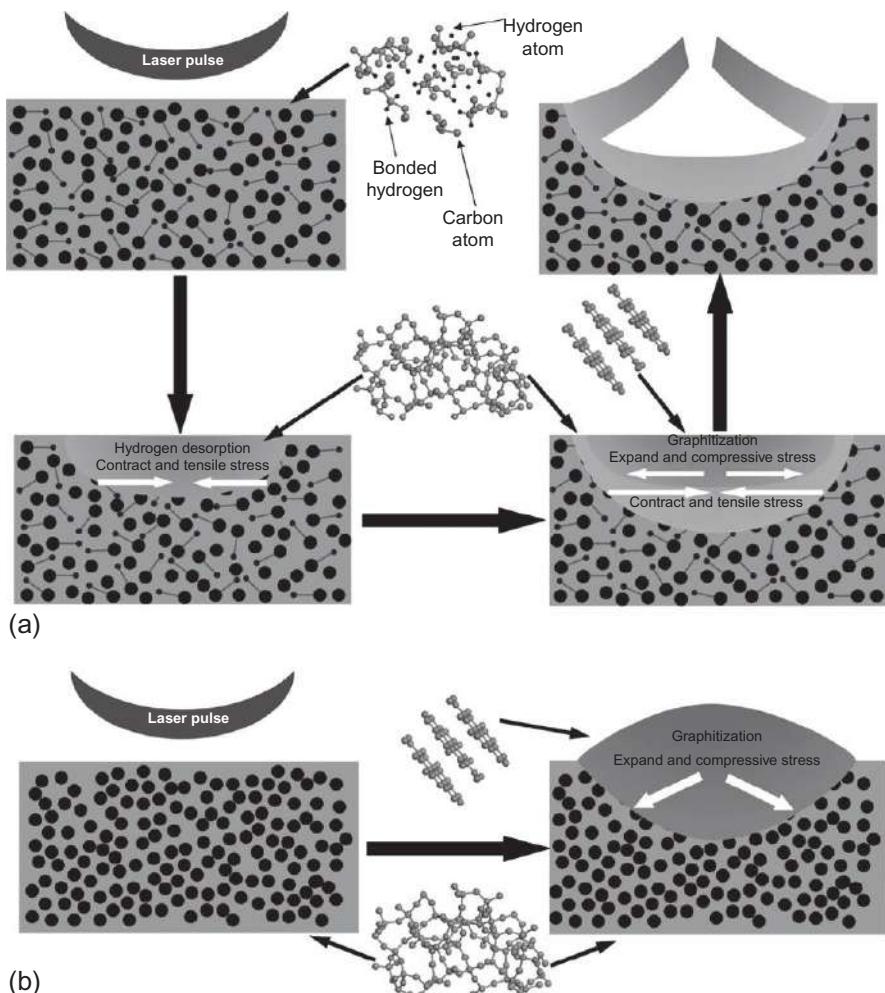
not lie in the laser parameter, but in the different film microstructure and its evolution process when irradiated by laser. Through the annealing experiments and subsequent structural and mechanical characterizations, it was found that after it had been heated, the nonhydrogenated DLC graphitized directly, while the DLC:H existed as a hydrogen desorption subprocess during the graphitization. From the point of view of structure evolution process of DLC during laser ablation, a mechanism was proposed.

Figure 16.3 illustrates the mechanisms of laser-induced spallation behavior in DLC:H and swelling in nonhydrogenated DLC. As shown in Figure 16.3a, at the beginning of the laser pulse, the surface layer of DLC:H is heated to the temperature at which the hydrogen mobilization and C—C network rearrangement occur. The heated region tends to contract due to network rearrangement and, thus, cause a radial tensile stress and tangential compressive biaxial stress. Then, as the laser pulse continues, the surface layer would be further heated to a higher temperature and trigger the graphitization transformation in this layer. Therefore, this layer would tend to expand and cause a radial compressive stress and tangential biaxial tensile stress. However, the layer below the surface layer (subsurface layer) just reaches the temperature at which the hydrogen mobilization and film densification take place, and thus radial tensile stress and tangential compressive biaxial stress are induced. Because these two processes occur at the same time dynamically at different depth, stress concentration, especially the tangential biaxial stress, would take place at the boundary between the layers. Once the concentrated stress exceeds the fracture threshold of modified layer, one can expect the appearance of a crack in the corresponding region. At last, as the temperature gradient extends deeper, the film would peel layer by layer. However, as shown in Figure 16.3b, the modified region in nonhydrogenated DLC just expands and causes radial compressive stress and tangential biaxial tensile stress. No stress concentration occurs between layers as happened in DLC:H. Therefore, the non-hydrogenated *a*-C surface just swells after being laser treated.

Then, the author proposes that two factors are crucial for the occurrence of such spalling effects: (1) the heat source, like laser pulse, with high power density and ultra-short duration, which could produce a high temperature gradient in very short time; and (2) the unique evolution process of film microstructure under heating.

## 16.3 Tribological application of laser surface texturing (LST) to bulk materials

As discussed in Section 16.1, the LST could improve the tribological properties by inducing extra hydrodynamic pressure, capturing the wear particles, storing the lubricants, and lowering the contact areas. Depending on different contact geometry, material properties, and operating conditions, one of above-mentioned effects may dominate. However, in order to obtain the maximum beneficial effects of LST, especially the hydrodynamic effects, large relative contact area and high sliding speed are the preferred working conditions such as that for seals and thrust bearings. Kovalchenko investigated the friction and wear behavior of laser-textured surface under



**Figure 16.3** Schematic diagrams of mechanisms for laser-induced: (a) spallation on DLC:H and (b) swelling on nonhydrogenated DLC. The microstructures for as-deposited films as well as the modified region are provided. The snapshot pictures illustrate the film temperature variation and microstructure evolution process during the laser pulse. The white arrows indicate the directions of modification-induced stress [25].

Reproduced with permission from Ref. [25]. Copyright (2011) AIP Publishing LLC.

lubricated point contact [29]. They found that the LST disks produced more abrasive wear on the counter ball. Nevertheless, the accelerated wear changes the contact geometry and facilitates the transition of lubrication from a high-friction boundary to lower-friction mixed regime. The author suggested that for nonconformal contact configuration, LST could be tribologically detrimental, especially in components requiring high precision and stability of dimensions in which wear is undesirable.

Therefore, the tribological tests for laser-textured materials often choose the surface-contact frictional pairs such as pin-on-disk or ring-on-disk configurations.

Hu experimentally investigated the tribological behavior of textured metallic materials including steel, aluminum alloy, and titanium alloy [30–36]. The textured patterns are micropits with different diameters and area coverage fraction. Frictional tests were performed on a pin-on-disk tribometer under dry friction, boundary lubrication, and solid ( $\text{MoS}_2$ ) lubrication. The friction coefficients and the corresponding optimal structure parameters are summarized in [Table 16.1](#).

As listed in [Table 16.1](#), in dry friction, the combination of large-diameter and high-textured area coverage is preferable. In unlubricated condition, the wear debris and material stick contribute the main friction forces, and the large dimple diameter with high-textured area proportion could be more effective in friction reduction by trapping debris and reducing contact area. It is noteworthy that the LST is more effective in friction reduction for titanium alloy, which is not easy to be lubricated due to high adhesive force. However, the functions of LST only maintain a short time and become ineffective after the surface structure is worn out.

For boundary lubrication and solid lubrication ( $\text{MoS}_2$ ) condition, the main effects of LST are to preserve the lubricants and feed the lubricants to the contact surfaces. Combined with lubricants, the textured samples exhibited lower friction coefficient and longer lifetime than the untextured ones, indicating that the surface texturing is beneficial for the maintaining and feeding of lubricants. The optimal textured parameters show a similar trend for both boundary lubrication and solid lubrication, that is, the preferred pattern is a medium dimple diameter with a medium area coverage fraction rather than the biggest dimple diameter with the largest area coverage, indicating

**Table 16.1 The friction coefficients and the corresponding optimal structure parameters for steel, aluminum alloy, and titanium alloy in dry friction, boundary lubrication, and solid lubrication [30–36].**

	Steel		Aluminium alloy		Titanium alloy	
	Polish	Textured (optimal structure)	Polish	Textured (optimal structure)	Polish	Textured (optimal structure)
Dry friction	0.5	0.2 ( $D = 300 \mu\text{m}$ ; 33%)	0.6	0.5 ( $D = 150 \mu\text{m}$ ; 18%)	0.7	0.2 ( $D = 300 \mu\text{m}$ ; 44%)
Boundary lubricated	0.4	0.1 ( $D = 160 \mu\text{m}$ ; 30%)	0.2	0.08 ( $D = 100 \mu\text{m}$ ; 8.5%)	0.3	0.18 ( $D = 160 \mu\text{m}$ ; 30%)
$\text{MoS}_2$ lubricated	0.3	0.075 ( $D = 65 \mu\text{m}$ ; 20%)	0.3	0.15 ( $D = 150 \mu\text{m}$ ; 37%)	0.5	0.2 ( $D = 160 \mu\text{m}$ ; 30%)

that a proper distribution of lubricant in the contact area is more important than the storage amount of lubricant.

To further improve the tribological performances of a solid lubricants/LST system, a hot press method could be applied to settle the solid lubricants on the textured surface [37]. The MoS<sub>2</sub> lubricating layer formed by hot pressing is thicker and denser than the ones formed by burnishing. The friction coefficient could be lowered to 0.05. Due to the high pressure, the micropits were well fulfilled with the lubricants. And such interlocking structure between the MoS<sub>2</sub> layer and textured substrate could greatly improve the load carry capacity and prolong the lubrication lifetime.

Due to high hardness, the texture fabricated on ceramics is more durable than the one on metals. Hu prepared the textured Al<sub>2</sub>O<sub>3</sub>-ZrO<sub>2</sub> disks with the pattern of micro-dimples. The produced dimples have a diameter of 150 μm and area coverage fraction of 6%, 12%, and 34%. When sliding against the steel pins under dry friction, the LST could reduce the friction coefficients about 40% more than the polished one, and high area coverage fraction is more effective in friction reduction. Surface analysis showed that the wear track on polished sample was covered with thick aggregates of steel debris, while the textured surface was clear and nearly intact with the dimples filled with wear debris.

Water lubrication is a typical working condition for ceramics such as Si<sub>3</sub>N<sub>4</sub> and SiC. Wang investigated the effects of LST on the load-carrying capability of SiC in water lubrication [14]. Microdimples were prepared on the SiC disk using a CO<sub>2</sub> laser system. The results showed that at the optimum structure parameter (diameter = 150 μm, area coverage = 2.8%), LST could raise the critical load of SiC by 20%. The author pointed out that the heat effects during the laser process resulted in the microcracks and lowered the material hardness, which affected the surface smoothing process in the running-in period. In their later studies, high-quality surface structure was fabricated using the RIE, and a substantial improvement in critical load (three times higher than the flat one) by surface texturing was evidenced [5]. Although such surface texture was produced by RIE technology, the laser technology is still capable to produce high-quality microstructure by using the ultra-short laser pulses or by optimizing the processing strategy as has been discussed in [Section 16.2](#).

In research work about LST, the circular dimple is the most selected structure due to its isotropy and convenience for simulation, and the influences of structure parameters (diameter, depth, and area coverage) on tribological performances has been deeply studied both in theoretical and experimental aspects. However, the circular dimple pattern might not be the most effective structure. Zum Gahr showed that the crossed channels pattern is more effective in friction reduction than the microdimple pattern for both steel self-mated and steel/Al<sub>2</sub>O<sub>3</sub> mated pairs [9]. Based on experimental and simulation results, Yu found that the ellipses placed perpendicular to the sliding direction exhibited a better result of load-carrying capacity than the circle dimples [4]. Some more complicated patterns that composed of texture units with different shapes or different scales also exhibited certain potential in tribological optimization [38,39]. However, due to the complicated geometry, such works are mainly focused on the experimental aspects.

## 16.4 Tribological application of LST to surface coatings

As discussed in [Section 16.2](#), to obtain coatings with specific surface structure, two approaches can be used: indirect processing, which is coating the already patterned substrates, or direct processing, which involves directly ablating the deposited coating by laser. However, due to the fact that the optimal pore depths yielding positive tribological effects are always larger than the thickness of common PVD coatings ( $\leq 5 \mu\text{m}$ ), the substrate also needs to be partially ablated in direct laser processing. Thus, the ultrashort pulses (ps or fs) should be the best choice for such precise laser processing.

### 16.4.1 Tribological performances of textured coatings fabricated by indirect processing

As for bulk materials, the beneficial effects of LST are also effective for coatings. However, in practical use, the main function of a surface coating is to protect the material from abrasive wear or to lubricate the contact surface in dry friction or boundary lubrication regime. Thus, the effects of debris trapping and lubricant storage should be more meaningful for textured coatings. Dumitru produced the textured DLC film by depositing DLC on laser-textured substrates, which had a pattern of micropits with a pore diameter of  $25 \mu\text{m}$  [\[21\]](#). The tribological test results showed that, under dry lubrication, the patterned surface could endure higher load without coating failure, while the untextured one was immediately worn out when the load was raised. The authors suggested that the hard debris were trapped into the surface pores, preventing the breakdown of the coating system.

However, Pettersson found that introducing texture into contact surfaces could bring beneficial results only in certain conditions, which depend on the coating instincts, lubrication condition, and structure parameters [\[40,41\]](#). For instance, in dry friction, the surface texture is beneficial for TiN but detrimental for DLC. Surface analyses suggest that, although the textured surface could lower the friction by debris trapping, the additional surface roughness caused by texture is harmful for the formation of tribofilm on counterbody, which is a key mechanism for self-lubrication of DLC. In boundary lubrication, due to the oil reservation effects, the textured coating could exhibit excellent tribological properties. However, to provide sufficient lubricant within the contact zone, the scale (diameter or width) of textured units (pores or grooves) need to be small enough compared with the contact areas.

Recently, when Ding prepared the textured DLC coating by depositing DLC on textured steel substrates, the inhomogeneous phase structure of deposited DLC was observed, implying that the substrate's morphology may affect the microstructure of deposited DLC [\[42\]](#). As shown in [Figure 16.4a](#), the DLC near the edge of grooves exhibited higher  $\text{sp}^2$  carbon fraction and lower coating hardness than the other regions. In a PVD system, a negative bias voltage is always applied on the substrate. From the simulation of an electric field around structured substrate, it was found that the local electric field was enhanced near the edges of grooves. Because the phase structure of

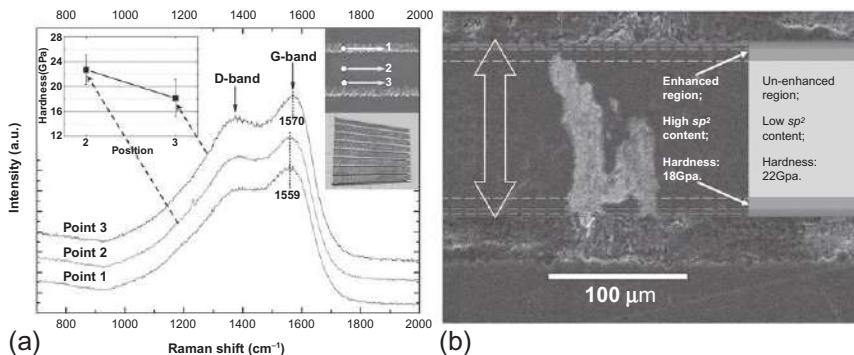


**Figure 16.4** (a) Raman frequency-intensity and the local nanohardness of deposited DLC at different locations on the textured substrates and (b) magnified SEM image of a delamination on the textured coating. The right part indicates the approximate spatial distribution of film microstructural gradient according to the corresponding electric field variation from the simulation. The double-headed arrow shows the sliding direction [42].

Reproduced with permission from Ref. [42]. Copyright (2010) Springer.

DLC is strongly depended on the deposition energy, the phase gradient in textured DLC coating might be ascribed to the electric field gradient on textured substrates. Further friction tests show that such phase-graded films exhibit better toughness, and the delamination tends to diminish when it comes into the electric-enhanced region, as shown in Figure 16.4b. The author thought that the  $\text{sp}^2$  carbon-enriched region with lower hardness could act as a kind of “buffer stripes” to terminate the cracks and suppress the enlargement of delamination by relieving the shear stress and dissipating the crack energy during friction.

Additionally, surface texture may affect the phase transformation of DLC during friction. Confirmed by the Raman spectra, it was found that the textured DLC coating experienced a much lower graphitizing transformation than the untextured one did [42]. The graphitization during friction is a degradation process for DLC, and such process is related to the factors including flash temperature between sliding surfaces and contact stress. As reported by Haque, high-contact pressure caused by wear debris could trigger the graphitizing transformation [43]. For the textured DLC, the wear debris is trapped by micropits or grooves during friction. Therefore, the wear-induced graphitization is relieved. This effect is beneficial for the maintenance of coating hardness during friction, and thus enhances the lifetime of DLC coatings.

#### 16.4.2 Tribological performances of textured coatings fabricated by direct processing

Direct processing is advantaged in simple procedure and low detrimental effects on coating adherence (with fs laser). Additionally, laser-induced local structural changes in coating could also bring unique effects in tribological properties. Through directly ablating with fs-laser, Dumitru successfully prepared the textured TiN and TiCN

coating with the pattern of micropits. When sliding against a steel cylinder under oil lubrication condition, significant differences in the friction evolution between the textured and untextured coating were observed [20]. The laser-textured surfaces maintained a low (0.11) and stable friction over a much longer duration than the untextured ones. Additionally, after friction test, the untextured coating showed severe damage with complete coating removal, while on the laser-patterned surfaces, only slight wear features were noticeable. Surface analysis showed that a large part of the pores in the wear track were filled with wear debris coming from the counterbody, suggesting that the laser texturing effectively prohibited the debris-induced wear processes.

Besides introducing specific depression patterns such as pores or grooves, swelling structures could also be produced to modify the coating tribological behavior. By using the unique structure response of DLC to fs-laser pulses, Yasumaru obtained the nanostructured DLC coatings. It was found that the tribological properties of the DLC surface could be controlled using such laser-induced nanostructure [44]. With a net-like pattern of nanostructure zone, the friction coefficient of DLC could be increased (from 0.08 to 0.45) when sliding against a hard metal WC-Co ball, while with a MoS<sub>2</sub> layer on the nanostructured surface, the frictional property of DLC can be greatly improved whether paired with steel or hard metal counterparts. The author thought the large reduction in friction with additional MoS<sub>2</sub> layer can be attributed to the following two reasons: The surface nanostructure acts as a lubricant reservoir to store the MoS<sub>2</sub> layer, and the induced GC layer improves the bonding interface between the DLC and MoS<sub>2</sub> layers.

Recently, Ding reported that the ns-laser pulse could also produce specific patterns on DLC coating [25]. The topography of produced pattern can be microbulges or micropits depending on different pulse power density. Additionally, besides change in morphology, localized GC phase was produced in the irradiated spot, which exhibited different mechanical properties from the original DLC film. The authors found the textured DLC with the pattern of microbulges exhibit superior tribological performances to the original one in both micro- and macroscale.

To evaluate the microtribological behavior, the load was limited to 100-1000 mN. It was found that laser treatment could produce different effects on the tribological performance depending on the friction pairs [45]. The laser treatment is negative for friction reduction when paired with Si<sub>3</sub>N<sub>4</sub> balls, especially in the small load range. When sliding against untreated DLC, the Si<sub>3</sub>N<sub>4</sub> ball exhibited low friction coefficients, which could be ascribed to low adhesion and slight plough effect. The inhomogeneous hardness generated by laser treatment invalidates the two above-mentioned beneficial factors and results in high friction. However, the laser treatment is very effective in friction reduction when the steel balls are paired. The high friction between the untreated DLC and the steel ball could be ascribed to the high adhesion and severe plough on steel balls. After laser irradiation, the adhesion between the steel ball and the DLC could be alleviated by reducing the contact area due to the formed microbulges. Additionally, a soft lubrication film enriched with GC is observed on textured DLC, which could relieve the plough wear and reduce the friction.

To investigate the macrotribological behavior of the above-mentioned textured DLC, the friction tests were performed on a CSM tribometer under the load of

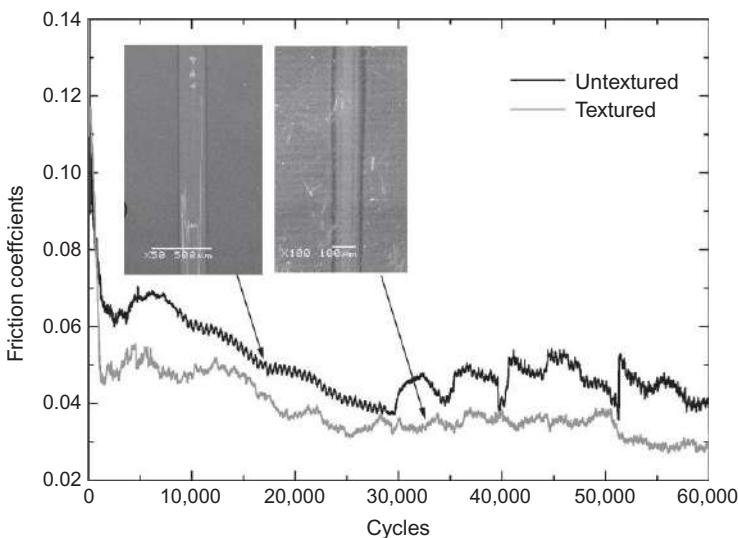


**Figure 16.5** Friction coefficients of untextured and textured DLC fabricated by direct laser process.

8 N. Rigid WC balls were selected as the counterbody to minimize the influence of counterbody wear. As shown in Figure 16.5, the friction coefficient curve of untextured DLC appeared to be unstable with some sudden jump after 30,000 cycles. However, the textured sample exhibited lower friction and the friction maintained stable during the whole test period. The insets in Figure 16.5 present the SEM images of wear tracks on coatings. It can be found that some delamination and long cracks appear in the wear track on the untextured coating. The sudden raise in the friction coefficients curve of untextured DLC should be correlated with these delaminations and cracks. However, no such damages could be observed on the textured sample. Confirmed by the mechanical characteristics, a soft/hard gradient exists from the laser-irradiated center to the untreated region, and such soft/hard gradients could improve the coating toughness and prohibit the cracks and delamination.

## 16.5 Conclusion and future trends

After LST having been studied for decades, a large number of results have confirmed the beneficial effects of LST in tribological optimization. However, the relative research works have been separately conducted in both theoretical and experimental aspects. Because the operating condition used in simulations is fixed (always in the hydrodynamic lubrication regime), the optimal texture obtained from the theoretical modeling might not be consistent with the actual experiment's results, due to the complicated working condition in tribological tests. Therefore, the two aspects should be organically combined, and an ideal state should be like this: (1) design the tribological experiments based on the actual working condition; (2) create the model and set the

boundary conditions according to the experimental configuration; (3) virtually “test” the textured specimen and obtain the optimal structure parameters; (4) send the selected parameters to the numerical control system of the laser processing machine to realize the textured specimen; and (5) conduct the tribological tests and feed back the results to simulation procedures to further correct the model and boundary conditions. Therefore, LST is a highly multidisciplinary technology, and the further development in it needs the efforts from mechanics, computing science, material science, and other areas.

For the design of surface texture, numerical simulation is an important method because the experimental evaluation of surface textures is costly and time-consuming. Not limited to the full film hydrodynamic lubrication, Zhu and Wang proposed the “virtual texturing” technology [2], which is capable of handling the contact and mixed lubrication analysis. This is a significant advancement toward the actual working situation. However, with the application of new tribomaterials, especially those surface coatings with extremely high or low surface energy, the interfacial action between the solid and lubricant oil also needs to be considered in the simulation. Additionally, the multiscale numerical simulation should be able to analyze the complicated surface textures such as the multiscale structures and bionic structures.

For the laser-processing aspect, with the fast development of laser technology, it is not challenging to produce high-quality microstructure on metals, ceramics, polymers, and surface coatings. However, in practice, the laser-textured components may exhibit poor performance in point-contact condition. To overcome this problem, it is suggested the size of texturing units (width or diameter) should be less than 10 µm for most point-contact conditions [41]. Thus, one of the future challenges in laser processing is to produce the fine surface structure of several micron or submicron scale. What’s more, fabrication of complicated texture with the multiscale feature is another challenge for LST, and the unique laser ablation behavior of some materials might be useful to achieve this task.

## Acknowledgments

The authors are grateful for financial support from the National Basic Research Program of China (973 Program) (Grant no. 2011CB706603) and the National Natural Science Foundation of China (Grant no. 51175493). The authors want to express their sincere gratitude to Dr. Tianchang Hu, Dr. Yongsheng Zhang, and Dr. Guangan Zhang for their great efforts and valuable discussions.

## References

- [1] I. Etsion, Improving tribological performance of mechanical components by laser surface texturing, *Tribol. Lett.* 17 (2004) 733–737, <http://dx.doi.org/10.1007/s11249-004-8081-1>.
- [2] Q.J. Wang, D. Zhu, Virtual texturing: modeling the performance of lubricated contacts of engineered surfaces, *J. Tribol. Trans. ASME* 127 (2005) 722–728, <http://dx.doi.org/10.1115/1.2000273>.

- [3] T. Nanbu, N. Ren, Y. Yasuda, D. Zhu, Q.J. Wang, Micro-textures in concentrated conformal-contact lubrication: effects of texture bottom shape and surface relative motion, *Tribol. Lett.* 29 (2008) 241–252, <http://dx.doi.org/10.1007/s11249-008-9302-9>.
- [4] H.W. Yu, X.L. Wang, F. Zhou, Geometric shape effects of surface texture on the generation of hydrodynamic pressure between conformal contacting surfaces, *Tribol. Lett.* 37 (2010) 123–130, <http://dx.doi.org/10.1007/s11249-009-9497-4>.
- [5] X.L. Wang, K. Kato, Improving the anti-seizure ability of SiC seal in water with RIE texturing, *Tribol. Lett.* 14 (2003) 275–280, <http://dx.doi.org/10.1023/A:1022650813314>.
- [6] X.L. Wang, K. Kato, K. Adachi, K. Aizawa, Loads carrying capacity map for the surface texture design of SiC thrust bearing sliding in water, *Tribol. Int.* 36 (2003) 189–197, [http://dx.doi.org/10.1016/S0301-679X\(02\)00145-7](http://dx.doi.org/10.1016/S0301-679X(02)00145-7).
- [7] M. Okoshi, W. Inoue, N. Inoue, Femtosecond laser ablation of frozen alcohols for deposition of diamond-like carbon thin films, *Jpn. J. Appl. Phys.* 47 (2008) 4572–4577, <http://dx.doi.org/10.1143/JJAP.47.4572>.
- [8] B. Bhushan, Adhesion and stiction: mechanisms, measurement techniques, and methods for reduction, *J. Vac. Sci. Technol. B* 21 (2003) 2262–2296, <http://dx.doi.org/10.1116/1.1627336>.
- [9] S. Schreck, K.H. Zum Gahr, Laser-assisted structuring of ceramic and steel surfaces for improving tribological properties, *Appl. Surf. Sci.* 247 (2005) 616–622, <http://dx.doi.org/10.1016/j.apsusc.2005.01.173>.
- [10] M.R.H. Knowles, G. Rutherford, D. Karnakis, A. Ferguson, Micro-machining of metals, ceramics and polymers using nanosecond lasers, *Int. J. Adv. Manuf. Technol.* 33 (2007) 95–102, <http://dx.doi.org/10.1007/s00170-007-0967-2>.
- [11] G. Dumitru, V. Romano, H.P. Weber, Y. Gerbig, H. Haefke, S. Bruneau, J. Hermann, M. Sentis, Femtosecond laser ablation of cemented carbides: properties and tribological applications, *Appl. Phys. A Mater. Sci. Process.* 79 (2004) 629–632, <http://dx.doi.org/10.1007/s00339-004-2675-1>.
- [12] H.C. Wong, N. Umehara, K. Kato, The effect of surface roughness on friction of ceramics sliding in water, *Wear* 218 (1998) 237–243, [http://dx.doi.org/10.1016/S0043-1648\(98\)00208-7](http://dx.doi.org/10.1016/S0043-1648(98)00208-7).
- [13] D. Sciti, A. Bellosi, Laser-induced surface drilling of silicon carbide, *Appl. Surf. Sci.* 180 (2001) 92–101, [http://dx.doi.org/10.1016/S0169-4332\(01\)00330-0](http://dx.doi.org/10.1016/S0169-4332(01)00330-0).
- [14] X.L. Wang, K. Kato, K. Adachi, K. Aizawa, The effect of laser texturing of SiC surface on the critical load for transition of water lubrication mode from hydrodynamic to mixed, *Tribol. Int.* 34 (2001) 703–711, [http://dx.doi.org/10.1016/S0301-679X\(01\)00063-9](http://dx.doi.org/10.1016/S0301-679X(01)00063-9).
- [15] C.Y. Chen, C.J. Chung, B.H. Wu, W.L. Li, C.W. Chien, P.H. Wu, C.W. Cheng, Microstructure and lubricating property of ultra-fast laser pulse textured silicon carbide seals, *Appl. Phys. A Mater. Sci. Process.* 107 (2012) 345–350, <http://dx.doi.org/10.1007/s00339-012-6822-9>.
- [16] T. Sugihara, T. Enomoto, Development of a cutting tool with a nano/micro-textured surface-improvement of anti-adhesive effect by considering the texture patterns, *Precis. Eng. J. Int. Soc. Precis. Eng. Nanotechnol.* 33 (2009) 425–429, <http://dx.doi.org/10.1016/j.precisioneng.2008.11.004>.
- [17] J. Robertson, Diamond-like amorphous carbon, *Mater. Sci. Eng. R Rep.* 37 (2002) 129–281, [http://dx.doi.org/10.1016/S0927-796X\(02\)00005-0](http://dx.doi.org/10.1016/S0927-796X(02)00005-0).
- [18] C. Chouquet, J. Gavillet, C. Ducros, F. Sanchette, Effect of DLC surface texturing on friction and wear during lubricated sliding, *Mater. Chem. Phys.* 123 (2010) 367–371, <http://dx.doi.org/10.1016/j.matchemphys.2010.04.016>.

- [19] G. Dumitru, V. Romano, H.P. Weber, M. Sentis, W. Marine, Femtosecond ablation of ultrahard materials, *Appl. Phys. A Mater. Sci. Process.* 74 (2002) 729–739, <http://dx.doi.org/10.1007/s003390101183>.
- [20] G. Dumitru, V. Romano, Y. Gerbig, H.P. Weber, H. Haefke, Femtosecond laser processing of nitride-based thin films to improve their tribological performance, *Appl. Phys. A Mater. Sci. Process.* 80 (2005) 283–287, <http://dx.doi.org/10.1007/s00339-003-2349-4>.
- [21] G. Dumitru, V. Romano, H.P. Weber, S. Pimenov, T. Kononenko, J. Hermann, S. Bruneau, Y. Gerbig, M. Shupugin, Laser treatment of tribological DLC films, *Diamond Relat. Mater.* 12 (2003) 1034–1040, [http://dx.doi.org/10.1016/S0925-9635\(02\)00372-2](http://dx.doi.org/10.1016/S0925-9635(02)00372-2).
- [22] C.Z. Wang, K.M. Ho, M.D. Shirk, P.A. Molian, Laser-induced graphitization on a diamond (111) surface, *Phys. Rev. Lett.* 85 (2000) 4092–4095, <http://dx.doi.org/10.1103/PhysRevLett.85.4092>.
- [23] G. Dumitru, V. Romano, H.P. Weber, S. Pimenov, T. Kononenko, M. Sentis, J. Hermann, S. Bruneau, Femtosecond laser ablation of diamond-like carbon films, *Appl. Surf. Sci.* 222 (2004) 226–233, <http://dx.doi.org/10.1016/j.apsusc.2003.08.031>.
- [24] G. Miyaji, K. Miyazaki, Origin of periodicity in nanostructuring on thin film surfaces ablated with femtosecond laser pulses, *Opt. Express* 16 (2008) 16265–16271, <http://dx.doi.org/10.1364/OE.16.016265>.
- [25] Q. Ding, L.P. Wang, L.T. Hu, T.C. Hu, Y.F. Wang, Y.N. Zhang, An explanation for laser-induced spallation effect in a-C:H films: altered phase evolution route caused by hydrogen doping, *J. Appl. Phys.* 109 (2011) 013501, <http://dx.doi.org/10.1063/1.3528223>.
- [26] T.V. Kononenko, V.G. Ralchenko, E.D. Obraztsova, V.I. Konov, J. Seth, S.V. Babu, E. N. Loubnin, Excimer-laser etching of diamond-like carbon-films—spalling effect, *Appl. Surf. Sci.* 86 (1995) 234–238, [http://dx.doi.org/10.1016/0169-4332\(94\)00417-X](http://dx.doi.org/10.1016/0169-4332(94)00417-X).
- [27] T.V. Kononenko, S.M. Pimenov, V.V. Kononenko, E.V. Zavedeev, V.I. Konov, G. Dumitru, V. Romano, Laser-induced spallation in diamond-like carbon films, *Appl. Phys. A Mater. Sci. Process.* 79 (2004) 543–549, <http://dx.doi.org/10.1007/s00339-003-2356-5>.
- [28] T.V. Kononenko, V.V. Kononenko, S.M. Pimenov, E.V. Zavedeev, V.I. Konov, V. Romano, G. Dumitru, Effects of pulse duration in laser processing of diamond-like carbon films, *Diamond Relat. Mater.* 14 (2005) 1368–1376, <http://dx.doi.org/10.1016/j.diamond.2005.02.009>.
- [29] A. Kovalchenko, O. Ajay, A. Erdemir, G. Fenske, Friction and wear behavior of laser textured surface under lubricated initial point contact, *Wear* 271 (2011) 1719–1725, <http://dx.doi.org/10.1016/j.wear.2010.12.049>.
- [30] T.C. Hu, L.T. Hu, Tribological properties of lubricating films on the Al-Si alloy surface via laser surface texturing, *Tribol. Trans.* 54 (2011) 800–805, <http://dx.doi.org/10.1080/10402004.2011.604761>.
- [31] T.C. Hu, L.T. Hu, The study of tribological properties of laser-textured surface of 2024 aluminium alloy under boundary lubrication, *Lubr. Sci.* 24 (2012) 84–93, <http://dx.doi.org/10.1002/lsc.11165>.
- [32] T.C. Hu, L.T. Hu, Q. Ding, The effect of laser surface texturing on the tribological behavior of Ti-6Al-4V, *Proc. Inst. Mech. Eng. J. Eng. Tribol.* 226 (2012) 854–863, <http://dx.doi.org/10.1177/1350650112450801>.
- [33] T.C. Hu, L.T. Hu, Q. Ding, Effective solution for the tribological problems of Ti-6Al-4V: combination of laser surface texturing and solid lubricant film, *Surf. Coat. Technol.* 206 (2012) 5060–5066, <http://dx.doi.org/10.1016/j.surfcoat.2012.06.014>.
- [34] T.C. Hu, Q. Ding, L.T. Hu, The effect of laser texturing of GCr15 steel surfaces on their tribological properties, *Tribology* 31 (2011) 447–451 (in Chinese).

- [35] T.C. Hu, L.T. Hu, Q. Ding, Tribological properties of laser textured surfaces of 45<sup>#</sup> steel under dry friction, *Tribology* 30 (2010) 46–52 (in Chinese).
- [36] T.C. Hu, L.T. Hu, Y.S. Zhang, Preparation of composite lubrication structure and its tribological properties on 45<sup>#</sup> steel surface, *Tribology* 32 (2012) 14–20 (in Chinese).
- [37] T.C. Hu, Y.S. Zhang, L.T. Hu, Tribological investigation of MoS<sub>2</sub> coatings deposited on the laser textured surface, *Wear* 278 (2012) 77–82, <http://dx.doi.org/10.1016/j.wear.2012.01.001>.
- [38] X.L. Wang, K. Adachi, K. Otsuka, K. Kato, Optimization of the surface texture for silicon carbide sliding in water, *Appl. Surf. Sci.* 253 (2006) 1282–1286, <http://dx.doi.org/10.1016/j.apsusc.2006.01.076>.
- [39] D.Z. Segu, S.G. Choi, J.H. Choi, S.S. Kim, The effect of multi-scale laser textured surface on lubrication regime, *Appl. Surf. Sci.* 270 (2013) 58–63, <http://dx.doi.org/10.1016/j.apsusc.2012.12.068>.
- [40] U. Pettersson, S. Jacobson, Influence of surface texture on boundary lubricated sliding contacts, *Tribol. Int.* 36 (2003) 857–864, [http://dx.doi.org/10.1016/S0301-679X\(03\)00104-X](http://dx.doi.org/10.1016/S0301-679X(03)00104-X).
- [41] U. Pettersson, S. Jacobson, Friction and wear properties of micro textured DLC coated surfaces in boundary lubricated sliding, *Tribol. Lett.* 17 (2004) 553–559, <http://dx.doi.org/10.1023/B:TRIL.0000044504.76164.4e>.
- [42] Q. Ding, L.P. Wang, Y.X. Wang, S.C. Wang, L.T. Hu, Q.J. Xue, Improved tribological behavior of DLC films under water lubrication by surface texturing, *Tribol. Lett.* 41 (2011) 439–449, <http://dx.doi.org/10.1007/s11249-010-9730-1>.
- [43] T. Haque, A. Morina, A. Neville, R. Kapadia, S. Arrowsmith, Effect of oil additives on the durability of hydrogenated DLC coating under boundary lubrication conditions, *Wear* 266 (2009) 147–157, <http://dx.doi.org/10.1016/j.wear.2008.06.011>.
- [44] N. Yasumaru, K. Miyazaki, J. Kiuchi, Control of tribological properties of diamond-like carbon films with femtosecond-laser-induced nanostructuring, *Appl. Surf. Sci.* 254 (2008) 2364–2368, <http://dx.doi.org/10.1016/j.apsusc.2007.09.037>.
- [45] Q. Ding, L.P. Wang, L.T. Hu, T.C. Hu, Y. Wang, The pairing-dependent effects of laser surface texturing on micro tribological behavior of amorphous carbon film, *Wear* 274 (2012) 43–49, <http://dx.doi.org/10.1016/j.wear.2011.08.008>.

# Fabrication of periodic submicrometer and micrometer arrays using laser interference-based methods

17

A.F. Lasagni<sup>1,2</sup>, E. Beyer<sup>1,2</sup>

<sup>1</sup>Fraunhofer Institute for Material and Beam Technology (IWS), Dresden, Germany;

<sup>2</sup>Technische Universität Dresden, Dresden, Germany

## 17.1 Introduction

Fabrication of period surfaces with micron and submicron features is a rapidly growing research field with applications in several technological areas. Such structures on the surface of metals, semiconductors, dielectrics, or polymers can generate new material properties with very special electrical, mechanical, or chemical characteristics. Depending on the specific material parameters and the morphology of the structures, new devices like biosensors [1], antifraud features, microfluidic devices [2–5], templates for biological applications [6], as well as photonic structures [7] can be realized. Furthermore, surface textures can be used to improve tribological properties of special tools [8], for the reduction of reflection losses [9] or as decoration elements for the refinement of precious goods.

Photon-based fabrication methods offer several advantages due to their remote and, thus, contactless operation, their flexibility during materials processing, as well as their precise energy deposition. Laser direct-writing and microstereolithography techniques are being utilized to pattern and process several materials with features in the range of 1–100 µm [10,11]. Furthermore, in some cases an imaging setup makes it possible in one single-step operation to reproduce a specific pattern by local ablation, photopolymerization, or surface modification processes. However, these methods require masks in order to obtain a specific geometry or pattern shape over a substrate, or can be quite time-consuming. In order to solve this problem, techniques involving large-area maskless lithography for rapid fabrication of two- and three-dimensional structures are required.

In this chapter, laser interference lithography (LIL) is introduced as new technology for the rapid fabrication of two- and three-dimensional structures. Different aspects of the laser interference-based methods, including LIL, and direct laser interference patterning (DLIP) using continuous wave, nanosecond, and femtosecond laser systems will be described.

## 17.2 Multibeam interference patterns

To calculate the intensity distribution of an interference pattern, all overlapping electromagnetic waves have to be added together:

Laser beams as follows:

$$E = \sum_{j=1}^N E_j = \sum_{j=1}^N E_{j0} e^{-ik \sin \alpha_j (x \cos \beta_j - y \sin \beta_j)} = \psi_i \quad (17.1)$$

where  $E_j$  are the amplitudes of electric field of each  $j$ -beam;  $\alpha_j$  and  $\beta_j$  are the angles of the beams with respect to the vertical (polar angle) and the horizontal axis (azimuthal angle) of the interference plane, respectively;  $\psi_i$  is the initial phase; and  $k$  is the wave number

$$k = \frac{2\pi}{\lambda} \quad (17.2)$$

with  $\lambda$  denoting wavelength.

Then, the total intensity of the interference pattern can be calculated as

$$I = \frac{c \epsilon_0}{2} |E|^2 \quad (17.3)$$

where  $c$  is the speed of light and  $\epsilon_0$  is the permittivity of free space. Using the last equation (Equation 17.3), the interference pattern of  $N$ -beams can be easily calculated [12,13].

For two-laser beams configuration, a one-dimensional (1-D) line-like interference pattern is obtained (Figure 17.1a, with  $\alpha_1 = \alpha_2 = 20.34^\circ$ ,  $\beta_1 = 0$ ,  $\beta_2 = \pi/2$ ,  $\lambda = 355$  nm, and  $\psi_1 = \psi_2 = 0$ ). In this case, independently if the polar angles  $\alpha_j$  are the same (with  $j = 1, 2$ ), no line defects are observed, as well as no changes in the intensity profile [14].

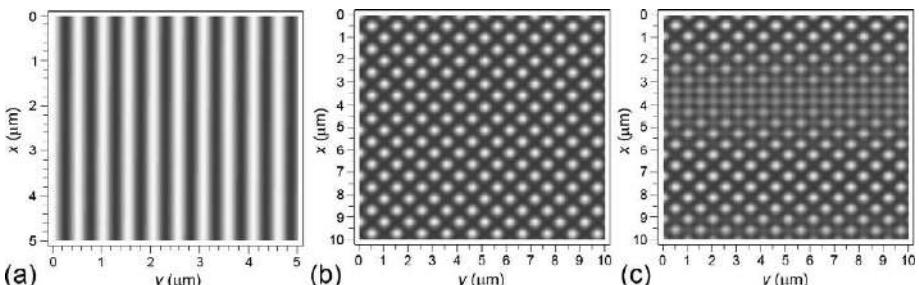


**Figure 17.1** (a) Calculated intensity distribution of a two-beam interference patterns with  $\alpha_1 = \alpha_2 = 20.34^\circ$ ,  $\beta_1 = 0$ ,  $\beta_2 = \pi/2$ ,  $\lambda = 355$  nm and  $\psi_1 = \psi_2 = 0$ . Calculated intensity distribution of four-beam interference patterns with  $\beta_1 = 0$ ,  $\beta_2 = \pi/2$ ,  $\beta_3 = \pi$ ,  $\beta_4 = 3/2 \pi$ ,  $\lambda = 355$  nm; (b)  $\alpha_1 = \alpha_2 = \alpha_3 = \alpha_4 = 20.34^\circ$ ,  $\psi_1 = \psi_2 = \psi_3 = \psi_4 = 0$ ; and (c)  $\alpha_1 = \alpha_2 = \alpha_3 = 20.34^\circ$ ,  $\alpha_4 = 23.34^\circ$ ;  $\psi_1 = \psi_2 = \psi_3 = \psi_4 = 0$ .

In the case of four-laser beam interference, a very different situation is observed. If the beams are incident on the sample having the same polar angles  $\alpha_j$  or satisfying the condition  $\alpha_1=\alpha_3 \neq \alpha_2=\alpha_4$  with  $\beta_1=0$ ,  $\beta_2=\pi/2$ ,  $\beta_3=\pi$ ,  $\beta_4=3/2\pi$ , a uniform intensity distribution is obtained ([Figure 17.1b](#), with  $\alpha_1=\alpha_2=\alpha_3=\alpha_4=20.34^\circ$ ,  $\lambda=355$  nm, and  $\psi_1=\psi_2=\psi_3=\psi_4=0$ ). On the contrary, for an asymmetric configuration that is not satisfied by the conditions previously mentioned, periodic or quasi-periodic linear defects appear in the pattern [15]. This effect is shown in [Figure 17.1c](#) for the condition  $\alpha_1=\alpha_2=\alpha_3=20.34^\circ$ ,  $\alpha_4=23.34^\circ$ ;  $\beta_1=0$ ,  $\beta_2=\pi/2$ ,  $\beta_3=\pi$ ,  $\beta_4=3/2\pi$ ;  $\lambda=355$  nm, and  $\psi_1=\psi_2=\psi_3=\psi_4=0$ . The line defects consist on a periodic variation of laser intensity perpendicular to the laser beam with the asymmetric angle (in this case the beam  $j=4$ , with a  $3^\circ$  difference compared to beams 1-3). Apart from that, for the symmetrical configuration case ( $\alpha_1=\alpha_2=\alpha_3=\alpha_4$ ) a phase change in one of the beams also produces a change in the shape of the intensity distribution of the interference pattern. On the other hand, for a nonsymmetrical configuration, variation of the phase  $\psi_j$  causes no changes in intensity profile but results in an offset of the whole pattern [15]. As a consequence, for a proper defect-free periodic structure fabrication using a four-laser beam setup, a perfect control of the initial phase, azimuthal angles, as well as a perfect positioning of the sample at the plane  $z=0$  is necessary.

### 17.3 Laser interference lithography

This technique is emerging as one of the simplest, fastest, and least expensive methods for producing highly ordered 1-D, 2-D, and 3-D structures with submicron periodicity over large areas.

LIL has been used to fabricate patterned substrates that are used in a variety of applications, including photonic crystal waveguides and field-emission flat-panel displays. In addition, patterned photoresist structures can be used to form templates for nanoparticle assemblies that can be incorporated into nanophotonic devices [16].

The dimensionality of the resultant periodic structure is determined by the number of beams involved. Interference among  $N < 4$  collimated, coherent beams produces an  $N - 1$  dimensional intensity gratings. Because the multiple beams must be coherent to produce an interference pattern, one laser beam from a visible (e.g., Ar-ion, frequency-doubled Nd:YAG, Nd:YVO<sub>4</sub>) or UV laser (e.g., frequency-tripled Nd:YAG, He-Cd, KrF) is typically divided into multiple beams [17].

In the process of LIL a small number of coherent optical beams incident from different directions are utilized to produce an interference pattern whose intensity distribution is recorded in the photosensitive layer and is later transferred (developed) by thermal and chemical processes. In conventional optical lithography, either a positive and negative photoresist is irradiated with the interference pattern [18]. Then, the irradiated samples are developed to remove the areas corresponding to nonpolymerized resist, and finally etched (chemically, plasma etching, etc.) obtaining the final structure on the substrate [19].

Two experimental arrangements are widely used for two-beam IL. The first setup utilizes a Lloyd's mirror interferometer as shown in [Figure 17.2a](#). This is a simple corner

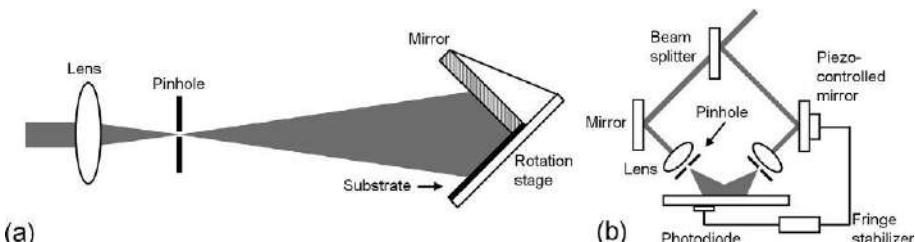


**Figure 17.2** (a) A Lloyd's mirror interference configuration to fabricate line-like arrays and (b) interference setup with a two-beam configuration with beam splitter using a piezo-electrically controlled mirror for phase stabilization.

cube arrangement with  $90^\circ$  geometry where the left and right halves of the beam are folded onto each other. This arrangement has been used successfully with sources having a high transverse coherence, such as a single-mode TEM Ar-ion laser [20]. Expanding the beam allows a large area overlap, especially when the angle of incidence is  $\sim 45^\circ$  and the sizes of beams incident on the sample and the mirror are equal.

The primary advantage of the Lloyd's mirror is that the spatial period of the exposed gratings can be easily and continuously varied from many microns down to  $\sim 150\text{-}170$  nm simply by rotating the stage without realigning the optical path [21]. See Figure 17.2a. However, the substrate areas that can be illuminated with any angles of incidence are small. Increasing the pattern area by increasing the mirror size can be expensive because the exacting smoothness and flatness tolerances of the mirrors are difficult to achieve over large areas.

These problems can be minimized by using other arrangements that involve splitting one coherent beam into two or more subbeams using beam splitters and then overlapping the beams over the sample (Figure 17.2b). Here, the longitudinal coherence (narrow spectral width) is important because the distances from the beam splitter to the image plane can vary for the two beams. Phase errors can accumulate when both beams travel long, separate paths and encounter different optics, vibrations, mirror imperfections, spurious scattering, and a variety of other deleterious effects. As both beams travel along separate paths, the effects of both vibration and air turbulences can easily disturb them [20]. This situation is common when using ion-argon lasers, where the exposure time ranges from some seconds up to several minutes. For the exposure of large surfaces, this problem can be overcome using a fringe-locking system (Figure 17.2b). Here, fringe movements detected by a photodiode generate signals that actuate a piezoelectrically driven optical element that stabilizes the phase of one of the beams [16,20].

If pulsed laser systems are utilized, this construction can be done without the fringe-locking systems, avoiding the use of the piezoelectric-supported mirrors to compensate low-frequency phase perturbations, keeping the interference fringes fixed during the exposure.

Interference patterns can also be created by passing one laser beam through a multiple grating configuration prior to exposing the photoresist [22]. In this case, an expanded incident beam is diffracted by three diffraction gratings incorporated into

one monolithic package, and aligned about the normal 120° to each other. This method is stable, fast, and easy because it entails using a single monolithic diffraction object.

As previously described, using a two-beam experimental setup, different line-like patterns can be reproduced on a photoresist. Using a negative resist (such as SU-8), the positions of the material exposed at the interference maxima became solid and after development of the sample we obtained the final structure. In general, several aspects are critical in order to fabricate stable polymeric structures such as pattern period ( $\Lambda$ ), thickness of the resist layer, width of the photopolymerized regions (wall width), pre- and postbaking temperatures and time, and surface tension of the developer and/or final wash solvent [23]. However, it can be assumed that line-like patterns are more stable for large periods, small height as well as wide wall widths.

Apart from line-like structures, the two-beam configuration setup can be also utilized to fabricate two-dimensional arrays. In the last case, a double exposure process must be performed consisting of irradiation of the sample with a line-like interference pattern followed by a rotation of the sample and a second irradiation of the sample. Moreover, because the periodic structured is cross-linked at the intercepting nodes due to the double exposure process, independently of spatial period, layer thickness or wall width, the structure is stable enough to resist the attractive capillary forces during the rinse and drying steps [24]. Moreover, no line defects appear on the structure because a two-beam configuration is used.

Examples of the cross-like structures are shown in [Figure 17.3](#) for 1500 nm of spatial period, respectively. By using different rotation angles (30°, 60°, and 90°) several periodic arrays could be fabricated. In addition, variation of the exposure dose (laser energy density) is permitted to control the width of the photopolymerized lines [14].

In order to qualitatively calculate the shape of the photopolymerized material with the different rotation angles, the following procedure was utilized. First, using [Equation \(17.3\)](#), the intensity distribution for a specific two-beam laser configuration was calculated. After that, we calculated the second line-like intensity distribution taking into account a specific sample rotation angle. Finally, both intensity distributions were added and using the Beer-Lambert's law ([Equation 17.4](#)), the local amount of photopolymerized material was calculated:

$$d = \frac{1}{\alpha} \ln \left( \frac{I}{I_{\text{th}}} \right) \quad (17.4)$$

where  $d$  is the photopolymerized depth at the position  $x, y$ ;  $\alpha$  the absorption coefficient of the photoresist;  $I$  the intensity of the total interference pattern at  $x, y$  ([Equation 17.3](#)); and  $I_{\text{th}}$  is a threshold value at which the material is polymerized.

The calculated surface structure for each fabricated pattern can be observed on the right side of [Figure 17.3](#). The results show a good agreement with the experimental results and permit us to qualitatively describe the shape of the fabricated structures as a function of experimental configuration and exposure dose [14].

As previously mentioned, in order to directly fabricate a 3-D pattern, at least four coherent beams are necessary ( $N - 1$ ). A particularly interesting application of such 3-D patterns is photonic crystals [25]. Multiple interference between waves scattered

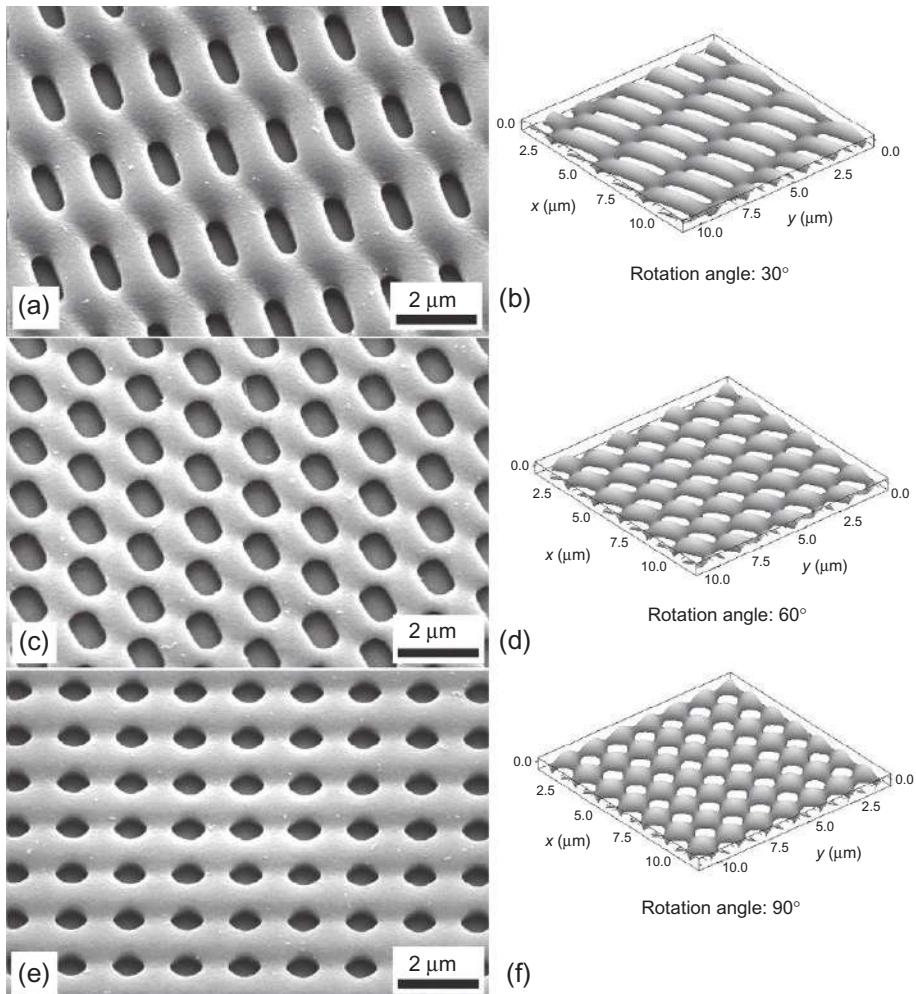


**Figure 17.3** Periodic two-dimensional patterns of photopolymerized SU-8 photoresist and their correspondent numerical calculation of solidified material. The period  $\Lambda$  of the line-like interference pattern was 1500 nm and the rotation angles were (a, b)  $30^\circ$ , (c, d)  $60^\circ$ , and (e, f)  $90^\circ$ . (a, c, e) Scanning electron micrographs with tilt angles of  $30^\circ$ . In all cases, the exposure dose per irradiation step was  $6.4 \text{ mJ/cm}^2$  [14].

from each unit cell of the structure may open a “photonic band gap”—a range of frequencies within which no propagating electromagnetic modes exist. Numerous device principles that exploit this property have been identified. Specifically related to interference lithography, 3-D polymer structures with submicrometer periodicity have been fabricated as templates and subsequently infiltrated with high-refractive-index materials. This 3-D-periodic structure is, in general, generated by interference of four noncoplanar laser beams in a film of photoresist of some tens of micrometers. For the

four-beam configuration, the intensity distribution of the interference pattern has three-dimensional translational symmetry; its primitive reciprocal lattice vectors are equal to the differences between the wave vectors of the beams. Highly exposed photoresist is rendered insoluble. Unexposed areas are dissolved away to reveal a three-dimensionally periodic structure formed of cross-linked polymer with air-filled voids. The four-laser beam wave vectors determine the translational symmetry and lattice constant of the interference pattern. There remain eight parameters, describing the intensities and polarization vectors of the four beams that are required to define the intensity distribution within a unit cell. These parameters allow considerable freedom in determining the distribution of dielectric material within the unit cell, which in turn determines the photonic band structure.

In Figure 17.4, different SEM micrographs of photonic crystals with fcc-like symmetry generated by holographic lithography are shown [26]. In this example, Cu<sub>2</sub>O (high-refractive index material) was electrodeposited into the photopolymerized SU-8 material over a glass substrate covered with a thin ITO layer. Then, the polymer template was removed by isotropic O<sub>2</sub> reactive-ion etching. As shown in Figure 17.4a and b, a highly ordered 3-D porous structure of Cu<sub>2</sub>O was successfully formed. However, although the images reveal that the Cu<sub>2</sub>O structure has well-defined smooth

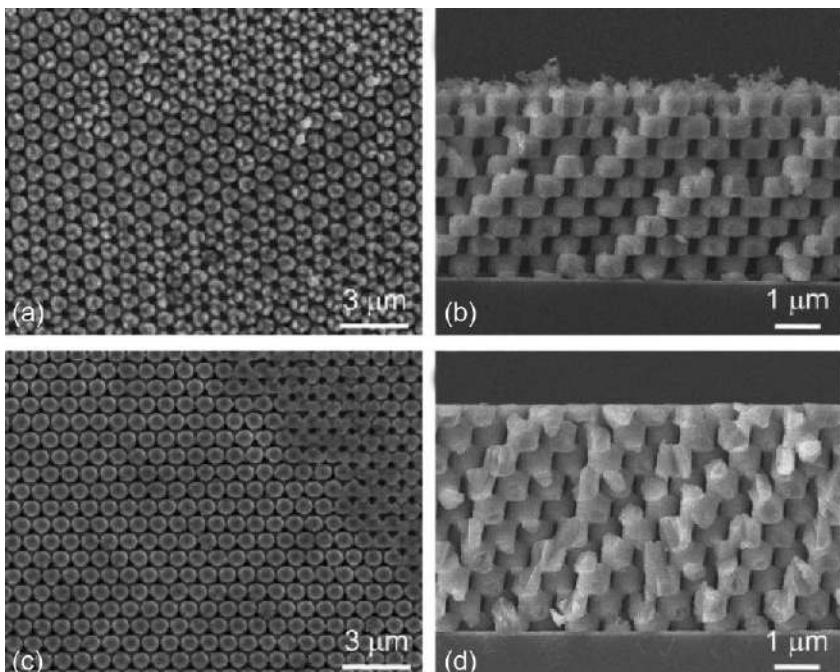


**Figure 17.4** SEM images of inverse 3D Cu<sub>2</sub>O photonic crystals after removal of polymer template. (a) Top surface and (b) fractured cross-section of a Cu<sub>2</sub>O photonic crystal electrodeposited within the template followed by reactive ion etching of the template. (c) Top surface and (d) fractured cross section of a polished Cu<sub>2</sub>O photonic crystal [26].

surfaces in the bulk of the structure, the top surface is relatively rough. This rough surface is not desirable because it causes diffuse scattering, which reduces the optical strength of the photonic crystal. To solve this problem, the rough surface can be eliminated using simple mechanical polishing with 50 nm alumina abrasive ([Figure 17.4c and d](#)).

## 17.4 Direct laser interference patterning

As has been introduced in [Section 17.2](#), in LIL low laser intensities (up to some tens of  $\text{mJ/cm}^2$ ) are utilized to locally activate a photosensitive material. This means that fabrication of periodic patterns using this approach directly on metals, ceramics, or polymers cannot be realized in one step and additional treatments are necessary. For example, using chemical or plasma etching, the substrate material can be etched at the regions not covered by the resist. After that, the photoresist is totally removed, generally using a specific solvent, obtaining the final structure on the substrate. However, using laser systems that can achieve higher power densities it is possible to directly fabricate 1-D and 2-D periodic patterns in one step. In the last case, the method has been called DLIP. In DLIP, nanosecond, picosecond, or femtosecond pulsed lasers are used in order to reach high energy densities at the interference maxima positions during the ultrashort laser pulse interaction with the material. In this way, high peak powers ranging from MW to several GW can be obtained during irradiation, permitting us to locally melt and/or ablate the irradiated substrates. The following examples for ns- and fs-DLIP are introduced describing the advantages and disadvantages of the methods.

### 17.4.1 DLIP using nanosecond laser pulses

A good option for the construction of a DLIP system with ns-pulsed laser is to utilize YAG lasers with harmonic generators. In this way, it is possible to select an appropriate wavelength at which the material has high absorption, and thus improve the interaction with the laser light. For example, Nd:YAG lasers (1064 nm) cover wavelengths ranging from the ultraviolet (UV) to the infrared spectrum by frequency doubling (532 nm), tripling (355 nm), and quadrupling (266 nm). Moreover, such systems have an impressive coherent length (on the order of some meters), which is necessary to make use of the so-called beam-splitter configuration.

The schematic setup for a beam-splitter interference setup is shown in [Figure 17.5a](#). As can be observed, the primary laser beam is split into two or more beams to interfere with each other on the sample surface. By the combination of a polarizer and a half-wave plate it is also possible to adjust the intensity impinging on the sample. The intensity can also be adjusted by selecting beam splitters with a specific reflection. Also a mechanical shutter can be used to control the number of pulses reaching the sample. By a two-lens telescope it is also possible to change the diameter of the laser beam and, therefore, the energy density received on the sample surface. To reduce

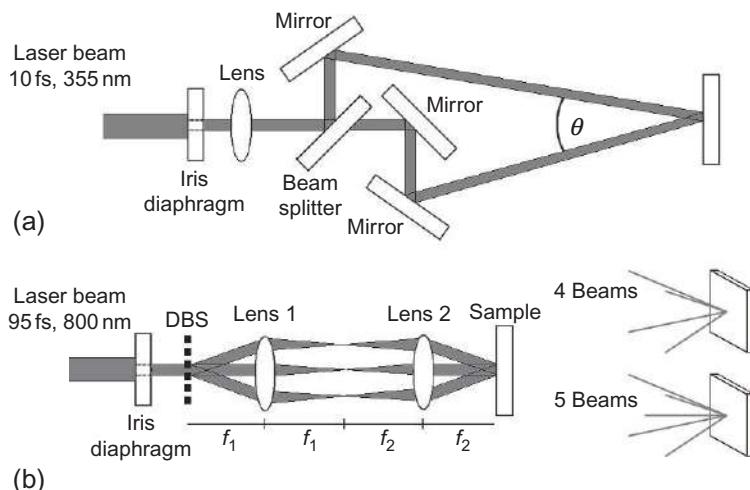


**Figure 17.5** (a) Experimental setup for nanosecond interference experiments (beam splitter configuration). The principal laser beam is split to obtain 2 individual laser beams interfering at the sample with an angle  $\theta$ . (b) Optical setup for the femtosecond interference patterns utilizing a DBS and confocal imaging system with two convex lenses with focal distances  $f_1$  and  $f_2$ . The four- and five-laser beam configurations are also shown [27].

influences from the optical elements, high flatness of the splitters and mirrors can also be utilized.

Examples of patterned metallic periodic structures with this configuration are shown in [Figure 17.6](#). Using two- and three-beam configurations, line-, cross-, and dot-like structures were fabricated on steel. The patterning process in this case involves a photothermal-induced local melting and/or ablation at the interference maxima positions. Moreover, from the SEM-micrographs of [Figure 17.6](#), the distribution of the molten material after the solidification can be observed.

According to previous investigations, depending on the pulse duration of the laser system, the laser energy density (laser fluence), the thermal properties of the irradiated materials, as well as the spatial period of the interference patterns, different temperature differences between the intensity maxima and minima positions (thermal gradient) can be induced [28,29]. For example, for  $5\text{ }\mu\text{m}$  periods, temperature differences over 2000–3000 K are usual; that means that the metal can be locally molten at the interference maxima positions. According to the Marangoni convection, an important temperature difference (in our case between the interference maxima and minima) can induce a flow of the molten material toward the cold regions. Consequently, the molten material at the interference minima is directed away and toward the minima positions. This convection is driven by the surface-tension gradient, which is induced by the temperature gradient as explained before. However, this effect dominates the formation of the periodic structures only if the temperature gradient is sufficiently high and the material is predominantly molten at the interference maxima.

Experimental observations in stainless steel substrates have shown that the laser fluence, which causes decreased on the pattern quality ranging from 1 to  $1.5\text{ J/cm}^2$ ,

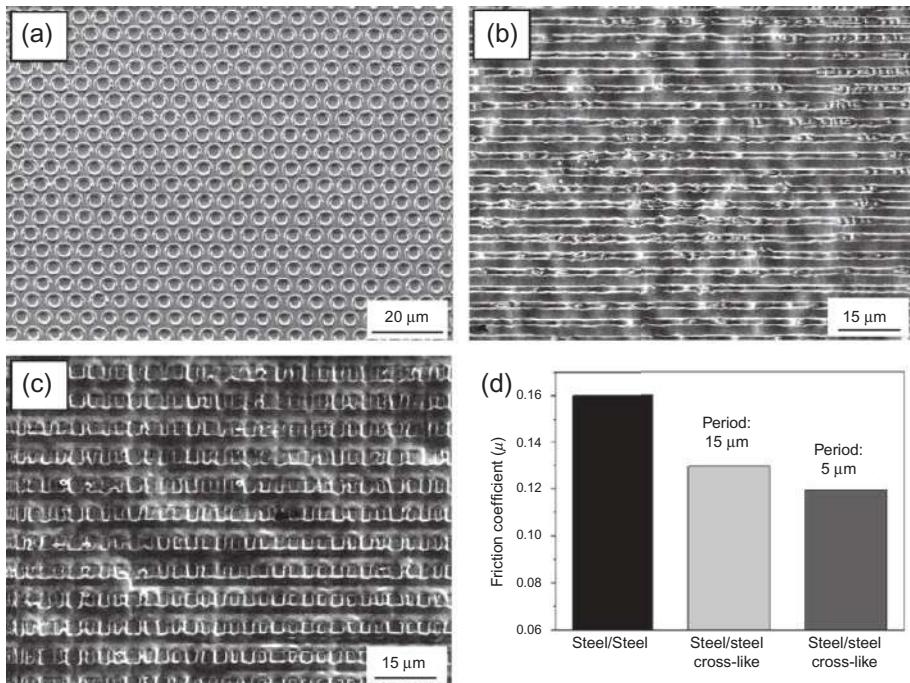


**Figure 17.6** DLIP patterning of steel (a) one-dimensional dot-like patterning with a period of 5  $\mu\text{m}$ , (b) line-like patterning with a period of 5  $\mu\text{m}$  and (c) crossed-like pattern with 10  $\mu\text{m}$ . (d) Friction coefficient of steel/steel, steel/patterned steel (15  $\mu\text{m}$ ), and steel/patterned steel (5  $\mu\text{m}$ ) (lubricated conditions).

depending on steel type. This data fits very well with the theoretically calculated energy density necessary to induce vaporization of the steel surface ( $\sim 0.9 \text{ J/cm}^2$ ) at the interference maxima position. Additionally, the thermal diffusion length of stainless steel is 1.3  $\mu\text{m}$  (for a laser pulse duration of 10 ns). This value fits very well to the smallest possible surface structures (1  $\mu\text{m}$ ) that can be fabricated on these materials. Consequently, the smallest possible periodic structure that can be fabricated on a metallic substrate is related to the thermal diffusion length, because smaller spatial periods of an interference pattern does not allow us to obtain a considerable temperature difference between maxima and minima positions.

Surface patterning of metallic surfaces can be also used to modulate tribological properties under lubricated and unlubricated conditions [30]. The requirements for surface patterns for tribological applications are smooth-shaped surfaces to avoid abrasive wear and minimize adhesive friction. Thus, the patterning parameters (especially for metals) have a high relevance for their tribological performance. In Figure 17.6d, the coefficient of friction of cross-like patterned steel samples is shown. The patterning period in these examples is varied between 5 and 15  $\mu\text{m}$ , respectively. The results indicate an improvement of 23% and 33% for the cross-like structures with 5 and 15  $\mu\text{m}$ , respectively. However, not only the spatial period is

relevant for the improvement of the tribological performance, but also the structure shape as well as the ratio between the structure depth and the spatial period, generally described as the aspect ratio. Previous tests have also demonstrated that such periodic surface patterns in the micronscale range (2–10  $\mu\text{m}$ ) can be used to increase the lubricant lifetime by a factor of 16 [8]. This effect is highly relevant in a case where insufficient lubrication at specific positions of a three-dimensional part takes place, since adhesive forces can result in a frictional welding-like event in steel components (i.e., piston seizures).

A second example is related to the patterning of polymer substrates. Using the setup described in Figure 17.7a, we fabricated periodic arrays on commercial polystyrene (PS) and polyimide (PI) substrates. Due to the low absorption of PS-substrates at both 355 and 532 nm wavelengths, the quadruple harmonic wavelength (266 nm) of the laser system was used. As can be observed in Figure 17.7a and b, well-defined periodic arrays could be fabricated. The ablated regions at the material's surface correspond to the interference maxima positions, where the threshold fluence is surpassed. Despite the short wavelength (266 nm) used to irradiate the PS substrates, a significant contribution of photothermal excitation is expected [31]. This means that the material is first melted before being ablated. Consequently, the obtained surface profile is quite smooth as shown in Figure 17.7b. Apart from that, the structure depth for single pulse irradiation can be varied with the laser fluence. The maximal achievable structure depth increases with increasing the spatial period up to values that are close to the absorption depth at the utilized laser wavelength.

To fabricate grid-like structures, the polymer substrate can be rotated a specific angle between two consecutive irradiation steps as described for LIL. This process is shown for PI substrates, in Figure 17.7c, for a rotation angle of 90°. The laser fluence utilized in this case was 0.5 J/cm<sup>2</sup>. PI polymer presents a high absorption at both 266 and 355 nm wavelengths [32]. Moreover, compared to PS, sharper edges were observed (even for 500 nm arrays, see Figure 17.7c).

Preliminary results of a bacterial adhesion test on these patterned polymers have demonstrated that by controlling the topographical characteristic (period and pattern shape) it is possible to fabricate antibacterial surfaces based only on topographical effects, without changing the surface chemistry [33].

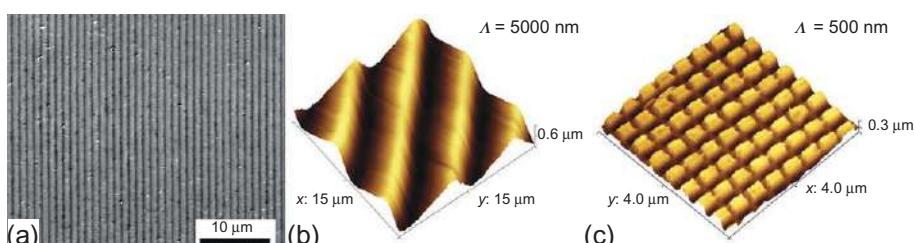


**Figure 17.7** Fabricated line-pattern on (a) PS with  $\Lambda = 1.0$  (SEM picture) and (b) 5.0  $\mu\text{m}$  (AFM). (c) Lattice-structure on PI with  $\Lambda = 500 \text{ nm}$  (AFM) [30].

### 17.4.2 DLIP using femtosecond laser pulses

It is common knowledge that the shorter the pulses, the smaller the area over which the pulses overlap. For example, in the case of two beams crossed at angle  $\theta$ , the size of the overlap area (OA) is given by

$$\text{OA} = c\tau(\sin \theta/2)^{-1} \quad (17.5)$$

where  $c$  is the speed of light in the medium and  $\tau$  is the pulse duration [34].

For example, for a 30 fs pulse duration and a moderate angle such as  $5^\circ$ , the beams overlap only within a strip approximately 200  $\mu\text{m}$  wide. The number of interference fringes ( $N_F$ ) produced by two beams is independent of the angle and, for transform-limited pulses, is roughly

$$N_F = 2c\tau/\lambda \quad (17.6)$$

With 30 fs pulses at  $\lambda = 800 \text{ nm}$ , only approximately 20 interference fringes can be produced. However, these limitations can be overcome if cross diffraction orders of a grating are crossed using the simple imaging system shown in Figure 17.5b [27,34].

In this setup, a femtosecond pulse is transmitted through a diffraction grating, which is then imaged with two confocal lenses, with the grating being placed in the front focal plane of the first lens. A spatial filter transmits only the desired number of laser beams corresponding to the different diffraction orders. Then the beams are recombined at the image plane (see Figure 17.5b). This setup not only provides pulse overlap in the image plane but also preserves short pulse duration [34].

Differently from the beam-splitter configuration (Figure 17.5a), in order to change the intercepting angle of the used beams, and in consequence the structure period, a set of lenses with appropriated focal distances ( $f_1$  and  $f_2$ ) must be selected. Due to the well-known interaction of fs lasers with materials, several effects can be explored. One possibility is to fabricate the periodic arrays by direct ablation of the material surface [35–37], and also by photopolymerization processes including multiphoton interactions [27,38]. This approach has also been utilized to fabricate photonic crystals [39], nanosized hole matrices and nanomeshes [36] between others.

Examples of patterned periodic structures on poly(3,4-ethylene dioxythiophene)-poly(styrene sulfonate) (PEDOT-PSS) thin films are shown in Figure 17.8 [40]. This conducting polymer is one of the most widely used materials in the field of organic electronics [41]. PEDOT-PSS has been used to fabricate neural electrodes [42], flexible photovoltaics [43] as well as batteries [44]. The irradiated films consist of electrochemically deposited PEDOT-PSS conducting polymers from a solution of PSS (0.2%, w/v) and ethylene dioxythiophene (EDOT) (0.1%, w/v) in deionized water, deposited over 100 nm gold-palladium thin films, sputtered on tin-doped indium oxide (ITO) substrates.

To fabricate the arrays, a Ti:sapphire fs-laser system with a pulse duration of 95 fs and a center wavelength of 800 nm was utilized. To split the main beam (Figure 17.5b), a polycarbonate diffractive beam splitter (DBS) was used. The zero and/or first-order beams were focused onto the sample by two biconvex lenses with

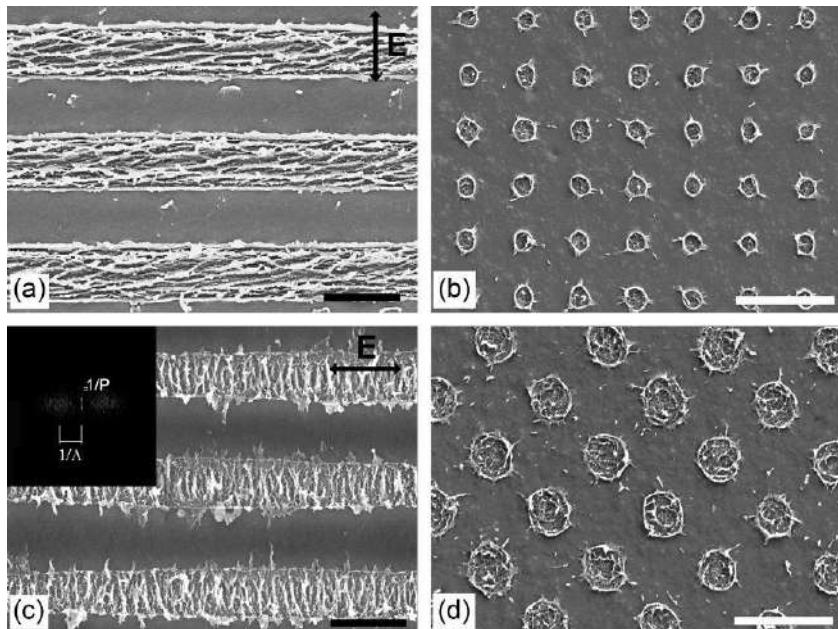


**Figure 17.8** Fabricated periodic arrays using (a, b) two-, (c) four-, and (d) five-laser beams configurations with (a)  $\alpha_{1,2}=11^\circ$ ,  $\beta_1=0^\circ$ ,  $\beta_2=180^\circ$  (two beams); (b)  $\alpha_{1,2}=11^\circ$ ,  $\beta_1=90^\circ$ ,  $\beta_2=270^\circ$  (two beams); (c)  $\alpha_{1,2,3,4}=11^\circ$ ,  $\beta_1=0^\circ$ ,  $\beta_2=90^\circ$ ,  $\beta_3=180^\circ$ ,  $\beta_4=270^\circ$  (four beams); and (d)  $\alpha_{1,2,3,4}=11^\circ$ ,  $\alpha_5=0^\circ$ ,  $\beta_1=0^\circ$ ,  $\beta_2=90^\circ$ ,  $\beta_3=180^\circ$ ,  $\beta_4=270^\circ$ ,  $\beta_5=0^\circ$  (five beams). The accumulated energy density was (a, b)  $0.21 \text{ J/cm}^2$ , (b)  $0.004 \text{ J/cm}^2$ , and (c)  $0.007 \text{ J/cm}^2$ . The orientation of the electric field  $E$  in (a) and (b) is denoted by the black. (a, b) Scale bar =  $2 \mu\text{m}$  and (c, d) scale bar =  $5 \mu\text{m}$  [40].

magnification factor  $M=f_2/f_1=20/75.6=0.265$ . To avoid distortion of the beam wave fronts due to nonlinear interactions of the high-field ultrashort pulses with air, a low humidity atmosphere is required.

Another important characteristic of the obtained periodic arrays is the subwavelength ripple structure when using several laser pulses (Figure 17.8a and b). In all cases, the ripple structure is perpendicular to the beam polarization, and independently of the number of laser beams used in interference set-up as well as accumulated energy density, the mean spatial period of the ripples was between 170 and 220 nm. The orientation of the subripples structure is also denoted by the Fourier transform in Figure 17.8b. A particular mechanism that can be regarded to explain the formation of these subwavelength ripples is a Coulombian explosion followed by self-organization [45]. The Coulombian explosion is the result of multiphoton ionization induced by the ultrashort laser pulses. In addition, interpulse mechanism could occur in the formation of subwavelength ripples if several pulses are applied [46]. However, as the PEDOT:PSS polymer is conductive, other processes may also be considered [46–48].

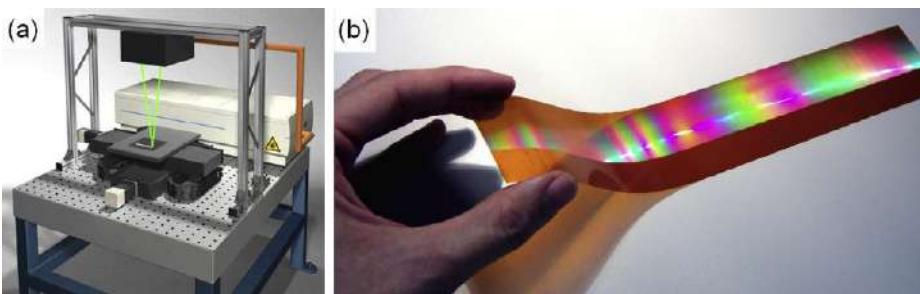


**Figure 17.9** (a) Schematic of DLIP system (Fraunhofer IWS, Dresden). (b) Structured polymer foil showing high homogeneity using DLIP (Fraunhofer IWS, Dresden).

## 17.5 Laser interference patterning systems

DLIP has been utilized in the past basically only at the laboratory scale. The method has shown high potential for application in several technological areas. In general, the laser interference experiments are carried out using high power pulsed Nd:YAG laser systems. Typical pulse durations range from 6 to 30 ns. In most of the cases, the infrared wavelength (1064 nm) of Nd:YAG lasers cannot be absorbed properly by several materials. The wavelength is normally shortened using nonlinear crystals. For instance, through frequency doubling the photons interacting with a nonlinear material are combined to form new photons with twice the energy and, therefore, half the wavelength of the initial photons. Similarly, UV wavelengths (e.g., 355 and 266 nm) can be generated by third (frequency tripling) or fourth (frequency quadrupling) harmonic generation.

Recently, compact interference patterning systems have been developed [49]. These systems offer the possibility to not only process planar surfaces but also to create complex three-dimensional mechanical components including mechanical seals, piston rings, and bearings. Moreover, the system can be adapted in order to precisely fabricate micro- or submicrometer arrays on flexible substrates. Figure 17.9a illustrates a DLIP system to produce  $1.5\text{ }\mu\text{m}$  line-like periodic arrays for the treatment of  $300 \times 300\text{ mm}^2$  substrates. The DLIP optical head is located 50 cm over the working plane and has a size of  $15 \times 20 \times 30\text{ cm}^3$ . In Figure 17.9b illustrates a structured PI foil with a total area of  $90\text{ cm}^2$  with a  $1.5\text{ }\mu\text{m}$  period line-like structure. The total length of the fabricated lines is 6.0 km.

## References

- [1] N. Ganesh, I.D. Block, B.T. Cunningham, Near ultraviolet-wavelength photonic-crystal biosensor with enhanced surface-to-bulk sensitivity ratio, *Appl. Phys. Lett.* 89 (2006) 023901.
- [2] H. Yu, O. Balogun, B. Li, T.W. Murray, X. Zhang, Building embedded microchannels using a single layered SU-8, and determining Young's modulus using a laser acoustic technique, *J. Micromech. Microeng.* 14 (11) (2004) 1576.

- [3] S.N. Bhatia, C.S. Chen, Tissue engineering at the micro-scale, *Biomed. Microdev.* 2 (1999) 131–144.
- [4] K. Hammerick, W. Ryu, R. Fasching, S.J. Bai, R. Smith, R. Greco, R. Lane Smith, R. S. Greco, F.B. Prinz, R.L. Smith, Chapter 5: synthesis of cell structures, in: R.S. Greco, F.B. Prinz, R.L. Smith (Eds.), *Nanoscale Technology in Biological Systems*, CRC Press, Boca Raton, FL, 2005, p. 93.
- [5] W.H. Ryu, S.W. Min, K.E. Hammerick, M. Vyakarnam, R.S. Greco, F.B. Prinz, R.J. Fasching, The construction of three-dimensional micro-fluidic scaffolds of biodegradable polymers by solvent vapor based bonding of micro-molded layers, *Biomaterials* 28 (2007) 1174–1184.
- [6] J. Zhang, S. Venkataramani, H. Xu, Y.-K. Song, H.K. Song, G. Palmore, J. Fallon, A.V. Nurmikko, Combined topographical and chemical micropatterns for templating neuronal networks, *Biomaterials* 27 (2006) 5734–5739.
- [7] J.D. Joannopoulos, P.R. Villeneuve, S. Fan, Photonic crystals: putting a new twist on light, *Nature* 386 (1997) 143–149.
- [8] M. Duarte, A. Lasagni, R. Giovanelli, J. Narciso, E. Louis, F. Mücklich, Increasing lubricant film lifetime by grooving periodical patterns using laser interference metallurgy, *Adv. Eng. Mater.* 10 (2008) 554–558.
- [9] A. Lasagni, M.R. Nejati, R. Clasen, F. Mücklich, Periodical surface structuring of metals by Laser Interference Metallurgy as a new fabrication method of textured solar selective absorbers, *Adv. Eng. Mater.* 6 (2006) 580–584.
- [10] A. Bertsch, S. Jiguet, P. Renaud, Microfabrication of ceramic components by microsterolithography, *J. Micromech. Microeng.* 14 (2004) 197–203.
- [11] F. Meriche, E. Neiss-Clauss, R. Kremer, A. Boudrioua, E. Dogheche, E. Fogarassy, R. Mouras, A. Bouabellou, Micro structuring of LiNbO<sub>3</sub> by using nanosecond pulsed laser ablation, *Appl. Surf. Sci.* 254 (2007) 1327.
- [12] A. Lasagni, C. Holzapfel, T. Weirich, F. Mücklich, Laser Interference Metallurgy: a new method for periodic surface microstructure design on multilayered metallic thin films, *Appl. Surf. Sci.* 253 (2007) 8070–8074.
- [13] M. Mütsel, S. Tandler, D. Haubrich, D. Meschede, K. Peithmann, M. Flaspöhler, K. Buse, Atom lithography with a holographic light mask, *Phys. Rev. Lett.* 88 (8) (2002) 83601.
- [14] A. Lasagni, B. Menéndez-Ormaza, How to fabricate two and three dimensional micro and sub-micrometer periodic structures using two-beam laser interference lithography, *Adv. Eng. Mater.* 12 (1–2) (2010) 54.
- [15] C. Tan, C.S. Peng, V.N. Petryakov, Y.K. Verevkin, J. Zhang, Z. Wang, S.M. Olaizola, T. Berthou, S. Tisserand, M. Pessa, Line defects in two-dimensional four-beam interference patterns, *New J. Phys.* 10 (2008) 023023.
- [16] R. Cheng Lu, H. Lipson, Interference lithography: a powerful tool for fabricating periodic structures, *Laser Photonics Rev.* 1 (13) (2009) 568–580.
- [17] J.H. Moon, J. Ford, S. Yang, Fabricating three-dimensional polymeric photonic structures by multi-beam interference lithography, *Polym. Adv. Technol.* 17 (2) (2006) 83–93.
- [18] V. Seidemann, J. Rabe, M. Feldmann, S. Buttgenbach, SU8-micromechanical structures with *in situ* fabricated movable parts, *Microsyst. Technol.* 8 (4) (2002) 348.
- [19] R. Rubner, Photoreactive polymers for electronics, *Adv. Mater.* 2 (10) (1990) 452–457.
- [20] S. Kuiper, H. van Wolferen, C. van Rijn, W. Nijdam, G. Krijnen, J. Elwenspoek, Fabrication of microsieves with sub-micron pore size by laser interference lithography, *Micro-mech. Microeng.* 11 (1) (2001) 33–37.
- [21] J.M. Carter, R.C. Fleming, T.A. Savas, M.E. Walsh, T.B. O'Reilly, M.L. Schattenburg, H.I. Smith, Interference lithography, MTL Annual Report, 2003.

- [22] C. Lu, X. Hu, I. Mitchell, R. Lipson, Diffraction element assisted lithography: pattern control for photonic crystal fabrication, *Appl. Phys. Lett.* 86 (2005) 193110-1–193110-3.
- [23] D. Wu, N. Fang, C. Sun, X. Zhang, Stiction problems in releasing of 3D microstructures and its solution, *Sens. Actuators A* 128 (2006) 109.
- [24] K.D. Vora, A.G. Peele, B.Y. Shew, E.C. Harvey, J.P. Hayes, Fabrication of support structures to prevent SU8 stiction in high aspect ratio structures, *Microsyst. Technol.* 13 (2007) 487–493.
- [25] M. Campbell, D.N. Sharp, M.T. Harrison, R.G. Denning, A.J. Turberfield, Fabrication of photonic crystals for the visible spectrum by holographic lithography, *Nature* 404 (2000) 53–56.
- [26] M. Miyake, Y.-C. Chen, P.V. Braun, P. Wiltzius, Fabrication of three-dimensional photonic crystals using multibeam interference lithography and electrodeposition, *Adv. Mater.* 21 (2009) 3012–3015.
- [27] A. Lasagni, D. Yuan, P. Shao, S. Das, Periodic micropatterning of polyethylene glycol diacrylate hydrogel by laser interference lithography using nano- and femtosecond pulsed, *Adv. Eng. Mater.* 113 (2009) B20.
- [28] M. Bieda, E. Beyer, A. Lasagni, Direct fabrication of hierarchical microstructures on metals by means of direct laser interference patterning, *J. Eng. Mater. Technol.* 132 (2010) 031015–031016.
- [29] A. Lasagni, T. Roch, D. Langheinrich, M. Bieda, A. Wetzig, Large area direct fabrication of periodic arrays using interference patterning, *Phys. Procedia* 12 (2011) 214–220.
- [30] A. Lasagni, M. Bieda, T. Roch, D. Langheinrich, Direct fabrication of periodic structures on surfaces, laser interference patterning as new scalable industrial tool, *Laser Tech. J.* 1 (2011) 45.
- [31] Y. Tsuboi, S.-I. Sakashita, K. Hatanaka, H. Fukumura, H. Masuhara, Photothermal ablation of polystyrene film by 248 nm excimer laser irradiation: a mechanistic study by time-resolved measurements, *Laser Chem.* 16 (1996) 167.
- [32] S. Küper, J. Brannon, K. Brannon, Threshold behavior in polyimide photoablation: single-shot rate measurements and surface-temperature modeling, *Appl. Phys. A* 56 (1993) 43–50.
- [33] S. Burgui, D. Langheinrich, C. Werner, R. Helbig, C. Gil, A. Lasagni, I. Lasa, J. Valle, Evaluation of *Staphylococcus aureus* adhesion to biomaterials with modified surfaces generated by direct laser interference patterning, *Acta Biomater.* (2014), submitted for publication.
- [34] A. Maznev, T.F. Crimmins, K.A. Nelson, How to make femtosecond pulses overlap, *Opt. Lett.* 23 (1998) 1378–1380.
- [35] Y. Nakata, T. Okada, M. Maeda, Nanosized hollow bump array generated laser by single femtosecond pulse, *Appl. Phys. Lett.* 81 (2002) 4239–4241.
- [36] Y. Nakata, T. Okada, M. Maeda, Lithographical laser ablation using femtosecond laser, *Appl. Phys. A* 79 (2004) 1481–1483.
- [37] B. Tan, N.R. Sivakumar, K. Venkatakrishnan, Direct grating writing using femtosecond-laser interference fringes formed at the focal point, *J. Opt. A: Pure Appl. Opt.* 7 (2005) 169–174.
- [38] T. Kondo, S. Matsuo, S. Juodkazis, V. Mizeikis, Multiphoton fabrication of periodic structures by multibeam interference of femtosecond pulses, *Appl. Phys. Lett.* 82 (2003) 2758–2760.
- [39] T. Kondo, S. Matsuo, S. Juodkazis, H. Misawa, A novel femtosecond laser interference technique with diffractive beam splitter for fabrication of three-dimensional photonic crystals, *Appl. Phys. Lett.* 79 (2001) 725–727.
- [40] A. Lasagni, P. Shao, J.L. Hendricks, C.M. Shaw, D. Yuan, D.C. Martin, S. Das, Direct fabrication of periodic patterns with hierarchical sub-wavelength structures on poly

- (3,4-ethylene dioxythiophene)-poly(styrene sulfonate) thin films using femtosecond laser interference patterning, *Appl. Surf. Sci.* 256 (6) (2010) 1708.
- [41] S. Beaupre, M. Leclerc, Optical and electrical properties of p-conjugated polymers based on electron-rich 3,6-dimethoxy-9,9-dihexylfluorene unit, *Macromolecules* 36 (2003) 8986–8991.
  - [42] J.Y. Yang, D.H. Kim, J.L. Hendricks, M. Leach, R. Northey, D.C. Martin, Ordered surfactant-templated poly(3,4-ethylenedioxythiophene) (PEDOT) conducting polymer on microfabricated neural probes, *Acta Biomater.* 1 (2005) 125.
  - [43] J. Reif, F. Costache, M. Henyk, S.V. Pandelov, Ripples revisited: non-classical morphology at the bottom of femtosecond laser ablation craters in transparent dielectrics, *Appl. Surf. Sci.* 197–198 (2002) 891.
  - [44] M. Guillermín, F. Garrelie, N. Sanner, E. Audouard, H. Soder, Single- and multi-pulse formation of surface structures under static femtosecond irradiation, *Appl. Surf. Sci.* 253 (2007) 8075–8079.
  - [45] H.M. van Driel, J.E. Sipe, J.F. Young, Laser-induced periodic surface structure on solids: a universal phenomenon, *Phys. Rev. Lett.* 49 (1982) 1955.
  - [46] J.F. Young, J.S. Preston, H.M. van Driel, J.E. Sipe, Laser-induced periodic surface structures. II. Experiments on Ge, Si, Al, and brass, *Phys. Rev. B* 27 (1983) 1155.
  - [47] T. Aernouts, P. Vanlaeke, W. Geens, J. Poortmans, P. Heremans, S. Borghs, R. Mertens, R. Andriessen, L. Leenders, Printable anodes for flexible organic solar cell modules, *Thin Solid Films* 451–452 (2004) 22–25.
  - [48] V.G. Khomenko, V.Z. Barsukov, A.S. Katašinkii, The catalytic activity of conducting polymers toward oxygen reduction, *Electrochim. Acta* 50 (2005) 1675–1683.
  - [49] Fraunhofer IWS Press Release VIII/2011, Low-Cost Laser Process Technology for Large-Area Micro/Nano-Fabrication, [www.iws.fraunhofer.de](http://www.iws.fraunhofer.de).

This page intentionally left blank

# Ultrashort pulsed laser surface texturing

18

E. Toyserkani, N. Rasti

University of Waterloo, Waterloo, ON, Canada

## 18.1 Introduction

For a few decades, ultrashort pulsed laser surface texturing/modification has been an attractive approach for surface alteration in terms of topological, chemical, and mechanical properties. The ease of the process for creating nano- and/or microscale texture on the surface has prompted many researchers to work extensively in this area while utilizing different types of ultrashort pulsed lasers. In this process, the surface of the material of interest is altered directly where a pulsed laser beam simply irradiates it without any masks, multiple beams, special positioning devices (e.g., atomic force microscope), and interference patterns. Different materials have been used to develop textured surfaces, so-called microstructures and nanostructures. Such textured surfaces have been used in many applications ranging from manufacturing, defense, and aerospace to medical industries.

In a generic fashion, the pulsed beam irradiates on a moving surface to create nano-, micro-, and/or macroscale structures with specific patterns. These patterns may be called self-assembled structures, pseudoperiodic structures, or engineered patterns, depending on the shape and physical mechanism behind the process that could be a pure thermal ablation and/or nonthermal process.

In this chapter, we try to shed some light on this process at different laser pulse durations through referring to several highly respected papers in this area to give readers some introductory understanding from its physics and applications.

## 18.2 Physics of thermal versus nonthermal ultrashort pulsed laser surface texturing

One of the premier studies on the physics of this process has been done in Mazur's group in Harvard. Their paper in *Nature* [1] explains the physics of ultrashort laser radiations on semiconductors. In general, the interaction of ultrashort laser beams with solids can be explained based on the pulse duration including nanosecond, picosecond, and femtosecond. Different physics govern each of these pulse duration regimes that can generally be named as thermal and nonthermal physics. Microstructures can be created on the materials in the form of craters (i.e., laser ablation and micromachining), or can grow from the substrate by protruding from

the surface. Different theories explain these structures, such as interference effect theory, which does not involve the photon wavelength explicitly [2], and fluid waves dictated by capillarity theory (i.e., surface energy) [3] due to instabilities from Marangoni effect. The first theory explains the structures with the periodic space equal to the laser wavelength.

The formation of microstructures, which have a period equal to the laser wavelength, has been explored by many authors [4–9]. However, the theory behind the self-assembled microstructures, with a higher period under pulsed laser irradiation, is still vague and is under investigation [10,11].

Where a laser irradiates the surface of materials, the electromagnetic waves interact with the materials. Usually, free or conductive electrons (called seed electrons) are available on the surface. The absorbed laser irradiation leads to energize the free electrons and cause further collisions of the electrons, resulting in ionization. By emitting more energy, the material is shattered as long as the system has not reached the critical plasma intensity. When it gets to the critical plasma intensity, the dielectric material becomes absorbable, known as the inverse Bremsstrahlung phenomenon [12].

Laser irradiation is one of the intense techniques that lead to the extreme thermodynamic nonequilibrium condition in very short timescale. Different phenomenon might occur as a consequence of laser irradiation to the material, such as optical breakdown, plasma formation, photomechanical effects, and thermal process. The main process affecting the material as a result of laser irradiation might differ based on the laser properties, especially the laser beam pulse duration. [Figure 18.1](#) represents different processes that occur at the surface of material as a result of laser irradiation

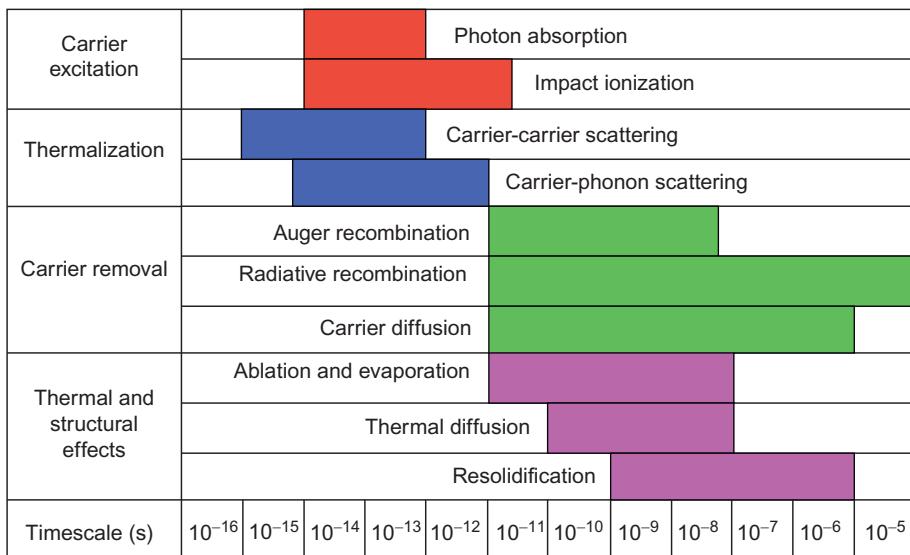


**Figure 18.1** Different processes associated with the different laser pulse durations. Adopted from Refs. [1,13].

that lead to the formation of microstructures for different laser pulses. These steps may overlap for nanosecond to femtosecond regimes [1]. For instance, in nonthermal processes, structural effects may happen when the lattice is cold [1].

In-depth explanations for all the four of these regimes are provided in Refs. [1,13]; however, a summary is given below where the dominant governing physics for the nanosecond range is first explained followed by the femtosecond regime:

- (a) *Thermal and structural effects*: Normally in the nano- and picoscale, the laser energy that is conducted to lattice results in electron resonance. If the resultant temperature is higher than the melting temperature, the material enters a liquid phase, and melting will happen where the temperature is higher than the boiling temperature, vaporization/ablation. The process may include resolidification from the melting phase with specific frequency, thermal diffusion, and ablation. According to Figure 18.1, the phenomenon that leads to the ablation of material in the range of 1-100 ns pulse is mostly thermal and structural effects. The effect of laser-material interaction and the ablation physics in the 1-100 ns range for metals are investigated by others [14]. Based on their theory, there are four different types of thermal sputtering: “(1) normal vaporization, (2) normal boiling, (3) phase explosion, and (4) subsurface heating” [14].
- (b) *Carrier removal*: Extra carriers/electrons can be removed from the materials by either the creation of electrons and holes in equilibrium or the diffusion associated with the excited area [1]. Excessive energy in a radiative condition will be converted to photons, known as luminescence, whereas in a nonradiative situation, it includes, “Auger recombination and defect and surface recombination/creation” [1]. Auger recombination refers to the situation where a hole combines again with an electron and a higher-level electron with less energy gains energy resulting in a lower density [1,14]. The diffusion process, however, results in electrons/carriers removal from the original excited area.
- (c) *Carrier excitation*: “Single photon absorption” is the main mechanism for excitation of electrons as long as the photon energy is larger than the energy difference between each energy level of atoms [1,13,14]. In the other way around, multiphoton absorption is dominant if the interval gap is larger than the photon energy. The latter one is more valid in transparent materials. If electrons are excited significantly such that their energy would be more than the orbit energy (bandgap), impact ionization may happen, resulting in extra excited electrons.
- (d) *Thermalization*: When excitation is over, redistribution of electrons and holes will happen in the material. It is mainly done by “carrier-carrier and carrier-phonon scattering” [1]. When the number of excited electrons/carriers remains unchanged, the energy lessens due to losing energy through phonon emission. In this case, the material starts to heat up regardless of the cold process that happened in a few femtoseconds.

These four phenomena during the ultrashort laser surface modification may result in nonthermal or thermal processes. Simple thermal process occurs in nanosecond and picosecond regions where the electrons at the outermost shell of the atom are excited and if the electrons resonance results in a case where the lattices are not in thermal equilibrium, melting or structural changes may occur.

In contrast, in the femtosecond and possibly attosecond regions, a nonthermal process results in material alterations. Normally, multiphoton excitation of electrons to the state of the conduction band is the main mechanism for structural changes. This excitation causes those particles to emit from ions to a larger cluster that is usually

more than 5-10 atoms. At high frequency of laser pulses, accumulation of temporary crystal defects causes structural changes. In a nutshell, the lattice alteration is subdued through self-organized creation of regular micro- and nanostructures in a rather non-thermal process than thermal [15].

### **18.2.1 *Physics of formation of pseudoperiodic and self-assembled microstructures during ultrashort pulsed laser processing***

The main mechanism of creation of self-assembled microstructures under irradiation of pulsed nanosecond and picosecond lasers is explained through melt displacement and the solidification process. The material deformation and resolidification theory is based on a two-coupled process of heat conduction and melt flow equations. Based on the thermal analysis, the temperature gradient is calculated based on the intensity absorption at a different part of the substrate. Then, the temperature gradient is coupled with fluid mechanic governing physics (i.e., Navier-Stokes equations). The temperature gradient will lead to the presence of surface tension and variation in tangential/interfacial force. The presence of this tangential force will lead to the melt pool displacement in the direction of increasing surface tension.

Microstructures can be created at the bottom of craters (i.e., laser ablation and micromachining), or can grow from the substrate by protruding from the surface. Different theories explain these structures that protrude from the surface of materials, such as interference effect theory, which does not include the photon wavelength explicitly [2], and fluid wave dictated by capillarity theory (i.e., surface energy) [3] due to instabilities from the Marangoni effect. The first theory explains the structures with the periodic space equal to the laser wavelength.

The formation of microstructures, which have a period the same as the laser wavelength, typically occur in the femtosecond region, and were explored by many authors [4]. However, the theory behind the self-assembled microstructures, with a higher period under pulsed laser irradiation, is still vague and is under investigation [5].

Where laser irradiates the surface of materials, the electron magnetic waves interact with the materials. Usually, free or conductive electrons are available on the surface. The absorbed laser irradiation leads to energizing the free electrons and causing the further collisions of the electrons, resulting in ionization. By irradiating more energy, the material is shattered, until critical plasma density is reached and the dielectric material becomes absorbable. When a high-intensity beam is used, the optical breakdown of the surface becomes a new issue to be considered in addition to the other thermal effects of the laser beam. The plasma, produced by a high-intensity laser beam in a short period of time (a range of a nanometer or less), facilitates the nonlocal deposition of laser energy, occurring below the critical electron density [6].

The vaporization temperature ( $T$ ) is linearly related to the laser beam intensity ( $I$ ), but it has the inverse relation to the pulse duration ( $\lambda$ ) (Equation 18.1). So, by

increasing the power intensity and decreasing the pulse duration, the temperature of the center of the spot increases, and it is represented as follows:

$$T = \frac{I\delta}{\lambda} \operatorname{erfc}\left(\frac{z}{\delta}\right) \quad (18.1)$$

where  $\delta = \sqrt{4\alpha t}$  is the depth of the laser penetration,  $\alpha$  is the thermal diffusivity,  $z$  is the penetrated depth (shown in Figure 18.2), and  $t$  is the time of irradiated laser.

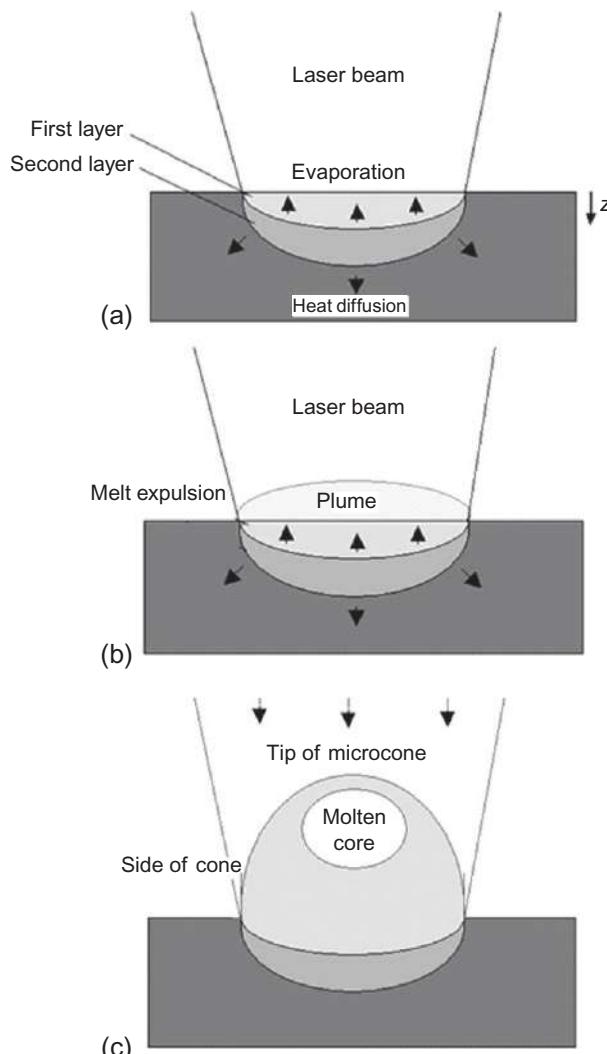


**Figure 18.2** (a–c) Schematic sequence processes of initiation and growth of microstructures under irradiation of ultrashort laser. Adapted from Ref. [7].

For a high-power intensity, the plume formation and vaporization of the material occur in an ultrashort period of time at the beginning of the laser pulse, shown by

$$t_p = \frac{\pi E}{4I^2} \quad (18.2)$$

where  $I$  is the laser intensity,  $E = \lambda\rho T_v^2$  is the erosion resistance of materials related to the pulse duration of the material density ( $\rho$ ), the vaporization temperature ( $T_v$ ), and the wavelength ( $\lambda$ ).

Where a laser with a high intensity of the order  $10^9$  W/cm<sup>2</sup> with a pulse length of a nanosecond or shorter heats the surface, the material reaches its vaporization temperature simultaneously. The nonlocalized absorption of irradiation results in a heat transport to the substrate and hardens the energy deposition. Therefore, because the energy dissipation of the laser pulse in the material is sluggish, compared to the width of the pulse, and the melting pool lifetime is, approximately, the same as the pulse periods before the surface vaporization, the underneath melted material, which is in the range of the depth of focus of the laser beam, reaches its vaporization temperature. As a result, the interaction between the melted part and the pressure of the plasma/vapor part in the near-surface layer increases temperature and pressure of the material. This induces a hydrodynamic instability of the melt, causing the working material to explode at the surface, forming some asperities on the surface [7].

Before the vaporization of the first layer, the second layer attains the vaporizing temperature. Pressure and temperature gradients in the layer beneath result in the material explosion shown in [Figure 18.2a and b](#).

In [Figure 18.2c](#), after the formation of the microstructures, three different regions can be distinguished on the microstructure. The sides, which are the coolest part of the cones and reflect most of the irradiated heat, and the tip of the cones, which is normally normal (perpendicular) to the laser beam, absorb the laser heat relative to its surface area, which is usually small. The inner cone has the highest temperature, because it is oriented normal to the laser beam and is exposed to the laser beam that is reflected from the side sections. By increasing the number of pulses per spot area, the newly formed asperities are accelerated to get away from the liquidified substrate at each laser pulse. This is due to the volume change caused by the dissolved oxygen, which decreases the surface tension of the melted area and the liquid thermal expansion in the center of the irradiated area. All these reasons, in addition to the varying surface tension due to the different temperatures of the surface, will lead to the increase in the height of self-assembled structures [8].

According to this theory, different shapes of the microstructures are observed for the different materials with different material properties (i.e., viscosity of melted material) through different stages of (i) temperature rising, (ii) diffusion of heat into the bulk, and (iii) convection. This has been reported before about the structures produced on stainless steel [6,8–11] compared to those on titanium [12,16–18], which is demonstrated to have considerable low-height structures on its surface.

### 18.3 Nanosecond pulsed surface texturing

A laser microablation method with nanosecond pulsed lasers has been recently used to modify the topography of many materials, including titanium, through the creation of microgrooves and also pseudoperiodic microstructures. The advantage of this method is the formation of the locally multiscaled (from a nano- to microroughness) roughened structures on the edges of the grooves under laser irradiation.

Different types of laser techniques have been utilized for the above-mentioned goal. Ricci *et al.* [19] used an excimer ultraviolet (UV) laser with large-area masking techniques and a top hat intensity profiles for creating the microgrooves. However, due to the high photon energy in UV wavelength range, microcracks and heat-affected zone (HAZ) appear on the surface [20,21]. To avoid such cracks, diode pumped solid-state lasers are substituted by UV lasers. Nd:YAG and Nd:YVO<sub>4</sub> IR wavelength lasers were also good alternatives to form microgrooves. It is because of their good laser beam quality with Gaussian beam intensity [22–24]. Both DIPSS and IR lasers provide a focused high-fluence laser beam for the creation of microgrooves on metal surfaces. The groove depth is affected by the laser energy per pulse, frequency of pulses, and translation distance through the ablation process [25]. This approach can be used to modify surfaces such that cell adhesion will be promoted in biomedical and implant applications. The roughness provides good sites for focal adhesion during cell locomotion and spreading. The microscale roughness activates the platelets, and retains the fibrin clot. Also, the roughness increases interfacial strength of the adhesive cells [19,23,24,26]. In an unpublished work of the authors, it is shown that the osteoblast cells may be attracted toward the area with higher surface as shown in Figure 18.3. The disadvantage of these methods is that microroughness still develops in the width and depth of microgrooves, which will act as sites for cell adhesion and eventually will affect the orientation of cells. There should be more roughness to act as adhesion sites on the spacing of the grooves, which are more in contact with the cell area [26].

Rasti *et al.* [27] used a nanosecond fiber laser to modify Ti surface. They showed the trend of initiation and growth of pseudoperiodic structures and their dependency on laser intensity and laser-effective energy. The surfaces shown in Figure 18.4 were all obtained at a laser intensity of 0.35 MW/cm<sup>2</sup> while the effective energy varied from: 5.13 J/cm<sup>2</sup> in Figure 18.4a to 10.26 J/cm<sup>2</sup> in Figure 18.4b, 25.65 J/cm<sup>2</sup> in Figure 18.4c, and 51.3 J/cm<sup>2</sup> in Figure 18.4d.

They have also shown that by varying the laser parameters in several experiments, it was observed that pseudoperiodic structures begin to appear at intensities close to the damage threshold of the material. They have shown that “such damage was very dependent on the surface absorbance and initial surface quality. For the prepared samples, the formation of the shown microstructures was initiated on the surface at the intensity of 0.35 MW/cm<sup>2</sup>, even at the low effective energy of 5.13 J/cm<sup>2</sup>. Then, by more irradiation, these structures continued to increase in size. The SEM and optical microscopy analyses revealed that pseudoperiodic structures do not develop at lower intensities. By increasing the effective energy, mostly by decreasing the scanning velocity, more laser energy is delivered to the spot area, which leads to the growth of microstructures as shown in Figure 18.4a-d” [27].

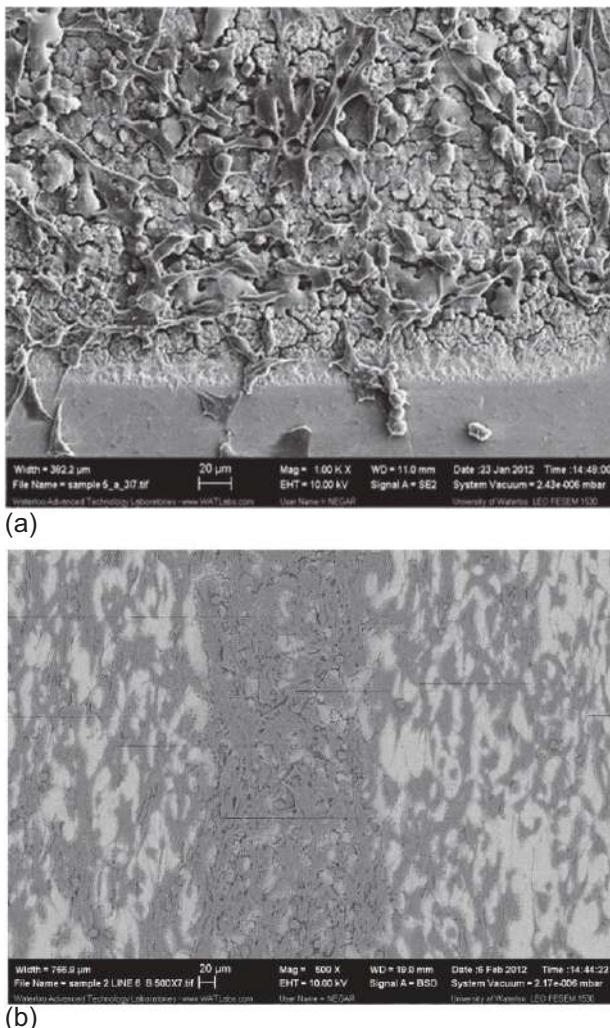


**Figure 18.3** (a) Cell elongation on rough surfaces and (b) cells migration in the direction of laser pass.

In general, nanosecond lasers can provide a great opportunity for surface modifications given their low cost.

## 18.4 Picosecond pulsed surface texturing

Picosecond lasers have been used in many applications and on many materials. For instance, SS304 is modified by picosecond pulse energies of 0.89-2.08 μJ at 100 ps [28]. It has been shown that for energy below 1 μJ, the periodic surface is visible

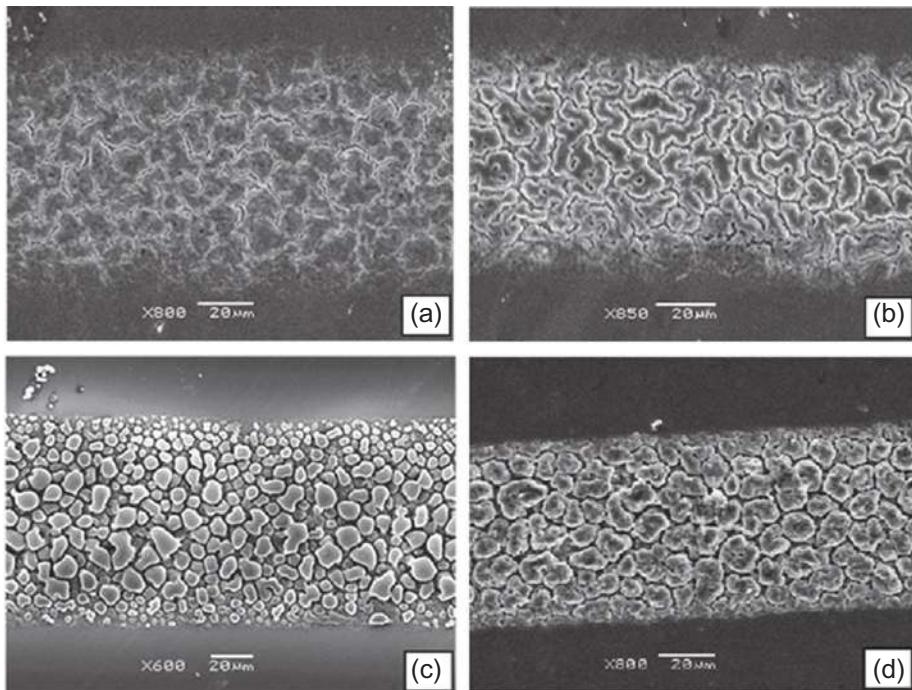


**Figure 18.4** Pseudoperiodic structures initiated at intensity of  $0.35 \text{ MW/cm}^2$  and at effective energy of (a) 5.13, (b) 10.26, (c) 25.65, and (d)  $51.3 \text{ J/cm}^2$  [27].

but not significant, whereas a remelting and periodic bandings are seen for energies above  $1.05 \mu\text{J}$  [28].

The surface of titanium nitride has been altered by a picosecond Nd:YAG laser [29]. It has been shown that at intensities higher than  $0.2 \text{ J/cm}^2$ , full melting occurs; whereas at a lower intensity, periodical surface structures with micro- and nanofeatures are developed.

Al, Ti, and SS316 are also reported to be modified by picosecond lasers. Zhao *et al.* [30] ablated stainless steel by a 10 ps Q-switched Nd:VAN pulsed laser to investigate ultrafast micromachining properties and optimize the performance parameters. Zhao *et al.* [31] irradiated amorphous  $\text{Ge}_2\text{Sb}_2\text{Te}_5$  films by a picosecond laser to study the morphology and crystalline phase changes.  $(\text{GeTe})_x(\text{Sb}_2\text{Te}_3)_y$  alloys with ultrashort phase change are considered as strong candidates to be used in phase-change memories. The HAZs formed by picosecond lasers are almost small and negligible due to very short interaction times with the material. Hafiz *et al.* [32] have used a picosecond laser for laser micropolishing of Inconel 718 (IN718).

The resulting surface was remarkably smooth and uniform and comparable in terms of surface roughness. Wang *et al.* [33] deployed a picosecond laser for laser-induced breakdown spectroscopy (LIBS) technology as an elemental analysis technique. They concluded that employment of a picosecond laser is extremely influential

to increase the LIBS detection limit. O'Brien *et al.* [34] also attempted to improve the corrosion rate of magnesium alloys as biodegradable implants using a picosecond laser. Surface treatment of the alloys using low- and high-power picosecond lasers helped to improve the corrosion resistance substantially.

## 18.5 Femtosecond pulsed laser surface texturing

Femtosecond lasers have shown promising applications in bio, energy, and aerospace sectors in recent years. As explained, the main mechanism behind the femtosecond laser surface modification is multiphoton phenomenon and nonthermal processes. This type of laser can form extremely uniform periodic structures in nano- and microscale with a minimum amount of deficiencies.

Nice self-assembled structures are produced on surfaces on a variety of materials like titanium, stainless steel, silicon, aluminum alloys, and many more. For instance, the surfaces of solar panels are altered by femtosecond lasers to increase solar cell efficiency [35]. In Mazur's group, femtosecond lasers are used to create periodic structures on black silicon with nano- and microsize features [36].

Modification of surface properties, nanoplasmonics, nanophotonics, metaoptics, and fiber Bragg grating inscribing are some of the fields of application of femtosecond lasers. Bashir *et al.* [37] have used Ti: Sapphire femtosecond lasers to study the formation of nanostructures on the surface of tin (Sn). They also explored the effect of laser fluence and pulse duration on surface modifications. Yong *et al.* [38] deployed a femtosecond laser to study superhydrophobic patterned polydimethylsiloxane (PDMS) surfaces. Ultralow to ultrahigh water adhesion of the PDMS surface was tuned using the femtosecond laser. Florian *et al.* [39] also ablated the surface of polymethyl-methacrylate by a focusing method named z-scan method. They employed a femtosecond laser with 450 fs pulses at a wavelength of 1027 nm. Bauer *et al.* [40] studied binary Li-silicate glasses as ion conductor and the lithium migration mechanisms. A femtosecond laser was employed to analyze the diffusion profiles and Li-dynamics. Zijlstra *et al.* [41] did a comprehensive study on bond strength and structural modifications of silicon, TiO<sub>2</sub>, and graphene using a femtosecond laser. Molecular dynamics and laser-induced atomic motions were also investigated to determine the thermal evolutions and structural response in the materials.

## 18.6 Attosecond pulsed laser surface texturing: would it reasonably be applicable to surface modifications?

The short answer is probably "No." This new laser may find its way to manipulate the surface molecules and find some ways to create novel material surface; however, there is a long way to go before offering stable attosecond lasers for such applications. In addition, the laser may not be suitable for scale-up surface modification.

## 18.7 Conclusion

Ultrashort laser surface modification (texturing) has opened up new venues to researchers and industry to benefit effectively from this emerging technology. In this chapter, we discussed the physics of thermal and nonthermal for such processes that are a function of laser pulse durations. In addition, some applications of ultrashort laser processing were discussed. It is noted that the cost of femtosecond and picosecond lasers is very high; therefore, an inexpensive nanosecond laser might be a better choice for some applications where compromises should be made to accept pseudo-periodic patterns with deficiencies as opposed to well-established self-assembled structures that could be created by picosecond and femtosecond lasers.

## References

- [1] S.K. Sundaram, E. Mazur, Inducing and probing non-thermal transitions in semiconductors using femtosecond laser pulses, *Nat. Mater.* 1 (2002) 217–224.
- [2] J.F. Young, J.S. Preston, H.M. van Driel, J.E. Sipe, Laser-induced periodic surface structure. II. Experiments on Ge, Si, Al, and Brass, *Phys. Rev. B* 27 (2) (1983) 1155–1172.
- [3] C.A. Coulson, A. Jeffery (Eds.), *Waves: A Mathematical Approach to the Common Types of Wave Motion*, second ed., Longman, London, 1977.
- [4] H.M. Driel, J.E. Sipe, F. Young, Laser induced periodic surface on solids: a universal phenomenon, *Phys. Rev. Lett.* 49 (26) (1982) 1955–1958.
- [5] S.R. Foltyn, in: D.B. Christy, G.K. Huber (Eds.), *Pulsed Laser Deposition of Thin Films*, Wiley, New York, 1994, pp. 89–113.
- [6] A. Abdolvand, R.W. Lloyd, M.J. Schmidt, D.J. Whitehead, Z. Liu, L. Li, Formation of highly organised, periodic microstructures on steel surfaces upon pulsed laser irradiation, *Appl. Phys. A* 95 (2) (2008) 447–452.
- [7] M.J. Jackson, *Micro and Nanomanufacturing*, Springer Science+Business Media, 2007.
- [8] S.I. Dolgaev, J.M. Fernández-Pradas, J.L. Morenza, P. Serra, G.A. Shafeev, Growth of large microcones in steel under multipulsed Nd:YAG laser irradiation, *Appl. Phys. Mater. Sci. Process.* 83 (3) (2006) 417–420.
- [9] R. Lloyd, A. Abdolvand, M. Schmidt, P. Crouse, D. Whitehead, Z. Liu, et al., Laser-assisted generation of self-assembled microstructures on stainless steel, *Appl. Phys. Mater. Sci. Process.* 93 (1) (2009) 117–122.
- [10] J. Schille, R. Ebert, U. Loeschner, T. Regenfuss, T. Suess, H. Exner, Micro structuring with highly repetitive ultra-short laser pulses, in: *Proceedings of LPM2008-the 9th International Symposium on Laser Precision Microfabrication*, 2008, pp. 1–6.
- [11] A. Bensaoula, C. Boney, R. Pillai, G.A. Shafeev, A.V. Simakin, D. Starikov, Arrays of 3D micro-columns generated by laser ablation of Ta and steel: modelling of a black body emitter, *Appl. Phys. Mater. Sci. Process.* 79 (4-6) (2004) 973–975.
- [12] E. György, I.N. Mihailescu, P. Serra, A. Perez Del Pino, J.L. Morenza, Crown-like structure development on titanium exposed to multipulse Nd:YAG laser irradiation, *Appl. Phys. A* 74 (2002) 755–759.
- [13] J.P. Calan, Ultrafast dynamics and phase changes in solids excited by femtosecond laser pulses (Ph.D. thesis), Harvard, 2000.
- [14] N.M. Bulgakova, A.V. Buglakov, Pulsed laser ablation of solids: transition from normal vaporization to phase explosion, *Appl. Phys. A* 73 (2001) 199–208.

- [15] J. Reif, Basic physics of femtosecond laser ablation, in: A. Miotello, P.M. Ossi (Eds.), *Laser-Surface Interactions for New Materials Production*, 2010 (Chapter 2).
- [16] S.I. Dolgaev, N.A. Kirichenko, A.V. Simakin, G.A. Shafeev, Initial stage of the development of three-dimensional periodic structures in laser melting, *Quantum Electron.* 34 (2004) 771–773.
- [17] E. György, A. Pérez del Pino, P. Serra, J.L. Morenza, Laser-induced growth of Titanium nitride microcolumns on biased Titanium targets, *J. Mater. Res.* 20 (1) (2005) 62–67.
- [18] E. György, A. Pérez del Pino, P. Serra, J.L. Morenza, Depth profiling characterization of the surface layer obtained by pulsed Nd:YAG laser irradiation of titanium in nitrogen, *Surf. Coat. Technol.* 173 (2002) 265–270.
- [19] J.L. Ricci, J.C. Grew, H. Alexander, Connective-tissue responses to defined biomaterial surfaces. I. Growth of rat fibroblast and bone marrow cell colonies on microgrooved substrates, *J. Biomed. Mater. Res. A* 85 (2) (2008) 313–325.
- [20] J.L. Ricci, H. Alexander, Laser microtexturing of implant surfaces for enhanced tissue integration, *Key Eng. Mater.* 198–199 (2001) 179–202.
- [21] W.O. Soboyejo, C. Mercer, S. Allameh, B. Nemetski, N. Marcantonio, J.L. Ricci, Multi-scale microstructural characterization of micro-textured Ti-6Al-4V surfaces, *Key Eng. Mater.* 198–199 (2001) 203–230.
- [22] S. Mwenifumbo, N.D. Morris, M. Li, M. Keirstead, W.O. Soboyejo, An investigation of nano-second UV laser processing parameters on surface micro-groove geometry and microstructure in Ti-6Al-4V, in: *Surface Engineering: In Materials Science II*; March 2-6, 2003, Minerals, Metals and Materials Society, Warrendale, PA, United States, 2003, pp. 141–150.
- [23] N. Mirhosseini, P.L. Crouse, M.J.J. Schmidth, L. Li, D. Garrod, Laser surface microtexturing of Ti-6Al-4V substrates for improved cell integration, *Appl. Surf. Sci.* 253 (19) (2007) 7738–7743.
- [24] A.C. Duncan, F. Rouais, S. Lazare, L. Bordenave, C. Baquey, Effect of laser modified surface microtopochemistry on endothelial cell growth, *Colloids Surf. B: Biointerfaces* 54 (2) (2007) 150–159.
- [25] J.P. Ulerich, L.C. Ionescu, J. Chen, W.O. Soboyejo, C.B. Arnold, Modifications of Ti-6Al-4V surfaces by direct-write laser machining of linear grooves, in: *Proceedings of the SPIE 6458, Photon Processing in Microelectronics and Photonics VI*, 645819, March 13, 2007.
- [26] Y. Cao, J. Chen, M.O. Adeoye, W.O. Soboyejo, Investigation of the spreading and adhesion of human osteosarcoma cells on smooth and micro-grooved polydimethylsiloxane surfaces, *Mater. Sci. Eng. C* 29 (1) (2009) 119–125.
- [27] N. Rasti, E. Toyserkani, F. Ismail, Formation of pseudo-periodic microstructure on titanium surfaces under pulsed nanosecond fiber laser irradiation: topographical and mechanical properties, *Lasers Eng.* 27 (3-4) (2014) 179–197.
- [28] K. Pangovski, K. Li, B. O'Neill, *Application of Picosecond Lasers for Surface Modification and Polishing*, Photonics London, London, UK, July 2011.
- [29] B. Gaković, M. Trtica, D. Batani, T. Desai, P. Panjan, D. Vasiljević-Radović, Surface modification of titanium nitride film by a picosecond Nd:YAG laser, *J. Opt. A: Pure Appl. Opt.* 9 (2007) S76.
- [30] W.Q. Zhao, W.J. Wang, G.D. Jiang, X.S. Mei, B. Liu, Improving the efficiency of picosecond laser micromachining of stainless steel, *Radiat. Eff. Defects Solids* (2013) 1–7.
- [31] J.J. Zhao, F.R. Liu, X.X. Han, N. Bai, Y.H. Wan, X. Lin, F. Liu, Morphology and crystalline phase characteristics of  $\alpha$ -GST films irradiated by a picosecond laser, *Appl. Surf. Sci.* 289 (2014) 160–166.

- [32] A.M.K. Hafiz, E.V. Bordatchev, R.O. Tutunea-Fatan, Experimental analysis of applicability of a picosecond laser for micro-polishing of micromilled Inconel 718 superalloy, *Int. J. Adv. Manuf. Technol.* 70 (9-12) (2014) 1963–1978.
- [33] Z.Z. Wang, Y. Deguchi, M. Kuwahara, J.J. Yan, J.P. Liu, Enhancement of laser-induced breakdown spectroscopy (LIBS) detection limit using a low-pressure and short-pulse laser-induced plasma process, *Appl. Spectrosc.* 67 (11) (2013) 1242–1251.
- [34] B.J. O'Brien, W.M. Carroll, J. Conneely, G.M. O'Connor, Combined anodizing and picosecond laser treatment to control the corrosion rate of biodegradable magnesium alloy AZ31. *Proc. Inst. Mech. Eng. Part L J. Mater. Des. Appl.* (2013), <http://dx.doi.org/10.1177/1464420713487648>.
- [35] T. Rublack, S. Krause, S. Schweizer, G. Seifert, Increasing solar-cell efficiency by femtosecond laser microstructuring. *SPIE Newsroom* (17 September 2012), <http://dx.doi.org/10.1117/2.1201209.004466>.
- [36] J.E. Carey, Femtosecond-laser microstructuring of silicon for novel optoelectronic devices (Ph.D. thesis), Harvard University, July 2004.
- [37] S. Bashir, M.S. Rafique, C.S. Nathala, W. Husinsky, The formation of nanodimensional structures on the surface of tin exposed to femtosecond laser pulses in the ambient environment of ethanol, *Appl. Surf. Sci.* 290 (2014) 53–58.
- [38] J. Yong, F. Chen, Q. Yang, D. Zhang, G. Du, J. Si, F. Yun, X. Hou, Femtosecond laser weaving superhydrophobic patterned PDMS surfaces with tunable adhesion. *J. Phys. Chem. C* (2013), <http://dx.doi.org/10.1021/jp408863u>.
- [39] C. Florian, F. Caballero-Lucas, J.M. Fernández-Pradas, J.L. Morenza, P. Serra, Surface ablation of transparent polymers with femtosecond laser pulses, *Appl. Surf. Sci.* 320 (2014) 226–230.
- [40] U. Bauer, A.M. Welsch, H. Behrens, J. Rahn, H. Schmidt, I. Horn, Li-diffusion and the role of local structure on Li-mobility in Li<sub>2</sub>O-SiO<sub>2</sub> glasses. *J. Phys. Chem. B* (2013), <http://dx.doi.org/10.1021/jp408805e>.
- [41] E.S. Zijlstra, T. Zier, B. Bauerhenne, S. Krylow, P.M. Geiger, M.E. Garcia, Femtosecond-laser-induced bond breaking and structural modifications in silicon, TiO<sub>2</sub>, and defective graphene: an ab initio molecular dynamics study. *Appl. Phys. A* (2013), <http://dx.doi.org/10.1007/s00339-013-8080-x>.

This page intentionally left blank

# Laser-guided discharge surface texturing

19

Z.-T. Wang, M.-J. Yang

Chinese Academy of Sciences, Shanghai, China

## 19.1 Introduction

Recently, the technology of roller surface texturing has been widely applied in the cold rolling industry. The surface texturing of the roller may increase the frictional coefficient between the roller and the steel sheet so as to decrease the surface defects of the steel sheet. On the other hand, the convex rims on the surface of the textured roller are converted to concave pits on the surface of the steel sheet in the cold rolling process. The concave pits on the surface of the steel sheet may improve the performance of stamping and painting; therefore, cold rolled textured sheets have been widely used in the body of cars and similar products.

The common techniques used for roller surface texturing include, shot blast texturing (SBT) [1], electrical discharge texturing (EDT) [2], and laser texturing (LT). LT can be further divided into two types: CO<sub>2</sub> laser texturing (CO<sub>2</sub>LT) [3] and Nd:YAG laser texturing (YAGLT) [4]. Furthermore, electron beam texturing (EBT) [5] and electrodeposited chromium texturing (TOPCROM) [6] have also been studied. EBT has been studied for many years and is still in the experimental stage, but TOPCROM with its different texturing mechanism is a promising technique.

The distribution and the shape of the textured craters on the surface of the textured steel sheet made by EDT are all random; therefore, in the stamping process the lubricating oil between the steel sheet and the mold will flow along the channels between the textured craters to weaken the lubricating condition. But the processing speed of EDT is the fastest among the existing texturing methods, except the traditional SBT; therefore, EDT has been popularly applied in the cold rolling industry. On the contrary, the distribution of the textured craters on the surface of the textured steel sheets by YAGLT is deterministic in two dimensions, and separated from each other so as to easily store the lubricating oil to improve the lubricating condition between the steel sheet and the mold; therefore, the stamping performance of the textured steel sheet made by YAGLT is perfect. But the Q-switcher power in the quasi-continuous YAG laser machine limits the output power of the laser. Therefore, the processing speed and the surface roughness are not increased at the same time, which restricts the application of YAGLT technology in the cold rolling industry. It is obvious that a new technique of surface texturing is needed to combine the advantages of laser processing and electrical discharge processing, for example, the technique of laser-induced discharge.

The studies of laser-induced discharge according to the property of laser plasma are mainly divided into two sides: the method of triggering the electrical discharge in an electrode gap with weak ionized plasma [7,8] and the method of guiding the breakdown channel in the medium with strong ionized plasma [9,10]. Triggering the electrical discharge by a laser beam is applied in the laser trigger spark gap (LTSG) technique [11,12], and guiding the discharge path by a laser beam is used to simulate lightning in the laboratory [13,14]. Furthermore, in the field of material processing, the laser-induced discharge technique is applied to locally removing material [15,16] and strengthening material [17].

In this chapter, a new technique of laser-guided discharge texturing (LGDT) is introduced. In this technique, the quasi-continuous Nd:YAG laser pulse is focused on the roller surface to trigger and guide the arc discharge in the electrode gap, and then to texture the roller surface. The mechanism of using a quasi-continuous Nd:YAG laser pulse to control the discharge is discussed. The processing methods of LGDT are studied. Three-dimensional surface profiles and microstructures of the textured craters made by LGDT are analyzed. Finally, the characters of three surface-texturing techniques, YAGLT, EDT, and LGDT, are compared.

## 19.2 Mechanisms of laser-guided discharge texturing (LGDT)

In the process of laser-induced discharge, the ionization degree or electron density of the laser plasma decides the method of triggering and guiding the electrical discharge. Next, the mechanism of laser plasma produced by a low-power laser, for example, a quasi-continuous Nd:YAG laser, is discussed, and the method of triggering and guiding it are studied.

### 19.2.1 Laser plasma formation

The formation of the laser plasma in the gas has two types of mechanism:

- *Multiphoton ionization*: The particles in the gas may absorb several photons at the same time. If the total energy of the photons reaches the ionization potential of the particle, then multiphoton ionization will be implemented. It is clearly noted that the laser beam with the higher power density and shorter wavelength is conducive to the creation of multiphoton ionization. Multiphoton ionization is likely to happen in a short laser pulse-width or at low pressure because of the limited electron avalanche [18].
- *Cascade ionization by inverse Bremsstrahlung (IB) heating electrons*: Free electrons in the gas are accelerated by the laser electric field within the laser focus in order to collide with the other particles. In the process of collision the particles gradually absorb photon energy by IB. If the absorbed photon energy reaches the ionization potential of the particle, then cascade ionization will be implemented. If the ionization rate is larger than the loss rate of the diffusion, attachment, and recombination, then gas breakdown will take place to produce plasma. In general the cascade ionization appears in high pressure or long laser pulse-widths [18].

In the atmosphere, when the quasi-continuous Nd:YAG laser used in this chapter is focused on the metal surface the laser power density is about  $10^9 \text{ W/cm}^2$  under the breakdown threshold value in air. However, in metal vapor there is an abundance of heated electrons from the metal surface. These heated electrons are conducive to produce the cascade ionization by IB.

## 19.2.2 Control in arc discharge by laser guiding

### 19.2.2.1 Triggering discharge

The property of laser triggering discharge is mainly represented through the breakdown voltage at a probability of 50% ( $U_{50}$ ). The contrasting experiment between the conditions of the laser triggering discharge and the free discharge is implemented with a copper needle electrode and a grounded plate of 1045 steel in the atmosphere. The result is shown in Figure 19.1. The  $U_{50}$  all is decreased to about one-tenth of the origin in the anodal discharge and the cathodal discharge by laser triggering. The  $U_{50}$  of the anodal discharge is lower than that of the cathodal discharge.

The breakdown threshold of the electrode gap in millimeter grade is decreased to about several hundred volts to avoid the use of high-voltage equipment, and to best achieve the discharge process with a high rate of repetition. In this kind of phenomenon, a laser pulse is used for the discharge switch as with the LTSG. In the experiment of the breakdown time jitter in the electrode gap less than 1.2 mm, it is found that the jitter is less in order to ensure the homogeneity of the discharge energy (Figure 19.2).

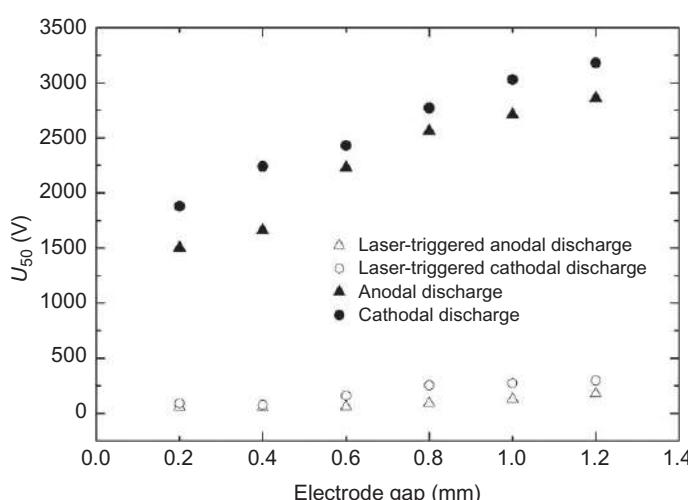


**Figure 19.1** Property of laser-triggered discharge.

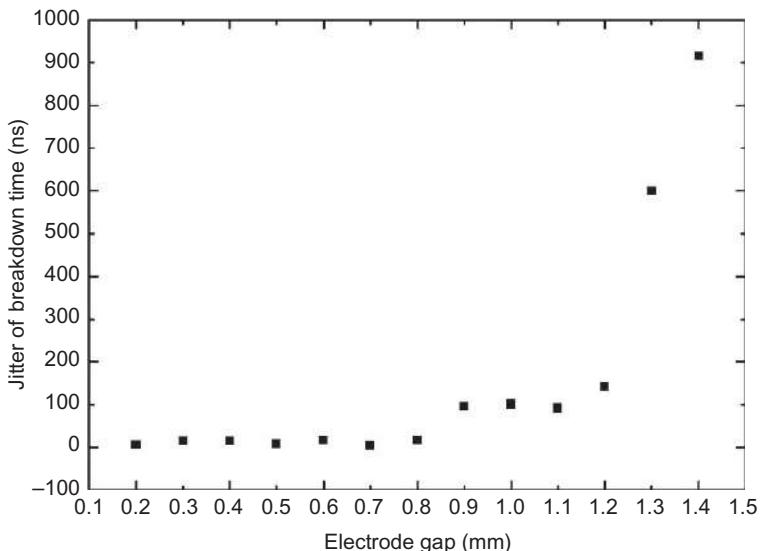


Figure 19.2 Relation between electrode gap and jitter of breakdown time.

### 19.2.2.2 Guiding discharge

In order to study how the laser guiding is used to control in such random processing as that of arc discharge, the textured surface created by laser guiding is compared with that created by free arc discharge. Figure 19.3 shows that without laser guiding, the distribution of the textured craters is random, the diameter of the textured craters is irregular, and some discharge pulses are not successfully triggered. Laser guiding can be used to combat these irregularity issues.

The control schematic in the free arc discharge by laser guiding is shown in Figure 19.4. Without laser guiding, the discharge position is determined by the microtopography of the electrode surface. The arc discharge is spread along the path of least energy, and the discharge position is random. With laser guiding, the arc discharge is spread along the plasma to arrive at the laser focuser with the highest degree of ionization, and the discharge position is overlapped with the laser focus. In addition, the laser triggering reduces the jitter of the breakdown time, and improves the regularity of the diameter of the textured craters.

## 19.3 Experiments of LGDT

After the property of the discharge induced by a quasi-continuous Nd:YAG laser has been discovered, the LGDT experiment can be implemented. The schematic is shown in Figure 19.5. A roller of 1045 steel is considered as an anode and grounded, and a round copper disk with a sharp edge is used as a cathode. During processing, the disk is

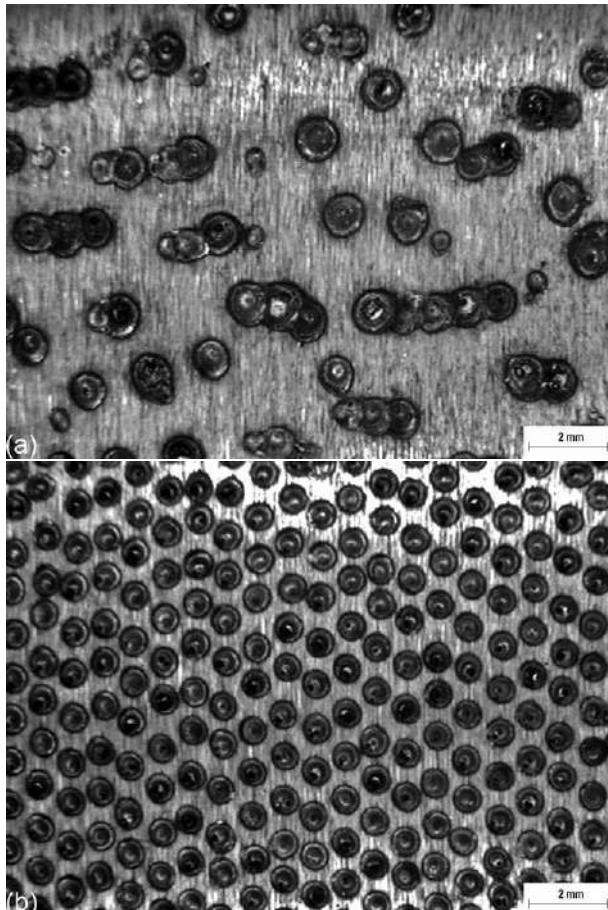


**Figure 19.3** Surface 3-D microscope photos of textured surfaces by (a) free arc discharge and (b) laser-guided discharge.

also rotated to separate the sequential discharge position on the disk edge. A quasi-continuous Nd:YAG laser is used to guide the arc discharge with 1.06  $\mu\text{m}$  wavelength. The laser pulse and the discharge pulse are triggered synchronously through the controlling signal. The transformer oil is initially laid on the roller surface to restrict the expansion of the textured craters.

During processing the roughness of the textured crater is determined by the discharge energy and the arc pressure. The discharge energy may be presented as:

$$E = U_{\text{arc}} I t_w \quad (19.1)$$

where  $U_{\text{arc}}$  is the arc voltage,  $I$  is the discharge current, and  $t_w$  is the discharge pulse-width. If the electrode gap is fixed,  $U_{\text{arc}}$  is nearly constant. Therefore, the discharge

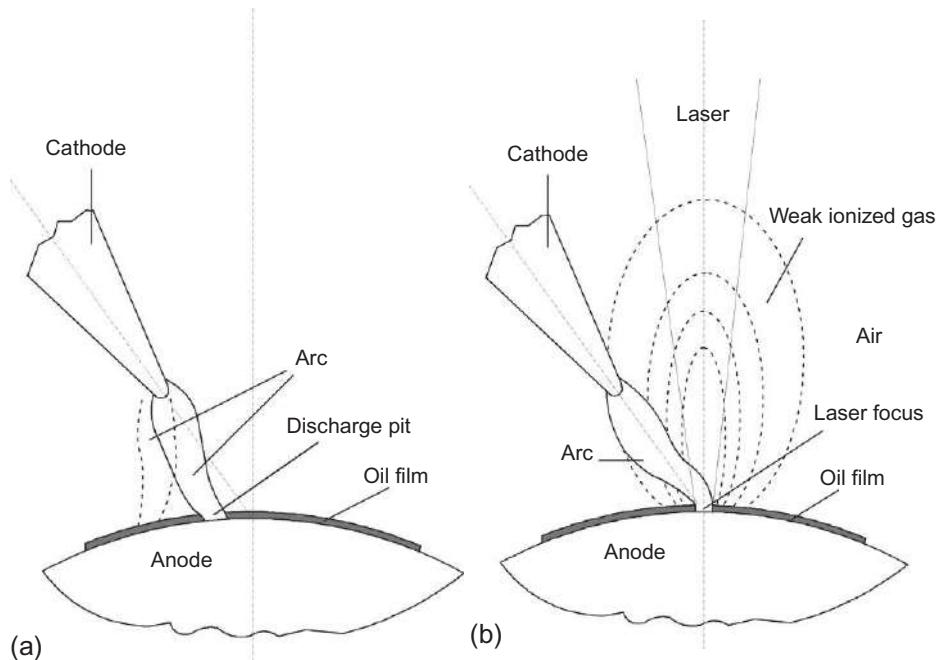


Figure 19.4 Control schematic by (b) laser guiding in the (a) free arc discharge.

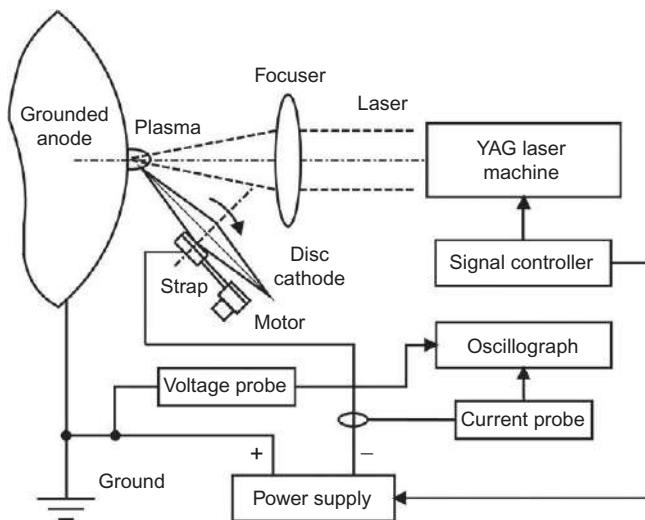


Figure 19.5 Schematic of LGDT.

energy is mainly determined by the discharge current and the discharge pulse-width. The arc pressure, in accordance with the discharge current and the current density is presented as:

$$P_a \propto Ij \quad (19.2)$$

where  $P_a$  is the arc pressure, and  $j$  is the current density. In the discharge process, while the discharge pulse-width is increased, the arc will be expanded to change the arc pressure. In the following experiment the combined parameters of the discharge current peak and the discharge pulse-width are used to study the 3-D surface profiles of the textured craters.

### 19.3.1 3-D surface profiles of textured craters

The four kinds of processing parameters and experimental results are shown in [Table 19.1](#). As a result of the augmentation of the discharge energy, the diameter of the textured craters is increased ([Figure 19.6](#)), the height of the convex rims in the textured craters is also increased from 38.1 to 55.3  $\mu\text{m}$  ([Figure 19.7](#)). In addition, the arc pressure has a significant influence on the height and shape of the convex rims in the textured craters. In spite of the discharge energy in parameter  $a$  being less than that in parameter  $b$ , the higher arc pressure in parameter  $a$  acquires, approximately, the same height as the convex rims in the textured craters with that in parameter  $b$ . In control of the high arc pressure the shape of the convex rims in the textured craters is sharp ([Figure 19.7a and c](#)). Otherwise, the shape of the convex rims in the textured craters is smooth ([Figure 19.7b and d](#)). It is easily found that the arc pressure determines the 3-D profiles of the textured craters, and the discharge energy and arc pressure together determine the height of the convex rims in the textured craters.

Given the frictional life, it is better for the textured crater to acquire a smooth shape than a sharp shape. The parameters of the short discharge pulse-width and the low discharge current peak may supply some textured craters with a small diameter, low height and smooth shape of convex rims adapted to produce the low roughened,

**Table 19.1 Parameters of textured craters**

	Parameter number			
	<i>a</i>	<i>b</i>	<i>c</i>	<i>d</i>
Pulse-width ( $\mu\text{s}$ )	150	100	100	150
Discharge current (A)	80	130	190	230
Pulsed discharge energy (J)	0.273	0.445	0.698	1.1
Diameter of textured crater (mm)	0.463	0.555	0.65	0.713
SRa of textured surface ( $\mu\text{m}$ )	3.27	6.03	8.46	13.2
Ratio of arc pressure	2.39	1.25	1.96	1

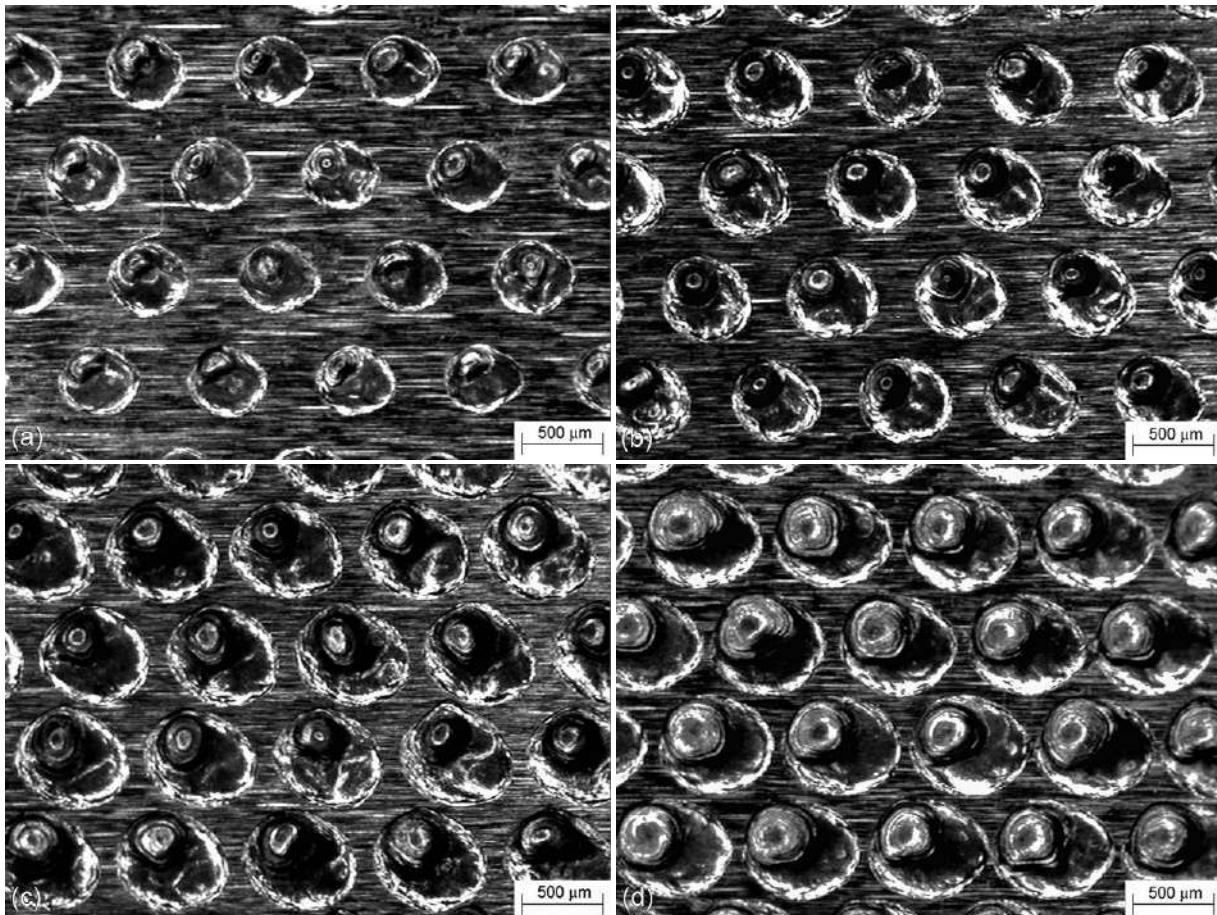


**Figure 19.6** 3-D microscope photos of the textured surfaces with different currents: (a) 150 A, 80  $\mu$ s; (b) 130 A, 100  $\mu$ s; (c) 190 A, 100  $\mu$ s; and (d) 150 A, 230  $\mu$ s.

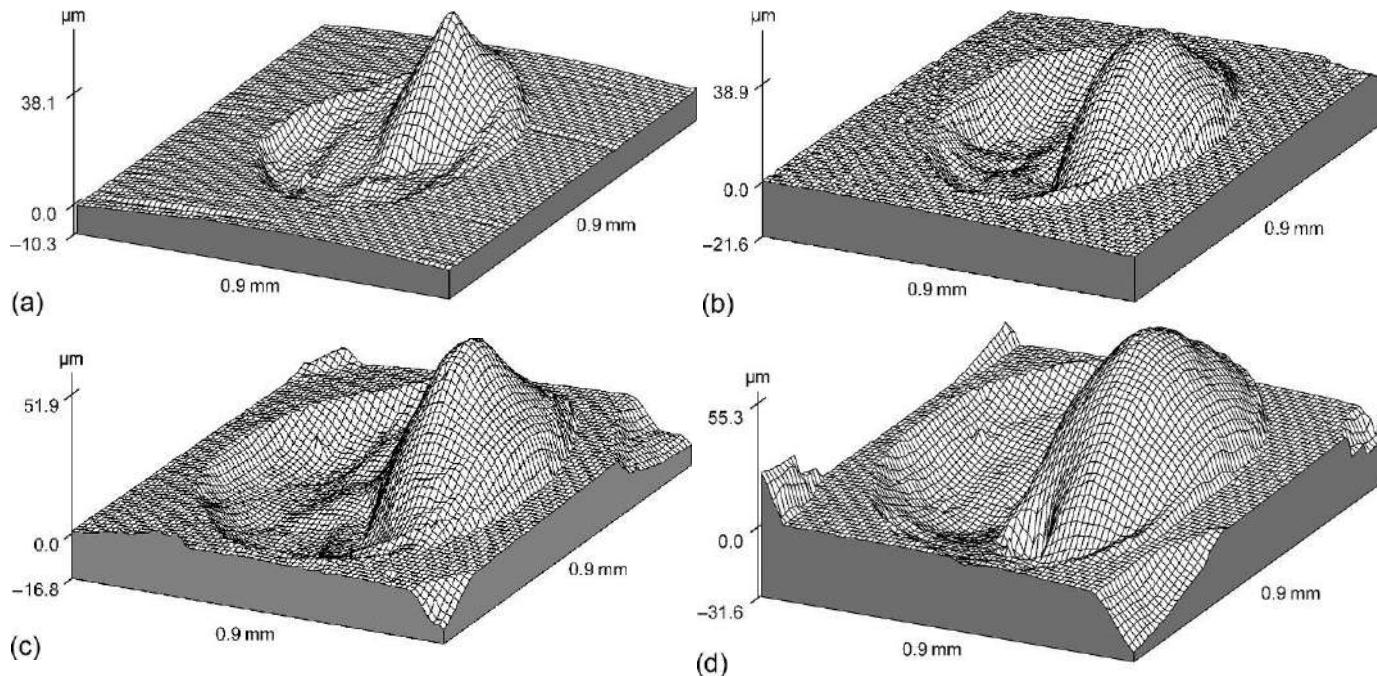


**Figure 19.7** 3-D surface profiles of the textured craters: (a) 150 A, 80  $\mu$ s; (b) 130 A, 100  $\mu$ s; (c) 190 A, 100  $\mu$ s; and (d) 150 A, 230  $\mu$ s.

textured surface. The parameters of a long-discharge pulse-width and a high discharge current peak may supply some textured craters with a larger diameter, high height and smooth shape to the convex rims adapted to produce a more highly roughened, textured surface ([Table 19.1](#)).

### 19.3.2 Microstructures of the textured craters

The microstructures of the textured craters decide the useful life of the textured surface. The optical microscope photograph of a cross section of a textured crater with the current peak of 150 A and pulse-width of 230  $\mu$ s is shown in [Figure 19.8](#). As can be seen, the microstructures of the textured crater can be divided into two sections: the melted section near the surface and the solid-state phase transition section near the base material. The hardness of the microstructures of the textured crater is measured, starting with the highest convex peak of the textured crater and ending at the base material. The hardness of the two textured craters in [Figure 19.9](#) is from 850 to

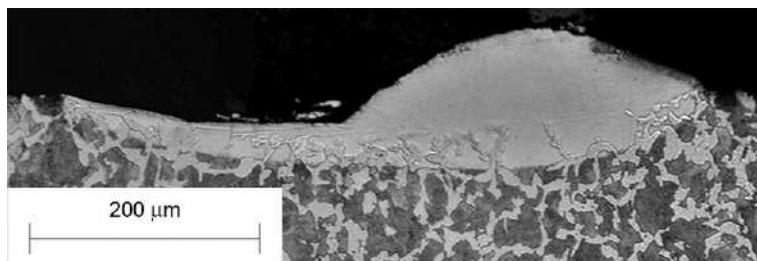


**Figure 19.8** Optical microscope photo of a cross section of a textured crater with a discharge current of 150 A and a pulse-width of 230  $\mu$ s.

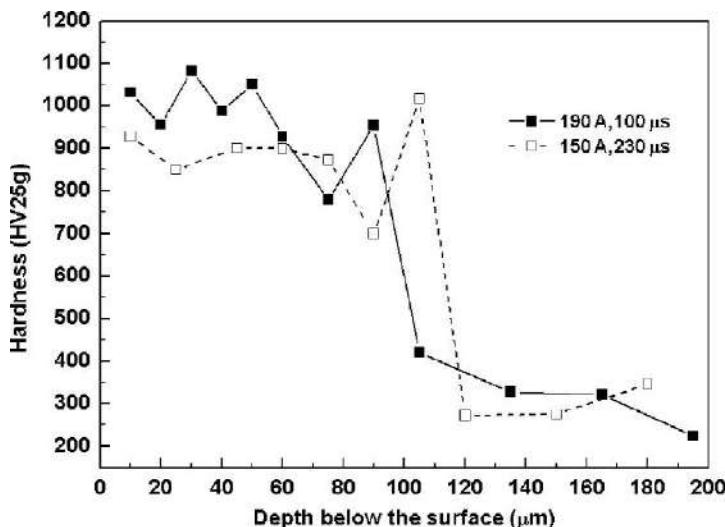


**Figure 19.9** Hardness of the textured craters.

1100 Vickers hardness, about three times that of the base material. The hardness of the textured craters with high-discharge current and the short-discharge pulse-width is higher than that with low-discharge current and the long-discharge pulse-width.

## 19.4 Comparison with Nd:YAG laser-textured surfacing (YAGLT) and electrical discharge surfacing (EDT)

The convex rims of Nd:YAG laser-textured craters are ringy and separated, with a height of about 10 µm (Figure 19.10). But on the textured surface by EDT [19] there are many burrs not clearly distinguishable in the textured craters. The height of the burrs ranges from 11.5 to 34 µm. It can be stated that the textured craters produced by LGDT have the combined advantages of using YAGLT and EDT, and have the separated deterministic distribution as produced by YAGLT, the height as produced by EDT, and the smoother and more regular shape of the convex rim than produced by EDT. In Table 19.2, the characters of three kinds of texturing techniques are collected together.

## 19.5 Conclusions

In the method of LGDT, the pulsed laser is focused on the roller surface to produce the metal plasma, and is then used to guide the arc discharge in the electrode gap to texture the roller surface. LDGT absorbs the advantages of EDT and YAGLT in order to (1) utilize the highly modulated frequency of a quasi-continuous Nd:YAG laser to supply the high processing speed and the large arc discharge energy to produce high surface roughness on the roller, and (2) control the randomization of the arc discharge, by laser

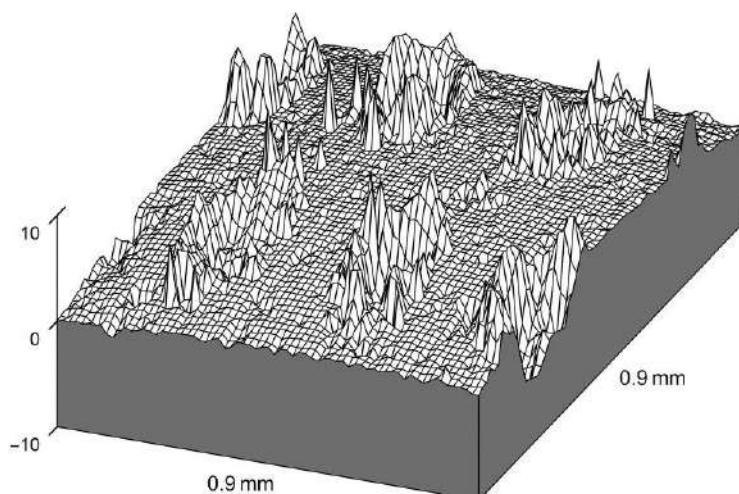


Figure 19.10 3-D profiles of YAG laser-textured crater.

**Table 19.2 Characters of three kinds of surface texturing methods**

Texturing method	Heat source	Texturing condition	Texturing speed	Design of roughness	Ra and homogeneity
LGDT	Laser-guided discharge	In air, surface oiled	40-60 m	Two-dimension	$R_a = 3.0\text{--}14.0 \mu\text{m}$
YAG LT	Laser	In air	2 h	Two-dimension	$R_a = 0.8\text{--}4.0 \mu\text{m}$ $\Delta R_a \leq 0.15\text{--}0.2 \mu\text{m}$
EDT	Electrical discharge	In oil	40-100 m	Arbitrary dimension	$R_a = 1.5\text{--}5.0 \mu\text{m}$ $\Delta R_a \leq 0.4 \mu\text{m}$

guiding to design the distribution and the surface profiles of the textured craters as well as enhancing the arc pressure to shape the surface of the textured craters. In general, LGDT tends to produce high surface roughness on the surface of the cold mill roller. This technique may be applied in the other surface shaping processing methods.

## References

- [1] W.J. Davies, Roll etching of cold mill workrolls, *Iron Steelmaker* 11 (1984) 37–41.
- [2] D.K. Aspinwall, F.L. Zhao, M.F. El-Menshawy, Electrodischarge texturing (EDT) of steel rolls, *Surf. Topogr.* 2 (1989) 123–141.
- [3] B. Snaith, S.D. Probert, R. Pearce, Characterization of laser-textured cold-rolled steel sheets, *Wear* 109 (1985) 87–97.
- [4] Y. Mingjiang, Technology and application of YAG laser texturing cold-roll, in: G. Zhenzhong (Ed.), *Manual of Laser Processing*, Metrology Publishing House, Beijing, China, 1998, pp. 338–346.
- [5] J. Dolves, Electron beam texturing of rolls, *Iron Steel Engineer* 68 (1991) 33–38.
- [6] M. Karl, M. Greg, B. Thomas, H. Manfred, TOPOCROM®—a superior method to texture work rolls, *Mater. Sci. Technol.* 1 (2004) 553–567.
- [7] V.N. Gusalov, K.I. Kozlovskii, A.S. Tsybin, An investigation of processes in a laser air spark gap, *Radiophys. Quantum Electron.* 27 (1984) 346–350.
- [8] R.A. Dougal, P.F. Williams, Fundamental processes in laser-triggered electrical breakdown of gases, *J. Phys. D Appl. Phys.* 17 (1984) 903–918.
- [9] D.W. Koopman, K.A. Saum, Formation and guiding of high-velocity electrical streamers by laser-induced ionization, *J. Appl. Phys.* 44 (1973) 5328–5336.
- [10] M. Miki, A. Wada, Guiding of electrical discharges under atmospheric air by ultraviolet laser-produced plasma channel, *J. Appl. Phys.* 80 (1996) 3208–3214.
- [11] F. Pinnekamp, G. Himmel, K. Bergstedt, Triggering of a spark gap with a low-power laser, *Opt. Commun.* 11 (1974) 225–226.
- [12] J.R. Woodworth, C.A. Frost, T.A. Green, UV laser triggering of high-voltage gas switches, *J. Appl. Phys.* 53 (1982) 4734–4739.
- [13] M. Miki, T. Shindo, Y. Aihara, Mechanisms of guiding ability of CO<sub>2</sub> laser-produced plasmas on pulsed discharges, *J. Phys. D Appl. Phys.* 29 (1996) 1984–1996.

- [14] T. Shindo, Y. Aihara, M. Miki, S. Toshio, Model experiments of laser-triggered lightning, *IEEE Trans. Power Delivery* 8 (1993) 311–317.
- [15] R.M. Gilgenbach, O.E. Ulrich, L.D. Horton, Localized metallic melting and hole boring by laser guided discharges, *Rev. Sci. Instrum.* 54 (1983) 109–113.
- [16] Y. Hoshi, H. Yoshida, Application of laser-guided discharge to processing, *Appl. Phys. A* 68 (1999) 93–98.
- [17] W. Zhitong, Y. Mingjiang, Laser guiding in the randomicity of discrete surface strengthening by arc discharge, *IEEE Trans. Plasma Sci.* 38 (2010) 943–947.
- [18] G. Bekefi, *Principles of Laser Plasmas*, Wiley-Interscience, New York, 1976.
- [19] J. Simäo, D. Aspinwall, F. El-Menshawy, K. Meadows, Surface alloying using PM composite electrode materials when electrical discharge hardened AISI D2, *J. Mater. Process. Technol.* 127 (2002) 211–216.

This page intentionally left blank

# Laser surface treatment to improve the surface corrosion properties of nickel-aluminum bronze

20

R. Cottam<sup>1,2</sup>, M. Brandt<sup>2,3</sup>

<sup>1</sup>Swinburne University of Technology, Melbourne, VIC, Australia; <sup>2</sup>Defence Materials Technology Centre, Melbourne, VIC, Australia; <sup>3</sup>RMIT University, Melbourne, VIC, Australia

## 20.1 Introduction

Nickel-aluminum bronze (NAB) is a copper-based alloy that has additions of between 9 and 12 wt.% Al, and up to 5 wt.% of Fe and Ni, depending on the application. This class of alloys have an excellent combination of strength and corrosion resistance and, as such, have found extensive maritime applications such as ship propellers and valves that handle sea water. While their corrosion behavior is good for the level of strength, there has nevertheless been ongoing research to improve it via several surface engineering methods. This has included laser cladding [1], friction stir processing [2–4], laser surface alloying [5], and laser surface melting [6]. While all of these treatment techniques have shown an improvement in mainly the cavitation corrosion behavior, the stagnant sea water corrosion resistance has suffered. This can be attributed to the formation of the Widmanstatten morphology of the microstructure due to the processing. It is also known that the  $\kappa_{\text{III}}$  phase present in the as-cast NAB microstructure promotes selective phase corrosion and is responsible for a deterioration in its stagnant sea water corrosion properties [7].

The above-mentioned surface treatments generally involve a phase change and the formation of the detrimental Widmanstatten morphology. Another approach that offers greater potential for improving the NAB's corrosion properties because of its composition and microstructure is the solid-state heat treatment. Our results show that solid-state heat treatment using a laser can be effective in producing a microstructure that is free from the Widmanstatten morphology, and free from the  $\kappa_{\text{III}}$  and, as such, shows an improvement in not only the cavitation corrosion behavior but also electrochemical corrosion behavior, which is linked to the behavior of the alloy in stagnate sea water. This chapter details the development of the solid-state approach, laser-processing parameters used, characterization of the processed NAB surface, and its subsequent corrosion performance.

## 20.2 Solid-state laser treatment and development of laser-processing parameters

As the phase diagram shown in Figure 20.1, NAB alloys that have between 9% and 12% aluminum at elevated temperatures form two phases,  $\alpha$  and  $\beta$ . The  $\alpha$  phase is an fcc phase and the  $\beta$  is a bcc phase. Then, upon slow cooling the  $\beta$  phase transforms to  $\alpha + \kappa_{\text{III}}$ . This reaction is the eutectoid reaction of NAB where the  $\kappa_{\text{III}}$  forms a lamella structure. At high cooling rates, this reaction does not take place and martensite or the Widmanstatten morphology microstructure forms. The eutectoid reaction can also take place in reverse and, as such, the  $\kappa_{\text{III}}$  precipitate is dissolved and the  $\beta$  phase forms. Therefore, with the right processing parameters it is possible to dissolve the  $\kappa_{\text{III}}$  phase and cool at a rate that the Widmanstatten morphology microstructure does not form and the  $\kappa_{\text{III}}$  is not precipitated. In this case, both elements of the NAB microstructure that are responsible for the poor corrosion performance can be eliminated with the right heating and cooling conditions. The reverse eutectoid reaction is diffusion dependant and the nature of the reaction is analogous to the perlite austenitization reaction in low-carbon steels [8]. Therefore, a two-phase diffusion model was employed to determine the kinetics of the reaction. This is detailed in the next section.

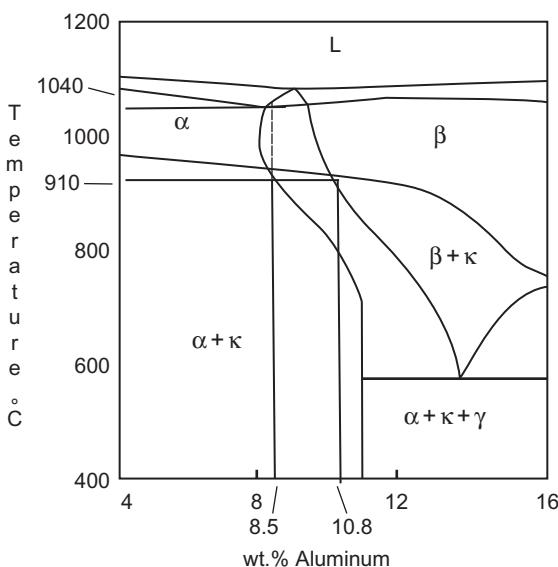


**Figure 20.1** NAB phase diagram for increasing aluminum content, where the iron and nickel contents are 5 wt.-%.

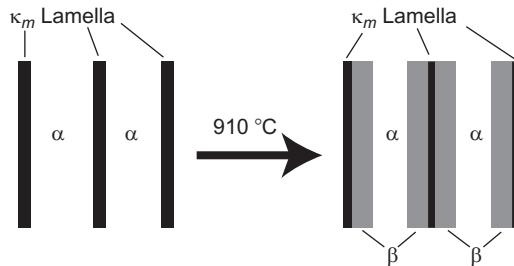


**Figure 20.2** The reverse reaction for the NAB eutectoid reaction.

### 20.2.1 Modeling of the reverse eutectoid reaction

During a reverse eutectoid reaction, the alloying elements that are precipitated, which for NAB are aluminum and nickel, are dissolved and their diffusion away from its precipitate form coincides with the growth of the new phase, which for NAB is the  $\beta$  phase, as shown by the schematic in Figure 20.2.

The kinetics of the reaction is governed by the diffusivity of aluminum in copper and the movement of the  $\alpha/\beta$  interface, which is given by the difference in composition between the  $\alpha$  and  $\beta$  phases at the interface, also known as the partition coefficient. The calculation of this rate allows a dwell time to be calculated for laser-processing parameter of laser-traversing speed, which eliminates the need for a trial and error determination of laser-processing parameters.

The two-phase diffusion problem involves solving its partial differential equations as shown in Equations (20.1)–(20.2):

$$\frac{\partial c}{\partial t} = \frac{1}{x^m} \frac{\partial}{\partial x} \left[ x^m D_\alpha(c) \frac{\partial c}{\partial x} \right] \quad (20.1)$$

$$\frac{\partial c}{\partial t} = \frac{1}{x^m} \frac{\partial}{\partial x} \left[ x^m D_\beta(c) \frac{\partial c}{\partial x} \right] \quad (20.2)$$

where  $c$  is the concentration of the diffusing element (wt.%),  $x$  is the position in meters,  $D$  is the diffusivity in meter square per second,  $t$  is the time in seconds, and  $m=0$  for planar geometry,  $m=1$  for cylindrical geometry, and  $m=2$  for spherical geometry. The interface mass balance and its velocity is given by Equation (20.3):

$$(c_{\alpha\beta} - c_{\beta\alpha}) \frac{\partial y}{\partial t} = D_\beta \left( \frac{\partial c}{\partial x} \right) - D_\alpha \left( \frac{\partial c}{\partial x} \right) \quad (20.3)$$

where  $\frac{\partial y}{\partial t}$  is the interface velocity in meter per second,  $c_{\alpha\beta}$  is the  $\alpha$ -phase side of the partition concentration, and  $c_{\beta\alpha}$  is the  $\beta$ -phase side of the partition concentration. There are several methods to solve the two-phase diffusion problem including the

finite element method [9], the finite volume method [10], and the finite difference method [8]. In this work, the finite difference scheme of Karlsson and Larsson [11] was employed to solve the diffusion equations, due to its relative simplicity to implement.

The boundary conditions used were as follows. The concentration of the  $\alpha$ -phase initially was 7.2 wt.% Al and was taken from the microprobe analysis of Hasan *et al.* [12]. The concentration of the  $\beta$ -phase was 50% because the  $\kappa_{\text{III}}$  precipitate is equal parts nickel and aluminum. The partition concentrations used were 8.5 wt.% Al for  $c_{\alpha\beta}$  and 10.8 wt.% Al for  $c_{\beta\alpha}$ , Figure 20.1. The spacing of the  $\kappa_{\text{III}}$  lamellae in the  $\alpha$ -matrix was taken from a scanning electron microscope (SEM) image of the alloy used in the investigation, Figure 20.2. The  $\kappa_{\text{III}}$  thickness was taken as 0.75  $\mu\text{m}$  and the spacing between them as 1.25  $\mu\text{m}$  for the larger spaced lamellae, which would take longer to transform.

The results of the calculation are shown in the reverse time-temperature-transformation diagram of Figure 20.3. The kinetics of the transformation of the boundary condition used in the model ranges from 0.2 to 0.75 s. The diffusion of aluminum in copper is quite fast; even though it is a substitution-based process (as opposed to an interstitial process) the diffusion rates at temperature are comparable with carbon in iron.

### 20.2.2 Modeling of the laser heating of NAB

The objective of modeling the heating behavior of NAB is to develop a relationship between the three main processing parameters of laser heating, namely, spot size,

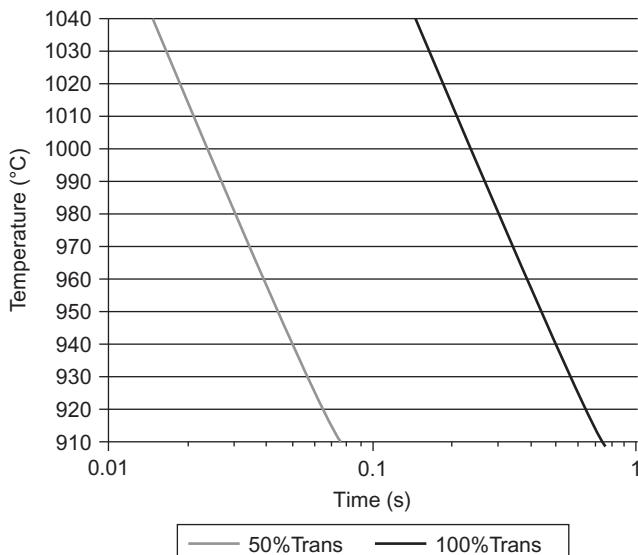


**Figure 20.3** Reverse time-temperature-transformation diagram for as-cast NAB for the  $\alpha + \kappa_{\text{III}} \rightarrow \beta$  reaction.

traversing speed, and power. Using the analytical heating model of Komanduri and Hou [13], the relationship between these variables was determined with NAB as the substrate material. The model and its associated equations are as follows:

$$T_{(x, y, z)} = \frac{AQv}{4\lambda a\pi^2/2r_L^2} \int \int_{r_i=0, w=0}^{r_i=r_L, w=v^2 t/4a} e^{-XV} Br_i \frac{1}{w^{3/2}} e^{(-w-u/4w)} I_0 dw dr_i \quad (20.4)$$

where  $T$  is the temperature rise at any position,  $x, y, z$ , in degree Celsius under the laser beam;  $A$  is a constant given in [Table 20.1](#), depending on the laser beam profile;  $Q$  is the absorbed laser power in Watts;  $\lambda$  is thermal conductivity in  $\text{W m}^{-1}\text{°C}^{-1}$ ;  $a$  is the thermal diffusivity of the medium in meter square per second;  $r_L$  is the radius of the laser in meters;  $r_i$  is the radius of that integration segment in meters;  $B$  is a mathematical function that is determined by the laser beam profile given in [Table 20.1](#);  $v$  is the laser traversing speed in meter per second; and  $t$  is the time the laser is on for in seconds.

[Equations \(20.5\)–\(20.7\)](#) are used to define the other variables:

$$u = \frac{Rv}{2a} \quad (20.5)$$

$$R = \sqrt{r_i^2 + X_0^2 + y^2 + z^2} \quad (20.6)$$

$$X_0 = x - vt \quad (20.7)$$

$(x, y, z)$  are any position relative to the starting position in meters.  $I_0$  is calculated from a function that has been defined mathematically in Ref. [14] and  $V=v/2a$ .

This heating model was programmed in MATLAB and was used to construct the theoretical processing map in [Figure 20.5](#). Using a melting point of  $1040\text{ °C}$ , a thermal diffusivity of  $1.32 \times 10^{-5}\text{ m}^2\text{ s}^{-1}$ , and a thermal conductivity of  $37.7\text{ W m}^{-1}\text{ °C}^{-1}$ , the laser power and traversing speed were varied to determine conditions where the above-mentioned parameters produced a temperature of  $1040\text{ °C}$  (a locus of points). Repeating this analysis for several laser spot sizes, a theoretical solid-state processing map was produced in [Figure 20.4](#). For each laser beam radius, the area above the line represents too much power and, consequently, surface melting, while the area below represents not enough heat and, consequently, a nonoptimized process.

**Table 20.1 Coefficients for beam profile used in analytical heating model, Equation (20.1)**

Distribution	A	B
Normal	9	$e^{-(3r_i/r_L)^2}$
Bimodal	4.3677	$e^{-(3.947(r_i/r_L)-0.947)^2} + e^{-(3.947(r_i/r_L)-0.947)^2}$
Uniform	1	1

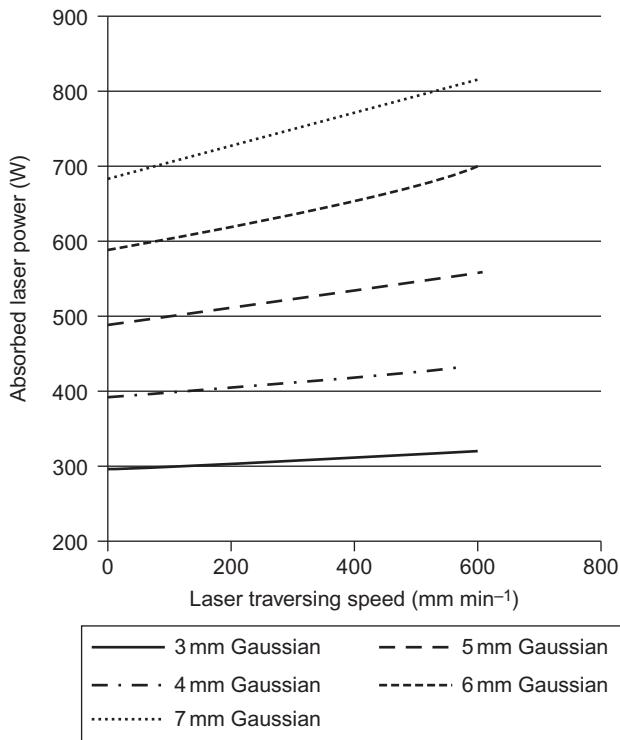


**Figure 20.4** Laser heating processing map for NAB for different laser spot dimensions. The laser spot sizes are a radius dimension.

Due to the processing limitations of the equipment used to do the experiments, a laser spot size of 4 mm radius with a processing traversing speed of 6 mm min<sup>-1</sup> and 780 W of dialed power were used.

## 20.3 Experimental procedure

Laser processing of as-cast NAB with nominal composition Cu-8.5Al-5Ni-4.5Fe (wt.%) was carried out with a fiber coupled, 3.5 kW Laserline diode laser. The beam was delivered via a 1-mm diameter optic fiber terminated with a 200 mm collimating and focusing optic attached to a Motoman UP20 robot (see Figure 20.5a). A processing speed of 6 mm min<sup>-1</sup> with a power setting of 780 W (taken from the map in Figure 20.4) and a 4 mm radius spot size was used. To maintain the ambient temperature of the substrate, a water-cooled plate was placed under 6-mm thick NAB plate during processing. Initially, a single track was trialed and then multitrack experiments were conducted with a 2-mm intertrack spacing (see Figure 20.5b).

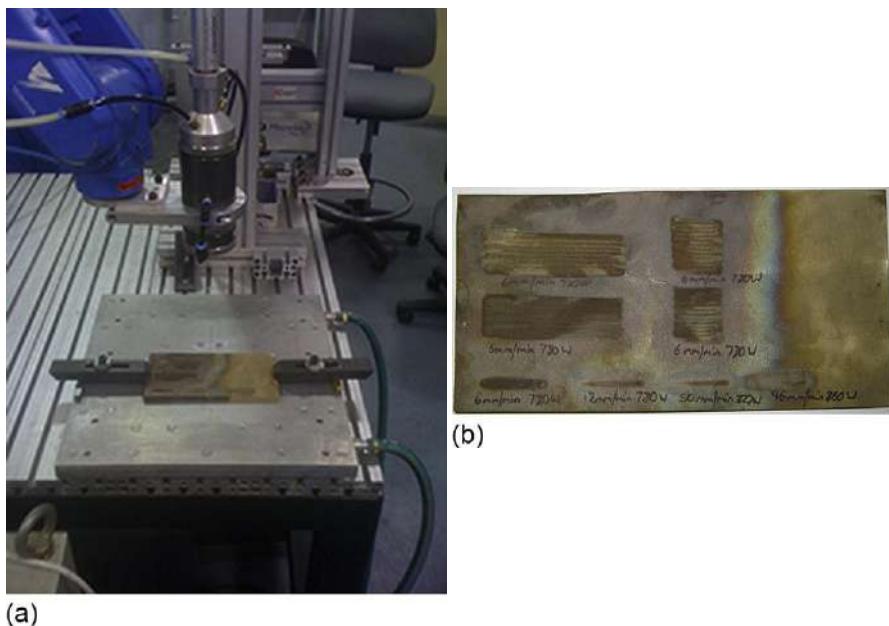
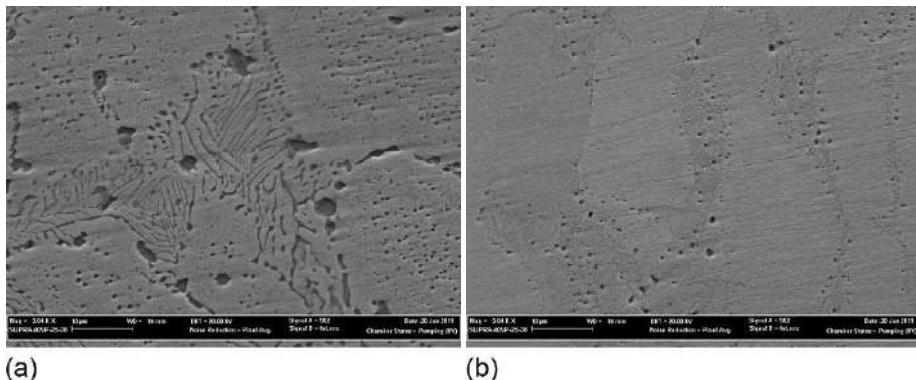


Figure 20.5 Picture of laser processing of NAB; (a) laser set up and (b) treated plate.

## 20.4 Characterization of laser-processed microstructure

Several techniques were employed to characterize the laser-processed layer. These included optical microscopy, SEM, neutron diffraction for residual stress measurements, and microhardness traverses. The SEM revealed that the results of the processing had achieved the goal; the  $\kappa_{\text{III}}$  phase of the as-cast NAB had been dissolved and the formation of a Widmanstatten microstructure had been avoided (see Figure 20.6). Figure 20.7 shows a macroshot of the treated area. The rough surface of the treated area is believed to be connected with the change in volume associated with dissolving the  $\kappa_{\text{III}}$  precipitate and is not due to local melting. To further understand the difference between a laser-melted and a laser-processed structure, microhardness traverses were conducted (see Figure 20.8). From this graph it is apparent that laser melting has a slightly harder microstructure than the laser-processed microstructure.

Residual stress analysis was also conducted on the laser-melted and laser-processed samples, and the results are shown in Figure 20.9. The residual stress analysis was conducted using neutron diffraction at the Australian Nuclear Science and Technology Organisation (ANSTO). From the results of the analysis, it is apparent that the tensile residual stress in the region of the laser-melted area is five times higher than the laser-processed sample at the same region. This can be attributed to a steeper thermal gradient in the laser-melted sample when compared with the processed sample. The



**Figure 20.6** Scanning electron microscopy micrographs of NAB in the (a) as-cast condition and (b) after laser heat treatment.

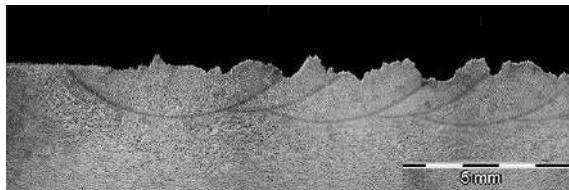


**Figure 20.7** Macrostructure of the laser-processed NAB showing the overlapping tracks.

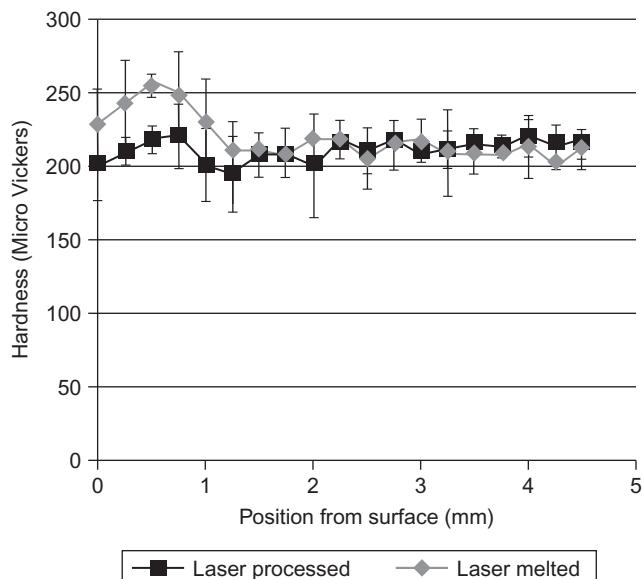


**Figure 20.8** Micro Vickers hardness traverses of NAB both laser melted and laser processed.

inflection of the laser-melted curve near the interface is as a result of the compressive stress exerted by the martensitic transformation during cooling of this zone.

XRD of the laser-treated samples shows that the phase of the as-cast, laser melted, and laser processed are all the same (see Figure 20.10). The shift in the peak position

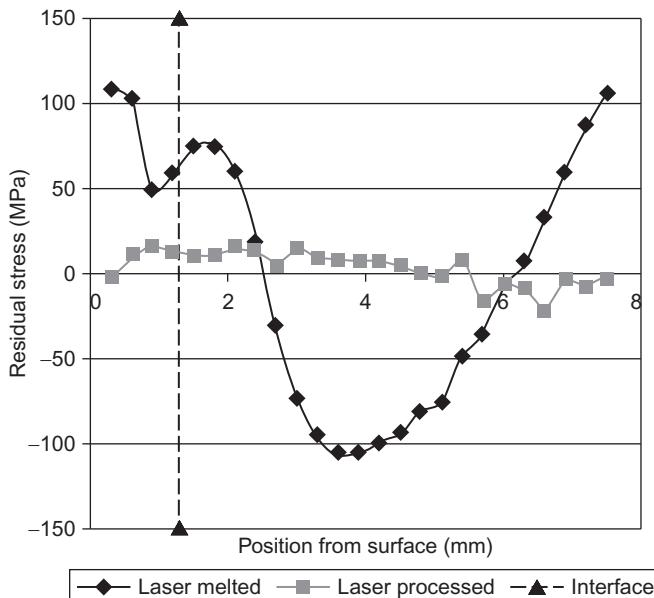


**Figure 20.9** Residual stress analysis of NAB in the laser-melted and laser-processed state using neutron diffraction.

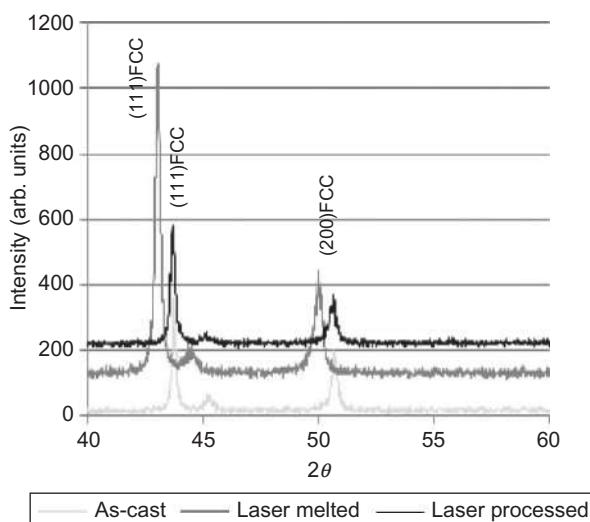


**Figure 20.10** XRD  $2\theta$  scan of NAB in the as-cast, laser-melted and laser-heated states.

for the laser-melted sample can be attributed to the Widmanstatten microstructure of this material. This graph supports the notion that the laser processing merely dissolves the  $\kappa_{\text{III}}$  precipitate in the solid state.

The characterization shows that the laser-processed NAB is different microstructurally to both the as-cast and laser-melted condition. Hence, this microstructure is new to the range of forms that NAB exhibits, which was the objective of the investigation.

## 20.5 Corrosion performance

The establishment of a new microstructure leads to an evaluation of its corrosion performance. For this investigation, this has included electrochemical corrosion performance, in the form of linear polarization and cavitation corrosion testing. These two tests give an indication of the performance of this new material in the stagnant and dynamic condition that most NAB parts experience in service.

### 20.5.1 Electrochemical corrosion

Three-electrode potentiostat testing was used to record polarization curves for laser-heated and as-cast NAB specimens immersed in a 3.5% NaCl solution. Samples were mounted in epoxy resin with an exposed area of  $1 \text{ cm}^2$  to the test solution. Prior to testing, the electrochemical cell was purged with air for several minutes. Upon termination of purging, a 30-min initial circuit delay was imposed to ensure a stable test environment. The potentiostat used was the Parstat 2273, which used the Powersuite software to control and monitor the cell. Polarization curves were recorded at a sweep rate of 0.166 mV/s. The results of the testing are shown in [Figure 20.11](#).

It is apparent from this graph that the corrosion current of the laser-processed sample is lower than that of the as-cast substrate but the potential is higher for its maximum corrosion current density. This is evidence that the stagnant sea water corrosion behavior of the laser-heated sample is superior. The origins of this improvement lie in the change in the microstructure brought about by the laser processing. Essentially, the laser processing dissolved the  $\kappa_{\text{III}}$  precipitate and more evenly redistributed the nickel and aluminum that the precipitate is composed of. Therefore, the aluminum is more evenly distributed throughout the microstructure, which in turn promotes the formation of  $\text{Al}_2\text{O}_3$  oxide, which is 11 times more stable than the  $\text{Cu}_2\text{O}$  oxide. The aluminum oxide film forms a highly impermeable layer that resists the transportation of cuprous ions, hence reducing the corrosion rate [7].

### 20.5.2 Cavitation erosion tests

Cavitation erosion testing was performed using an ultrasonic horn (Sonic VCX) with a replaceable tip made from Ti-6Al-4V. Testing was conducted in 3.5% NaCl solution, with the specimen held at a depth of 10 mm. The horn was operated at a frequency of 20 kHz and amplitude 50  $\mu\text{m}$ , and the horn tip was 1 mm above the specimen. The

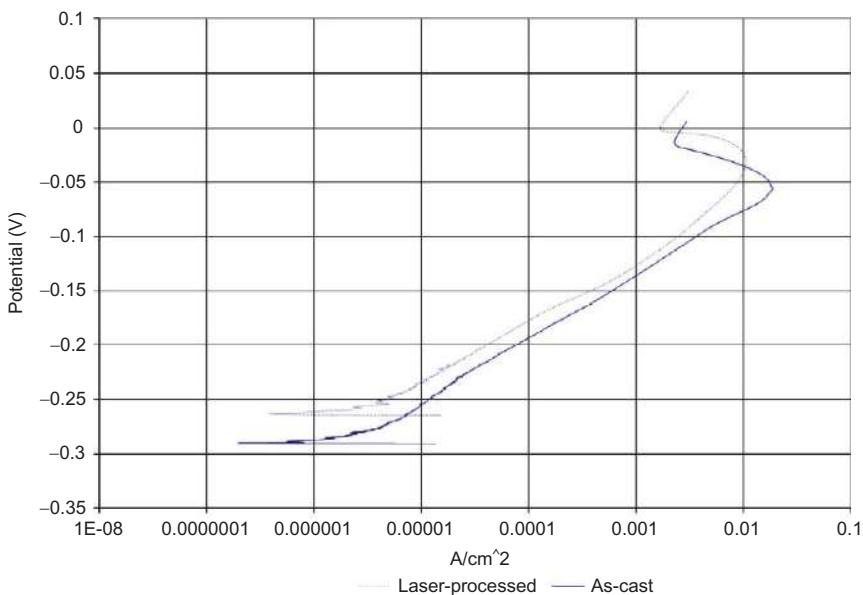


**Figure 20.11** Linear polarization curves for as-cast substrate and laser-heated NAB.

temperature was controlled using a coil to  $25 \pm 2$  °C. Disc-shaped specimens (12.8 mm diameter) were machined from NAB coupons. These were polished to 1200 grit with SiC paper prior to testing. Each specimen was cleaned with ethanol, dried, and weighed before and after testing. The duration of each test was 6 h, and weight loss was measured by interrupting testing at regular intervals (1, 3 and 6 h). The results of the testing are shown in Figure 20.12.

It is apparent from these results that both laser-melted and laser-processed samples are far superior to the as-cast and extruded materials. This shows that the laser-processed material is not only superior in stagnant sea water but it also performs well when exposed to cavitation. The fact that laser processed behavior is similar to laser melted is of interest. Reference to the hardness of laser melted versus laser processed (see Figure 20.7) shows that the melted sample is harder and, given that hardness and cavitation erosion resistance scale [15], it would be expected that the performance of the laser-melted sample would be significantly superior. The reason that this is not the case can be explained by the difference in the residual stress. The laser-melted sample has a tensile residual stress level of 100 MPa (see Figure 20.8), which reduces the strength of the material and evens up the difference in the strength between the two materials.

## 20.6 Conclusion

A new approach to improve the corrosion resistance of NAB at the surface by laser processing has been developed. The technique produced a new type of microstructure for NAB, which has been developed by heating the surface with a laser near to

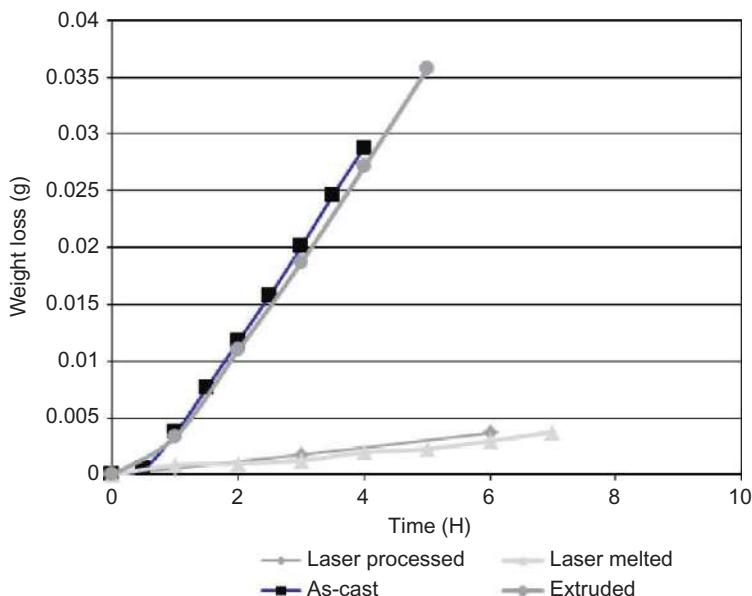


**Figure 20.12** Cavitation erosion testing result for NAB in the laser-processed, as-cast, extruded, and laser-melted conditions.

its melting point for a long enough period to dissolve the  $\kappa_{\text{III}}$  phase in the solid state and cooled at a rate where the Widmanstatten morphology microstructure is avoided. The processing parameters required to do this were developed with the aid of mathematical modeling of both the reverse phase transformation and laser heating. The resulting microstructure exhibited a low residual stress, no significant increase in hardness, and a crystal structure the same as the cast material. The corrosion performance of the new microstructure showed improved electrochemical performance and cavitation erosion performance when compared with as-cast NAB, thus proving the value of this new processing technique for extending the life of NAB components.

## Acknowledgments

This work has been conducted by funding from the Defence Materials Technology Centre, Program 2, Project 2.2 “Surface Processing Technologies for Repair and Improved Performance of Submarine and Surface Ship Components.” The authors would like to acknowledge Brian Dempster for conducting the laser-processing experiments and the valuable help of Dr Lenore Pedrina of DSTO with corrosion testing. As well as for ANSTO and AINSE for providing neutron beam time through neutron proposal ID 2310 “Residual stress analysis of laser-treated nickel-aluminum bronze.”

## References

- [1] J.C. Bennett, C.V. Hyatt, Microstructural characterisation of laser-clad nickel aluminium bronze alloys by TEM, Defence Research Establishment Atlantic, 2007.
- [2] M.D. Fuller, S. Swaminathan, A.P. Zhilyaev, T.R. McNelley, Microstructural transformations and mechanical properties of cast NiAl bronze: effects of fusion welding and friction stir processing, Mater. Sci. Eng. A 463 (2007) 128–137.
- [3] D.R. Ni, P. Xue, D. Wang, B.L. Xiao, Z.Y. Ma, Inhomogeneous microstructure and mechanical properties of friction stir processed NiAl bronze, Mater. Sci. Eng. A 524 (2009) 119–128.
- [4] D.R. Ni, B.L. Xiao, Z.Y. Ma, Y.X. Qio, Y.G. Zheng, Corrosion properties of friction-stir processed cast NiAl bronze, Corros. Sci. 52 (2010) 1610–1617.
- [5] C.H. Tang, F.T. Cheng, H.C. Man, Laser surface alloying of a marine propeller bronze using aluminium powder. Part I: microstructural analysis and cavitation erosion study, Surf. Coat. Technol. 200 (2006) 2602–2609.
- [6] C.H. Tang, F.T. Cheng, H.C. Man, Improvement in cavitation erosion resistance of a copper-based propeller alloy by laser surface melting, Surf. Coat. Technol. 182 (2004) 300–307.
- [7] J.A. Wharton, R.C. Barik, G. Kear, R.J.K. Wood, K.R. Stokes, F.C. Walsh, The corrosion of nickel-aluminium bronze in sea water, Corros. Sci. 47 (2005) 3336–3367.
- [8] T. Akbay, R.C. Reed, C. Atkinson, Modelling reaustenitisation from ferrite/cementite mixtures in Fe-C steels, Acta Metall. Mater. 47 (1994) 1469–1480.
- [9] A. Jacot, M. Rappaz, R.C. Reed, Modeling of reaustenitization from the pearlite structure in steel, Acta Mater. 46 (1998) 3949–3962.
- [10] A. Jacot, M. Rappaz, A two-dimensional diffusion model for the prediction of phase transformations: application to austenitization and homogenization of hypoeutectoid Fe-C steels, Acta Mater. 45 (1997) 575–585.
- [11] B. Karlsson, L.E. Larsson, Homogenization by two-phase diffusion, Mater. Sci. Eng. 20 (1975) 161–170.
- [12] F. Hasan, A. Jahanafrooz, G.W. Lorimer, N. Ridley, The morphology, crystallography, and chemistry of phases in As-cast nickel-aluminium bronze, Metall. Trans. A 13A (1982) 1337–1345.
- [13] R. Komanduri, Z.B. Hou, Thermal analysis of laser surface transformation hardening—optimisation of process parameters, Int. J. Mach. Tools Manuf. 44 (2004) 991–1008.
- [14] Z.B. Hou, R. Komanduri, Magnetic field assisted finishing of ceramics—Part I: thermal model, J. Tribol. 120 (1998) 645–651.
- [15] C.T. Kwok, H.C. Man, F.T. Cheng, Cavitation erosion and pitting corrosion behaviour of laser surface-melted martensitic stainless steel UNS S42000, Surf. Coat. Technol. 126 (2000) 238–255.

This page intentionally left blank

# Laser surface engineering of titanium and its alloys for improved wear, corrosion and high-temperature oxidation resistance

21

J. Dutta Majumdar, I. Manna  
Indian Institute of Technology, Kharagpur, India

## 21.1 Introduction

Titanium-based alloys (especially titanium-based intermetallic phases and compounds) are known to possess very high specific strength and positive temperature coefficient of strength at elevated temperatures. However, titanium is known to suffer substantial scale or oxidation loss during prolonged exposure to high temperatures in oxidising atmosphere. The poor high-temperature oxidation resistance of titanium and its alloys may be attributed to the high solubility and diffusivity of oxygen in titanium and fast counter ionic mobility of  $\text{Ti}^{4+}$  and  $\text{O}^{2-}$  through the oxide scale above 823 K. Furthermore, the oxide scale turns porous and loses adherence with the surface at elevated temperatures due to considerable differences in specific volume and coefficients of thermal expansion between the concerned regions. Similarly, wear/erosion is a serious impediment against universal application of titanium in components subjected to a high rate of friction/wear and relative motion. Wear or progressive loss of material from the surface due to friction and contact-fatigue/impact is essentially a surface-related phenomenon. Oxidation is a similar progressive degradation of the component surface due to the formation of a more thermodynamically stable chemical state dictated by the prevailing environmental condition.

The extent and rate of oxidation and wear are mainly dependent on microstructure and/or composition of the surfaces concerned. Therefore, resistance to oxidation and wear may be imparted or improved primarily by suitable modification of the microstructure and/or composition of the near-surface region. Application of surface coatings by diffusion bonding, pack cementation, and so on, have been the conventional practices for ages; however, they are often time-consuming, not environmentally friendly, and necessitate a complex heat treatment schedule. The directed energy beams (ion, electron, and laser) assisted surface engineering offer excellent scope of tailoring the surface properties and have proved superior to conventional treatment. However, ion beam processing is suitable for a very shallow depth surface engineering and electron beam-assisted surface engineering is ideal for deeper penetration of

surface processing. In terms of the process economy, flexibility, and ease of operation, laser surface engineering is more appropriate for surface treatment of metallic substrates, especially for the development of an exotic range of composition and/or microstructural changes. Laser surface engineering is of great significance in modifying the surface region of reactive metals like titanium. Laser surface engineering may be applied to melt the near-surface region of titanium-based components for the refinement of microstructure. Laser surface melting may be used to change the microstructure and composition for improvement of properties by surface alloying, and is termed laser surface alloying. Because the melted/alloyed zone is confined to a very shallow depth from the surface, the process may safely be applied to finished/semitinished components with a great deal of economy in materials, time, and energy. In the present contribution, detailed studies on the application of laser surface melting and alloying of titanium and its alloys on the characteristics of the surface and its properties are discussed in detail.

## 21.2 Titanium and its alloys

Titanium is abundantly (0.6%) available in the universe, especially on earth and also was detected in meteorites, on the moon, and other stars [1,2]. The important physical properties of titanium are summarized in Table 21.1 [3]. Due to its interesting properties of high strength to weight ratio, good corrosion resistance, and reasonably good toughness, titanium and its alloys find a wide-ranging engineering application in aerospace, marine, and biomedical sectors [1]. The Titanium Metals Company of America (TMCA) produced the first commercial products in 1950 [1,4]. Since then, the production of titanium and its alloys has grown at an average annual rate of about 8%. Over the past 50 years, titanium and its alloys have proven to be technically superior and cost-effective materials for structures in aerospace, marine, and other industrial applications [1]. A few titanium-based alloys developed over this period are summarized in Table 21.2 [5,6]. The important properties, applications, and the surface engineering of titanium and its alloys are discussed in the following section.

The properties and characteristics of titanium that are important to design engineers are listed below [4]:

- Superior strength to weight ratio*—The densities of current commercial titanium-based alloys range between 4420 and 4850 kg/m<sup>3</sup>. Yield strengths range from 172 MPa for commercially pure (CP) Grade 1 to above 1380 MPa for heat-treated beta alloys. The combination of

**Table 21.1 Physical properties of titanium [3]**

Name of element	Atomic symbol	Atomic number	Atomic weight	Density (g/cm <sup>3</sup> )	Boiling point (°C)	Melting point (°C)
Titanium	Ti	22	47.90	4.5	3130	1812

**Table 21.2 Working temperature of a few commercially available titanium alloys [5,6]**

Sl. no.	Alloy	Composition (wt.%)	Introduction year	Maximum working temperature
1	Ti64	6Al, 4V	1954	300
2	IMI-550	4Al, 2Sn, 4Mo, 0.5Si	1956	425
3	Ti-811	8Al, 1Mo, 1V	1961	400
4	IMI-679	2Al, 11Sn, 5Zr, 1Mo, 0.2Si	1961	450
5	Ti-6246	6Al, 2Sn, 4Zr, 6Mo	1966	450
6	Ti-6242	6Al, 2Sn, 4Zr, 2Mo	1967	450
7	IMI-685	6Al, 2Zr, 0.5Mo, 0.25Si	1969	520
8	Ti-11	5Al, 2Sn, 1.5Zr, 1Mo, 0.1Si, 0.3Bi	1972	540
9	Ti-17	5Al, 2Sn, 2Zr, 4Mo, 4Cr	1973	350
10	Ti-6242S	6Al, 2Sn, 4Zr, 2Mo, 0.1Si	1974	520
11	IMI-829	5.5Al, 3.5Sn, 3Zr, 0.3Mo, 1Nb, 0.3Si	1976	580
12	IMI-834	5.5Al, 4Sn, 4Zr, 0.3Mo, 1Nb, 0.5Si, 0.06C	1984	590

high strength and low density results in exceptionally favorable strength to weight ratios for titanium-based alloys.

2. *Excellent corrosion resistance*—Titanium is immune to corrosive attack by saltwater or marine atmospheres. It also exhibits exceptional resistance to a broad range of acids, alkaline, natural waters, and industrial chemicals.
3. *Superior erosion resistance*—Titanium offers superior resistance to erosion, cavitation, or impingement attack and is very much more erosion resistant than copper-nickel alloys, which were the most corrosion-resistant and erosion-resistant materials used in heat exchanger tubes prior to the introduction of titanium.
4. *High heat transfer efficiency*—In service conditions, the heat transfer properties of titanium approximate those of admiralty brass and copper-nickel.
5. *Superior room and low temperature oxidation resistance*—Titanium possesses a relatively superior room temperature oxidation resistance due to the presence of an inherent oxide film. The relative absence of corrosion in media where titanium is generally used leaves the surface bright.

## 21.3 Physical metallurgy of titanium and its alloys

To understand the microstructure of any alloy system, it is necessary to outline the phase relationships and constitution of the system being studied. Titanium can exist in two crystal forms [6]. The first one is alpha ( $\alpha$ ), which has a hexagonal close-packed crystal structure, and the second one is beta ( $\beta$ ), which has a body-centered cubic

**Table 21.3 Effects of alloying elements on microstructures of titanium alloys [6,7]**

Alloying element	Range (approx) (wt.%)	Effect on structure
Aluminum	2-7	Alpha stabilizer
Tin	2-6	Alpha stabilizer
Vanadium	2-20	Beta stabilizer
Molybdenum	2-20	Beta stabilizer
Chromium	2-12	Beta stabilizer
Copper	2-6	Beta stabilizer
Zirconium	2-8	Alpha and beta strengthener
Silicon	0.2-1	Improves creep resistance

structure. In unalloyed titanium, the alpha phase ( $\alpha$ ) is stable at all temperatures up to 1153 K, above which it transforms to beta ( $\beta$ ) phase. This temperature is known as the beta ( $\beta$ ) transition temperature. The beta ( $\beta$ ) phase is stable from 1153 K to the melting point. Alloying of titanium changes the temperature of the alpha to beta transformation, and also stabilizes either the alpha or beta phase, and thereby controls the amount of each phase in the alloy. Elements known as alpha stabilizers raise the beta transition temperature, while beta stabilizers lower the beta transition temperature. Table 21.3 summarizes the effect of a few commonly used alloying elements on microstructures [7].

## 21.4 Alloy classification

Depending on the microstructure of the alloy phase, there are three main structural types of titanium alloys. Different microstructures are achieved by adding different alloying elements, which stabilize the desired phase [6].

### 21.4.1 Alpha alloys

The alpha alloys possess the highest strength and oxidation resistance at elevated temperatures (588-811 K), and they possess the best weldability among the other titanium grades. However, they do not respond to heat treatment and they have lowest room temperature strength [6]. The most popular alpha alloy is Ti-5Al-2.5Sn and the extra low interstitial grade of the same composition. Under the alpha alloy classification, five alloys are classified as near alpha. Of these five grades, Ti-8Al-1Mo-1V is most commonly used. Special annealing cycles have been developed for this grade, which enhances its creep strength and fracture toughness while permitting it to maintain good strength levels. A few near-alpha alloys are: Ti-2.25Al-11Sn-5Zr-1Mo-0.2Si, Ti-5Al-6Sn-2Zr-1Mo-0.25Si, and Ti-6Al-2Sn-1.5Zr-1Mo-0.35Bi-0.15Si (Ti-11).

### **21.4.2 Alpha-beta alloys**

Alpha-beta alloys have higher strength and respond to heat treatment, but they are less formable than alpha alloys. Fusion weld efficiencies up to 100% are attainable. This class of titanium alloys account for more than 70% of all commercially available titanium alloys. A few important alpha-beta alloys include Ti-3Al-2.5V, Ti-5Al-2Sn-2Zr-4Mo-4Cr (Ti-17), Ti-6Al-2Sn-2Zr-2Mo-2Cr-0.25 Si, Ti-6Al-2Sn-4Zr-6Mo, and Ti-6Al-6V-2Sn.

### **21.4.3 Beta alloys**

The beta alloys are readily heat treatable, with increased hardenability compared with alpha or alpha-beta alloys. Though the room temperature strength of this alloy is high, its high temperature strength is poor. Excellent formability can be expected of the beta alloys in the solution-treated condition. Examples of a few commercially available beta alloys include Ti-3Al-8V-6Cr-4Mo-4Zr, Ti-4.5Sn-6Zr-11.5Mo, Ti-8Mo-8V-2Fe-3Al, and Ti-13V-11Cr-3Al.

## **21.5 Surface dependent engineering properties**

Prior to the application of surface engineering techniques for the improvement of surface properties, it is important to know the surface-dependent engineering properties in detail. The engineering properties dependent on surface microstructure and composition include surface appearance, color, fatigue, friction and wear, corrosion, oxidation, and catalysis. Among these varied physical and chemical surface-dependent properties, wear, erosion, corrosion, and oxidation are the common modes of mechanical and electrochemical failure experienced by engineering materials in real service conditions, and the probability of failure may be minimized by a suitable modification of surface microstructure and composition. In this section, common modes of surface-related failure will be briefly introduced and discussed.

### **21.5.1 Wear**

Wear can be defined as the progressive loss of material from the operating surface of a solid occurring as a result of relative motion between two surfaces [8]. Wear constitutes an important design consideration in applications likely to encounter friction and relative motion between the solid component and surrounding medium.

The various modes of wear include adhesion (e.g., scuffing, galling, welding, scoring, wiping, and smearing), abrasion, fatigue, erosion, and corrosion. However, most important among them are adhesive and abrasive wear.

### **21.5.2 Adhesive wear**

Adhesive wear [8] refers to a type of wear generated by sliding one solid surface along another surface. When two surfaces are loaded against each other, the whole of the contact load is carried only by the very small area of asperity contacts. The real contact pressure over the asperity is very high, leading to adhesion between them. If one of the surfaces slides against the other, the adhesive junction may break. As sliding continues, fresh junctions will form and rupture in succession. The probability of adhesive wear may be minimized by the application of lubricants or by the application of hard coating with a low coefficient of friction.

### **21.5.3 Abrasive wear**

Abrasive wear [8] is due to hard particles or protuberances that are forced against and move along a solid surface. Wear, in turn, is defined as damage to a solid surface that generally involves progressive loss of materials and is due to relative motion between the surface and a contacting substance. The rate at which the surfaces abrade depends on the characteristics of each surface, the presence of abrasives between the first and second surfaces, the speed of contact, and other environmental conditions. The abrasive wear resistance property may be improved by application of a hard coating with a hardness level 1-1.2 times that of the counterbody.

### **21.5.4 Erosion**

Erosion is the damage produced by the impingement of sharp particles on a solid surface causing progressive material loss [8]. Among the possible variables, the number, direction, and velocity of the particles striking the surface constitute an important consideration to determine the rate of erosion [8]. Erosion, in most cases, is accelerated by corrosion when the media is corrosive. Hence, erosion-resistance property may be improved by application of a hard coating along with improved corrosion resistance.

### **21.5.5 Corrosion**

Corrosion can be defined as the progressive loss of material in an aqueous environment in the presence of oxidizing or reducing species. The various forms of corrosive attacks are listed below [9]:

1. General (uniform) corrosion
2. Galvanic corrosion
3. Pitting corrosion
4. Crevice corrosion
5. Intergranular corrosion
6. Stress corrosion cracking
7. Erosion corrosion

The corrosion-resistance property of the surface may be improved by the application of noble material coating or sacrificial coating.

### 21.5.6 Oxidation

Oxidation may be defined as the failure of materials due to reaction with the oxidizing environment at room or high temperature in dry conditions [10]. The rate of formation of oxide on a metal surface is governed by the progress of the following reaction:  $2M + O_2 = 2MO$ . The rate of oxidation may be measured by measuring (a) the amount of metal consumed, (b) the amount of oxygen consumed, or (c) the amount of oxide produced. Surface alloying is an important route for improving high-temperature oxidation resistance of any metallic components. Usually, silicon, aluminum, or chromium are the alloying elements commonly applied for improving the high-temperature oxidation resistance property of metallic materials.

## 21.6 Surface engineering

Surface engineering aims at the modification of microstructure and/or composition of the near-surface region of a component to improve surface-dependent engineering properties. Conventionally, equilibrium or near-equilibrium processing (e.g., heat treatment, coating, painting) is applied for the modification of microstructure and/or composition of the surface of any component. Conventional surface engineering practices are diverse in methodology and scope of application. In general, surface engineering (both conventional and advanced) practices involve either microstructural modification or compositional changes or both. Figure 21.1 presents a general classification of surface engineering practices used in metallurgical industries. Surface engineering may broadly be classified into microstructural modification, where a suitable heat treatment is applied to modify microstructure. On the other hand, compositional modification involves changing the composition of the surface. Among all the compositional surface engineering processes mentioned above, metallic coating is one of the most economical and convenient treatments.

Before discussing the advantages and characteristics of laser surface engineering, a comparative study of all the above-mentioned processing techniques, including lasers, will be presented in the following section.

## 21.7 Laser surface engineering

Light amplification by stimulated emission of radiation or laser is a coherent, convergent, and monochromatic beam of electromagnetic radiation with a wavelength ranging from ultraviolet to infrared [11]. Laser can deliver very low ( $\sim mW$ ) to extremely high (1-100 kW) focused power with a precise spot size/dimension and interaction/pulse time ( $10^{-3}$  to  $10^{-15}$  s) onto any kind of substrate through any medium [12-15]. Table 21.4 summarizes the commercially available lasers and their main areas of application. The important properties that enable and justify the use of a laser in such a wide spectrum of applications are (a) spatial and temporal coherence (i.e., phase and amplitude are unique), (b) low divergence (parallel to the optical axis), (c) high continuous or

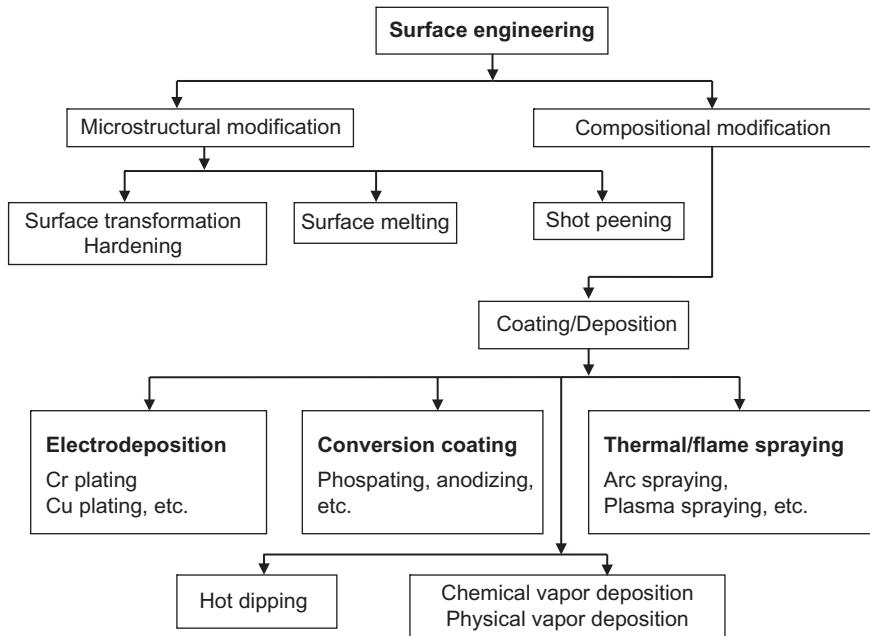


**Figure 21.1** General classification of surface engineering practices used in metallurgical industries [17].

**Table 21.4 Commercially available lasers and their industrial applications [16]**

Laser	Discovery	Commercialization	Wavelength (nm)	Application
Ruby	1960	1963	628	Metrology, medical applications, inorganic material processing
Nd-glass	1961	1968	1060	Length and velocity measurement
Diode	1962	1965	780-905	Semiconductor processing, biomedical applications, welding

**Table 21.4 Continued**

Laser	Discovery	Commercialization	Wavelength (nm)	Application
He-Ne	1962		1152	Light pointers, length/velocity measurement, alignment devices
Carbon dioxide	1964	1966	10,200	Material processing, cutting/joining, atomic fusion
Nd-YAG	1964	1966	1064	Material processing, joining, analytical technique
Argon ion	1964	1966	480-515	Powerful light, medical applications
Dye (sodium fluorescein)	1966	1969	535-600	Pollution detection, isotope separation
Copper	1966	1989	511	Isotope separation
Excimer	1975	1976	300-350	Medical application, material processing, coloring
Free electron laser	1971	1997	2000-10,000	Medical surgery, surface modification of polymer

pulsed power density, and (d) monochromaticity. Depending on the type of laser and wavelength desired, the laser medium could be solid, liquid, or gaseous. Different laser types are commonly named according to the state or the physical properties of the active medium. Consequently, there are glass or semiconductor, solid-state, liquid, and gas lasers. Gas can be further subdivided into neutral atom lasers, ion lasers, molecular lasers, and excimer lasers. The typical commercially available lasers are (a) solid state or glass laser—Nd:YAG, (b) semiconductor laser—AlGaAs, GaAsSb, and GaAlSb, (c) dye or liquid lasers—solutions of dyes in water/alcohol and other solvents, (d) neutral or atomic gas lasers—He-Ne, Cu or Au vapor, (e) ion lasers—argon ( $\text{Ar}^+$ ) and krypton ( $\text{Kr}^+$ ) ion, (f) molecular gas lasers— $\text{CO}_2$  or CO, and (g) excimer laser— $\text{XeCl}$ ,  $\text{KrF}$ . The wavelengths of the presently available lasers cover a wide spectral range from the far infrared to the soft X-ray.

A laser, as a source of intense heat, is capable of heating, melting, and evaporating materials from the surface [12–15]. The laser may be used to modify the microstructure and/or composition of the near-surface region and offers advantages in terms of economy, precision, flexibility, and novelty (thermodynamic and kinetic) of processing and improvement in the surface-dependent properties of interest [12–15]. The process is characterized by an extremely fast heating/cooling rate ( $10^4$ - $10^{11}$  K/s), high thermal gradient ( $10^6$ - $10^8$  K/m), and ultrarapid resolidification velocity (1-30 m/s) [16–18]. These extreme processing conditions often develop an exotic microstructure and composition in the near-surface region with large extension of solid solubility and formation of metastable including nanocrystalline and amorphous phases. The overall classification of laser surface engineering as applicable to metallic materials is shown in Figure 21.2 [16–18]. Figure 21.3 shows the fields of application of lasers in surface engineering according to the power density of the laser and interaction time for

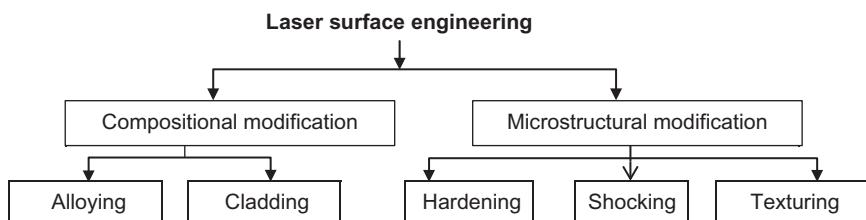


**Figure 21.2** General classification of laser surface engineering [17].

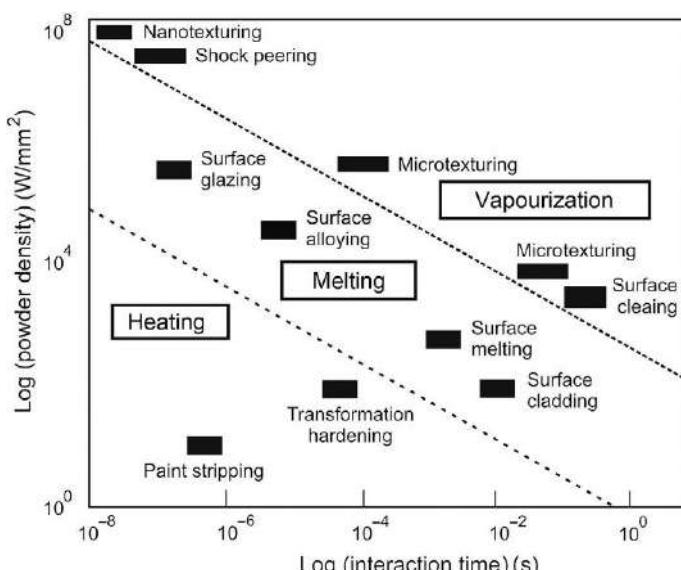


**Figure 21.3** Fields of application of lasers in surface engineering according to its energy density of laser and interaction time [17].

continuous wave (CW) laser treatment. [Figure 21.3](#) will serve as a guideline for the choice of appropriate laser parameters in terms of power density and interaction time for any surface engineering, as specified in [Figure 21.3](#). Laser surface engineering has certain specific and notable advantages over other methods [16–18], for example, (a) controlled quantum of directed energy delivery with precise spatial and temporal distribution, (b) extremely rapid processing with minimum heat-affected zone and distortion, (c) clean and nontoxic processing devoid of contamination, (d) economy in materials and energy consumption, (e) circumvention of thermodynamic and kinetic constraints faced during conventional surface engineering, and (f) the possibility of attaining novel microstructures and surface properties not achievable by conventional materials processing routes.

## 21.8 Laser surface engineering of titanium and its alloys

In the past, laser surface engineering was successfully applied on titanium and its alloys to improve its wear, corrosion, and high-temperature oxidation resistance properties [16–28]. Laser surface engineering was applied for microstructural modification, which was achieved by melting of the surface followed by rapid quenching (e.g., laser surface melting). On the other hand, microstructural and compositional modification of the surface was achieved by predeposition of the surface with alloying ingredients and its subsequent melting along with a part of the underlying substrate to cause surface alloying, resulting in partial or complete modification of the near-surface region of a component. In the following sections, examples of laser surface engineering of titanium and its alloys will be discussed.

### 21.8.1 *Laser surface melting of titanium and its alloys*

Laser surface melting involves heating the surface of the substrate to its melting point to cause it to melt and subsequent rapid solidification to refine the surface microstructure [16]. In the past, the process was applied on magnesium, magnesium-based alloys, and steel to improve their corrosion-resistance property by grain refinement and microstructural homogenization [16]. Studies on laser surface melting of Ti-6Al-4V were carried out in detail using a 2 kW CW diode laser with rectangular beam (3.5 mm × 2 mm area) using argon as shrouding gas to understand the effect of laser surface melting on microstrucrure, mechanical, and electrochemical properties.

[Figure 21.4a and b](#) shows the scanning electron micrographs of the top surface of (a) as-received and (b) laser surface melted Ti-6Al-4V lased with an applied power of 600 W, scan speed of 6 mm/s, and gas flow rate of 5 l/min. The microstructure of as-received Ti-6Al-4V consists of elongated  $\alpha$ -Ti and the presence of lamellae of  $\beta$ -Ti at the intergranular region (as shown by arrowheads) (cf. [Figure 21.4a](#)). The as-received microstructure consists of elongated grains of  $\alpha$ -Ti and the presence of  $\alpha$ - $\beta$  lamellae at the grain boundary regions. The average grain size

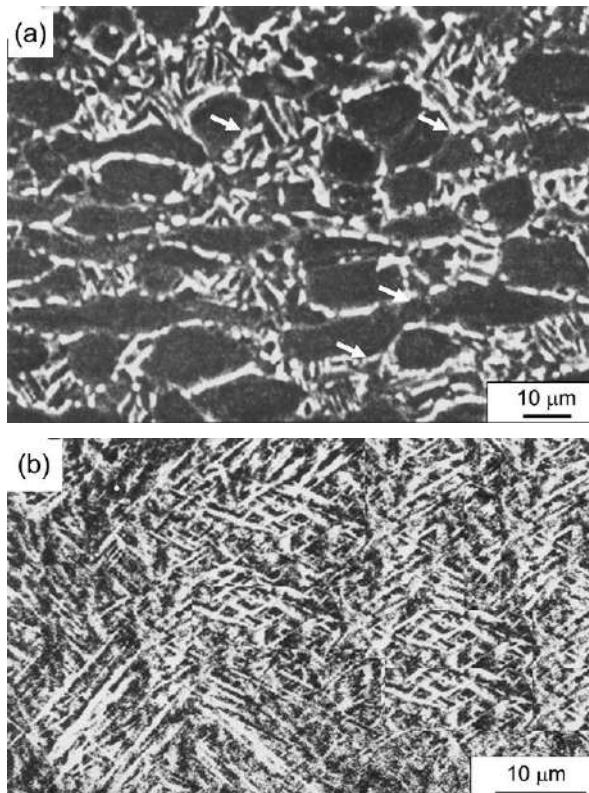


**Figure 21.4** Scanning electron micrographs (SEI) of the top surface of (a) as-received Ti-6Al-4V, and laser surface melted Ti-6Al-4V (b) lased with a power of 600 W and argon gas flow rate of 5 l/min.

and aspect ratio of  $\alpha$ -Ti grains were 5-15  $\mu\text{m}$  and 1.2-2, respectively. Laser surface melting leads to formation of acicular  $\alpha'$ -martensite in the microstructure. However, the mass fraction of  $\beta$ -Ti phase, as commonly observed in as-received microstructure, is suppressed (cf. Figure 21.4b). Similar  $\alpha'$ -martensite was also reported to be formed in laser surface melted titanium sheet with Nd:YAG laser due to a rapid quenching during solidification [18]. Acicular martensitic is having a hexagonal close-packed crystal structure and similar lattice parameters as that of  $\alpha$  phase, but possessing a very high hardness and relatively low ductility [19,20]. A detailed study shows that increasing laser power leads to coarsening of microstructure with decreased mass fraction of  $\alpha'$  martensite. On the other hand, the microstructure is refined and there is an increase in volume fraction of  $\alpha'$  martensite with increase in gas flow rate (this is also confirmed by X-ray diffraction analysis). Increase in applied power during laser surface melting leads to decreased cooling rate, resulting in coarsening of microstructure and decrease in volume fraction of acicular martensitic phase. Similarly, application of a high gas flow rate possibly results in a large cooling rate due to increased convective-dominated heat flow and, hence, causes the formation of more-refined

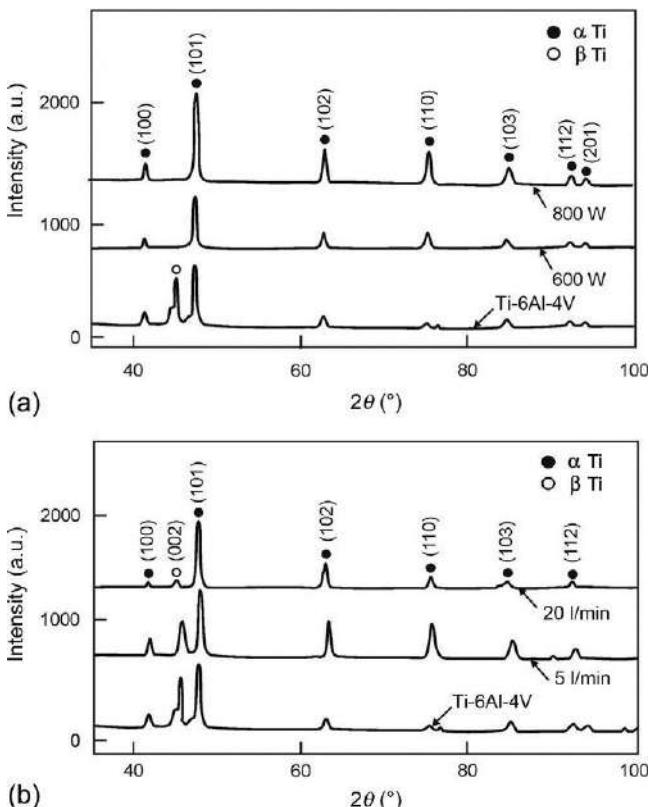


**Figure 21.5** X-ray diffraction profiles of as-received and laser surface melted Ti-6Al-4V lased with (a) a power of 600 and 800 W (at an argon gas flow rate of 5 l/min) and (b) with an Ar gas flow rate of 5 and 20 l/min (at an applied power of 800 W).

microstructure with a large volume fraction of martensite. Figure 21.5 shows the X-ray diffraction profiles of the top surface of as-received and laser surface melted Ti-6Al-4V processed under different processing conditions (as mentioned in the figures) showing (a) the effect of applied power and (b) the effect of gas flow rate. A detailed comparison of X-ray diffraction profiles of as-received and laser surface melted Ti-6Al-4V shows the presence of  $\alpha$ -Ti and  $\beta$ -Ti in as-received Ti-6Al-4V (Figure 21.5a). Due to laser surface melting, the intensity of  $\beta$ -titanium is almost diminished and  $\alpha$ -titanium is increased, which is evident from the X-ray diffraction profiles (cf. Figure 21.5). The intensity of  $\alpha'$ -titanium was found to vary with laser parameters. Increasing applied power from 600 to 700 W decreases the relative mass fraction of  $\alpha'$ -martensite significantly. However, application of a very high power (800 W) marginally increases the relative mass fraction of  $\alpha'$ -martensite in the melt zone. On the other hand, increase in gas flow rate increases relative mass fraction of  $\alpha'$ -martensite in the melt zone (plot 2 vis-à-vis plot 1 in Figure 21.5b). Change in relative mass fraction of  $\alpha'$ -martensite with applied power and gas flow rate is attributed to change in thermal profile and, hence, variation in cooling rate during laser surface melting of Ti-6Al-4V.

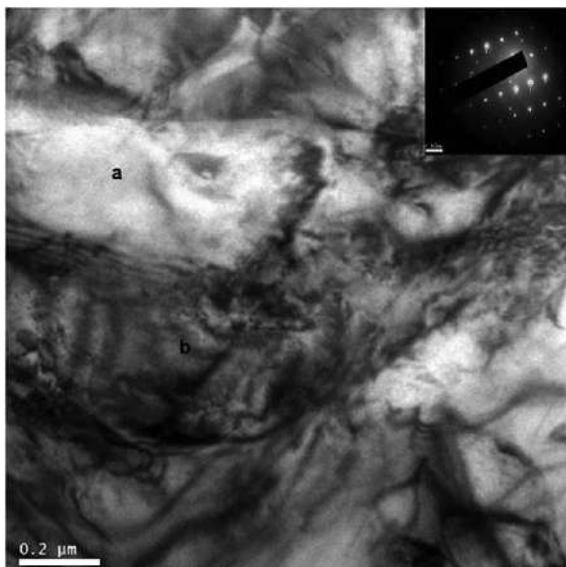


**Figure 21.6** High-resolution transmission electron micrograph of the top surface of laser surface melted Ti-6Al-4V lased with a power of 700 W and argon gas flow rate of 20 l/min.

[Figure 21.6](#) shows the high-resolution transmission electron micrograph of laser surface melted Ti-6Al-4V revealing the presence of  $\alpha'$  martensite (as shown in region A and evident from the SAD pattern as embedded on it) and a mixture of  $\alpha$ -titanium and  $\beta$ -titanium (shown as region B). The quantity of  $\beta$  phase in laser surface melted Ti-6Al-4V was, however, lower than in as-received Ti-6Al-4V. There are a large area fraction of dislocations in the microstructure. [Figure 21.7](#) shows the variation of average microhardness in the melt zone as a function of (a) applied power (at an argon gas flow rate of 5 l/min) at a gas flow rate of 5 l/min (plot 1), 20 l/min (plot 2), and (b) argon gas flow rate at an applied power of 600 W (plot 1), and 800 W (plot 2) in laser surface melted Ti-6Al-4V. From [Figure 21.7](#), it is evident that the average microhardness of the melt zone is significantly increased to as high as 550 VHN as compared to 280 VHN of as-received Ti-6Al-4V. The increase in microhardness in the melt zone is attributable to grain refinement and the formation of accicular  $\alpha'$  martensite in the microstructure [19]. From [Figure 21.7a](#), it is observed that, with an increase in laser power, there is a decrease in microhardness of the melt zone up to 700 W, following which it increases marginally. A decrease in microhardness of the melt zone with an increase in applied power is attributed to a decrease in mass fraction of  $\alpha'$  martensite and a coarsening of microstructure. Further enhancement of microhardness by the application of high power is possibly due to a marginal increase in volume fraction of  $\alpha'$ -martensite in the microstructure (as was also confirmed by the X-ray diffraction study). [Figure 21.7b](#) shows that the microhardness increases with an increase in gas flow rate from 5 to 10 l/min, following which it remains constant. Increase in average microhardness with increase in gas flow rate is attributed to refinement of microstructure and presence of  $\alpha'$  martensite in the microstructure.

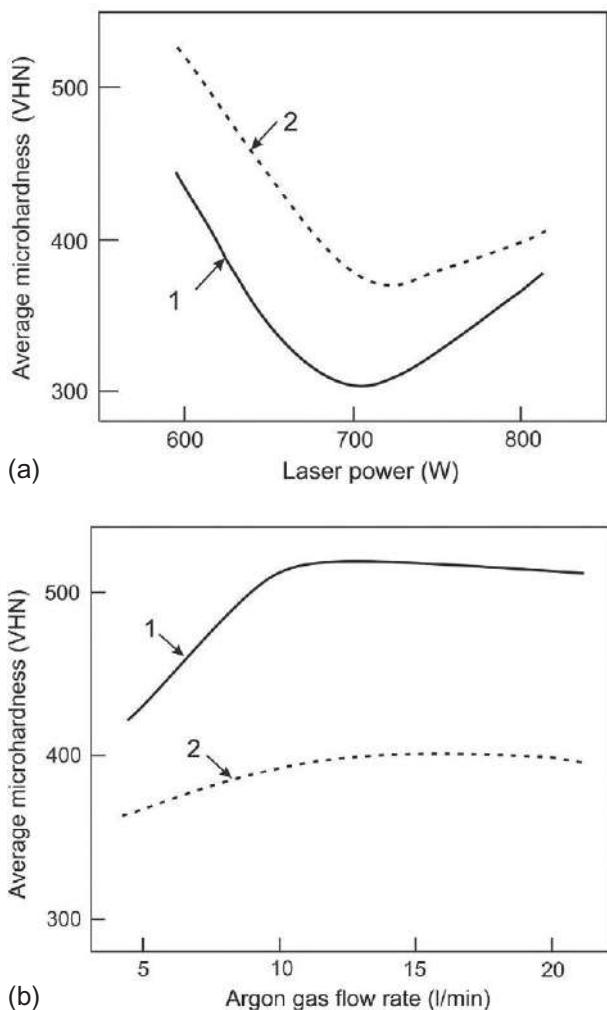


**Figure 21.7** Variation of average microhardness with (a) laser power at a gas flow rate of 5 l/min (plot 1), (2) 20 l/min (plot 2) and (b) argon gas flow rate at an applied power of 600 W (plot 1), 800 W (plot 2) in laser surface melted Ti-6Al-4V.

The corrosion-resistance property of the surface was evaluated in Hank's solution using potentiodynamic polarization technique, and the results are presented in terms of critical potential for pit formation ( $E_{\text{pit}}$ ). Table 21.5 summarizes the measured potential for pit formation ( $E_{\text{piu}}$ ) for as-received vis-à-vis laser surface melted Ti-6Al-4V for different laser parameters. It is interesting to note that the measured critical potential for pit formation ( $E_{\text{pit}}$ ) of the melted surface (in SBF) has increased significantly as compared to as-received Ti-6Al-4V, though its magnitude was found to vary with laser

**Table 21.5 Summary of physical and electrochemical properties of laser surface melted Ti-6Al-4V**

Applied power, W (gas flow rate, l/min)	Average surface roughness, $R_a$ ( $\mu\text{m}$ )	Contact angle ( $^\circ$ )	Critical potential for pit formation V (SCE)
600(5)	0.060	$48 \pm 1^\circ$	2.0
600(10)	0.058	$58 \pm 1^\circ$	6.5
600(20)	0.057	$52 \pm 1^\circ$	2.6
700(10)	0.059	$56 \pm 1^\circ$	4.8
800(5)	0.060	$43 \pm 1^\circ$	2.5
800(20)	0.061	$41 \pm 1^\circ$	2.0
As-received Ti-6Al-4V	0.044	$60 \pm 1^\circ$	1.3

parameters. Increasing applied power was found to increase  $E_{\text{pit}}$ , however, at a very high applied power, there is a marginal decrease in  $E_{\text{pit}}$ . Decrease in  $E_{\text{pit}}$  at a very high applied power is possibly due to a reduced mass fraction of  $\alpha'$ -martensite. On the other hand, increasing gas flow rate reduced the magnitude of  $E_{\text{pit}}$ , which is also attributed to grain refinement with increases in gas flow rate. Hence, it may be concluded that the improvement in pitting corrosion resistance (increased  $E_{\text{pit}}$ ) of laser surface melted surface is attributed to formation of  $\alpha'$ -martensite due to rapid quenching and microstructural homogenization [18–20].

Figure 21.8a and b shows the microstructures of corroded films formed on (a) as-received and (b) laser surface melted (with a power of 700 W and gas flow of 5 l/min) Ti-6Al-4V followed by immersion in simulated body fluid for 72 h. Figure 21.8a shows that the microstructure of the corroded surface of as received Ti-6Al-4V mainly consists of localized pitted regions (labeled as 1). In as-received Ti-6Al-4V, the area fraction of pit is significantly higher. The greater area of pit in as-received Ti-6Al-4V is mainly because of the interconnection of pits for a longer duration. Very finely distributed  $\text{Ca}_3(\text{PO}_4)_2$  was also found to be present in both the microstructures (labeled as 2). The area fraction of pits was reduced by laser surface melting as shown in Figure 21.8b and very fine pits are randomly distributed throughout the corroded surface (labeled as 1 in Figure 21.8b). A detailed study also reveals that there is significant reduction in contact angle of simulated body fluid on laser-melted surface (to  $41\text{--}58^\circ$ ) as compared to as-received Ti-6Al-4V ( $60^\circ$ ) (cf. Table 21.5), indicating an increased wettability of the surface against simulated body fluid. The increased wettability is possibly due to the increase in surface roughness by laser surface melting. Hence, laser surface melting is a unique and simple processing technique for modification of surface microstructure of Ti-6Al-4V to improve its hardness and corrosion resistance. In addition, the processing also changes the surface topography and, hence, increases the wettability of the surface for its application as a bioimplant.

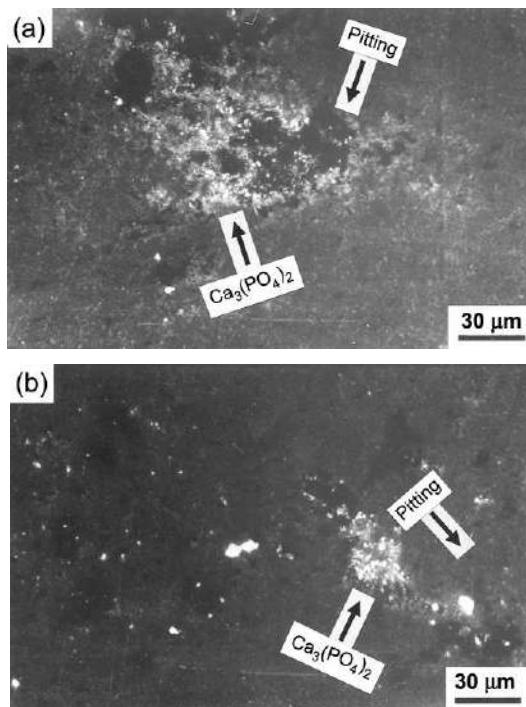


**Figure 21.8** Scanning electron micrograph of the top surface of (a) as-received and (b) laser surface melted (lased with a power of 700 W and nitrogen gas flow of 5 l/min) Ti-6Al-4V followed by immersion in simulated body fluid for 72 h.

### 21.8.2 *Laser surface alloying of titanium and its alloys*

Laser surface alloying is a material-processing method that utilizes high power density available from focused laser sources to melt pre- or co-deposited alloying elements/compounds and a portion of the underlying substrate [21]. Because melting occurs in a very short time and only at the surface, the bulk of the material remains cool, thus serving as an infinite heat sink. Large temperature gradients exist across the boundary between the melted surface region and the underlying solid substrate. This results in rapid self-quenching and resolidification. Quench rates as great as  $10^{11}$  K/s and concomitant resolidification velocities of 30 m/s have already been achieved. What makes laser surface alloying both attractive and interesting is the possibility of retention of metastability in the microstructure because of the rapid quenching from the liquid phase. These include chemical profiles where the “alloyed” element is highly concentrated near the surfaces and decreases in concentration over a shallow depth, and uniform profiles where the concentration is the same throughout the entire melted region. The types of microstructures observed include extended solid solution, metastable crystalline phase, and metallic glass. **Figure 21.9** illustrates the schematic of

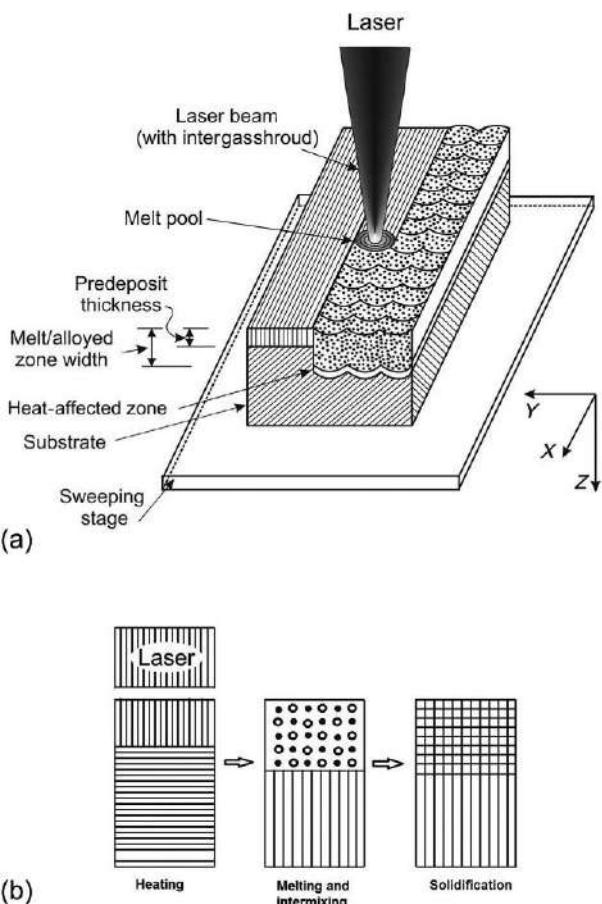


**Figure 21.9** Stages involved in laser surface alloying from arrival of laser pulse to complete resolidification: (a) laser irradiation, (b) start of melting, (c) interdiffusion in liquid state, (d) start of solidification, and (e) end of solidification [17].

laser surface alloying [21]. Figure 21.9a, shows the irradiation of a coated substrate with a CW laser beam. When the energy density of the laser beam reaches a threshold value, the surface region starts melting and, subsequently, there will be diffusion of atoms from both the coating toward the substrate and vice versa, which is mostly convection dominated (cf. Figure 21.9b). Finally, there is rapid solidification to form a homogeneous alloyed zone. Laser surface alloying may be achieved by applying the coating (by any of the deposition techniques) on the surface of the substrate prior to laser surface melting (may be termed as predeposition) or by concomitant addition of alloying elements during laser surface melting at the melt zone (may be termed as codeposition) [21]. Predeposition methods may be any of the conventional coating techniques such as vacuum evaporation, sputtering, or ion implantation, which are used for very thin films (less than 500 nm). Thicker predeposited films are more

commonly electroplated, sprayed, or rolled onto the substrates. The ideal predeposited film would be of uniform thickness, low in porosity, having good adherence, possessing a clean substrate/film interface, and having an optically clean surface. Codeposition is attractive because it implies single-step processing. Particle injection directly into the melt trail produced by a CW-CO<sub>2</sub> laser is the most popular codeposition method. The powder feed rate may be changed during laser melting by design or in response to real-time changes or fluctuations in other processing variables.

In the past, laser surface alloying was successfully applied on titanium and its alloys to improve its wear, corrosion, high-temperature oxidation resistance, and biocompatibility. The alloying elements mostly applied for surface alloying included nitrogen, silicon, aluminum, and boron [22–28]. In the following sections, a few examples of application of laser surface alloying in improving the mechanical and electrochemical properties of titanium and its alloys will be presented.

The most successful alloying addition in titanium and its alloys leading to tailoring of wear resistance property is nitrogen. Nitrogen, as an alloying ingredient, is added in laser-melted titanium. During the process, a high-power laser is used to melt the surface of titanium and there is continuous feeding of nitrogen in the molten zone. In an earlier attempt, laser surface nitriding was carried out by irradiating the Ti-6Al-4V substrate using a 2 kW CW laserline diode laser with mixed 810 and 940 nm wavelengths (maximum power of 1.5 kW) and with an optical fiber beam delivery system (with a spot area of  $3.5 \times 2 \text{ mm}^2$ ) using nitrogen as the shrouding gas, with an overlap of 25% between the successive melt tracks (to ensure a uniform depth of nitriding). **Table 21.6** summarizes the laser parameters used for laser surface nitriding [22]. **Figure 21.10a and b** shows the scanning electron micrographs of the cross section of laser surface-nitrided Ti-6Al-4V (lased with a power of 700 W, scan speed of 6 mm/s, and gas flow rate of 5 l/min) showing (a) the size and shape of the nitrided zone and a higher-magnification view of (b) the nitroded zone. From **Figure 21.10a** it may be noted that laser surface nitriding caused formation of a continuous and defect-free nitride zone, the shape of which was semicircular as an evidence of conduction-dominated heat flow. From **Figure 21.10a** it is also seen that the thickness of heat-affected zone is negligible and found to vary from 10 to 50 μm. A higher magnification view of the nitrided layer shows that it consists of dendrites of titanium nitride and α-Ti (as confirmed by X-ray diffraction analysis) with an average interdendritic spacing of 2–4 μm for different conditions of lasing (cf. **Figure 21.10b**). However, the mass fraction of titanium nitride phase and the interdendritic spacing

**Table 21.6 Summary of the laser parameters used for laser surface nitriding of Ti-6Al-4V [22]**

Substrate	Laser power (W)	Scan speed (mm/s)	Nitrogen gas flow rate (l/min)
Ti-6Al-4V	600	6	5-20
	700	6	5-20
	800	6	5-20

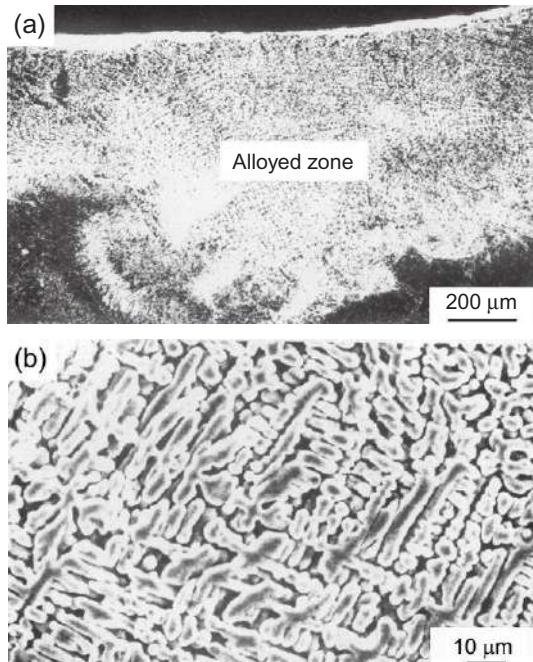


**Figure 21.10** Scanning electron micrograph of the (a) cross section of laser surface nitrided Ti-6Al-4V and the higher magnification view of the (b) alloyed zone lased with a power of 700 W, scan speed of 6 mm/s, and gas flow rate of 5 l/min [22].



**Figure 21.11** Scanning electron micrograph of the top surface of laser surface nitrided Ti-6Al-4V lased with a power of 700 W, scan speed of 6 mm/s, and gas flow rate of 20 l/min.

were found to vary with laser parameters [22]. It was observed that the secondary arm spacing of dendrites were marginally coarsened with increase in applied power and decrease in gas flow rate. When a very high gas flow rate (20 l/min) was applied, there was formation of fragmented dendrites with the presence of titanium nitride needle and a decreased mass fraction of titanium nitrides (cf. [Figure 21.11](#)). The decreased

mass fraction of titanium nitride phase with increase in gas flow rate is attributed to less availability of time for gas alloying in the liquid state due to a very high cooling rate at an increased gas flow rate. The fragmentation of dendrites and needle shape appearance of the nitride phase are due to a forced convection in the melt pool due to a high gas flow rate during laser processing. In this regard, it is relevant to mention that the fragmented dendrites would lead to an increased toughness property as compared to thick and continuous dendrites. There is a significant enhancement in surface roughness after laser surface nitriding. The calculated average surface roughness ( $R_a$ ) was found to vary from 0.25 to 0.30  $\mu\text{m}$  for different conditions of lasing as compared to 0.044  $\mu\text{m}$  for as-received Ti-6Al-4V. The increase in surface roughness level following laser surface nitriding is beneficial for improved biocompatibility, and hence, the possible application of the surface treatment as bioimplant.

A detailed X-ray diffraction study of the top surface of as-received and laser surface nitrided Ti-6Al-4V was undertaken to understand the phases present and quantify its volume fraction. Figure 21.12 compares the X-ray diffraction patterns of the surface of as-received (plot 1) with laser surface nitrided Ti-6Al-4V lased with a power of 600 W (plot 2) and 800 W (plot 3) at a gas flow rate of 10 l/min. From the X-ray diffraction patterns, it is evident that the as-received Ti-6Al-4V used in the present study consists of a mixture of  $\alpha$  and  $\beta$  titanium. Laser surface nitriding of Ti-6Al-4V led to formation of TiN and a few  $\alpha$ -Ti. A detailed comparison of the individual peaks in Figure 21.12 shows that the intensity of  $\alpha$ -Ti peak decreases after nitriding. Furthermore, the intensities of TiN peaks were also found to vary marginally with applied power.

Figure 21.13 shows the variation of microhardness with depth from the surface of laser surface nitrided Ti-6Al-4V lased with (a) applied power of 600 W (plot 1), and 800 W (plot 2) at a nitrogen gas flow rate of 10 l/min and (b) with a gas flow rate of

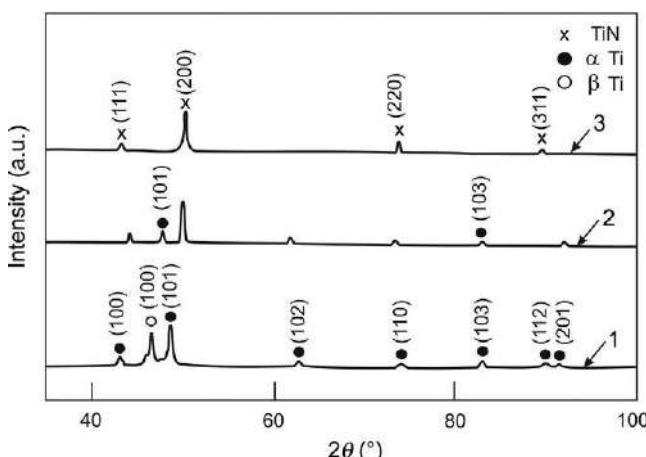


**Figure 21.12** X-ray diffraction patterns of as-received (plot 1) and laser surface nitrided Ti-6Al-4V lased with a power of 600 W (plot 2) and 800 W (plot 3) at a gas flow rate of 10 l/min [22].

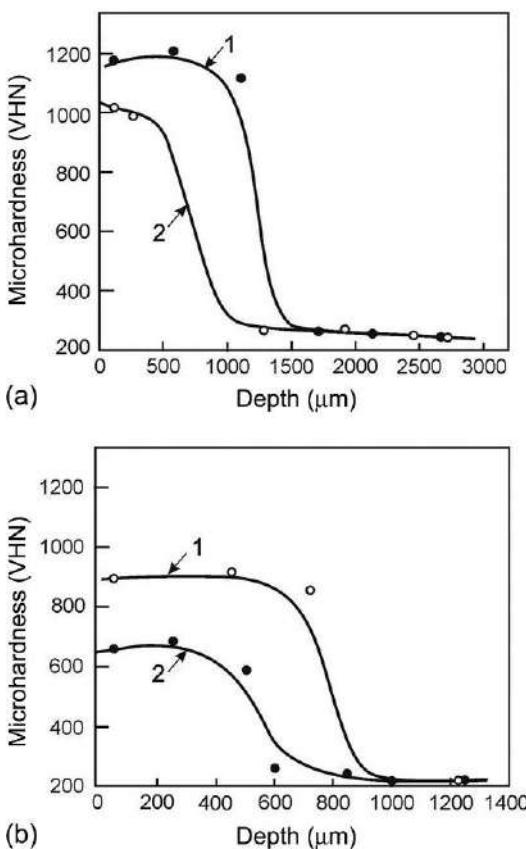


**Figure 21.13** Variation of microhardness with depth from the surface of laser surface nitrided Ti-6Al-4V lased with (a) applied power of 600 W (plot 1), and 800 W (plot 2) at a nitrogen gas flow rate of 10 l/min and (b) at an applied power of 700 W with a gas flow rate of 5 l/min (plot 1), and 20 l/min (plot 2) [22].

5 l/min (plot 1), and 20 l/min (plot 2) at an applied power of 700 W. From Figure 21.13 it is evident that microhardness in the nitrided zone is almost uniform along the cross section with depth. Furthermore, with increase in laser power the microhardness of the nitrided layer decreases (cf. Figure 21.13a). Decreased microhardness with increase in applied power is due to the coarsening of microstructure. From Figure 21.13b it is clear that the microhardness of the nitrided layer decreases (plot 2) with increase in gas flow rate from 5 to 20 l/min. Maximum surface hardness was developed when laser surface nitrided at an applied power of 600 W and gas flow rate of 10 l/min (1175 VHN), which is over four times higher than the base hardness (280 VHN). Hence, it may be concluded that the mechanism of hardening in laser surface nitrided Ti-6Al-4V is because of formation of nitrides and refinement of microstructures.

Cracking was found to be a critical problem in laser surface nitriding of titanium alloys due to a large residual stress developed in the nitrided zone. Figure 21.14 shows

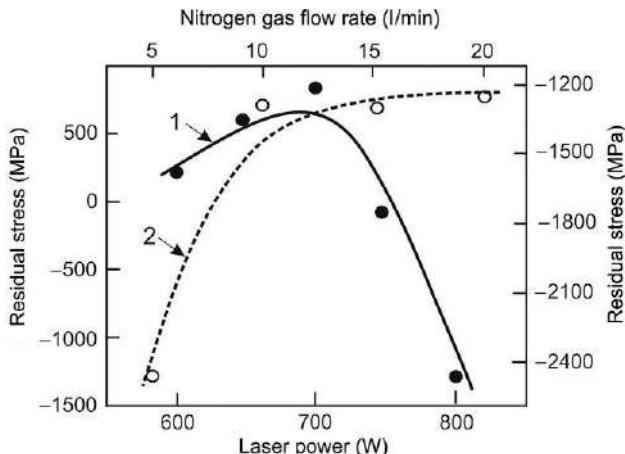


**Figure 21.14** Variation of average residual stress developed in the nitrated layer with applied power at a gas flow rate of 10 l/min (plot 1 solid line and left axis) and gas flow rate at an applied power of 800 W (plot 2 dotted line and right axis) [22].

the variation of average residual stress developed in the nitrated layer with applied power at a gas flow rate of 10 l/min (plot 1 solid line and left axis) and gas flow rate at an applied power of 800 W (plot 2 dotted line and right axis). Increase in applied power from 600 to 700 W was found to increase residual stress from 250 to 750 MPa. A further increase in applied power to 800 W decreased the residual stress level to -1400 MPa. The origin of the residual stress is thermal (mainly because of a large difference in thermal gradient between the surface and the interior) as well as due to the presence of nitrogen in solution along with nitride formation. Thermal stress leads to the development of tensile residual stress. On the other hand, nitride formation and the presence of nitrogen in solution leads to the development of compressive residual stress. The increased level of tensile residual stress in the nitrated zone at 600 and 700 W applied power is possibly due to a significant contribution of quench stress toward the residual stress distribution and the presence of lower mass fraction of TiN phase in the microstructure. On the other hand, at high power, the effect of quench stress is reduced (because of a slower cooling rate) but the transformation stress predominates. Furthermore, the presence of a higher mass fraction of TiN contributes toward the compressive stress distribution. At a lower gas flow rate (5 l/min), residual stress was compressive and as low as -2500 MPa (for an applied power of 800 W). The decreased magnitude of tensile residual stress at a very low gas flow rate is attributed to a reduction in cooling rate. The residual stress increased with increase in gas flow rate to 10 l/min following which it remained the same. Increased magnitude of residual stress with increase in gas flow rate is due to increased quenching rate and a reduced volume fraction of nitrides (cf. [Figure 21.14](#), plot 2 dotted line)).

[Figure 21.15](#) presents bar charts comparing the measured potential for pit formation ( $E_{pit}$ ) for as-received vis-à-vis laser surface nitrified Ti-6Al-4V for different laser parameters. It is interesting to note that measured pitting potential ( $E_{pit}$ ) of the nitrified

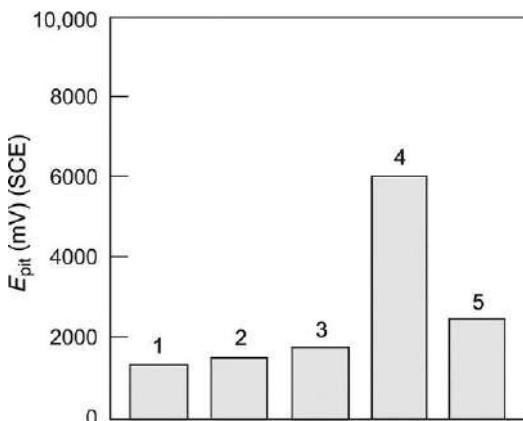


**Figure 21.15** Bar charts comparing the measured potential for pit formation ( $E_{\text{pit}}$ ) of as-received (plot 1) and laser surface nitrided Ti-6Al-4V lased with an applied power of 800 W, powder flow rate of 5 l/min (plot 2), 700 W, 5 l/min (plot 3), 600 W, 5 l/min (plot 4) and received vis-à-vis laser surface nitrided Ti-6Al-4V for different laser parameters [22].

surface (in simulated body fluid plus bovine serum albumin) is similar or superior to the as-received Ti-6Al-5V, though its magnitude was found to vary with laser parameters. Increasing applied power was found to decrease  $E_{\text{pit}}$ . On the other hand,  $E_{\text{pit}}$  of the nitrided surface decreased with an increase in nitrogen gas flow rate. Increased pitting potential due to surface nitriding is due to the presence of TiN on the surface and nitrogen in solution. A maximum improvement of pitting corrosion resistance was achieved when lased with an applied power of 600 W and powder flow rate of 5 l/min. The presence of surface microdefects and surface roughness, deteriorates pitting corrosion property. Increasing power was found to coarsen the microstructure and increase the surface roughness, which is possibly responsible for decreasing  $E_{\text{pit}}$  at higher power level. On the other hand, increasing gas flow rate leads to the formation of fragmented dendrites and, hence, the presence of large numbers of interfaces and a reduced mass fraction of titanium nitride in the alloyed zone. As a result,  $E_{\text{pit}}$  is lowered at a higher nitrogen flow rate.

Hence, laser surface nitriding is effective in improving the hardness and corrosion resistance of the surface of Ti-6Al-4V. However, the process parameters should be optimized to achieve an alloyed zone with a minimum residual stress level and improved mechanical/electrochemical properties.

Silicon as an alloy is known to improve high-temperature oxidation resistance of metallic materials. Conventional diffusion-assisted surface alloying of Si on titanium is extremely difficult due to its poor solid solubility. Laser surface alloying of titanium with silicon was carried out by a 6 kW CW CO<sub>2</sub> laser with a rectangular beam of 3.45 mm × 2.4 mm beam area (with the focal point 35 mm above the surface) by codeposition or simultaneous feeding of (99.5 wt.% purity) elemental Si (22–45 mm size) through an Ar gas driven (at a flow rate of 6 l/min) powder delivery system onto a sandblasted titanium surface. The process parameters selected for determining the optimum

conditions for LSA were incident laser power ( $P$ : 2-4.5 kW), linear speed of the sample ( $v$ : 150-600 mm/min), and powder feed rate ( $F_p$ : 16-80 mg/s), respectively.

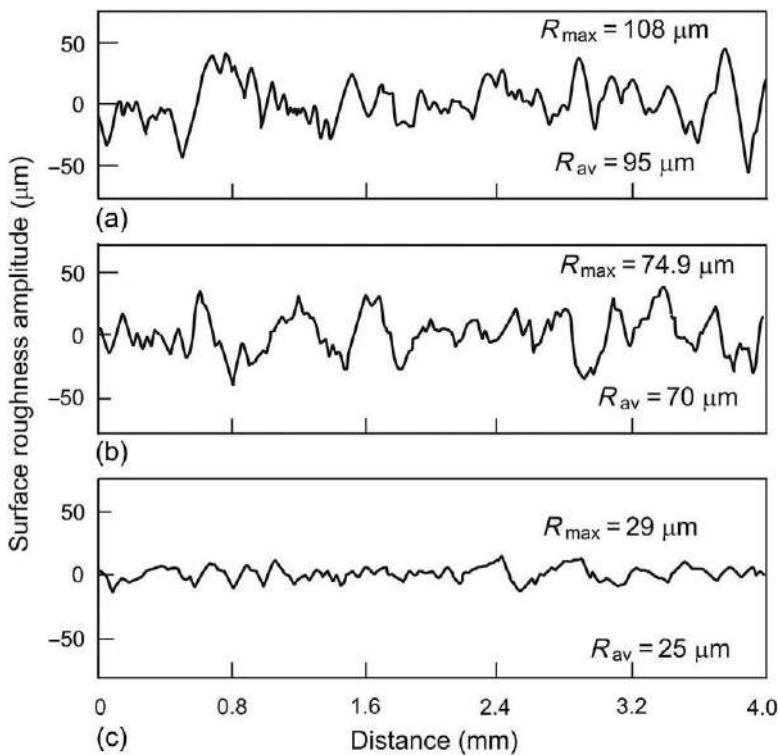
A large number of defects (porosities, microcracks, and an increased surface roughness) were associated with laser surface alloying of titanium with silicon. A careful set of dye penetration tests on the laser-alloyed surface revealed the presence of isolated microcracks and porosities under unfavorable laser processing routines. The overall crack distribution in the alloyed zone for different combinations of applied power ( $P$ ) and scan speed ( $v$ ) for laser surface-alloyed titanium with silicon is summarised in [Table 21.7](#). From [Table 21.7](#) it is evident that too low  $P$  or too high  $v$  leads to incomplete melting and formation of fine micro/macrocraacks. On the other hand too high  $P$  or too low  $v$  leads to surface evaporation or surface cracks due to very high powder feeding. Appropriate selection of laser parameters leads to the formation of crack-free alloyed zone as shown by cross mark in [Table 21.7](#). From [Table 21.7](#) it is also evident that the number of cracks is more at too low a scan speed due to increased powder delivery because of high interaction time, or at a very high scan speed for improper intermixing and, hence, generation of a crack from the high-concentration region for both Ti(Si). An improper selection of laser parameters leads to either incomplete melting or surface boiling and, consequently, a worse surface contour following laser surface alloying (cf. [Figure 21.16a and b](#)). On the other hand, an adequate level of  $P$  and  $v$  required for proper melting/intermixing and formation of the alloyed zone may yield a smoother surface contour ([Figure 21.16c](#)).  $R_{\max}$  decreases with a decrease in  $P$  or increase in  $v$  provided the selected  $P$  or  $v$  is sufficient to melt, intermix, and form the alloyed zone.

[Figure 21.17a-d](#) presents the scanning electron micrographs of the cross section of laser surface-alloyed titanium with silicon lased with a (a) power of 3 kW, and scan speed of 300 mm/min, powder feed rate of 72 mg/s, (b) 4 kW, 500 mm/min, 17 mg/s, (c) 4 kW, 300 mm/min, 17 mg/s, and (d) 4 kW, 300 mm/min, 16 mg/s, respectively. From [Figure 21.17](#) it may be noted that based on the width of the alloyed zone, its microstructure and phase distribution vary with laser parameters. The microstructure of the alloyed zone on the cross-sectional plane of Ti(Si) is heterogeneous with nonuniform  $H_v$  and  $X_{Si}$  in different regions of the alloyed zone (as revealed in [Figure 21.17a-d](#) and summarized in [Table 21.8](#)). Perhaps, a combined effect of inadequate  $P$  and higher  $F_p$  ([Figure 21.17a](#)), or lower  $P$  and faster  $v$  ([Figure 21.17b](#)) has been responsible for the incomplete melting/intermixing of the alloying powders during laser surface alloying in this case. On the other hand, application of appropriate  $P$ ,  $v$  and  $F_p$  leads to homogeneous and crack-free alloyed zone with uniformly dispersed  $Ti_5Si_3$  (detected by X-ray diffraction analysis) primary precipitates in the eutectic aggregate of  $\alpha$ -Ti and  $Ti_5Si_3$  ([Figure 21.17c](#)). Therefore, it is important to determine the optimum conditions of laser surface alloying in terms of  $P$ ,  $v$  and  $F_p$  to achieve homogeneous microstructure in the alloyed zone. A detailed EDS analysis of the surface shows that the silicon content in the alloyed zone varied from 6 to 15 wt.% for the different conditions of lasing and decreases with increase in applied power, due to increased degree of dilution. However, the effect of scan speed ( $v$ ) on the composition of the alloyed zone is too complex. At higher scan speed ( $v$ ), a nonuniform elemental distribution results from improper melting and intermixing. On the

**Table 21.7 Defects in the alloyed for different combinations of applied power,  $P$  and scan speed,  $v$  ( $F_p = 16 \text{ mg/s}$ )**

$v$ (mm/min)		150	200	225	250	300	350	375	400	425	450	475	500
System	$P$ (kW)	Number of cracks per unit area (%)											
Ti(Si)	2.75	No melting (NM)/incomplete intermixing (II)											
Ti(Si)	3	30	X	X	X	30	30	50	II	NM			
Ti(Si)	3.25	SE	50	X	X	X	20	40	70	NM			
Ti(Si)	3.5	SE	SE	60	X	X	X	X	40	80	NM		
Ti(Si)	4.0	SE	SE	SE	60	50	X	X	X	X	X	X	30
Ti(Si)	4.5	Surface evaporation (SE)											

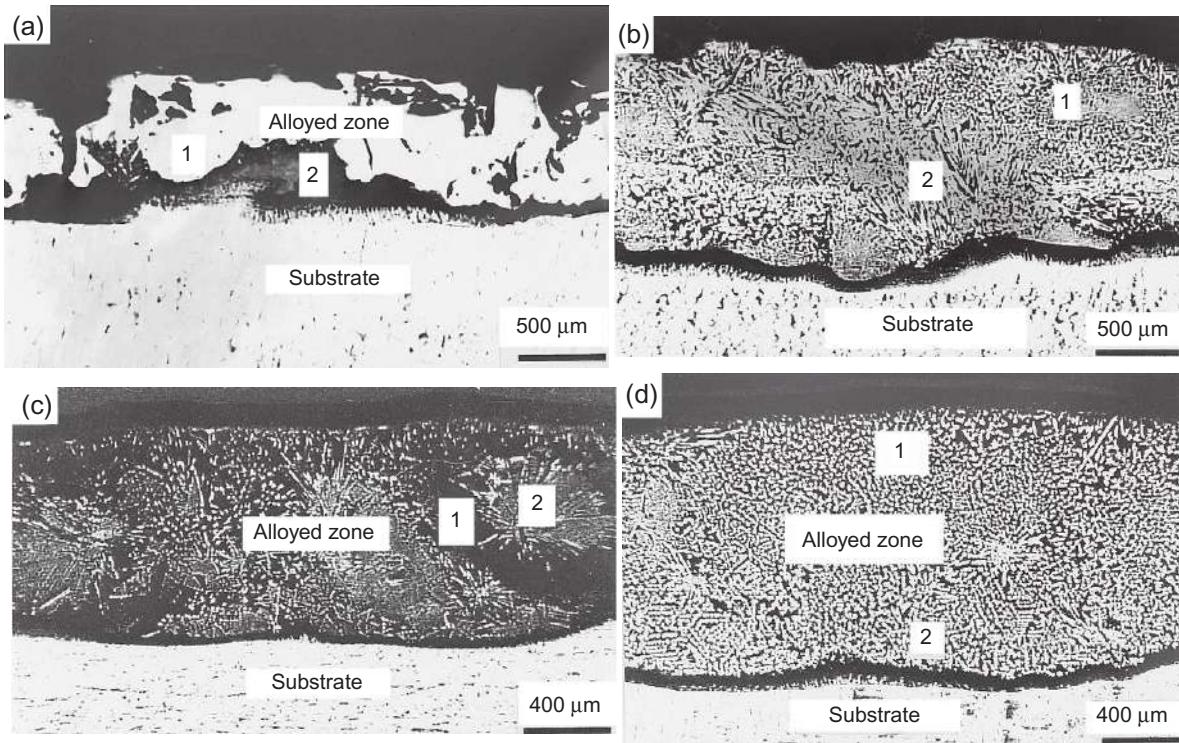
No defect: X.



**Figure 21.16** Variation in maximum surface roughness ( $R_{\max}$ ) within a track (perpendicular to the direction of lasing) on laser surface alloyed titanium with silicon lased with (a) an applied power ( $P$ ) = 3 kW, scan speed ( $v$ ) = 300 mm/min,  $F_p$  = 85 mg/s, (b) 4 kW, 300 mm/min, 17 mg/s, and (c) 3 kW, 300 mm/min, 17 mg/s [27].

other hand, both powder feeding rate and interaction time increase at a very low scan speed ( $v$ ). Thus, both dilution (due to higher depth of melting) and increase in elemental concentration (due to higher time of interaction) play important roles. Unfavorable choice of  $P$  and  $v$  leads to nonuniform composition distribution in the alloyed zone. Hence, a suitable combination of  $P$  or  $v$  is necessary to achieve a uniform alloyed zone with the desired level of Si. [Figure 21.18a and b](#) presents the respective X-ray diffraction profiles obtained from (a) as-received Ti and (b) top surface of the laser-alloyed titanium with silicon lased with an applied power of 4 kW, scan speed of 300 mm/min, and a powder flow rate of 16 mg/s using Cu-K $\alpha$  radiation. It may be noted that the X-ray diffraction profile of Ti(Si) consists of only the  $\alpha$ -Ti and of  $\text{Ti}_5\text{Si}_3$  peaks ([Figure 21.18b](#)). The mass fraction of  $\text{Ti}_5\text{Si}_3$  was, however, found to vary with laser parameters.

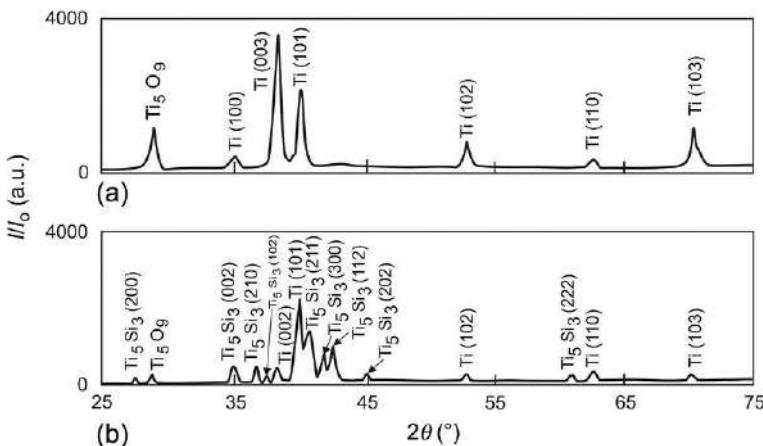
[Figure 21.19a](#) reveals a typical hypereutectic microstructure on the top surface of the alloyed zone in Ti(Si) (processed with  $P$  = 4 kW,  $v$  = 300 mm/min, and  $F_p$  = 17 mg/s). The microstructure consists of particles of faceted  $\text{Ti}_5\text{Si}_3$  phase uniformly distributed in a two-phase eutectic aggregate of  $\alpha$ -Ti and  $\text{Ti}_5\text{Si}_3$ . The high



**Figure 21.17** Variation of the alloyed zone microstructure in the cross-sectional plane of Ti(Si) subjected to laser surface alloying with (a)  $P = 3$  kW,  $v = 300$  mm/min,  $F_p = 72$  mg/s, (b) 4.5 kW, 200 mm/min, 16 mg/s, (c) 4 kW, 500 mm/min, 16 mg/s, and (d) 4 kW, 300 mm/min, 16 mg/s, respectively. Note that only (d) shows a homogeneous and defect-free microstructure in the alloyed zone. The arabic numerals (1, 2) indicate the locations for the EDS analysis [27].

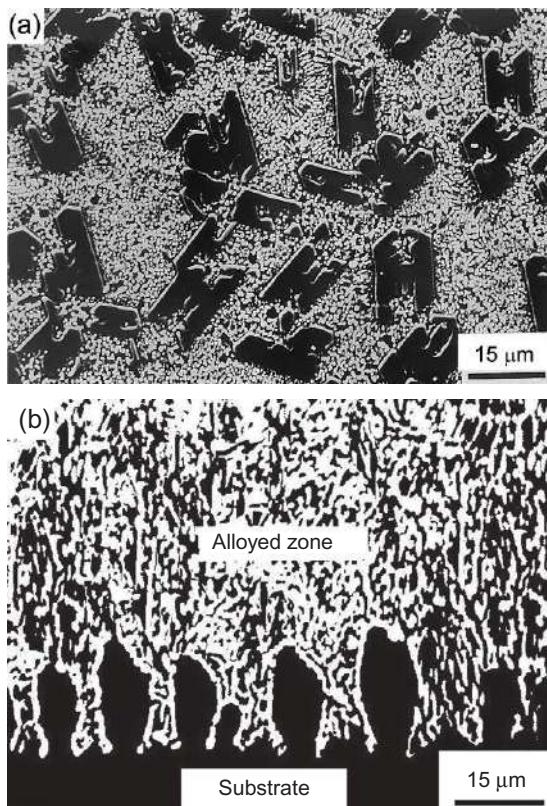
**Table 21.8 Average silicon content ( $X_{\text{Si}}$ ) and microhardness ( $H_v$ ) of the selected regions in Figure 21.17 [27]**

Figure number	Region	$X_{\text{Si}}$ (at.%)	$H_v$ (VHN)
21.17a	1	52	1380
	2	9	710
21.17b	1	12	750
	2	10	735
21.17c	1	17	780
	2	2	450
21.17d	1	13	763
	2	12	760



**Figure 21.18** X-ray diffraction profiles obtained from (a) as-received Ti and (b) top surface of the laser-alloyed titanium with silicon lased with an applied power of 4 kW, scan speed of 300 mm/min, and a powder flow rate of 16 mg/s [27].

volume fraction of the primary phase and degree of fineness of the eutectic products signify complete dissolution and uniform intermixing of Si in the alloyed zone, and a rapid quenching experienced by the latter, respectively. In contrast, the interfacial region of the same alloyed zone consists of fine eutectic lamellae of  $\alpha$ -Ti and  $\text{Ti}_5\text{Si}_3$  with a few coarse  $\alpha$ -Ti dendrites growing from the alloyed zone-substrate interface (Figure 21.19b). It should be mentioned that  $X_{\text{Si}}$  (determined by energy dispersive spectroscopic analyser) near the alloyed zone-substrate interface is significantly lower than that in the upper portion of the alloyed zone. The average microhardness ( $H_v^{\text{av}}$ ) of the alloyed zone was improved 2-4 times due to laser surface alloying as compared to the substrate Ti ( $H_v^{\text{av}} = 216$  VHN). The improved microhardness of the alloyed zone due to laser surface alloying is attributed to dispersion strengthening by the  $\text{Ti}_5\text{Si}_3$  precipitates in the alloyed zone in Ti(Si). Furthermore, the microhardness of the surface is inversely proportional to the applied power. As microhardness depends on the



**Figure 21.19** Scanning electron micrographs of the (a) top surface and (b) solid liquid interface (cross-sectional plane) of laser-alloyed Ti(Si) lased with an applied power of 4 kW, scan speed of 300 mm/min, and a powder flow rate of 16 mg/s [27].

microstructure, microhardness distribution in the alloyed zone is related to the choice of laser parameters. Figure 21.20 displays the optimum processing range for laser surface alloying of Ti with Si derived from a detailed correlation of microstructure, composition, surface roughness, and mechanical properties (in terms of  $H_v^{\text{av}}$ ) of the alloyed zone with laser parameters ( $P$  and  $v$ ). It is apparent that an insignificant  $P$  or too high a  $v$  during laser surface alloying leads to improper melting, higher level of  $R_{\max}$ , and heterogeneous microstructure/composition (Figure 21.18a-d) in the alloyed zone. On the other hand, too high a  $P$  or too low a  $v$  leads to surface boiling and crater formation and, hence, increases in  $R_{\max}$ . Figure 21.19 acts as a suitable guideline for selection of laser parameters to attain the desired type of microstructure/composition in the alloyed zone. It may be noted that a detailed study on the influence of  $F_p$  on the alloyed zone characteristics have revealed that the optimum level of  $F_p$  required for formation of a homogeneous and defect-free alloyed zone lies in the narrow range of 16–18 g/s. A similar process map has also been drawn for Ti(3Si + Al) and Ti(Si + 3Al), respectively. Accordingly, the optimum range of process parameters for laser

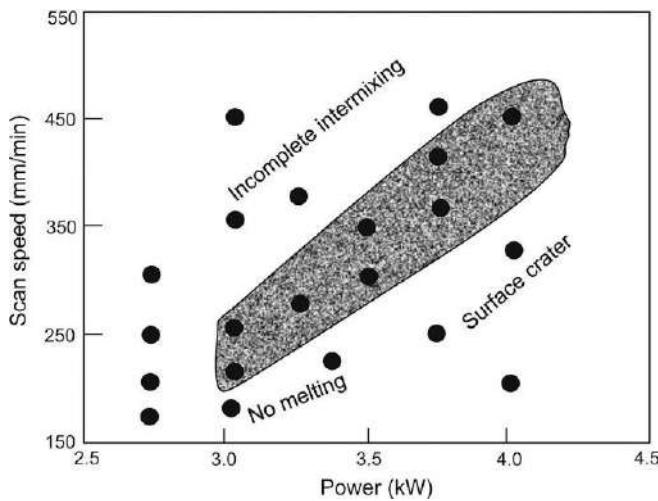


**Figure 21.20** Process optimization diagram correlating composition, microstructure, and properties of the alloyed zone in laser-alloyed titanium with silicon [27].

surface alloying of titanium with silicon, which could lead to homogeneous and defect-free microstructures are as follows: laser power: 3–4.2 kW; scan speed: 175–450 mm/min; and powder flow rate: 16–20 mg/s. Laser surface alloying using optimum process parameter could produce alloyed zone with an average surface roughness ranging from 25 to 29 µm, an average silicon content of 12–14 at.%, and an average surface microhardness of 700 to 750 VHN.

A detailed study of the high-temperature oxidation behavior of the surface-alloyed samples was evaluated under both isothermal and cyclic condition. [Figure 21.21a and b](#) presents the results of cyclic oxidation studies (with 10–15 cycles) on pure Ti and laser surface-alloyed titanium with silicon, and Ti(Si) in terms of weight gain per unit area ( $\Delta m$ ) as a function of time of exposure ( $t$ ) at (a) 950, and (b) 1150 K, respectively. From [Figure 21.21](#) it is evident that the oxidation rate is much higher in pure Ti, which significantly decreases with addition of Si at all temperatures of study. The much higher oxidation rate of Ti may be attributed to the higher diffusivity and solubility of  $O_2$  in Ti, and the ease of uninhibited counterionic transport of the species concerned. With increase in temperature, the oxidation loss increases by an order of magnitude to 1050 K. At this temperature, the oxide scale tends to spall only after 48 h in pure Ti. On the other hand, the oxide scale is strongly adherent to the surface in laser-alloyed samples. With further rise in temperature ( $T=1150$  K in [Figure 21.21b](#)), oxidation increases further. At this temperature, loose oxide surface gets sintered and adheres to the surface during the initial period (72 h), following which they get detached from the surface due to the difference in coefficient of linear expansion between pure Ti and  $TiO_2$ . Thus, the results of cyclic oxidation demonstrate that the oxidation resistance of Ti has been significantly improved by laser surface alloying with Si. [Figure 21.22a and b](#) shows the kinetics

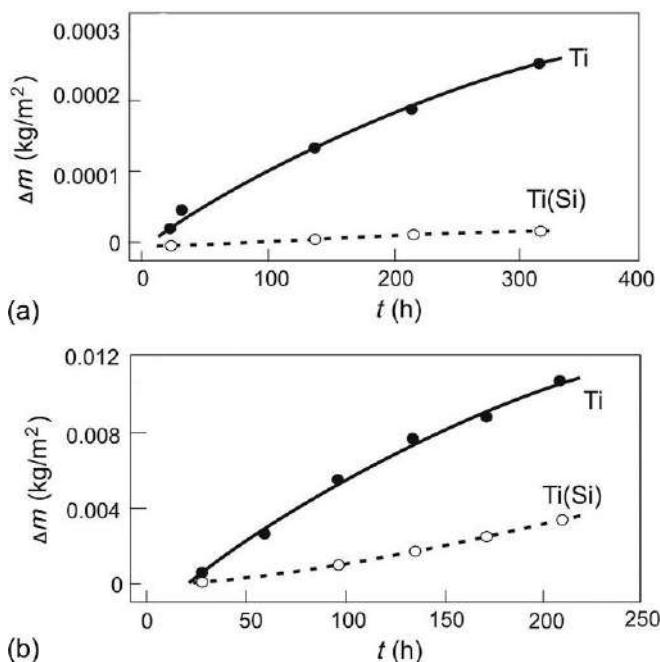


**Figure 21.21** Variation of the total weight gain per unit area ( $\Delta m$ ) as a function of time ( $t$ ) in Ti, and Ti(Si) following cyclic oxidation studies between room temperature and (a) 923 K and (b) 1150 K for 360 h [28].

of isothermal oxidation of Ti and Ti(Si) for an exposure of 5–360 h at (a) 923, and (b) 1150 K, respectively. The oxidation loss is significantly higher in pure Ti as compared to that in Ti(Si) at all temperatures of study. Furthermore, a comparison between Figure 21.22 with Figure 21.21 shows that the kinetics of cyclic oxidation is significantly higher as compared to isothermal oxidation in both as-received and laser surface-alloyed titanium for all temperatures studied. The higher rate of cyclic oxidation as compared to isothermal oxidation is attributed to the thermal stress-assisted failure due to the former mode of oxidation. A detailed kinetic analysis showed that the activation energy of oxidation ( $E_a$ ) of pure Ti,  $E_a$  is very high ( $=230 \text{ J/mol}$ ) at the initial period of oxidation ( $t \leq 120 \text{ h}$ ) following which it decreases ( $=190 \text{ J/mol}$ ). On the other hand, in Ti(Si),  $E_a$  increases from 260 to 312 J/mol from initial to final stage of oxidation.

The mechanism of oxidation has been extensively studied by phase analysis using X-ray diffractometry and microstructural studies with the help of scanning electron microscopy [28]. It was concluded that the enhanced oxidation resistance of laser surface-alloyed titanium with silicon up to 1050 K is attributed to the presence of a  $\text{SiO}_2$  at the scale-alloyed-zone interface. Moreover, the uniformly distributed  $\text{Ti}_5\text{Si}_3$  particles in the alloyed zone underneath may reduce the oxidation rate and provide an

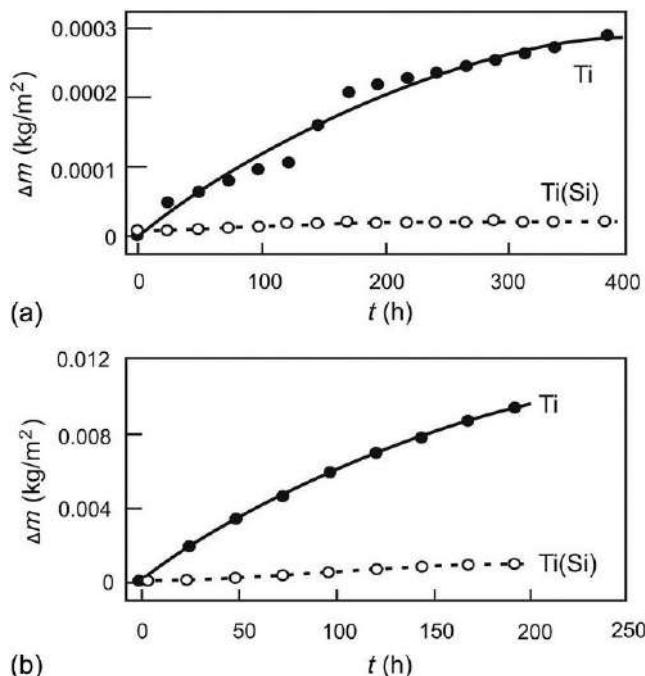


**Figure 21.22** Variation of the total weight gain per unit area ( $\Delta m$ ) as a function of time ( $t$ ) in Ti, and Ti(Si) following isothermal oxidation at (a) 923 K and (b) 1150 K, respectively [28].

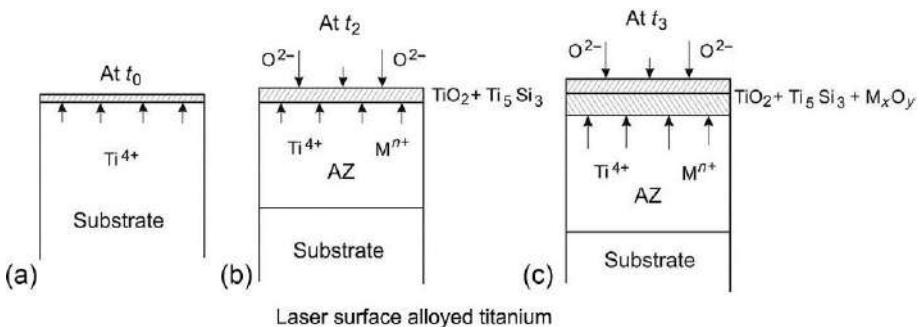


**Figure 21.23** (a–c) Schematic representation of mechanism of oxidation in as-received and laser surface alloyed (with silicon) titanium [28].

indirect diffusion barrier against the countertransportation of ions through the alloyed zone. Figure 21.23a-c shows the schematic representation of the mechanism of oxidation. From Figure 21.23 it is apparent that, initially, all the species (Ti or Si) would diffuse outward from the substrate to the external gas/oxide interface. According to the calculated required activity of oxide phases at the scale-metal

interface, titanium oxide followed by silicon oxide are the favored reaction products. On the other hand, oxygen species would diffuse inward to the oxide-substrate interface and react with Ti or Si to form  $\text{TiO}_2$  and increase the thickness of the  $\text{TiO}_2$  and  $\text{SiO}_2$  layer. Consequently, Ti or Si would be trapped at the oxide-substrate interface. With the growth of this double-layered oxide scale, there is a problem due to the difference in thermal expansion coefficients between the substrate and oxide. At the initial stage of oxidation, there is a good adherence between the substrate and oxide scale by the plastic flow of oxide scale. Because the plasticity of thin oxide scale is limited, cracks would form between the oxide scale and substrate once a critical thickness of the oxide scale is exceeded. The stress caused by the mismatch in expansion coefficients between the oxide scale and substrate can be released by cracking initially at the edges of the specimen and then expanding progressively through the entire specimen surface. The inner surface of  $\text{TiO}_2$  layer would no longer be saturated with Ti species. In contrast, the oxygen species would diffuse inward and, as a result, the partial pressure of oxygen in the crack would increase significantly and the equilibrium state of the O- $\text{TiO}_2$ -Ti would no longer exist. On the substrate side, the establishment of high-oxygen partial pressure in the crack would produce conditions favorable for the formation of a second  $\text{TiO}_2$  layer.

The resistance to wear of pure Ti and laser surface-alloyed titanium with silicon, Ti (Si) has been studied by: (a) determining the variation of the scratch depth with applied load and time of scratching, (b) monitoring the change in friction coefficient with load and time of scratching, and (c) investigating the microstructure of the scratched surface following wear. Finally, the mechanism of wear active for the present systems has been proposed. The variation of wear depth ( $z_{sc}$ ) with load ( $L$ ) due to scratching of pure Ti and Ti(Si), against a hardened 100Cr6 steel ball is presented in Figure 21.24. It should be noted that  $z_{sc}$  varies linearly with  $L$  for all the cases. The effect of  $L$  on  $z_w$  is more significant at higher  $n_{sc}$  (=1000) than that at a lower value of the same (=25). Ti(Si) undergoes the minimum wear loss. Figure 21.25 shows the variation of  $z_{sc}$  with  $n_{sc}$  (or  $t_i$ ) due to scratching at two different  $L$ . The extent and rate of wear increase with an increase in  $n_{sc}$  (or  $t_{sc}$ ), especially at higher  $L$ . Comparison of the scratch depth and slopes of the plots suggest that the rate of wear loss is maximum in Ti and minimum in Ti(Si). The coefficient of friction ( $\mu$ ) is expressed as:  $\mu = L/L_n$  (where  $L_n$  is the frictional force measured during the scratch testing operation).

Figure 21.26 shows the variation of coefficient of friction ( $\mu$ ) as a function of time of scratching ( $t_{sc}$ ) during a real-time wear test with an applied load ( $L$ )=40 N. Following an initial surge due to interlocking and smoothening of asperities to increase the real area of contact, a steady state wear initiates in all the samples nearly at the same instant of time. The extent of wear is minimum in Ti(Si) and maximum in pure Ti. In as-received Ti, the steady state wear is followed by a gradual decrease in the  $\mu$  value with an increase in  $t_{sc}$ . On the other hand, wear in Ti(Si) undergoes a low friction event following a sharp or gradual changeover from the steady state, respectively. This low friction event may arise due to partial lubrication offered by the three-body wear condition involving the worn out debris. It is anticipated that the softer phase in the two-phase eutectic aggregate in Ti(Si) facilitates accumulation of debris

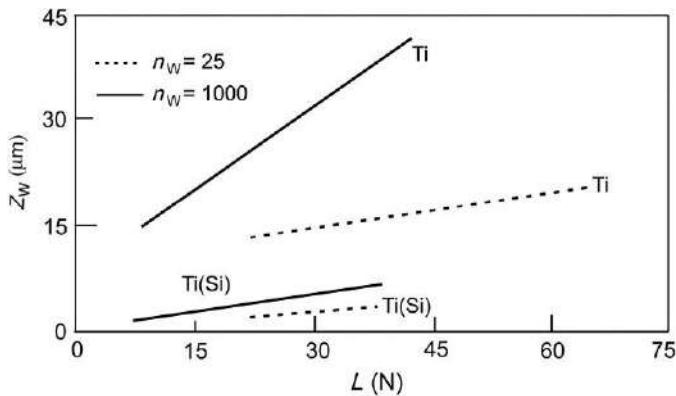


**Figure 21.24** Variation of depth of scratches ( $z_{sc}$ ) due to wear against hardened steel ball as a function of applied load ( $L$ ) in (a) pure Ti, and (b) Ti(Si). Note that scratch depth increases with an increase in  $L$  [26].

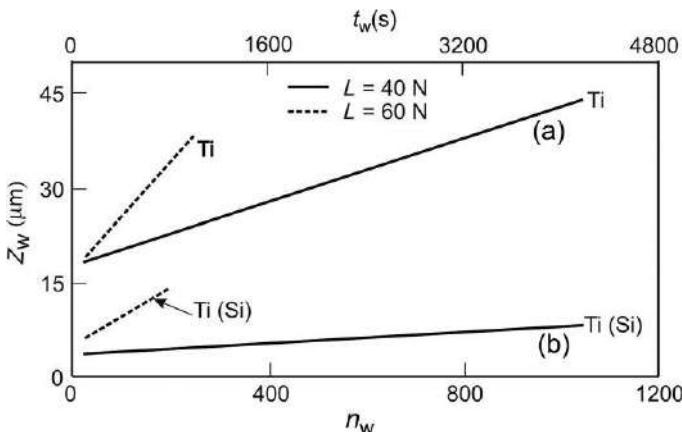


**Figure 21.25** Variation of depth of scratches due to wear against hardened steel ball as a function of number of cycles ( $n_{sc}$ ) in (a) pure Ti, and (b) Ti(Si). Note that scratch depth increases with an increase in  $n_{sc}$  under comparable conditions, and the damage is minimal in Ti(Si) [26].

at the initial stage, which subsequently acts as loose solid lubricant between the indenter and high silicide rich surface during the low friction steady state event. It is interesting to note that the  $\mu$  values for all the samples tends to coverage within a narrow range in the final stage (Figure 21.26). This may be attributed to a possible three-body wear condition at the final stage offered by the loose debris at the final stage.

Figure 21.27a-e schematically illustrates the general wear behavior of laser-alloyed samples investigated in this study. Accordingly, the overall mechanism of wear may be divided into the following four intermediate stages as shown in Figure 21.27e:

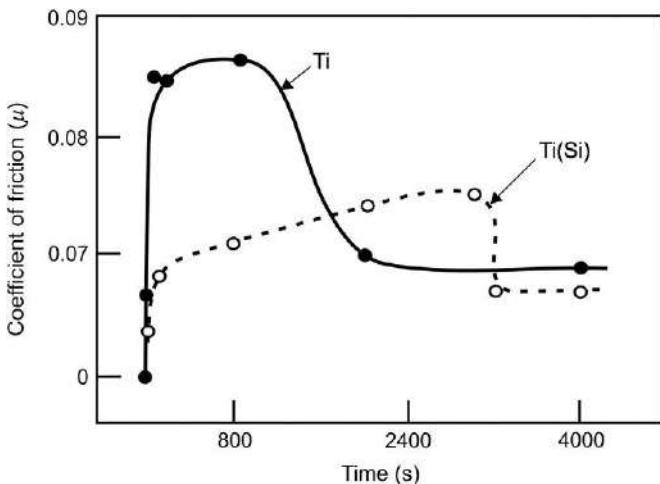


**Figure 21.26** Variation of coefficient of friction ( $\mu$ ) with time of scratch,  $t_{sc}$  on at an applied load,  $L=40$  N for pure Ti, and laser-alloyed titanium with silicon, Ti(Si) [26].

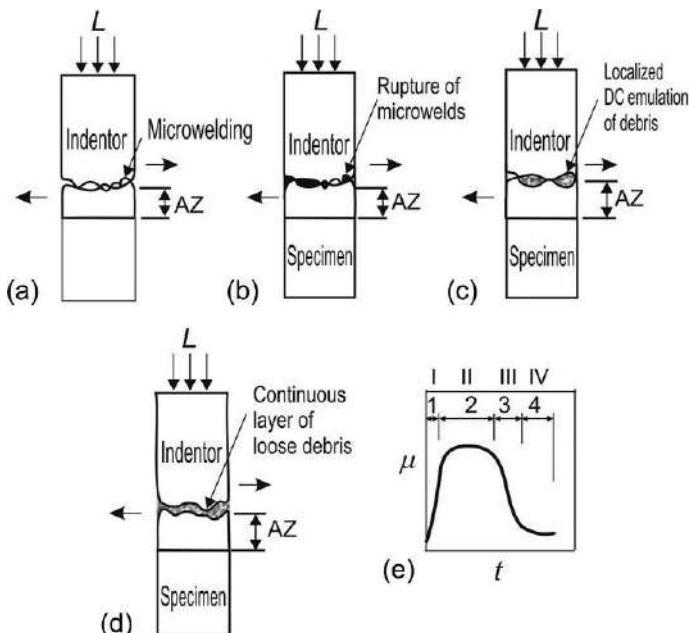


**Figure 21.27** Schematic illustration of the mechanism of wear in laser-alloyed samples: (a) interlocking and smoothening phenomenon (stage I), (b) adhesive wear (stage II), (c) low-friction event (stage III), (d) three-body wear condition (stage IV), and (e) variation of  $\mu$  with  $t$  showing the respective stages of wear [26].

- Stage I** Microwelding/interlocking phenomenon (sudden rise in  $\mu$ ): It causes an increase in  $\mu$  because of alternate sequence of interlocking of surface asperities and smoothening of the contact surface, leading to an increase in total area of frictional contact.
- Stage II** Steady state wear (constant  $\mu$ ): During this stage, wear starts due to adhesion or abrasion, depending on the nature of the contact surface and the surface contour, while  $\mu$  remains almost constant or slightly increases if the adhesive bonding between the interacting surfaces is high.
- Stage III** Low friction or interface wearing event (gradual decreases in  $\mu$ ): During this stage, the contact surfaces are set free due to detachment of worn-out debris as a result of which the  $\mu$  decreases.
- Stage IV** Three-body steady state phenomenon (constant  $\mu$ ): Once the worn-out debris get detached and occupy the space in between the contact surface, the system converts from a two-body to a three-body wear condition, during which  $\mu$  remains constant as the loose powder particles tend to act as lubricants and reduce wear.

Hence, it may be concluded that laser surface alloying with silicon is an effective way of improving high-temperature oxidation resistance (up to 1050 K) along with wear resistance property. The possible applications of laser surface alloying of silicon on titanium and its alloys include different components in aero engines like the fan and compressor discs and blades, ducts, and casings.

## 21.9 Conclusion and future trends

Laser surface engineering is an emerging technique for the tailoring of microhardness, wear, and corrosion resistance of titanium and its alloys by modification of microstructures and composition of the near-surface region. Laser surface melting is the simplest treatment for grain refinement and formation of metastable phase leading to improved mechanical and electrochemical properties of the surface. However, process parameters need to be optimized for reducing the surface roughness and minimization of residual stress level on the surface. Laser surface alloying of titanium and its alloys are another effective way to improve wear, corrosion, and high-temperature oxidation resistance of the surface. However, proper shrouding needs to be maintained and optimum processing parameters need to be selected due to high reactivity of titanium and the possibility of introduction of residual stress on the surface. In this chapter, it has been shown that laser surface nitriding develops a defect-free microstructure and improves corrosion resistance if it's designed properly and under optimum parameters. Similarly, surface alloying with silicon significantly reduces the high-temperature oxidation resistance of titanium and its alloys. However, systematic studies on the effect of microstructure (grain size and morphology, texture, and degree of metastability) on wear, corrosion, and high-temperature oxidation resistance properties need to be undertaken and correlated through a proper process modelling for optimization of process parameters. The role of the femtosecond laser processing on the microstructure and microtexture is another open area of investigation where attention is needed.

## References

- [1] R. Boyer, G. Welsh, E.W. Collings, Materials Properties Handbook—Titanium Alloys, ASM International, Materials Park, OH, 1994.
- [2] T. Bell, H. Dong, in: Proceedings of the 12th IFHT and SE Congress, vol. 2, 2000, p. 1.
- [3] W. Smith, Structure and Properties of Engineering Alloys, second ed., McGraw-Hill, New York, 1993.
- [4] E.W. Collings, The Physical Metallurgy of Titanium Alloys, American Society for Metals, 1984.
- [5] D. Eylon, S. Fujishiro, P.J. Postans, F.H. Froes, High-temperature titanium alloys—a review, *J. Met.* 36 (1984) 55–62.
- [6] R. Pederson, Microstructure and phase transformation of Ti-6Al-4V, (Licentiate thesis) Lulea University of Technology, 2002.
- [7] M.J. Donachie Jr. (Ed.), Titanium-Technical Guide, ASM International, Metals Park, OH, 1988.
- [8] K.G. Budinski (Ed.), Surface Engineering for Wear Resistance, Prentice Hall, New Jersey, 1988.
- [9] M.G. Fontana, Corrosion Engineering, third ed., McGraw-Hill Book Company, ISBN 0-07-100360-6, 1987 (Chapter 3, p. 67).
- [10] N. Briks, G.H. Meier (Eds.), Introduction to High Temperature Oxidation of Metals, Edward Arnold (Publishers) Ltd., London, 1983, p. 32.
- [11] A. Einstein, Stimulated and spontaneous emission, *Z. Phys.* 18 (1917) 121–128.
- [12] W.M. Steen, K. Watkins, in: Laser Material Processing, vol. 1, Springer Verlag, NY, 2003.
- [13] B.L. Mordike, in: R.W. Cahn, P. Haasen, E.J. Kramer (Eds.), Materials Science and Technology, vol. 15, VCH, Weinheim, 1993, p. 111.
- [14] J. Mazumdar, in: M. Bass (Ed.), Lasers for Materials Processing, North-Holland Publishing Company, New York, 1983, p. 113.
- [15] S.T. Picraux, D.M. Follstaedt, in: J. Narayan, W.L. Brown, R.A. Lemons (Eds.), Laser-Solid Interactions and Transient Thermal Processing of Materials, North-Holland Publishing Company, NY, 1983, p. 751.
- [16] J. Dutta Majumdar, I. Manna, Laser processing of materials, *Sadhana* 28 (2003) 495–562.
- [17] J. Dutta Majumdar, I. Manna, Laser material processing, *Int. Mater. Rev.* 56 (2001) 341–388.
- [18] J. Dutta Majumdar, I. Manna (Eds.), Laser Assisted Fabrication of Materials, Springer Verlag, Heidelberg, 2013, <http://dx.doi.org/10.1007/978-3-642-28359-8>. 516 pp.
- [19] Z. Sun, I. Annergren, D. Pan, T.A. Mai, Effect of laser surface remelting on the corrosion behavior of commercial pure titanium sheet, *Mater. Sci. Eng. A345* (2003) 293–300.
- [20] A.S.M. Handbook, Welding, Brazing and Soldering, vol. 6, ASM International, Materials Park, OH, 1993.
- [21] C.W. Draper, J.M. Poate, Laser surface alloying, *Int. Mater. Rev.* 30 (1985) (1985) 2.
- [22] A. Biswas, L. Li, U.K. Chatterjee, I. Manna, J. Dutta Majumdar, Diode laser assisted surface nitriding of Ti-6Al-4V: properties of the nitrided surface, *Metall. Mater. Trans. A Phys. Mater. Sci.* 40 (2009) 3031–3037.
- [23] A. Biswas, L. Li, U.K. Chatterjee, I. Manna, S.K. Pabi, J. Dutta Majumdar, Mechanical and electrochemical properties of laser surface nitrided Ti-6Al-4V, *Scr. Mater.* 59 (2008) 239–242.
- [24] A. Biswas, L. Li, U.K. Chatterjee, I. Manna, J. Dutta Majumdar, Laser assisted surface modification of Ti-6Al-4V for bio-implant application, *Surf. Rev. Lett.* 14 (2007) 531–534.

- [25] J. Dutta Majumdar, Laser surface alloying of titanium with silicon, aluminium and silicon +aluminium to enhance oxidation and wear resistance, (Ph.D. dissertation) TU Clausthal, Germany, ISBN 3-89720-385-5, 2000.
- [26] J. Dutta Majumdar, B.L. Mordike, I. Manna, Friction and wear behaviour of Ti following laser surface alloying with Si, Al and Si+Al, Wear 242 (2000) 18–27.
- [27] J. Dutta Majumdar, A. Weisheit, B.L. Mordike, I. Manna, Laser surface alloying of Ti with Si, Al and Si+Al for improved oxidation resistance, Mater. Sci. Eng. A 266 (1999) 123–134.
- [28] J. Dutta Majumdar, B.L. Mordike, S.K. Roy, I. Manna, High temperature oxidation behavior of laser surface alloyed Ti with Si and Si+Al, Oxid. Met. 57 (2002) 473–498.

This page intentionally left blank

# Laser-initiated ablation of materials

22

C. Dowding, A. Borman  
University of Lincoln, Lincoln, UK

## 22.1 Introduction

Ablation is the principle means of material removal when using pulsed lasers. Ablation is an obscure term; first, it is sensible to note its definition in the Oxford dictionary: “1. n. the loss of solid material by melting, evaporation, or erosion. 2. n. the surgical removal of body tissue.” [1]. “Ablatio” is Latin for “to remove” [2]. It is clear from these definitions that this is a blanket term to describe many instances.

Laser ablation was originally envisioned as a possible alternative or complimentary manufacturing technique to conventional photolithography; however, traditional engineering polymers, such as polymethylmethacrylate (PMMA), polyimide (PI), or polycarbonate (PC) have severe limitations, including low sensitivity, carbonization during irradiation, and ablation-generated debris issues [3,4].

Laser ablation is the irradiation of a material causing removal of said material [5] with accuracies as resolved as one monolayer per pulse [6]. This accuracy enables its use in micromachining, for industries such as biomedical (such as controlled removal of tissue [5]) and material sciences [6], mass spectrometry and the construction of new microartificial structures [5] such as the *via* holes on circuit boards [7]. The energy absorbed by the target material converts the material to either a liquid that is expelled from the material through recoils or else a vapor, expelled through pressure.

While it can be flexible in its uses as well as cost-effective [7], an understanding of the chemical physics involved in laser ablation is, as yet, incomplete [8]. This is, in part, due to the difficult nature of ablation to simulate with the potential of 10-1000 atoms to simulate in an ablation event [5].

Zhigilei describes an approximate process for laser ablation as excitation (by laser) of molecules that transfer energy to modes in the solid, causing disintegration and forward ejection and formation of a plume, noting the complexity of the event and, hence, the difficulty in modelling such a system, leading to varied assumptions as the starting point for discussions on the subject [5].

The ejection of material begins within picoseconds, thus, unless picosecond laser pulses are being used, the end of the pulse will irradiate the ejected material [8]. This results in both attenuation of the beam and excitation of the plume, resulting in plume ionization, forming a plasma [8].

## 22.2 Mechanisms involved in ablation

Both ablation threshold (the minimum amount of energy required for ablation to occur) and ablation rate are dependent upon the mechanism of ablation being followed [9] with lower fluencies meaning lower rates of ablation [10]. The ablation rate and threshold can be calculated following the procedures of Dyer [11].

Liu *et al.* [12] note in their work that ultrashort laser pulses, capable of greater intensities, are both able to micromachine to more precise tolerances as well as facilitate modelling of their mechanisms more easily through the absence of any fluid dynamic contributions. In their work, Liu *et al.* defined a short pulse as less than 1 picosecond. Regarding longer pulses, the mechanisms behind ablation are somewhat different with the generated plasma plume absorbing a greater amount of energy. Yang [13] specifies that in pulsed laser ablation, the gaseous products from the solid target material subsequently condense to form a plasma plume, therefore, at a macroscale, elements of the mechanism are understood. Furthermore, Kelly and Miotello [14], when considering specifically UV ablation at 248 nm, state that both photochemical and photothermal interactions are taking place between photons and the atomic matrix.

With the fact that mechanisms are governed by many variables, some of these shall be discussed below; however, no single complete mechanism for ablation of a material can be outlined, as there are too many permutations. Ablation caused by short pulse laser-material interactions are dependent upon the photon absorption depth, not the thermal diffusion of the material that is critical for these short (nanosecond) pulse lengths [13]. The main stages of the debris highlighted by Dowding and Lawrence [10] are generation, transformation, and condensation.

- (a) Generation begins with absorption of energy. At the focal point of the laser, material is heated to melting point with the possibility of continued heating to vaporization point, dependent on intensity and pulse width of the beam [12]. Both linear and nonlinear mechanisms are involved in this process, dependent on factors such as the transparency of a material and the number of free electrons it contains. The initial phase of the pulse will instigate ablation; the gaseous materials ejected from the target will form a plasma, as depicted in Figure 22.1a. The plasma formed will be partially confined by the surrounding gaseous environment; however, continued ablation and excitation of the plume will cause the plume to expand, as shown in Figure 22.1b.
- (b) Transformation. The ablated species originating from the target material are not suspended in the plasma plume. Because both the plasma and the surrounding environment are gaseous in nature, the two tend to mix. The high energy and temperature state of the plume allows chemical reactions to occur between molecules from the two substances to form new compounds. The latter part of the pulse adds energy to instigate these reactions; the mixing of the gas and plume continues after the pulse has ended and the next phase begins, as described in Figure 22.1c.
- (c) Condensation. The heat contained within the plume begins to diffuse into the surrounding environment at the end of the pulse. The intense thermal diffusion of the species in the plasma plume can result in collisions, leading to aggregations. Thus, thermal diffusion is also critical in transformation, before eventually leading to condensation of the new mixed species into melt form and finally to solidification resulting in particulate matter, as shown in Figure 22.1d.

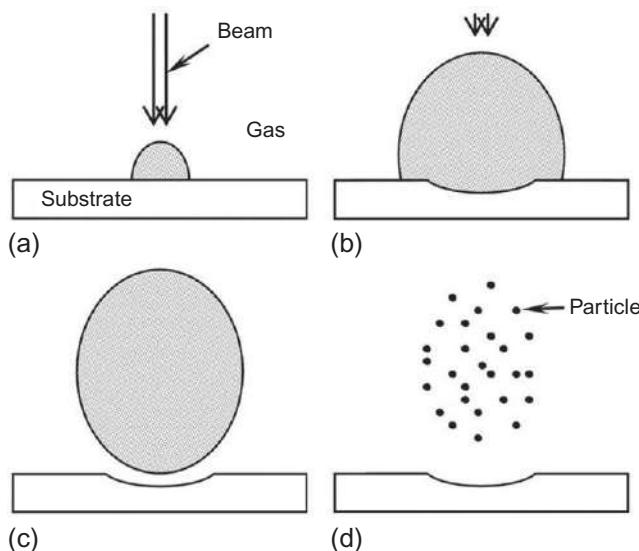


**Figure 22.1** Schematic diagram of the four stages of PLA in gasses: (a) initial phase of the beam interaction; (b) further irradiation; (c) pulse ends; and (d) plume condenses to form multiple nanoscale particulates [13].

It must be noted that this entire process is completed in just a few nanoseconds, being complete in time for the beginning of the next pulse and the start of another of these cycles.

In transparent materials, the initial mechanisms of ablation are nonlinear. Because transparent materials hold many bound electrons, the absorption of energy through these is minimal. Impurities, photothermal and photochemical ionization introduce free or conduction electrons into the medium. While these free electrons cannot absorb energy directly from the laser easily, they can absorb energy from collisions with the lattice structure of their host material. When a free electron has gained enough energy through such collisions, a further collision results in a transfer of the free electron's energy, giving a bound electron enough energy to escape its atom. If this occurs, where once there was one free electron, there will be two by the end of a single mechanism. Therein, both free electrons can complete the cycle once more and the number of free electrons grows exponentially. When the number of electrons released is great enough, transparent materials become absorptive and irreversible breakdown and ablation of the material begins [12].

Energy transferred to the material increases the temperature, diffusing along a thermal gradient from the focal point. The pulse length and area of the heat-affected zone are proportional. Longer pulse lengths tend toward possessing a larger area of melt, yet a smaller area of vaporization [12].

In contrast to this, short pulse lengths used in ablation result in electrons being driven to high temperatures, significantly higher than that of the surrounding ions. The electrons transfer the heat energy to ions in the material through collision,

continuing their heating effect after the pulse has finished; heating the material to higher temperatures than would be reached with a longer pulse. As a result of this, the melt phase is completed extremely quickly with a large transition to vaporization. The area is smaller and more precise due to the shorter nature of the pulse.

Alternatively, metals and semiconductors on the other hand have a greater number of free valence electrons that enable Joule heating, a process whereby energy is absorbed linearly. The rate of heating is determined directly from the rate of heating by the laser minus the rate of loss from the material to its surroundings [12].

Irrespective of pulse length, energy deposition occurs in a layer with thickness related to the penetration depth. This is governed by the absorption coefficient of the material [12]

$$l_s = \frac{1}{\alpha} \quad (22.1)$$

where  $l_s$  is the thickness of the layer the absorbed energy initially penetrates and  $\alpha$  is the absorption coefficient.

Heat then diffuses through the material in a layer of thickness,  $l_d$ . This variable is governed by the heat diffusion coefficient,  $D$ , as well as the laser pulse width,  $\tau_1$ , in the equation [12]

$$l_d = \sqrt{D\tau_1} \quad (22.2)$$

These critical dimensions are illustrated in Figure 22.2. For long pulses, the diffusion layer is thicker than the deposition surface layer thickness; therefore, the temperature is governed by the heat diffusion thickness [12]. For shorter pulses however, the layer of absorption is greater than the layer of diffusion during the pulse, making temperature during short laser pulses reliant on the absorption coefficient but independent of the pulse width and, thus, not the heat diffusion depth [12].

To summarize, long pulse length ablation causes large volumes to be heated and melted. Driven by vapor pressures, resolidification of melt leads to irregularities in the finish. Short pulse ablation conversely relies upon direct vaporization to remove material from the sample, because heat diffuses over a smaller thickness and plays a lesser role resulting in lower liquid generation, making the ablation more precise [12].

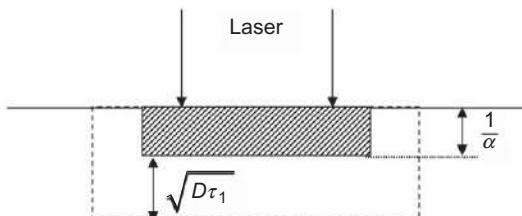


**Figure 22.2** Schematic diagram of the absorption and thermal diffusion depth of an incident laser pulse.

## 22.3 Demagnified image ablation machining using excimer laser beams

The excimer laser offers great potential for the use of fine-image etching because of the fundamental attributes of the typical cavity output: large cross-sectional beam area; high energy density; short wavelength (and small associated thermal dissipation depth); and easily variable pulse energy and repetition rate. However, to access these attributes, some potential barriers must be overcome: approximately Gaussian cross-sectional beam energy distribution; often nonsymmetrical cross-sectional beam dimensions; and relatively high beam divergence. All of these barriers can be corrected or ignored due to their minimal impact upon machining quality. This section will describe common mitigation techniques for these issues.

### 22.3.1 *Modifying the cross-sectional beam dimensions to suit the imaging technique*

The fundamental beam dimensions generated by the laser may not be ideal for the features to be machined or the process to be used to achieve those features. To correct this, the beam can be expanded or reduced along one or more (rarely more than two) axis. For instance the laser used in the laboratory of the Photonics and Laser Engineering Group at the University of Lincoln (LPX120i, Lambda Physik, GmbH.) has the fundamental beam dimensions of  $23\text{ mm} \times 6.3\text{ mm}$  at the cavity exit for 248 nm radiation. The users of this laser find it most convenient to image using a square beam profile; hence, the optical system has been designed to expand the beam in one axis to have the corrected beam dimensions of  $23\text{ mm} \times 23\text{ mm}$ . Obviously, the optical design is utterly dependent upon the specific output characteristics of the specific laser being used.

### 22.3.2 *Preparing the cross-sectional beam energy distribution for imaging*

Laser mask imaging can be considered by using the analogy of a spray paint canister. If the user were to use a stencil with the spray delivery method with a desire to uniformly cover a shaped area of surface with paint, it would be ideal if the paint was to be evenly distributed across the cross section of the ejection cone, as shown in [Figure 22.3a](#). However, the excimer spray canister delivers its paint with a Gaussian paint distribution, as given in [Figure 22.3b](#). This is because of the fundamental cavity characteristics of the laser (which uses spherically dished mirrors for focusing resonating light within the cavity to ensure maximum lasing efficiency).

There are two common optical solutions to this problem; both involve “mixing up” the cross-sectional distribution of energy within the beam. The first employs an optical toy familiar to most children: the kaleidoscope, which is shown in [Figure 22.4](#). This technique is commonly installed in output optical train of laser systems (hence

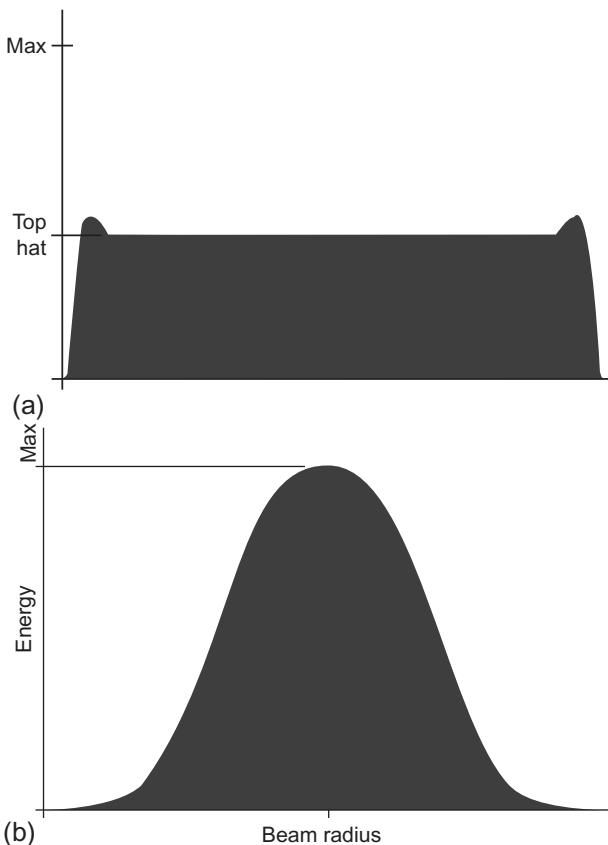


**Figure 22.3** Schematic plot describing across a single axis: (a) “top hat” cross-sectional beam energy distribution and (b) Gaussian cross-sectional beam energy distribution.

allowing them to deliver a nominally “top hat” profile) that are intended for laser micropatterning applications. This technique is simple to arrange, has no prerequisite for a specific beam shape, and is relatively robust; but has the disadvantage of resulting in relatively high losses (as every reflection has an optical efficiency). It should be noted that an optical fiber can also offer the same homogenizing function to a laser beam, giving an extremely uniform energy distribution across the cross section of the fiber due to the large ratio between fiber length and diameter.

The other common technique is the application of microlens array homogenizers. These use the refractive property of lenses to expand the beam to varying degrees with respect to the position of the microlens in the input beam, as shown schematically in [Figure 22.5](#). Notice that in the case of [Figure 22.5](#), the overall beam dimensions are changed; this is not an absolute requirement of homogenizing lens arrays for functionality, but is very common. As a result of this overall dimensional reduction, the final beam dimensions at the mask of the University of Lincoln excimer laser system are 12 mm × 12 mm. Microlens arrays are normally applied externally to the laser source

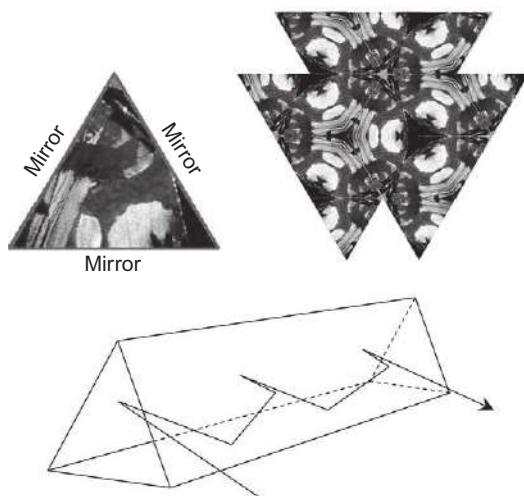


**Figure 22.4** A schematic diagram describing the input, arrangement, optical path, and result of applying a kaleidoscope for the purpose of laser beam homogenizing.

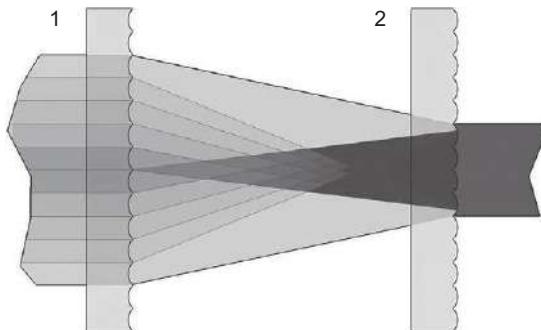


**Figure 22.5** Schematic diagram of the operation of an optical homogenizer across a single plane; the diffuser lens array (1) mixes the differing local energy densities of the beam into a single, homogenous whole, at which point a collimating lens array sets the output beam energy distribution.

(allowing a high degree of user control, but less functional stability) and must be adjusted regularly to cater to operational drift of the laser.

The specific application of these must be chosen with respect to the input beam characteristics. If the input beam has only one axis of symmetry, two sets of linear homogenizing lens arrays must be applied: one pair for the horizontal plane and a second pair for the vertical plane. If the input beam has two (or more) planes of symmetry (as the University of Lincoln system has because of the single-plane beam expansion in [Section 22.3.1](#)) a radial homogenization can be performed, requiring just one pair of homogenizing lens arrays for total beam energy density uniformity. This second technique is cheaper than linear homogenization, because microlens arrays are costly to manufacture.

### 22.3.3 Beam masking

The geometry of the features to be machined are most commonly depicted by a boundary area of chrome that is electroplated onto a thin quartz plate (for wavelengths greater than 308 nm, high-purity fused silica is sufficient), as shown in [Figure 22.6](#). The geometry to be machined is able to pass through the transparent mask base material (quartz or fused silica) and unwanted laser energy is reflected by the chrome layer.

This reflected energy could pose a risk to the laser, hence, it is common practice to place a low-magnification “field lens” just before the mask to expand any reflected light to a level that is so defuse at the laser that no damage can result. The field lens specification is also often chosen to correct (or slightly overcorrect) any beam divergence that is existent in the beam.

Following the mask, the beam is demagnified by a desired ratio, as shown in [Figure 22.6](#), to yield microfacsimiles of the masked feature geometries. The diffractive limit of the laser wavelength being used limits both the minimum feature size that can be transmitted through the mask and the minimum feature detail size that can be machined. As a result, narrow triangular structures are best avoided when using masking techniques.

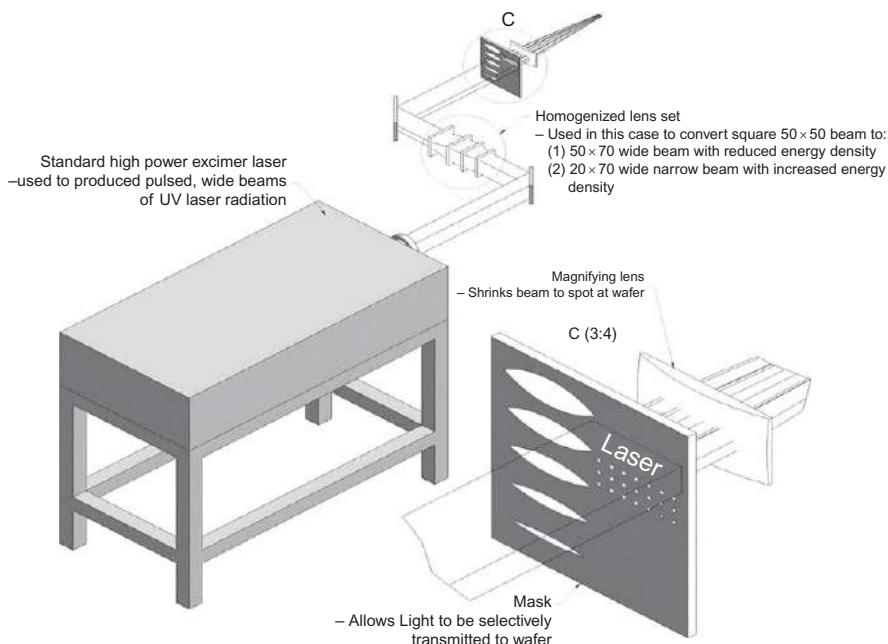


**Figure 22.6** Technical drawing of a hypothetical excimer laser mask imaging system that modifies a square source beam to a rectangular, homogenized beam that is masked and demagnified.

### 22.3.4 Applications of laser beam mask imaging techniques

The beam manipulations described in this section are the foundation for a number of technologies that can produce 2-D features, 2-D feature arrays, and even arrays of 2.5-D features. 2.5-D features have geometry that can be controlled in width, length, and height, but cannot include undercuts. Two commonly applied techniques are producing 2.5-D feature arrays are known as mask dragging [15] and synchronized image scanning [16]. Mask dragging is a fast and repeatable noncontact method for producing complex shaped troughs in materials *via* the process described schematically in [Figure 22.7](#). Synchronized image scanning relies on exactly the same principle but relies upon horizontal steps between pulse locations that match the largest plan dimensions of the feature being machined; thus, allowing feature contours to be machined on top of each other to produce fully defined 2.5-D feature arrays as shown in [Figure 22.8](#).

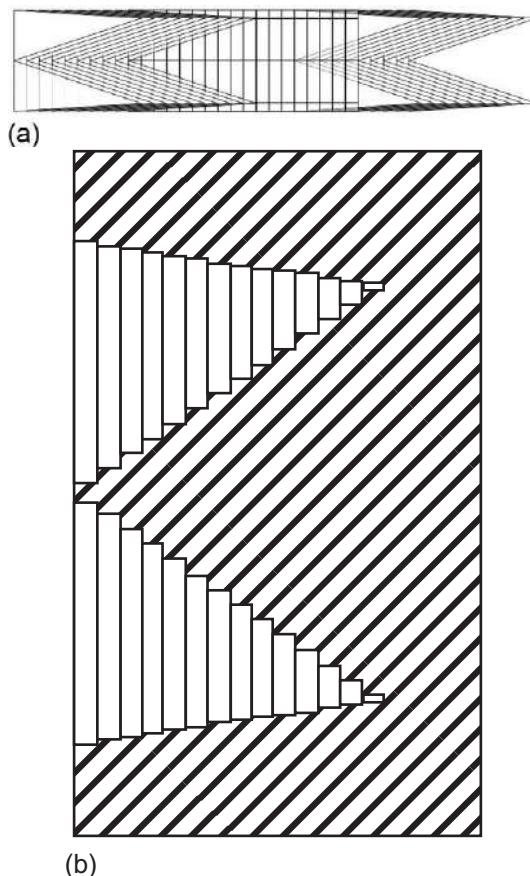


**Figure 22.7** Schematic representation of (a) the pulse locations of a mask dragged trough, resulting in (b) the cross-sectional trough geometry in the material.

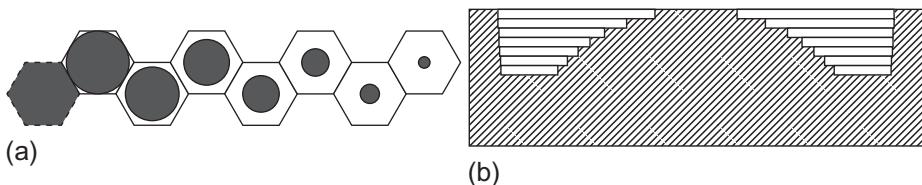


**Figure 22.8** Schematic synchronized image scanning diagrams of (a) the mask pattern required to machine a basic microlens geometry where the colored circles are reflective to the incident beam; and (b) the resulting cross-sectional layers.

## 22.4 Issues arising from ablation

Arising from ablation, there are multiple issues dependent on the material interface between which ablation happens: the size of hole, depth achieved, taper, level of contamination, degree of thermal damage, and amount of cracking can vary [17]. Additionally, the plume ejected from the surface continues to interact with the ‘ablating laser, attenuating the beam [8] and, thus, reduces the effectiveness and efficiency of the process.

### 22.4.1 Ablation product trajectory

Equally important as the phase and chemical composition of the ablation product are the speed and flight path of the material. Knowledge of this issue allows prediction of where to concentrate efforts toward material removal for a given situation.

Weisbuch *et al.* examine the ablation products of a KrF laser with microcrystalline PET [18]. A subsequent review of the samples machined during these experiments demonstrates an apparent melt phase ejection from the ablation zone, with spatter patterns extending radially from the shot area. The work of Weisbuch *et al.* [18] is supported by Yung *et al.* [9], who explore the interaction of a 355-nm-wavelength pulsed beam with Vectra A950, a liquid crystal polymer, and the topographical and chemical modifications caused by this interaction. At low fluences, close to and just above the threshold value, no surface melting is evident, suggesting that in this situation photochemical decomposition dominates the ablation process. However, melting becomes more apparent in the samples as fluence is increased. Melt is indicated by solidified radial spatter surrounding the ablation zone. This result suggests that photothermal reactions become more dominant in the ablation process with increasing fluence. Yoo *et al.* [19] postulate a reason for the ejection of materials from the ablation zone: evaporation is thought to take place both on the irradiated surface and in the superheated melt produced during the initial period of the pulse. This event has become colloquially known as “explosive evaporation.” This process is covered in detail by Dyer *et al.* [20] who investigated the interaction of a KrF beam with a metallic ceramic film and also cite the explosive evaporation mechanism as being responsible for the debris created in that scenario. First, strong superheating of the surface liquid layer occurs under the nonisotropic conditions of pulsed

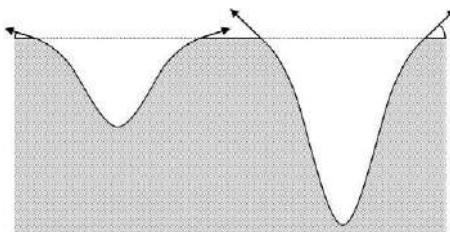


**Figure 22.9** Graphical representation of the relationship between ejection angle and crater depth for a Gaussian laser beam profile [9].

laser irradiation. Heat loss by boiling within the liquid layer is prevented, as the local vapor pressure is too low to support bubble growth from atomic scale voids. Secondly, ablation commences at a maximum superheating temperature, where the tensile strength of the liquid falls to zero. Pressure fluctuation in the liquid then instigates explosive boiling.

The recoil pressure developed by the evaporation of the superheated liquid expels mass molten material from the ablation zone. The depth and shape of the crater are critical in the angle of ejection of the materials, as described in Figure 22.9, where the ejection angle ( $a$ ) for the shallow crater is smaller than the ejection angle ( $b$ ) for the deep crater. The depth of a crater is directly related to two variables: the ablation rate and the number of pulses over the same area. Bauerle [21] has formulated a relationship to predict the ablation depth of a single pulse. This model of the ablation rate was found to closely approximate the experimental results of tests conducted, except for low fluences, where the absorption coefficient fluctuates with laser fluence.

Torrissi *et al.* [22] examined the normalized yield of ablation products at a range of angles away from the normal to the target surface, which in this case is a copper plate. The results clearly show that over half of the ablation products are ejected in a  $40^\circ$  range around the normal to the material surface. Furthermore, at angles greater than  $30^\circ$  from the normal to the copper plate, as shown in Figure 22.10, there is very little possibility of ablation products being ejected through that angle. This distribution would tend to support the theory of Yung *et al.* [9] described in Figure 22.9. This is important, as this knowledge allows for the assumption to be made that control of debris is only important at a  $90^\circ$  range around the normal to the surface being machined.

#### 22.4.2 Size and form of ablation products

During ablation large amounts of gaseous products are ejected, but these carry both liquid and some solid products via entrapment. These products are deposited on the area surrounding the machined area in a manner similar to that shown in Figure 22.11. Some research has used lasers specifically to produce particulate debris for use in other research fields. Ullmann *et al.* [23] examine the relationship between laser parameters and the debris produced from various ceramics and metals in a number

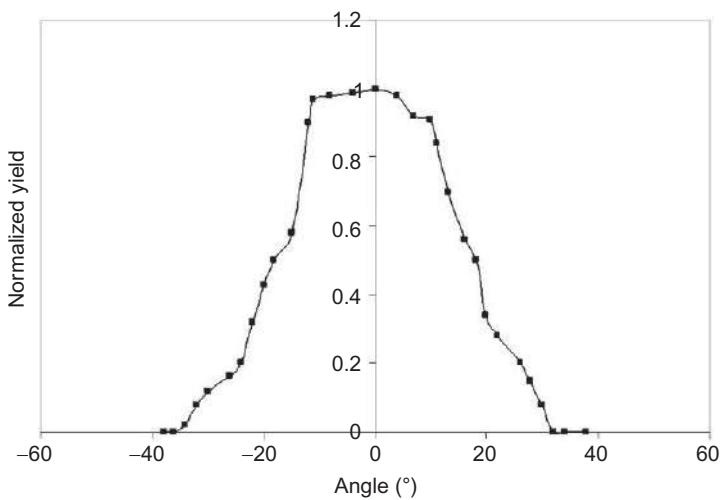


**Figure 22.10** Plot depicting the yield/trajecory angle of particles ejected from the ablation spot [22].

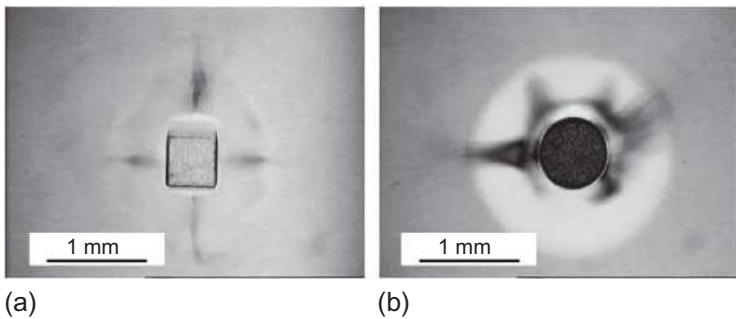


**Figure 22.11** Deposited debris surrounding a KrF excimer laser ablation machined area on bisphenol A PC using a (a) square and (b) circular mask.

of carrier gasses, claiming that the purity of particles produced is governed by the purity of the carrier gas and target material itself. Gartner *et al.* [24] generated  $\text{Y}_2\text{O}_3$ ,  $\text{SiO}_2$ , and  $\text{Cs}_2\text{O}_3$  nanoparticles with mean primary particle size between 4 and 40 nm dependent upon gas pressure and velocity over the ablation zone. Sasaki *et al.* [25] achieved control of particle size and composition of calcium-iron oxide particles by varying the gas pressure from 0.133 to 133 Pa, particle size increasing with pressure from 2 to 26 nm, while the Ca/Fe reduced from 0.9 to 0.2 during the same pressure change. Ogawa *et al.* [26] showed that an increase in flow rate produces smaller aggregates and smaller primary particles, but at an increased number concentration. Also increased pulse energy results in an increase in aggregate size. Similar effects were achieved with increased pulse frequency. The geometry dependent deposition pattern that is clearly evident in Figure 22.5 is interesting. Dowding

and Lawrence [27] propose a hypothesis for this phenomenon based upon the interaction ablation seed nodes in varying feature shapes.

Larger particles can form from coalescence of multiple smaller particles [23] or from the solidification of molten ablation products [9,18]. The collision of primary particles at a high temperature early in the cooling process leads to coalescence. As the gas cools, coalescence ends and further particles that collide with the new body tend to adhere themselves to the main body and form aggregates; this aggregation process can then continue to build larger composite debris. The aggregation process could also perceptively occur for melt products that solidify before landing back on the substrate surface.

The work of Bereznai *et al.* [28] supports the claims of Ullmann *et al.*: B<sub>4</sub>C was ablated with an ArF beam. Low fluences produced mostly particles of less than 20 nm diameter. Increasing the fluence up to approximately 2 J/cm<sup>2</sup> the size of the particles produced did not change; however, the amount produced did increase. Above this fluence the mean size of particles produced begins to increase, with a reduced population of smaller debris.

#### 22.4.3 Debris deposition

Without liquid submersion, both Van der Waals and electrostatic forces act to hold particles to the material surface [29]. Dowding and Lawrence concluded that strong arguments were made for liquid immersion to reduce Van der Waals and electrostatic forces [27]. In ablation using liquids, Sasaki and Takada [30] note the colloidal suspension of nanoparticles and constraint of plume formation by the liquid itself. Dowding and Lawrence [27] note the four main stages of immersion ablation as interaction of the laser with the material generating a plume; confined expansion of the plasma by the liquid, as also noted by Sasaki and Takada [30]; chemical reactions between the confined plasma and liquid; and, finally, colloidal particle formation. Without immersion, the plume would form and attenuate the beam in a similar way initially. This would lead to increased heating and expansion of the plume, due to lack of confinement, followed by thermal diffusion, condensation, and eventual plume collapse [31].

### 22.5 Possible solutions to such issues

The resolution of the plasma plume attenuating the beam may be overcome through the use of immersion in flowing liquid; in the case of Dowding and Lawrence, deionized water [10,27], which yielded the reduction in debris shown in Figure 22.12. When immersed, homogeneity of the debris increased, deposition occurring in ripple patterns consistent with fluid transport [27], contrasting with nonimmersed deposition patterns. Suggestions made by Dowding and Lawrence include the idea that increasing flow rates and eradication of surface ripples could lead to increased accuracy as well as better debris control [27,32]. Immersion does, however, both increase the

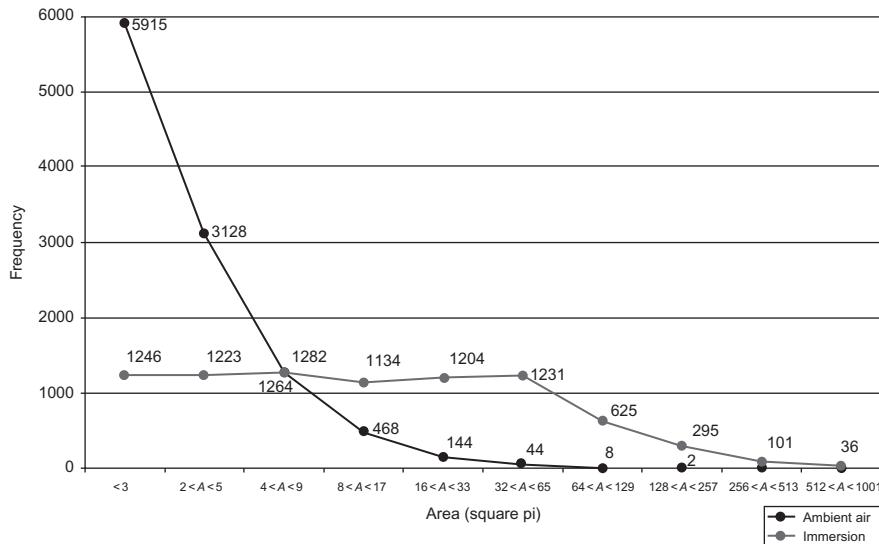


**Figure 22.12** Debris reduction achieved around a sample machined using KrF excimer laser ablation under flowing thin film deionized water immersion.

threshold fluence for ablation as well as decrease the rate of ablation, even when using fluids with insignificant attenuation effects themselves, such as deionized water [10]. This change in rate was theorized to be due to plume confinement by the immersion, leading to increased inverse Bremsstrahlung attenuation and a decreased etching rate from the plume when compared to a thicker immersion layer, which usually results from increased pressure from confinement of the plume [10]. Thin film immersion did, however, yield a reduction in the range covered by debris as well as increasing particulate size from an average of 3-4 square pixels in open air to between 33 and 71 square pixels [27]. With reduced small debris and greater proportions of larger debris, cleaning and removal is easier, because a greater amount of force can be applied to larger debris [27].

Reduction in surface ripples was deemed to be necessary to increase immersion ablation accuracy [27,32], Dowding *et al.* examined a closed water immersion system [32]. Here, the closed immersion (in this case filtered water) showed no splashing and, hence, a repeatable set of machining conditions with the effect of varying flow velocity being studied. A closed system, compared to ambient air, demonstrated 53% pressure increases [31] as well as a plume with a longer existence, increased thermal effects, and increased density leading to increased attenuation and, hence, increased temperature. A reduction in depth of focus was also noted; this, not being attributable to the additional equipment used compared to ablation in air, was attributed to the effect of plume etching [31].

Closed flowing immersion techniques delivered a far superior solution to open thin film flowing techniques, as shown in Figure 22.13, indicating a 93% decrease in debris and increase in average particle size, attributed to gas microbubbles caused by the

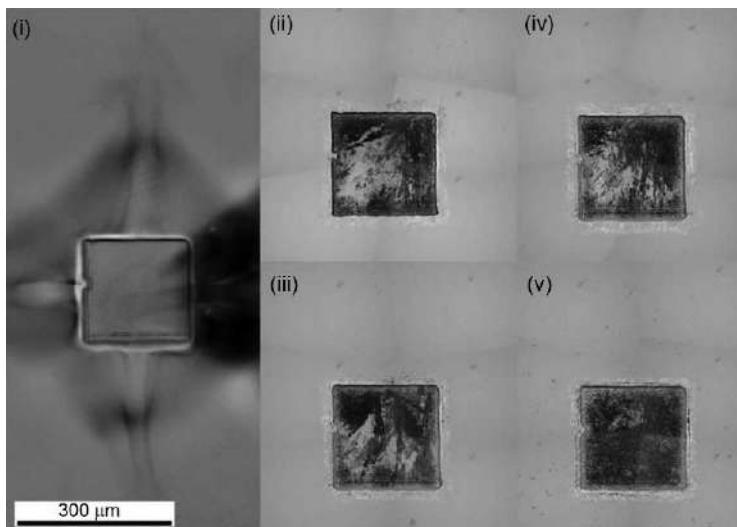


**Figure 22.13** Comparison between features machined by KrF excimer laser under (i) ambient air; (ii) 3.70 m/s flowing filtered water; (iii) 2.78 m/s flowing filtered water; (iv) 1.85 m/s flowing filtered water; and (v) 0.03 m/s flowing filtered water.

plume dispersion, cooling, and contracting, bringing together debris particles that bond through capillary action and Van der Waals intermolecular forces to form medium-sized debris from the small debris. These same mechanisms were too weak to combine medium into larger debris. Thick, closed immersion outperform thin, open immersion as debris control techniques [32]. Dowding *et al.* suggested there are several possible reasons for this: prevention of fluid rupture, leading to a more stable mechanism; symmetrical drag from all boundaries of the immersion, maintaining that particles were not subjected to turbulent forces guiding them to a surface; and a different fluid being used compared to the thin, open immersion [32].

Within the thick, closed system, deposition was found to be variable with fluid flow: laminar flow gives a more even distribution than air whereas turbulence transported debris downstream. However, population size was found to be inversely proportional to flow velocity [32]. Dowding *et al.* suggested that lower flow rates suspend particles within the working area of the beam for a longer duration, interacting and lowering the fluence across the work area and, thus, decreasing both the etch rate and, hence, the amount of debris produced [32]. Regarding distribution, for any given flow velocity, large debris is displaced more than small debris, the latter being affected to a greater extent by turbulence, which was the influential factor in debris distribution at high flow rates; whereas, at lower flow rates the immersion was less effective [32]. Dowding *et al.* found the optimum flow rate for debris control for the thick, closed system to be  $1.85 \text{ m s}^{-1}$ .

The choice of liquid is important. Chang and Molian [17] noted self-focussing, chemical reactions, pressure waves, and thermal quenching as causes of some of the issues when considering different liquid immersed ablation events. Their study

compared methanol and ethyl alcohol to air and demonstrated the differences in geometry of hole, zone of thermal damage, and amount of cracking when using liquids instead of air.

Liquid is not the only change in atmosphere that can occur. Chang and Molian [17] suggest that, while ablation in air produces particulate contaminants, a vacuum environment for ablation may both eliminate contamination as well as improve ablation rates. Lazare and Granier [33] showed that the ablation rate was not to be influenced to a significant degree by the surrounding atmosphere, though the threshold fluence was higher in a vacuum than in ambient air, particularly at longer wavelengths. Spiess and Strack [34] go on to demonstrate that, whether in ambient air or a vacuum, debris is always present to a greater or lesser degree. The composition of debris is dependent on the oxygen concentration in which the ablation is occurring. Using similar debris control methods to Dowding *et al.* [32], Spiess and Strack used a purge gas in their study nitrogen or oxygen, passing over the top of the ablation zone through a 5 µm opening at 3.5 bar. As with liquid immersion [32], the particulate debris was shown to be deposited in the direction of the gas flow, concentrated beyond the area exposed to the laser beam [34].

Techniques that do not require immersion of the target sample into an environment alternative to ambient air may make use of postablation processing techniques to remove the debris. These techniques include the use of laser irradiation, such as techniques by Koren and Donelon [35] using CO<sub>2</sub> lasers, absorbed strongly by the debris yet significantly less strongly by the PI, therefore, doing no damage to the finished product while cleanly removing the debris.

Gu *et al.* [36] also make use of laser irradiation in the form of a frequency doubled Nd:YAG at 10 Hz, showing it to shorten the postablation cleaning cycle. Their technique also demonstrated no damage to the substrate and lower oxygen/carbon ratios than other cleaning methods; hence, demonstrating the effectiveness of this laser at this wavelength in debris removal [36].

A further postablation debris removal technique examined is the electrostatic collection of the debris postprocessing [37]; Von Gutfeld and Srinivasan examined the use of 150 µm tungsten wires, thin (0.5 mm depth) and thick (67 mm depth) plates with variable high voltages up to 10<sup>3</sup> V to collect the debris from ablation. With a standard separation of 10 mm, the wire was found to have 2.5 times the field strength of the plates. Results from this showed “very little (if any)” debris remaining on the PI surface when using voltages of 300 V or greater [37]. Observations of structures formed on the surface of the electrodes from the particulates suggest the initial collection points for the first molecules become high-intensity field points, acting as nucleation sites upon which further particulates can bind. These structures grew both thicker and spread more branching structures with higher fluencies to a point with densification of the structures also observed. For high fluences, black structures postulated to be carbon-based on previous studies [38] were observed, and higher fluences still noting a thinner structure once more that extended further [37].

When comparing the positive and negative electrodes, von Gutfeld and Srinivasan found approximately equal numbers of particulate debris collected on each; the population increased approximately proportionally to the voltage applied across the

electrodes. This fifty-fifty distribution of the debris lead to two possible mechanisms being suggested: the charging of neutral molecules *via* triboelectric friction from high numbers of collisions, or the plasma formed from the laser pulse charging neutral debris as they come into contact with each other. Further examination of the debris distribution on the electrodes and comparison with models suggested the second mechanism was more likely [37].

Other collection techniques include debris collection *via* a localized vacuum nozzle [39] or chemical treatment following processing in the successful removal of all debris from ablated PI through the use of acetone [34]. When considering which approach to take with regards debris, it should be considered that additional, postablation cleaning leads to extra processing steps and is, therefore, undesirable [39]. A technique wherein the debris does not contact the substrate at all in the first place would not require additional processes postablation.

Ablation does not only require the use of lasers; one patented method that has been developed for collection of debris from ablation by charged particles accelerated to ultrasonic speeds involved the triboelectric effect to attract the charged debris from the ablation zone [40,41].

## 22.6 Methods of examining ablation mechanisms

There are three commonly practiced methods for attempting to identify and understand the ablation mechanisms at work between a laser beam and a material [42]: the modifications to a polymer structure can be examined following ablation; time-resolved measurements can be made during ablation; or the laser pulse lengths and wavelengths can be modified and the differing effect they have upon a specific material can be examined following ablation.

Modifying the pulse lengths and wavelengths is typically implemented while using the other two experimental techniques; however, it is a powerful tool in helping the practitioner to gain an understanding of the mechanisms at work.

Several authors make use of analysis of the debris left over from ablation [8,10,27], as well as velocity, angle, and radius of the plume emanating from the ablation event [5], suggesting possible methods of analysis.

A relevant example of investigations made to the polymer structure of a material have been conducted by Lippert *et al.* [43]. Excimer lamps were alternately employed to study the effect of low fluence irradiation at 222 and 308 nm wavelengths where linear photochemistry could be expected; that is, without ablation. Excimer lamps emit incoherent, quasi-continuous radiation at the same wavelength as an excimer laser; however, these emit far lower photon fluxes and so multiphoton processes can be neglected. This experiment showed that the triazine-chromophore decomposes at a fluence well below the ablation threshold and is clearly the most sensitive chromophore in any triazine-based polymer. As a consequence, the possibility of a photochemical interaction during ablation by irradiation at 308 nm must be considered to be likely.

A wide choice of time-resolved methods to examine the ablation mechanism are available: picosecond anti-Stokes coherent Raman scattering spectroscopy [44]; time-resolved transmission [45]; high-speed Schlieren imaging [46]; nanosecond shadowgraphy [42]; nanosecond surface interferometry [47]; nanosecond photoacoustic analysis [20]; and time-of-flight mass spectrometry (ToF-MS) are all common. Time-resolved measurements are useful in examining the transient processes in laser ablation. The shadowgraphy method, described in detail by Hauer *et al.* [48], has been used by Lippert [42] to image the shockwave and ablation products at different times during and after the pulse. Lippert's results confirm the absence of solid products in the ablation plume for irradiation of a triazene-polymer, at 308 nm; this was a result expected by Lippert due to the lack of redeposited material found after ablation. But, further investigation found that the use of different wavelength-material combinations can generate solid ablation products. The shadowgraphy technique can also yield an insight toward the nature of the shockwave being found to be wavelength dependent [42]. The use of surface interferometry has been used alongside shadowgraphy to examine changes in surface morphology on ns timescales both during and after the laser pulse [47]. This imaging technique demonstrated that when machining a triazene polymer at 193, 308, and 351 nm [47], etching begins and ends with the laser pulse; however, use of the same wavelengths with other polymers, such as PI [48], PMMA, and PS [49], results in pronounced swelling, followed by material removal that continues for several  $\mu\text{s}$  after the laser pulse has ended (Figure 22.14).

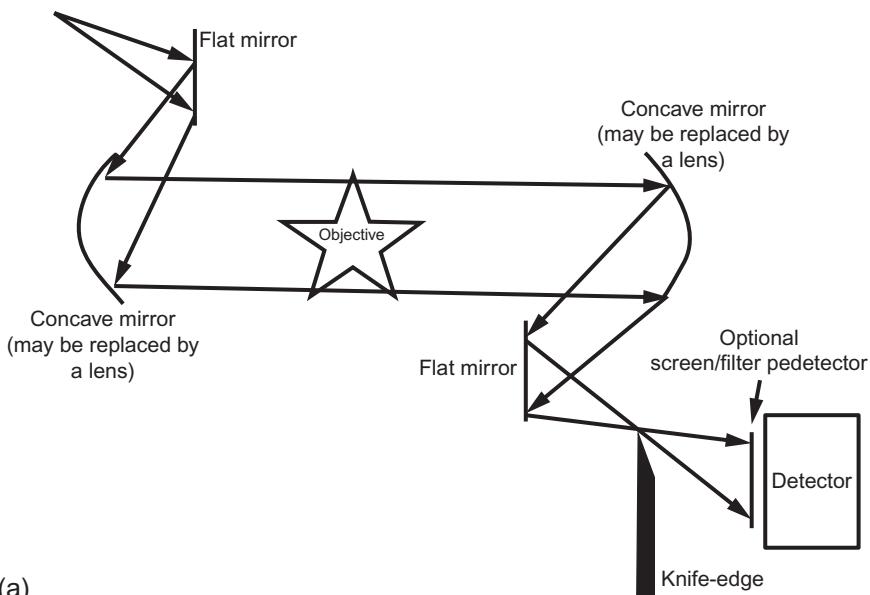
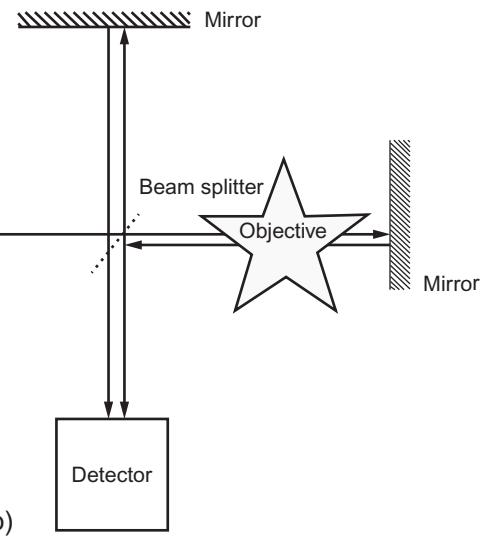
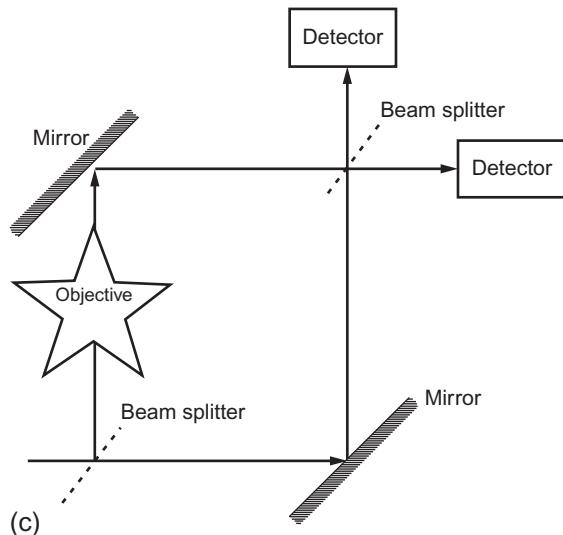


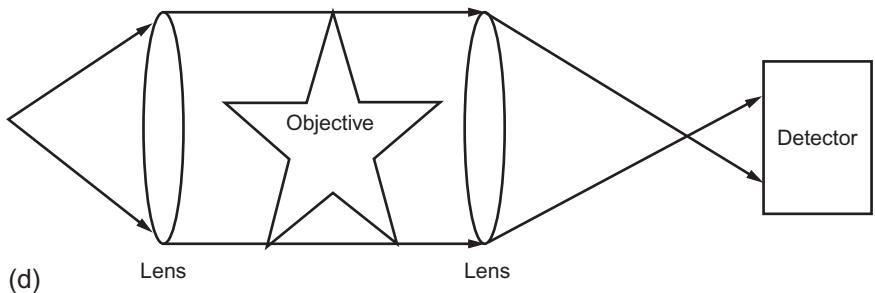
**Figure 22.14** Illustration of some of the imaging techniques applicable to ablation events: (a) Schlieren imaging arrangement [50]; (b) Michelson interferometry arrangement [51]; (c) Mach-Zehnder interferometry arrangement [51]; and (d) shadowgraphy arrangement [52].



(b)



(c)



(d)

Lens

Lens

Figure 22.14 Continued.

### 22.6.1 *The role of high-speed imaging in the observance of these solutions*

Masubuchi *et al.* [49] note that the expansion starts in the initial half of the excimer laser peak and reaches a maximum value at around 50 ns, before beginning to contract back to a flat surface. These peers explain that the contraction process should be controlled by the thermal dissipation of the material; however, the time taken for contraction is of the microsecond order and this is outside the scale of thermal dissipation predictions; thus, the contraction mechanism is unexplained. Photothermal ablation is often associated with pronounced surface swelling and delayed material ejection and photochemical ablation is considered to yield less swelling and instantaneous etching [42].

Multiple fields are described wherein ablation can be made use of [5–7], yet the specific mechanisms or reaction pathways are not yet fully understood [8]. In order to continue to refine and develop the process, more data is required to analyze and, thus, surmise the processes involved. As the pulse length used for ablation decreases, the amount of data required to accurately analyze the event increases. With material ejection beginning picoseconds after the initial interaction between the laser and objective material [8], finely time-resolved techniques are required in order to observe the initiation of ablation.

Furthermore, in order to observe plume development, highly resolved, short time-frame images will be required. In order to achieve this using Gregorčič's technique [53,54], a short pulse length is required in order to enable quick succession between the two frames, quality time-delay generation required to ensure accurate timing between the initiation of the event laser and the imaging laser to capture development of the relatively short event.

## 22.7 Conclusion

To summarize, this chapter has considered the process of ablation, noting its broad definition and focussing specifically on laser-initiated ablation and the instance of excimer laser ablation, an example of a short wavelength, UV laser. The ability to produce accurate geometric modifications has been noted and the application of this with excimer lasers in micromachining has been discussed.

The limits of ablation within the application of micromachining have been highlighted, before considering possible solutions. Following this breakdown of drawbacks, the technique of applying closed, thick flowing films of water across the surface was described in detail, to reduce the wall gradient of the machined features and remove the debris from an ablation event from the zone being machined, thus enabling an increase in feature resolution.

While noting incomplete understanding of the chemical physics taking place within ablation, general mechanisms involved in ablation have been considered; no one specific mechanism can be offered due to the multitude of variables upon which such a mechanism is dependent.

Beam modifications, including techniques for homogenizing the beam from a Gaussian to “top hat” profile and beam masking were discussed, including examples of 2.5-D features and their complementary beam masks.

Another consideration of laser-initiated ablation examined was the issues arising from the procedure. These issues include size of hole, depth of hole, taper, contaminant level, degree of thermal damage, level of cracking, and interaction of and attenuation by ejected debris plume, limiting efficiency. Two key variables considered when dealing with ejected debris have been discussed: the product’s trajectory and size, these affecting the debris’ final location prior to reinteracting with the surface being ablated.

The solution offered to engage with the issue of debris is the use of liquid immersion. Proven to play a role in transport of the debris, the drawbacks of the technique have been noted along with the advantages. Consideration of alternative atmospheres have also briefly been considered, as well as methods for debris collection such as electrostatically, rather than passive transport from the ablation event.

The final consideration made in this chapter briefly examines the methods of investigating laser-initiated ablation. Of the three methods discussed, two rely on setting preablation conditions followed by postablation analysis. The third, time-resolved measurements made during ablation, is noted to offer insight into both the initiation, debris formation, effect of control measures on debris formation and deposition, as well as shockwave formation resulting from ablation. With publications as recent as 2012, developments to the analytical techniques continue to be made in this area.

With incomplete understanding regarding the chemical physics involved in laser ablation, combined with the known mechanisms being governed by an array of variables, techniques such as the immersed ablation technique continue to improve ablation resolution and push back constraints. As new analytical techniques develop that can further improve our understanding of the processes involved in ablation and their optimization, this field continues to offer vast potential as a novel and expanding research area in the future.

## References

- [1] D. Thompson, The Concise Oxford Dictionary of Current English, Clarendon, Oxford, 1995.
- [2] T. Sakka, K. Takatani, Y. Ogata, M. Mabuchi, Laser ablation at the solid-liquid interface: transient absorption of continuous spectral emission by ablated aluminium atoms, *J. Appl. Phys.* 35 (1) (2002) 65–73.
- [3] K.H. Song, X. Xu, Explosive phase transformation in excimer laser ablation, *Appl. Surf. Sci.* 127 (1998) 111–116.
- [4] T. Lippert, M. Hauer, C.R. Phipps, A. Workaun, Fundamentals and applications of polymers designed for laser ablation, *Appl. Phys. A* 77 (2) (2003) 259–264.
- [5] L.V. Zhigilei, P.B. Kodali, B.J. Garrison, A microscopic view of laser ablation, *J. Phys. Chem. B* 102 (1998) 2845–2853.
- [6] R.F. Haglund Jr., Microscopic and mesoscopic aspects of laser-induced desorption and ablation, *Appl. Surf. Sci.* 96–98 (1996) 1–13.

- [7] K. Coupland, P.R. Herman, B. Gu, Laser cleaning of ablation debris from CO<sub>2</sub>-laser-etched vias in polyamide, *Appl. Surf. Sci.* 127–129 (1998) 731–737.
- [8] M.N. Ashfold, F. Claeysens, G.M. Fuge, S.J. Henley, Pulsed laser ablation and deposition of thin films, *R. Soc. Chem.* 33 (2004) 23–31.
- [9] K.C. Yung, S.M. Mei, T.M. Yue, Pulsed UV laser ablation of a liquid crystal polymer, *Int. J. Adv. Manuf. Technol.* 26 (11) (2005) 1231–1236.
- [10] C.F. Dowding, J. Lawrence, Impact of open de-ionized water thin film laminar immersion on the liquid immersed ablation threshold and ablation rate of features machined by KrF excimer laser ablation of bisphenol A polycarbonate, *Opt. Lasers Eng.* 47 (11) (2009) 1169–1176.
- [11] P.E. Dyer, Excimer laser ablation and thermal coupling efficiency to polymer films, *J. Appl. Phys.* 57 (4) (1985) 1420–1422.
- [12] X. Liu, D. Du, G. Mourou, Laser ablation and micromachining with ultrashort laser pulses, *IEEE J. Quantum Electron.* 33 (10) (1997) 1706–1716.
- [13] G.W. Yang, Laser ablation in liquids: applications in the synthesis of nanocrystals, *Prog. Mater. Sci.* 52 (4) (2006) 648–698.
- [14] R. Kelly, A. Miotello, On the role of thermal processes in sputtering and composition changes due to ions or laser pulses, *Nucl. Instrum. Methods Phys. Res. Sect. B: Beam Interact. Mater. At.* 141 (1–4) (1998) 49–60.
- [15] E. Harvey, P. Rumsby, Fabrication techniques and their application to produce novel micromachined structures and devices using excimer laser projection, *Micromach. Microfab.* 26–33 (1997).
- [16] H.J. Booth, Recent applications of pulsed lasers in advanced materials processing, *Thin Solid Films* 453 (2004) 450–457.
- [17] T.-C. Chang, P.A. Molian, Excimer pulsed laser ablation of polymers in air and liquids for micromachining applications, *J. Manuf. Processes* 1 (1) (1999) 1–17.
- [18] F. Weisbuch, V.N. Tokarev, S. Lazare, D. Débarre, Ablation with a single micropatterned KrF laser pulse: quantitative evidence of transient liquid microflow driven by the plume pressure gradient at the surface of polyesters, *Appl. Phys. A* 76 (4) (2003) 613–620.
- [19] J.H. Yoo, S.H. Jeong, R. Greif, R.E. Russo, Explosive changes in crater properties during high power nanosecond laser ablation of silicon, *J. Appl. Phys.* 88 (3) (2000) 1638–1649.
- [20] P.E. Dyer, S. Farrar, P.H. Key, Investigation of excimer ablation of ceramic and thin film Y-Ba-Cu-O using nanosecond photoacoustic techniques, *Appl. Phys. Lett.* 60 (15) (1890–1892) 1992.
- [21] D. Bauerle, Laser processing and chemistry: recent developments, *Appl. Surf. Sci.* 186 (1) (2002) 1–6.
- [22] L. Torrisi, S. Gammino, L. Andò, V. Nassisi, D. Doria, A. Pedone, Comparison of nanosecond ablation at 1064 and 308 nm wavelength, *Appl. Surf. Sci.* 210 (3–4) (2003) 262–273.
- [23] M. Ullmann, S.K. Friedlander, A. Schmidt-Ott, Nanoparticle formation by laser ablation, *J. Nanopart. Res.* 4 (6) (2002) 499–509.
- [24] G. Gartner, P. Janiel, H. Lydtin, L. Rehder, *Synthesis and Measurement of Ultrafine Particles*, Delft University Press, Netherlands, 1993, p. 41.
- [25] T. Sasaki, S. Teraguchi, N. Koshizaki, H. Umehara, The preparation of iron complex oxide nanoparticles by pulsed-laser ablation, *Appl. Surf. Sci.* 127–129 (1998) 398–402.
- [26] K. Ogawa, T. Vogt, M. Ullmann, S. Johnson, S.K. Friedlander, Elastic properties of nanoparticle chain aggregates of TiO<sub>2</sub>, Al<sub>2</sub>O<sub>3</sub>, and Fe<sub>2</sub>O<sub>3</sub> generated by laser ablation, *J. Appl. Phys.* 87 (1) (2000) 63–73.

- [27] C.F. Dowding, J. Lawrence, Use of thin laminar liquid flows above ablation area for control of ejected material during excimer machining, *Proc. Inst. Mech. Eng. Part B J. Eng. Manuf.* 223 (2009) 759–773.
- [28] M. Bereznai, P. Heszler, Z. Tóth, O. Wilhelmsen, M. Boman, Measurements of nanoparticle size distribution produced by laser ablation of tungsten and boron-carbide in N<sub>2</sub> ambient, *Appl. Surf. Sci.* 252 (13) (2006) 4368–4372.
- [29] R.A. Bowling, A theoretical review of particle adhesion, in: *Particles on Surfaces: Detection, Adhesion and Removal*, CRC Press, New York, 1988, pp. 129–142.
- [30] K. Sasaki, N. Takada, Liquid-phase laser ablation, *Pure Appl. Chem.* 82 (6) (2010) 1317–1327.
- [31] C. Dowding, J. Lawrence, Analysis of KrF excimer laser beam modification resulting from ablation under close thick film flowing filtered water, *Opt. Laser Technol.* 43 (6) (2011) 1026–1035.
- [32] C. Dowding, J. Lawrence, A. Holmes, Ablation debris control by means of closed thick film filtered water immersion, *Proc. Inst. Mech. Eng. Part B J. Eng. Manuf.* 224 (5) (2010) 753–768.
- [33] S. Lazare, V. Granier, Excimer laser light induced ablation and reactions at polymer surfaces as measured with a quartz-crystal microbalance, *J. Appl. Phys.* 63 (6) (1988) 2110–2115.
- [34] W. Spiess, H. Strack, Structuring of polyimide by ArF excimer laser ablation, *Semicond. Sci. Technol.* 4 (6) (1989) 486–490.
- [35] G. Koren, J.J. Donelon, CO<sub>2</sub> laser cleaning of black deposits formed during the excimer laser etching of polyimide in air, *Appl. Phys. B Photophys. Laser Chem.* 45 (1) (1988) 45–46.
- [36] J. Gu, J. Low, P.K. Lim, P. Lim, Nd:YAG laser cleaning of ablation debris from excimer laser ablated polyimide, in: *Photonic Systems and Applications—Proceedings of SPIE—The International Society for Optical Engineering*, Singapore, 2001.
- [37] R.J. von Gutfeld, R. Srinivasan, Electrostatic collection of debris resulting from 193 nm laser etching of polyimide, *Appl. Phys. Lett.* 51 (1) (1987) 15–17.
- [38] R. Srinivasan, B. Braren, R.W. Dreyfus, Ultraviolet laser ablation of polyimide film, *J. Appl. Phys.* 61 (1) (1987) 372–376.
- [39] D.E. Seeger, M.G. Rosenfeld, Clearing resist from alignment mark areas using an excimer laser, *J. Vac. Sci. Technol. B: Microelectron. Nanometer Struct.* 6 (1) (1988) 399–402.
- [40] H. Gabel, R.M. Tapphorn, Coating or ablation applicator with a debris recovery attachment. United States Patent 5,795,626, 18 August 1998.
- [41] R.M. Tapphorn, H. Gabel, Coating or ablating applicator with debris recovery attachment. United States Patent 6,074,135, 13 June 2000.
- [42] T. Lippert, Interaction of photons with polymers: from surface modification to ablation, *Plasma Processes Polym.* 2 (2005) 525–546.
- [43] T. Lippert, C. David, J.T. Dickinson, M. Hauer, U. Kogelschatz, S.C. Langford, O. Nuyken, C. Phipps, J. Robert, A. Wokaun, Structure property relations of photoreactive polymers designed for laser ablation, *J. Photochem. Photobiol. A* 145 (3) (2001) 145–157.
- [44] D.E. Hare, J. Franken, D.D. Dlott, Coherent Raman measurements of polymer thin-film pressure and temperature during picosecond laser ablation, *J. Appl. Phys.* 77 (11) (1995) 5950–5960.
- [45] Y. Tsuboi, K. Hatanaka, H. Fukumura, H. Masuhara, The 248-nm excimer-laser-ablation mechanism of liquid benzene derivatives: photochemical formation of benzyl radical leads to ablation, *J. Phys. Chem.* 102 (10) (1998) 1661–1665.

- [46] G. Paltauf, E. Reichel, H. Schmidt-Kloiber, Study of different ablation models by use of high-speed-sampling photography, in: Proceedings of the SPIE 1646, Laser-Tissue Interaction III, Los Angeles, CA, 1992.
- [47] H. Furutani, H. Fukumura, H. Masuhara, T. Lippert, A. Yabe, Laser-induced decomposition and ablation dynamics studied by nanosecond interferometry 1. A triazene polymer film, *J. Phys. Chem. A* 101 (32) (1997) 5742–5747.
- [48] M. Hauer, D.J. Funk, T. Lippert, A. Wokaun, Time-resolved techniques as probes for the laser ablation process, *Opt. Lasers Eng.* 43 (2005) 545–556.
- [49] T. Masubuchi, H. Fukumura, H. Masuhara, K. Suzuki, N. Hayashi, Laser induced decomposition and ablation dynamics studied by nanosecond interferometry 3. A polyurethane film, *J. Photochem. Photobiol. A* 145 (3) (2001) 215–222.
- [50] E. Hecht, Sundry topics from contemporary optics—lasers and laserlight, in: *Optics*, Addison-Wesley Publishing Company, Reading, Massachusetts, 1974, pp. 577–593.
- [51] E. Hecht, Interference, in: *Optics*, Addison-Wesley Publishing Company, Reading, Massachusetts, 1974, pp. 333–391.
- [52] P.K. Panigrahi, K. Muralidhar, Laser schlieren and shadowgraph, in: *Schlieren and Shadowgraph Methods in Heat and Mass Transfer*, Springer, New York, 2012, pp. 23–46.
- [53] P. Gregorčič, J. Možina, High-speed two-frame shadowgraphy for velocity measurements of laser-induced plasma and shock-wave evolution, *Opt. Lett.* 36 (15) (2011) 2782–2784.
- [54] P. Gregorčič, J. Diaci, J. Možina, Two-dimensional measurements of laser-induced breakdown in air by high-speed two-frame shadowgraphy, *Appl. Phys. A Mater. Sci. Process.* 112 (1) (2013) 49–55.

## **Part Four**

# **Chemical and biological applications of laser surface engineering**

This page intentionally left blank

# Luminescence spectroscopy as versatile probes for chemical diagnostics on the solid–liquid interface

23

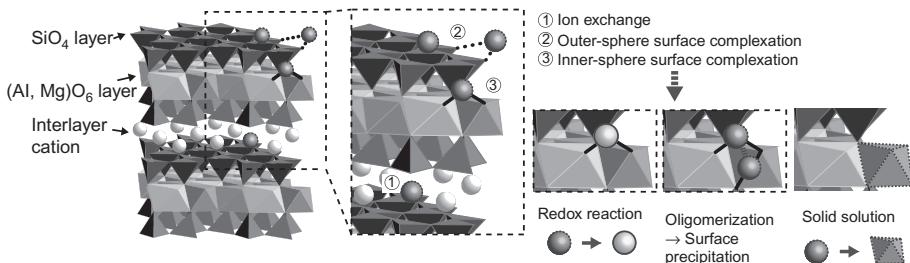
N. Aoyagi<sup>1</sup>, T. Saito<sup>2</sup>

<sup>1</sup>Japan Atomic Energy Agency (JAEA), Ibaraki, Japan; <sup>2</sup>The University of Tokyo, Tokyo, Japan

## 23.1 Introduction

Solid-water interfaces play a significant role in various aspects related to our daily life. For instance, they are invaluable in material production as solid catalysts, in biological functions facilitating transport of chemicals through cell membranes, and in mitigating environmental pollution through the interaction of pollutants with mineral and biological surfaces. The characteristics of these interfaces arise from their ability to provide unique places for chemical processes that would proceed less effectively in the bulk. Although solid-water interfaces are involved in various processes and reactions surrounding us, one should also remember the following words by Pauli: *God made the bulk; surfaces were invented by the Devil* [1]. This implies that it could be difficult to describe the phenomena occurring at such interfaces.

The management and disposal of nuclear waste is an impending issue in many countries that use nuclear power to generate a part of their electricity. Underground geological disposal is the only well-accepted and well-established solution for spent nuclear fuels and vitrified high-level wastes after reprocessing. The safety of geological disposal is strengthened by combining engineered and natural barriers. Engineered barriers, such as vitrified glass, carbon steel canister or overpack, and bentonite buffer, are used to retard the release of radionuclides. In contrast, natural barriers rely on sorption and buffering functions of subsurface environments. For instance, sorption on rocks retards the migration of radionuclides and the reductive atmosphere of deep underground maintains low oxidation states of redox-sensitive radionuclides like U and Pu. At low oxidation states, these metal ions are sparsely soluble and their migration is retarded. Chemical reactions and processes that occur at solid–water interfaces are crucial for achieving reliable geological disposal (see [Scheme 23.1](#)). For this, it is first necessary to determine the various processes at the interfaces that could help in gaining a better understanding of the radionuclide migration; thus, any analytical techniques should possess the following prerequisites: (a) high selectivity for the element, (b) high detection limit, (c) nondestructive, (d) prompt measurement, (e) a small volume, and (f) qualitative and



**Scheme 23.1** Examples of chemical reactions and processes at the solid-water interface (ex. montmorillonite). Metal ions can be immobilized by sorption (ion exchange, outer-sphere and inner-sphere surface complexation), accompanying redox reaction, oligomerization, surface precipitation, and solid solution.

quantitative speciation analyses. Spectroscopic methods using lasers are promising because they can satisfy these requirements.

Several previous studies have aimed at understanding the complexation of actinide ions by inorganic/organic ligands in aqueous solutions [2]. Spectroscopic methods such as UV-Vis absorption spectroscopy, Raman spectroscopy, IR/NIR (infrared/near infrared) spectroscopy, NMR (nuclear magnetic resonance) spectroscopy, and XAS (X-ray absorption spectroscopy) are used for characterizing the chemical states of actinide compounds, whereas radiation measurements or mass spectrometry techniques such as ICP-MS (inductively coupled plasma mass spectrometry) are superior in quantitative detection. In addition, laser spectroscopy [3] is applied to probe the chemical state of the actinide (An) ions as well as to quantify their concentrations in certain chemical forms because the majority of their optical emission levels are in the visible-NIR region and depend on their surrounding chemical environments. Time-resolved laser-induced fluorescence spectroscopy (TRLFS) permits *in situ* measurements of the luminescence from fluorescent An ions with moderately low detection limits and is speciation-sensitive as the luminescence is measured as a function of excitation and emission wavelength and time.

The aquo ions of lanthanide ranging from  $\text{Nd}^{3+}$  to  $\text{Yb}^{3+}$  are luminescent and predominantly exist as trivalent cations. The same applies to some of the trivalent actinides:  $\text{Am}^{3+}$ ,  $\text{Cm}^{3+}$ ,  $\text{Bk}^{3+}$ ,  $\text{Cf}^{3+}$ , and  $\text{Es}^{3+}$ . Physicochemical properties of the lanthanide (Ln) ions including the electron configurations, the oxidation states, the ionic radii, or the hydration number and coordination geometry in the first coordination shell have a certain similarity to those of actinide (An) ions. Thus, owing to the difficulties in handling An ions, Ln ions are used as chemical analogs to An ions at the corresponding position in the periodic table. However, a closer comparison between An and Ln reveals certain differences between the two. The thermodynamic constants such as the formation constant of a metal complex and a dissociation constant of a proton,  $pK_a$ , are normally measured by potentiometric titration under normal light except for reagents that are reactive in the photoexcited state. Some studies have determined these constants by TRLFS, and for  $\text{UO}^{2+}$  or  $\text{Cm}^{3+}$  ions, in the photoexcited state, these constants are not necessarily identical to those in the ground state [4]. Therefore, these effects should be taken into consideration when determining these constants by spectrofluorimetry.

A myriad of lanthanide and actinide complexes have been investigated using TRLFS to determine their hydration states and coordination structures in homogeneous aqueous solutions. An empirical linear relationship has been established between the hydration number and the kinetic constant of de-excitation, that is, a reciprocal number of the fluorescence lifetime [5–8]. Emission and excitation spectra have been used to differentiate coexisting species and discuss their structures based on the spectral shapes. Nowadays, actinide chemistry studies are increasingly evidencing chemical processes in nonaqueous solvents such as ionic liquids (ILs) and those at environmental interfaces, including the incorporation of actinide ions into solid, and adsorption of actinides onto the surface of minerals or organic macromolecules. Laser spectroscopy is effective for chemical diagnostics of such processes because actinide ions exhibit a high quantum yield of luminescence. Herein, we describe the recent progress in the analysis of actinides and lanthanides at interfaces using TRLFS as well as other more recent and advanced techniques, such as cryogenic TRLFS, interface-specific nonlinear spectroscopy, near-field imaging spectroscopy, and the possible combination of quantum chemical simulations.

## 23.2 Chemical analysis of lanthanide and actinide ions by time-resolved laser-induced fluorescence spectroscopy (TRLFS)

As mentioned in the previous section, laser spectroscopy enables probing of the chemical states of lanthanide and actinide ions in various environments. This section describes the relationship of the fluorescence spectrum and lifetime with the chemical environment in the close vicinity of a fluorescent metal ion.

Fluorescence is one of the de-excitation processes from the excited states of a fluorescent ion or molecule [9]. After excitation by absorbing a photon with a certain energy, fluorophores in their highly excited states immediately de-excite to their lowest excited singlet state,  $S_1$ . This nonradiative process is called internal conversion. Fluorescence emission occurs when fluorophores on the  $S_1$  level transit to the ground state,  $S_0$  (see Figure 23.1). This fluorescence emission competes with other transition processes such as nonradiative transition, in which atoms in the excited state dissipate through vibrational energy transfer to their surroundings, and radiative transition through intersystem crossing to their triplet states, namely phosphorescence emission. Some fluorescent transitions in lanthanide ions involve transitions between f-electron orbitals, which are parity forbidden (i.e., La Porte forbiddance) and exhibit relatively small transition probability and long lifetime [10].

Luminescence, which is a collective term for fluorescence and phosphorescence, is sensitive to the surrounding environments of the central fluorescent ions. The transitions from the  $^5D_0$  state of  $\text{Eu}^{3+}$  and  $^6D_{7/2}$  state of  $\text{Cm}^{3+}$  involve various ground states with slightly different energies, which can be modulated by the interaction with surrounding atoms, and thus, the associated excitation and emission spectra exhibit characteristic shapes, corresponding to the surrounding ligand fields. This tendency is rather prominent for  $\text{Cm}^{3+}$ , which possesses delocalized and more chemically sensitive 5f orbitals [10]. In addition, the indicative transition from the  $^5D_0$  to  $^7F_1$  of  $\text{Eu}^{3+}$  is

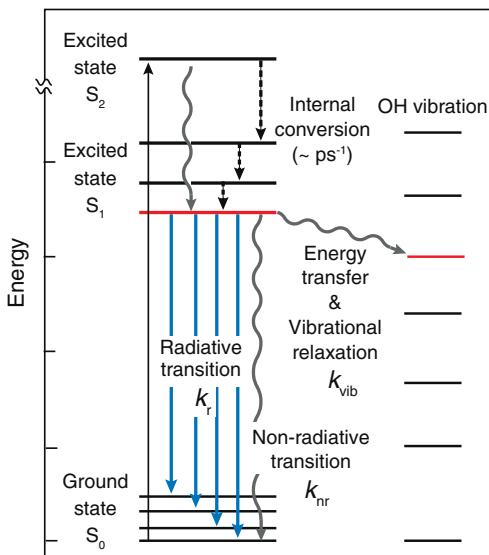


**Figure 23.1** Schematic diagram of the excitation and emission energy levels owing to the luminescence of a  $\text{Eu}^{3+}$  ion surrounded by an O—H oscillator as a quencher.

an electron dipole allowed transition, and its fluorescence intensity increases with a decrease in the centrosymmetry around the  $\text{Eu}^{3+}$  ion. Fluorescence from hexavalent uranium,  $\text{UO}_2^{2+}$ , occurs from the transition between different vibrational ground-state energy levels of  $\text{U}=\text{O}$  bonds, which can be modulated by temperature and ligand fields [3]. In addition, the fluorescence of central metal ions can be sensitized by utilizing the energy transfer from organic ligands with large molar absorption coefficients (the antenna effect) [11]. The lifetime of fluorescence emission depends on the balance between radiative and nonradiative transitions as well as energy transfer to quencher molecules. For  $\text{Cm}^{3+}$  and  $\text{Eu}^{3+}$  in aqueous solution, a part of the excited energy dissipates through energy transfer from their  $S_1$  levels to a closely lying O—H vibrational mode of the water molecules. For such ions, complexation with ligand molecules replaces some of the water molecules, resulting in an increase of their fluorescence lifetimes. Indeed, there are good linear relationships between the reciprocal of their lifetimes and the number of hydration water molecules [6–8].

The symmetry around the metal center affects the electronic spectra. Namely, the chemical structure or state of the sample, which are difficult to directly measure in the bulk solution or on the surface, can be determined by observing the speciation corresponding to the spectral shape. The information necessary to assess the species involved in the possible surface reactions include the hydration/solvation state, the symmetry in the conformation of the ligands, and the dynamics in solvation. Actinide complexes are, in this sense, thought to be a luminescence probe in the chemical analyses of heterogeneous surface of the environmental concern.

The aforementioned sensitivity of the fluorescence of lanthanide and actinide ions to their local environments have been used to determine their speciation in complex media

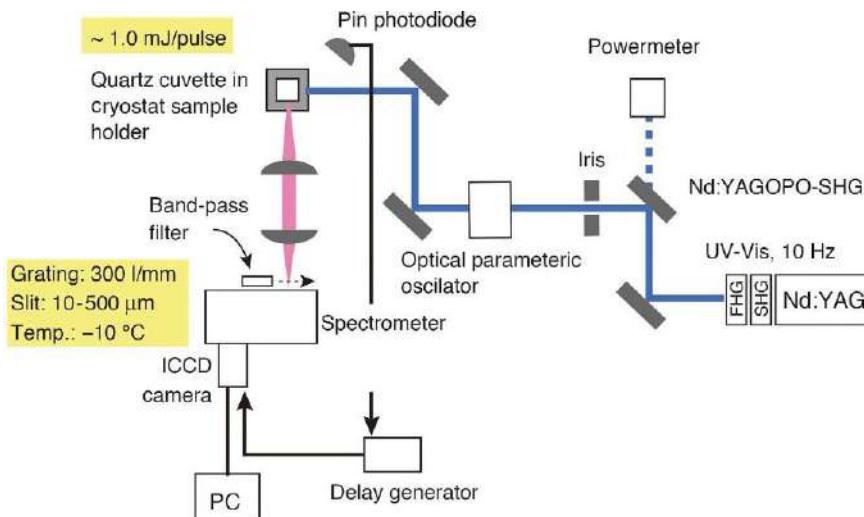


**Figure 23.2** Example of TRLFS setup using variable wavelength, spectrometer, ICCD camera, and a cryostat to maintain the temperature of the sample.

or to probe the characteristics of their binding sites on mineral or biological surfaces. The main advantages of fluorescence spectroscopy, especially TRLFS, over other analytical techniques are a relatively low detection limit, *in situ* measurement, and multivariate nature, which is particularly favorable for studying systems with multiple species of target fluorescent ions. Statistical techniques are often employed to analyse the multidimensional TRLFS data. Recently, the authors have demonstrated the applicability of multi-way factor analytic method, PARAFAC (PARAllel FACtor analysis), to simultaneously obtain spectra, decay curves, and intensity profiles as a function of a certain chemical variable (such as pH or ligand concentration) from TRLFS data [12–14].

Figure 23.2 shows the instrumentation used in TRLFS. An essential component for the measurement is a pulsed laser having pulse width shorter than the lifetimes of the species of a target fluorescent ion. Nd:YAG lasers with nanosecond pulses or Ti:sapphire lasers with femtosecond pulses are frequently used, combined with dye lasers or optical parametric oscillator units to convert the energy of the laser emission to that appropriate for the target ion excitation. The fluorescence from the samples is typically detected at a 90° angle. For simple lifetime measurements at single emission wavelength, a combination of a monochromator and a photo multiplier tube is used; however, for TRLFS, a polychromator with grating and a fast-gated intensified CCD camera or streak camera are necessary.

### 23.3 Analysis of TRLFS data

The data of TLRFS of a fluorescent ion is expressed as follows:

$$f(\lambda_{\text{ex}}, \lambda_{\text{em}}, t, x) = AI_0 \sum_i \varepsilon_i(\lambda_{\text{ex}}) \varphi_i(\lambda_{\text{em}}) c_i(x) e^{-t/\tau_i} \quad (1)$$

where  $f$  is the fluorescence intensity at the excitation and emission wavelengths  $\lambda_{\text{ex}}$  and  $\lambda_{\text{em}}$ , respectively, elapsed at time,  $t$ , after irradiation by the incident laser;  $\epsilon_i$  is the molar absorption coefficient at  $\lambda_{\text{ex}}$ ;  $\varphi_i$  is the quantum coefficient at  $\lambda_{\text{em}}$ ;  $c_i$  is the concentration of the species as a function of chemical variables such as pH and ligand concentration, denoted as  $x$ ; and  $\tau_i$  is the lifetime that characterizes the decay term. The fluorescence intensity is equal to the sum of the products of four terms— $\epsilon_i$ ,  $\varphi_i$ ,  $c_i$ ,  $\tau_i$ —across different species,  $i$ , multiplied by the proportional constant,  $A$ , determined by the geometry of the sample, detector, and optics of TRLFS, and the intensity of the incident laser,  $I_0$ . As mentioned above,  $\epsilon_i$  and  $\varphi_i$  depend on the adjacent chemical structure around the central fluorescent ion and  $\tau_i$  on the number of quencher molecules such as  $\text{H}_2\text{O}$  in their coordination sphere; the TRLFS data contain a great deal of information useful for revealing the speciation of the target ion, that is, information about their chemical structures and concentrations as a function of  $x$ . However, in most of the cases, only a part of the data have been used because of the intractable data reduction from the complete TRLFS data. In the analyses of the TRLFS data, it has been frequently observed that exponential fitting occurs for decay curves at fixed  $\lambda_{\text{ex}}$ ,  $\lambda_{\text{em}}$ , and  $x$  or peak deconvolution of the spectrum occurs at fixed  $\lambda_{\text{ex}}$  ( $\lambda_{\text{em}}$ ),  $t$ , and  $x$ . Two-dimensional (2-D) factor analysis (FA) such as evolving FA has been applied for a single list of TRLFS data defined by 2-D matrices using  $\lambda_{\text{em}}$  and  $t$  [15,16].

More recently, Saito *et al.* [14] demonstrated the applicability of multimode FA known as PARAFAC for the simultaneous analysis of a series of TRLFS data ( $\lambda_{\text{em}} \times t \times x$ ) (see Figure 23.3). Compared with 2-D FA, PARAFAC is more robust, as separating the contributions of different species of a target ion is more constrained by increased data dimension. Furthermore, relationship between samples, that is, concentration profiles are more easily attained, as all data measured at different chemical conditions are treated at the same time. By using this technique, the authors successfully separated the fluorescence spectra, decay curves, and intensity profiles of the complexation of  $\text{Eu}^{3+}$  with an acetate ligand, which agreed well with the known speciation and stoichiometry of the complexes.

## 23.4 Recent progress in chemical analysis of actinides by laser spectroscopy

### 23.4.1 Analysis of fluorescent ions in solution

An early TRLFS study on the hydration states of  $\text{Eu}^{3+}$  and  $\text{Tb}^{3+}$  ions in the first coordination sphere in aqueous solutions was conducted in the late 1970s by Horrocks and Sudnick [5]. However, it was only in the mid-1990s (Kimura and Choppin) that a corresponding study for actinide ions such as  $\text{Cm}^{3+}$  and  $\text{Am}^{3+}$  was conducted [7,17,18]. The hydration study of Ln and An is summarized in Table 23.1 [19]. Recent years have witnessed a series of fundamental studies on the hydration structures of trivalent actinide ions [ $\text{An}(\text{H}_2\text{O})_9](\text{CF}_3\text{SO}_3)_3$  ( $\text{An}^{3+} = \text{Cm}^{3+}, \text{Am}^{3+}$ ) and their TRLFS properties [20]. Although the only known example of the first coordination sphere of actinides had been that of a Pu complex with CN (coordination number)=9, Lindqvist-Reis

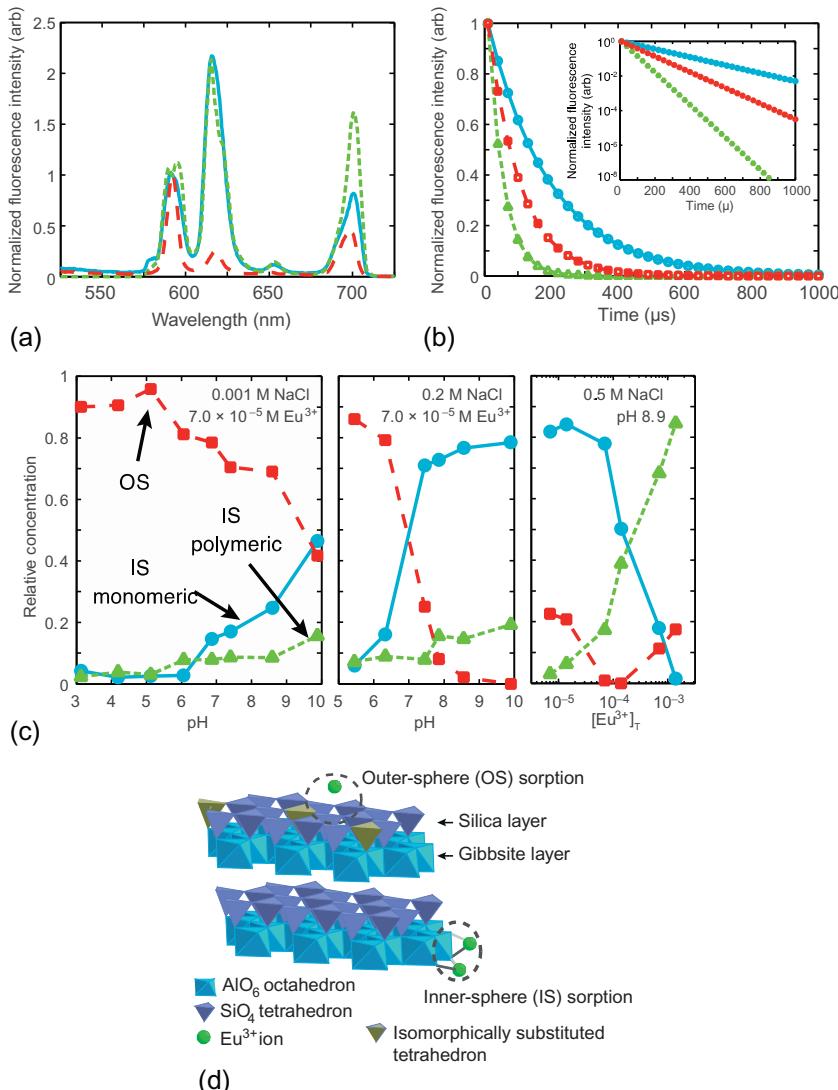


**Figure 23.3** Fluorescence spectra (a), fluorescence decays (b), and relative intensity profiles (c) of the three factors from the PARAFAC decomposition. The three factors correspond to outer-sphere (OS) and inner-sphere (IS) sorption complexes in the schematic (d); the IS sorption complexes are further divided to monomeric and polymeric complexes. The spectra are normalized by the intensities at 592 nm, and the decay curves are normalized by the intensities at the first point in the kinetic series at  $t = 10 \mu$ s. The resulting normalization coefficients are used to calculate the relative intensity profiles. For (b), the results of exponential fitting to the obtained fluorescence decays (symbols) are shown as solid, dashed, and dotted curves for the OS, monomeric IS, and polymeric IS sorption complexes, respectively. For (c), similar curves as in (b) simply serve as guides for the eyes [12].

**Table 23.1 Constants obtained to describe the correlation between hydration number and the observed decay rate ( $k_i$ ) for the trivalent ions europium, terbium, and curium using Model I or Model II**

	Model <sup>†</sup>	C	D	Uncertainty in $n_{\text{H}_2\text{O},i}^{\ddagger}$	Reference
Eu <sup>3+</sup>	I	1.07	-0.62	$\pm 0.5$	[7]
	I	1.05	-0.44	$\pm 0.4$	[18]
	II	1.05	0	$\pm 0.5$	[5]
	II	1.11	-0.34	$\pm 0.1$	[8]
	II	1.2	-0.3	<0.4	[6]
	I	4.03	-0.87	$\pm 0.4$	[18]
Tb <sup>3+</sup>	II	4.2	0	$\pm 0.5$	[5]
	II	5	-0.3	<0.4	[6]
Cm <sup>3+</sup>	I	0.65	-0.88	$\pm 0.5$	[7]

$k_i$  must be measured before  $n_{\text{H}_2\text{O},i}$  can be calculated with the equations used in Models I and II. Note that  $k_i$ ,  $k_{i,\text{H}_2\text{O}}$ , and  $k_{i,\text{D}_2\text{O}}$  are reciprocals of the observed lifetimes [19].

<sup>†</sup>Model I:  $n_{\text{H}_2\text{O},i} = Ck_i + D$ ; Model II:  $n_{\text{H}_2\text{O},i} = C(k_{i,\text{H}_2\text{O}} - k_{i,\text{D}_2\text{O}}) + D$ .

<sup>‡</sup> $n_{\text{H}_2\text{O},i}$ , hydration number. Uncertainty associated with  $n_{\text{H}_2\text{O},i}$  assigned by authors.

*et al.* found that other actinides also favor similar hydration structures,  $[\text{M}(\text{H}_2\text{O})_9](\text{CF}_3\text{SO}_3)_3$ , with  $C_{3h}$  symmetry around the metal centers [21,22]. Furthermore, the incorporation of a trace amount of Cm<sup>3+</sup> into the above complex with M=La<sup>3+</sup>, Y<sup>3+</sup> for the *tris*-triflate salt provides the well-defined spectra and lifetimes at low temperature ranging from 20 to 293 K.

An emerging topic about actinide chemistry in solutions is found not only in water or organic solvents but also in ILs. The spectroscopic properties or complexation of Ln and An in ILs are described in several reports (see Figure 23.4). Readers may refer to the review papers of Binnemans [25] and Takao *et al.* [26], and references therein. Stumpf *et al.* [27] demonstrated TRLFS measurement on Eu(CF<sub>3</sub>SO<sub>3</sub>)<sub>3</sub> and Cm(ClO<sub>4</sub>)<sub>3</sub> in a hydrophobic IL [C<sub>4</sub>mim][Tf<sub>2</sub>N], discussing the differences in their quenching processes in the presence of Cu<sup>2+</sup> ion. Nockemann *et al.* [28] observed the absorbance spectra of [UO<sub>2</sub>Br<sub>4</sub>]<sup>2-</sup>, which possesses CN=4 in an equatorial plane of a uranyl ion, in detail. We recently reported that low-melting complexes based on uranium, such as [C<sub>4</sub>mim][UO<sub>2</sub>(NCS)<sub>5</sub>], show thermochromism [24]. Though this material does not emit luminescence at room temperature because of self-quenching, it becomes luminescent at 77 K. The corresponding data obtained using <sup>15</sup>N NMR and crystallography reveal that the chromic reaction upon heating is caused by the shift of the equilibrium reaction in the ligand dissociation reaction and a concomitant decrease in CN on the equatorial plane.

### 23.4.2 Analysis of fluorescent ions at interfaces

TRLFS has been applied for adsorption reactions on mineral surfaces and soft surfaces such as bacterial and macromolecular surfaces. Stumpf *et al.* [29] studied the adsorption of Cm<sup>3+</sup> on clay minerals such as smectite and kaolinite and revealed that Cm<sup>3+</sup>

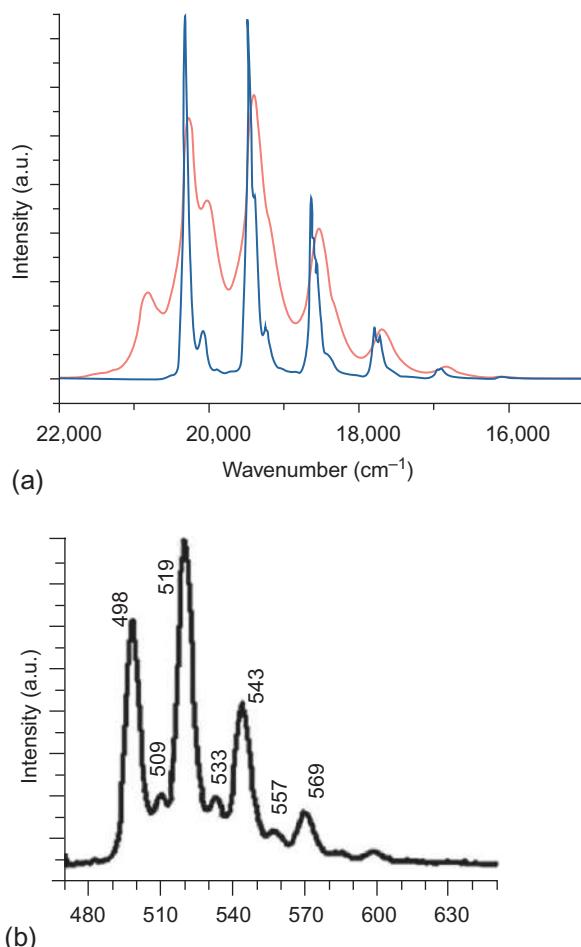


**Figure 23.4** Typical luminescence spectra of uranium compounds in ILs: (a) Luminescence spectrum of a powder of  $[(\text{UO}_2)_2(\text{bet})_6(\text{H}_2\text{O})_2][\text{Tf}_2\text{N}]_4$  (betainium bis[(trifluoromethyl)sulfonyl]imide) dispersed in vacuum grease, measured at room temperature (red) and at 77 K (blue) [23] and (b) that of  $[\text{C}_4\text{mim}]_3[\text{UO}_2(\text{NCS})_5]$  (1-butyl-3-methylimidazolium thiocyanate) at 77 K [24].

Adapted from Ref. [24] with permission from the Royal Society of Chemistry.

formed outer-sphere surface complexes with intact hydration water at relatively low pH and inner-sphere surface complexes showing coordination of surface hydroxyl groups at neutral to alkaline pH. The results of TRLFS can be readily combined with thermodynamic modelling. Based on these results, Rabung and coauthors [30,31] modelled the adsorption of  $\text{Cm}^{3+}$  and  $\text{Eu}^{3+}$  on montmorillonite by combining a surface complexation model with an ion-exchange model. Ishida *et al.* [12] employed PAR-AFAC for the analysis of a series of TRLFS data measured as a function of pH and  $\text{Eu}^{3+}$  concentration for the  $\text{Eu}^{3+}$ /kaolinite system and proposed the detailed speciation over

a wide range of concentration, pH, and ionic strength (Figure 23.3). The adsorption of  $\text{UO}_2^{2+}$  on various minerals has been studied [32] by employing the cryogenic TRLFS method. Wang and coauthors used this technique to study  $\text{UO}_2^{2+}$  species with weak fluorescence and its speciation in soil samples contaminated by low concentration of  $\text{UO}_2^{2+}$  [33,34]. The quantum efficiency of the fluorescence emission of  $\text{UO}_2^{2+}$  species is significantly improved by measuring the samples at liquid He temperature, which enables one to detect weakly fluorescent species of  $\text{UO}_2^{2+}$  that otherwise cannot be measured.

Adsorption on soft surfaces is ubiquitous in the environment. Natural organic matters (NOM) resulting from the decomposition of animal and plant remains and microorganisms such as bacteria possess active functional groups for metal adsorption, which affect their speciation in soil and aquatic systems. The interaction of fluorescence metal ions ( $\text{Eu}^{3+}$ ,  $\text{Cm}^{3+}$ ,  $\text{UO}_2^{2+}$ ) to NOM has been studied using the TRLFS analysis, exhibiting the presence of multiple species and binding sites [35–37]. Lukman *et al.* [13] used  $\text{Eu}^{3+}$  to probe the characteristics of various binding sites in heterogeneous NOM from various sources with the help of TRLFS and PARAFAC. The presence of two different binding environments were elucidated by their study, based on the correlation of the obtained fluorescence properties (i.e., spectra, lifetimes, and intensities of  $\text{Eu}^{3+}$ -NOM species) with the physicochemical properties of NOM. One binding environment comprises  $\text{Eu}^{3+}$  bound to carboxylic, phenolic, and N-containing functional groups of NOM with increasing contribution of the latter two groups at higher pH and the accompanying chelate formation. The second comprises  $\text{Eu}^{3+}$  bound to O-containing functional groups, whose fluorescence properties are strongly affected by the structures of the carbon backbones of NOM (i.e., aliphaticity and aromaticity) and the direct energy transfer from  $\text{Eu}^{3+}$  to NOM. Mineral surfaces encountered in nature are frequently covered by the adsorbed organic materials and may exhibit the properties of soft surfaces. Takahashi *et al.* [38] studied the interaction of  $\text{Cm}^{3+}$  in the  $\text{Cm}^{3+}$ /NOM/mineral ternary systems, using TRLFS.

The application of TRLFS for the interaction of lanthanide and actinide ions with microorganisms and biofilms has been an active research topic for decades [39–42]. Herein, the recent progresses in this field are briefly mentioned. Most of the biological surfaces are complex mixtures of various binding sites. This is especially true for natural biofilms used for the uptake of lanthanide and actinide ions. Therefore, TRLFS is used together with other techniques to reveal the underlying speciation of target ions. Ozaki *et al.* [39] studied the interaction of  $\text{Eu}^{3+}$  with *Bacillus subtilis* and *Halobacterium salinarum* using TRLFS to supplement their sorption results. The numbers of hydration water molecules calculated from the obtained lifetimes were used for the discussion of different binding modes of  $\text{Eu}^{3+}$  to these bacteria. The comparison with the fluorescent spectra of model compounds is sometimes effective to understand the speciation of unknown samples. Knopp *et al.* [40] and Koban and Bernhard [43] used a series of  $\text{UO}_2^{2+}$  phosphate and phospholipid compounds to study the interaction of lanthanides and actinides with bacteria. Lütke *et al.* [41] combined the TRLFS data with potentiometric titration results to reveal the speciation of  $\text{UO}_2^{2+}$  in the presence of *Pseudomonas fluorescens*, proposing the relevant stability constants of the (surface) complexes.

## 23.5 Recent trends in chemical analysis of actinides by laser spectroscopy

Chemical analyses of actinides through laser spectroscopy have been developed using measurements conducted in bulk solutions and at interfaces. Innovation in spectroscopic technologies allows the detection of a target molecule or complex at an ultra-trace level, as well as the probing of relevant fast chemical processes. The local adsorption behavior or dynamics of the chemical species containing radionuclides at the heterogeneous solid-water interface will be observed using novel methods such as SNOM (scanning near-field optical microscopy). Such type of nonaveraged information captured by ultrafast spectroscopy or imaging provides a deeper understanding of the photochemical reactions occurring at the heterogeneous interface. The findings obtained through advanced laser spectroscopies can be further combined with quantum chemical modelling or electronic structure calculations; these findings also allow for the prediction and assessment of radionuclides transport in heterogeneous geochemical environments, particularly in soils and in groundwater conditions.

### 23.5.1 Interface-specific laser spectroscopy

As mentioned above, TRLFS has been used for the chemical analysis of actinide compounds. There are also other techniques involving the use of lasers: LIPAS (laser-induced photoacoustic spectroscopy), LIBS (laser-induced breakdown spectroscopy), and so on. These techniques are based on the physical processes that convert light into other forms of energy, such as heat or sound, and are therefore considered as advanced methods owing to the remarkable development in laser technologies during the 1990s. With regard to conducting an analysis at the interface, some of the promising methods currently used for ultrafast spectroscopy since 2000s are nonlinear spectroscopy such as SHG (second-harmonic generation) and SFG (sum-frequency generation) [44]. These emerging methods enable us to probe the quantities and chemical states of target ions localized on surfaces, irrespective of whether they exhibit fluorescent; the concept and the setup is designed in conformity with methods that utilize the nonlinear phenomena occurring at interfaces, where the refractive index varies from one phase to another. In particular, studies on actinides using nonlinear spectroscopy is uncommon. Geiger *et al.* [45–47] applied resonantly enhanced SHG on the water-silica and water-mica interface to study uranyl adsorption and speciation, determining the charge density for uranyl hydrolysis and carbonates species at the water-silica interface in mononuclear and poly-nuclear forms via the Eisenthal  $\chi^{(3)}$  technique (see Figure 23.5). They also evaluated the free energy of adsorption using the assumption of surface complexation modelling.

### 23.5.2 Advanced fluorescence imaging

All the laser spectroscopy methods introduced so far provide information averaged over a certain volume of a bulk solution or an interface. Spatially nonaveraged information, that is, local information is invaluable particularly for interfacial processes

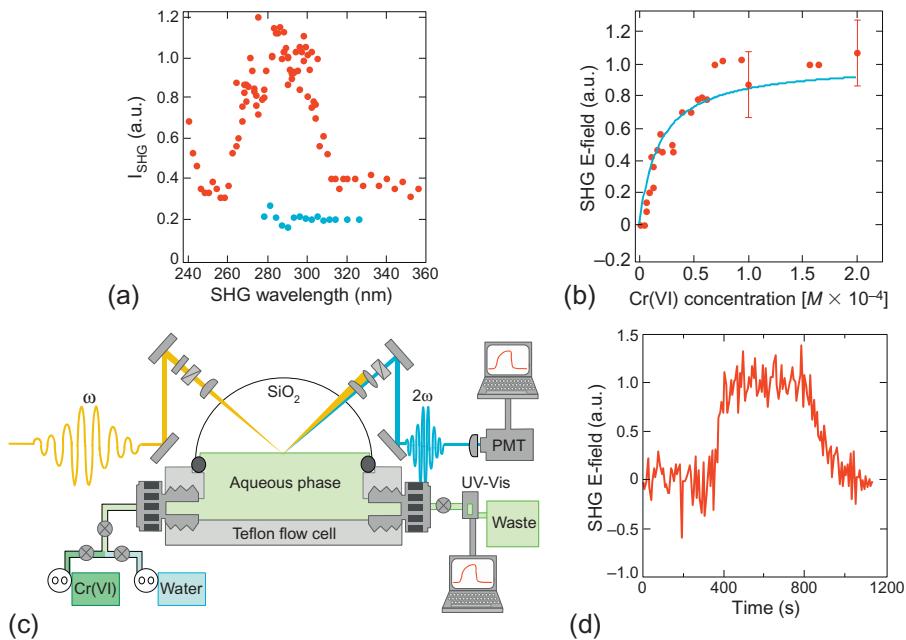


**Figure 23.5** (a) SHG spectrum of a fused quartz-water interface maintained at pH 7 in the presence (red circles) and absence (blue circles) of adsorbed chromate at the monolayer coverage, assessed through adsorption isotherm measurements (vide infra). (b) SHG adsorption isotherm recorded at 290 nm and at pH 7 as a function of chromate concentration. (c) Dual-pump flow systems used in our experiments, PMT, and photomultiplier tube. (d) Time-dependent SHG electric field (E-field) recorded while exposing a fused quartz-water interface to chromate at a concentration resulting in a monolayer coverage (near 400 s) and again to background electrolyte solution (near 800 s).

Figure adapted from Refs. [45,48].

with heterogeneous surfaces. Fluorescence microscopy serves such a purpose, as manifested in the staining of cells with fluorescent tags to investigate the location of a certain biochemical process. By combining fluorescence microscopy with TRLFS, the local chemical states of fluorescence ions on mineral surfaces and in biological samples [49] can also be obtained. For instance, radioisotopes used in the field of medicine have a variety of applications in terms of molecular labelling. Although the radiation measurement has an advantage over the quantitative observation for the environmental or biological samples, chemical speciation of the radionuclide at a specific point can be determined. Fluorescence spectra and the lifetimes of An ions at a certain crystal face of a mineral will aid in the development of a robust adsorption model. Diffraction limits the spatial resolution of classical optical microscopy to about half the wavelength of light, and this technical difficulty has long posed a challenge for engineers and scientists to overcome, especially for achieving microscopy at a nano-scale resolution. Lately, SNOM or NSOM and hyphenated infrared spectroscopy or SERS (surface-enhanced Raman scattering) have been seen as potential applications

to further understand biological macromolecules such as DNA with a 100 nm resolution, which is less than  $\sim\lambda/2$ , given by the Rayleigh criterion [50–52]. However, the combination of TRLFS with SNOM is not common, although there are a few rare examples [53–56]. Most likely, avoiding possible breakage of an optical fiber used for illuminating a sample and collecting the resulting fluorescence by a short-pulsed laser with a high peak intensity is necessary for rendering this technique applicable for various interfacial processes. A schematic setup of the interferometer and SNOM is shown in Figure 23.6.

### 23.5.3 Quantum chemical simulation for supplemental information

The chemical species and the structural geometry in aqueous solutions, found with laser spectroscopy, can be further supplemented by the subsequent theoretical prediction or substantiation. The orbital energy levels among actinide ions, which have a remarkable relativistic effect, are close to each other and are strongly influenced by the electron-electron interaction. This makes the quantum chemical modelling of reactions with An ions difficult, though it is not entirely intractable, in the following methods: *ab initio* molecular orbital (MO) theory, DFT (density functional theory), and so on. The interpretation of computational results can be complicated, so an

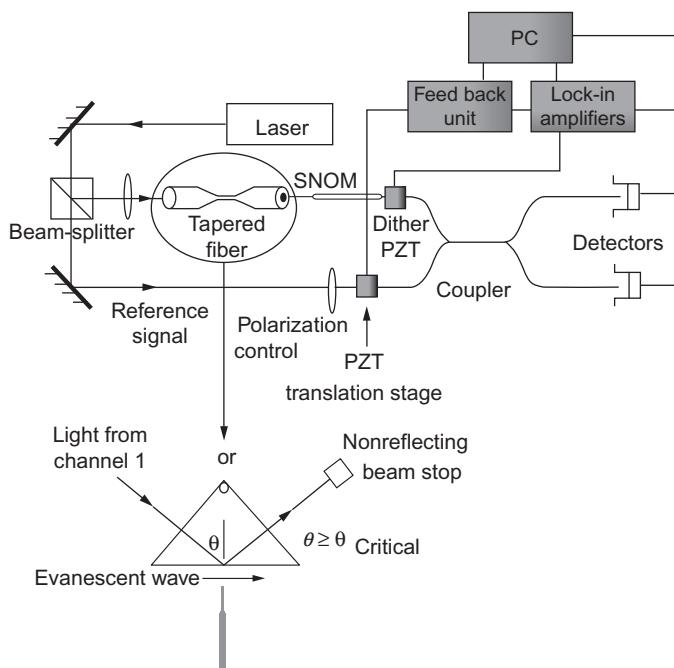


**Figure 23.6** Schematic representation of interferometer and scanning near-field optical microscope [57].

alternative method is required to interpret the results. As for the comparison of the calculated result with the spectral information, the vibrational spectroscopy has been recognized as a better modelling about the symmetry of coordination compounds. In contrast, recent studies using DFT particularly shed light on the applications of fluorescence, NMR, and photoelectron spectroscopies [58–62]. Thus, the new terminology “computational spectroscopy” suggested by Wei *et al.* [63] seems to be a more familiar expression of quantum chemical calculation for the experimentalists.

## 23.6 Future trends in laser spectroscopy

The traditional actinide studies based on laser spectroscopic techniques such as TRLFS have hitherto dealt with the complexes or colloids as the bulk existence in solutions or solids. Current interests of scientists are found more on the site-specific bonding and structure, namely, heterogeneity of interfacial chemistry [64–66]. There are versatile potential utilities that have not appeared in this chapter: for example, 2-D-IR spectroscopy [67], CARS microscopy [68], and so on. The research frontier of actinides at interfaces approaches the level of sophistication using hyphenated/combined technology among these key methods.

## References

- [1] B. Jamtveit, P. Meakin, *Growth, Dissolution and Pattern Formation in Geosystems*, Springer, The Netherlands, 1999, p. 291.
- [2] G. Bernhard, G. Geipel, V. Brendler, H. Nitsche, *Radiochim. Acta* 74 (1996) 87.
- [3] C. Moulin, P. Decambox, V. Moulin, J.G. Decaillon, *Anal. Chem.* 67 (1995) 348.
- [4] I. Billard, K. Lutzenkirchen, *Radiochim. Acta* 91 (2003) 285.
- [5] W.D. Horrocks, D.R. Sudnick, *J. Am. Chem. Soc.* 101 (1979) 334.
- [6] A. Beeby, I.M. Clarkson, R.S. Dickins, S. Faulkner, D. Parker, L. Royle, A.S. de Sousa, J.A.G. Williams, M. Woods, *J. Chem. Soc. Perkin Trans.* (1999) 493.
- [7] T. Kimura, G.R. Choppin, *J. Alloys. Compd.* 213/214 (1994) 313.
- [8] R.M. Supkowski, W.D. Horrocks, *Inorg. Chim. Acta* 340 (2002) 44.
- [9] J.R. Lakowicz, *Principles of Fluorescence Spectroscopy*, third ed., Springer, New York, 2006.
- [10] S. Cotton, *Lanthanide and Actinide Chemistry*, John Wiley & Sons, Ltd., Chichester, 2006.
- [11] E.G. Moore, A.P.S. Samuel, K.N. Raymond, *Acc. Chem. Res.* 42 (2008) 542.
- [12] K. Ishida, T. Saito, N. Aoyagi, T. Kimura, R. Nagaishi, S. Nagasaki, S. Tanaka, *J. Colloid Interface Sci.* 374 (2012) 258.
- [13] S. Lukman, T. Saito, N. Aoyagi, T. Kimura, S. Nagasaki, *Geochim. Cosmochim. Acta* 88 (2012) 199.
- [14] T. Saito, H. Sao, K. Ishida, N. Aoyagi, T. Kimura, S. Nagasaki, S. Tanaka, *Environ. Sci. Tech.* 44 (2010) 5055.
- [15] H. Chang, G.V. Korshin, Z. Wang, J.M. Zachara, *Environ. Sci. Tech.* 40 (2006) 1244.
- [16] U. Gabriel, L. Charlet, C.W. Schlapfer, J.C. Vial, A. Brachmann, G. Geipel, *J. Colloid Interface Sci.* 239 (2001) 358.

- [17] T. Kimura, G.R. Choppin, Y. Kato, Z. Yoshida, *Radiochim. Acta* 72 (1996) 61.
- [18] T. Kimura, Y. Kato, *J. Alloys Compd.* 271-273 (1998) 867.
- [19] R.N. Collins, T. Saito, N. Aoyagi, T.E. Payne, T. Kimura, T.D. Waite, *J. Environ. Qual.* 40 (2011) 731.
- [20] P. Lindqvist-Reis, C. Apostolidis, J. Rebizant, A. Morgenstern, R. Klenze, O. Walter, T. Fanghänel, R.G. Haire, *Angew. Chem. Int. Ed.* 46 (2007) 919.
- [21] P. Lindqvist-Reis, C. Walther, R. Klenze, N.M. Edelstein, *J. Phys. Chem. C* 113 (2008) 449.
- [22] A. Skerencak, P.J. Panak, V. Neck, M. Trumm, B. Schimmelpfennig, P. Lindqvist-Reis, R. Klenze, T. Fanghänel, *J. Phys. Chem. B* 114 (2010) 15626.
- [23] P. Nockemann, R. Van Deun, B. Thijs, D. Huys, E. Vanecht, K. Van Hecke, L. Van Meervelt, K. Binnemans, *Inorg. Chem.* 49 (2010) 3351.
- [24] N. Aoyagi, K. Shimojo, N.R. Brooks, R. Nagaishi, H. Naganawa, K.V. Hecke, L.V. Meervelt, K. Binnemans, T. Kimura, *Chem. Commun.* 47 (2011) 4490.
- [25] K. Binnemans, *Chem. Rev.* 107 (2007) 2592.
- [26] K. Takao, T.J. Bell, Y. Ikeda, *Inorg. Chem.* 52 (2013) 3459–3472.
- [27] S. Stumpf, I. Billard, P.J. Panak, S. Mekki, *Dalton Trans.* (2007) 240.
- [28] P. Nockemann, K. Servaes, R. Van Deun, K. Van Hecke, L. Van Meervelt, K. Binnemans, C. Görller-Walrand, *Inorg. Chem.* 46 (2007) 11335.
- [29] T. Stumpf, A. Bauer, F. Coppin, J.I. Kim, *Environ. Sci. Tech.* 35 (2001) 3691.
- [30] M.H. Bradbury, B. Baeyens, H. Geckeis, T. Rabung, *Geochim. Cosmochim. Acta* 69 (2005) 5403.
- [31] T. Rabung, M.C. Pierret, A. Bauer, H. Geckeis, M.H. Bradbury, B. Baeyens, *Geochim. Cosmochim. Acta* 69 (2005) 5393.
- [32] T. Arnold, S. Utsunomiya, G. Geipel, R.C. Ewing, N. Baumann, V. Brendler, *Environ. Sci. Tech.* 40 (2006) 4646.
- [33] Z. Wang, J.M. Zachara, J.P. McKinley, S.C. Smith, *Environ. Sci. Tech.* 39 (2005) 2651.
- [34] Z. Wang, J.M. Zachara, W. Yantasee, P.L. Gassman, C. Liu, A.G. Joly, *Environ. Sci. Tech.* 38 (2004) 5591.
- [35] S. Pompe, A. Brachmann, M. Bubner, G. Geipel, K.H. Heise, G. Bernhard, H. Nitsche, *Radiochim. Acta* 82 (1998) 89.
- [36] P.E. Reiller, J. Brevet, *Spectrochim. Acta A* 75 (2010) 629.
- [37] F. Claret, T. Schafer, T. Rabung, M. Wolf, A. Bauer, G. Buckau, *Appl. Geochem.* 20 (2005) 1158.
- [38] Y. Takahashi, T. Kimura, Y. Minai, *Geochim. Cosmochim. Acta* 66 (2002) 1.
- [39] T. Ozaki, J.B. Gillow, A.J. Francis, T. Kimura, T. Ohnuki, Z.J. Yoshida, *Nucl. Sci. Technol. (Suppl. 3)* (2002) 950.
- [40] R. Knopp, P.I. Panak, L.A. Wray, N.S. Renninger, J.D. Keasling, H. Nitsche, *Chem. Eur. J.* 9 (2003) 2812.
- [41] L. Lütke, H. Moll, G. Bernhard, *Dalton Trans.* 41 (2012) 13370.
- [42] E. Krawczyk-Bärsch, H. Lünsdorf, K. Pedersen, T. Arnold, F. Bok, R. Steudtner, A. Lehtinen, V. Brendler, *Geochim. Cosmochim. Acta* 96 (2012) 94.
- [43] A. Koban, G. Bernhard, *J. Inorg. Biochem.* 101 (2007) 750.
- [44] S. Nihonyanagi, S. Yamaguchi, T. Tahara, *J. Chem. Phys.* 130 (2009) 204704.
- [45] F.M. Geiger, *Annu. Rev. Phys. Chem.* 60 (2009) 61.
- [46] J.N. Malin, J.G. Holland, S.A. Saslow, F.M. Geiger, *J. Phys. Chem. C* 115 (2011) 13353.
- [47] S.A. Saslow Gomez, D.S. Jordan, J.M. Troiano, F.M. Geiger, *Environ. Sci. Tech.* 46 (2012) 11154.
- [48] A.L. Mifflin, M.J. Musorrafati, C.T. Konek, F.M. Geiger, *J. Phys. Chem. B* 109 (2005) 24386.

- [49] K. Ishida, T. Kimura, T. Saito, S. Tanaka, Environ. Sci. Technol. 43 (2009) 1744.
- [50] V. Deckert, D. Zeisel, R. Zenobi, T. Vo-Dinh, Anal. Chem. 70 (1998) 2646.
- [51] T. Taubner, D. Korobkin, Y. Urzumov, G. Shvets, R. Hillenbrand, Science 313 (2006) 1595.
- [52] M. Brehm, T. Taubner, R. Hillenbrand, F. Keilmann, Nano Lett. 6 (2006) 1307.
- [53] K.A. Ghaleb, F. Viala, F. Miserque, L. Salmon, P. Reiller, G. Moutiers, Appl. Spectrosc. 62 (2008) 213.
- [54] J. Grausem, M. Dossot, S. Cremel, B. Humbert, F. Viala, P. Mauchien, J. Phys. Chem. B 110 (2006) 11259.
- [55] A. Cadby, R. Dean, A.M. Fox, R.A.L. Jones, D.G. Lidzey, Nano Lett. 5 (2005) 2232.
- [56] A.J. Cadby, R. Dean, C. Elliott, R.A.L. Jones, A.M. Fox, D.G. Lidzey, Adv. Mater. 19 (2007) 107.
- [57] P.L. Phillips, J.C. Knight, J.M. Pottage, G. Kakarantzas, P.S. Russell, J. Appl. Phys. Lett. 76 (2000) 541.
- [58] S. Tsushima, Dalton Trans. (2011) 6732.
- [59] A. Ikeda-Ohno, S. Tsushima, K. Takao, A. Rossberg, H. Funke, A.C. Scheinost, G. Bernhard, T. Yaita, C. Hennig, Inorg. Chem. 48 (2009) 11779.
- [60] V. Vallet, A. Fischer, Z. Szabo, I. Grenthe, Dalton Trans. (2010) 7666.
- [61] L. Gagliardi, B.O. Roos, Nature 433 (2005) 848.
- [62] T. Toraishi, T. Tsuneda, S. Tanaka, J. Phys. Chem. A 110 (2006) 13303.
- [63] F. Wei, G. Wu, W.H.E. Schwarz, J. Li, Theor. Chem. Acc. 129 (2011) 467.
- [64] H. Geckeis, J. Lützenkirchen, R. Polly, T. Rabung, M. Schmidt, Chem. Rev. 113 (2013) 1016.
- [65] M. Altmaier, X. Gaona, T. Fanghänel, Chem. Rev. 113 (2013) 901.
- [66] C. Walther, M.A. Denecke, Chem. Rev. 113 (2013) 995.
- [67] L. Fu, J. Liu, E.C.Y. Yan, J. Am. Chem. Soc. 133 (2011) 8094.
- [68] J.X. Cheng, X.S. Xie, J. Phys. Chem. B 108 (2004) 827.

# Ablation effects of femtosecond laser functionalization on surfaces

24

*B. Raillard, F. Mücklich*

Saarland University, Saarbrücken, Germany

## 24.1 Introduction

The laser functionalization of surfaces has been the subject of multiple research studies during recent decades. Functionalization is a technique or process that transforms a low-cost material or surface into a highly valuable system. The material functionalization can be performed for multiple applications and with various methods. Numerous techniques involving different kinds of lasers are used for various functionalization. Due to the achievement of femtosecond laser techniques during the last few years, new possibilities and properties are offered to material engineers and scientists. Femtosecond laser ablation is a method that requires a simple optical setup in comparison to other light-activated methods such as replica molding or laser interference patterning.

Laser-matter interaction is a very complex phenomenon involving multiple parameters such as material chemical composition, ambient atmosphere, and laser parameters. In this chapter, we provide an overview of the technique itself and the potential effects that can be observed.

## 24.2 Laser techniques and materials

Laser functionalization using a femtosecond laser does not require a complex setup to elaborate surface patterns, which has a significant role. In fact, because laser functionalization became a common method to improve material properties in modern industries, cost-effectiveness is a common topic and target for improvement. In opposition to historical techniques such as lithography and replica moulding, the setup and optical elements required include a shutter to control the pulse number, a lens, and an aperture to control and influence the laser-irradiated area. As showed in the schematic representation of Figure 24.1, the laser light directly goes through the shutter system, the aperture, and finally the lens.

The focus of the laser beam is of crucial importance in the patterning process, and has to be carefully considered regarding the thickness of the samples and depth of the cavities ablated. Indeed, as the lens used in the work [1] has a focal length (FL) of

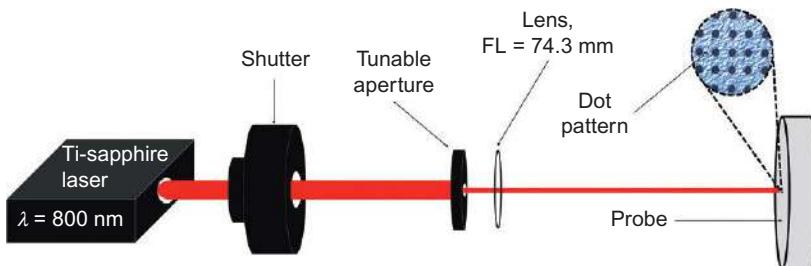


**Figure 24.1** Femtosecond laser setup for the ablation process. The laser power is controlled by the power meter. The main laser beam goes through a standard shutter and the diameter of the irradiated zone is controlled by a tunable aperture. The laser beam is focused by a lens with a FL of 74.3 mm.

Reproduced with the authorization of Raillard *et al.* [1].

about 74.3 mm, the value of the maximum cavity depth has to be previously considered. As the hole does not become deeper than 100  $\mu\text{m}$ , the laser beam is still considered as focused onto the surface of the sample. If the ablated volume becomes deeper than 100  $\mu\text{m}$ , the laser light is not focused anymore, and then the ablation process occurs at laser fluences that cannot be further assumed as constant. The effects of defocusing have not been investigated for this system but might be very interesting for the authors and their potential industrial applications because it will allow them to establish the boundaries of their method.

The femtosecond laser ablation can be applied to all kinds of materials: ceramics, polymers, metals, and also bulk or thin films, but of course certain ablation structures cannot be successfully applied to certain materials, for example, thin films of a few 100 nm thickness won't present the same aspect ratios as bulk metal matrix with ripples thickness of about 100 nm high.

A similar reflexion has to be done when the laser ablation is performed onto bulk samples. Indeed, the functionalization makes sense only if the cavity induced by the laser irradiation is in a higher scale than the original roughness. According to these observations, a preliminary study of the surface roughness has to be performed; the roughness characteristics such as root mean square and skewness values have to be studied.

## 24.3 Topographical effects

### 24.3.1 Zones

The topographical investigation of femtosecond laser-irradiated metallic samples is of prior interest in comparison to other materials such as ceramics or polymers. Indeed, because the ablation of polymers using long-pulsed laser allows a precise and tunable ablation of the material, the functionalization made by femtosecond laser is not relevant.

In comparison to nanosecond laser ablation, the femtosecond system drills holes in metallic samples without any melting phenomenon. Because the laser ablation is related to the time of relaxation of electrons in metallic materials, the ablation process strongly varies with the incident laser beam. The relaxation time can be situated around 1-10 ps for metallic materials. Using a long or very long pulsed (e.g.,  $10^{-12}$  or  $10^{-9}$  s) laser induces the complete melting of the irradiated zone, including flows or uncontrolled ejections of the molten material leading to random distributed patterns. It should be noted that this quenching phenomenon involving long-pulsed laser can be easily controlled, and is then a successful patterning technique [2]. In comparison, when the pulse duration is shorter than the relaxation time, which is the case for femtosecond laser and metallic materials, the material is not melted but ablated.

Femtosecond laser irradiation involves several phenomena depending on the working conditions, laser parameters, and material properties, which will be detailed in the following sections. Moreover, the femtosecond laser-matter interaction does not always lead to the creation of a precise and well-designed hole. Different zones and patterns clearly appeared at the surface of the samples such as ripples, cones, and their dimensions, and density and shape of the structures vary as well.

### 24.3.2 Ripples

The ripples occurring during femtosecond laser irradiation are defined as periodical patterns; they might be also described as laser induced periodic surface structures (LIPSS) in the literature [3]. Their formation directly occurs from the femtosecond laser irradiation but cannot be strictly related to the ablation mechanisms. The investigation on the morphology of the ripples is a common research topic for laser scientists. Indeed, their geometrical parameters, periodicity (periodicity, which is defined as the distance between the two highest peaks of two neighbored ripples), and height depend on multiple working conditions. The laser wavelength and the angle of incidence [4] are, first of all, the two main parameters that control the morphology of the ripples. The periodicity of the ripples is related to the wavelength of the laser. In the laser community, the first approximation of the LIPSS periodicity estimates it in the same order of magnitude as the laser wavelength. Chakravarty *et al.* [4] studied the formation of ripples using a Ti:sapphire laser (45 fs pulse duration, 800 nm wavelength) to irradiate the surfaces of semiconductors such as GaAs and SiC. The authors assumed in their work that the periodicity varies in the range  $\lambda/9$  to  $\lambda$ , where  $\lambda$  is the wavelength of the incident laser beam. These two simple estimations are correct but are clearly not relevant to precisely characterize the periodicity of the ripples. A formula ( $P = \lambda/(\lambda/\lambda_{sp} \pm i \sin \theta)$ ) has been proposed by Huang *et al.* [5], Han and Shiliang [6], and Chakravarty *et al.* [4] to calculate it. The periodicity depends on the incident wavelength of the laser beam ( $\lambda$ ), the surface plasmon wavelength ( $\lambda_{sp}$ ), the refractive index of the ambient atmosphere ( $i$ ), and the angle of incidence of the laser beam ( $\theta$ ). The surface plasmon might be defined according to the works of Homola [7], Wood [8], and Fano [9] as “*narrow dark bands in the spectrum of the diffracted light [...] referred as anomalies [...] associated with the excitation of electromagnetic waves on the surface of the diffraction grating.*”

The surface plasmon was also described by Kooymani in the *Handbook of Surface Plasmon Resonance* [10], edited by Schasfoort and Tudos, as “*propagating electron density waves occurring at the interface between metal and dielectric.*”

The formula above shows that the ripples morphology depends on several parameters, and all of them have to be carefully considered. The laser operation itself has an influence on the period because the wavelength is involved in the period calculation. The laser setup also plays a major role and the angle of incidence might have an effect. Then, the ambient atmosphere (air or controlled environment) might also influence the formation of ripples (presence of the refractive index of the media), but probably at a lower scale.

Finally, the nature of the material is also strongly involved in the formation phenomena of the ripples. The surface plasmon, arising from the interaction of the laser and the material, changes depending on the surface properties. The absorption, and then the original roughness, is induced and enhanced by the multiphoton ionization of the laser irradiation as the laser irradiation starts [11,12].

The formation of ripples induced by femtosecond laser irradiation is still a research topic for laser and material scientists. The previously given explanations and parameters are only a basic and fundamental knowledge to understand the ripples formation.

### 24.3.3 Cones

Cone structures, also called spikes or peaks, are a typical structure created by the femtosecond laser irradiation of materials. The growing of cone structures is of crucial importance in the ablation effects by femtosecond laser because their geometrical parameters (height, periodicity, and density of the forest) are directly related to the depth and shape of the ablated cavities. Their formation clearly varies with multiple parameters such as the laser parameters (laser polarization [13]) or the atmosphere [14], which can be easily controlled, or other parameters such as the chemical composition of the irradiated samples or their preferential orientation for thin films might influence the cone growth. Indeed, cone-like structures have been observed at the surface of various materials such as silicon films [13], bearing steel 100Cr6 [1,15], stainless steel [14], aluminium [14], and titanium [16], for example. The formation of the spikes, just as the formation of ripples, must be considered as a combination of multiple phenomena. For the previous reason, the formation of cones is not an exact science yet and is a challenging research topic for laser scientists.

Wu reported in her doctoral thesis [17] the femtosecond mechanisms involved in the formation of conical structures and linked it to the above-mentioned parameters. Wu [17] and Her *et al.* [13] found that the ambient atmosphere had crucial effects on the spike formation.

Wu compared the formation of conical structures under several distinct atmospheres: SF<sub>6</sub>, Cl<sub>2</sub>, nitrogen, helium, argon, and vacuum. She observed that the shape and the regularity of the spikes drastically changed. The cones had a sharp and regular shape only under SF<sub>6</sub> and Cl<sub>2</sub> atmospheres. Nayak *et al.* [18] performed similar investigations using SF<sub>6</sub> and HCl environments combined with laser irradiation. They found first that the cone sizes changed depending on the atmosphere.

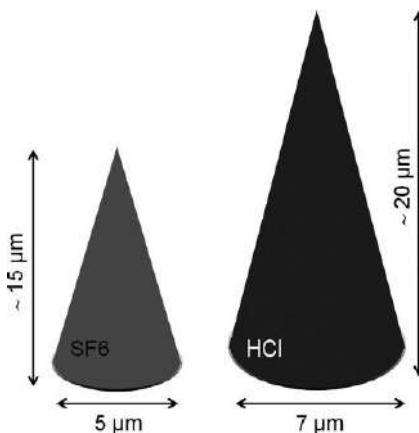


**Figure 24.2** Effects reported on the formation of conical structures by Nayak *et al.* using the two different atmospheres SF6 and HCl for the femtosecond laser irradiation [18]. The authors have established that the formation of peaks is a combination of chemical etching and laser ablation.

The SF6 atmosphere provided smaller conical structures with thinner bases than the HCl as it is schematically represented in Figure 24.2.

Nayak *et al.* could not observe a difference in the spike density (number of spikes per unit surface area) between the two cone forests. Finally, they observed that the HCl atmosphere provided pillars, which have a stronger mechanical resistance but a coarse and curvy aspect. According to the authors, this topographical difference might be explained by the different etching properties involved in the laser ablation process for the two pairs F/Si and Cl/Si. Similar aspect differences were made by the authors while using germanium samples, which confirmed the importance of the ambient atmosphere for the growing of such pillars [18].

It has been clearly established that the laser fluence (incident energy per unit surface area) had a crucial influence in the formation phenomena of the spikes. By increasing the laser energy density from 0.36 to 3.6 J/cm<sup>2</sup>, Fadeeva *et al.* [19] changed drastically the aspect and height of the spikes formed at the surface of Si samples. Her *et al.* [13] and Wu [17] observed a similar growing behavior. They increased the laser fluence from less than 5 up to 10 kJ/m<sup>2</sup>, and studied the periodicity (tip-to-tip distance) of the cones. The periodicity was found to increase nonlinearly from approximately 3.5 μm at 5 kJ/m<sup>2</sup> to 10.8 μm at 10 kJ/m<sup>2</sup>. The authors had previously established a relation between the periodicity and spike height, which lead them to affirm that multiplying the laser fluence by a factor of two led to increasing the height by a factor of 12 [13]. Wu observed that the cones' height was increasing near to the center of the laser-irradiated zone [17]. Because the laser intensity is distributed according to a Gaussian curve, the highest intensity appears in the middle of the laser zone. The cone formation results from the laser ablation phenomena, which happens if the laser fluence is above the ablation threshold of the material [17].

As it has been previously described in this chapter, the formation of ripples and cones are a combination of multiple parameters. The ablation study of Mourier *et al.* [15] revealed that the deepest ablation holes were not always induced by the highest laser fluence, but by the highest pulse number. Moreover, Her *et al.* observed that the conical structures appeared above  $2 \text{ kJ/m}^2$ , while below this threshold the laser irradiation induced only submicron ripples even using 500 pulses [13]. The following section will show the role played by the pulse number in the spikes formation. Mourier *et al.* [15] studied the combined effects of laser fluence and pulse number on the ablated depth at the surface of 100Cr6 steel samples. First, at the lowest fluence ( $0.09 \text{ J/cm}^2$ ) at any pulse number, almost no ablation effect could be observed, because this fluence is below the ablation threshold of steel. In order to understand this affirmation, the ablation threshold of stainless steel is approximately  $0.16 \text{ J/cm}^2$  according to Mannion *et al.* [20], which confirms that no ablation could be induced even if the chemistry of the two materials are different.

At a constant fluence above the assumed ablation threshold of 100Cr6 steel, Raillard *et al.* [1] studied the effects of the pulse number. Cones clearly appeared in the so-called ablation zone above a certain pulse number, after 66 pulses. Their formation was initiated by the prior laser shots and then enhanced by ablated volume and the roughness of the irradiated areas. Indeed, the spikes clearly appear when enough material is ablated from the metallic surface. Each previous pulse enhances the roughness (root mean square), which increases linearly with the pulse number [1]. According to the studies performed by many researchers such as Ang *et al.* [11] and Stern [12], the absorption properties of a material are generally enhanced by the asperities of a rough surface due to the multiple reflections of the laser light.

In the study performed by Raillard *et al.* [1], and as is clearly shown in the SEM images (see Figure 24.3c and d [1]), cones appear randomly, disordered and with various sizes in the middle of the irradiated zones. Nevertheless, studies performed at the surface of silicon samples [3] revealed that increasing the pulse number leads to the creation of highly ordered and sharper conical structures. A similitude with the random distribution of cones (Figure 24.3d) can be found for the sample irradiated with 50 pulses, but when the pulse number is increased by a factor of 10 or at least doubled, the orientation and shape of the cones become significantly regular.

The laser polarization has an influence on the growing of spikes, which can be compared to the effects observed in the formation of ripples. By changing the polarization of their laser using a half-wave plate, Her *et al.* [13] observed a corresponding change in the orientation of the basis of the cones. In the case of a linear polarized laser, the cones have an asymmetric basis and their observation revealed that the major diameter of the basis is aligned perpendicular to the laser polarization [3]. These results are in agreement with the formation process of the ripples. Wu [17] calculated the reflectance of crystalline silicon depending on the refractive index of silicon, the incident wavelength, the angle of incidence, and theoretical values. The reflectance (i.e., the absorption) strongly varies with the type of polarization of the laser and, for this reason, the cones grow asymmetrically.

As can be observed in the SEM picture (see Figure 24.4), the shape, profile, aspect, thickness, size, and then the repartition are obviously not regular. According to the

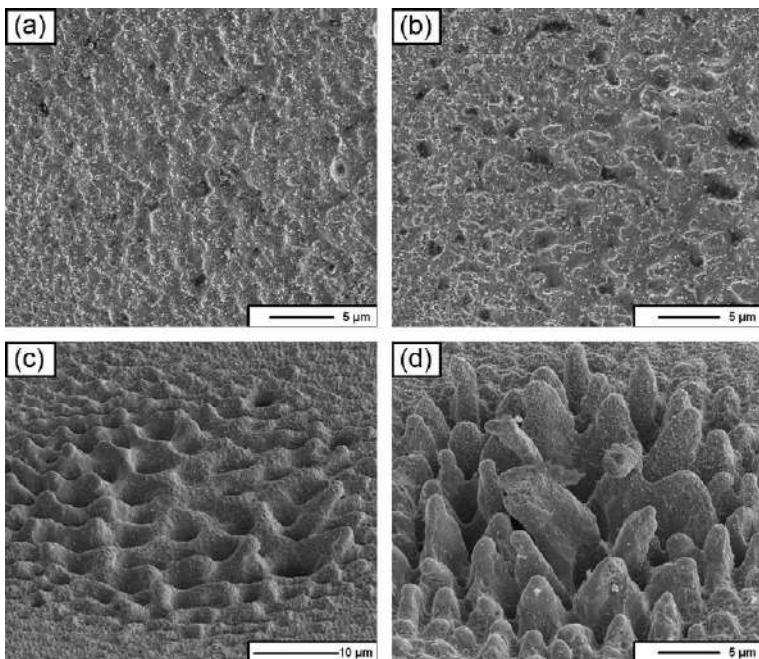


**Figure 24.3** SEM images of the four ablated areas in the laser cavities depending on the number of pulses: (a) 9, (b) 20, (c) 66, and (d) 100 pulses. For a low number of pulses (9 and 20 pulses), the ablated zone is almost flat, while for higher pulse counts (66 and 100 pulses), it becomes rough and irregular.

Reproduced with the authorization of Raillard *et al.* [1].

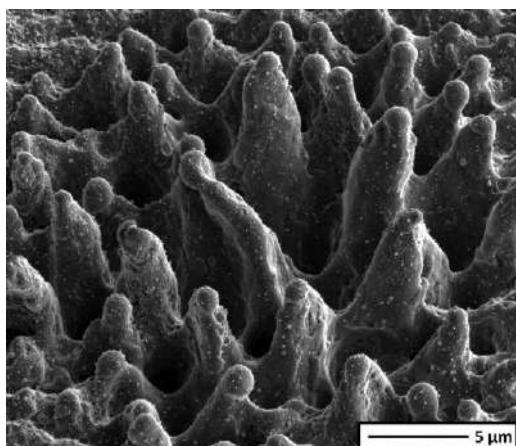


**Figure 24.4** SEM image of spikes created at the surface of a 100Cr6 steel sample with 100 pulses. The irradiation was performed with similar laser parameters and experimental setup as in the study of Raillard *et al.* [1]. Cones are randomly distributed, while the tallest spikes are in the center of the zone due to the Gaussian distribution of the laser intensity.

influences previously described, the aspects of the cones should be regular as is the case for pure materials such as Si thin films [3,19]. The choice of parameters such as the pulse number plays an important role, as it is of prior importance to determine the form of the cones. As written previously, the setup parameters used for the laser irradiation in Figure 24.4 may be partially responsible for the irregularity of the spikes' aspect, but the chemical nature of the material has also a strong effect on the growing of cones.

Her *et al.* revealed in their work [13] that the presence of cones was related to the distribution of impurities at the surface of the material. Indeed, the presence of impurities such as oxide particles at the surface of the samples significantly changes the absorption of the laser energy. The presence of oxides or, more generally, impurities at the surfaces of the samples, depends on parameters such as the elaboration process, the ambient atmosphere, and the storage conditions of the samples. These resistant particles or impurities prevent the ablation at this exact location. The distribution may not be perfectly controlled, but the chemical nature of the material will determine if the cones' forest will be strongly random distributed or more regular. In the case of pure materials and stability under ambient atmosphere, such as the Si (100) wafers used by Her *et al.* [13], the forest appears more regularly distributed than is the case of 100Cr6 steel [1], for example. Indeed, Raillard *et al.* [1] used 100Cr6 samples that were prepared by grinding and polishing techniques. These standard techniques remove most of the impurities and the roughness, but they cannot remove all the oxides and, because they are performed under air and with aqueous solutions, the presence of residual oxides appears to be obvious after the metallographic treatment. Moreover, because the samples were irradiated under air conditions, oxidation may occur before and during the process.

## 24.4 Chemical and microstructural effects

The previous section resumed the main and common topographical changes that can be observed after a standard femtosecond laser ablation. This part of the chapter will focus on certain chemical and microstructural effects due to the laser ablation process.

As the femtosecond laser irradiation removes matter, molecules, and atoms, it is important to think about the behavior of the residual and ejected matter. As previously described, the topography of the material was significantly changed and the cones and ripples themselves can have different microstructures in comparison to the nonirradiated material. After the laser irradiation of silicon wafers, Amer *et al.* [21] observed amorphization and recrystallization phenomena. Using micro-Raman spectroscopy, the authors observed that the fluence and pulse duration induced internal stresses and microstructural changes, while no heat-affected zone was always observed. Raman spectra revealed the presence of amorphous silicon, while the original Si wafer was a single crystal. The threshold of induced amorphization oscillates in an irregular way, while the laser fluence increases. Moreover, the type of the laser polarization is also found to change the proportion of amorphized silicon for a given fluence.

Bonse *et al.* [22] established that femtosecond laser irradiation also led to modifications of their crystalline silicon samples, which can be identified as amorphization and recrystallization. These phenomena appeared at low pulse numbers and are located on the external circular zone of the laser-irradiated areas. The authors found that these modifications were related to the oxidation resulting from the laser irradiation.

Raillard *et al.* [1] studied the chemical composition of 100Cr6 bearing steel irradiated by a femtosecond laser system and compared to the as-delivered state of the samples. X-ray photoelectron spectroscopy (XPS) analyses were first conducted on two different types of samples. A sample with a higher structure density (or “density of the irradiated spots”) was previously prepared to obtain a 50% pattern density in order to get sufficient information. The study was focused on the oxygen, carbon, and iron species by analyzing the behaviors of the O-1s, C-1s, and Fe-2p core levels. As shown in the nonirradiated case (see Figure 24.5, bottom), the extinctions of the metal and iron oxide peaks on the O-1s and Fe-2p spectra, respectively, are both related to the presence of oxidized species. They prove the presence of a 4.1 nm thick oxide layer. The analysis of the laser-irradiated surface reveals a significant increase of the thickness from 4.1 to 6.9 nm. The oxidation phenomena are based on the thermal and nonthermal excitations of species present at the surface of the material [23]. In the present case there is no thermal excitation because the ultrafast pulse duration of the femtosecond laser is shorter than the relaxation time of the steel. Then, the ablation process removes the native oxide layer and the atoms below [24]. Based on the works of Mott [25] and Cabrera and Mott [26], the authors affirm that the dioxide molecules present in atmosphere dissociate upon contact with the irradiated surface. Indeed, the irradiated surfaces became reactive and favorable sites for the metallic oxidation.

Moreover, the apparition of the metal carbide peaks deep inside the bulk matrix of the samples did not allow the authors to clearly speak about the concentration or the exact location of the metal carbides.

Confocal Raman spectroscopy was performed in order to collect more detailed information on the oxide and metallic species present on the different irradiated zones, as it has been represented by the authors in Figure 24.6. Figure 24.6 represents Raman spectra of the nonirradiated ripples and ablation zones of samples irradiated at a constant fluence and 20 pulses. The Raman spectra reveal that iron and chromium oxide bands appear in the three previously mentioned zones. Moreover, carbon D (disorder) and G (graphite) bands appeared on the spectra, also without depending on the location of the measurement. The presence of these peaks in all of the investigated regions is related to the original chemical composition of the 100Cr6 steel, while a significant difference of peak intensity is observed between the nonirradiated and laser-irradiated zones. This difference proves that the femtosecond laser ablation increases the quantity of the detected compounds.

Further analyses were performed in the ripple and ablation zones using higher (66) and lower (9) pulse numbers. The normalized spectra of the ripple zones showed that increasing the pulse number did not significantly change the composition of the ripples. Nevertheless, in the ablation zone, Raman spectroscopy revealed that

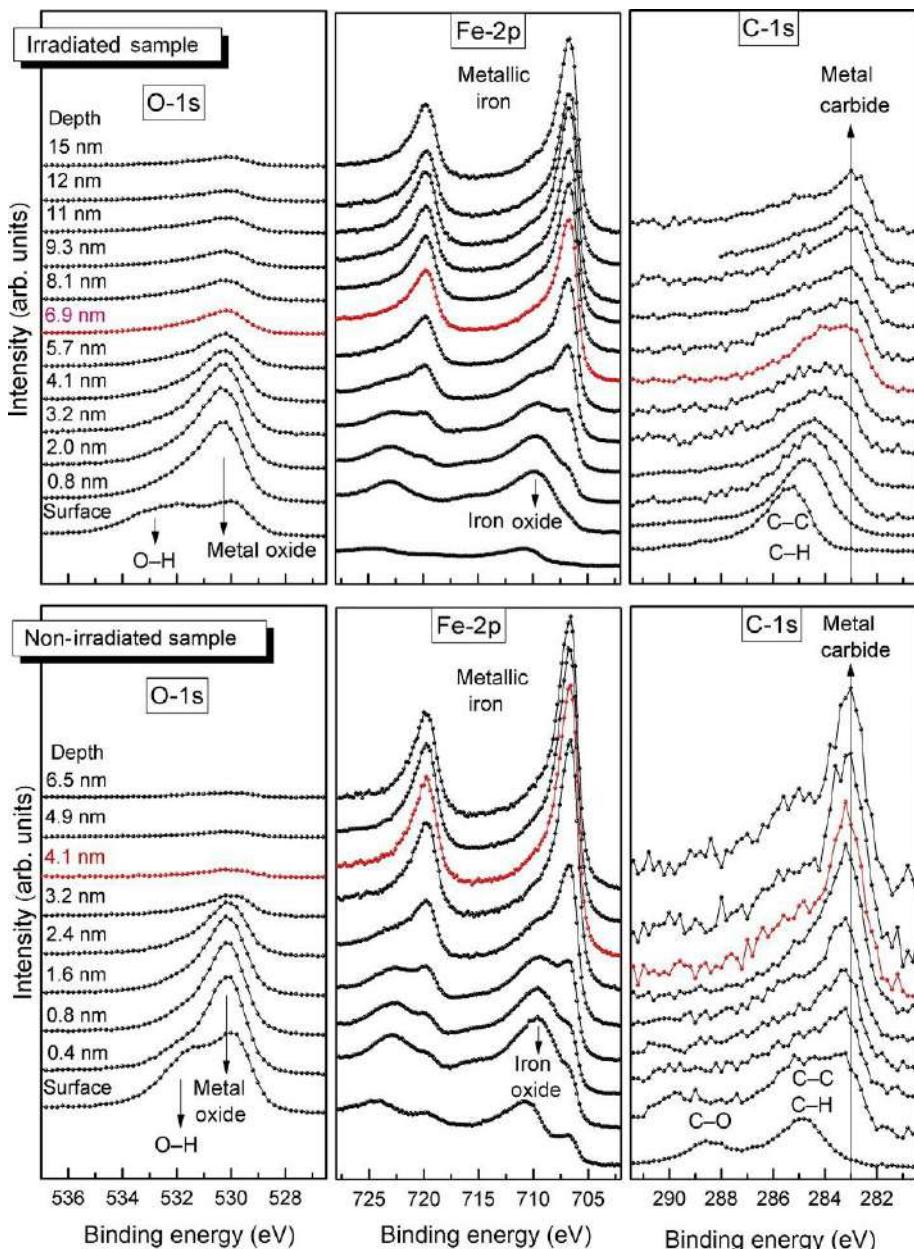


**Figure 24.5** XPS oxygen (O-1s), iron (Fe-2p), and carbon (C-1s) signals of the (top) femto-irradiated and (bottom) nonirradiated samples. The thickness of the surface layer containing iron oxide is defined by the depth at which the oxide satellite contribution vanishes [1].

Reproduced with the authorization of Raillard *et al.* [1].

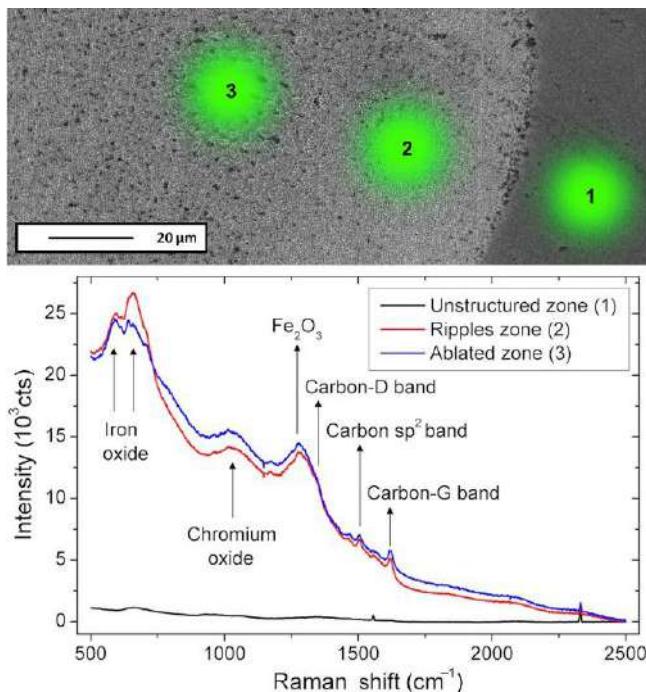


**Figure 24.6** Raw confocal Raman spectra of the unstructured (1), ripple (2), and ablated (3) zones measured on the 20 pulses sample, using an optical magnification of  $50\times$  (spot size showed in green). Iron and chromium oxides were observed in all the zones, whereas the carbon D, G, and  $\text{sp}^2$  bands were observed in the modified zones [1].

Reproduced with the authorization of Raillard *et al.* [1].

increasing the pulse number leads to amorphous-shaped spectra. Indeed, the fluorescence of the spectrum significantly increases and confirms the presence of more amorphous species in this region. Similar results can be found in the literature [27] for different systems after laser treatment and lets the authors assume that this amorphization involves melt-quenching phenomena.

Complementary Raman analyses were performed on the samples irradiated with 20 pulses, as is shown in the SEM picture (see Figure 24.7). The analysis was performed from the outer (i.e., nonirradiated) zone toward the center of the irradiated zone (i.e., the ablation zone) at regular distance. The study was focused on the D and G bands in order to observe the evolution of the ordered and disordered carbides. It revealed that the Raman intensity of the D bands was decreasing from the outer to the center of the irradiated zone, while the intensity of the G bands was increasing. It means that the femtosecond laser irradiation tends to increase the amount of ordered carbons according to the Gaussian distribution of the laser intensity. The phenomena are not yet completely understood, but the authors suggest that a recombination occurs. Indeed, they suggested that the ablation removes iron atoms and then carbon atoms can recombine in the irradiated zone regarding the energy transmitted by the laser. For these

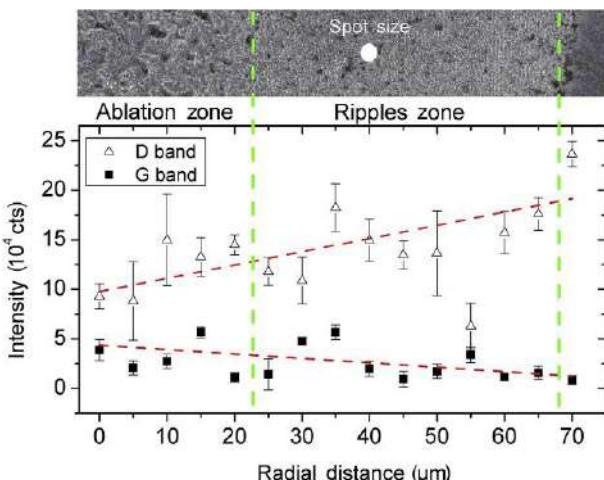


**Figure 24.7** Fitted amplitude of the Raman peaks corresponding to the carbon D and G bands measured on the 20 pulses sample using an optical magnification of  $100\times$ , which corresponds to about  $1\ \mu\text{m}$  information depth. The global tendency shows an increase of the crystallinity of the carbon toward the center of the structured zone [1].

Reproduced with the authorization of Raillard *et al.* [1].

reasons, the amount of ordered carbons increases from the nonirradiated zones, where the laser fluence is minimal toward the center of the irradiated regions. Because the binding energy is higher in the case of Fe—C in comparison to the Fe—Fe bond [28], the dissociation appears at different energy states. Thus, the authors assume that the iron and carbide species will be in their most favorable states after the femtosecond laser ablation.

## 24.5 Potential applications

In this section, potential applications for materials treated using femtosecond laser systems are briefly presented. Because femtosecond laser ablation is a recent and pioneering material treatment, the applications are still limited to research topics such as tribology and wetting. Most of them result from the previously described topographical or chemical ablation effects.

Mourier *et al.* [15] used femtosecond laser ablation in order to create microcavities. The structures have strong effects regarding the lubrication phenomena. The authors created regular holes at the surface of 100Cr6 steel with various diameters. Because different fluences and pulse numbers were used to create various dimples, their aspects and profiles drastically changed in comparison to the smooth surfaces. A film thickness evolution in the elastohydrodynamic lubrication regime proved the reservoir role of the microcavities for the lubricant.

Sugihara and Enomoto [29] used femtosecond laser to generate ripples or so-called nano- and microgrooves at the surface of a cutting tool. First, the laser irradiation significantly changed the adhesion of a wet or a dry contact. Second, the orientation of the ripples, either parallel or perpendicular to the edge, also has an influence on the friction behavior and clearly decreases the coefficient of friction in comparison to the polished tool. Finally, a combination of unstructured and laser-irradiated zones present interesting properties because it provides the lowest friction coefficient.

The use of femtosecond laser sources is not yet a common solution to tune and control the wettability of materials, as we will now show.

The wetting behavior of structured ZnO surfaces using a combination of femto- and nanosecond pulses was tailored, leading to a reversible hydrophobicity and superhydrophilicity depending on the external influences such as UV illumination and thermal heating [30]. Fadeeva *et al.* [31] irradiated silicon samples using femtosecond laser inducing spikes. The so-formed cones were used as a mold for silicone elastomers, and the replicated and original structures provided an increase of the hydrophobicity because the surfaces were in the Cassie-Baxter regime. Indeed, the authors assumed that air pockets are trapped between the fluid and the structured materials, which led to composite (solid-liquid-air) interfaces.

Femtosecond laser ablation is also of interest for the tailoring of surfaces in comparison to techniques involving melting of the matter, such as laser-interference patterning [32]. Indeed, because the femtosecond laser system allows the ablation of very precise cavities, the load-bearing properties can be tailored depending on the pulse number as it is shown in the Abbott-Firestone curves plotted by Raillard *et al.* [1] (see Figure 24.8).

The curves plotted in Figure 24.8 show that as the pulse number (i.e., the maximal depth of the cavities) increases, the bearing capacity of the surface decreases. This way of tailoring metallic materials is very promising because the ablation cavities might also be used as lubricant “reservoir.” Indeed, depending on their shape and geometrical parameters (diameter, presence of cones, slope of the wall), the ablation holes will retain the fluid with different behaviors. This process is actually developed by research labs such as the Chair of Functional Materials to create superwetting structures or to design the wettability of a surface. As is shown in Figure 24.9, the contact angle varies as a function of the maximal depth of the laser cavities. After 6 s (the most stabilized measurement), the highest contact angle appears for 5  $\mu\text{m}$  depth configuration. The laser-ablated zones corresponding to a 5  $\mu\text{m}$  depth show very deep and steep profiles plus the presence of conical structures in the middle of the ablated zone. Then, the fluid requires more energy to pass such high energetically barriers, which significantly slows down the spreading of the metallic surface. These kinds of asperities trap the liquid between them in comparison to the 1  $\mu\text{m}$  depth surface, which is very regular and relatively flat. The 3  $\mu\text{m}$  depth configuration presents the lowest contact angle after 6 s. The 3  $\mu\text{m}$  depth cavities are very regular in comparison to the 5  $\mu\text{m}$  patterns, and no cone and sharp asperity were observed in this configuration. Then, the ablated holes have a perfect role of “lubricant reservoir.”

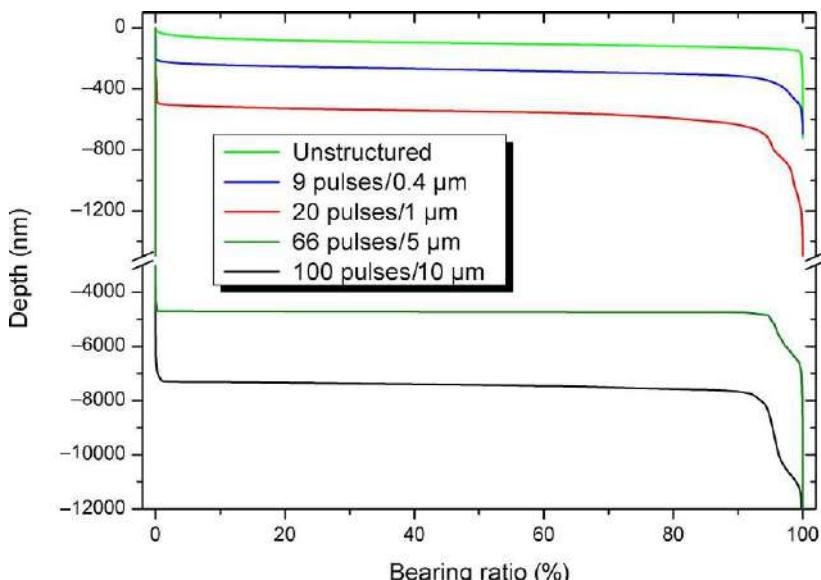


**Figure 24.8** Abbott-Firestone curves of femtosecond laser structured 100Cr6 samples. The samples irradiated with a low number of pulses (9 and 20 pulses) have a bearing behavior similar to the unstructured samples. For a high number of pulses (66 and 100 pulses), the bearing properties decrease [1].

Reproduced with the authorization of Raillard *et al.* [1].

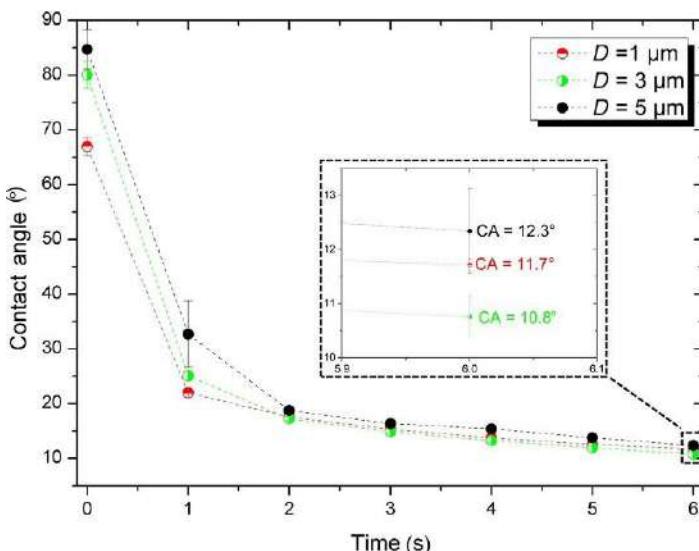


**Figure 24.9** Contact angle measurements performed using FVA 2 oil (BP) on various laser-irradiated steel samples as a function of the time. The contact angle varies depending on the maximal depth found in the ablation zone. The distance between the laser zones and the diameter were kept constant (500 and 110  $\mu\text{m}$ , respectively).

The laser ablation might then also be used for tribological applications in new processes because it successfully combines good bearing properties and a lubricant reservoir effect.

## 24.6 Conclusions

Femtosecond laser ablation is obviously an effective technique to functionalize surfaces but should be carefully considered because a profound knowledge of the phenomena involved is required to understand and apply the femtosecond laser functionalization. Indeed, while the setup used for femtosecond laser ablation might be described as simple in comparison to other patterning techniques, the phenomena involved in this technique are really complex and related to multiple parameters. Indeed, the ablation results in various topographical (cones, ripples) and microstructural (recombination, oxidation, amorphization) effects, which depend on the laser parameters (pulse number, intensity distribution, angle incidence, etc.), the atmosphere conditions, the wished geometrical parameters of the structure, and, of course, the material itself. Moreover, the functionalization of surfaces by using femtosecond laser ablation is of interest because it allows the texturing of multiple materials. It seems to be a source of material patterning for various applications such as low-friction material or controlled-surface wettability. Because femtosecond laser ablation is a high-precision technique allowing a fine material texturation (ripples, cones, cavities) with multiple geometries (period, orientation, structure density), it will be used in the future by engineers and scientists to expand their choice in material functionalization.

## References

- [1] B. Raillard, L. Gouton, E. Ramos-Moore, S. Grandthyll, F. Müller, F. Mücklich, Ablation effects of femtosecond laser functionalization on steel surfaces, *Surf. Coat. Technol.* 207 (2012) 102–109.
- [2] C. Daniel, F. Mücklich, Z. Liu, Periodical micro-nano-structuring of metallic surfaces by interfering laser beams, *Appl. Surf. Sci.* 208-209 (2003) 317–321.
- [3] B.R. Tull, J.E. Carey, E. Mazur, J.P. McDonald, S.M. Yalisove, Silicon surface morphologies after femtosecond laser irradiation, *MRS Bull.* 31 (08) (2006) 626–633.
- [4] U. Chakravarty, R.A. Ganeev, P.A. Naik, J.A. Chakera, M. Babu, P.D. Gupta, Nano-ripple formation on different band-gap semiconductor surfaces using femtosecond pulses, *J. Appl. Phys.* 109 (8) (2011) 084347.
- [5] M. Huang, et al., Origin of laser-induced near-subwavelength ripples: interference between surface plasmons and incident laser, *ACS Nano* 3 (12) (2009) 4062–4070.
- [6] Y. Han, Q. Shiliang, The ripples and nanoparticles on silicon irradiated by femtosecond laser, *Chem. Phys. Lett.* 495 (4) (2010) 241–244.
- [7] J. Homola, in: *Surface Plasmon Resonance Based Sensors*, vol. 4, Springer, 2006.

- [8] R.W. Wood, On a remarkable case of uneven distribution of light in a diffraction grating spectrum, *Philos. Mag.* 4 (1902) 396.
- [9] U. Fano, The theory of anomalous diffraction gratings and of quasi-stationary waves on metallic surfaces (Sommerfeld's waves), *J. Opt. Soc. Am.* 31 (1941) 321.
- [10] R.B.M. Schasfoort, A.J. Tudos, *Handbook of Surface Plasmon Resonance*, Royal Society of Chemistry, 2008.
- [11] L.K. Ang, Y.Y. Lau, R.M. Gilgenbach, H.L. Spindler, Analysis of laser absorption on a rough metal surface, *Appl. Phys. Lett.* 70 (6) (1997) 696–698.
- [12] G. Stern, Absorptivity of cw CO<sub>2</sub>, CO and YAG laser beams by different metallic alloys, in: *Proceedings of ECLAT*, vol. 90, 1990, September, pp. 25–35.
- [13] T.H. Her, R.J. Finlay, C. Wu, E. Mazur, Femtosecond laser-induced formation of spikes on silicon, *Appl. Phys. A* 70 (4) (2000) 383–385.
- [14] B.K. Nayak, M.C. Gupta, Self-organized micro/nano structures in metal surfaces by ultrafast laser irradiation, *Opt. Lasers Eng.* 48 (10) (2010) 940–949.
- [15] L. Mourier, D. Mazuyer, A.A. Lubrecht, C. Donnet, E. Audouard, Action of a femtosecond laser generated micro-cavity passing through a circular EHL contact, *Wear* 264 (5) (2008) 450–456.
- [16] V. Oliveira, S. Ausset, R. Vilar, Surface micro/nanostructuring of titanium under stationary and non-stationary femtosecond laser irradiation, *Appl. Surf. Sci.* 255 (17) (2009) 7556–7560.
- [17] C. Wu, Femtosecond laser-gas-solid interactions, Ph.D. Thesis, Harvard University, 2001.
- [18] B.K. Nayak, M.C. Gupta, K.W. Kolasinski, Ultrafast-laser-assisted chemical restructuring of silicon and germanium surfaces, *Appl. Surf. Sci.* 253 (15) (2007) 6580–6583.
- [19] E. Fadeeva, S. Schlie, J. Koch, A. Ngezahayo, B.N. Chichkov, The hydrophobic properties of femtosecond laser fabricated spike structures and their effects on cell proliferation, *Phys. Status Solidi A* 206 (6) (2009) 1348–1351.
- [20] P. Mannion, J. Magee, E. Coyne, G.M. O'Connor, Ablation thresholds in ultrafast laser micromachining of common metals in air, in: *Opto Ireland*, International Society for Optics and Photonics, 2003, March, pp. 470–478.
- [21] M.S. Amer, M.A. El-Ashry, L.R. Dosser, K.E. Hix, J.F. Maguire, B. Irwin, Femtosecond versus nanosecond laser machining: comparison of induced stresses and structural changes in silicon wafers, *Appl. Surf. Sci.* 242 (1) (2005) 162–167.
- [22] J. Bonse, S. Baudach, J. Krüger, W. Kautek, M. Lenzner, Femtosecond laser ablation of silicon-modification thresholds and morphology, *Appl. Phys. A* 74 (1) (2002) 19–25.
- [23] D. Bäuerle, *Laser Processing and Chemistry*, Springer Verlag, Berlin, Heidelberg, 2011.
- [24] R. Holenstein, S.E. Kirkwood, R. Fedosejevs, Y.Y. Tsui, Simulation of femtosecond laser ablation of silicon, in: *Photonics North*, International Society for Optics and Photonics, 2004, November, pp. 688–695.
- [25] N.F. Mott, The theory of the formation of protective oxide films on metals—III, *Trans. Faraday Soc.* 43 (1947) 429–434.
- [26] N. Cabrera, N.F. Mott, Theory of the oxidation of metals, *Rep. Prog. Phys.* 12 (1) (1949) 163.
- [27] Y. Hirayama, M. Obara, Heat-affected zone and ablation rate of copper ablated with femtosecond laser, *J. Appl. Phys.* 97 (6) (2005) 064903.
- [28] L. Pauling, Atomic radii and interatomic distances in metals, *J. Am. Chem. Soc.* 69 (3) (1947) 542–553.

- [29] T. Sugihara, T. Enomoto, Development of a cutting tool with a nano/micro-textured surface—improvement of anti-adhesive effect by considering the texture patterns, *Precis. Eng.* 33 (4) (2009) 425–429.
- [30] E.L. Papadopoulou, et al., Reversible photoinduced wettability transition of hierarchical ZnO structures, *J. Phys. Chem. C* 113 (7) (2009) 2891–2895.
- [31] E. Fadeeva, et al., The hydrophobic properties of femtosecond laser fabricated spike structures and their effects on cell proliferation, *Phys. Status Solidi A* 206 (6) (2009) 1348–1351.
- [32] M. Frank, et al., Laser interference metallurgy—using interference as a tool for micro/nano structuring, *Int. J. Mater. Res.* 97 (10) (2006) 1337–1344.

This page intentionally left blank

# Laser surface engineering in dentistry

25

R.S. Oliveira, J.T. Pereira, C.M. Assunção, S.B. Werle,  
J.A. Rodrigues

Federal University of Rio Grande do Sul (UFRGS), Porto Alegre, Brazil

## 25.1 Introduction

Since the 1960s, laser therapy has been used in dentistry as an adjunct or an alternative to traditional approaches, being nowadays a well-known technique and widely used on different oral surfaces, which means hard, soft, and dental tissues [1–3].

The laser application in the oral cavity depends on the following parameters: desired penetration depth of the radiation into the different tissues (given by the radiation wavelength); the duration of this interaction (continuous versus pulsed laser regime); pulse repetition rate, the energy, radiation power, irradiated area, energy density, and length of pulse [4].

These properties define the interaction of the laser and the oral cavity, once specific wavelength and fluence (continuous wave or pulsed laser) are required to each tissue (hard, soft, or dental tissue) for different actions [2]. This complete description of the parameters' function would assist the professional in applying laser therapy to clinically replicate the findings in experimental trials.

In dentistry, low- and high-intensity lasers are used with different applications. Low-intensity laser (i.e., He-Ne, Ga-As, As-Ga-Al, In-Ga-Al-P) can be helpful for caries detection, treatment of pain, neuromuscular disorders, inflammatory process control, and acceleration of the healing process. High-intensity lasers (i.e., Er:YAG, Nd:YAG, Ho: YAG, Argon, CO<sub>2</sub>, excimer, Alexandrite) are used for surgical treatments such as excision or incision of soft tissues and dental caries and calculus removal [5–9].

The dental applications can be divided into the following:

Effect of lasers on soft tissues:

- Therapeutic use: recurrent aphthous ulcer, ulcers, mucositis;
- Surgical treatments: excision or incision of lesions without bleeding;
- Periodontal: surgery and disinfection;
- Endodontic applications: disinfection using lasers.

Effect of lasers on hard tissues:

- Caries detection;
- Caries removal;
- Caries prevention—enhancing enamel resistance;
- Treatment of dentin hypersensitivity by laser radiation;
- Dental bleaching.

## 25.2 Effect of lasers on soft tissues

On soft tissues, two types of lasers can be used depending on the therapy purpose: low- and high-intensity lasers. The first acts as a cellular biomodulator, guiding the inflammatory response, accelerating epithelialization, increasing vascularization, and collagen synthesis. The red laser operates in the most superficial tissue layer and is indicated mainly for healing. The infrared laser is suitable for analgesia and inflammation, acting in deeper tissues [10,11]. High-intensity lasers operate on soft tissue cutting and excisioning lesions through light absorption, generating heat, dehydrating, coagulating, vaporizing, or charring. When the surface is irradiated three well-defined zones are formed over the healthy tissue: vaporized, necrotic, and coagulated [5,12].

Low-level laser therapy (LLLT) uses low-powered laser light in the range of 1-1000 mW, at wavelengths from 632 to 1064 nm, to stimulate a biological response. Instead of generating a thermal effect, LLLT acts by inducing a photochemical reaction in the cell, a process referred to as biostimulation or photobiomodulation. It works on the principle that, when light hits certain molecules called chromophores, the photon energy causes electrons to be excited and jump from low-energy orbits to higher-energy orbits [10]. LLLT induces DNA synthesis in myofibroblasts and conversion of fibroblasts to myofibroblasts, energy production at mitochondrial level, and finally an increase in vascularity and reepithelialization of injured tissues. The anti-inflammatory and analgesic effects of low-power lasers might be attributed to a decrease in proinflammatory cytokines, a decrease in free oxygen radicals, and alterations in nerve impulse conduction [8,10,11].

LLLT benefits can be achieved with various wavelengths and units with different outputs. The first working laser was a ruby laser (a solid-state laser using a single, rod-shaped ruby crystal). It emitted pulsed light at a wavelength of 694 nm. The ruby laser was also the first to be used in biostimulatory research in the mid-1960s. Among its successors was the HeNe (Helium-Neon) laser, a gas laser emitting at 632.8 nm with a power output of 1-5 mW. The most popular lasers are relatively inexpensive diode units that were developed in the 1980s. The GaAs (gallium-arsenide; 904 nm) diode laser was developed in the early 1980s and was typically 1-4 mW. Pulse-train modulated GaAs lasers entered the market in the late 1980s. The GaAlAs (gallium-aluminum-arsenide; 780-890 nm) was developed in the late 1980s. It was originally designed as a 10- to 30-mW unit but since in the late 1990s has been featured up to 500 mW. The InGaAlP (indium-gallium-aluminium-phosphide; 630-700 nm) diode lasers were developed in the mid-1990s. Typically, 25-50 mW devices offer an alternative to the HeNe laser for surface wound healing. The power of the GaAlAs lasers should not be less than 100 mW to obtain the desired biologic effect in a reasonable time [11].

Dental therapeutic lasers usually are the size of an electric toothbrush and come with an attachable intraoral probe shaped like the wand used in composite curing light units.



**Figure 25.1** (a) Low-power laser therapy XT (DMC). (b) Patients with cancer, preventive application for mucositis. Figures provided by the group of the Mãe de Deus Hospital Dentistry, Porto Alegre, Brazil.

### 25.2.1 Therapeutic indications

In recent years some researchers have focused attention on the use of LLLT to treat and prevent chemotherapy- and radiotherapy-induced oral mucositis (Figure 25.1). This is one of the serious complications of patients receiving radiotherapy or chemotherapy. There are reports that around 50% of patients with different cancers, who undergo chemotherapy and bone marrow transplantation, develop oral mucositis [13–15].

This oral injury is a result of a complicated biologic process, involving direct damage to the oral epithelium during cell division, decrease of the basal cell counts in the epithelium, the immune system modulation weakness, intensification of the inflammatory processes, and super infection by the oral bacterial flora. It gives rise to a painful inflammatory process, which might be debilitating and might need the use of opioid analgesics for pain relief [13].

Moreover, severe mucositis might have a detrimental effect on the patients' therapeutic protocol, leading to the cessation of the treatment in some cases. It is usually manifested in the first and second weeks of chemotherapy sessions, subsiding during the third or fourth weeks after chemotherapy [14,16].

In recent years, some researchers have focused attention on the use of low-power lasers to treat and prevent chemotherapy- and radiotherapy-induced oral mucositis. At the beginning of 2013, a systematic review with meta-analyses about the "Interventions for treating oral mucositis for patients with cancer receiving treatment" [17], concluded that there is weak and unreliable evidence that low-level laser treatment reduces the severity of mucositis. But, only the low-level laser showed a reduction in severe mucositis when compared with the sham procedure. Another systematic review with meta-analysis about the effects on prevention and treatment of LLLT in cancer therapy-induced oral mucositis was recently published [16]. It showed that there is consistent evidence from small high-quality studies that red and infrared LLLT can partly prevent the development of cancer therapy-induced oral mucositis.

LLLT also significantly reduced pain and severity and duration of symptoms in patients with cancer therapy-induced oral mucositis [16].

A recent double-blind randomized controlled study with patients who underwent chemotherapy showed that LLLT was able to decrease the effect of chemotherapy on oral mucositis, xerostomia, and pain in a variety of malignancies, concluding that low-level laser might decrease the intensity of mucositis [14].

The most recent review analyzed the available literature on this issue and defined clinical practice guidelines for the use of laser therapies for the prevention and treatment of oral mucositis. A new recommendation was made for the use of low-level laser for the prevention of oral mucositis in adult patients receiving hematopoietic stem cell transplantation conditioned with high-dose chemotherapy, with or without total body irradiation. It was, to use wavelength at 650 nm, power of 40 mW, and each square centimeter treated for the required time with a tissue energy dose of  $2 \text{ J/cm}^2$  (2 s/point). A new suggestion was made for low-level laser—wavelength around 632.8 nm—for the prevention of oral mucositis in patients undergoing radiotherapy, without concomitant chemotherapy, for head and neck cancer [18].

A common pathological change found in the oral mucosa is the recurrent aphthous ulcer (RAU), characterized by painful single or multiple ulcers. This is a result of an oral epithelium lesion, which typically exposed nerve endings and results in pain or soreness, especially when eating spicy foods or citrus fruits [19,20].

The ulcers and erosions may also come from local manifestations of systemic diseases. These range from epithelial damage resulting from trauma; from an immunological attack as in lichen planus, pemphigoid, or pemphigus; damage because of an immune defect as in HIV disease and leukemia; infections such as herpes viruses, tuberculosis, and syphilis; cancer; and nutritional defects such as vitamin deficiencies and some gastrointestinal disorders [19]. Some predisposing factors may be identifiable for RAU: stress; trauma; deficiencies of iron, folic acid, or vitamin B12; sodium lauryl sulfate; cessation of smoking; gastrointestinal disorders; and food allergies. HIV is also considered as a predisposing factor for RAU due to immune deficiency [21].

There is no curative treatment for RAU, and few randomly controlled trials have investigated treatments [19], although a consensus approach was recently published [20]. Currently, the best that can be achieved is avoiding local traumatic precipitants, decreasing the pain and duration of ulceration by suppressing the local immune response, and preventing secondary infection. RAU management has traditionally included medication with different categories of drugs. More recently, lasers have been used because they improve the efficacy of wound healing and eliminate the potential adverse effects caused by drugs. More specifically, Nd:YAG lasers are currently used for a wide range of dental applications [19,20].

Published controlled clinical trials show a trend in favor of the use of laser, suggesting that the use of Nd:YAG laser provides better patient acceptance, shorter treatment time, and lower rates of pain and post-treatment adverse events among patients with RAU. Besides, studies with LLLT have demonstrated analgesic and healing effects with regard to RAU [20]. However, the use of LLLT on the oral lesions has still not been widely accepted by the dental community due to the lack of sufficient numbers of controlled clinical trials.

## 25.2.2 *Laser and soft tissues surgery*

Recent studies have demonstrated the use of lasers in soft tissue surgery on the dental area [22–27]. The common laser advantages comparing with conventional treatments are: low bleeding, reduced bacterimia, reduction of scar formation and swelling, generally does not require sutures, reduced postoperative pain, and greater precision and control of cut [27]. Thus, the laser has been an auxiliary tool for oral surgeries such as gingivectomy, gingivoplasty, frenectomy, and excisional and incisional biopsies.

The most commonly used lasers for surgical purposes in oral soft tissues are carbon dioxide (CO<sub>2</sub>); neodimium doped yttrium aluminum garnet (Nd:YAG); erbiumdoped yttrium aluminum garnet (Er:YAG); and laser diode [27,28]. The choice of which laser should be used is based on the intrinsic characteristics of the oral soft tissue to be irradiated, such as pigmentation, vascularization, and water content [6].

The CO<sub>2</sub> laser (wavelength of 10.6 mm) has been used since the early 1970s [22]. It has become one of the most useful tools in oral surgery because of its advantages, such as hemostasis of small blood vessels, maintenance of a sterile environment (due to the high temperature of the laser beam), and reduced acute inflammatory reactions and postoperative pain (due to sensory nerve endings sealing). The CO<sub>2</sub> laser has a high coefficient of water absorption and causes vaporization of water-rich tissues, such as oral tissues (70-90% water). Thus, it is applied ideally for excision, vaporization, and coagulation of these tissues [6,25–27].

The main disadvantages of CO<sub>2</sub> lasers are the collateral effects, such as thermal damage, which could complicate the histological analysis of the manipulated lesion [28]. However, recent clinical trials show that the thermal damage does not affect the histological diagnosis [25,26] when 1 mm is maintained as a safety margin.

The Nd:YAG laser is absorbed by pigments with depth tissue penetration [6]. When used in contact mode, the Nd:YAG laser has excellent ablation of soft tissue, cutting with precision and adequate hemostasis, which is useful in procedures such as gingivectomy and gingivoplasty. This laser also sterilizes while it cuts, thus decreasing the rate of postoperative infection. When pulsed, Nd:YAG laser does not cause thermal damage, and produces a reduction in postoperative pain compared to conventional surgery [23].

The Er:YAG laser operates at a wavelength of 2.94, which is well absorbed by water and therefore is also recommended to be used on soft tissues [6]. The Er: YAG laser coefficient of water absorption is greater than that of CO<sub>2</sub> and Nd:YAG lasers, thus Er:YAG laser seems to be particularly useful for soft tissue surgery, when a coagulation effect is required. The operator should be careful with iatrogeny to adjacent tissues, such as bone, cementum, and dentin [29]. Moreover, Er:YAG laser promotes less inflammation and improved wound healing compared to CO<sub>2</sub> laser [28].

Diode lasers with wavelengths ranging from 810 to 980 nm, from a pulsed or continuous mode, are a possible instrument for soft tissue surgery [24]. Its relatively small size and lower cost has made its use very attractive [6]. The application without contact is made to coagulate superficial lesions with moderate power densities,

while the contact mode is used to cut tissue, which can seal vessels up to 2 mm in diameter.

Although the use of lasers during surgeries of soft tissue has become a reality in clinical dentistry and numerous studies have involved its use, few quality clinical trials are found in the literature. This emphasizes the need for further studies on laser technique standardization and optimization.

### **25.2.3 *Laser and periodontal therapy***

Conventional treatment of periodontitis consists of eliminating biofilm and calculus from periodontal pocket with the use of manual instruments such as curettes in order to scale and root plane (SRP) [30]. To optimize therapy, the use of lasers has been studied as an adjunct treatment [7]. The laser may contribute to bacterial reduction in periodontal pockets, conforming the pigmentation of the cell membranes, morphology, and water content of the bacteria [31], as well as contribute to the removal of calculus and granulation tissue of tooth and soft tissues wall [32].

The most common devices studied in periodontics include the semiconductor diode laser, the Er:YAG laser; the Nd:YAG laser; and the CO<sub>2</sub> laser [33]. The CO<sub>2</sub> laser and the Nd:YAG laser have shown nonfavorable outcomes [34]. Regarding the Nd:YAG laser, clinical trials have not found superior clinical or microbiological effects compared with conventional treatment [30,32], and the CO<sub>2</sub> laser treatment needs further studies to better understand its usefulness in root conditioning [35].

The Er:YAG laser, approved by the U.S. Food and Drug Administration (FDA) for sulcular debridement in 1999, seems to be the best alternative [31,33]. The Er:YAG laser has a bactericidal effect [33], and the potential to remove bacterial endotoxins from the root surface by high coefficient of absorption of the light frequency applied by lipopolysaccharides (LPS) [36,37]. Moreover, the Er:YAG laser has the ability of tissue ablation with minimal thermal damage, especially when used in association with irrigation [37].

Some clinical trials failed to demonstrate any advantage of using the Er:YAG laser for subgingival debridement compared with conventional treatment [31,34], although less discomfort has been demonstrated by the patients [37]. However, the use of the Er:YAG laser as an adjunct to surgical treatment has been demonstrated, and good clinical results have been achieved. These results might be explained by detoxification of lipopolysaccharide-contaminated root surfaces. Moreover, Er:YAG laser irradiation causes microcracking, disorganization, slight recrystallization of the original apatites, and reduction of surrounding organic matrix [33].

In the last years, photodynamic (Pd) therapy has been studied in periodontology. This technique combines diode lasers and photosensitizer substances, such as methylene blue, which make it able to interact with LPS and deactivate it. A recent study associated Pd with conventional treatment, and a significant clinical improvement and reduction of microbiota was found, when compared with conventional treatment alone [36].

Thus, although previous studies using the laser in periodontal therapy started in the 1990s, up to now there is still controversy about its effectiveness [32,33]. The lack of clinical trials with long follow-up and the diversity of laser application techniques leads to difficulty in comparing these techniques to conventional treatment (SRP). In this way, there is a lack of consensus that laser application improves clinical parameters in periodontal treatment [35,36].

#### **25.2.4 *Laser and endodontics***

The success of endodontic therapy consists of the elimination of microorganisms from the root canal system to allow tissue reparation [38,39]. However, complete removal of these microorganisms and their toxins is difficult to obtain [40,41]. Therefore, new strategies supplementing conventional treatment, such as the application of laser, have been studied [40]. Different types of lasers with an optical fiber device (Nd:YAG, argon, and diode) or made from a hollow tube ( $\text{CO}_2$  and Er:YAG) have shown good ability for microbial reduction in root canals, as well as in removing debris from the dentine surface [29,40,41].

The use of Nd:YAG laser for photothermal disinfection has been effective and safe. Moreover, its thermic effect can be absorbed by mineral structures and it disrupts crystal structures, promoting morphological changes by dentin melting and resolidification of dentin, which can reduce dentinal permeability [38,42]. However, the literature indicates that Nd:YAG laser irradiation is only a possible supplement for canal disinfection [42], and requires several cycles of application as an adjunct to conventional treatment protocol.

The diode laser seems to be a safe option. Due to its low interaction with water and hydroxyapatite, it might be attractive for endodontic treatments, because its transmission is made by flexible, thin fibers that can adapt to the dimensions of curved root canals [43]. Its efficacy and safety have been demonstrated in the literature, mainly when it is applied in the root canal at 1.5 W in all operating modes, and 3.0 W in the pulsed mode, for 20 s [41]. Furthermore, the use of photoactivated disinfection using dye activator can have a lethal effect on bacteria membrane, with a high level of selectivity for killing microorganisms. However, the diode laser is considered to be only an additional tool to conventional endodontic treatments [43].

There are important limitations on the use of lasers in root canals. The first concerns energy emission, which is guided longitudinally along the axis of the canal and does not achieve the lateral walls, reducing the laser's effectiveness. However, alternative devices, which enable lateral light emission, have been studied [40].

The second limitation includes thermal damage due to the transmission of radiation (converted into thermal energy) to the root apex. This may affect the support tissues and cause significant clinical effects, such as a predisposition to root reabsorption and periodontal ligament fibers, periradicular and alveolar bone necrosis, ankylosis, and pain. The severity of these effects is determined by the quantity of heat generated and by the time that it persists in the area [39–41].

Despite the promising effect of laser in endodontic treatment, more studies with clinical assessments are necessary, considering parameters of safety and effectiveness [39,41]. The results published to date, most of them from *in vitro* studies, must be interpreted with caution in view of the costs involved and, especially, of the adverse effects [42].

## 25.3 Effect of lasers on hard tissues

### 25.3.1 Caries detection

The use of lasers for detecting caries lesions has been studied for some years. This new technology was developed to aid clinical lesion assessment, the first method of choice during the process of caries diagnosis. However, this method is subjective and dependent on the clinical experience of the dentist [44–47].

The device works based on the principle of laser-emitted fluorescence. This tool can identify tooth demineralization because caries lesions emit stronger fluorescence than sound tissues when stimulated by the visible red laser light [48–50]. The two devices currently available on the market are the DIAGNOdent 2095 and the DIAGNOdent 2190 (LF and LFpen, DIAGNOdent, KaVo, Biberach, Germany). The first LF device has a laser diode that emits red light at 655 nm, which reaches the tooth surface using a central light guide contained within a flexible shaft. A photodetector quantifies the emitted fluorescence from bacterial metabolites (fluorophores known as porphyrins) present in the decayed tissues. This emitted fluorescence is captured by nine fibers concentrically arranged with the central light guide and transformed into numerical values varying from 0 to 99 [47,51–53]. These values, according to the manufacturer, are related to the lesion depth. This first developed device can be used with two types of tips, one for occlusal and one for smooth surfaces.

In 2006, an improved device was developed (LFpen). This laser fluorescence device functions on the same principle as LF. However, the device's components were condensed into one piece and the structure of the tips was changed. The tips used in this device are made of sapphire fiber and the excitation and fluorescence light follow the same optic path of propagation inside the solid fiber tip, but in opposite directions and in different wavelengths [52,54]. The LFpen can be used on approximal and occlusal surfaces.

Prior to use, these devices should be calibrated on a standard ceramic supplied by the manufacturer whose fluorescence value is known and stable [50].

Thus, the laser fluorescence devices allow caries severity to be estimated. Another advantage is that both the devices are safe in view of the excitatory light, because they are in the range of the visible spectrum and have low power intensity (Figure 25.2).

An important limitation of both devices is that they do not allow the assessment of lesion activity (i.e., whether it is progressing or arrested). This is an important point in dentistry, because it is an essential factor for the treatment decision. Furthermore, the differentiation between caries lesion and some another developmental defect that involves mineral loss or surface stain cannot be verified [53–55].



**Figure 25.2** (a) Use for caries lesions detection. (b) DIAGNOdent hand-held caries detection pen—KaVo. Device calibrated to use.

Some studies assessed the performance of laser fluorescence devices for detecting caries [47,50–52,54,56–61]. One of these studies compared the performance of traditional (visual and radiograph examination) and fluorescence-based methods (LF, LFpen, and a fluorescence camera), on occlusal surfaces *in vitro*. The results showed good sensitivity and specificity values for the LFpen and LF, respectively. However, the best combination for detecting caries was a visual examination with a radiographic examination [60].

Diniz *et al.* [56] evaluated the performance of these conventional and fluorescence-based methods on occlusal caries lesions in an *in vivo* study with histologic validation. For this, 105 teeth were assessed by using all methods. Afterwards, the teeth were extracted and assessed histologically. The results demonstrated good clinical performance for the visual examination and both LF and LFpen. The authors concluded that laser technology may be used as an adjunct in caries detection in clinical practice. Likewise, the results of other studies demonstrate that these devices are adjunct tools in caries detection and their use alone needs to be done with care [57–59,61].

In view of the results of the studies, currently the laser fluorescence devices are indicated as auxiliary methods. Their use is indicated in conjunction with traditional methods of detecting caries.

### 25.3.2 Caries removal

Caries removal in dentistry is traditionally performed by using rotary or manual instruments. In view of some disadvantages presented by these methods (heat generation, noise, time required for the procedure, and the need for anesthesia), new technologies have been developed.

In the literature, several types of lasers for caries removal and cavity preparation are mentioned (Er:YAG, Er:YSGG, and Er,Cr:YSGG) [3]. However, the most studied is the Er:YAG laser [62–67].

The Er:YAG laser has a yttrium-aluminum-garnet crystal doped with erbium ions as its active component. This laser operates at wavelengths of 2940 nm [3]. This laser-emitted wavelength coincides with the maximum absorption of water and hydroxyl radicals of dental tissues and, therefore, the use of this technique in biological tissues is allowed. The exposition to laser seems to promote water vaporization as well as dehydration of the component tissues, producing a rapid heating followed by a micro-explosion. This microexplosion is caused by increased pressure within the molecules of the tissue that generates a photomechanical effect. In this way, cavity preparation is achieved by selective ablation of caries without damage to the surrounding dental structures [66,68,69].

Some studies demonstrated that the Er:YAG laser can be used for caries removal as well as cavity preparation without significant thermal effects or patient discomfort [68,70]. However, those studies have varied aims and this makes results comparison very difficult.

In this way, a systematic review assessed the scientific evidence regarding laser technology for removal of carious tissue. The results showed that the substitution of rotatory burr for removing carious tissue should be viewed with care. This systematic review evaluated several points regarding the use of a laser: (1) effectiveness for removing carious tissue, (2) biological potential complications associated with the method, (3) longevity of the restorations, (4) if the patients respond more favorably to laser treatment than conventional caries excavation, and (5) the cost of the laser treatment. The studies found and included were of low and medium quality. Based on the studies reviewed, the authors concluded that the scientific evidence that the laser treatment is as effective as a rotary burr for removing carious tissue is limited. Regarding patients' perception, the results indicated that adults prefer laser treatment although the evidence was also limited. These results are probably related to the fact that local anesthetic is not required [71].

Taking into account the studies to date, the use of lasers for caries removal and cavity preparation is not yet fully settled, but these technologies used in conjunction with traditional methods seem to be an important component of contemporary dental practice.

### **25.3.3 Caries prevention—enhancing enamel resistance**

Low-intensity lasers, either alone or in combination with topical fluoride treatment, could be considered a relatively simple and noninvasive caries preventive treatment, resulting in reduced enamel solubility and dissolution [72,73].

High-intensity lasers can be used in mineralized tissues preventing dental decay, improving surface strength. As a preventive treatment, the laser can seal pits and fissures through surface ablation, hydroxyapatite conversion, and can promote greater penetration of fluoride ions. As a therapeutic effect, melting followed by vitrification

of dental tissues is obtained, making the tissues more resistant and less permeable to the bacterial acidic products [72].

The CO<sub>2</sub> laser can modify the fissure system to increase its resistance to future carious attack, either acting on fissure sealing or increasing the preventive fluoride content in the enamel [72].

The lasers are not used only to achieve ablation or melting, but also to change the chemical composition of the dental structure to achieve surfaces more resistant to demineralization and, consequently, reduce the susceptibility to incipient and secondary caries [74]. The effects depend upon the energy density applied on the surface as well as on the laser's focal distance, beam spot size, repetition rate, and pulse duration. Previous studies have reported dentin ablation after Er,Cr:YSGG laser irradiation at 0.25 and 0.5 W, with water cooling.

In a blind *in vitro* study, Ana *et al.* [75] compared professional fluoride application and laser irradiation on demineralization of enamel and on fluoride formation and retention. This study showed that both methods enhance enamel resistance, and no additional effect was demonstrated associating both of them, although a greater concentration of retained CaF<sub>2</sub>-like material was found in the laser group. Formation and retention of CaF<sub>2</sub> were also improved with laser irradiation.

The wavelengths absorbed most strongly in dental enamel are the 9.3- and 9.6-μm CO<sub>2</sub>-laser wavelengths. The loss of the carbonate phase from the enamel crystals due to the irradiation heat is reported to be responsible for the reduction in acid dissolution of enamel. Rechmann *et al.* [72] demonstrated in vital teeth in human mouths that the specific short-pulsed 9.6-μm CO<sub>2</sub>-laser irradiation reduced enamel mineral loss by up to 46% in 4 weeks. This scheme could be successfully used for the inhibition of enamel caries without any harm to the pulpal tissue of those irradiated teeth. Further clinical studies could verify the efficacy of CO<sub>2</sub>-laser irradiation with respect to its long-term capability in caries resistance.

### 25.3.4 Treatment of dentin hypersensitivity by laser radiation

Dentin tissue is mainly constituted by hydroxyapatite, type I collagen, and water. Collagen is a structural protein that underlies mechanical properties of the supporting tissues [76]. Dentin hypersensitivity (DH) is characterized by short, sharp pain arising from exposed dentin as a response to thermal, tactile, osmotic, or chemical stimulus, which cannot be ascribed to any other dental pathology [77].

The lasers used for treating DH may be divided into two groups according to output powers. The middle output power lasers are neodymium doped:yttrium, aluminum, and garnet (Nd:YAG); erbium doped:YAG (Er:YAG); and carbon dioxide (CO<sub>2</sub>) lasers. The low-level lasers are helium-neon (He-Ne,  $\lambda=632.8$  nm) and gallium-aluminumarsenide (GaAlAs) (diode) lasers ( $\lambda=780\text{--}900$  nm). Energy setting and wavelengths could range from 632.8 nm (He-Ne) to 10,600 nm (Er:YAG, CO<sub>2</sub>) [78].

There are several different theories to explain the effect of laser irradiation on dentine, but the most accepted one for the middle output lasers indicates sealing or occluding the dentinal tubules by melting and recrystallization of dentin. While the beam of the Er:YAG and CO<sub>2</sub> lasers acts on the dentin surface, a diode laser, at a

wavelength of 810 nm, acts on a relatively deeper area of tissue [76]. Recently, studies showed that LLLT can occlude dentinal tubules by increasing the cellular metabolic activity of odontoblasts that promote tertiary dentine production [79].

Low output power laser therapy has an anti-inflammatory effect and stimulates nerve cells. The mechanism of Nd:YAG and CO<sub>2</sub> laser is the narrowing of dentinal tubules as well as direct nerve analgesia [72]. A protein such as collagen is more sensitive to heat than an inorganic crystal such as hydroxyapatite. Therefore, the collagen in dentin would possibly be affected by dental laser treatment. Collagen in dentin was severely damaged or completely changed, while the inorganic crystal was improved by Er:YAG laser application [76].

Clinical trials have shown a significant decrease in DH, especially in patients that responded poorly to conventional treatment with fluoride or desensitizers. Some studies demonstrated that the association of laser and fluoride or other desensitizers is an effective treatment strategy to reduce DH that has immediate and long-lasting effects [76,79,80].

On the other hand, a recent systematic review showed divergent results as to the effectiveness of laser therapy for DH [78]. Wide variations are seen in the effectiveness rate, which reflects the percentage of teeth or patients showing a reduction in DH-related pain. Effectiveness rates range from 53.3% to 94.2% for the GaAlAs laser at 1-month follow-up, 50% to 94.5% for the CO<sub>2</sub> laser at 3 months, and 51.5% to 100% for the Nd:YAG laser. The reduction in DH at 6 months with the Er:YAG laser reportedly ranges from 38.2% to 47%. On the other hand, the therapeutic power of this placebo effect on DH reduction ranges from 20% to 60% for treatment with desensitizing toothpastes.

In a meta-analysis, Sgolastra *et al.* [81] looked over the results of 13 clinical trials, and concluded that Er:YAG, Nd:YAG, and GaAlAs lasers appear to be efficacious in reducing DH. At wavelengths and energy settings, no pulp damages or major adverse effects have been reported [78]. However, given the high heterogeneity of the included studies, future randomized controlled clinical trials are needed to confirm these results [81].

### 25.3.5 Dental bleaching

The term “bleaching” means chemical destruction through groups of chromophore compounds. Power bleaching has resulted in easy-to-use bleaching agents, essentially using highly concentrated hydrogen peroxide mixed with thickening or additional buffering agents, catalysts, or coloring agents [82].

The energy source can be derived from blue-colored halogen curing lamps, infrared CO<sub>2</sub> lasers, and blue-colored plasma arc lamps as well as the cool blue argon and GaAlAs lasers. Laser systems for bleaching applications usually employ a handpiece that expands the laser beam such that the laser is not used in point focus. By expanding the laser beam, the laser light spreads over the surface of a few teeth. Consequently, some typical properties of the laser are lost, but the risk of tissue damage is reduced [82]. Today there are three lasers approved by the FDA for tooth whitening: argon, carbon dioxide, and diode.

The knowledge of some absorption properties of light in tooth tissue is helpful in assessing the risks associated with laser and light-activated bleaching. Wavelengths with a high

absorption coefficient in water and in tooth mineral are readily absorbed at the tooth surface, and are converted on heat. Wavelengths, around 3000 nm, hardly penetrate deeper into dental hard tissue and, therefore, hardly damage the living pulp [82].

The pulse modus of laser systems is another important factor for efficacy and safety. Pulsed laser systems can create very high power densities within a very short time (milliseconds and less). Thermal tissue damage can be minimized by the appropriate choice of pulse duration and repetition rate. Pulsed laser systems can be used in a more tissue friendly manner compared to continuous wave lasers with comparable energy output [82].

The use of an LED or Nd:Yag laser for activation of the hydrogen peroxide 35% allows for higher degree of penetration in the direction of the chamber pulp (20 min after the gel application), in comparison to the groups without photoactivation [83]. The Nd:YAG laser has a strong potential in whitening teeth, because it produces the heat necessary for activating the hydrogen peroxide and the analgesia produced in the pulp by biostimulation.

Therefore, to increase the interaction of visible light with the bleaching gel, manufacturers have incorporated coloring agents or pigments into their products, which have colors capable of promoting maximum absorption of this light and subsequent conversion into heat. The application of dyes, which have a wavelength similar to that of the Nd:YAG laser, on dental hard tissues, allows the surfaces to absorb the laser light efficiently, with a lower percentage of reflection or transmission by tissues [83,84].

Moreover, the interaction between the light sources and the dyes played a major role in the pulp temperature decrease. The different laser types should be used with dental bleaching agents that contain dyes with wavelengths similar to theirs. This is relevant when considering the pulp heat transmission, because when the dye absorbs the light source energy, it increases the gel temperature and transmits less heat to the deepest dental structures. The irradiation intensity and the exposure time of the light source on the tooth are very important, because the critical temperature that leads to irreversible pulp damage is 5.6 °C above body temperature [85].

The association of five brands of agents with halogen light, infrared, argon laser, and carbon dioxide laser have been demonstrated to show significant correlation between the type of bleaching agent and the light source, as regards shade change and temperature generated on tooth surfaces [86]. The clinical chair time could be reduced using some diode laser systems to activate peroxide-based bleaching agents [2].

On the other hand, it is still debatable whether the laser activation results in superior tooth brightening as compared to nonactivated bleaching therapies. Therefore, application of laser-activated bleaching procedures should be critically weighed, keeping in mind the physical, physiological, and pathophysiological implications.

## 25.4 Future trends

There is a large research effort looking for new applications for the laser in dentistry. In the last few years, several studies were developed in order to investigate the mechanism of the laser in different oral superficies. However, the evidence produced

by these researches could not demonstrate that laser therapies were much better than traditional treatments. For specific uses, such as dentine hypersensitivity and mucositis, laser achieves results comparable to traditional treatments. This suggests that more clinical trials, focused on standardization, improvement, and long term follow-up of the several lasers techniques, should be performed.

There are other challenges for future research. The improvement of lasers devices to enable better access to dental surfaces, especially on root canals and periodontal pockets, is necessary. In addition, Pd therapy deserves full attention, once it has a greater efficacy and fewer adverse effects. The use of laser radiation offers a new possibility for minimally invasive tissue interventions and overall better patient acceptance than that found with some traditional techniques.

In conclusion, the application of laser therapy in dentistry seems to be a real trend and good results have been shown in several areas. These therapies still have limitations and, therefore, the devices as well as the protocols need to be improved in order to try to make its use routine and not just as an adjunct tool.

## References

- [1] D.N. Dederich, R.D. Bushick, Lasers in dentistry: separating science from hype, *J. Am. Dent. Assoc.* 135 (2004) 204–212 (quiz 229).
- [2] T. Dostalova, H. Jelinkova, Lasers in dentistry: overview and perspectives, *Photomed. Laser Surg.* 31 (2013) 147–149, <http://dx.doi.org/10.1089/pho.2013.3493>.
- [3] L.J. Walsh, The current status of laser applications in dentistry, *Aust. Dent. J.* 48 (2003) 146–155, <http://dx.doi.org/10.1111/j.1834-7819.2003.tb00025.x> (quiz 198).
- [4] T.Y. Fukuda, C.A. Malfatti, Analysis of low-level laser therapy doses in Brazilia equipment, *Rev. Bras. Fisioter.* 12 (2008) 5.
- [5] D.J. Coluzzi, Fundamentals of dental lasers: science and instruments, *Dent. Clin. N. Am.* 48 (2004) 751–770, v. <http://dx.doi.org/10.1016/j.cden.2004.05.003>.
- [6] R.A. Convissar, The biologic rationale for the use of lasers in dentistry, *Dent. Clin. N. Am.* 48 (2004) 771–794, v. <http://dx.doi.org/10.1016/j.cden.2004.06.004>.
- [7] N. Raffetto, Lasers for initial periodontal therapy, *Dent. Clin. N. Am.* 48 (2004) 923–936, vii. <http://dx.doi.org/10.1016/j.cden.2004.05.007>.
- [8] L.J. Walsh, The current status of low level laser therapy in dentistry. Part 1. Soft tissue applications, *Aust. Dent. J.* 42 (1997) 247–254.
- [9] L.J. Walsh, The current status of low level laser therapy in dentistry. Part 2. Hard tissue applications, *Aust. Dent. J.* 42 (1997) 302–306.
- [10] J.T. Hashmi, Y.Y. Huang, B.Z. Osmani, S.K. Sharma, M.A. Naeser, M.R. Hamblin, Role of low-level laser therapy in neurorehabilitation, *PM R* 2 (2010) S292–S305, <http://dx.doi.org/10.1016/j.pmrj.2010.10.013>.
- [11] G. Sun, J. Tuner, Low-level laser therapy in dentistry, *Dent. Clin. N. Am.* 48 (2004) 1061–1076, viii. <http://dx.doi.org/10.1016/j.cden.2004.05.004>.
- [12] S. Coleton, Lasers in surgical periodontics and oral medicine, *Dent. Clin. N. Am.* 48 (2004) 937–962, vii. <http://dx.doi.org/10.1016/j.cden.2004.05.008>.
- [13] F. Arbab-Kalati, T. Moridi, Evaluation of the effect of low level laser on prevention of chemotherapy-induced mucositis, *Acta Med. Iran.* 51 (2013) 157–162.

- [14] P.A. Carvalho, G.C. Jaguar, A.C. Pellizzon, J.D. Prado, R.N. Lopes, F.A. Alves, Evaluation of low-level laser therapy in the prevention and treatment of radiation-induced mucositis: a double-blind randomized study in head and neck cancer patients, *Oral Oncol.* 47 (2011) 6, <http://dx.doi.org/10.1016/j.oraloncology.2011.08.021>.
- [15] A.F. Qutob, S. Gue, T. Revesz, R.M. Logan, D. Keefe, Prevention of oral mucositis in children receiving cancer therapy: a systematic review and evidence-based analysis, *Oral Oncol.* 49 (2013) 102–107, <http://dx.doi.org/10.1016/j.oraloncology.2012.08.008>.
- [16] J.M. Bjordal, R.J. Bensadoun, J. Tuner, L. Frigo, K. Gjerde, R.A. Lopes-Martins, A systematic review with meta-analysis of the effect of low-level laser therapy (LLLT) in cancer therapy-induced oral mucositis. *Support. Care Cancer* 19 (2011) 1069–1077, <http://dx.doi.org/10.1007/s00520-011-1202-0>.
- [17] J.E. Clarkson, H.V. Worthington, S. Furness, M. Mccabe, T. Khalid, S. Meyer, Interventions for treating oral mucositis for patients with cancer receiving treatment, *Cochrane Database of Systematic Reviews*, The Cochrane Library, Issue 4, Art. No. CD001973, 2010, doi: <http://dx.doi.org/10.1002/14651858.CD001973.pub4>.
- [18] C. Migliorati, I. Hewson, R.V. Lalla, H.S. Antunes, C.L. Estilo, B. Hodgson, N.N. Lopes, M.M. Schubert, J. Bowen, S. Elad, Systematic review of laser and other light therapy for the management of oral mucositis in cancer patients, *Support. Care Cancer* 21 (2013) 333–341, <http://dx.doi.org/10.1007/s00520-012-1605-6>.
- [19] B.V. Caputo, G.A. Noro Filho, C.C. Dos Santos, Y. Okida, E.M. Giovani, Laser therapy of recurrent aphthous ulcer in patient with HIV infection, *Case Rep. Med.* 2012 (2012) 695642, <http://dx.doi.org/10.1155/2012/695642>.
- [20] A. Tezel, C. Kara, V. Balkaya, R. Orbak, An evaluation of different treatments for recurrent aphthous stomatitis and patient perceptions: Nd:YAG laser versus medication, *Photomed. Laser Surg.* 27 (2009) 101–106, <http://dx.doi.org/10.1089/pho.2008.2274>.
- [21] C. Scully, D.H. Felix, *Oral medicine-update for the dental practitioner. Aphthous and other common ulcers*, *Br. Dent. J.* 199 (2005) 259–264.
- [22] M.C. Haytac, O. Ozcelik, Evaluation of patient perceptions after frenectomy operations: a comparison of carbon dioxide laser and scalpel techniques, *J. Periodontol.* 77 (2006) 1815–1819, <http://dx.doi.org/10.1902/jop.2006.060043>.
- [23] C. Kara, T. Demir, R. Orbak, A. Tezel, Effect of Nd:YAG laser irradiation on the treatment of oral malodour associated with chronic periodontitis, *Int. Dent. J.* 58 (2008) 151–158.
- [24] H.M. Saleh, A.M. Saafan, Excision biopsy of tongue lesions by diode laser, *Photomed. Laser Surg.* 25 (2007) 45–49, <http://dx.doi.org/10.1089/pho.2006.2014>.
- [25] V.G. Suter, H.J. Altermatt, P. Sendi, G. Mettraux, M.M. Bornstein, CO<sub>2</sub> and diode laser for excisional biopsies of oral mucosal lesions. A pilot study evaluating clinical and histopathological parameters, *Schweiz. Monatsschr. Zahnmed.* 120 (2010) 664–671.
- [26] V.G. Suter, H.J. Altermatt, R.P.A. Dietrich, M.M. Bornstein, Does a pulsed mode offer advantages over a continuous wave mode for excisional biopsies performed using a carbon dioxide laser? *J. Oral Maxillofac. Surg.* 70 (2012) 1781–1788, <http://dx.doi.org/10.1016/j.joms.2012.01.023>.
- [27] I. Tuncer, C. Ozcakir-Tomruk, K. Sencift, S. Cologlu, Comparison of conventional surgery and CO<sub>2</sub> laser on intraoral soft tissue pathologies and evaluation of the collateral thermal damage, *Photomed. Laser Surg.* 28 (2010) 75–79, <http://dx.doi.org/10.1089/pho.2008.2353>.
- [28] D. Zaffe, M.C. Vitale, A. Martignone, F. Scarpelli, A.R. Botticelli, Morphological, histochemical, and immunocytochemical study of CO<sub>2</sub> and Er:YAG laser effect on oral soft tissues, *Photomed. Laser Surg.* 22 (2004) 185–189.

- [29] V.A. Glenn, Erbium lasers in dentistry, *Dent. Clin. N. Am.* 48 (2004) 1017–1059.
- [30] P. Ambrosini, N. Miller, S. Briançon, S. Gallina, J. Penaud, Clinical and microbiological evaluation of the effectiveness of the Nd:YAP laser for the initial treatment of adult periodontitis. A randomized controlled study, *J. Clin. Periodontol.* 32 (2005) 670–676.
- [31] F.V. Derdilopoulou, J. Nonhoff, K. Neumann, A.M. Kielbassa, Microbiological findings after periodontal therapy using curettes, Er:YAG laser, sonic, and ultrasonic scalers, *J. Clin. Periodontol.* 34 (2007) 588–598.
- [32] C. Gómez, A. Domínguez, A.I. García-Kass, J.A. García-Nuñez, Adjunctive Nd:YAG laser application in chronic periodontitis: clinical, immunological, and microbiological aspects, *Lasers Med. Sci.* 26 (2011) 453–463, <http://dx.doi.org/10.1007/s10103-010-0795-8>.
- [33] B. Gaspiric, U. Skaleric, Clinical evaluation of periodontal surgical treatment with an Er: YAG laser: 5-year results, *J. Periodontol.* 78 (2007) 1864–1871.
- [34] I. Krohn-Dale, O.E. Bøe, M. Enersen, K.N. Leknes, Er:YAG laser in the treatment of periodontal sites with recurring chronic inflammation: a 12-month randomized, controlled clinical trial, *J. Clin. Periodontol.* 39 (2012) 745–752, <http://dx.doi.org/10.1111/j.1600-051X.2012.01912.x>.
- [35] R. Crespi, A. Barone, U. Covani, Histologic evaluation of three methods of periodontal root surface treatment in humans, *J. Periodontol.* 76 (2005) 476–481.
- [36] M. Giannelli, D. Bani, C. Viti, A. Tani, L. Lorenzini, S. Zecchi-Orlandini, L. Formigli, Comparative evaluation of the effects of different photoablative laser irradiation protocols on the gingiva of periodontopathic patients, *Photomed. Laser Surg.* 30 (2012) 222–230, <http://dx.doi.org/10.1089/pho.2011.3172>.
- [37] C. Tomasi, K. Schander, G. Dahlén, J.L. Wennström, Short-term clinical and microbiologic effects of pocket debridement with an Er:YAG laser during periodontal maintenance, *J. Periodontol.* 77 (2006) 111–118.
- [38] C. Moura-Netto, C.A.B. Guglielmi, A.C.V. Mello-Moura, R.M. Palo, D.P. Raggio, C. L. Caldeira, Nd:YAG laser irradiation effect on apical intracanal dentin—a microleakage and SEM evaluation, *Braz. Dent. J.* 22 (2011) 377–381.
- [39] A. Rios, J. He, G.N. Glickman, R. Spears, E.D. Schneiderman, A.L. Honeyman, Evaluation of photodynamic therapy using a light-emitting diode lamp against *Enterococcus faecalis* in extracted human teeth, *J. Endod.* 37 (2011) 856–859, <http://dx.doi.org/10.1016/j.joen.2011.03.014>.
- [40] A. Stabholz, S. Sahar-Helft, J. Moshonov, Lasers in endodontics, *Dent. Clin. N. Am.* 48 (2004) 809–832.
- [41] E. Alfredo, M.A. Marchesan, M.D. Sousa-Neto, A. Brugnera-Junior, Y.T.C. Silva-Sousa, Temperature variation at the external root surface during 980-nm diode laser irradiation in the root canal, *J. Dent.* 36 (2008) 529–534.
- [42] L. Bergmans, P. Moisiadis, W. Teughels, B. Van Meerbeek, M. Quirynen, P. Lambrechts, Bactericidal effect of Nd:YAG laser irradiation on some endodontic pathogens ex vivo, *Int. Endod. J.* 39 (2006) 547–557.
- [43] L. Bergmans, P. Moisiadis, B. Huybrechts, B. Van Meerbeek, M. Quirynen, P. Lambrechts, Effect of photo-activated disinfection on endodontic pathogens ex vivo, *Int. Endod. J.* 41 (2008) 227–239.
- [44] M.B. Diniz, J.A. Rodrigues, I. Hug, C. Cordeiro Rde, A. Lussi, Reproducibility and accuracy of the ICDAS-II for occlusal caries detection, *Community Dent. Oral Epidemiol.* 37 (2009) 399–404, <http://dx.doi.org/10.1111/j.1600-0528.2009.00487.x>.
- [45] K.R. Ekstrand, S. Martignon, D.J. Ricketts, V. Qvist, Detection and activity assessment of primary coronal caries lesions: a methodologic study, *Oper. Dent.* 32 (2007) 225–235, <http://dx.doi.org/10.2341/06-63>.

- [46] A. Jablonski-Momeni, V. Stachniss, D.N. Ricketts, M. Heinzel-Gutenbrunner, K. Pieper, Reproducibility and accuracy of the ICDAS-II for detection of occlusal caries *in vitro*, *Caries Res.* 42 (2008) 79–87, <http://dx.doi.org/10.1159/000113160>.
- [47] J.F. Souza, T. Boldieri, M.B. Diniz, J.A. Rodrigues, A. Lussi, R.C. Cordeiro, Traditional and novel methods for occlusal caries detection: performance on primary teeth, *Lasers Med. Sci.* (2012), <http://dx.doi.org/10.1007/s10103-012-1154-8>.
- [48] J.D. Bader, D.A. Shugars, A systematic review of the performance of a laser fluorescence device for detecting caries, *J. Am. Dent. Assoc.* 135 (2004) 1413–1426.
- [49] A. Braun, F. Krause, S. Jepsen, The influence of the calibration mode of a laser fluorescence device on caries detection, *Caries Res.* 39 (2005) 144–149, <http://dx.doi.org/10.1159/000083161>.
- [50] R. Hibst, R. Paulus, A. Lussi, A detection of occlusal caries by laser fluorescence: basic and clinical investigations, *Med. Laser Appl.* 16 (2001) 205–213.
- [51] A. Lussi, A. Hack, I. Hug, H. Heckenberger, B. Megert, H. Stich, Detection of approximal caries with a new laser fluorescence device, *Caries Res.* 40 (2006) 97–103, <http://dx.doi.org/10.1159/000091054>.
- [52] A. Lussi, E. Hellwig, Performance of a new laser fluorescence device for the detection of occlusal caries *in vitro*, *J. Dent.* 34 (2006) 467–471.
- [53] A. Lussi, R. Hibst, R. Paulus, DIAGNOdent: an optical method for caries detection, *J. Dent. Res.* 83 (Spec No C) (2004) C80–C83, <http://dx.doi.org/10.1177/154405910408301S16>.
- [54] A. Lussi, S. Imwinkelried, N. Pitts, C. Longbottom, E. Reich, Performance and reproducibility of a laser fluorescence system for detection of occlusal caries *in vitro*, *Caries Res.* 33 (1999) 261–266, <http://dx.doi.org/10.1159/000016527>.
- [55] I.A. Pretty, G. Maupome, A closer look at diagnosis in clinical dental practice: part 5. Emerging technologies for caries detection and diagnosis, *J. Can. Dent. Assoc.* 70 (2004) 540, 540a–540i.
- [56] M.B. Diniz, T. Boldieri, J.A. Rodrigues, L. Santos-Pinto, A. Lussi, R.C. Cordeiro, The performance of conventional and fluorescence-based methods for occlusal caries detection: an *in vivo* study with histologic validation, *J. Am. Dent. Assoc.* 143 (2012) 339–350.
- [57] K.C. Huth, A. Lussi, M. Gygax, M. Thum, A. Crispin, E. Paschos, R. Hickel, K. W. Neuhaus, In vivo performance of a laser fluorescence device for the approximal detection of caries in permanent molars, *J. Dent.* 38 (2010) 1019–1026, <http://dx.doi.org/10.1016/j.jdent.2010.09.001>.
- [58] K.W. Neuhaus, J.A. Rodrigues, I. Hug, H. Stich, A. Lussi, Performance of laser fluorescence devices, visual and radiographic examination for the detection of occlusal caries in primary molars, *Clin. Oral Investig.* 15 (2011) 635–641, <http://dx.doi.org/10.1007/s00784-010-0427-5>.
- [59] J.A. Rodrigues, M.B. Diniz, E.B. Josgrilberg, R.C. Cordeiro, In vitro comparison of laser fluorescence performance with visual examination for detection of occlusal caries in permanent and primary molars, *Lasers Med. Sci.* 24 (2009) 501–506, <http://dx.doi.org/10.1007/s10103-008-0552-4>.
- [60] J.A. Rodrigues, I. Hug, M.B. Diniz, A. Lussi, Performance of fluorescence methods, radiographic examination and ICDAS II on occlusal surfaces *in vitro*, *Caries Res.* 42 (2008) 297–304, <http://dx.doi.org/10.1159/000148162>.
- [61] J.A. Rodrigues, I. Hug, K.W. Neuhaus, A. Lussi, Light-emitting diode and laser fluorescence-based devices in detecting occlusal caries, *J. Biomed. Opt.* 16 (2011) 107003, <http://dx.doi.org/10.1117/1.3631796>.

- [62] J. Eberhard, K. Bode, J. Hedderich, S. Jepsen, Cavity size difference after caries removal by a fluorescence-controlled Er:YAG laser and by conventional bur treatment, *Clin. Oral Investig.* 12 (2008) 311–318, <http://dx.doi.org/10.1007/s00784-008-0203-y>.
- [63] J. Eberhard, A.K. Eisenbeiss, A. Braun, J. Hedderich, S. Jepsen, Evaluation of selective caries removal by a fluorescence feedback-controlled Er:YAG laser in vitro, *Caries Res.* 39 (2005) 496–504, <http://dx.doi.org/10.1159/00008186>.
- [64] F. Krause, A. Braun, G. Lotz, S. Kneist, S. Jepsen, J. Eberhard, Evaluation of selective caries removal in deciduous teeth by a fluorescence feedback-controlled Er:YAG laser in vivo, *Clin. Oral Investig.* 12 (2008) 209–215, <http://dx.doi.org/10.1007/s00784-007-0169-1>.
- [65] D.R. Schwass, J.W. Leichter, D.G. Purton, M.V. Swain, Evaluating the efficiency of caries removal using an Er:YAG laser driven by fluorescence feedback control, *Arch. Oral Biol.* 58 (2012) 603–610, <http://dx.doi.org/10.1016/j.archoralbio.2012.09.017>.
- [66] C.V. Toro, R. Derceli Jdos, J.J. Faraoni-Romano, P. Marchi, J.D. Pecora, R.G. Palma-Dibb, The use of an Er:YAG laser to remove demineralized dentin and its influence on dentin permeability, *Microsc. Res. Tech.* 76 (2013) 225–230, <http://dx.doi.org/10.1002/jemt.22156>.
- [67] K. Yonemoto, T. Eguro, T. Maeda, H. Tanaka, Application of DIAGNOdent as a guide for removing carious dentin with Er:YAG laser, *J. Dent.* 34 (2006) 269–276, <http://dx.doi.org/10.1016/j.jdent.2005.07.001>.
- [68] R. Hibst, U. Keller, Experimental studies of the application of the Er:YAG laser on dental hard substances: I. Measurement of the ablation rate, *Lasers Surg. Med.* 9 (1989) 338–344.
- [69] K. Osuka, T. Amagai, N. Kukidome, Y. Takase, S. Aida, Y. Hirai, Effect of dentin hardness on ablation rate with Er:YAG laser, *Photomed. Laser Surg.* 27 (2009) 395–399, <http://dx.doi.org/10.1089/pho.2008.2163>.
- [70] J.T. Walsh Jr., T.J. Flotte, T.F. Deutsch, Er:YAG laser ablation of tissue: effect of pulse duration and tissue type on thermal damage, *Lasers Surg. Med.* 9 (1989) 314–326.
- [71] T. Jacobsen, A. Norlund, G.S. Englund, S. Tranaeus, Application of laser technology for removal of caries: a systematic review of controlled clinical trials, *Acta Odontol. Scand.* 69 (2011) 65–74, <http://dx.doi.org/10.3109/00016357.2010.536901>.
- [72] P. Rechmann, D. Fried, C.Q. Le, G. Nelson, M. Rapozo-Hilo, B.M. Rechmann, Caries inhibition in vital teeth using 9.6- $\mu\text{m}$  CO<sub>2</sub>-laser irradiation, *J. Biomed. Opt.* 16 (2011) 071405.
- [73] G.R. Sant'anna, E.A. Santos, L.E. Soares, A.M. Espírito Santo, A.A. Martin, D.A. Duarte, C. Pacheco-Soares, A. Brugnera Jr., Dental enamel irradiated with infrared diode laser and photo-absorbing cream: part 2—EDX study, *Photomed. Laser Surg.* 27 (2009) 771–782, <http://dx.doi.org/10.1089/pho.2008.2401>.
- [74] S.B. Botta, P.A. Ana, F.S. Teixeira, M.C.B.S. Salvadori, A.B. Matos, Relationship between surface topography and energy density distribution of Er,Cr:YSGG beam on irradiated dentin: an atomic force microscopy study, *Photomed. Laser Surg.* 4 (2011) 261–269, <http://dx.doi.org/10.1089/pho.2010.2812>.
- [75] P.A. Ana, C.P. Tabchoury, J.A. Cury, D.M. Zezell, Effect of Er,Cr:YSGG laser and professional fluoride application on enamel demineralization and on fluoride retention, *Caries Res.* 46 (2012) 441–451, <http://dx.doi.org/10.1159/000333603>.
- [76] K. Tonami, H. Takahashi, J. Kato, F. Nakano, F. Nishimura, Y. Takagi, N. Kurosaki, Effects of laser irradiation on tensile strength of bovine dentin, *Photomed. Laser Surg.* 23 (2005) 278–283, <http://dx.doi.org/10.1089/pho.2005.23.278>.
- [77] G.R. Holland, M.N. Närhi, M. Addy, L. Gangarosa, R. Orchardson, Guidelines for the design and conduct of clinical trials on dentine hypersensitivity, *J. Clin. Periodontol.* 24 (1997) 808–813, <http://dx.doi.org/10.1111/j.1600-051X.1997.tb01194>.

- [78] F. Sgolastra, A. Petrucci, R. Gatto, A. Monaco, Effectiveness of laser in dentinal hypersensitivity treatment: a systematic review, *J. Endod.* 37 (2011) 297–303, <http://dx.doi.org/10.1016/j.joen.2010.11.034>.
- [79] H.G. Yilmaz, S. Kurtulmus-Yilmaz, E. Cengiz, Long-term effect of diode laser irradiation compared to sodium fluoride varnish in the treatment of dentine hypersensitivity in periodontal maintenance patients: a randomized controlled clinical study, *Photomed. Laser Surg.* 29 (2011) 721–725, <http://dx.doi.org/10.1089/pho.2010.2974>.
- [80] A.O. Lopes, A.C. Aranha, Comparative evaluation of the effects of Nd:YAG laser and a desensitizer agent on the treatment of dentin hypersensitivity: a clinical study, *Photomed. Laser Surg.* 31 (2013) 132–138, <http://dx.doi.org/10.1089/pho.2012.3386>.
- [81] F. Sgolastra, A. Petrucci, M. Severino, R. Gatto, A. Monaco, Lasers for the treatment of dentin hypersensitivity: a meta-analysis, *J. Dent. Res.* 92 (2013) 492–499, <http://dx.doi.org/10.1177/0022034513487212>.
- [82] W. Buchalla, T. Attin, External bleaching therapy with activation by heat, light or laser—a systematic review, *Dent. Mater.* 23 (2007) 586–596, <http://dx.doi.org/10.1016/j.dental.2006.03.018>.
- [83] R.F. Mondelli, J.F. Azevedo, A.C. Francisconi, C.M. Almeida, S.K. Ishikirama, Comparative clinical study of the effectiveness of different dental bleaching methods—two year follow-up, *J. Appl. Oral Sci.* 20 (2012) 435–443, <http://dx.doi.org/10.1590/S1678-77572012000400008>.
- [84] A. Strobl, N. Gutknecht, R. Franzen, R.D. Hilgers, F. Lampert, J. Meister, Laser-assisted in-office bleaching using a neodymium:yttrium-aluminum-garnet laser: an *in vivo* study, *Lasers Med. Sci.* 25 (2010) 503–509, <http://dx.doi.org/10.1007/s10103-009-0675-2>.
- [85] M. Marcondes, M.P. Paranhos, A.M. Spohr, E.G. Mota, I.N. Da Silva, A.A. Souto, L.H.J. R. Burnett, The influence of the Nd:YAG laser bleaching on physical and mechanical properties of the dental enamel, *J. Biomed. Mater. Res. B Appl. Biomater.* 90 (2009) 388–395, <http://dx.doi.org/10.1002/jbm.b.31297>.
- [86] K. Luk, L. Tam, M. Hubert, Effect of light energy on peroxide tooth bleaching, *J. Am. Dent. Assoc.* 135 (2004) 194–201.

This page intentionally left blank

# Laser-assisted fabrication of tissue engineering scaffolds from titanium alloys

26

I.V. Shishkovsky<sup>1,2</sup>

<sup>1</sup>Lebedev Physics Institute (LPI) of Russian Academy of Sciences, Samara, Russia; <sup>2</sup>Moscow State Technological University named "STANKIN", Moscow, Russia

## 26.1 Introduction

Several millions of reparative operations for replacing bone tissue with metallic implants and endoprostheses are performed every year. These operations are typical for maxillofacial surgery, neurosurgery, traumatology, orthopedics, and stomatology. The main property required for an implant is reliability; it must be able to function as a bone tissue substitute over a long period of time. The reliability is affected most of all by the possibility of osteointegration, the durable ingrowth of an implant into a bone without inflammatory reactions, which facilitates implant rejection. The implant should be made of a biocompatible material, possess sufficient durability, and have a large surface area in contact with the bone.

Of the metals used for implants, about 50% are titanium and its alloys. These are optimal materials for implants in terms of their biocompatibility and strength-to-weight ratio. Their comparatively low usage is due to the low manufacturability of titanium, and, consequently, the expense of the implants, prepared mainly by mechanical treatment. Further, final polishing of the surfaces in contact with the bone is quite complex. There are basically no cast implants, although titanium alloy molding is widely applied in the aerospace industry. This is because pure titanium has low casting properties and its castable alloys contain components like nickel or vanadium, which have a detrimental influence on the tissues around the implant. In order to increase the application of titanium in medicine, special durable alloys and new implant constructions and technologies for designing them are needed.

Tens of firms around the world are engaged in the design and production of implants and endoprostheses. Most of the recognized constructions are fixed to bones by their external surface. To increase the contact surface, the implants are applied using macroretention systems like incisions and excavations or deposited with special coverings. The helical implants used in stomatology have their surface treated in order to obtain the special microrelief that increases the contact surface. Recently, porous implants have been manufactured by casting cobalt-chrome alloys or sintering titanium grains. The most complete (and most expensive) endoprostheses have a porous surface composed of a layer of spatial multiradial "stars." The porous implant is fixed to a bone by its external surface, due to the tissue invasion into the pores. However,

the porous surfaces of the implants are not regular because the cells differ in size and monolithic zones can occur. The tissue invading the pores is not always sufficiently supplied, which can lead to osteoporosis and other complications. All the implant systems are unified; this means that all the implants being manufactured vary in size but are similar in form. This seriously constrains the use of implantation in complicated cases.

In neurosurgery and maxillofacial surgery, titanium implants in the form of perforated plates are used. The position of the plates is adjusted during the operation. This prolongs the operation (and the time under anaesthetic for the patient), leads to deformation of the mounting holes and, above all, to the occurrence of stress concentration zones, which lowers the durability of the implant.

The results of many research studies [1,2] show the many possibilities of applying an intermetallic nickel-titanium NiTi, which has the useful property of shape memory even in the porous form, as a biocompatible material for medical implants. This substance is promising for orthopaedy as well as manufacturing of prosthetic elements capable of self-righting, self-fixing, and self-functioning at physiological temperature.

The traditional methods of obtaining this material have an essential disadvantage, which is the laboriousness of fabricating functional medical implants with individual predetermined size and shape.

The idea of using rapid prototyping (RP) technology and the selective laser sintering (SLS) method in medicine is common [3–14]. But the problem at issue is how to synthesize the models of the implants' forms or the implants themselves from powder materials such as titanium, its alloys (Ti-Al-V), and stainless steel. The next logical step for practical implantology has been made. It consists of the direct SLS of intermetallic phase NiTi in a controlled laser influence (LI) space [15]. This way of fabricating medical implants with their individual form predetermined by three-dimensional computer modelling is quite promising. At the same time, the initial powder of NiTi can be saturated with hydroxyapatite to increase the biocompatibility of the implants [2]. Biosimulating additives can also be infiltrated to accelerate the process of implantation.

The abstract mentioned [16] some factors to consider for the better use of implants: (a) the bone quality in patients over 60 is lowered; (b) the majority of high-strength materials for prostheses have higher modules of elasticity compared to bone tissue, so stress concentration zones can appear; and (c) micromotion on the implant-bone interface leads to the instability of that interface, the deterioration of the implant, and damage to the bone. The transitional zone between the implant and the bone is therefore of great importance and should have an optimal macro-, micro-, and probably nanostructure as well as a strong linkage.

Gaggl *et al.* [17] demonstrated in their research that the interfacial durability between the implant and a bone essentially increases when using a rough surface at the place of contact. This guarantees reliable growth of the tissue into the pores and durable mechanical bonding between the implant and the substrate [18]. Also the topography of the contact surface should be adjusted to the real structure of the bone. Different types of bones in the human body have different structures, making it quite difficult to ensure the durability of the implant and bone join with ingrowth of the tissue only. Consequently, it is essential to search for some methods that allow

the use of alternative ways of fixing to the bone surface, taking into account the individual structural characteristics of different people. The gradient porosity structure can be realized through the SLS method [2,15]. A shielding medium prevents oxidation of the nitinol particles in the sintering process, although in some studies titanium oxide is seen as a favorable phase [16,19].

Nitinol powders (NiTi phase >99.7 wt.%) of P55H45 grade and titanium powders (Ti > 98.1 wt.%) of PTOM grade were purchased at the Polema Company (Tula, Russia). Prior to laser sintering, the powders were dried in a vacuum oven for 2 h at 300 °C. The particle size of all starting powders was ~100 µm (in order to be commensurate with the diameter of the laser spot) and was checked using a sieve analysis.

The SLS requires sensitive selective treatment of the powder composition for layer-by-layer synthesis of the premodelled implants. Choosing the laser beam (LB) parameters, including power density, scanning velocity, and focusing spot diameter and its overlap coefficient, is therefore of fundamental importance.

The RP process via the SLS of biomaterials involves the following steps [2,20] (Figure 26.1):

- Preparation of a computer-aid design (CAD) of a future scaffold.
- Program-based fabrication of the transversal sections of a 3-D object.
- Layer-by-layer superposition of these sections during the laser additive process.

The CAD stage (Figure 26.1, stage I) is conducted in the framework of CAD-CAE packages such as *Solid Work* (Dassault Systems), or *Pro-Engineering* (Parametric Technology), or the specialized package *Mimic* (Materialize) used in medical tomography treatment. Such packages have utilities for modelling the internal porous structure, including a gradient of some biophysical properties (porosity, permeability,

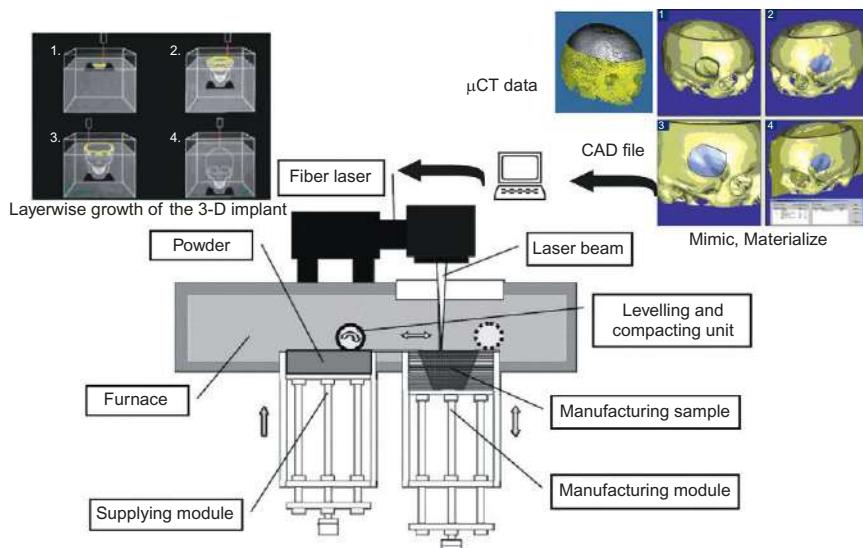


**Figure 26.1** Schematic diagram of the SLS setup by 3-D data of tomography.

element concentration, etc.). The program divides the image into sections to render it in its actual size later on.

The SLS machine ([Figure 26.1](#), stage II) consists of a table with two containers attached to it. The bottom of each container is a piston. Initially, one of the containers (the left one) is filled with the powder while the other is left empty with its piston placed at table level. The agglomeration can be carried out in an argon or nitrogen medium at low or high temperature. The untapped powder in one of the containers “supports” the implant during its formation while the powder from the other container can be recycled.

Provided that the laser power is high, the sintering process is transformed into the melting one. Thus a solid, practically cast 3-D part (implant) can be created that is very important for bone reconstruction.

In the photo in [Figure 26.2](#), samples of the synthesized 3-D parts are shown: a pure titanium plate for maxillofacial surgery (a), a molar of nickel titanium (b) and a layered 3-D titanium cladding on a stomatological dowel (c).

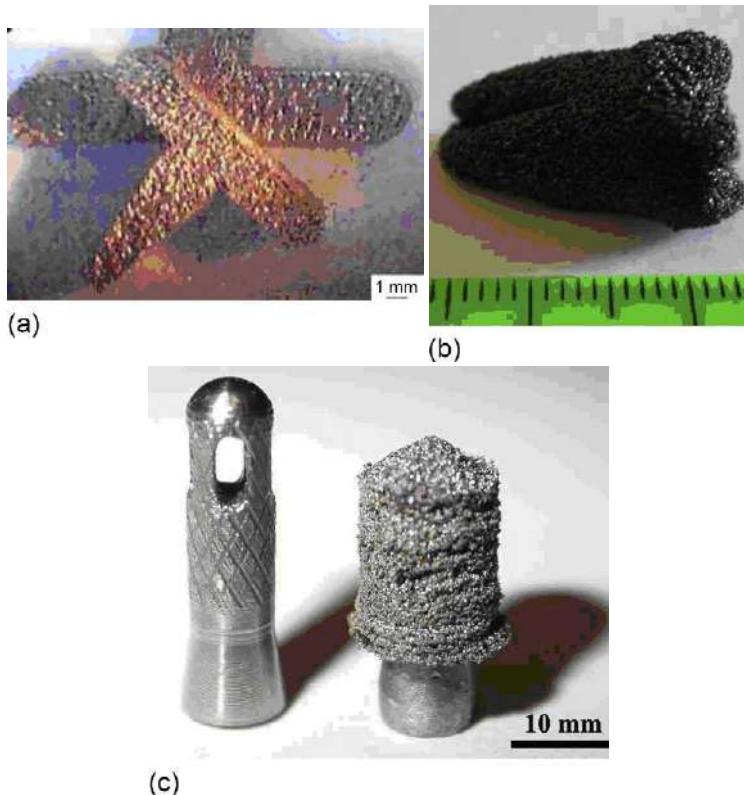


**Figure 26.2** (a–c) 3-D parts for use in stomatology.

Using the SLS method can reduce the period of fabrication of the prosthetic parts by accelerating the stages of designing, modelling, and adjustment. It will also reduce the cost of the suggested technology in comparison with traditional methods. Material resources are also saved because cheaper domestically produced powders are used. At the same time, the new properties and functional characteristics of the biocompatible titanium and nickel titanium implants and their influence on the cost of prosthetics in the fields of their application (sports medicine, stomatology, orthopaedy) are yet to be valued.

## **26.2 Influence of the selective laser sintering (SLS)-technique-obtained 3-D porous matrix for tissue engineering on the culture of multipotent mesenchymal stem cells**

In traumatology, maxillofacial surgery, and stomatology, the application of implants is very important for various pathologies. The quality and biological compatibility of the implant material and its structure influence the efficiency of the implant applications [21]. At present, most of the implant producers are testing their products on animals. However it cannot be assumed that these results can be extrapolated directly to human beings [22]. Besides, it should be noted that the use of animals for such experiments is not ethical, especially now that alternative techniques are available. Implant testing on cellular cultures is commonly used as the first stage of biological testing for biocompatibility and toxicity of implants [23].

Multipotent mesenchymal stromal stem cells (MMSC) are a promising autologous material for cell therapy and tissue engineering because they can be found inside almost any conjunctive tissue [24]. Active participation of the MMSC in the regeneration processes has been proven by many authors [25]. MMSC usage allows one to show the properties of the implant material on the cell level. This provides the opportunity to study the biological properties of implants, such as a cytodifferentiation induction, stimulation and suppression of proliferation and migration, and mutagenic and toxic effects of implants. Provided that there are not toxic effects, it is possible to estimate the adhesion properties, velocity and depth of the growth of stem cells in the implant, and hence to conjecture the degree of integrity of the tissue with the implant material [26]. The MMSC approach allows us to gather information about the implant biological properties prior to animal testing, and thus to improve and change the material properties until the desired ones are achieved.

Today tissue scaffold engineering is a widely developed line of the regenerative medicine that covers *in vivo* cultivation of stem cells, fabrication and restoration of damaged or lost tissue, control and testing systems, biological studies and the synthesis of new pharmaceutical products [5,27]. Within this concept, the main interest is building (or stimulating the synthesis) of tissue and organs *in vivo* due to stem cell implantation of the extracellular matrix. In contrast to the conventional method of cell culturing *in vitro*, tissue-engineering scaffolds can be designed so that the shape

strictly meets the individual peculiarities of each patient. A scaffold will not only ensure a support function but also determine the direction of stem cell growth into the extracellular matrix. The matrix structure and contents promote the artificial differentiation of cell and tissue regeneration. This sophisticated approach to tissue synthesis *in vivo* matches their natural development *in situ* [28,29].

In regenerative surgery, it is currently important to replace cast implant materials by porous 3-D matrices having the shape of the body (bone) to be replaced to restore the defective areas. It is generally known that the topography of a porous surface in comparison with a smooth one has an impact on the morphological behavior of cells while stem cell proliferation is influenced by the synergistic action of micron and submicron scale topography [2,30]. A further problem is that the stem cell matrix must have bioptic properties over the whole porous structure where the stem cell mass and newly formed tissue become ingrown during their evolution.

The investigation of regeneration mechanisms for tissues and organs is a relatively new research field. Research into new technologies, which could restore a lost function of an organ or a system, has led to the application of RP and manufacturing technology (RPMT) in biotechnology, tissue engineering, regenerative implant medicine, and organogenesis. These are all based on the transplantation of stem cells into carrier matrices.

A carrier matrix is a synthetic or biological complex with sufficient mechanical strength to act as a support. It is normally made from a porous layered construction. It can be synthesized via the SLS technique using the CAD file for each individual layer by referring to 3-D tomography data. After synthesis of the porous scaffold, the stem cells are adopted inside (i.e., penetrate into) the matrix. The following basic criteria for building a biologically compatible matrix for use in tissue-engineering constructions have been established through experiments: prevention of cytotoxicity; maintenance of adhesion; fixation; proliferation and differentiation of the cells located on its surface; prevention of inflammatory reaction on the material surface and immune response; and sufficient mechanical strength and bioresorption by normal metabolic routes [31,32].

Adult bone tissue is practically incapable of regeneration. As a result of disturbing factors, its defects gradually lead to deterioration or even loss of mobility. Current technologies for prosthetic repair allow complete rehabilitation. However, progress in modern organotypic regenerative medicine encourages research into technologies for bone replacement using natural transplants.

New technologies of bone building using tissue engineering have been developed in several directions. The following process has been called osteogenesis. The cellular mass, consisting of the osteoblasts and human MSSCs, is slurried and jointly cultivated. Biodegradable polymers based on organic acids (polyetheretherketone, polycaprolactone, e-caprolactone/hydroxyapatite, PGA, PGLA), traditionally used as matrices, are then formed into three-dimensional implants [33–35]. The cellular mass culture is placed inside the matrix, and, during preparation, transplanted into

the alveolar socket. Here, because of the cellular and tissue properties of the microenvironment, osteogenesis takes place [34].

The present study outlines the results of research into the stem cell adhesion, morphology, and proliferation. It looks at differentiation of porous 3-D tissue-engineering matrices of NiTi synthesized by the SLS process with the aid of dynamic SEM optical microscopy. Comparative morphological analysis of stem cell growth was also carried out in Ref. [2]. All of the titanium graded PTOM and nitinol graded PV N55 T45 powders were obtained from the Russian chemical market and used as supplied. Mixtures of Ti or nitinol with hydroxyapatite (graded HA:GAP-85d) were prepared in order to increase the implant biocompatibility. As a result of LB sintering, flat monolayers were used for morphological analysis ( $10 \times 30 \times d$  mm, where  $d$  is the depth of monolayer).

According to a technique developed previously [20], the external appearance of the porous matrix of NiTi proper and NiTi with HA additives was modelled via CAD-CAE and synthesized by previously determined LI methods. Figure 26.3 shows a common scheme for the medical experiment and the configuration of the nitinol scaffolds.

Morphological analysis was carried out in collaboration with CRL SamSMU (Prof. Volova L.T.) for Case Study 1 and with the Cell Technologies Centre of Samara Ministry of Health (Ph.D. Volchkov S.E.) for Case Study 2. In Case Study 1, the experiments were conducted on the primary cultures of dermal fibroblasts and human MMSCs of 4–18 passages. The dermal fibroblast culture was taken from the musculocutaneous tissue within a 6–10 week period using the method of primary explants.

The cells were cultured in standard conditions (thermostat Sanyo, Incubator MIR-262) at 37 °C in the MEM growth medium with 10% embryo beef serum in plastic culture vials (Orange Scientific; Corning) with  $2500 \text{ mm}^2$  surface area. The testing process was conducted inside cultured Petri dishes (Sarstedt) with internal

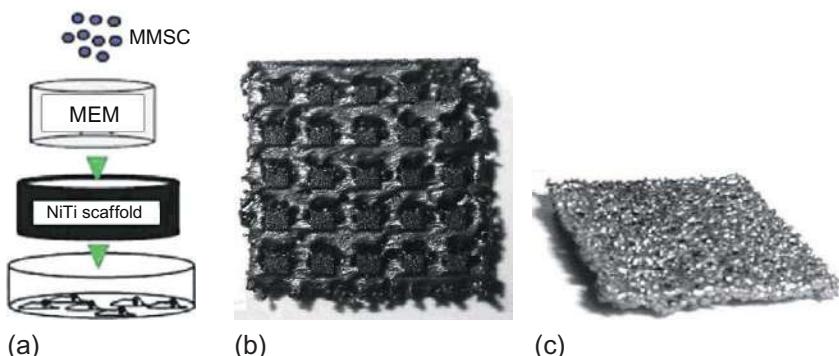


**Figure 26.3** Experiment scheme: (a) configuration of porous NiTi scaffolds with regular (b) and tessellation (c) structures (size of squares were  $10 \times 10 \text{ mm}^2$ ).

diameter 30 mm. Experiments were carried out by the direct contact method with two variants, as explained below:

1. Fibroblasts were reseeded from the culture vial onto the Petri dish and then cultured for 24 h. Over this time cellular monolayers with a density of about  $315 \text{ cells/mm}^2$  were fabricated. The implants to be studied were inserted into the monolayers.
2. Fibroblasts were reseeded and the implant was inserted simultaneously in the Petri dish. The cell dose was constant in all cases at  $200 \text{ cells/mm}^2$ .

The following control parameters were used:

1. Petri dishes with culture growth medium and implants with fibroblasts were not reseeded.
2. Petri dishes with fibroblast culture were passivated and observed simultaneously with experimental samples, but without any supplementary treatment.

Native cultures were studied by using an inverted microscope, called “Biolam P-2-1,” with magnifications of  $100\times$  and  $150\times$ . Daily visual examination and morphometry of the native culture were undertaken. Cell consistency in each individual monolayer was estimated visually and the desquamation was determined numerically. Size, shape, and cytotoxicity effects were also observed. Usually, in the normal primary culture the fibroblasts had an elongated form, 2-4 appendices, homogeneous cytoplasm, and clear boundaries. The nucleus was generally situated eccentrically and 1-3 nuclei were kept (see [Figure 26.4](#)). After reseeding, the culture medium was checked for common protein content. It was then controlled using a microbiuretic method involving estimation of the free and protein bound oxyproline. Statistical processing was estimated using both parametric and nonparametric tests.

The MMSC were received from the *Wharton's Jelly* of the umbilical cord of newborns (with the authorization of the mother). Stem cells were singled out by the explant method. The materials under consideration were washed with the sterile

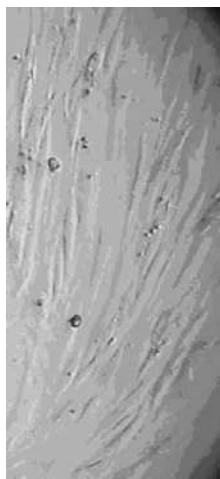


**Figure 26.4** Primary culture of dermal fibroblasts, native culture.

phosphate salt buffer, and then sterilized in the autoclave at a temperature under 121 °C over 30 min.

Two groups were included in the study:

1. Reference or control group, containing only MMSC.
2. NiTi (10 samples for statistics), see [Figure 26.3](#).

The culturing process in the three groups lasted for 26 days under standard cultivation conditions (37 °C, 5% CO<sub>2</sub> in MCO-20AIC (Sanyo) incubator). The nutrient medium comprised  $\mu$ MEM (Sigma) with the following additives: 10% FBS (Gibco), 2 mM L-alanyl-glutamine (Invitrogen). This was changed either every 5 days, or at the moment when the medium indication altered.

We used studies recommended by the international community involved in stem cell therapy to verify that the obtained cells belonged to the MMSC [36]. Immunophenotyping was carried out using these antigens: CD90, CD44, CD106, CD45, HLA-ABC, HLA-DR, 73, 34, 144, 105, 117, 62L, 133, 14, on a continuous-flow cytofluorometer (Becton Dickinson). The induction of cytodifferentiation in osteogenic, chondrogenic, and adipogenic directions was conducted in the following commercially available media: NH Osteodiff, NH Chondrodif, and NH Adipodif (Miltenyi Biotec) according to the producer's recommendations. The cytodifferentiation was estimated by measuring the stem cell morphology change and the reaction to the specific staining agents (also according to the producer's recommendations). OilRed O (Sigma) was used for the adipogenous estimation, alkaline phosphatase FAST BCIP/NBT (Sigma) for the osteogenesis evaluation, and aggrecan (Abcam) for testing the antibodies. The proliferation activity was estimated with a cellular analyzer of concentration and viability, ViCell XR (Beckman Coulter). The proliferation activity was determined by the equation:

$$X = [\log 10(\text{NH}) - \log 10(\text{NI})] / \log 10(2)$$

where NI is the inoculum cell number, NH is the cell harvest number and X is the amount of doubling that occurs during each cultivation time.

In order to determine the toxicity of the material, the cellular morphology and morphometry were studied and the velocity of duplication was calculated. The migration ability of stem cells (mechanotaxis) was determined using a time-lapse experiment with the aid of the AxioObserver A1 microscope (Carl Zeiss) with an incubation system. The time-lapse method involves filming MMSC cultivation for 4 h at a video-filming rate of 10 frames per min. The migration ability (mechanotaxis) was evaluated by the comparative method, in which the trajectories of the cell motion between the reference and nitinol groups were compared. The assessment of the video, calculation of the cell migration distance, and morphological analysis were supported by the *Image-Pro PLUS 6.0* (Media Cybernetics) and *AxioVision 4.8* (Carl Zeiss) software. Cluster analysis, which shows a display of moving objects (cells) and calculates their trajectories and distances, was carried out with the bundled software *ImageJ* and *Image Pro Plus*. From this software, division of the cells into groups was estimated according to the density of pixels per object.

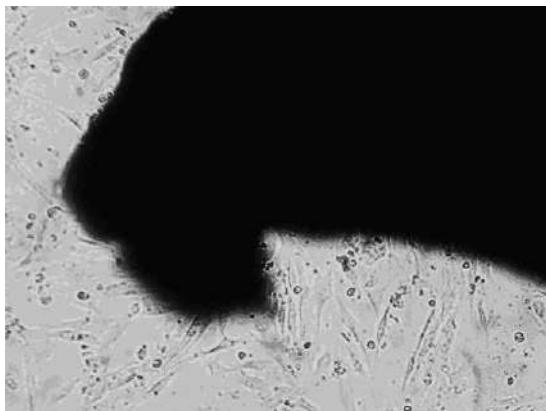


**Figure 26.5** Titanium sample (black) on the fibroblast monolayer (first variant, first day of experiment). Fusiform cells with central nuclei grow in the manner of “scythes” parallel to each other without adhesion. Native culture. Inverting optical microscope (OM). 100 × .

## 26.2.1 First series of experiments

### 26.2.1.1 SLS of titanium powder, first variant

After one day the monolayer density was measured in the regions around the porous implant and was shown to have reduced its coverage by 136 cell/mm<sup>2</sup>. This was probably a consequence of damage because of sample mobility in the culture solution. The percentage of damaged cells in each individual monolayer was up to 10.2%. The majority of the fibroblasts kept all the characteristics of normal cells. The form and size of cells were not changed, their cytoplasm was homogeneous, and their nuclei were of the light bubble-type with 1-2 nuclei ([Figure 26.5](#)).

The monolayer on the bottom surface of the dish was integral and uniform; fibroblasts kept their normal structure, forms, and sizes. Monolayer shape and cell structure were not notably different from normal during all four days of observations. The percentage of damaged cells was about 5-10%. No morphological signs of the implant influencing the fibroblast culture were observed. The cells formed a uniform monolayer. Its density corresponded to the process of culture growth after passivation and was also dependent on distance. The nature and direction of the cell growth for those in close proximity to the sample were constant.

### 26.2.1.2 SLS of titanium powder, second variant

Observation after one day showed that the fibroblasts had adhered to the bottom of the culture dish near the implant edges. The cell body was located around and under the objects being studied ([Figure 26.6a and c](#)). The sample itself was on the bottom of the Petri dish. In the detached zone, the fibroblasts produced an incomplete monolayer. The fibroblasts had clearly incorporated into and penetrated the implant.

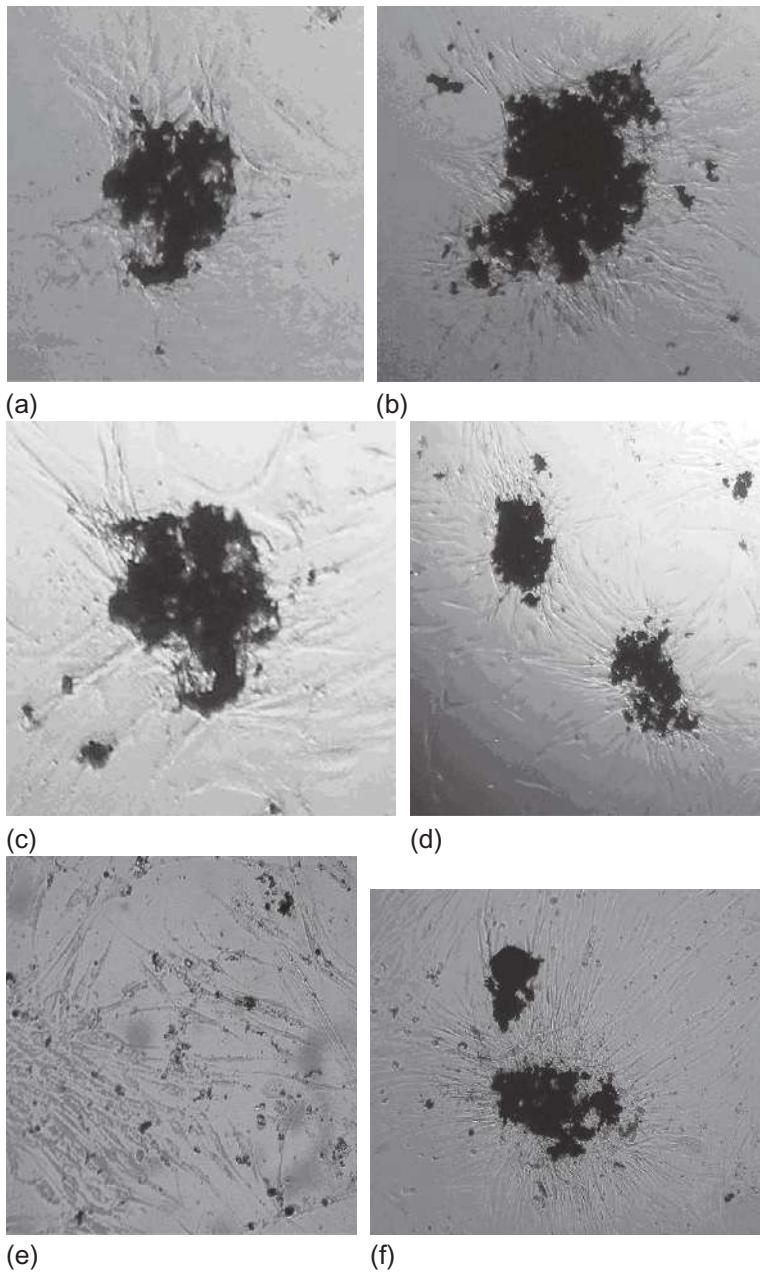


**Figure 26.6** Titanium (a, c, e, g) and nitinol (b, d, f, h) samples on the fibroblastmonolayer (second variant of experiments). Native culture. Inverting OM  $\times 100$ ). Scales point out in Figure 26.7.

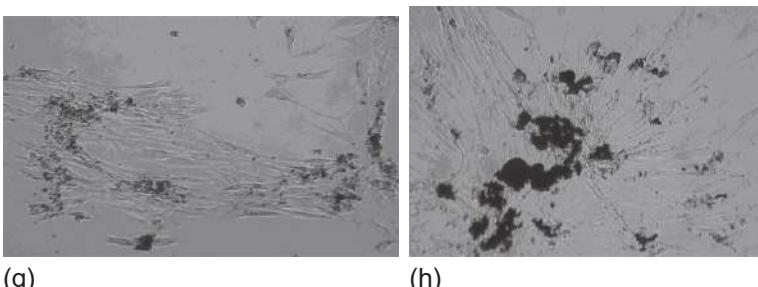


**Figure 26.6** Continued.

These experimental results showed that fibroblasts in the culture demonstrated vastly greater affinity for the very small edges of the porous titanium structure. The process of fibroblast growth (formation of the distinctive “scythes”) occurs in the pore direction and leads to texture formation (Figure 26.6c). Cell density on the surface around these pores quickly increased (Figure 26.6e and f) and by the fourth day of the experiment had achieved saturation density. Fibroblast colonies penetrated into the titanium pores and diffused into its highly porous structure.

After day one of the experiment, near the low-porosity region of the implant, the fibroblast monolayer was noticeably rarer. The cell density had begun to increase and by day four some uniform structure had formed in the regions around the samples. However, these structures had still not reached saturation density. Cells were not located along the edges of the titanium implants.

## 26.2.2 Second series of experiments

### 26.2.2.1 SLS of the nitinol powder, first variant

After the first day, a reduction of the monolayer density was observed on the whole surface of the culture dish caused by the implant mobility at the bottom of the Petri dish. During the three subsequent days the view of the monolayer was perfected; the monolayer density increased; and the structure, shape, and size of its cells were not distinguishable from normal.

### 26.2.2.2 SLS of the nitinol powder, second variant

Under the influence of the testing material, the cells were fixed to the bottom of the culture dish. As a result, the monolayer density had decreased significantly after one day. There was a greater local focus of mass reproduction, where the cells tended to be normal (Figure 26.6b). This focus was much greater than that of the titanium experiments (Figure 26.6a and b). Throughout the observations the fibroblasts had a distinctive morphology, velocity, and growth pattern (Figure 26.6d, f, and h).

### **26.2.3 Third series of experiments**

#### **26.2.3.1 SLS of the titanium powder+HA, first variant**

After one day, a reduction of the monolayer density was observed in cells placed on the culture dish. On the fourth and final day of the experiment the bottom surface of the dish was not distinguishable from normal. The monolayer was homogeneous and fibroblasts kept their usual structure, forms, and sizes.

#### **26.2.3.2 SLS of the titanium powder+HA, second variant**

A significant reduction in the speed of the monolayer growth was observed after 24 h. The cells were mainly concentrated around the small implant pores. On the fourth day of the experiment the cells had practically died. It seems that this is because, in the presence of HA, the reproduction conditions were so favorable that cells had used up the whole nutrient solution and perished.

### **26.2.4 Fourth series of experiments**

#### **26.2.4.1 SLS of the nitinol powder+HA, first variant**

Under the influence of combined intermetallic and hydroxyapatite, the cells were fixed to the bottom of the culture dish very weakly. This meant that after one day the monolayer density was considerably lower than in the control sample. At this point, the cells were attached to the whole area of the bottom of the dish without showing any affinity to the sample. Throughout the observation the fibroblasts kept a distinctive morphology, velocity, and growth.

#### **26.2.4.2 SLS of the nitinol powder+HA, second variant**

Observation over 24 h showed that the fibroblasts were concentrated mainly around the small implant pores. In other areas, the fibroblasts formed a thin monolayer. The shape, size, and fibroblast location in the culture dish were similar to the results of previous observations.

During the investigation of the *in vitro* cultivation process, it was established that initially so-called round cells dominated. After 4 days they were transformed into different cell lines. The dominant population had the fibroblast elements in all the cells. After that, separate processes occurred, including distinct fixing to the dish walls and to the titanium or nitinol samples. This resulted in different cell lines merging and forming the cell monolayers inside the pores. Under cultivation *in vivo*, it was shown that stable chondrogenic and osteogenous elements grew inside the titanium and nitinol pores. Osteoblast colonies in the porous nitinol were formed corresponding to chondro- or bone matrix.

The initial results of Case Study 2 are shown in [Figure 26.7a and b](#). The cells of the reference group proliferated actively compared with this same process nearby the implant edge, which was minimal.

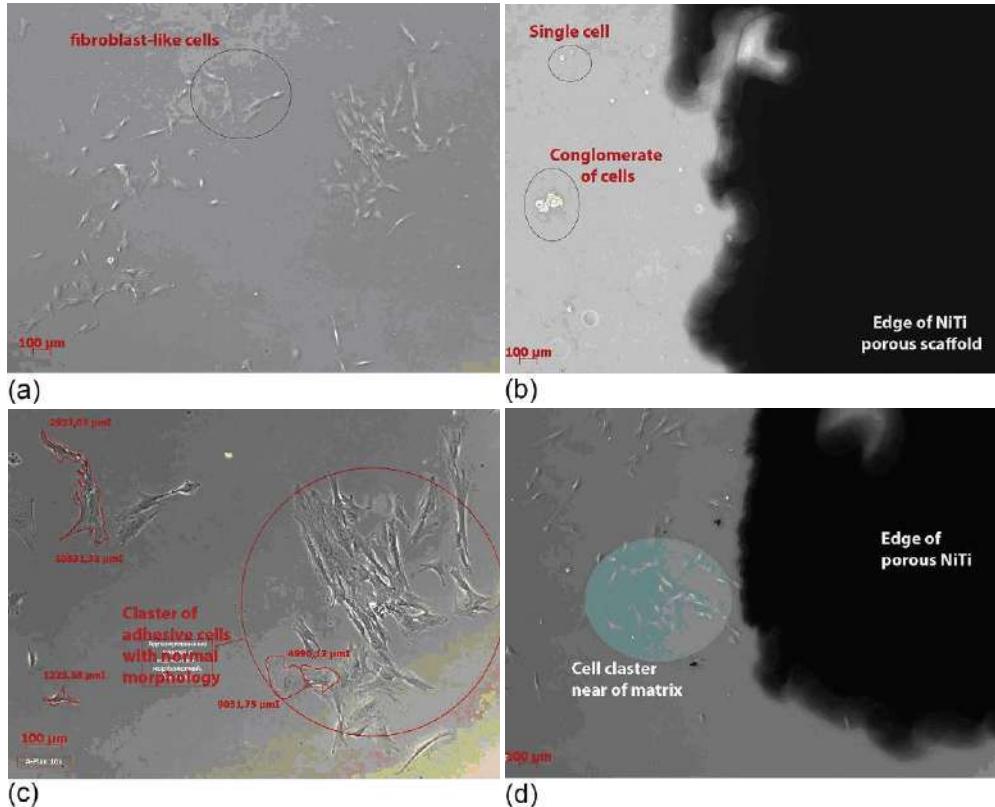


**Figure 26.7** OM images of the start (a, b) and the second day (c, d) of the experiment: (a, c) for the reference group and (b, d) for the edge of the NiTi sample.

By the next day, there was full adhesion of 90% of cells to the Petri dishes in the reference group. The majority of the cells had a typical fibroblast-like (spindle-shaped) shape and a clearly visible nucleus with two or four nucleoli (Figure 26.7a). The increase of the cell population near the NiTi sample edge was less remarkable (Figure 26.7d).

After a week of experiments, the reference group's cellular mass had increased smoothly during the process of cultivation. Culture density increased from 35% to 100% in 10 days of cultivation.

In the NiTi groups (Figure 26.8b), for 10 days the culture density grew substantially slower than the reference group and nonuniformly between the samples in this group (from 75% up to 95%). On the tenth day, maximum densities were registered for group 1 (95%), group 3 (85%), and group 4 (60%). In addition, small colonies were observed in immediate proximity to the material, with the morphological image that suggested "aging" cells. On the material, the first signs of the stem cells were noticed (Figure 26.8c).

These colonies can be seen more clearly in Figure 26.9, after the cellular study had been completed. There is a thin layer of cells visible in the porous 3-D matrix structure.

Hence, in the reference group the formation of a cellular monolayer lasted for 16 days, the proliferation speed was 0.03 and doubled each hour or 0.694 and doubled each day, and the total number of doublings within the period of cultivation was 11.11 (Figure 26.10). A cellular morphology was normal during the whole cultivation process. The natural emergence of "aging" cells in the culture didn't exceed 20% of the whole population. The aging processes were characterized by the increase of cytoplasm and nucleus volume, a growing cell area, cell shape changing into cubic, cellular arrest, and close death (Figure 26.9, *vide supra*).

At the nitinol group, the proliferation speed was 0.02 doubling per hour or 0.532 doubling per day, and the total number of reduplications within the cultivation period was 10.69. An insignificant effect of proliferation oppression was mentioned as a result of the research in the NiTi series. This was probably related to the heightened porosity of the material.

Depending on the intensity of the stem cell population growth, the analysis and separate samplings of cells were carried out at different stages of the maturing process that characterize the cells' aging according to their morphological characteristics (Figure 26.11). In Figure 26.11 (from right to left and bottom-up) the cells are shown separated by their "age," beginning with the youngest.

A morphological assessment of the pictures was carried out for each group and experiment series on the 3rd, 15th (Figure 26.11), and 25th day of the culturing process. The cells were then sorted into three groups (Table 26.1, Figures 26.11 and 26.12):

- "Immature" (red) cells: these are young, actively dividing cells, spindle-shaped, with an area not exceeding  $5000 \mu\text{m}^2$ . These cells are actively participating in fission and migration.
- "Adult" (blue) cells: these have a triangular or irregular form, with areas ranging from 5000 to  $16,000 \mu\text{m}^2$ . These cells are also taking part in proliferation and migration but are much slower.
- "Giant" (yellow-green) cells: these have an irregular shape, sharpened edges, and an enormous surface area ranging from 16,000 to  $40,000 \mu\text{m}^2$  and, occasionally, even higher. They are not involved in the division process and are not practically migrating.

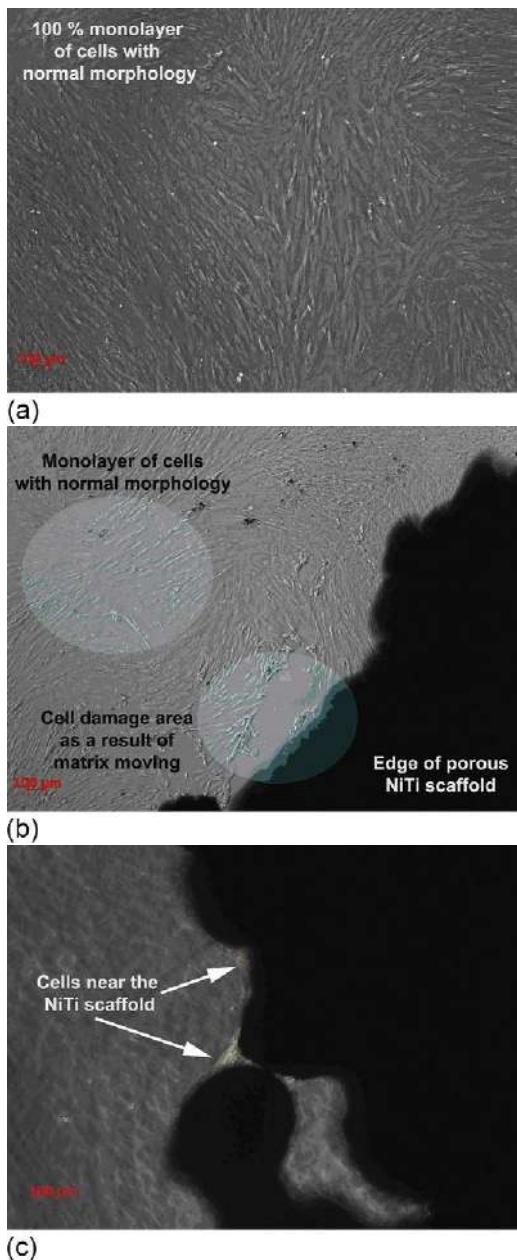


**Figure 26.8** OM images after the week of experiments (a, b): (a) the reference group; (b) the border of the NiTi matrix; and (c) the cell culture near the matrix on the 13th day.

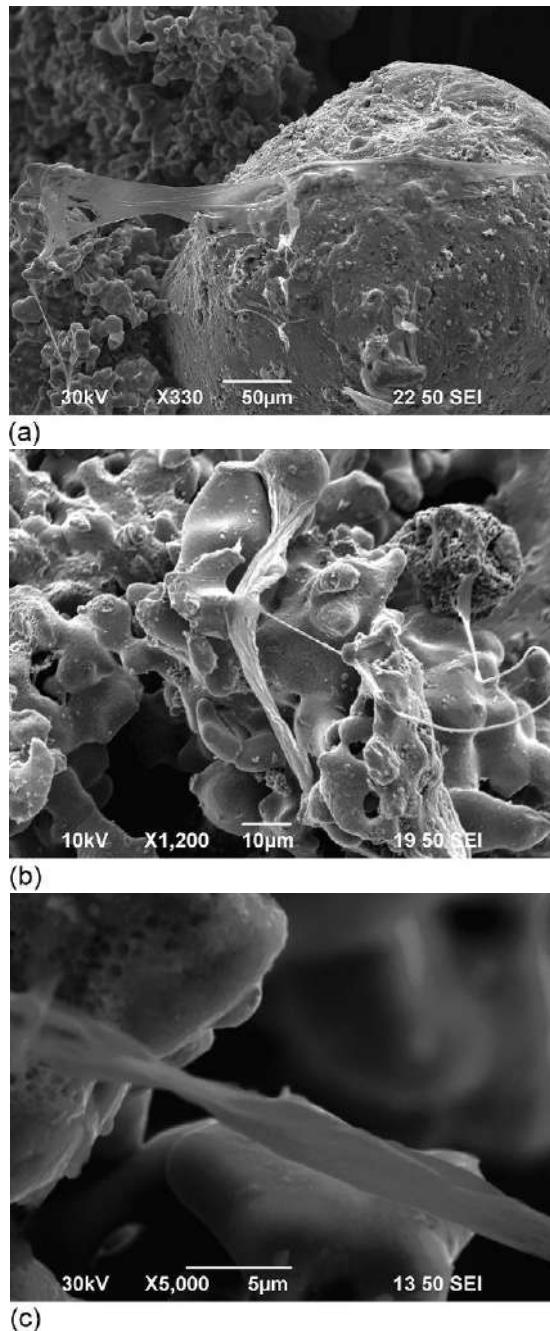


**Figure 26.9** (a–c) Scanning electron microscope investigation of the porous NiTi matrices.

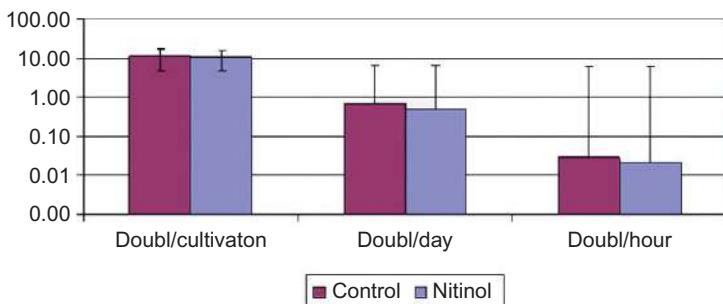


**Figure 26.10** Logarithmic speed of proliferative activity. Root-mean-square difference from the average by vertical lines.



**Figure 26.11** Number and configuration of MMSC colonies.

**Table 26.1 Morphological groups ratio**

No. of a group	Reference group	NiTi	Reference group	NiTi
	Quantity of objects/% ratio of objects	Aver. area/standard deviation (square/pixel)		
1 group (red)	1797/60.57	1154/ 65.27	201.5/60.8	174.0/53.8
2 group (blue)	1169/39.41	547/30.94	543.4/210.6	426.6/111.1
3 group (green)	1/0.034	67/3.79	2708.5/0.1	1143.7/ 482.7

[Figure 26.12](#) shows that the reference group of “young” and actively propagating cells is dominant but, near the 3-D NiTi matrix, the reverse is the case. In the latter, there is a high population of “aging giant” and slow-moving cells. This is why the proliferation velocity in the near-matrix zone is much lower than that in the reference group.

The migration ability (mechanotaxis) was evaluated by comparing the trajectories of the cells motion between the reference and nitinol groups ([Figure 26.13](#) and [Table 26.2](#)). During the observation, the average distance covered by the cells in the reference group was ~350 µm, while in the NiTi group the cells covered an average ~42 µm under similar conditions.

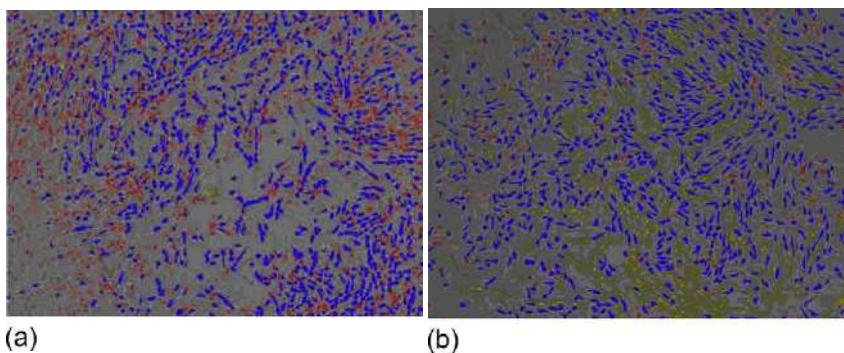


**Figure 26.12** Cluster analysis of the stem cells population (“young” cells—red color, “adult” cells—blue color, and “aging” cells—green color): (a) reference group cells and (b) cells in near-scaffold zones.

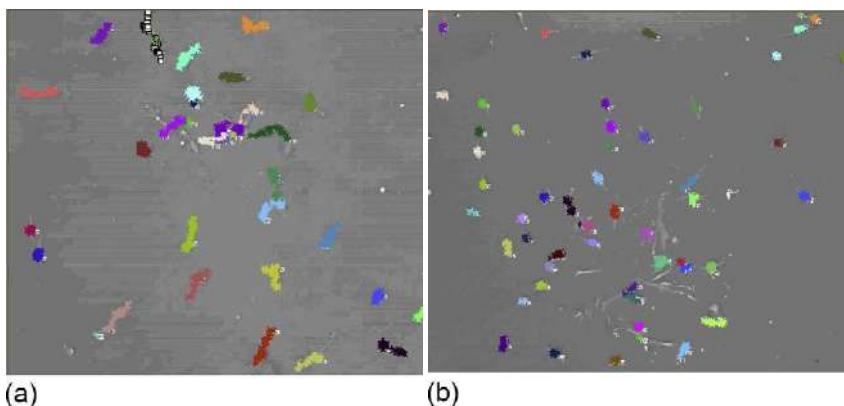


**Figure 26.13** Motion path and calculation of the distance passed by cells. Duration is 4 h. Magnification of image is 50×: (a) reference group and (b) near-matrix zone.

**Table 26.2 Migration activity**

Group	Cells per analysis	Distance ( $\mu\text{m}$ )	Minimum ( $\mu\text{m}$ )	Maximum ( $\mu\text{m}$ )	St. deviation ( $\mu\text{m}$ )
Reference NiTi	34	350.4238	78.70689	768.6559	187.0104
	56	42.494089	8.173793	153.891548	29.881101

The experiments on the cell migration ability revealed that in the reference group, over 4 h, the average distance covered by the stem cells was 350.42  $\mu\text{m}$  (minimum 78.70, maximum 768.65, standard deviation 187.01), as shown in [Table 26.2](#). The stem cell in the near-nitinol zone, under similar conditions, covered an average 42.49  $\mu\text{m}$  (minimum 8.17, maximum 153.89, standard deviation 29.88).

The immunophenotypic study showed that the stability of the testing cells was due to the MMSC group and the absence of the hemopoietic transformation or changes in the linear origin. The testing cells contained the following antigens: CD 90, CD44, HLA-ABC, 73, 105. These are characteristic of stromal cells. The absence of the antigens CD 45, CD106, CD34, CD144, 62L, HLA-DR, 133, 14, confirmed the presence of the MMSC group. In the course of the experiment, the weak positive expression of the marker CD 117 (C-kit) was revealed. This is a receptor for the stem cell factor of stem cell growth. The positive expression of this factor makes it possible to assume that the cells were immature.

As seen in [Section 26.1](#), we have discovered that porosity alone is not enough to grow cells into an implant. The size of the pores is also very important and should be commensurable with the size of the cells (compare [Figures 26.7d](#) and [26.8b](#)). The cells were pulled transversely to the matrix and their density was higher near certain pores, as mentioned in Ref. [29]. Excessive submicron porosity is probably as unfavorable for stem cells of  $\sim$ 50–100  $\mu\text{m}$  as its complete lack.

The study presents comparative results of morphological analysis of stem cell growth on porous matrices created by SLS on titanium and nitinol for tissue engineering. It is clear that the creation of tissue scaffolds (for example, for oral and maxillo-facial surgery) is relevant and promising [37]. In particular, it is possible that:

1. The SLS method allows layer-by-layer synthesis of biocompatible implants from pure titanium or nitinol powders, which do not possess measured cytotoxicity. Cell adhesion in the presence of such implants has demonstrated good monolayer conditions in and near the sample area with high cell density. Stem cells retained their structure and proliferative activity.
2. Implants made from Ti, NiTi, Ti + HA and NiTi + HA have high porosity, which provides the possibility for germination and adhesion, although their hardness is problematic.
3. Both options for stem cell proliferation are characterized by high chemotaxis of the cells to the samples, which decreases the number of cells in intermediate areas.
4. The presence of hydroxyapatite does not significantly influence the cell reproduction, indicating the high biocompatibility of titanium and nitinol. The nature of cell growth suggests that titanium is a biotolerant material for implantation, while nitinol is a biocompatible material.
5. The results of the proliferative activity and dynamic differentiation of the MMSC on the SLS-obtained porous Ni-Ti scaffold have been shown. According to the morphometry data, backed up by the SEM, the first MMSC colonies in the NiTi pores were registered on the tenth day. The proliferation speed was 0.694 doubling per day and 0.532 doubling per day for the reference group and the NiTi group, respectively.
6. Another fundamental result still requires explanation. While the percentage of small, but actively proliferating, “young” cells is comparatively high (50%) in the reference group (without scaffold), the stem cells grow up to an enormous size (which is aging) and their proliferation activity slows significantly after bringing in the matrix (the exogenous irritant).

The damaging effect of fibroblasts on the first day of experiments and the inadequate mechanical strength of porous scaffolds mean that they cannot be recommended as a universal material for substrate matrices. Despite these drawbacks, these materials can compete with organotypic polymers. In the future, laser sintering should be adapted for layer-by-layer fusion of such implants, which will allow their use in the replacement of skin, cartilage, and bone defects in surgical practices.

It is important that the issue of supplying the stem cells remains unsolved in the case of using porous Ni and NiTi as a stem cell repository. In the synthesis of bone by the SLS method, the question of blood supply after grafting is not clear either. The technology of direct osteogenesis can cause several problems connected with the creation of a certain tissue microenvironment for the developing bone over 30–35 weeks. Equally, one must admit that the creation of an organ *de novo* will be a major breakthrough for reconstructive orthopaedics.

## **26.3 Preclinical testing of SLS-obtained titan and nitinol implants' biocompatibility and biointegration**

Preclinical research on biointegration of porous nitinol implants compared with that of porous and cast titanium was carried out on a group of 21 laboratory rats over a three-month period at SamSMU (Prof. Volova T.V., M.D. Fokeev S.V.) [38]. All the porous nitinol implants were obtained by the SLS method. The animals were divided into three groups. Implants made of porous sintered nitinol were implanted in the first group, implants of porous titanium in the second one, and the third was the reference group with implants of pure titanium “Rema,” as used in stomatology. The appearance of the implants is represented in [Figure 26.14](#).

The area for surgery was prepared using standard techniques with all the common rules regarding asepsis and antiseptics ([Figure 26.15](#)). The insertion site within the bone was formed using a hollow dental burr. The wound was repaired with sutures and treated with iodine solution. Primary intention healing was typical for the wound. Material extraction was carried out after 1, 2, and 3 days and at 1, 2, and 3 months. In all cases the implant remained in a steady position inside the shoulder blade. The color of the implants did not change, possibly indicating a lack of material corrosion. The extracted material was then submerged in formalin solution for four days. After that the specimens were embedded with paraffin and stained with hematoxylin and eosin.

Seven days after implantation, macroscopic analysis showed no signs of edema in the operation area. After the implant extraction in the osteal tissue, a cylindrical defect was observed. From investigation, using optical microscopy, of the tissue specimens of the scapulas, it was established that spongiform osteal tissue was present transformed into trabecules and lacunas. Between the trabecules there was reticular tissue with blood vessels. At the same sites, intensive bone formation was detected by observing the young osteal and reticulofibrous tissue. There were no signs of inflammation. The histological picture for the porous nitinol implants was similar to that of

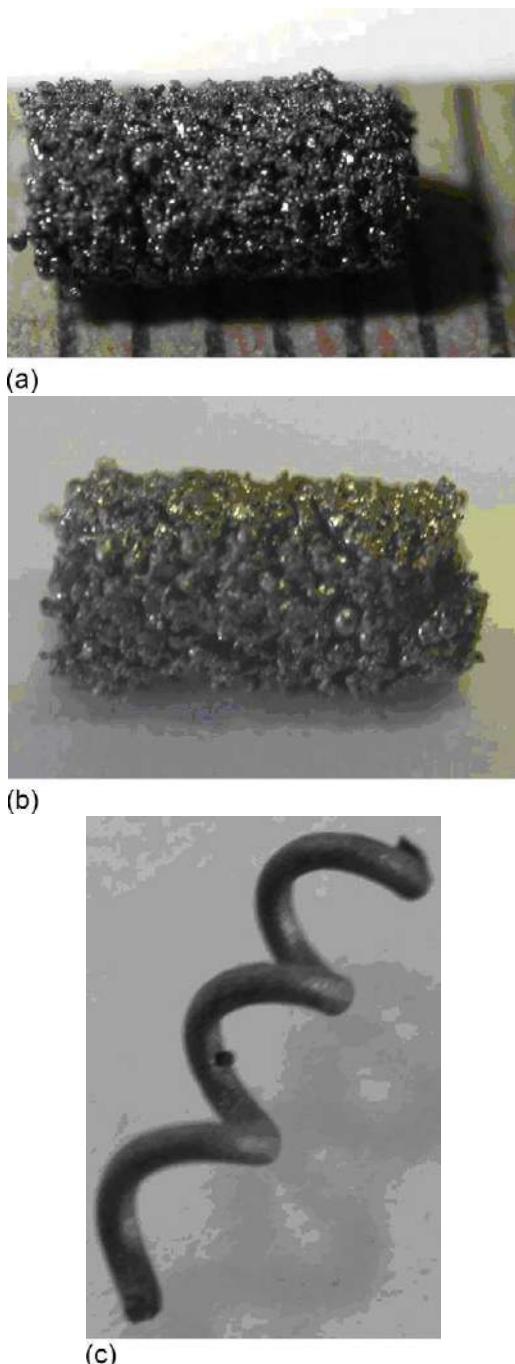


**Figure 26.14** Appearance of the porous implants of nitinol (a), and titanium (b), synthesized by the layer-by-layer SLS method, and cast titanium (c—spiral) “Rema”.

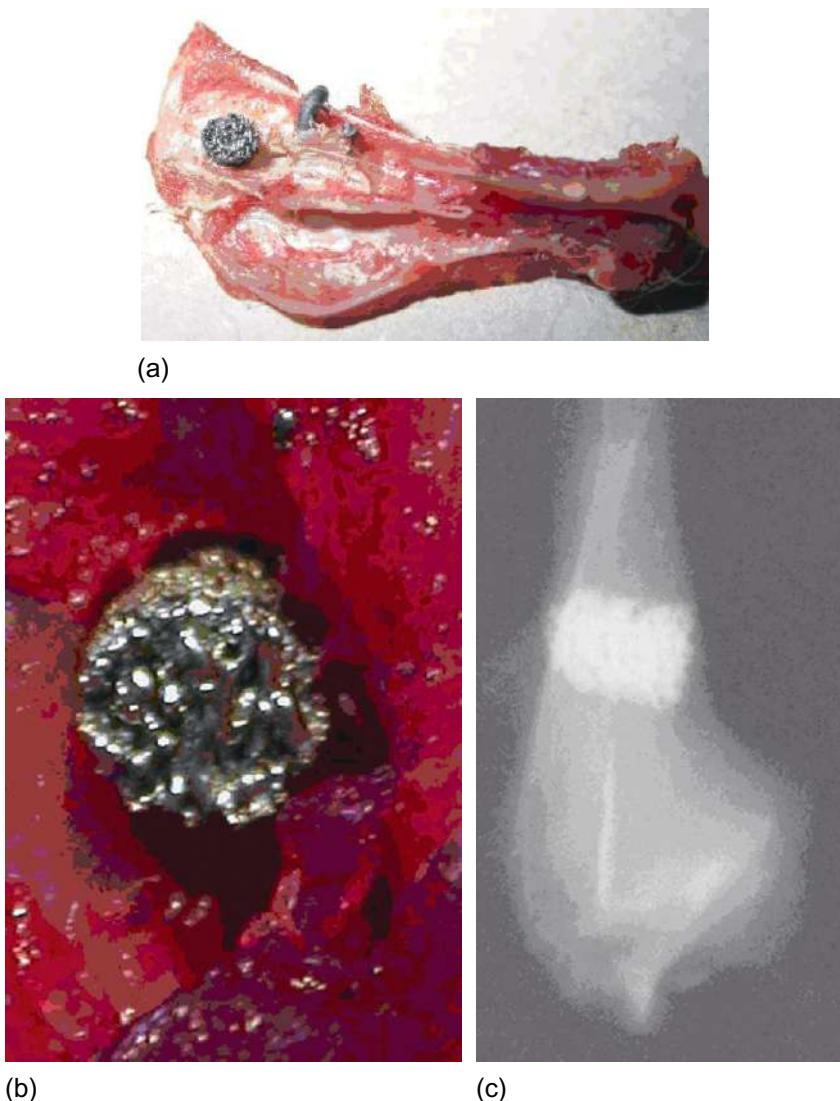


**Figure 26.15** Scapula with the porous implant in it (a), the process of implantation (b), roentgenogram of the implant topography *in vivo* (c—axial view).

the experiments with porous titanium implants (compare Figures 26.16 and 26.17 after 1 week and after 2 months). This suggests both of the materials could be used in implantology.

Microscopic analysis of the bone tissue near the titanium spiral revealed the presence of huge cells with 2-3 large nuclei. Among the connective tissue cells, macrophages, fibroblasts, lymphocytes, and plasmocytes were discernible. Reticulofibrous tissue

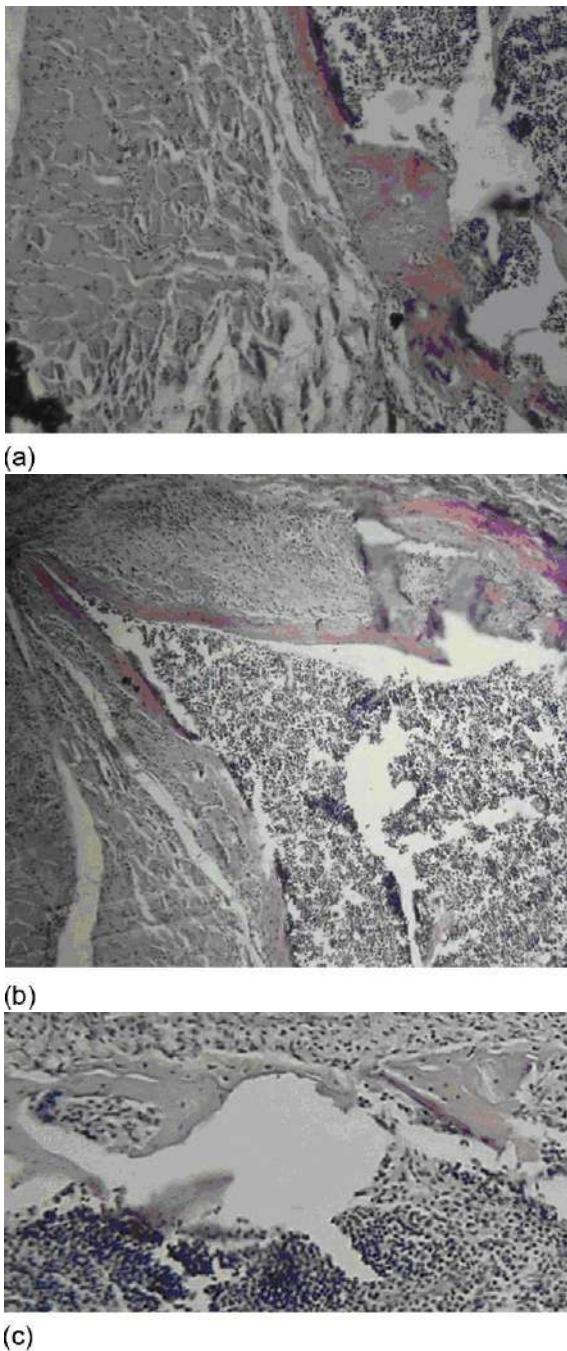


**Figure 26.16** Periosteal tissue structures after implantation, 1 week. OM, magnification  $40 \times 10$ : (a) porous titanium; (b) porous nitinol; and (c) cast titanium spiral.

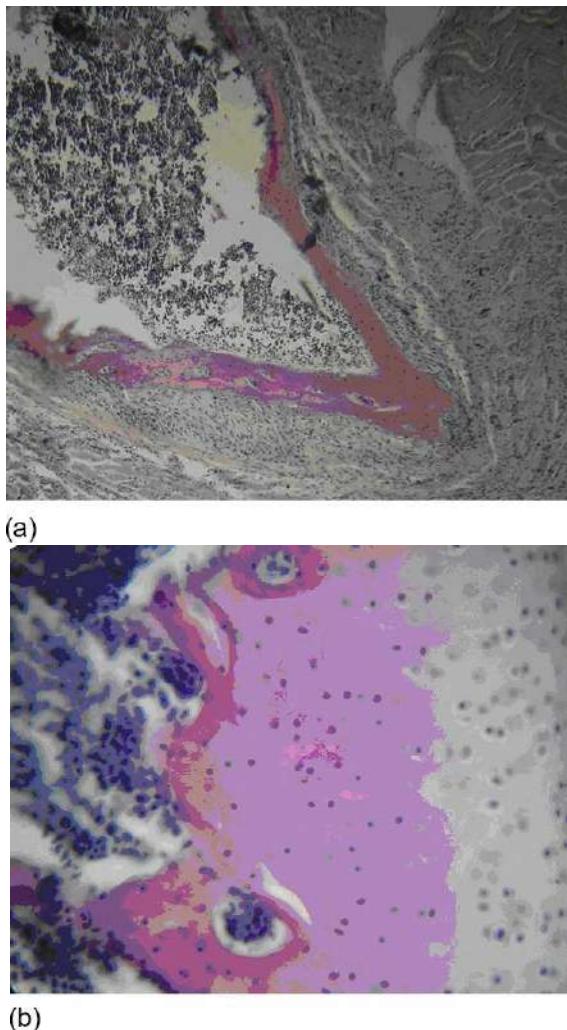
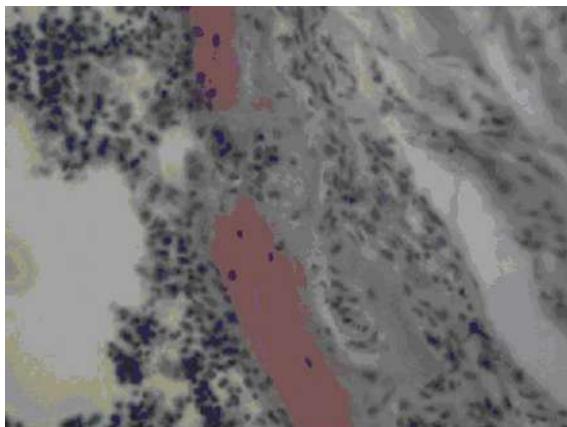


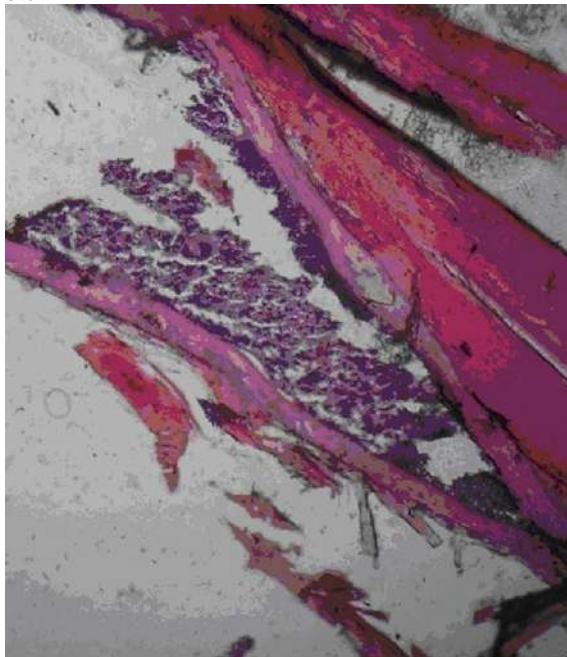
**Figure 26.17** Osseous tissue mount after implantation, 2 months. OM, magnification  $40 \times 10$ : (a) porous titanium and (b) porous nitinol.

accretion toward the muscular tissue was observed in the periosteal area. Histological analysis revealed an osteoplastic process accompanied by the growth of young osteal beams on the edge of the defect ([Figure 26.16c](#)).

In the later weeks and months ([Figure 26.18](#)), the osteoblasts and osteocytes in the scapula's structures actively rejuvenated. In the connective tissue, randomly located fascicles of collagenic fibers dividing cellular elements were visible. Fibroblasts, macrophages, and lymphocytes were found between the osteal beams as well. A white color ([Figure 26.18](#)) showed the formation of fatty tissue. The osteal beams had



(a)

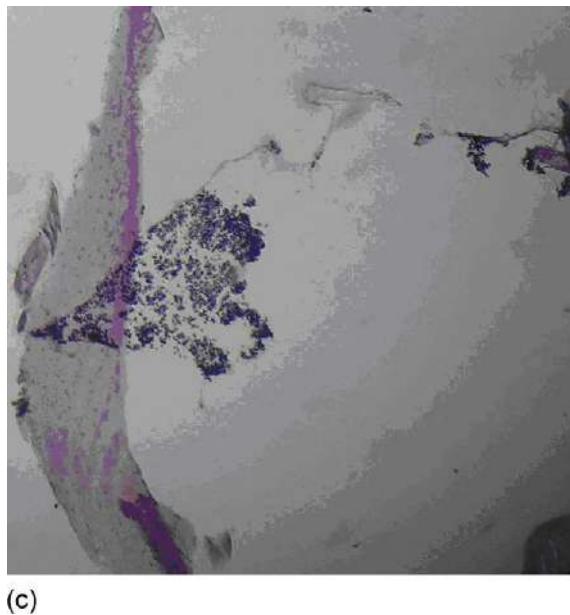


(b)

**Figure 26.18** Periosteal tissue structures after implantation, 3 months. OM, magnification  $40 \times 10$ : (a) porous titanium; (b) porous nitinol; and (c) cast titanium spiral.

the organotypical structure of young spongy bone tissue with lacunas. The lacunas were filled with actively proliferating cells of red bone marrow reticular tissue.

A morphological study of the implant structure, once it had been contained in living tissue, was carried out after the histological study at the SEM (LEO EVO-50 XVP + INCA). [Figure 26.19](#) shows an example of effective penetration of the connective



(c)

**Figure 26.18** Continued.

tissue between the darker granular materials consisting of titanium particles without any signs of necrosis.

[Figure 26.19a](#) shows an organotypic structure of the young tissue with lacunae between two large (150–200 mm) titanium globules. Elemental analysis (EDX—S3, [Figure 26.19b](#)) showed the presence of titanium 18.35%, nickel 21.88%, and carbon 59.77%. The nickel to titanium ratio affected the stoichiometry of NiTi intermetallic phase, and the higher quantity of carbon indicated the presence of conjunctive cartilaginous tissue. White areas in [Figure 26.19](#) were caused by fluorescence from electron-beam excited organic structures during SEM.

[Figure 26.20](#) shows clearly that the young conjunctive tissue has grown into a gap between two big particles of titanium. The element analysis (EDX—S3, [Figure 26.19b](#)) showed, apart from titanium, the presence of carbon, oxygen, and phosphor, which are constituents of connective cartilaginous tissue.

Nitinol was completely osseointegrated after three months of biointegration in organotypic structures ([Figure 26.21a](#)). Bone/nitinol contacts were close, indicating good tissue tolerance. The implant has a regular open structure ([Figure 26.21a](#)), which facilitates the bony tissue ingrowth into the body of the implant resulting in the desirable firm fixation to the bone. Free nickel ([Figure 26.21e](#)) was not observed on the nitinol surface, which is important because of its potential toxicity. The presence of calcium in the element composition was due to the decalcination process before the histological study and showed that there was good bone formation. Dark areas

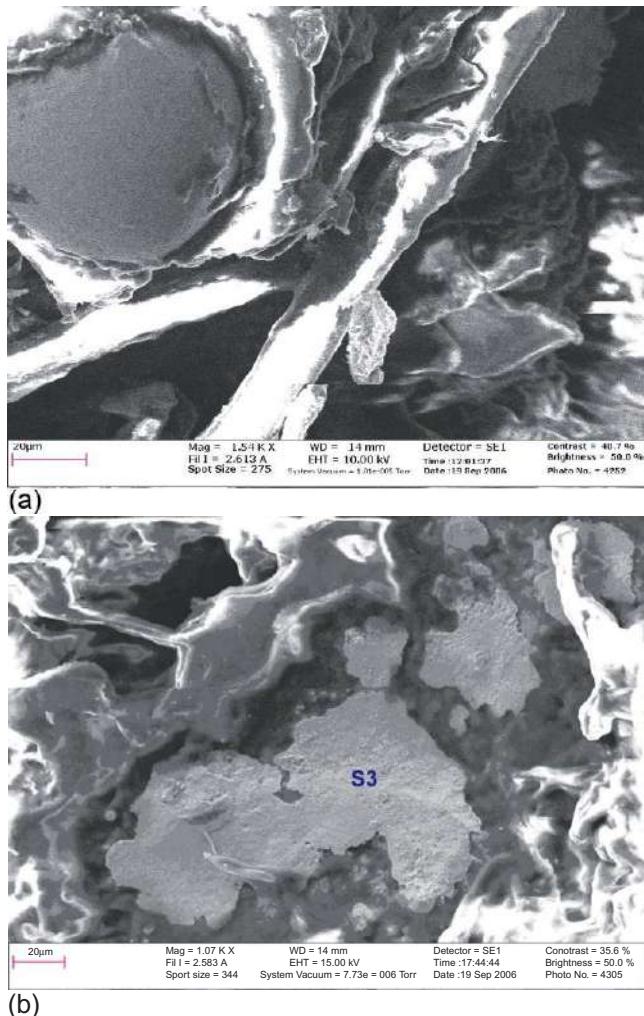


**Figure 26.19** The titanium implant after 3 months: (a) SEM microstructure, magnification 1530×, accelerating potential of 10.00 (kV) and (b) the nitinol implant after 3 months. SEM microstructure, magnification: 1070×, accelerating potential 15.00 (kV).

in Figures 26.20a, 26.21a, and 26.22a (see S2 in Table 26.3) correspond to carbon inclusions covered with titanium or nitinol particles.

A slight bone resorption could be seen under a microscope at the contact area of the implants. This bone resorption activity was caused by removal of the bone tissue with the dentist's burr during the implant operations. The defect zone kept the organotypic structure. Neutrophilic exudate was not found in any series of probes.

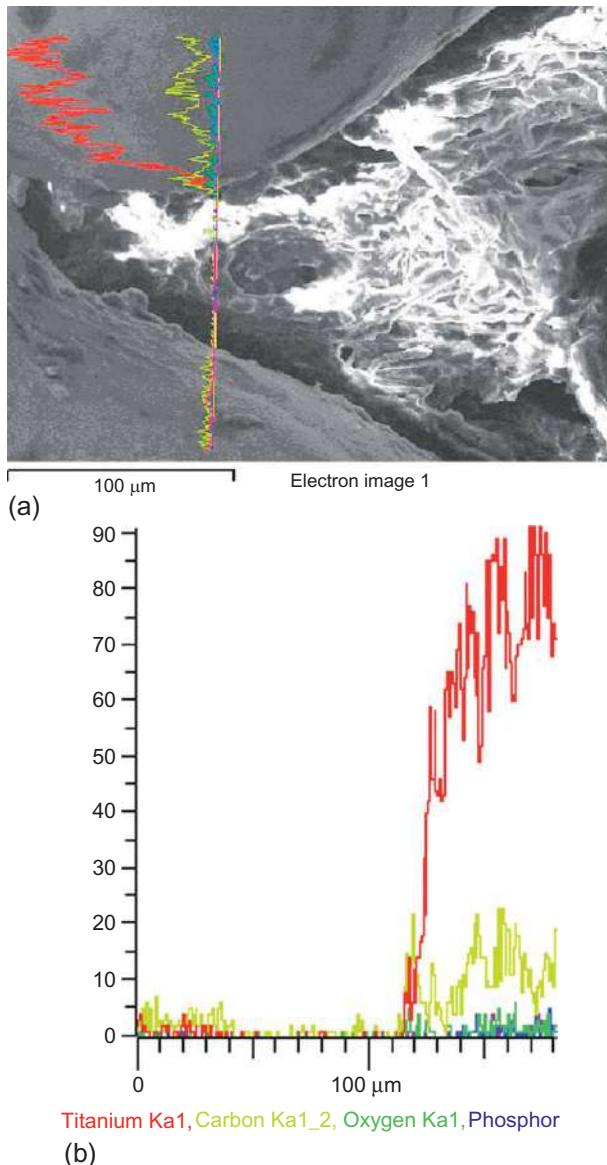
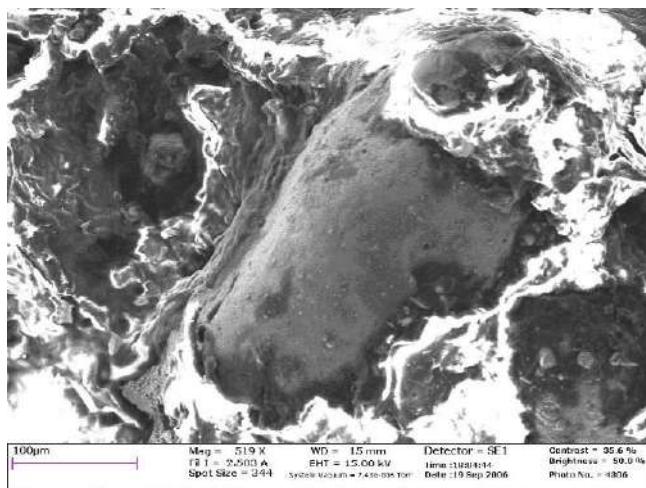
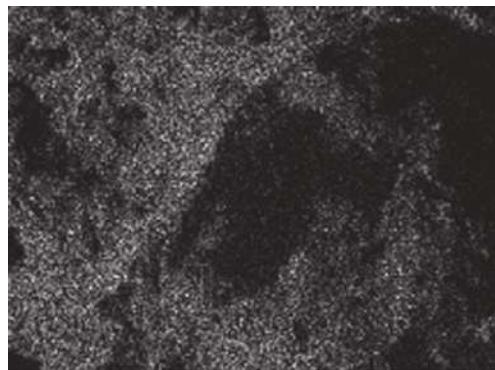


**Figure 26.20** Titanium implant after 3 months: (a) microstructure at magnification of 1186 $\times$ , accelerating potential of 15.00 (kV) and (b) elements' distribution.

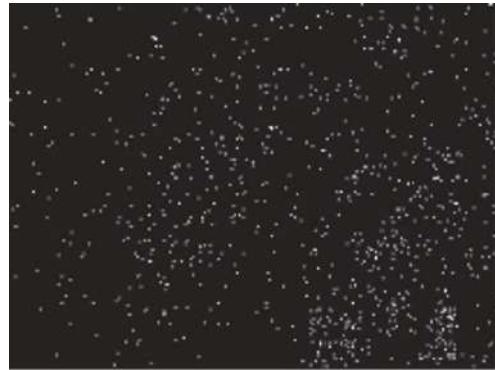
Once the observations had been completed, porous nitinol and titanium implants were closely embedded in the living tissue and were difficult to extract. The osteal tissue surrounding the defect zone had an organotypical structure. The periosteum did not change in thickness, which was slightly different from normal values, and consisted of a cellular and a fibrous layer. Histological analysis showed that the



(a)



(b) O Ka1\_2

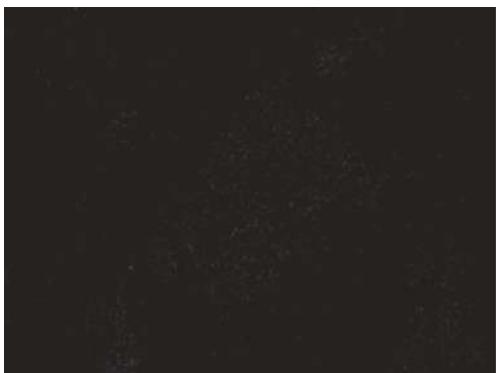


(c) O Ka1

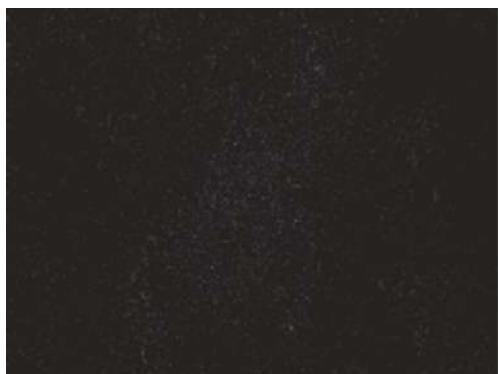
**Figure 26.21** Nitinol implant, 3 months after implantation. (a) Microstructure, magnification: 519×, acceleration potential 15.00 (kV) and (b-f) elemental structure.



(d) Ca Ka1



(e) Ni Ka1



(f) O Ka1

**Figure 26.21** Continued.

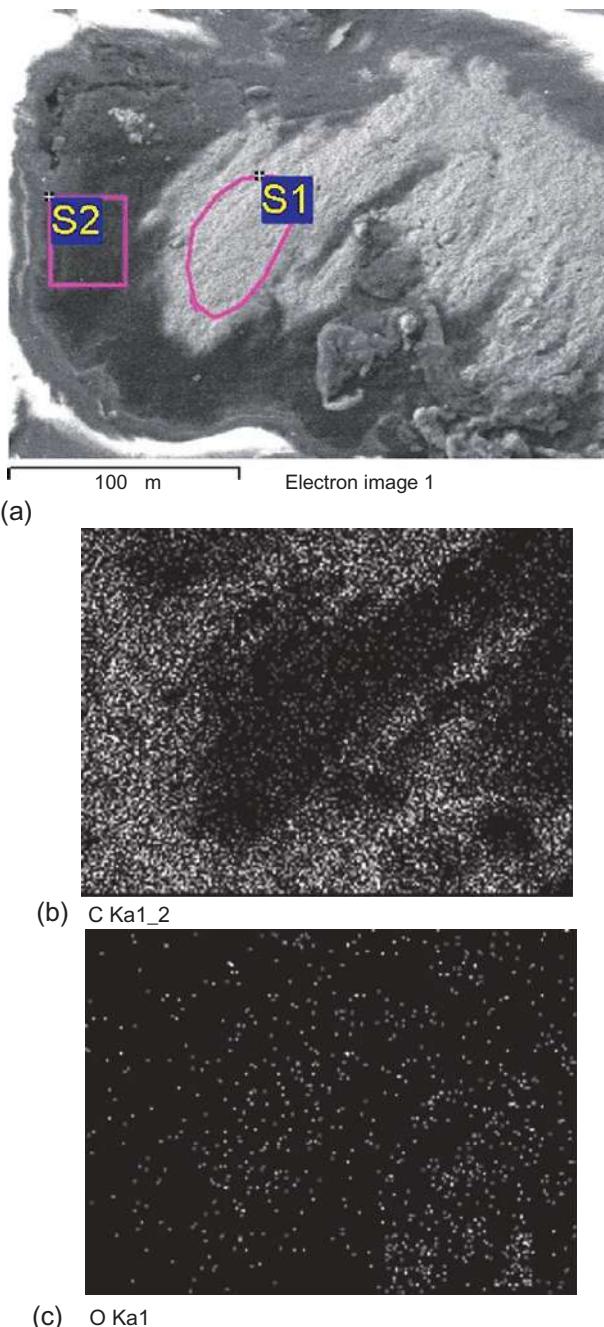
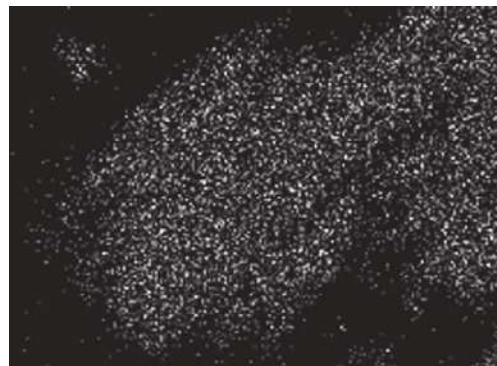


**Figure 26.22** Microstructure of the accreted nitinol magnification: 1220 $\times$ , acceleration potential (kV): 15.00. (b-e) Elemental structure.



(d) Ti Ka1



(e) Ni Ka1

**Figure 26.22** Continued.

**Table 26.3 EDX-analysis of the place shown in Figure 26.22a**

Spectrum	C	O	Ti	Ni	Total
S1	49.44	13.27	26.05	11.23	100.0
S2	98.93		1.07		100.0
Max.	98.93	13.27	26.05	11.23	
Min.	49.44	13.27	1.07	11.23	

internal space around the spongiform osteal tissue defect had connecting tissue in the form of trabecules and lacunae, which were filled in by osteal bone and spongy material. From the medullar spaces of an osteal bed, trabecules could be seen, consisting of reticulofibrous osteal tissue. The osteal beams were wide with considerable quantities of osteocytes densely packed together and surrounded by thick rows of osteoblasts. Around the trabecules, considerable quantities of osteoblasts were observed.

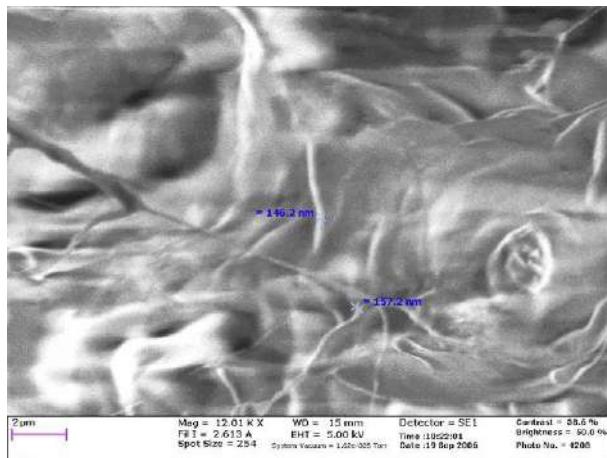


**Figure 26.23** The organotypical structures near to the titanium implant.

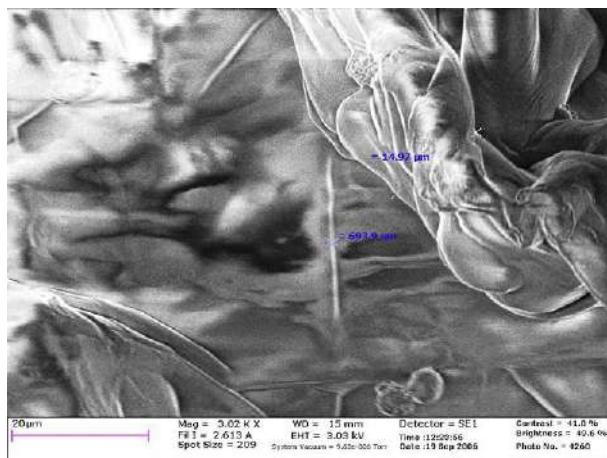


**Figure 26.24** The organotypical structures near to the nickel-titanium implant.

The development of connective tissue ([Figures 26.23](#) and [26.24](#)) in the implantation zone confirmed that the process of osseointegration had occurred. Measurements showed that if near an NiTi implant their characteristic dimensions ranged from 700 nm up to 15 mm ([Figure 26.23](#)), whereas around porous Ti more shallow bonds of about 150 nm were formed.

Due to their low durability, nitinol implants can only be recommended for use as plastics for soft and hard tissues defects. Another interesting aspect of developing this branch of implantology is the possibility for CAD-supported creation of objects with controllable porosity. These have better reconciliation of parameters (modulus of elasticity, Poisson's ratio, coefficient of thermal expansion, etc.) between bone tissue and implant material.

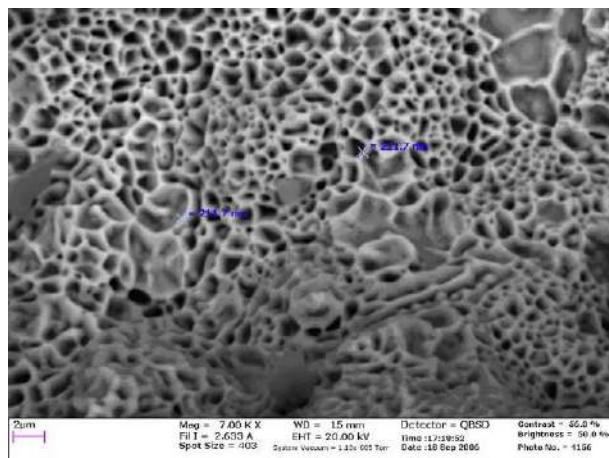


**Figure 26.25** SHS + SLS-synthesized nitinol surface with a developed nanofractal structure.

Highly magnified SEM imaging of the implant surface was used to thoroughly examine the effect that the surface morphology and implant porosity had on the biomechanical integration of the implant with the surrounding bone tissue (see Chapter 11 and [2]). Figure 26.25 shows a close up of Figure 2 from Chapter 11, which shows the sintered nitinol surface (Figure 26.22 shows the surface at lower magnification) at a magnification of 7.000 KX. It was found that the synthesized nitinol surface had a developed nanofractal structure. The nanostructures had a low dimensional self-organization. The wall size of the synthesized nanostructures ranges from about 140 to 460 nm, while the structure itself is about 2–5 μm. It is therefore possible that the developed micro- and nanostructured nitinol surface promotes biointegration.

Histological analysis showed that there was active biointegration of the porous implants with the bones of the animals under consideration. The NiTi implants showed no adverse tissue reactions and there was no evidence of either localized or general corrosion of the bone surface. The implants were assessed according to their biocompatibility, bone contact, and ingrowth. The bone histology and microhardness parameters showed that the bone behavior in contact with the implants was similar to that of the surrounding cranial bone. The SLS-made porous nitinol therefore appears to be a suitable material for craniofacial applications.

## 26.4 Finite-elemental optimization of SLS-obtained implants' porous structure

Intaosseous dental implants are effective for dentition correction. The development of dental implantation depends on achieving osteointegration by improving the intraosseous parts of the implants. Implants with the open type of porosity can manage the load if used as one-root teeth substitutes, but break under the load of the first molars.

Therefore studies of the stress-strain behavior of porous implants under the masticatory load or pressure are needed. The structural and strength properties of the porous implant are also important. The finite element approach (*ANSYS*) is used for solving related problems [39].

One way of approaching implant synthesis is the process of an SLS allowing the manufacture of dental implants with open porosity. Earlier we showed the possibility of the layer-by-layer laser synthesis of titanium and nitinol scaffolds with complex porosity architecture and controllable permeability and particle size, in order to confirm their suitability for tissue engineering.

We now turn to the use of *ANSYS* bundled software to study the SLS-obtained porous implants' mode of deformation. *ANSYS* is already widespread among development-engineers because it can solve the most complex problems of deformable body mechanics and it is adaptable for different end-consumers. Further, it can be used in constructional stomatology.

The different studies in this area are listed below (see references in Ref. [40]):

- “Removable prosthesis—implant—bone” numerical modelling. Variable parameters of size and density of the bone allow the study of the biomechanical foundations of the interaction between the osseous structures of the lower jaw and the full removable prostheses, of a different construction, with the intraosseous implants fixing them.
- Research into the peculiarities of tooth and periodont when in a deflected mode under the dynamic load and into the protective role of the snag. This is carried out by using the finite-elemental model of the teeth-jaw segment of the central maxillary incisor area.
- Investigation of the stress distribution in hard tooth crown tissues with different scopes for defect as well as in the inserts under exposure to physiological loads.
- Comparative analysis of the results of modelling the deflected mode of different pivot crown constructions mathematically.
- Finite-elemental analysis of deflected mode with cavities replaced, in a medial-occlusive way, by the distal insertion of ceramic material or by the plug of a photocurable composite.

However, the exact interaction between the porous structure of the implant and the bone tissue is still unclear.

It is important to know how porosity size influences the interaction between the tissue and the bone. For both particle shapes, the implant is synthesized by the SLS method. Their spatial orientation contributes to the deflected mode of the system. The objective of the analysis was to calculate how to optimize the structure of the implant. The analysis allows one to establish a system to form the prosthesis, which will be both porous enough and meet the masticating pressures of the other. A bone-implant interaction model is needed to carry out the calculations.

It was proposed the changes of the stress at the contact zone should be observed while changing the porosity size. Further, the influence of the internal structure (the particle size) and the shape of the implant upon the originating stresses, resultant deflections, and unit strains are of interest.

A simplified implant model of cylindrical shape (Figure 26.27a) was used for the numerical simulations. Its diameter was 8 mm and length was 14 mm. This construction was placed in the cavity of the spongy bone tissue. To shorten the simulation process,

the model volume was quartered by symmetrically scaled meshing. However, the boundary conditions were imposed on the symmetrical model faces (Figure 26.27c).

As the SLS-obtained implants have a porous structure, the pictorial representation of the model was changed. The implant porosity was determined by the structure of the ordering objects (that is, the particles of the sintered powder) with regular shape (balls or cylinders were used) (Figure 26.26).

The porosity value was adjusted for the change in ball diameter (Figure 26.26a-c). This value was also expressed by changing how much the ball overlapped with its diameter, evaluated in percent. The relative configuration of the objects didn't vary through the study. For the balls, only density packing was appropriate, and every following layer was placed in the holes formed by the previous one.

The material was designed as follows:

1. One object (for example, the ball) is created.
2. This object was copied several times (four times for this study) along the X-axis of the distance defining the porosity. (This could be 98% or 95% of the ball diameter, so that overlapping was of 2% or 5%, respectively.)
3. The duplicated process is along the Y (4 times) and the Z (10 times) directions also. In these cases, it was necessary to calculate that objects fell into the holes of the close-packed structure.

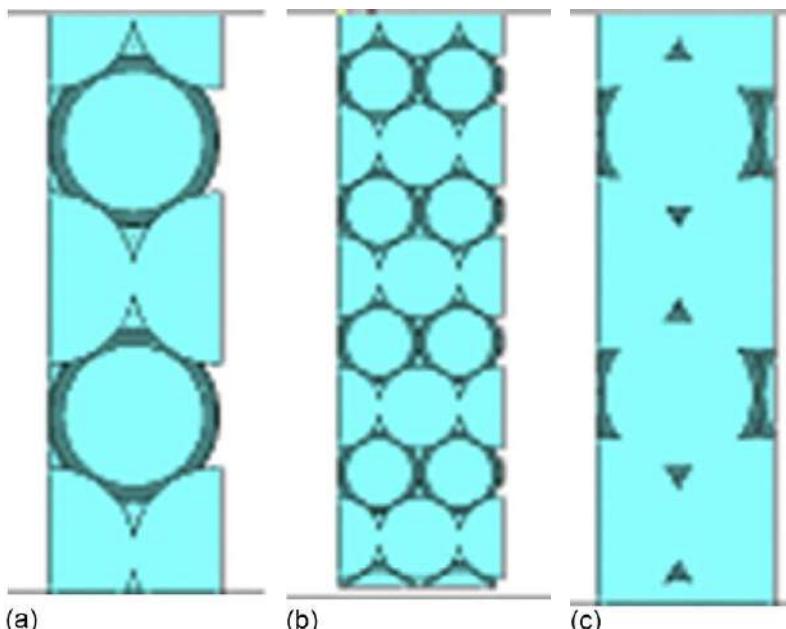


**Figure 26.26** Changing of the calculation model porosity: (a) ball  $d=2$  mm, overlapping of 2% from  $d$ ; (b) ball  $d=1$  mm, overlapping of 2% from  $d$ ; and (c) ball  $d=2$  mm, overlapping of 9% from  $d$ .

Using the built in ANSYS function (VINV), a cut-and-paste model was produced. This was done either by a volumetrical cylinder modelled using this program or by another figure built in a different CAD-system. The dowel model was built in the *Solid Works* program and then imported to ANSYS as a \*.sat file (Figure 26.27). At this stage, the problem is the appearance of improper surfaces, volumes, and small lines when the intersection of complex-shaped volumes is being built. This causes difficulties in building. Hence, volume size was measured by SCAL throughout the building process. The volume obtained by cutting should be restored to its original size. A process of fragmentation of a construction with a coarse grid of finite elements to optimize the time of the calculations is often not available after such operations. Though a finer grid gives a more accurate result, the time it takes for the calculations becomes unacceptable. Therefore, it was necessary to reject some intermediate constructions (for example, 7% overlapping for 2 mm ball's diameters).

The spongy bone (Figure 26.27b) formed the surrounding volume, remotely attached at a distance of 6 cm. The cylindrical or complex dowels were 1.5 cm × 2 cm. The study used 20-node SOLID95 element to assess the structure of the titanium. It allowed for modelling of the transitional tasks and stress-strain behavior, as well as importing of the model from the CAD system. However, this element is not suitable for materials with shape-memory capabilities because hyperelasticity was not among the special properties of ANSYS.

Nitinol is defined as a hyperelastic material as it has an elastic potential energy (or function of the deformation energy density), which is a scalar function of one deformation or strain tensor. Its existent stress component is determined by a derivative of a component of strain. It can be exposed to heavy deformations and displacements without sizeable volume changes occurring. For materials of this kind, the theory of heavy deformations should be applied. Thus, for nitinol, the SOLID187 3-D-element with 10 nodes was used. In the interaction (contact) zone between the implant and bone tissue, the mesh of FE was concentrated. The boundary of the contact was described via TARGE170 and CONTA174 contact elements. The TARGE170 element was generated on the implant surface while the CONTA174 element was used on the internal surface of the bone cavity. We considered a yielding-yielding contact that implies a deformation of both materials.

For the sake of this experiment, it was important to calculate the stresses at the contact zone and in the bone tissue and porous metal part of the model. A comparative analysis of the behaviors of the two types of titanium alloys was undertaken. For titanium, the Young modulus was  $E_X = 1.1025 \times 10^{11}$  Pa and Poisson ratio  $\nu_{XY} = 0.32$ , while for nitinol (NiTi-phase)  $E_X = 48 \times 10^9$  Pa and  $\nu_{XY} = 0.33$ . The spongy tissue parameters were  $E_X = 6.89 \times 10^9$  Pa,  $\nu_{XY} = 0.33$ .

The following boundary conditions were applied to the construction being modelled (Figure 26.27c). The chewing load experienced by teeth is 240 N [1]. Taking the size of the implant into consideration, the pressure applied to the top external surface of implant was set at 1.19 MPa. As mentioned above, the same conditions were set for the construction's cut. The bottom of the bone surface was fastened so that it was prevented from displacing relative to the Z-axis or to the X-Y axes, at the front.

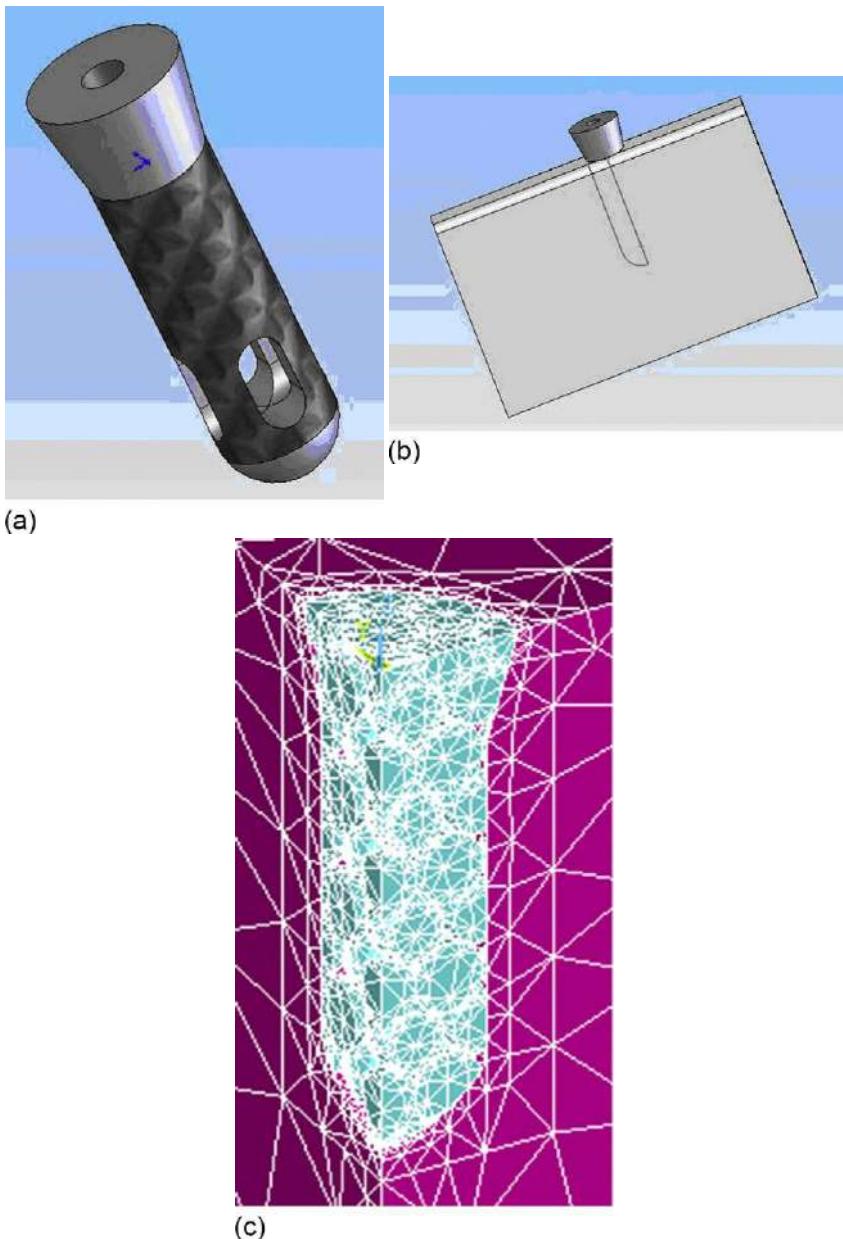


**Figure 26.27** Modelling the implant by *SolidWorks* (a), the implant inserted in the bone tissue (b), and *ANSYS* meshing (c).

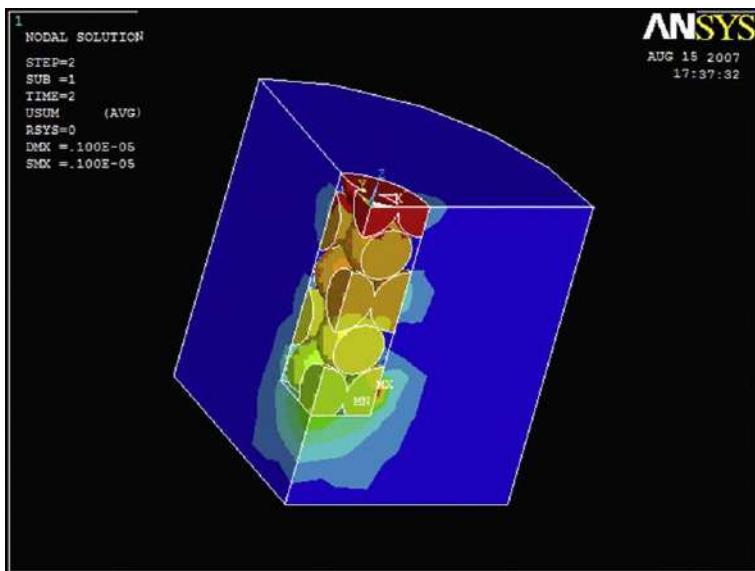
The solution was produced in two steps with the ANSYS solver. First, the implant “penetration” was achieved in the contact area of the spongy bone. This is achieved by the displacement of the top surface layer along the Z-axis. The solution did not disturb this and the loading from the first step was kept. In the second step of the solver, the chewing load was put into force. In the case of the nitinol implant, the “Large Displacement Static” solver was used during the first step of loading because of the “shape-memory effect” characteristic of this material.

Originally, a cylinder-shaped implant of the same size was used to adjust the model. During the first stage of simulation we changed the powder size from 2 to 4 mm. This shortens the calculation time. The diameter overlapping was also increased from 2% to 9%. For the purposes of comparison, we studied two materials, titanium and nitinol. At the second stage of comparison, the model structure was in the cylindrical form of particles. Here we changed the structure of the porosity as a percentage of the cylinder overlapping by height from 2% to 4%. At the third stage of modeling, we studied the influence that the common implant shape had when introduced into the spongy bone construction. The shape of the prosthesis (cylinder or dowel, [Figure 26.27](#)) and its porous internal structure were designed at this stage. Finally, the dependency of the simulation results on the loading direction was shown, that is, how the results of the simulation changed under both normal and tangential deformation, compared to their absolute values, applied to the upper implant surface.

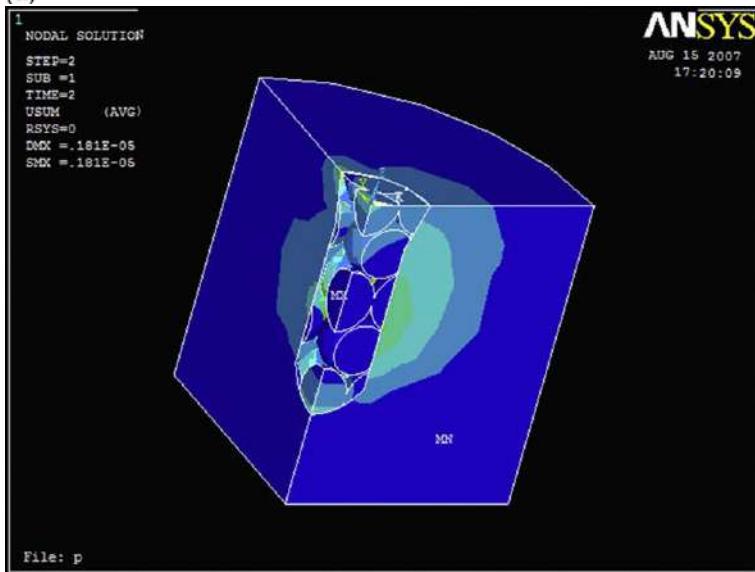
The results of the stress and displacement simulation show that when the overlap of the small particles that constitute the implant (“balls” or “cylinders”) increases, strains and displacements in titanium increase, while stresses drop. For the nitinol structure, when overlapping was increased (in a material approaching a cast one rather than a porous one) stresses, stains, and displacements decreased. Judging by the absolute value, the stress-displacement parameters for titanium are lower than those of the nitinol. Variation of the particle size from 2 to 4 mm shifts the tendencies insignificantly.

The influence of the internal and external shape of the implant upon the strains, stresses, and displacements is complex. First, the implant of a complex shape has higher values of strains, stresses, and displacements than one with a simple cylindrical shape. The shape of the powder particles also influenced the stress-strain behavior: cylinder-shaped particles had higher values of displacements but lower ones of stresses and strains. Generally, the behavior of the nitinol structure is preferable to that of the titanium structure.

Looking at the stress diagram in the graphics mode, we can observe the environmental stress in the implant-bone system in the contact zone, but also in the place of connection between the objects constituting the model. The diagrams are presented in [Figure 26.28](#) for comparison. The cast implant provided the normal loads as well as the tangential ones. The cylinder-shaped implant was a heavy load upon the surface and likely to damage it. The porous dowel of the complex shape tended to release its loads into the space around it and relieve the bottom of the dental alveolus from it. This transforms a part of the implant-bone load into the internal load of the prosthesis. The internal loads can then fasten to the deterioration of the implant. But, because the implant is porous, the tissue will grow into the pores and increase the reliability of osteointegration. Though this was not taken into consideration while making the calculations, it can still be studied afterwards.

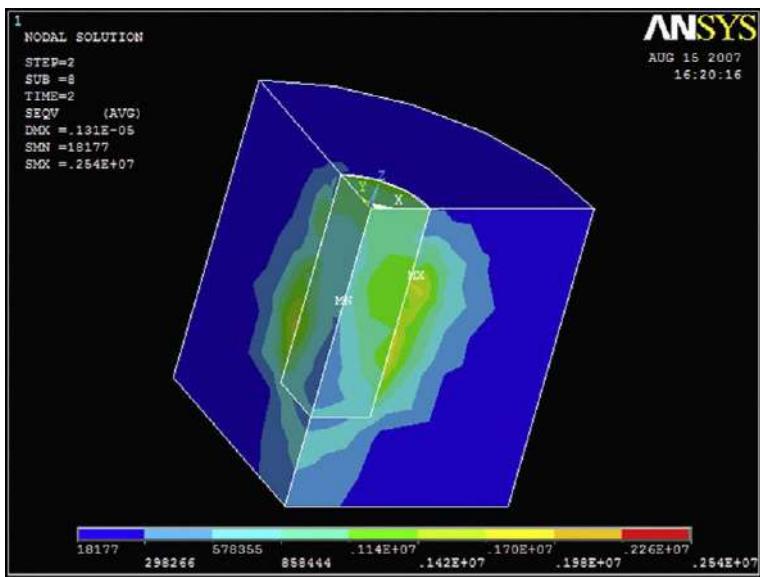


(a)



(b)

**Figure 26.28** Assumption diagram for stresses and strains in the cylinder-shaped (a), in the complex-shaped [Figure 26.27a](#) (b) and cast (c) implant in the bone tissue.



(c)

**Figure 26.28** Continued.

Research has shown that a rough or porous implant surface ensures that there is substantial contact between the bone tissue and the prosthetic device. This results in a more efficient, stronger biomechanical relationship between the implant and the bone. It is also desirable that the contact surface topography corresponds to the bone structure.

The SLS technique allows for picking the right approach to form the prosthesis with a certain structure and, at the same time, regulates its surface roughness and porosity. These characteristics can be controlled to provide a better penetration of the tissues into the implant material.

The study therefore revealed that the absolute values of stresses, strains, and displacements decrease and the implant density increases when the overlapping degree is increased. A comparative simulation has shown that the maximum values of all the investigated parameters observed for the porous nitinol are different for porous Ti. Further, it has shown that bigger displacements and strains occurred with smaller stresses.

## 26.5 The SLS-assisted functional design of porous drug delivery systems based on nitinol

For the last decade, the application of microfabrication methods has led to the development of microelectromechanical systems (MEMS), bio-MEMS, total analysis microsystems, lab-on-a-chip, and other microdevices [41,42]. For instance, the

microfabrication techniques facilitated the creation of novel drug-delivery microdevices and components of microdevices that improve the therapeutic effect of drugs, such as microneedles, micropumps, microvalves and implantable drug delivery systems (DDSs) [43]. Major microfluidic components include:

- sample introduction, loading, and, in some cases, sample preparation
- fluid propulsion, for example reagents, washing or calibration fluids, through micron-sized channels
- valve functioning
- fluid mixing and/or isolation
- small volume sample metering
- sample splitting and washing
- temperature control of the fluids.

A wide range of microfluidic products such as pumps, valves, mixers, and flow sensors has been demonstrated [44,45]. The main challenge is how to create miniaturized systems that integrate different microfluidic components to perform certain functions at high speeds throughput.

In general, the fluid propulsion can be put into action mechanically, electrically, or thermally [41,44,45]. Each of these approaches has its own advantages. Here, the thermal methods of propulsion will be discussed. In the case of phase-change pumping, the driving pressure is caused by the volume change due to the phase transformation from one state to another under the temperature variation. Owing to a high heat exchange rate in small channels, this mechanism scales down well to the microdomain. However, thermal methods require careful control of the local temperature. An essential component in the microfluidic system is that the control can stop and start the fluid flow. Different designs use different methods of actuation, such as magnetic, pneumatic, hydraulic, or thermal-electric. The delivery of precisely metered fluids from one reservoir to another in a well-controlled sequence is important for many microfluidic applications. Inkjet print cartridges are one of the most well-known commercial applications of microfluidic devices.

Various microfluidic propulsion technologies have been reviewed and compared with regard to the choice of materials, the maturity of the technology, and the possible volumetric flow rates. Intermetallic NiTi has, even in a porous state, a high specific strength, corrosion resistance, damping characteristics, and a unique shape memory effect (SME) [2,46]. In the case of nitinol, its biocompatibility, physical properties, and the SME observed, even in a porous state, suggests that this material may offer substantial gains in orthopaedic implants and DDS [47–49]. To achieve these gains, implant elements need to be created that can change their shape after implantation. This would be achieved by exploiting the SME of nitinol that can be initiated at the temperature of a living organism. These shape changes have three primary benefits: (1) enhanced bone fixation, (2) minimally invasive surgery, and (3) improved drug saturation. In the field of controlled drug delivery, self-expanding (which occurred here owing to the SME) in *in vivo* devices that use diagnostic measurements to control the drug release will be widely developed in future. Microscale therapeutic and diagnostic systems are fundamental for the development of these self-regulated

(within a close loop) drug delivery devices. They can be implanted inside the body to monitor concentrations of specific target drugs and deliver therapeutic agents if necessary.

RP technology has great potential for engineering implants, scaffolds, and DDS with a pre-specified and reproducible external and internal surface morphology useful for bioengineering applications [5,9,29,38,43,50]. The SLS method is able to rapidly synthesize reproducible, highly complex three-dimensional data ( $\mu$ CT or MRS) for each patient, and internal structural features as well. Another application for the porous structures is in membrane technologies [2] and in the creation of dosing devices for the pharmaceutical (medical) industry. Studies have suggested [9] synthesizing a porous polymeric DDS implant with a bioactive preparation by the method of SLS. The implant dissolves after a time in the patient.

In earlier studies, it was shown that the SLS process typically produces materials with high values of corrosion resistance and porosity, significant water absorption ability, and a well-developed surface structure [2,20]. A controllable internal structure of the interconnected porous channels provides a framework for the bone that ensures it grows into the matrix of the material, thus increasing the interfacial area between the implant and the tissue, and thereby reducing the shift of the implant in the tissue. Also, some suitable channels could be available for drug release into the blood, aimed at reaching the connective ingrown tissue, thereby preventing necrosis of the penetrated cells. The present report is dedicated to the functional design of porous DDSs based on laser-assisted-manufactured nitinol.

The possibility for monitoring and control of the drug release within a spatial and temporary scale is a key requirement for therapeutic use of 3-D porous matrices for storage and medical feeding. To achieve this, it has been suggested that we create porous matrices out of nitinol with encapsulated drugs and/or nanoparticles. Depending on the type of 3-D matrices (CAD structure, as in [Figure 26.14a](#)) the penetration speed can be controlled. Since the synthesized 3-D nitinol matrices possess the SME, the drug release velocity should be regulated by changing the pore sizes in the nitinol when under the austenite-martensite phase transformation.

During the heating stage, in which body temperature rises (curves (a), (b), and (d) in [Figure 26.29](#)), the load of the stress condition in the NiTi occurs, the pore sizes decrease, and the biological solution is “extruded” from the pores ([Figure 26.30a](#)). During the cooling stage, in which the body temperature reverts to its normal state (i.e., “a patient is recovered,” curves (d), (c), and (a) in [Figure 26.29](#)), the drug solution intake stops ([Figure 26.30b](#)).

Shishkovsky *et al.* [46] have shown that in the presence of porosity, a change of the NiTi stoichiometric composition (even by a few percent) or the addition of alloying elements (Fe, Mo, etc.) can all shift the interval of the back and forward reactions of the austenite-martensite transformations with regard to higher and lower temperatures (compared with cast NiTi). Besides, in the study [46], the method of measuring the dependence of specific resistance upon temperature revealed that changes in SLS and SHS processing influenced the temperature range of SPE in NiTi. Determining all the parameters can therefore lead to the therapeutic effect of delivering the drugs through SPE.

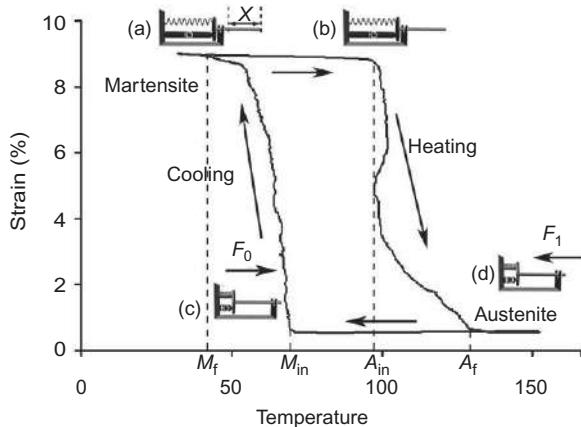


**Figure 26.29** The main steps of the DDS functioning based on the SME. See text for explanation.

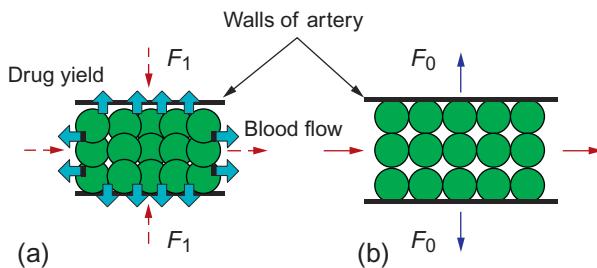


**Figure 26.30** (a, b) The porous 3-D NiTi scaffold behavior during the blood vessels flow.

A general model can be created of the functioning of DDS based on SPE in a porous biocompatible nitinol matrix obtained by SLS, in turn based on individual tomography data. The SME temperature range shift is facilitated by changing the conditions of the SLS and/or the composition and porosity of the sample.

Deformation and stress produced in NiTi creates a useful displacement and produces a force necessary to cause drug release from the pores. The basic stages of the DDS functioning are connected with a complete or incomplete martensite transformation at the body temperature level. We suggest after theoretical modelling and numerical simulations [51] that microdevices of this type can be used repeatedly.

## 26.6 Future remarks

Humans' average lifespan continues to increase. As a result, there is a significant and growing portion of the population, evident from clinical medical practice, that is experiencing serious problems associated with old age, including organ, tissue, bone, and joint degradation. Advances in orthopedics have helped to enhance quality of life

for many individuals; however, there is still further room for improvement. Future progress in orthopedics will rely on the development of novel biocompatible materials and new ways of producing implants and tissue engineering scaffolds with improved functionality of materials. In order to address this problem, we have studied a combination of novel biocompatible materials and advanced laser-assisted manufacturing technology to produce orthopedic implants that will exceed the functionality and benefits of current implant technologies.

Orthopedic implants must be designed to act as substitutes for human tissues. Hence, the implants should combine, along with other parameters, characteristics like biocompatibility, durability, and physical properties that match the underlying tissue, simplicity of manufacturing, and geometrical accuracy. As mentioned above, several studies have shown that the application of a rough (uneven) or porous surface at the bone/implant interface makes adhesion between bone tissue and implant/scaffold substantially higher. This results in a more effective, stronger biomechanical connection between implant and bone.

The topography of the contact surface should also match bone structure. Bone shape and size in the human body differ from person to person. It is therefore difficult to achieve a durable, solid connection when relying only upon biological fixation with noncustomized geometries. Hence, development of a method that allows for alternative types of fixation to the bone surface that can be adapted for individual structural peculiarities would be highly advantageous.

A conventional material used for implantation is pure titanium. It has high biocompatibility and corrosion resistance in comparison with steel and other materials. Alloys based on Ti-6Al-4V are also widely used. Our research suggests that nickel titanium (NiTi, intermetallic phase) is a suitable material due its properties, even in a porous state, of high specific strength, of corrosion resistance, its damping characteristics, and its unique SME that is the result of thermoelastic martensite transformations within the material.

The biocompatibility of nitinol, its physical properties, and the SME peculiar to it, even in a porous state, suggests that there might be substantial gains in orthopedic implants from using this material. These gains center on creating implant elements that change shape after implantation due to the SME being initiated at the temperature of a living organism. These shape changes have primary beneficial effects: (1) enhanced bone fixation, (2) minimally invasive surgeries, and (3) improved drug delivery. Understanding the effect that varying manufacturing process parameters and material powder composition has on nitinol structures and their physical and mechanical characteristics, including thermally induced shape changes, stiffness, and porosity, allows us to design the optimum implants.

With the use of advanced manufacturing methodologies combined with medical imaging, it is now possible to scan the geometry of a specific patient, and thus customize the implant for that patient. This can be achieved by using modern CT or MRI devices combined with digitally driven manufacturing processes. Two such manufacturing processes are the SLS/M and the LENS. Both technologies are capable of forming a structure layer-by-layer directly from digital data that represents the geometry of the intended structure.

Developing near-net shape methods of tissue engineering scaffold and implant manufacturing is crucial to the future of laser-additive technology. In the long term, artificial bio-MEMS devices (implants with SME, DDS) will find a substantial market in the medicine and pharmacological industries. Interdisciplinary cooperation in research and development is important in order to achieve breakthroughs and to find new approaches to designing products such as biodegraded scaffolds and implants.

## Acknowledgments

This chapter was completed while the author was at P.N. Lebedev Physics Institute of the Russian Academy of Sciences. All the studies were conducted in the framework of the research grants (N 13-08-97001p Povoljie-a; N 10-08-00208-a; N 07-08-12048-ofi) of the Russian Foundation of Basis Researches and the Grants of Presidium of Russian Academy of Sciences in the framework program, “Fundamental sciences for medicine”—stages 2005-2006 and 2009-2010. The author is grateful to Prof. Morozov Yu.G. for his assistance with SEM, Prof. Volova L.T. with Ass. Fokeev S. for the preclinical trial, and Ph.D. Volchkov S.E. for the biomedical testing with MMSC on proliferation activity and cell aging.

## References

- [1] V.E. Gunter, Delay Law a New Class of Materials and Implants in Medicine, STT Publishing, Northampton, MA, 2000.
- [2] I.V. Shishkovsky, Laser Synthesis of Functional Mesostructures and 3D Parts, Fizmatlit Publications, Moscow, 2009.
- [3] S. Swann, Integration of MRI and stereolithography to build medical models: a case study, *Rapid Prototyp. J.* 2 (4) (1996) 41–46.
- [4] J.M. Taboas, R.D. Maddox, P.H. Krebsbacha, S.J. Hollister, Indirect solid free form fabrication of local and global porous, bio-mimetic and composite 3D polymer-ceramic scaffolds, *Biomaterials* 24 (2003) 181–194.
- [5] K.F. Leong, K.K.S. Phua, C.K. Chua, et al., Fabrication of porous polymeric matrix drug delivery devices using the selective laser sintering technique, *Proc. Inst. Mech. Eng. Part H* 215 (2001) 191–201.
- [6] E. Berry, J.M. Brown, M. Connell, et al., Preliminary experience with medical applications of rapid prototyping by selective laser sintering, *Med. Eng. Phys.* 19 (1) (1997) 90–96.
- [7] K.H. Tan, C.K. Chua, K.F. Leong, et al., Scaffold development using selective laser sintering of polyetheretherketone—hydroxyapatite biocomposite blends, *Biomaterials* 24 (2003) 3115–3123.
- [8] N.K. Vail, L.D. Swain, W.C. Fox, et al., Materials for biomedical applications, *Mater. Des.* 20 (1999) 123–132.
- [9] C.L. Liew, K.F. Leong, C.K. Chua, Z. Du, Dual material rapid prototyping techniques for the development of biomedical devices. Part 1: space creation, *Int. J. Adv. Manuf. Technol.* 18 (2001) 717–723.
- [10] N.K. Tolochko, V.V. Savich, T. Laoui, et al., Dental root implants produced by the combined selective laser sintering/melting of titanium powders, *Proc. Inst. Mech. Eng. Part L* 216 (2002) 267–270.

- [11] R. Jamieson, B. Holmer, A. Ashby, Development of new orthopaedic products, *Rapid Prototyp. J.* 1 (4) (1995) 34–41.
- [12] L.C. Hieu, E. Bohez, J.V. Sloten, et al., Design for medical rapid prototyping of cranioplasty implants, *Rapid Prototyp. J.* 9 (3) (2003) 175–186.
- [13] S. Gopakumar, RP in medicine: a case study in cranial reconstructive surgery, *Rapid Prototyp. J.* 10 (3) (2004) 207–211.
- [14] Z. Chen, D. Li, B. Lu, et al., Fabrication of artificial bioactive bone using rapid prototyping, *Rapid Prototyp. J.* 10 (5) (2004) 327–333.
- [15] D.M. Gureev, A.L. Petrov, I.V. Shishkovsky, Method of medical implants fabrication from the biocompatible materials, Patent Russian Federation No. 2218242, claim N 99102751/02, 1999, date of priority 11.02.1999.
- [16] V.I. Kalita, Physics and chemistry of bioinert and bioactive implant surface fabrication. Review, *Fiz. Khim. Obrab. Mater.* 5 (2000) 28–45(in Russian).
- [17] A. Gagg, G. Schultes, W.D. Mukller, H. Karrcher, Scanning electron microscopical analysis of laser-treated titanium implant surfaces: a comparative study, *Biomaterials* 21 (2000) 1067–1073.
- [18] S. Hansson, A conical implant-abutment interface at the level of the marginal bone improves the distribution of stresses in the supporting bone, *Clin. Oral Implants Res.* 14 (2003) 286–293.
- [19] O.H. Surov, *Teeth Prosthesis on Implants*, Medicine Publications, Mocsow, 1993.
- [20] I.V. Shishkovskii, I.A. Yadroitsev, I.Y. Smurov, Selective laser sintering/melting of nitinol-hydroxyapatite composite for medical applications, *Powder Metall. Met. Ceram.* 50 (5-6) (2011) 275–283.
- [21] G. Binyamin, B.M. Shafi, C.M. Mery, Biomaterials: a primer for surgeons, *Semin. Pediatr. Surg.* 15 (4) (2006) 276–283.
- [22] A.S. Fauci, et al., *Harrison's Principles of Internal Medicine*. seventeenth ed., McGraw-Hill Medical, 2008 <http://dx.doi.org/10.1036/0071466339> American textbook of internal medicine.
- [23] P.E. Murray, C. Garcia Godoy, F. Garcia Godoy, How is the biocompatibility of dental biomaterials evaluated? *Med. Oral Patol. Oral Cir. Bucal* 12 (3) (2007) E258–E266.
- [24] S.E. Volchkov, O.V. Tumina, et al., Comparative characteristics of multipotent mesenchymal stem cells from different sources, *Cell Transplant. Tissue Eng.* 3 (2009) 8–9.
- [25] A. Salamon, E. Toldy, Use of mesenchymal stem cells from adult bone marrow for injured tissue repair, *Orv. Hetil.* 150 (27) (2009) 1259–1265.
- [26] V.S. Nirmalanandhan, G.S. Sittampalam, Stem cells in drug discovery, tissue engineering, and regenerative medicine: emerging opportunities and challenges, *J. Biomol. Screen.* 14 (7) (2009) 755–768.
- [27] J.M. Kanczler, S. Mirmalek-Sani, N.A. Hanley, et al., Biocompatibility and osteogenic potential of human fetal femur-derived cells on surface selective laser sintered scaffolds, *Acta Biomater.* 5 (2009) 2063–2071.
- [28] N. Ogura, M. Kawada, W. Chang, et al., Differentiation of the human mesenchymal stem cells derived from bone marrow and enhancement of cell attachment by fibronectin, *J. Oral Sci.* 46 (4) (2004) 207–213.
- [29] I.V. Shishkovskii, Y.G. Morozov, S.V. Fokeev, et al., Laser synthesis and comparative testing of a three-dimensional porous matrix of titanium and titanium nickelide as a repository for stem cells, *Powder Metall. Met. Ceram.* 50 (9/10) (2012) 606–618.
- [30] O. Zinger, K. Anselme, A. Denzer, et al., Time-dependent morphology and adhesion of osteoblastic cells on titanium model surfaces featuring scale-resolved topography, *Biomaterials* 25 (14) (2004) 2695–2711.

- [31] E. Behravesh, et al., Synthetic biodegradable polymers for orthopedic applications, *Clin. Orthop.* 367S (1999) 118–185.
- [32] K.J.L. Burg, et al., Biomaterials development for bone tissue engineering, *Biomaterials* 21 (2000) 2347–2359.
- [33] M.T. Duailibi, et al., Bioengineered teeth from cultured rat tooth bud cells, *J. Dent. Res.* 83 (7) (2004) 523–528.
- [34] A. Smith, Tooth tissue engineering and regeneration, *J. Dent. Res.* 83 (7) (2004) 517.
- [35] C.S. Young, et al., Tissue engineering of complex tooth structures on biodegradable polymer scaffolds, *J. Dent. Res.* 81 (10) (2004) 695–700.
- [36] C.Y. Fong, L.L. Chak, A. Biswas, et al., *Stem Cell Rev.* 7 (2011) 1.
- [37] S.E. Volchkov, I.V. Shishkovsky, I.V. Barikov, Influence of porous three-dimensional implants from nitinol on culture of multipotent mesenchymal stromal cells, *Cell Transplant. Tissue Eng.* 8 (1) (2013) 51–56.
- [38] I.V. Shishkovsky, M.V. Kuznetsov, Y.G. Morozov, Porous titanium and nitinol implants synthesized by SHS/SLS: microstructural and histomorphological analyses of tissue reactions, *Int. J. Self Propag. High Temp. Synth.* 19 (2) (2010) 157–167.
- [39] A.B. Kaplun, et al., ANSYS for Engineers: Handbook, Editorial URSS, Moscow, 2003.
- [40] I.V. Shishkovsky, Stress-strain analysis of porous scaffolds made from titanium alloys synthesized via SLS method, *Appl. Surf. Sci.* 255 (24) (2009) 9902–9905.
- [41] J.Z. Hilt, N.A. Peppas, Microfabricated drug delivery devices, *Int. J. Pharm.* 306 (2005) 15–23.
- [42] F.N. Pirmoradi, J.K. Jackson, H.M. Burt, M.A. Chiao, Magnetically controlled MEMS device for drug delivery: Design, fabrication, and testing, *Lab Chip Miniaturisat. Chem. Biol.* 11 (18) (2011) 3072–3080.
- [43] I.V. Shishkovsky, Functional design of porous drug delivery systems based on laser assisted manufactured nitinol, *MRS Proc.* 1415 (2012) mrsf11-1415-ii03-10.
- [44] J.L. Moore, A. McCuiston, I. Mittendorf, R. Ottway, R.D. Johnson, Behavior of capillary valves in centrifugal microfluidic devices prepared by three-dimensional printing, *Microfluid. Nanofluid.* 10 (4) (2010) 877–888.
- [45] E. Gultepe, D. Nagesha, S. Sridhar, M. Amiji, Nanoporous inorganic membranes or coatings for sustained drug delivery in implantable devices, *Adv. Drug Deliv. Rev.* 62 (2010) 305–315.
- [46] I. Shishkovsky, V. Sherbakoff, I. Yadroitsev, I. Smurov, Particularities of electrical resistivity and phase structure in the 3D porous nitinol after SLS/SLM, *Proc. Inst. Mech. Eng. Part C* 226 (12) (2012) 2982–2989.
- [47] S.-R. Guo, Z.-M. Wang, Y.-Q. Zhang, et al., *In vivo* evaluation of 5-fluorouracil-containing self-expandable nitinol stent in rabbits: efficiency in long-term local drug delivery, *J. Pharm. Sci.* 99 (7) (2010) 3009–3018.
- [48] M.D. Dake, W.G. Van Alstine, Q. Zhou, A.O. Ragheb, Polymer-free paclitaxel-coated silver PTX stents—evaluation of pharmacokinetics and comparative safety in porcine arteries, *J. Vasc. Interv. Radiol.* 22 (2011) 603–610.
- [49] S. Sato, Y. Nakayama, Y. Miura, et al., Development of self-expandable covered stents, *J. Biomed. Mater. Res. Part B Appl. Biomater.* 83 (2) (2007) 345–353.
- [50] C.M. Cheah, K.F. Leong, C.K. Chua, K.H. Low, H.S. Quek, Characterization of microfeatures in selective laser sintered drug delivery devices, *Proc. Inst. Mech. Eng. Part H: J. Eng. Med.* 216 (2002) 369–383.
- [51] I.V. Shishkovsky, Simulation of thermomechanical and electrothermal hysteresis phenomena in porous nickel titanium, *Tech. Phys.* 59 (2) (2014) 297–303.

This page intentionally left blank

# Laser melting of NiTi and its effects on *in vitro* mesenchymal stem cell responses

27

D.G. Waugh<sup>1</sup>, J. Lawrence<sup>1</sup>, C.W. Chan<sup>2</sup>, I. Hussain<sup>3</sup>, H.C. Man<sup>2</sup>

<sup>1</sup>University of Chester, Chester, UK; <sup>2</sup>The Hong Kong Polytechnic University, Hong Kong, China; <sup>3</sup>University of Lincoln, Lincoln, UK

## 27.1 Introduction

The control of cell adhesion to materials is a key factor in tissue engineering and bioengineering, resting on the ability to direct specific cell types to proliferate, migrate, and express physiological behaviors to support cellular architecture. A considerable amount of research effort has been devoted to the surface modification of materials to enhance different cell line responses [1–11]. The growth of stem cells *in vitro* can benefit from laser surface treatment insofar as cell signalling is likely to be modulated on account of the laser surface modifications. This is owed to variations in stem cell signalling, especially with regards to mesenchymal stem cells (MSCs), leading to the formation of different cell types including osteoblast, chondrocyte, and adipocyte cells. In this chapter, the bioactivity of NiTi after laser melting is investigated implementing *in vitro* techniques for studying MSC responses at different sets of time varying from early (4–12 h) to intermediate phases (1 and 4 days) of cell culture. The effects of physical (surface roughness and topography) and chemical (surface Ti/Ni ratio) modifications as a consequence of laser melting in different regions on the cell morphology and cell coverage are studied. These regions are the melt zone (MZ), the heat-affected zone (HAZ), and base material (BM).

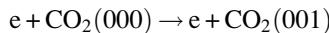
### 27.1.1 Lasers for melting

Over the last 10 years lasers have become more commonly implemented in the field of melting [12–21] with some of the main applications being modification of microstructure and hardness [12,15,19], damage repair [16], manufacturing [17,18], and biomedical [14]. Many of the lasers used for the technique of melting fall within the near-infrared and infrared spectrum. That is, lasers that usually operate at wavelengths between approximately 700 nm and 11 µm. This is owed to the fact that those lasers operating within this wavelength range can be seen, generally, to be discrete, highly localized heat sources. On account of this, this section will detail three of the main laser types that operate within this spectral region: CO<sub>2</sub> lasers, Nd:YAG lasers, and fiber lasers.

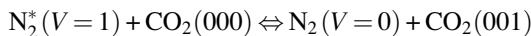
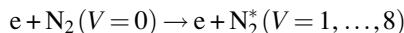
### 27.1.1.1 $\text{CO}_2$ lasers

The  $\text{CO}_2$  laser is one of the most used lasers throughout the scientific world and within many industries due to this laser being one of the most versatile. It is capable of emitting radiation within the IR region of the electromagnetic spectrum on rotational-vibrational transitions with wavelengths ranging from 9 to 11  $\mu\text{m}$  [22]. This laser gives rise to the possibility of operating in either continuous wave (CW) or pulsed using different types of gas discharge configurations. The gases generally used to achieve these configurations are  $\text{CO}_2$ ,  $\text{N}_2$ , and He with ratios of  $\text{CO}_2:\text{N}_2$  usually being around 0.8:1 with commonly more helium than nitrogen and gas pressures ranging from 50 to 760 torr [22]. Each gas within this type of laser plays a distinct role to the production of population inversion. The  $\text{CO}_2$  is the gas that allows the laser light to be emitted and is first excited such that the molecules vibrate in an asymmetrical stretching mode. After a time, the  $\text{CO}_2$  molecules begin to lose their excitation energy by dropping to one of two lower vibrational energy states, which are two of the principal laser transitions for this system [23]. The nitrogen is utilized within the system to allow more efficient excitation of the  $\text{CO}_2$  molecules up to the upper laser level. This is done efficiently due to the fact that the lowest vibrational energy state of the nitrogen molecules is equivalent to that of the upper laser level for the  $\text{CO}_2$  molecules, giving rise to a high probability of energy transfer between the two different molecules. It should be noted here that the  $\text{CO}_2$  molecules can be excited in other ways, such as directly absorbing the energy from electrons; however, with the presence of the nitrogen the system becomes considerably more efficient. The helium on the other hand has two distinct roles to the functioning of the  $\text{CO}_2$  laser, with the first being that it acts as a buffer gas to aid in heat transfer within the system and, secondly, to efficiently attempt and relax the  $\text{CO}_2$  molecules back down to the ground state in the attempt to achieve efficient population inversion. To fully understand the way in which a  $\text{CO}_2$  laser functions it is possible to take an energy level diagram into consideration showing the energy transfers as seen in [Figure 27.1](#).

Elaborating in [Figure 27.1](#), it can be seen that the upper laser level excitation can be achieved via direct electron collisional excitation in the form



However, this process is not particularly selective, giving rise to many other vibrational modes of  $\text{CO}_2$  becoming populated. As it has been discussed and can be visualized in [Figure 27.1](#), the lasing process can be made more efficient by vibrational energy transfer from the nitrogen present in the form of



The second step in the vibrational energy transfer from the nitrogen is more commonly known as the  $V-V$  resonant transfer, and is very selective due to the close coincidence of the nitrogen ( $V=1$ ) and  $\text{CO}_2$  (001) levels allowing very efficient population of the

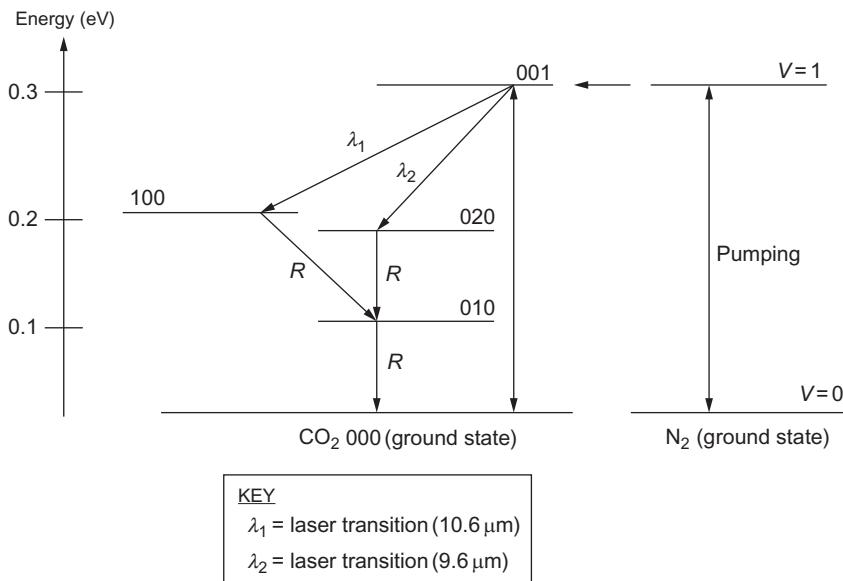
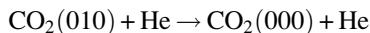
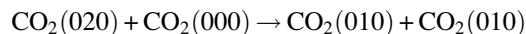


**Figure 27.1** An energy-level diagram showing the main energy transfers and laser transitions for the CO<sub>2</sub> laser.

upper laser level. To allow for efficient lasing, the lower level relaxation must be taken into account and, in this case, the (100) level shares energy rapidly with the (020) level due to the fact that they are mixed-states as a result of a Fermi resonance. From this, it can then be seen that the relaxation proceeds via



It should be noted here that the deactivation of the (010) state to the (000) ground state is vital for recycling molecules for reexcitation in the attempt to prevent degrading population inversion.

For cw CO<sub>2</sub> lasers, powers of 100 kW and pulse energies of up to 10 kJ can easily be achieved [22,23]. In addition to this, there are a number of different laser structures that have been developed for this laser type: sealed-off tube, longitudinal flow, waveguide, and transversely excited [22]. Due to the versatility and high powers that this laser can achieve, it has been implemented for many years in the general field of materials processing from cutting to alloying.

### 27.1.1.2 Nd:YAG lasers

The Nd:YAG laser is one of the most common lasers within the solid-state family with a fundamental operating wavelength of 1.064 μm. This type of laser incorporates a four-level system, resulting in a low pumping threshold. All solid-state lasers that

incorporate neodymium crystals rely on light from an external source to excite the Nd atoms to the upper-laser levels. Through development of this technology, this can be done in three main structures: flashlamp-pumped Q-switched, flashlamp-Pumped cw, and diode-pumped [22–24]. As a result of the compactness and relatively lower cost compared to other laser types, Nd:YAG lasers have many applications with one of the major ones being various areas of materials processing, such as drilling, spot welding, and laser marking. Also, due to the fact that the beam can be focused to very small spot, applications that require a high degree of accuracy can take advantage of this laser.

### 27.1.1.3 Fiber lasers

High-power fiber lasers are a relatively new technology but researchers realize that they can be utilized for many applications within the materials processing industry. For instance, a comprehensive literature review has been produced by Canning [25] on fiber lasers and related technologies. From this review, Canning found that high-power lasers are attractive for use within numerous industries. He also indicated that extensive research had been undertaken to understand the way in which these lasers operate; this can be seen throughout the published literature [26–30]. This research has covered many areas of fiber laser technology ranging from large mode area fibers [26,29], to internal thermal effects [27], to the investigation of utilizing different materials for the construction of high-power fiber lasers [30]. In addition to this, others have already researched the possibility of using high-power fiber lasers for welding and cutting various materials; for example, Quintino *et al.* [31] have recently carried out preliminary studies to determine the quality of welding pipeline steel with an 8 kW fiber laser.

### 27.1.2 Mesenchymal stem cells

MSCs are known to play important roles in development, postnatal growth, repair, and regeneration of mesenchymal tissues [32]. This is owed to the relative ease of isolation, high proliferative potential, and multipotentiality to differentiate into specialized cell types (such as osteoblasts, chondrocytes, and tenocytes). On account of this, MSCs have become an extremely promising cell type for tissue engineering and regenerative medicine. In tissue engineering applications, MSCs are grown on biomaterial scaffolds that provide structural support and a substrate for cellular adhesion [33]. Currently, most MSCs research has been conducted on Ti-based alloys such as CP Ti and Ti6Al4V, and only limited attention has been given to the shape memory NiTi, despite its importance as a biomaterial. Habijan *et al.* [34] studied the effect of dynamic loading on the viability of adherent human MSCs on NiTi, and they found that the nickel ion release due to dynamic loading did not necessarily affect the biocompatibility of NiTi. Meisner *et al.* [35] indicated that the MSCs proliferation improved for the ion-implanted NiTi specimens with Si Ti, or Zr. On the other hand, the biocompatibility of NiTi comes from the surface passive layer, which is composed of  $\text{TiO}_2$ .  $\text{TiO}_2$  is a known biocompatible material and the chemistry of  $\text{TiO}_2$  is favorable for cell adhesion. The deposition of  $\text{TiO}_2$  can increase the proliferation and

attachment of mouse MSCs [36]. Because the amount of TiO<sub>2</sub> in the passive film is controlled by the substrate Ti concentration, alternation of Ti concentration between the MZ, HAZ, and BM in the NiTi melt would inevitably affect the TiO<sub>2</sub> content in the passive film and may influence the biocompatibility.

### 27.1.3 *NiTi and biomaterials*

Owing to the unique shape memory and superelastic effects, and apparent biocompatibility, NiTi has become an important biomaterial for orthopaedic applications in the last decade [37]. Also, due to the increasing demand for miniaturization of medical implants, laser micromelting has been treated as the most promising joining technique in the clinical and medical device industry by virtue of its capability to deliver the advantages of high precision with small and localized heat input [13,38–45]. Orthopaedic implants such as mono-bloc hip stems are often made of two elements welded together [46]. Furthermore, implantable prosthetic devices in medicine require hermetic encapsulation to isolate internal components from the chemically aggressive *in vivo* environment [47]. In laser micromelting, three distinct regions have been found in the melt: MZ, HAZ, and BM, which result from variation of thermal excursions in different regions of the material [48]. A well-defined and directional dendritic pattern as a result of rapid cooling effect from laser melting is always observed from the surface of MZ, whereas grain growth due to recrystallization of material is found in the HAZ [44].

The interaction between cells and biomaterial is considered to be an essential indication for biocompatibility, and such interaction is often affected by a list of surface properties, such as surface roughness, topography, chemistry, and hydrophilicity. Curtis and Wilkinson [49] stated that cells are able to discriminate among subtle differences in surface roughness and topography, resulting in different protein adsorption and cellular responses of morphology, differentiation, proliferation, and orientation. The degree of responses varies from one type of cell to another. Generally, osteoblasts prefer rough surfaces while fibroblasts prefer smooth surfaces [50,51]. Previous studies with the MSCs performed on the materials indicate that MSCs are sensitive to the surface roughness and topography. Kommireddy *et al.* [36] reported cell attachment of MSCs is affected by the surface roughness and increased cell attachment is found on the rougher surface than on the smoother surfaces. Myllymaa *et al.* [33] found that MSCs are sensitive to the topographical variations and it is likely to interact with the physical environment by aligning its orientation along the physical shape and edges.

## 27.2 Experimental details

### 27.2.1 *Laser melting procedure*

Flat annealed Ti-55.91 wt.% Ni foil in the form of 50 × 50 × 0.25 mm<sup>3</sup> (Johnson Matthey, Inc.) was ground using SiC papers of 600 grit to remove oxide scales on the sample surface. The samples were ultrasonically degreased in pure alcohol for

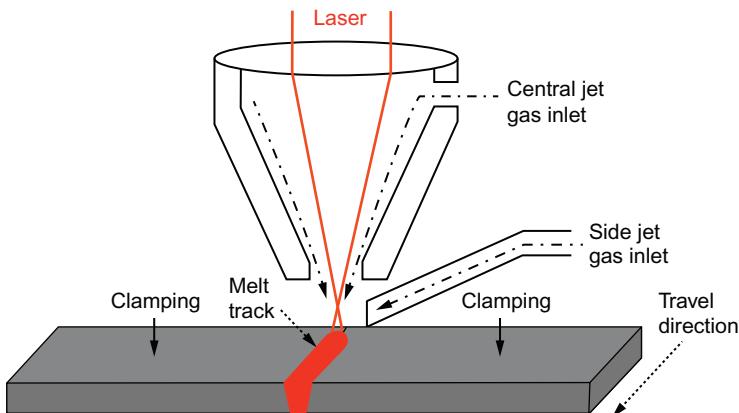


**Figure 27.2** Schematic diagram for the laser melting of the NiTi samples.

10 min, followed by 5 min of cleaning in distilled water, and dried thoroughly in air before laser melting. A 100-W CW fiber laser (SP-100C-0013; SPI and A&P Co., Ltd.) with a wavelength of 1091 nm was then implemented for autogenous melting. A schematic diagram of the laser setup can be seen in Figure 27.2. An  $x$ - $y$ - $z$  multistage manipulator (or welding jig) was used to adjust the samples in an appropriate position for the laser melting, and to apply a clamping force to the samples for minimizing thermal distortion. Argon was used as the shielding gas to suppress the formation of plasma in the vapor over the MZ by blowing them away and to prevent the samples from oxidizing during laser melting. The Ar gas was delivered to the MZ via the laser nozzle (central jet) of 10 mm in diameter and a copper pipe (side jet) of 6 mm in diameter. The side jet was tilted at  $30^\circ$  to the horizontal plane. The gas flow rate was controlled by a flow meter. The melting parameters chosen in this study were optimized by a fractional factorial experimental design to guarantee a full-penetration melt [9]. The optimized parameters of laser power, speed, focus position, gas flow rate, and shielding environment were: 70 W, 300 mm/min, +1.6 mm (away from the top surface of samples), 35 l/min, and under Ar shielding.

### 27.2.2 Sample preparation

The sample used for cell culture was the single-track laser melt that included the MZ, HAZ, and BM, which altogether had an area of  $5 \times 10 \text{ mm}^2$ . It should be noted that each of the regions (approximately) contributed one-third of the total surface area. In order to characterize the effect of surface topography on the cell behaviors, some MZ samples were mechanically ground by 180-grit sandpaper using a zig-zag motion to remove the surface dendritic pattern, and kept the surface roughness similar to the MZ. The effect of roughness on the cell behaviors was studied by comparing the MZ samples after grinding and polishing with sandpapers up to 2400-grit.

### **27.2.3 Surface roughness and surface topography analysis**

The surface profiles were determined using a white light interferometer (WLI) (NewView 500; Zygo, Ltd.). The WLI was setup using a  $50 \times$  Mirau lens ( $NA = 0.55$ ) with working distance of 3.4 mm. The Ra and maximum peak-to-valley height roughness parameters for each sample were determined using the *MetroPro* software, where Ra can be defined as the arithmetic average of the absolute values along a single specified direction. The mean and experimental standard deviation of the roughness parameters were obtained from five measurements.

### **27.2.4 Surface compositional analysis**

The compositions at the surface without sputter cleaning were analyzed using X-ray photoelectron spectroscopy (XPS) (PHI5600, Physical Electronics, Inc.) with a take-off angle of  $45^\circ$  normal to the sample surface. The X-ray source was monochromatic Al K alpha (15 kV, 25 W) and the beam size was 100  $\mu\text{m}$  in diameter. The pass energy for survey scan and narrow scan spectra were 187.5 and 58.7 eV, respectively.

### **27.2.5 Phase structure and transformation temperature analysis**

The phase structure of the MZ and BM samples was characterized by the selected area diffraction pattern (SADP) using TEM (JEOL 2010). The TEM study was done by operating the electron microscope at 200 keV. The TEM samples were prepared by mechanical grinding, polishing, and dimpling, followed by twin-jet Ar-ion milling at 5 keV. A differential scanning calorimeter (DSC, Perkin Elmer DSC 7) was used to determine the phase transformation temperatures of the MZ and BM samples. The MZ and BM samples were cut from the melt, and then heated and cooled in the range of  $-70$  to  $100^\circ\text{C}$  at  $10^\circ\text{C}/\text{min}$ . The phase transformation temperatures are denoted as  $A_s$  (austenite start),  $A_m$  (austenite peak),  $A_f$  (austenite finish),  $M_s$  (martensite start),  $M_m$  (martensite peak), and  $M_f$  (martensite finish).

### **27.2.6 In vitro biological stem cell experimentation**

A research laboratory safety protocol was followed. To avoid contamination of the cells, the culture work was conducted within a Class II Microbiological Safety Cabinet, and sterile conditions were maintained. All used items were correctly discarded in accordance with the laboratory safety protocol. The MSCs (Stem Cell Bank, Japan) were grown in a tissue culture medium consisting of DMEM (with L-glutamine) (Sigma Aldrich, Ltd.), supplemented with 10% fetal calf serum (Sigma Aldrich, Ltd.), and 100 units/ml of penicillin and 0.1 mg/ml of streptomycin (Sigma Aldrich, Ltd.), and placed in an incubator set at  $37^\circ\text{C}$ , 5% humidified  $\text{CO}_2$  (Wolf Laboratories, Ltd.), throughout the study. When the cells reached subconfluent (70-80%), they were retrieved with 0.25% trypsin and 0.02% EDTA. The retrieved cells were washed twice with phosphate-buffered saline (PBS), centrifuged at 1200 rpm for 12 min at room temperature, reseeded into four 24-well plates

cell culture at the initial seeding density of  $5 \times 10^4$  cells per well, and maintained under the same culture conditions mentioned before [52]. The four well plates were then placed in the incubator for different sets of time: 4 h, 12 h, 24 h (1 day), and 96 h (4 days).

### 27.2.7 Scanning electron microscopy and cell coverage measurement

After 4 h to 4 days cell culture, morphology of the attached cells were analyzed by SEM in the secondary imaging mode and the following procedures were undertaken to produce a sample that was dehydrated, ready for Au coating. After removal of the culture media, the samples were initially rinsed with PBS (Sigma-Aldrich, Ltd.) to remove any unattached cells and then adherent cells were fixed using 1.2% glutaraldehyde in water (Sigma-Aldrich, Ltd.) at room temperature for 1 h within the BSC. After an hour, the glutaraldehyde solution was removed and the fixed cells were washed with PBS prior to carrying out a graded series of ethanol/distilled water mixtures of 50%, 80%, 90%, 95%, 98%, and 100%. Each sample was left in these mixtures for 10 min and dried in air. The samples were sputter coated with Au for cell morphology observation by SEM. The cell coverage (or cover density per  $\text{cm}^2$ ) was determined following the 4 h to 4 days incubation. This was done by analyzing the cell coverage on each sample using SEM and optical micrographs with the *ImagePro* software. The optical micrographs were obtained using an up-right optical microscope (Flash 200 Smartscope; OGP, Ltd.) with magnifications varying between  $100 \times$  and  $500 \times$ .

### 27.2.8 Statistical analysis

The significance of the observed difference between different samples was tested by Student *t*-test using the *SPSS* software, version 12 (SPSS, Inc.). The probability below  $p < 0.05$  was considered as statistically significant.

## 27.3 Results and discussion

### 27.3.1 Surface morphology following laser melting

Figure 27.3a-c shows the surface morphology of the laser melt in different regions (MZ, HAZ, and BM), while Figure 27.3d gives the morphology of the MZ after polishing. As observed from Figure 27.3a, a typical tree-like or dendritic pattern as a result of rapid solidification of grains along the energetically favorable crystallographic direction in laser melting can be seen in the MZ. The morphology of the HAZ and BM was similar in Figure 27.3b and c and exhibited some surface defects, such as pores and grooves, which came from the manufacturing processes. For the MZ (ground), obvious grooves as a result of mechanical grinding by sandpaper were clearly found on the sample surface. No visible grooves were observed from the MZ (polished) as given in Figure 27.3d. The effect of topography could be considered as negligible.

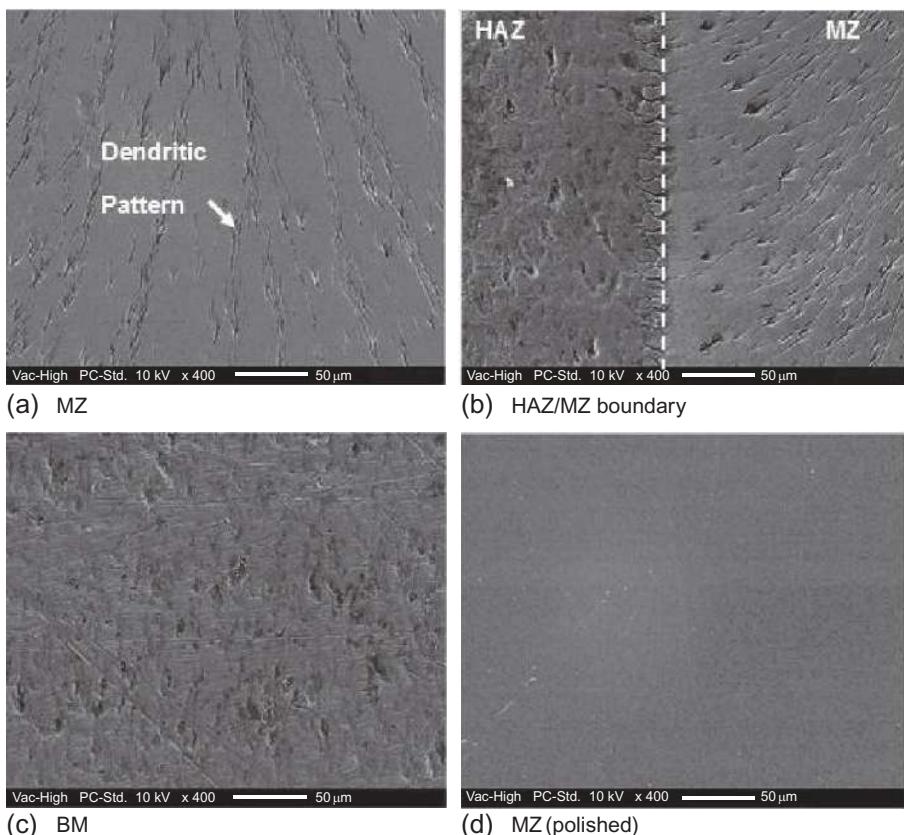


**Figure 27.3** SEM morphology of different samples: (a) MZ; (b) HAZ/MZ boundary; (c) BM; and (d) MZ (polished).

### 27.3.2 Phase structure and transformation temperature analysis

The phase structure of the MZ and BM samples has been determined by XRD, and reported in the authors' previous paper [53]. The XRD results indicated that the MZ was of the parent austenite structure at room temperature, similar to the BM, and did not contain any Ni-rich or Ti-rich precipitates. The phase structure and non-existence of the precipitates in the MZ and BM samples was further confirmed by the SADP using TEM. As shown in the SADP (in the inset of Figure 27.4a), the grains in the BM were preferentially oriented along the [111] B2 direction. The SADP (in the inset of Figure 27.4b) for the grains in the MZ showed a single crystalline pattern and the presence of B2 phase in the [111] zone. The TEM results showed that the MZ and BM were composed of austenite at room temperature, and no precipitate could be found in the grains of the MZ and BM.

The transformation temperatures of the MZ and BM samples are given in Table 27.1. The results showed that both the austenitic and martensitic transformation

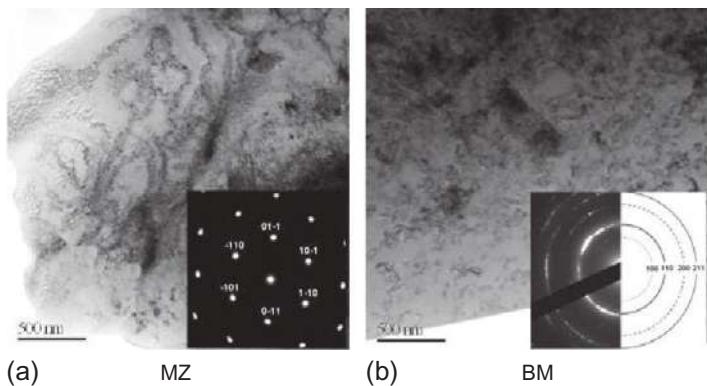


**Figure 27.4** TEM micrographs and the corresponding SADP (shown in the inset) of the MZ and BM samples: (a) MZ and (b) BM.

**Table 27.1 Transformation temperatures of MZ and BM from DSC measurements**

Sample	Transformation temperature (°C)					
	Heating curve			Cooling curve		
	$A_s$	$A_m$	$A_f$	$M_s$	$M_m$	$M_f$
MZ	-20.6	-14.2	-5.8	-40.5	-45.6	-52.3
BM	-3.6	2.3	8.8	2.2	-4.0	-7.0

The transformation temperatures are denoted as  $A_s$  (austenite start),  $A_m$  (austenite peak),  $A_f$  (austenite finish),  $M_s$  (martensite start),  $M_m$  (martensite peak), and  $M_f$  (martensite finish).

temperatures of the MZ were considerably depressed as compared to the BM. Such a decrease could be attributed to the presence of thermal-induced defects and the removal of cold working effect after laser melting [44]. The DSC measurements confirmed that the MZ and BM samples were in the austenite state at or above room temperature. Because the cell culture was done in the incubator at 37 °C, it is believed that the effect of phase switching on the cell responses could be neglected.

### 27.3.3 Surface roughness analysis

White light interferometry (WLI) was employed to obtain the roughness parameters of the samples in a quantitative way, and allowed for the generation of continuous axonometric images and surface profile extractions. Figure 27.5a-e shows the continuous axonometric images for different samples. The Ra and maximum peak-to-valley height of the samples are given in Table 27.2. The results in Table 27.2 indicate that the Ra and maximum peak-to-valley height of the MZ was  $0.375 \pm 0.038 \mu\text{m}$  and  $2.49 \pm 0.314 \mu\text{m}$ , respectively. Compared with the MZ in Figure 27.5a, a relatively

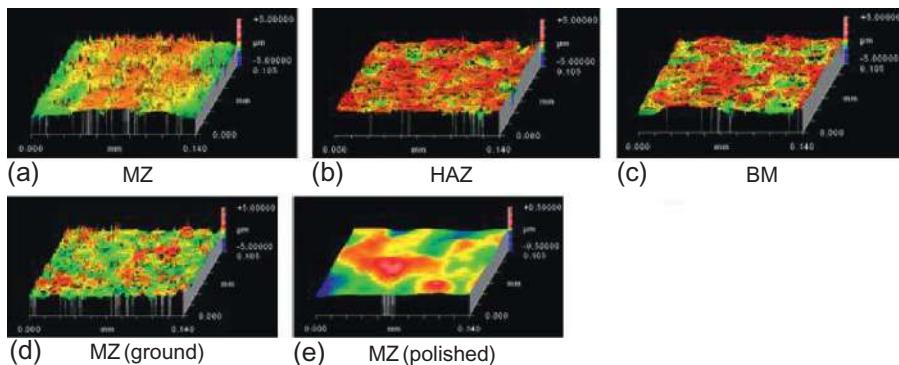


**Figure 27.5** Continuous axonometric 3-D profile images for different samples: (a) MZ; (b) HAZ; (c) BM; (d) MZ (ground); and (e) MZ (polished).

**Table 27.2 Ra and maximum peak-to-valley height of different samples (mean and experimental standard deviation based on five measurements)**

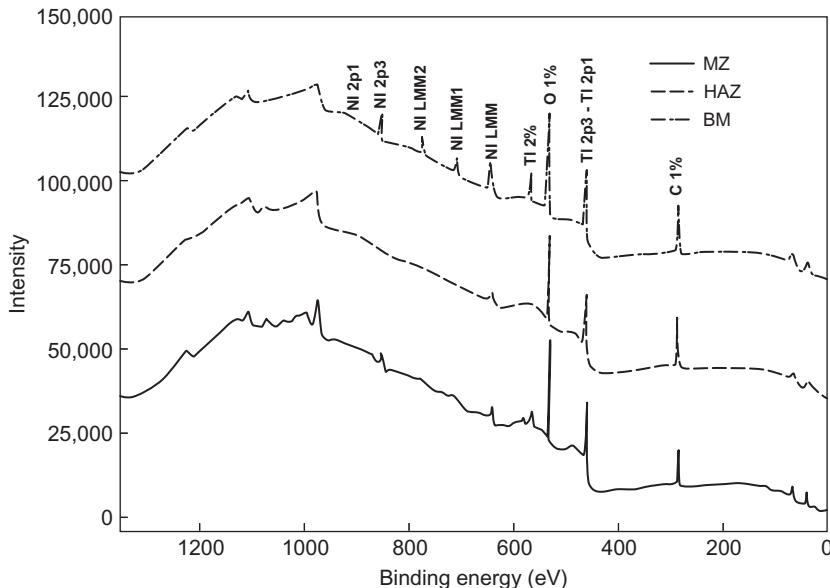
Sample	Ra ( $\mu\text{m}$ )	Maximum peak-to-valley height ( $\mu\text{m}$ )
MZ	$0.375 \pm 0.038$	$2.49 \pm 0.314$
HAZ	$0.289 \pm 0.017$	$1.46 \pm 0.195$
BM	$0.301 \pm 0.022$	$1.53 \pm 0.174$
MZ (ground)	$0.362 \pm 0.031$	$1.67 \pm 0.243$
MZ (polished)	$0.017 \pm 0.006$	$0.14 \pm 0.039$

smoother surface can be observed from the HAZ and BM (in Figure 27.5b and c, respectively) as evidenced by the smaller Ra and maximum peak-to-valley height. The dendritic pattern caused by the rapid cooling effect of laser melting induced a roughening effect in the MZ compared to the HAZ and BM, while the grain growth effect in the HAZ did not cause any observable changes in the surface roughness, as evidenced by the similar Ra and maximum peak-to-valley height to the BM. In contrast to the MZ, the MZ (ground) showed completely different topography (in Figure 27.5d) with smaller maximum peak-to-valley height of  $1.67 \pm 0.243 \mu\text{m}$ , though their Ra was similar. The MZ (polished) showed a smoother surface (in Figure 27.5e) as compared to that of the MZ. The Ra of the MZ (polished) was  $0.017 \pm 0.006 \mu\text{m}$  and the maximum peak-to-valley height was  $0.14 \pm 0.039 \mu\text{m}$ .

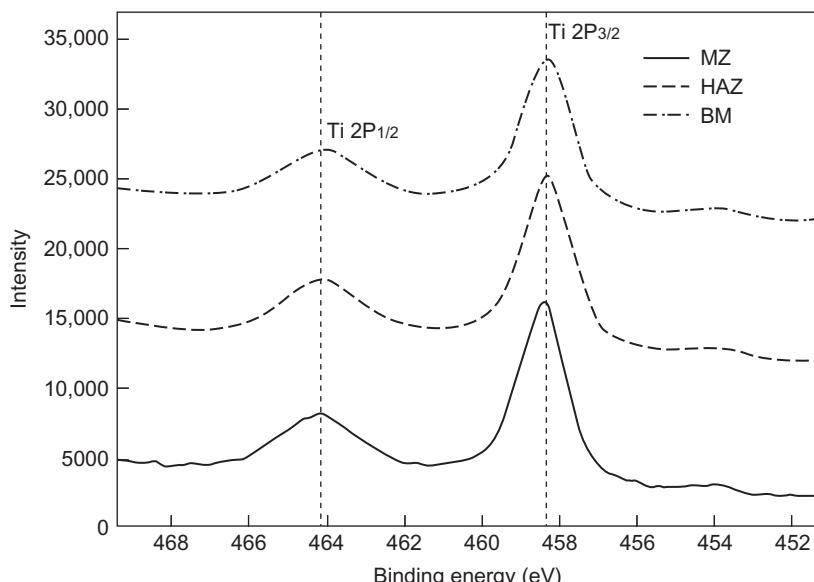
### 27.3.4 Surface chemistry analysis

Figure 27.6 shows the XPS survey scans at the surface (without sputter cleaning) for the melt in different regions: MZ, HAZ, and BM. As shown in the figure, the surface element of the samples was composed of carbon, oxygen, nitrogen, titanium, and

nickel. The nature of passive film on the samples is characterized by plotting the narrow scan of Ti 2P region in Figure 27.7. The two peaks in Figure 27.7 at 458.4 and 464.2 eV were identified as Ti 2P<sub>3/2</sub> and Ti 2P<sub>1/2</sub>, respectively, and were corresponding to the presence of Ti<sup>4+</sup>, which is responsible for the TiO<sub>2</sub> formation. The results



**Figure 27.6** XPS survey scans at the surface for MZ, HAZ, and BM.



**Figure 27.7** XPS narrow scans of Ti 2P region for MZ, HAZ, and BM.

**Table 27.3 XPS surface atomic composition and the corresponding Ti/Ni ratio of the melt in different regions: MZ, HAZ, and BM**

Sample	Ni (at.%)	Ti (at.%)	O (at.%)	C (at.%)	N (at.%)	Ti/Ni ratio
MZ	1.5	15.6	48.1	33.0	1.8	10.4
HAZ	2.2	14.9	44.7	35.1	3.1	6.8
BM	2.6	14.3	43.6	36.9	2.6	5.5

from the survey scan and the narrow scan for the Ti 2P region suggested that the major component of the outermost surface layer of the samples was  $\text{TiO}_2$ , with some other Ti suboxides and intermediate NiTi. The surface atomic compositions and the corresponding Ti/Ni ratio of those samples are given in [Table 27.3](#). The presence of C and N can be attributed to the surface contamination from the environment. As observed from [Table 27.3](#), the surface Ti/Ni ratio of the MZ is 10.4 and is higher than that found in the HAZ and BM; namely 6.8 and 5.5, respectively.

It is widely accepted that higher surface Ti/Ni ratio can suppress the rate of Ni release and be beneficial to form a more protective surface passive film because of more titanium available to react with oxygen and combine into the  $\text{TiO}_2$  [12]. The increase of atomic Ti/Ni ratio in the MZ is a consequence of local vaporization of Ni during laser melting of NiTi alloy [54,55]. Such vaporization of Ni would enrich the MZ with higher concentration of Ti, which helps to increase the surface Ti/Ni ratio and also the  $\text{TiO}_2$  content in the passive film [56].

### 27.3.5 Stem cell morphology

#### 27.3.5.1 Early phase (4-12 h) of stem cell culture

Biocompatibility of biomaterials is closely related to cell adhesion and spreading on the material surface. Initial adhesion and spreading of the cells usually determines the long-term viability of cells on substrates designed for various biomedical applications. Stiehler *et al.* [57] stated that the attachment, adhesion, and spreading in the early phase (minutes to hours) of cell-substrate interactions influence the capacity of a cell to proliferate and to differentiate itself on contact with the implant. In order to capture the effect of laser melting on the intimate contact between the MSCs and NiTi, SEM was carried out on the samples after 4 and 12 h. The morphology of MSCs after 4 and 12 h are given in [Figures 27.8](#) and [27.9](#), respectively. It could be observed from the SEM micrographs in the figures that the MSCs successfully adhered to all of the samples by stretching out pseudopodia after 4 h of cell culture. More importantly, it was found that the cells preferably adhered onto the surface discontinuities existing in the sample surface, such as dendritic pattern in MZ ([Figure 27.8a](#)), pores in HAZ and BM ([Figure 27.8b and c](#)), and grooves in MZ (ground) ([Figure 27.8d](#)). An interesting phenomenon about the cell adhesion can be noted from the morphology

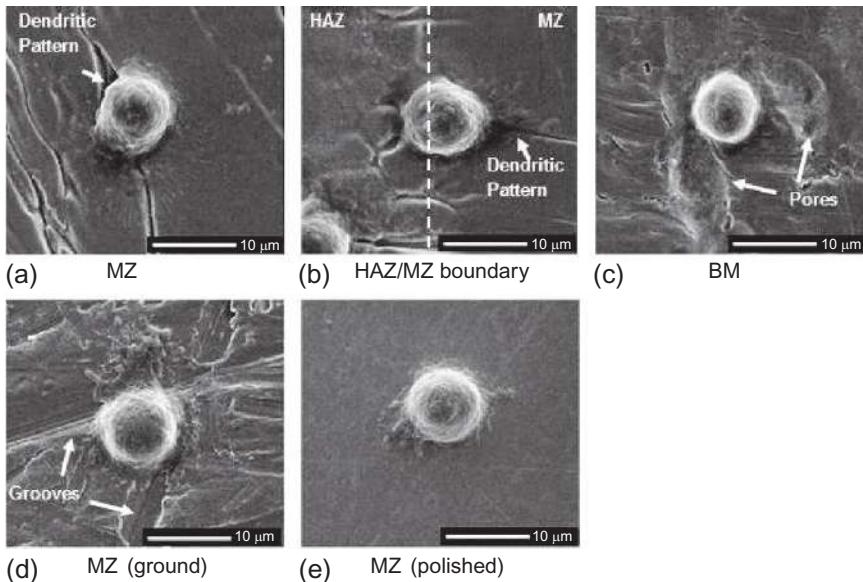


**Figure 27.8** SEM images showing the morphology of MSCs after 4 h cell culture: (a) MZ; (b) HAZ/MZ boundary; (c) BM; (d) MZ (ground); and (e) MZ (polished).

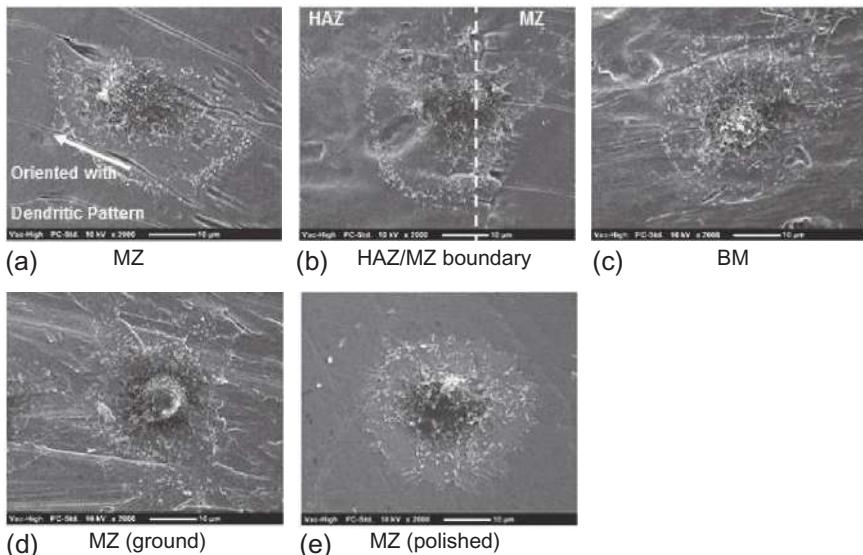


**Figure 27.9** SEM images of the morphology of MSCs after 12 h cell culture: (a) MZ; (b) HAZ/MZ boundary; (c) BM; (d) MZ (ground); and (e) MZ (polished).

of the MZ and HAZ/MZ boundary at lower magnification, as given in [Figure 27.10a and b](#), respectively. The cells were found to preferably distribute and adhere along the edges of the dendritic pattern.

On the other hand, the morphology after 12 h culture in [Figure 27.9](#) shows that the MSCs on all the samples emitted flattened cytoplasmic prolongations and spread over the sample surface, but with different morphology. For the BM, MZ (ground), and MZ (polished) (in [Figure 27.9c-e](#)), a typical spherical cell was observed, and this finding

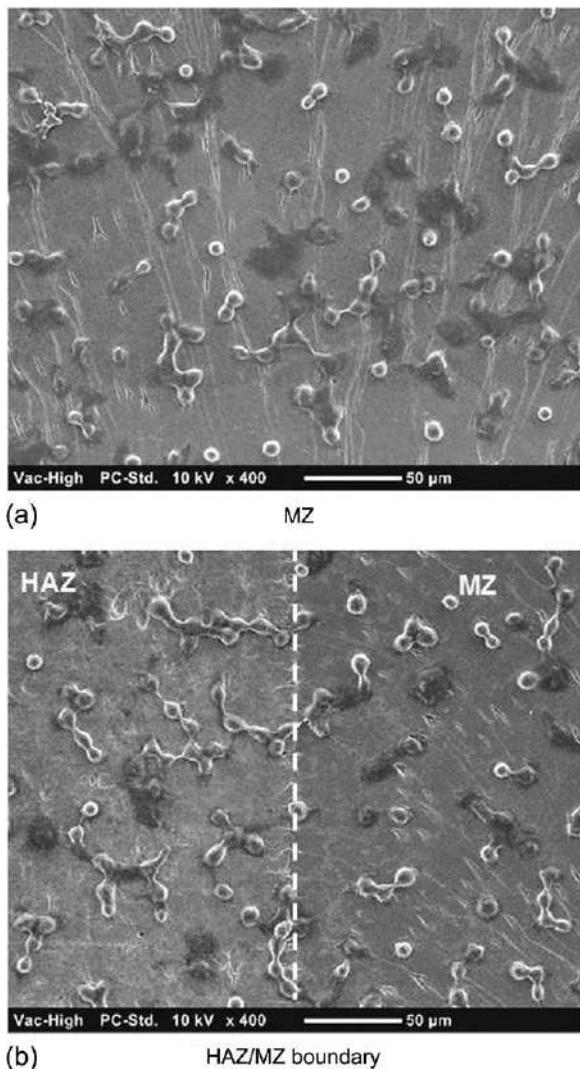


**Figure 27.10** SEM images of the morphology of MSCs on the MZ and HAZ/MZ boundary at lower magnification: (a) MZ and (b) HAZ/MZ boundary.

indicated that the surface roughness may not significantly modulate the morphology of MSCs. In contrast, an oriented and elliptical cell was found in the MZ as shown in [Figure 27.9a](#), and it seems that the cell bent to conform to the dendritic pattern. The effect of the dendritic pattern on the morphology of MSCs was further verified by examining the cell located between the HAZ/MZ boundary (in [Figure 27.9b](#)). It was observed that one half of the cell in the HAZ remained semispherical while another half of it that is located in the MZ distorted and tended to align along with the dendritic pattern. Such guiding effect of MSCs due to the direct physical cell-substrate contact has been reported by Myllymaa *et al.* [33]. They pointed out that MSCs can react to the physical environment and prefer to extend the pseudopodia along with the physical shape and edges.

In comparison to the MZ, even though some obvious grooves were found from the surface of the MZ (ground), no distinct guiding effect could be observed. Therefore, it is reasonable to assume that the guiding effect of MSCs was originated from two topographical factors due to laser melting: (i) the well-defined and directional dendritic pattern, and (ii) the presence of deeper grooves. First, as reported by Dalby *et al.* [58], the pseudopodia of MSCs have a sensory role to detect and react with the physical environment even at the nanometer scale. Therefore, the dendritic pattern of the MZ provided a clear physical guidance for the pseudopodia to align and orient along with the defined direction. Without the clearly defined physical guidance, or when the grooves were randomly oriented as the case in the MZ (ground), the cell would be likely to remain spherical in shape and the pseudopodia no longer actively interact with the physical shape and edges. Second, it has been demonstrated by many authors that the deeper the grooves the greater the guidance, and the degree of guidance depending on the type of cells [59]. As discussed in [Section 27.3.3](#), the MZ showed similar surface roughness but deeper grooves than that after grinding, as evidenced by the higher maximum peak-to-valley height. Such deeper grooves are believed to be beneficial for the enhancement of the guiding effect for the cell.

### 27.3.5.2 Intermediate phase (1-4 days) of stem cell culture

To study the spreading of MSCs, the cells were incubated for 1 and 4 days, respectively. The morphology of MSCs after 1 and 4 days culture were captured by SEM and given in [Figure 27.11](#). As seen in [Figure 27.11a\(i\)](#), the morphology of MSCs on the MZ after 1 day culture indicated that the guiding effect of the dendritic pattern was still clear and the cells tended to bridge over the edges of the dendritic pattern so that cell-substrate contact was confined to the dendrite surface between the edges. Furthermore, a more flattened form of cells was also observed when compared to those in the early phase (after 12 h culture). When looking into the SEM at higher magnification in [Figure 27.12a and b](#), the cells adopted a well-spread and flattened morphology and extended many pseudopodia along the surface between the edges of the dendritic pattern.

Similar observations about the cell morphology after 1 day culture can be found from surfaces of other samples: BM, MZ (ground), and MZ (polished) as shown in [Figure 27.11c\(i\)-e\(i\)](#). No particular orientation could be identified and obvious

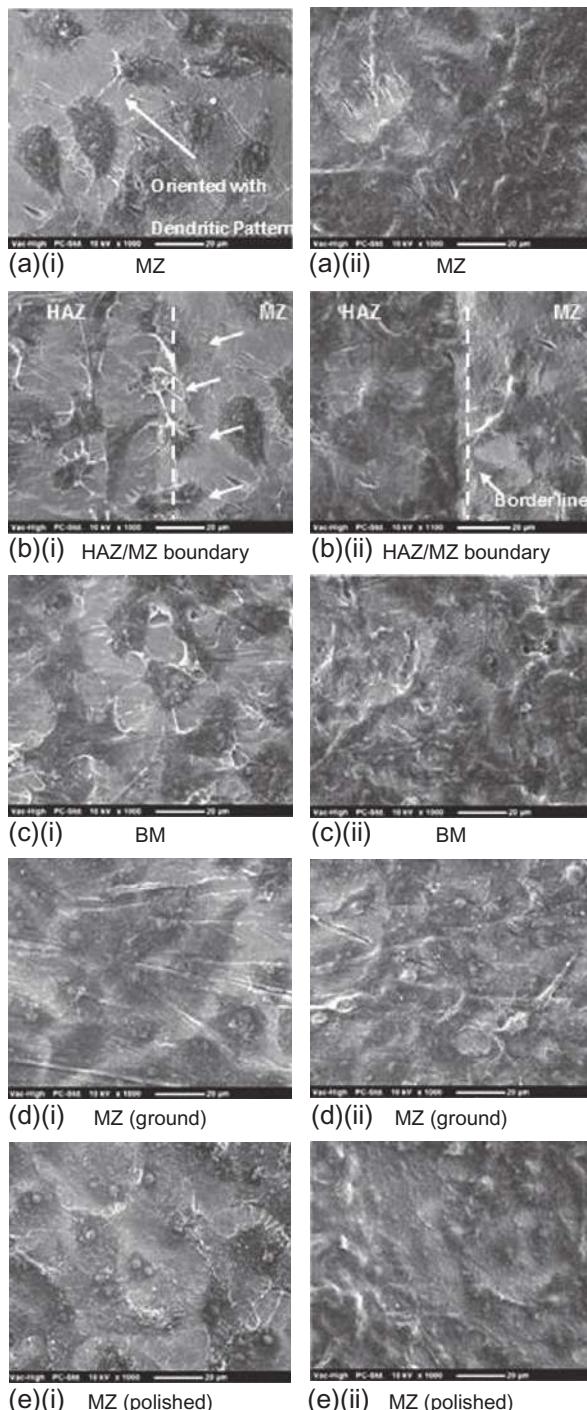


**Figure 27.11** SEM images of the morphology of MSCs after (i) 1 day and (ii) 4 days cell culture: (a)(i) MZ; (a)(ii) MZ; (b)(i) HAZ/MZ boundary; (b)(ii) HAZ/MZ boundary; (c)(i) BM; (c)(ii) BM; (d)(i) MZ (ground); (d)(ii) MZ ground; (e)(i) MZ (polished); and (e)(ii) MZ (polished).

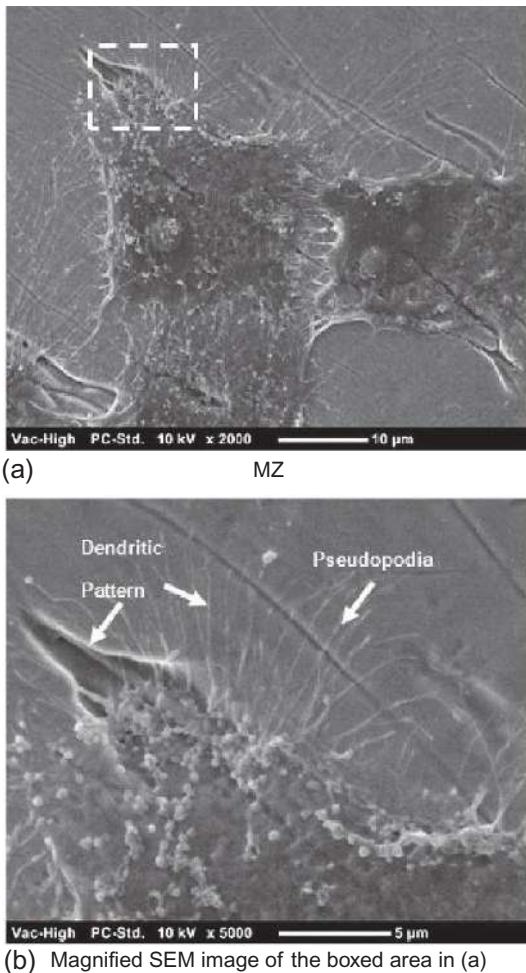


**Figure 27.12** SEM images showing the morphology of MSCs on MZ after 1 day cell culture:  
(a) MZ and (b) magnified SEM image of the boxed area in (a).

pseudopodia, which are an indication of good cell adhesion, were found from the sample surfaces. This also reinforced the argument that surface roughness may not be the crucial factor to affect the cell morphology in the early phase of cell culture. The morphology between the HAZ/MZ boundary in Figure 27.11b(i) gives an important indication about the cell adhesion and spreading behaviors between the regions with different surface topography and roughness being identified. As observed from the figure, the cell was able to bridge across the HAZ/MZ boundary (as pointed by the arrow), with more orientation and elongation compared to the MZ. On the other hand, after 4 days culture the guiding effect of the dendritic pattern was not so clear, as most of the sample area was already covered by the cells as shown in Figure 27.11a(ii), and similar observations could be found from other samples: BM, MZ (ground), and MZ

(polished) in Figure 27.11c(ii)-e(ii). However, a clear borderline that resulted from different cell morphology in the MZ and HAZ was found along the HAZ/MZ boundary as shown in Figure 27.11b(ii). Two important factors could be drawn from the above results. First, the cell was still sensitive to the dendritic pattern after 4 days culture and likely to adapt to the shape and edges of the pattern, resulting in different morphology between the MZ and HAZ. Second, the cell morphology was still predominantly controlled by the surface topography after 4 days culture and the effect of surface roughness seemed to be small.

### 27.3.6 Cell coverage measurement

The effect of laser melting on the cell adhesion of MSCs on NiTi was estimated by the surface area covered by the cells, and the corresponding cell coverage (per  $\text{cm}^2$ ) is plotted in Figure 27.13. From the results, the MZ showed higher cell coverage than the MZ (ground), HAZ, and BM after 1 day culture, but only differences between the MZ and HAZ or BM was significant ( $p < 0.02$  and  $p < 0.05$ , respectively). No remarkable difference can be seen in the results between the MZ and MZ (polished). However, the results were found to be different after 4 days culture. The cell coverage between the MZ, MZ (ground), and BM was similar, but the MZ showed higher cell coverage than the MZ (polished) and HAZ. Differences between the MZ and MZ (polished) or HAZ were significant ( $p < 0.02$ ). Based on the results in Section 27.3.3, the Ra of MZ was higher than that of the MZ (polished) and HAZ. This indicated that the cell coverage is probably related to the surface roughness, with rougher surface corresponding to higher cell coverage. The cellular responses are

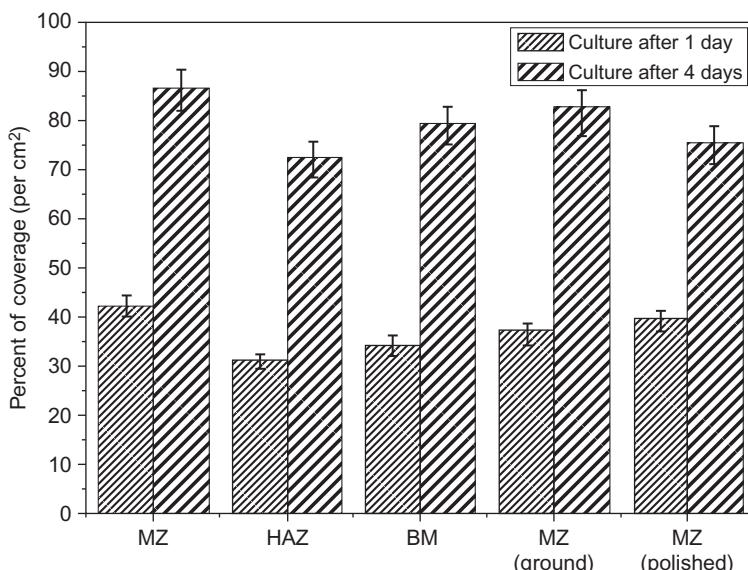


**Figure 27.13** Cell coverage (per  $\text{cm}^2$ ) of different samples after 1 and 4 days cell culture.

reported to be cell-type dependent: osteoblasts prefer rough surfaces, while fibroblasts prefer smooth surfaces [50,51]. The cell adhesion of MSCs preferably increases on a rougher surface due to the increased surface area available for the cells to interact with the material [36]. As a result, the higher cell coverage of the MZ compared to the MZ (polished) and HAZ after 4 days culture was possibly due to the higher amount of surface area available on the surface of MZ to interact with the cells. Furthermore, the richness of surface topography, which came from the well-defined and directional dendritic pattern, might help to increase the cell coverage due to the better organization of the cytoskeleton, as reported by Eisenbath *et al.* [60]. They showed that oriented cells that aligned with the defined pattern have higher density of focal contact when they are in contact with the edges of the grooves. On the other hand, the chemistry of  $\text{TiO}_2$  is reported to be good for the cell attachment of the MSCs [36]. The higher cell coverage of the MZ than the HAZ, in addition to the effects of surface roughness and topography, might be due to the higher surface Ti/Ni ratio (as shown in Table 27.3), which helps to form the passive film with a higher amount of  $\text{TiO}_2$ .

Although the cell coverage was not a quantitative method to count the cell adhesion, the results at least indicated that the degree of surface roughness, topography, and chemistry could modulate the MSCs adhesion of NiTi after laser melting. However, the underlying mechanisms for how these factors interact with the cell adhesion and also proliferation are still inconclusive. As a result, quantitative measurements such as cell counting by hemocytometer and cell proliferation by MTT array are currently being conducted in line with this research. On the other hand, despite the possible initial Ni release in the medium during the cell culture, no toxic effects have been observed on MSCs, as evidenced by the success of cell adhesion and spreading of the cells onto different regions (MZ, HAZ, and BM) in the laser melt. This is due to cell spreading often being an indicator of the nontoxicity of NiTi [50].

## 27.4 Conclusions

The biocompatibility of NiTi laser melting was investigated by examining the cell adhesion and cell spreading of MSCs after early (4 and 12 h) and intermediate phases (1 and 4 days) of cell culture. The effects of surface roughness, topography, and chemistry of the melt on the cell morphology and cell coverage were also determined. The findings have addressed a new research window of applying laser surface treatments, such as laser surface melting, to modulate the MSCs cellular responses on the substrate by modifying the surface roughness, topography, and chemistry. It is also possible to guide the migration of MSCs to a predefined direction by the laser-induced dendritic pattern. The following conclusions were drawn in accordance of the results obtained in this study:

1. The dendritic pattern caused by rapid cooling of laser melting induced a roughening effect in the MZ compared to the HAZ and BM, while the grain growth effect in the HAZ did not cause any observable changes in the surface roughness.

2. The XPS results indicated that the passive films at different regions of the melt were mainly composed of TiO<sub>2</sub>, and the MZ showed a higher surface atomic Ti/Ni ratio as compared to the HAZ and BM.
3. The morphology of MSCs were primarily affected by the richness of topography in the MZ: the well-defined and directional dendritic pattern and the presence of deeper grooves. The surface roughness might not significantly modulate the morphology of MSCs.
4. The good biocompatibility of the NiTi following laser melting has been first demonstrated in this study, as evidenced by the success of cell adhesion and cell spreading of MSCs onto different regions (MZ, HAZ, and BM) in the melt.

## References

- [1] L. Hao, J. Lawrence, *Laser Surface Treatment of Bio-Implant Materials*, John Wiley & Sons Inc., New Jersey, USA, 2005.
- [2] D.G. Waugh, J. Lawrence, D.J. Morgan, C.L. Thomas, Interaction of CO<sub>2</sub> laser-modified nylon with osteoblast cells in relation to wettability, *Mater. Sci. Eng. C* 29 (2009) 2514–2524.
- [3] W. Pfleging, M. Bruns, A. Welle, S. Wilson, Laser-assisted modification of polystyrene surfaces for cell culture applications, *Appl. Surf. Sci.* 253 (2007) 9177–9184.
- [4] H. Mirzadeh, M. Dadsetan, Influence of laser surface modifying of polyethylene terephthalate on fibroblast cell adhesion, *Radiat. Phys. Chem.* 67 (2003) 381–385.
- [5] Y. Mei, A. Kumar, W. Gao, R. Gross, S.B. Kennedy, N.R. Washburn, E.J. Amis, J. T. Elliott, Biocompatibility of sorbitol-containing polyesters. Part I: synthesis, surface analysis and cell response *in vitro*, *Biomaterials* 25 (2004) 4195–4201.
- [6] F.Z. Cui, Z.S. Luo, Biomaterials modification by ion-beam processing, *Surf. Coat. Technol.* 112 (1999) 278–285.
- [7] M. Dadsetan, H. Mirzadeh, N. Sharifi-Sanjani, M. Daliri, Cell behaviour on laser surface-modified polyethylene terephthalate *in vitro*, *J. Biomed. Mater. Res.* 57 (2001) 183–189.
- [8] M.D. Ball, R. Sherlock, T. Glynn, Cell interactions with laser-modified polymer surfaces, *J. Mater. Sci. Mater. Med.* 15 (2004) 447–449.
- [9] P.K. Chu, Bioactivity of plasma implanted biomaterials, *Nucl. Instrum. Methods Phys. Res. B* 242 (2006) 1–7.
- [10] P.K. Chu, Enhancement of surface properties of biomaterials using plasma-based technologies, *Surf. Coat. Technol.* 201 (2007) 8076–8082.
- [11] C.M. Chan, T.M. Ko, H. Hiraoka, Polymer surface modification by plasmas and photons, *Surf. Sci. Rep.* 24 (1996) 1–54.
- [12] Z.D. Cui, H.C. Man, X.J. Yang, The corrosion and nickel release behavior of laser surface-melted NiTi shape memory alloy in Hanks solution, *Surf. Coat. Technol.* 192 (2005) 347–353.
- [13] H. Gugel, A. Schuermann, W. Theisen, Laser welding of NiTi wires, *Mater. Sci. Eng. A* 481–482 (2008) 668–671.
- [14] X.J. Yan, H. Gugel, S. Huth, W. Theisen, Microstructures and properties of laser cladding NiTi alloy with W for biomedical applications, *Mater. Lett.* 65 (2011) 2934–2936.
- [15] B.S. Yilbas, S.S. Akhtar, Laser re-melting of HVOF coating with WC blend: thermal stress analysis, *J. Mater. Process. Technol.* 212 (2012) 2569–2577.

- [16] M. Cabeza, G. Castro, P. Merino, G. Pena, M. Roman, Laser surface melting: a suitable technique to repair damaged surfaces made in 14 Ni (200 grade) maraging steel, *Surf. Coat. Technol.* 212 (2012) 159–168.
- [17] E. Yasa, J.P. Kruth, J. Deckers, Manufacturing by combining selective laser melting and selective laser erosion/laser re-melting, *CIRP Ann. Manuf. Technol.* 60 (2011) 263–266.
- [18] I. Shishkovsky, I. Yadroitsev, I. Surov, Direct selective laser melting of nitinol powder, *Phys. Procedia* 39 (2012) 447–454.
- [19] G. Sun, Y. Zhang, C. Liu, Effects of laser surface re-melting on the microstructure and hardness of laser deposited Co-285+WC coatings, *Lasers Eng.* 20 (2010) 9–20.
- [20] T. Bormann, R. Schaumacher, B. Muller, M. Wilde, Controlling mechanical properties of NiTi scaffolds built by selective laser melting, *Biomed. Technol.* 57 (2012) 568.
- [21] J. Susnik, R. Sturm, J. Grum, Influence of laser surface remelting on Al-Si properties, *J. Mech. Eng.* 58 (2012) 614–620.
- [22] W.T. Silfvast, *Laser Fundamentals*, Cambridge University Press, Cambridge, UK, 1996.
- [23] J. Hecht, *The Laser Guidebook*, second ed., McGraw-Hill Inc., USA, 1992.
- [24] W. Koechner, *Solid-State Laser Engineering*, sixth revised and updated ed., Springer Sciences and Business Media, New York, USA, 2006.
- [25] J. Canning, Fibre lasers and related technologies, *Opt. Lasers Eng.* 44 (2006) 647–676.
- [26] L. Li, Q. Lou, J. Zhuo, J. Dong, Y. Wei, S. Du, B. He, High power single transverse mode operation of a tapered lare-mode-area fiber laser, *Opt. Commun.* 281 (2007) 655–657.
- [27] P. Li, C. Zhu, S. Zou, H. Zhao, D. Jiang, G. Li, M. Chen, Theoretical and experimental investigation of thermal effects in a high power Yb<sup>3+</sup>-doped double-clad fiber laser, *Opt. Laser Technol.* 40 (2008) 360–364.
- [28] T. Beck, N. Reng, H. Weber, Optical fibres for material processing lasers, *Opt. Lasers Eng.* 34 (2000) 255–272.
- [29] N.G.R. Broderick, H.L. Offerhaus, D.J. Richardson, R.A. Sammut, J. Caplen, L. Dong, Large mode area fibers for high power applications, *Opt. Fiber Technol.* 5 (1999) 185–196.
- [30] J. Kirchhof, S. Unger, A. Schwuchow, S. Grimm, V. Reichel, Materials for high-power fiber lasers, *J. Non Cryst. Solids* 352 (2006) 2399–2403.
- [31] L. Quintino, A. Costa, R. Miranda, D. Yapp, V. Kumar, C.J. Kong, Welding with high power fiber lasers—a preliminary study, *Mater. Des.* 28 (2007) 1231–1237.
- [32] H. Koga, L. Engebretsen, J.E. Brinchmann, T. Muneta, I. Sekiya, Mesenchymal stem cell-based therapy for cartilage repair: a review, *Knee Surg. Sports Traumatol. Arthrosc.* 17 (2009) 1289–1297.
- [33] S. Myllymaa, E. Kaivosa, K. Myllymaa, T. Sillat, H. Korhonen, R. Lappalainen, Y. T. Konttinen, Adhesion, spreading and osteogenic differentiation of mesenchymal stem cells cultured on micropatterned amorphous diamond, titanium, tantalum, and chromium coatings on silicon, *J. Mater. Sci. Mater. Med.* 21 (2010) 329–341.
- [34] T. Habijan, S. Glogowski, S. Kuhn, M. Pohl, J. Wittsiepe, C. Greulich, G. Eggler, T. A. Schildhauer, M. Koller, Can human mesenchymal stem cells survive on a NiTi implant material subject to cyclic loading, *Acta Biomater.* 7 (2011) 2733–2739.
- [35] L.L. Meisner, A.I. Lotkov, A. Matveeva, L.V. Artemieva, S.N. Meisner, A.L. Mtveev, Effect of silicon, titanium, zirconium ion implantation on NiTi biocompatibility, *Adv. Mater. Sci. Eng.* 2012 (2012), Article ID—706094.
- [36] D.S. Kommireddy, S.M. Sriram, Y.M. Lvov, D.K. Mills, Stem cell attachment to layer-by-layer assembled TiO<sub>2</sub> nanoparticle thin films, *Biomaterials* 27 (2006) 4296–4303.
- [37] T. Duerig, A. Pelton, D. Stockel, An overview of Nitinol medical applications, *Mater. Sci. Eng. A* 273–275 (1999) 149–160.

- [38] E. Hornbogen, V. Mertinger, D. Wurzel, Microstructure and tensile properties to two binary NiTi-alloys, *Scr. Mater.* 44 (2001) 171–178.
- [39] Y.G. Song, W.S. Li, L. Li, Y.F. Zheng, The influence of laser welding parameters on the microstructure and mechanical property of the as-jointed NiTi alloy wires, *Mater. Lett.* 62 (2008) 2325–2328.
- [40] A. Tuissi, S. Besseghini, T. Ranucci, F. Squatrito, M. Pozzi, Effect of Nd-YAG laser welding on the functional properties of the Ni-49.6 at.%Ti, *Mater. Sci. Eng. A* 273–275 (1999) 813–817.
- [41] Y.T. Hsu, Y.R. Wang, S.K. Wu, C. Chen, Effect of CO<sub>2</sub> laser welding on the shape-memory and corrosion characteristics of TiNi alloys, *Metall. Mater. Trans. A* 32 (2001) 569–576.
- [42] Y. Ogata, M. Takatugu, T. Kunimasa, K. Uenishi, K.F. Kobayashi, Tensile strength and pseudo-elasticity of YAG laser spot melted TiNi shape memory alloy wires, *Mater. Trans.* 45 (2004) 1070–1076.
- [43] A. Falvo, F.M. Furgiuele, C. Maletta, Laser welding of a NiTi alloy: mechanical and shape memory behaviour, *Mater. Sci. Eng. A* 412 (2005) 235–240.
- [44] C.W. Chan, H.C. Man, T.M. Yue, Effect of postweld heat treatment on the microstructure and cyclic deformation behavior of laser-welded NiTi-shape memory wires, *Metall. Mater. Trans. A* 43 (2012) 1956–1965.
- [45] B. Tam, M.I. Khan, Y. Zhou, Mechanical and functional properties of laser-welded Ti-55.8 wt pct Ni nitinol wires, *Metall. Mater. Trans. A* 42 (2011) 2166–2175.
- [46] M. Dadfar, M.H. Fathi, F. Karimzedah, M.D. Dadfar, A. Saatchi, Effect of TIG welding on corrosion behaviour of 316L stainless steel, *Mater. Lett.* 61 (2007) 2343–2346.
- [47] N. Amanat, N.L. James, D.R. McKenzie, Welding methods for joining thermoplastic polymers for the hermetic enclosure of medical devices, *Med. Eng. Phys.* 32 (2010) 690–699.
- [48] C.W. Chan, H.C. Man, T.M. Yue, Effects of process parameters upon the shapoe memory and pseudo-elestic behaviors of laser-welded NiTi thin foil, *Metall. Mater. Trans. A* 42 (2011) 2264–2270.
- [49] A.S.G. Curtis, C.D.W. Wilkinson, Reactions of cells to topography, *J. Biomater. Sci. Polym. Ed.* 9 (1998) 1313–1329.
- [50] C. Wirth, V. Comte, C. Lagneau, P. Exbrayat, M. Lissac, N. Jaffrezic-Renault, L. Ponsonnet, Nitinol surface roughness modulates *in vitro* cell responses: a comparison between fibroblasts and osteoblasts, *Mater. Sci. Eng. C* 25 (2005) 51–60.
- [51] T.P. Kunzler, C. Huwiler, T. Drobek, J. Voros, N.D. Spencer, Systematic study of osteoblast response to nanotopography by means of nanoparticle-density gradients, *Biomaterials* 28 (2007) 5000–5006.
- [52] I. Hussain, S.A. Magd, O. Eremin, M. El-Sheemy, New approach for isolation of mesenchymal stem cells (MSCs) from human umbilical cord blood, *Cell Biol. Int.* 36 (2012) 595–600.
- [53] C.W. Chan, H.C. Man, T.M. Yue, Susceptibility to environmentally induced cracking of laser-welded NiTi wires in Hanks' solution at open-circuit potential, *Mater. Sci. Eng. A* 544 (2012) 38–47.
- [54] M.I. Khan, Y. Zhou, Effects of local phase conversion on the tensile loading of pulsed Nd: YAG laser processed Nitinol, *Mater. Sci. Eng. A* 527 (2010) 6235–6238.
- [55] X.J. Yan, D.Z. Yang, X.P. Liu, Corrosion behavior of a laser-welded NiTi shape memory alloy, *Mater. Charact.* 58 (2007) 623–628.
- [56] H.C. Man, Z.D. Cui, T.M. Yue, Corrosion properties of laser surface melted NiTi shape memory alloy, *Scr. Mater.* 45 (2001) 1447–1453.

- [57] M. Stiehler, M. Lind, T. Mygind, A. Batrup, A.D. Pirouz, H. Li, M. Foss, F. Besenbacher, M. Kassem, C. Bunger, Morphology, proliferation, and osteogenic differentiation of mesenchymal stem cells cultured on titanium, tantalum, and chromium surfaces, *J. Biomed. Mater. Res. A* 86A (2008) 448–458.
- [58] M.J. Dalby, D. McCloy, M. Robertson, H. Agheli, D. Sutherland, S. Affrossman, Osteoprogenitor response to semi-ordered and random nanotopographies, *Biomaterials* 27 (2006) 2980–2987.
- [59] P. Clark, P. Connolly, A.S.G. Curtis, J.A.T. Dow, C.D.W. Wilkinson, Topographical control of cell behaviour: II. Multiple grooved substrata, *Development* 108 (1990) 635–644.
- [60] E. Eisenbath, P. Linez, V. Biehl, D. Velten, J. Breme, H.F. Hildebrand, Cell orientation and cytoskeleton organization on ground titanium surfaces, *Biomol. Eng.* 19 (2002) 233–237.

# Index

*Note:* Page numbers followed by *f* indicate figures and *t* indicate tables.

## A

### Ablation

- ceramics, 407–408
- closed flowing immersion techniques, 536–537, 537*f*
- condensation, 524, 525*f*
- conventional photolithography, 523
- debris deposition, 535
- definition, 523
- demagnified image, excimer laser beams, 527–531
- electrons transfer, 525–526
- excimer lamps, 539
- free valence electrons, 526
- fs laser functionalization
  - (*see* Femtosecond laser functionalization, ablation effects)
- generation, 524, 525*f*
- high-speed Schlieren imaging, 540, 540*f*
- laser irradiation, 538
- liquid selection, 537–538
- long pulses, absorption and thermal diffusion, 526, 526*f*
- mechanisms, 524–526
- metals, laser ablation behavior, 406–407
- micromachining, 523
- nanosecond photoacoustic analysis, 540
- nanosecond shadowgraphy, 540, 540*f*
- nanosecond surface interferometry, 540, 540*f*
- photothermal, 542
- picosecond anti-Stokes coherent Raman scattering spectroscopy, 540
- product, size and form, 533–535
- product trajectory, 532–533
- pulsed laser deposition (PLD), 288
- short pulse laser-material interactions, 524–525
- surface coatings, laser ablation behavior, 408–411

### surface micro-nano structures (SMNS), 215

- surface ripples reduction, 536
- threshold and rate, 524
- time-of-flight mass spectrometry (ToF-MS), 540
- time-resolved transmission, 540
- transformation, 524, 525*f*
- in transparent materials, 525
- van der waals intermolecular forces, 536–537

### Abrasive wear, 488

### Actinide (An) ions

- advanced fluorescence imaging, 559–561
- hydration study, 554–556, 556*t*
- at interfaces, analysis, 556–558
- interface-specific laser spectroscopy, 559
- quantum chemical simulation, 561–562
- in solution, analysis, 554–556
- spectroscopic properties, 556, 557*f*
- TRLFS data analysis, 551–553

### Additive layer manufacturing (ALM) 3D, 182, 183*f*

- processes classification, 181–182, 182*t*

### Additive manufacturing (AM)

- application, 177–178
- metallic components, 177
- microstructure development and metallurgical mechanisms, 178
- physical and chemical metallurgy, 177
- processes database, 178
- treatment, versatile powder materials, 178

### Adhesive wear, 70–72, 85–87, 488, 518*f*

### AISI 304 steel surface

- B<sub>4</sub>C particles, 99
- EDS, 102–104, 103*t*
- high-speed tool steel, 97–98
- laser heating conditions, 98, 99*t*
- laser treatment, 98, 99, 100*f*
- melting temperature, 99–101

- AISI 304 steel surface (*Continued*)  
 microhardness, 102–104  
 SEM, 101–102, 102*f*  
 surface properties, 97  
 XRD, 99, 102–104, 103*f*
- Alloyed layers  
 heat-affected zones (HAZ), 75  
 microhardness, 69, 69*f*, 76–79  
 microstructure, 74, 74*f*, 82, 83*f*  
 molten pool, 82–83  
 morphology, 74, 74*f*, 81, 82*f*  
 thicknesses values, 73–74  
 wear properties, 76–79, 84–88  
 wear surface, 72  
 weight loss, 70, 70*f*  
 worn surface, 70–72, 71*f*  
 XRD pattern, 75–76, 76*f*, 83, 84*f*
- Alloying, titanium  
 alloyed zone microstructure variation, 507–513, 510*f*, 512*f*  
 average surface roughness, 501–503  
 coated substrate, irradiation, 499–501, 500*f*  
 codeposition, 499–501  
 coefficient of friction, variation, 516–517, 518*f*  
 cracking, 504–505  
 cyclic oxidation studies, 513–514, 514*f*, 515*f*  
 defects, 507, 508*t*  
 definition, 499–501  
 elements, 501  
 expansion coefficients mismatch, 514–516  
 laser surface nitriding, parameters, 501–503, 501*t*  
 microhardness variation, 503–504, 504*f*  
 nitroded zone, scanning electron micrographs, 501–503, 502*f*  
 nitrogen, 501–503  
 pit formation potential measurement, 505–506, 506*f*  
 process optimization diagram, 509–513, 513*f*  
 silicon, 506–507  
 solidification, 499–501, 500*f*  
 stages, 499–501, 500*f*  
 surface roughness, 507, 509*f*  
 temperature gradients, 499–501  
 wear behavior, 517–519, 518*f*
- wear depth variation, 516, 517*f*  
 X-ray diffraction patterns, 503, 503*f*, 507–509, 511*f*
- Alpha alloys, 486  
 Alpha-beta alloys, 487  
 ANSYS bundled software, 638, 640, 641*f*, 642
- Attosecond pulsed laser surface texturing, 450
- Australian Nuclear Science and Technology Organisation (ANSTO), 475–477
- Avalanche ionization, 360
- AZ91D Mg alloy  
 acid-base theory or three-liquid method, 350–351  
 Al and Mg elements, 345–346, 345*f*  
 contact angle measurement, 349, 350*f*  
 laser-treated alloy, surface energy, 350–351, 351*t*  
 microstructural evolution, 346–349, 349*t*  
 m-SBF, 349, 350*f*  
 phase transformation, 346, 347*f*  
 solidification microstructure, 344–345, 344*f*  
 surface energy components, 350–351, 351*t*  
 wettability, 351  
 XRD patterns, 344–345, 344*f*
- B**
- Backscattered electron microscopy (BSEM) methods, 245
- B<sub>4</sub>C particles, AISI 304 steel. *See* AISI 304 steel
- Beam masking, 530
- Beam-splitter configuration, 430
- Beta alloys, 487
- Biocompatible implants, titanium and nickel-titanium  
 biomatrices, RP process, 605, 605*f*  
 biostimulating additives, 604
- CAD stage, 605–606
- cobalt-chrome alloys, porous, 603–604
- gradient porosity structure, 604–605
- helical, in stomatology, 603–604
- interfacial durability, 604–605
- intermetallic nickel-titanium NiTi, 604
- laser beam (LB) parameters, 605
- laser influence (LI) space, 604

- machine, 605*f*, 606  
in neurosurgery and maxillofacial surgery, 604  
nitinol powders, 605  
rapid prototyping (RP) technology, 604  
synthesized 3-D parts, 606, 606*f*  
titanium alloys, 603
- C**
- CA. *See* Contact angle (CA)  
Carbon dioxide ( $\text{CO}_2$ ) laser, 587, 589, 593  
Carbon nitride thin films  
    C–N/C=N integrated intensity ratio, 298–299, 300*t*  
    C1s XPS spectra, 298, 299*f*  
    hardness values, 297, 297*f*, 298*t*  
    Lorenzian-Gaussian profiles, 298, 300*t*  
    nitrogen pressure, 298  
    Oliver and Pharr method, 296  
    RPLD, 296  
    sp<sup>3</sup> hybridization state, 298  
    XPS analysis, 297
- Carburization  
    aluminum, 47–48, 49*f*  
    carbides formation, 44–46  
    description, 44  
    iron, 46  
    methane atmosphere, 46, 47*f*  
    nanoindentation measurement, 47–48, 48*f*  
    nitrocarburisation, 50  
    nonferrous materials, 47  
    RBS measurement, 47–48, 48*f*  
    silicon matrix, 49, 49*f*  
    stainless steel, 47
- Caries  
    detection, 590–591  
    prevention, 592–593  
    removal, 591–592
- Cast steel rolls  
    alloyed layers, 80–81  
    chemical composition, 85–87, 87*t*  
    EDX analysis, 87–88  
    layers depth, 84–85, 85*f*  
    microstructure and phases, 80, 81*f*  
    processing parameters, 80, 80*t*  
    relative wear resistance, 85, 85*t*  
    worn surfaces, 85–87, 86*f*  
    XRD pattern, 88, 88*f*
- C-B-W-Cr nano-powders, 62–72  
Cell coverage measurement, 671–672  
Ceramics  
     $\text{Al}_2\text{O}_3$  layer, 108–109  
    characterization techniques, 110–111  
    cold isostatic pressed  $\text{ZrO}_2$ , 109–110  
    HPDL, 109  
    laser ablation behavior, 407–408  
    laser processing parameters, 111–112  
    laser surface treatment, 107, 110  
     $\text{Si}_3\text{N}_4$ , coal isostatic pressed, 109–110  
    temperature distribution and phase transition, 129–131, 130*f*  
     $\text{ZrO}_2$  and the  $\text{Si}_3\text{N}_4$ , 108
- Chemotherapy, effect, 586
- Chirped pulse amplification (CPA) systems, 386–387
- Coaxial nozzle gas supply, 38
- $\text{CO}_2$  lasers, 654–655
- Cones, fs laser ablation  
    ablation zone, 570  
    atmospheres, 568–569, 569*f*  
    100Cr6 samples, 570, 571*f*  
    fluence and pulse number, 570  
    laser parameters (laser polarization), 568, 570  
    materials, 568  
    oxide particles, 572  
    setup parameters, 570, 571*f*  
    spike density, 569
- Confocal Raman spectroscopy, 573, 575*f*
- Contact angle (CA)  
    laser texturing, 231–232, 231*f*  
    measurements, 230  
    and roughness, 231–232, 232*f*  
    superhydrophobic surface, 230
- Continuous wave mode (cw-mode)  
    coaxial nozzle gas supply, 38  
    equipment, 38  
    gas chamber arrangement, 38  
    Nd:YAG ns-laser, 407*f*  
    shroud arrangement, 38  
    side nozzle gas supply, 38  
    swivelling clamping device, 38–39
- Corrosion  
    aluminium oxide film, 478  
    cavitation erosion testing, 478–479, 480*f*  
    laser-heated sample, 478  
    laser-melted sample, 479

**Corrosion (*Continued*)**

- linear polarization curves, 478, 479*f*
  - surface dependent engineering properties, 488
  - three-electrode potentiostat testing, 478
- Coulomb explosion, 361
- CPA. *See* Chirped pulse amplification (CPA) systems
- Crack propagation
- alloyed layer, NCIR, 68–69, 68*f*
  - backscatter electron (BSE) SEM image, 139–140, 153–155
  - Cr borides, 155–156, 155*f*
  - Cr-rich precipitates, 139*f*
  - hardness and fracture toughness, 138
  - intergranular and transgranular crack, 69
  - microstructure, 66–68, 67*f*
  - rolling work condition, 68

**Crystallization**

- convective mixing task, 272
- intermetallic compounds, 271
- kinetic and diffusion processes, 275
- LC, 271–272
- MeAl redistribution, 274
- phase transformation (PT), 272
- polycrystalline silicon, 15–18
- relative volume, 273
- self-propagated high-temperature synthesis (SHS), 270
- silicon, laser texturing, 318–324, 351–352

**D**

- Demagnified image ablation machining
- beam masking, 530
  - cross-sectional beam dimensions modification, 527
  - excimer laser, 527
- Gaussian cross-sectional beam energy distribution, 527, 528*f*
- input beam characteristics, 529
- kaleidoscope, 527–528, 529*f*
- laser beam mask imaging techniques, application, 531
- microlens array homogenizers, 528–529, 529*f*
- Density functional theory (DFT), 561–562
- Dental bleaching, 594–595
- Dentin hypersensitivity (DH), 593–594

**Dentistry, laser applications**

- hard tissues, 583–584, 590–595
- low-and high-intensity lasers, 583
- soft tissues, 583–590

**DIAGNOdent, 590, 591*f***

- Diamond-like carbon (DLC) coating**
- friction coefficients, 417–418, 418*f*
  - on laser-textured substrates, 415
  - ns-laser pulse, 417
  - phase transformation, 416
  - Raman frequency-intensity, 416*f*
  - textured steel substrates, 415–416, 417
  - tribological properties, 415

**Direct laser interference patterning (DLIP)**

- bacterial adhesion test, 433
- beam-splitter interference setup, 430–431, 431*f*
- femtosecond laser pulses, 434–435
- laser energy density, 431
- Marangoni convection, 431
- metallic surfaces, surface patterning, 432–433
- ns-pulsed laser, 430
- patterned metallic periodic structures, 431, 432*f*
- polystyrene (PS) and polyimide (PI) substrates, 433

**Direct writing, 362–363, 362*f***

- 3-D laser processing, ultrashort pulses**
- advantages, 383–384
  - beam shaping techniques, 385
  - direct-writing scheme, 392
  - enhanced fs laser filamentation, 397–400
  - experimental setup, 390–391, 391*f*
  - Foturan glass samples, 391–392
  - Gaussian beam, 390
  - heat treatment, 392
  - LDW processes, 384, 384*f*
  - at low numerical apertures (NAs), 389–392

MPA initiated process, 383–384

peak-intensity distributions, 389–390

slit beam shaping method, 392

spatial chirp, 390

spatiotemporal manipulation, 385–389

TPFE process, 393–397

transparent materials, 384

- DLC. *See* Diamond-like carbon (DLC) coating**

- DLIP. *See* Direct laser interference patterning (DLIP)
- 3D manganese-based nanoporous structure (3D-Mn-NPS)  
fabrication, 220  
FESEM image, 221, 221*f*  
melting point, 222–223  
microstructure, 220, 220*f*  
nanostructure, 221, 221*f*  
surface structural evolution, 222–223, 223*f*  
tunability, 221–222
- 3D-Mn-NPS. *See* 3D manganese-based nanoporous structure (3D-Mn-NPS)
- 3-D porous matrix, tissue engineering  
adult bone tissue, 608  
biodegradable polymers, 608–609  
carrier matrix, 608  
control parameters, 610  
experiment scheme, 609, 609*f*  
fibroblast monolayer, titanium sample, 612*f*  
immunophenotyping, 611, 622  
implant testing, 607  
migration ability evaluation, 620  
MMSC colonies, 607, 610–611, 620*f*  
morphological groups ratio, 620*t*  
native cultures, 610  
nitinol powder, 613*f*, 614  
nitinol powder+HA, 615–623, 616*f*, 618*f*, 619*f*  
osteogenesis, 608–609  
proliferative activity, 620*f*  
quality and biological compatibility, 607  
in regenerative surgery, 608  
RP and manufacturing technology (RPMT), 608  
stem cells population, cluster analysis, 621*f*  
time-lapse method, 611  
tissue scaffold engineering, 607–608  
titanium graded PTOM, 609  
titanium powder, 612–614, 612*f*, 613*f*  
titanium powder+HA, 615  
toxicity determination, 611
- Drug delivery systems  
bioengineering applications, 646  
DDS functioning, 647*f*  
drug solution intake, 646
- fluid propulsion, 645  
interconnected porous channels, 646  
intermetallic NiTi, 645–646  
laser fluence, 300–301  
microelectromechanical systems (MEMS), 644–645  
microfabrication techniques, 644–645  
microfluidic components, 644–645  
microfluidic propulsion technologies, 645–646  
monitoring and control, 646  
nitinol, 645–646  
NiTi stoichiometric composition, 646  
porous 3-D NiTi scaffold, 647*f*  
RP technology, 646
- E**
- Early transition metals (ETMs), 140–141, 141*t*
- EDT. *See* Electrical discharge texturing (EDT)
- EHL. *See* Elastohydrodynamic lubrication (EHL) regime
- Eisenthal  $\chi^{(3)}$  technique, 559, 560*f*
- Elastohydrodynamic lubrication (EHL) regime, 576
- Electrical discharge texturing (EDT)  
cold rolling industry, 455  
roller surface texturing, 455  
YAGLT and, 465
- Electroplating method  
copper nanoparticles, 193, 203–206, 203*t*  
deposition rate, 193  
device, 194–195, 194*f*  
EDS, copper particles, 206, 209*f*  
experimental setups, laser power measurement, 196, 197*f*  
mechanisms, 195–196  
metallic nanoparticles, 193  
numerical and experimental results, 196, 199*f*  
numerical simulation, 200, 200*f*, 201*f*  
power absorptions, 196, 198*f*  
stainless steel substrate, 196, 197*f*  
temperature profiles, 196, 198*t*, 200, 202*f*  
water jet, heating, 200, 201*t*  
W Q-switched laser interaction, 203–206, 205*f*

- Enamel resistance, 594–595  
 Endodontics, 589–590  
 Energy dispersive spectroscopy (EDS)  
     laser-treated surface, 102–104, 103*t*  
     phases, mutual solubility, 144–145  
 EPD. *See* Equilibrium phase diagram (EPD)  
 Equilibrium phase diagram (EPD), 244–245,  
     272, 275  
 Erbiumdoped yttrium aluminum garnet  
     (Er:YAG), 587, 588, 589, 592  
 Erosion, 488  
 Explosive evaporation, 532–533
- F**
- Fabry-Perot interferometer, 365–366, 369,  
     371–372, 372*f*  
 Femtosecond laser filamentation  
     experimental setup, 397–398  
     laser energy, 399, 399*f*  
     nitrogen fluorescence, 398–399  
     peak intensity, 399  
     spatiotemporal focusing technique,  
         398, 398*f*  
 Femtosecond laser functionalization,  
     ablation effects  
     amorphization and recrystallization  
         phenomena, 572, 573  
     chemical and microstructural effects,  
         572–576  
     confocal Raman spectroscopy, 573, 575*f*  
     contact angle measurements, 577, 578*f*  
     100Cr6 samples, Abbott-Firestone curves,  
         573, 577, 578*f*  
     EHL regime, 576  
     femtosecond laser setup, 565, 566*f*  
     laser-interference patterning, 577  
     laser techniques and materials,  
         565–566  
     lubricant reservoir, 577  
     metal carbides, 573  
     micro-Raman spectroscopy, 572  
     nano-and microgrooves, 577  
     oxidation phenomena, 573  
     potential applications, 576–579  
     Raman analyses, 575–576, 576*f*  
     ripple and ablation zones, 573–575  
     topographical effects, 566–572  
     UV illumination and thermal heating, 577
- X-ray photoelectron spectroscopy (XPS),  
     573, 574*f*  
 Femtosecond laser micromachining  
     avalanche ionization, 360  
     beam interference, 361–362  
     Coulomb explosion, 361  
     inner air cavity, microfiber, 376, 377*f*  
     laser direct writing, 362–363  
     microfiber, 376  
     microhole fabrication, ablation,  
         376–378, 377*f*  
     multiphoton ionization and tunneling  
         ionization, 359–360  
     optical fiber microstructures, 363–366  
     recent progress and future development  
         trend, 375–378  
     sensing devices, optical fiber  
         microstructures, 367–375
- Femtosecond laser pulses  
     beam-splitter configuration, 434  
     Coulombian explosion, 435  
     ethylene dioxythiophene (EDOT), 434  
     overlap area (OA), 434  
     PEDOT-PSS thin films, 434  
     subwave-length ripple structure, 435  
     surface texturing, 450  
     Ti:sapphire fs-laser system, 434–435
- Fiber Bragg grating (FBG)  
     Corning SMF-28, 363  
     damaged FBG, axial morphology, 363, 363*f*  
     sensors, 367–368
- Fiber in-line interferometer  
     Fabry-Perot interferometer, 365–366, 369,  
         371–372, 372*f*  
     liquid refractive index measurement, 369,  
         370*f*  
     Mach-Zehnder interferometer, 365–366,  
         369–370, 373*f*  
     Michelson interferometer, 365–366,  
         370–371, 371*f*  
     reflection spectra, 372, 373*f*  
     sensors, 369–372  
     transmission spectra, 369–370, 370*f*
- Fiber lasers, 656
- Flat-jet powder nozzles, 188, 188*f*
- Fracture toughness  
     crack healing, 129  
     laser-engineered surfaces, ZrO<sub>2</sub> and Si<sub>3</sub>N<sub>4</sub>,  
         128, 128*t*

- surface hardness, 128
- Fresnel-Kirchhoff's diffraction theory, 387, 395
- Full width at half maximum (FWHM), 319
- Functionally graded structures (FGS)  
aluminum powder, 259  
fabrication, 249  
structures, 248
- G**
- GaAs (gallium-arsenide) diode laser, 584
- Gaussian cross-sectional beam energy distribution, 527, 528*f*
- H**
- Hard tissues, lasers effect  
caries detection, 590–591  
caries prevention, 592–593  
caries removal, 591–592  
dental bleaching, 594–595  
dentin hypersensitivity, treatment, 593–594
- Heat-affected zone (HAZ)  
alloyed layers, 74, 75  
laser surface treatment, 3  
light metal casting alloys, 14, 17*f*  
nanosecond pulsed surface texturing, 447  
 $\text{Si}_3\text{N}_4$  technical ceramics, 125
- Helium-Neon (HeNe) laser, 584
- High-intensity lasers, 583, 584, 592–593
- High power diode laser (HPDL), 11, 109
- High productivity processing  
and cost efficiency, 187  
flat-jet powder nozzles, 188, 188*f*  
high-power laser systems, 187  
induction-assisted laser cladding, 188–189
- High-speed imaging  
Gregorčič's technique, 542  
multiple fields, 542  
photothermal ablation, 542
- High-speed tool steel, 97–98
- Hot-work tool steels  
 $\text{Al}_2\text{O}_3$  counterspecimen wear, 7–9, 9*f*  
32CrMoV12-28 steel surface, 5–6, 6*f*  
fatigue strength, 11  
friction coefficient, surface layers, 9, 10*f*  
hardness, 6–7  
laser power and scanning rate, 11
- laser surface treatment, 5–6  
material surface layers, 4–5  
NbC alloying, 5–6, 5*f*  
structure changes, laser remelting, 5–6, 6*f*  
surface layer wear profile, 7–9, 9*f*  
thin foil structures, 6, 7*f*  
TiC alloying, 5–6, 5*f*
- Hydrogenated DLCs (DLC:H), 410–411, 412*f*
- I**
- Induction-assisted laser cladding  
cracking reduction, 181  
hybrid process, 189  
hybrid technology, 188, 189*f*  
temperature profile, 188–189, 190*f*
- InGaAlP (indium-gallium-aluminium-phosphide) diode lasers, 584
- Interference patterning  
DLIP system, 436, 436*f*  
four-laser beam interference, 425  
intensity distribution calculation, 424  
nonsymmetrical configuration, 425  
two-beam interference patterns, 424*f*
- Iron aluminides (Fe-Al) system  
bottom cladding layers, 255, 255*f*  
dissimilar materials, laser welding, 254  
EDS, 257, 258*f*  
element analysis, 259  
intermetallic samples and coating, 254  
LAM, 254  
metastable phases, 256  
microelement analysis data, 257, 258*f*  
microhardness distributions, 256, 256*f*  
MMC, 254  
powders, 254  
temperature applications, 253–254  
X-ray analysis, 256–257, 257*f*
- K**
- Kaleidoscope, 527–528, 529*f*
- L**
- Lanthanide (Ln) ions  
hydration study, 554–556, 556*t*  
physicochemical properties, 550  
spectroscopic properties, 556, 557*f*  
TRLFS, 551–553

- Laser additive manufacturing (LAM)  
 metallic matrix, 248  
 micro-and macroalloying, 254
- Laser annealing, 317–318, 323–324
- Laser-assisted cold spray (LACS), 237, 238–239
- Laser cladding (LC)  
 additive layer manufacturing, 181–182, 182*t*  
 camera-based closed loop control, 189, 191*f*  
 2D-and 3D-processing, 185  
 energy efficiency, 181  
 fabrication and repair, 186  
 filigree functional parts, 185  
 $\beta$ -grain morphology, 184  
 hot-wire INCONEL 625 coating, 184, 184*f*  
 industrial technique, 181
- LACS, 237
- melt pool dimensions, 189–190
- metallurgical bond, 182, 183*f*
- nozzle designs, 185, 185*f*
- plasma spraying, 237
- powder compositions, 237
- powder/wire material, 182, 183*f*
- SHS (*see* Self-propagated high-temperature synthesis (SHS))
- slim nozzle design, 186, 187*f*
- soldering, 237
- substrate material, 189
- temperature distribution, 263–268
- triple-helix structure, 185, 186*f*
- Laser cooling, 242, 245–246, 251
- Laser deposition methods  
 calcium phosphates thin films, 291–292  
 carbon nitride thin films, 296–299  
 fluence, drug delivery systems, 300–301  
 protein films for biofouling, 302–303  
 solvent, drug delivery and implants, 301–302  
 ZnO thin films, 293–296
- Laser diode, 587–588, 589
- Laser direct-write (LDW) processes, 384, 384*f*
- Laser-guided discharge texturing (LGDT)  
 arc discharge control, 457–458  
 cascade ionization, inverse  
 Bremsstrahlung (IB) heating electrons, 456
- laser plasma formation, 456–457
- multiphoton ionization, 456
- quasi-continuous Nd:YAG laser, 458–459
- schematic, 460*f*
- surface texturing methods, 466
- textured craters (*see* Textured crater, 3-D surface profile)
- YAGLT and EDT comparison, 465
- Laser-induced breakdown spectroscopy (LIBS), 449–450, 559
- Laser induced periodic surface structures (LIPSS), 567–568
- Laser-induced photoacoustic spectroscopy (LIPAS), 559
- Laser interference-based methods  
 DLIP, 430–435  
 laser interference patterning systems, 436  
 LIL, 425–430  
 multibeam interference patterns, 424–425
- Laser interference lithography (LIL)  
 3D Cu<sub>2</sub>O photonic crystals, SEM micrographs, 429–430, 429*f*  
 double exposure process, 427  
 four-laser beam wave vectors, 427–429  
 fringe-locking system, 426, 426*f*  
 interference patterns creation, 426–427  
 Lloyd's mirror interferometer, 425–426, 426*f*  
 longitudinal coherence, 426  
 patterned substrates fabrication, 425  
 phase errors, 426  
 “photonic band gap,”, 427–429  
 photopolymerized material, 427, 428*f*  
 pulsed laser systems, 426  
 resultant periodic structure, 425
- Laser mask imaging, 527, 530*f*
- Laser processing parameters  
 establishment, 111–112  
 laser surface alloying, 80*t*  
 laser traversing speed, 471  
 Si<sub>3</sub>N<sub>4</sub> technical ceramics, 111  
 solid-state laser treatment and development, 470–474
- ZrO<sub>2</sub> technical ceramics, 111–112
- Laser surface alloying  
 C-B-W-Cr nano-powders, 62–72  
 metallic rolls, 60–62  
 NiCr-Cr<sub>3</sub>C<sub>2</sub> powders, 72–80  
 titanium and its alloys, 499–519

- Laser surface melting, titanium acicular martensitic, 493–495 corroded films, microstructures, 498, 499<sup>f</sup> corrosion-resistance property, 497–498 grain refinement, 493 high-resolution transmission electron micrograph, 496, 496<sup>f</sup> laser surface melted, physical and electrochemical properties, 498<sup>t</sup> microhardness, in melt zone, 496, 497<sup>f</sup> microstructural homogenization, 493 scanning electron micrographs (SEI), 493–495, 494<sup>f</sup> solidification, 493 X-ray diffraction profiles, 493–495, 495<sup>f</sup>
- Laser surface processing magnesium alloy, Nd:YAG laser melting, 318, 342–351, 352 PMMA, fs laser interactions, 333–341 silicon, laser texturing, 318–332, 351–352 surface wettability improvement, 342–351
- Laser surface texturing (LST) boundary and solid lubrication (MoS<sub>2</sub>) condition, 413–414 ceramics fabrication, 414 friction coefficients and parameters, 413, 413<sup>t</sup> laser ablation behavior, ceramics, 407–408 laser-textured surface, friction and wear behavior, 411–413 metals, laser ablation behavior, 406–407 surface coatings, 408–411, 415–418 “virtual texturing” technology, 419 water lubrication for ceramics, 414
- Laser surface treatment advantages, 4 computer-integrated methodology, 21–22 dendrological matrix, technology value, 22–23, 22<sup>f</sup> heat-affected zone (HAZ), 3 hot-work tool steels, 4–11 laser-processed NAB, macrostructure, 476<sup>f</sup> laser set up, 475<sup>f</sup> light metal casting alloys, 11–15 matrix of strategies, technologies, 25, 25<sup>f</sup> meteorological matrix, environment influence, 23–25, 24<sup>f</sup> methodology, 110
- Micro Vickers hardness traverses, laser-melted and laser-processed, 476<sup>f</sup> NAB, scanning electron microscopy micrographs, 476<sup>f</sup> polycrystalline silicon, 15–21 processing map, 474, 474<sup>f</sup> remelted zone (RZ), 3 residual stress analysis, 475–477 technology electronic transfer, 27 technology information sheets, 25–27, 28<sup>f</sup> technology road map, 25–27, 26<sup>f</sup> treated plate, 475<sup>f</sup> Widmanstätten microstructure formation, 475 XRD, 477–478, 477<sup>f</sup>
- Laser texturization, 4
- Laser triggering discharge arc discharge, 457 control schematic, 460<sup>f</sup> electrode gap and breakdown time disturbance, relation, 458<sup>f</sup> guiding discharge, 458 property, 457<sup>f</sup> textured surfaces, surface 3D microscope photos, 459<sup>f</sup>
- Laser welding, 254
- LDW. *See* Laser direct-write (LDW) processes
- LFpen, 590, 591
- LGDT. *See* Laser-guided discharge texturing (LGDT)
- LIBS. *See* Laser-induced breakdown spectroscopy (LIBS)
- Light metal casting alloys AlSi9Cu alloy, 13, 13<sup>f</sup> aluminium casting alloys, 11–13 HPDL, 11 laser surface treatment, 11 magnesium alloys, 11, 12<sup>f</sup> MCMgAl9Zn1 casting magnesium, 14, 17<sup>f</sup> RZ and HAZ, 14, 17<sup>f</sup> thin foil, magnesium, 14, 15<sup>f</sup> vanadium carbide, 14 WC particles, 13–14, 14<sup>f</sup>
- LIL. *See* Laser interference lithography (LIL)
- LIPAS. *See* Laser-induced photoacoustic spectroscopy (LIPAS)

- LIPSS. *See* Laser induced periodic surface structures (LIPSS)
- Long period fiber grating (LPFG)  
 experimental setup, 364, 364/*f*  
 microhole-structured, 368–369  
 resonance wavelength, 368, 368/*f*  
 sensors, 368–369  
 tensile strain test, 368, 368/*f*  
 UV-laser irradiation, 368
- Low friction/interface wearing event, 519
- Low-intensity lasers, 592
- Low-level laser therapy (LLLT), 584, 585, 585/*f*
- LST. *See* Laser surface texturing (LST)
- Luminescence spectroscopy, f-block metal complexes  
 actinides, recent progress/trends in  
 chemical analysis, 554–558, 559–562  
 geological disposal, barriers, 549–550  
 lanthanide and actinide ions, 551–553  
 solid-water interfaces, 549
- TRLFS data analysis, 553–554
- M**
- Mach-Zehnder interferometer, 365–366, 369–370, 373/*f*
- Magnesium alloy, Nd:YAG laser melting  
 AZ91D Mg alloy, 344–346  
 corrosion resistance, 346–349, 352  
 heat transport mechanism, 342  
 laser irradiation, 318  
 liquid flow, 342  
 material loss, 342–344, 343/*f*  
 m-SBF, degradation behavior, 346–349  
 surface energy and wettability  
     characteristics, 349–351, 352
- Mask dragging, 531, 531/*f*
- Matrix-assisted pulsed laser evaporation (MAPLE)  
 advantages, 290–291  
 applications, 291  
 degree of polymerization, 289  
 desorption process, 290, 290/*f*  
 laser-based vapor deposition  
     technique, 289  
 multipulse KrF\* laser irradiation, 289, 290/*f*  
 (bio)polymers, 289
- Mesenchymal stem cell (MSC) responses  
 biomaterial scaffolds, 656–657  
 early phase (4–12 h), 665–668  
 intermediate phase (1–4 days), 668–671  
 ion-implanted NiTi specimens, 656–657  
 laser melting, 656–657  
 pseudopodia, 668  
 SEM images, 666/*f*, 667/*f*, 668, 670/*f*  
 in tissue engineering applications, 656–657
- Metallic materials development  
 AM, 163  
 porous stainless steel, 172–177  
 SLM (*see* Selective laser melting (SLM))  
 TiC/Ti nanocomposites (*see* TiC/Ti nanocomposites)
- Metallic rolls  
 application, material processing, 59  
 chemical composition, 60, 61/*t*  
 corrosion and wear resistance, 59  
 hot rolls, 60–62  
 laser surface alloying (*see* Laser surface alloying)  
 material processing, 59  
 measurement, 60  
 NCIR (*see* Nodular cast-iron rolls (NCIR))  
 surface alloying, 59
- Metal-the matrix composites (MMC), 254, 271, 278
- Michelson interferometer, 365–366, 370–371, 371/*f*
- Microlens array homogenizers, 528–529, 529/*f*
- Micro-nano hierarchical Cu/Cu<sub>2</sub>O structures  
 dealloying process, 224  
 fabrication process, 223, 224/*f*  
 laser ablated surface, 223–224, 225/*f*  
 laser ablation parameters, 224, 227/*t*  
 laser deposition and dealloying  
     process, 224  
 microstructure and composition, 224, 226/*f*  
 morphologies, laser ablation parameters, 224–225, 227/*f*  
 Rz and Ra, 225–226, 228/*f*
- Microstructural refinement-cracking relationship  
 crack growth paths and fracture surfaces, 158–159

- Fe-base alloys, 158  
fracture mechanism and toughening, 159  
PTA, 159
- Microstructures and phases, nickel alloys  
boride and carbide precipitates, 140  
characterization, 146–147  
cracking susceptibility, deposits, 151–152  
Cr-rich precipitates, 139–140, 139f  
Cr-rich rods, 149, 149f  
EBSD patterns, 147–149  
equilibrium phase fractions, 147–149, 148f  
hardness graphs, deposits, 149–151, 151f  
HPD, 147  
map, 149, 150f  
Nb-rich precipitates, 145–146, 146f  
refining elements, 156–157  
rejected indent, 152–153, 153f  
SEM-BSE images, 145, 146f  
solid-liquid interface energy, 157  
surface energy, 158  
thermodynamic calculation software, 157
- Microwelding/interlocking phenomenon, 519
- MMSC. *See* Multipotent mesenchymal stromal stem cells (MMSC)
- Modified body simulated fluid (m-SBF)  
corrosion rate, 346–349, 349t  
polarization curves, AZ91D alloy, 349, 350f
- MPA. *See* Multiphoton absorption (MPA) initiated process
- Multiphoton absorption (MPA) initiated process, 383–384
- Multiphoton ionization and tunneling ionization, 359–360
- Multiple parameter sensing, microstructures  
FBG sensor, 374, 374f  
Mach-Zehnder interferometer, 372–373, 373f  
refractive index measurement, 375, 375f  
sensor, transmission spectrum, 373–374, 374f  
temperature measurement, 375, 376f
- Multipotent mesenchymal stromal stem cells (MMSC)  
cell therapy and tissue engineering, 607  
dermal fibroblasts and human, 609  
immunophenotypic study, 622
- number and configuration, 620f  
SLS, 3-D porous matrix, 607–623  
*Wharton's Jelly*, umbilical cord, 610–611
- N**
- NAB. *See* Nickel-aluminium bronze (NAB)
- Nanobump arrays, silicon  
AFM characterization, 324–325, 326f, 327f  
EDX result, 324–325, 329f  
Gaussian-like intensity distribution, 325–328  
Mie scattering law, 325–328  
polystyrene (PS) spheres, 325  
pulsed KrF excimer laser, 324–325, 324f, 325f  
Rayleigh scattering, 325–328  
solidification, 325–328
- Nanoporous copper structures  
composition and phase characterization, 216–217, 216f  
hybrid laser deposition and chemical dealloying, 215  
micro-nano structures tunability, 217–220
- Nanosecond pulsed surface texturing  
cell elongation and migration, 448f  
excimer ultraviolet (UV) laser, 447  
Gaussian beam intensity, 447  
pseudoperiodic structures, 449f  
Ti surface modification, 447
- Nanostructuring and crystallization, silicon film  
AFM images, 319, 321f  
amorphous and crystalline silicon, 322  
'black silicon', 319  
continuous wave and excimer laser annealing, 323–324  
fs laser-treated a-Si:H thin film, 318–319, 319f  
laser surface texturing process, 323  
micro-Raman analysis, 319–320, 322f  
reflectance and transmittance, 322, 323f  
SEM images, 319, 320f
- Natural organic matters (NOM), 558
- Nd:YAG lasers, 655–656
- Neodium doped yttrium aluminum garnet (Nd:YAG), 587, 588, 589, 595
- Ni-Al system
- 3D laser cladding, 262–263

- Ni-Al system (*Continued*)  
 FGS fabrication, 259  
 microhardness measurement, 260, 261*f*  
 optical metallography, 259–260, 260*f*  
 SEM data, 261–262, 262*f*  
 superalloys, 259  
 XRD pattern, 260–261, 261*f*
- Nickel alloys  
 Colmonoy 69, 142–144, 153–155, 154*f*  
 cracks, 137–138, 155–156, 155*f*  
 EDS, 144–145  
 fracture surface, ductile failure, 154*f*, 155  
 hardness and fracture toughness, 138  
 laser cladding, 137  
 microstructural design, 139–140, 156, 156*f*  
 Ni-Cr-B-Si-C hardfacing alloys, 137  
 refining element selection, 140–142
- Nickel-aluminium bronze (NAB)  
 aluminium content, phase diagram, 470*f*  
 as-cast NAB, reverse time-temperature-transformation diagram, 472, 472*f*  
 corrosion performance (*see* Corrosion)  
 laser heating modelling, 472–474  
 reverse eutectoid reaction, 471–472, 471*f*  
 strength and corrosion resistance, 469  
 surface engineering methods, 469
- Widmanstatten morphology  
 microstructure forms, 470
- Ni-Cr-B-Si-C hardfacing alloys, 137
- NiCr-Cr3C2 powders  
 cast steel rolls (*see* Cast steel rolls)  
 semisteel rolls (*see* Semisteel rolls)
- NiTi, laser melting  
 and biomaterials, 657  
 cell coverage measurement, 671–672, 671*f*  
 CO<sub>2</sub> lasers, 654–655  
 fiber lasers, 656  
*in vitro* biological stem cell  
 experimentation, 659–660  
 mesenchymal stem cells, 656–657  
 Nd:YAG lasers, 655–656  
 near-infrared and infrared spectrum, 653  
 phase structure and transformation  
 temperature analysis, 659, 661–662,  
 662*f*, 662*t*  
 procedure, 657–658, 658*f*  
 sample preparation, 658  
 scanning electron microscopy and cell  
 coverage measurement, 660
- statistical analysis, 660  
 stem cell morphology, 665–671  
 surface chemistry analysis, 663–665, 664*f*  
 surface compositional analysis, 659  
 surface morphology, 660, 661*f*  
 surface roughness and surface topography  
 analysis, 659, 662–663, 663*f*
- Nitriding and carburization  
 absorption and local heating, 35  
 aluminium and AlSi alloys, 33  
 cracking, 40  
 cw-mode, 38–43  
 description, 33  
 dissociation/ionization, 35  
 fatigue testing, 41–42, 41*f*  
 gas adsorption and absorption, 36  
 gas atomic transport, 36  
 gas pressure/flow, 36  
 laser pulses, 43–44  
 melt and evaporation processes, 35  
 nitrogen concentrations, 40  
 nitrogen process gas conditions, 39–40, 40*t*  
 nucleation and solidification, 36  
 parameters, 39  
 plasma expansion, gas, 35  
 and plasma spraying, 33  
 power density, 36  
 properties, 37  
 pulsed treatments, 33–34  
 sliding wear protection, 40  
 solid-state phase transformation, 36  
 strengthening, 43  
 structural evolution, 42–43, 43*f*  
 surface grinding, 41–42  
 temperature dependencies and  
 mechanisms, 34, 35*f*  
 time scales, 36–37
- Nodular cast-iron rolls (NCIR)  
 alloyed layer, 62–63, 64*f*, 65–66, 65*f*  
 chemical composition, 65–66, 65*t*  
 crack propagation, 66–69  
 dendrites and interdendrites, 62  
 Gibbs formation energies, 66  
 laser-alloyed layer, 69–72  
 microstructure, 62, 63*f*
- Nonlinear spectroscopy  
 second-harmonic generation (SHG),  
 559, 560*f*  
 sum-frequency generation (SFG), 559

**O**

- Octocalcium phosphate (OCP)  
3D structure, 291, 292*f*  
SAED pattern, 291, 292, 292*f*  
thin film deposition, 291
- Optical fiber microstructures  
FBG, 363  
fiber in-line interferometer, 365–366  
LPFG, 364  
microhole structure, 364–365
- Optical fiber sensing devices  
fs laser fabricated FBG sensors, 367–368  
fs laser fabricated fiber in-line interferometer sensors, 369–372  
fs laser fabricated LPFG sensors, 368–369  
for multiple parameter sensing, 372–375
- Oral cavity  
laser therapy, 583  
parameters, 583
- Oxidation  
alloying, titanium, 513–514, 514*f*, 515*f*  
alpha alloys, 486  
component surface, progressive degradation, 483  
resistance, 485, 489, 493, 501, 506–507  
surface dependent engineering properties, 489

**P**

- PARAFAC (PARAllel FACtor analysis), 554
- Parallel/perpendicular writing, 363
- Percolation cluster, 242
- Periodontal therapy, 588–589
- Photodynamic (Pd) therapy, 588, 596
- Photon-based fabrication methods, 423
- Picosecond pulsed surface texturing, 448–450
- Plasma spraying, 33, 237
- Plasma transferred arc (PTA), 152, 159
- PMMA. *See* Polymethyl methacrylate (PMMA)
- Polycrystalline silicon  
alkaline texturization, 18, 19*f*  
chemical etching and laser texturization, 20, 20*f*
- crystallization process, 15–18  
laser texturization, 18, 19*f*  
light reflection coefficient, 20–21, 21*f*  
monocrystalline silicon surface, 18, 18*f*  
solar cells production, 15–18
- Polymer structure, time-resolved measurements, 539
- Polymethyl methacrylate (PMMA)  
femtosecond laser interactions, 352  
surface hydrophilicity and hydrophobicity, 318, 333–338  
wettability modification of microfluidic channels, 318, 338–341
- Polyvinyl alcohol (PVACOOH) thin films, 300
- Porous stainless steel  
characteristic microstructure, 172–173, 173*f*  
controlling mechanisms, 176–177  
formation, 175, 176*f*  
powder system, 172  
scan speed, 173, 174*f*  
SLM processing, 172
- Pressure fluctuation, 532–533
- Protein films, biofouling  
contact angle measurements, 303  
DOPA-PF68 thin films, 302
- Pseudoperiodic and self-assembled microstructures  
creation, 444  
free/conductive electrons, 444  
initiation and growth, schematic process, 445*f*
- Marangoni effect, 444  
pressure and temperature gradients, 445*f*, 446  
regions, 445*f*, 446  
solidification process, 444  
vaporization temperature, 444–445
- Pulsed laser deposition (PLD)  
advantages and disadvantages, 288–289  
applications, 289  
direct surface processing, 287  
RPLD, 288  
thin films synthesis method, 288
- Pulsed laser systems, 595
- Pulse lengths and wavelengths modification, 539

**Q**

Quasi-continuous Nd:YAG laser  
 arc discharge, 458–459  
 Q-switcher power, 455  
 roller surface, 456  
 schematic, 458–459, 460*f*

**R**

Raman analyses, 575–576, 576*f*  
 Reaction-capable powdered compositions  
 laser scan velocity, 276, 277  
 measured and calculated temperatures,  
 278, 280*f*  
 numerical results, LC, 278, 279*f*  
 SLS/M, powder compositions, 275–276  
 velocity, SLS/M, 277  
 Reactive pulsed laser deposition  
 (RPLD), 288  
 Recurrent aphthous ulcer (RAU), 586  
 Refining element selection, nickel alloys  
 Colmonoy 69 alloy powder, 140  
 equilibrium phase fraction *vs.* temperature,  
 142, 143*f*  
 ETM, 140–141  
 Zr and Nb form borides/carbides, 142  
 Residual stress, 475–477, 477*f*, 479  
 Ripples, fs laser ablation, 408, 567–568  
 Root canals, 589  
 RPLD. *See* Reactive pulsed laser deposition  
 (RPLD)

**S**

Scale and root plane (SRP), 588  
 Scanning near-field optical microscopy  
 (SNOM), 559–561, 561*f*  
 Selected area electron diffraction (SAED),  
 291, 292, 292*f*  
 Selective laser melting (SLM)  
 porous stainless steel, 172–177  
 TiC/Ti nanocomposites, 166–167  
 Selective laser sintering (SLS)  
 artificial bio-MEMS devices, 649  
 biocompatible implants, titanium and  
 nickel-titanium, 603–607  
 contact surface topography, 648  
 drug delivery systems, 644–647  
 implants' porous structure, finite-  
 elemental optimization, 637–644

medical imaging, 648  
 MMSC, 3-D porous matrix for, 607–623  
 orthopedic implants, 648  
 titan and nitinol implants, biocompatibility  
 and biointegration, 623–637

## Selective laser sintering/melting (SLS/M)

Al-Ti systems, 239–240, 241*t*  
 depth variation, 239, 240*f*  
 exothermal reaction, 238  
 laser alloying, 239  
 laser-controlled combination, 238  
 laser energy dosing, 241  
 LI, 239  
 LPASS and LACS, 238–239  
 Ni-Al systems, 239–240, 241*t*  
 Ni powder, PGSR-4 grade, 239, 240*f*  
 SHS and LI processes, 238  
 and SHS hybrid processes, 268–278

Self-propagated high-temperature synthesis  
 (SHS)

aluminium, 248–249  
 conservation equations, 269–270  
 crystallization, 270  
 3D LC, 268–269  
 and DMD process, 249–250, 249*f*  
 EDX microanalysis, 245  
 EPD, 244–245  
 Fe-Al system, 253–259  
 $\text{Fe}_x\text{Ti}_y$  and  $\text{Ni}_x\text{Ti}_y$  intermetallic  
 phases, 246  
 FGS, 248  
 fractal dimension, 246–247, 247*f*  
 graded structure fabrication, 249, 249*f*  
 intermetallic compounds, 242  
 intermetallide synthesis, 242–244, 243*f*  
 laser cooling, 245–246  
 laser melting, 248  
 Maxwell equation system, 270  
 melting and exothermal reaction, Fe-Al  
 system, 245

nanosurface roughness *vs.* fractal

dimension, 246–247, 247*f*  
 nano wall thickness, 246, 246*f*  
 Ni-Al system, 259–263  
 percolation cluster, 242  
 prealloying intermetallide, 242  
 and SLS, 238–242  
 solid-liquid, 270  
 Ti-Al system, 250–253

- XRD, SEM and BSEM, 245
- Semisteel rolls  
alloyed layers, 73–74, 76–77, 77*f*  
microstructure and phases, 73, 73*f*  
oxidation film, 78  
processing parameters, 72, 72*t*  
weight loss comparison, 77–78, 78*t*  
worn surfaces, 78, 79*f*
- SERS. *See* Surface enhanced Raman spectrum (SERS)
- Shape memory effect (SME), 642, 645–646
- Silicon femtosecond laser processing,  
far-and near-field  
contact angle measurements, 304–305,  
305*f*  
experimental setup, 303–304, 304*f*  
and gallium arsenide fs laser processing,  
306–307  
overlap (OL) factor, 305–306, 306*f*  
ripple structures, 305–306, 306*f*  
SEM micrographs, 305–306, 306*f*  
two dimensional Fourier transforms  
(2D-FFT), 304, 305*f*
- Silicon, laser texturing  
a-Si:H thin film surface, 319, 319*f*  
nanobump arrays, fabrication, 324–328  
nanostructuring and crystallization,  
318–324, 351–352
- $\text{Si}_3\text{N}_4$  technical ceramics  
argon and oxygen, 121  
as-received surface, 122, 123*f*  
chemical composition, 119–121, 120*f*  
fiber laser engineer, 119–120, 120*f*  
HAZ and laser treated zone, 125  
laser-engineered, 122–124, 123*f*  
material removal, 118–119, 118*f*  
oxide layer, 120–121  
processing gases, 114  
surface finish, 119, 119*f*  
surface hardness, 112–113  
surface topography, 114–116, 115*f*
- Slit beam shaping method, 391*f*, 392
- SLM. *See* Selective laser melting (SLM)
- SLS. *See* Selective laser sintering (SLS)
- SLS-obtained implants' porous structure,  
optimization
- ANSYS bundled software, 638
- biomechanical relationship, 644
- implant modelling, 641*f*
- material design, 639–640
- nitinol, 640
- porosity determination, 639, 639*f*
- relative configuration, 639
- solution production, 642
- spongy bone formation, 640
- stress and displacement simulation, 642
- stress-strain behavior, 638, 642, 643*f*
- SME. *See* Shape memory effect (SME)
- SMNS. *See* Surface micro-nano structures (SMNS)
- Soft tissues, lasers effect  
cancer therapy, 585–586  
dental therapeutic lasers, 584  
effect of chemotherapy, 586  
endodontics, 589–590  
GaAs diode laser, 584  
HeNe laser, 584  
InGaAlP diode lasers, 584  
LLLT, 584, 585, 585*f*  
low-and high-intensity lasers, 584  
mucositis, 585  
Nd:YAG lasers, 586  
opioid analgesics, 585  
periodontal therapy, 588–589  
recurrent aphthous ulcer (RAU), 586  
soft tissues surgery, 587–588  
surgery, 587–588  
therapeutic indications, 585–586
- Solvent, drug delivery and implants  
dimethyl sulfoxide (DMSO), 301–302  
levan and oxidized levan coatings,  
3D-AFM images, 302, 302*f*
- Spatiotemporal focusing technique  
CPA systems, 386–387  
direct writing method, 388  
enhanced femtosecond laser  
filamentation, 397–400
- Fresnel-Kirchhoff's diffraction theory, 387
- fs laser micromachining, experiment  
set-up, 386–387, 386*f*
- intensity distributions, 387–388, 388*f*
- ultrashort laser pulse duration, 389
- SPPs. *See* Surface plasmon polaritons (SPPs)
- Steady state wear, 519
- Surface alloying  
laser nitriding and carburizing, 34–37
- materials and applications, 37

- Surface coatings, LST tribological application  
 direct processing, fabrication, 416–418  
 DLC coating, 408, 409  
 DLC:H, 410–411, 412*f*  
 graphitization, 409  
 indirect processing, fabrication, 415–416  
 laser ablation behavior, 408–411  
 ns-laser to fs-laser ablation, 408–409  
 SPPs, 409–410  
 textured coatings, 408–409  
 Ti:sapphire fs-laser system, 407*f*, 409
- Surface dependent engineering properties  
 abrasive wear, 488  
 adhesive wear, 488  
 corrosion, 488  
 erosion, 488  
 oxidation, 489  
 wear, 487
- Surface enhanced Raman spectrum (SERS)  
 description, 230  
 rhodamine 6G (R6G), 230, 230*f*
- Surface hydrophilicity and hydrophobicity  
 DPSS UV laser direct pit ablation, 328, 329*f*  
 imprinted pattern, sol gel film surface, 330, 334*f*  
 laser direct pit ablation texturing method, 328, 330–332, 330*f*  
 laser textured Si surface morphology, 330, 333*f*  
 original sol gel film, 330, 335*f*  
 PMMA, 318, 333–338  
 pulse numbers, laser-induced texturing, 328, 331*f*, 332*t*  
 surface contact angle measurement, 328–330, 332*f*, 335*f*  
 surface texture, 328, 329*f*
- Surface micro-nano structures (SMNS)  
 animals/plants, 213  
 chemical dealloying, 215  
 Cu/Cu<sub>2</sub>O structures, 223–227  
 CuMn alloy, 215  
 dealloying hybrid approach, 214  
 3D-Mn-NPS, 220–223  
 laser remelting, 215  
 limitations, fabrication, 214  
 nanoporous copper structures  
 (*see* Nanoporous copper structures)
- nanosecond laser ablation, 215  
 properties, 213  
 technical road map, hybrid method, 214–215, 214*f*  
 tunable micro-nano surface structures, 228–232
- Surface plasmon polaritons (SPPs), 409–410
- Surface wettability improvement, 342–351
- Swivelling clamping device, 38–39
- Synchronized image scanning, 531
- T**
- Technology road map, 25–27, 26*f*
- Textured crater, 3-D surface profile  
 3-D microscope photos, 462*f*  
 D surface profiles, 461–464  
 3-D surface profiles, 463*f*  
 hardness, 463*f*  
 microstructures, 464–465  
 parameters, 461*t*  
 roller surface texturing, 455  
 YAG laser-textured crater, 465, 465*f*
- Thermocouples, 264, 264*f*, 265*f*
- Thin film transistor (TFT), 317, 351–352
- Thin solid structures, high-intensity pulsed laser irradiation  
 direct fs laser surface processing in far and near-field, 303–307  
 laser deposition methods, 288–291  
 one parameter variation, laser deposition, 291–303  
 resources, 307–308
- TiC/Ti nanocomposites  
 characteristic microstructures, 164, 165*f*  
 laser energy densities, 166, 168*f*  
 linear laser energy density, 166, 167*f*  
 melting/solidification mechanism, 168–170  
 melt viscosity, 166, 168*f*  
 microhardness, 170, 171*f*  
 microstructures, 168, 169*f*  
 powder components, 164  
 SLM process, 164, 165*f*  
 surface morphologies, 166, 167*f*  
 wear rate, 170–172
- Time-resolved laser-induced fluorescence spectroscopy (TRLFS)  
 data analysis, 553–554, 555*f*

- fluorescence, 551  
hydration/solvation state, 552  
*in situ* measurements, 550  
instrumentation, 553, 553*f*  
internal conversion, 551, 552*f*  
lanthanide and actinide ions, 552–553  
luminescence, 551–552  
phosphorescence emission, 551, 552*f*
- Titan and nitinol implants, SLS  
accreted nitinol magnification, 634*f*  
appearance, 623, 624*f*  
biocompatibility, 637  
biointegration, 623  
connective tissue penetration, 628–629, 630*f*  
EDX-analysis, 635*t*  
element analysis, 629, 631*f*  
healing, 623  
histological analysis, 637  
macroscopic analysis, after implantation, 623–625  
organotypical structures, 636, 636*f*  
osteoblasts and osteocytes, 627–628, 628*f*  
porous implant, scapula, 625*f*  
SHS+SLS-synthesized nitinol surface, 637, 637*f*
- Titanium  
alloy classification, 486–487  
alloying, 499–519  
characteristics and properties, 484–485  
classification, 490*f*, 492*f*  
continuous wave (CW) laser treatment, 492–493  
fields of application, 492*f*  
lasers and their industrial applications, 490*t*  
lasers nitriding (*see* Nitriding and carburization)  
melting, 493–498  
metallic materials, 492–493  
microstructure modification, 492–493  
oxidation, 483  
physical metallurgy, 485–486, 486*t*  
physical properties, 484*t*  
surface-dependent properties, 492–493  
surface engineering, 489  
tissue engineering scaffolds, alloy  
(*see* Selective laser sintering (SLS))
- Titanium aluminides (Ti-Al) system  
clad coatings, 252–253, 253*f*  
3D laser clad coating, 250–251, 250*f*  
gamma alloys, 250  
micro-and substructures, 253, 253*f*  
microhardness, 251, 251*f*  
nonremelted particle, 250*f*, 251  
phase diagram, 250  
powder particles, 250  
X-ray diffraction patterns, 251–252, 252*f*
- Titanium Metals Company of America (TMCA), 484
- Tunable micro-nano surface structures  
catalysis performance, 228–230  
contact angle (CA) (*see* Contact angle (CA))  
photodegradation performance, 232, 233*f*  
SERS, 230
- Two-photon fluorescence excitation (TPFE)  
process  
beamlet angle, frequency dependence, 395–396  
experimental setup, 393–394  
femtosecond LDW, 396–397, 396*f*  
Fresnel-Kirchhoff's diffraction theory, 395  
images, 394, 394*f*  
intensity distribution, 395  
IPT angle, 396  
nonreciprocal writing process, 393, 397  
optical nonreciprocal or quill writing, 393  
pulse front tilt (PFT), 393, 395  
with spatiotemporal focusing method, 393  
spectral phase, 396  
without spatiotemporal focusing, 394–395
- U**
- Ultrashort pulsed laser surface texturing  
attosecond, 450  
carrier removal, 443  
femtosecond, 450  
laser irradiation, 442–443, 442*f*  
microstructures, 442  
nanosecond, 447–448  
picosecond, 448–450  
pseudo-periodic and self-assembled  
microstructures, 444–446  
seed electrons, 442  
single photon absorption, 443  
thermal and structural effects, 443  
thermalization, 443

- W**
- Wear
- abrasive, 488
  - adhesive, 488
  - alloyed layer quality, 91–92, 91*f*
  - alloying, titanium behavior, 517–519, 518*f*
  - austenite, 90–91
  - cast steel rolls and alloyed layers, 90
  - defintion, 487
  - depth variation, 516, 517*f*
  - low friction/interface wearing event, 519
  - NCIR and alloyed layers, 89
  - semisteel rolls and alloyed layers, 89–90
  - steady state, 519
- Wettability modification, PMMA
- fabrication of microchannels, 338–339, 339*f*, 340*f*
  - laser irradiation, 333–336, 335*f*
  - liquid flow, 339–341, 340*f*, 341*f*
  - of microfluidic channels, 318, 338–341
  - oxygen/carbon functional groups, 337, 337*t*
  - surface hydrophilicity and hydrophobicity, 336–337
  - WCA and surface roughness, 337–338, 338*f*
  - XPS-spectra, 336–337, 336*f*
- White light interferometry (WLI), 662–663
- WLI. *See* White light interferometry (WLI)
- Worn surfaces
- wear morphology, 70–72
  - XRD pattern, 88*f*
- X**
- X-ray photoelectron spectroscopy (XPS), 573, 574*f*
- Z**
- ZnO thin films
- contact angle measurement, 294, 294*f*
  - hydrophilic and hydrophobic deposition, 293, 293*f*
  - oxygen flux, 294–296, 296*f*
  - rocking curves, FWHM, 294
  - wetting properties, 293–294, 294*f*
  - XRD patterns, 294, 295*f*
- Zones, fs laser ablation, 566–567
- ZrO<sub>2</sub> technical ceramics
- as-received surface, 121–122
  - gas compositions, 122
  - laser engineered, 127–128
  - material removal, 118–119, 118*f*
  - micrographs, 125–127, 126*f*
  - surface topography, 112–113, 116–117, 116*f*, 119, 119*f*